



Special Issue Reprint

75 Years of the Casimir Effect

Advances and Prospects

Edited by
Galina L. Klimchitskaya and Vladimir M. Mostepanenko

mdpi.com/journal/physics



75 Years of the Casimir Effect: Advances and Prospects

75 Years of the Casimir Effect: Advances and Prospects

Editors

Galina L. Klimchitskaya

Vladimir M. Mostepanenko



Basel • Beijing • Wuhan • Barcelona • Belgrade • Novi Sad • Cluj • Manchester

Editors

Galina L. Klimchitskaya
Department of Astrophysics
Pulkovo Observatory of the
Russian Academy of Sciences
St. Petersburg
Russia

Vladimir M. Mostepanenko
Department of Astrophysics
Pulkovo Observatory of the
Russian Academy of Sciences
St. Petersburg
Russia

Editorial Office

MDPI AG
Grosspeteranlage 5
4052 Basel, Switzerland

This is a reprint of articles from the Special Issue published online in the open access journal *Physics* (ISSN 2624-8174) (available at: www.mdpi.com/journal/physics/special_issues/75yearsCasimir).

For citation purposes, cite each article independently as indicated on the article page online and as indicated below:

Lastname, A.A.; Lastname, B.B. Article Title. <i>Journal Name</i> Year , <i>Volume Number</i> , Page Range.
--

ISBN 978-3-7258-2144-0 (Hbk)

ISBN 978-3-7258-2143-3 (PDF)

doi.org/10.3390/books978-3-7258-2143-3

© 2024 by the authors. Articles in this book are Open Access and distributed under the Creative Commons Attribution (CC BY) license. The book as a whole is distributed by MDPI under the terms and conditions of the Creative Commons Attribution-NonCommercial-NoDerivs (CC BY-NC-ND) license.

Contents

Preface	ix
Galina L. Klimchitskaya and Vladimir M. Mostepanenko Advances and Prospects in Casimir Physics Reprinted from: <i>Physics</i> 2024 , <i>6</i> , 66, doi:10.3390/physics6030066	1
Giuseppe Bimonte and Thorsten Emig Surface Scattering Expansion of the Casimir–Polder Interaction for Magneto-Dielectric Bodies: Convergence Properties for Insulators, Conductors, and Semiconductors Reprinted from: <i>Physics</i> 2024 , <i>6</i> , 14, doi:10.3390/physics6010014	12
César D. Fosco, Fernando C. Lombardo and Francisco D. Mazzitelli Casimir Physics beyond the Proximity Force Approximation: The Derivative Expansion Reprinted from: <i>Physics</i> 2024 , <i>6</i> , 20, doi:10.3390/physics6010020	24
Shunashi Guadalupe Castillo-López, Raúl Esquivel-Sirvent, Giuseppe Pirruccio and Carlos Villarreal Casimir Forces with Periodic Structures: Abrikosov Flux Lattices Reprinted from: <i>Physics</i> 2024 , <i>6</i> , 26, doi:10.3390/physics6010026	51
Noah Graham Electromagnetic Casimir–Polder Interaction for a Conducting Cone Reprinted from: <i>Physics</i> 2023 , <i>5</i> , 65, doi:10.3390/physics5040065	64
Madhav Dhital and Umar Mohideen A Brief Review of Some Recent Precision Casimir Force Measurements Reprinted from: <i>Physics</i> 2024 , <i>6</i> , 55, doi:10.3390/physics6020055	74
Fatemeh Tajik and George Palasantzas Dynamical Sensitivity of Three-Layer Micro Electromechanical Systems to the Optical Properties of the Intervening Liquid Layer Reprinted from: <i>Physics</i> 2023 , <i>5</i> , 70, doi:10.3390/physics5040070	88
Hamid Haghmoradi, Hauke Fischer, Alessandro Bertolini, Ivica Galić, Francesco Intravaia, Mario Pitschmann, Raphael A. Schimpl and René I. P. Sedmik Force Metrology with Plane Parallel Plates: Final Design Review and Outlook Reprinted from: <i>Physics</i> 2024 , <i>6</i> , 45, doi:10.3390/physics6020045	101
Vitaly B. Svetovoy Casimir Forces between a Dielectric and Metal: Compensation of the Electrostatic Interaction Reprinted from: <i>Physics</i> 2023 , <i>5</i> , 51, doi:10.3390/physics5030051	153
Galina L. Klimchitskaya and Vladimir M. Mostepanenko Casimir Effect Invalidates the Drude Model for Transverse Electric Evanescent Waves Reprinted from: <i>Physics</i> 2023 , <i>5</i> , 62, doi:10.3390/physics5040062	162
Carsten Henkel Rectified Lorentz Force from Thermal Current Fluctuations Reprinted from: <i>Physics</i> 2024 , <i>6</i> , 37, doi:10.3390/physics6020037	178
Galina L. Klimchitskaya and Vladimir M. Mostepanenko The Casimir Force between Two Graphene Sheets: 2D Fresnel Reflection Coefficients, Contributions of Different Polarizations, and the Role of Evanescent Waves Reprinted from: <i>Physics</i> 2023 , <i>5</i> , 66, doi:10.3390/physics5040066	189

Manuel Asorey, Claudio Iuliano and Fernando Ezquerro Casimir Energy in (2 + 1)-Dimensional Field Theories Reprinted from: <i>Physics</i> 2024 , 6, 40, doi:10.3390/physics6020040	207
Philippe Brax and Sylvain Fichet Casimir Forces in CFT with Defects and Boundaries Reprinted from: <i>Physics</i> 2024 , 6, 36, doi:10.3390/physics6020036	223
Nail Khusnutdinov and Natalia Emelianova The Normal Casimir Force for Lateral Moving Planes with Isotropic Conductivities Reprinted from: <i>Physics</i> 2024 , 6, 11, doi:10.3390/physics6010011	247
George V. Dedkov Casimir–Lifshitz Frictional Heating in a System of Parallel Metallic Plates Reprinted from: <i>Physics</i> 2024 , 6, 2, doi:10.3390/physics6010002	263
Norio Inui Stabilizing Diamagnetic Levitation of a Graphene Flake through the Casimir Effect Reprinted from: <i>Physics</i> 2023 , 5, 60, doi:10.3390/physics5030060	281
Iver Brevik, Subhojit Pal, Yang Li, Ayda Gholamhosseinian and Mathias Boström Axion Electrodynamics and the Casimir Effect Reprinted from: <i>Physics</i> 2024 , 6, 27, doi:10.3390/physics6010027	294
Mathias Boström, Ayda Gholamhosseinian, Subhojit Pal, Yang Li and Iver Brevik Semi-Classical Electrodynamics and the Casimir Effect Reprinted from: <i>Physics</i> 2024 , 6, 30, doi:10.3390/physics6010030	309
Valery N. Marachevsky and Arseny A. Sidelnikov Casimir Interaction of Chern–Simons Layers on Substrates via Vacuum Stress Tensor Reprinted from: <i>Physics</i> 2024 , 6, 33, doi:10.3390/physics6020033	321
Evgenii Ievlev and Michael R. R. Good Larmor Temperature, Casimir Dynamics, and Planck’s Law Reprinted from: <i>Physics</i> 2023 , 5, 50, doi:10.3390/physics5030050	341
Matthew J. Gorban, William D. Julius, Patrick M. Brown, Jacob A. Matulevich, Ramesh Radhakrishnan and Gerald B. Cleaver First- and Second-Order Forces in the Asymmetric Dynamical Casimir Effect for a Single $\delta - \delta'$ Mirror Reprinted from: <i>Physics</i> 2024 , 6, 47, doi:10.3390/physics6020047	358
Michael Bordag and Irina G. Pirozhenko Mass and Magnetic Moment of the Electron and the Stability of QED—A Critical Review Reprinted from: <i>Physics</i> 2024 , 6, 17, doi:10.3390/physics6010017	378
Aram Saharian Surface Casimir Densities on Branes Orthogonal to the Boundary of Anti-De Sitter Spacetime Reprinted from: <i>Physics</i> 2023 , 5, 74, doi:10.3390/physics5040074	392
Yuri V. Grats and Pavel Spirin Vacuum Interaction of Topological Strings at Short Distances Reprinted from: <i>Physics</i> 2023 , 5, 75, doi:10.3390/physics5040075	410

**Valdir Barbosa Bezerra, Herondy Francisco Santana Mota, Augusto P. C. M. Lima,
Geová Alencar and Celio Rodrigues Muniz**
The Casimir Effect in Finite-Temperature and Gravitational Scenarios
Reprinted from: *Physics* **2024**, *6*, 65, doi:10.3390/physics6030065 **428**

Preface

This reprint contains articles belonging to the Special Issue of the Journal *Physics* devoted to the 75th anniversary of the physical effect predicted by Hendrik Brugt Gerhard Casimir 75 years ago. Currently, this effect is being intensively studied both experimentally and theoretically. The multidisciplinary character of the Casimir effect is caused by the fact that it is determined by the zero-point and thermal fluctuations of quantized fields, which play an important role in any physical system. Modern discussions deal with concepts such as the Casimir force, Casimir torque, Casimir energy and free energy, the Casimir entropy, non-equilibrium Casimir and Casimir–Polder forces, etc. These concepts are used in quantum field theory, condensed matter physics, nanotechnology, atomic physics, physics of elementary particles, gravitation, and cosmology. Experiments that measure the Casimir force have already covered a wide class of physical systems, ranging from metallic, dielectric, and semiconductor test bodies to nanostructured devices, metamaterials, and 2D materials, including graphene. Despite the great achievements in this field, the Lifshitz theory of Casimir forces, which was proposed by Evgeny M. Lifshitz in 1954, has long suffered from unresolved problems. These problems arose when describing the electromagnetic response of different materials to the low-frequency electromagnetic field by using simple, partially phenomenological models of dielectric permittivity. The articles contained in this reprint cover the state-of-the-art advances in the above-mentioned subjects.

Galina L. Klimchitskaya and Vladimir M. Mostepanenko

Editors

Advances and Prospects in Casimir Physics

Galina L. Klimchitskaya ^{1,2} and Vladimir M. Mostepanenko ^{1,2,3*}

¹ Central Astronomical Observatory, Pulkovo of the Russian Academy of Sciences, 196140 Saint Petersburg, Russia; g.klimchitskaya@gmail.com

² Peter the Great Saint Petersburg Polytechnic University, 195251 Saint Petersburg, Russia

³ Kazan Federal University, 420008 Kazan, Russia

* Correspondence: vmostepa@gmail.com

Abstract: In the present introductory to the Special Issue “75 Years of the Casimir Effect: Advances and Prospects”, we summarize the state of the art in this field of physics, briefly describe the topics of the contributing papers, formulate several unresolved problems, and outline possible pathways towards their resolution. Special attention is given to experiments on measuring the Casimir force, to the known problem of the dissipation of conduction electrons when one compares experiment with theory, and to the Casimir effect in novel materials and non-traditional situations. We conclude that in the future, this multidisciplinary quantum effect will continue to play a crucial role in both fundamental physics and its applications.

1. Introduction

The Casimir effect [1] was discovered 75 years ago, and now is an appropriate time to summarize its role in different physical phenomena, the results thus far obtained, and the unsolved problems, as well as to outline possible pathways towards their resolution.

At first sight, the Casimir prediction of the attractive force acting between two parallel, uncharged ideal metal planes kept at zero temperature could be considered to have a rather modest physical significance. The reason is that this force takes noticeable values only at extremely short separations between the plates, and both the ideal metal and the zero temperature are idealizations which are literally unrealizable in physical experiments.

The importance of the Casimir discovery greatly exceeded these expectations. The Casimir force is determined by the vacuum fluctuations of the electromagnetic and other quantum fields. These fluctuations are inherent to all physical phenomena in which Casimir forces may play some role. A few years after its discovery, the Casimir effect was generalized for the case of ideal metal planes kept at non-zero temperatures [2–4] and, within the framework of the Lifshitz theory [5–7], for two thick plates made of any material. It was shown that the Casimir force is a generalization of the van der Waals force [8] for separations where relativistic effects come into play, and to any temperature. The forces in question also act between atoms, molecules, and material surfaces, and in this case they are called Casimir–Polder forces [9].

There are a great number of applications of the Casimir force caused by the zero-point and thermal fluctuations of the electromagnetic field in condensed matter physics and atomic physics. In condensed matter physics, the Casimir force acts between any closely spaced surfaces made of metallic, dielectric, and semiconductor materials (see, e.g., Refs. [10–31], reviews [32,33], and monographs [34,35]). In atomic physics, the Casimir–Polder force has been calculated in many systems [36–47]. It plays a primary role in the phenomena of quantum reflection [48–55] and Bose–Einstein condensation [56–61] (see also the monograph [62,63]).

Many measurements of the Casimir force have been performed by means of an atomic force microscope, where the sharp tip was replaced with a relatively large sphere (see Refs. [32,34,64–78]), and by means of a micromechanical torsional oscillator [32,34,79–85].

Citation: Klimchitskaya, G.L.; Mostepanenko, V.M. Advances and Prospects in Casimir Physics. *Physics* **2024**, *6*, 1072–1082. <https://doi.org/10.3390/physics6030066>

Received: 10 July 2024

Accepted: 16 August 2024

Published: 22 August 2024



Copyright: © 2024 by the authors. Licensee MDPI, Basel, Switzerland. This article is an open access article distributed under the terms and conditions of the Creative Commons Attribution (CC BY) license (<https://creativecommons.org/licenses/by/4.0/>).

Based on these measurement results, the Casimir force was applied for the creation of various next-generation micro- and nanoelectromechanical devices [86–99]. The Casimir–Polder force has been measured in experiments on quantum reflection [49–52] and Bose–Einstein condensation [56,57,60,61].

The Casimir effect for other than electromagnetic (scalar, spinor, gluon, etc.) fields has found prospective applications in elementary particle physics, for instance, in the bag model of hadrons (see Refs. [100–106] and the monograph [107]). It has been demonstrated that the Casimir effect is also of high importance in topologically non-trivial cosmological models, where the identification conditions play the same role as the materials boundaries, changing the spectrum of the vacuum fluctuations and leading to non-zero Casimir energy density [108–113]. A similar effect was found in multi-dimensional physics, where the extra spatial dimensions are compactified at some energy scale [114–116].

All of the above permits us to conclude that the Casimir force, regarded initially as an interesting but toy and somewhat exotic example, has developed over time into a broad research area, which is often called Casimir physics.

2. The Topics Highlighted in This Special Issue

This Special Issue, entitled “75 Years of the Casimir Effect: Advances and Prospects”, presents several scientific directions within the wide research area of Casimir-related phenomena. After the creation of the Lifshitz theory, which allows for the calculation of the Casimir force in plane-parallel configurations only, it was generalized for the case of arbitrary-shaped bodies [117–126] and, specifically, for the experimentally important configuration of a sphere above a plate [127–135]. In this Special Issue, this line of research is represented by Ref. [136], which is devoted to the application of the scattering approach for calculating the Casimir–Polder interaction with magnetodielectric bodies, by Ref. [137], which reviews an application of the method of derivative expansion in Casimir physics, by Ref. [138], which considers the Casimir forces with periodic structures, and by Ref. [139], calculating the Casimir–Polder force for a conducting cone.

Special attention in this Special Issue is devoted to recent progress in measuring the Casimir force. Reference [140] reviews the last experiments performed by means of an atomic force microscope. This includes measuring the normal Casimir force between the smooth surfaces of both non-magnetic and magnetic metals, normal and lateral Casimir forces between the corrugated surfaces, and the thermal Casimir force in graphene systems. The comparison of the experimental results with theory for graphene systems required the development of a novel approach to describing the response of graphene to the electromagnetic field because the previously used semi-phenomenological approaches, based on the Kubo formula, the two-dimensional Drude model, and density–density correlation functions [141–144], turned out to be insufficient. The new approach, which was found to be in agreement with the measurement data, uses the polarization tensor of graphene with non-zero values of the energy gap and the chemical potential found within the framework of thermal quantum field theory in $(2 + 1)$ dimensions [145–148].

Two other experimental papers are devoted to the dynamical sensitivity of three-layer microelectromechanical systems exploiting the Casimir force to the optical properties of the intervening liquid layer [149] and to the planned experiment on measuring the Casimir pressure between two parallel plates spaced at micrometer separations [150]. Realization of the last experiment will allow to strengthen the constraints on the Yukawa-type corrections to the Newton law of gravitation and on the hypothetical constituents of dark matter and dark energy, such as axions, chameleons, symmetrons, and environment-dependent dilatons [151–155], which are often constrained from measuring the Casimir force [156–162]. One more experimentally oriented paper considers the possibility of compensating the electrostatic interaction between dielectric and metallic test bodies [163]. This investigation is directed towards solving the problem of surface patches, which complicates measurements of the Casimir force [164,165].

The major problem of Casimir physics, which has remained unresolved over the last 25 years, is the question of how to describe the free charge carriers correctly when calculating the Casimir force. It has been shown Refs. [32,34,72,74,75,80,81,85] that for metallic test bodies the Casimir force, calculated by means of the Lifshitz theory using the dissipative Drude model at low frequencies, is excluded by the measurement data. If the dissipationless plasma model is used in the calculations, the theoretical results agree with all precise experiments on measuring the Casimir force [32,34,72,74,75,80,81,85]. For the dielectric test bodies, theory comes into agreement with the measurement data only if the role of free charge carriers, which are present in all real dielectrics at any non-zero temperature, is omitted in the computations [32,34,65,69,70,166].

According to the results of Ref. [167] published in this Special Issue, the roots of the problem are not in accounting for or disregarding the dissipation properties of the conduction electrons in calculations of the Casimir force, but in the necessity of accounting for these properties correctly. It is shown that an account of the relaxation properties of conduction electrons at low frequencies by means of the Drude model in the region of propagating waves with any polarization and transverse magnetic evanescent waves does not lead to contradictions with the measurement data. The contradiction between the calculated and measured Casimir forces arises only when the Drude model is used to describe the response of metals to the low-frequency evanescent waves with transverse electric polarization.

It is common knowledge that the Drude model has numerous experimental confirmations in the region of propagating waves. It has also been confirmed by special experiments in the area of transverse magnetic evanescent waves [168]. As to the area of transverse electric evanescent waves, the Drude model lacks any reliable experimental confirmation. On this basis, it was concluded [167] that the experiments on measuring the Casimir force invalidate the Drude model in the area of transverse electric evanescent waves. An alternative experiment in the field of classical electrodynamics was proposed, which can independently confirm this important conclusion [169,170]. Reference [171] of this Special Issue suggests another experimental means of distinguishing between the Drude and plasma models, which is based on measuring the Lorentz force originating from thermal fluctuations.

It is interesting that for the Casimir force between two graphene sheets considered in Ref. [172] of this Special Issue, theory is in good agreement with the measurement data. The reason for this is that the electromagnetic response of graphene is described on the rigorous basis of quantum electrodynamics at non-zero temperature do not using any phenomenological approach like the Drude model. This is reached by employing the polarization tensor of graphene with any energy gap and the chemical potential found in the framework of thermal quantum field theory [145–148].

Several papers belonging to this Special Issue are devoted to the investigation of the Casimir effect in various specific configurations. Thus, in Ref. [173] the Casimir energy in $(2 + 1)$ -dimensional field theories is considered which is interesting in connection with its application to novel two-dimensional materials, such as graphene, silicene, stanene, phosphorene, and others [174–177]. The Casimir forces in conformal field theories with defects and boundaries are discussed in Ref. [178]. The normal Casimir force for the planes with isotropic conductivity in the state of lateral motion is found in Ref. [179]. In Ref. [180], the Casimir–Lifshitz force of friction, which arises due to the relative motion of interacting bodies, and resulting heating are considered in the framework of fluctuational electrodynamics. Finally, it is explained in Ref. [181] how the Casimir force can be used to stabilize the levitation of a graphene sheet lifted by the repulsive force arising in an inhomogeneous magnetic field.

In a few papers included in this Special Issue, the Casimir effect is considered in rather non-standard situations and using some alternative approaches. For instance, in Ref. [182] the Casimir effect in axion electrodynamics is investigated where, due to the presence of an additional pseudoscalar quantity, the relationship between the vectors of the electric field, magnetic induction, electric displacement, and the magnetic field

becomes more complicated than in the standard electrodynamics of continuous media. This subject is closely related to new materials called topological insulators, which are of great practical interest.

An interesting approach to the Casimir effect based on semi-classical electrodynamics is discussed in Ref. [183] in this Special Issue. This paper includes a preface discussing different concepts of intermolecular forces in the early history of physics. It is shown how the semi-classical approach results in the familiar Lifshits formula for Casimir free energy. One more study [184] is devoted to a derivation of the Casimir pressure between two Chern–Simons boundary layers deposited on dielectric substrates. For this purpose, gauge-invariant formalism was developed using the electric and magnetic Green functions. Two more papers are devoted to the dynamical Casimir effect. One of them [185] considers an analogy between the dynamical Casimir effect, black holes, and the radiation temperature of an accelerated electron. The other one [186] investigates an asymmetric force acting on a moving mirror modeled by the potential, which is equal to the difference between the delta function and its derivative in two-dimensional space–time. We also list one more paper published in this Special Issue which is devoted to the one-loop correction to the mass of an electron in a homogeneous magnetic field [187]. This issue has been considered by several authors but with somewhat differing results. Keeping in mind that the radiative corrections are similar in their physical nature to the Casimir effect, it is necessary to resolve all existing discrepancies.

As was discussed in Section 1, the Casimir effect arises not only in configurations with material boundaries but also in spaces with non-trivial topology. Because of this, it plays a significant role in gravitation and cosmology and in multi-dimensional theories of elementary particle physics. Four papers in this Special Issue represent this scientific direction in the field of Casimir physics. It is known that anti-de Sitter space–time plays a significant role in cosmology. Generally speaking, the braneworld model contains the fields propagating in the bulk or localized on the branes. The boundary conditions on the branes induce Casimir-type contributions to the expectation values of physical observables. In Ref. [188], the vacuum expectation of the surface stress–energy tensor for a scalar field is calculated in the configuration of two parallel branes orthogonal to the boundary of anti-de Sitter space–time.

Other objects of importance to cosmology are the so-called cosmic strings, i.e., the topological defects which could have been created in the early Universe during cosmological phase transitions. The Casimir interaction between two cosmic strings arising due to vacuum fluctuations of the scalar field with minimal coupling is considered in Ref. [189] in the cases both small and large separation distances, taking into account the transverse size of a string.

Finally, the Casimir effect for two parallel plates in a weak gravitational field and the wormholes determined by the Casimir energy densities of the Yang–Mills field are discussed in Ref. [190]. The same paper studies the Casimir energy density in Euclidean space–time with a non-trivial topology, equivalent to imposing the so-called helix identification conditions.

3. Future Prospects

As has been demonstrated above, the Casimir effect is a wide research area, with implications for practically all branches of modern physics. It is actively investigated both theoretically and experimentally by many research groups working in many countries. Over the last few years, a number of new breakthrough results have been obtained. Below, we outline the most crucial problems in this research area to be solved in the future.

Although for metallic test bodies at separations below several micrometers, the Casimir force was already measured with high precision, at larger separations, and for the test bodies made of semiconductor and dielectric materials, new breakthrough experimental results are expected in near future. Progress in precise force measurements can be stimulated using the traditional and novel techniques (see Refs. [140,150] published in this Special Issue)

and by compensating for the spurious electric forces [163–165]. The obtained results are considered to be used for the creation of next-generation micro- and nanoelectromechanical devices driven by the Casimir force (see Ref. [149] of this Special Issue, elaborating this scientific direction).

One can expect that the problem of disagreement between experiment and theory, taking into account the dissipation of conduction electrons by means of the Drude model (this problem is often called the Casimir puzzle [32,34,75]), will be solved soon. In this Special Issue, the problem has already been narrowed down to the inapplicability of the Drude model in the region of transverse electric evanescent waves [167]. It has been shown [191–193] that if to modify the Drude model in this area phenomenologically by adding a spatially non-local contribution, the theoretical predictions come to an agreement with the measurement data. It remains to put the phenomenology on a solid fundamental basis as has already been made for the electromagnetic response of graphene [77,78,145–148].

In near future, Casimir physics is going also to find new applications in modern theoretical approaches beyond the Standard Model, e.g., in the brane models, multi-dimensional physics with compacted extra dimensions, the theory of topological defects, etc. It is to be used for obtaining stronger constraints on the Yukawa-type corrections to Newtonian gravity and the hypothetical particle constituents of dark matter and dark energy.

We hope that the papers published in this Special Issue, “75 Years of the Casimir Effect: Advances and Prospects”, will be helpful by stimulating further developments in this prospective field of physics.

Author Contributions: Conceptualization, G.L.K. and V.M.M.; investigation, G.L.K. and V.M.M.; writing—original draft, V.M.M.; writing—review and editing, G.L.K. All authors have read and agreed to the published version of the manuscript.

Funding: The work of G.L.K. and V.M.M. was partially funded by the Ministry of Science and Higher Education of Russian Federation as part of the World-Class Research Center program: Advanced Digital Technologies (contract No. 075-15-2022-311 dated 20 April 2022). The research of V.M.M. was also partially carried out in accordance with the Strategic Academic Leadership Program “Priority 2030” of the Kazan Federal University.

Conflicts of Interest: The authors declare no conflicts of interest.

References

1. Casimir, H.B.G. On the attraction between two perfectly conducting plates. *Proc. Kon. Ned. Akad. Wetensch. B* **1948**, *51*, 793–795. Available online: <https://dwc.knaw.nl/DL/publications/PU00018547.pdf> (accessed on 11 August 2024).
2. Fierz, M. Zur Anziehung leitender Ebenen im Vakuum. *Helv. Phys. Acta* **1960**, *33*, 855–858. [CrossRef]
3. Mehra, J. Temperature correction to Casimir effect. *Physica* **1967**, *37*, 145–152. [CrossRef]
4. Brown, L.S.; Maclay, G.J. Vacuum stress between conducting plates—An image solution. *Phys. Rev.* **1969**, *184*, 1272–1279. [CrossRef]
5. Lifshitz, E.M. The theory of molecular attractive forces between solids. *Zh. Eksp. Teor. Fiz.* **1955**, *29*, 94–110 (In Russian); *Sov. Phys. JETP* **1956**, *2*, 73–83. Available online: <http://jetp.ras.ru/cgi-bin/e/index/e/2/1/p73?a=list> (accessed on 11 August 2024).
6. Dzyaloshinskii, I.E.; Lifshitz, E.M.; Pitaevskii, L.P. The general theory of van der Waals’ forces. *Usp. Fiz. Nauk* **1961**, *73*, 381–422 (In Russian); *Sov. Phys. Uspekhi* **1961**, *4*, 153–176. [CrossRef]
7. Lifshitz, E.M.; Pitaevskii, L.P. *Statistical Physics, Part 2*; Pergamon: Oxford, UK, 1980. Available online: <https://haidinh89.files.wordpress.com/2015/08/landau-l-d-lifshitz-e-m-course-of-theoretical-physics-vol-09-statistical-physics-part-2-3455.pdf> (accessed on 11 August 2024).
8. Parsegian, V.A. *Van der Waals Forces: A Handbook for Biologists, Chemists, Engineers, and Physicists*; Cambridge University Press: New York, NY, USA, 2005. [CrossRef]
9. Casimir, H.B.G.; Polder, D. The influence of retardation on the London–van der Waals forces. *Phys. Rev.* **1948**, *73*, 360–372. [CrossRef]
10. Hargreaves, C.M. Corrections to retarded dispersion force between metal bodies. *Proc. Kon. Ned. Akad. Wetensch. B* **1965**, *68*, 231–236.
11. Boyer, T.H. Quantum electromagnetic zero-point energy of a conducting spherical shell and Casimir model for a charged particle. *Phys. Rev.* **1968**, *174*, 1764–1776. [CrossRef]
12. Richmond, P.; Ninham, B.W. A note on the extension of the Lifshitz theory of van der Waals forces to magnetic media. *J. Phys. C* **1971**, *4*, 1988–1993. [CrossRef]

13. Boyer, T.H. Van der Waals forces and zero-point energy for dielectric and permeable materials. *Phys. Rev. A* **1974**, *9*, 2078–2084. [CrossRef]
14. Boström, M.; Sernelius, B.E. Comment on “Calculation of the Casimir force between imperfectly conducting plates”. *Phys. Rev. A* **2000**, *61*, 046101. [CrossRef]
15. Boström, M.; Sernelius, B.E. Thermal effects on the Casimir force in the 0.1–5 μm range. *Phys. Rev. Lett.* **2000**, *84*, 4757–4760. [CrossRef] [PubMed]
16. Lambrecht, A.; Reynaud, S. Casimir force between metallic mirrors. *Eur. Phys. J. D* **2000**, *8*, 309–318. [CrossRef]
17. Genet, C.; Lambrecht, A.; Maia Neto, P.; Reynaud, S. The Casimir force between rough metallic plates. *EPL (Europhys. Lett.)* **2003**, *62*, 484–490. [CrossRef]
18. Boström, M.; Sernelius, B.E. Entropy of the Casimir effect between real metal plates. *Phys. A* **2004**, *339*, 53–59. [CrossRef]
19. Torgerson, J.R.; Lamoreaux, S.K. Low-frequency character of the Casimir force between metallic films. *Phys. Rev. E* **2004**, *70*, 047102. [CrossRef] [PubMed]
20. Bimonte, G.; Calloni, E.; Esposito, G.; Milano, L.; Rosa, L. Towards measuring variations of Casimir energy by a superconducting cavity. *Phys. Rev. Lett.* **2005**, *94*, 180402. [CrossRef]
21. Bimonte, G.; Calloni, E.; Esposito, G.; Rosa, L. Variations of Casimir energy from a superconducting transition. *Nucl. Phys. B* **2005**, *726*, 441–463. [CrossRef]
22. Bimonte, G. Comment on “Low-frequency character of the Casimir force between metallic films”. *Phys. Rev. E* **2006**, *73*, 048101. [CrossRef]
23. Bimonte, G. A theory of electromagnetic fluctuations for metallic surfaces and van der Waals interactions between metallic bodies. *Phys. Rev. Lett.* **2006**, *96*, 160401. [CrossRef]
24. Bimonte, G. Bohr-van Leeuwen theorem and the thermal Casimir effect for conductors. *Phys. Rev. A* **2009**, *79*, 042107. [CrossRef]
25. Levin, M.; McCauley, A.P.; Rodrigues, A.W.; Reid, M.T.H.; Johnson, S.G. Casimir repulsion between metallic objects in vacuum. *Phys. Rev. Lett.* **2010**, *105*, 090403. [CrossRef] [PubMed]
26. Bimonte, G. Making precise predictions of the Casimir force between metallic plates via a weighted Kramers-Kronig transform. *Phys. Rev. A* **2011**, *83*, 042109. [CrossRef]
27. Schwinger, J.; DeRaad, L.L.; Milton, K.A. Casimir effect in dielectrics. *Ann. Phys.* **1978**, *115*, 1–23. [CrossRef]
28. Inui, N. Temperature dependence of the Casimir force between silicon slabs. *J. Phys. Soc. Jpn.* **2003**, *72*, 2198–2202. [CrossRef]
29. Canaguier-Durand, A.; Gérardin, A.; Guérou, R.; Maia Neto, P.A.; Nesvizhevsky, V.V.; Voronin, A.Y.; Lambrecht, A.; Reynaud, S. Casimir interaction between a dielectric nanosphere and a metallic plane. *Phys. Rev. A* **2011**, *83*, 032508. [CrossRef]
30. Rosa, F.S.S.; Dalvit, D.A.R.; Milonni, P.W. Electrodynamic energy, absorption, and Casimir forces. II. Inhomogeneous dielectric media. *Phys. Rev. A* **2011**, *84*, 053813. [CrossRef]
31. Inui, N. Temperature dependence of the Casimir force between a superconductor and a magnetodielectric. *Phys. Rev. A* **2012**, *86*, 022520. [CrossRef]
32. Klimchitskaya, G.L.; Mohideen, U.; Mostepanenko, V.M. The Casimir force between real materials: Experiment and theory. *Rev. Mod. Phys.* **2009**, *81*, 1827–1885. [CrossRef]
33. Woods, L.M.; Dalvit, D.A.R.; Tkatchenko, A.; Rodriguez-Lopez, P.; Rodriguez, A.W.; Podgornik, R. Materials perspective on Casimir and van der Waals interactions. *Rev. Mod. Phys.* **2016**, *88*, 045003. [CrossRef]
34. Bordag, M.; Klimchitskaya, G.L.; Mohideen, U.; Mostepanenko, V.M. *Advances in the Casimir Effect*; Oxford University Press: Oxford, UK, 2015. doi:10.1093/oso/9780199238743.001.0001 [CrossRef]
35. Sernelius, B.E. *Fundamentals of van der Waals and Casimir Interactions*; Springer: Cham, Switzerland, 2018. doi:10.1007/978-3-319-99831-2 [CrossRef]
36. Zhou, F.; Spruch, L. Van-der-Waals and retardation (Casimir) interactions of an electron or an atom with multilayered walls. *Phys. Rev. A* **1995**, *52*, 297–310. [CrossRef] [PubMed]
37. Caride, A.O.; Klimchitskaya, G.L.; Mostepanenko, V.M.; Zanette, S.I. Dependences of the van der Waals atom-wall interaction on atomic and material properties. *Phys. Rev. A* **2005**, *71*, 042901. [CrossRef]
38. Babb, J.F. Long-range atom–surface interactions for cold atoms. *J. Phys. Conf. Ser.* **2005**, *19*, 1. [CrossRef]
39. Safari, H.; Welsch, D.-G.; Buhmann, S.Y.; Scheel, S. van der Waals potentials of paramagnetic atoms. *Phys. Rev. A* **2008**, *78*, 062901. [CrossRef]
40. Haakh, H.; Intravaia, F.; Henkel, C.; Spagnolo, S.; Passante, R.; Power, B.; Sols, F. Temperature dependence of the magnetic Casimir–Polder interaction. *Phys. Rev. A* **2009**, *80*, 062905. [CrossRef]
41. Ellingsen, S.; Buhmann, S.Y.; Scheel, S. Temperature-independent Casimir–Polder forces despite large thermal photon numbers. *Phys. Rev. Lett.* **2010**, *104*, 223003. [CrossRef]
42. Passante, R.; Rizzuto, L.; Spagnolo, S.; Tanaka, S.; Petrosky, T.Y. Harmonic oscillator model for the atom-surface Casimir–Polder interaction energy. *Phys. Rev. A* **2012**, *85*, 062109. [CrossRef]
43. Sun, W. Interaction forces between a spherical nanoparticle and a flat surface. *Phys. Chem. Chem. Phys.* **2014**, *16*, 5846–5854. [CrossRef]
44. Khusnutdinov, N.; Kashapov, R.; Woods, L.M. Casimir–Polder effect for a stack of conductive planes. *Phys. Rev. A* **2016**, *94*, 012513. [CrossRef]

45. Fuchs, S.; Crosse, J.A.; Buhmann, S.Y. Casimir–Polder shift and decay rate in the presence of nonreciprocal media. *Phys. Rev. A* **2017**, *95*, 023805. [CrossRef]
46. Milton, K.A.; Li, Y.; Kalauni, P.; Parashar, P.; Guérout, P.; Ingold, G.-L.; Lambrecht, A.; Reynaud, S. Negative entropies in Casimir and Casimir–Polder interactions. *Fortschr. Phys./Prog. Phys.* **2017**, *65*, 1600047. [CrossRef]
47. Fuchs, S.; Bennett, R.; Krems, R.V.; Buhmann, S.Y. Nonadditivity of optical and Casimir–Polder potentials. *Phys. Rev. Lett.* **2018**, *121*, 083603. [CrossRef] [PubMed]
48. Berkhout, J.J.; Luiten, O.J.; Setija, I.D.; Hijmans, T.W.; Mizusaki, T.; Walraven, J.T.M. Quantum reflection: Focusing of hydrogen atoms with a concave mirror. *Phys. Rev. Lett.* **1989**, *63*, 1689–1693. [CrossRef]
49. Yu, I.A.; Doyle, M.J.; Sandberg, J.C.; Cesar, C.L.; Kleppner, D.; Greytak, T.J. Evidence for universal quantum reflection of hydrogen from liquid ^4He . *Phys. Rev. Lett.* **1993**, *71*, 1589–1593. [CrossRef] [PubMed]
50. Shimizu, F. Specular reflection of very slow metastable neon atoms from a solid surface. *Phys. Rev. Lett.* **2001**, *86*, 987–991. [CrossRef] [PubMed]
51. Friedrich, H.; Jacoby, G.; Meister, C.J. Quantum reflection by Casimir–van der Waals potential tails. *Phys. Rev. A* **2002**, *65*, 032902. [CrossRef]
52. Druzhinina, V.; DeKieviet, M. Experimental observation of quantum reflection far from threshold. *Phys. Rev. Lett.* **2003**, *91*, 193202. [CrossRef]
53. Oberst, H.; Tashiro, Y.; Shimizu, K.; Shimizu, F. Quantum reflection of He^* on silicon. *Phys. Rev. A* **2005**, *71*, 052901. [CrossRef]
54. Madroñero, J.; Friedrich, H. Influence of realistic atom wall potentials in quantum reflection traps. *Phys. Rev. A* **2007**, *75*, 022902. [CrossRef]
55. Bezerra, V.B.; Klimchitskaya, G.L.; Mostepanenko, V.M.; Romero, C. Lifshitz theory of atom–wall interaction with applications to quantum reflection. *Phys. Rev. A* **2008**, *78*, 042901. [CrossRef]
56. Harber, D.M.; McGuirk, J.M.; Obrecht, J.M.; Cornell, E.A. Thermally induced losses in ultra-cold atoms magnetically trapped near room-temperature surfaces. *J. Low Temp. Phys.* **2003**, *133*, 229–238. [CrossRef]
57. Leanhardt, A.E.; Shin, Y.; Chikkatur, A.P.; Kielpinski, D.; Ketterle, W.; Pritchard, D.E. Bose–Einstein condensates near a microfabricated surface. *Phys. Rev. Lett.* **2003**, *90*, 100404. [CrossRef]
58. Antezza, M.; Pitaevskii, L.P.; Stringari, S. Effect of the Casimir–Polder force on the collective oscillations of a trapped Bose–Einstein condensate. *Phys. Rev. A* **2004**, *70*, 053619. [CrossRef]
59. Lin, Y.-J.; Teper, I.; Chin, C.; Vuletić, V. Impact of the Casimir–Polder potential and Johnson noise on Bose–Einstein condensate stability near surfaces. *Phys. Rev. Lett.* **2004**, *92*, 050404. [CrossRef] [PubMed]
60. Harber, D.M.; Obrecht, J.M.; McGuirk, J.M.; Cornell, E.A. Measurement of the Casimir–Polder force through center-of-mass oscillations of a Bose–Einstein condensate. *Phys. Rev. A* **2005**, *72*, 033610. [CrossRef]
61. Obrecht, J.M.; Wild, R.J.; Antezza, M.; Pitaevskii, L.P.; Stringari, S.; Cornell, E.A. Measurement of the temperature dependence of the Casimir–Polder force. *Phys. Rev. Lett.* **2007**, *98*, 063201. [CrossRef]
62. Buhmann, S.Y. *Dispersion Forces I: Macroscopic Quantum Electrodynamics and Ground-State Casimir, Casimir–Polder and van der Waals Forces*; Springer: Berlin/Heidelberg, Germany, 2012. [CrossRef]
63. Buhmann, S.Y. *Dispersion Forces II: Many-Body Effects, Excited Atoms, Finite Temperature and Quantum Friction*; Springer: Berlin/Heidelberg, Germany, 2012. [CrossRef]
64. Mohideen, U.; Roy, A. Precision measurement of the Casimir force from 0.1 to 0.9 μm . *Phys. Rev. Lett.* **1998**, *81*, 4549–4552. [CrossRef]
65. Chen, F.; Klimchitskaya, G.L.; Mostepanenko, V.M.; Mohideen, U. Control of the Casimir force by the modification of dielectric properties with light. *Phys. Rev. B* **2007**, *76*, 035338. [CrossRef]
66. de Man, S.; Heeck, K.; Wijngaarden, R.J.; Iannuzzi, D. Halving the Casimir force with Conductive Oxides. *Phys. Rev. Lett.* **2009**, *103*, 040402. [CrossRef]
67. de Man, S.; Heeck, K.; Iannuzzi, D. Halving the Casimir force with conductive oxides: Experimental details. *Phys. Rev. A* **2010**, *82*, 062512. [CrossRef]
68. Torricelli, G.; van Zwol, P.J.; Shpak, O.; Binns, C.; Palasantzas, G.; Kooi, B.J.; Svetovoy, V.B.; Wuttig, M. Switching Casimir force with phase-change materials. *Phys. Rev. A* **2010**, *82*, 010101. [CrossRef]
69. Chang, C.-C.; Banishev, A.A.; Klimchitskaya, G.L.; Mostepanenko, V.M.; Mohideen, U. Reduction of the Casimir force from indium tin oxide film by UV treatment. *Phys. Rev. Lett.* **2011**, *107*, 090403. [CrossRef] [PubMed]
70. Banishev, A.A.; Chang, C.-C.; Castillo-Garza, R.; Klimchitskaya, G.L.; Mostepanenko, V.M.; Mohideen, U. Modifying the Casimir force between indium tin oxide film and Au sphere. *Phys. Rev. B* **2012**, *85*, 045436. [CrossRef]
71. Laurent, J.; Sellier, H.; Mosset, A.; Huant, S.; Chevrier, J. Casimir force measurements in Au–Au and Au–Si cavities at low temperature. *Phys. Rev. B* **2012**, *85*, 035426. [CrossRef]
72. Banishev, A.A.; Klimchitskaya, G.L.; Mostepanenko, V.M.; Mohideen, U. Demonstration of the Casimir force between ferromagnetic surfaces of a Ni-coated sphere and a Ni-coated plate. *Phys. Rev. Lett.* **2013**, *110*, 137401. [CrossRef]
73. Sedighi, M.; Svetovoy, V.B.; Palasantzas, G. Casimir force measurements from silicon carbide surfaces. *Phys. Rev. B* **2016**, *93*, 085434. [CrossRef]
74. Liu, M.; Xu, J.; Klimchitskaya, G.L.; Mostepanenko, V.M.; Mohideen, U. Examining the Casimir puzzle with an upgraded AFM-based technique and advanced surface cleaning. *Phys. Rev. B* **2019**, *100*, 081406. [CrossRef]

75. Liu, M.; Xu, J.; Klimchitskaya, G.L.; Mostepanenko, V.M.; Mohideen, U. Precision measurements of the gradient of the Casimir force between ultraclean metallic surfaces at larger separations. *Phys. Rev. A* **2019**, *100*, 052511. [CrossRef]
76. Svetovoy, V.B.; Postnikov, A.V.; Uvarov, I.V.; Stepanov, F.I.; Palasantzas, G. Measuring the dispersion forces near the van der Waals–Casimir transition. *Phys. Rev. Appl.* **2020**, *13*, 064057. [CrossRef]
77. Liu, M.; Zhang, Y.; Klimchitskaya, G.L.; Mostepanenko, V.M.; Mohideen, U. Demonstration of unusual thermal effect in the Casimir force from graphene. *Phys. Rev. Lett.* **2021**, *126*, 206802. [CrossRef] [PubMed]
78. Liu, M.; Zhang, Y.; Klimchitskaya, G.L.; Mostepanenko, V.M.; Mohideen, U. Experimental and theoretical investigation of the thermal effect in the Casimir interaction from graphene. *Phys. Rev. B* **2021**, *104*, 085436. [CrossRef]
79. Decca, R.S.; López, D.; Fischbach, E.; Krause, D.E. Measurement of the Casimir force between dissimilar metals. *Phys. Rev. Lett.* **2003**, *91*, 050402. [CrossRef]
80. Decca, R.S.; López, D.; Fischbach, E.; Klimchitskaya, G.L.; Krause, D.E.; Mostepanenko, V.M. Precise comparison of theory and new experiment for the Casimir force leads to stronger constraints on thermal quantum effects and long-range interactions. *Ann. Phys.* **2005**, *318*, 37–80. [CrossRef]
81. Decca, R.S.; López, D.; Fischbach, E.; Klimchitskaya, G.L.; Krause, D.E.; Mostepanenko, V.M. Tests of new physics from precise measurements of the Casimir pressure between two gold-coated plates. *Phys. Rev. D* **2007**, *75*, 077101. [CrossRef]
82. Decca, R.S.; López, D.; Osquiguil, E. New results for the Casimir interaction: Sample characterization and low temperature measurements. *Int. J. Mod. Phys. A* **2010**, *25*, 2223–2230. [CrossRef]
83. Bao, Y.; Guérou, R.; Lussange, J.; Lambrecht, A.; Cirelli, R.A.; Klemens, F.; Mansfield, W. M.; Pai, C.S.; Chan, H.B. Casimir force on a surface with shallow nanoscale corrugations: Geometry and finite conductivity effects. *Phys. Rev. Lett.* **2010**, *105*, 250402. [CrossRef]
84. Intravaia, F.; Koev, S.; Jung, I.W.; Talin, A.A.; Davids, P.S.; Decca, R.S.; Aksyuk, V.A.; Dalvit D.A.R.; López, D. Strong Casimir force reduction through metallic surface nanostructuring. *Nat. Commun.* **2013**, *4*, 2515. [CrossRef]
85. Bimonte, G.; López, D.; Decca, R.S. Isoelectronic determination of the thermal Casimir force. *Phys. Rev. B* **2016**, *93*, 184434. [CrossRef]
86. Buks, E.; Roukes, M.L. Stiction, adhesion, and the Casimir effect in micromechanical systems. *Phys. Rev. B* **2001**, *63*, 033402. [CrossRef]
87. Buks, E.; Roukes, M.L. Metastability and the Casimir effect in micromechanical systems. *EPL (Europhys. Lett.)* **2001**, *54*, 220–226. [CrossRef]
88. Chan, H.B.; Aksyuk, V.A.; Kleiman, R.N.; Bishop, D.J.; Capasso, F. Quantum mechanical actuation of microelectromechanical system by the Casimir effect. *Science* **2001**, *291*, 1941–1944. [CrossRef] [PubMed]
89. Chan, H.B.; Aksyuk, V.A.; Kleiman, R.N.; Bishop, D.J.; Capasso, F. Nonlinear micromechanical Casimir oscillator. *Phys. Rev. Lett.* **2001**, *87*, 211801. [CrossRef]
90. Barcenas, J.; Reyes, L.; Esquivel-Sirvent, R. Scaling of micro- and nanodevices actuated by the Casimir force. *Appl. Phys. Lett.* **2005**, *87*, 263106. [CrossRef]
91. Palasantzas, G. Contact angle influence on the pull-in voltage of microswitches in the presence of capillary and quantum vacuum effects. *J. Appl. Phys.* **2007**, *101*, 053512. [CrossRef]
92. Palasantzas, G. Pull-in voltage of microswitch rough plates in the presence of electromagnetic and acoustic Casimir forces. *J. Appl. Phys.* **2007**, *101*, 063548. [CrossRef]
93. Esquivel-Sirvent, R.; Pérez-Pascual, R. Geometry and charge carrier induced stability in Casimir actuated nanodevices. *Eur. Phys. J. B* **2013**, *86*, 467. [CrossRef]
94. Broer, W.; Palasantzas, G.; Knoester, G.; Svetovoy, V.B. Significance of the Casimir force and surface roughness for actuation dynamics of MEMS. *Phys. Rev. B* **2013**, *87*, 125413. [CrossRef]
95. Sedighi, M.; Broer, W.; Palasantzas, G.; Kooi, B.J. Sensitivity of micromechanical actuation on amorphous to crystalline phase transformations under the influence of Casimir forces. *Phys. Rev. B* **2013**, *88*, 165423. [CrossRef]
96. Zou, J.; Marcet, Z.; Rodriguez, A.W.; Reid, M.T.H.; McCauley, A.P.; Kravchenko, I.I.; Lu, T.; Bao, Y.; Johnson, S.G.; Chan, H.B. Casimir forces on a silicon micromechanical chip. *Nat. Commun.* **2013**, *4*, 1845. [CrossRef]
97. Broer, W.; Waalkens, H.; Svetovoy, V.B.; Knoester, J.; Palasantzas, G. Nonlinear actuation dynamics of driven Casimir oscillators with rough surfaces. *Phys. Rev. Appl.* **2013**, *4*, 054016. [CrossRef]
98. Liu, X.-F.; Li, Y.; Jing, H. Casimir switch: Steering optical transparency with vacuum forces. *Sci. Rep.* **2016**, *6*, 27102. [CrossRef] [PubMed]
99. Inui, N. Optical switching of a graphene mechanical switch using the Casimir effect. *J. Appl. Phys.* **2017**, *122*, 104501. [CrossRef]
100. Milton, K.A. Fermionic Casimir stress on a spherical bag. *Ann. Phys.* **1983**, *150*, 432–438. [CrossRef]
101. Baacke, J.; Igarashi, Y. Casimir energy of confined massive quarks. *Phys. Rev. D* **1983**, *27*, 460–463. [CrossRef]
102. Bordag, M.; Elizalde, E.; Kirsten, K.; Leseduarte, S. Casimir energies for massive scalar fields in a spherical geometry. *Phys. Rev. D* **1997**, *56*, 4896–4904. [CrossRef]
103. Elizalde, E.; Santos, F.C.; Tort, A.C. The Casimir energy of a massive fermionic field confined in a $(d + 1)$ -dimensional slab-bag. *Int. J. Mod. Phys. A* **2003**, *18*, 1761–1772. [CrossRef]
104. Cruz, M.B.; Bezerra de Mello, E.R.; Petrov A.Y. Fermionic Casimir effect in a field theory model with Lorentz symmetry violation. *Phys. Rev. D* **2019**, *99*, 085012. [CrossRef]

105. Mandlecha, Y.V.; Gavai, R.V. Lattice fermionic Casimir effect in a slab bag and universality. *Phys. Lett. B* **2022**, *835*, 137558. [CrossRef]
106. Rohim, A.; Romadani, A.; Adam, A.S. Casimir effect of Lorentz-violating charged Dirac field in background magnetic field. *Prog. Theor. Exp. Phys.* **2024**, *2024*, 033B01. [CrossRef]
107. Milton, K.A. *The Casimir Effect: Physical Manifestations of Zero-Point Energy*; World Scientific: Singapore, 2001. [CrossRef]
108. Ford, L.H. Quantum vacuum energy in a closed universe. *Phys. Rev. D* **1976**, *14*, 3304–3313. [CrossRef]
109. Dowker, J.S.; Critchley, R. Covariant Casimir calculations. *J. Phys. A Math. Gen.* **1976**, *9*, 535–540. [CrossRef]
110. Isham, C.J. Twisted quantum fields in a curved space-time. *Proc. R. Soc. Lond. A Math. Phys. Sci.* **1978**, *362*, 383–404.
111. DeWitt, B.S.; Hart, C.F.; Isham, C.J. Topology and quantum field theory. *Phys. A* **1979**, *96*, 197–211. [CrossRef]
112. Ford, L.H. Vacuum polarization in a non-simply connected spacetime. *Phys. Rev. D* **1980**, *21*, 933–948. [CrossRef]
113. Helliwell, T.M.; Konkowski, D.A. Vacuum fluctuations outside cosmic strings. *Phys. Rev. D* **1986**, *34*, 1918–1920. [CrossRef]
114. Candelas, P.; Weinberg, S. Calculation of gauge couplings and compact circumferences from self-consistent dimensional reduction. *Nucl. Phys. B* **1984**, *237*, 397–441. [CrossRef]
115. Chodos, A.; Myers, E. Gravitational contribution to the Casimir energy in Kaluza-Klein theories. *Ann. Phys.* **1984**, *156*, 412–441. [CrossRef]
116. Birmingham, D.; Kantowski, R.; Milton, K.A. Scalar and spinor Casimir energies in even-dimensional Kaluza-Klein spaces of the form $M^4 \times S^{N_1} \times S^{N_2} \times \dots$. *Phys. Rev. D* **1988**, *38*, 1809–1822. [CrossRef]
117. Emig, T.; Jaffe, R.L.; Kardar, M.; Scardicchio, A. Casimir interaction between a plate and a cylinder. *Phys. Rev. Lett.* **2006**, *96*, 080403. [CrossRef]
118. Emig, T.; Graham, N.; Jaffe, R.L.; Kardar, M. Casimir forces between arbitrary compact objects. *Phys. Rev. Lett.* **2007**, *99*, 170403. [CrossRef] [PubMed]
119. Kenneth, O.; Klich, I. Casimir forces in a T-operator approach. *Phys. Rev. B* **2008**, *78*, 014103. [CrossRef]
120. Emig, T.; Graham, N.; Jaffe, R.L.; Kardar, M. Casimir forces between compact objects: The scalar case. *Phys. Rev. D* **2008**, *77*, 025005. [CrossRef]
121. Rahi, S.J.; Emig, T.; Graham, N.; Jaffe, R.L.; Kardar, M. Scattering theory approach to electromagnetic Casimir forces. *Phys. Rev. D* **2009**, *80*, 085021. [CrossRef]
122. Fosco, C.D.; Lombardo, F.C.; Mazzitelli, F.D. Proximity force approximation for the Casimir energy as a derivative expansion. *Phys. Rev. D* **2011**, *84*, 105031. [CrossRef]
123. Bimonte, G.; Emig, T.; Jaffe, R.L.; Kardar, M. Casimir forces beyond the proximity force approximation. *EPL (Europhys. Lett.)* **2012**, *97*, 50001. [CrossRef]
124. Bimonte, G.; Emig, T.; Kardar, M. Material dependence of Casimir force: Gradient expansion beyond proximity. *Appl. Phys. Lett.* **2012**, *100*, 074110. [CrossRef]
125. Graham, N. Electromagnetic Casimir forces in elliptic cylinder geometries. *Phys. Rev. D* **2013**, *87*, 105004. [CrossRef]
126. Spreng, B.; Hartmann, M.; Henning, V.; Maia Neto, P.A.; Ingold, G.-L. Proximity force approximation and specular reflection: Application of the WKB limit of Mie scattering to the Casimir effect. *Phys. Rev. A* **2018**, *97*, 062504. [CrossRef]
127. Bulgac, A.; Magierski, P.; Wirzba, A. Scalar Casimir effect between Dirichlet spheres or a plate and a sphere. *Phys. Rev. D* **2006**, *73*, 025007. [CrossRef]
128. Bordag, M. Casimir effect for a sphere and a cylinder in front of a plane and corrections to the proximity force theorem. *Phys. Rev. D* **2006**, *73*, 125018. [CrossRef]
129. Maia Neto, P.A.; Lambrecht, A.; Reynaud, S. Casimir energy between a plane and a sphere in electromagnetic vacuum. *Phys. Rev. A* **2008**, *78*, 012115. [CrossRef]
130. Canaguier-Durand, A.; Maia Neto, P.A.; Cavero-Pelaez, I.; Lambrecht, A.; Reynaud, S. Casimir interaction between plane and spherical metallic surfaces. *Phys. Rev. Lett.* **2009**, *102*, 230404. [CrossRef] [PubMed]
131. Bordag, M.; Pirozhenko, I. Casimir entropy for a ball in front of a plane. *Phys. Rev. D* **2010**, *82*, 125016. [CrossRef]
132. Teo, L.P. Material dependence of Casimir interaction between a sphere and a plate: First analytic correction beyond proximity force approximation. *Phys. Rev. D* **2013**, *88*, 045019. [CrossRef]
133. Bimonte, G. Going beyond PFA: A precise formula for the sphere-plate Casimir force. *EPL (Europhys. Lett.)* **2017**, *118*, 20002. [CrossRef]
134. Hartmann, M.; Ingold, G.-L.; Maia Neto, P.A. Plasma versus Drude modeling of the Casimir force: Beyond the proximity force approximation. *Phys. Rev. Lett.* **2017**, *119*, 043901. [CrossRef]
135. Hartmann, M.; Ingold, G.-L.; Maia Neto, P.A. Advancing numerics for the Casimir effect to experimentally relevant aspect ratios. *Phys. Scr.* **2018**, *93*, 114003. [CrossRef]
136. Bimonte, G.; Emig, T. Surface scattering expansion of the Casimir-Polder interaction for magneto-dielectric bodies: Convergence properties for insulators, conductors, and semiconductors. *Physics* **2024**, *6*, 194–205. [CrossRef]
137. Fosco, C.D.; Lombardo, F.C.; Mazzitelli, F.D. Casimir Physics beyond the Proximity Force Approximation: The Derivative Expansion. *Physics* **2024**, *6*, 290–316. [CrossRef]
138. Castillo-López, S.G.; Esquivel-Sirvent, R.; Pirruccio, G.; Villarreal, C. Casimir forces with periodic structures: Abrikosov flux lattices. *Physics* **2024**, *6*, 394–406. [CrossRef]
139. Graham, N. Electromagnetic Casimir-Polder interaction for a conducting cone. *Physics* **2023**, *5*, 1003–1012. [CrossRef]

140. Dhital, M.; Mohideen, U. A Brief review of some recent precision Casimir force measurements. *Physics* **2024**, *6*, 891–904. [CrossRef]
141. Hult, E.; Hyldgaard, P.; Rossmesl, J.; Lundqvist, B.I. Density-functional calculation of van der Waals forces for free-electron-like surfaces. *Phys. Rev. B* **2001**, *64*, 195414. [CrossRef]
142. Drosdoff, D.; Woods, L.M. Casimir forces and graphene sheets. *Phys. Rev. B* **2010**, *82*, 155459. [CrossRef]
143. Sernelius, B.E. Retarded interactions in graphene systems. *Phys. Rev. B* **2012**, *85*, 195427. [CrossRef]
144. Zhu, T.; Antezza, M.; Wang, J.-S. Dynamical polarizability of graphene with spatial dispersion. *Phys. Rev. B* **2021**, *103*, 125421. [CrossRef]
145. Bordag, M.; Fialkovsky, I.V.; Gitman, D.M.; Vassilevich, D.V. Casimir interaction between a perfect conductor and graphene described by the Dirac model. *Phys. Rev. B* **2009**, *80*, 245406. [CrossRef]
146. Fialkovsky, I.V.; Marachevsky, V.N.; Vassilevich, D.V. Finite-temperature Casimir effect for graphene. *Phys. Rev. B* **2011**, *84*, 035446. [CrossRef]
147. Bordag, M.; Klimchitskaya, G.L.; Mostepanenko, V.M.; Petrov, V.M. Quantum field theoretical description for the reflectivity of graphene. *Phys. Rev. D* **2015**, *91*, 045037. [CrossRef]
148. Bordag, M.; Fialkovskiy, I.; Vassilevich, D. Enhanced Casimir effect for doped graphene. *Phys. Rev. B* **2016**, *93*, 075414. [CrossRef]
149. Tajik, F.; Palasantzas, G. Dynamical sensitivity of three-layer micro electromechanical systems to the optical properties of the intervening liquid layer. *Physics* **2023**, *5*, 1081–1093. [CrossRef]
150. Haghmoradi, H.; Fischer, H.; Bertolini, A.; Galić, I.; Intravaia, F.; Pitschmann, M.; Schimpl, R.; Sedmik, R.I.P. Force metrology with plane parallel plates: Final design review and outlook. *Physics* **2024**, *6*, 690–741. [CrossRef]
151. Khoury, J.; Weltman, A. Chameleon fields: Awaiting surprises for tests of gravity in space. *Phys. Rev. Lett.* **2004**, *93*, 171104. [CrossRef] [PubMed]
152. Olive, K.A.; Pospelov, M. Environmental dependence of masses and coupling constants. *Phys. Rev. D* **2008**, *77*, 043524. [CrossRef]
153. Hinterbichler, K.; Khoury, J. Screening long-range forces through local symmetry restoration. *Phys. Rev. Lett.* **2010**, *104*, 231301. [CrossRef] [PubMed]
154. Hinterbichler, K.; Khoury, J.; Levy, A.; Matas, A. Symmetron cosmology. *Phys. Rev. D* **2011**, *84*, 103521. [CrossRef]
155. Brax, P.; Fischer, H.; Käding, C.; Pitschmann, M. The environment dependent dilaton in the laboratory and the solar system. *Eur. Phys. J. C* **2022**, *82*, 934. [CrossRef]
156. Decca, R.S.; López, D.; Chan, H.B.; Fischbach, E.; Krause, D.E.; Jamell, C.R. Constraining new forces in the Casimir regime using the isoelectronic technique. *Phys. Rev. Lett.* **2005**, *94*, 240401. [CrossRef]
157. Antoniadis, I.; Baessler, S.; Bücher, M.; Fedorov, V.V.; Hoedl, S.; Lambrecht, A.; Nesvizhevsky, V.V.; Pignol, G.; Protasov, K.V.; Reynaud, S.; et al. Short-range fundamental forces. *Comptes Rendus Phys.* **2011**, *12*, 755–778. [CrossRef]
158. Klimchitskaya, G.L.; Mostepanenko, V.M. Improved constraints on the coupling constants of axion-like particles to nucleons from recent Casimir-less experiment. *Eur. Phys. J. C* **2015**, *75*, 164. [CrossRef]
159. Chen, Y.-J.; Tham, W.K.; Krause, D.E.; López, D.; Fischbach, E.; Decca, R.S. Stronger limits on hypothetical Yukawa interactions in the 30–8000 nm range. *Phys. Rev. Lett.* **2016**, *116*, 221102. [CrossRef] [PubMed]
160. Klimchitskaya, G.L.; Mostepanenko, V.M. Constraints on axionlike particles and non-Newtonian gravity from measuring the difference of Casimir forces. *Phys. Rev. D* **2017**, *95*, 123013. [CrossRef]
161. Klimchitskaya, G.L. Recent breakthrough and outlook in constraining the non-Newtonian gravity and axion-like particles from Casimir physics. *Eur. Phys. J. C* **2017**, *77*, 315. [CrossRef]
162. Klimchitskaya, G.L.; Kuusk, P.; Mostepanenko, V.M. Constraints on non-Newtonian gravity and axionlike particles from measuring the Casimir force in nanometer separation range. *Phys. Rev. D* **2020**, *101*, 056013. [CrossRef]
163. Svetovoy, V.B. Casimir forces between a dielectric and metal: Compensation of the electrostatic interaction. *Physics* **2023**, *5*, 814–822. [CrossRef]
164. Speake, C.C.; Trenkel, C. Forces between conducting surfaces due to spatial variations of surface potential. *Phys. Rev. Lett.* **2003**, *90*, 160403. [CrossRef]
165. Behunin, R.O.; Dalvit, D.A.R.; Decca, R.S.; Genet, C.; Jung, I.W.; Lambrecht, A.; Liscio, A.; López, D.; Reynaud, S.; Schnoering, G.; et al. Kelvin probe force microscopy of metallic surfaces used in Casimir force measurements. *Phys. Rev. A* **2014**, *90*, 062115. [CrossRef]
166. Klimchitskaya, G.L.; Mostepanenko, V.M. Conductivity of dielectric and thermal atom-wall interaction. *J. Phys. A Math. Theor.* **2008**, *41*, 312002. [CrossRef]
167. Klimchitskaya, G.L.; Mostepanenko, V.M. Casimir effect invalidates the Drude model for transverse electric evanescent waves. *Physics* **2023**, *5*, 952–967. [CrossRef]
168. Törmä, P.; Barnes, W.L. Strong coupling between surface plasmon polaritons and emitters: A review. *Rep. Prog. Phys.* **2015**, *78*, 013901. [CrossRef] [PubMed]
169. Klimchitskaya, G.L.; Mostepanenko, V.M.; Svetovoy, V.B. Probing the response of metals to low-frequency s-polarized evanescent fields. *EPL (Europhys. Lett.)* **2022**, *139*, 66001. [CrossRef]
170. Klimchitskaya, G.L.; Mostepanenko, V.M.; Svetovoy, V.B. *Experimentum crucis* for electromagnetic response of metals to evanescent waves and the Casimir puzzle. *Universe* **2022**, *8*, 574. [CrossRef]
171. Henkel, C. Rectified Lorentz force from thermal current fluctuations. *Physics* **2024**, *6*, 568–578. [CrossRef]
172. Klimchitskaya, G.L.; Mostepanenko, V.M. The Casimir force between two graphene sheets: 2D Fresnel reflection coefficients, contributions of different polarizations, and the role of evanescent waves. *Physics* **2023**, *5*, 1013–1030. [CrossRef]

173. Asorey, M.; Iuliano, C.; Ezquerro, F. Casimir energy in $(2 + 1)$ -dimensional field theories. *Physics* **2024**, *6*, 613–628. [CrossRef]
174. Geim, A.K.; Novoselov, K.S. The rise of graphene. *Nat. Mater.* **2007**, *6*, 183–191. [CrossRef]
175. Lalmi, B.; Oughaddou, H.; Enriquez, H.; Kara, A.; Vizzini, S.B.; Ealet, B.N.; Aufray, B. Epitaxial growth of a silicene sheet. *Appl. Phys. Lett.* **2010**, *97*, 223109. [CrossRef]
176. Garcia, J.C.; de Lima, D.B.; Assali, L.V.C.; Justo, J.F. Group IV graphene- and graphane-like nanosheets. *J. Phys. Chem. C* **2011**, *115*, 13242. [CrossRef]
177. Carvalho, A.; Wang, M.; Zhu, X.; Rodin, A.S.; Su, H.; Castro Neto, A.H. Phosphorene: From theory to applications. *Nat. Rev. Mater.* **2016**, *1*, 16061. [CrossRef]
178. Brax, P.; Fichet, S. Casimir forces in CFT with defects and boundaries. *Physics* **2024**, *6*, 544–667. [CrossRef]
179. Khusnutdinov, N.; Emelianova, N. The normal Casimir force for lateral moving planes with isotropic conductivities. *Physics* **2024**, *6*, 148–163. [CrossRef]
180. Dedkov, G.V. Casimir–Lifshitz frictional heating in a system of parallel metallic plates. *Physics* **2024**, *6*, 13–30. [CrossRef]
181. Inui, N. Stabilizing diamagnetic levitation of a graphene flake through the Casimir effect. *Physics* **2023**, *5*, 923–935. [CrossRef]
182. Brevik, I.; Pal, S.; Li, Y.; Gholamhosseinian, A.; Boström, M. Axion electrodynamics and the Casimir effect. *Physics* **2024**, *6*, 407–421. [CrossRef]
183. Boström, M.; Gholamhosseinian, A.; Pal, S.; Li, Y.; Brevik, I. Semi-classical electrodynamics and the Casimir effect. *Physics* **2024**, *6*, 456–467. [CrossRef]
184. Marachevsky, V.N.; Sidelnikov, A.A. Casimir interaction of Chern–Simons layers on substrates via vacuum stress tensor. *Physics* **2024**, *6*, 496–514. [CrossRef]
185. Ievlev, I.; Good, M.R.R. Larmor temperature, Casimir dynamics, and Planck’s law. *Physics* **2023**, *5*, 797–813. [CrossRef]
186. Gorban, M.J.; Julius, W.D.; Brown, P.M.; Matulevich, J.A.; Radhakrishnan, R.; Cleaver, G.B. First and second-order forces in the asymmetric dynamical Casimir effect for a single δ – δ' mirror. *Physics* **2024**, *6*, 760–779. [CrossRef]
187. Bordag, M.; Pirozhenko, I.G. Mass and magnetic moment of the electron and the stability of QED— A critical review. *Physics* **2024**, *6*, 237–250. [CrossRef]
188. Saharian, A. Surface Casimir densities on branes orthogonal to the boundary of anti-de Sitter spacetime. *Physics* **2023**, *5*, 1145–1162. [CrossRef]
189. Grats, Y.V.; Spirin, P. Vacuum interaction of topological strings at short distances. *Physics* **2023**, *5*, 1163–1180. [CrossRef]
190. Bezerra, V.B.; Mota, H.F.S.; Lima, A.P.C.M.; Alencar, G.; Muniz, C.R. Casimir effect in finite temperature and gravitational scenarios. *Physics* **2024**, *6*, 1046–1071. [CrossRef]
191. Klimchitskaya, G.L.; Mostepanenko, V.M. An alternative response to the off-shell quantum fluctuations: A step forward in resolution of the Casimir puzzle. *Eur. Phys. J. C* **2020**, *80*, 900. [CrossRef]
192. Klimchitskaya, G.L.; Mostepanenko, V.M. Casimir effect for magnetic media: Spatially nonlocal response to the off-shell quantum fluctuations. *Phys. Rev. D* **2021**, *104*, 085001. [CrossRef]
193. Klimchitskaya, G.L.; Mostepanenko, V.M. Theory-experiment comparison for the Casimir force between metallic test bodies: A spatially nonlocal dielectric response. *Phys. Rev. A* **2022**, *105*, 012805. [CrossRef]

Disclaimer/Publisher’s Note: The statements, opinions and data contained in all publications are solely those of the individual author(s) and contributor(s) and not of MDPI and/or the editor(s). MDPI and/or the editor(s) disclaim responsibility for any injury to people or property resulting from any ideas, methods, instructions or products referred to in the content.

Article

Surface Scattering Expansion of the Casimir–Polder Interaction for Magneto-Dielectric Bodies: Convergence Properties for Insulators, Conductors, and Semiconductors

Giuseppe Bimonte ^{1,*} and Thorsten Emig ²

¹ Dipartimento di Fisica E. Pancini, Università di Napoli Federico II, Complesso Universitario di Monte S. Angelo, Via Cintia, I-80126 Napoli, Italy

² Laboratoire de Physique Théorique et Modèles Statistiques, CNRS UMR 8626, Université Paris-Saclay, CEDEX, 91405 Orsay, France; thorsten.emig@cnrs.fr

* Correspondence: giuseppe.bimonte@na.infn.it

† INFN Sezione di Napoli, I-80126 Napoli, Italy.

Abstract: Fluctuation-induced forces are a hallmark of the interplay between fluctuations and geometry. We recently proved the existence of a multi-parametric family of exact representations of Casimir and Casimir–Polder interactions between bodies of arbitrary shape and material composition, admitting a multiple scattering expansion (MSE) as a sequence of inter-body and intra-body multiple wave scatterings. The approach requires no knowledge of the scattering amplitude (T-matrix) of the bodies. In this paper, we investigate the convergence properties of the MSE for the Casimir–Polder interaction of a polarizable particle with a macroscopic body. We consider representative materials from different classes, such as insulators, conductors, and semiconductors. Using a sphere and a cylinder as benchmarks, we demonstrate that the MSE can be used to efficiently and accurately compute the Casimir–Polder interaction for bodies with smooth surfaces.

Keywords: Casimir–Polder force; scattering expansion; surface integral equation; silicon; gold; polystyrene

Citation: Bimonte, G.; Emig, T. Surface Scattering Expansion of the Casimir–Polder Interaction for Magneto-Dielectric Bodies: Convergence Properties for Insulators, Conductors, and Semiconductors. *Physics* **2024**, *6*, 194–205. <https://doi.org/10.3390/physics6010014>

Received: 6 December 2023

Revised: 2 January 2024

Accepted: 9 January 2024

Published: 9 February 2024



Copyright: © 2024 by the authors. Licensee MDPI, Basel, Switzerland. This article is an open access article distributed under the terms and conditions of the Creative Commons Attribution (CC BY) license (<https://creativecommons.org/licenses/by/4.0/>).

1. Introduction

Following the seminal paper of Hendrick Casimir, who discovered that two discharged perfectly conducting parallel plates at zero temperature attract each other with a force originating from quantum fluctuations of the electromagnetic (EM) field [1], Evgeny Lifshitz successfully used the then-new field of fluctuational electrodynamics to compute the Casimir force between two parallel, infinite surfaces of dispersive and dissipative dielectric bodies at finite temperature [2]. By taking the dilute limit for one of the two bodies, Lifshitz could also compute the Casimir–Polder (CP) force between a small polarizable particle and a planar surface. Lifshitz’s results remained unsurpassed for a long time, because it was not understandable how to extend his computation beyond planar surfaces. Computing the Casimir and CP interactions in non-planar geometries is actually a notoriously complicated problem, due to the collective and non-additive character of dispersion forces. For many years, the only method to estimate dispersion forces in non-planar setups was the Derjaguin additive approximation [3], the so-called Proximity Force Approximation (PFA), which expresses the Casimir force between two non-planar surfaces as the sum of the forces between pairs of small opposing planar portions of the surfaces. Because of its simplicity, the PFA is still often used to interpret modern experiments with curved bodies; for reviews, see [4–9].

A significant step forward in the study of curved surfaces was made in the 1970s by Dieter Langbein, who used scattering methods to study the Casimir interaction between spheres and cylinders [10]. The remarkable study of Langbein went quite unnoticed, and it was quickly forgotten. A new wave of strong interest in the problem arose at the beginning

of this century, spurred by modern precision experiments on the Casimir effect [11–18]. The intense theoretical efforts that were put forward culminated in the discovery of the scattering Formula [19–21]. According to this formula, which was initially devised for non-planar mirrors [22,23], the interaction between dielectric bodies is expressed in terms of their scattering amplitude, known as T-operator. While this formalism has been the basis of the theoretical advancements made in recent years, its practical use is limited by the feature that the T-operator is known only for highly symmetric bodies, such as spheres and cylinders, or for a few perfectly conducting shapes [24]. Remarkably enough, it has been found that the scattering formula can be computed exactly for the sphere–plate and sphere–sphere systems for Drude conductors in the high temperature limit [25,26]. By improved numerical methods, the scattering formula for a dielectric sphere and a plate at finite temperature can be computed with high precision also for experimentally relevant small separations [27]. To note, however, is that the precision of current experiments using a simple enough sphere–plate geometry has not yet reached the point where deviations from the PFA to be observed.

As mentioned above, the practical use of the scattering approach is limited to the few simple shapes for which the scattering amplitude is known. A more fundamental limitation of the scattering approach is that interlocked geometries evade this method due to lack of convergence of the mode expansion [28]. The necessity of theoretical formulations for a precise force computation in complex geometries has become urgent lately, because recent experiments using micro-fabricated surfaces [28–30] have indeed shown large deviations from the PFA. Theoretical progress has been made for the special case of dielectric rectangular gratings by using a generalization of the Rayleigh expansion in Refs. [31–33]. On a different route, a general approach has been devised for gently curved surfaces, for which a gradient expansion can be used to obtain first order curvature corrections to the proximity force approximation for the Casimir force [34–37]. In this approach, the Casimir energy is expanded in powers of derivatives of the height functions of the surfaces, whose coefficients can be computed analytically by matching the gradient expansion with the perturbative expansion of the energy in the common domain of validity of both expansions.

A breakthrough occurred in 2013 [38] when it was shown that surface integral-equations methods [39,40], which have been used for a long time in computational electromagnetism, can also be used to compute, at least in general, Casimir interactions for arbitrary arrangements of any number of (homogeneous) magneto-dielectric bodies of any shape. The formulation in [38] expresses Casimir forces and energies as traces of certain expressions involving a surface operator, evaluated along the imaginary frequency axis. The surface operator consists of linear combinations with constant coefficients of free Green tensors of the EM field of $N + 1$ *homogeneous* infinite media, having the permittivities of the N bodies, and of the medium surrounding them. A potential problem with the approach of Ref. [38] is that the expression for the Casimir interaction contains the inverse of the surface operator, which has to be computed numerically by replacing the continuous surfaces with a suitable discrete mesh. This operation replaces the surface operator by a large matrix whose elements involve double surface integrals of the free Green tensors over all pairs of small surface elements composing the mesh. The generation of the matrix is time consuming because of the strong inverse-distance cubed singularity of the surface operator in the coincidence limit. In addition, the size of the non-sparse matrix for sufficiently fine meshes can quickly exceed the memory-usage limit, preventing the matrix numerical inversion.

Inspired by earlier papers of Roger Balian and Bertrand Duplantier on the Casimir effect for perfect conductors [41,42], we have recently derived a multiple scattering expansion (MSE) of Casimir and CP interactions for magneto-dielectric bodies of arbitrary shape [43,44]. Similar to Ref. [38], in the MSE approach the interactions have the form of traces of expressions involving the inverse of a surface operator, $\mathbb{M}(i\bar{\zeta})$, evaluated along the imaginary frequency axis. A crucial difference with respect to Ref. [38] is that the MSE kernel \mathbb{M} has the form of a Fredholm surface integral operator of the second kind,

$$\mathbb{M} = \mathbb{I} - \mathbb{K} . \quad (1)$$

Here, \mathbb{I} and \mathbb{K} represent the identity and the surface scattering operator (SSO), respectively.

The Fredholm form implies that the inverse \mathbb{M} can be computed as a power (Neumann) series,

$$\mathbb{M}^{-1} = \mathbb{I} + \mathbb{K} + \mathbb{K}^2 + \dots, \quad (2)$$

which converges, provided that the spectral radius of \mathbb{K} is less than one. Hence, one obtains an expansion of Casimir and CP interaction in the powers of \mathbb{K} , which can be interpreted as an expansion in the number of scatterings off the surfaces of the bodies. Specifically, the MSE has the form of an iterated series of surface integrals of elementary functions, running over the surfaces of the bodies. Let us note that a particular choice of the free coefficients in the kernel \mathbb{K} exists, such that the kernel has a weak $1/|\mathbf{u} - \mathbf{u}'|$ singularity, where \mathbf{u} and \mathbf{u}' are the points on the surface. The weak singularity feature should simplify and expedite numerical evaluations on a mesh. An additional advantage implied by the MSE, if implemented on a mesh, is that one does not need to store the matrix for \mathbb{K} in memory, since its elements can be computed at the moment of performing the matrix multiplication.

Considering specifically the CP interaction of a polarizable particle with a dielectric body, let us note that the problem has been studied by many authors in the past, using a variety of methods. A distinction can be made between approaches devised for bodies of special shapes, as opposed to formulations that can handle bodies of arbitrary shapes. The first group includes spheres and cylinders, for which the scattering formula leads to a simple exact expression for the CP energy in terms of the exactly known T-operator [45–48]. This group also includes the computation of the exact CP interaction between an atom and a rectangular dielectric grating [32,49], based on the Rayleigh expansion. Regarding the second group of approaches, it has been shown [50,51] that the gradient expansion [34–37] can be used to compute the leading and the next-to-leading curvature corrections beyond the PFA for the CP energy of an atom in front of a gently curved surface of any shape. A numerical time-domain approach to compute the CP interaction of an atom with an arbitrary micro-structured body has been recently discussed [52]. Let us stress that this elegant approach offers the possibility of dealing with a broad range of dielectric materials, including inhomogeneous and possibly non-local materials.

In this paper, we investigate the power of the MSE in the computation of CP interactions. In its present formulation, the MSE allows one to deal with homogeneous and local magneto-dielectric bodies of any shapes, which is the situation of interest in experiments carried out so far. In [43], we showed that only a few terms of the MSE are sufficient to obtain a fairly accurate estimate of the Casimir energy between a Si wedge and a Au plate. The purpose of the present study is to investigate the convergence properties of the MSE for the CP interaction between a polarizable isotropic particle and a dielectric body. We use as benchmarks two shapes that can be solved exactly by using the scattering approach, namely a sphere or a cylinder. We consider different types of materials for the sphere and the cylinder in order to see how the material properties of the bodies affect the rate of convergence of the MSE. We demonstrate that, in all the cases considered, the MSE converges quite fast and uniformly with respect to the particle-surface separation. Since there is no reason to expect that the convergence properties of the MSE bring whatever difference for bodies that are smooth deformations of a sphere or a cylinder, we argue that the findings of the current study imply that the MSE can be used to efficiently compute the CP interactions for compact and non-compact dielectric bodies with smooth surfaces of an arbitrary shape.

2. Casimir–Polder Energy of a Polarizable Particle and a Magneto-Dielectric Body

We study the CP interaction between a small polarizable particle and a magneto-dielectric body (see Figure 1). The optical response of the particle is described by its (complex) electric, $\alpha(\omega)$, and magnetic, $\beta(\omega)$, polarizability tensors, where ω is the fre-

quency. It is known [6,44] that the CP energy can be expressed in terms of the *scattering* Green tensor $\Gamma(\mathbf{r}, \mathbf{r}')$ evaluated at the particle's position \mathbf{r}_0 , as

$$E_{\text{CP}} = -4\pi k_B T \sum_{n=0}^{\infty} \kappa_n \sum_{i,j=1}^3 \left[\alpha_{ij}(i\zeta_n) \Gamma_{ij}^{(\text{EE})}(\mathbf{r}_0, \mathbf{r}_0; \kappa_n) + \beta_{ij}(i\zeta_n) \Gamma_{ij}^{(\text{HH})}(\mathbf{r}_0, \mathbf{r}_0; \kappa_n) \right], \quad (3)$$

where k_B is Boltzmann constant, T is the temperature, $\zeta_n = 2\pi n k_B T / \hbar$, with \hbar the reduced Planck's constant and $n = 0, 1, 2, \dots$, are the Matsubara frequencies, $\kappa_n = \zeta_n / c$ with c the speed of light, the prime in the sum indicates that the $n = 0$ terms has to be taken with a weight of $1/2$. The superscripts 'EE' and 'HH' denote the electric and the magnetic fields, respectively. Here, only one scattering at the particle is considered, which is completely justified for particles that are much smaller than the distance from the surface, d . However, multiple scatterings at the body need to be considered. Using the surface integral-equation formulation of EM scattering by a dielectric body [44], one can show that $\Gamma(\mathbf{r}, \mathbf{r}')$ can be expressed as a surface integral extending over the surface, S , of the body,

$$\Gamma(\mathbf{r}, \mathbf{r}') = \int_S ds_{\mathbf{u}} \int_S ds_{\mathbf{u}'} \mathbb{G}_0(\mathbf{r}, \mathbf{u}) (\mathbb{I} - \mathbb{K})^{-1}(\mathbf{u}, \mathbf{u}') \mathbb{M}(\mathbf{u}', \mathbf{r}'), \quad (4)$$

where $\mathbb{K}(\mathbf{u}, \mathbf{u}')$ denotes the following SSO,

$$\mathbb{K}(\mathbf{u}, \mathbf{u}') = 2\mathbb{P}(\mathbb{C}^i + \mathbb{C}^e)^{-1} \mathbf{n}(\mathbf{u}) \times \left[\mathbb{C}^i \mathbb{G}_1(\mathbf{u}, \mathbf{u}') - \mathbb{C}^e \mathbb{G}_0(\mathbf{u}, \mathbf{u}') \right], \quad \mathbb{P} = \begin{pmatrix} 0 & -1 \\ 1 & 0 \end{pmatrix}, \quad (5)$$

$\mathbb{M}(\mathbf{u}, \mathbf{u}')$ is the surface operator,

$$\mathbb{M}(\mathbf{u}, \mathbf{r}) = -2\mathbb{P}(\mathbb{C}^i + \mathbb{C}^e)^{-1} \mathbb{C}^e \mathbf{n}(\mathbf{u}) \times \mathbb{G}_0(\mathbf{u}, \mathbf{r}), \quad (6)$$

In Equations (4)–(6), \mathbb{G}_0 and \mathbb{G}_1 are the empty-space Green tensors for the homogenous media with the permittivities ϵ_0 and ϵ_1 and the permeabilities μ_0 and μ_1 , respectively (see Appendix E of Ref. [44] for the definition of \mathbb{G}_0 and \mathbb{G}_1), while $\mathbf{n}(\mathbf{u})$ is the outward unit normal vector to the surface S at point \mathbf{u} . The action $\mathbf{n}(\mathbf{u}) \times$ on the 3×3 matrices $\mathbb{G}_1^{(pq)}$ and $\mathbb{G}_0^{(pq)}$ ($p, q \in \{E, H\}$) is respectively defined by $(\mathbf{n}(\mathbf{u}) \times \mathbb{G}_1^{(pq)}) \mathbf{v} \equiv \mathbf{n}(\mathbf{u}) \times (\mathbb{G}_1^{(pq)} \mathbf{v})$ and $(\mathbf{n}(\mathbf{u}) \times \mathbb{G}_0^{(pq)}) \mathbf{v} \equiv \mathbf{n}_\sigma(\mathbf{u}) \times (\mathbb{G}_0^{(pq)} \mathbf{v})$, for any vector \mathbf{v} . To note is that \mathbb{K} and \mathbb{M} depend on four *arbitrary* coefficients, which must form two invertible diagonal 2×2 matrices, \mathbb{C}^i and \mathbb{C}^e .

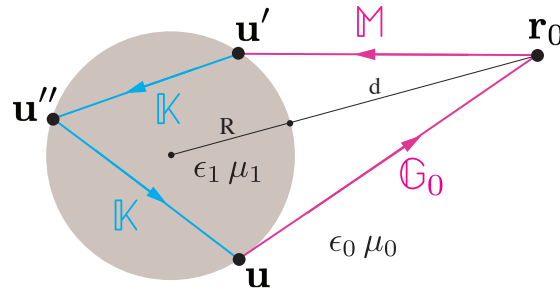


Figure 1. Configuration of a dielectric body (sphere, cylinder) of radius R with the permittivity ϵ_1 and permeability μ_1 interacting with a polarizable particle at position \mathbf{r}_0 outside the object at a distance d from the surface. ϵ_0 and μ_0 denote, respectively, the permittivity and permeability of the surrounding medium. \mathbb{M} , \mathbb{G}_0 and \mathbb{K} are the operators of the multiple scattering expansion. \mathbf{u} , \mathbf{u}' and \mathbf{u}'' mark some positions on the surface of the dielectric body. The arrows denote ordering of the operators. See text for more details.

The existence of an MSE follows from the Fredholm type of the operator $(\mathbb{I} - \mathbb{K})^{-1}$ in Equation (4), which permits an expansion of $\Gamma(\mathbf{r}, \mathbf{r}')$ in powers of \mathbb{K} . This in turn leads to an MSE expansion of the CP energy in Equation (3) in terms of the number of scatterings at

the surface of the body. It is useful to show the first terms of the MSE of the CP energy for the simple case of a particle having an isotropic electric polarizability, $\alpha_{ij} = \alpha \delta_{ij}$ with δ_{ij} the Kronecker delta, and a negligible magnetic polarizability, β ,

$$E_{\text{CP}} = -4\pi k_B T \sum_{n=0}^{\infty} \kappa_n \alpha(i \zeta_n) \left\{ \sum_{p=\text{E,H}} \int_S ds_{\mathbf{u}} \text{tr} \left[\mathbb{G}_0^{(\text{Ep})}(\mathbf{r}_0, \mathbf{u}; \kappa_n) \mathbb{M}^{(p\text{E})}(\mathbf{u}, \mathbf{r}_0; \kappa_n) \right] \right. \\ \left. + \sum_{p,q=\text{E,H}} \int_S ds_{\mathbf{u}} \int_S ds_{\mathbf{u}'} \text{tr} \left[\mathbb{G}_0^{(\text{Ep})}(\mathbf{r}_0, \mathbf{u}; \kappa_n) \mathbb{K}^{(pq)}(\mathbf{u}, \mathbf{u}'; \kappa_n) \mathbb{M}^{(q\text{E})}(\mathbf{u}', \mathbf{r}_0; \kappa_n) \right] \right\} + \dots, \quad (7)$$

where the symbol 'tr' denotes a trace over the tensor spatial indices. Since the kernels \mathbb{K} and \mathbb{M} are combinations of free-space Green tensors \mathbb{G}_0 and \mathbb{G}_1 , which are elementary functions of the coordinates, it is understandable that the CP energy involves an iterated series of integrals of elementary functions running over the surface, S , of the body. Since the Green tensors decay exponentially with distance for imaginary frequencies, one immediately sees from Equation (7) that the CP interaction is dominated by the region of the surface that is most closer to the particle. However, one notes that, for the classical term $n = 0$, the Matsubara frequency vanishes and the operators decay only according to a power law.

3. Equivalent Expressions of the SSO

It has to be noticed that different choices of the matrices for the interior, \mathbb{C}^i , and the exterior, \mathbb{C}^e , coefficients lead to *equivalent* SSO, in the sense that the right-hand side of Equation (4) provides different representations of the same scattering tensor for all coefficients [44], given that neither the interior nor the exterior matrices vanish, and that the sum $\mathbb{C}^i + \mathbb{C}^e$ is invertible. This in turn also implies that the CP energy is independent of the values of these coefficients. However, at any *finite* order of the MSE, the CP energy does depend on the chosen coefficients, which implies that the *rate of convergence* of the MSE depends in general on this choice. This important property gives one the possibilities of optimizing convergence of the MSE by suitably choosing the coefficients, dependent on the optical properties of the surfaces. Among the infinite number of the choices for the coefficients, there are two cases which we consider of most importance and describe in detail here.

C1. When the two surface positions, \mathbf{u} and \mathbf{u}' , are close one to another, the SSO has, in general, a $1/|\mathbf{u} - \mathbf{u}'|^3$ singularity. However, a unique choice of the coefficients exists [53], for which the singularity is reduced to a weaker $1/|\mathbf{u} - \mathbf{u}'|$ divergence. The coefficient matrices ensuring this remarkable property are

$$\mathbb{C}^i = \text{diag}(\epsilon_1, \mu_1), \quad \mathbb{C}^e = \text{diag}(\epsilon_0, \mu_0). \quad (8)$$

The corresponding surface operator \mathbb{K} has unique mathematical properties (see Section 6 of Ref. [44]).

C2. A fully asymmetric, material independent choice of coefficient matrices is

$$\mathbb{C}^i = \text{diag}(1, 0), \quad \mathbb{C}^e = \text{diag}(0, 1). \quad (9)$$

For good conductors, one observes relatively fast convergence of the MSE with this choice what is consistent with the observation made in Ref. [42].

4. Results and Discussion

The MSE of the CP energy (7) converges if all eigenvalues of the SSO \mathbb{K} are less than 1 in modulus which to be called here the boundedness property. No a general bound on the eigenvalues of \mathbb{K} was possible to be derived. However, we can prove [44] the boundedness property for the choice case C1 of the coefficients (see Equation (8)) in the asymptotic limit of infinite frequencies for bodies of any shape. For compact bodies, the boundedness

property also holds in the static limit $\kappa = 0$. For the special case of perfect conductors of compact shape, the boundedness property was proven much earlier for all frequencies [41].

While having a proof of convergence of the MSE is well desirable, from the practical point of view it is of more need to know if the convergence is fast enough for the first few terms of the MSE, in order to provide a good approximation of an entire series. Given the current status of experiments, obtaining the CP energy with an error of less than a percent would be acceptable. To investigate this problem, we consider using as a benchmark the CP interaction of a particle with a body for which the scattering amplitude (T-matrix) is known exactly, and then to verify in such a setup the rate of convergence of the MSE expansion to the energy exact formula. In what follows, choose to study a dielectric sphere and a dielectric cylinder. We consider three different materials: a conductor (gold), a semiconductor (silicon), and an insulator (polystyrene). Since these materials have quite different permittivities, one can check how the rate of convergence of the MSE is affected by the magnitude of the permittivity. We compare the rate of convergence of the MSE for the two cases of choice C1 and C2, of the free coefficients that enter in the definition of the SSO. We Let us denote by $MSE_k, k = 0, 1, \dots$, the estimate of the CP energy corresponding to the inclusion of \mathbb{K} up to the k power into the MSE (3).

4.1. Materials

In the computations here, the following expressions for the permittivities of the materials are used:

$$\epsilon_{\text{Au}}(i\zeta_n) = 1 + \frac{\Omega_p^2}{\zeta(\zeta + \gamma)} + \sum_{j=1}^6 \frac{f_j}{\omega_j^2 + g_j\zeta + \zeta^2}, \quad (10)$$

$$\epsilon_{\text{Si}}(i\zeta_n) = \epsilon_{\infty}^{(\text{Si})} + \frac{\epsilon_0^{(\text{Si})} - \epsilon_{\infty}^{(\text{Si})}}{1 + \zeta^2/\omega_{\text{UV}}^2}, \quad (11)$$

$$\epsilon_{\text{polystyrene}}(i\zeta_n) = 1 + \sum_{j=1}^4 \frac{f_j}{\omega_j^2 + g_j\zeta + \zeta^2}, \quad (12)$$

where $\Omega_p = 9 \text{ eV}/\hbar$, $\gamma = 0.035 \text{ eV}/\hbar$, $\epsilon_{\infty}^{(\text{Si})} = 1.035$, $\epsilon_0^{(\text{Si})} = 11.87$, and $\omega_{\text{UV}} = 4.34 \text{ eV}/\hbar$; the oscillator parameters ω_j, f_j, g_j for Au and polystyrene are listed in Tables 1 and 2, respectively. The particle's polarizability, α , is assumed to be frequency-independent.

Table 1. Oscillator parameters for Au [54]. See Equation (10).

j	$\omega_j \text{ (eV}/\hbar)$	$f_j \text{ (eV}^2/\hbar^2)$	$g_j \text{ (eV}/\hbar)$
1	3.05	7.091	0.75
2	4.15	41.46	1.85
3	5.4	2.7	1.0
4	8.5	154.7	7.0
5	13.5	44.55	6.0
6	21.5	309.6	9.0

Table 2. Oscillator parameters for polystyrene [4]. See Equation (12).

j	$\omega_j \text{ (eV}/\hbar)$	$f_j \text{ (eV}^2/\hbar^2)$	$g_j \text{ (eV}/\hbar)$
1	6.35	14.6	0.65
2	14.0	96.9	5.0
3	11.0	44.4	3.5
4	20.1	136.9	11.5

4.2. CP Energy for a Sphere

The scattering approach yields the following Formula [45,46] for the CP interaction energy of a polarizable particle at distance d from the surface of a sphere of radius R in vacuum ($\epsilon_0 = \mu_0 = 1$):

$$E_{\text{CP}}^{(\text{exact})} = \frac{k_B T}{a^2} \sum_{n=0}^{\infty} \kappa_n \alpha(i \xi_n) \sum_{l=1}^{\infty} (2l+1) \times \left\{ T_l^{\text{HH}}(i \xi_n) \mathcal{K}_l^2(\kappa_n a) - T_l^{\text{EE}}(i \xi_n) \left[\mathcal{K}_l'^2(\kappa_n a) + \frac{l(l+1)}{\kappa_n^2 a^2} \mathcal{K}_l^2(\kappa_n a) \right] \right\}, \quad (13)$$

where $a = R + d$, l is the multipole index, $\mathcal{K}_l(x) = x k_l(x)$, $k_l(x) = \sqrt{\frac{2}{\pi x}} K_{l+1/2}(x)$ is the modified spherical Bessel function of the third kind, $\mathcal{K}_l'(x) = d\mathcal{K}_l/dx$, and $T_l^{\text{HH}}, T_l^{\text{EE}}$ are the T-matrix elements (Mie coefficients) of the sphere,

$$T_l^{\text{HH}}(i \xi) = \frac{\sqrt{\mu/\epsilon} \mathcal{I}_l(\sqrt{\epsilon \mu} \kappa R) \mathcal{I}_l'(\kappa R) - \mathcal{I}_l'(\sqrt{\epsilon \mu} \kappa R) \mathcal{I}_l(\kappa R)}{\mathcal{K}_l(\kappa R) \mathcal{I}_l'(\sqrt{\epsilon \mu} \kappa R) - \sqrt{\mu/\epsilon} \mathcal{I}_l(\sqrt{\epsilon \mu} \kappa R) \mathcal{K}_l'(\kappa R)}, \quad (14)$$

$$T_l^{\text{EE}}(i \xi) = \frac{\sqrt{\epsilon/\mu} \mathcal{I}_l(\sqrt{\epsilon \mu} \kappa R) \mathcal{I}_l'(\kappa R) - \mathcal{I}_l'(\sqrt{\epsilon \mu} \kappa R) \mathcal{I}_l(\kappa R)}{\mathcal{K}_l(\kappa R) \mathcal{I}_l'(\sqrt{\mu/\epsilon} \kappa R) - \sqrt{\epsilon/\mu} \mathcal{I}_l(\sqrt{\epsilon \mu} \kappa R) \mathcal{K}_l'(\kappa R)}, \quad (15)$$

$$T_l^{\text{EH}}(i \xi) = T_l^{\text{HE}}(i \xi) = 0, \quad (16)$$

where $\xi = \kappa c$, $\mathcal{I}_l(x) = x i_l(x)$, and $\mathcal{I}_l'(x) = d\mathcal{I}_l/dx$, with $i_l(x) = \sqrt{\frac{\pi}{2x}} I_{l+1/2}(x)$ the modified spherical Bessel function of the first kind.

The matrix elements of the SSO \mathbb{K} and the operator \mathbb{M} can be straightforwardly computed in the basis of vector spherical harmonics. The corresponding matrices are both diagonal with respect to multipole indices, (l, m) , $-l \leq m \leq l$, and, in addition, these matrices are independent of m . Therefore, the matrix for \mathbb{K} has the structure of l -dependent 4×4 blocks $K_{p,r,l,m;q,s,l',m'} = \delta_{ll'} \delta_{mm'} K_{p,r;q,s}^{(l)}$, where $r, s = 1, 2$ label the tangential fields $Y_{1,lm}(\hat{r})$ and $Y_{2,lm}(\hat{r})$, introduced in Equation (8.1) of Ref. [42].

In Figures 2–4, we show the ratios of the MSE for the CP energy $E_{\text{CP}}^{(\text{MSE}_k)}$ and the exact result for the CP energy $E_{\text{CP}}^{(\text{exact})}$ obtained from Equation (13) versus d/R for Au, Si, and polystyrene. In the case of Au, a comparison of Figure 2a with Figure 2b shows that the rate of convergence is much faster with the asymmetric choice C2 of the coefficients. Actually, with the C2 choice, MSE_3 already differs from the energy exact values by less than one percent for all displayed separations: specifically, the maximum error is of 0.6% for $d/R = 1$, while for $d/R = 0.03$ the error is as small as 0.1%. In the case of Si, the performance of the choice C1 is better than that for C2. Indeed, with the C1 choice, the maximum error of MSE_4 is 0.8% for $d/R = 0.03$, while the minimum error is 0.2% for $d/R = 1$, while for the choice C2, the maximum error is 3.4% for $d/R = 1$. In the case of polystyrene, the performance of C1 case is amazingly good, since with MSE_3 the maximum error is 0.6% for $d/R = 1$, while for $d/R = 0.04$ the error is as low as 0.003%. For polystyrene, the rate of convergence of (C2) is instead quite poor.

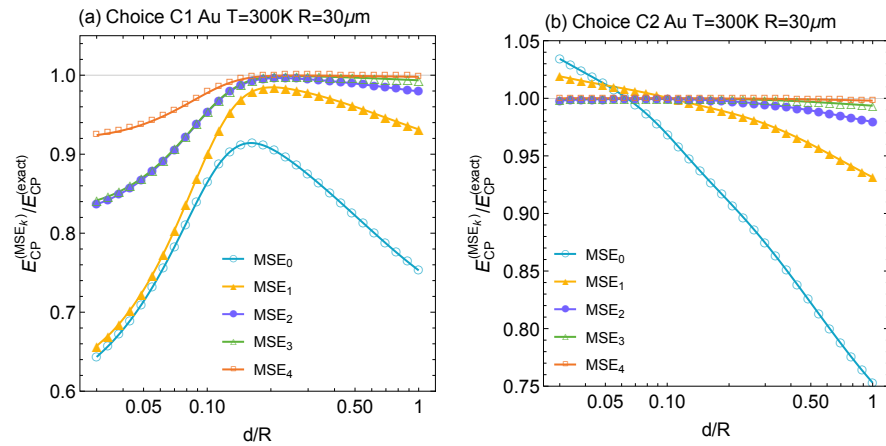


Figure 2. The ratio of MSE of the CP energy (7) up to the k -power of the kernel \mathbb{K} to the energy exact Formula (13) for an Au sphere of radius $R = 30 \mu\text{m}$ at room temperature versus d/R , where d is the distance from the surface, for (a) C1 and (b) C2 choices. See text for details.

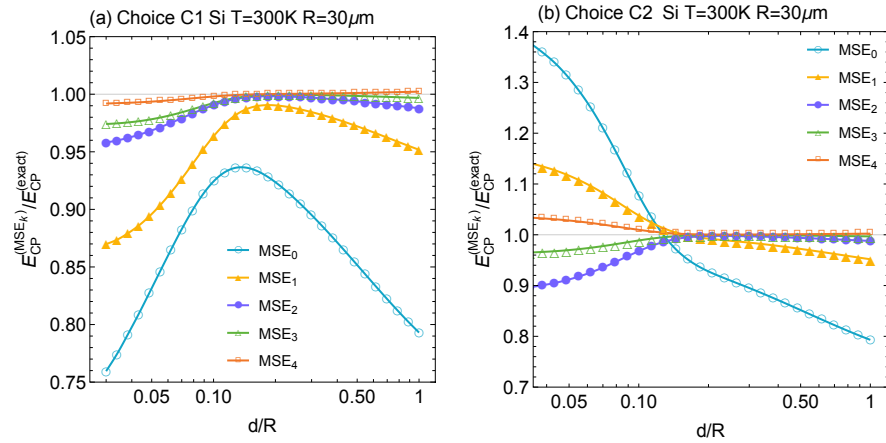


Figure 3. The ratio of MSE of the CP energy (7) up to the k -power of the kernel \mathbb{K} to the energy exact Formula (13) for a Si sphere of radius $R = 30 \mu\text{m}$ at room temperature versus d/R for (a) C1 and (b) C2 choices. See text for details.

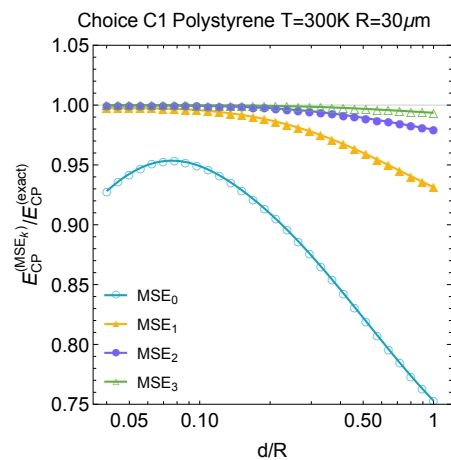


Figure 4. The ratio of MSE of the CP energy (7) up to the k -power of the kernel \mathbb{K} to the energy exact Formula (13) for a polystyrene sphere of radius $R = 30 \mu\text{m}$ at room temperature versus d/R , for C1 choice. See text for details.

4.3. CP Energy for a Cylinder

Within the scattering T-matrix approach, the CP interaction energy of a polarizable particle at distance d from the surface of an infinitely long cylinder of radius R with the permittivity $\epsilon_1 = \epsilon$ permeability $\mu_1 = \mu$ in vacuum ($\epsilon_0 = \mu_0 = 1$) is

$$\begin{aligned}
 E_{\text{CP}}^{(\text{exact})} &= \frac{k_B T}{\pi} \sum_{n=0}^{\infty} \kappa_n^2 \alpha(i\zeta_n) \int_{-\infty}^{\infty} dk_z \sum_{m=-\infty}^{\infty} \\
 &\times \left\{ T_{k_z m}^{\text{EE}}(i\zeta_n) \frac{1}{\kappa_n^2} \left[k_z^2 K_m'^2(p_0 a) + \left(\frac{m^2 k_z^2}{p_0^2 a^2} + p_0^2 \right) K_m^2(p_0 a) \right] \right. \\
 &- T_{k_z m}^{\text{HH}}(i\zeta_n) \left[K_m'^2(p_0 a) + \frac{m^2}{p_0^2 a^2} K_m^2(p_0 a) \right] \\
 &\left. + T_{k_z m}^{\text{EH}}(i\zeta_n) \frac{4mk_z}{\kappa_n p_0 a} K_m(p_0 a) K_m'(p_0 a) \right\}, \quad (17)
 \end{aligned}$$

where $a = R + d$, $p_0 = \sqrt{\kappa^2 + k_z^2}$, m is the multipole index, K_m is the modified Bessel function of second kind and K_m' its derivative, and $T_{k_z m}^{NM}$, ($N, M \in \{E, H\}$) are the T-matrix elements of a dielectric cylinder [48],

$$T_{k_z m}^{\text{HH}}(i\zeta) = -\frac{I_m(p_0 R)}{K_m(p_0 R)} \frac{\Delta_1 \Delta_4 + Y^2}{\Delta_1 \Delta_2 + Y^2}, \quad (18)$$

$$T_{k_z m}^{\text{EE}}(i\zeta) = -\frac{I_m(p_0 R)}{K_m(p_0 R)} \frac{\Delta_2 \Delta_3 + Y^2}{\Delta_1 \Delta_2 + Y^2}, \quad (19)$$

$$T_{k_z m}^{\text{HE}}(i\zeta) = -T_{k_z m}^{\text{EH}}(i\zeta) = \frac{Y}{\sqrt{\epsilon \mu} (p_0 R)^2 K_m(p_0 R)^2} \frac{1}{\Delta_1 \Delta_2 + Y^2}, \quad (20)$$

with I_m the modified Bessel function of first kind and

$$Y = \frac{mk_z}{\sqrt{\epsilon \mu} R^2 \kappa} \left(\frac{1}{p^2} - \frac{1}{p_0^2} \right), \quad (21)$$

with $p = \sqrt{\epsilon \mu \kappa^2 + k_z^2}$ and

$$\Delta_1 = \frac{I_m'(pR)}{pRI_m(pR)} - \frac{1}{\epsilon} \frac{K_m'(p_0 R)}{p_0 RK_m(p_0 R)}, \quad (22)$$

$$\Delta_2 = \frac{I_m'(pR)}{pRI_m(pR)} - \frac{1}{\mu} \frac{K_m'(p_0 R)}{p_0 RK_m(p_0 R)}, \quad (23)$$

$$\Delta_3 = \frac{I_m'(pR)}{pRI_m(pR)} - \frac{1}{\epsilon} \frac{I_m'(p_0 R)}{p_0 RI_m(p_0 R)}, \quad (24)$$

$$\Delta_4 = \frac{I_m'(pR)}{pRI_m(pR)} - \frac{1}{\mu} \frac{I_m'(p_0 R)}{p_0 RI_m(p_0 R)}. \quad (25)$$

To notice is that, in general, the polarization is *not conserved* under scattering, i.e., $T_{k_z m}^{\text{EH}} \neq 0 \neq T_{k_z m}^{\text{HE}}$. This property, together with its quasi-2D shape, makes the cylinder an important benchmark test for the convergence of the MSE.

The CP energy can be straightforwardly obtained as an MSE since the SSO \mathbb{K} and the operator \mathbb{M} can be computed by substituting for the free Green functions in Equations (5) and (6) an expansion in vector cylindrical waves. In Figure 5, we again show the numerical results for the ratio of the MSE for the CP energy $E_{\text{CP}}^{(\text{MSE}_k)}$ at MSE of the order k and the exact result for the CP energy $E_{\text{CP}}^{(\text{exact})}$ obtained from Equation (18). The materials, temperature, and geometric lengths are the same as in the case of a sphere. For Si, one observes that the MSE with the choice case C1 has converged at order MSE₃ to the energy exact calculations

within approximately 3%, with the largest deviations at the shortest (2.4%) and longest (3.3%) considered separation. The deviation is minimal at intermediate distances around $d/R = 0.2$, with an error of only 0.1%. Hence, the performance of the MSE for an infinite cylinder is quite similar to a compact sphere. We do not consider the coefficients from the C2 choice as they performed worse than the choice case C1 for a sphere. For polystyrene, we consider again only the choice case C1, for the same reason. Due to its low dielectric contrast, one expects the choice C1 to give good convergence of the MSE at low orders. Indeed, the rate of convergence is quite fast so that the MSE can be terminated at the order MSE_1 already, with a maximum deviation from the energy exact value of only 1.9% at the separation $d = R$. Let us note that, in general, that with the choice case C1, the lowest order MSE_0 , the estimate of the energy for the cylinder is not as good as that for the sphere. This is presumably due to arbitrarily long-range charge and current fluctuations along the cylinder, which require at least one power of the operator \mathbb{K} to be described properly.

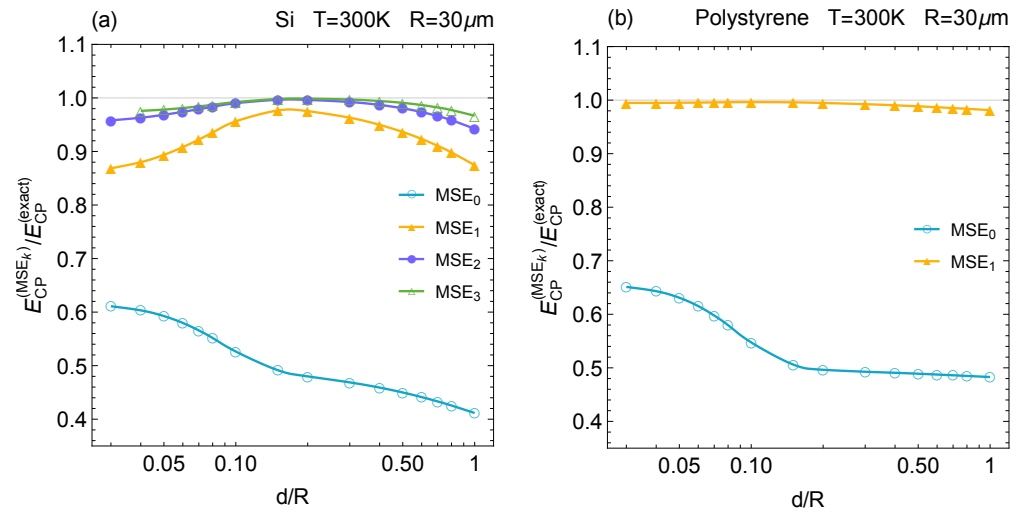


Figure 5. The ratio of MSE of the CP energy (7) up to the k -power of the kernel \mathbb{K} to the energy exact Formula (18) for (a) a Silicon cylinder and (b) a polystyrene cylinder of radius $R = 30 \mu m$ at room temperature $T = 300 K$, for the choice case C1. See text for details.

Finally, it is necessary to discuss the case of a metal, such as Au. As the dielectric function diverges in the limit $\kappa \rightarrow 0$, the classical term $n = 0$ of the Matsubara sum resembles that of a perfect conductor. We have shown that, for a cylinder, the SSO \mathbb{K} , for the choice case C1, in the partial wave channel $m = 0$, has an eigenvalue that approaches unity when $\kappa \rightarrow 0$ and $\epsilon \rightarrow \infty$ [44]. For the choice case C2 the situation is even worse as there is an eigenvalue approaching unity in all partial wave channels. This property is expected to persist for all quasi-2D shapes with a compact cross section. Hence, for such metallic shapes the classical term $n = 0$ cannot be obtained from an MSE. However, the surface scattering approach as developed by us is also useful for zero frequency $\kappa = 0$ as the inverse of $\mathbb{M} = \mathbb{I} - \mathbb{K}$ can be computed directly, without resorting to an MSE. We note that for $\kappa = 0$ the expression for \mathbb{K} simplifies considerably, in particular in the perfect conductor limit [44].

To conclude, we have demonstrated that the MSE provides an especially well-suited tool to compute Casimir–Polder interactions with high precision for a quite wide range of materials. Let us stress that this conclusion is not specific to the shapes considered here but is expected to hold generically for any compact 3D shape or quasi-2D shape. Here, we considered a sphere and a cylinder just because, for those shapes, the exact results are known and hence the convergence of our MSE can be tested. Most essentially, for general shapes where the T-matrix is not known the SSO \mathbb{K} can be computed and the MSE implemented to obtain high precision results for the interaction.

Author Contributions: Both authors contributed equally to this work. All authors have read and agreed to the published version of the manuscript.

Funding: This research received no external funding.

Data Availability Statement: No external data used.

Conflicts of Interest: The authors declare no conflict of interest.

References

- Casimir, H.B.G. On the attraction between two perfectly conducting plates. *Proc. Kon. Ned. Akad. Wetensch. B* **1948**, *51*, 793–795. Available online: <https://dwc.knaw.nl/DL/publications/PU00018547.pdf> (accessed on 6 January 2024).
- Lifshitz, E.M. The theory of molecular attractive force between solids. *Sov. Phys. JETP (J. Exp. Theoret. Phys.)* **1956**, *2*, 73–83. Available online: <http://jetp.ras.ru/cgi-bin/e/index/e/2/1/p73?a=list> (accessed on 6 January 2024).
- Deriaguin, B.V.; Abrikosova, I.I. Direct measurement of the molecular attraction of solid bodies. 1. Statement of the problem and method of measuring forces by using negative feedback. *Sov. Phys. JETP (J. Exp. Theoret. Phys.)* **1957**, *3*, 819–829. Available online: <http://jetp.ras.ru/cgi-bin/e/index/e/3/6/p819?a=list> (accessed on 6 January 2024).
- Parsegian, V.A. *Van der Waals Forces: A Handbook for Biologists, Chemists, Engineers, and Physicists*; Cambridge University Press: New York, NY, USA, 2006. [CrossRef]
- Klimchitskaya, G.L.; Mohideen, U.; Mostepanenko, V.M. The Casimir force between real materials: Experiment and theory. *Rev. Mod. Phys.* **2009**, *81*, 1827–1885. [CrossRef]
- Buhmann, S.Y. *Dispersion Forces. I: Macroscopic Quantum Electrodynamics and Ground-State Casimir, Casimir–Polder, and van der Waals Forces*; Springer: Berlin/Heidelberg, Germany, 2012. [CrossRef]
- Rodriguez, A.W.; Hui, P.C.; Woolf, D.P.; Johnson, S.G.; Loncar, M.; Capasso, F. Classical and fluctuation-induced electromagnetic interactions in micron-scale systems: Designer bonding, antibonding, and Casimir forces. *Ann. Phys.* **2014**, *527*, 45. [CrossRef]
- Woods, L.M.; Dalvit, D.A.R.; Tkatchenko, A.; Rodriguez-Lopez, P.; Rodriguez, A.W.; Podgornik, R. Materials perspective on Casimir and van der Waals interactions. *Rev. Mod. Phys.* **2016**, *88*, 045003. [CrossRef]
- Bimonte, G.; Emig, T.; Kardar, M.; Krüger, M. Nonequilibrium fluctuational quantum electrodynamics: Heat radiation, heat transfer, and force. *Annu. Rev. Condens. Matter Phys.* **2017**, *8*, 119–143. [CrossRef]
- Langbein, D. *Theory of van der Waals Attraction*; Springer: Berlin, Heidelberg, Germany, 1974. [CrossRef]
- Lamoreaux, S.K. Demonstration of the Casimir force in the 0.6 to 6 μm range. *Phys. Rev. Lett.* **1997**, *78*, 5–8. [CrossRef]
- Mohideen, U.; Roy, A. Precision measurement of the Casimir force from 0.1 to 0.9 μm . *Phys. Rev. Lett.* **1998**, *81*, 4549–4552. [CrossRef]
- Chan, H.B.; Aksyuk, V.A.; Kleiman, R.N.; Bishop, D.J.; Capasso, F. Quantum mechanical actuation of microelectromechanical systems by the Casimir force. *Science* **2001**, *291*, 1941–1944. [CrossRef]
- Bressi, G.; Carugno, G.; Onofrio, R.; Ruoso, G. Measurement of the Casimir force between parallel metallic surfaces. *Phys. Rev. Lett.* **2002**, *88*, 041804. [CrossRef]
- Decca, R.S.; López, D.; Fischbach, E.; Krause, D.E. Measurement of the Casimir force between dissimilar metals. *Phys. Rev. Lett.* **2003**, *91*, 050402. [CrossRef]
- Munday, J.N.; Capasso, F.; Parsegian, V.A. Measured long-range repulsive Casimir–Lifshitz forces. *Nature* **2009**, *457*, 170–173. [CrossRef] [PubMed]
- Sushkov, A.O.; Kim, W.J.; Dalvit, D.A.R.; Lamoreaux, S.K. Observation of the thermal Casimir force. *Nat. Phys.* **2011**, *7*, 230–233. [CrossRef]
- Tang, L.; Wang, M.; Ng, C.Y.; Nikolic, M.; Chan, C.T.; Rodriguez, A.W.; Chan, H.B. Measurement of non-monotonic Casimir forces between silicon nanostructures. *Nat. Photon.* **2017**, *11*, 97–101. [CrossRef]
- Emig, T.; Graham, N.; Jaffe, R.L.; Kardar, M. Casimir forces between arbitrary compact objects. *Phys. Rev. Lett.* **2007**, *99*, 170403. [CrossRef] [PubMed]
- Kenneth, O.; Klich, I. Casimir forces in a T-operator approach. *Phys. Rev. B* **2008**, *78*, 014103. [CrossRef]
- Rahi, S.J.; Emig, T.; Graham, N.; Jaffe, R.L.; Kardar, M. Scattering theory approach to electrodynamic Casimir forces. *Phys. Rev. D* **2009**, *80*, 085021. [CrossRef]
- Genet, C.; Lambrecht, A.; Reynaud, S. Casimir force and the quantum theory of lossy optical cavities. *Phys. Rev. A* **2003**, *67*, 043811. [CrossRef]
- Lambrecht, A.; Maia Neto, P.A.; Reynaud, S. The Casimir effect within scattering theory. *New J. Phys.* **2006**, *8*, 243. [CrossRef]
- Maghrebi, M.F.; Rahi, S.J.; Emig, T.; Graham, N.; Jaffe, R.L.; Kardar, M. Analytical results on Casimir forces for conductors with edges and tips. *Proc. Natl. Acad. Sci. USA* **2011**, *108*, 6867–6871. [CrossRef]
- Bimonte, G.; Emig, T. Exact results for classical Casimir interactions: Dirichlet and Drude model in the sphere-sphere and sphere-plane geometry. *Phys. Rev. Lett.* **2012**, *109*, 160403. [CrossRef] [PubMed]
- Schoger, T.; Ingold, G.L. Classical Casimir free energy for two Drude spheres of arbitrary radii: A plane-wave approach. *SciPost Phys. Core* **2021**, *4*, 011. [CrossRef]

27. Hartmann, M.; Ingol, G.L.; Maia Neto, P.A. Plasma versus Drude modeling of the Casimir force: Beyond the proximity force approximation. *Phys. Rev. Lett.* **2017**, *119*, 043901. [CrossRef] [PubMed]
28. Wang, M.; Tang, L.; Ng, C.Y.; Messina, R.; Guizal, B.; Crosse, J.A.; Antezza, M.; Chan, C.T.; Chan, H.B. Strong geometry dependence of the Casimir force between interpenetrated rectangular gratings. *Nat. Commun.* **2021**, *12*, 600. [CrossRef]
29. Banishev, A.A.; Wagner, J.; Emig, T.; Zandi, R.; Mohideen, U. Demonstration of angle-dependent Casimir force between corrugations. *Phys. Rev. Lett.* **2013**, *110*, 250403. [CrossRef]
30. Intravaia, F.; Koev, S.; Jung, I.W.; Talin, A.A.; Davids, P.S.; Decca, R.S.; Aksyuk, V.A.; Dalvit, D.A.R.; López, D. Strong Casimir force reduction through metallic surface nanostructuring. *Nat. Commun.* **2013**, *4*, 2515. [CrossRef]
31. Lambrecht, A.; Marachevsky, V.N. Casimir interaction of dielectric gratings. *Phys. Rev. Lett.* **2008**, *101*, 160403. [CrossRef]
32. Bender, H.; Stehle, C.; Zimmermann, C.; Slama, S.; Fiedler, J.; Scheel, S.; Buhmann, S.Y.; Marachevsky, V.N. Probing atom-surface interactions by diffraction of Bose-Einstein condensates. *Phys. Rev. X* **2014**, *4*, 011029. [CrossRef]
33. Antezza, M.; Chan, H.; Guizal, B.; Marachevsky, V.N.; Messina, R.; Wang, M. Giant Casimir torque between rotated gratings and the $\theta = 0$ anomaly. *Phys. Rev. Lett.* **2020**, *124*, 013903. [CrossRef]
34. Fosco, C.D.; Lombardo, F.C.; Mazzitelli, F.D. Proximity force approximation for the Casimir energy as a derivative expansion. *Phys. Rev. D* **2011**, *84*, 105031. [CrossRef]
35. Bimonte, G.; Emig, T.; Jaffe, R.L.; Kardar, M. Casimir forces beyond the proximity approximation. *Europhys. Lett. (EPL)* **2012**, *97*, 50001. [CrossRef]
36. Bimonte, G.; Emig, T.; Kardar, M. Material dependence of Casimir forces: Gradient expansion beyond proximity. *Appl. Phys. Lett.* **2012**, *100*, 074110. [CrossRef]
37. Bimonte, G. Going beyond PFA: A precise formula for the sphere-plate Casimir force. *Europhys. Lett.* **2017**, *118*, 20002. [CrossRef]
38. Reid, M.T.H.; White, J.; Johnson, S.G. Fluctuating surface currents: An algorithm for efficient prediction of Casimir interactions among arbitrary materials in arbitrary geometries. *Phys. Rev. A* **2013**, *88*, 022514. [CrossRef]
39. Chew, W.C.; Tong, M.S.; Hu, B. *Integral Equations Methods for Electromagnetic and Elastic Waves*; Springer Nature Switzerland AG: Cham, Switzerland, 2022. [CrossRef]
40. Volakis, S.K.; Sertel, K. *Integral Equations Methods for Electromagnetics*; SciTech Publishing: Raleigh, NC, USA, 2012.
41. Balian, R.; Duplantier, B. Electromagnetic waves near perfect conductors. I. Multiple scattering expansions. Distribution of modes. *Ann. Phys.* **1977**, *104*, 300–335. [CrossRef]
42. Balian, R.; Duplantier, B. Electromagnetic waves near perfect conductors. II. Casimir effect. *Ann. Phys.* **1978**, *112*, 165–208. [CrossRef]
43. Emig, T.; Bimonte, G. Multiple scattering expansion for dielectric Media: Casimir effect. *Phys. Rev. Lett.* **2023**, *130*, 200401. [CrossRef]
44. Bimonte, G.; Emig, T. Casimir and Casimir-Polder interactions for magneto-dielectric materials: Surface scattering expansion. *Phys. Rev. A* **2023**, *108*, 052807. [CrossRef]
45. Marachevsky, V.N. Casimir effect and quantum field theory in dielectrics. *Theor. Math. Phys.* **2002**, *131*, 468–482. [CrossRef]
46. Buhmann, S.Y.; Dung, H.T.; Welsch, D.G. The van der Waals energy of atomic systems near absorbing and dispersing bodies. *J. Opt. B Quantum Semiclass. Opt.* **2004**, *6*, S127–S135. [CrossRef]
47. Milton, K.A.; Parashar, P.; Pourtolami, N. Casimir-Polder repulsion: Polarizable atoms, cylinders, spheres and ellipsoids. *Phys. Rev. D* **2012**, *85*, 025008. [CrossRef]
48. Noruzifar, E.; Emig, T.; Mohideen, U.; Zandi, R. Collective charge fluctuations and Casimir interactions for quasi-one-dimensional metals. *Phys. Rev. B* **2012**, *86*, 115449. [CrossRef]
49. Contreras-Reyes, A.M.; Guérout, R.; Neto, P.A.M.; Dalvit, D.A.R.; Lambrecht, A.; Reynaud, S. Casimir-Polder interaction between an atom and a dielectric grating. *Phys. Rev. A* **2010**, *82*, 052517. [CrossRef]
50. Bimonte, G.; Emig, T.; Kardar, M. Casimir-Polder interaction for gently curved surfaces. *Phys. Rev. D* **2014**, *90*, 081702. [CrossRef]
51. Bimonte, G.; Emig, T.; Kardar, M. Casimir-Polder force between anisotropic nanoparticles and gently curved surfaces. *Phys. Rev. D* **2015**, *92*, 025028. [CrossRef]
52. Kristensen, P.T.; Beverungen, B.; Intravaia, F.; Busch, K. High-accuracy Casimir-Polder force calculations using the discontinuous Galerkin time-domain method. *Phys. Rev. B* **2023**, *108*, 205424. [CrossRef]
53. Müller, C. *Foundations of the Mathematical Theory of Electromagnetic Waves*; Springer: Berlin/Heidelberg, Germany, 1969. [CrossRef]
54. Decca, R.S.; Lopez, D.; Fischbach, E.; Klimchitskaya, G.K.; Krause, D.E.; Mostepanenko, V.M. Novel constraints on light elementary particles and extra-dimensional physics from the Casimir effect. *Eur. Phys. J. C* **2007**, *51*, 963–975. [CrossRef]

Disclaimer/Publisher's Note: The statements, opinions and data contained in all publications are solely those of the individual author(s) and contributor(s) and not of MDPI and/or the editor(s). MDPI and/or the editor(s) disclaim responsibility for any injury to people or property resulting from any ideas, methods, instructions or products referred to in the content.

Review

Casimir Physics beyond the Proximity Force Approximation: The Derivative Expansion

César D. Fosco¹, Fernando C. Lombardo^{2,3} and Francisco D. Mazzitelli^{1,*}

¹ Centro Atómico Bariloche, Instituto Balseiro, Comisión Nacional de Energía Atómica, Bariloche 8400, Argentina; fosco@cab.cnea.gov.ar

² Departamento de Física, Facultad de Ciencias Exactas y Naturales, Universidad de Buenos Aires, Buenos Aires 1428, Argentina; lombardo@df.uba.ar

³ Consejo Nacional de Investigaciones Científicas y Técnicas (CONICET), Instituto de Física de Buenos Aires (IFIBA), Universidad de Buenos Aires, Buenos Aires 1428, Argentina

* Correspondence: fdmazzi@cab.cnea.gov.ar

Abstract: We review the derivative expansion (DE) method in Casimir physics, an approach which extends the proximity force approximation (PFA). After introducing and motivating the DE in contexts other than the Casimir effect, we present different examples which correspond to that realm. We focus on different particular geometries, boundary conditions, types of fields, and quantum and thermal fluctuations. Besides providing various examples where the method can be applied, we discuss a concrete example for which the DE cannot be applied; namely, the case of perfect Neumann conditions in $2 + 1$ dimensions. By the same example, we show how a more realistic type of boundary condition circumvents the problem. We also comment on the application of the DE to the Casimir–Polder interaction which provides a broader perspective on particle–surface interactions.

Keywords: Casimir effect; derivative expansion; proximity force approximation; Casimir–Polder force

Citation: Fosco, C.D.; Lombardo, F.C.; Mazzitelli, F.D. Casimir Physics beyond the Proximity Force Approximation: The Derivative Expansion. *Physics* **2024**, *6*, 290–316. <https://doi.org/10.3390/physics6010020>

Received: 9 December 2023

Revised: 5 January 2024

Accepted: 8 January 2024

Published: 27 February 2024



Copyright: © 2024 by the authors. Licensee MDPI, Basel, Switzerland. This article is an open access article distributed under the terms and conditions of the Creative Commons Attribution (CC BY) license (<https://creativecommons.org/licenses/by/4.0/>).

1. Introduction

Casimir forces are one of the most intriguing macroscopic manifestations of quantum fluctuations in Nature. Their existence, first realized in the specific context of the interaction between the quantum electromagnetic (EM) field and the boundaries of two neutral bodies, manifests itself as an attractive force between them. That force depends, in an intricate manner, on the shape and EM properties of the objects. Since the discovery of this effect by Hendrik Casimir 75 years ago [1] this, and closely related phenomena, have been subjected to intense theoretical and experimental research [2–5]. The outcome of that work has not just revealed fundamental aspects of quantum field theory, but also subtle aspects of the models used to describe the EM properties of material bodies. Besides, it has become increasingly clear that this research has potential applications to nanotechnology.

Theoretical and experimental reasons have called for the calculation of the Casimir energies and forces for different geometries and materials [6], and with an ever increasing accuracy. The simplicity of the theoretical predictions when two parallel plates are involved, corresponds to a difficult experimental setup, due to alignment problems (in spite of this, the Casimir force for this geometry has been measured at the 10% accuracy level [7]). Equivalently, geometries which are more convenient from the experimental point of view, and allow for higher precision measurements, lead to more involved theoretical calculations. Such is the case of a cylinder facing a plane [8], or a sphere facing a plate, which is free from the alluded alignment problems [9–15].

From a theoretical standpoint, finding the dependence of the Casimir energies and forces on the geometry of the objects, poses an interesting challenge. Indeed, even when evaluating the self-energies which result from the coupling on an object to the vacuum

field fluctuations, results may be rather non-intuitive; as in the case of a single spherical surface [16].

For a long time, calculations attempting to find analytical results for the Casimir and related interactions had been restricted to using the so called proximity force approximation (PFA). In this approach, the interaction energies and the resulting forces are computed approximating the geometry by a collection of parallel plates and then adding up the contributions obtained for this approximate geometry. This procedure was presumed to work well enough, at least for smooth surfaces when they are sufficiently close to each other; in more precise terms: when the curvature radii of the surfaces R_i are much larger than the distance d between them. Indeed, this is the main content of the Derjaguin approximation (DA), developed by Boris Derjaguin in the 1930s [17–19], which is pivotal in the study of surface interactions, especially in the context of colloidal particles and biological cells. This approach has significant implications in understanding colloidal stability, adhesion, and thin film formation.

It is worth introducing some essentials of the DA, in particular, of the geometrical aspects involved. Assuming the interaction energy per unit area between two parallel planes at a distance h is known, and given by $E_{11}(h)$, the DA yields an expression for the interaction energy between two curved surfaces, U_{DA} [2,4,17–20]. Indeed,

$$U_{DA}(a) = 2\pi R_{\text{eff}} \int_a^{\infty} E_{11}(h) dh, \quad (1)$$

where a denotes the distance between the surfaces, R_1 and R_2 are their curvature radii (at the point of closest distance), while $R_{\text{eff}} = R_1 R_2 / (R_1 + R_2)$. It is rather straightforward to implement the approximation at the level of the force f_{DA} between surfaces:

$$f_{DA}(a) = 2\pi R_{\text{eff}} E_{11}(a). \quad (2)$$

This approximation is usually derived from a quite reasonable assumption, namely, that the interaction energy can be approximated by means of the PFA expression:

$$U_{\text{PFA}} = \int dS E_{11}. \quad (3)$$

Here, the surface integration may be performed over one of the participating surfaces, but it could also be over an imaginary, “interpolating surface”, which lies between them. The DA is obtained from the expression above, by approximating the surfaces by (portions of) the osculating spheres (with radii R_1 and R_2) at the point of closest approach.

Based on this hypothesis, on dimensional grounds one can expect the corrections to the PFA to be of order $\mathcal{O}(a/R_i)$. Note, however, that since the PFA had not been obtained as the leading-order term in a well-defined expansion, the approximation itself did not provide any quantitative method to assess the validity of that assumption.

A need for reliable measure of the accuracy of the results obtained using different methods became increasingly crucial, specially since the development of the “precision era” in the measurement of the Casimir forces [9–15]. It was in this context that the Derivative Expansion (DE) approach, was first introduced by us in 2011 [21], as a tool to assess the validity of the PFA, by putting it in the framework of an expansion, and to calculate corrections to the PFA using that very same expansion. When one realizes that the PFA had previously been proposed in contexts which are rather different to Casimir physics, it becomes clear that the improvement on the PFA which represents the DE may and does have relevance on those realms, regardless of them having an origin in vacuum fluctuations or not. Indeed, when one strips off the DE of the particularities of Casimir physics, one can see the ingredients that allowed one to implement it are also found, for example, in electrostatics, nuclear physics, and colloidal surface interactions.

Here, we present the essential features of the DE, its derivation, and consider some examples of its applications. The review is organized as follows. In Section 2, we recall

some aspects of the DA which stem from its application to nuclear and colloidal physics. We start with the DA not just for historical reasons, but also because we believe that this sheds light on some geometrical aspects of the approximation, in a rather direct way (like the relevance of curvature radii and distances).

Then, in Section 3, we introduce the DE in one of its simplest realizations, namely, in the context of electrostatics, for a system consisting of two conducting surfaces kept at different potentials [22]. We first evaluate the PFA in this example, and then introduce the DE as a method to improve on that approximation. In Section 4, we introduce a more abstract, and therefore more general, formulation of the DE [23]. By putting aside the particular features of a specific interaction, and keeping just the ones that are common to all of them, we are led to formulate the problem as follows: the DE is a particular kind of expansion of a functional having as argument a surface (or surfaces). We mean “functional” here in its mathematical sense: a function that assigns a number to a function or functions. We elucidate and demonstrate some of the aspects of the DE in this general context; the purpose of presenting those aspects are not just a matter of consistency or justification, but they also provide a concrete way of applying and implementing the DE to any example where it is applicable.

Then, in Section 5, we focus on the DE in the specific context of the Casimir interaction between surfaces, for perfect boundary conditions at zero temperature; i.e., vacuum fluctuations [21,24]. Then in Section 6 we review the extension of those results to the case of finite temperatures and real materials [25,26]. As we shall see, the temperature introduces another scale, which affects the form one must adopt for the different terms in the DE. Then we comment on an aspect which first manifests itself here: as it happens with any expansion, it is to be expected to break down for some specific examples, when the hypothesis that justified it are not satisfied. We show this for the case of the Casimir effect with Neumann conditions at finite temperatures [26,27]. We also show that the application of the DE to the EM field is free of this problem, if dissipative effects are included in the model describing the media [28].

The application of the DE to Casimir-Polder forces for atoms near smooth surfaces [29] is described in Section 7. Other alternatives to compute Casimir energies beyond PFA [30] are described in Section 8. Section 9 contains our conclusions.

2. Proximity Approximations in Nuclear and Colloidal Physics

The introduction of the Derjaguin Approximation (DA) to nuclear physics dates back to the seminal paper [31]. In this paper, the DA was rediscovered and applied to calculate nuclear interactions, starting with a Derjaguin-like formula for the surface interaction energies. The approach was based on a crucial “universal function”—a term referring here to the interaction energy between flat surfaces, calculated using a Thomas-Fermi approximation. In spite of the rather different context, the analogy with the approach followed in the DA becomes clear when one introduces three surfaces, the physical ones, Σ_L and Σ_R , and the intermediate one Σ which one uses to parametrize the interacting ones. Then, if the physical surfaces are sufficiently smooth, the interaction energy should, to a reasonable approximation, be described by the PFA, in a similar fashion as in Equation (3). To render the assertion above more concrete, we yet again use the function $h : \Sigma \rightarrow \mathbb{R}$, measuring the distance between Σ_L and Σ_R at each point on Σ . Since h will have level sets which are, except for a zero measure set, one-dimensional (closed curves), and the interaction depends just on h , the PFA expression for the interaction energy U may be rendered as a one-dimensional integral:

$$U_{\text{PFA}} = \int dh J(h) E_{\parallel}(h), \quad (4)$$

where $J(h)dh$ is the infinitesimal area between two level curves on Σ : the ones between h and $h + dh$, while E_{\parallel} is the universal function.

We now assume that Σ is a plane, and that the physical surfaces may be both described by means of just one Monge patch based on Σ . This surface is then naturally thought of (in descriptive geometry terms) as the projection plane. Using Cartesian coordinates $(x_1, x_2) \equiv \mathbf{x}_\parallel$ on Σ , assuming (for smooth enough surfaces) that J may be regarded as constant, and using a second-order Taylor expansion of h around a (the distance of closest approach):

$$h(\mathbf{x}_\parallel) \simeq a + \frac{1}{2} \left(\frac{x_1^2}{R_1} + \frac{x_2^2}{R_2} \right) \quad (5)$$

produces, when evaluating the PFA interaction energy (4), the DA energy (1). Here, R_1 and R_2 are the radii of curvature of the surface by $x_3 = h(\mathbf{x}_\parallel)$ at $x_3 = a$.

This result may be improved, even within the spirit of the PFA, by introducing some refinements. Indeed, in Ref. [32], a generalization of the PFA has been introduced such that the starting point was Equation (4), but now allowing for the surfaces to have larger curvatures, as long as they remained almost parallel locally. The main difference that follows from those weaker assumptions is that, now, the Jacobian J may become a non-trivial function of h . For instance, introducing a linear expansion:

$$J(h) \approx J_0 + J_1 h, \quad (6)$$

a straightforward calculation shows that the force f becomes:

$$f_{\text{PFA}}(a) = J_0 E_{\parallel}(a) - J_1(a) \int_a^{\infty} dh E_{\parallel}(h). \quad (7)$$

Note that the result is the sum of the DA term plus a second term proportional to the derivative of the Jacobian with respect to h . This is a correction to the DA obtained from the same starting point we used for the DA: U_{PFA} . In other words, Equation (7) is still determined by the energy density for parallel plates. As we shall see, the DE will introduce corrections that go beyond $E_{\parallel}(a)$. The correction will depend on both the geometry and the nature of the interaction.

We wish to point out that the lack of knowledge of an exact expression for E_{\parallel} is not specific to nuclear physics, but of course it may appear in other applications. The general PFA approach can nevertheless be introduced; the accuracy of its predictions will then be limited not just by the fulfillment or not of the geometrical assumptions, but also by the reliability of the expression for E_{\parallel} . Using different approximations for E_{\parallel} gives as many results for the PFA. For a recent review in the case of nuclear physics, see Refs. [33,34].

An apparently unrelated approximation, based on different physical assumptions, was introduced in the context of colloidal physics. Let us now see how it yields a result which agrees with the DA: it is the so called Surface Element Integration (SEI) [35], or Surface Integration Approach (SIA) [36]. This approach may be introduced as follows: let us consider a compact object facing the $x_3 = 0$ plane. x_3 is then the normal coordinate to the plane, pointing towards the compact object. With this conventions, the SEI approximation applied to the interaction energy amounts to the following:

$$U_{\text{SEI}} = - \int_{\text{plane}} dx_1 dx_2 \frac{\hat{n} \cdot \hat{e}_3}{|\hat{n} \cdot \hat{e}_3|} E_{\parallel}. \quad (8)$$

Here \hat{n} denotes the outwards pointing unit normal to each surface element of the object. We see that, when the compact object may be thought of as delimited by just two surfaces, one of them facing the plane and the other away from it, the SEI consists of the difference between the PFA energies of those surfaces. This (possibly startling) fact is, as we shall see, related to the fact that the SEI becomes exact for almost transparent bodies, a situation characterized by the fact that the interaction is the result of adding all the (volumetric) pairwise contributions.

In the context of colloidal physics, the SEI method relies heavily upon the existence of a pressure on the compact object. The effect of that pressure should be integrated over the closed surface surrounding the compact object, in order to find the total force [35]. An alternative route to understand the SEI is to show that Equation (8) becomes exact when the interaction between macroscopic bodies is the superposition of the interactions for the pair potentials of their constituents [36]. That may be interpreted by using a simple example. Consider two media, one of them, the left medium L , corresponding to the $x_3 \leq 0$ half-space, while the right medium, R , is defined as the region:

$$R = \{(x_1, x_2, x_3) : \psi_1(\mathbf{x}_{||}) \leq x_3 \leq \psi_2(\mathbf{x}_{||})\}. \quad (9)$$

The interaction energy U is a functional of the two functions $\psi_{1,2}$. When the media are diluted, we expect the interaction energy to have the form

$$U[\psi_1, \psi_2] = \int d^2\mathbf{x}_{||} (E_{||}(\psi_1) - E_{||}(\psi_2)), \quad (10)$$

where $E_{||}(a)$ is the interaction energy per unit area, between two half-spaces at a distance a . This formula can be interpreted as follows: to obtain the interaction energy for the configuration described by ψ_1 and ψ_2 , one must certainly subtract from $E_{||}(\psi_1)$ the contributions from $x_3 > \psi_2$. This “linearity” is expected to be valid only for dilute media, and in that situation it coincides with the result obtained using the SEI. One expects then the SEI to give an exact result for almost-transparent media, for which the superposition principle holds true, and the total interaction energy is due to the sum of all the different pairwise potentials [36]. It is worth noting, at this point, the important fact that the PFA also becomes exact in Casimir physics when the media constituting the objects are dilute. Indeed, this has been pointed out in Refs. [37,38].

The examples just described illustrate the relevance of the DA, and of some of its variants, to different areas of physics. At the same time, the main drawback is made rather evident: in spite of being based on reasonable physical assumptions, it is difficult to assess its validity. The reason for this difficulty is that the approximation is uncontrolled, and therefore the estimation of the error incurred is difficult, within a self-contained approach.

The DE provides a systematic method to improve the PFA, and to compute its next-to-leading-order (NTLO) correction in a consistent set up.

3. Introducing the Derivative Expansion

3.1. The PFA in an Electrostatic Example

We introduce the PFA, and then the DE, in an example which neatly illustrates the DE main aspects, in the context of electrostatics. Here, contrary to what happens when dealing with more involved systems, like, say, Van der Waals, nuclear or Casimir forces, the physical assumptions and their implementations are more transparent. We follow closely Ref. [22]

The set-up we want to describe consists of two perfectly-conducting surfaces, one of them an infinite grounded plane and the other a smoothly curved surface kept at an electrostatic potential V_0 . We use coordinates such that the plane corresponds to $z = 0$ while the smooth surface is such that it can be described by a single function, namely, by an equation of the form $z = \psi(x_{||})$. The electrostatic energy contained between surfaces can then be written as follows:

$$U = \frac{\epsilon_0}{2} \int d^2\mathbf{x}_{||} \int_0^{\psi(x_{||})} dz |\mathbf{E}|^2, \quad (11)$$

where ϵ_0 denotes the permittivity of vacuum. In terms of U and V_0 , the capacitance C of the system is then given by $C = 2U/V_0^2$.

Let us see how one implements the PFA in order to calculate U (from which one can extract, for instance, an approximate expression for C) expecting it to be accurate when

the distance between the two surfaces is shorter than the curvature radius of the curved conductor. To that end, one first finds an approximation to the electric field between the conductors, by proceeding as follows: the smooth conductor is regarded as a set of parallel plates (Figure 1), in the sense that the electric field \mathbf{E} points along the z direction and has a z -independent value. The electric field does, however, depend on $x_{||}$ since it is assumed to have, for every $x_{||}$, the same intensity as the electric field due to two (infinite) conducting planes at a distance $\psi(x_{||})$. Namely, $\mathbf{E}(x) = -V_0/\psi(x_{||}) \hat{\mathbf{z}}$. Therefore, the approximated expression for the electrostatic energy becomes:

$$U_{\text{PFA}} = \frac{\epsilon_0 V_0^2}{2} \int d^2 \mathbf{x}_{||} \frac{1}{\psi(x_{||})}. \quad (12)$$

It is implicitly understood in the equation above, that the region to integrate is such that the assumption on the distance and curvature is satisfied. On the contrary, regions such that the assumption is not satisfied can be consistently ignored (see the example below).

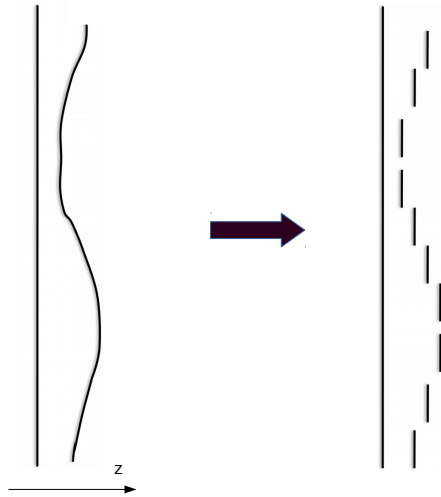


Figure 1. In the PFA, the interaction between a smoothly curved surface and a plane is approximated by that of a set of parallel plates. For each pair of parallel plates, border effects are ignored.

It should be evident that Equation (12) provides a rather convenient tool to obtain estimates for the electrostatic energy in many relevant situations. Indeed, to illustrate this point we consider a cylinder of length L and radius R in front of a plane, and denote by a the minimum distance between the two surfaces. The cylinder is not a surface that can be described by a single patch; namely, one needs at least two functions. However, in the context of the PFA, it is reasonable to assume that only the half that is closer to the plane should be relevant. Assuming the axis of the cylinder to be along y , the function ψ reads:

$$\psi(x) = a + R \left(1 - \sqrt{1 - \frac{x^2}{R^2}} \right), \quad (13)$$

with the variable x assumed to be in the range $-x_M < x < x_M < R$. Note that for $x_M/R = \mathcal{O}(1) < 1$ the assumption on the distance and the curvature is satisfied. It is to be expected that, as long as $R \gg a$ (where the PFA gives an accurate value of the electrostatic energy), the final result will not depend on x_M . This can be readily checked by inserting Equation (13) into Equation (12), computing the integral, and expanding that result for $a \ll R$. Doing this we obtain:

$$U_{\text{PFA}}^{\text{cp}} \approx \frac{\epsilon_0 V_0^2 L \pi}{\sqrt{2}} \sqrt{\frac{R}{a}}, \quad (14)$$

which is independent of x_M . An immediate consequence of this is that, when the cylinder approaches the plane, the electrostatic force behaves as $a^{-3/2}$.

Let us check now the accuracy of $U_{\text{PFA}}^{\text{CP}}$. We take advantage of the knowledge of the exact expression for the electrostatic interaction energy:

$$U^{\text{CP}} = \frac{\pi L \epsilon_0 V_0^2}{\text{arccosh}(1 + \frac{a}{R})}. \quad (15)$$

For $a/R \ll 1$, U^{CP} yields the PFA result $U_{\text{PFA}}^{\text{CP}}$ (14). The relevance of the corrections to the PFA can be estimated by expanding the exact result, but keeping also the next-to-leading order (NTLO) when $a \ll R$:

$$U^{\text{CP}} \approx \frac{\epsilon_0 V_0^2 L \pi}{\sqrt{2}} \sqrt{\frac{R}{a}} \left(1 + \frac{1}{12} \frac{a}{R}\right). \quad (16)$$

We will now introduce the DE. By construction, it should produce the NTLO result (for this and other surfaces), without resorting to the expansion of any exact expression (the knowledge of which, needless to say, is usually lacking).

3.2. Improvement of the PFA Using a Derivative Expansion

We begin by noting that the electrostatic energy is a functional of the function which defines the shape of the surface. A second observation is that, in principle, there is no reason to assume that the functional is local in ψ . Here, “local” means that it contains just one integral over \mathbf{x}_{\parallel} of a sum of terms involving powers of $\psi(\mathbf{x}_{\parallel})$ and derivatives at $\psi(\mathbf{x}_{\parallel})$. On the contrary, the exact functional will generally involve terms where, for example, there are two or more integrals over \mathbf{x}_{\parallel} , and kernels depending of those variables, and products of ψ with different arguments. However, regardless of the non locality of the exact expression, it must become local when the surfaces are sufficiently smooth and close to each other. Indeed, if the PFA becomes valid asymptotically in that limit, then the energy must approach a result which is a local function of ψ . Not whatever local functional but just one without derivatives.

The way we found to depart slightly but significantly from the PFA, has been to add terms involving derivatives of ψ . Namely, we shall assume that the electrostatic energy can be expanded in local terms involving derivatives of ψ . One can think of the condition $|\nabla\psi| \ll 1$, as introducing a small, dimensionless expansion parameter. In physical terms, this means that the curved surface is almost parallel to the plane on the points where it is satisfied.

To introduce the first departure from the PFA, we include terms with up to two derivatives. Then the electrostatic energy has to be (up to this order) of the form:

$$U_{\text{DE}} \simeq \int d^2\mathbf{x}_{\parallel} \left[V(\psi) + Z(\psi) |\nabla\psi|^2 \right], \quad (17)$$

for some functions V and Z . The gradient is the two-dimensional one, and it can only appear in such a way that the energy is a scalar (ψ is a scalar under changes of coordinates on the plane). Besides, recalling the equations of electrostatics, and on dimensional grounds, the result must be proportional to $\epsilon_0 V^2$. On top of that it must reproduce U_{PFA} for constant ψ . Furthermore, as ψ is the only other dimensionful quantity, both functions V and Z have to be proportional to ψ^{-1} . Thus, we have restricted even further the functional to:

$$U_{\text{DE}} \simeq \frac{\epsilon_0 V_0^2}{2} \int d^2\mathbf{x}_{\parallel} \frac{1}{\psi} (1 + \beta_E |\nabla\psi|^2), \quad (18)$$

where β_E is a numerical coefficient to be determined (the subindex E stands for electrostatics). It is worth stressing that β_E is independent of the specific surface being considered, as long as it is smooth. Therefore, it can be obtained once and for all just from its evaluation

for a particular case. A simple procedure to obtain the coefficient β_E , when an exact analytic solution to the problem is known, would be to retrieve its value by expanding that solution. Let us do that for the configuration of a cylinder in front of a plane. Inserting Equation (13) into Equation (18), and performing the integrals, an expansion of the result in powers of a/R , allow us to fix β_E . Indeed, in order to agree with the expansion of the exact result in Equation (16), this fixes its value to $\beta_E = 1/3$. Of course, one will obtain the same value for any other particular example for which the exact solution was known.

It is worthy of noting that, since the DE is a perturbative approach, it should be desirable to have a perturbative method to calculate the coefficient β_{EM} . In other words, to compute it from first principles, using the appropriate expansion. One can do that, for instance, by solving perturbatively the Laplace equation and then resorting to the method described in Section 5. We have performed that calculation in Ref. [22], and refer the reader to that work for details, and also for the application of the DE to other electrostatic examples.

3.3. Two Smooth Surfaces

As a natural generalization of the previously discussed situation, let us now consider two surfaces described by the two functions $\psi_1(\mathbf{x}_\parallel)$ and $\psi_2(\mathbf{x}_\parallel)$, each one of them measuring the respective height of a surface with respect to a reference plane Σ . This geometry was first considered in the context of the DE for the Casimir effect in Ref. [24].

To construct the DE for the electrostatic energy in this case, we keep up to two derivatives of the functions. This allows we to write the general expression:

$$U_{DE}[\psi_1, \psi_2] = \int_{\Sigma} d^2\mathbf{x}_\parallel U_\parallel(\psi) \left[1 + \beta_1 |\nabla\psi_1|^2 + \beta_2 |\nabla\psi_2|^2 + \beta_\times \nabla\psi_1 \cdot \nabla\psi_2 + \beta_- \hat{\mathbf{z}} \cdot \nabla\psi_1 \times \nabla\psi_2 + \dots \right], \quad (19)$$

where $\psi = |\psi_2 - \psi_1|$ is the height difference, $U_\parallel(\psi) = \epsilon_0 V_0^2 / (2\psi)$ is the electrostatic energy between parallel plates, and the dots denote higher derivative terms. Equation (19) actually contains four numerical constants: β_1 , β_2 , β_\times , and β_- . However, symmetry considerations imply some constraints on them: the energy must be invariant under the interchange of ψ_1 and ψ_2 , since that is just a relabeling: $\beta_1 = \beta_2$ and $\beta_- = 0$. Furthermore, in order to reproduce the result for a single smooth surface in front of a plane we must have $\beta_1 = \beta_2 = 1/3$. The coefficient β_\times can be determined taking into account that the energy should be invariant under a simultaneous rotation of both surfaces [24]. Indeed, for an infinitesimal rotation of each surface by an angle ϵ in the plane (x, z) , the changes induced on the functions ψ_i are $\delta\psi_i = \epsilon(x + \psi_i \partial_x \psi_i)$, for $i = 1, 2$. To simplify the determination of β_\times we can assume that, initially, $\psi_1 = 0$ and that ψ_2 is only a function of x . Computing explicitly the variation of U_{DE} to linear order in ϵ one can show that

$$\delta U_{DE} = 0 \Rightarrow \beta_\times = 1/3, \quad (20)$$

and therefore

$$U_{DE}[\psi_1, \psi_2] = \frac{\epsilon_0 V_0^2}{2} \int_{\Sigma} d^2\mathbf{x}_\parallel \frac{1}{\psi} \left[1 + \frac{1}{3} \left(|\nabla\psi_1|^2 + |\nabla\psi_2|^2 + \nabla\psi_1 \cdot \nabla\psi_2 \right) \right]. \quad (21)$$

Note that, by taking the variation of the electrostatic energy Equation (19) with respect to translations or rotations of one of the surfaces, one can obtain the vertical and lateral components of the force, as well as the torque, due to the remaining surface.

The identities $\beta_1 = \beta_2$ and $\beta_- = 0$ are universally valid, regardless of the interaction (as long as the surfaces are of an identical nature), but $\beta_\times = \beta_1$ holds true for the electrostatic interaction. This depends upon the fact that the leading term is proportional to ψ^{-1} (i.e., it is then not valid for the Casimir energy).

For later use, let us recall that, for a general function $E_{ii}(\psi)$, the relation between the different coefficients becomes [24]:

$$2(\beta_1 + \beta_2) + 2\beta_\times + \psi \frac{d \log E_{ii}}{d\psi} = 1. \tag{22}$$

The relation (22) shows that, for any interaction, the DE for the interaction energy between two curved surfaces can be reduced to the problem of a single surface in front of a plane. Indeed, in the later case one can determine β_1 and β_2 , while Equation (22) determines the remaining coefficient β_\times .

To summarize: when computing the electrostatic energy associated with a configuration of two conductors at different potentials, with smoothly curved surfaces, one can go beyond the PFA by simply assuming that the energy admits an expansion in derivatives of the functions that define the shapes of the conductors. If the exact electrostatic energy for a single non trivial curved configuration is known, one can determine all the free parameters in the expansion.

Finally, the NTLO correction produces an appreciable improvement in the DA and, by the same token, also provides an assessment for its validity. An interesting alternative approach to compute electrostatic forces beyond the PFA can be found in Ref. [39].

4. Obtaining the DE from a Perturbative Expansion

Regardless of the interaction considered, the DA and its improvement, the DE, can be obtained by performing the proper resummation of a perturbative expansion [23]. The required expansion is in powers of the departure of the surfaces, about a two flat parallel planes configuration. This connection yields a systematic and quite general approach to obtain the DE, even when an exact solution is not available.

To keep things general, we work with a general functional of the surface; that functional may correspond to an energy, free energy, force, etc. Besides, we do not make any assumption about the kind of interaction involved, not even about whether it satisfies a superposition principle or not.

To begin, let us we assume a geometry where there are two surfaces, one of which, L , is a plane, which with a proper choice of Cartesian coordinates (x_1, x_2, x_3) , is described by $x_3 = 0$. The other one, R , is assumed to be describable by $x_3 = \psi(\mathbf{x}_{ii})$.

The object for which we implement the approximation is denoted by $F[\psi]$, a functional of ψ . Then we note that the PFA for F , to be denoted here by F_0 , is obtained as follows: add, for each \mathbf{x}_{ii} , the product of a local surface density $\mathcal{F}_0(\psi(\mathbf{x}_{ii}))$ depending only on the value of ψ at the point \mathbf{x}_{ii} , times the surface element area; namely,

$$F_0[\psi] = \int d^2\mathbf{x}_{ii} \mathcal{F}_0(\psi(\mathbf{x}_{ii})). \tag{23}$$

The surface density is, in turn, determined by the (assumed) knowledge of the exact form of F for the case of two parallel surfaces, as follows:

$$\mathcal{F}_0(a) = \lim_{S \rightarrow \infty} \frac{F[a]}{S}, \tag{24}$$

where S denotes the area of the L plate and a is a constant. Namely, to determine the density one needs to know the functional F just for constant functions $\psi \equiv a$. Note that, if the functional F is the interaction energy between the surfaces, \mathcal{F}_0 becomes the interaction energy per unit area E_{ii} , and F_0 becomes U_{PFA} (see Equation (3)).

Let us now show how to derive the PFA (and its corrections) by the resummation of a perturbative expansion. To that end, we evaluate F for a ψ having the form:

$$\psi(\mathbf{x}_{ii}) = a + \eta(\mathbf{x}_{ii}). \tag{25}$$

and write the resulting perturbative expansion in powers of η , which has the general form:

$$F[\psi] = \mathcal{S}\mathcal{F}_0(a) + \sum_{n \geq 1} \int \frac{d^2 k_{\parallel}^{(1)}}{(2\pi)^2} \dots \frac{d^2 k_{\parallel}^{(n)}}{(2\pi)^2} \delta(k_{\parallel}^{(1)} + \dots + k_{\parallel}^{(n)}) h^{(n)}(k_{\parallel}^{(1)}, \dots, k_{\parallel}^{(n)}) \tilde{\eta}(k_{\parallel}^{(1)}) \dots \tilde{\eta}(k_{\parallel}^{(n)}), \quad (26)$$

where $\delta(\cdot)$ is the Dirac delta function, and the form factors $h^{(n)}$ can be computed by using perturbative techniques. For the Dirichlet-Casimir effect, this can be done in a rather systematic way [40]. Although the approach to follow in order to obtain those form factors may depend strongly on the kind of system considered, the form of the expansion shall be the same. Note that the form factors may depend on a , although, in order to simplify the notation, we will not make that dependence explicit.

Up to now, we have not used the hypothesis of smoothness of the R surface. We do that now by assuming that the Fourier transform $\tilde{\eta}$ is peaked at the zero momentum. What follows is to make use of this assumption for all terms in the expansion. In Equation (26), we set then: $h^{(n)}(k_{\parallel}^{(1)}, \dots, k_{\parallel}^{(n)}) \simeq h^{(n)}(0, \dots, 0)$, and, as a consequence:

$$F(\psi) \simeq \mathcal{S}\mathcal{F}_0(a) + \sum_{n \geq 1} h^{(n)}(0, \dots, 0) \int d^2 \mathbf{x}_{\parallel} [\eta(\mathbf{x}_{\parallel})]^n. \quad (27)$$

One could evaluate the form factors at the zero momentum straightforwardly. However, there is a shortcut here that allows one to obtain all of them immediately: consider a constant $\eta(\mathbf{x}_{\parallel}) = \eta_0$, so that the interaction energy is given by Equation (27) with the replacement $\int d^2 \mathbf{x}_{\parallel} \eta(\mathbf{x}_{\parallel})^n \rightarrow \mathcal{S}\eta_0^n$. For this particular case, F becomes just the functional corresponding to parallel plates, which are separated by a distance $a + \eta_0$:

$$\mathcal{F}_0(a + \eta_0) = \mathcal{F}_0(a) + \sum_{n \geq 1} h^{(n)}(0, \dots, 0) \eta_0^n. \quad (28)$$

We then conclude that, in this low-momentum approximation, the series can be summed up with the result:

$$F_0[\psi] \simeq \int d^2 \mathbf{x}_{\parallel} \mathcal{F}_0(a + \eta(\mathbf{x}_{\parallel})) = \int d^2 \mathbf{x}_{\parallel} \mathcal{F}_0(\psi), \quad (29)$$

which is just the PFA.

The calculation just above shows that, for the class of geometries considered in this paper, the PFA can be justified from first principles as the result of a resummation of a perturbative calculation corresponding to almost flat surfaces. In order to be well defined, the PFA requires that the form factors $h^{(n)}(k_{\parallel}^{(1)}, \dots, k_{\parallel}^{(n)})$ have a finite limit as $k_{\parallel}^{(i)} \rightarrow 0$.

This procedure also suggests how the PFA could be improved; one can include the NTLO terms in the low-momentum expansions of the form factors. We assume that they can be expanded in powers of the momenta up to the second order. We stress that this is by no means a trivial assumption. Indeed, depending on the the interaction considered, the form factors could include nonanalyticities (we will discuss some explicit examples below). In case of no nonanalyticities, one can introduce the expansions:

$$h^{(n)}(k_{\parallel}^{(1)}, \dots, k_{\parallel}^{(n)}) = h^{(n)}(0, \dots, 0) + \sum_{i,\alpha} A_{i\alpha}^{(n)} k_{\parallel\alpha}^{(i)} + \sum_{i,j,\alpha,\beta} B_{ij\alpha\beta}^{(n)} k_{\parallel\alpha}^{(i)} k_{\parallel\beta}^{(j)} \dots, \quad (30)$$

for some a -dependent coefficients $A_{i\alpha}^{(n)}$ and $B_{ij\alpha\beta}^{(n)}$. Here $i, j = 1, \dots, n$ label arguments while $\alpha, \beta = 1, 2$ label their components. Symmetry considerations are crucial, since they allow us to simplify the above expression (30), as follows: rotational invariance implies that the form factors depend only on the scalar products $k_{\parallel}^{(i)} \cdot k_{\parallel}^{(j)}$. Additionally, they have to be symmetric under the interchange of any two momenta. This thus leads to

$$h^{(n)}(k_{\parallel}^{(1)}, \dots, k_{\parallel}^{(n)}) = h^{(n)}(0, \dots, 0) + B^{(n)} \sum_i k_{\parallel}^{(i)2} + C^{(n)} \sum_{i \neq j} k_{\parallel}^{(i)} \cdot k_{\parallel}^{(j)}, \quad (31)$$

for some coefficients $B^{(n)}$ and $C^{(n)}$.

Inserting Equation (31) into Equation (26) and taking integrations by parts, one then finds the form of the first correction to the PFA:

$$F_2[\psi] = \int d^2\mathbf{x}_\parallel \left[\sum_{n \geq 2} D^{(n)} \eta^{n-2} \right] |\nabla \eta|^2, \quad (32)$$

where the coefficients $D^{(n)}$ are linear combinations of $B^{(n)}$ and $C^{(n)}$. The subindex 2 in F indicates that this is the part of the functional containing two derivatives.

We complete the calculation by calculating the sum in Equation (32). To that end, we evaluate the correction F_2 for a particular case: $\eta(\mathbf{x}_\parallel) = \eta_0 + \epsilon(\mathbf{x}_\parallel)$, with $\epsilon \ll \eta_0$, and expand up to the second order in ϵ . Thus,

$$F_2[a + \eta_0 + \epsilon] = \int d^2\mathbf{x}_\parallel \left[\sum_{n \geq 2} D^{(n)} \eta_0^{n-2} \right] |\nabla \epsilon|^2. \quad (33)$$

The resummation can be obtained in this case, by considering the usual perturbative evaluation of the interaction energy up to second order in ϵ . This evaluation does, naturally, depend on the interaction considered, but, once one has that result one can obtain the sum of the series above. We will denote by Z that sum, namely:

$$Z(a + \eta_0) \equiv \sum_{n \geq 2} D^{(n)} \eta_0^{n-2}. \quad (34)$$

Upon replacement $\eta_0 \rightarrow \eta$ in Equation (34), one obtains

$$F_2[\psi] = \int d^2\mathbf{x}_\parallel Z(\psi) |\nabla \psi|^2. \quad (35)$$

This is the NTLO correction to the PFA. This concludes our systematic derivation of the PFA, including its first correction, a result which may be put as follows:

$$F_{\text{DE}}[\psi] = \int d^2\mathbf{x}_\parallel \left[V(\psi) + Z(\psi) |\nabla \psi|^2 \right], \quad (36)$$

where $V(\psi) = \mathcal{F}_0(\psi)$ is determined from the (known) expression for the interaction energy between parallel surfaces, while $Z(\psi)$ can be computed using a perturbative technique. In practice, $Z(\psi)$ can be evaluated setting $\eta_0 = 0$ in Equation (34).

The higher orders may be derived by an extension of the procedure described just above. It should be evident that, for the expansion to be well-defined, the analytic structure of the form factors is quite relevant. Indeed, the existence of nonanalytic zero-momentum contributions can render the DE non applicable. This should be expected on physical grounds, since the presence of nonanalytic terms implies that the functional cannot be approximated, in coordinate space, by the single integral of a local density. Physically, it is a signal that the nonlocal aspects of the interaction cannot be ignored. That should not come up as a surprise, when one recalls that the same kind of phenomenon does happen when evaluating the effective action in quantum field theory, and the quantum effects contain contributions due to virtual massless particles. In this case, the effective action may develop nonanalyticities at zero momentum.

The main messages of this Section are the following: irrespective of the nature of the interaction, the energy and forces between objects are functionals of their shapes. The PFA is recovered when the form factors of the functionals are evaluated at zero momentum. Enhancements to this approximation are achievable by expanding these form factors at low momenta. If the expansion is analytic, a resummation of the form factors produces the DE.

5. DE for the Zero-Temperature Casimir Effect

The application of the DE to the Casimir interaction energy between two objects was, actually, our original motivation to introduce the approximation, and it is useful briefly review some aspects of this application here. We consider first a real vacuum scalar field satisfying Dirichlet boundary conditions (Section 5.1) and then we move to the EM field with perfect-conductor boundary conditions (Section 5.2). We follow Ref. [21] for the derivation of the DE in the Dirichlet case.

5.1. Scalar Field with Dirichlet Boundary Conditions

We consider here a massless real scalar field φ in $3 + 1$ dimensions, coupled to two mirrors which impose Dirichlet boundary conditions. In our Euclidean conventions, we use x_0, x_1, x_2, x_3 to denote the spacetime coordinates, x_0 being the imaginary time. As before, the mirrors occupy two surfaces, denoted by L and R , defined by the equations $x_3 = 0$ and $x_3 = \psi(\mathbf{x}_\parallel)$, respectively.

On only dimensional grounds, and using natural units ($\hbar \equiv c \equiv 1$), the DE approximation to the interaction energy to be of the form

$$E_{DE} = -\frac{\pi^2}{1440} \int d^2\mathbf{x}_\parallel \frac{1}{\psi^3} [\alpha_D + \beta_D(\partial_\alpha\psi)^2], \tag{37}$$

where α_D and β_D are dimensionless coefficients that do not depend on the geometry. The subindex D stands for Dirichlet. An evaluation of the above expression for parallel plates fixes $\alpha_D \equiv 1$. As in the electrostatic case, the coefficient β_D could be computed from explicit examples where the interaction energy is known exactly.

Let us recall, from Section 4, that the interaction energy can also be computed from an expansion of the Casimir energy in powers of η for

$$\psi(\mathbf{x}_\parallel) = a + \eta(\mathbf{x}_\parallel), \tag{38}$$

where a (assumed to be greater than zero) is the spatial average of ψ whereas η contains its varying piece. The expansion needed is of the second order in η , and with up to two spatial derivatives.

To obtain such an expansion, we start from a rather general yet formal expression for the energy (for earlier perturbative computations of the Casimir force see, for example, Refs. [41,42]). That formal expression follows from the functional approach to the Casimir effect, where we deal with \mathcal{Z} , the zero-temperature limit of a partition function. That partition function, for a scalar field in the presence of two Dirichlet mirrors is given by

$$\mathcal{Z} = \int \mathcal{D}\varphi \delta_L(\varphi) \delta_R(\varphi) e^{-S_0(\varphi)}, \tag{39}$$

with S denoting the real scalar field free (Euclidean) action

$$S_0(\varphi) = \frac{1}{2} \int d^4x (\partial\varphi)^2, \tag{40}$$

while the δ_L and δ_R impose Dirichlet boundary conditions on the L and R surface, respectively.

The vacuum energy, E , is then obtained as follows:

$$E = -\lim_{T \rightarrow \infty} \log \mathcal{Z} / T, \tag{41}$$

where T is the extent of the time dimension (or β^{-1} , in a thermal partition function setting). We discard from E the terms that do not contribute to the Casimir interaction energy between the two surfaces. These terms will appear as factors in \mathcal{Z} ; among them the one describing the zero point energy of the field in the absence of the plates, and also the

‘self-energy’ contributions, due to the vacuum distortion produced by each mirror, even when the other is infinitely far apart.

Exponentiating the two Dirac delta functions by introducing two auxiliary fields, λ_L and λ_R , we obtain for \mathcal{Z} an equivalent expression:

$$\mathcal{Z} = \int \mathcal{D}\varphi \mathcal{D}\lambda_L \mathcal{D}\lambda_R e^{-S(\varphi; \lambda_L, \lambda_R)}, \tag{42}$$

with

$$S(\varphi; \lambda_L, \lambda_R) = S_0(\varphi) - i \int d^4x \varphi(x) \left[\lambda_L(x_{||}) \delta(x_3) + \lambda_R(x_{||}) \sqrt{g_R(\mathbf{x}_{||})} \delta(x_3 - \psi(\mathbf{x}_{||})) \right]$$

where we have introduced $x_{||} \equiv (x_0, x_1, x_2) = (x_0, \mathbf{x}_{||})$. The factor depending on the determinant of the induced metric on the R , $g_R(\mathbf{x}_{||}) \equiv 1 + |\nabla\psi(\mathbf{x}_{||})|^2$ makes the expression above reparametrization invariant. However, by a redefinition of the auxiliary field λ_R one gets rid of that factor, at the expense of generating a Jacobian. That Jacobian does not depend on the distance between the two surfaces, since only derivatives of ψ are involved. Therefore it will not contribute to the Casimir interaction energy and thus we shall subsequently ignore such factor, as well as others that will appear in the course of the calculations.

Integrating out φ , we see that \mathcal{Z}_0 , corresponding to the field φ in the absence of boundary conditions factors out, while the rest becomes an integral over the auxiliary fields:

$$\mathcal{Z} = \mathcal{Z}_0 \int \mathcal{D}\lambda_L \mathcal{D}\lambda_R e^{-\frac{1}{2} \int d^3x_{||} \int d^3y_{||} \sum_{\alpha, \beta} \lambda_\alpha(x_{||}) \mathbb{T}_{\alpha\beta} \lambda_\beta(y_{||})}, \tag{43}$$

with:

$$\mathcal{Z}_0 = \int \mathcal{D}\varphi e^{-S_0(\varphi)}, \tag{44}$$

and $\alpha, \beta = L, R$. We have introduced the objects:

$$\mathbb{T}_{LL}(x_{||}, y_{||}) = \langle x_{||}, 0 | (-\partial^2)^{-1} | y_{||}, 0 \rangle, \tag{45}$$

$$\mathbb{T}_{LR}(x_{||}, y_{||}) = \langle x_{||}, 0 | (-\partial^2)^{-1} | y_{||}, \psi(\mathbf{y}_{||}) \rangle, \tag{46}$$

$$\mathbb{T}_{RL}(x_{||}, y_{||}) = \langle x_{||}, \psi(\mathbf{x}_{||}) | (-\partial^2)^{-1} | y_{||}, 0 \rangle, \tag{47}$$

$$\mathbb{T}_{RR}(x_{||}, y_{||}) = \langle x_{||}, \psi(\mathbf{x}_{||}) | (-\partial^2)^{-1} | y_{||}, \psi(\mathbf{y}_{||}) \rangle, \tag{48}$$

where we use a ‘bra-ket’ notation to denote matrix elements of operators, and ∂^2 is the four-dimensional Laplacian. Thus, for example,

$$\langle x | (-\partial^2)^{-1} | y \rangle = \int \frac{d^4k}{(2\pi)^4} \frac{e^{ik \cdot (x-y)}}{k^2}. \tag{49}$$

A subtraction of the zero point contribution contained in \mathcal{Z}_0 leads to:

$$E = \lim_{T \rightarrow \infty} \left(\frac{1}{2T} \text{Tr} \log \mathbb{T} \right), \tag{50}$$

which still contains self-energies. Up to now, we have obtained a formal expression for the vacuum energy; let us now proceed to evaluate its DE.

We need to expand E to the second order in η , keeping up to the second order term in an expansion in derivatives. It is convenient to do so first for $\Gamma \equiv \frac{1}{2} \text{Tr} \log \mathbb{T}$. Namely,

$$\Gamma(a, \eta) = \Gamma^{(0)}(a) + \Gamma^{(1)}(a, \eta) + \Gamma^{(2)}(a, \eta) + \dots \tag{51}$$

where the upper index denotes the order in derivatives. Each term will be a certain coefficient times the spatial integral over $\mathbf{x}_{||}$ of a local term, depending on a and on η -derivatives. Additionally, because the configuration is time-independent, they should be

proportional to T (a factor that will cancel out). Expanding first the matrix \mathbb{T} in powers of η

$$\mathbb{T} = \mathbb{T}^{(0)} + \mathbb{T}^{(1)} + \mathbb{T}^{(2)} + \dots, \quad (52)$$

we obtain: $\Gamma = \Gamma^{(0)} + \Gamma^{(1)} + \Gamma^{(2)} + \dots$,

$$\begin{aligned} \Gamma^{(0)} &= \frac{1}{2} \text{Tr} \log \mathbb{T}^{(0)}, \\ \Gamma^{(1)} &= \frac{1}{2} \text{Tr} \log \left[(\mathbb{T}^{(0)})^{-1} \mathbb{T}^{(1)} \right], \\ \Gamma^{(2)} &= \frac{1}{2} \text{Tr} \log \left[(\mathbb{T}^{(0)})^{-1} \mathbb{T}^{(2)} \right] - \frac{1}{4} \text{Tr} \log \left[(\mathbb{T}^{(0)})^{-1} \mathbb{T}^{(1)} (\mathbb{T}^{(0)})^{-1} \mathbb{T}^{(1)} \right], \end{aligned} \quad (53)$$

where, in $\Gamma^{(l)}$, we need to keep up to l derivatives of η .

Then, the zeroth-order term is obtained as follows: replace ψ by a constant, a , and then subtract from the result its $a \rightarrow \infty$ limit (this gets rid of self-energies). This leads to:

$$\Gamma^{(0)}(a) = \frac{1}{2} \text{Tr} \log \left[1 - (T_{LL}^{(0)})^{-1} T_{LR}^{(0)} (T_{RR}^{(0)})^{-1} T_{RL}^{(0)} \right]. \quad (54)$$

Here, the $T_{\alpha\beta}^{(0)}$ are identical to the ones for two flat parallel mirrors separated by a distance a .

Taking the trace, leads to:

$$\Gamma^{(0)} = \frac{T}{2} \int d^2 \mathbf{x}_{\parallel} \int \frac{d^3 k_{\parallel}}{(2\pi)^3} \log[1 - e^{-2k_{\parallel} a}]. \quad (55)$$

Then, we recall the general derivation to note that the replacement $a \rightarrow \psi$ leads to:

$$\begin{aligned} E^{(0)} &= \frac{1}{2} \int d^2 \mathbf{x}_{\parallel} \int \frac{d^3 k_{\parallel}}{(2\pi)^3} \log[1 - e^{-2k_{\parallel} \psi(\mathbf{x}_{\parallel})}] \\ &= -\frac{\pi^2}{1440} \int d^2 \mathbf{x}_{\parallel} \frac{1}{\psi(\mathbf{x}_{\parallel})^3}, \end{aligned} \quad (56)$$

which is the PFA expression for the vacuum energy.

To improve on the previous result, we consider its first non trivial correction. There can be no first order term because of symmetry considerations. while to terms contribute to the second order

$$\Gamma^{(2)} = \Gamma^{(2,1)} + \Gamma^{(2,2)}, \quad (57)$$

where,

$$\Gamma^{(2,1)} = \frac{1}{2} \text{Tr} \log \left[(\mathbb{T}^{(0)})^{-1} \mathbb{T}^{(2)} \right] \quad (58)$$

and

$$\Gamma^{(2,2)} = -\frac{1}{4} \text{Tr} \log \left[(\mathbb{T}^{(0)})^{-1} \mathbb{T}^{(1)} (\mathbb{T}^{(0)})^{-1} \mathbb{T}^{(1)} \right]. \quad (59)$$

In the terms above, we have to keep just up to two derivatives of η . We see that, in Fourier space, and before implementing any expansion in momentum (derivatives), they have the structure:

$$\Gamma^{(2,j)} = \frac{T}{2} \int \frac{d^2 \mathbf{k}_{\parallel}}{(2\pi)^2} f^{(2,j)}(\mathbf{k}_{\parallel}) |\tilde{\eta}(\mathbf{k}_{\parallel})|^2 \quad (60)$$

($j = 1, 2$), with $\tilde{\eta}$ denoting the Fourier transform of η , and with the $f^{(2,j)}$ kernels denoting the $k_0 \rightarrow 0$ (i.e., static) limits of the more general expressions:

$$\begin{aligned} f^{(2,1)}(k_{||}) &= - \int \frac{d^3 p_{||}}{(2\pi)^3} \frac{|p_{||}| |p_{||} + k_{||}|}{1 - e^{-2|p_{||} + k_{||}|a}}, \\ f^{(2,2)}(k_{||}) &= - \int \frac{d^3 p_{||}}{(2\pi)^3} \frac{|p_{||}| |p_{||} + k_{||}| e^{-2|p_{||} + k_{||}|a} (1 + e^{-2|p_{||}|a})}{(1 - e^{-2|p_{||}|a})(1 - e^{-2|p_{||} + k_{||}|a})}. \end{aligned}$$

By subtracting all the a -independent contributions, one finds:

$$\Gamma^{(2)} = \frac{T}{2} \int \frac{d^2 \mathbf{k}_{||}}{(2\pi)^2} f^{(2)}(\mathbf{k}_{||}) |\tilde{\eta}(\mathbf{k}_{||})|^2 \quad (61)$$

with:

$$f^{(2)}(k_{||}) = -2 \int \frac{d^3 p_{||}}{(2\pi)^3} \frac{|p_{||}| |p_{||} + k_{||}|}{(1 - e^{-2|p_{||}|a})(e^{2|p_{||} + k_{||}|a} - 1)}. \quad (62)$$

The low-momentum behaviour of $f^{(2)}$ determines whether the DE can be applied or not. In this case, the function is analytic and therefore a local expansion of the vacuum energy exists. We need to extract its \mathbf{k}^2 order term in a Taylor expansion at zero momentum, namely $f^{(2)}(\mathbf{k}_{||}) \simeq \chi \mathbf{k}_{||}^2$. We find:

$$\chi = -\frac{\pi^2}{1080 a^3}. \quad (63)$$

Thus,

$$\begin{aligned} \Gamma^{(2)}(a, \eta) &= -\frac{T}{2} \frac{\pi^2}{1080} \int \frac{d^2 \mathbf{k}_{||}}{(2\pi)^2} \frac{\mathbf{k}_{||}^2}{a^3} |\tilde{\eta}(\mathbf{k}_{||})|^2 \\ &= -\frac{T}{2} \frac{\pi^2}{1080} \int d^2 \mathbf{x}_{||} \frac{1}{a^3} (\partial_\alpha \eta)^2. \end{aligned} \quad (64)$$

Therefore, the NTLO term in the DE becomes:

$$E^{(2)} = \frac{\Gamma^{(2)}(\psi)}{T} = -\frac{1}{2} \frac{\pi^2}{1080} \int d^2 \mathbf{x}_{||} \frac{(\partial_\alpha \psi)^2}{\psi^3}, \quad (65)$$

where the index α runs from 1 to 2.

Putting together the terms up to second order,

$$E_{\text{DE}} \equiv E^{(0)} + E^{(2)} = -\frac{\pi^2}{1440} \int d^2 \mathbf{x}_{||} \frac{1}{\psi^3} \left[1 + \frac{2}{3} (\partial_\alpha \psi)^2 \right]. \quad (66)$$

The leading-order term above is the Casimir energy according to the PFA, while the second order one represents the first significant deviation from it. We note that the structure of both terms had been anticipated by dimensional analysis and symmetry considerations. The overall normalization, on the other hand, had been fixed by our previous knowledge of the (well-established) result for parallel plates.

We would like to insist on the fact that the relative weight between the PFA and its correction term—the factor $\beta_{\text{D}} = 2/3$ —is independent of the surface geometry. This value of β_{D} has been independently corroborated in concrete examples by expanding the exact Casimir energy expressions. Interesting cases among them are, for example, either a sphere or a cylinder positioned in front of a plane.

We conclude this Section with an application of the DE to the particular geometry of a sphere in front of a plane. Let us express the function ψ of Equation (13) in polar coordinates ρ , with R the radius of the sphere and d the distance to the plane. The function $\psi(\rho)$ describes an hemisphere when $0 \leq \rho \leq R$. By inserting the expression of ψ into the

DE for the Casimir energy, it becomes possible to explicitly calculate the integrals, to get a rather compact analytical expression:

$$E_{DE} = E_{PFA} \left(1 + \frac{1}{3} \frac{a}{R} \right), \tag{67}$$

where $E_{PFA} = -\hbar c \pi^3 R / (1440 a^2)$.

5.2. The EM Case

The results for the scalar field satisfying Dirichlet boundary conditions, described in Section 5.1 above, have been generalized to different boundary conditions and fields. Results for the EM field case and two curved surfaces have been presented in Ref. [24]. Note that, as pointed out at the end of Section 3.3, symmetry considerations allow for the two-surface problem to be reduced to the one of a curved surface facing a plane, namely, the geometry we have just dealt with in the Dirichlet case above. Indeed, as shown in Ref. [24], the extension of Ref. [21] to two curved surfaces is restricted among other things by the tilt invariance of the reference plane, to which the two surfaces can be projected. This served as a rigorous test for the self-consistency of perturbative results.

Venturing beyond the scalar Dirichlet (D) case of Ref. [21], they calculated the DE for Neumann (N), mixed D/N, and electromagnetic (EM) (perfect metal) surfaces. Interestingly, they observed that the EM correction must align with the sum of D and N corrections. They also replicated previous findings for cylinders under D, N, and mixed D/N conditions, as well as for the sphere with D boundary conditions. However, their calculations did not confirm previous results for the sphere/plane geometry, either with N or EM boundary conditions. Indeed, the results for β were found to disagree with those obtained from Refs. [43–45]. This discrepancy was later resolved in Ref. [46] in favour of the results in Ref. [24].

Another interesting concrete example presented in Ref. [24] is the DE for two spheres of radii R_1 and R_2 , both imposing the same boundary conditions. It was found there that

$$E = E_{PFA} \left[1 - \frac{a}{R_1 + R_2} + (2\beta - 1) \left(\frac{a}{R_1} + \frac{a}{R_2} \right) \right], \tag{68}$$

where $E_{PFA} = -(\alpha \pi^3 R_1 R_2) / [1440 a^2 (R_1 + R_2)]$; a is chosen to be the distance of closest separation, and β is a number that depends on the type of boundary condition, as can be seen from Table 1. $\alpha = \alpha_{EM} = 2$ in the EM boundary conditions case. The corresponding formula for the sphere/plane case can be obtained by taking one of the two radii to infinity (in fact it coincides with the D case in Equation (67) when $\alpha = \alpha_D = 1$ and $\beta = \beta_D = 2/3$).

A rather different example corresponds to two circular cylinders (with identical boundary conditions) whose axes are inclined at a relative angle θ . Using the DE, the interaction Casimir energy reads:

$$E = -\frac{\alpha \pi^3 \sqrt{R_1 R_2}}{1440 a^2 \sin \theta} \left[1 + \left(\beta - \frac{3}{8} \right) \frac{a}{R_1 + R_2} \right]. \tag{69}$$

For this particular geometry, the interaction energy has been computed numerically in Ref. [47]. The numerical results reproduce Equation (69) at short distances.

The results obtained for the β -coefficients in each case are summarized in Table 1.

Having presented in this Section a derivation and some interesting results obtained by applying the DE to the Casimir effect at zero temperature and for perfect boundary conditions, we present in the rest of the review some generalizations and applications.

Table 1. β coefficient from (68) for the following five cases: a scalar field obeying Dirichlet (D) or Neumann (N) boundary conditions on both surfaces, or D boundary condition on one surface and N boundary condition on the other, or vice versa, and for the electromagnetic (EM) field with ideal metal boundary conditions [24].

β_D	β_N	β_{DN}	β_{ND}	β_{EM}
2/3	$2/3(1 - 30/\pi^2)$	2/3	$2/3 - 80/7\pi^2$	$2/3(1 - 15/\pi^2)$

6. Finite Temperature, Nonanalyticities, and DE

The DE can be extended to the finite temperature case [25,26,28], the free energy being the relevant functional to approximate. There are at least two reasons why this extension is not trivial: firstly, the temperature introduces a dimensionful magnitude, and this will reflect itself in the form of the DE (part of it was fixed by dimensional analysis). Second, a known phenomenon in quantum field theory at finite temperature is the so-called “dimensional reduction”, by which a bosonic model which is defined in $d + 1$ dimensions at zero temperature, becomes effectively d -dimensional at high temperatures. The DE should therefore manifest (and interpolate between) those two cases.

We first describe, in Section 6.1, the results for a scalar field satisfying Dirichlet conditions [26] in $d + 1$ dimensions. Then, Section 6.2 discusses the appearance of nonanalyticities for Neumann boundary conditions [26,27]. Finally, we comment on the results for the EM field with imperfect boundary conditions [25,28] (Section 6.3) and on semianalytic formula for plane–sphere geometry (Section 6.4).

6.1. Dirichlet Boundary Conditions

In the finite-temperature case, and for the same geometry that we have considered in the zero temperature case, the functions $V(\psi)$ and $Z(\psi)$ cannot be completely determined from dimensional analysis alone. Indeed, on general grounds, we can assert that the Casimir free energy in $d + 1$ dimensions, if the DE is applicable, must have the form:

$$F_{DE}[\psi] = \int d^{d-1} \mathbf{x}_\parallel \left\{ b_0 \left(\frac{\psi}{\beta}, d \right) \frac{1}{[\psi(\mathbf{x}_\parallel)]^d} + b_2 \left(\frac{\psi}{\beta}, d \right) \frac{(\nabla\psi)^2}{[\psi(\mathbf{x}_\parallel)]^d} \right\}, \tag{70}$$

where b_0 and b_2 are dimensionless and depends on the ratio of the local distance between surfaces ψ and the inverse temperature β . They can be obtained from the knowledge of the Casimir free energy for small departures around $\psi(\mathbf{x}_\parallel) = a = \text{constant}$. They are given by [26]

$$b_0(\xi) = \frac{\xi}{2} \sum_{n=-\infty}^{\infty} \int \frac{d^{d-1} \mathbf{p}_\parallel}{(2\pi)^{d-1}} \log \left(1 - e^{-2\sqrt{(2\pi n\xi)^2 + (\mathbf{p}_\parallel)^2}} \right), \tag{71}$$

$$b_2(\xi) = \frac{1}{2} \left[\frac{\partial F^{(2)}(\xi, n, \mathbf{l}_\parallel)}{\partial |\mathbf{l}_\parallel|^2} \right]_{n \rightarrow 0, |\mathbf{l}_\parallel| \rightarrow 0}, \tag{72}$$

where

$$F^{(2)}(\xi; n, |\mathbf{l}_\parallel|) = -2\xi \sum_{m=-\infty}^{+\infty} \int \frac{d^{d-1} \mathbf{p}_\parallel}{(2\pi)^{d-1}} \left\{ \frac{\sqrt{(2\pi m\xi)^2 + \mathbf{p}_\parallel^2}}{1 - \exp \left[-2\sqrt{(2\pi m\xi)^2 + \mathbf{p}_\parallel^2} \right]} \times \frac{\sqrt{(2\pi(m+n)\xi)^2 + (\mathbf{p}_\parallel + \mathbf{l}_\parallel)^2}}{\exp \left\{ 2\sqrt{[2\pi(m+n)\xi]^2 + (\mathbf{p}_\parallel + \mathbf{l}_\parallel)^2} \right\} - 1} \right\}. \tag{73}$$

In the zero-temperature limit, the Matsubara sum becomes an integral that can be analytically computed. The results are described in Table 2. The ratio b_2/b_0 tends to 1 for large values of d .

Table 2. Values of the ratio $b_2(d)/b_0(d)$ for different dimensions. The ratio tends to 1 for $d \rightarrow \infty$. See text for details.

Dimension	$b_2(d)/b_0(d)$	Approximate Value
$d = 1$	$\frac{1}{\pi^2} \left(1 + \frac{\pi^2}{3} \right)$	0.435
$d = 2$	$\frac{1+6\zeta(3)}{12\zeta(3)}$	0.569
$d = 3$	$2/3$	0.667
$d = 4$	$\frac{-\zeta(3)+10\zeta(5)}{12\zeta(5)}$	0.737
$d = 5$	$\frac{10\pi^2-21}{10\pi^2}$	0.787
$d = 6$	$\frac{-2\zeta(5)+7\zeta(7)}{6\zeta(7)}$	0.824

In the high temperature limit, we find

$$\begin{aligned} [b_0(\xi, d)]_{\xi \gg 1} &\simeq \xi [b_0(\xi, d - 1)]_{\xi \rightarrow 0} \equiv \xi b_0(d - 1), \\ [b_2(\xi, d)]_{\xi \gg 1} &\simeq \xi [b_2(\xi, d - 1)]_{\xi \rightarrow 0} \equiv \xi b_2(d - 1), \end{aligned} \tag{74}$$

where $\xi = \psi/\beta$. The coefficients $b_0(d - 1)$ and $b_2(d - 1)$ agree with those for perfect mirrors at zero temperature, but in $d - 1$ dimensions, i.e., the “dimensional reduction” effect.

An interesting result is found when this is applied to the (Dirichlet) Casimir interaction for a system consisting of a sphere in front of an infinite plane. Denoting by a the distance between the surfaces, and by R the radius of the sphere, we get for the free energy at high temperatures:

$$F_{DE}[\psi]_{|\psi/\beta \gg 1, d=3} \sim -\frac{\zeta(3)R}{8\beta a} \left(1 - \frac{1}{6\zeta(3)} \frac{a}{R} \log\left(\frac{a}{R}\right) \right). \tag{75}$$

We see that the R/a^2 -behavior corresponding to the dominant contribution at zero temperature changes to $R/a\beta$ in the high temperature case. This could be expected on dimensional grounds, if one assumes that the free energy is linear in the temperature in this limit. Note that the same problem has been exactly solved in Ref. [48], and one can show that Equation (75) does agree with the small-distance expansion obtained from the exact solution.

It is worth to remark that the NTLO correction from the DE becomes nonanalytic, because of the integration, in the ratio a/R . This behavior has been observed in numerical calculations of the Casimir interaction energy for this geometry, in the infinite temperature limit, for the electromagnetic case (see Refs. [48,49]). It is important to recognize that this nonanalyticity has nothing to do with the nonanalyticity in momenta of the form factors described in Section 4, and is a non trivial prediction of the DE.

6.2. Neumann Boundary Conditions

This case, discussed in Ref. [27], highlights a potential warning to the applicability of the DE, already mentioned previously: the appearance of nonanalyticities in the form factors. To begin with, we deal with the zero temperature case in $2 + 1$ dimensions, since the nonanalyticity appears because of the existence of a Matsubara mode which behaves as a massless field in $2 + 1$ dimensions, with Neumann boundary conditions.

The free Euclidean action for the vacuum (i.e., $T = 0$) field φ is given by

$$S_0 = \frac{1}{2} \int d^3x (\partial\varphi)^2, \tag{76}$$

and, instead of imposing perfect Neumann boundary conditions on the surfaces, we add the following action to describe the interaction between the vacuum field and the mirrors:

$$\mathcal{S}_I[\varphi] = \frac{1}{2\bar{\mu}} \int d^3x \left[\delta(x_2)(\partial_2\varphi(x))^2 + \sqrt{g(x_{\parallel})}\delta(x_2 - \psi(x_{\parallel}))(\partial_n\varphi(x))^2 \right]. \quad (77)$$

The constant $\bar{\mu}$, which has the dimensions of a mass, is used to impose Neumann boundary conditions in the $\bar{\mu} \rightarrow 0$ limit. We use the same $\bar{\mu}$ on both L and R mirrors, since we will assume them to have identical properties, differing just in their position and geometry.

The DE approximation to the Casimir energy can be computed following standard steps. The result reads, in the limit $\bar{\mu}\psi \rightarrow 0$ [27],

$$E_{DE}[\psi] = -\frac{1}{16\pi} \int_{-\infty}^{\infty} dx_1 \frac{1}{\psi(x_1)^2} \left[\zeta(3) + \log[\bar{\mu}\psi(x_1)] \left(\frac{d\psi(x_1)}{dx_1} \right)^2 \right]. \quad (78)$$

In the expression above, the first term is the PFA contribution while the second one is a non trivial correction to it, and depends on the shape of the boundary (defined by ψ). It is then clear that, as this equation shows, the DE is well posed when imposing imperfect Neumann boundary conditions in 2 + 1 dimensions. On the contrary, it cannot be applied when the boundary conditions become perfect ($\bar{\mu} = 0$). The reason is that the hypothesis of analyticity in momentum, used to derive the DE, is clearly violated. The non-existence of a local expansion is due to the existence of massless modes, allowed by Neumann boundary conditions.

At finite temperatures, a 3 + 1 dimensional theory may be decomposed into the sum of an infinite tower of decoupled 2 + 1 dimensional Matsubara modes, each one satisfying N boundary conditions, and with a mass $\frac{2n\pi}{\beta}$, $n = 0, 1, 2, \dots$. The existence of the massless $n = 0$ mode (the only one surviving in the high temperature limit) means that analyticity will be lost in 3 + 1 dimensions, for any non zero temperature. That is indeed the case [26]. We summarize here some of the main features of that example: the free energy in the $d + 1$ dimensional Neumann case can again be written as before (see Equation (70), but with coefficients c_0 and c_2 instead of b_0 and b_2 . The zero order term coincides with the one for the Dirichlet case; namely: $c_0 = b_0$.

When $d = 3$, the NTLO term contains, besides a local term, a nonlocal contribution which is linear in T , and thus present for any $T > 0$. Hence, there is no local DE for perfect Neumann boundary conditions at $d = 2$ at zero temperature and for $d = 3$ at any finite temperature. Indeed, an expansion for small values of $|k_{\parallel}|$ of the form factor contains, in addition to a term proportional to k_{\parallel}^2 , one proportional to $(Ta)k_{\parallel}^2 \log(k_{\parallel}^2 a^2)$.

6.3. The Electromagnetic Case for Imperfect Boundary Conditions

We have seen that, for a real scalar field in the presence of Neumann boundary conditions, the DE cannot be applied when in 2 + 1 dimensions at zero temperature, or in 3 + 1 dimensions at a non-zero temperature [26]. The reason is that, as we have shown, nonanalyticities in the form factors appear. We have shown that the nonanalyticity could be cured by introducing a small departure from perfect Neumann conditions [27]. It is natural to wonder whether the nonanalyticities could also be cured by a similar approach for the EM field in 3 + 1 dimensions at finite temperatures. We know, based on the insight obtained from Ref. [27], that nonanalyticities are originated in contributions due to dimensionally reduced massless modes: zero Matsubara frequency terms. To obtain an answer to this question, in Ref. [28] we singled out in detail the zero-mode contributions to the free energy, for a media described by non trivial permittivity $\epsilon(\omega)$ and permeability $\mu(\omega)$ functions.

We start from the free energy F for the EM field, which can be written in terms of the partition function $\mathcal{Z}(\psi)$, as follows:

$$F(\psi) = -\frac{1}{\beta} \log \left[\frac{\mathcal{Z}(\psi)}{\mathcal{Z}_0} \right], \quad (79)$$

where the denominator, \mathcal{Z}_0 , denotes the partition function for the EM field in the absence of media and

$$\mathcal{Z}(\psi) = \int [\mathcal{D}A] e^{-\mathcal{S}_{\text{inv}}(A)}. \quad (80)$$

The gauge invariant action $\mathcal{S}_{\text{inv}}(A)$ reads

$$\begin{aligned} \mathcal{S}_{\text{inv}}(A) = & \int_0^\beta d\tau \int_0^\beta d\tau' \int d^3\mathbf{x} \left[\frac{1}{2} F_{0j}(\tau, \mathbf{x}) \epsilon(\tau - \tau', \mathbf{x}) F_{0j}(\tau', \mathbf{x}) \right. \\ & \left. + \frac{1}{4} F_{ij}(\tau, \mathbf{x}) \mu^{-1}(\tau - \tau', \mathbf{x}) F_{ij}(\tau', \mathbf{x}) \right]. \end{aligned} \quad (81)$$

Here, indices like $i, j \dots$ run over spatial indices, Einstein summation convention is assumed, and $\epsilon(\tau - \tau', \mathbf{x})$ and $\mu(\tau - \tau', \mathbf{x})$ denote the imaginary time versions of the permittivity and permeability, respectively (μ^{-1} is the inverse integral kernel of μ).

The geometry of the system is determined by same two surfaces L and R we have considered before, and defined by $x_3 = 0$ and $x_3 = \psi(\mathbf{x}_\parallel)$, but now they correspond to the boundaries of the media, i.e.,

$$\begin{aligned} \epsilon(\tau - \tau', \mathbf{x}) &= \theta(-x_3) \epsilon_L(\tau - \tau') + \theta(x_3) \theta(\psi(\mathbf{x}_\parallel) - x_3) + \theta(x_3 - \psi(\mathbf{x}_\parallel)) \epsilon_R(\tau - \tau'), \\ \mu(\tau - \tau', \mathbf{x}) &= \theta(-x_3) \mu_L(\tau - \tau') + \theta(x_3) \theta(\psi(\mathbf{x}_\parallel) - x_3) + \theta(x_3 - \psi(\mathbf{x}_\parallel)) \mu_R(\tau - \tau'), \end{aligned}$$

where $\epsilon_{L,R}(\tau - \tau')$ and $\mu_{L,R}(\tau - \tau')$ characterize the permittivity and permeability of the respective mirror.

We can expand the fields and the electromagnetic properties as

$$\begin{aligned} A_\mu(\tau, \mathbf{x}) &= \frac{1}{\beta} \sum_{n=-\infty}^{+\infty} \tilde{A}_\mu^{(n)}(\mathbf{x}) e^{i\omega_n \tau}, \\ \epsilon(\tau - \tau', \mathbf{x}) &= \frac{1}{\beta} \sum_{n=-\infty}^{+\infty} \tilde{\epsilon}^{(n)}(\mathbf{x}) e^{i\omega_n(\tau - \tau')}, \\ \mu(\tau - \tau', \mathbf{x}) &= \frac{1}{\beta} \sum_{n=-\infty}^{+\infty} \tilde{\mu}^{(n)}(\mathbf{x}) e^{i\omega_n(\tau - \tau')}, \end{aligned} \quad (82)$$

where $\omega_n \equiv 2\pi n / \beta$ ($n \in \mathbb{Z}$) are the Matsubara frequencies.

Inserting these expansions into the partition function one can readily check the factorization

$$\mathcal{Z}(\psi) = \prod_{n=0}^{\infty} \mathcal{Z}^{(n)}(\psi), \quad (83)$$

and therefore

$$F(\psi) = \sum_{n=0}^{\infty} F^{(n)}(\psi). \quad (84)$$

As mentioned, we are particularly interested in the $n = 0$ contribution,

$$\mathcal{Z}^{(0)}(\psi) = \int [\mathcal{D}\tilde{A}_0^{(0)} \mathcal{D}\tilde{A}_j^{(0)}] e^{-\mathcal{S}^{(0)}(\tilde{A}_0^{(0)}, \tilde{A}_j^{(0)})}, \quad (85)$$

where

$$\mathcal{S}^{(0)}(\tilde{A}_0^{(0)}, \tilde{A}_j^{(0)}) = \frac{1}{\beta} \int d^3\mathbf{x} \left[\frac{1}{2} \tilde{\epsilon}^{(0)}(\mathbf{x}) (\partial_j \tilde{A}_0^{(0)})^2 + \frac{1}{4 \tilde{\mu}^{(0)}(\mathbf{x})} (\tilde{F}_{jk}^{(0)})^2 + \frac{1}{2} \Omega_0^2(\mathbf{x}) (\tilde{A}_j^{(0)})^2 \right], \quad (86)$$

and

$$\Omega_0^2(\mathbf{x}) \equiv \lim_{n \rightarrow 0} [\omega_n^2 \tilde{\epsilon}^{(n)}(\mathbf{x})]. \quad (87)$$

Note that Ω_0 vanishes for a dielectric and also for a metal described by the Drude model. On the other hand, it equals the plasma frequency for a metal described by the plasma model.

The zero mode contribution to the free energy therefore splits into a scalar (s) and a vector (v) contribution, the former associated to the field $\tilde{A}_0^{(0)}$ and the later to $\tilde{A}_j^{(0)}$

$$F^{(0)} = F_s(\psi) + F_v(\psi). \tag{88}$$

To discuss the emergence of nonanalyticities in the derivative expansion we computed F_s and F_v assuming $\psi(\mathbf{x}_\parallel) = a + \eta(\mathbf{x}_\parallel)$ up to second order in η . The quadratic contributions can be written as

$$F_{s,v}^{(2)} = \frac{1}{2} \int \frac{d^2k_\parallel}{(2\pi)^2} f_{s,v}^{(2)}(k_\parallel, a) |\tilde{\eta}(k_\parallel)|^2, \tag{89}$$

and the crucial point is whether the functions $f_{s,v}^{(2)}$ are analytic or not in k_\parallel .

Omitting the details, we summarize the main results [28]: for finite values of μ and ϵ , the scalar contribution $f_s^{(2)}$ analytic, including the limit $\epsilon \rightarrow \infty$, in which it tends to the $2 + 1$ dimensional Dirichlet value. It develops a nonanalytic (logarithmic) contribution for $\mu = \infty$, since the kernel corresponds in this case to that of a scalar field in $2 + 1$ dimensions satisfying Neumann boundary conditions. In other words, magnetic materials regulate the non-analyticity of the TE zero mode.

On the other hand, the TM zero mode is nonanalytic whenever $\omega^2\epsilon(\omega) \rightarrow \Omega^2 \neq 0$ as $\omega \rightarrow 0$ for both mirrors. In terms of the models usually considered in the Casimir literature to describe real materials, this condition corresponds to the plasma model.

In summary, the nonanalyticities we observed for perfect conductors in our previous work [26], survive only under the assumption of perfectly lossless materials. The NTLO corrections to PFA for metals (gold) at room temperature have been computed in Ref. [25].

6.4. A Semianalytic Formula for Plane-Sphere Geometry

As a final application of the DE to compute the Casimir free energy we mention the results of Ref. [50], where the author combined exact calculations for the zero mode and the DE to obtain a precise formula for the interaction between a sphere and a plane at a finite temperature which is valid at all separations. We briefly describe here these findings.

Formally, the free energy for this geometry can be written as

$$F = k_B T \sum_{n \geq 0} \text{Tr} \log[1 - \hat{M}(i\zeta_n)], \tag{90}$$

where the sum is over the Matsubara frequencies $\zeta_n = 2\pi n k_B T / \hbar$ and \hat{M} denotes scattering matrix elements for this geometry. The prime on the sum indicates that the $n = 0$ term has an additional $1/2$ factor.

The $n = 0$ contribution can be computed exactly using the Drude model to describe the materials of the plane and the sphere, and plays a crucial role. Indeed, the proposed approximation for the Casimir force on the sphere of radius R at a distance a from the plane is

$$F_{\text{approx}} = F_{n=0}^{(\text{exact})} + F_{n>0}^{(\text{PFA})} \left(1 - \theta \frac{a}{R}\right), \tag{91}$$

where θ can be computed using the DE. Notably, F_{approx} describes with high precision the Casimir force at all separations, as can be checked by comparison with high precision numerical simulations of the exact scattering formula.

These results have been generalized in subsequent studies to the case of the two spheres- geometry [51], also considering the differences that come from the use of the Drude vs plasma models, as well as for grounded vs isolated spheres [52]. The relevance of the use of grounded conductors in Casimir experiments has also been discussed in Ref. [53].

7. Casimir-Polder Forces

The DE approach has also been applied to the calculation of the Casimir-Polder interaction between a polarizable particle and a gently curved surface [29]. We present in this Section a simplified version of the results contained in that reference.

When a small polarizable particle is at a distance a of a planar surface, the Casimir-Polder potential reads [4]

$$U(a) = -\frac{1}{a^4} \int \frac{d\zeta}{2\pi} \alpha(i\omega_c \zeta) \beta^{(0)}(\zeta), \tag{92}$$

where $\alpha(\omega)$ is the frequency dependent polarizability (which is assumed isotropic), $\omega_c = c/a$, and

$$\beta^{(0)} = \frac{e^{-2\zeta}}{2} (1 + 2\zeta + 2\zeta^2). \tag{93}$$

For moderate distances such that $\alpha(\omega) \approx \alpha(0)$ one obtains the usual Casimir-Polder potential [54]

$$U(a) = -\frac{3}{8\pi} \frac{\alpha(0)}{a^4}. \tag{94}$$

Assume now that the particle is in front of a slightly curved surface. The particle is at the origin of coordinates, and the surface is described, as usual, by the height function $z = \psi(x_{||})$. The DE for the Casimir-Polder interaction U_{DE} assumes that the interaction depends on the derivatives of the height function ψ evaluated at $x_{||} = 0$, the point on the surface closest to the particle (a local minimum for ψ). If the surface is homogeneous and isotropic, then the interaction energy must be invariant under rotations of the $x_{||}$ coordinates. The more general expression compatible with this properties describes the Casimir-Polder interaction energy at $T = 0$ reads [29]:

$$U_{DE} = -\frac{1}{\psi^4} \int \frac{d\zeta}{2\pi} \alpha(i\omega_c \zeta) \left(\beta^{(0)}(\zeta) + \beta^{(1)}(\zeta) \psi \nabla^2 \psi \right). \tag{95}$$

The dimensionless function $\beta^{(1)}$ can be read from the perturbative expansion of the potential U , carried to second order in the deformation, that is, for $\psi(x_{||}) = a + \eta(x_{||})$ with $\eta(x_{||}) \ll a$. We stress that here the Casimir-Polder energy is not a functional but a function of ψ and its derivatives evaluated at the origin of coordinates (recall that $\nabla \psi(\mathbf{0}) = 0$). The DE is expected to be valid when $a \ll R_1, R_2$, the radii of curvature of the surface at $x_{||} = 0$. Note that $\psi(\mathbf{0}) = d$ and

$$\nabla^2 \psi(\mathbf{0}) = \frac{1}{R_1} + \frac{1}{R_2}. \tag{96}$$

Using again the static polarizability approximation, $\alpha(\omega) \approx \alpha(0)$, one obtains

$$U_{DE} = -\frac{1}{\pi a^4} \alpha(0) \left[\frac{3}{8} - \frac{13}{60} a \left(\frac{1}{R_1} + \frac{1}{R_2} \right) \right]. \tag{97}$$

The results presented in Ref. [29] are much more general than those described here: they include the Casimir-Polder potential for a general polarization tensor $\alpha_{\mu\nu}(\omega)$ and higher order corrections proportional to $(a/R_i)^2$, as well as the details of the computation of the corresponding functions $\beta^{(p)}$. Additional applications can be found in Refs. [55,56].

8. Other Techniques Beyond PFA

In Ref. [57] a detailed analysis of the Casimir effect's roughness correction in a setting involving parallel metallic plates is presented. The plates were defined through the plasma model. The approach used is perturbative, factoring in the roughness amplitude and allowing for the consideration of diverse values of the plasma wavelength, plate separation, and roughness correlation length. A notable finding was that the roughness correction exceed the predictions of the PFA. The authors have calculated the second-order response

function, $G(k)$, across a spectrum of values encompassing the plasma wavelength (λ_p), distance (a), and roughness wave vector (k):

$$G(k) = -\frac{A}{8\pi^2} \frac{1}{a^5 q} \int_0^\infty \frac{dK e^{-2K}}{1 - e^{-2K}} \int_{|K-q|}^{K+q} dK' \frac{(KK')^2 + \frac{1}{4}(K^2 + K'^2 - q^2)^2}{1 - e^{-2K'}}, \quad (98)$$

applicable when $\lambda_p \rightarrow 0$. Here, A represents the plate surface area, K the dimensionless integration variable denoting the imaginary wave vector's z -component scaled by plate separation d , K' the longitudinal component of the imaginary wave vector for the diffracted wave, and $q = ka$.

The calculation in Ref. [57] helps to compute the second-order roughness correction as a function of the surface profiles, h_1 and h_2 . Analytical solutions were determined for specific limiting cases, revealing a more complex relationship with the perfect reflectors model than previously recognized [58,59], particularly in scenarios involving extended distances and small roughness wavelengths. While the asymptotic case of long roughness wavelengths aligns with PFA predictions, it was established that PFA generally underestimates the roughness correction, a critical aspect for exploring constraints on potentially new weak forces at sub-millimeter ranges.

As a further expansion to Ref. [57], in Ref. [60], the authors explored the Casimir interaction between a plane and a sphere of radius R at a finite temperature T , in terms of the distance of closest approach, a . Noting that, under the usual experimental conditions, the thermal wavelength λ_T satisfies $a \ll \lambda_T \ll R$, they evaluated the leading correction to the PFA, applicable to such intermediate temperatures. They resorted to developing the scattering formula in the plane-wave basis. The result captures the combined effect of spherical geometry and temperature, and is expressed as a sum of temperature-dependent logarithmic terms. Remarkably, two of these logarithmic terms originated from the Matsubara zero-frequency contribution.

Defining the variables $x = a/R$ and $\tau = a/\lambda_T$, and the deviation $\delta F(T) = F(T) - F(0)$, in the intermediate temperature regime $x \ll \tau \ll 1$, it is found in Ref. [60] that

$$\begin{aligned} \Delta &= \frac{\delta F(T) - \delta F_{\text{PFA}}(T)}{F_{\text{PFA}}(T)} \\ &\approx \frac{45}{\pi^3} x\tau \left[-\log^2(x) + 2[1 - \log(2)] \log(x) + 2\log^2(\tau) + \mathcal{O}(\log(\tau)) \right]. \quad (99) \end{aligned}$$

The leading neglected terms stem from non-zero Matsubara frequencies.

In Ref. [61], the leading-order correction to PFA in a plane-sphere geometry was derived. The momentum representation connected this with geometrical optics and semi-classical Mie scattering. The primary contributions are shown to come from diffraction, with TE polarization becoming more relevant than TM polarization. The diffraction contribution is calculated at leading order, using the saddle-point approximation, considering leading order curvature effects at the sphere tangent plane.

Additionally, the next-to-leading order (NTLO) term in the saddle-point expansion contributed to the PFA correction. This involved computing the round-trip operator within the WKB (Wentzel–Kramers–Brillouin) approximation, representing sequences of reflections between the plane and the sphere. A key aspect was the tilt in the scattering planes, allowing TE and TM polarizations to mix.

Comprehending the implications of polarization mixing channels on the geometric optical correction applied to PFA holds considerable importance. Indeed, these channels are recognized for inducing negative Casimir entropies with a geometric foundation [62–67]. In spite of the non-vanishing contribution of the polarization mixing matrix elements, the total correction associated with the tilt between the scattering and Fresnel planes is zero at NTLO. This implies that the primary correction to the PFA would remain unchanged even if the complexities arising from the differences between the Fresnel and scattering polarization bases were initially ignored. The latter points to the fact that a different approach, one that

completely omits the effect of polarization mixing, could directly produce the leading order correction to PFA. Plane waves proved to be a well-suited basis for studying the Casimir effect, as has been evidenced in the more recent study [30]. The utility of that basis ranges from analytical to numerical applications, particularly when dealing with objects in close proximity, the most relevant situation in experiments. It has been also shown that the use of plane waves was notably effective in improving the interpretation of results in the realms of geometrical optics and diffractive corrections.

In the context of a setup involving two spheres with arbitrary radii in vacuum, it was shown in Ref. [30] that the PFA emerged as the leading term in an asymptotic expansion for large radii. Extending a prior calculation based on the saddle-point approximation, involving a trace over multiple round-trips of electromagnetic waves between the spheres, the study encompassed spheres made of bi-isotropic material, requiring the consideration of polarization mixing during reflection processes. The result was naturally elucidated within the framework of geometrical optics.

Then, by relying on a saddle-point approximation framework, the authors derived leading-order corrections, of geometrical and diffractive origins. Explicit results, at first obtained for perfect electromagnetic conductors (PEMC) spheres at zero temperature, indicated that for certain material parameters, the PFA contribution vanishes; should that be the case, the leading-order correction would be the dominant term in the Casimir energy.

In the lowest-order saddle-point approximation, but including diffractive corrections, one can show that the expression for the Casimir energy becomes:

$$E_{\text{LO-SPA}} = -\frac{\pi^3 R_{\text{eff}}}{720a^2} \left[1 - \frac{15}{\pi^2} x + \frac{15(10 + 3\pi)}{4\pi^3} x^{3/2} + \dots \right], \quad (100)$$

where $x = a/R_{\text{eff}}$. As expected, this result reproduces the PFA result and its leading-order diffractive correction. The NTLO correction behaves as $x^{3/2}$. However, the prefactor obtained accounts for about 90% of the one coming from numerical results [61]. This discrepancy may be traced back to having neglected the NTLO-SPA and NNTLO-SPA contributions.

9. Conclusions

In this review, we have discussed several properties and applications of the DE approach, mostly as a method to improve the predictions of the Proximity Force Approximation, of long standing use in many different fields.

We started the review by briefly discussing the precursor of the PFA: the Derjaguin (and related) approximations, since we have found them rather appropriate in order to display the essentially geometric nature of the kind of problem we discuss: two quite close smooth surfaces, and an interaction energy between them. Depending on the kind of system being considered, that interaction between the two surfaces may or not be the result of the superposition of the interactions between pairs. An example of an interaction which is not the result of such a superposition is the Casimir effect. Note, however, that even when the fundamental interaction satisfies a superposition principle, like in electrostatics, the actual evaluation of the Coulomb integral to calculate the total interaction energy could be a rather involved problem because the actual charge density may not be known a priori. That is indeed the case when the surfaces involved are conductors, since that usually requires finding the electrostatic potential. We have used precisely this problem in order to present the idea of the DE in a concrete example: to calculate the electrostatic energy between two conducting surfaces held at different potentials.

After introducing and applying the DE in that example, we have discussed its more general proof of that expansion, by first putting the problem in a more general and abstract way: how to approximate, under certain smoothness assumptions, a functional of a pair of surfaces. At the same time, the proof provides a concrete way to determine the PFA and its NTLO correction, the DE: one just needs to perform an expansion in powers of the deformation of the surfaces about the situation of two flat and parallel surfaces.

The derivations and examples here have been presented for a geometrical setting where one surface is a plane, while the other may be described by a single Monge patch based on that plane. However, as shown by other authors, under quite reasonable and general assumptions, the results obtained for that situation may be generalized to the case of two curved surfaces parametrized by their respective patches, based on a common plane (which now does not coincide with one of the physical surfaces).

Then we reviewed different applications of the DE to the zero temperature Casimir effect, considering different fields and boundary conditions, starting from the cases of the scalar field with Dirichlet boundary conditions, then the EM field in the presence of perfectly conducting surfaces, and commented on the scalar field with Neumann conditions.

We afterwards presented a description and brief review of the extension of DE to finite temperature cases, and different numbers of spatial dimensions. The temperature is a dimensionful magnitude and the phenomenon of dimensional reduction presents a problem when there are Neumann boundary conditions or when an EM field is involved. Indeed, dimensional reduction implies the existence of a massless $2 + 1$ dimensional field (with Neumann conditions), and this mode introduces a nonanalyticity in momentum space, which violated one of the hypothesis of the DE, and therefore it cannot be applied. Nevertheless, we have shown that the introduction of a small departure from ideal Neumann conditions solves this issue, namely, analyticity is recovered and the DE may be applied.

We also mentioned the application of DE to the Casimir-Polder interaction, particularly between a polarizable particle and a gently curved surface. This example highlights the broader implications of DE in understanding particle-surface interactions beyond the Casimir force itself.

To conclude, we have presented in this review the main features of the DE approach, with a focus in the Casimir effect, but pointing at the fact that its applicability can certainly go beyond that realm. We have shown that explicitly for electrostatics, but we expect it to be applicable to, for example, the same kind of systems where the DA, SEI and SIA were introduced.

Author Contributions: All authors contributed equally to this work. All authors have read and agreed to the published version of the manuscript.

Funding: This research received no external funding.

Data Availability Statement: Not applicable.

Acknowledgments: The authors acknowledge the support from Agencia Nacional de Promoción Científica y Tecnológica (ANPCyT), Consejo Nacional de Investigaciones Científicas y Técnicas (CONICET), Universidad de Buenos Aires (UBA), and Universidad Nacional de Cuyo (UNCuyo), Argentina.

Conflicts of Interest: The authors declare no conflicts of interest.

References

1. Casimir, H.B.G. On the attraction between two perfectly conducting plates. *Proc. Kon. Ned. Akad. Wetensch. B* **1948**, *51*, 793–795. Available online: <https://dwc.knaw.nl/DL/publications/PU00018547.pdf> (accessed on 6 January 2023).
2. Milonni, P.W. *The Quantum Vacuum. An Introduction to Quantum Electrodynamics*; Academic Press, Inc.: San Diego, CA, USA, 1994. [CrossRef]
3. Milton, K.A. *The Casimir Effect. Physical Manifestations of Zero-Point Energy*; World Scientific: Singapore, 2001. [CrossRef]
4. Bordag, M.; Klimchitskaya, G.L.; Mohideen, U.; Mostepanenko, V.M. *Advances in the Casimir Effect*; Oxford University Press: Oxford, UK, 2009. [CrossRef]
5. Dalvit, D.; Milonni, P.; Roberts, D.; da Rosa, F. (Eds.) *Casimir Physics*; Springer: Berlin/Heidelberg, Germany, 2011. [CrossRef]
6. Mostepanenko, V.M. Casimir puzzle and Casimir conundrum: Discovery and search for resolution. *Universe* **2021**, *7*, 84. [CrossRef]
7. Bressi, G.; Carugno, G.; Onofrio, R.; Ruoso, G. Measurement of the Casimir force between parallel metallic surfaces. *Phys. Rev. Lett.* **2002**, *88*, 041804. [CrossRef] [PubMed]
8. Brown-Hayes, M.; Dalvit, D.A.R.; Mazzitelli, F.D.; Kim, W.J.; Onofrio, R. Towards a precision measurement of the Casimir force in a cylinder-plane geometry. *Phys. Rev. A* **2005**, *72*, 052102. [CrossRef]
9. Lamoreaux, S.K. Demonstration of the Casimir force in the 0.6 to 6 μm range. *Phys. Rev. Lett.* **1997**, *78*, 5–8. [CrossRef]

10. Mohideen, U.; Roy, A. Precision measurement of the Casimir force from 0.1 to 0.9 μm . *Phys. Rev. Lett.* **1998**, *81*, 4549–4552. [CrossRef]
11. Chan, H.B.; Aksyuk, V.A.; Kleiman, R.N.; Bishop, D.J.; Capasso, F. Quantum mechanical actuation of microelectromechanical system by the Casimir effect. *Science* **2001**, *291*, 1941–1944. [CrossRef]
12. Decca, R.S.; López, D.; Fischbach, E.; Klimchitskaya, G.L.; Krause, D.E.; Mostepanenko, V.M. Precise comparison of theory and new experiment for the Casimir force leads to stronger constraints on thermal quantum effects and long-range interactions. *Ann. Phys.* **2005**, *318*, 37–80. [CrossRef]
13. Chang, C.C.; Banishev, A.A.; Castillo-Garza, R.; Klimchitskaya, G.L.; Mostepanenko, V.M.; Mohideen, U. Gradient of the Casimir force between Au surfaces of a sphere and a plate measured using an atomic force microscope in a frequency-shift technique. *Phys. Rev. B* **2012**, *85*, 165443. [CrossRef]
14. Bimonte, G.; López, D.; Decca, R.S. Isoelectronic determination of the thermal Casimir force. *Phys. Rev. B* **2016**, *93*, 184434. [CrossRef]
15. Bimonte, G.; Spreng, B.; Maia Neto, P.A.; Ingold, G.-L.; Klimchitskaya, G.L.; Mostepanenko, V.M.; Decca, R.S. Measurement of the Casimir force between 0.2 and 8 μm : Experimental procedures and comparison with theory. *Universe* **2021**, *7*, 93. [CrossRef]
16. Boyer, T.H. Quantum electromagnetic zero point energy of a conducting spherical shell and the Casimir model for a charged particle. *Phys. Rev.* **1968**, *174*, 1764–1774. [CrossRef]
17. Derjaguin, B.V. Untersuchungen über die Reibung und Adhäsion, IV. *Koll.-Z.* **1934**, *69*, 155–164. [CrossRef]
18. Deriagin, B.V.; Abrikosova, I.I. Direct measurement of the molecular attraction of solid bodies. I. Statement of the problem and method of measuring forces by using negative feedback. *Sov. Phys. JETP* **1957**, *4*, 819–829. Available online: <http://jetp.ras.ru/cgi-bin/e/index/e/3/6/p819?a=list> (accessed on 6 January 2024).
19. Derjaguin, B.V. The force between molecules. *Sci. Am.* **1960**, *203*, 47. [CrossRef]
20. Israelachvili, J.N. *Intermolecular and Surface Forces*; Academic Press/Elsevier, Inc.: Oxford, UK, 2011. [CrossRef]
21. Fosco, C.D.; Lombardo, F.C.; Mazzitelli, F.D. The proximity force approximation for the Casimir energy as a derivative expansion. *Phys. Rev. D* **2011**, *84*, 105031. [CrossRef]
22. Fosco, C.D.; Lombardo, F.C.; Mazzitelli, F.D. An improved proximity force approximation for electrostatics. *Ann. Phys.* **2012**, *327*, 2050–2059. [CrossRef]
23. Fosco, C.D.; Lombardo, F.C.; Mazzitelli, F.D. Derivative-expansion approach to the interaction between close surfaces. *Phys. Rev. A* **2014**, *89*, 062120. [CrossRef]
24. Bimonte, G.; Emig, T.; Jaffe, R.; Kardar, M. Casimir forces beyond the proximity approximation. *Europhys. Lett.* **2012**, *97*, 50001. [CrossRef]
25. Bimonte, G.; Emig, T.; Kardar, M. Material dependence of Casimir forces: Gradient expansion beyond proximity. *App. Phys. Lett.* **2012**, *100*, 074110. [CrossRef]
26. Fosco, C.D.; Lombardo, F.C.; Mazzitelli, F.D. Derivative expansion for the Casimir effect at zero and finite temperature in $d + 1$ dimensions. *Phys. Rev. D* **2012**, *86*, 045021. [CrossRef]
27. Fosco, C.D.; Lombardo, F.C.; Mazzitelli, F.D. Derivative expansion for the electromagnetic and Neumann Casimir effects in $2 + 1$ dimensions with imperfect mirrors. *Phys. Rev. D* **2015**, *91*, 105019. [CrossRef]
28. Fosco, C.D.; Lombardo, F.C.; Mazzitelli, F.D. On the derivative expansion for the electromagnetic Casimir free energy at high temperatures. *Phys. Rev. D* **2015**, *92*, 125007. [CrossRef]
29. Bimonte, G.; Emig, T.; Kardar, M. Casimir-Polder interaction for gently curved surfaces. *Phys. Rev. D* **2014**, *90*, 081702. [CrossRef]
30. Schoger, T.; Spreng, B.; Ingold, G.L.; Neto, P.A.M. Casimir effect between spherical objects: Proximity-force approximation and beyond using plane waves. *Int. J. Mod. Phys. A* **2022**, *37*, 2241009. [CrossRef]
31. Blocki, J.; Randrup, J.; Swiatecki, W.J.; Tsang, C.F. Proximity forces. *Ann. Phys.* **1977**, *105*, 427–462. [CrossRef]
32. Blocki, J.; Swiatecki, W.J. A generalization of the proximity force theorem. *Ann. Phys.* **1981**, *132*, 53–65. [CrossRef]
33. Myers, W.D.; Swiatecki, W.J. Nucleus-nucleus proximity potential and superheavy nuclei. *Phys. Rev. C* **2000**, *62*, 044610. [CrossRef]
34. Dutt, I.; Puri, R.K. Comparison of different proximity potentials for asymmetric colliding nuclei. *Phys. Rev. C* **2010**, *81*, 064609. [CrossRef]
35. Bhattacharjee, S.; Elimelech, M. Surface element integration: A novel technique for evaluation of DLVO interaction between a particle and a flat plate. *J. Colloid. Interface Sci.* **1997**, *193*, 273–285. [CrossRef] [PubMed]
36. Dantchev, D.; Valchev, G. Surface integration approach: A new technique for evaluating geometry dependent forces between objects of various geometry and a plate. *J. Colloid Interface Sci.* **2012**, *372*, 148–163. [CrossRef]
37. Decca, R.S.; Fischbach, E.; Klimchitskaya, G.L.; Krause, D.E.; Lopez, D.; Mostepanenko, V.M. Application of the proximity force approximation to gravitational and Yukawa-type forces. *Phys. Rev. D* **2009**, *79*, 124021. [CrossRef]
38. Milton, K.A.; Parashar, P.; Wagner, J.; Shajesh, K.V. Exact Casimir energies at nonzero temperature: Validity of proximity force approximation and interaction of semitransparent spheres. *arXiv* **2009**, arXiv:0909.0977. [CrossRef]
39. Hudlet, S.; Saint Jean, M.; Guthmann, C.; Berger, J. Evaluation of the capacitive force between an atomic force microscopy tip and a metallic surface. *Eur. Phys. J. B.* **1998**, *2*, 5–10. [CrossRef]
40. Fosco, C.D.; Lombardo, F.C.; Mazzitelli, F.D. Fourth order perturbative expansion for the Casimir energy with a slightly deformed plate. *Phys. Rev. D* **2012**, *86*, 125018. [CrossRef]

41. Emig, T.; Hanke, A.; Golestanian, R.; Kardar, M. Normal and lateral Casimir forces between deformed plates. *Phys. Rev. A* **2003**, *67*, 022114. [CrossRef]
42. Lambrecht, A.; Neto, P.A.M.; Reynaud, S. The Casimir effect within scattering theory. *New J. Phys.* **2006**, *8*, 243. [CrossRef]
43. Bordag, M.; Nikolaev, V. Casimir force for a sphere in front of a plane beyond proximity force approximation. *J. Phys. A* **2008**, *41*, 164001. [CrossRef]
44. Bordag, M.; Nikolaev, V. Analytic corrections to the electromagnetic Casimir interaction between a sphere and a plate at short distances. *Int. Mod. J. Phys. A* **2010**, *25*, 2171–2176. [CrossRef]
45. Bordag, M.; Nikolaev, V. First analytic correction beyond the proximity force approximation in the Casimir effect for the electromagnetic field in sphere-plane geometry. *Phys. Rev. D* **2010**, *81*, 065011. [CrossRef]
46. Teo, L.P.; Bordag, M.; Nikolaev, V. Corrections beyond the proximity force approximation. *Phys. Rev. D* **2011**, *84*, 125037. [CrossRef]
47. Rodriguez-Lopez, P.; Emig, T. Casimir interaction between inclined metallic cylinders. *Phys. Rev. A* **2012**, *85*, 032510. [CrossRef]
48. Bimonte, G.; Emig, T. Exact results for classical Casimir interactions: Dirichlet and Drude model in the sphere-sphere and sphere-plane geometry. *Phys. Rev. Lett.* **2012**, *109*, 160403. [CrossRef]
49. Canaguier-Durant, A.; Ingold, G.L.; Jaekel, M.T.; Lambrecht, A.; Neto, P.A.M.; Reynaud, S. Classical Casimir interaction in the plane-sphere geometry. *Phys. Rev. A* **2012**, *85*, 052501. [CrossRef]
50. Bimonte, G. Going beyond PFA: A precise formula for the sphere-plate Casimir force. *EPL (Europhys. Lett.)* **2017**, *118*, 20002. [CrossRef]
51. Bimonte, G. Beyond-proximity-force-approximation Casimir force between two spheres at finite temperature. *Phys. Rev. D* **2018**, *97*, 085011. [CrossRef]
52. Bimonte, G. Beyond-proximity-force-approximation Casimir force between two spheres at finite temperature II: Plasma versus Drude modeling, grounded versus isolated spheres. *Phys. Rev. D* **2018**, *98*, 105004. [CrossRef]
53. Fosco, C.D.; Lombardo, F.C.; Mazzitelli, F.D. Difference between the vacuum Casimir energies for grounded and isolated conductors. *Phys. Rev. D* **2016**, *94*, 085024. [CrossRef]
54. Casimir, H.B.G.; Polder, D. The Influence of retardation on the London–van der Waals forces. *Phys. Rev.* **1948**, *73*, 360–372. [CrossRef]
55. Bimonte, G.; Emig, T.; Kardar, M. Casimir-Polder force between anisotropic nanoparticles and gently curved surfaces. *Phys. Rev. D* **2015**, *92*, 025028. [CrossRef]
56. Bimonte, G.; Emig, T. Interplay of curvature and temperature in the Casimir–Polder interaction. *J. Phys. Condens. Mater.* **2015**, *27*, 214018. [CrossRef] [PubMed]
57. Neto, P.A.M.; Lambrecht, A.; Reynaud, S. Roughness correction to the Casimir force: Beyond the proximity force approximation. *Europhys. Lett.* **2005**, *69*, 924–930. [CrossRef]
58. Genet, C.; Lambrecht, A.; Maia, Neto, P.; Reynaud, S. The Casimir force between rough metallic plates. *Europhys. Lett.* **2003**, *62*, 484–490. [CrossRef]
59. Emig, T.; Hanke, A.; Golestanian, R.; Kardar, M. Probing the strong boundary shape dependence of the Casimir force. *Phys. Rev. Lett.* **2001**, *87*, 260402. [CrossRef]
60. Henning, V.; Spreng, B.; Neto, P.A.M.; Ingold, G.L. Casimir interaction between a plane and a sphere: Correction to the proximity-force approximation at intermediate temperatures. *Universe* **2021**, *7*, 129. [CrossRef]
61. Henning, V.; Spreng, B.; Hartmann, M.; Ingold, G.L.; Neto, P.A.M. Role of diffraction in the Casimir effect beyond the proximity force approximation. *J. Opt. Soc. Am. B* **2019**, *36*, C77–C87. [CrossRef]
62. Canaguier-Durand, A.; Neto, P.A.M.; Lambrecht, A.; Reynaud, S. Thermal Casimir effect in the plane-sphere geometry. *Phys. Rev. Lett.* **2010**, *104*, 040403. [CrossRef]
63. Canaguier-Durand, A.; Neto, P.A.M.; Lambrecht, A.; Reynaud, S. Thermal Casimir effect for Drude metals in the plane-sphere geometry. *Phys. Rev. A* **2010**, *82*, 012511. [CrossRef]
64. Zandi, R.; Emig, T.; Mohideen, U. Quantum and thermal Casimir interaction between a sphere and a plate: Comparison of Drude and plasma models. *Phys. Rev. B* **2010**, *81*, 195423. [CrossRef]
65. Milton, K.A.; Guérout, R.; Ingold, G.-L.; Lambrecht, A.; Reynaud, S. Negative Casimir entropies in nanoparticle interactions. *J. Phys. Condens. Matter* **2015**, *27*, 214003. [CrossRef] [PubMed]
66. Ingold, G.-L.; Umrath, S.; Hartmann, M.; Guérout, R.; Lambrecht, A.; Reynaud, S.; Milton, K.A. Geometric origin of negative Casimir entropies: A scattering-channel analysis. *Phys. Rev. E* **2015**, *91*, 033203. [CrossRef] [PubMed]
67. Umrath, S.; Hartmann, M.; Ingold, G.-L.; Neto, P.A.M. Disentangling geometric and dissipative origins of negative Casimir entropies. *Phys. Rev. E* **2015**, *92*, 042125. [CrossRef] [PubMed]

Disclaimer/Publisher’s Note: The statements, opinions and data contained in all publications are solely those of the individual author(s) and contributor(s) and not of MDPI and/or the editor(s). MDPI and/or the editor(s) disclaim responsibility for any injury to people or property resulting from any ideas, methods, instructions or products referred to in the content.

Article

Casimir Forces with Periodic Structures: Abrikosov Flux Lattices

Shunashi Guadalupe Castillo-López, Raúl Esquivel-Sirvent, Giuseppe Pirruccio and Carlos Villarreal *

Instituto de Física, Universidad Nacional Autónoma de México, Apdo. Postal 20-364, Mexico City 01000, Mexico; shunashi@fisica.unam.mx (S.G.C.-L.); raul@fisica.unam.mx (R.E.-S.); pirruccio@fisica.unam.mx (G.P.)

* Correspondence: carlos@fisica.unam.mx

Abstract: We investigate the influence of the Abrikosov vortex lattice on the Casimir force in a setup constituted by high-temperature superconductors subject to an external magnetic field. The Abrikosov lattice is a property of type II superconductors in which normal and superconducting carriers coexist and the latter define a periodic pattern with square symmetry. We find that the optical properties determined by spatial redistribution of the superconducting order parameter induce Casimir forces with a periodic structure whose minimal strengths coincide with the vortex cores.

Keywords: Casimir force; superconductor; quantum vortex; fluxon; Abrikosov lattice; vortex matter

1. Introduction

Seventy-five years have passed since, motivated by a suggestion by Niels Bohr during a walk, Hendrik Casimir proposed that vacuum fluctuations could induce an attractive force per unit area between two perfectly conducting parallel plates, a distance d apart, given by $F = -\hbar c \pi^2 / 240 d^4$ [1] with $\hbar = h/2\pi$ the reduced Planck constant and c the speed of light. A more realistic theory was proposed by Evgeny Lifshitz in 1956 by considering fluctuating electrodynamics, based on the fluctuation–dissipation mechanism. Lifshitz theory allows to determine the Casimir force in terms of the dispersive and dissipative properties of the materials [2], as described by its optical properties. Grounded on Lifshitz formulation, numerous experiments [3–13] have been performed on measuring the Casimir forces involving a diversity of experimental arrangements and materials [14,15]. The influence and taming of these forces in the design and construction of micro- and nanodevices is a current field of research. Extensive treatments of the Casimir effect and its applications, are presented in Refs. [16–20].

In spite of the fruitful advances in the investigations of the Casimir effect there exist yet pending fundamental problems on the basic theory, concerning the role of dissipative mechanisms on the strength of the force between metallic bodies. These may involve electron scattering by impurities, other electrons, phonons, etc., yielding a total scattering rate $\tau^{-1} = \tau_{\text{el-imp}}^{-1} + \tau_{\text{el-el}}^{-1}(T) + \tau_{\text{el-ph}}^{-1}(T) + \dots$. Actually, the inclusion of this kind of contributions in the theoretical characterization of the optical response of materials involved in a given setup should be necessary to achieve congruence with the fluctuation–dissipation theorem underlying the Lifshitz theory. However, earlier measurements of Casimir forces in metals at room temperature at body separations $d \approx 50\text{--}600$ nm showed consistence with theoretical predictions if dissipative effects are neglected. This hypothesis is also consistent with more recent experimental studies of the gradient of the Casimir force between metallic surfaces performed at larger separations, $d > 700$ nm, such that $k_B T \sim \hbar c/d$ [21–23], with k_B the Boltzmann constant. On the contrary, experiments carried out at micrometer distances to measure the total magnitude of the Casimir force display a better agreement with predictions including electronic relaxation [19]. The main difference between the results at small and large separations, is that in the latter thermal effects become important.

Citation: Castillo-López, S.G.; Esquivel-Sirvent, R.; Pirruccio, G.; Villarreal, C. Casimir Forces with Periodic Structures: Abrikosov Flux Lattices. *Physics* **2024**, *6*, 394–406. <https://doi.org/10.3390/physics6010026>

Received: 4 December 2023

Revised: 27 January 2024

Accepted: 30 January 2024

Published: 12 March 2024



Copyright: © 2024 by the authors. Licensee MDPI, Basel, Switzerland. This article is an open access article distributed under the terms and conditions of the Creative Commons Attribution (CC BY) license (<https://creativecommons.org/licenses/by/4.0/>).

It has been proposed that the study of the Casimir effect in superconducting (SC) materials may constitute an excellent scenario to assess the influence of relaxation phenomena on the strength of the Casimir force between metallic bodies [24–28]. This is motivated by the finding that charge carriers in these materials exhibit a transition from dissipative transport to a dissipationless coherent behavior at a critical temperature $T = T_c$. However, measurements of the influence of the SC transition on the Casimir force in setups involving conventional BCS (Bardeen–Cooper–Schrieffer) superconductors turn out to be extremely difficult, since for typical values $T_c \sim 1$ K, and $k_B T_c \ll \hbar c/d$ for sub- μm body separations. Therefore, indirect approaches have been proposed based on observations of the Casimir-induced shift of the critical magnetic field H_c of a thin superconducting film, or differential measurements of the Casimir force [29,30].

This suggests that the use of high-temperature superconductors (HTSCs), with $T_c \approx 100$ K, could constitute a suitable alternative to perform a direct analysis of the effect of the SC transition on the Casimir effect. In previous studies, we investigated the Casimir forces between objects made of optimally doped $\text{YBa}_2\text{Cu}_3\text{O}_{7-\delta}$ (YBCO), with $T_c = 93$ K, either in thermal [31], or out of thermal equilibrium [32]. In the first case, we found that the Casimir force displays an abrupt increment as T approaches T_c from above, $T \rightarrow T_c$. On the other hand, for $T < T_c$, the (force \times distance) approaches a constant in the limit $T \ll T_c$. In the second case, each slab was in local equilibrium with a thermal reservoir at respective temperatures, $T_1 = 300$ K and T_2 , where $300 \geq T_2 \geq 0$ K. In contrast with the thermal equilibrium situation, the Casimir force displays an abrupt decrement in the transit from normal metal to the SC state as $T_2 \rightarrow T_c$. The low-temperature asymptotic behavior of the force is similar to that displayed in the equilibrium situation.

To get further insight on the influence of superconductivity-related effects on the Casimir effect, in this paper, we study the effect of the Abrikosov lattice (AL) [33] on the local properties of Casimir forces associated to high-temperature superconductors (HTSCs). The AL is a manifestation of the Meissner effect, in which the presence of an external magnetic field induces surface screening supercurrents, which expel out the magnetic field lines from the material's interior within a London penetration length $\lambda_L(T) \sim n_s(T)^{-1/2}$. Here, $n_s(T)$ is the number density of Cooper pairs (CPs) at a temperature T . In the case of type-II superconductors, such as YBCO, the Meissner effect involves the existence of a mixed phase of coexistence of normal and SC charge carriers determined by two critical magnetic fields, $H_{c1} < H_{c2}$. For values of the applied field higher than H_{c1} , magnetic flux lines penetrate the sample in the form of quantum vortices, $\Phi_0 = h/2e$, with e the elementary charge, thus inducing local screening currents to overcome the applied field [34]. Upon increasing magnitude of the field, the vortex density increases and saturates at the upper critical field H_{c2} , where superconductivity disappears. Remarkably, as shown by Alexei Abrikosov [33], for intensities of the applied field just below H_{c2} the vortices align in a compact square lattice with period $L_x = L_y = \sqrt{2\pi}\zeta(T)$, where $\zeta(T)$ is the CP coherence length. In the case of YBCO, $\zeta(0) \equiv \zeta_0 \approx 1.65$ nm, and $\lambda_L(0) \equiv \lambda_0 \approx 156$ nm, while the temperature-independent ratio $\kappa = \lambda_L(T)/\zeta(T) \approx 95$ [34].

It can be shown that the AL vortices strongly repel each other, giving rise to highly correlated configurations which are stable when thermal fluctuations and disorder are both negligible. A measure of the magnitude of the energy associated to thermal fluctuations with respect to the magnetic condensation energy is provided by the Ginzburg number [35], $G_i = 2\gamma^2\kappa^4(k_B T_c / H_{c2}(0)^2 \zeta_0^3)^2$, where γ is a measure of the anisotropic conductivity (discussed below). In the case of conventional BCS superconductors, $G_i = 10^{-7}$. In comparison, in the case of HTSCs, $T_c \sim 10^2$ K and $\kappa \sim 10^2$, implying that $G_i \sim 10^{-2}$. This relatively large value of G_i joined with the feature that these materials display a layered anisotropic structure at the atomic level, leads to the manifestation of a manifold of phenomena generally termed as vortex matter, encompassing a complex phase diagram under different environmental conditions and material compositions [36]. Thus, thermal fluctuations may significantly alter the properties of the AL, generally leading to melting towards a liquid phase displaying vortex deformation, entanglement or migration. Superposed with repul-

sive interactions and thermal fluctuations, disorder due to material imperfections induce vortex pinning, which may conduce to the formation of glassy configurations [35–37]. Vortex matter has been investigated by recurring to techniques such as scanning tunneling microscopy [38] or muon spin rotation [39]. In addition, the possibility of using cold atoms to asses vortex-noise has been considered in the literature [40].

In order to examine the influence of the AL on the Casimir force, in this study we consider a setup, depicted in Figure 1, constituted by a spherical Au nanoparticle located at a minimum distance d from a planar YBCO substrate, in presence of an applied magnetic field directed along the z -axis. We show that the force acquires a spatial structure congruent with the AL due to the modulation imparted by the vortices on the dielectric permittivity.

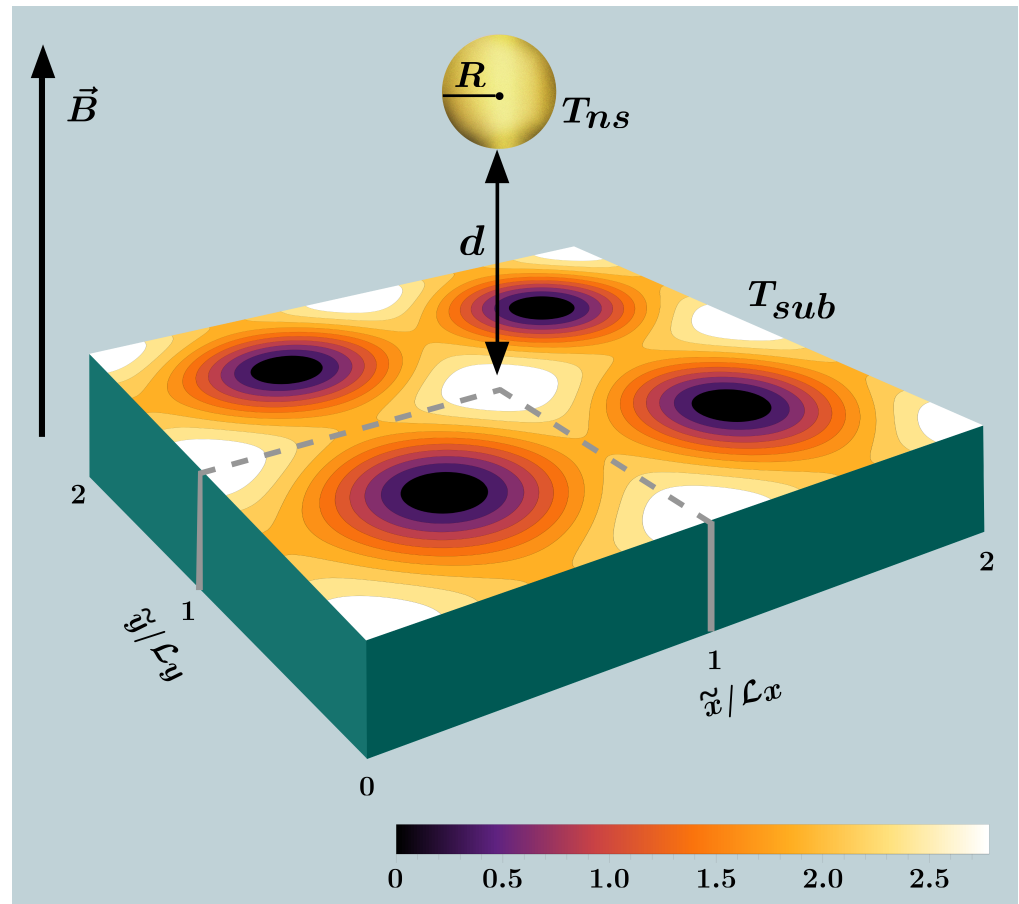


Figure 1. Setup consisting of a spherical Au nanoparticle of radius R located at a minimum distance d from a planar substrate made of optimally-doped YBCO ($\text{YBa}_2\text{Cu}_3\text{O}_{7-\delta}$), both at the same temperature $T = T_{\text{ns}}$ and T_{sub} , respectively,—in presence of an applied magnetic field directed along the z axis. We show the resulting lattice structure with elementary cells of nondimensional spatial periods $a = \mathcal{L}_x = \mathcal{L}_y$. Induced supercurrents coincide with equiprobability contours defined by the number density of Cooper pairs, $n_s = |\Psi(\tilde{\mathbf{r}})|^2$, where $\Psi(\tilde{\mathbf{r}})$ is the superconducting order parameter. The vortex cores of radius ζ correspond to the darkest inner zones. \vec{B} denotes the magnetic field, and the tilde stands for adimensional variables, $\tilde{x} = x/\lambda_{ab}$ and $\tilde{y} = y/\lambda_{ab}$, where λ_{ab} represents the ab -plane penetration length.

In what follows, we present the formalism aimed to evaluate the Casimir force between a planar substrate and a nanosphere, which relies upon the frequency-dependent optical properties of the involved materials. To investigate the optical response of YBCO under the action of an external magnetic field, we then discuss a generalization of the Ginzburg–Landau (GL) theory of superconductivity, which allows the consideration of the anisotropic properties HTSCs, allowing the characterization of the number density of SC pairs, $n_s(\mathbf{r})$,

with a spatial dependence induced by the action of the applied magnetic field, as provided by the Abrikosov solution of the GL equation. We then discuss the thermal behavior of $n_s(\mathbf{r})$ by taking into account that SC charge carriers in HTSCs may be described as a 2D (2-dimensional) gas of weakly-interacting CPs able to form a Bose–Einstein condensate (BEC). In Section 2, we model the optical response of YBCO by combining the derived expression for $n_s(\mathbf{r}, T)$ with experimental data for the YBCO dielectric function obtained in the normal ($T = 100$ K) and SC regime ($T = 2$ K). We then integrate the former antecedents to evaluate the Casimir force associated to the AL, and discuss the derived results.

2. Theory and Definitions

2.1. Casimir Force between a Nanosphere and a Planar Substrate

The theory of the Casimir effect between a sphere and a planar surface beyond the Proximity Force Approximation has been investigated within alternative perspectives, including some developed by authors of the present study [18,41–47]. In this Section, we extend the formalism previously presented in Refs. [41–43] to calculate the finite-temperature Casimir force for the nanosphere-substrate setup displayed in Figure 1, with the corresponding dielectric function of the nanosphere, $\epsilon_{\text{ns}}(\omega)$, and substrate, $\epsilon_{\text{sub}}(\mathbf{r}, \omega)$. We first evaluate the zero-temperature interaction energy as a sum over proper frequencies, $\omega_k(\mathbf{r}_\perp; d)$, of the considered configuration:

$$\mathcal{E}(\mathbf{r}_\perp; d) = \frac{1}{2} \sum_k (\hbar\omega_k(\mathbf{r}_\perp; d) - \hbar\omega_k(\mathbf{r}_\perp; d \rightarrow \infty)), \quad (1)$$

where $\mathbf{r}_\perp(x, y)$. Straightforward use of the argument principle method lets us express the sum over proper mode frequencies as a sum over the zeros of a spectral function $G(\omega; \mathbf{r}_\perp; d)$ (discussed below). This is determined by the solutions of Maxwell equations with boundary conditions satisfied by the plate-sphere setup:

$$\mathcal{E}(\mathbf{r}_\perp; d) = \frac{1}{2\pi i} \oint_{\mathcal{C}} \frac{\hbar\omega}{2} \frac{\partial}{\partial\omega} [\log G(\omega; \mathbf{r}_\perp, d) - \log G(\omega; \mathbf{r}_\perp, d \rightarrow \infty)] d\omega. \quad (2)$$

Here, the (counter clock-wise) contour \mathcal{C} is defined along the imaginary axis of the complex ω -plane and a semicircle in the right hand of this plane with its radius tending to infinity. The integral along the semicircle yields a null contribution, and the integral in Equation (3) may be evaluated by considering a contour between $-i\infty$ and $i\infty$. An integration by parts leads to

$$\mathcal{E}(\mathbf{r}_\perp; d) = -\frac{\hbar}{4\pi} \int_{-\infty}^{\infty} [\log G(\omega; \mathbf{r}_\perp, d) - \log G(i\zeta; \mathbf{r}_\perp, \infty)] d\zeta. \quad (3)$$

The Casimir force is then obtained by calculating the derivative $F(\mathbf{r}_\perp; d) = -\partial\mathcal{E}(\mathbf{r}_\perp; d)/\partial d$. The eigenfrequency set of the sphere-substrate setup $\{\omega_k(\mathbf{r}_\perp; d)\}$ is obtained by assuming that the vacuum fluctuations induce a charge distribution on the sphere, described at lowest level, as a point dipole moment located at its center:

$$\mathbf{p}_{\text{ns}}^0(\omega) = \alpha(\omega) \mathbf{E}^{\text{vac}}(\omega), \quad (4)$$

where $\alpha(\omega) = 4\pi R^3(\epsilon_{\text{ns}} - 1)/(\epsilon_{\text{ns}} + 2)$ denotes the nanosphere polarizability with R the nanosphere radius and \mathbf{E}^{vac} denoting the electric field in vacuum. This dipole moment introduces in turn a charge distribution in the YBCO half-space. By using the images method it follows that the total induced dipole moment on the sphere is

$$\mathbf{p}_{\text{ns}}(\omega; \mathbf{r}_\perp) = \alpha(\omega) [\mathbf{E}^{\text{vac}}(\omega) + \mathbb{T} \cdot \mathbf{p}_{\text{sub}}(\mathbf{r}_\perp)]. \quad (5)$$

Here, \mathbb{T} is the dipole-dipole interaction tensor $\mathbb{T} = (3\mathbf{r}_0\mathbf{r}_0 - r_0^2\mathbb{I})/r_0^5$, with \mathbf{r}_0 a vector joining the center of the sphere and its image dipole below the substrate surface. In turn,

the relation between the dipole moment on the sphere and the dipole moment induced on the YBCO substrate is $\mathbf{p}_{\text{sub}}(\omega; \mathbf{r}_{\perp}) = f_c(\omega; \mathbf{r}_{\perp}) \mathbb{M} \cdot \mathbf{p}_{\text{ns}}(\mathbf{r}_{\perp})$, where $\mathbb{M} = \text{diag}(-1, -1, 1)$ is a diagonal matrix in the chosen coordinate frame, and the contrast factor $f_c(\omega; \mathbf{r}_{\perp}) \equiv (1 - \epsilon_{\text{sub}}(\omega; \mathbf{r}_{\perp})) / (1 + \epsilon_{\text{sub}}(\omega; \mathbf{r}_{\perp}))$. By substituting $\mathbf{p}_{\text{sub}}(\omega; \mathbf{r}_{\perp})$ into Equation (5), one obtains:

$$\left[\alpha^{-1}(\omega) \mathbb{I} + f_c(\omega; \mathbf{r}_{\perp}) \mathbb{M} \cdot \mathbb{T} \right] \cdot \mathbf{p}_{\text{ns}}(\omega; \mathbf{r}_{\perp}) = \mathbf{E}^{\text{vac}}(\omega), \quad (6)$$

which, by introducing the function $u(\omega) = [1 - \epsilon_{\text{ns}}(\omega)]^{-1}$ and explicitly substituting $\alpha(\omega)$, may be re-expressed as the secular equation:

$$[-u(\omega) \mathbb{I} + \mathbb{H}(\mathbf{r}_{\perp})] \cdot \mathbf{p}_{\text{ns}}(\omega; \mathbf{r}_{\perp}) = \tilde{\mathbf{E}}^{\text{vac}}(\omega), \quad (7)$$

where $\mathbb{H}(\mathbf{r}_{\perp}) = (1/3)[\mathbb{I} + R^3 f_c(\omega; \mathbf{r}_{\perp}) \mathbb{M} \cdot \mathbb{T}]$, and $\tilde{\mathbf{E}}^{\text{vac}} = (1/3)R^3 \mathbf{E}^{\text{vac}}$. By performing the change of variable $\omega \rightarrow i\zeta$, it follows that the matrix \mathbb{H} in Equation (7) is real. This allows us to introduce the spectral function such that

$$G(i\zeta; \mathbf{r}_{\perp}, d) \equiv \prod_l [-u(i\zeta) + \eta_l(i\zeta; \mathbf{r}_{\perp}, d)] = 0, \quad (8)$$

which in the present case implies three eigenvalues,

$$\eta_{1,2}(i\zeta; \mathbf{r}_{\perp}, d) = \frac{1}{3} \left[1 + \frac{f_c(i\zeta; \mathbf{r}_{\perp})}{[2(1 + d/R)]^3} \right]; \quad \eta_3(i\zeta; \mathbf{r}_{\perp}, d) = \frac{1}{3} \left[1 + \frac{2f_c(i\zeta; \mathbf{r}_{\perp})}{[2(1 + d/R)]^3} \right], \quad (9)$$

whose structure reflects the dipole–dipole interaction described by the tensor \mathbb{T} , and $\eta_{1,2}$ correspond to dipoles parallel to the surface, while η_3 is perpendicular. Substitution of $G(i\zeta; \mathbf{r}_{\perp}, d)$ into Equation (2) leads to a final expression for Casimir force at null temperature:

$$\begin{aligned} F(\mathbf{r}_{\perp}, d) &= \frac{\hbar}{4\pi} \frac{\partial}{\partial d} \sum_l \int_{-\infty}^{\infty} \log[-u(i\zeta) + \eta_l(i\zeta; \mathbf{r}_{\perp}, d)] d\zeta \\ &= \frac{\hbar}{16\pi R} \frac{1}{(1 + d/R)^4} \int_{-\infty}^{\infty} \left[\frac{f_c(i\zeta; \mathbf{r}_{\perp})}{-u(i\zeta) + \eta_1(i\zeta; \mathbf{r}_{\perp}, d)} + \frac{f_c(i\zeta; \mathbf{r}_{\perp})}{-u(i\zeta) + \eta_3(i\zeta; \mathbf{r}_{\perp}, d)} \right] d\zeta, \end{aligned} \quad (10)$$

where the feature that $\eta_1(i\zeta; \mathbf{r}_{\perp}, d) = \eta_2(i\zeta; \mathbf{r}_{\perp}, d)$ has been considered.

This result may be generalized to the finite-temperature regime by use of the Matsubara formalism. In this approach, the frequency integration is replaced by a summation over discrete frequencies $\zeta_n = 2\pi k_B T n / \hbar$, with n an integer number. In that case, the final expression for temperature-dependent Casimir force is:

$$F(\mathbf{r}_{\perp}, d; T) = \frac{k_B T}{4R} \frac{1}{(1 + d/R)^4} \sum_{n=0}^{\infty} \left[\frac{f_c(i\zeta_n; \mathbf{r}_{\perp})}{-u(i\zeta_n) + \eta_1(i\zeta_n; \mathbf{r}_{\perp})} + \frac{f_c(i\zeta_n; \mathbf{r}_{\perp})}{-u(i\zeta_n) + \eta_3(i\zeta_n; \mathbf{r}_{\perp})} \right], \quad (11)$$

where the prime implies that the $n = 0$ term should be multiplied by a factor $1/2$.

The influence of higher-order multipoles on the Casimir force for the present configuration has been studied in Refs. [42,43]. It follows that for sphere–substrate multipolar interaction of order l and l' , respectively, the interaction energy $\mathcal{E}(\mathbf{r}_{\perp}; d) \sim f(\mathbf{r}_{\perp}) / (2[R + d])^{l+l'+1}$, and therefore, $F(\mathbf{r}_{\perp}; d) \sim f(\mathbf{r}_{\perp}) / (2[R + d])^{l+l'+2}$. However, specific calculations [42] indicate that the contributions for $l, l' > 1$, only become relevant for distances $d/R < 2$, consistently with the dipolar approximation considered in this study.

2.2. Ginzburg–Landau Theory and the Optical Response of the YBCO Substrate

In the expressions derived in Section 2.1, the functions $u(\omega)$ and $f_c(\omega)$ are respectively determined by the dielectric response of the nanosphere, ϵ_{ns} , and the planar substrate, ϵ_{sub} . The dielectric properties of the gold nanosphere may be straightforwardly represented by a Drude function $\epsilon_{\text{ns}}(\omega) = 1 - \omega_{Au}^2 / (\omega^2 + i\gamma_{Au}\omega)$, where the gold plasma

frequency, $\omega_{Au} = 9.1$ eV, and the inverse scattering rate, $\gamma_{Au} = 0.02$ eV. Therefore, $u(i\zeta) = -(\zeta^2 + \gamma_{Au}\zeta)/\omega_{Au}^2$.

On the other hand, to characterize the dielectric response of the YBCO subject to the action of an applied magnetic field, \mathbf{H} , we put forth a straightforward variation of the GL theory of superconductivity that takes into account specific SC features of HTSCs, such as YBCO. In the GL theory, the transit to the SC state is described as a second-order phase transition determined by a complex order parameter, $\Psi(\mathbf{r})$, null in the normal phase, but finite in the SC phase, characterizing a long-range order specified by the number density of SC pairs, $n_s(\mathbf{r}) = |\Psi(\mathbf{r})|^2$. We incorporate in the GL formalism the following findings [48]: (i) cuprate superconductors exhibit a layered crystallographic structure in which superfluid transport of CPs occurs mainly along CuO_2 planes (the ab -planes), whereas CP transport along the perpendicular c -axis occurs due to Josephson tunneling, with respective effective masses, m_{ab}^* and m_c^* , reflecting an anisotropic charge transport measured by the ratio $\gamma^2 = m_c^*/m_{ab}^* \approx 50$, (ii) an extremely short CP coherence length, such that the GL parameter $\kappa \gg 1$. The finding that $\gamma^2 \gg 1$ implies that YBCO is an uniaxial material with a concomitant anisotropic dielectric response characterized by the diagonal tensor $\varepsilon = \text{diag}(\varepsilon_{ab}, \varepsilon_{ab}, \varepsilon_c)$ in the coordinate system depicted in Figure 1. However, a related study on the radiative heat transfer between nearby YBCO surfaces [49] revealed that electromagnetic mode contributions involving ε_c are relevant only for thin film configurations. Therefore, in the following, we assume that $\varepsilon_{\text{sub}} = \varepsilon_{ab}$. On the other hand, the joint conditions (i) and (ii) are indicative of a strongly binding pair interaction, leading the formation of a 2D gas of weakly-interacting particles, able to form a BEC [50].

In this framework, the anisotropic free energy density in the SC state in presence of a magnetic field $\mathbf{B}(\mathbf{r}) = \nabla \times \mathbf{A}(\mathbf{r})$, with \mathbf{A} the electromagnetic potential, can be expressed as

$$f_s(T) = f_n(T) + \frac{1}{2}(\hat{\pi}\Psi)^\dagger \cdot \left(\frac{1}{m^*}\right) \cdot (\hat{\pi}\Psi) + a_T|\Psi|^2 + \frac{b}{2}|\Psi|^4 + \frac{1}{2\mu_0}\mathbf{B}^2(\mathbf{r}), \quad (12)$$

where $f_n(T)$ is the normal state contribution, Ψ is the superconducting order parameter, the symbol † denotes hermitian conjugate, μ_0 is magnetic permeability of free space, the canonical momentum $\hat{\pi} = -i\hbar\nabla + e^*\mathbf{A}$, with $e^* = 2e$ the CP charge, and the reciprocal mass tensor is also diagonal in the chosen coordinate system: $(1/m^*) = \text{diag}(1/m_{ab}^*, 1/m_{ab}^*, 1/m_c^*)$. In the original GL approach, $a_T = a_0(T - T_c)$ and $b > 0$; however, as shown in Section 2.3, a more accurate description of the physical properties of SC materials can be achieved by considering alternative temperature parameterizations.

In the SC state, the total energy is obtained by spatial integration of Equation (12), $F_s = \int f_s(T)d^3r$. It follows that the functional differentiation, $\delta F_s(T)/\delta\Psi^*(\mathbf{r})$, then leads to the anisotropic GL equation

$$-\frac{\hbar^2}{2}\left[\nabla - \frac{ie^*}{\hbar}\mathbf{A}\right] \cdot \left(\frac{1}{m^*}\right) \cdot \left[\nabla - \frac{ie^*}{\hbar}\mathbf{A}\right]\Psi + (a_T + b|\Psi|^2)\Psi = 0, \quad (13)$$

while the differentiation $\delta F_s(T)/\delta\mathbf{A}(\mathbf{r})$ yields the current density

$$\mathbf{J}_s = -\frac{i\hbar e^*}{2}\left(\frac{1}{m^*}\right) \cdot [\Psi^*\nabla\Psi - \Psi\nabla\Psi^*] - \left(\frac{1}{m^*}\right) \cdot e^{*2}\mathbf{A}|\Psi|^2. \quad (14)$$

It can be shown that the mass anisotropy induces in turn anisotropic coherence lengths, $\xi_j(T)$, satisfying the relations $\xi_{ab}^2(T) = \hbar^2/2m_{ab}^*|a_T|$, and $\xi_c^2(T) = \hbar^2/2m_c^*|a_T|$ [48]. In absence of external fields or material boundaries, the former equations predict a second-order phase transition, with an order parameter magnitude, $|\Psi_\infty|^2 = 0$, for $a_T > 0$, and $n_s = |\Psi_\infty|^2 = -a_T/b$, for $a_T < 0$, and a null current density. In this case, the condensation energy of the superconductor (per unit volume) is given by [48]

$$f_s(T) - f_n(T) = -a_T^2/2b = -\mu_0 H_{c2}^2(T)/4\kappa^2, \quad (15)$$

with $H_{c2}(T) = \Phi_0/2\pi\zeta_{ab}^2(T)$. In the general case, Equations (13) and (14) represent a coupled equation system; however, for type II materials this system uncouples by taking into account that a thermodynamic phase transition also occurs for magnetic fields $H = H_{c2}$. Since the phase transition is of second order, Ψ is small and so is the magnetization \mathbf{M} . Therefore, $\mathbf{B} = \mu_0(\mathbf{H} + \mathbf{M}) \approx \mu_0\mathbf{H}$, where \mathbf{H} is the applied field. This implies that, near H_{c2} , the spatial variation in $\mathbf{B}(\mathbf{r})$ can be neglected and consider that it has the form $\mathbf{B} = B\mathbf{e}_z$, where \mathbf{e}_z is directed along the crystallographic c -axis. Then, in the Landau gauge, the vector potential $\mathbf{A} = Bx\mathbf{e}_y$. A further consequence of the smallness of Ψ is that the GL equation may be linearized by dropping cubic term in Equation (13). Then, the GL equation becomes

$$\frac{-\hbar^2}{2m_{ab}^*} \left(\nabla_{\perp} - \frac{ie^*}{\hbar} Bx\mathbf{e}_y \right)^2 \Psi - \frac{\hbar^2}{2m_c^*} \frac{\partial^2}{\partial z^2} \Psi = |a_T| \Psi. \quad (16)$$

As shown by Abrikosov [33], Equation (16) admits Landau-level solutions of the form $\Psi(\mathbf{r}) = \Phi(\mathbf{r}_{\perp})e^{ik_z z}$, where the ground state is given by $k_z = 0$, and

$$\Phi(\mathbf{r}_{\perp}) = \sum_{n=-\infty}^{\infty} C_n e^{i(2\pi n y)/L_y} \exp[-(x + n\Phi_0/BL_y)^2 / \zeta_{ab}^2(T)], \quad (17)$$

which is a periodic function provided $C_n = C_{n+\nu}$, for some integer ν . The case $\nu = 1$ corresponds to a square lattice as displayed by HTSCs, while the case $\nu = 2$ yields a triangular lattice, characteristic of conventional superconductors [34]. The stability of these solutions can be analyzed by incorporating the effects of nonlinear terms in the description. This is determined by the Abrikosov parameter, $\beta_A = \langle |\Psi|^4 \rangle / \langle |\Psi|^2 \rangle^2$. In the homogeneous case, $\beta_A = 1$, whereas $\beta_A > 1$ implies less favorable energies. In particular, the energy of the triangular configuration is smaller than that of the square one by less than 1% [34]. In the square lattice configuration, the summation may be re-expressed in terms of a Jacobi theta function, $\theta_3(z; q) = \sum_{n=-\infty}^{\infty} q^{n^2} e^{2inz}$, so that

$$\Phi(\tilde{x}, \tilde{y}) = C e^{-\frac{1}{2}\kappa^2 \tilde{x}^2} \theta_3 \left[1; \sqrt{2\pi} \kappa i(\tilde{x} + i\tilde{y}) \right]. \quad (18)$$

In this case, $\kappa = \lambda_{ab}/\zeta_{ab}$ where λ_{ab} is the ab -plane penetration length, while $\tilde{x} = x/\lambda_{ab}$, $\tilde{y} = y/\lambda_{ab}$. Notice that λ_{ab} describes the magnetic field screening by supercurrents flowing along the ab -plane. Figure 1 depicts the resulting contours of constant probability defined by $|\Phi(\tilde{\mathbf{r}}_{\perp})|^2$. We observe a lattice structure with square elementary cells with dimensionless periods $\mathcal{L}_x = \mathcal{L}_y = \sqrt{2\pi}/\kappa$. By writing $\Phi(\tilde{\mathbf{r}}_{\perp}) = |\Phi(\tilde{\mathbf{r}}_{\perp})| e^{i\chi(\tilde{\mathbf{r}}_{\perp})}$ it follows that the GL current density is given by $\mathbf{J}_s = (\hbar e^*/2m_{ab}^*) |\Phi|^2 (\nabla\chi - (e^*/\hbar)\mathbf{A})$, indicating that supercurrent lines coincide with the equi-probability contours, being the vortex cores located at the darkest zones of the figure. Notice that the vortex size can be tuned by the substrate temperature T , which modulates the lattice parameter. In normal units, it follows that $L_x(T) = L_y(T) = \sqrt{2\pi}\zeta_{ab}(T)$, so that $L_x(2\text{ K}) \approx 4\text{ nm}$, whereas $L_x(90\text{ K}) \approx 16\text{ nm}$.

2.3. Thermal Properties of the Order Parameter

We describe the thermal properties of the order parameter by recurring to the London two-fluid model of superconductivity, inspired in turn by the two-fluid model of the superfluid He^4 . This model assumes that the charge density, n , at a fixed position, is split as a sum of normal and SC contributions, $n = n_n(T) + n_s(T)$. The temperature behavior of $n_s(T)$ is frequently described according to the Casimir–Gorter model, $n_s(T)/n = 1 - (T/T_c)^4$ [51]. However, this empirical relation is in clear disagreement with experimental observations [48].

We consider instead, as mentioned above, that CPs define a 2D gas of weakly-interacting particles with BE statistical properties. As a consequence, the energy excitation spectrum is given by Bogoliubov expression $E_k = \left[(\hbar c_s k)^2 + (\hbar^2 k^2 / 2m^*)^2 \right]^{1/2}$ which, in the low-momentum limit, leads to a phonon dispersion relation, $E_k \approx \hbar c_s k$, with c_s the

sound's speed, consistent with Landau's criterion for superfluid particle transport [52]. In that case, we assume the pair occupancy density at any given position can be expressed, for $T < T_{\text{BEC}}$, in the form [53]

$$n^{2D} = n_0^{2D}(T) + \sum_{\mathbf{k} \neq 0} \frac{1}{\exp(\hbar c_s k / k_B T) - 1}. \quad (19)$$

Here, $T_{\text{BEC}} = \left(2\pi\hbar^2 c_s^2 n^{2D} / k_B^2 \zeta(2)\right)^{1/2}$, and $\zeta(2)$ is a Riemann's zeta function. The summation in Equation (19) can be straightforwardly evaluated by integrating over a 2D density of states. It follows that $n_0^{2D}(T) / n^{2D} = 1 - (T/T_c)^2$ [53,54]. Taking into account that in the dilute regime the condensate and the density of superfluid charge carriers coincide, we identify $T_{\text{BEC}} = T_c$. This latter result implies, in particular, that the penetration length satisfies the universal relation $\lambda_{ab}^2(0) / \lambda_{ab}^2(T) = 1 - (T/T_c)^2$, which has shown to represent an accurate description of experimental data for YBCO systems under an ample range of doping levels in the whole temperature interval $0 < T < T_c$ [54–56]. By assuming now that the former results hold at every position over the SC substrate, $n_0^{2D}(\mathbf{r}, T) \approx n_s^{2D}(\mathbf{r}, T)$, and then

$$n_s^{2D}(\mathbf{r}_\perp, T) = |\Phi(\mathbf{r}_\perp)|^2 \left[1 - (T/T_c)^2\right]. \quad (20)$$

2.4. YBCO Dielectric Response

The optical properties of HTSCs have been experimentally investigated for different compounds at several temperatures and frequencies using reflectivity and impedance-type measurements [57–59]. In particular, the dielectric function, $\varepsilon(\omega)$, of YBCO samples has been measured in the normal and SC states at $T = 100$ K and $T = 2$ K, respectively. Notably, the estimated values of the optical parameters remain practically unaltered in these temperature extremes. In particular, the plasma frequency, $\omega_p^2 = e^{*2}n / \varepsilon_0 m^*$, satisfies $\omega_p(2\text{K}) = \omega_p(100\text{K}) = 0.75$ eV, suggesting that London's two-fluid model of superconductivity can be employed to derive an interpolation, $\varepsilon(\omega; T)$, valid in the entire temperature range $2 < T < 100$ K. For $T > T_c$, an accurate representation of the dielectric response includes a constant term, ε_∞ , in the optical spectrum, as well as Drude, mid-infrared (MIR), and N_{ph} phonon contributions:

$$\varepsilon_{ab}^{(n)}(\omega) = \varepsilon_\infty - \frac{\omega_p^2}{\omega^2 + i\gamma(T)\omega} - \frac{\Omega_{\text{MIR}}^2}{\omega^2 - \omega_{\text{MIR}}^2 + i\Gamma_{\text{MIR}}\omega} - \sum_{r=1}^{N_{\text{ph}}} \frac{\Omega_{\text{ph}}^2}{\omega^2 - \omega_r^2 + i\gamma_r\omega}. \quad (21)$$

Here, $\varepsilon_\infty = 3.8$, the inverse scattering rate $\gamma(T) = 0.037 + \gamma_1 T$ eV, with $\gamma_1 = 8 \times 10^{-15}$ eV/K, and the MIR parameters $\Omega_{\text{MIR}} = 2.6$ eV, $\omega_{\text{MIR}} = 0.26$ eV, $\Gamma_{\text{MIR}} = 1$ eV, whereas the phonon parameters are given in Refs. [57,58]. In the SC regime, dissipative scattering does not occur, so that $\gamma \rightarrow 0$. In that limit, $(\omega \pm i\gamma)^{-1} \rightarrow \mathcal{P}(1/\omega) \mp i\pi\delta(\omega)$, with $\delta(\omega)$ the Dirac delta function, and the dielectric function becomes:

$$\begin{aligned} \varepsilon_{ab}^{(s)}(\omega; \mathbf{r}_\perp) = \varepsilon_\infty & - \left[\frac{i\pi\omega_p^2}{2\omega} \delta(\omega) + \frac{\omega_p^2}{\omega^2} \right] \left(1 - (T/T_c)^2 \right) |\Psi(\mathbf{r})|^2 - \frac{\omega_p^2 (T/T_c)^2}{\omega^2 + i\gamma(T)\omega} \quad (22) \\ & - \frac{\Omega_{\text{MIR}}^2}{\omega^2 - \omega_{\text{MIR}}^2 + i\Gamma_{\text{MIR}}\omega} - \sum_{r=1}^{N_{\text{ph}}} \frac{\Omega_{\text{ph}}^2}{\omega^2 - \omega_r^2 + i\gamma_r\omega}. \end{aligned}$$

As explained in Section 2.1, the dielectric function has to be calculated in the rotated frequency space $i\zeta$ where the details can be found in Ref. [60]. In this scheme, the nanosphere and substrate permittivities are respectively given by $\varepsilon_{\text{ns}}(i\zeta) = \varepsilon_{\text{Au}}(i\zeta)$, $\varepsilon_{\text{sub}}(i\zeta, \mathbf{r}_\perp, T) = \varepsilon_{ab}^{(n)}(i\zeta, \mathbf{r}_\perp, T > T_c)$ and $\varepsilon_{\text{sub}}(i\zeta, \mathbf{r}_\perp, T) = \varepsilon_{ab}^{(s)}(i\zeta, \mathbf{r}_\perp, T < T_c)$.

3. Results

We show in Figure 2 the structure of Casimir force at $T = 2$ K, as a function of the position of the Au nanosphere over the AL. Here, the nanosphere radius $R = 4$ nm, and $d = 2R$. Although the dipole approximation requires, actually, $d \gg R$, as mentioned above, in a previous study, it was found that higher multipolar contributions to the force become negligible at this separation [42]. This figure reveals that the Casimir force displays a periodic structure congruent with the spatial charge distribution induced by the AL. It can be observed that the modulation amplitude $\Delta F = |F_{\max} - F_{\min}|$ is maximized at regions corresponding to the vortex cores, consistently with the finding that the material reflectivity is strongly reduced at these zones. In order to compare how these results are altered with increasing temperature, we present in Figure 3 a cross-section of the Casimir force surface at a fixed value of $\mathcal{L}_x = 0.5$, for three different temperatures: $T = 2$ K, $T = 40$ K, and $T = 90$ K, with corresponding lattice size: $L_x(2 \text{ K}) = 4.1$ nm, $L_x(40 \text{ K}) = 4.6$ nm, and $L_x(90 \text{ K}) = 16.4$ nm. We observe that in the low-temperature regime, $2 \leq T \leq 40$ K, quite similar periodic patterns arise, essentially independent of the temperature, with a relatively small modulation amplitude $\Delta F \approx 0.04$ pN. On the other hand, for $T \approx T_c$ the vortex cell size increases, but the force modulation is drastically reduced.

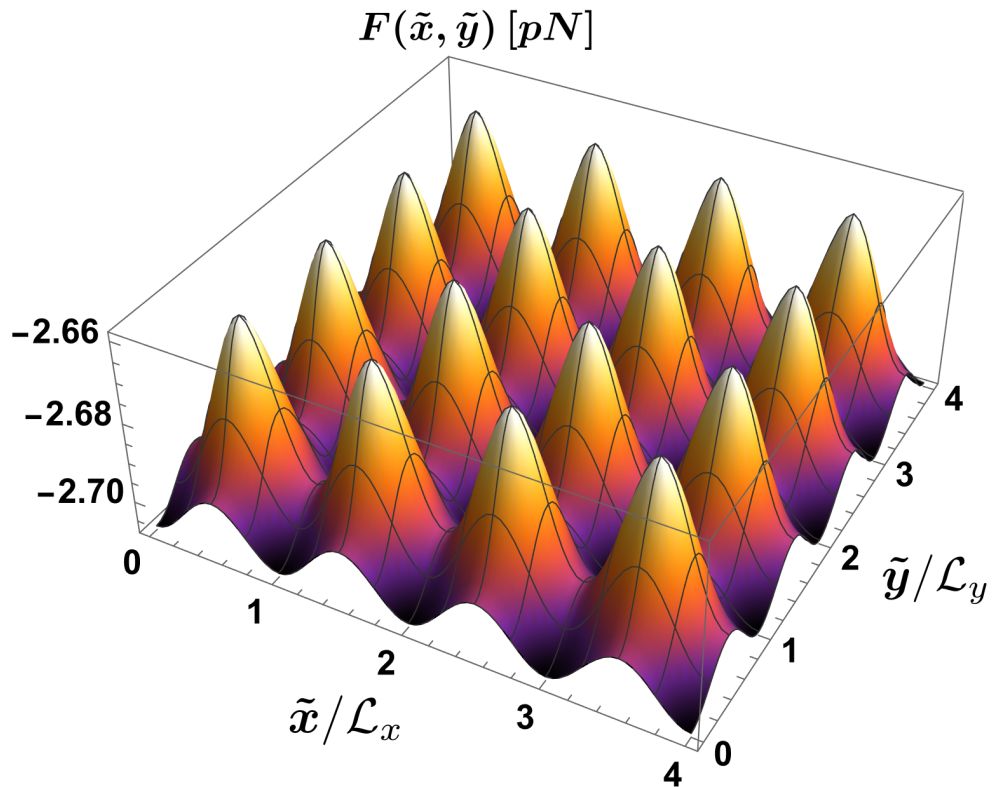


Figure 2. Periodic structure of the Casimir force as a function of the location of the Au nanosphere over the Abrikosov lattice at $T = 2$ K, for a fixed distance $d = 2R$. Here, $R = \mathcal{L}_x(2 \text{ K}) \approx 4$ nm. It can be observed that the minimal strength of the Casimir force corresponds to the vortex cores.

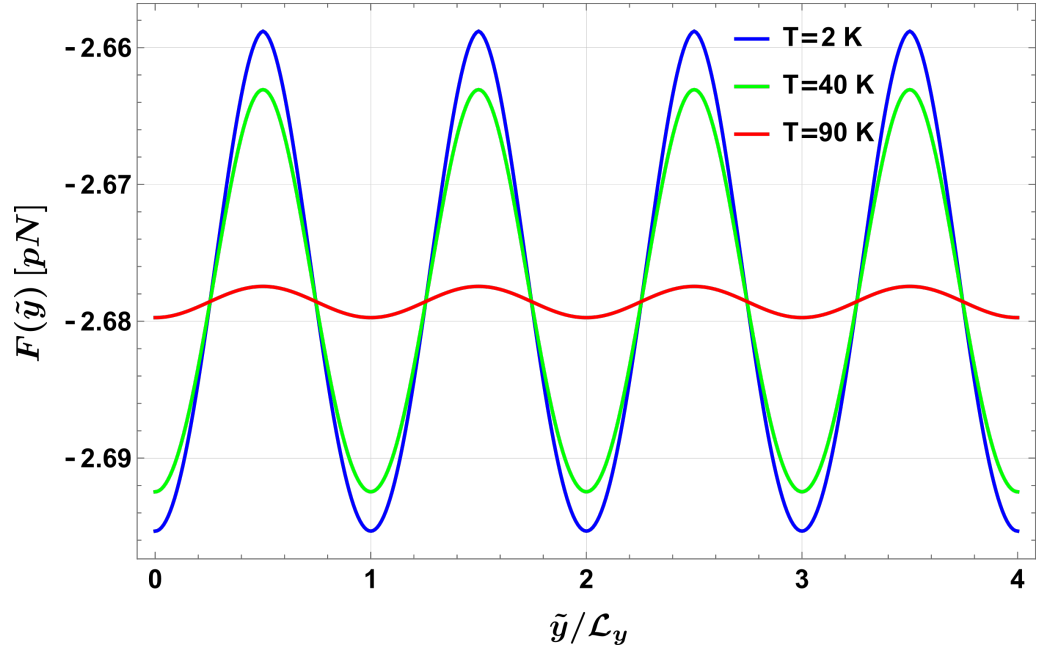


Figure 3. Comparison of the Casimir force profiles as a function of the normalized coordinate \tilde{y}/\mathcal{L}_y along a line passing right above the vortex core ($\tilde{x}/\mathcal{L}_x = 0.5$), and $d = 2R = 8$ nm, at three different temperatures: $T = 2$ K, $T = 40$ K and $T = 90$ K as indicated. Depending on the temperature, each unit period \mathcal{L}_y corresponds to spatial periods: $L_y(2 \text{ K}) = 4.1$ nm, $L_y(40 \text{ K}) = 4.6$ nm, and $L_y(90 \text{ K}) = 16.4$ nm. We observe that in the low-temperature regime the force magnitude shows almost coincident values up to $T = 40$ K, consistent with expectations that vacuum fluctuations ($\sim \hbar c/d$) overwhelm thermal fluctuations ($\sim k_B T$) at nanometer separations. Here, \hbar , c , and k_B denote the reduced Planck constant, the speed of light, and the Boltzmann constant, respectively.

4. Discussion and Conclusions

The former results have been derived within a mean-field approach that neglects thermal fluctuations of the order parameter and pinning disorder. However, in the weak-interacting limit of Cooper pairs, thermal effects can be taken into account [36]. The effect of disorder in the vortex array can be introduced by adding white noise to the coefficients of the GL free energy and performing the \mathcal{Z} functional integration, or by performing vortex matter simulations based on the numerical analysis of the time-dependent GL formulation [35,36].

Although the present study was focused on the action of magnetic fields just below the upper critical field, $H \leq H_{c2}$, the effect of fields near the lower critical value, $H \geq H_{c1}$ can be straightforwardly discussed within the clean-limit of the London theory [34]. In that case, the order parameter is given by $|\phi(r)|^2 \approx (1 + 2\zeta_{ab}^2/r^2)^{-1}$, while the local magnetic induction $B(r) = \Phi_0 K_0\left(\sqrt{r^2 + 2\zeta_{ab}^2}/\lambda_{ab}\right)/2\pi\lambda_{ab}^2$, where $K_0(x)$ is a modified Bessel function. Then, the total order parameter can be built as the product $\prod_i \phi(|\mathbf{r} - \mathbf{r}_i|)$, where \mathbf{r}_i denotes the localization of the different vortices, whereas the total magnetic induction $\mathbf{B}(\mathbf{r}) = \sum_i \mathbf{B}(|\mathbf{r} - \mathbf{r}_i|)$ [61].

The periodic structure of the system could, actually, induce diffractive effects in the predicted spatial-pattern observed in the Casimir force. Indeed it has been shown how diffraction gratings modify the force [62]. We did not consider this kind of effects because they would occur for wavelengths of the order of the period of the Abrikosov lattice, about 4–16 nm in our case. This corresponds to frequencies higher than 300 eV. For these high values of energy, the dielectric function is constant (tends to the high-frequency value, ϵ_∞), and no position dependence will be observed.

In conclusion, we presented a general methodology aimed to evaluate the Casimir force in setups constituted by SC materials under the action of an external magnetic field.

We have shown that the Abrikosov vortex lattice displayed by a type II superconductor induces Casimir forces with a periodic structure that mirrors the local charge redistribution due to superconducting currents conducting to magnetic fluxon confinement within the vortex cores. This approach may be applied to SC systems under different conditions of temperature, oxygen doping, and magnetic field configurations, allowing the analysis of alternative orderings competing with vortex matter, such as charge density waves [63], or the investigation of normal matter inside the vortices subject to multiple Andreev reflections [64].

Author Contributions: Conceptualization, S. G.C.-L., R.E.-S., G.P. and C.V.; formal analysis, S.G.C.-L., R.E.-S., G.P. and C.V.; methodology, S.G.C.-L., R.E.-S., G.P. and C.V.; software, S.G. C.-L. and C.V.; writing—original draft, S.G. C.-L., R.E.-S., G.P. and C.V.; writing—review and editing, S.G.C.-L., R.E.-S., G.P. and C.V. All authors have read and agreed to the published version of the manuscript.

Funding: S.G.C-L acknowledges financial support from UNAM DGAPA PAPIIT Grant No. TA100724. G.P. acknowledges financial support from UNAM DGAPA PAPIIT Grant No. IN104522, UNAM DGAPA PAPIME PE101223 and CONACyT Projects No. 1564464 and No. 1098652. R.E.-S. acknowledges partial support from CONACyT Project No. A1-S-10537.

Data Availability Statement: The data presented in this study are available on request from the corresponding author.

Conflicts of Interest: The authors declare no conflict of interest.

References

1. Casimir, H.B.G. On the attraction between two perfectly conducting plates. *Proc. Kon. Ned. Akad. Wet. B* **1948**, *51*, 793–795. Available online: <https://dwc.knaw.nl/DL/publications/PU00018547.pdf> (accessed on 29 January 2024).
2. Lifshitz, E.M. The theory of molecular attractive forces between solids. *Sov. Phys. JETP* **1956**, *2*, 73–83. Available online: <http://jetp.ras.ru/cgi-bin/e/index/e/2/1/p73?a=list> (accessed on 29 January 2024).
3. Lamoreaux, S.K. Demonstration of the Casimir force in the 0.6 to 6 μm range. *Phys. Rev. Lett.* **1997**, *78*, 5–8. [CrossRef]
4. Harris, B.W.; Chen, F.; Mohideen, U. Precision measurement of the Casimir force using gold surfaces. *Phys. Rev. A* **2000**, *62*, 052109. [CrossRef]
5. Bressi, G.; Carugno, G.; Onofrio, R.; Ruoso, G. Measurement of the Casimir force between parallel metallic surfaces. *Phys. Rev. Lett.* **2002**, *88*, 041804. [CrossRef] [PubMed]
6. Decca, R.S.; López, D.; Fischbach, E.; Krause, D.E. Measurement of the Casimir force between dissimilar metals. *Phys. Rev. Lett.* **2003**, *91*, 050402. [CrossRef] [PubMed]
7. Chen, F.; Klimchitskaya, G.L.; Mohideen, U.; Mostepanenko, V.M. Theory confronts experiment in the Casimir force measurements: Quantification of errors and precision. *Phys. Rev. A* **2004**, *69*, 022117. [CrossRef]
8. Decca, R.S.; López, D.; Fischbach, E.; Klimchitskaya, G.L.; Krause, D.E.; Mostepanenko, V.M. Precise comparison of theory and new experiment for the Casimir force leads to stronger constraints on thermal quantum effects and long-range interactions. *Ann. Phys.* **2005**, *318*, 37–80. [CrossRef]
9. Krause, D.E.; Decca, R.S.; López, D.; Fischbach, E. Experimental investigation of the Casimir force beyond the proximity-force approximation. *Phys. Rev. Lett.* **2007**, *98*, 050403. [CrossRef]
10. Jourdan, G.; Lambrecht, A.; Comin, F.; Chevrier, J. Quantitative non-contact dynamic Casimir force measurements. *EPL (Europhys. Lett.)* **2009**, *85*, 31001. [CrossRef]
11. Chang, C.-C.; Banishev, A.A.; Castillo-Garza, R.; Klimchitskaya, G.L.; Mostepanenko, V.M.; Mohideen, U. Gradient of the Casimir force between Au surfaces of a sphere and a plate measured using an atomic force microscope in a frequency-shift technique. *Phys. Rev. B* **2012**, *85*, 165443. [CrossRef]
12. Banishev, A.A.; Klimchitskaya, G.L.; Mostepanenko, V.M.; Mohideen, U. Demonstration of the Casimir force between ferromagnetic surfaces of a Ni-coated sphere and a Ni-coated plate. *Phys. Rev. Lett.* **2013**, *110*, 137401. [CrossRef] [PubMed]
13. Castillo-Garza, R.; Xu, J.; Klimchitskaya, G.L.; Mostepanenko, V.M.; Mohideen, U. Casimir interaction at liquid nitrogen temperature: Comparison between experiment and theory. *Phys. Rev. B* **2013**, *88*, 075402. [CrossRef]
14. Klimchitskaya, G.L.; Mohideen, U.; Mostepanenko, V.M. The Casimir force between real materials: Experiment and theory. *Rev. Mod. Phys.* **2009**, *81*, 1827–1885. [CrossRef]
15. Rodriguez, A.W.; Capasso, F.; Johnson, S.G. The Casimir effect in microstructured geometries. *Nat. Phot.* **2011**, *5*, 211–221. [CrossRef]
16. Milonni, P.W. *The Quantum Vacuum: An Introduction to Quantum Electrodynamics*; Academic Press, Inc.: San Diego, CA, USA, 2013. [CrossRef]
17. Milton, K.A. *The Casimir Effect: Physical Manifestations of Zero-Point Energy*; World Scientific Co., Ltd.: Singapore, 2001. [CrossRef]

18. Bordag, M.; Klimchitskaya, G.L.; Mohideen, U.; Mostepanenko, V.M. *Advances in the Casimir Effect*; Oxford University Press Inc.: New York, NY, USA, 2009. [CrossRef]
19. Sushkov, A.; Kim, W.; Dalvit, D.; Lamoreaux, S. Observation of the thermal Casimir force. *Nat. Phys.* **2011**, *7*, 230–233. [CrossRef]
20. Simpson, W.M.R.; Leonhardt, U. *Forces of the Quantum Vacuum: An Introduction to Casimir Physics*; World Scientific: Singapore, 2015. [CrossRef]
21. Bimonte, G.; López, D.; Decca, R.S. Isoelectronic determination of the thermal Casimir force. *Phys. Rev. B* **2016**, *93*, 184434. [CrossRef]
22. Liu, M.; Xu, J.; Klimchitskaya, G.L.; Mostepanenko, V.M.; Mohideen, U. Precision measurements of the gradient of the Casimir force between ultraclean metallic surfaces at larger separations. *Phys. Rev. A* **2019**, *100*, 052511. [CrossRef]
23. Bimonte, G.; Spreng, B.; Maia Neto, P.A.; Ingold, G.L.; Klimchitskaya, G.L.; Mostepanenko, V.M.; Decca, R.S. Measurement of the Casimir force between 0.2 and 8 mm: Experimental procedures and comparison with theory. *Universe* **2021**, *7*, 93. [CrossRef]
24. Bimonte, G.; Calloni, E.; Esposito, G.; Milano, L.; Rosa, L. Towards measuring variations of Casimir energy by a superconducting cavity. *Phys. Rev. Lett.* **2005**, *94*, 180402. [CrossRef]
25. Bimonte, G.; Born, D.; Calloni, E.; Esposito, G.; Il'ichev, E.; Rosa, L.; Scaldaferrì, O.; Tafuri, F.; Vaglio, R.; Hübner, U. The Aladin2 experiment: Status and perspectives. *J. Phys. A Math. Gen.* **2006**, *39*, 6153–6159. [CrossRef]
26. Bimonte, G.; Calloni, E.; Esposito, G.; Rosa, L. Casimir energy and the superconducting phase transition. *J. Phys. A Math. Gen.* **2006**, *39*, 6161–6171. [CrossRef]
27. Bimonte, G.; Born, D.; Calloni, E.; Esposito, G.; Huebner, U.; Il'ichev, E.; Rosa, L.; Tafuri, F.; Vaglio, R. Low noise cryogenic system for the measurement of the Casimir energy in rigid cavities. *J. Phys. A Math. Theor.* **2008**, *41*, 164023. [CrossRef]
28. Bimonte, G. Casimir effect in a superconducting cavity and the thermal controversy. *Phys. Rev. A* **2008**, *78*, 062101. [CrossRef]
29. Norte, R.A.; Forsch, M.; Wallucks, A.; Marinković, I.; Gröblacher, S. Platform for measurements of the Casimir force between two superconductors. *Phys. Rev. Lett.* **2018**, *121*, 030405. [CrossRef]
30. Bimonte, G. Casimir effect between superconductors. *Phys. Rev. A* **2019**, *99*, 052507. [CrossRef]
31. Villarreal, C.; Caballero-Benitez, S.F. Casimir forces and high- T_c superconductors. *Phys. Rev. A* **2019**, *100*, 042504. [CrossRef]
32. Castillo-López, S.G.; Esquivel-Sirvent, R.; Pirruccio, G.; Villarreal, C. Casimir forces out of thermal equilibrium near a superconducting transition. *Sci. Rep.* **2022**, *12*, 2905. [CrossRef]
33. Abrikosov, A.A. Nobel Lecture: Type-II superconductors and the vortex lattice. *Rev. Mod. Phys.* **2004**, *76*, 975–979. [CrossRef]
34. Annett, J.F. *Superconductivity, Superfluids and Condensates*; Oxford University Press Inc.: New York, NY, USA, 2004. Available online: <https://archive.org/details/superconductivity000anne/> (accessed on 29 January 2024).
35. Blatter, G.; Feigel'man, M.V.; Geshkenbein, V.B.; Larkin, A.I.; Vinokur, V.M. Vortices in high-temperature superconductors. *Rev. Mod. Phys.* **1994**, *66*, 1125–1388. [CrossRef]
36. Rosenstein, B.; Li, D. Ginzburg-Landau theory of type II superconductors in magnetic field. *Rev. Mod. Phys.* **2010**, *82*, 109–168. [CrossRef]
37. Kwok, W.K.; Welp, U.; Glatz, A.; Koshchev, A.E.; Kihlstrom, K.J.; Crabtree, G.W. Vortices in high-performance high-temperature superconductors. *Rep. Prog. Phys.* **2016**, *79*, 116501. [CrossRef] [PubMed]
38. Suderow, H.; Guillaumon, I.; Rodrigo, J.G.; Vieira, S. Imaging superconducting vortex cores and lattices with a scanning tunneling microscope. *SuST* **2014**, *27*, 063001. [CrossRef]
39. Sonier, J.E.; Brewer, J.H.; Kiefl, R.F. μ SR studies of the vortex state in type-II superconductors. *Rev. Mod. Phys.* **2000**, *72*, 769–811. [CrossRef]
40. Scheel, S.; Fermini, R.; Hinds, E. Feasibility of studying vortex noise in two-dimensional superconductors with cold atoms. *Phys. Rev. A* **2007**, *75*, 064901. [CrossRef]
41. Román-Velázquez, C.E.; Noguez, C.; Villarreal, C.; Esquivel-Sirvent, R. Spectral representation of the nonretarded dispersive force between a sphere and a substrate. *Phys. Rev. A* **2004**, *69*, 042109. [CrossRef]
42. Noguez, C.; Román-Velázquez, C.E.; Esquivel-Sirvent, R.; Villarreal, C. High-multipolar effects on the Casimir force: The non-retarded limit. *EPL (Europhys. Lett.)* **2004**, *67*, 191–197. [CrossRef]
43. Noguez, C.; Román-Velázquez, C.E. Dispersive force between dissimilar materials: Geometrical effects. *Phys. Rev. B* **2004**, *70*, 195412. [CrossRef]
44. Neto, P.A.M.; Lambrecht, A.; Reynaud, S. Casimir energy between a plane and a sphere in electromagnetic vacuum. *Phys. Rev. A* **2008**, *78*, 012115. [CrossRef]
45. Canaguier-Durand, A.; Neto, P.A.M.; Cavero-Pelaez, I.; Lambrecht, A.; Reynaud, S. Casimir interaction between plane and spherical metallic surfaces. *Phys. Rev. Lett.* **2009**, *102*, 230404. [CrossRef]
46. Canaguier-Durand, A.; Neto, P.A.M.; Lambrecht, A.; Reynaud, S. Thermal Casimir effect in the plane-sphere geometry. *Phys. Rev. Lett.* **2010**, *104*, 040403. [CrossRef]
47. Bimonte, G. Going beyond PFA: A precise formula for the sphere-plate Casimir force. *EPL (Europhys. Lett.)* **2017**, *118*, 20002. [CrossRef]
48. Tinkham, M. *Introduction to Superconductivity*; Dover Publications, Inc.: Mineola, NY, USA, 2004.
49. Castillo-López, S.; Villarreal, C.; Esquivel-Sirvent, R.; Pirruccio, G. Enhancing near-field radiative heat transfer by means of superconducting thin films. *Int. J. Heat Mass Transf.* **2022**, *182*, 121922. [CrossRef]

50. Nozières, P.; Schmitt-Rink, S. Bose condensation in an attractive fermion gas: From weak to strong coupling superconductivity. *J. Low Temp. Phys.* **1985**, *59*, 195–211. [CrossRef]
51. Pal, S.; Ganguly, K.; Basu, A.; Sharma, U.D. Gorter-Casimir two fluid model revisited and possible applications to superconductivity. *Int. J. Innov. Res. Phys.* **2019**, *1*, 17–26. [CrossRef]
52. Landau, L.D.; Lifshitz, E.M. *Statistical Physics*; Elsevier Butterworth-Heinemann: Oxford, UK, 2013. [CrossRef]
53. Fujita, S.; Godoy, S. *Quantum Statistical Theory of Superconductivity*; Springer Science + Business Media: New York, NY, USA, 1996. [CrossRef]
54. Lomnitz, M.; Villarreal, C.; de Llano, M. BEC model of high- T_c superconductivity in layered cuprates. *Int. J. Mod. Phys. B* **2013**, *27*, 1347001. [CrossRef]
55. Zuev, Y.; Kim, M.S.; Lemberger, T.R. Correlation between superfluid density and T_c of underdoped $\text{YBa}_2\text{Cu}_3\text{O}_{6+x}$ near the superconductor-insulator transition. *Phys. Rev. Lett.* **2005**, *95*, 137002. [CrossRef] [PubMed]
56. Chen, Q.; Stajic, J.; Tan, S.; Levin, K. BCS–BEC crossover: From high temperature superconductors to ultracold superfluids. *Phys. Rep.* **2005**, *412*, 1–88. [CrossRef]
57. Bonn, D.A.; O’Reilly, A.H.; Greedan, J.E.; Stager, C.V.; Timusk, T.; Kamarás, K.; Tanner, D.B. Far-infrared properties of ab-plane oriented $\text{YBa}_2\text{Cu}_3\text{O}_{7-\delta}$. *Phys. Rev. B* **1988**, *37*, 1574–1579. [CrossRef] [PubMed]
58. Timusk, T.; Herr, S.L.; Kamarás, K.; Porter, C.D.; Tanner, D.B.; Bonn, D.A.; Garrett, J.D.; Stager, C.V.; Greedan, J.E.; Reedyk, M. Infrared studies of ab-plane oriented oxide superconductors. *Phys. Rev. B* **1988**, *38*, 6683–6688. [CrossRef] [PubMed]
59. Basov, D.N.; Timusk, T. Electrodynamics of high- T_c superconductors. *Rev. Mod. Phys.* **2005**, *77*, 721–779. [CrossRef]
60. Klimchitskaya, G.L.; Mohideen, U.; Mostepanenko, V.M. Kramers–Kronig relations for plasma-like permittivities and the Casimir force. *J. Phys. A Math. Theor.* **2007**, *40*, F339–F346. [CrossRef]
61. Brandt, E.H. The flux-line lattice in superconductors. *Rep. Prog. Phys.* **1995**, *58*, 1465–1594. [CrossRef]
62. Intravaia, F.; Koev, S.; Jung, I.W.; Talin, A.A.; Davids, P.S.; Decca, R.S.; Aksyuk, V.A.; Dalvit, D.A.; López, D. Strong Casimir force reduction through metallic surface nanostructuring. *Nat. Commun.* **2013**, *4*, 2515. [CrossRef]
63. Chang, J.; Blackburn, E.; Holmes, A.T.; Christensen, N.B.; Larsen, J.; Mesot, J.; Liang, R.; Bonn, D.A.; Hardy, W.N.; Watenphul, A.; et al. Direct observation of competition between superconductivity and charge density wave order in $\text{YBa}_2\text{Cu}_3\text{O}_{6.67}$. *Nat. Phys.* **2012**, *8*, 871–876. [CrossRef]
64. Huebener, R.P. The Abrikosov vortex lattice: Its discovery and impact. *J. Supercond. Nov. Magn.* **2019**, *32*, 475–481. [CrossRef]

Disclaimer/Publisher’s Note: The statements, opinions and data contained in all publications are solely those of the individual author(s) and contributor(s) and not of MDPI and/or the editor(s). MDPI and/or the editor(s) disclaim responsibility for any injury to people or property resulting from any ideas, methods, instructions or products referred to in the content.

Electromagnetic Casimir–Polder Interaction for a Conducting Cone

Noah Graham

Department of Physics, Middlebury College, Middlebury, VT 05753, USA; ngraham@middlebury.edu

Abstract: Using the formulation of the electromagnetic Green’s function of a perfectly conducting cone in terms of analytically continued angular momentum, we compute the Casimir–Polder interaction energy of a cone with a polarizable particle. We introduce this formalism by first reviewing the analogous approach for a perfectly conducting wedge, and then demonstrate the calculation through numerical evaluation of the resulting integrals.

Keywords: Casimir–Polder interaction; Kontorovich–Lebedev transformation; electromagnetic Green’s function

1. Introduction

The Casimir–Polder interaction between an uncharged conducting object on a polarizable particle [1–3] provides one of the simplest examples of a mesoscopic fluctuation-based force. Since the particle can be treated as a delta-function potential, its effects can be evaluated in any basis. As a result, in the scattering formalism, the interaction energy between the particle and conducting object can be determined directly from the full electromagnetic Green’s function in the presence of the object. In contrast, for the Casimir force between two objects, one needs the scattering T -matrices for each object connected by the free Green’s function expressed in each object’s scattering basis to propagate fluctuations between objects [4–9].

Along with the standard plane, cylinder, and sphere geometries, for which there exist analytic expressions in terms of scattering modes for the Green’s function in the presence of a perfect conductor, the conducting wedge [10,11], which also models a cosmic string [12], is a case where the Green’s function can be obtained analytically as a mode sum, by imposing the wedge boundary conditions through a discrete, fractional, angular momentum index. However, one can also use analytic continuation to a continuous, complex angular momentum to express this Green’s function in terms of the T -matrix for scattering in the angular (rather than radial) variable [13–16], an approach that then extends to the case of the cone [16] and puts the Green’s function into a form that is more directly analogous to the sphere, cylinder, and plane results. Mathematically, this approach is based on the Mehler–Fock and Kontorovich–Lebedev transforms [17]. The complex angular momentum approach requires that one consider only imaginary frequencies, however, so though it is well-suited to equilibrium problems at both zero and nonzero temperature, it cannot be applied to heat transfer [18], which must be computed on the real axis.

All of these calculations allow for investigation of the Casimir–Polder interaction near a sharp edge or tip, where the derivative expansion approach [19–23] is not applicable, yielding semi-analytic results in terms of a small number of integrals and sums. However, this approach is limited to perfect conductors and, as a result, complements calculations based on surface current methods [24–27], which are more complex numerically, but applicable to more general geometries and materials. Recent work using the multiple scattering surface method, in which one combines expansions in scattering between and within objects [28], provides a particularly relevant comparison by demonstrating the Casimir force between a dielectric wedge and plane.

Citation: Graham, N.

Electromagnetic Casimir–Polder Interaction for a Conducting Cone. *Physics* **2023**, *5*, 1003–1012. <https://doi.org/10.3390/physics5040065>

Received: 23 August 2023

Revised: 14 September 2023

Accepted: 16 September 2023

Published: 12 October 2023



Copyright: © 2023 by the author. Licensee MDPI, Basel, Switzerland. This article is an open access article distributed under the terms and conditions of the Creative Commons Attribution (CC BY) license (<https://creativecommons.org/licenses/by/4.0/>).

Here we use the analytically continued scattering formalism to calculate the Casimir–Polder force of a conducting cone on a polarizable atom, as might arise, for example, in the case of a particle beam passing by an atomic force microscope. We begin by reviewing the wedge calculation in the discrete angular momentum approach, and show how to obtain the same result using the analytic continuation approach. We then extend this calculation to the case of the cone, obtaining a result in terms of a sum and integral over angular momentum variables. For a special case where the particle lies on the cone axis, the calculation simplifies to a single integral. This calculation can be straightforwardly extended to frequency-dependent polarizability and nonzero temperature, although, in those cases, an additional sum or integral over frequency must be done numerically.

2. Review of Casimir–Polder Wedge

Let us begin by reviewing the Casimir–Polder interaction energy for a conducting wedge, which was computed in Refs. [10,29] and considered in the context of repulsive forces in Refs. [30,31]. Let the wedge run parallel to the z-axis and have a half-opening angle $0 < \theta_0 < \pi$ around $\theta = 0$ with the wedge vertex located at $x = y = 0$, and consider imaginary wavenumber $k = i\kappa$ with $\kappa > 0$. Note that by allowing $\theta_0 > \frac{\pi}{2}$, one is able to consider a case where the particle is inside the wedge. For a particle located at angle $\theta \in [0, 2\pi]$ obeying $\theta_0 < \theta < 2\pi - \theta_0$, one can write the full Green’s function for the wedge in terms of ordinary cylindrical wavefunctions of fractional order [10,11],

$$\mathfrak{G}(\mathbf{r}_1, \mathbf{r}_2, \kappa) = -\frac{p}{\pi} \int_{-\infty}^{\infty} \frac{dk_z}{2\pi} \sum_{\ell=-\infty}^{\infty} \left(M_{\ell k_z \kappa}^{\text{outgoing}} \otimes M_{\ell k_z \kappa}^{\text{regular}*} - N_{\ell k_z \kappa}^{\text{outgoing}} \otimes N_{\ell k_z \kappa}^{\text{regular}*} \right), \tag{1}$$

in terms of the magnetic (transverse electric) and electric (transverse magnetic) modes, respectively,

$$\begin{aligned} M_{\ell k_z \kappa}(\mathbf{r}) &= \frac{1}{\sqrt{\kappa^2 + k_z^2}} \nabla \times \left[\hat{\mathbf{z}} f_{|\ell p|} \left(\sqrt{\kappa^2 + k_z^2} r \right) e^{ik_z z} \cos(\ell p(\theta - \theta_0)) \right] \\ N_{\ell k_z \kappa}(\mathbf{r}) &= \frac{1}{\kappa \sqrt{\kappa^2 + k_z^2}} \nabla \times \nabla \times \left[\hat{\mathbf{z}} f_{|\ell p|} \left(\sqrt{\kappa^2 + k_z^2} r \right) e^{ik_z z} \sin(\ell p(\theta - \theta_0)) \right] \end{aligned} \tag{2}$$

with ℓ the quantum number, the hat denoting unit vector, and $p = \frac{\pi}{2(\pi - \theta_0)}$, where the regular (outgoing) function is evaluated at the point \mathbf{r}_1 or \mathbf{r}_2 with the smaller (larger) value of the cylindrical radius r and the radial functions given in terms of Bessel functions for regular and outgoing modes as:

$$f_{|\ell p|}^{\text{regular}}(\sqrt{\kappa^2 + k_z^2} r) = I_{|\ell p|}(\sqrt{\kappa^2 + k_z^2} r) \quad \text{and} \quad f_{|\ell p|}^{\text{outgoing}}(\sqrt{\kappa^2 + k_z^2} r) = K_{|\ell p|}(\sqrt{\kappa^2 + k_z^2} r). \tag{3}$$

This Green’s function then obeys:

$$(\nabla \times \nabla \times + \kappa^2) \mathfrak{G}(\mathbf{r}_1, \mathbf{r}_2, \kappa) = \delta^{(3)}(\mathbf{r}_1 - \mathbf{r}_2) \tag{4}$$

in the presence of the conducting wedge, whereas the free Green’s function $\mathfrak{G}_0(\mathbf{r}_1, \mathbf{r}_2, \kappa)$, given by setting $p = 1$ and replacing the trigonometric functions $\sin(\ell p(\theta - \theta_0))$ and $\cos(\ell p(\theta - \theta_0))$ in Equation (2) with $e^{i\ell\theta}/\sqrt{2}$, obeys the same equation in empty space.

One can then use the “TGTG” (T-matrix/free Green’s function) [4–9] formulation of the Casimir energy, considering only the lowest-order interaction with the potential for a particle with polarizability α at position \mathbf{r} ,

$$V(\mathbf{r}') = -4\pi\alpha\kappa^2 \delta^{(3)}(\mathbf{r} - \mathbf{r}'), \tag{5}$$

which can be expressed in any basis since it is a delta function, $\delta^{(3)}(\mathbf{r} - \mathbf{r}')$.

The result for the interaction energy of a particle with isotropic polarizability α becomes [10,29]:

$$\begin{aligned}
 U(\mathbf{r}) &= -\frac{\hbar c}{2\pi} \int_0^\infty \text{Tr}[V(\mathbf{r})(\mathfrak{G}(\mathbf{r}, \mathbf{r}', \kappa) - \mathfrak{G}_0(\mathbf{r}, \mathbf{r}', \kappa))] d\kappa \\
 &= 2\alpha\hbar c \int_0^\infty \kappa^2 \text{tr}[\mathfrak{G}(\mathbf{r}, \mathbf{r}, \kappa) - \mathfrak{G}_0(\mathbf{r}, \mathbf{r}, \kappa)] d\kappa \\
 &= -\frac{3\alpha\hbar c}{8\pi r^4 \sin^4(p(\theta - \theta_0))} \left[p^4 - \frac{2}{3} p^2 (p^2 - 1) \sin^2(p(\theta - \theta_0)) - \frac{1}{135} (p^2 - 1)(p^2 + 11) \sin^4(p(\theta - \theta_0)) \right], \quad (6)
 \end{aligned}$$

where \hbar is the reduced Planck's constant, c denotes the speed of light, 'Tr' denotes the trace, which includes the trace over the spatial coordinate, and 'tr' denotes the trace only over polarizations. In this approach, there is not a straightforward way to subtract the free contribution mode-by-mode, so one instead uses a point-splitting argument to subtract the entire contribution from the free Green's function at once.

For the case of the cone, there does not exist an analog of this full Green's function written in terms of a rescaled order. As a result, we next recompute the result for the wedge using a different form of the Green's function, which generalizes more readily to the case of the cone. In this approach, the angular momentum sum is replaced via analytic continuation by an integral, yielding for the free Green's function [13,16]:

$$\begin{aligned}
 \mathfrak{G}_0(\mathbf{r}_1, \mathbf{r}_2, \kappa) &= -\frac{1}{\pi^2} \int_{-\infty}^\infty \frac{dk_z}{2\pi} \int_0^\infty d\lambda \left(M_{\lambda k_z \kappa}^{\text{outgoing},+} \otimes M_{\lambda k_z \kappa}^{\text{regular},+*} + M_{\lambda k_z \kappa}^{\text{outgoing},-} \otimes M_{\lambda k_z \kappa}^{\text{regular},-*} \right. \\
 &\quad \left. - N_{\lambda k_z \kappa}^{\text{outgoing},+} \otimes N_{\lambda k_z \kappa}^{\text{regular},+*} - N_{\lambda k_z \kappa}^{\text{outgoing},-} \otimes N_{\lambda k_z \kappa}^{\text{regular},-*} \right), \quad (7)
 \end{aligned}$$

where the transverse modes are:

$$M_{\lambda k_z \kappa}(\mathbf{r}) = \frac{1}{\sqrt{\kappa^2 + k_z^2}} \nabla \times \left[\hat{\mathbf{z}} K_{i\lambda} \left(\sqrt{\kappa^2 + k_z^2} r \right) e^{ik_z z} f_\lambda(\theta) \right] \quad \text{and} \quad N_{\lambda k_z \kappa}(\mathbf{r}) = \frac{1}{\kappa} \nabla \times M_{\lambda k_z \kappa}(\mathbf{r}) \quad (8)$$

and $\theta \in [-\pi, \pi]$. One has both even and odd modes, with regular modes given by:

$$f_\lambda^{\text{regular},+}(\theta) = \cosh(\lambda\theta) \quad \text{and} \quad f_\lambda^{\text{regular},-}(\theta) = \sinh(\lambda\theta) \quad (9)$$

and outgoing modes given by

$$f_\lambda^{\text{outgoing},+}(\theta) = \cosh(\lambda(\pi - |\theta|)) \quad \text{and} \quad f_\lambda^{\text{outgoing},-}(\theta) = \sinh(\lambda(\pi - |\theta|)) \text{sgn } \theta, \quad (10)$$

where λ denotes the analytically continued angular quantum number, and the regular (outgoing) functions are evaluated at the point \mathbf{r}_1 or \mathbf{r}_2 with the smaller (larger) value of $|\theta|$. Note that the star indicates the conjugation of the complex exponential part of the function only.

Although not needed for the computation, the corresponding longitudinal mode is:

$$L_{\lambda k_z \kappa}(\mathbf{r}) = \frac{1}{\kappa} \nabla \left[K_{i\lambda} \left(\sqrt{\kappa^2 + k_z^2} r \right) e^{ik_z z} f_\lambda(\theta) \right]. \quad (11)$$

If its contribution is added to the free Green's function, the result is equal to the scalar Green's function, $\frac{1}{2\pi} \int_{-\infty}^\infty \frac{dk_z}{2\pi} K_0 \left(\sqrt{\kappa^2 + k_z^2} \left| r_1 e^{i\theta_1} - r_2 e^{i\theta_2} \right| \right) e^{ik_z(z_>-z_<)}$, times the identity matrix; without this contribution, one obtains the same scalar times the projection matrix on to the transverse components. Here, $z_>$ ($z_<$) is the z coordinate associated with the point with the larger (smaller) value of $|\theta|$.

In this approach, we take the wedge to be located at $\theta = \pm\theta_0$ and the particle's location will always have $|\theta| > \theta_0$. One then obtains the full Green's function by replacing the

regular solution with a combination of regular and outgoing solutions given in terms of the T -matrix:

$$\mathcal{T}_\lambda^{M,+} = \frac{\sinh(\lambda\theta_0)}{\sinh(\lambda(\pi - \theta_0))} = -\mathcal{T}_\lambda^{N,-} \quad \text{and} \quad \mathcal{T}_\lambda^{M,-} = \frac{\cosh(\lambda\theta_0)}{\cosh(\lambda(\pi - \theta_0))} = -\mathcal{T}_\lambda^{N,+}, \quad (12)$$

so that it now obeys the conducting boundary conditions on the wedge, yielding:

$$\begin{aligned} \mathfrak{G}(\mathbf{r}_1, \mathbf{r}_2, \kappa) = & -\frac{1}{\pi^2} \int_{-\infty}^{\infty} \frac{dk_z}{2\pi} \int_0^{\infty} d\lambda \left[\mathbf{M}_{\lambda k_z \kappa}^{\text{outgoing},+} \otimes \left(\mathbf{M}_{\lambda k_z \kappa}^{\text{regular},+*} + \mathcal{T}_\lambda^{M,+} \mathbf{M}_{\lambda k_z \kappa}^{\text{outgoing},+*} \right) \right. \\ & + \mathbf{M}_{\lambda k_z \kappa}^{\text{outgoing},-} \otimes \left(\mathbf{M}_{\lambda k_z \kappa}^{\text{regular},-*} + \mathcal{T}_\lambda^{M,-} \mathbf{M}_{\lambda k_z \kappa}^{\text{outgoing},-*} \right) \\ & - \mathbf{N}_{\lambda k_z \kappa}^{\text{outgoing},+} \otimes \left(\mathbf{N}_{\lambda k_z \kappa}^{\text{regular},+*} + \mathcal{T}_\lambda^{N,+} \mathbf{N}_{\lambda k_z \kappa}^{\text{outgoing},+*} \right) \\ & \left. - \mathbf{N}_{\lambda k_z \kappa}^{\text{outgoing},-} \otimes \left(\mathbf{N}_{\lambda k_z \kappa}^{\text{regular},-*} + \mathcal{T}_\lambda^{N,-} \mathbf{N}_{\lambda k_z \kappa}^{\text{outgoing},-*} \right) \right]. \end{aligned} \quad (13)$$

In this form, one can subtract the free Green's function mode-by-mode, leaving only the terms with outgoing waves multiplied by the T -matrix. One obtains for the energy:

$$\begin{aligned} U(\mathbf{r}) = & -\frac{\alpha\hbar c}{\pi^3 r^2} \int_0^{\infty} d\kappa \int_{-\infty}^{\infty} dk_z \int_0^{\infty} d\lambda \frac{1}{\sinh(2(\pi - \theta_0)\lambda)} \\ & \left\{ K_{i\lambda}(\sqrt{\kappa^2 + k_z^2} r) \left[\left(r^2(\kappa^2 + k_z^2) + \lambda^2 \right) \cosh(2(\pi - \theta)\lambda) \sinh \pi\lambda \right. \right. \\ & \left. \left. + \left(r^2(\kappa^2 + k_z^2) + \frac{\kappa^2 - k_z^2}{\kappa^2 + k_z^2} \lambda^2 \right) \sinh((\pi - 2\theta_0)\lambda) \right] \right. \\ & \left. + r^2 \left(\frac{\partial}{\partial r} K_{i\lambda}(\sqrt{\kappa^2 + k_z^2} r) \right)^2 \left(\cosh(2(\pi - \theta)\lambda) \sinh \pi\lambda + \frac{k_z^2 - \kappa^2}{k_z^2 + \kappa^2} \sinh((\pi - 2\theta_0)\lambda) \right) \right\} \\ = & -\frac{\alpha\hbar c}{\pi r^4} \int_0^{\infty} d\lambda \left[\frac{\lambda + \lambda^3}{3} \coth \pi\lambda - \frac{1}{3} \coth(2(\pi - \theta_0)\lambda) + \frac{\cosh(2(\pi - \theta)\lambda)}{\sinh(2(\pi - \theta_0)\lambda)} \right], \end{aligned} \quad (14)$$

where the integrals over κ and k_z are done using polar coordinates. After carrying out the λ integral, one obtains agreement with Equation (6).

3. Electromagnetic Cone Green's Function

Let us now construct the Green's function for the perfectly conducting cone with half-opening angle $0 < \theta_0 < \pi$, centered on the z -axis with the cone vertex at $z = 0$, as shown in Figure 1. We again consider imaginary wavenumber $k = i\kappa$ with $\kappa > 0$. Note that by allowing $\theta_0 > \frac{\pi}{2}$, one can consider a case where the particle is inside the cone. From Ref. [16], one has magnetic (transverse electric) and electric (transverse magnetic) transverse modes:

$$\mathbf{M}_{\lambda m \kappa}(\mathbf{r}) = \nabla \times \left[\mathbf{r} k_{i\lambda - \frac{1}{2}}(\kappa r) e^{im\phi} f_{\lambda m}(\mathbf{r}) \right] \quad \text{and} \quad \mathbf{N}_{\lambda m \kappa}(\mathbf{r}) = \frac{1}{\kappa} \nabla \times \mathbf{M}_{\lambda m \kappa}(\mathbf{r}) \quad (15)$$

with

$$f_{\lambda m}^{\text{regular}}(\mathbf{r}) = P_{i\lambda - \frac{1}{2}}^{-m}(\cos \theta) \quad \text{and} \quad f_{\lambda m}^{\text{outgoing}}(\mathbf{r}) = P_{i\lambda - \frac{1}{2}}^m(-\cos \theta), \quad (16)$$

where $P_{i\lambda - \frac{1}{2}}^m(\cos \theta)$ is the Legendre function of the first kind and $k_{i\lambda - \frac{1}{2}}^m(\kappa r) = \sqrt{\frac{2}{\pi \kappa r}} K_{i\lambda}(\kappa r)$ is the modified spherical Bessel function of the third kind, both with complex degree/order $\ell = i\lambda - \frac{1}{2}$. The "ghost" mode [16] is:

$$\mathbf{R}_{\lambda m \kappa} = \mathbf{r} \times \nabla \left[k_{i\lambda - \frac{1}{2}}(\kappa r) P_{i\lambda - \frac{1}{2}}^{-|m|}(\pm \cos \theta) e^{im\phi} \right], \quad (17)$$

where the \pm sign is for regular ('+') and outgoing ('-') modes. Its contribution arises from the contour integral used to turn the sum over the angular momentum quantum number ℓ into the integral over its analytic continuation λ , in which it cancels the contribution from the $\ell = 0$ mode, since that mode does not exist in electromagnetism. As a result, it is only ever evaluated at $\lambda = \frac{1}{2i}$, corresponding to $\ell = 0$.

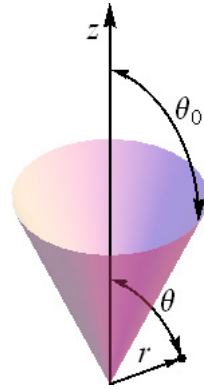


Figure 1. Geometry of cone with half-opening angle θ_0 and particle at radius r and angle $\theta > \theta_0$.

In this basis, the free Green’s function is [16]:

$$\mathfrak{G}_0(r_1, r_2, \kappa) = -\frac{\kappa}{4\pi} \left[\sum_{m=-\infty}^{\infty} \int_0^{\infty} \frac{\lambda \tanh \pi\lambda}{\lambda^2 + \frac{1}{4}} d\lambda \left(M_{\lambda m \kappa}^{\text{outgoing}} \otimes M_{\lambda m \kappa}^{\text{regular}*} - N_{\lambda m \kappa}^{\text{outgoing}} \otimes N_{\lambda m \kappa}^{\text{regular}*} \right) + \sum_{\substack{m=-\infty \\ m \neq 0}}^{\infty} \Gamma(|m|)\Gamma(|m| + 1) R_{\lambda m \kappa}^{\text{outgoing}} \otimes R_{\lambda m \kappa}^{\text{regular}*} \Big|_{\lambda=\frac{1}{2i}} \right], \tag{18}$$

where the regular (outgoing) function is evaluated at the point r_1 or r_2 with the smaller (larger) value of $|\theta|$, and $\Gamma(x)$ is the gamma function. Note that, as above, the star indicates the conjugation of the complex exponential part of the function only. Here, the integral over $\lambda = \frac{1}{i} \left(\ell + \frac{1}{2} \right)$ represents the analytic continuation of the sum over ℓ .

For completeness, we also give the longitudinal mode:

$$L_{\lambda m \kappa} = -\frac{\sqrt{\lambda^2 + \frac{1}{4}}}{\kappa} \nabla \left[k_{i\lambda-\frac{1}{2}}(\kappa r) e^{im\phi} f_{\lambda m}(r) \right] \tag{19}$$

for this geometry. If its contribution is added to the free Green’s function, the result is equal to the scalar Green’s function $\frac{\kappa}{4\pi} k_0(\kappa|r_1 - r_2|)$ times the identity matrix; without this contribution, one obtains the same scalar times the projection matrix on to the transverse components.

The full Green’s function in the presence of the conducting boundary \mathfrak{G} is then given by the same expression with the replacement, $\chi^{\text{regular}*} \rightarrow \chi^{\text{regular}*} + \mathcal{T}_{\lambda m}^{\chi} \chi^{\text{outgoing}*}$, where $\chi = M, N, R$; again, the star indicates the conjugation of the complex exponential part of the function only, and $\mathcal{T}_{\lambda m}^{\chi}$ is the corresponding T -matrix element [16],

$$\mathcal{T}_{\lambda m}^N = -\frac{P_{i\lambda-\frac{1}{2}}^{-m}(\cos \theta_0)}{P_{i\lambda-\frac{1}{2}}^m(-\cos \theta_0)}, \quad \mathcal{T}_{\lambda m}^M = -\frac{\frac{\partial}{\partial \theta_0} P_{i\lambda-\frac{1}{2}}^{-m}(\cos \theta_0)}{\frac{\partial}{\partial \theta_0} P_{i\lambda-\frac{1}{2}}^m(-\cos \theta_0)}, \quad \text{and} \quad \mathcal{T}_{\lambda m}^R = \frac{P_{i\lambda-\frac{1}{2}}^{-|m|}(\cos \theta_0)}{P_{i\lambda-\frac{1}{2}}^{-|m|}(-\cos \theta_0)}, \tag{20}$$

in terms of θ_0 , the half-opening angle of the cone. Subtracting the contribution from the free Green’s function then cancels the term with the regular solution, leaving only the product of outgoing solutions in the interaction energy.

4. Electromagnetic Cone Casimir–Polder Energy

After some algebra and simplification, one obtains the Casimir–Polder interaction energy for an atom with isotropic and frequency-independent polarizability α at distance r from the cone vertex and angle θ from the cone axis, with $|\theta| > \theta_0$, as:

$$\begin{aligned}
 U(\mathbf{r}) &= 2\alpha\hbar c \int_0^\infty \kappa^2 \text{tr}[\mathfrak{G}(\mathbf{r}, \mathbf{r}, \kappa) - \mathfrak{G}_0(\mathbf{r}, \mathbf{r}, \kappa)] d\kappa \\
 &= -\frac{\alpha\hbar c}{2\pi} \int_0^\infty \kappa^3 \text{tr} \left[\sum_{m=-\infty}^\infty \int_0^\infty \frac{\lambda \tanh \pi\lambda}{\lambda^2 + \frac{1}{4}} d\lambda \left(\mathcal{T}_{\lambda m}^M \mathbf{M}_{\lambda m \kappa}^{\text{outgoing}} \otimes \mathbf{M}_{\lambda m \kappa}^{\text{outgoing}*} - \mathcal{T}_{\lambda m}^N \mathbf{N}_{\lambda m \kappa}^{\text{outgoing}} \otimes \mathbf{N}_{\lambda m \kappa}^{\text{outgoing}*} \right) \right. \\
 &\quad \left. + \sum_{\substack{m=-\infty \\ m \neq 0}}^\infty \Gamma(|m|)\Gamma(|m|+1) \mathcal{T}_{\lambda m}^R \mathbf{R}_{\lambda m \kappa}^{\text{outgoing}} \otimes \mathbf{R}_{\lambda m \kappa}^{\text{outgoing}*} \Big|_{\lambda=\frac{1}{2i}} \right] d\kappa \\
 &= \frac{\alpha\hbar c}{2\pi r^2} \sum_{m=-\infty}^\infty \int_0^\infty \kappa d\kappa \left\{ \int_0^\infty d\lambda \lambda \tanh \pi\lambda \left[\left(\frac{\partial}{\partial \theta} P_{i\lambda-\frac{1}{2}}^m(-\cos \theta) \right)^2 + \frac{m^2}{\sin^2 \theta} P_{i\lambda-\frac{1}{2}}^m(-\cos \theta)^2 \right] \right. \\
 &\quad \left. \times \left(\mathcal{T}_{\lambda m}^N \left(\frac{\partial}{\partial r} (rk_{i\lambda-\frac{1}{2}}(\kappa r)) \right) \right)^2 - \mathcal{T}_{\lambda m}^M \kappa^2 r^2 k_{i\lambda-\frac{1}{2}}(\kappa r)^2 \right) \frac{1}{\left(\lambda^2 + \frac{1}{4} \right)} \right. \\
 &\quad \left. + \mathcal{T}_{\lambda m}^N \left(\lambda^2 + \frac{1}{4} \right) P_{i\lambda-\frac{1}{2}}^m(-\cos \theta)^2 k_{i\lambda-\frac{1}{2}}(\kappa r)^2 \right] - \left(\frac{1 + \cos \theta}{1 - \cos \theta} \right)^{|m|} \left(\frac{1 - \cos \theta_0}{1 + \cos \theta_0} \right)^{|m|} \frac{2|m|}{\sin^2 \theta} e^{-2\kappa r} \left. \right\} \\
 &= \frac{\alpha\hbar c}{8r^4} \left\{ \sum_{m=-\infty}^\infty \int_0^\infty d\lambda \lambda \operatorname{sech} \pi\lambda \tanh \pi\lambda \left[2\mathcal{T}_{\lambda m}^N \left(\lambda^2 + \frac{1}{4} \right) P_{i\lambda-\frac{1}{2}}^m(-\cos \theta)^2 \right. \right. \\
 &\quad \left. \left. + \left(\mathcal{T}_{\lambda m}^N - \mathcal{T}_{\lambda m}^M \right) \left(\left(\frac{\partial}{\partial \theta} P_{i\lambda-\frac{1}{2}}^m(-\cos \theta) \right)^2 + \frac{m^2}{\sin^2 \theta} P_{i\lambda-\frac{1}{2}}^m(-\cos \theta)^2 \right) \right] - \frac{1}{\pi} \frac{\sin^2 \theta_0}{(\cos \theta - \cos \theta_0)^2} \right\}, \tag{21}
 \end{aligned}$$

where the last term arises from the “ghost” mode contribution. Here,

$$\frac{\lambda^2 + \frac{1}{4}}{2r^2} \int_0^\infty \kappa k_{i\lambda-\frac{1}{2}}(\kappa r)^2 d\kappa = \int_0^\infty \kappa^3 k_{i\lambda-\frac{1}{2}}(\kappa r)^2 d\kappa = \int_0^\infty \frac{\kappa}{r^2} \left[\frac{\partial}{\partial r} (rk_{i\lambda-\frac{1}{2}}(\kappa r)) \right]^2 d\kappa = \frac{\pi}{4r^4} \left(\lambda^2 + \frac{1}{4} \right) \operatorname{sech} \pi\lambda \tag{22}$$

is used [32] to carry out the integral over κ , with integrals involving derivatives with respect to r obtained by differentiating under the integral sign. The ghost term can be computed using the derivative of a geometric series,

$$\sum_{m=1}^\infty m \left(\frac{1 + \cos \theta}{1 - \cos \theta} \right)^m \left(\frac{1 - \cos \theta_0}{1 + \cos \theta_0} \right)^m = \frac{\sin^2 \theta \sin^2 \theta_0}{4(\cos \theta - \cos \theta_0)^2}, \tag{23}$$

along with an elementary κ integral.

One can check the result (21) numerically in the case of $\theta_0 = \pi/2$, when this result becomes the Casimir–Polder energy of a particle at a distance $d = r|\cos \theta|$ from a conducting plane, $U(r) = -\frac{3\alpha\hbar c}{8\pi d^4}$. Let us also note that the difference of T -matrices simplifies to

$$\mathcal{T}_{\lambda m}^N - \mathcal{T}_{\lambda m}^M = \frac{4 \cosh \pi\lambda}{\pi \sin \theta_0} \frac{1}{\frac{\partial}{\partial \theta_0} [P_{i\lambda-\frac{1}{2}}^m(-\cos \theta_0)^2]} \tag{24}$$

by using the Wronskian relation between $P_\ell^m(z)$ and $P_\ell^m(-z)$.

Carefully taking the limit $\theta \rightarrow \pi$, one obtains a special case where the particle lies on the cone axis. Here, the only contributions arise from $m = -1, 0, +1$, leading to a result that simplifies to:

$$U(r) = \frac{\alpha\hbar c}{2\pi r^2} \int_0^\infty \kappa d\kappa \left\{ \int_0^\infty d\lambda \lambda \left(\lambda^2 + \frac{1}{4} \right) \tanh \pi\lambda \left[\left(\mathcal{T}_{\lambda 0}^N - \kappa^2 r^2 \mathcal{T}_{\lambda 1}^M \right) k_{i\lambda-\frac{1}{2}}(\kappa r)^2 \right. \right.$$

$$\begin{aligned}
 & \left. + \mathcal{T}_{\lambda 1}^N \left(\frac{\partial}{\partial r} \left(r k_{i\lambda - \frac{1}{2}}(\kappa r) \right) \right)^2 \right] - e^{-2\kappa r} \tan^2 \frac{\theta_0}{2} \left. \right\} \\
 = & \frac{\alpha \hbar c}{8r^4} \left\{ \int_0^\infty d\lambda \lambda \left(\lambda^2 + \frac{1}{4} \right) \operatorname{sech} \pi \lambda \tanh \pi \lambda \left[2\mathcal{T}_{\lambda 0}^N + \left(\lambda^2 + \frac{1}{4} \right) \left(\mathcal{T}_{\lambda 1}^N - \mathcal{T}_{\lambda 1}^M \right) \right] - \frac{1}{\pi} \tan^2 \frac{\theta_0}{2} \right\} \quad (25)
 \end{aligned}$$

for the cone-particle interaction energy when $\theta = \pi$. Here, it is helpful to obtain the result in the first line, before integration over κ , because that result can straightforwardly be extended to nonzero temperature and frequency-dependent polarization, as will be described in more detail below.

Within this special case, it is illustrative to consider $\theta_0 = \frac{\pi}{2}$, where the cone becomes a plane, for which $\mathcal{T}_{\lambda 0}^N = -1$ and $\mathcal{T}_{\lambda 1}^N = -\mathcal{T}_{\lambda 1}^M = -\frac{1}{\left(\lambda^2 + \frac{1}{4}\right)}$. One then uses the κ integrals above along with the integrals [32,33] (the second integral does not appear to have been obtained previously):

$$\begin{aligned}
 \int_0^\infty k_{i\lambda - \frac{1}{2}}(\kappa r)^2 \lambda \tanh \pi \lambda d\lambda &= \frac{1}{2\kappa r} e^{-2\kappa r} \\
 \int_0^\infty k_{i\lambda - \frac{1}{2}}(\kappa r)^2 \lambda^3 \tanh \pi \lambda d\lambda &= \frac{1}{2\kappa r} \left(\kappa r + \frac{1}{4} \right) e^{-2\kappa r} \\
 \int_0^\infty \left(\frac{\partial}{\partial r} \left(r k_{i\lambda - \frac{1}{2}}(\kappa r) \right) \right)^2 \lambda \tanh \pi \lambda d\lambda &= \frac{1}{2\kappa r} \left(\kappa^2 r^2 - \kappa r + \frac{1}{2} \right) e^{-2\kappa r} \\
 \int_0^\infty d\lambda \lambda \left(\lambda^2 + \frac{1}{4} \right) \operatorname{sech} \pi \lambda \tanh \pi \lambda &= \frac{1}{2\pi}, \quad (26)
 \end{aligned}$$

where, again, the integrals involving derivatives with respect to r are obtained by differentiating under the integral sign, to do both the κ and λ integrals explicitly and in either order and obtain the standard results for the plane,

$$\begin{aligned}
 U(r) &= -\frac{\alpha \hbar c}{2\pi r^2} \int_0^\infty \kappa d\kappa \left\{ \int_0^\infty d\lambda \lambda \tanh \pi \lambda \left[\left(\lambda^2 + \frac{1}{4} + \kappa^2 r^2 \right) k_{i\lambda - \frac{1}{2}}(\kappa r)^2 + \left(\frac{\partial}{\partial r} \left(r k_{i\lambda - \frac{1}{2}}(\kappa r) \right) \right)^2 \right] + e^{-2\kappa r} \right\} \\
 &= -\frac{\alpha \hbar c}{4\pi r^3} \int_0^\infty d\kappa \left(2\kappa^2 r^2 + 2\kappa r + 1 \right) e^{-2\kappa r} \\
 &= -\frac{\alpha \hbar c}{2r^4} \left[\int_0^\infty d\lambda \lambda \left(\lambda^2 + \frac{1}{4} \right) \operatorname{sech} \pi \lambda \tanh \pi \lambda + \frac{1}{4\pi} \right] = -\frac{3\alpha \hbar c}{8\pi r^4}, \quad (27)
 \end{aligned}$$

where, in the second line, we have done the λ integral first and, in the third line, we have done the κ integral first. The former expression shows that if the ghost contribution is grouped with the electric modes, the contributions from the electric and magnetic modes match the planar calculation individually as functions of κ , and, as a result, reproduce the 5:1 ratio of the total contributions of the electric and magnetic modes [34].

5. Anisotropic Polarizability

By repeating the above calculation in the case where α is a matrix, one can extend these results to the case of an anisotropic particle. We write the polarizability in the general form:

$$\alpha = \begin{pmatrix} \alpha_\perp \cos^2 \beta & \alpha_{xy} - i\gamma_z & \alpha_{xz} + i\gamma_y \\ \alpha_{xy} + i\gamma_z & \alpha_\perp \sin^2 \beta & \alpha_{yz} - i\gamma_x \\ \alpha_{xz} - i\gamma_y & \alpha_{yz} + i\gamma_x & \alpha_{zz} \end{pmatrix}, \quad (28)$$

which includes both the symmetric and antisymmetric (nonreciprocal) off-diagonal components. Without loss of generality, we take the particle to be at $\phi = 0$, so that it lies in the xz -plane. In terms of these parameters, one obtains for the energy:

$$\begin{aligned}
 U(r) = & \frac{\hbar c}{8r^4} \left\{ \sum_{m=-\infty}^{\infty} \int_0^{\infty} d\lambda \lambda \operatorname{sech} \pi \lambda \tanh \pi \lambda \right. \\
 & \times \left[\left(\frac{\partial}{\partial \theta} P_{i\lambda-\frac{1}{2}}^m(-\cos \theta) \right)^2 \left((\alpha_{\perp} \cos^2 \beta \cot^2 \theta - 2\alpha_{xz} \cot \theta + \alpha_{zz}) \mathcal{T}_{\lambda m}^N - \alpha_{\perp} \sin^2 \beta \mathcal{T}_{\lambda m}^M \right) \right. \\
 & + 2m \frac{\gamma_x + \gamma_z \cot \theta}{\sin \theta} \left(\frac{\partial}{\partial \theta} P_{i\lambda-\frac{1}{2}}^m(-\cos \theta) \right) P_{i\lambda-\frac{1}{2}}^m(-\cos \theta) (\mathcal{T}_{\lambda m}^N - \mathcal{T}_{\lambda m}^M) \\
 & + P_{i\lambda-\frac{1}{2}}^m(-\cos \theta)^2 \left(m^2 (2\alpha_{xz} \cot \theta - \alpha_{\perp} \cos^2 \beta \cot^2 \theta - \alpha_{zz}) \mathcal{T}_{\lambda m}^M \right. \\
 & \left. \left. + 2 \left(\frac{1}{4} + \lambda^2 \right) \left(\alpha_{zz} \cos^2 \theta + \frac{2m^2 \alpha_{\perp}}{(1+4\lambda^2)} \csc^2 \theta \sin^2 \beta + 2\alpha_{xz} \cos \theta \sin \theta + \alpha_{\perp} \cos^2 \beta \sin^2 \theta \right) \mathcal{T}_{\lambda m}^N \right) \right] \\
 & \left. + \frac{(2\alpha_{xz} \cos \theta \sin \theta - \alpha_{\perp} + (\alpha_{\perp} \cos^2 \beta - \alpha_{zz}) \sin^2 \theta) \sin^2 \theta_0}{2\pi(\cos \theta - \cos \theta_0)^2} \right\}, \tag{29}
 \end{aligned}$$

which, on the axis $\theta = \pi$, simplifies to

$$U(r) = \frac{\hbar c}{4r^4} \left\{ \int_0^{\infty} d\lambda \lambda \left(\frac{1}{4} + \lambda^2 \right) \operatorname{sech} \pi \lambda \tanh \pi \lambda \left[\alpha_{zz} \mathcal{T}_{\lambda 0}^N + \left(\frac{\alpha_{\perp}}{4} + \frac{\gamma_z}{2} \right) \left(\frac{1}{4} + \lambda^2 \right) (\mathcal{T}_{\lambda 1}^N - \mathcal{T}_{\lambda 1}^M) \right] - \frac{\alpha_{\perp} \tan^2(\theta_0/2)}{4\pi} \right\}. \tag{30}$$

Of particular interest is the γ_z term, which generates a nonreciprocal torque around the z-axis. Comparing the α_{zz} and α_{\perp} contributions also enables us to compare whether a particle with a single polarization axis prefers to be aligned with or perpendicular to the axis of the cone.

6. Results and Discussion

To visualize these results numerically, in Figure 2, the Casimir–Polder interaction energy of an isotropic particle is plotted scaled by the fourth power of $r \sin(\theta - \theta_0)$, which gives the perpendicular distance from the particle to the plane in the case where $\theta - \theta_0 < \frac{\pi}{2}$. For $\theta_0 = \pi/2$, the result in units of $\alpha \hbar c$ is $-\frac{3}{8\pi} \approx -0.1194$, and past this inflection point, as the the cone envelops the particle, its interaction becomes much stronger.

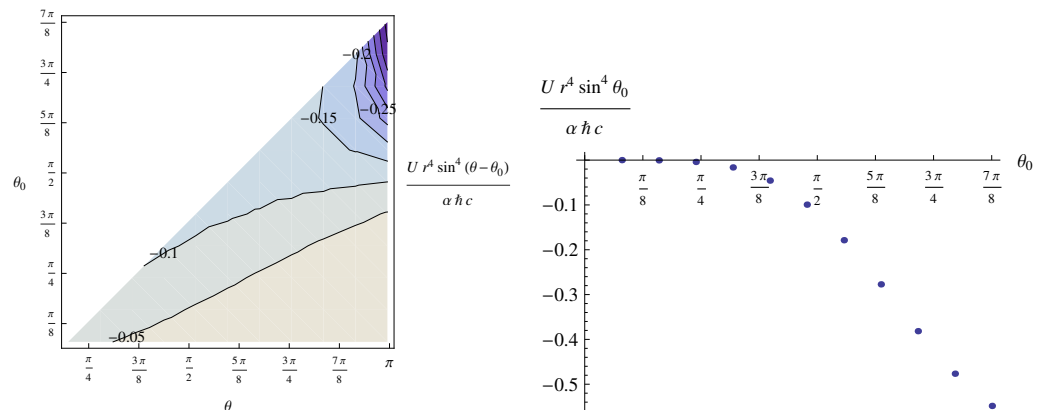


Figure 2. Scaled Casimir–Polder interaction energy, $\frac{U r^4 \sin^4(\theta - \theta_0)}{\alpha \hbar c}$, for an isotropic particle as a function of θ and θ_0 (left) and as a function of θ_0 for $\theta = \pi$ (right). See text for details.

All of the above calculations can be extended to nonzero equilibrium temperature T , in which case the integral over κ from 0 to ∞ is replaced by $\frac{2\pi k_B T}{\hbar c}$ times the sum

over Matsubara frequencies, $\kappa_n = \frac{2\pi n k_B T}{\hbar c}$, for all $n = 0, 1, 2, 3, \dots$, where the $n = 0$ contribution is counted with a weight of $\frac{1}{2}$. This term must be considered carefully, since the Bessel function has a logarithmic singularity as $\kappa \rightarrow 0$ for fixed λ . For the special case of $\theta_0 = \pi/2$, one can see explicitly from the above that this singularity disappears when the integral over λ is done first, which should remain the case in general. In all of these calculations, one can also straightforwardly move α inside the κ integral or sum to model a frequency-dependent polarizability. However, introducing either or both nonzero temperature and frequency-dependent polarizability then requires the κ sum or integral to be carried out numerically.

Funding: N.G. is supported in part by the National Science Foundation (NSF) through grant PHY-2205708.

Data Availability Statement: All supporting data are available on request.

Acknowledgments: It is a pleasure to thank M. Kardar for suggesting this problem and, along with K. Asheichyk, T. Emig, D. Gelbwaser, and M. Krüger, for helpful conversations and feedback.

Conflicts of Interest: The author declares no conflict of interest.

References

1. Casimir, H.B.G.; Polder, D. The influence of retardation on the London-van der Waals forces. *Phys. Rev.* **1948**, *73*, 360–372. [CrossRef]
2. Sukenik, C.I.; Boshier, M.G.; Cho, D.; Sandoghdar, V.; Hinds, E.A. Measurement of the Casimir–Polder force. *Phys. Rev. Lett.* **1993**, *70*, 560–563. [CrossRef] [PubMed]
3. Harber, D.M.; Obrecht, J.M.; McGuiirk, J.M.; Cornell, E.A. Measurement of the Casimir–Polder force through center-of-mass oscillations of a Bose-Einstein condensate. *Phys. Rev. A* **2005**, *72*, 033610. [CrossRef]
4. Langbein, D. *Theory of Van der Waals Attraction*; Springer: Berlin/Heidelberg, Germany, 1974. [CrossRef]
5. Lambrecht, A.; Maia Neto, P.A.; Reynaud, S. The Casimir effect within scattering theory. *New J. Phys.* **2006**, *8*, 243. [CrossRef]
6. Emig, T.; Jaffe, R.L.; Kardar, M.; Scardicchio, A. Casimir interaction between a plate and a cylinder. *Phys. Rev. Lett.* **2006**, *96*, 080403. [CrossRef] [PubMed]
7. Kenneth, O.; Klich, I. Opposites attract: A theorem about the Casimir force. *Phys. Rev. Lett.* **2006**, *97*, 160401. [CrossRef] [PubMed]
8. Emig, T.; Graham, N.; Jaffe, R.; Kardar, M. Casimir forces between arbitrary compact objects. *Phys. Rev. Lett.* **2007**, *99*, 170403. [CrossRef] [PubMed]
9. Rahi, S.J.; Emig, T.; Graham, N.; Jaffe, R.L.; Kardar, M. Scattering theory approach to electrodynamic Casimir forces. *Phys. Rev. D* **2009**, *80*, 085021. [CrossRef]
10. Deutsch, D.; Candelas, P. Boundary effects in quantum field theory. *Phys. Rev. D* **1979**, *20*, 3063–3080. [CrossRef]
11. Brevik, I.; Lygren, M. Casimir effect for a perfectly conducting wedge. *Ann. Phys.* **1996**, *251*, 157–179. [CrossRef]
12. Helliwell, T.M.; Konkowski, D.A. Vacuum fluctuations outside cosmic strings. *Phys. Rev. D* **1986**, *34*, 1918–1920. [CrossRef] [PubMed]
13. Oberhettinger, F. Diffraction of waves by a wedge. *Commun. Pure Appl. Math.* **1954**, *7*, 551–563. [CrossRef]
14. Carslaw, H.S. The scattering of sound waves by a cone. *Math. Ann.* **1914**, *75*, 133–147. [CrossRef]
15. Felsen, L. Plane-wave scattering by small-angle cones. *IEEE Trans. Anten. Propag.* **1957**, *5*, 121–129. [CrossRef]
16. Maghrebi, M.F.; Rahi, S.J.; Emig, T.; Graham, N.; Jaffe, R.L.; Kardar, M. Analytical results on Casimir forces for conductors with edges and tips. *Proc. Natl. Acad. Sci. USA* **2011**, *108*, 6867–6871. [CrossRef]
17. Yakubovich, S.B. *Index Transforms*; World Scientific: Singapore, 1996. [CrossRef]
18. Krüger, M.; Bimonte, G.; Emig, T.; Kardar, M. Trace formulas for nonequilibrium Casimir interactions, heat radiation, and heat transfer for arbitrary objects. *Phys. Rev. B* **2012**, *86*, 115423. [CrossRef]
19. Fosco, C.D.; Lombardo, F.C.; Mazzitelli, F.D. Proximity force approximation for the Casimir energy as a derivative expansion. *Phys. Rev. D* **2011**, *84*, 105031. [CrossRef]
20. Bimonte, G.; Emig, T.; Kardar, M. Casimir–Polder interaction for gently curved surfaces. *Phys. Rev. D* **2014**, *90*, 081702. [CrossRef]
21. Bimonte, G.; Emig, T.; Jaffe, R.L.; Kardar, M. Casimir forces beyond the proximity approximation. *Europhys. Lett. (EPL)* **2012**, *97*, 50001. [CrossRef]
22. Bimonte, G.; Emig, T.; Jaffe, R.L.; Kardar, M. Spectroscopic probe of the van der Waals interaction between polar molecules and a curved surface. *Phys. Rev. A* **2016**, *94*, 022509. [CrossRef]
23. Bimonte, G.; Emig, T.; Kardar, M. Material dependence of Casimir forces: Gradient expansion beyond proximity. *Appl. Phys. Lett.* **2012**, *100*, 074110. [CrossRef]

24. Rodriguez, A.; Ibanescu, M.; Iannuzzi, D.; Joannopoulos, J.D.; Johnson, S.G. Virtual photons in imaginary time: Computing exact Casimir forces via standard numerical electromagnetism techniques. *Phys. Rev. A* **2007**, *76*, 032106. [CrossRef]
25. Homer Reid, M.T.; Efficient computation of Casimir interactions between arbitrary 3D objects. *Phys. Rev. Lett.* **2009**, *103*, 040401. [CrossRef] [PubMed]
26. Homer Reid, M.T.; White, J.; Johnson, S.G. Fluctuating surface currents: An algorithm for efficient prediction of Casimir interactions among arbitrary materials in arbitrary geometries. *Phys. Rev. A* **2013**, *88*, 022514. [CrossRef]
27. Bimonte, G.; Emig, T. Unifying theory for Casimir forces: Bulk and surface formulations. *Universe* **2021**, *7*, 225. [CrossRef]
28. Emig, T.; Bimonte, G. Multiple scattering expansion for dielectric media: Casimir effect. *Phys. Rev. Lett.* **2023**, *130*, 200401. [CrossRef] [PubMed]
29. Brevik, I.; Lygren, M.; Marachevsky, V. Casimir–Polder effect for a perfectly conducting wedge. *Ann. Phys.* **1998**, *267*, 134–142. [CrossRef]
30. Milton, K.A.; Abalo, E.K.; Parashar, P.; Pourtolami, N.; Brevik, I.; Ellingsen, S.Å. Casimir–Polder repulsion near edges: Wedge apex and a screen with an aperture. *Phys. Rev. A* **2011**, *83*, 062507. [CrossRef]
31. Milton, K.A.; Abalo, E.K.; Parashar, P.; Pourtolami, N.; Brevik, I.; Ellingsen, S.Å. Repulsive Casimir and Casimir–Polder forces. *J. Phys. Math. Theor.* **2012**, *45*, 374006. [CrossRef]
32. Gradshteyn, I.S.; Ryzhik, I.M. *Table of Integrals, Series, and Products*; Academic Press: San Diego, CA, USA, 2007. Available online: <https://www.sciencedirect.com/book/9780123736376/table-of-integrals-series-and-products> (accessed on 15 September 2023).
33. Oberhettinger, F.; Higgins, T.P. *Tables of Lebedev, Mehler and Generalized Mehler Transforms*; Boeing Scientific Research Laboratories: Washington, DC, USA, 1961. Available online: <https://apps.dtic.mil/sti/tr/pdf/AD0267210.pdf> (accessed on 15 September 2023).
34. Milton, K.A. Casimir–Polder forces in inhomogeneous backgrounds. *J. Opt. Soc. Am. B* **2019**, *36*, C41–C45. [CrossRef]

Disclaimer/Publisher’s Note: The statements, opinions and data contained in all publications are solely those of the individual author(s) and contributor(s) and not of MDPI and/or the editor(s). MDPI and/or the editor(s) disclaim responsibility for any injury to people or property resulting from any ideas, methods, instructions or products referred to in the content.

Review

A Brief Review of Some Recent Precision Casimir Force Measurements

Madhav Dhital and Umar Mohideen *

Department of Physics & Astronomy, University of California, Riverside, CA 92521, USA

* Correspondence: umar.mohideen@ucr.edu

Abstract: Here, we review recent advances in precision Casimir force measurements with both non-magnetic and magnetic materials. In addition, the measurement of the geometric dependence of the Casimir force, both lateral and normal, using uniformly corrugated surfaces is briefly presented. Finally, the measurement of the thermal Casimir force in graphene is discussed.

Keywords: precision Casimir force measurements; geometric dependence of Casimir force; normal Casimir force measurements; lateral Casimir force measurements

1. Introduction

Precision measurements of the Casimir force have been ongoing since they were first published, more than two decades ago [1,2]. The rapid progress in precision measurements between metallic test bodies over this period [3–6] has revealed a puzzling problem through disagreement between experiment and theory. In many experiments performed by different groups, it was found that the predictions of the Lifshitz theory came into conflict with the measurement data if the much-studied relaxation properties of conduction electrons at low frequencies were taken into account in computations (detailed in monograph [7]) and reviews [8,9]. In this paper, we briefly review some of the experimental advances in the University of California(UC)-Riverside group since the publication of the previous reviews [7,10]. In Section 2, we recap the results from the recent precision measurement of the Casimir force between smoother Au-coated surfaces of a sphere and plate for much larger separations from 250 nm to 1300 nm in an ultra-high vacuum, using a more force-sensitive cantilever in the custom-built dynamic atomic force microscope (AFM)-based setup. Here, both ultraviolet (UV) light and Ar-ion cleaning of the Au surfaces were carried out to remove ambiguities of electrostatic patches. In Section 3, we briefly consider experiments on the geometric dependence of the Casimir force using sinusoidal corrugated surfaces. Here, measurements of the lateral Casimir force as well as the normal Casimir force between the two uniformly corrugated surfaces are reviewed. In Section 4, earlier experiments on the role of magnetic fluctuations are reviewed. These experiments, in addition to demonstrating the effect of magnetic permeability, were also able to rule out any prominent role for electrostatic patches as an explanation for the disagreement between experiment and theory. Finally, in Section 5, we review our recent experiment measuring the Casimir force from graphene. Graphene provides many advantages towards understanding the disagreement between precision measurements of the Casimir force and the Lifshitz theory. The reason is that the response of graphene to electromagnetic fluctuations can be deduced from the first principles of quantum electrodynamics, thus eliminating the key uncertainty of the material properties in theoretical calculations of the Casimir force when metal test bodies are used where tabulated values of the permittivity [11] and its extrapolation to zero frequency are needed. Key details in all the experiments mentioned above are (i) independent measurement of the residual electrostatic force between the interacting surfaces; (ii) keeping the contribution of this residual electrostatic force either negligible or small compared with the Casimir force, by using clean experimental surfaces in an ultra-high vacuum chamber; and

Citation: Dhital, M.; Mohideen, U. A Brief Review of Some Recent Precision Casimir Force Measurements. *Physics* **2024**, *6*, 891–904. <https://doi.org/10.3390/physics6020055>

Received: 30 November 2023

Revised: 13 February 2024

Accepted: 22 March 2024

Published: 13 June 2024



Copyright: © 2024 by the authors. Licensee MDPI, Basel, Switzerland. This article is an open access article distributed under the terms and conditions of the Creative Commons Attribution (CC BY) license (<https://creativecommons.org/licenses/by/4.0/>).

(iii) using only surfaces where the residual electrostatic force is independent of distance, allowing its definitive subtraction. In the precision Casimir force measurements with normal metals such as Au, the disagreement between the experimental measurement and the Lifshitz theory, using tabulated values of the permittivity and its extrapolation including the dissipation of the free conduction electrons, remains an unresolved puzzle to date. Note that in Refs. [12,13], an agreement was obtained only by subtracting a hypothetical electrostatic force between a centimeter-size spherical lens and a plate that was ten times larger than the Casimir force. The measurements reviewed below, acquired using magnetic metal surfaces [14,15] and difference force measurements using over layers [16], reconfirm this conclusion to high precision.

2. Recent Precision Casimir Force Measurements to 1.3 μm

The most recent direct precision measurements of the gradient of the Casimir force between an Au-coated surface of a sphere and a plate for separations to 1.3 μm were reported in Refs. [17–20]. A large sphere and plate, rather than two plates, were used to avoid problems with keeping two plates parallel. The schematic of the experiment is shown in Figure 1a. A custom-built ultra-high vacuum atomic force microscope cantilever technique was used to measure the Casimir force between an Au-coated sphere and plate. The resonance frequency shift of this microcantilever is related to the sphere-plate force gradient, as:

$$\Delta f = -\frac{f_0}{2k} \left(\frac{\partial F_{\text{el}}}{\partial z} + \frac{\partial F_{\text{Cas}}}{\partial z} \right), \quad (1)$$

where Δf is the frequency shift, f_0 is the cantilever resonant frequency when no force is applied, k is the cantilever spring constant, F_{el} and F_{Cas} are electrostatic force and Casimir force, respectively. The electrostatic force F_{el} is used for calibration. The following improvements over our previous measurements were achieved [17–20]:

- i. Force measurement sensitivity improved by a factor of 10.
- ii. An in situ Ar ion beam and UV cleaning procedure for the interacting surfaces were introduced, eliminating the effects of ambiguous electrostatic forces and achieving ultra-high vacuum.
- iii. The surface roughness of the plate was reduced by a factor of 2 to 1.08 nm through the use of polished Si wafer substrates and e-beam Au coating, which eliminated uncertainties in separation distance (reduced to a smaller than 10^{-4} effect).
- iv. Measurements were made to larger separation distances from 250 to 1300 nm (factor of 2 larger than previously).

The gradient of the Casimir force was measured between the Au-coated hollow glass sphere of $R = 43.446 \pm 0.042 \mu\text{m}$ radius and the Au-coated silicon plate. The hollow glass spheres were made from liquid phase and had negligible asphericity with the difference along two perpendicular axes being less than or equal to 0.1%. The spring constant k of this cantilever was reduced by decreasing its thickness through etching with 60% KOH (potassium hydroxide) solution. The electron micrograph of the Au-coated hollow glass spheres attached to the cantilever end is shown in Figure 1b. The use of polished silicon wafer as the base plate instead of sapphire or fused silica plates used previously [6] and an e-beam evaporator for making the Au coatings instead of a thermal evaporator allowed a decrease in the surface roughness by up to a factor of 2. The root-mean square (rms) roughness on the sphere and the plate was 1.13 nm and 1.08 nm, respectively (compared with 2.0 nm and 1.8 nm, respectively, in Ref. [6]). The Au-coated plate was mounted on a piezoelectric tube which helped to precisely control its position, see Figure 1a. The precise plate position was measured with the 520 nm interferometer shown in Figure 1a. The cantilever oscillation was monitored with a 1550 nm laser optical interferometer. The finesse of the cavity was maximized by Au coating the cantilever top end. Care needed to be taken, as Au coating of the cantilever would reduce the oscillator quality factor, Q .

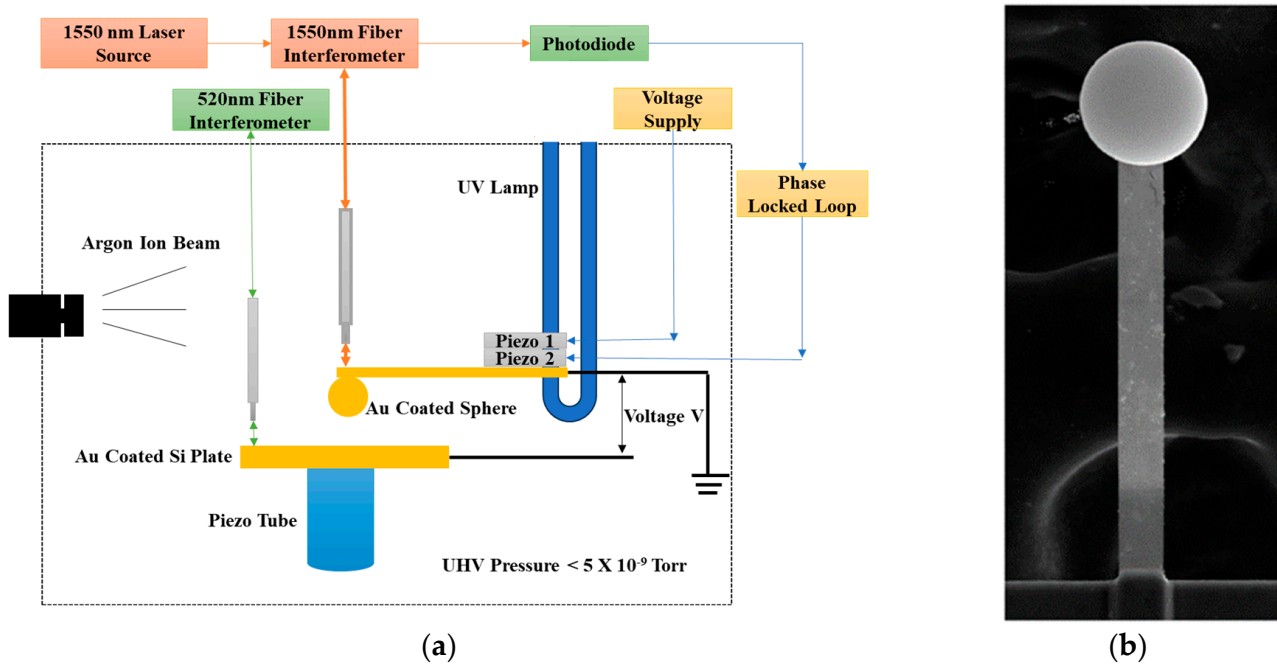


Figure 1. (a) Schematic of the experimental setup. “UV” stands for “ultraviolet” and “UHV” stands for “ultra-high vacuum”. (b) SEM (scanning electron microscope) micrograph of a microcantilever with attached Au-coated sphere.

Removing Ambiguity from Electrostatic Patches

A major improvement over all previous experiments is the in situ UV followed by Ar-ion cleaning of the test bodies and surfaces inside the vacuum chamber. The in situ cleaning of interacting surfaces in Casimir force measurements is critical for the removal of any surface contaminants that lead to background electrostatic forces. In particular, the contaminants lead to inhomogeneous work functions of the Au surface, resulting in patch potentials [21–24]. Such patch potentials result in electrostatic forces having a distance dependence (electric multipole effects), complicating their subtraction and leading to ambiguity in precision measurements of the Casimir force. Traditional vacuum cleaning by baking to high temperatures is not suitable, as the interferometer alignment is destroyed by thermal stress. In Figure 2, the sphere–plate residual potential is shown as a function of separation distance before and after UV plus Ar-ion-beam cleaning. In Ar-ion cleaning, the ions are focused on the interacting sphere–plate surfaces, as shown in Figure 1a, and the adsorbed contaminants on the experimental chamber walls are not completely removed. Thus, over time, the desorption of contaminants from the chamber walls leads to the redeposition of some of the contaminant molecules on the Au surfaces of the test samples, resulting in an increase in residual electric potential difference. First, applying UV light leads to desorption of surface contaminants from the entire chamber, either through direct ionization or reaction with generated ozone, which is then pumped out. As a result of the UV light followed by Ar-ion-beam cleaning, the residual potential difference between sphere and plate, as shown in Figure 2, was lowered by an order of magnitude, leading to the near elimination of electrostatic forces, as discussed in the literature [18,19]. Its value is also independent of sphere–plate separation distance, pointing to the absence of electric multipole effects from any patch effects. In addition, the residual potential difference between the two surfaces remains near zero for considerably longer, allowing stable Casimir force measurements.

The measurement results [18,19] for the gradient of the Casimir force obtained are shown in Figure 3a,b over the separation range from 250 to 950 for 10 nm cantilever oscillation amplitude.

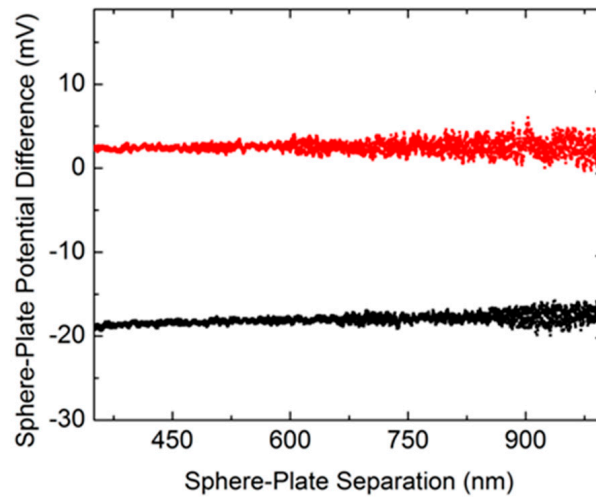


Figure 2. The Au sphere–plate residual potential difference as a function of the separation before (black) and after (red) UV and Ar-ion cleaning [20]. Reproduced under the copyright permission from World Scientific.

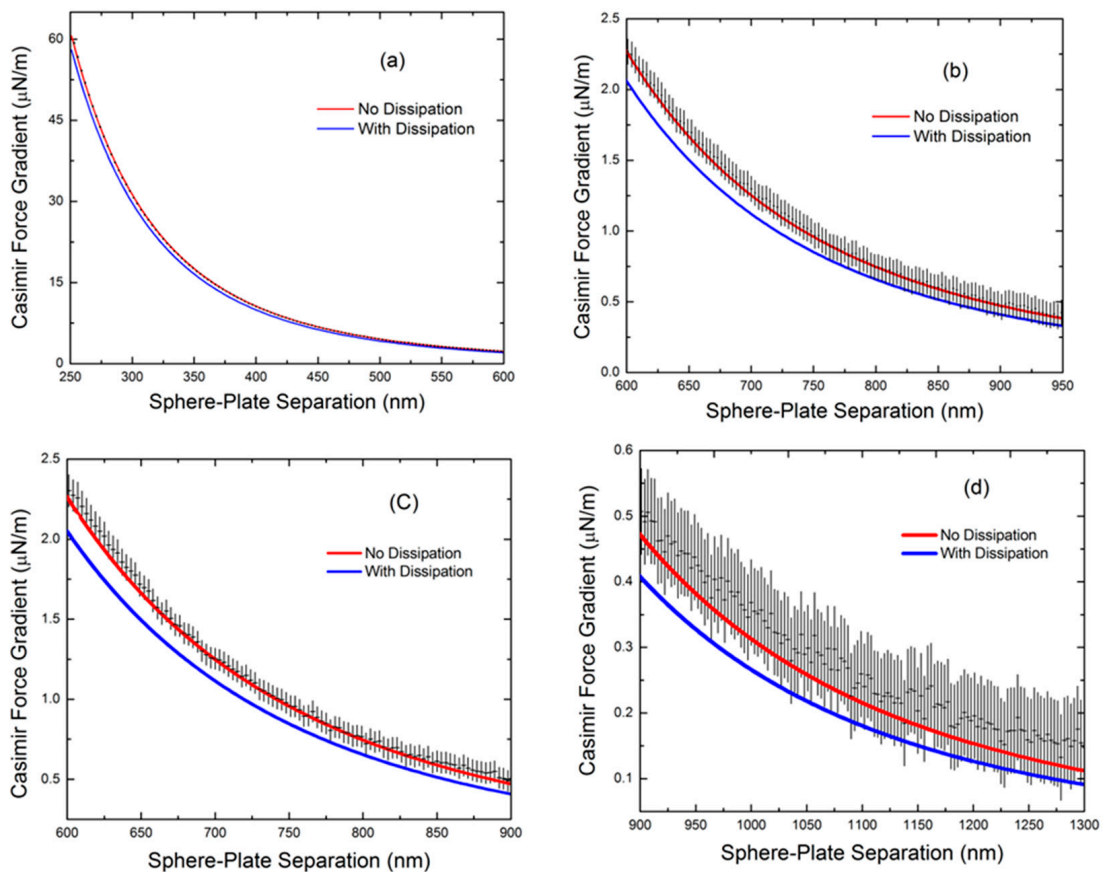


Figure 3. The Casimir force gradient measured as a function of the sphere–plate separation for (a,b) 10 nm cantilever oscillations and (c,d) 20 nm cantilever oscillations [18]. The experimental data (error bars) for the force gradient and separation agree with the no-dissipation theory calculations (lines) for zero-point photon-free electron scattering for all separations shown.

Using larger cantilever oscillation amplitudes of 20 nm, the frequency shift measurement can be improved, allowing Casimir force gradient measurements to 1300 nm. The measured gradients are shown as crosses in Figure 3c,d over the separation region from 600 nm to 1.3 μm. The vertical size of the crosses indicates the total error in measuring

the force gradient at the 67% confidence level. The horizontal size is determined by the constant error in measuring the absolute separations $\Delta z = 0.5$ nm in Figure 3a,b and 1.1 nm in Figure 3c,d. For ease of visualization, only every third data point is plotted. In the theory calculations, the Au metal response is given by the permittivity $\epsilon(\omega)$, where the tabulated values in Ref. [11] were used along with the extrapolation to low frequencies made using $\epsilon(\omega) = \frac{\omega_p^2}{\omega(\omega+i\gamma)}$, where $\omega_p = 9.0$ eV is the plasma frequency and the relaxation frequency is $\gamma = 35$ meV [11] for the dissipative Drude model and $\gamma = 0$ for the dissipationless plasma model. The theoretical values represented by the solid blue line were calculated with the tabulated Au permittivity [11] and dissipative Drude extrapolation to zero frequency. The theoretical values represented by the solid red line were calculated with the tabulated Au permittivity [11] and dissipationless plasma extrapolation to zero frequency. As is seen in Figure 3a–d, the theoretical predictions using the dissipationless plasma model are consistent with the measurement data over the entire range from 250 nm to 1.3 μm . The predictions of the Lifshitz theory using the dissipative Drude model are excluded at all separations up to 1.1 μm . Thus, the range of separations where the dissipative Drude model is excluded has been significantly extended.

3. Geometric Dependence of the Casimir Force with Sinusoidally Corrugated Surfaces

3.1. Demonstration of Asymmetry and Nonadditivity in Lateral Casimir Force

Controlling the length scale of the zero-point photon fluctuations using boundary geometry, dielectric properties, and temperature leads to profoundly interesting effects. In particular, uniformly corrugated boundaries are of interest due to the diffraction-type coherent scattering effects of zero-point photons that have been reported in these systems [23,25–34]. The zero-point photon wavelengths that matter are those that correspond to the separation distance. Additional important length scales in the problem are the corrugation period, λ , separation between the corrugations, z , the thermal wavelength $\hbar c/k_B T$, the temperature, T , and the material reflectivity through the plasma wavelength $2\pi c/\omega_p$, where ω_p is the plasma frequency, \hbar is the reduced Planck constant, c denotes the speed of light, and k_B is the Boltzmann constant. The coupling of scales of different lengths and the angle between the two corrugations led to rich behavior, making it a promising probe into these interconnected phenomena [35–40].

Of the above, the most intriguing feature is the nonadditive behavior of the Casimir force and, thus, the complicated dependence on the shape of the boundary surfaces connected with diffraction effects. The nontrivial behavior of the normal Casimir force was experimentally demonstrated in the configuration of a smooth sphere above a sinusoidally corrugated plate [25]. For the case of the additive regime, we reported measurement of the lateral Casimir force between two aligned sinusoidally corrugated surfaces of a sphere and a plate [26]. In the case of the nonadditive regime, the deviation of both the experimental data and the exact theory from the prediction of the proximity force approximation (PFA) was quantified in Refs. [29,30]. PFA approximates curved surfaces as a collection of infinitesimal flat surface elements and the local parallel plate contributions are added [27,28]. Thus, PFA neglects the diffraction effects of the zero-point photons. Compared with our previous lateral force measurement [2,26], this demonstration [29,30] of asymmetry and nonadditivity required many improvements such as a decrease of more than 50% in the grating period along with a 71% increase in the amplitude of the aligned imprinted grating. Here, the experimental chamber with a pressure less than 10 mTorr contained a sinusoidally corrugated Au-coated grating of size 5×5 mm² vertically mounted on the piezotube of the AFM. In order to achieve the nonadditive regime, the corrugations had an average period of 574.7 nm, i.e., less than half of that in Refs. [2,26] and an amplitude of 85.4 ± 0.3 nm, compared with 59 nm in Refs. [2,26]. This flat grating served as the first test body. A 320 μm long V-shaped silicon nitride cantilever for the AFM was specially prepared first by uniformly coating it with 40 nm of Al to improve its thermal and electric conductivity and to prevent deformation due to differential thermal expansion in a vacuum. The lateral Casimir force results from the interaction between two perfectly aligned uniaxially corrugated surfaces of

the same period. With the goal to keep the contact region for the imprinting of the grating and to make the second corrugated surface far away from the silicon nitride cantilever, a $200 \pm 4 \mu\text{m}$ diameter polystyrene sphere was placed at the end of the cantilever, to the bottom of which a freshly cleaved mica sheet of $400 \mu\text{m}$ length, $200 \mu\text{m}$ width, and a few micrometers thickness was attached. A second polystyrene sphere was then attached to the bottom free end of the mica sheet. The complete system was uniformly coated with a 10 nm layer of Cr and then with a 50 nm layer of Au in a thermal evaporator. The corrugations of the flat grating were imprinted on the Au-coated sphere using a stepper motor and by applying a voltage to the AFM piezo, as has been described. The lateral Casimir force between the two aligned sinusoidally corrugated Au-coated surfaces was measured for separation distances between 121.1 nm and 175.3 nm, much smaller than the 221–257 nm measured previously. The uncertainty in the measured separation distances was reduced to 4 nm, compared with 32 nm previously [6].

In addition, an independent electrostatic measurement of the separation distance was taken [2,26–30]. The measured asymmetric lateral Casimir force was observed from its nonsinusoidal phase dependence, as shown in Figure 4a. Here, the measurement data are compared with the exact theory describing the Rayleigh scattering [31] of the electromagnetic oscillations on the sinusoidally corrugated boundary surfaces of a sphere and plate with no fitting parameters. In Figure 4a, both the experimental data shown as dots and the theoretical line shown in red demonstrate that the lateral Casimir force is asymmetric and that the dependence of the lateral Casimir force as function of the phase is purely sinusoidal only if the calculation is restricted to the lowest order in the corrugation amplitudes. The asymmetry of the lateral Casimir force can be clearly observed even without the red theoretical curve, because the average shift of the maxima from the midpoint of two adjacent minima is $(0.12 \pm 0.02)\lambda$. The experimental data of the measured lateral Casimir force amplitude as a function of separation are shown in Figure 4b as crosses, along with error bars. These data were found to be in good agreement with the theory, which takes into account the photon correlation. In Figure 4b, the measured forces are found to deviate from the PFA, which neglects diffraction effects. This experiment using large amplitude corrugations with a significantly smaller period allowed demonstration of the asymmetry of the lateral Casimir force and had the ability to quantify deviations from the PFA.

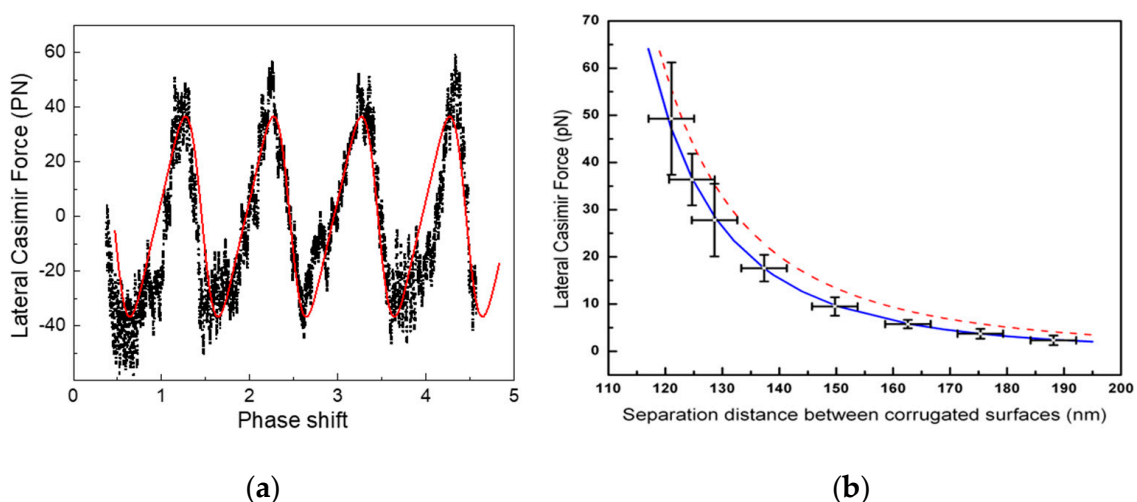


Figure 4. (a) The measured lateral Casimir force for a separation distance of $z = 124.7 \pm 4.0 \text{ nm}$ as a function of the phase shift between the corrugations (black dots) compared with the theory (red solid line) given by the Rayleigh scattering approach [29]. Note that the maximum is not at the midpoint of the minima, demonstrating asymmetry. (b) The amplitude as a function of separation distance (shown with error bars) compared to the Rayleigh scattering theory, which includes photon correlation (blue solid line), and to the PFA with no photon correlation (red dashed line) [30].

3.2. Role of Coherent Scattering in the Normal Casimir Force between Two Uniformly Corrugated Surfaces

Whereas the lateral Casimir force acts parallel to the two corrugated surfaces, the normal Casimir force is measured perpendicular to the periodically corrugated surfaces and provides us with valuable insight into the macroscopic geometric effects of vacuum fluctuations. As in Section 3.1, these geometry effects are quantified in terms of deviation from PFA where the Casimir energy is treated as the simple addition of flat infinitesimal surface elements which represent the curved surface. In addition to neglecting diffraction effects, the PFA ignores correlations from the interplay of geometry, material properties, and temperature.

The measurement of the normal Casimir force between two sinusoidally corrugated diffraction gratings on a gold-coated plate and sphere at various angles between corrugations was previously reported in Refs. [32,41]. The data are shown in Figure 5a where the measured Casimir force is shown to increase by 15% at 130 nm separation when the orientation angle between corrugations increased from 0 to 2.4. Figure 5b shows the deviation of the measured force from PFA for an angle between the corrugations of 1.2°. The measured forces are seen to deviate from the PFA (deviations measure diffraction-like coherent effects not included in PFA) and to be in agreement with the gradient approximation theory [42,43] including correlation effects of geometry and real metal–dielectric properties. The system is also seen to be highly sensitive to the role of thermal photons and is thus a measurement of the thermal Casimir effect between corrugated surfaces.

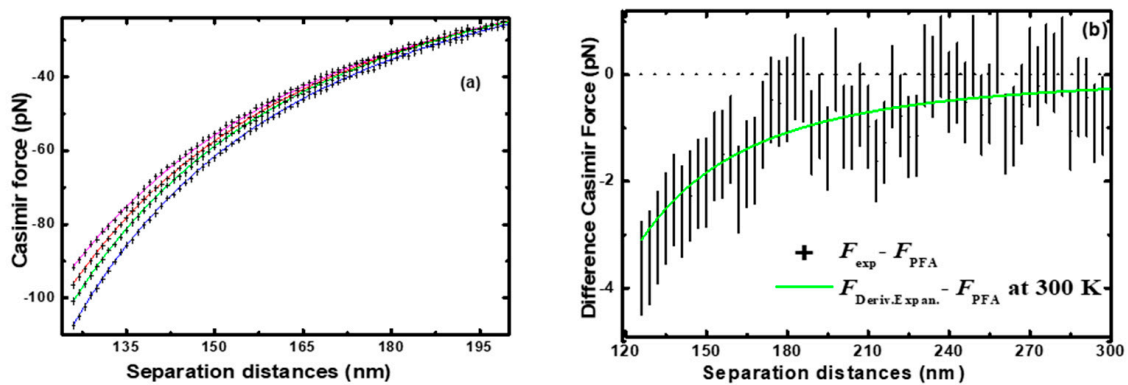


Figure 5. (a) Measured (shown with error bars) normal Casimir force between two sinusoidally corrugated surfaces corresponding to corrugation orientation angles of 0°, 1.2°, 1.8°, and 2.4° (top to bottom) compared to the theory (solid lines) using the derivative expansion [32]. (b) The difference ($F_{\text{exp}} - F_{\text{PFA}}$) between the measured and PFA-predicted Casimir forces (shown with error bars) for a corrugation orientation angle of 1.2° compared to the corresponding difference ($F_{\text{Deriv. Expan.}} - F_{\text{PFA}}$) between the gradient expansion and PFA theories at $T = 300$ K [41]. This difference a measure of the correlation and diffraction effects (see text for details). The bars represent the total (combined systematic and random) errors at a 67% confidence level.

The above results experimentally demonstrate the angle dependence of the normal Casimir force between a corrugated plate and corrugated sphere. The strong angular and temperature dependences of normal Casimir force for two oriented corrugations make it a uniquely important system for understanding the nontrivial combined interactions of geometry, material properties, and temperature.

4. Role of Magnetic Fluctuations in the Casimir Force

More than 40 years after the prediction of potentially repulsive contributions from magnetic fluctuations [44,45], the first experimental demonstration of the role of magnetic permeability, μ , was reported [14,15] and the results were compared to a new measurement with non-magnetic Au surfaces [6]. The use of materials such as Ni with $\mu > 0$ reduces

the Casimir force by adding a repulsive contribution. The experiments also showed that the role of electrostatic patch charges on surfaces was negligible in our experimental scheme. In Ref. [14], we reported the first demonstration of the Casimir force between two ferromagnetic Ni boundary surfaces. The experimental data, as shown in Figure 6, were found to be in good agreement with the predictions of the Lifshitz theory for magnetic boundary surfaces combined with the dissipation-less plasma model approach to describe the low-frequency permittivity of the metal. Tabulated [11] values of ϵ and μ were used, except for the dissipation $\gamma = 0$ (plasma) or $\gamma > 0$ (Drude model) for the low-frequency response of Au.

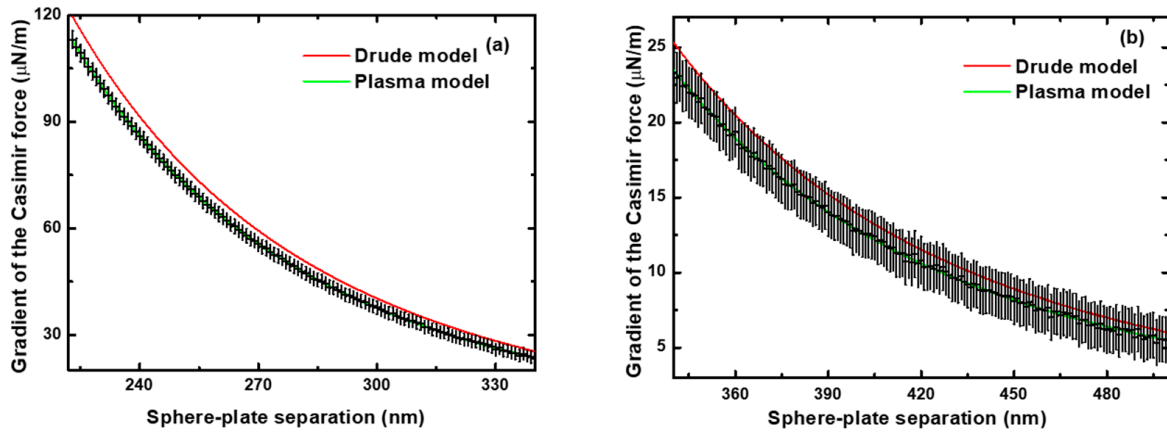


Figure 6. Measured (shown with error bars) Casimir force gradient between a ferromagnetic Ni-coated sphere and plate at small (a) and large (b) separation distances [14]. The bars represent total error at a 67% confidence level. The experimental data are in remarkable agreement with the plasma model with magnetic properties of Ni included. There are no fitting parameters used.

In Ref. [15], the measured gradient of the Casimir force between a Ni plate and the non-magnetic Au sphere was reported. The mean gradient of the Casimir force (see Figure 7) was compared with theoretical predictions of the Lifshitz theory with no fitting parameters. The data are in good agreement with both the plasma model and Drude model description of the metal-free electrons as they coincide for these separations.

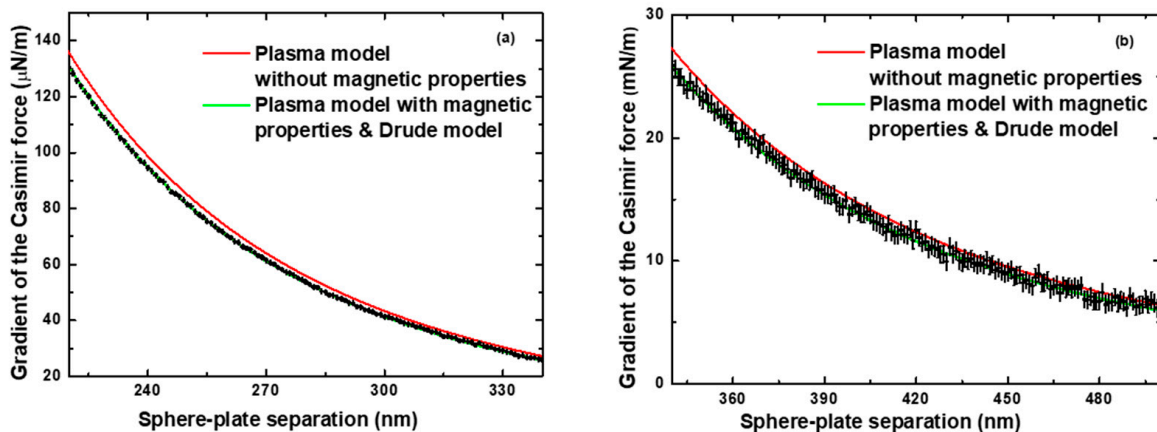


Figure 7. Measured (shown with error bars) Casimir force between an Au sphere–ferromagnetic Ni plate versus small (a) and large (b) surface separation distances [15]. The error bars represent total error bars at a 67% confidence level. The experimental data are in good agreement with both the plasma model ($\gamma = 0$) and the Drude model for low-frequency metal response with the tabulated ϵ and μ of Ni included. The Drude and plasma models overlap for the μ of Ni in this region. No fitting parameters were used in comparison.

Conclusion on Role of Electrostatic Patches

To answer the critical question of whether zero-point photons dissipate energy on free electron scattering, one has to show agreement with either the plasma (no dissipation) or Drude (dissipative) model. For the Au-coated sphere and plate, using a different tabulated ϵ and μ to calculate the theoretical Casimir force makes a negligible difference [14,15] to the agreement with the dissipationless plasma model. However, for non-magnetic materials, an agreement can possibly be brought about by using electrostatic forces [21,23] with specialized charge density and size distributions. Yet, from the results of the experiments indicated in Figures 3, 6 and 7, one can see that anomalous forces from electrostatic patches in the experiments (a) have to be negligible and (b) cannot explain the difference from the Drude model consistently. To bring about an agreement with Drude model, one needs positive contribution in Figure 6 (two magnetic material surfaces), but a negative one in Figure 3 (non-magnetic material surfaces). In the experiment in Figure 7 with one magnetic material and one non-magnetic material, both models overlap and agree with data for this separation region. As electric patch forces only add to the total force, the only consistent explanation is that they have to be negligible [46,47]. Following these results, a difference force measurement [16] showed that the non-dissipative plasma model was in remarkable agreement and the dissipative Drude model in disagreement with their data by a factor of 10^3 .

5. Precision Casimir Force Measurements with Graphene

Unlike normal metals, where for comparison between experiment and theory, the metal properties have to be input from tabulated values with extrapolation to zero frequency, the non-local response function of graphene to electromagnetic fluctuations can be calculated from the first principles of quantum electrodynamics [48–50]. Another interesting feature is an unusually large thermal correction to the Casimir force between two parallel graphene sheets spaced at separations of less than $1 \mu\text{m}$, first predicted by Gómez-Santos [51]. Many physical effects in graphene have also been described [52]. In a more recent measurement [53], the gradient of the Casimir force between an Au-coated microsphere and a graphene sheet deposited on a silica glass (SiO_2) plate obtained in a high vacuum using a custom dynamic AFM was performed. In the previous experiment [53], the graphene sheet was deposited on a SiO_2 film covering a Si plate. The gradient of the Casimir force was measured and found to be in good agreement with the theory. However, the thermal effect could not be identified because of the large uncertainty in the charge carrier concentration of the Si plate used.

In this Casimir force gradient measurement system, a tipless AFM cantilever was used whose spring constant was reduced through chemical etching, as described above. As in previous experiments, a hollow glass microsphere attached to the end of the cantilever using silver epoxy and coated with Au was used as the second surface. The thickness of the Au coating and the diameter of the coated sphere were measured to be 120.3 nm and $120.7 \mu\text{m}$, using an AFM and a scanning electron microscope, respectively. The rms roughness of the Au coating was measured to be $\delta = 0.9 \text{ nm}$. The resonant frequency of the complete Au-coated cantilever–sphere system in the vacuum was measured to be $\omega_0 = 6.1581 \times 10^3 \text{ rad/s}$.

A large area of graphene monolayer originally grown by chemical vapor deposition on a Cu foil was transferred onto a polished JGS2 grade fused silica double-sided optically polished substrate of 100 mm diameter and $500 \mu\text{m}$ thickness through an electro-chemical delamination procedure. A $1 \times 1 \text{ cm}^2$ piece of the graphene-coated fused silica wafer was then cut from the large sample and used. After the force gradient measurements, the roughness of the graphene on the fused silica substrate was measured to be $\delta = 1.5 \pm 0.1 \text{ nm}$ using an AFM. After the Casimir force gradient measurement, the impurity concentration of graphene was determined utilizing Raman spectroscopy. The respective zero-temperature value of the chemical potential for our sample is given by $\mu = 0.24 \pm 0.01 \text{ eV}$. The values of the energy gap Δ for graphene on a SiO_2 substrate vary between 0.01 eV and 0.2 eV .

The fused silica-supported graphene sample and gold sphere probe were loaded into the vacuum chamber which was pumped down to a pressure below 9×10^{-9} Torr. Because of the sensitive nature of the graphene sample, the UV/Ar-ion radiation treatment described in Section 2 for cleaning the Au surfaces was not implemented, to avoid potential damage to the single atomic layer of graphene. To ensure the accuracy of the measurement, the residual potential difference between the gold and graphene surfaces was determined through the same standard electrostatic calibration procedure as stated in Section 2. The change in the resonant frequency Δf in the presence of external force was recorded by the PLL (phase-locked loop) every 0.14 nm while the graphene plate was moved toward the grounded sphere, starting at the maximum separation. This was repeated with one of ten different voltages V_i that varied between 0.083 V and 0.183 V and eleven voltages equal to the residual potential difference V_0 (see below) applied to the graphene using ohmic contacts while the sphere remained grounded.

The gradients of the total and Casimir forces were calculated from the measured frequency shifts using electrostatic calibration. At each separation, the gradient of the Casimir force was measured 21 times with the different applied voltages mentioned above. The random errors of the mean were determined at a 67% confidence level and combined in quadrature with the systematic errors originating primarily from the errors in measuring the frequency shifts. The obtained measurement data for the force gradient with their errors are shown in Figure 8 as crosses corresponding to error bars. For visual clarity, in Figure 8a, all data points are indicated, whereas in Figure 8b,c, every other data point and in Figure 8d, only every third are shown. For the comparison with the theory, the relativistic version of the Lifshitz formula with reflection coefficients expressed via the exact polarization tensor of graphene in the framework of the Dirac model takes into account the nonzero energy gap, Δ , and chemical potential, μ [54–57]. The computational results for the boundaries of allowed theoretical bands are shown in Figure 8 by the two bands, computed at $T = 294$ K and $T = 0$ K. The upper line in each band was computed for $\mu = 0.25$ eV, $\Delta = 0$ eV, and the lower line for $\mu = 0.23$ eV, $\Delta = 0.2$ eV. As shown in Figure 8, the measurement data are in very good agreement with the theory at $T = 294$ K. The unusually large thermal effect in the force gradient equal to the difference between the top and bottom bands is clearly demonstrated over the region from 250 to 590 nm. For example, at sphere–plate separations of 250, 300, 400, 500, and 590 nm, the thermal corrections were 4%, 5%, 7%, 8.5%, and 10% of the total force gradient, respectively.

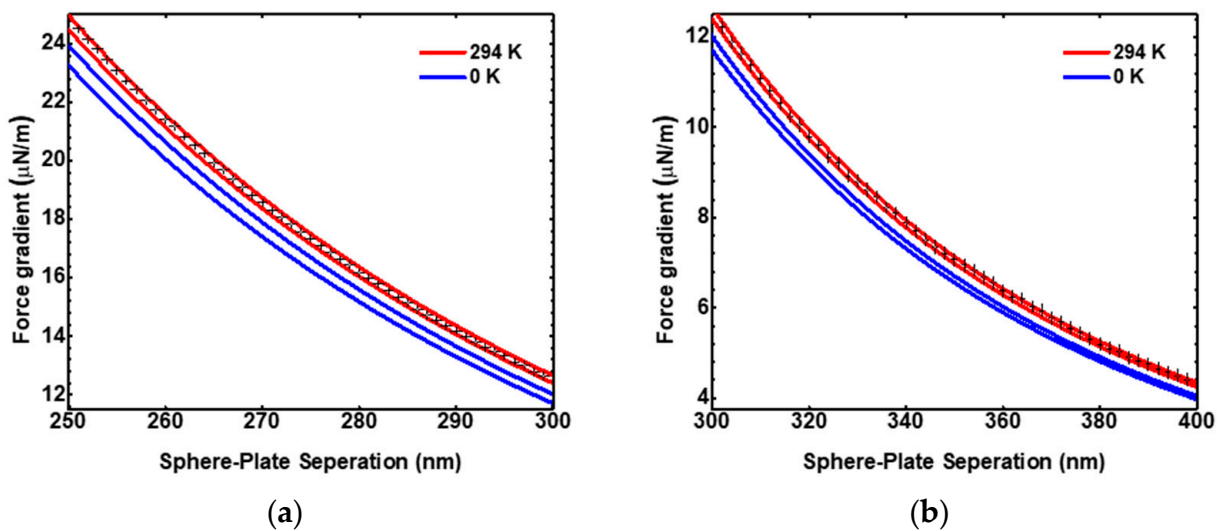


Figure 8. Cont.

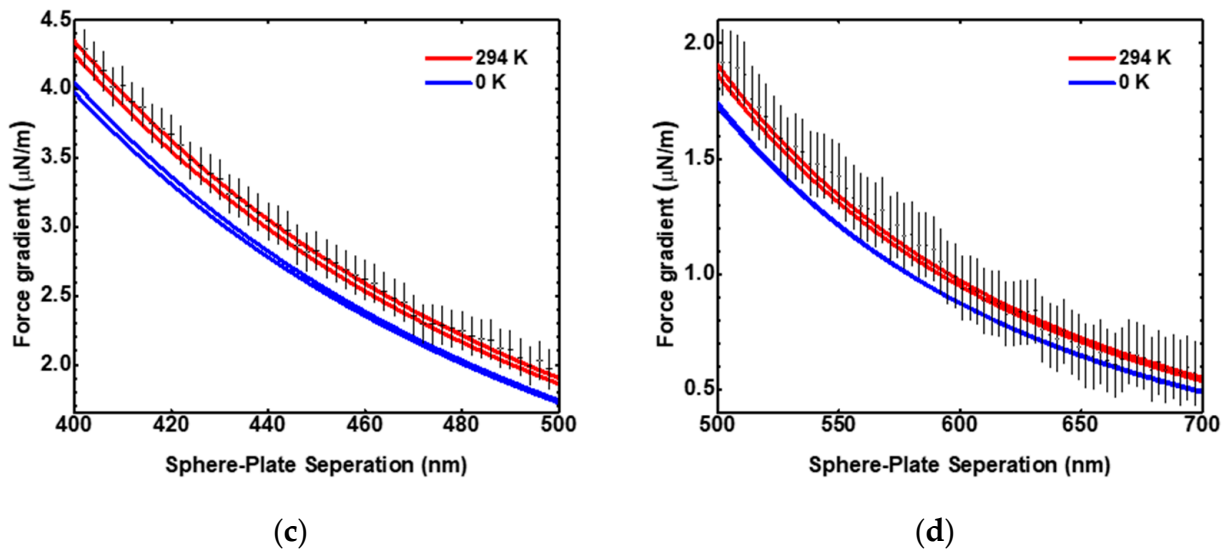


Figure 8. The measured (shown with error bars) mean gradient of the Casimir force as a function of separation compared to the calculations at $T = 294$ K (red) and 0 K (blue) with the upper lines for each T band computed for the chemical potential $\mu = 0.25$ eV and the gap $\Delta = 0$ eV, and the lower lines for $\mu = 0.23$ eV, $\Delta = 0.2$ eV [58,59]. The agreement of the data with the $T = 294$ K band is the detection of the thermal Casimir effect with graphene at sphere–plate separations of 250–300 nm (a), 300–400 nm (b), 400–500 nm (c), and 500–700 nm (d).

6. Conclusions

Precision Casimir force measurements have undergone remarkable progress over the last two decades. Some of the results of the UC Riverside group are presented above. The experimental results have, in turn, encouraged a tremendous amount of theoretical developments, some detailed in Ref. [60]. In addition to improvements in experimental methodology, considerable progress has also been achieved with the use of complicated geometries [61,62] other than the sinusoidally corrugated cases discussed above. Many other exciting geometric dependences [63–66] and material-dependent repulsive forces [9,67–71] remain to be investigated and exploited in nanomechanical devices [72,73]. Casimir torques [74,75] and their experimental exploitation represent another area of much promise. An exciting and as yet unresolved issue that remains is the disagreement between the experiment and the Lifshitz theory [76–79] when the dielectric response of metals is deduced from the optical data extrapolated down to zero frequency by means of the Drude model, where the relaxation parameter γ describes the energy losses of conduction electrons due to phonon scattering. It has been a puzzle that agreement between experiment and theory is obtained only if one makes γ equal to zero. This might lead to the conclusion that there are no energy losses at low frequencies for zero-point photon interactions with materials, unlike the case of real photons. However, this hypothesis alone would lead to the violation of the fluctuation dissipation theorem which is central to all of physics. Much light was shed from the precision experiments with graphene, discussed above, where the dielectric response of graphene was calculated from first principles of quantum electrodynamics. Based on the graphene’s dielectric response, it appears that it is the phenomenological character of the Drude model at low frequencies that might be in error. In particular, the Drude model does not capture the complete wave vector dependence of the dielectric response for evanescent waves, which are electromagnetic fluctuations that are not on the mass shell. Here again, there have been suggestions [80] for how to bring about a resolution to this long-standing problem, which are discussed elsewhere in Ref. [60].

Author Contributions: Both authors contributed equally to this work. All authors have read and agreed to the published version of the manuscript.

Funding: The work of M.D. and U.M. was partially supported by the National Science Foundation Grant No. PHY-2012201.

Data Availability Statement: The data are from the references cited.

Conflicts of Interest: The authors declare no conflict of interest.

References

- Mohideen, U.; Roy, A. Precision measurement of the Casimir force from 0.1 to 0.9 mm. *Phys. Rev. Lett.* **1998**, *81*, 4549–4552. [CrossRef]
- Chen, F.; Mohideen, U.; Klimchitskaya, G.L.; Mostepanenko, V.M. Experimental and theoretical investigation of the lateral Casimir force between corrugated surfaces. *Phys. Rev. A* **2002**, *66*, 032113. [CrossRef]
- Harris, B.W.; Chen, F.; Mohideen, U. Precision measurement of the Casimir force using gold surfaces. *Phys. Rev. A* **2000**, *62*, 052109. [CrossRef]
- Decca, R.S.; Lopez, D.; Fischbach, E.; Klimchitskaya, G.L.; Krause, D.E.; Mostepanenko, V.M. Precise comparison of theory and new experiment for the Casimir force leads to stronger constraints on thermal quantum effects and long-range interactions. *Ann. Phys.* **2005**, *318*, 37–80. [CrossRef]
- Decca, R.S.; Lopez, D.; Fischbach, E.; Klimchitskaya, G.L.; Krause, D.E.; Mostepanenko, V.M. Tests of new physics from precise measurements of the Casimir pressure between two gold-coated plates. *Phys. Rev. D* **2007**, *75*, 077101. [CrossRef]
- Chang, C.-C.; Banishev, A.A.; Castillo-Garza, R.; Klimchitskaya, G.L.; Mostepanenko, V.M.; Mohideen, U. Gradient of the Casimir force between Au surfaces of a sphere and a plate measured using an atomic force microscope in a frequency-shift technique. *Phys. Rev. B* **2012**, *85*, 165443. [CrossRef]
- Bordag, M.; Klimchitskaya, G.L.; Mohideen, U.; Mostepanenko, V.M. *Advances in the Casimir Effect*; Oxford University Press: Oxford, UK, 2015. [CrossRef]
- Klimchitskaya, G.L.; Mohideen, U.; Mostepanenko, V.M. The Casimir force between real materials: Experiment and theory. *Rev. Mod. Phys.* **2009**, *81*, 1827–1885. [CrossRef]
- Woods, L.M.; Dalvit, D.A.R.; Tkatchenko, A.; Rodriguez-Lopez, P.; Rodriguez, A.W.; Podgornik, R. Materials perspective on Casimir and van der Waals interactions. *Rev. Mod. Phys.* **2016**, *88*, 045003. [CrossRef]
- Bordag, M.; Mohideen, U.; Mostepanenko, V. New developments in the Casimir effect. *Phys. Rep.* **2001**, *353*, 1–205. [CrossRef]
- Palik, E.D. (Ed.) *Handbook of Optical Constants of Solids*; Academic Press: San Diego, CA, USA, 1985. [CrossRef]
- Garcia-Sanchez, D.; Fong, K.Y.; Bhaskaran, H.; Lamoreaux, S.; Tang, H.X. Casimir force and in situ surface potential measurements on nanomembranes. *Phys. Rev. Lett.* **2012**, *109*, 027202. [CrossRef]
- Sushkov, A.O.; Kim, W.J.; Dalvit, D.A.R.; Lamoreaux, S.K. Observation of the thermal Casimir force. *Nat. Phys.* **2011**, *7*, 230–233. [CrossRef]
- Banishev, A.; Klimchitskaya, G.; Mostepanenko, V.; Mohideen, U. Demonstration of the Casimir force between ferromagnetic surfaces of a Ni-coated sphere and a Ni-coated plate. *Phys. Rev. Lett.* **2013**, *110*, 137401. [CrossRef] [PubMed]
- Banishev, A.A.; Chang, C.-C.; Klimchitskaya, G.L.; Mostepanenko, V.M.; Mohideen, U. Measurement of the gradient of the Casimir force between a nonmagnetic gold sphere and a magnetic nickel plate. *Phys. Rev. B* **2012**, *85*, 195422. [CrossRef]
- Bimonte, G.; Lopez, D.; Decca, R.S. Isoelectronic determination of the thermal Casimir force. *Phys. Rev. B* **2016**, *93*, 184434. [CrossRef]
- Xu, J.; Klimchitskaya, G.L.; Mostepanenko, V.M.; Mohideen, U. Reducing detrimental electrostatic effects in Casimir-force measurements and Casimir-force-based microdevices. *Phys. Rev. A* **2018**, *97*, 032501. [CrossRef]
- Liu, M.Y.; Xu, J.; Klimchitskaya, G.L.; Mostepanenko, V.M.; Mohideen, U. Precision measurement of the gradient of the Casimir force between ultraclean metallic surfaces at larger separations. *Phys. Rev. A* **2019**, *100*, 052511. [CrossRef]
- Liu, M.Y.; Xu, J.; Klimchitskaya, G.L.; Mostepanenko, V.M.; Mohideen, U. Examining the Casimir puzzle with an upgraded AFM-based technique and advanced surface cleaning. *Phys. Rev. B* **2019**, *100*, 081406. [CrossRef]
- Liu, M.Y.; Schafer, R.; Xu, J.; Mohideen, U. Elimination of electrostatic forces in precision Casimir force measurements using UV and Ar ion radiation. *Mod. Phys. Lett. A* **2020**, *35*, 2040001. [CrossRef]
- Behunin, R.; Intravaia, F.; Dalvit, D.; Neto, P.M.; Reynaud, S. Modeling electrostatic patch effects in Casimir force measurements. *Phys. Rev. A* **2012**, *85*, 012504. [CrossRef]
- Behunin, R.O.; Dalvit, D.A.R.; Decca, R.S.; Genet, C.; Jung, I.W.; Lambrecht, A.; Liscio, A.; Lopez, D.; Reynaud, S.; Schnoering, G.; et al. Kelvin probe force microscopy of metallic surfaces used in Casimir force measurements. *Phys. Rev. A* **2014**, *90*, 062115. [CrossRef]
- Behunin, R.O.; Zeng, Y.; Dalvit, D.A.R.; Reynaud, S. Electrostatic patch effects in Casimir-force experiments performed in the sphere-plane geometry. *Phys. Rev. A* **2012**, *86*, 052509. [CrossRef]
- Naji, A.; Dean, D.S.; Sarabadani, J.; Horgan, R.R.; Podgornik, R. Fluctuation-induced interaction between randomly charged dielectrics. *Phys. Rev. Lett.* **2010**, *104*, 060601. [CrossRef] [PubMed]

25. Roy, A.; Mohideen, U. Demonstration of the nontrivial boundary dependence of the Casimir force. *Phys. Rev. Lett.* **1999**, *82*, 4380–4383. [CrossRef]
26. Chen, F.; Mohideen, U.; Klimchitskaya, G.L.; Mostepanenko, V.M. Demonstration of the lateral Casimir force. *Phys. Rev. Lett.* **2002**, *88*, 101801. [CrossRef] [PubMed]
27. Derjaguin, B. Untersuchungen über die Reibung und Adhäsion, IV. Theorie des Anhaftens kleiner Teilcher. *Kolloid-Zeitschrift* **1934**, *69*, 155–164. [CrossRef]
28. Blocki, J.; Randrup, J.; Swiatecki, W.J.; Tsang, C.F. Proximity forces. *Ann. Phys.* **1977**, *105*, 427–462. [CrossRef]
29. Chiu, H.C.; Klimchitskaya, G.L.; Marachevsky, V.N.; Mostepanenko, V.M.; Mohideen, U. Demonstration of the asymmetric lateral Casimir force between corrugated surfaces in the nonadditive regime. *Phys. Rev. B* **2009**, *80*, 121402. [CrossRef]
30. Chiu, H.C.; Klimchitskaya, G.L.; Marachevsky, V.N.; Mostepanenko, V.M.; Mohideen, U. Lateral Casimir force between sinusoidally corrugated surfaces: Asymmetric profiles, deviations from the proximity force approximation, and comparison with exact theory. *Phys. Rev. B* **2010**, *81*, 115417. [CrossRef]
31. Lord Rayleigh, Strutt, J.W. On the dynamical theory of gratings. *Proc. R. Soc. Lond. A* **1907**, *79*, 399–416. [CrossRef]
32. Banishev, A.; Wagner, J.; Emig, T.; Zandi, R.; Mohideen, U. Demonstration of angle-dependent Casimir force between corrugations. *Phys. Rev. Lett.* **2013**, *110*, 250403. [CrossRef]
33. Chan, H.B.; Bao, Y.; Zou, J.; Cirelli, R.; Klemens, F.; Mansfield, W.; Pai, C. Measurement of the Casimir force between a gold sphere and a silicon surface with nanoscale trench array. *Phys. Rev. Lett.* **2008**, *101*, 030401. [CrossRef] [PubMed]
34. Bao, Y.; Gue'rou, R.; Lussange, J.; Lambrecht, A.; Cirelli, R.A.; Klemens, F.; Mansfield, W.M.; Pai, C.S.; Chan, H.B. Casimir force on a surface with shallow nanoscale corrugations: Geometry and finite conductivity effects. *Phys. Rev. Lett.* **2010**, *105*, 250402. [CrossRef]
35. Golestanian, R.; Kardar, M. Mechanical Response of Vacuum. *Phys. Rev. Lett.* **1997**, *78*, 3421–3425. [CrossRef]
36. Rodrigues, R.B.; Neto, P.A.M.; Lambrecht, A.; Reynaud, S. Lateral Casimir force beyond the proximity-force approximation. *Phys. Rev. Lett.* **2006**, *96*, 100402. [CrossRef]
37. Canaguier-Durand, A.; Neto, P.A.M.; Lambrecht, A.; Reynaud, S. Thermal Casimir effect for Drude metals in the plane-sphere geometry. *Phys. Rev. A* **2010**, *82*, 012511. [CrossRef]
38. Zandi, R.; Emig, T.; Mohideen, U. Quantum and thermal Casimir interaction between a sphere and a plate: Comparison of Drude and plasma models. *Phys. Rev. B* **2010**, *81*, 195423. [CrossRef]
39. Rosa, F.S.S.; Dalvit, D.A.R.; Milonni, P.W. Casimir-Lifshitz theory and metamaterials. *Phys. Rev. Lett.* **2008**, *100*, 183602. [CrossRef] [PubMed]
40. Rodrigues, R.B.; Neto, P.A.M.; Lambrecht, A.; Reynaud, S. Vacuum-induced torque between corrugated metallic plates. *Europhys. Lett.* **2006**, *76*, 822. [CrossRef]
41. Banishev, A.A.; Wagner, J.; Emig, T.; Zandi, R.; Mohideen, U. Experimental and theoretical investigation of the angular dependence of the Casimir force between sinusoidally corrugated surfaces. *Phys. Rev. B* **2014**, *89*, 235436. [CrossRef]
42. Bimonte, G.; Emig, T.; Jaffe, R.L.; Kardar, M. Casimir forces beyond the proximity approximation. *Europhys. Lett.* **2012**, *97*, 50001. [CrossRef]
43. Bimonte, G.; Emig, T.; Kardar, M. Material dependence of Casimir forces: Gradient expansion beyond proximity. *Appl. Phys. Lett.* **2012**, *100*, 074110. [CrossRef]
44. Barash, Y.S.; Ginzburg, V.L. Electromagnetic fluctuations in matter and molecular (Van-der-Waals) forces between them. *Sov. Phys. Usp.* **1975**, *18*, 305–322. [CrossRef]
45. Kenneth, O.; Klich, I.; Mann, A.; Revzen, M. Repulsive Casimir forces. *Phys. Rev. Lett.* **2002**, *89*, 033001. [CrossRef] [PubMed]
46. Bezerra, V.B.; Klimchitskaya, G.L.; Mohideen, U.; Mostepanenko, V.M.; Romero, C. Impact of surface imperfections on the Casimir force for lenses of centimeter-size curvature radii. *Phys. Rev. B* **2011**, *83*, 075417. [CrossRef]
47. Decca, R.S.; Fischbach, E.; Klimchitskaya, G.L.; Krause, D.E.; Lopez, D.; Mohideen, U.; Mostepanenko, V.M. Capacitance measurements and electrostatic calibrations in experiments measuring the Casimir force. *Int. J. Mod. Phys. A* **2011**, *26*, 3930–3943. [CrossRef]
48. Drosdoff, D.; Woods, L.M. Quantum and thermal dispersion forces: Application to graphene nanoribbons. *Phys. Rev. Lett.* **2014**, *112*, 025501. [CrossRef]
49. Rodriguez-Lopez, P.; Kort-Kamp, W.J.M.; Dalvit, D.A.R.; Woods, L.M. Casimir force phase transitions in the graphene family. *Nat. Commun.* **2017**, *8*, 14699. [CrossRef]
50. Klimchitskaya, G.L.; Mohideen, U.; Mostepanenko, V.M. Theory of the Casimir interaction from graphene-coated substrates using the polarization tensor and comparison with experiment. *Phys. Rev. B* **2014**, *89*, 115419. [CrossRef]
51. Gomez-Santos, G. Thermal van der Waals interaction between graphene layers. *Phys. Rev. B* **2009**, *80*, 245424. [CrossRef]
52. Sarabadani, J.; Naji, A.; Asgari, R.; Podgornik, R. Many-body effects in the van der Waals–Casimir interaction between graphene layers. *Phys. Rev. B* **2011**, *84*, 155407. [CrossRef]
53. Banishev, A.A.; Wen, H.; Xu, J.; Kawakami, R.K.; Klimchitskaya, G.L.; Mostepanenko, V.M.; Mohideen, U. Measuring the Casimir force gradient from graphene on a SiO₂ substrate. *Phys. Rev. B* **2013**, *87*, 205433. [CrossRef]
54. Bordag, M.; Klimchitskaya, L.; Mostepanenko, M.; Petrov, M. Quantum field theoretical description for the reflectivity of graphene. *Phys. Rev. D* **2016**, *93*, 089907. [CrossRef]

55. Bimonte, G.; Klimchitskaya, G.L.; Mostepanenko, V.M. Thermal effect in the Casimir force for graphene and graphene-coated substrates: Impact of nonzero mass gap and chemical potential. *Phys. Rev. B* **2017**, *96*, 115430. [CrossRef]
56. Sernelius, B.E. Retarded interactions in graphene systems. *Phys. Rev. B* **2014**, *89*, 079901. [CrossRef]
57. Klimchitskaya, G.L.; Mostepanenko, V.M.; Sernelius, B.E. Two approaches for describing the Casimir interaction in graphene: Density-density correlation function versus polarization tensor. *Phys. Rev. B* **2014**, *89*, 125407. [CrossRef]
58. Liu, M.; Zhang, Y.; Klimchitskaya, G.L.; Mostepanenko, V.M.; Mohideen, U. Demonstration of an unusual thermal effect in the casimir force from graphene. *Phys. Rev. Lett.* **2021**, *126*, 206802. [CrossRef] [PubMed]
59. Liu, M.; Zhang, Y.; Klimchitskaya, G.L.; Mostepanenko, V.M.; Mohideen, U. Experimental and theoretical investigation of the thermal effect in the Casimir interaction from graphene. *Phys. Rev. B* **2021**, *104*, 085436. [CrossRef]
60. Klimchitskaya, G.L.; Mostepanenko, V.M. (Eds.) *Special Issue: 75 Years of the Casimir Effect: Advances and Prospects; Physics, in print.* Available online: https://www.mdpi.com/journal/physics/special_issues/75yearsCasimir (accessed on 17 March 2024).
61. Intravaia, F.; Koev, S.; Jung, I.W.; Talin, A.A.; Davids, P.S.; Decca, R.S.; Aksyuk, V.A.; Dalvit, D.A.R.; López, D. Strong Casimir force reduction through metallic surface nanostructuring. *Nat. Commun.* **2013**, *4*, 2515. [CrossRef]
62. Tang, L.; Wang, M.; Ng, C.Y.; Nikolic, M.; Chan, C.T.; Rodriguez, A.W.; Chan, H.B. Measurement of non-monotonic Casimir forces between silicon nanostructures. *Nat. Photon.* **2017**, *11*, 97–101. [CrossRef]
63. Rahi, S.J.; Emig, T.; Graham, N.; Jaffe, R.L.; Kardar, M. Scattering theory approach to electrodynamic Casimir forces. *Phys. Rev. D* **2009**, *80*, 085021. [CrossRef]
64. Lambrecht, A.; Neto, P.A.; Reynaud, S. The Casimir effect within scattering theory. *New J. Phys.* **2006**, *8*, 243. [CrossRef]
65. Maghrebi, M.F.; Rahi, S.J.; Emig, T.; Graham, N.; Jaffe, R.L.; Kardara, M. Analytical results on Casimir forces for conductors with edges and tips. *Proc. Natl. Acad. Sci. USA* **2011**, *108*, 6867–6871. [CrossRef]
66. Milton, K.A.; Wagner, J. Multiple scattering methods in Casimir calculations. *J. Phys. A Math. Theor.* **2008**, *41*, 155402. [CrossRef]
67. Grushin, A.G.; Cortijo, A. Tunable Casimir repulsion with three-dimensional topological insulators. *Phys. Rev. Lett.* **2011**, *106*, 020403. [CrossRef]
68. Jiang, Q.; Wilczek, F. Chiral Casimir forces: Repulsive, enhanced, tunable. *Phys. Rev. B* **2019**, *99*, 125403. [CrossRef]
69. Somers, D.A.; Munday, J.N. Conditions for repulsive Casimir forces between identical birefringent materials. *Phys. Rev. A* **2017**, *95*, 022509. [CrossRef]
70. Tajik, F.; Palasantzas, G. Sensitivity of actuation dynamics of Casimir oscillators on finite temperature with topological insulator materials: Response of repulsive vs attractive interactions. *Phys. Lett. A* **2023**, *481*, 129032. [CrossRef]
71. Gelbwaser-Klimovsky, D.; Graham, N.; Kardar, M.; Krüger, M. Equilibrium forces on nonreciprocal materials. *Phys. Rev. B* **2022**, *106*, 115106. [CrossRef]
72. Rodriguez, A.W.; Capasso, F.; Johnson, S.G. The Casimir effect in microstructured geometries. *Nat. Photon.* **2011**, *5*, 211–221. [CrossRef]
73. Javor, J.; Yao, Z.; Imboden, M.; Campbell, D.K.; Bishop, D.J. Analysis of a Casimir-driven parametric amplifier with resilience to Casimir pull-in for MEMS single-point magnetic gradiometry. *Microsyst. Nanoeng.* **2021**, *7*, 73. [CrossRef] [PubMed]
74. Munday, J.N.; Iannuzzi, D.; Barash, Y.; Capasso, F. Torque on birefringent plates induced by quantum fluctuations. *Phys. Rev. A* **2005**, *71*, 042102. [CrossRef]
75. Broer, W.; Lu, B.; Podgornik, R. Qualitative chirality effects on the Casimir-Lifshitz torque with liquid crystals. *Phys. Rev. Res.* **2021**, *3*, 033238. [CrossRef]
76. Boström, M.; Sernelius, B.E. Thermal effects on the Casimir force in the 0.1–5 μm range. *Phys. Rev. Lett.* **2000**, *84*, 4757–4760. [CrossRef] [PubMed]
77. Genet, C.; Lambrecht, A.; Reynaud, S. Temperature dependence of the Casimir effect between metallic mirrors. *Phys. Rev. A* **2000**, *62*, 012110. [CrossRef]
78. Bordag, M.; Geyer, B.; Klimchitskaya, G.L.; Mostepanenko, V.M. Casimir force at both nonzero temperature and finite conductivity. *Phys. Rev. Lett.* **2000**, *85*, 503–506. [CrossRef] [PubMed]
79. Milton, K.A. The Casimir effect: Recent controversies and progress. *J. Phys. A Math. Gen.* **2004**, *37*, R209–R277. [CrossRef]
80. Klimchitskaya, G.L.; Mostepanenko, V.M.; Svetovoy, V.B. Probing the response of metals to low-frequency s-polarized evanescent fields. *EPL (Europhys. Lett.)* **2022**, *139*, 66001. [CrossRef]

Disclaimer/Publisher’s Note: The statements, opinions and data contained in all publications are solely those of the individual author(s) and contributor(s) and not of MDPI and/or the editor(s). MDPI and/or the editor(s) disclaim responsibility for any injury to people or property resulting from any ideas, methods, instructions or products referred to in the content.

Article

Dynamical Sensitivity of Three-Layer Micro Electromechanical Systems to the Optical Properties of the Intervening Liquid Layer

Fatemeh Tajik ^{1,*} and George Palasantzas ²¹ Department of Condensed Matter Physics, Faculty of Physics, Alzahra University, Tehran 1993891167, Iran² Zernike Institute for Advanced Materials, University of Groningen, Nijenborgh 4, 9747 AG Groningen, The Netherlands; g.palasantzas@rug.nl

* Correspondence: f.tajik@alzahra.ac.ir

Abstract: Here, we investigate the actuation dynamics of a micro device with different intervening liquids between the actuating components under the influence of Casimir and dissipative hydrodynamic forces. This is enabled via phase space portraits, which demonstrate that by increasing the dielectric response of the intervening layer the autonomous device may not come into stiction due to the decreasing in magnitude Casimir force. Unlike the micro devices that are placed in vacuum with an intervening liquid, the phase portraits show only a spiral trajectory which eventually stops at a rest position due to the strong energy dissipation by the position dependent hydrodynamic drag forces, even when considering sufficiently strong restoring forces. Moreover, it is feasible to expand the area of motion using intervening liquids with lower dynamic viscosity or increasing the slip length of the intervening fluid. Finally, under the influence of an external driven force, which is the realistic case for possible applications, the system can reach stable oscillation at larger separations with an amplitude higher for the liquid that led to lower Casimir and hydrodynamic forces. Hence, the results presented in this study are essential for studying the dynamical behavior of MEMS and their design in liquid environments.

Keywords: Casimir effect; hydrodynamic force; MEMS; NEMS; actuation dynamics; stiction

Citation: Tajik, F.; Palasantzas, G. Dynamical Sensitivity of Three-Layer Micro Electromechanical Systems to the Optical Properties of the Intervening Liquid Layer. *Physics* **2023**, *5*, 1081–1093. <https://doi.org/10.3390/physics5040070>

Received: 27 September 2023

Revised: 19 October 2023

Accepted: 27 October 2023

Published: 21 November 2023



Copyright: © 2023 by the authors. Licensee MDPI, Basel, Switzerland. This article is an open access article distributed under the terms and conditions of the Creative Commons Attribution (CC BY) license (<https://creativecommons.org/licenses/by/4.0/>).

1. Introduction

During the past decades the emergence of rapid development in micro/nano fabrication has led to scaling down of electromechanical systems into submicron-length scales. This opens new areas for the application of the Casimir forces, since they could inevitably play role in the operation of micro/nano systems [1–8]. These devices have sufficiently large surface areas and gaps small enough for the Casimir force to pull components together leading to permanent adhesion, a phenomenon known as stiction [9–12]. This malfunction in many cases is unavoidable for the dynamical stability of micro/nano electromechanical systems (MEMS/NEMS) such as sensors, micro switches, actuators. Hence, a comprehensive knowledge about the magnitude and direction of the Casimir force can provide strong insight into the design and architecture of MEMS/NEMS.

The Casimir force, which originates from perturbations of fluctuating electromagnetic (EM) fields [13,14], was discovered in 1948 by the Dutch physicist Hendrick Casimir [15]. This is a quantum mechanical attractive force between two parallel, neutral, and perfectly conducting flat plates, and without considering thermal fluctuations (at temperature $T = 0$ K) [15]. In the 1950s, Evgeny Lifshitz and collaborators proposed the general theory for the Casimir force between parallel flat plates made of real dielectric materials [16]. For this purpose, the fluctuation–dissipation theorem was utilized to relate the dissipative properties of the plates (optical absorption by many microscopic dipoles) and EM fluctuations. The Lifshitz theory predicts the attractive force between the two parallel plates of arbitrary

materials and covers both at short ranges (non-retarded regime) the van der Waals forces, and at longer ranges (retarded regime) the Casimir forces. [16,17].

Furthermore, the Lifshitz theory enables the prediction of the actuation dynamics of micro/nano devices actuation since the omnipresent Casimir force could play a significant role. This is because the Lifshitz theory allows to compute the tuning of the Casimir force, actually, for both the magnitude and direction, by a suitable choice of the interacting materials with the necessary optical properties [18–21]. As a result, several studies have been performed on the effect of optical properties on the actuation dynamic of devices in order to widen the range of their applications [22–25]. For example, in Ref. [23], it was illustrated how the use of phase change materials can delay chaotic motion in MEMS without changing the materials. Also, in Ref. [24], it was investigated how one can decrease the influence of the temperature on the magnitude of the Casimir force with the use of suitable materials in order to survive operation at low or high temperatures. Finally, in Ref. [25], it was demonstrated how the magnetoelectric effect in micro devices consisting of topological insulators can become dominant on the operation of MEMS and taking into account its sensitive dependence on thermal fluctuations.

Actually, a three-layer system consisting of two actuating components immersed inside a liquid has attracted extensive attention because it provides unique advantages. In this system, under certain conditions, it is possible to generate repulsive Casimir forces leading to stable operation without employing a restoring mechanical spring [26–36]. Moreover, with a ferrofluid between the actuating components one can open new opportunities in nanotechnology [29], for instance, in micromechanical sensors [30], microfluidics [31,36], and micro robotics [37]. Therefore, we consider here a MEMS operating inside a fluid, and the main aim is to investigate how stable operation is sensitive to optical properties of the intervening layer by taking also into account the dynamic viscosity of the intervening fluids as well as the fluid slip length on the walls of the actuating plate. Hence, the results presented in this study are essential for studying the dynamical behavior of MEMS and their design in liquid environments.

2. Methods and Materials

Here, we assume that the actuating components of the MEMS device are coated with Au, which is a good conductor. The latter has static conductivity $\omega_p^2/\omega_\tau|_{Au} \approx 1600$ eV [38] (ω_p and ω_τ define the plasma and relaxation frequencies, respectively), and it is also extensively used for Casimir force measurements. Moreover, ethanol and kerosene are used as the intervening layer between the Au plates. Previous studies have shown that ethanol could produce repulsive Casimir forces in a system consisting of different interacting bodies (with dielectric functions ϵ_{Liquid} , ϵ_1 , ϵ_2 , respectively) if the condition $\epsilon_1 < \epsilon_{Liquid} < \epsilon_2$ is satisfied [26–28], and kerosene is also used in ferrofluid-based microdevices. In any case, both materials, as an intervening medium, have attracted attention in investigations related to Casimir forces [29–32]. The dielectric response of ethanol at imaginary frequencies can be described by a three-oscillator Ninham–Parsegian model [29]:

$$\epsilon_E(i\zeta) = 1 + \frac{\epsilon_0 - \epsilon_{IR}}{1 + (\zeta/\omega_{MW})} + \frac{\epsilon_{IR} - (n_0)^2}{1 + (\zeta/\omega_{IR})^2} + \frac{(n_0)^2 - 1}{1 + (\zeta/\omega_{UV})^2}, \quad (1)$$

where ζ is the Matsubara frequency, $n_0 = 1.35$ is the refractive index in the visible range, $\epsilon_0 = 25.07$ is the static dielectric constant, and $\epsilon_{IR} = 4.2$ is the dielectric constant where the microwave (MW) relaxation ends and the infrared (IR) begins. $\omega_{MW} = 6.97 \times 10^9$ rad/s, $\omega_{IR} = 2.588 \times 10^{14}$ rad/s, and $\omega_{UV} = 1.924 \times 10^{16}$ rad/s are the characteristic MW, IR, and ultraviolet (UV) absorption frequencies, respectively. Similarly, one has for the dielectric function of kerosene at imaginary frequencies [29]:

$$\epsilon_K(i\zeta) = 1 + \frac{B}{1 + (\zeta\tau)} + \frac{C_{IR}}{1 + (\zeta/\omega_{IR})^2} + \frac{C_{UV}}{1 + (\zeta/\omega_{UV})^2}, \quad (2)$$

where the second term on the right-hand side describes the contribution to the dielectric permittivity from the orientation of permanent dipoles. The values of $B = 0.020$ and $1/\tau = 8.0 \times 10^8$ rad/s were determined from the measured data of Ref. [38] in the MW region. The third term shows the effect of ionic polarization with $C_{IR} = 0.007$ and $\omega_{IR} = 2.14 \times 10^{14}$ rad/s as obtained using the infrared optical data of Ref. [39]. The fourth term describes the optical data in the UV region with the values $C_{UV} = 0.773$ (obtained from the static dielectric permittivity at zero frequency $\epsilon_K = 1.8$ [38] since $\epsilon_K = 1 + B + C_{IR} + C_{UV}$) and $\omega_{UV} = 1.0 \times 10^{16}$ rad/s. Finally, the dielectric functions, $\epsilon(i\zeta)$, of all media at imaginary frequencies, which are vital as input for the calculations of the Casimir force via the Lifshitz theory, are shown in Figure 1a.

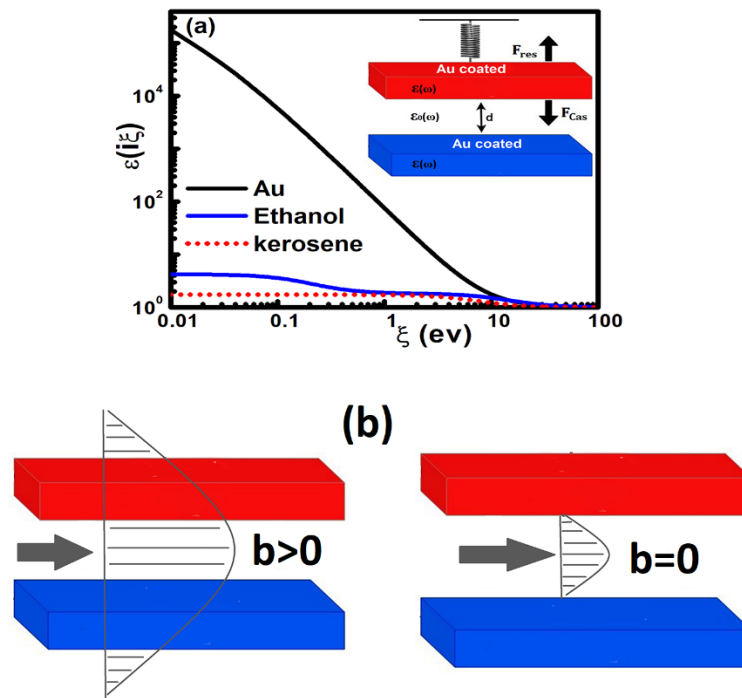


Figure 1. (a) Dielectric functions $\epsilon(i\zeta)$ of imaginary Matsubara frequencies for the materials considered in this study. The inset shows the MEMS design for this study. (b) Schematic of three-layer Au micro system with no-slip/slip (having slip length, b) boundary conditions. See text for details.

The dielectric function $\epsilon(i\zeta)$ is a vital input function to compute the Casimir force using the Lifshitz theory [16]. The Casimir force between two parallel plates at $T = 300$ K is given in terms of the Lifshitz theory (at the imaginary frequency representation) by the equation

$$F(T, z) = \frac{kT}{\pi} \sum'_{n=0} \int_0^\infty dq q |k_0| g(q, i\zeta_n), \tag{3}$$

where z denotes the separation, q denotes the in-plane vector, the imaginary frequencies (ζ) describe the discrete Matsubara frequencies ($\zeta = 2\pi kTn/\hbar$). Here, \hbar is the reduced Planck's constant, k denotes the Boltzmann constant, and the prime in the sum of Equation (3) means that the $n = 0$ term must be taken with half weight. The term $g(q, i\zeta_n)$ describes the multiple reflections from the inner surfaces of the interacting bodies, which is represented by the equation

$$g(q, i\zeta_n) = \sum_{\nu=s,p} r_1^\nu r_2^\nu e^{-2k_0 z} / (1 - r_1^\nu r_2^\nu e^{-2k_0 z}), \tag{4}$$

where the Fresnel reflection coefficients are given by

$$r_i^s = (k_0 - k_i) / (k_0 + k_i) \tag{5}$$

and

$$r_i^p = (\epsilon_i k_0 - \epsilon_0 k_i) / (\epsilon_i k_0 + \epsilon_0 k_i) \tag{6}$$

where the superscript “s” indicates the transverse electric polarization (TE), and the subscript “p” indicates the transverse magnetic polarization (TM) of the electromagnetic field, respectively. $\epsilon_0(i\zeta)$ and $\epsilon_i(i\zeta)$ are the dielectric functions of the intervening layer and the interacting components, respectively. $k_i = \sqrt{\epsilon_i(i\zeta) \zeta^2 / c^2 + q^2}$ ($i = 0,1,2$) describes the out-of-plane wave vector in the intervening layer between the interacting components (k_0), and in each of the interacting components ($k_{i=1,2}$), c is the speed of light, and q is the in-plane wave vector.

Moreover, we consider a typical MEMS, which is shown in the inset of Figure 1a, consisting of two plates with the upper one being able to move. Both components are assumed to be coated with Au, (with a coating thickness of more than 100 nm in order to be considered optically bulk material) [40]. Moreover, we assume flat plates because, at short separations ($\ll 100$ nm), nanoscale roughness can significantly affect the Casimir force. The initial distance of the parallel plates is assumed to be $d = 300$ nm, and the system temperature being $T = 300$ K. The intervening medium between these components is assumed to be ethanol or kerosene. The equation of motion for the MEM system without any external driven force is given by

$$M \frac{d^2z}{dt^2} + \left(\frac{M\omega_0}{Q} \right) \frac{dz}{dt} = F_{res} + F_{Cas} + F_h, \tag{7}$$

where M is the mass of the moving plate. The term $(M\omega_0/Q) (dz/dt)$ describes the Stokes term for the energy losses of the moving plate, whereas Q defines the quality factor of the MEMS (in this study, $Q = 400$ is considered, while the calculations performed with low values of $Q = 10$ do not have significant effect). We also assume $\omega = 300$ kHz, which is a typical frequency for Atomic Force Microscopy cantilevers and MEMS [41]. $F_{res}(z) = -k(d - z)$ is the restoring force, where k is the elastic spring stiffness, and $F_{Cas}(z)$ is the Casimir force, which is computed via the Lifshitz theory. Finally, F_h defines the separation-dependent hydrodynamic force, which is the dominant dissipation term due to its $1/z$ dependence at short separations, and it is given by [42–51]

$$F_h(z) = -\frac{A\mu}{z} \frac{dz}{dt} f^*, \tag{8}$$

where A is the area of the plates, and we consider for both the length (L_x) and width (L_y) of the plates the value of $10\mu\text{m}$. μ is the dynamic viscosity of the intervening liquid. The latter at 300 K has the value $\mu = 0.001$ kg/ms and $\mu = 0.0016$ kg/ms for ethanol and kerosene, respectively. f^* is the correction due to deviations from the Reynolds flow because of fluid slip on solid surfaces (see Figure 1b). In this study we consider the same slip length b on the surface of both plates. If $b = 0$ then $f^* = 1$, otherwise it is given by [42–51]

$$f^* = \frac{1}{4} \left\{ 1 + \frac{3z}{2b} \left[\left(1 + \frac{z}{4b} \right) \left(1 + \frac{4b}{z} \right) - 1 \right] \right\}. \tag{9}$$

Equation (8) is valid for fluid flow with low Reynolds numbers and short separations between the interacting components.

3. Results and Discussion

Before analyzing the actuation dynamics, we illustrate the influence of the optical properties of the intervening layer on the Casimir force via Lifshitz theory calculations. In order to achieve the aim, we introduce the reduction factor $\eta_p(z)$ (< 1) to normalize the Casimir force, with respect to the maximum Casimir force ($F_C = \pi^2 \hbar c / 240z^4$) [15] between ideal metals at $T = 0$ K. The Casimir force calculations are shown in Figure 2 and confirm that, by increasing the magnitude of the dielectric function $\epsilon(i\zeta)$ of the intervening layer (since $\epsilon_{Au}(i\zeta) > \epsilon_{ethanol}(i\zeta) > \epsilon_{kerosene}(i\zeta)$), the strength of the Casimir force is reduced.

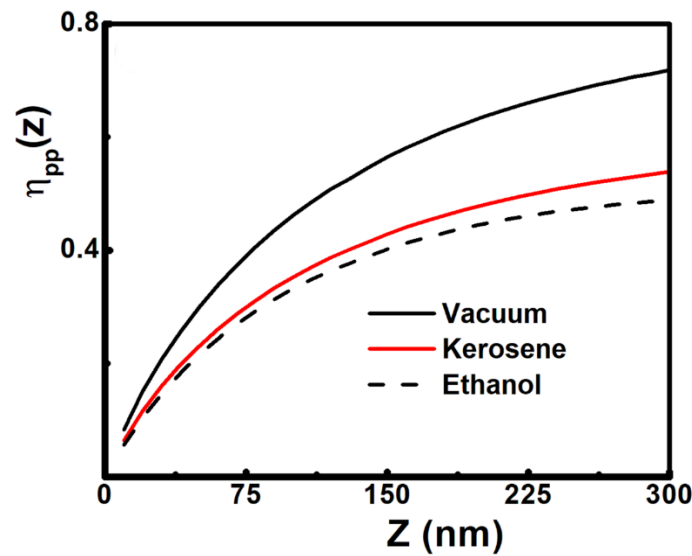


Figure 2. Casimir reduction factor for different three-layer micro systems versus separation between the plates. The fixed and moving components are assumed to be decorated Au with 100 nm thickness in order to be considered optically bulk. The intervening liquid layer is indicated.

Furthermore, for the discussion of the actuation dynamics for the three-layer micro device, it is helpful to consider the separation of z^* , where there is equilibrium between the Casimir and the restoring forces or $F_c(z^*) + F_{res}(z^*) = 0$. The latter yields the characteristic spring stiffness, $K^* = (z^*)/(d - z^*)$. d defines the initial separation between plates where the spring is supposed to be unstretched ($d = 300$ nm). Indeed, K^* determines the minimum spring stiffness for the system to be able to sustain some form of motion against the stiction of the moving component on the fixed plate.

In the beginning, in order to show how the presence of the hydrodynamic drag force can change the motion and consequently the phase portrait, we have considered a micro device which is placed in vacuum or air. Under these conditions, the energy dissipation is described only by the Stokes dissipation term $(M\omega_0/Q) (dz/dt)$, where the values of the Q factor considered here are typical for a multitude of MEMS/NEMS operating in vacuum [4,41]. Figure 3 shows the corresponding phase portraits for a microsystem consisting of Au coated components that are placed in vacuum. As it can be seen in Figure 3a, when the stiffness of the restoring force is sufficiently strong the phase portrait reveals closed orbits, which correspond to periodic motion around a stable center equilibrium point. Also, by decreasing the magnitude of the restoring force for lower stiffness, the size of orbits enlarges, allowing the moving plate to come rather close to the fixed plate and preserve its stable operation. Notably, the stable operation can be preserved until the restoring force is stronger than the force corresponding to K^* for a considered initial condition. Hence, if the restoring force becomes smaller than the force corresponding to K^* , there is no more closed orbit. Indeed, according to Figure 3b, by considering a weak value of the restoring force ($K < K^*$), it can be seen that the close orbit changes into an open orbit, which is the evidence of motion of the moving plate towards the fixed one, leading to irreversible adhesion between the components. This phenomenon is called stiction. If, however, the restoring force is increased, the dissipation energy, or equivalently the quality factor Q is decreased, then it is still possible to decrease the possibility to drive the system into stiction. The effect of the finite value of Q , due to intrinsic and extrinsic dissipation mechanisms of the oscillating plate, is shown in Figure 3b. Indeed, calculations illustrate that the transition from unstable motion towards stiction to stable oscillation is possible if dissipative motion takes place. Therefore, proper tuning of the system Q factor can also aid to prevent the permanent adhesion of an otherwise unstable micro system.

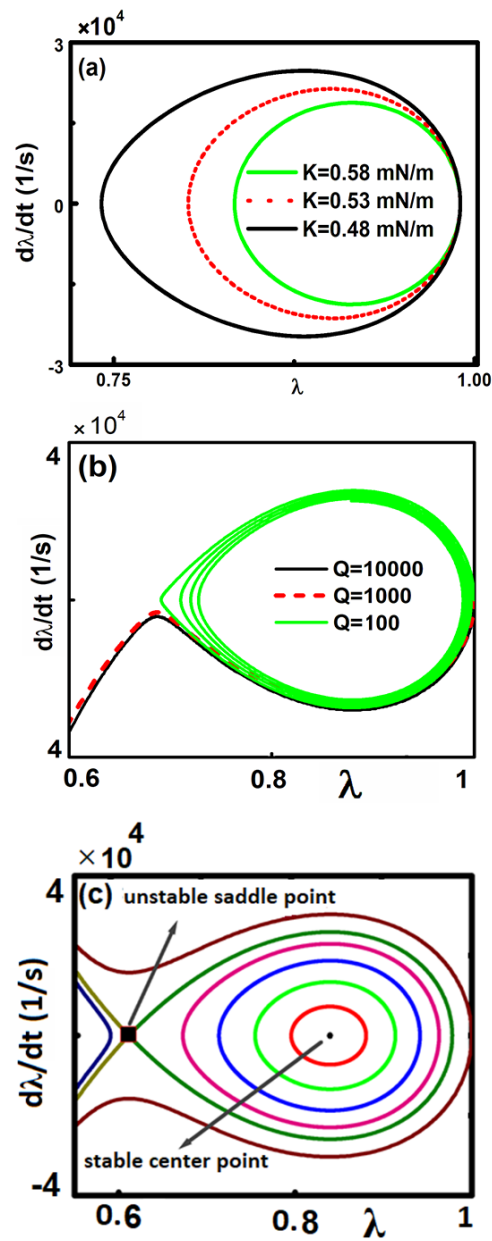


Figure 3. Phase portraits for micro system coated with Au. $Q = 10,000$, $\lambda = 0.95$ ($\lambda = z^*/d$), $d = 300$ nm, and $K^* = 0.000465$ are used. (a) $K \gg K^*$, where the value of K is indicated. (b) Influence of the damping term on the actuation dynamics of the Au–Au micro device with $K = 0.000464$ ($K < K^*$), and different values of the quality factor Q as indicated. The closed orbits indicate stable motion, while an open orbit is the sign of unstable motion leading to stiction. (c) Phase portraits for $K = 0.000465$ ($K = K^*$), and initial conditions inside and outside the homoclinic orbit. The stable center point and unstable saddle point are indicated. See text for details.

Figure 3a,b is considered with an initial condition ($z = 0.95d$) and for different values of the stiffness for the restoring force ($K < K^*$ and $K > K^*$). In Figure 3c, a fixed stiffness K (which corresponds to $z = 0.95d$) is assumed, and different initial conditions are considered. According to Figure 3c, there is a homoclinic orbit, including one unstable equilibrium point on the sharp side of the orbit and one stable equilibrium inside it. This homoclinic curve can sharply separate unstable motion (leading to stiction within one period) from the periodic closed orbits around the stable center point. Any solution of the equation of motion with initial conditions within the homoclinic orbit that goes until the unstable saddle point (square in shape in Figure 3c) will lead to stable periodic motion around the

stable center. However, for any other initial conditions outside of the homoclinic orbit, the upper plate will perform unstable motion, leading to collapse on the fixed plate. In the latter case, the micro system is unstable during oscillation around these points due to the stronger Casimir force which leads to the collapse of the moving plate on the fixed one. The periodic solutions indicate that the restoring force is strong enough to keep system in operation and avoid any stiction instabilities.

Further, we consider the three-layer microsystem consisting of Au-coated components within a liquid (ethanol or kerosene) playing the role of an intervening layer. In this system, besides the Stokes dissipation term $(M\omega_0/Q) (dz/dt)$, the additional hydrodynamic force also describes dissipation for the micro system, and consequently can play an inevitable role for the motion and phase portrait of these devices. In this case, the phase portraits related to the autonomous micro device containing liquid do not reveal closed orbits or equivalently continuous oscillation. Unlike the micro device, which is placed in vacuum, even by considering a sufficiently strong restoring force, the phase portraits show a spiral trajectory which eventually stops at the resting position $z = d$. This is shown in the calculations in Figure 4, where $\lambda^* (=z^*/d) = 0.5$ is considered as an initial position to activate the actuation. If the spring stiffness is $K > K^*$, then for both micro systems the moving component approaches slowly the resting position toward $z = d$ and eventually stops. By considering $K \gg K^*$, the corresponding curve in phase space shows that the moving component exhibits stronger velocity due to the enhancement of the restoring force. For the value of $K < K^*$, the moving component eventually collapses on fixed plate leading to permanent adhesion or stiction.

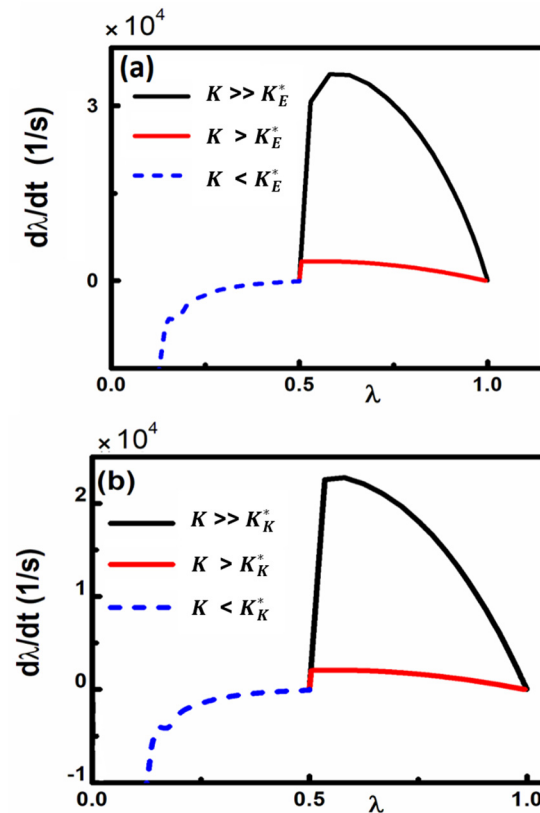


Figure 4. Phase portraits for the three-layer Au microsystem with (a) ethanol (b) kerosene. $z^* = 0.5d$, $d = 300$ nm, and $b = 0$ are used. Phase space dissipative motion for various values of K (0.0005, 0.005, 0.05 N/m). $K_E^* = 0.000635$ N/m and $K_K^* = 0.000675$ N/m are considered for the micro systems containing ethanol and kerosene, respectively.

Further, Figure 5 shows phase space portraits using as initial condition $\lambda^* = 0.5$ and significant spring stiffness $K \gg K^*$, leading to spiral trajectory towards immobility.

By increasing the restoring force, the spiral curve and consequently the velocity of the moving component becomes wider. Also, by increasing the slip length b , the hydrodynamic dissipation, which acts against the motion, reduces and, as a consequence, the spiral trajectory is more extended for both liquids. However, the effect of the slip length (b), as the spring stiffness increases, becomes more pronounced for the micro system containing kerosene, for which the Casimir force is stronger than that of micro system containing ethanol as shown also in Figure 2. However, both micro systems preserve the ability to move if the spring stiffness K is stronger than the value that corresponds to λ^* (K_E^* and K_K^* for micro system containing ethanol and kerosene, respectively), while for both micro systems stiction occurs if $K < K^*$. Although the hydrodynamic force cannot influence the magnitude of K^* (which depends on the magnitude of the Casimir force), this term is significantly important in phase space. Indeed, as Figure 6 shows, for $K < K^*$ the reduction of the hydrodynamic force causes the approach to stiction to take place significantly faster. Therefore, increasing the slip length (b), or equivalently decreasing the hydrodynamic dissipation in the system containing kerosene, it is possible to make the trajectory of both micro systems similar to each other (Figure 6b).

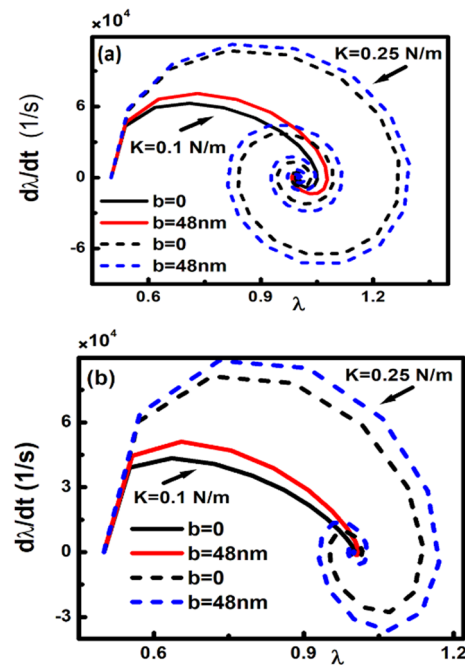


Figure 5. Phase portraits for the three-layer Au–Au microsystem with (a) ethanol and (b) kerosene. $z^* = 0.5d$, $d = 300$ nm, and $K \gg K^*$ are used. The value of the slip length, b , is indicated. $K_E^* = 0.000635$ N/m and $K_K^* = 0.000675$ N/m are considered for the micro systems containing ethanol and kerosene, respectively.

Figure 7 compares the magnitudes of Casimir and hydrodynamic forces for a three-layer system including ethanol for the spring stiffness $K = 0.008$ N/m. As can be seen for small and large separations, the magnitudes of both forces become comparable and consequently both forces play role in the dynamical behavior of the microsystem.

Finally, in Figure 8, we investigate the response of the three-layer micro device with a liquid as an intervening medium under the presence of an external driven periodic force ($F(t) = F_0 \cos(\omega_d t)$), which is a realistic case for possible applications. In this case, the equation of motion has the more general form:

$$M \frac{d^2z}{dt^2} + \left(\frac{M\omega_0}{Q} \right) \frac{dz}{dt} = F_{res} + F_{Cas} + F_h + F_0 \cos(\omega_d t) \tag{10}$$

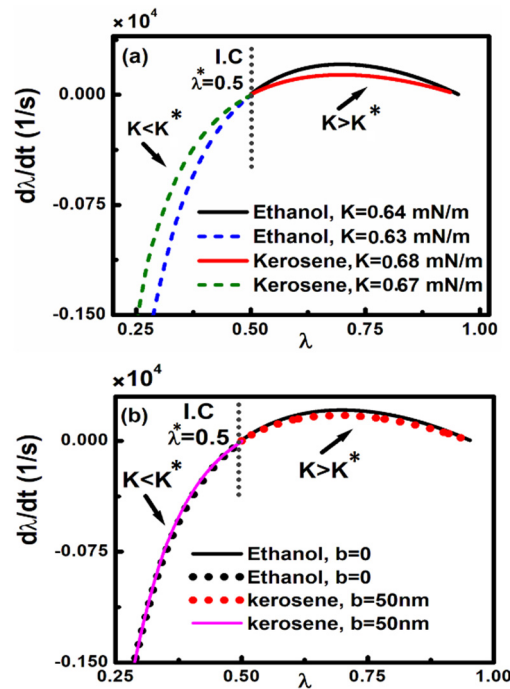


Figure 6. Phase portraits for the both three–layer Au microsystem with ethanol and kerosene. $z^* = 0.5d$ and $d = 300$ nm are used. (a) $b = 0$ and the value of K as indicated; (b) the previous values of K are applied, and the value of slip length, b , as indicated. $K_E^* = 0.000635$ N/m and $K_K^* = 0.000675$ N/m are considered for the micro systems containing ethanol and kerosene, respectively. $\lambda = 0.5$ is considered as initial condition (I.C).

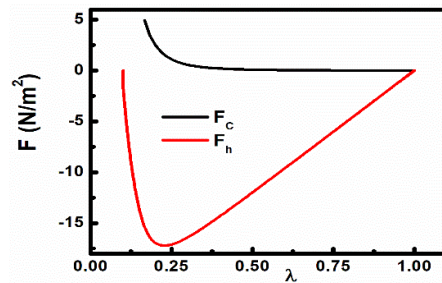


Figure 7. Casimir and hydrodynamic forces for the three–layer Au microsystem with ethanol. $\lambda = z/d$ and $d = 300$ nm are used. For computing hydrodynamic force z^*/d is considered of 0.1 and $K = 0.008$ N/m.

By decreasing the magnitude of the Casimir force (for large value of λ or, equivalently, larger separations) and the hydrodynamic force, the influence of the periodic driven force becomes dominant, and the micro system can achieve continuous stable oscillation around the resting position ($z = d$). Indeed, according to Figure 8a, the amplitude of the stable oscillation is higher for micro system containing ethanol due to the lower magnitude of Casimir and hydrodynamic forces. This is also depicted in Figure 8b,c, where the amplitude of the continuous oscillation is smaller in the micro system containing kerosene due to the stronger magnitude of the Casimir force and hydrodynamic force. Moreover, as Figure 8b,c indicate, an increasing amplitude of the external driven periodic force (F_0) leads to significant influence on the continuous oscillation, while decreasing the hydrodynamic force (by increasing slip length) is no longer making significant difference on the oscillatory motion for both liquids.

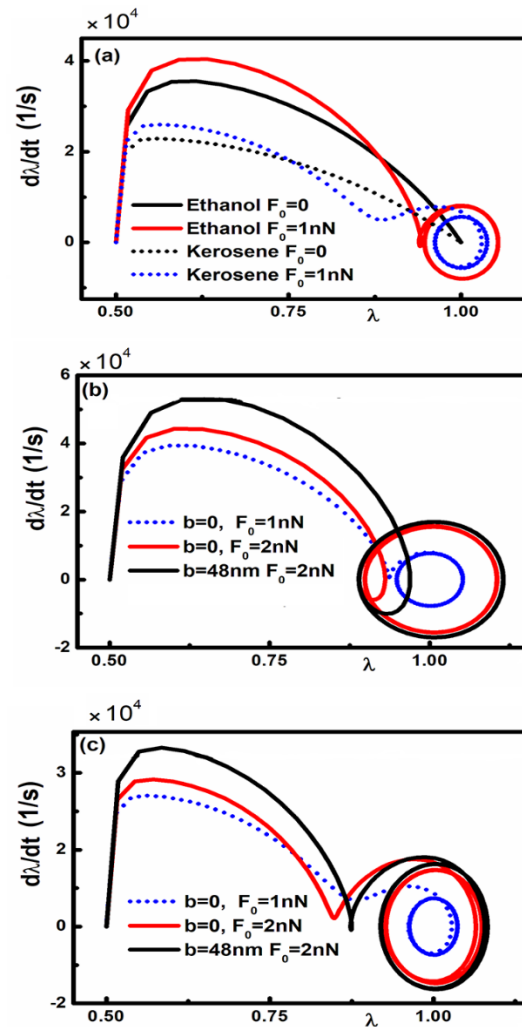


Figure 8. Phase portraits for the driven microsystem with an external applied force $F_0\cos(\omega_d t)$ with $\omega_d = 0.5\omega_0$. $z^* = 0.5d$, $d = 300$ nm, and $K = 0.05$ N/m are used. (a) Three–layer Au micro systems (containing ethanol or kerosene) under the presence and absence of external driven periodic force without slip length ($b = 0$). Three–layer Au micro systems containing (b) ethanol and (c) kerosene under different applied driven periodic forces and various slip lengths as indicated.

4. Conclusions

In this study, we investigated the actuation dynamics of a micro device consisting of Au-coated components with different intervening liquids between the actuating components under the influence of Casimir and separation-dependent dissipative hydrodynamic drag forces. This is accomplished via phase space portraits, which demonstrate that by increasing the dielectric response of the intervening layer, one can prevent the microdevice to come into stiction due to decreasing in magnitude Casimir forces. Using the phase portraits of a microsystem that is placed in vacuum or air, it has been shown how the presence of a liquid and, as a consequence, the additional dissipation term due the position dependent hydrodynamic drag force can significantly influence the actuation dynamics of MEMS/NEMS. By assuming vacuum or air between the actuating components, there are closed or open orbits inside the phase portraits providing evidence that the restoring force is sufficiently strong or very weak in order to preserve stable operation of the micro devices. In addition, it is shown how the reduction of the quality factor Q or, equivalently, by enhancing the Stoke energy dissipation can change an unstable motion towards stiction to stable dissipative motion.

However, by considering liquid (ethanol or kerosene) as the intervening medium, and as a consequence the existence of the additional hydrodynamic force between the components of MEMS the actuation dynamics changes drastically. Indeed, for both at the absence and presence of the external driven force, it is illustrated that it is feasible to expand area of motion using intervening liquids with lower dynamic viscosity or increasing the slip length (b) of the surrounding fluid leading to weaker hydrodynamic forces. It is indicated that the phase portraits related to the autonomous micro device containing liquid do not reveal closed orbit or, equivalently, continuous oscillation. Even by considering sufficiently strong restoring force, the phase portraits show spiral trajectory which eventually terminates the motion at a rest position. Finally, we investigated the influence of an external driven periodic force, which is the realistic case for device applications. It is demonstrated that the system can reveal continuous stable oscillation with an amplitude higher for the liquid that led to lower Casimir and hydrodynamic drag forces. Notably the amplitude of the driven force leads to significant influence on the continuous stable oscillation that takes place at relatively larger separations, while any decrease in hydrodynamic force via increasing the slip length has limited influence. Therefore, this study addresses the influence of the optical properties of the intervening layer for the three-layer actuating micro system. And the results presented in this study are essential for studying the dynamical behavior of three-layer micro devices, and for the designing and manufacturing of MEMS in order to operate in a stable manner in different environments.

Author Contributions: Writing—original draft: F.T.; Writing—review & editing: F.T. and G.P.; Formal analysis: F.T. All authors have read and agreed to the published version of the manuscript.

Funding: This research received no external funding.

Data Availability Statement: The data that support the findings of this study are available from the corresponding author upon reasonable request.

Acknowledgments: G.P. acknowledges support from the Zernike Institute for Advanced Materials, University of Groningen. F.T. acknowledges support from the Faculty of Physics, Alzahra University.

Conflicts of Interest: The authors declare no conflict of interest.

References

- Rodriguez, A.W.; Capasso, F.; Johnson, S.G. The Casimir effect in microstructured geometries. *Nat. Photonics* **2011**, *5*, 211–221. [CrossRef]
- Capasso, F.; Munday, J.N.; Iannuzzi, D.; Chan, H.B. Casimir forces and quantum electrodynamical torques: Physics and nanomechanics. *IEEE J. Sel. Top. Quant. Electron.* **2007**, *13*, 400–414. [CrossRef]
- Bordag, M.; Klimchitskaya, G.L.; Mohideen, U.; Mostepanenko, V.M. *Advances in the Casimir Effect*; Oxford University Press: Oxford, UK, 2015. [CrossRef]
- Decca, R.S.; López, D.; Fischbach, E.; Klimchitskaya, G.L.; Krause, D.E.; Mostepanenko, V.M. Precise comparison of theory and new experiment for the Casimir force leads to stronger constraints on thermal quantum effects and long-range interactions. *Ann. Phys.* **2005**, *318*, 37–80. [CrossRef]
- Decca, R.S.; López, D.; Fischbach, E.; Klimchitskaya, G.L.; Krause, D.E.; Mostepanenko, V.M. Tests of new physics from precise measurements of the Casimir pressure between two gold-coated plates. *Phys. Rev. D* **2007**, *75*, 077101. [CrossRef]
- Ashourvan, A.; Miri, M.F.R.; Golestanian, R. Noncontact rack and pinion powered by the lateral Casimir force. *Phys. Rev. Lett.* **2014**, *98*, 140801. [CrossRef] [PubMed]
- Miri, M.F.; Golestanian, R. A frustrated nanomechanical device powered by the lateral Casimir force. *Appl. Phys. Lett.* **2011**, *92*, 113103. [CrossRef]
- Ashourvan, A.; Miri, M.F.; Golestanian, R. Rectification of the lateral Casimir force in a vibrating noncontact rack and pinion. *Phys. Rev. E* **2007**, *75*, 040103. [CrossRef]
- DelRio, F.W.; de Boer, M.P.; Knapp, J.A.; Reedy, E.D.; Clews, P.J.; Dunn, M.L. The role of van der Waals forces in adhesion of micromachined surfaces. *Nat. Mater.* **2005**, *4*, 629–634. [CrossRef]
- Serry, F.M.; Walliserand, D.; Maclay, G.J. The role of the Casimir effect in the static deflection and stiction of membrane strips in microelectromechanical systems. *J. Appl. Phys.* **1998**, *84*, 2501–2506. [CrossRef]
- Serry, F.M.; Walliser, D.; Maclay, G.J. The anharmonic Casimir oscillator (ACO)—The Casimir effect in a model microelectromechanical system. *J. Microelectromech. Syst.* **1995**, *4*, 193–205. [CrossRef]

12. Palasantzas, G.; DeHosson, J.T.M. Phase maps of microelectromechanical switches in the presence of electrostatic and Casimir forces. *Phys. Rev. B* **2005**, *72*, 121409. [CrossRef]
13. Milonni, P.W. *The Quantum Vacuum. An Introduction to Quantum Electrodynamics*; Academic Press, Inc.: San Diego, CA, USA, 1994. [CrossRef]
14. Sciamia, D.W. The physical significance of the vacuum state of a quantum field. In *The Philosophy of Vacuum*; Saunders, S., Brown, H.R., Eds.; Clarendon Press/Oxford University Press: Oxford, UK, 1991; pp. 137–158. [CrossRef]
15. Casimir, H.B.G. On the Attraction between Two Perfectly Conducting Plates. *Indag. Math.* **1948**, *10*, 261–263. Available online: <https://dwc.knaw.nl/DL/publications/PU00018547.pdf> (accessed on 24 October 2023).
16. Lifshitz, E.M. The Theory of Molecular Attractive Forces between Solids. *Sov. Phys. JETP* **1956**, *2*, 73–83. Available online: <http://jetp.ras.ru/cgi-bin/e/index/e/2/1/p73?a=list> (accessed on 24 October 2023).
17. Ball, P. Feel the force. *Nature* **2007**, *447*, 772–774. [CrossRef] [PubMed]
18. Chan, H.B.; Aksyuk, V.A.; Kleiman, R.N.; Bishop, D.J.; Capasso, F. Quantum mechanical actuation of microelectromechanical systems by the Casimir force. *Science* **2001**, *291*, 1941–1944. [CrossRef]
19. Pawlowski, P.; Zielenkiewicz, P. The quantum Casimir effect may be a universal Force organizing the bilayer structure of the cell membrane. *J. Membr. Biol.* **2013**, *246*, 383–389. [CrossRef] [PubMed]
20. Svetovoy, V.B.; Postnikov, A.; Uvarov, I.; Stepanov, F.; Palasantzas, G. Measuring the dispersion forces near the van der Waals–Casimir transition. *Phys. Rev. Appl.* **2020**, *13*, 064057. [CrossRef]
21. Velichko, E.N.; Klimchitskaya, G.L.; Mostepanenko, V.M. Dispersion forces between metal and dielectric plates separated by a magnetic fluid. *Techn. Phys.* **2019**, *64*, 1260–1266. [CrossRef]
22. Sedighi, M.; Svetovoy, V.B.; Broer, W.H.; Palasantzas, G. Casimir forces from conductive silicon carbide surfaces. *Phys. Rev. B* **2014**, *89*, 195440. [CrossRef]
23. Tajik, F.; Sedighi, M.; Khorrami, M.; Masoudi, A.A.; Palasantzas, G. Chaotic behavior in Casimir oscillators: A case study for phase-change materials. *Phys. Rev. E* **2017**, *96*, 042215. [CrossRef] [PubMed]
24. Tajik, F.; Sedighi, M.; Babamahdi, Z.; Masoudi, A.A.; Waalkense, H.; Palasantzas, G. Sensitivity of chaotic behavior to low optical frequencies of a double-beam torsional actuator. *Chaos* **2019**, *29*, 093126. [CrossRef]
25. Tajik, F.; Palasantzas, G. Sensitivity of actuation dynamics of Casimir oscillators on finite temperature with topological insulator materials: Response of repulsive vs attractive interactions. *Phys. Lett. A* **2023**, *481*, 129032. [CrossRef]
26. Klimchitskaya, G.L.; Mohideen, U.; Mostepanenko, V.M. Pulsating Casimir force. *J. Phys. A* **2007**, *40*, F841–F847. [CrossRef]
27. van Oss, C.J.; Chaudhury, M.K.; Good, R.J. Interfacial Lifshitz-van der Waals and polar interactions in macroscopic systems. *Chem. Rev.* **1988**, *88*, 927–941. [CrossRef]
28. Munday, J.N.; Capasso, F. Precision measurement of the Casimir–Lifshitz force in a fluid. *Phys. Rev. A* **2007**, *75*, 0601062(R). [CrossRef]
29. Klimchitskaya, G.L.; Mohideen, U.; Nepomnyashchaya, E.K.; Velichko, E.N. Effect of agglomeration of magnetic nanoparticles on the Casimir pressure through a ferrofluid. *Phys. Rev. B* **2019**, *99*, 045433. [CrossRef]
30. Goubault, C.; Jop, P.; Fermigier, M.; Baudry, J.; Bertrand, E.; Bibette, J. Flexible magnetic filaments as micromechanical sensors. *Phys. Rev. Lett.* **2003**, *91*, 260802. [CrossRef]
31. Pekas, N.; Porter, M.D.; Tondra, M.; Popple, A.; Jander, A. Giant magnetoresistance monitoring of magnetic picodroplets in an integrated microfluidic system. *Appl. Phys. Lett.* **2004**, *85*, 4783–4785. [CrossRef]
32. Inglis, D.W.; Riehn, R.; Austin, R.H.; Sturm, J.C. Continuous microfluidic immunomagnetic cell separation. *Appl. Phys. Lett.* **2004**, *85*, 5093–5095. [CrossRef]
33. Nishat, S.; Jafry, A.T.; Martinez, A.W.; Awan, F.R. Paper-based microfluidics: Simplified fabrication and assay methods. *Sens. Actuators B Chem.* **2021**, *336*, 129681. [CrossRef]
34. Philip, J.; Laskar, J.M. Optical properties and applications of ferrofluids. *J. Nanofluids* **2012**, *1*, 3–20. [CrossRef]
35. Mao, L.; Elborai, S.; He, X.; Zahn, M.; Koser, H. Direct observation of closed-loop ferrohydrodynamic pumping under traveling magnetic fields. *Phys. Rev. B* **2011**, *84*, 104431. [CrossRef]
36. Lin, W.; Miao, Y.; Zhang, H.; Liu, B.; Liu, Y.; Song, B. Fiber-optic in-line magnetic field sensor based on the magnetic fluid and multimode interference effects. *Appl. Phys. Lett.* **2013**, *103*, 151101. [CrossRef]
37. Saga, N.; Nakamura, T. Elucidation of propulsive force of microrobot using magnetic fluid. *J. Appl. Phys.* **2002**, *91*, 7003–7005. [CrossRef]
38. Fannin, P.C.; Marin, C.N.; Malaescu, I.; Stefu, N. Microwave dielectric properties of magnetite colloidal particles in magnetic fluids. *J. Phys. Condens. Matter* **2007**, *19*, 036104. [CrossRef]
39. Qi, H.; Zhang, X.; Jiang, M.; Wang, Q.; Li, D. A method to determine optical properties of kerosene using transmission spectrum. *Optik* **2016**, *127*, 8899–8906. [CrossRef]
40. Svetovoy, V.B.; Van Zwol, P.J.; Palasantzas, G.; De Hosson, J.T.M. Optical properties of gold films and the Casimir force. *Phys. Rev. B* **2008**, *77*, 035439. [CrossRef]
41. Garcia, R.; Perez, R. Dynamic atomic force microscopy methods. *Surf. Sci. Rep.* **2002**, *47*, 197–301. [CrossRef]
42. Vinogradova, V.O. Drainage of a thin liquid film confined between hydrophobic surfaces. *Langmuir* **1995**, *11*, 2213–2220. [CrossRef]
43. Vinogradova, O.I.; Yakubov, G.E. Dynamic effects on force measurements. 2. Lubrication and the atomic force microscope. *Langmuir* **2003**, *19*, 1227–1234. [CrossRef]

44. Vinogradova, O.I.; Yakubov, G.E. Surface roughness and hydrodynamic boundary conditions. *Phys. Rev. E* **2006**, *73*, 045302. [CrossRef] [PubMed]
45. Neto, C.; Evans, D.R.; Bonaccorso, E.; Butt, H.J.; Craig, V.S.J. Boundary slip in Newtonian liquids: A review of experimental studies. *Rep. Prog. Phys.* **2005**, *68*, 2859–2897. [CrossRef]
46. Bonaccorso, E.; Butt, H.J.; Craig, V.S.J. Surface roughness and hydrodynamic boundary slip of a Newtonian fluid in a completely wetting system. *Phys. Rev. Lett.* **2003**, *90*, 144501. [CrossRef] [PubMed]
47. Zhu, L.; Attard, P.; Neto, C. Reliable measurements of interfacial slip by colloid probe atomic force microscopy. II. Hydrodynamic force measurements. *Langmuir* **2011**, *27*, 6712–6719. [CrossRef] [PubMed]
48. Granick, S.; Zhu, Y.; Lee, H. Slippery questions about complex fluids flowing past solids. *Nat. Mater.* **2003**, *2*, 221–227. [CrossRef]
49. Siria, A.; Drezet, A.; Marchi, F.; Comin, F.; Huan, S.; Chevrier, J. Viscous cavity damping of a microlever in a simple fluid. *J. Phys. Rev. Lett.* **2009**, *102*, 254503. [CrossRef]
50. Maali, A.; Bhushan, B. Slip-length measurement of confined air flow using dynamic atomic force microscopy. *Phys. Rev. E* **2008**, *78*, 027302. [CrossRef] [PubMed]
51. Pan, Y.; Bhushan, B.; Maali, A. Slip length measurement of confined air flow on three smooth surfaces. *Langmuir* **2013**, *29*, 4298–4302. [CrossRef] [PubMed]

Disclaimer/Publisher’s Note: The statements, opinions and data contained in all publications are solely those of the individual author(s) and contributor(s) and not of MDPI and/or the editor(s). MDPI and/or the editor(s) disclaim responsibility for any injury to people or property resulting from any ideas, methods, instructions or products referred to in the content.

Article

Force Metrology with Plane Parallel Plates: Final Design Review and Outlook

Hamid Haghmoradi ^{1,*}, Hauke Fischer ¹, Alessandro Bertolini ², Ivica Galić ³, Francesco Intravaia ⁴, Mario Pitschmann ¹, Raphael A. Schimpl ¹ and René I. P. Sedmik ^{1,*}

¹ Atominstitut, TU Wien, Stadionallee 2, 1020 Vienna, Austria; hauke.fischer@tuwien.ac.at (H.F.); mario.pitschmann@tuwien.ac.at (M.P.); raphael.schimpl@tuwien.ac.at (R.A.S.)

² Nikhef, Science Park, 1098 XG Amsterdam, The Netherlands; a.bertolini@nikhef.nl

³ Faculty of Mechanical Engineering and Naval Architecture, University of Zagreb, 10000 Zagreb, Croatia; ivica.galic@fsb.unizg.hr

⁴ Institut für Physik, Humboldt Universität zu Berlin, Newtonstraße 15, 12489 Berlin, Germany; francesco.intravaia@physik.hu-berlin.de

* Correspondence: hamid.haghmoradi@tuwien.ac.at (H.H.); rene.sedmik@tuwien.ac.at (R.I.P.S.)

Abstract: During the past few decades, abundant evidence for physics beyond the two standard models of particle physics and cosmology was found. Yet, we are tapping in the dark regarding our understanding of the dark sector. For more than a century, open problems related to the nature of the vacuum remained unresolved. As well as the traditional high-energy frontier and cosmology, technological advancement provides complementary access to new physics via high-precision experiments. Among the latter, the Casimir And Non-Newtonian force EXperiment (CANNEX) has successfully completed its proof-of-principle phase and is going to commence operation soon. Benefiting from its plane parallel plate geometry, both interfacial and gravity-like forces are maximized, leading to increased sensitivity. A wide range of dark sector forces, Casimir forces in and out of thermal equilibrium, and gravity can be tested. This paper describes the final experimental design, its sensitivity, and expected results.

Keywords: Casimir effect; dark sector; force metrology; seismic isolation

Citation: Haghmoradi, H.; Fischer, H.; Bertolini, A.; Galić, I.; Intravaia, F.; Pitschmann, M.; Schimpl, R.A.; Sedmik, R.I.P. Force Metrology with Plane Parallel Plates: Final Design Review and Outlook. *Physics* **2024**, *6*, 690–741. <https://doi.org/10.3390/physics6020045>

Received: 31 December 2023

Revised: 5 February 2024

Accepted: 11 February 2024

Published: 7 May 2024



Copyright: © 2024 by the authors. Licensee MDPI, Basel, Switzerland. This article is an open access article distributed under the terms and conditions of the Creative Commons Attribution (CC BY) license (<https://creativecommons.org/licenses/by/4.0/>).

1. Introduction

Continuous improvements in measurement methods during the past few decades have unveiled a number of tensions between predictions of the standard models of particle physics (SM) and cosmology (Λ CDM) with observations. Since the 1970s, the development and testing the SM have been dominated by collider experiments culminating in the experimental discovery of the Higgs particle. However, further advancement on the high-energy frontier appears difficult, as the required technological and financial efforts grow over-proportionally with the gain in energy. Yet there are still sixteen orders of magnitude missing between the current 10 TeV scale and the Planck scale. Therefore, precision measurements at lower energy have established themselves as an alternative route to test existing theories and to search for the physics beyond.

Precision tests have unveiled a growing number of ‘tensions’ in various fields that cannot be explained well on the basis of existing theory. We can highlight only a few of these here. For quantum electrodynamics, measurements of the relative gyromagnetic moments, $(g - 2)/2$, of fermions have revealed values [1] that differ from theoretical expectations by 2.5σ (standard deviation) for electrons and 4.2σ for muons, giving a strong signal of an incomplete understanding of either vacuum fluctuation contributions or new physics. Charge radii of the proton and the deuteron have been determined using precision (Lamb-shift) spectroscopic measurements with H and D, as well as from electron and muon scattering experiments (see review [2]). Even after a recent re-analysis of experimental

errors, and new measurements, tensions at the 2σ [3] and 3.5σ [2] level, respectively, exist between different experiments and between experiments and theory. While QED is still referred to as the ‘best-tested theory’, even after about 150 years, the question of whether the electromagnetic energy momentum tensor is traceless or not in materials remains open [4]. Tensions are also known for other elements of the SM. For example, the Cabibbo–Kobayashi–Maskawa (CKM) quark mixing matrix of QCD shows increasing signs of non-unitarity (currently 2.2σ [5] or up to 2.8σ [6]), which, if confirmed, would be an indication for beyond SM physics. In QCD, the breaking of CP symmetry being suppressed by a factor 10^{-10} creates a fine tuning problem that could be resolved [7,8] by an additional spontaneously broken ‘Peccei–Quinn’ symmetry leading to the axion as its associated Nambu–Goldstone boson [9,10]. The latter is constrained strongly but is not yet excluded. Another strong motivation for the axion is due to it providing an excellent candidate for dark matter (DM).

DM has a solid basis of evidence, as galaxy rotation curves have been measured since the early 20th century [11], and newer probes, such as cosmic microwave background or weak lensing data indicate that a fraction $\Omega_{\text{DM}} \approx 0.27$ [12] of the total mass in the universe can be attributed to DM (see [5] for a review). Numerical simulations [13] show that the current large-scale structure of the universe can only be obtained if DM is taken into account, with baryonic matter ($\Omega_b \approx 0.05$) playing a sub-leading role.

Twenty five years ago after the discovery of accelerated expansion [14–16], there are clear indications that by far the largest fraction of the energy/mass content of our universe ($\Omega_{\text{DE}} \approx 0.68$) is due to the existence of what is generically termed ‘dark energy’ (DE). In general relativity (GR), dark energy can effectively be described in terms of a cosmological constant Λ providing the negative pressure necessary to account for an accelerated expansion of our universe. In combination with ‘cold’ DM this constitutes the cosmological standard model Λ CDM. However, as the Hubble constant H_0 —being a measure of expansion—obtained from data on the cosmic microwave background at large redshift z , is at significant tension (5σ) with the one obtained from local distance ladder measurements at $z < 2.36$ and a range of other measurements [17], speculations arise (among others) if Λ is a constant after all [18]. Significant tensions exist not only in measurements of H_0 but also for several other parameters of Λ CDM [19]. Since DE accounts for the largest fraction of the energy/mass content of our universe, the quest for an answer to the question what the dark sector is composed of has received significant attention. It is currently unknown whether DE and DM are composed of new particles or not, but the answer lies probably beyond the current SM/ Λ CDM framework.

While amending general relativity by the cosmological constant enables us to describe an accelerated expansion, such a procedure would lead to a severe fine-tuning problem, which is the so-called ‘(old) cosmological constant problem’ [20]. This is due to contributions in addition to Einstein’s original (bare) cosmological constant, coming from the zero-point energies of all quantum fields (SM fields as well as possible unknown ones), as well as the Higgs potential during its phase transition related to electroweak symmetry breaking [21]. Introducing a cutoff at the Planck scale or electroweak unification scale in order to render the zero-point energies finite, these contributions provide values for Λ that are 123 or 55 orders of magnitude above the measured value containing all contributions [20]. This may suggest that quantum fluctuations of the vacuum do not seem to gravitate [22], which has cast some doubt on their reality. Some authors have resorted to the rather metaphysical anthropological principle [23] to explain the ‘cosmological constant problem’ [24], while others, just to give an example, have attempted to find explanations in terms of a natural cutoff given by metric feedback at high energies [25]. If there existed additional interactions, cancellations of the zero-point energies of these new fields and the ones of the standard model [26] could explain the smallness of Λ . However, we would be left with a severe fine tuning problem, which adds to the problem of the non-gravitation of vacuum fluctuations. By now, a whole host of conceptually distinct approaches has been devised to avoid this problem (see, e.g., [20,21,27]) with no final solution.

While no general consensus has been found on the above tensions, one approach to explain them is to introduce new interactions. The historically very successful approach to search for the associated new particles in colliders, however, has not led to any discoveries so far, for either DM or DE. Indications for weakly interacting massive particles (WIMPs) have not been found at high energies. Lighter particles searched for by recoil experiments have also eluded detection (the DAMA experiment's periodic DM signal [28] is not generally considered to be confirmed at the time of writing) despite quite large international efforts. Astronomical observations, on the other hand, may have found indications for sterile neutrinos [29,30] and WIMPS [31]. Indications were also found in long baseline nuclear experiments but are still being discussed. As no clear signs regarding the type or energy range of new interactions have been found, theoreticians have turned to the broad field of effective field theories to give generic predictions that allow experimentalists to narrow down the possibilities for DM and DE models. Irrespective of the true physical origin, an effective field theory enables describing and classifying the low-energy behavior of the corresponding fundamental theory in a model-independent way. As such, the 'Standard Model Extension' [32] covers all possible $CP(T)$ -violating terms that could be added to the SM. Several of these can also be written in terms of bosonic spin-0 or spin-1, scalar, vector, or tensor interactions (and their respective pseudo or axial counterparts) between SM fermions [33,34]. The latter leads to a class of effective potentials that can be tested in a large number of experiments [35]. For DE, besides modified gravity, variable dark energy models, and black holes, a class of screened scalar fields has been investigated that would describe dynamical 'quintessence' scalar fields with an effective potential depending on the local mass density. This local variability permits them to 'hide' in denser environments and evade stringent astrophysical bounds while still being able to prevail in low density regions, thereby describing DE. However, these models have several free parameters, and only a few, such as the string-inspired dilaton, have a more solid motivation.

In any case, the cosmological constant problem provides further indications that our understanding of the quantum vacuum may be incomplete. This has been one of many motivations for investigations of the Casimir effect. Being the only known quantum effect causing forces between separated macroscopic objects, experiments have been performed since its prediction in 1948 [36]. Modern experiments starting in the 1990s [37–39] have tested non-trivial boundary dependence [40,41] and lateral forces [42,43], thin layers [44], dielectric properties [45–51], influence on micro-electromechanical elements [52,53], torque [54], and repulsion [55–57], to name just a few topics. Regarding the description of the dielectric properties, especially for the thermal contribution to the Casimir effect, there has been a discussion going on for more than two decades (see review [58]). Specifically, a disagreement between theoretical predictions and experimental results put the focus on the proper account of dissipation in the description of the material optical response. Surprisingly, a simple non-dissipative model provides a better description of several experiments measuring the Casimir interaction between metallic objects. Consequently, the same experiments appear to exclude an account of dissipation in terms of the commonly used Drude model [59]. A similar issue was noticed for free electrons in semiconductors [60]. Within the same context, attention has also been devoted to surface roughness [61] and patch potentials [62,63] as a possible source for the disagreement between theory and experiment. Other material properties were investigated and, in particular, non-locality (spatial dispersion) has also attracted attention [64] in relation to thermodynamic inconsistencies, which may appear when the Drude model is adopted for the description of a metal [65]. However, up to now, all attempts have failed to reach an unanimous consensus, and more precise experimental data are required to settle the controversy [58]. More recently, it was pointed out that a non-equilibrium configuration in which the objects are at different temperatures, T_1 and T_2 , can serve as an additional benchmark of the theoretical framework surrounding the Casimir effect [66]. In this case, an additional contribution to the interaction, anti-symmetric under the exchange $T_1 \leftrightarrow T_2$, has been predicted. Still, this contribution has not yet been quantitatively confirmed in a Casimir experiment.

Experimentally, precision Casimir experiments have also been used to set limits on new interactions [67–79] at small separation a , as proposed four decades ago [80]. However, the sensitivity is limited [81], as one of the strongest uncertainties in such measurements comes from local surface charges that are hard to quantify and control [62,81]. These uncertainties can be mostly avoided by using the ‘iso-electronic’ technique [59,70,82] (allowing only relative measurements) or by placing an electrostatic shield between the test objects, leading to the Cavendish configuration that has been extensively used in torsion balance experiments [83–96] to measure gravity-like interactions. However, a shield between the interacting objects precludes the measurement of Casimir forces and DE screened scalar fields. Another common disadvantage of most existing precision force experiments in either configuration is that they use curved surfaces of some radius R_s . Depending on the distance dependence of the investigated interaction, the effective surface area generating the force is thereby dramatically reduced from $A = R_s^2\pi$ to $A_{\text{eff}} \approx \pi R_s a$ [97,98] with $a \ll R_s$. Therefore, one loses a factor $\eta_{\text{eff}} \equiv a/R_s = 10^{-2}$ to 10^{-4} in force sensitivity [99]. This problem is maximally avoided for plane parallel plates, where $\eta_{\text{eff}} = 1$. The downside is that one has to measure and control parallelism and use perfectly flat surfaces, which introduces significant technical complications. Previous attempts to measure Casimir force gradients between parallel plates [100,101] have suffered from electrostatic and other unresolved offsets for which the results included a free fit parameter.

The Casimir And Non-Newtonian force EXperiment (CANNEX) has been designed from the onset to perform measurements between macroscopic plane parallel plates [102]. After a first proof of principle [103], we continuously updated the design [99,104] to characterize, attenuate, or actively control all relevant disturbances. The setup allows synchronous measurements of the pressure and pressure gradient with nominal sensitivities of 1 nN/m^2 and 1 mN/m^3 , respectively, in both the Cavendish and Casimir configurations, in the distance regime $3 \mu\text{m}$ to $30 \mu\text{m}$. Recently, we selected the Conrad Observatory (COBS), a geoseismic and geomagnetic surveillance station inside a tunnel system in the Alps as a location. The seismic and thermal stability there will reduce errors and technical requirements of isolation systems for CANNEX. Operations at COBS are expected to commence in the summer of 2024.

In this paper, we present the final design and its predicted performance in Cavendish and interfacial (Casimir) configurations in Section 2. Subsequently, we update our recent error budget [99] taking into account actual device specifications and preliminary noise measurements. We then give an update on prospects for measurements of in- and out-of-equilibrium Casimir forces [66] in Section 4.1. Finally, we present updated prospects for DE screened scalar field limits [99,102,105] in Section 4.2, based on fully consistent numerical calculations taking into account the experimental and theoretical uncertainties, and close with a short outlook in Section 5.

2. Experimental Design

CANNEX is a metrological setup designed to synchronously measure forces and force gradients between plane parallel plates at separations between $3 \mu\text{m}$ and $30 \mu\text{m}$ in interfacial and Cavendish configurations. Force (gradients) are measured by interferometrically detecting (see Section 2.5) the movement of a mass-spring system consisting of a ‘sensor’ plate and a set of helical springs. Forces onto the sensor plate are sourced by a second fixed ‘lower’ parallel plate, as shown in Figure 1d. Since this mechanical detection system is highly sensitive to mechanical vibrations, surface charges, and thermal changes, we have included countermeasures for all of these disturbances in terms of active control and attenuation systems into the design, described in detail in Sections 2.1, 2.2, and 2.4, respectively. In what follows in this section, we give an overview of the setup.

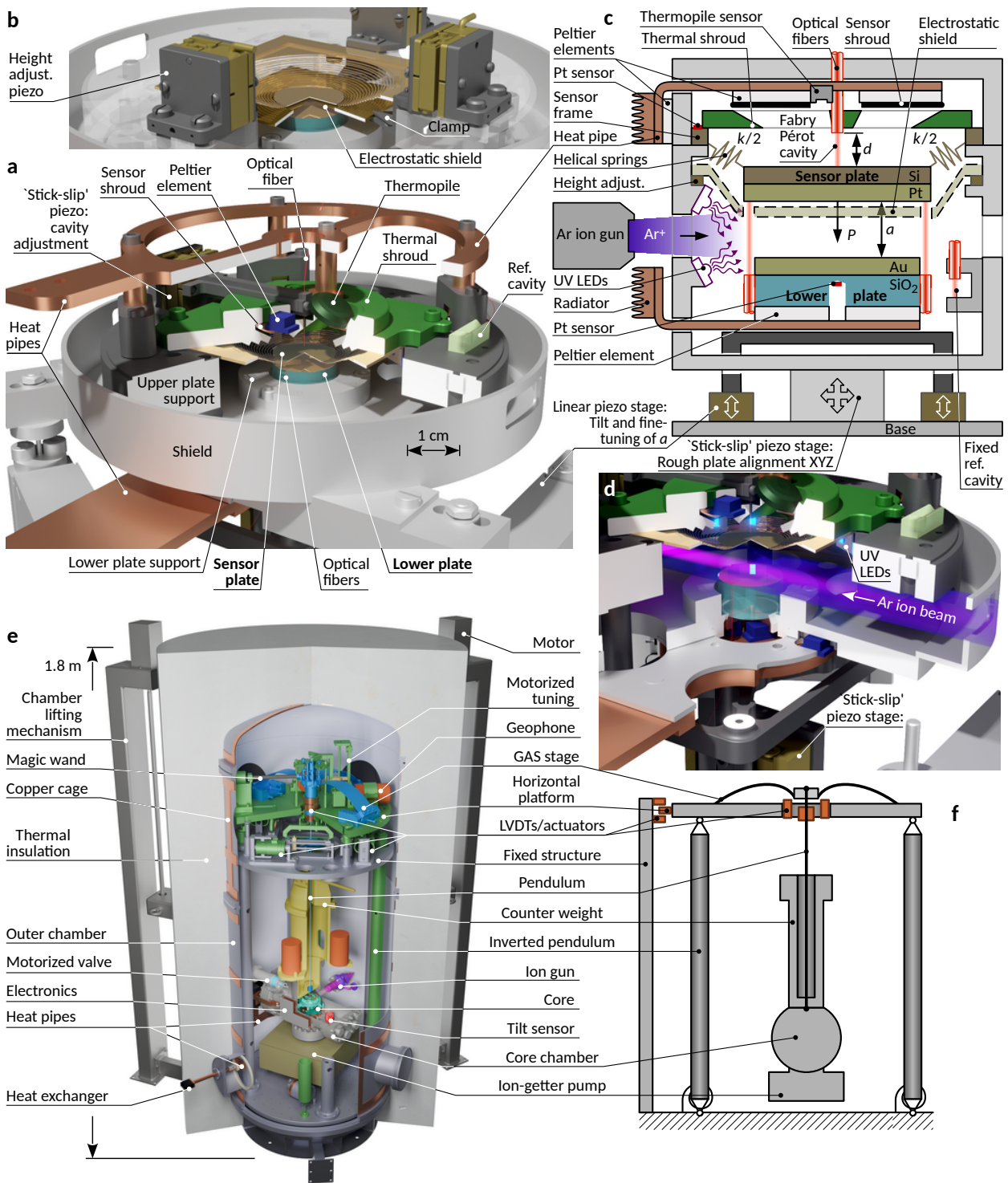


Figure 1. The CANNEX setup. (a) Simplified cut view of the actual core design in interfacial configuration. (b) Simplified focus view of the Cavendish configuration with the electrostatic shield and associated adjustment stages. (c) Schematic representation of the core including all elements and configurations. (d) View of the core with the translator stages in their upper position, in which the ion tunnels are opened for Ar ion cleaning and UV irradiation. (e) Cut view of the complete setup. (f) Schematic view of the seismic attenuation system (SAS).

The setup's 'core' contains the actual measuring device. Here, the lower plate, made of silica glass, is mounted in a fitting (light gray in Figure 1a–d) that isolates it thermally and electrically from the rest of the setup. The fitting is supported by three linear piezo

transducers with a range of 200 μm , allowing us to fine-tune the parallelism and separation between the plates. Thermal control of the lower plate can be achieved via Peltier elements (PE)s below it and a platinum sensor at its center. Attached to the side of the lower plate are three optical fibers used to measure the plate separation and tilt (see Section 2.5).

The force sensor is fabricated from a silicon single crystal (Norcada Inc., Edmonton, AB, Canada) and placed directly above the lower plate. Its position can be adapted by a three-axis drift-free stick-slip stage (SLC-1720, Smaract GmbH, Oldenburg, Germany) supporting the entire upper part of the core. The sensor's frame is connected to a massive support structure (middle gray in Figure 1a,c,d) that is thermally controlled by distributed PEs, and electrically grounded. The support carries a thermal shroud (green) allowing for non-contact thermal control of the sensor and its springs.

Sensor movements are detected via an optical fiber placed above its center (see Section 2.5). The fiber is attached to a drift-free stick-slip piezo transducer allowing us to adjust the cavity size. Similarly, the separation a between the lower and upper plate is monitored by three interferometers arranged around the rim of the lower plate. The fibers' end faces are polished optically together with the lower plate in order for them to be at exactly the same height. CANNEX implements three different configurations. In the first—interfacial—configuration, the sensor plate directly faces the top surface of the lower plate. In the second—Cavendish—configuration, we add a gold-coated silicon nitride membrane acting as an electrostatic shield (ESS) between the two plates. The ESS is held by three stick-slip piezos (see Figure 1b) to change its height and orientation. Despite its relatively large area (1 cm^2) and small thickness ($<1 \mu\text{m}$), the ESS has an extremely low hang-through under gravity of about 1 μm . Three pinholes in the ESS allow the lower plate's interferometers to operate both through the ESS (to measure a) and when shifted slightly to the side to monitor the separation between the ESS and the lower plate. This mechanism allows us to unambiguously determine and control the relative position of all three plates with respect to each other. In the third configuration discussed in Section 2.4, which is only used for surface characterization, either the sensor and the shroud, or the lower plate and its fitting, are replaced by a Kelvin probe setup able to scan the surface potential and topology of the entire surface area of the remaining plate.

The core assembly, Figure 1a, is enclosed inside an ultra-high vacuum (UHV) 'core' chamber. This chamber can be evacuated down to a pressure of 10^{-9} mbar by using an ion-getter pump or be filled with up to 500 mbar of Xe gas for measurements of screened DE interactions [106]. On the outside of the core chamber wall, the core electronics are placed on a copper plate that allows generated heat to be guided away without mechanical contact to the outside of the outer chamber (shown partially in Figure 1e). A similar but independent mechanism exists for the heat pipes emerging from the core itself. Details on these systems are given in Section 2.3. The core chamber is suspended on a 6-axis seismic attenuation system (SAS) shown in Figure 1e,f. The SAS comprises an inverted pendulum (green) for horizontal isolation, a geometric anti-spring (GAS) filter (blue) for vertical isolation, and a mass tower (yellow) improving tilt isolation, as described in more detail below. Additionally, a hollow silicon carbide rod, known as a compensation wand (magic wand), is connected to the tip of the GAS filter to improve the attenuation performance [107]. Vertical and horizontal positions of the SAS can be sensed by linear variable differential transformer (LVDT) sensors, and controlled by motorized pre-tension springs. In addition, the dynamical behavior in translational degrees of freedom can be influenced by voice coil actuators. For higher sensitivity at intermediate frequencies, geophones are used to monitor all but the vertical rotation degree of freedom. Inverted pendulums (IPs) support the base plate of the GAS filter, thereby combining vertical and horizontal attenuation systems.

The entire SAS with the core is enclosed in an 'outer' vacuum chamber at 10^{-6} mbar providing further isolation against sound, thermal, and other environmental disturbances. This chamber is mechanically decoupled from the SAS, to ensure deformations due to pressure differences do not influence the performance of the SAS. The outer chamber is fitted with a dense grid of copper bars and a 25 cm insulation layer to reduce temperature

gradients on the chamber wall. We use PEs on the mentioned copper bars to control the chamber temperature with a precision of about 4 mK. Eventually, the chamber includes several exterior mechanisms (not shown) to open it, and to extract the core with minimum mechanical input to the sensor. The entire setup is placed inside an ISO class 7 cleanroom inside the tunnels at COBS.

2.1. Seismic Attenuation

Seismic vibrations present a significant impediment to the precision of small-distance metrology setups, necessitating a comprehensive understanding of their impact on the respective measurements. CANNEX uses non-linear mechanical elements developed for gravitational wave detectors [108–110]. For vertical isolation, a geometric anti-spring (GAS) filter [111] (blue in Figure 1e) provides 40 dB/decade attenuation from roughly 100 mHz. We employ so-called ‘magic wands’ [107] to augment filter performance at low frequencies and near the sensor resonances. Horizontal isolation is achieved by inverted pendula [112] (green) carrying the GAS filter and a regular pendulum suspending the core chamber. The tilt of the core chamber around the horizontal axes is attenuated by the core chamber being mounted on the pendulum close to its center of gravity. The latter is raised to the hinge point by means of a massive tower (yellow), which reduces the tilt resonance frequency.

Previously, the Atominstut (ATI) of TU Wien, Austria, was considered as the location for CANNEX [99]. We have identified a more suitable location in the underground laboratory of the Conrad observatory, roughly 50 km southwest of Vienna. Seismic spectra have been recorded at both locations and are shown in Figure 2. As we discuss in Section 3.1 below, a one-staged passive SAS at COBS already fulfills all requirements for the targeted error level, while at ATI, a two-stage isolation system would be required [99]. In what follows here, we describe the final system, which is similar to already realized systems in the literature [109,110].

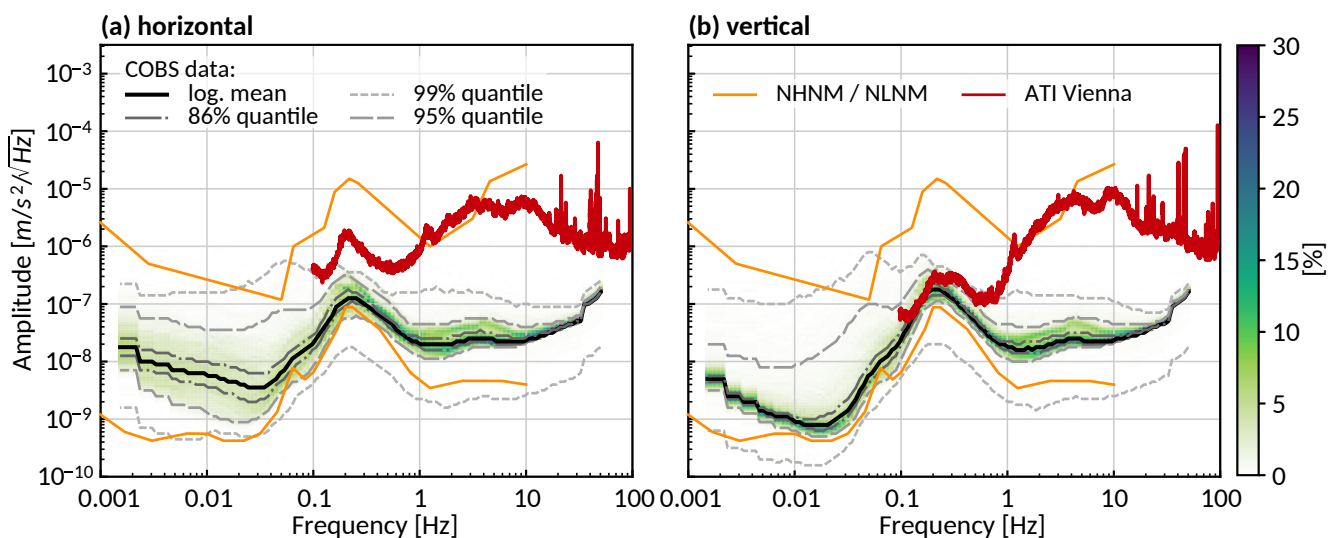


Figure 2. Seismic background in (a) vertical and (b) horizontal (eastern) direction. Data were recorded at COBS using calibrated STS-2 seismometers between 30 April 2023 and 30 June 2023, including four earthquakes of magnitude up to 3.3. The black line is the logarithmic mean of the data, while the dashed gray lines represent the quantiles obtained from histograms at each frequency. The green and blue color encodes the probability. In comparison, the seismic background at the Atominstut (ATI) in Vienna, recorded using calibrated Sercel L4C geophones during 24 h starting 28 September 2018, is significantly higher due to a nearby highway, subway, and in-house noise sources. For reference, we give Peterson’s new high- and low-noise models [113] (NHNM and NLNM, respectively).

The principle of GAS filters [111] and inverted pendula [112] relies on the instability of non-linear mechanical systems at which the stable operating point splits into two distinct solutions. Such points lead (theoretically) to zero resonance frequency and thereby ideal isolation. In practice, internal damping and creep set limits on the achievable minimum resonance frequencies. We can describe our SAS by the model shown in Figure 3. The respective small-signal Lagrange functions \mathcal{L}_D for the horizontal ($D = h$) and vertical ($D = v$) directions are given by

$$\mathcal{L}_h = \mathcal{T}_h - \mathcal{V}_h \tag{1}$$

$$\text{with } \mathcal{T}_h = \frac{1}{2} \left[I_0 (\partial_t \alpha_0)^2 + I_2 (\partial_t \alpha_2)^2 + m_1 (\partial_t x_1)^2 + m_2 (\partial_t x_2)^2 + m_0 (\partial_t x_c)^2 \right],$$

$$\mathcal{V}_h = \frac{1}{2} \left[k_0 (x_1 - x_0)^2 + k_{w2} (\delta_{1l}^2 + \delta_{2u}^2) \right] + m_0 g y_0 + m_1 g y_1 + m_2 g y_2,$$

$$\mathcal{R}_h = \frac{1}{2} \left[\gamma_{2h} (\partial_t x_2 - \partial_t x_0)^2 + \gamma_{1h} (\partial_t x_2 - \partial_t x_1)^2 + \gamma_{0h} (\partial_t x_1 - \partial_t x_0)^2 \right],$$

$$x_c = x_0 \left(1 - \frac{l_{0cm}}{l_0} \right) + x_1 \frac{l_{0cm}}{l_0},$$

$$y_0 = -\frac{1}{2} \alpha_0^2 l_{0cm}, \quad y_1 = -\frac{1}{2} \alpha_0^2 l_0, \quad y_2 = y_1 + \frac{1}{2} (\delta_{1l}^2 l_2 + \alpha_2^2 a_{2u}),$$

$$\delta_{1l} = \frac{x_2 - x_1 - a_{2u} \alpha_2}{l_2}, \quad \delta_{2u} = \alpha_2 - \delta_{1l}, \quad \alpha_0 = \frac{x_1 - x_0}{l_0}, \quad \partial_t \alpha_0 = \frac{\partial_t x_1 - \partial_t x_0}{l_0}.$$

$$\mathcal{L}_v = \mathcal{T}_v - \mathcal{V}_v, \tag{2}$$

$$\text{with } \mathcal{T}_v = \frac{1}{2} \left[m_2 (\partial_t z_2)^2 + m_c \left(\frac{l_c}{l_w} (\partial_t z_2 - \partial_t z_0) \right)^2 \right],$$

$$\mathcal{V}_v = \frac{1}{2} k_{v1} (z_2 - z_0)^2, \quad \mathcal{R}_v = \frac{1}{2} \gamma_1 (\partial_t z_2 - \partial_t z_0)^2.$$

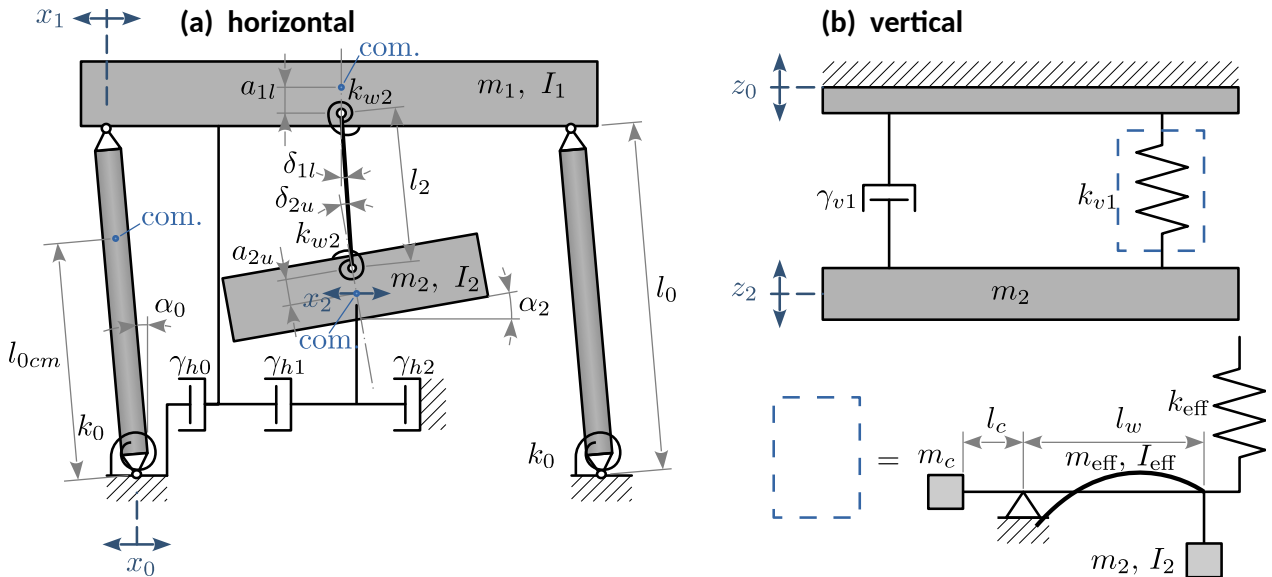


Figure 3. Model for the dynamical behavior of the CANNEX SAS in (a) horizontal and (b) vertical direction. The centers of mass are indicated by ‘com.’. See text for details.

Here, in \mathcal{T}_h , the first two terms describe the angular kinetic energy of the top and payload masses m_1 and m_2 , respectively. The last three terms are the linear kinetic energies of the top, payload, and inverted pendulum (m_0) masses. Potential energies for the inverted pendulum tilt and wire tilt are given by the first two terms in \mathcal{V}_h , while the last two terms

regard the change in the absolute height of m_1 and m_2 due to rotary (sideways) movements of the inverted pendulum and pendulum, respectively. The wire is resisting with elastic constant k_{w2} its deformation at both fixed ends with angles δ_{1l} and δ_{2u} due to the swing x_2 and tilt α_2 of the payload. Viscous damping between all parts is considered by the Rayleigh dissipation terms in \mathcal{R}_h , while internal friction is added ad hoc by adding to the effective values $k_i = \omega_i^2 m_i$ (for masses $i = 1, 2$ and resonance frequencies ω_i), representing the spring constant of system i a factor $(1 + i\phi)$ with $\phi < 1$ [107], which is not shown here for brevity. Similarly, for the vertical direction, we have the linear kinetic energy of the payload mass and wand counter weight μ_c in \mathcal{T}_v . Deformation of the GAS filter gives a contribution to the potential energy \mathcal{V}_v , while viscous damping between the top stage and the payload contributes to the damping term \mathcal{R}_v . y_1 approximates the vertical shift of m_1 for small angle, α_0 . Consequently, y_2 is the vertical shift of m_2 due to the combined action of the pendulum and inverted pendulum. The I_x denote the moments of inertia of the inverted pendula ($x = 0$), the upper platform ($x = 1$), the payload (core chamber, $x = 2$), and the GAS springs ($x = \text{eff}$) obtained numerically from CAD software. γ_x denote damping coefficients, k_x are (effective) elastic constants, and m_x are masses as defined in Figure 3. Note that we use the notation $\partial_x \equiv \partial/\partial x$.

The Euler–Lagrange equations giving the dynamical behavior of the system are then

$$\frac{\partial \mathcal{L}}{\partial u} - \frac{\partial}{\partial t} \frac{\partial \mathcal{L}}{\partial(\partial_t u)} - \frac{\partial \mathcal{R}}{\partial(\partial_t u)} = 0, \quad (3)$$

for $u = x_i, z_i, \alpha_i$. Equation (3) can be resolved for the transfer functions $T_{x_0x_2} \equiv X_2/X_0$, $T_{x_0\alpha_2} \equiv \alpha_2/X_0$, and $T_{z_0z_2} \equiv Z_2/Z_0$ for the horizontal, tilt, and vertical degrees of freedom. We have optimized the system’s parameters with respect to low resonance amplitude and maximum attenuation around the sensor resonance frequency $f_0 = 9.8$ Hz, resulting in the responses shown in Figure 4. We obtain a vibration suppression of about 77 dB and 66 dB in the horizontal (both axes) and vertical direction, respectively, at f_0 , which suffices to achieve the targeted sensitivity under all circumstances, as discussed further in Section 3.

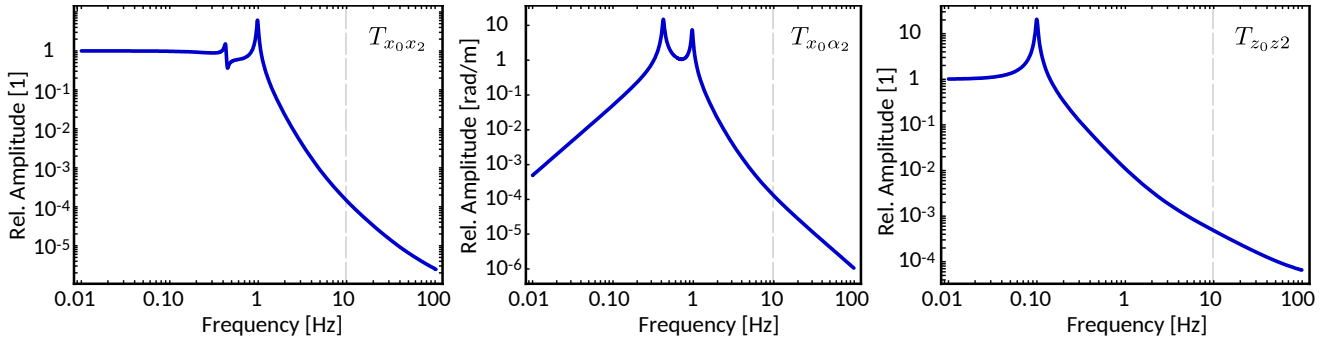


Figure 4. Transfer functions of the passive CANNEX SAS from horizontal and vertical vibrations to core movement and tilt, respectively, as indicated. The vertical dashed lines indicate the position of the sensor resonance.

The current design includes linear variable differential transformers (LVDT) combined with voice coils for force feedback on the horizontal and vertical degrees of freedom as well as geophones. These sensors and actuators shall be used to reduce the amplitude of resonances and improve the overall performance, as described for similar systems [114]. The design of the feedback system is still in progress.

2.2. Surface Charge Cancellation

Electrostatic patch potentials due to local variations in the Fermi potential of surfaces, chemical impurities, and charge accumulation [115] are a major nuisance in all interfacial force experiments [81,116,117]. Over the years, several methods to characterize and compute these forces (gradients) have been developed [62,116,118–120]. Recently, a new ex-

perimental approach was presented to reduce surface charges in situ [121]. UV irradiation can be used to dissociate larger molecules and extract electrons from surfaces. The residual impurities can then easily be removed by a variant of plasma cleaning using a low-energetic beam of Ar ions. After the process, the surfaces have been demonstrated to exhibit strongly reduced local variations in the potential and a low overall force minimizing potential.

In CANNEX, we implement a dual strategy. Firstly, in all configurations (interfacial and Cavendish), active surface cleaning using an Ar ion source and UV irradiation are possible without the need to break the vacuum. This is enabled by the vertical translator stage of the upper plate being able to lift the sensor to a distance of about 5 mm above the lower plate and simultaneously open a window in the shield to clear the path for an Ar ion beam (see Figure 1d). Using eight high-power LEDs viewing the gap between the plates, we can apply UV irradiation at 275 nm wavelength with up to 2 W in short pulses (visible in Figure 1c,d). Secondly, the performance of the cleaning procedure can be monitored in situ using a custom-built Kelvin probe setup (see Section 2.4) mounted in place of the force sensor. Once the distribution, stability, and amplitude of the surface potentials after cleaning and intermittent exposure to air [115] have been determined on both interacting surfaces, the regular force measuring configuration is restored to perform exactly the same cleaning procedures as before.

Apart from patch potentials, two opposing surfaces differ in their absolute potential even if grounded together due to contact potentials. To cancel these, we use an active homodyne compensation method that was successfully applied in recent measurements of Casimir forces [122–124] and in the proof of principle for CANNEX [103]. The method is similar to amplitude modulation Kelvin probe force microscopy (see below), and relies on a small electrostatic excitation, $v_{AC}(t) = V_{ac} \sin \omega_{AC} t$, being applied to the lower plate, resulting in signals at frequencies ω_{AC} and $2\omega_{AC}$, whose amplitudes are measured using a lock-in amplifier. The prior signal is then used to drive a feedback circuit that applies an additional potential V_{DC} to the plate, thereby driving $(V_{DC} - V_0)$ to zero [103,122] with high accuracy. The signal at $2\omega_{AC}$ can be used to independently measure the surface separation electrostatically or what is not required in CANNEX due to the optical method, to perform an independent measurement of the mechanical properties of the sensor. Importantly, all potentials are applied to the lower plate, while the sensor and all other parts are kept on the ground potential. Note also that all surfaces and contacts, except for isolating spacers, are coated by gold to exhibit the same absolute surface potential. The real potentials applied to both plates are measured at all times using a calibrated in situ electrometer amplifier.

2.3. Temperature Control

According to the error budget described in Ref. [99], achieving the targeted error levels of 1 nN/m^2 and 1 mN/m^3 is only possible if the thermal stability of the sensor and optical cavities of 0.1 mK is guaranteed. In order to comply with this requirement, both plates have an independent thermal control system responsible for providing the desired thermal stability. We use calibrated custom-made low-noise controllers with 24-bit converters. The lower plate's thermal system is based on thermal conduction and consists of several PEs located below a copper plate attached to the bottom of the lower plate and a platinum sensor situated in a hole at the center of the lower plate body to read the temperature as close as possible to the top surface of the plate. The copper plate is insulated thermally from other parts by reflective coatings and mechanically by a gap to suppress heat transfer via radiation and conduction, respectively, between the lower plate and other parts of the core. The lower plate itself is clamped down onto the copper plate and into its fitting using spring-loaded ruby balls, which minimizes mechanical contact area and limits heat loss towards the sides. The sensor plate's temperature is stabilized with a combination of a contact and a non-contact feedback loop. The contact loop consists of several platinum sensors and PE combinations on a copper plate between the upper plate support (Figure 1a) and the thermal shroud on top of it, thereby controlling the sensor frame. The central disk of the sensor is connected to its frame only via the long and

thin spring arms, for which thermal conduction plays a minor role. On the other hand, the sensor plate exchanges radiation with the lower plate. Despite highly reflective metal coatings on both sides, heat will be transferred between the two plates as soon as they have different temperature setpoints. As the function of the sensor precludes any mechanical contact with its center, the only option to stabilize the upper plate's temperature is via radiation. For this purpose, a blackened copper ring being controlled in temperature by a separate circuit is placed inside the shroud such that it is visible from the sensor plate's surface. This ring counteracts radiation heating or cooling of the sensor plate by the lower plate. Importantly, we optimized the view factor to the sensor's springs such that they are minimally influenced by radiation from either the ring or the lower plate. Another opening in the shroud allows a thermopile to view the sensor plate and monitor its temperature with <0.1 m°C precision. This input is used to control the temperature of the ring and in consequence the temperature of the sensor disk. A finite element method (FEM) study was conducted using COMSOL Multiphysics to examine the temperature and respective gradients in all parts of the core. Figure 5a,b show the preliminary results of this study for the temperature distributions of both plates for a temperature setpoint of the lower plate being 10 °C higher than the ambient temperature. The deviation on the upper plate with respect to the setpoint (293.130 K) is kept below 0.27 mK, while on the lower plate, the deviation reaches 3.31 mK.

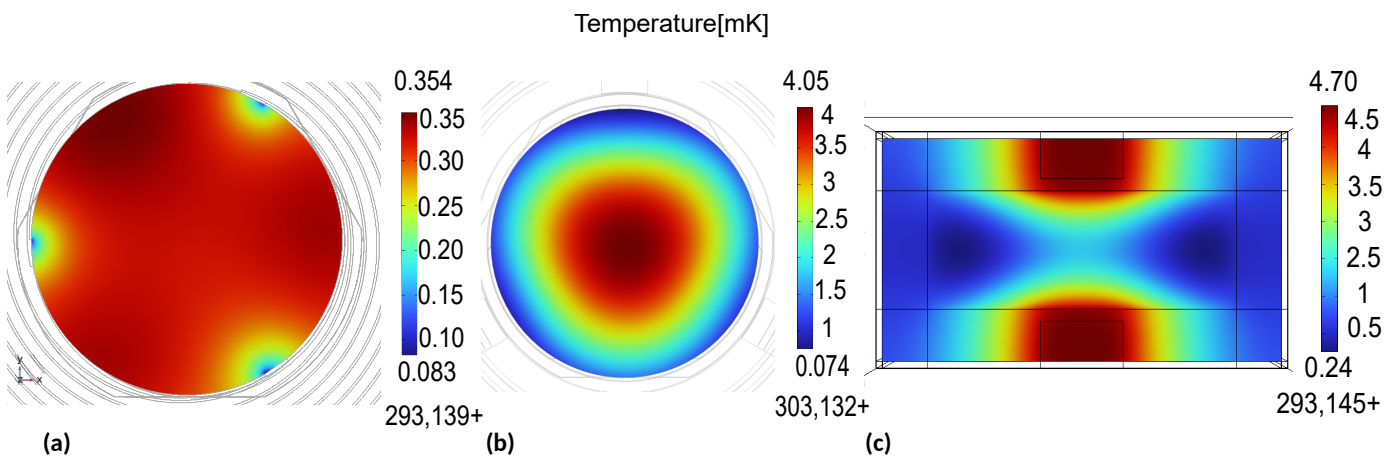


Figure 5. Results of an FEM analysis of thermal distributions. (a) sensor plate (b) lower plate in the core for a nominal difference of 10 °C between the two plates. (c) chamber wall grid cell (see text). Here, only the relative deviations on the parts are accurate, while the absolute temperatures may contain relatively small offsets due to fixed power input instead of feedback control in the numerical computations.

Proper operation of a PE requires the side opposite to the controlled surface to be connected to a heatsink. Therefore, all PEs atop the upper plate, support, and shroud are connected via vertical copper columns to the large circular heatpipe on top connected via flexible parts (not shown) to a thermal feedthrough at the back chamber wall. Below the lower plate, the non-control side of the PEs is connected to a heat pipe (shown on the lower left of Figure 1d), which leads to a radiator permitting contactless heat transmission between the core and a feedthrough at the back chamber wall of the core. Similarly, there are two radiators between the core chamber and outer chamber that contactlessly exchange heat with their respective counterpart, partially visible in Figure 1e. These radiators on the inner side of the outer walls are connected to heat pipes leading through the outer wall to a thermal controller regulating the heat pipe temperature and effectively releasing excess heat via a heat exchanger to the environment. The radiators themselves are interleaved comb-like structures with a relatively large overlap between the interacting parts, blackened on the inside and reflective on the outside. Optimization and testing of these structures is still in progress.

The strong dependency of the working point of the non-linear mechanical elements of the SAS on thermal variations [111] makes it crucial to actively stabilize the temperature of the outer chamber wall as well to within about 5 mK. This requirement is not changed by our DC-feedback with the pre-tension springs. The low amount of power produced by CANNEX's SAS, which still could be a critical thermal disturbance, is dissipated via radiation interaction with the wall. At the setup's location at COBS, the ambient temperature changes by much less than 0.1 °C per day with an average of roughly 10 °C, for which we expect little exterior thermal fluctuations. To keep the chamber close to the setpoint (about 290 K), we add 25 cm of passive thermal isolation around the entire chamber. Below the isolation, the entire chamber wall is covered with a dense grid of 5 mm thick copper bars to improve the heat conduction on the walls. On top of the copper bars, we add 50 independent calibrated control units each consisting of two PEs and two platinum resistors. In Figure 5c, we show the results of an FEM study of the resulting temperature distribution on the inside of the chamber wall for one representative unit cell of the gridded chamber wall.

2.4. AFM/KPFM Setup

In Section 2.2, we discussed the setup for surface charge cancellation by the combined action of an Ar-ion beam and UV irradiation cleaning. To ensure the consistency and performance of these methods, to investigate the long-time evolution of the surface potentials, and to measure the influence of exposure of the setup to the atmosphere [125] (which is inevitable while working on it), we add a Kelvin probe force microscope (KPFM) to the setup. The KPFM has been designed to offer two configurations. In the first one shown in Figure 6, the surface charge distribution on the lower plate can be investigated in situ before and after cleaning. The sensor plate and shroud (see Figure 1) of the force sensing setup are replaced by a u-shaped structure (green) carrying an AFM cantilever. The optical fiber, which is otherwise used for measurements on the sensor plate, is remounted at an angle to detect the movement of the cantilever interferometrically, in a similar way as demonstrated previously [124,126]. In order to align the fiber with the cantilever tip in situ, we use a stack of horizontal stick-slip translators. The scanning motion of the tip and vertical coarse alignment is carried out by the movement of the 3-axis stick-slip piezo translator stack (golden, at the bottom in Figure 6). Note that these stages have a range of more than 12 mm, for which they can be used to investigate the entire area of the lower plate with the KPFM. Because of the comparably large surface separation in CANNEX, only patches of size $\lambda_p \gtrsim a/10$ are of interest [127], with a being the separation between the plates. Therefore, the tip of the cantilever is chosen to be of spherical shape with a diameter of a few μm . Using a common sharp tip, the same setup can also be used to characterize the roughness (and potentials) on all scales with lateral resolution <10 nm. In the vertical direction, we implement a common tapping mode method, where the height adaptation with 0.2 nm resolution is enabled by the three linear piezo-electric stages otherwise used for tilt adjustment of the lower plate.

In the second configuration (not shown in this paper) the KPFM is turned upside down and the lower plate is replaced by the cantilever holder, allowing an in situ measurement of the upper plate's lower surface or the electrostatic shield's potential distribution in the same way as described above. With these two configurations, we can achieve a complete characterization of all surfaces that can then be used to compute the patch potential contribution to the measurements based on actual data instead of statistics.

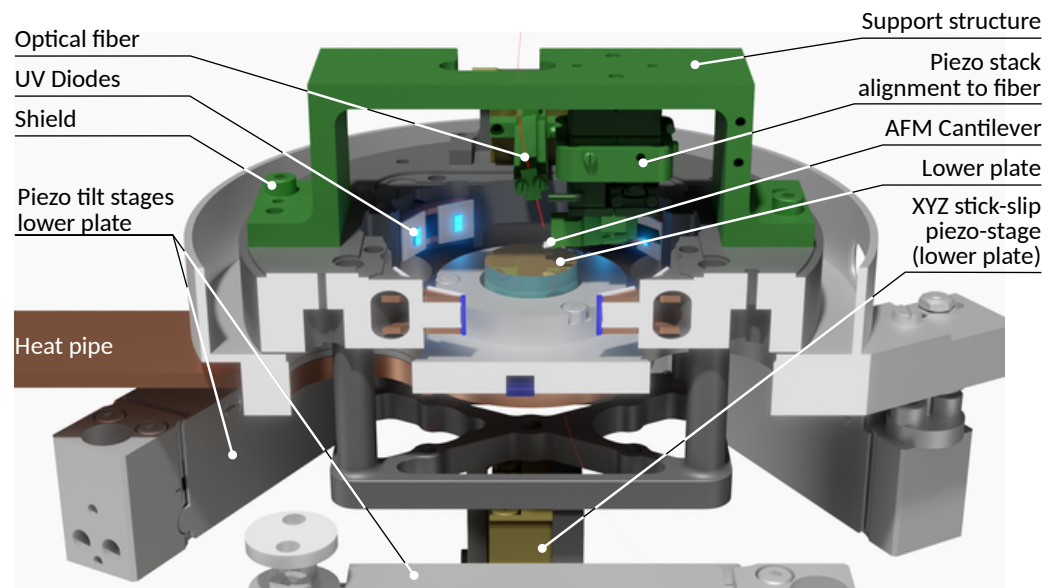


Figure 6. Rendering of the AFM/KPFM configuration for measurements of potentials and topology of the lower plate.

It has been demonstrated that frequency-modulated (FM)-KPFM is able to achieve higher resolutions than amplitude-modulated (AM)-KPFM, as artifacts caused by the capacitance of the cantilever are more prominent in AM-mode operation [128–130]. On the other hand, lower bias voltages in AM KPFM reduce the distance dependence of the minimizing potential [131] and result in a higher reliability for the topological loop to prevent damaging the surface or the tip [132]. Recently, the introduction of heterodyne detection methods in both AM [133] and FM [134] KPFM has been shown to yield improved resolution and speed. In CANNEX, we intend to use heterodyne AM. In contrast to the literature, our cantilever is excited at its resonance frequency ω_{c0} electrostatically. This method is less prone to artifacts and offers increased resolution compared to both classical AM and FM KPFM. Moreover, heterodyne KPFM enables us to detect the contact potential difference simultaneously to $\partial^2 C / \partial a^2$, where C is the capacitance and a is the distance between the tip and the surface [134–136]. In the potential domain, we expect the resolution to be better than 0.1 mV [137]. This setup can easily be adjusted to any homo- or heterodyne detection method. If necessary, we will diverge from the intended use of heterodyne AM-KPFM if other methods prove to lead to higher resolutions.

2.5. Optical Detection System: Force and Distance Measurements

A major problem in the proof of principle for CANNEX [103,104] was the parasitic coupling of AC signals into the cavity. We have, therefore, replaced the capacitive detection system by a entirely optical one to detect all relevant parameters. Electrical potentials between the plates are now defined by a single source driven by the active potential compensation circuit described in Section 2.2.

2.5.1. Force and Force Gradient Detection

CANNEX uses Fabry–Pérot cavities formed by the polished ends of optical fibers and the reflecting surfaces of the sensor plate to measure the extension of the latter and its distance to the opposing lower plate. An overview of the complete optical setup is given in Figure 7.

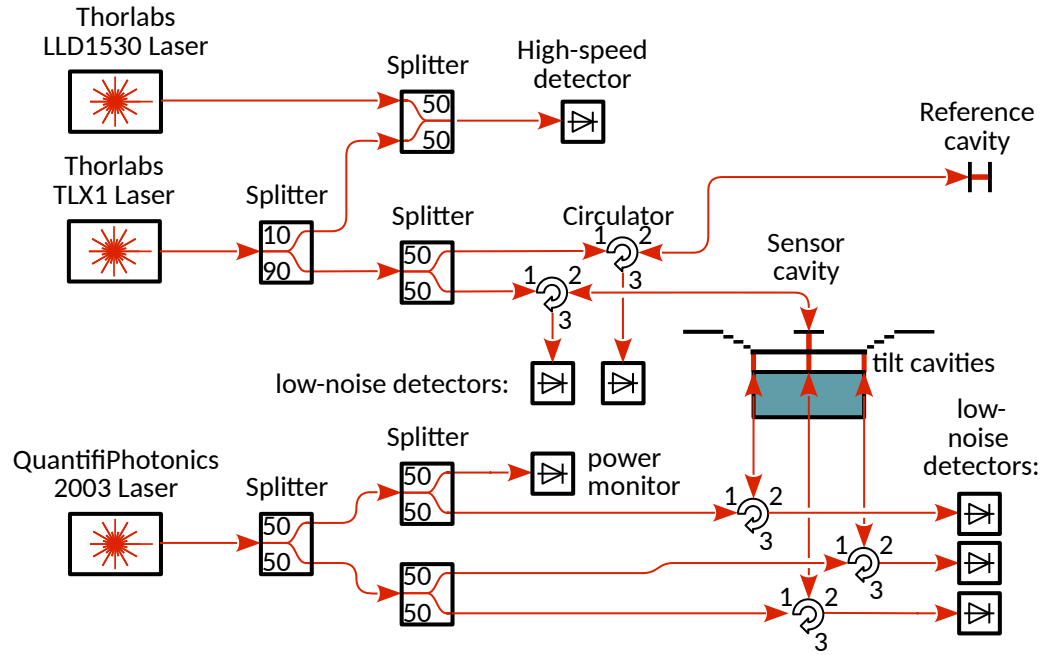


Figure 7. Complete schematic of the optical detection system.

A periodic force F or movement of the sensor base z_0 at circular frequency ω leads to a displacement amplitude Δz of the sensor plate according to the transfer functions

$$T_{Fz} \equiv \frac{\Delta z}{F} = \frac{1}{m(\omega_0^2 - \omega^2 - \partial_a F/m - i\omega\omega_0/Q)}, \quad \text{and} \quad T_{z_0z} \equiv \frac{\Delta z}{z_0} = \frac{\omega^2}{(\omega_0^2 - \omega^2 - \partial_a F/m - i\omega\omega_0/Q)}. \quad (4)$$

Here, $Q \approx 10^4$ is the quality factor of the sensor.

Note that at $\omega = 0$, the transfer function reduces only approximately to Hooke's law, as $T_{Fz} \rightarrow (m\omega_0^2 - \partial_a F)^{-1} = (k - \partial_a F)^{-1}$. We denote the sensor spring constant by k , the free resonance frequency by ω_0 , and the effective mass by m , which is larger than the physical plate mass m_0 due to the dynamical contribution of the spring elements. At the smallest separations $a \rightarrow 3 \mu\text{m}$, the ratio $(\partial_a F)/k$ reaches values up to 0.01 such that the force gradient $\partial_a F$ cannot be neglected when evaluating DC extension data. We, therefore, have to either measure or calculate $\partial_a F$ for all measurements. The sensor resonance frequency ω_r (defined as the frequency at which the mechanical system has $\pi/2$ phase shift with respect to the sinusoidal force excitation signal) shifts according to

$$\omega_r = \sqrt{\omega_0^2 - \frac{\partial_a F}{m} + \frac{1}{m} \mathcal{O}((\partial_a^2 F)T_{Fz}F)}, \quad (5)$$

where the relative error due to the last term is smaller by four orders of magnitude than the effect of the second at all separations.

We use the single interferometer above the sensor (see Figure 7, 'sensor cavity') to synchronously detect the DC extension Δz in response to constant forces acting onto the plate, and the dynamical response $\Delta z(t)$ to an electrostatic excitation $F_{\text{exc}}(t) = (\epsilon_0/4a^2)V_{\text{exc}}^2 \cos \omega_r t$ (with the vacuum permittivity ϵ_0).

Due to the voltage V_{exc} applied between the plates at frequency $\omega_r/2$. Using a phase-locked loop (PLL), we can track ω_r and detect the shift $\Delta\omega = \omega_r - \omega_0$ of the resonance frequency, from which we extract $\partial_a F$ by inverting Equation (5). For measurements in Xe gas, the sensor is over-critically damped, such that $\Delta\omega$ cannot be measured. In these measurements, we move to $a > 10 \mu\text{m}$, where $\partial_a F/k \ll 10^{-2}$ and the error by using the computed values for the force gradients due to the dominant electrostatic and Casimir force contributions is negligible.

The value of $\Delta z(t)$ is extracted from the optical signal

$$S = S_A + S_B \cos \frac{4\pi(d - \Delta z)}{\lambda}, \quad (6)$$

where the offset S_A and the amplitude S_B are determined by the optical and geometric properties of the cavity, the laser power P_L and the wavelength λ , and the sensitivity of the detector. All appearing parameters are calibrated independently (see Section 2.5.2). In order to maximize the sensitivity of S to Δz in Equation (6), we need to adjust λ such that $\cos 4\pi d/\lambda = 0$, which we call the ‘quadrature point’. Before data taking, we ensure the latter condition by performing a sweep of λ at large distance, where Δz can be calculated with sufficient precision. The sweep data are then fitted by Equation (6), with free parameters S_A , S_B , and d . Note that for all a the interferometric cavity size d only changes by $|\Delta z| \ll |d - \lambda/2|$ (the size of a fringe) due to the sensor’s reaction to forces applied between the two plates. We can, thus, measure d and adjust λ to be at quadrature. The same sweep method with a wide range of λ allows us to measure the absolute distance a_i between the two plates at the position of the lower three interferometers; see Figures 1 and 7. We extract a_i either from fits as described above or from the peaks appearing in the Fourier transformed data $\tilde{S}(d)$ of $S(\lambda)$. Which method is used depends on the cavity size. At large $a \gtrsim 20 \mu\text{m}$, where sufficiently many fringes can be covered by the modulation range (1520–1620 nm) of the QuantifiPhotonics 2003 laser (QuantifiPhotonics Ltd., Auckland, New Zealand) laser, the Fourier method gives fast and accurate values of a_i , while at the smallest separations, not even one fringe can be covered and only the fit method can be applied.

The optical paths $2d$ and $2a_i$ of our cavities change with the vacuum pressure and are significantly influenced during the measurements in Xe gas. For this reason, we use an auxiliary fixed-distance cavity made of a material with an effectively zero thermal expansion coefficient, sourced by the same laser driving the upper sensor cavity. Being located next to the sensor, this cavity gives a reference signal $S_R(P_L, \lambda, \rho_G)$ depending on the density ρ_G of the gas and fluctuations in both the laser power and wavelength. For the three interferometers below the sensor, we use a power monitor to eliminate power fluctuations from the signal. As all excitations and resonances are well below 20 Hz, we use slow low-noise detectors with cutoff-frequency 1 kHz to eliminate high-frequency noise.

Measurements in the interfacial and Cavendish configurations are performed in sweeps starting at the maximum separation $a_{\text{max}} = 30 \mu\text{m}$, reducing the separation for each measurement point in discrete logarithmic steps towards $a_{\text{min}} = 3 \mu\text{m}$. Before each sweep, a full re-calibration is performed (see below) to cancel drifts. The cavity size d and wavelength λ are re-calibrated before each single measurement point. For measurements in Xe, a is kept constant and sets of several consecutive measurements are performed at the same pressure. Each set is preceded by a full calibration with d and λ recalibrations in between single measurements.

2.5.2. Calibration

In order to perform an absolute measurement of forces, we need to calibrate all the optical, mechanical, and electric properties of our detection system. Some calibrations are invalidated only by ageing for which one measurement per experimental campaign is sufficient, while others have to be repeated as often as possible to compensate drift. Constant offsets requiring only few re-calibrations concern the dependence of laser power on the wavelength, transmission functions of wiring and electronics, etc., taken into account in the error calculations in Section 3. The remainder of this Section focuses on the frequent calibration of physical properties of the sensor and optical system. Mechanically, the sensor response is influenced by thermal fluctuations, long-term changes in the residual water layer on its surface, and surface charges. Even if these effects are expected to be relatively small, only a calibration can exclude them with certainty.

We start by re-calibrating the time-dependent wavelength offset of our lasers using a second laser with wavelength locked to an acetylene transition at $\lambda_{\text{ref}} = 1532.832\,30(8) \text{ nm}$

and a beat technique [138]. For this method, the output of the tested laser is combined with that of the reference laser and lead to a high-frequency detector (see Figure 7). Then, the λ_{set} setting of the TLX1 is adjusted to result in a minimum beat frequency, $\Delta f = (c/2)(\lambda_{\text{set}}^{-1} - \lambda_{\text{ref}}^{-1})$ (with c the speed of light), using a lock-in amplifier. From the difference between λ_{set} and λ_{ref} , and from the residual Δf (resolution of λ_{set}), we can determine the (constant) error in λ_{set} to within about 0.1 pm.

Next, in a similar way as in the proof of principle [103], we increase the plate separation in high vacuum to $a_{\text{cal}} \approx 5$ mm, where all interactions (electrostatic, Casimir, and gravity) between the plates fall off by at least two orders of magnitude with respect to their values at $a = 30$ μm . In this position, the properties of the sensor cavity (see Figure 7) and the reference cavity are determined by a wavelength sweep as described above. Subsequently, at $\lambda_{\text{set}} \approx \lambda_{\text{ref}}$, d is adapted iteratively to match that of the reference cavity such that both cavities are of the same size and at quadrature. Then, a precisely known electrostatic excitation is applied at frequency ω_{exc} that is swept over a range from $\omega_0/2$ to $2\omega_0$ and the signal amplitude and phase are decoded by a lock-in amplifier. Finally, a DC voltage is applied between the plates and its value is swept over a range around zero, resulting in similar signal levels as in the actual measurement of the Casimir force. Both the extension Δz and the frequency shift $\Delta\omega$ in response to the electrostatic force are recorded. Then, a synchronous fit of data from both sweeps (frequency and voltage) to Equations (4) and (5), considering the signal non-linearity from Equation (6), with all separately recorded voltages, power fluctuations (see below), and calculated forces and their gradients contributing to Δz at $a = a_{\text{cal}}$, is performed. This fit results in accurate values for m , ω_0 , and Q .

3. Error Budget

We already published a complete error budget [99] on the basis of a preliminary design considering a two-stage SAS, but at a location inside a (seismically and thermally) noisy lab in Vienna. The leading reason to relocate CANNEX to COBS is significantly lower environmental disturbances. Here, we update the previous error budget, firstly, with respect to the new location, and, secondly, for the final design and the characteristics of the actually used devices. As we show subsequently, the final design implements major improvements with respect to the previous conservative estimations, leading to expected final sensitivities of 0.259 nN/m² and 0.0179 mN/m³, with projected uncertainties (of statistical (stat.), systematic (syst.) and constant (const.) errors) 0.119 nN/m²(stat.+ syst.) + 0.139 nN/m²(const.) and 8.6 $\mu\text{N}/\text{m}^3$ (stat.+ syst.) + 9.3 $\mu\text{N}/\text{m}^3$ (const.), respectively, at the 68% confidence level (1σ) for 100 days of measurements at $a = 20$ μm . These figures represent an improvement by factors 2 and 30 for measurements of the pressure and pressure gradient between the flat parallel plates, respectively, in comparison to our previous estimate.

3.1. Seismic Noise

As shown in Figure 2 above, the seismic noise at the COBS is significantly lower than in Vienna at all frequencies above the micro-seismic peak. Due to a near seismically active zone in the Pannonian basin south of Vienna, earthquakes of low magnitude are frequent. However, the observatory houses official geomagnetic, seismic, and meteorological surveillance stations, including several STS-2 seismometers (Streckeisen GmbH, Pfungen, Switzerland), which can be used not only to veto affected data but also to correct variations in the gravitational acceleration g due to Earth tides and irregular local mass shifts at the location of CANNEX.

The lower seismic noise at the COBS relaxes our requirements for the SAS such that the one-staged system described in Section 2.1 suffices. In Figure 8, we show the expected spectral seismic disturbance together with the limits from RMS noise, signal non-linearity, and the signal-to-noise ratio (SNR). At all frequencies at COBS, the passive SAS alone already fulfills the requirement with 53 dB and 22 dB (amplitude) buffers in the horizontal and vertical directions, respectively, around the sensor resonance. Near the resonance of the GAS filter (assumed 100 mHz) in the vertical direction, the buffer reduces to 14 dB.

Such a low resonance frequency is usually not achieved by a passive system but since active feedback can lower the resonance frequency and the corresponding amplitude even further, we use this assumption in our calculations. At frequencies below 30 mHz, RMS noise becomes an issue. However, all data below 10 s^{-1} will be corrected by STS-2 data, which eliminates the constraint. Furthermore, the current error budget does not include additional damping by active feedback, as the respective design is not yet complete. We conservatively expect 2 dB additional damping around the sensor resonance and about twice this reduction for the amplitude of the primary GAS filter and pendulum resonances.

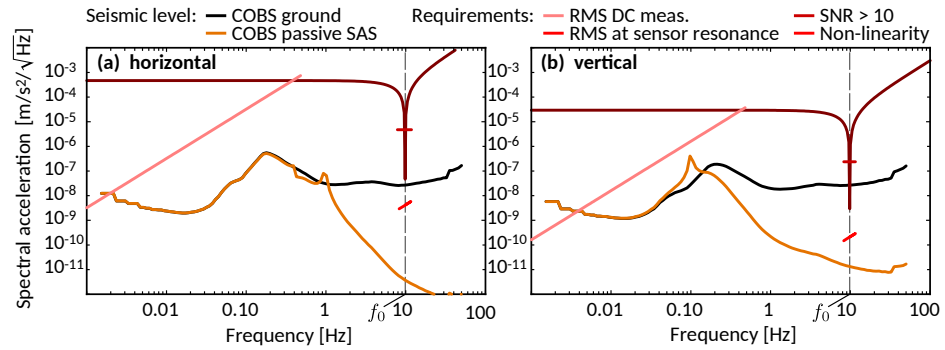


Figure 8. Numerical result of the passive (a) horizontal and (b) vertical seismic background on the core chamber, compared to updated requirements (red lines) representing upper limits (for details see [99]). The vertical dashed lines indicate the position of the vertical sensor resonance.

3.2. Detection Noise

For the error budget, we have to consider the time-dependent offsets and noise in all the calibrated quantities, parameters, inputs, excitation and detection signal paths, and measurement devices. With respect to the previous error budget, we now have detailed and specific information about most quantities available, which allows us to compute the final error level expected for the measurements.

General boundary conditions are a total number of 100 distance sweeps, each including a re-calibration of the cavity sizes, laser wavelength and sensor parameters, and elimination of seismic disturbances at frequencies lower than $(10\text{ s})^{-1}$ using seismometer data. In the following, we construct the error budget by first analyzing the signal paths for DC and AC measurements independently, leading to a voltage and frequency signal, respectively, mentioned. Please confirm or revise naming “first step” clearly. Those signals are then converted to the pressure and pressure gradient using the calibrated mechanical properties of the sensor. In each of these two stages and for the calibration, we perform a detailed and—to the best of our knowledge—complete error analysis assuming small and normally distributed statistical errors and time-dependent drifts wherever manufacturer data are available. Details on each considered error are given in Appendix A.

For DC signals of the extension Δz , we consider variations δd in the cavity size d due to seismic vibrations and thermal drift. Note that errors σd in the cavity size determination are constant offsets that need to be considered only for the conversion to a force below, as they are nullified for the voltage signal at quadrature. Wavelength errors $\delta \lambda$ are due to the laser bandwidth and spectral frequency noise as well as time-dependent wavelength accuracy errors $\sigma \lambda(t)$. The latter can be reduced by first assuring the independence (specifications obtained directly from the manufacturer) of the offset $\sigma \lambda(\lambda)$ from the wavelength, for all λ values in the tuning range of the TLX1 laser, using a spectrometer with less than 0.1 pm accuracy. Then, during operation, $\sigma \lambda$ will be measured repeatedly (before each force measurement) at one single wavelength using a frequency-locked reference laser as described above. According to the manufacturer’s information, the uncertainty of the reference laser wavelength is mainly limited by thermal drift. The given uncertainty value $\sigma \lambda = 0.08\text{ pm}$ is specified for $\delta T = 3.5^\circ$, for which we reduce this value by a factor 0.1/3.5 for operation at COBS. For the signal error, we further consider the relative power fluctuations δP_L of the

laser leading to intensity fluctuations affecting both the signal of the measuring cavity and the one of the reference cavity, S_R . As both signals are measured independently, this allows us to normalize the signal in realtime. Both optical signals contain stochastic noise δV_{det} of the detectors, and δV_{DAQ} of the two Keysight 34470A voltmeters, discretization error δV_{alias} , voltage offsets $\sigma V_{\text{DAQ}}(T)$, depending on fluctuations of the ambient temperature T , and a stochastic component for cable pickup noise. This leads to an expression for the total measured signal V_{sig} , where for brevity, we combine for some quantities the respective constant and systematic errors $\sigma X(t)$ that may contain drift depending on time t and the stochastic noise δX as $\delta X(t)$:

$$V_{\text{sig}} = \frac{V_R(0) + \delta V_{R0}}{V_R(t) + \delta V_R} \left(\delta V_{\text{DAQ}}(t) + \delta V_{\text{det}} + [1 + \delta P_L(t)] \left[S_A + S_B \frac{4\pi[d + \delta d(t)]}{\lambda + \delta \lambda(t)} \right] \right), \quad (7)$$

with $V_R(t) = \delta V_{\text{DAQ}}(t) + \delta V_{\text{det}}(t) + [1 + \delta P_L] \left[S_{A,R} + S_{B,R} \frac{4\pi[d_R + \sigma_R]}{\lambda + \delta \lambda(t)} \right]$.

The reference signal $V_R(0)$ is measured before the start of the measurements with long integration time τ_R (see below), determined from the minimum between noise averaging and the rising influence of long-term variations (drift). The measured ambient temperature in the tunnel at COBS generally changes over periods of weeks rather than hours and has a typical fluctuation amplitude of 5×10^{-3} °C per day. As a worst case (in the case of work being performed in the tunnel), we consider a sinusoidal diurnal temperature deviation with peak amplitude 0.1° with zero transition at the start of the measurement. For the resulting offset errors, we use manufacturer specifications for the voltmeters amended by noise measurements with the actual devices. The lasers are temperature-stabilized but nonetheless are affected by changes in T . For the TLX1, the power noise has a $1/f$ characteristic for frequencies below 10 Hz extrapolated from -105 dBc at 10 Hz to smaller frequencies, and flattening off at -40 dBc at around 2×10^5 s due to the power regulation circuit; specifications were confirmed by actual measurements over 3 h [139]. We computed the Allan deviation from these data, showing no clear minimum but flattening around 5 ks). The laser frequency noise δf_L is most pronounced around 1 Hz and reduced for smaller frequencies by a dither keeping the DC value of the wavelength constant within 10 kHz (approximately 0.1 fm). Due to the periodic laser frequency offset calibration between measurements, continuous power normalization, internal temperature calibration of the data acquisition system, and all-year temperature stability at COBS, any long-term drift is expected to be insignificant for the period of data taking (100 days). We, thus, cut off drift contributions ($\delta V_{\text{DAQ}}(t)$, $\delta f_L(t)$, δP_L) at the integration time $\tau = 1 \times 10^{-5}$ s by integrating over the fluctuation spectra from $f = t^{-1}$ to ∞ with a cutoff function, $f_I(f) = 1/(1 + 2\pi f\tau)$, provided by the detector with $\tau = \tau_{\text{det}} = 10^{-3}$ s and $\tau = t$ for a variable integration time (2 s for DC measurements and 83 s for AC measurements, 1000 s with averaging for one measurement point) to obtain the respective RMS error. This procedure replaces the $1/\sqrt{\tau}$ factor considered generally for stochastic quantities for all errors for which we have spectral information. The cavity size d has an uncertainty due to seismic disturbances ($\delta d = 4 \text{ pm}_{\text{RMS}}$ for $\tau = 2$ s and $\delta d = 2.8 \times 10^{-2}$ pm for $\tau = 1000$ s). Another contribution to δd comes from the thermal drift. Based on the thermal expansion coefficients and geometry, we expect an effective coefficient of about 5×10^{-8} m/°C (with rather large uncertainty), which translates to 5 pm maximum amplitude. This error needs to be evaluated carefully but our results here indicate that in order to keep the effect of this error small, we need to re-calibrate d after each measurement point. Note that for δV_{sig} , constant errors in d are irrelevant, as they cancel out by subtracting the signal from the one at a_{cal} .

Without error normalization (i.e., by setting $V_R(t) = V_R(0)$), we obtain for an integration time of $\tau_i = 1000$ s a total (statistical and systematic) detection error, $\delta V_{\text{sig}} = 4.85 \times 10^{-6}$ V, which is dominated by stochastic δP_L at short times and $\delta \lambda$ drift at times larger than approximately 100 s. Including the reference measurement, which has a fixed-length cavity without distance fluctuations or temperature drift, this figure can be reduced (assuming even 10% mismatch between sensor and reference cavity) to 8.90×10^{-7} V,

which is dominated by seismic vibration at short times, and δV_{DAQ} at $\tau \gtrsim 500$ s. Error contributions for a single measurement and 500 sequential measurements comprising one force (gradient) measurement are given in Table 1. For comparison, a pressure of 1 nN/m^2 would result in a signal of $3.03 \times 10^{-6} \text{ V}$. Note that δV_{DC} has no significant dependence on a .

Table 1. Components of the DC signal error for fixed $a = 3 \mu\text{m}$ and $\tau_{\text{DC}} = 2$ s for a single datum ($N = 1$) and for $N = 500$ ($\tau = 1000$ s) representing one single measurement point, considering drift models and constant deviations $\sigma_{\text{R}} = d + 10 \text{ nm}$, $S_{\text{A,R}} = 1.1S_{\text{A}}$, and $S_{\text{B,R}} = 1.1S_{\text{B}}$. See text for details.

Error	Symbol	Value [V]		Error Type
		$N = 1$	$N = 500$	
Detector noise	δV_{det}	6.0×10^{-8}	2.7×10^{-9}	stat.
DAQ input noise	δV_{DAQ}	8.9×10^{-8}	4.0×10^{-9}	stat.
Laser power fluct. (canceled)	δP_{L}	0	0	stat.
Laser bandwidth	$\delta \lambda$	2.1×10^{-12}	9.3×10^{-14}	stat.
Laser frequency noise	$\delta \lambda$	1.6×10^{-10}	7.6×10^{-12}	stat.
Seismic vibrations	δd	3.3×10^{-5}	1.3×10^{-7}	stat.
Tot. ref. measurement noise (72 h)	δV_{R}	8.2×10^{-8}		stat.
DAQ input error	$\sigma V_{\text{DAQ}}(t)$	2.3×10^{-11}	1.3×10^{-11}	syst.
Laser wavelength drift	$\sigma \lambda(t)$	7.0×10^{-13}	1.3×10^{-10}	syst.
Cavity size drift	$\sigma d(t)$	2.9×10^{-9}	8.3×10^{-7}	syst.
Tot. ref. measurement error (72 h)	σV_{R}	7.9×10^{-7}		syst.
DAQ calibration	σV_{DAQ}	1×10^{-7}		const.
Tot. ref. measurement error (72 h)	σV_{R}	1×10^{-7}		const.

For AC measurements of the frequency shift, $\Delta\omega = 2\pi\Delta f$, we consider the inherent phase stability of the lock-in amplifier and PLL feedback circuitries, δf_{LI} and δf_{PID} , respectively. There is no simple expression, such as Equation (7) that could be used for direct error propagation, since the frequency measurement involves numerical operation of the PLL. Therefore, we measured the noise and stability of the actual lock-in amplifier and feedback using a first-order passive RC-lowpass filter as the test device. This measurement results in higher noise than in measurements with the CANNEX sensor, as the Q -factor is significantly lower. Aiming to give a (quite) conservative estimate, we consider these measurements representative, nonetheless. Furthermore, we consider the uncertainty in the ω_0 calibration obtained from simulations (see below). Constant offsets σf of the lock-in amplifier clock are reduced to $< 5 \times 10^{-10} \text{ Hz}$ by referencing the PLL to an external Rubidium clock. In addition, the Allan deviation of the clock between calibrations (once per 24 h) could give an error at the level $0.05 \text{ ppm}/^\circ\text{C}$, which we take into account. Voltage noise sources as described for DC measurements, vibrations, and laser frequency noise are considered indirectly by expressing the amplitude noise of the sensor signal in terms of a phase ϕ at the zero transition, $\delta\phi = (\partial V/\partial\omega t)^{-1}\delta V$ and $\delta\phi = [\partial\text{Arg}(T_{\text{Fz}})(\omega)/\partial\omega]\delta\omega$, where $\text{Arg}()$ is the argument function. This computation over-estimates the real phase error by at least a factor of two but we consider it as a worst case. We obtain $\delta f_{\text{V}} = \omega_0\lambda/(16\pi Q\Delta z_{\text{exc}})\delta V$, with the excitation displacement amplitude Δz_{exc} depending on V_{exc} and a , and $\delta V_{\text{sig}} = 7.33 \times 10^{-7}$, $\sigma V_{\text{sig}} = 5.58 \times 10^{-7} \text{ V}$, evaluated as described above for DC measurements but with $\tau_i = 83$ s. Note that we adapt $V_{\text{exc}}(a) = V_{\text{exc}}(10 \mu\text{m}) \times (a/10 \mu\text{m})^{3/2}$ to render the excitation and associated shift in the sensor resonance frequency independent of a . The same uncertainties lowered by longer integration time are used for the calibration of ω_0 (see Section 2.5.2). We then obtain the total frequency shift measurement error by adding all the constant, systematic, and statistical errors listed in Table 2, as described in Section 3.3 below, leading at the shortest separation $a = 3 \mu\text{m}$ to a single point ($\tau = 1000$ s) frequency determination error $\delta f = 4.68 \times 10^{-7} \text{ Hz}$ dominated by δf_{LI} at all integration times (up to $\tau \sim 10^4$ s) and $\sigma f = 8.31 \times 10^{-9} \text{ Hz}$. This

has to be compared by a minimum signal $\Delta f = 4.95 \times 10^{-6}$ Hz for a pressure gradient of 1 mN/m^3 .

Table 2. Components of the AC signal error for fixed $a = 3 \mu\text{m}$ and $\tau_{\text{AC}} = 83 \text{ s}$ for a single datum ($N = 1$) and for $N = 12$ ($\tau = 1000 \text{ s}$) representing one single measurement point, considering drift models. See text for details.

Error	Symbol	Value [Hz]		Error Type
		$N = 1$	$N = 12$	
Signal noise	δf_V	3.9×10^{-9}	1.4×10^{-10}	stat.
f -detection	δf_{PID}	2.2×10^{-6}	6.3×10^{-7}	stat.
PLL frequency noise	δf_{LI}	1.8×10^{-9}	5.2×10^{-10}	stat.
Signal drift	$\sigma f \delta_V(t)$	3.0×10^{-10}	1.6×10^{-11}	syst.
PLL phase stability	$\sigma f_{\text{LI}}(\tau)$	8.8×10^{-10}	1.1×10^{-8}	syst.
Resonance freq. error	$\sigma \omega_0$	2.3×10^{-10}	2.3×10^{-10}	syst.
Signal noise	σf_V		4.5×10^{-9}	const.
PLL phase error	σf_{LI}		5×10^{-10}	const.
Resonance freq. error	$\sigma \omega_0$		8.8×10^{-11}	const.

The measured frequency shift can be converted to a total force gradient by inverting Equation (5), where we require the effective mass m and ω_0 from the calibration. In order to determine the error on m , Q , and ω_0 , we performed a Monte Carlo simulation of complete calibration data on V_{sig} and ω_r considering all the voltage and frequency measurement errors discussed in this Section as normally distributed random quantities with the known width, and offsets depending on time. For frequency data, we created voltage signals containing δV_{sig} and extracted the resulting amplitude and phase using a software lock-in amplifier. We then selected 300 arbitrary sets of frequency shift and voltage shift data, from which we extracted values for m , Q , ω_0 , as described in Section 2.5.2. Eventually, we computed the standard deviation of the fit results, which we interpret as a systematic error (i.e., statistical, averaging with the number of calibrations only). The difference between the mean fit value and the originally used parameter value is representative of a constant error for this parameter. We obtain $\delta m = 58.6 \times 10^{-12} \text{ kg}$, $\sigma m = 1.42 \times 10^{-12} \text{ kg}$, $\delta Q = 1.30 \times 10^{-5}$, $\sigma Q = 2.83 \times 10^{-2}$, $\delta \omega_0 = 1.44 \times 10^{-9} \text{ rad/s}$, $\sigma \omega_0 = 4.4 \times 10^{-11} \text{ rad/s}$. For m and ω_0 , the constant errors are significantly smaller than the systematic ones, which indicates that repeated calibrations may be required to average out the systematic errors. For further computation, we use the constant frequency detection error $\sigma f = 5.53 \times 10^{-10} \text{ Hz}$ for $\sigma \omega_0 / (2\pi)$ instead of the smaller constant error from the simulation given above. We consider a measurement scheme in which one calibration is performed per distance sweep (i.e., per day) and assume that due to the thermal stability of the system, σm and $\sigma \omega_0$ can be reduced as $1/\sqrt{N_{\text{cal}}}$ with the number N_{cal} of calibrations. We then resolve $\omega_r + \delta \omega_r(t) = \sqrt{(\omega_0 + \sigma \omega_0)^2 - \partial_a F / (m + \sigma m)}$ for the total gradient $\partial_a F$, and propagate all errors. To evaluate the latter expression, we require a value for ω_r , where we assume the Casimir force gradient (see Section 4.1) and an electrostatic interaction $\partial_a F_{\text{ES}} = \epsilon_0 A V^2 / a^3$, with $V = 0.5 \text{ mV} \times (a/10 \mu\text{m})^{3/2}$ for the excitation and the sensor interaction area A . Using the quantities just above and the frequency determination error $\delta \Delta f(t)$, we finally obtain the errors listed in Table 3 for $a = 3 \mu\text{m}$, yielding a total pressure gradient detection errors $\delta \partial_a F / A = 0.097 \text{ mN/m}^3$ (stat. + syst.) and $\sigma \partial_a F / A = 0.001 \text{ mN/m}^3$ (const.), dominated by the frequency measurement error δf_{PID} , which is based on our test measurements at low Q -factor.

Table 3. Components of the pressure gradient error for fixed $a = 3 \mu\text{m}$ and $\tau_{AC} = 83 \text{ s}$ for a single datum ($N = 1$) and for $N = 12$ ($\tau = 1000 \text{ s}$) representing one single measurement point, considering drift models.

Error	Symbol	Value [N/m^3]		Error Type
		$N = 1$	$N = 12$	
Frequency detection error	δf	3.3×10^{-4}	9.4×10^{-5}	stat.
Mass calibr. uncertainty	σm	4.8×10^{-5}	4.8×10^{-5}	syst.
Resonance freq. uncert.	$\sigma \omega_0$	4.6×10^{-8}	4.6×10^{-8}	syst.
Frequency detection error	$\sigma f(t)$	1.4×10^{-7}	1.6×10^{-6}	syst.
Mass calibration error	σm		1.2×10^{-6}	const.
Resonance freq. error	$\sigma \omega_0$		1.1×10^{-7}	const.
Frequency detection error	σf		1.1×10^{-7}	const.

The measured DC signal voltage can be interpreted as an extension $\Delta d = FT_{Fz}|_{\omega \rightarrow 0}$ of the sensor due to a force F and its transfer function T_{Fz} , given in Equation (4). In order to evaluate the latter quantity, we require the errors of $\partial_a F$, m , d , as well as the optical amplitude S_B and V_{sig} . Eventually, we propagate the errors according to

$$F(a) = \frac{1}{4\pi} \left[\partial_a F + \delta \partial_a F(t) - (m + \sigma m)(\omega_0 + \sigma \omega_0)^2 \right] \quad (8)$$

$$\times \left[4\pi \sigma d - (\lambda + \delta \lambda(t)) \text{asin} \left(\frac{V_{\text{sig}} + \delta V_{\text{sig}}(t)}{S_B + \sigma S_B} + \sin \frac{4\pi \sigma d}{\lambda + \delta \lambda(t)} \right) \right],$$

resulting in an error of $\delta F/A = 0.324 \text{ nN/m}^2$ and $\sigma \partial F/A = 0.167 \text{ nN/m}^2$, for a single measurement of 1000 s at $a = 3 \mu\text{m}$ dominated by the uncertainty δV_{sig} and uncertainty σd in the cavity size. The value of σd is the parameter error obtained by the wavelength sweep fit during repeated calibrations, for which we categorize it as systematic error, influenced by thermal variation. The corresponding offset (constant error) was below machine precision in the fit. We, thus, consider in the final budget a factor $1/\sqrt{N_{\text{sweep}}}$ with $N_{\text{sweep}} = 500$ for σd . All errors contributing to $\delta F/A$ are listed in Table 4. These results highlight again the need for thermal stability and vibration attenuation as well as proper thermal design. In Figure 9a,b, we show the detection errors for the pressure and its gradient as a function of the integration time. In light of the considerations of this section, the previous error budget [99] is thereby improved by up to one order of magnitude in both measured quantities. For the pressure error, the main contributions are the drift and uncertainty (σd) in the cavity size, the DC measurement noise, which, in turn, depends on vibrations, and the uncertainty σm in the mass of the sensor. For the pressure gradient, the most important contributions come from the frequency measurement that depends strongly on the internal stability of the PLL and the sensor mass. The temperature drift is a crucial parameter influencing most systematic errors considered here.

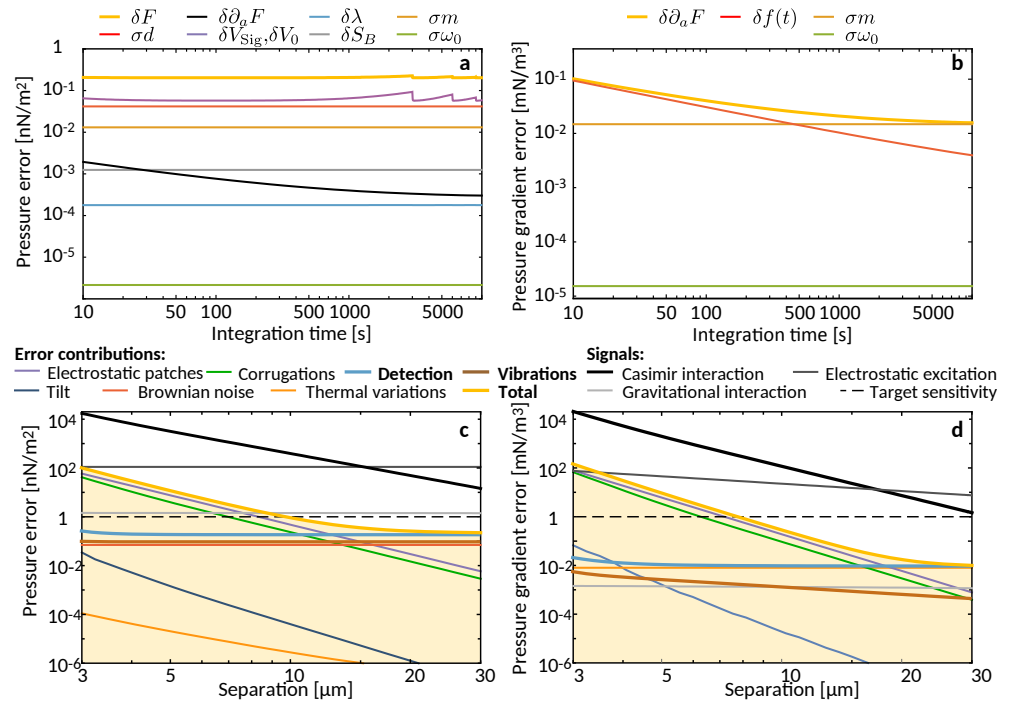


Figure 9. Updated error budget for CANNEX. (a,b) Time dependence of the detection error in the pressure and pressure gradient, respectively, for a single calibrated measurement at fixed separation $a = 3 \mu\text{m}$. (c,d) Error contributions from Ref. [99] with only detection errors and seismic errors updated. Note that here, δX denotes the total error of quantity X and σX denotes the the corresponding combined systematic and constant error.

Table 4. Components of the pressure error for fixed $a = 3 \mu\text{m}$, $\tau_{\text{DC}} = 2 \text{ s}$ and $\tau_{\text{AC}} = 83 \text{ s}$ for a single datum ($N = 1$) and for $N = 12$ ($\tau = 1000 \text{ s}$) representing one single measurement point, considering drift models.

Error	Symbol	Value [N/m^2]		Error Type
		$N = 1$	$N = 12$	
Force gradient error	$\delta \partial_a F$	6.0×10^{-12}	5.0×10^{-13}	stat.
DC signal error	δV_{sig}	1.8×10^{-10}	2.0×10^{-12}	stat.
Zero force DC signal error	δV_0	1.8×10^{-10}	2.4×10^{-11}	stat.
Mass calibr. uncertainty	σm	4.1×10^{-11}	1.2×10^{-11}	syst.
Resonance freq. uncertainty	$\sigma \omega_0(t)$	8.6×10^{-16}	2.5×10^{-16}	syst.
Cavity size error	$\sigma d(t)$	4.2×10^{-10}	1.2×10^{-10}	syst.
Wavelength drift	$\sigma \lambda(t)$	1.4×10^{-12}	4.0×10^{-13}	syst.
Fringe amplitude uncertainty	σS_B	1.3×10^{-11}	3.6×10^{-12}	syst.
Force gradient error	$\sigma \partial_a F$	6.6×10^{-13}	1.9×10^{-13}	syst.
DC signal error	σV_{sig}	9.0×10^{-11}	4.9×10^{-11}	syst.
Zero force DC signal error	σV_0	9.1×10^{-11}	1.7×10^{-10}	syst.
Mass cal. uncertainty	σm	9.0×10^{-12}		const.
Resonance freq. uncertainty	$\sigma \omega_0(t)$	2.1×10^{-15}		const.
Cavity size error	$\sigma d(t)$	6.7×10^{-11}		const.
Wavelength accuracy	$\sigma \lambda(t)$	3.9×10^{-14}		const.
Force gradient error	$\sigma \partial_a F$	2.2×10^{-13}		const.
DC signal error	σV_{sig}	4.8×10^{-11}		const.
Zero force DC signal error	σV_0	4.8×10^{-11}		const.

3.3. Updated Error Budget

Apart from the seismic and detection errors updated above in Sections 3.1 and 3.2, respectively, we also improved our statistical methods. Following Ref. [140], we compute the total error σ_p^{tot} at probability p for N_δ statistical errors σ_j^{stat} , N_σ systematic errors σ_k^{sys} , and N_{const} independent constant errors σ_i^{const} using

$$\sigma_p^{\text{tot}} = \sum_i \sigma_i^{\text{const}} + \sqrt{t_p^2(\nu_\delta) \sum_j^{N_\delta} [\delta_j^{\text{stat}}]^2 + t_p^2(\nu_\sigma) \sum_k^{N_\sigma} [\sigma_k^{\text{sys}}(\tau)]^2}. \quad (9)$$

Note that constant errors occur for many devices and are not limited to the aliasing error, as mentioned in the literature [141]. For example, consider an internal calibration offset of a voltmeter due to aging that may change on timescales larger than the experimental period. Even if a traceable certified calibration is performed before the experiment, the error cannot be determined during the experiment but has to be considered as a maximum offset. Such errors are not statistically distributed (varying) over the timescales of the experiment and can only be estimated conservatively from the accuracy limit given by the manufacturer. They are linearly added and do not reduce with time. δ_j are statistical random errors varying on timescales shorter than any integration time τ , such that they properly probe a (normal) distribution and can be reduced by a factor $1/\sqrt{\tau}$. $\sigma_k^{\text{sys}}(t)$ are the (statistical components of) systematic errors. In this category, we have any offset that has changes that are quick enough to exhibit a distribution during the experiment that may probably not be sampled completely. For example, we have aliasing errors and temperature drift as well as errors of parameters determined in repeated calibrations. These errors average with the number of calibrations or the number of measurements obtained at the same conditions and parameters. $t_p(\nu)$ is the p -% point of the student distribution that depends on the number ν of degrees of freedom, $\nu_x = N_x - 1$, for x being δ or σ . Note that for $p = 0.68$ at 1σ level, $t_p < 1$ for which the total error is smaller than the single errors in Figure 9. For all δ_i determined from N_i individual measurements x_j , each with a total error σ_j , it is common to consider the (weighted) error of the mean

$$\delta = \left[\sum_{j=1}^{N_i} \frac{\sigma_j^{-2} (x_j - \bar{x}_w)}{\sum_{k=1}^{N_i} \sigma_k^{-2}} \right]^{\frac{1}{2}}, \quad \text{with } \bar{x}_w = \frac{\sum_{j=1}^{N_i} \sigma_j^{-2} x_j}{\sum_{k=1}^{N_i} \sigma_k^{-2}}, \quad (10)$$

where we have introduced the weighted mean \bar{x}_w . While for experimental data points, weighted quantities can differ from unweighted ones due to singular noise events, in the present estimation of the error to the total mean, it holds that $\sigma_j = \sigma \forall j$ for which Equation (10) reduces to the geometric mean and its error.

With the seismic and detection errors updated, we achieve the prospective error budget in Figure 9c,d. We replot the errors discussed in Ref. [99] with only the seismic and detection errors updated. All the detection errors have a mild dependence on separation due to the adaptation of V_{exc} . For details on other errors, see the detailed discussion in Ref. [99]. The detection error is the main limitation at separations $a \gtrsim 10 \mu\text{m}$, for which the updated error budget presented here improves the prospects for measurements at large separations. Deformation errors, including the sag of the surfaces due to the measured pressures and gravity, are the second-strongest error contribution at small consider replacing. separations after residual patch effects. Using Talbot interferometry on the actual plate surfaces, we are able to measure the deformation and take it into account, for which the error given here (green line), which considers a *residual* spherical deformation of 4 nm amplitude, can be considered as an absolute worst case. Note further that local differences in the Xe density in the gas pressure modulation measurements near the surfaces due to temporal adsorption, rarefaction, or other stratification effects would cause only negligible errors not influencing the budget presented here. As the present error budget is still partially based on models,

we nonetheless present the updated prospects below considering the previous worse error budget.

4. Prospective Results

Recently [99], we gave prospective limits on axion-like interactions, Symmetron DE interactions, and measurements of the Casimir effect. Although the error budget in Section 3 demonstrates a further improvement in both the pressure and pressure gradient measurements, we conservatively keep the baseline of 1 nN/m^2 and 1 mN/m^3 . In this section, we present updated calculations regarding equilibrium and non-equilibrium Casimir forces and limits on a range of DE interactions with updated theoretical methods and consider the final design. The latter limits supersede the previous ones in Refs. [99,102].

4.1. Casimir Effect

Casimir force experiments open an extensive window into the quantummechanical behavior of physical systems. Since the prediction of the Casimir effect in 1948 [36], the theoretical framework characterizing this phenomenon has substantially evolved, and nowadays it is situated at the intersection of very diverse areas of physics, ranging from material science and statistical physics to quantum field theory. An accurate measurement of the Casimir force has, therefore, the potential not only to offer more information about the behavior of the system’s quantum fluctuations but also to test how different theories merge together, possibly providing a new window into fundamental physics.

One of the most remarkable aspects of the Casimir interaction is its dependence on the involved materials, the thermodynamic state, and the geometry of the system. Indeed, investigations have shown that by modifying these properties the Casimir force can be tuned, with interesting implications both for fundamental research and modern quantum technologies. Below, we provide a brief review of how these three aspects affect the Casimir interaction and the role that CANNEX may play in approaching them separately or also simultaneously.

4.1.1. Material Properties

Already from Casimir’s original paper on the force between two parallel perfect reflecting plates, it appears clear that the properties of the materials involved in the system can play a role in determining the behavior of the force. The work by Evgeny Lifshitz in 1955 [142] underlined this aspect even further. The celebrated Lifshitz formula,

$$P_{\text{Lif}}(a, T) = -\text{Im} \int_0^\infty \frac{d\omega}{\pi} \int \frac{d\mathbf{k}}{(2\pi)^2} \sum_\sigma \hbar \coth \left[\frac{\hbar\omega}{2k_B T} \right] \kappa \frac{r_1^\sigma(\omega, k)r_2^\sigma(\omega, k)e^{-2\kappa a}}{1 - r_1^\sigma(\omega, k)r_2^\sigma(\omega, k)e^{-2\kappa a}}, \quad (11)$$

provides the force per unit of area between two parallel planar structures separated by a distance a in terms of the planes’ reflection coefficients $r_i^\sigma(\omega, k)$. In Equation (11), σ defines the polarization (TE or TM) of the electromagnetic field, \mathbf{k} is the component of the wave vector parallel to the surfaces, $k = |\mathbf{k}|$ and $\kappa = \sqrt{k^2 - \omega^2/c^2}$ ($\text{Im}[\kappa] \leq 0; \text{Re}[\kappa] \geq 0$) and k_B denotes the Boltzmann constant. Considering materials with different reflection properties, several experimental groups have shown that the Casimir pressure can be substantially modified [46,47,49,50,54,57,143–146]. In particular, leveraging the interplay between optical properties and geometry (see also Section 4.1.2), not only the strength but also the sign of interaction can be changed [146–150].

One of the most representative and, at the same time, most controversial examples highlighting the relevance of material properties in the Casimir interaction is provided by their role in determining the finite-temperature correction to the Casimir force between parallel metal plates. For more than two decades now this has been a topic of intense investigation and debate. A description of the metal in terms of the commonly used Drude model,

$$\varepsilon(\omega) = 1 - \frac{\Omega^2}{\omega(\omega + i\gamma)}, \quad (12)$$

where Ω is the plasma frequency and γ a non-zero dissipation rate, gives rise to a temperature dependence of the force, which considerably differs from that obtained for perfect reflectors [151]. (For recent reviews on the debate around the thermal correction of the Casimir force, see [152,153] and references therein.) This is particularly relevant at large temperatures and/or distances where the force predicted by the Drude model is half the value obtained for perfect reflectors. Puzzlingly, such behavior is not found in many precise measurements of the Casimir force [49,59,145,154–156]. Experiments where the reduction in strength predicted by the Drude model was observed [63,144,157] needed to consider systematic effects, such as the presence of patch potentials in their setups [127,158,159]. Perhaps even more surprising is that the experiments disagreeing with the prediction of the Drude model (12) are in very good agreement with the result obtained by setting $\gamma = 0$ in the same model. This quite suggestive behavior highlights the role of the material properties and, for the present model, of dissipation in the controversy. More generally, within the Lifshitz framework, the disagreement between the experimental measurements and theoretical predictions obtained using the Drude model is related to the description of the optical response of metals at low frequency. This can substantially affect the contribution of the transverse electric ($\sigma = \text{TE}$) polarization [160–163]. More specifically, in the limit of large separations a , the difference between the two models discussed here arises because for the Drude model with $\gamma \neq 0$, in agreement with the Bohr–van Leeuwen theorem [164,165], the contribution of the TE-polarization in Equation (11) vanishes at large distance [163]. The model resulting by setting $\gamma = 0$ in Equation (12), often called the plasma model, is equivalent to a relatively simple description of a superconductor [166], which does not fulfill the Bohr–van Leeuwen theorem.

A complementary perspective can be given in terms of specific solutions of the Maxwell equations corresponding to purely dissipative (i.e., over-damped) modes [167], which are physically connected with the Foucault current or ‘eddy current’ in the interior of the plate’s material [162,168–170] (see also Refs. [171,172] for related investigations). These modes have pure imaginary frequencies (see Figure 10) and their dynamics are described by a diffusion equation. The diffusion constant is given by $D = \gamma\lambda^2$, where γ is the dissipation rate of the metal and $\lambda \equiv c/\Omega$ is the plasma penetration depth. The electromagnetic field associated with these currents is evanescent in vacuum, i.e., it exponentially decays with the distance from the surface of the metal. In superconductors, eddy current modes are suppressed by the Meissner effect, explaining the behavior of the Casimir effect with the plasma model. It was shown that the eddy current contribution alone accounts for the difference in the prediction for the Casimir effect at finite temperature obtained with the Drude and the plasma model [162,168]. In particular, in agreement with earlier observations [160,161], the largest contribution of these modes arises for the TE-polarization [163]. Eddy currents are also helpful to understand why accounting for spatial dispersion in light–matter interaction [173] can remove pathologies occurring in the thermodynamic behavior of the Casimir entropy when the Drude model is used [65,174–177]. In particular, they enable discerning among the different models describing spatial dispersion, showing also that not all of them are able to eliminate these inconsistencies [170].

Due to the accuracy and the flexibility of the measurements, as well as the possibility to approach the system in its simplest geometry (two parallel plates), CANNEX allows approaching the study of the interplay between material properties and the Casimir effect from a new perspective. The same flexibility also allows probing the impact on the interaction of materials with special or exotic properties, such as magnetic materials [145,178,179], graphene [51,180–182], and others [183–186], using planar structures. This can offer new understandings for the resolution of the controversy and, in general, additional information about the behavior of the Casimir force in regimes and, in particular, for distances that were not explored before in experiments.

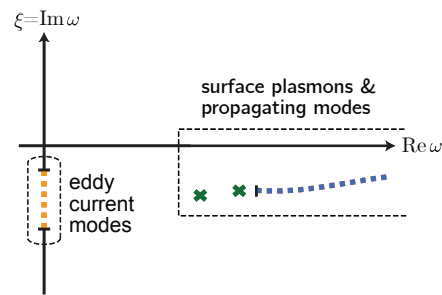


Figure 10. Schematic representation of the typical electromagnetic mode-frequencies vibrating within a planar cavity made by dispersive and dissipative metallic mirrors described in terms of the Drude model [167]. Due to dissipation and according to causality, all modes are resonances described by a complex frequency located in the lower half of the complex-frequency plane. Typical resonances include surface plasmons (green crosses) and cavity modes (blue dots) [187,188]. Due to their diffusive nature, the eddy currents are described in terms of a pure imaginary frequency and are, therefore, located along the negative imaginary axis [162,168].

4.1.2. The Geometry of the System

It was recognized early on that the Casimir effect can be substantially modified by changing the geometry of the involved objects. One of the most remarkable examples is probably the calculation of T. Boyer in 1968 predicting a repulsive Casimir force on a perfectly conducting spherical shell cavity [189] (see also Ref. [190] for recent evaluations with the same geometry). In the last decade, theoretical developments have shown how to efficiently compute the Casimir interaction in systems involving complex structures. A large variety of methods, ranging from semi-analytical [191–199] to full numerical [199–204], have been developed. The main drives of this progress have been, on the one side, the necessity to accurately interpret measurements of the Casimir force in realistic setups, and, on the other side, the ambition to deterministically tune the interaction. Controlling the Casimir force can help in reducing unwanted stiction in microscopic devices like MEMS and NEMS, and it can serve as an additional contactless mechanical actuator for similar devices [205,206].

Among the most studied geometries different from plane–plane originally considered by Casimir, one finds the plane–sphere configuration. As a matter of fact, this geometry has been for a long time the workhorse in experiments aiming to measure the Casimir force [37,38,156,205,207,208]. Considering a sphere in front of a plane indeed releases the constraint of parallelism, drastically simplifying the experimental setup. The price to pay is, however, a smaller signal and a more difficult interpretation of the measurement. The latter has for a long time relied on the so-called proximity force approximation, sometimes also called the Derjaguin approximation [207]. If the radius of the sphere is larger than the distance between the surfaces of the two objects, this approximation connects the sphere–plane Casimir force to the energy in the plane–plane configuration. Although previous experiments have directly investigated the plane–plane configuration [100,209], CANNEX is one of the first modern apparatuses designed to reexamine this geometry without strongly penalizing compromises between control, accuracy, and strength of the signal. This same characteristic and the flexibility of this setup can be employed in order to investigate from a new perspective the interaction between different planar structures, ranging from multilayer stacks to nanostructured surfaces, like periodic gratings [191,193–195,197,210–214] or more modern and complex arrangements, such as, for example, metasurfaces [215–217].

Specifically, the one-dimensional lamellar grating structure has already found its way into Casimir physics. Its relative simplicity has allowed for an accurate theoretical description of the Casimir interaction between two vacuum-separated gratings with commensurable periods. Within the framework of the scattering approach [218–221] the evaluation is essentially reduced to the calculation of the scattering matrices of the two nanostructured objects. For instance, the Casimir pressure at temperature T between

two parallel gratings with the same period p separated by the distance a can be obtained from [192,193].

$$P(a) = -4k_B T \sum_{l=0}^{\infty}{}' \int_0^{\infty} dk_y \int_0^{\pi/p} d\alpha_0 \partial_a \log \det \left[1 - \underline{\mathcal{R}}^L \mathcal{P}(a) \underline{\mathcal{R}}^R \mathcal{P}(a) \right]. \quad (13)$$

Here, \mathcal{P} are the matrices describing the propagation of the electromagnetic field in the vacuum between the gratings, and \mathcal{R} are the gratings' reflection matrices. The arrows under the reflection and propagation matrices indicate the direction of propagation of light, and their expression can be obtained using rigorous coupled wave approaches (RCWA), as in classical photonics [222]. The propagation matrices are diagonal in a plane-wave, Rayleigh basis (see for example [192] for explicit expressions). All these matrices are evaluated at the Matsubara imaginary frequencies, $\omega_l = i\zeta_l = i2\pi l k_B T / \hbar$ [223], and the primed sum indicates that the $l = 0$ term has half weight. A particular example of this geometry is represented in Figure 11, left, where the depth h of one of the gratings was reduced to zero to recover a plane. For a grating structure with specific geometrical parameters and comprised by a metal described using the Drude model, the predictions corresponding to Equation (13) are reported in Figure 11, right. At short separations, due to the finite grating conductivity, the pressure scales as $\propto a^{-3}$. At large separations, the pressure tends towards the value $\zeta(3)k_B T / (8\pi a^3)$, which is the same limiting behavior for the Casimir pressure predicted for the plane–plane configuration using the Drude model.

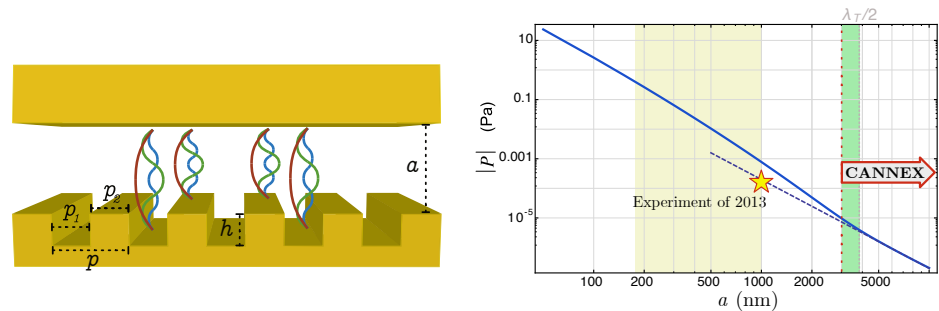


Figure 11. **Left:** A schematic representation of one of the simplest configurations for investigating the impact of nanostructuring on the Casimir effect: a one dimensional lamellar grating facing a plane. The grating can be characterized with the help of the following parameters: width of the grooves p_1 , width p_2 , and height h of the teeth. **Right:** Casimir pressure between a metallic grating and a metallic plane (see Ref. [194] for further details). The metal is modeled using the Drude model with $\Omega = 8.39$ eV and $\gamma = 0.043$ eV, corresponding to the values of gold. The grating is characterized by the following parameters: $p_1 = 160$ nm, $p_2 = 90$ nm, and height $h = 216$ nm. The temperature of the system is set to $T = 300$ K. At separations larger than the thermal wavelength [$\lambda_T = \hbar c / (k_B T)$], the pressure tends towards the value $\zeta(3)k_B T / (8\pi a^3)$ (dashed curve), which is the same limiting behavior for the Casimir pressure predicted for the plane–plane configuration using the Drude model. At short separations, the pressure is proportional to a^{-3} because of the finite grating conductivity. The yellow shadow region describes the distance range investigated in Ref. [213] and the star indicates the value of the Casimir pressure measured around 1 μm in the same experiment. See text for details.

Despite systems involving ‘simple’ one-dimensional grating structures having been actively investigated both theoretically [191,193–195,197,212,213] and experimentally [43,210,211,213,214,224], some disagreements between the predictions and measurements of the corresponding Casimir pressure remain. For example, an experiment reported in Ref. [213] measuring the Casimir force between a gold sphere and a one-dimensional gold grating at finite temperature has shown that the Casimir force can be tailored in a nontrivial way by modifying the grating’s period [213]. Conversely to comparable measurements involving a dielectric grating [210,211,214], however, the theoretical predictions and the experimental results do not agree, indicating once again the possibility that when metals are involved something in the physics of the system still needs to be understood.

In Figure 11, right, we depict the theoretical predictions for the Casimir pressure between a plane and a grating with dimensions quite similar to those used in Ref. [213], as well as the designated working range of the CANNEX setup. The distance range, as well as the value of the pressure measured for the largest plane–sphere separation in the experiment reported in Ref. [213], are also represented, showing that CANNEX has the potential to inspect a complementary regime. Specifically, the device’s accuracy of 1 nPa could allow to investigate the pressure behavior within a range of distances corresponding to the transition to the thermal regime. This is expected to occur for distances of the order of $\lambda_T = \hbar c / (k_B T) \simeq 7.6 \mu\text{m}$ (green shadowed region in Figure 11), considerably higher than the largest separation considered in many experiments. Shorter separations could be investigated using the same setup with a slightly more rigid sensor. This would reduce the sensitivity, but as the Casimir forces in this distance range scale as a^{-n} with n between 3 and 4, while other disturbing effects, such as patches or electrostatics scale with $2 \leq n < 4$, the precision of the measurement would not be reduced.

4.1.3. The Thermodynamic State of the System: Configurations out of Thermal Equilibrium

The Lifshitz theory of Casimir interactions assumes that the whole system is at thermal equilibrium at temperature T . Recent investigations have shown, however, that when non-equilibrium configurations are taken into account, interesting phenomena can occur [225–227]. Out-of-equilibrium configurations can be realized with different expedients, including temperature gradients [66,225,228–230], moving objects [226,227], and also scenarios where external lasers act on a system initially in thermal equilibrium [231,232]. In many experiments, non-equilibrium physics are more the rule than the exception. In particular, the presence of different temperatures in the system can considerably affect the Casimir force’s behavior, giving rise to repulsive interactions and different power-law dependencies [66,225,229,230]. In addition to providing alternative ways to tailor Casimir forces, non-equilibrium configurations also offer opportunities to differently investigate the interplay between the Casimir interaction, the material’s optical properties, and the system geometry, possibly adding new relevant information for solving some of the issues mentioned above.

The high symmetry of the plane–plane configuration has allowed in Ref. [228] for a detailed calculation of the thermal non-equilibrium Casimir pressure acting on the inside faces of two planar plate configuration. As in the Lifshitz Formula (11), the planes can be characterized using the corresponding reflection coefficients r_i^σ , $i = 1, 2$. If each planar plate is assumed to be locally in thermal equilibrium at the temperature T_i within an environment that is kept at temperature T_3 , the total Casimir pressure on the plate i can be written as follows [66]:

$$P^{(i)}(a, T_1, T_2) = \frac{1}{2} \sum_{i=1,2} \left[P_{\text{Lif}}(a, T_i) + \frac{4\sigma_{\text{SB}}}{3c} T_i^4 \right] + \Delta P_{\text{neq}}(a, T_1, T_2) - \frac{2\sigma_{\text{SB}}}{3c} (T_i^4 + T_3^4), \quad (14)$$

where σ_{SB} is the Stefan–Boltzmann (SB) constant. The first term is equivalent to the average equilibrium pressure predicted by the Lifshitz formula and the SB law evaluated at the two different plates’ temperatures. The last term is the pressure of the environmental radiation on the plate i (for both plates, we assumed the external surfaces to be blackened [66,233]). The second term, ΔP_{neq} , is a pure non-equilibrium contribution: It can be written as the sum of two contributions arising from evanescent and propagating waves, respectively. Moreover, ΔP_{neq} is non-zero only if the two planar structures are different such that $r_1^\sigma \neq r_2^\sigma$ and it is odd if the plates’ temperatures are swapped $\Delta P_{\text{neq}}(a, T_1, T_2) = -\Delta P_{\text{neq}}(a, T_2, T_1)$ (see Appendix B for more details).

The direct connection between the detailed expression for $P^{(i)}(a, T_1, T_2)$ and their reflection coefficients (from the inside of the resulting cavity) allows for some flexibility in the description of the planar structure and, in particular, for the consideration of multilayered structures [234,235]. An example is given in Figure 12, left, which represents a typical configuration used in the CANNEX setup. A possible measurement scheme in-

volves the upper plate, which is kept at equilibrium with the surrounding environment, i.e., $T_1 = T_3 = T_{\text{eq}} = 293$ K, while the lower plate is cooled by $\Delta T_2 = 10$ K during a first measurement campaign and then warmed by the same quantity during a second campaign. According to Equation (14), the difference between the two sets of measurements considering the pressures acting on the CANNEX's sensor plate is given by

$$P_{\text{diff}}^{(1)}(a) = P^{(1)}(a, T_{\text{eq}}, T_{\text{eq}} + \Delta T_2) - P^{(1)}(a, T_{\text{eq}}, T_{\text{eq}} - \Delta T_2). \quad (15)$$

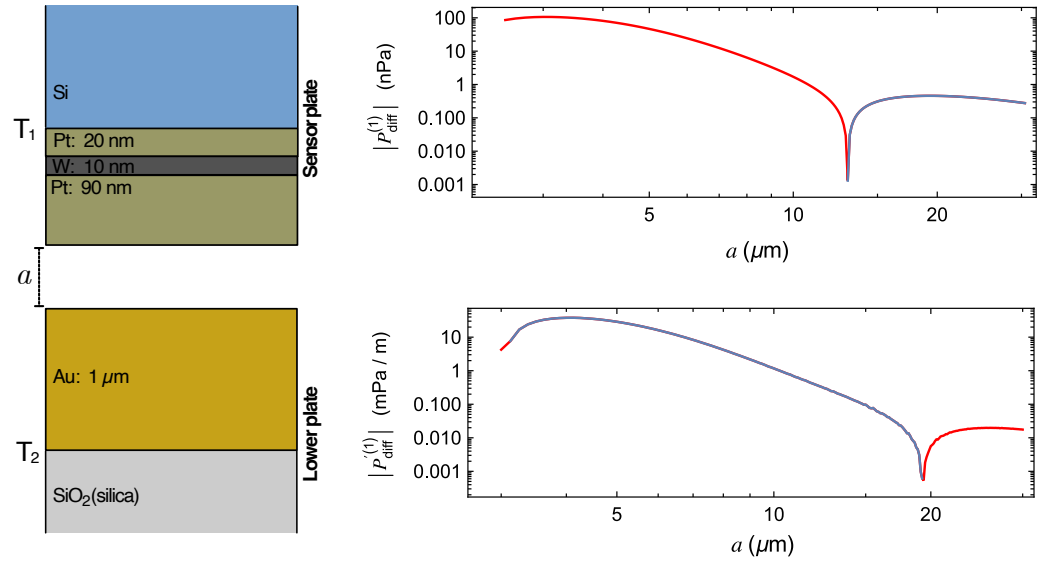


Figure 12. **Left:** Schematic configuration of the two planar multilayer structures which shall be used in the CANNEX setup for interfacial measurements (not to scale). The lower plate is made by a $1 \mu\text{m}$ thick gold layer over a silica substrate. The upper/sensor plate is made of a platinum/tungsten/platinum multilayer deposited over a silicon structure. For describing the metals, we use the Drude model (12) with the following parameters: $\Omega_{\text{Au}} = 8.39$ eV, $\gamma_{\text{Au}} = 43.4$ meV [213]; $\Omega_{\text{Pt}} = 5.48$ eV, $\gamma_{\text{Pt}} = 86.5$ meV [236]; $\Omega_{\text{W}} = 6.41$ eV, $\gamma_{\text{W}} = 60.4$ meV [237]. For simplicity, we described the silicon and silica layers using the same dielectric function described in terms of the Lorentz model (A8), with the following parameters: $\epsilon_0 = 11.87$, $\epsilon_\infty = 1.035$, $\Omega_0 = 4.346$ eV, and $\Gamma = 43.5$ meV [238]. **Right:** Differential pressure $P_{\text{diff}}^{(1)}(a)$ (see Equation (15)) (**top**) and its gradient (**bottom**) corresponding to out-of-equilibrium configurations, where $T_1 = T_3 = T_{\text{eq}} = 293$ K, while the lower plate's temperature is in one case at temperature $T_2 = T_{\text{eq}} + \Delta T_2$, and $T_2 = T_{\text{eq}} - \Delta T_2$ in the other case. The value of ΔT_2 is taken to be 10 K corresponding to the temperature difference, which can be obtained in CANNEX. The red curves indicate a negative difference while the blue curves describe positive ones. See text for more details.

Since CANNEX can simultaneously measure both the pressure and the pressure gradient, in Figure 12, right, we plot the prediction corresponding to these two quantities for the differential measurement described above and in relation to the material configuration in Figure 12, left. For comparison, in Figure 13, we also report the corresponding equilibrium values ($T_i = T_{\text{eq}} = 293$ K) for both the pressure and its gradient calculated using the Lifshitz Formula (11). Notice that over a range of 3–30 μm , we can predict a maximal value for $P_{\text{diff}}^{(1)}(a)$ of about -0.1 mPa for a distance $a = 3$ to $4 \mu\text{m}$ and a change in sign from negative ($P^{(1)}(a, T_{\text{eq}}, T_{\text{eq}} + \Delta T) < P^{(1)}(a, T_{\text{eq}}, T_{\text{eq}} - \Delta T_2)$) to positive ($P^{(1)}(a, T_{\text{eq}}, T_{\text{eq}} + \Delta T_2) > P^{(1)}(a, T_{\text{eq}}, T_{\text{eq}} - \Delta T_2)$) around $a = 13 \mu\text{m}$. This means that for sufficiently short distances, the pressure measured by the sensor plate when the lower plate is warmer than the environment is larger than the corresponding pressure measured for a plate which is cooler than the environment. This balance, however, changes as a

function of the separation between the plates. Coherently, Figure 12, bottom right, shows that the pressure gradient, in the range of distance considered in our analysis, changes sign between 3 and 4 μm and again around 20 μm .

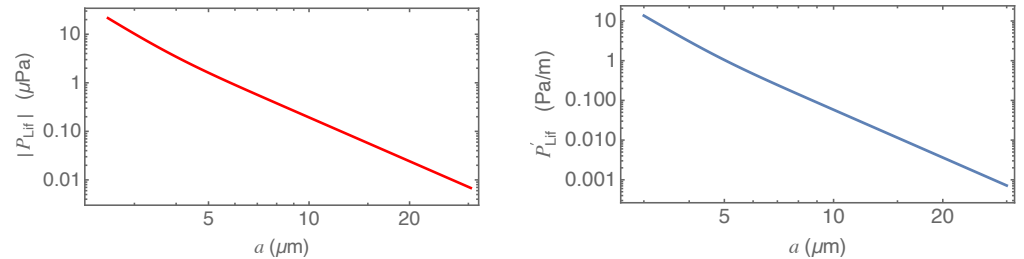


Figure 13. Pressure (left) and its gradient (right) in equilibrium at temperature $T = T_{\text{eq}} = 293$ K for the configuration depicted in Figure 12. The pressure is negative (attraction) while its gradient is positive. The values of both quantities are evaluated using the Lifshitz Formula (11) (see Appendix B) and the material parameters reported in the caption of Figure 12.

4.2. Scalar Dark Energy

A common approach to solving the cosmological constant problem proposes the existence of new hypothetical scalar fields. However, these scalar fields typically introduce so-called fifth forces. Since such additional forces are tightly constrained by ongoing high-precision experiments, these scalar fields must incorporate some kind of ‘screening mechanism’ to avoid conflict with current experimental results. Several such screening mechanisms have been suggested, such as the chameleon [239,240], K-mouflage [241,242], Vainsthein [243], and Damour–Polyakov [244] mechanisms. All these mechanisms have in common that the fifth force is suppressed in high-density environments. For this reason, high-precision vacuum experiments, such as CANNEX, are ideal tools to probe these hypothetical forces.

The investigations in this paper cover the environment-dependent dilaton [245,246], symmetron [247–249], and chameleon field theories [250]. Notably, the self-interaction potential of the dilaton finds its theoretical origin in the strong coupling limit of string theory [251–253]. The corresponding screening mechanism is highly sensitive to the parameter values and the corresponding behavior has been investigated in detail in [105]. In contrast, symmetrons, resembling the Higgs, employ spontaneous symmetry breaking to realize a screening mechanism. In low-density regions, the field is in its spontaneously broken phase and, hence, acquires a non-vanishing vacuum expectation value (VEV), resulting in a fifth force. However, in high-density regions, the symmetry is restored and the fifth force vanishes. Still another screened scalar field theory is the chameleon with a screening mechanism, which increases the mass in dense environments (see, e.g., [250,254] for reviews concerning the symmetron and chameleon field).

While the chameleon and the symmetron field have been constrained by several experiments, such as atomic interferometry [255,256], Eöt–Wash experiments [257], gravity resonance spectroscopy [247,248,258], precision atomic measurements [259], and others [250,254], more recent investigations on the dilaton model have so far provided only constraints by gravity resonance spectroscopy, lunar laser ranging, and neutron interferometry [105,260]. Concerning CANNEX, prospective constraints have been derived for either of these fields [99,102,105]. However, these earlier analyses suffer from various shortcomings, e.g., the chameleon analysis has neglected the vacuum region above the setup’s movable mirror in the calculation of the induced pressure. Furthermore, the chameleon parameter Λ has been fixed to the specific value of 2.4 meV. As of now, pressure gradients have not been considered and investigations related to chameleons and symmetrons have not taken variations in the vacuum pressure and plate separation into account. Herein, the most rigorous and complete investigation, closing the discussed gaps, has been carried out.

4.2.1. Theoretical Background

The effective potential of the scalar fields considered herein is given by

$$V_{\text{eff}}(\phi; \rho) = V(\phi) + \rho A(\phi), \quad (16)$$

where $V(\phi)$ is the self-interaction potential and $A(\phi)$ the ‘Weyl factor’ providing the coupling to the ambient matter density ρ . For all models investigated in this paper, $A(\phi) \simeq 1$ holds. The dilaton (D), symmetron (S), and chameleon (C) models are defined by [250,254]

$$\begin{aligned} V_D(\phi) &= V_0 e^{-\lambda_D \phi / m_{\text{pl}}}, \\ V_S(\phi) &= -\frac{\mu^2}{2} \phi^2 + \frac{\lambda_S}{4} \phi^4, \\ V_C(\phi) &= \frac{\Lambda^{n+4}}{\phi^n}, \end{aligned} \quad (17)$$

together with the Weyl factors

$$\begin{aligned} A_D(\phi) &= 1 + \frac{A_2}{2} \frac{\phi^2}{m_{\text{pl}}^2}, \\ A_S(\phi) &= 1 + \frac{\phi^2}{2M^2}, \\ A_C(\phi) &= e^{\phi/M_c} \simeq 1 + \frac{\phi}{M_c}. \end{aligned} \quad (18)$$

The dilaton field is characterized by three parameters, i.e., V_0 , an energy scale associated with DE, λ_D , a numerical constant, and A_2 , a dimensionless coupling parameter. Then, m_{pl} denotes the reduced Planck mass. Furthermore, the symmetron parameters are given by the tachyonic mass μ , a dimensionless self-coupling constant λ_S , and M as a coupling constant to matter with a dimension of a mass. Finally, for chameleons, $n \in \mathbb{Z}^+ \cup 2\mathbb{Z}^- \setminus \{-2\}$ determines the power of the self-interaction potential, Λ defines an energy scale that is sometimes related to DE, $M_c = m_{\text{pl}}/\beta$ is a coupling constant with dimension of a mass, and β being the dimensionless coupling. To justify the neglect of any higher-order couplings, the analysis herein is restricted to

$$\frac{A_2}{2} \frac{\phi^2}{m_{\text{pl}}^2}, \frac{\phi^2}{2M^2}, \frac{\phi}{M_c} \ll 1. \quad (19)$$

The resulting equations of motion are given by

$$\square\phi + V_{\text{eff},\phi}(\phi; \rho) = 0, \quad (20)$$

while the non-relativistic force acting on a point particle with mass m is [249]

$$\vec{f}_\phi = -m \vec{\nabla} \ln A(\phi). \quad (21)$$

For the analysis herein, the CANNEX setup is approximated in one dimension along the z -axis as follows: The fixed lower mirror is located at $z < 0$ with density $\rho_M = 2514 \text{ kg/m}^3$, while the movable upper mirror with density ρ_M and thickness $D = 100 \text{ }\mu\text{m}$ is located at $a < z < a + D$ with $3 \text{ }\mu\text{m} \leq a \leq 30 \text{ }\mu\text{m}$. Between both mirrors and above the upper mirror, vacuum prevails with an adjustable density of $5.3 \times 10^{-12} \text{ kg/m}^3 \leq \rho_V \leq 2.6 \text{ kg/m}^3$. To justify the neglect of the vacuum chamber above the upper plate, an interaction range cut-off at 1 mm has been applied in our analysis. For even greater interaction ranges, the matter content of the vacuum chamber induces a pull on the upper plate, thereby

effectively lowering the pressure on the upper plate. Hence, the force on the upper mirror is given by [261].

$$\vec{f}_\phi = -\rho_M \int_{-\infty}^{\infty} dx \int_{-\infty}^{\infty} dy \int_a^{a+D} dz \partial_z \ln A(\phi) \vec{e}_z, \quad (22)$$

and the pressure in the z-direction on the movable mirror is, therefore,

$$\begin{aligned} P &= \rho_M (\ln A(\phi(a)) - \ln A(\phi(a + D))) \\ &\simeq \rho_M (A(\phi(a)) - A(\phi(a + D))). \end{aligned} \quad (23)$$

If the field reaches its potential minimum value ϕ_M inside the upper mirror, the latter expression can be simplified further to [105]

$$P = \frac{\rho_M}{\rho_M - \rho_V} (V_{\text{eff}}(\phi_V, \rho_V) - V_{\text{eff}}(\phi_0, \rho_V)), \quad (24)$$

where $\phi_0 := \phi(a/2)$ is the value of the scalar field in the middle between both plates. This assumption, however, is not very restrictive, since the screening mechanism typically suppresses the field inside the mirror such that the field can effectively reach its potential minimum value. We have checked explicitly that this assumption is actually satisfied for parameter values where limits were set. In order to obtain ϕ_0 , the following differential equation has to be solved:

$$\frac{d^2\phi}{dz^2} - V_{\text{eff},\phi}(\phi(z), \rho(z)) = 0. \quad (25)$$

Since the field effectively reaches its potential minimum values inside both mirrors, $\phi(z) = \phi_M$ has been set as a boundary condition deep inside the mirrors. For some cases, analytical solutions to this equation exist [248,249,262]. However, for the new limits obtained herein, we solved this equation numerically. Whenever possible, we performed a comparison with analytical solutions as an additional check. This allowed the reliable computation of the pressure as a function of the plate distance as well as the vacuum density. The pressure gradients can straightforwardly be computed by using

$$\partial_a P \simeq \frac{P(a + \delta) - P(a - \delta)}{2\delta}, \quad (26)$$

for small enough δ .

4.2.2. Dilaton Constraints

The resulting constraints for the dilaton field theory are shown in Figure 14. CANNEX will indeed be able to probe parts of the dilaton parameter space that have not been excluded by existing experiments. However, adding pressure gradients to the existing analysis does not improve the constraints that can be obtained with CANNEX.

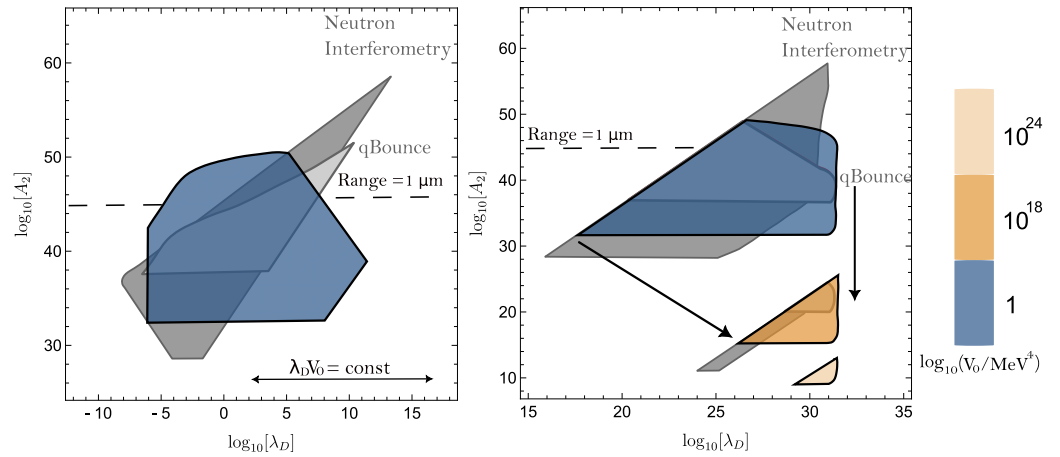


Figure 14. Prospective CANNEX limits on dilaton interactions (in color) alongside the already existing constraints from q Bounce and neutron interferometry (assuming the Fermi-screening approximation [105]). The combined constraints from pressure and pressure gradient measurements are plotted. The parameter space of the dilaton field naturally falls into two regimes. **Left:** For small values of the parameter λ_D , the model has an additional parameter symmetry, such that the physics only depend on the product $\lambda_D V_0$ rather than λ_D or V_0 individually. Therefore, the shape of the excluded parameter areas remains the same for increasing V_0 , but only shifts towards lower values of λ_D . **Right:** For large values of λ_D , the dilaton approximately depends only on $A_2 \ln(V_0/\rho)$, but not on their individual values. Therefore, the excluded parameter areas shift towards lower A_2 for increasing V_0 without changing their shape. However, in contrast to the small λ_D regime, the areas are cut by an ever stronger cut-off as indicated by the arrows.

4.2.3. Symmetron Constraints

The resulting constraints for the symmetron field theory are shown in Figure 15. For too small values of μ , the field vanishes entirely and with it the induced pressure as well. This happens approximately for [248]

$$\sqrt{\mu^2 - \frac{\rho V}{M^2} a} < \frac{\pi}{2}. \quad (27)$$

For too large μ values, however, the force between the plates gets very weak. Hence, CANNEX can only probe a small interval of μ values. It has been found that in some cases the pressure gradients provide better constraints than the pressure itself and that the plate separation has strong impact on the limits. The analysis herein significantly improves on the analysis in Ref. [99]. Specifically, for $\mu = 1$ eV, corresponding roughly to an interaction range of $0.2 \mu\text{m}$, the CANNEX limits have previously been underestimated by a factor of $\sim 10^{20}$ on the λ_S axis, since a plate separation of $10 \mu\text{m}$ was assumed. Clearly, a smaller plate separation of $3 \mu\text{m}$ yields an enormously stronger pressure and consequently better constraints. Due to the same reason, previous limits for $\mu = 10^{-0.5}$ eV have also been underestimated by several orders of magnitude. Based on Equation (27), in combination with a value of $a = 10 \mu\text{m}$, the conclusion was drawn in [99] that CANNEX can probe only parameter values $M > 10^2$ GeV for $\mu = 10^{-3/2}$ eV, resulting in weak limits. However, increasing a to $20 \mu\text{m}$ removes this constraint and more substantial limits with $M > 10^{-4.5}$ GeV can be obtained, resulting in significant improvements with respect to the existing constraints. Indeed, CANNEX will be able to improve upon existing table-top experiment constraints by several orders of magnitude.

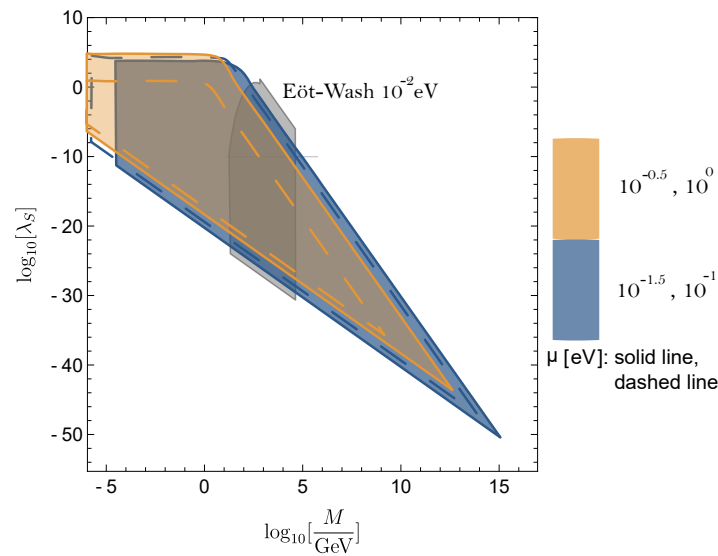


Figure 15. Prospective constraints on symmetron interactions from CANNEX. The colored areas refer to the constraints for $\mu \in \{10^{-1.5}, 10^{-0.5}\}$ eV, the colored dashed lines enclose the constraints for $\mu \in \{10^{-1}, 10^0\}$ eV, as indicated. Only the combined constraints from pressure and pressure gradient measurements are shown, alongside already existing constraints.

4.2.4. Chameleon Constraints

Since each value of n is typically considered as a separate chameleon model, the analysis herein has been restricted to two cases. The most commonly studied model is $n = 1$ and, hence, limits have been computed for $n = 1$ and varying Λ . However, within the current limits of the applied theoretical analysis, no new parts of the parameter space can be probed using CANNEX. Nevertheless, fixing $\Lambda = 2.4$ meV to the DE scale and varying $1 \leq n \leq 10$, which is also commonly studied, will indeed result in narrowing the gap between the existing limits, as shown in Figure 16.

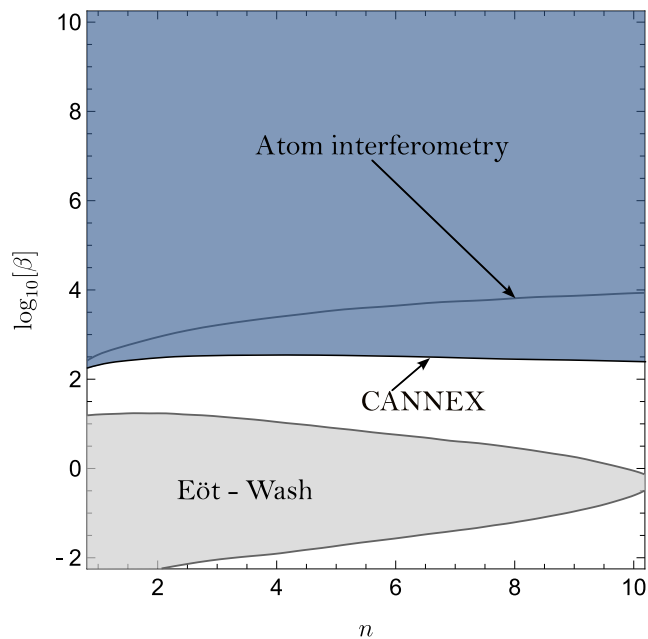


Figure 16. The blue area shows the combined prospective constraints of pressure and pressure gradient measurements on chameleon interactions resulting from CANNEX, while gray areas indicate parameter combinations already excluded by torsion balances and atom interferometry. The parameter Λ has been fixed here to the DE scale of 2.4 meV. See text for details.

5. Discussion

CANNEX has completed its design phase and is about to be realized, with the first results expected in 2024. It is the first experiment to perform highly accurate measurements of both interfacial and gravity-like forces and force gradients in the distance regime 3–30 μm with truly plane parallel plates. This geometry increases the sensitivity to distance-dependent forces by several orders of magnitude with respect to the curved interacting surfaces used in most other experiments. High accuracy naturally demands control of various disturbing effects. We have designed and (partially) tested thermal control at the (sub-)mK precision level both in thermal equilibrium and with the two interacting plates being out of thermal equilibrium by 10 °C. We also designed a six-axis passive seismic attenuation system, in situ surface charge and impurity removal by UV irradiation and Ar ions, purely optical detection systems, and an in situ Kelvin probe/AFM setup to characterize the surfaces. Importantly, our calibration procedures rely on references that can be traced to metrological standards (wavelengths, voltages, frequencies).

In the present paper, we give a final update on the design and measurement procedures, on the basis of which we compute a detailed update of the detection error and seismic disturbances. Using specifications of and noise measurements with the actual devices, we find that the error at large separation $a \gtrsim 15 \mu\text{m}$ can realistically be reduced by factors 2 and 30 in the pressure and its gradient, respectively, with respect to the previous error budget in Ref. [99].

CANNEX can be operated in different configurations. In the interfacial configuration, the two plates directly face each other, which allows us to measure the Casimir forces, and the hypothetical screened scalar DE forces. Measuring the former at the percent level at separations both smaller and larger than the thermal wavelength allows us for the first time to probe the transition from a predominantly quantum mechanical origin to a thermal origin in the Casimir force at high accuracy. The respective data may lead to further insights regarding longstanding problems regarding the role of dissipation and locality in the description of the dielectric response of metals. CANNEX could also perform the first quantitative measurements of Casimir forces out of thermal equilibrium, thereby testing the respective theory. Eventually, the plates can easily be modified by structuring. Thanks to control of parallelism at the μrad level, gratings or cylinders at arbitrary angles could be investigated, thereby generating high-precision data that can be used to further verify theoretical approaches currently disagreeing with the measurement results for such geometries. While the Casimir force is a worthwhile subject to study, it also poses a problem if we aim to measure screened scalar DE forces which have a similar distance dependence, but in comparison, several orders of magnitude lower strength. An electrostatic shield would entirely block these interactions. For this reason, we adapt our measurement procedure by remaining in interfacial configuration at the same surface separation but changing the ambient pressure of the Xe gas. In the presence of the gas, electrostatic, Casimir and gravitational forces only show a negligible and calculable increase, while screened DE forces would decrease in strength. In a relative measurement with and without Xe, our sensitivity to such hypothetical forces is maximized. Here, we have presented updated prospective exclusion graphs for the most prominent representatives of screened scalar fields: dilatons, symmetrons, and chameleons. The new calculations properly take into account the finiteness and geometry of the interacting objects, the formation of the field within the vacuum chamber, and the validity limits of the theory—aspects that have mostly been neglected in the literature. For all three scalar fields, even considering only the most conservative error budget, CANNEX will be able to extend the present limits by several orders of magnitude.

The second possible configuration is the one of Cavendish, where a thin flat conducting shield is added between the two plates in order to remove electrostatic and Casimir forces from the balance. In this configuration, volume-sourced forces, such as gravity or hypothetical fifth forces between fermions in the two plates, can be measured with high sensitivity. As we now reconfirm the previous error budget and prospective limits on

a variety of such forces that have been presented recently [99], we do not update these data here but refer to the literature [99]. With this in mind, CANNEX is considered to be able to measure gravity (and thereby Newton's constant, G) at the 10%-level in a distance regime down to 10 μm with active masses of roughly 30 mg, thereby probably exceeding recent experiments with torsion balances and spherical objects probing in this direction. We remark that, since the thick metal coatings on the plates of CANNEX have densities that exceed those of the carrier material by an order of magnitude, the effective separation between the masses sourcing the gravitational interaction lies close to the actual surface separation, in stark difference to spherical objects.

Author Contributions: Conceptualization, R.I.P.S., H.F., M.P. and F.I.; methodology, R.I.P.S. and M.P.; software, H.F., R.I.P.S. and R.A.S.; design and simulation: I.G., A.B., R.A.S., H.H. and R.I.P.S.; formal analysis, H.F., H.H. and R.I.P.S.; writing—original draft preparation, H.F., R.A.S., H.H., F.I. and R.I.P.S.; writing—review and editing, R.I.P.S., M.P., R.A.S., I.G. and A.B.; visualization, R.A.S. and R.I.P.S.; supervision, M.P. and R.I.P.S.; project administration, R.I.P.S.; funding acquisition, R.I.P.S. and M.P. All authors have read and agreed to the published version of the manuscript.

Funding: This research was funded by the Austrian Science Fund (FWF) under grant No. P 36577-N and P 34240-N.

Data Availability Statement: Data are contained within the article.

Acknowledgments: The authors thank Roman Gergen, Heinz Matusch, Andrzej Pelczar, Thomas Dokulil, and Piotr Suprunowicz for technical support, Max Maichanitsch for analyses of the SAS design, and Hartmut Abele for administrative support. The previous version of this experiment was funded by the Netherlands Organization for Scientific Research (NWO) and donations via the CANNEX crowd funding campaign by ASML and others.

Conflicts of Interest: The authors declare no conflicts of interest.

Abbreviations

The following abbreviations are used in this manuscript:

AC	Alternate Current
AFM	Atomic Force Microscope
AM	Amplitude Modulation
ATI	Atominstitut
CANNEX	Casimir And Non-Newtonian force EXperiment
COBS	Conrad OBServatory
CKM	Cabibbo–Kobayashi–Maskawa matrix
$CP(T)$	Charge Parity (Time)
cal	calibration
DAMA	DARk MATter
DAQ	Data Acquisition
DC	Direct Current
DE	Dark Energy
DM	Dark Matter
det	detector
ESS	Electrostatic Shield
EW	Evanescence Wave
exc	excitation
FEM	Finite Element Method
FM	Frequency Modulation
GAS	Geometric Anti-Spring
GR	General Relativity
KPFM	Kelvin Probe Force Microscopy
LED	Light-Emitting Diode
LI	Lock-In amplifier
Lif	Lifshitz

LVDT	Linear Variable Differential Transformer
Λ CDM	Lambda Cold Dark Matter model
MC	Monte Carlo
MEMS	MicroElectroMechanical System
NHNM	New High-Noise Model
NEMS	NanoElectroMechanical System
NLNM	New Low-Noise Model
PE	Peltier Element
PID	Proportional–Integral–Derivative
PLL	Phase-Locked Loop
PW	Propagating Wave
QCD	Quantum ChromoDynamics
QED	Quantum ElectroDynamics
RC	Resistor–Capacitor
RCWA	Rigorous Coupled Wave Approach
RMS	Root Mean Square
SAS	Seismic Attenuation System
SB	Stefan–Boltzmann
STS	S’Treckeisen Seismometer
SM	Standard Model
SNR	Signal-to-Noise Ratio
SpI	Spectral Integration
sig	signal
TD	Temperature Drift
TE	Transverse Electric
TM	Transverse Magnetic
TU	Technische Universität
UHV	Ultra-High Vacuum
UV	UltraViolet
WIMP	Weakly Interacting Massive Particle

Appendix A. Details of the Error Budget

In this Appendix, we give the models used for the calculation of various specific detection errors. For easier reference, we give them in a listed format below in their original units, while their effects on the respective measurement were listed in Tables 1–4.

As a general model for drift estimation, we assume a generic diurnal sinus model with $A_T = 0.1$ °C amplitude,

$$TD(t) = A_T \sin \frac{2\pi t}{24 \times 3600 \text{ s}}, \quad (\text{A1})$$

which over-estimates the actual temperature variation at COBS and statistically exceeds the error for a normal distribution by up to two orders of magnitude, but serves as a worst-case scenario. Table A1 lists further parameters assumed throughout the analysis. For RMS quantities x_{RMS} , we do not use a sharp cutoff at the bandwidth $1/\tau$ but integrate the spectrum $x(\omega)$ up to the maximum frequency ω_{max} with a first-order low-pass $T_I(\omega, \tau) = [1 + i\omega\tau]^{-1}$ yielding a more realistic estimate

$$x_{\text{RMS}}(\tau) = \left[\int_0^{\omega_{\text{max}}} \frac{d\omega}{2\pi} x^2(\omega) |T_I|^2(\omega) \right]^{\frac{1}{2}}. \quad (\text{A2})$$

Table A1. Global parameters assumed for the error analysis.

Parameter	Value	Description
τ_{DC}	2.0 s	integration time for a single DC voltage measurement
τ_{AC}	83.0 s	lock-in integration time for a single AC amplitude, frequency, or phase measurement
m	26.13 mg	effective dynamic sensor mass
ω_0	$2\pi \times 9.8 \text{ s}^{-1}$	free sensor resonance frequency
d	500 μm	nominal sensor cavity size
A	1.035 cm^2	sensor interaction area

Note again that all statistical errors where we do not have information on the spectral dependence, are time-averaged with $1/\sqrt{t/\tau}$, where τ is the time constant of the actual measurement as listed in Table A1. Systematic errors are averaged with $1/\sqrt{N_{\text{cal}}}$, where N_{cal} is the number of calibrations. We furthermore use the following indicators on statistics: ‘SpI’ means that spectral integration is performed according to Equation (A2) instead of regular time averaging (which includes low-frequency thermal drifts); ‘TD’ indicates that temperature drift is considered on this error according to Equation (A1).

Appendix A.1. DC Signals

Appendix A.1.1. Statistical Errors

DAQ noise, δ_{DAQ} . $\delta_{\text{DAQ}} = (\frac{1}{2} + 1) \times 10^{-7} \text{ V}$, containing the aliasing error from 34470A datasheet (first term). Keysight specifies [263] that the error given in the datasheet is for a temperature range of $\pm 1^\circ\text{C}$ and can be adapted if the real temperature variation is below that. We add 1 μV (second term) to account for noise picked up by cabling, estimated from actual measurements with the device.

Cavity size fluctuations, δd . We consider the RMS value according to Equation (A2) of the measured vertical vibration spectrum (see Figure 2) at COBS, the passive SAS $T_{x0x2}(\omega)$, and the sensor response $T_{z0z}(\omega)$ up to $1/\tau \text{ Hz}$ with $\tau \geq \tau_{DC}$. For $\tau = \tau_{DC}$, we have $\delta d = 8.5 \text{ pm}$.

Detector noise, δV_{det} . At $\lambda = 1550 \text{ nm}$, the detectors have a noise level of $0.19 \text{ pW}/\sqrt{\text{Hz}}$, at a total incident flux of 1 mW from the fiber interferometer into the detector (based on laser power and the optical properties of the cavity and fiber). We consider a 1 kHz bandwidth for the low-pass filter, resulting in 60 nV RMS noise.

Laser power fluctuations, δP_L (SpI). We received actual TLX1 intensity noise spectra from the manufacturer ranging from $1/(3 \times 3600) \text{ s}$ to 10 kHz. From these data, we determined a temperature correlation coefficient of $4.38 \pm 0.03 \times 10^{-6} \text{ K}^{-1}$, but not all of the drift is temperature-related. We, thus, use the measured Allan deviation as error here. For integration times 2, 83, and 1000 s, using Equation (A2), we obtain RMS relative intensity errors 5.53×10^{-4} , 1.51×10^{-5} , and 1.54×10^{-6} , respectively. To the first order, this error is canceled exactly by the normalization in Equation (7).

Laser bandwidth, $\delta \lambda_{\text{BW}}$. Given by the datasheet to be 10 kHz (0.08 fm), nominally, as the low-frequency limit of the frequency noise.

Laser frequency noise, $\delta \lambda_f$ (SpI). Derived from manufacturer data of the spectral frequency noise δf in the range 3 Hz–100 MHz. At lower frequencies, the noise is assumed to stay constant at $6.8 \text{ MHz}/\sqrt{\text{Hz}}$, which is three orders of magnitude larger than the specified linewidth but serves as a worst-case estimate. We convert these data to wavelength noise by $\delta \lambda_f = (\lambda^2/c)\delta f$ for the mean wavelength $\lambda = 1590 \text{ nm}$ after integration over the spectrum as described at the start of Appendix A, resulting in RMS values 6.28 fm, 1.04 fm, and 0.31 fm for $\tau = 2, 83$ and 1000 s, respectively.

Reference cavity signal, δV_R . Respective values are obtained from the total δV_{DC} without seismic vibrations and thermal distance fluctuations, as the reference cavity is a monolithic block made of a material with thermal expansion coefficient of less than $2 \times 10^{-8} \text{ K}^{-1}$. We obtain a total $\delta V_{\text{ref}} = 4.82 \times 10^{-6} \text{ V}$ and $1.06 \times 10^{-6} \text{ V}$ for 1000 s and 72 h integration time, indicating the errors for $V_R(t)$, and $V_R(0)$, respectively. This error could be reduced in practice, as power fluctuations being the main error here also have a significant temperature dependence.

Appendix A.1.2. Systematic Errors

DAQ error, σV_{DAQ} (TD). We use the temperature drift according to manufacturer specifications $\sigma_{\text{DAQ}} = (S_A \times 1 \mu\text{V} + 1 \mu\text{V}) \times TD(\tau)$ with $S_A = 0.55 \text{ V}$. For longer measurements, we consider a reset of this error by the Keysight 34470A's auto-calibration routing after $\tau = 1000 \text{ s}$.

Cavity drift, $\sigma d(t)$ (TD). The effective temperature coefficient of d can only be measured, as uncertainties in the material properties lead to rather different values. Considering the actual geometry and materials, we obtain an estimate of $5 \times 10^{-8} \text{ m/K}$, which, together with a preliminary stability 0.1 mK of the core temperature and $TD(\tau)$, results in the second-strongest error at large τ . Knowing the actual temperature, this error could be removed from the results but we do not consider this possibility in the error budget here. We rather assume that $\sigma d(t)$ can be reset using a λ -sweep calibration preceding each measurement point, leading to respective statistical averaging and consider $TD(\tau)$ with amplitude 5 pm. We add to $\sigma d(t)$ the uncertainty of determination obtained from simulated calibration data. For this purpose, we computed 100 λ -sweep datasets considering independently randomized $\delta\lambda$, δV_{sig} , δd , and fixed $\sigma\lambda$ with their respective known statistical widths. The single sweep data are fit to Equation (6) with free parameters S_A , S_B , d , and $\sigma\lambda$. σd is then the standard deviation of all the MC results and the mean parameter error (added as systematic errors) of the fits. The same procedure is used for the reference cavity size determination error σd_{ref} , where we set $\delta d = 0$ for data generation. For the computation of the 72 h reference signal, we assume periodic re-calibration and reset of $\sigma d(t)$ every $500\tau_{\text{DC}} + \tau_{\text{cal}}$, with calibration time $\tau_{\text{cal}} = 2800 \text{ s}$.

Wavelength drift, $\sigma\lambda(t)$ (TD), is derived from the 1.5 GHz accuracy of the TLX1 for a range 10–40 °C. As the absolute wavelength can be re-calibrated using the frequency-locked reference laser, we assume for operation at COBS a pessimistic maximal error of 12.6 pm/100 as amplitude for $TD(\tau)$. This error averages with the number of measurement points of both data and reference signal; we assume periodic re-calibration and reset of $\sigma\lambda(t)$ every $500\tau_{\text{DC}} + \tau_{\text{cal}}$.

Reference cavity signal (TD): systematic component of $\sigma V_R = 4.7$ and $0.79 \mu\text{V}$ for 1000 s and 72 h integration time, respectively. Obtained in the same way as σV_{DAQ} .

Appendix A.1.3. Constant Errors

DAQ error, $\sigma_{\text{DAQ}} = 0.1 \mu\text{V}$, for the Keysight 34470A offset error, exceeding the specifications from the datasheet.

Reference cavity signal: constant component of $\sigma V_{\text{ref}} = 0.1 \mu\text{V}$, similar as for σ_{DAQ} .

Note that constant errors in d and λ do not appear as voltage errors due to measurement at quadrature. The constant errors are considered in Appendixes A.3 and A.4.

Appendix A.2. AC Signals

Appendix A.2.1. Statistical Errors

PLL frequency noise, δf_{LI} . The short-time stability of the lock-in amplifier's phase-tracking based on phase stability $\delta\phi_{\text{LI}}$ was measured as the RMS value of the phase using

a first-order passive RC-lowpass as a device under test over 3 h, without feedback. This error combines internal electrical noise, aliasing errors, and internal oscillator stability (without an external Rubidium reference clock). We obtained $\delta f_{\text{LI}} \leq \delta \phi_{\text{LI}} \omega_0 / (4\pi Q) = 1.80 \text{ nHz}$ (for $Q = 10^4$ and $\delta \phi_{\text{LI}} = 2.4 \times 10^{-4}$ °).

Frequency measurement, δf_{PID} . This noise quantifies the stability of the frequency tracking algorithm of the PLL together with PID feedback. We measured it using the same first-order passive RC lowpass, resulting in $\delta f_{\text{PID}} = 2.2 \text{ } \mu\text{Hz}$.

Signal noise, δf_V (SpI, indirectly; see Appendix A.1). Voltage noise (containing all error sources described in Appendix A.1) can be converted into time jitter of a sinusoidal signal at frequency ω , as explained in the main text in Section 3.2, resulting in $\delta V_{\text{sig}} = 7.39 \times 10^{-7}$ and $5.59 \times 10^{-7} \text{ V}$, $\sigma f_V = 3.90$ and 0.51 nHz for τ_{AC} and 1000 s integration time, respectively and $a = 3 \text{ } \mu\text{m}$.

Appendix A.2.2. Systematic Errors

PLL phase stability, $\sigma f_{\text{LI}}(t)$ (TD). This error quantifies the 0.05 ppm/°C drift of the internal oscillator of the lock-in amplifier with temperature, and the respective deviation at COBS. For multiple measurements, we consider periodic re-calibration to average this error. $\sigma f_V(t) = 0.88$ and 10.5 nHz for τ_{AC} and 1000 s integration time, respectively.

Resonance frequency calibration error, $\sigma \omega_0$. The resonance frequency is calibrated prior to each distance sweep or once per day. We use the combined standard deviation and parameter error obtained from MC simulations of the calibration data as described in Section 2.5.2. $\sigma \omega_0 = 1.44 \times 10^{-9} \text{ s}^{-1}$.

Signal drift, $\sigma f_V(t)$ (TD, indirectly; see Appendix A.1). Drifts of the voltage signal, converted to frequency error, as described in Section 3.2. We obtain $\sigma V_{\text{sig}} = 3.64 \times 10^{-7}$ and $6.69 \times 10^{-7} \text{ V}$, $\sigma f_V(t) = 1.92$ and 3.63 nHz for τ_{AC} and 1000 s integration time, respectively, and $a = 3 \text{ } \mu\text{m}$.

Appendix A.2.3. Constant Errors

PLL phase error, σf_{LI} . This error reflects the absolute 0.05 ppm frequency accuracy of the reference Rubidium atomic clock, applied to the sensor resonance frequency ($f_0 = 10 \text{ Hz}$).

Resonance frequency calibration error, $\sigma \omega_0$. This error comes from the mean constant offset error seen in our MC simulations. It is caused by non-linearities in combination with other errors, leading to a constant estimation error $\sigma \omega_0 = 5.53 \times 10^{-7} \text{ s}^{-1}$.

Signal error: constant component of the signal error, amounting to $\sigma f_V = 0.1 \text{ } \mu\text{V}$ or 0.53 nHz (see Section 2.5.2).

Appendix A.3. Pressure Gradient

Appendix A.3.1. Statistical Errors

Frequency measurement, δf (SpI, indirectly; see Appendix A.1). This error is propagated from the AC error described in Appendix A.2 and amounts for τ_{AC} to $\delta f = 1.62$ and $0.47 \text{ } \mu\text{V}$ for $\tau = \tau_{\text{AC}}$ and 1000 s, respectively, at $a = 3 \text{ } \mu\text{m}$.

Appendix A.3.2. Systematic Errors

Frequency measurement, $\sigma f(t)$ (TD, indirectly; see Appendix A.1). This error is propagated from the AC error described in Appendix A.2. We obtain $\sigma f = 0.71$ and 7.76 nHz for $\tau = \tau_{\text{AC}}$ and 1000 s, respectively.

Resonance frequency calibration error, $\sigma \omega_0$. This error (described already in Appendix A.2) is considered separately here, as it appears in the expression for the total gradient $\partial_a F$, expressed from Equation (5). $\sigma \omega_0 = 1.44 \times 10^{-9} \text{ s}^{-1}$.

Mass calibration error, σm . We again use the standard deviation and parameter error determined from MC simulations of calibration data (see Section 2.5.2). $\sigma m = 5.86 \times 10^{-11}$ kg.

Appendix A.3.3. Constant Errors

Frequency measurement, $\sigma f = 5.13$ nHz, is the constant part of the error propagated from the AC frequency detection.

Resonance frequency error, $\sigma\omega_0 = 5.53 \times 10^{-7}$ s⁻¹. Mean parameter offset from fits to MC simulation data (see Section 2.5.2).

Mass calibration error, $\sigma m = 1.28 \times 10^{-11}$ kg. Mean parameter offset from fits to MC simulation data (see Section 2.5.2).

Appendix A.4. Pressure

Appendix A.4.1. Statistical Errors

Signal fluctuation, δV_{sig} . Propagated statistical error from the DC signal. Amounts to $\delta V_{\text{sig}} = 0.74$ and 0.10 μV for τ_{AC} and 1000 s integration time, respectively, at $a = 3$ μm .

Reference signal, δV_0 . Statistical error of the zero-force reference signal taken at a_{cal} (do not confuse with δV_{R} from the reference cavity). As DC detection is independent of a , we use the same models as for δV_{sig} described in Appendix A.1. $\delta V_0 = 0.01$ μV for $\tau = 1000$ s integration time.

Force gradient, $\delta\partial_a F$. Correcting the spring constant k introduces a dependence on the force gradient. We propagate the corresponding error described in Appendix A.3, resulting in $\delta\partial_a F = 32.5$ and 9.36 nN/m for τ_{AC} and 1000 s integration time, respectively.

Appendix A.4.2. Systematic Errors

Mass calibration error, $\sigma m = 5.86 \times 10^{-11}$ kg, was described in Appendix A.3.

Resonance frequency error, $\sigma\omega_0 = 1.44 \times 10^{-9}$ s⁻¹. This is the same error described in Appendix A.2.

Wavelength error, $\sigma\lambda(t)$ (TD, partially). While $\sigma\lambda$ can be measured and brought close to zero by the beat method (see Section 2.5.2), it can also be obtained from a fit to a λ -sweep (see σd above). We use the average parameter uncertainty of the fits combined with the standard deviation of the results using 300 sets of calibration data, resulting in $\sigma\lambda = 0.16$ pm. In addition, we use the known temperature dependence, as described in Appendix A.1: $\sigma\lambda = 12.6$ pm/100 \times TD(τ), and add the two uncertainties.

Cavity size determination error, $\sigma d(t)$. Same as described in Appendix A.1.

Signal error, σV_{sig} (TD, indirectly; see Appendix A.1). Systematic component of the signal error from Appendix A.1. We use $\sigma V_{\text{sig}} = 0.36$ and 0.69 μV for τ_{AC} and 1000 s, respectively.

Reference signal error, σV_0 (TD, indirectly; see Appendix A.1). Systematic error of the zero-force reference, from Appendix A.1 for $\tau = 1000$ s. $\sigma V_0 = 0.69$ μV .

Force gradient error, $\sigma\partial_a F$ (TD, indirectly; see Appendix A.3). Systematic error of the synchronous force gradient measurement, considering all errors from Appendix A.3, $\sigma\partial_a F = 3.55$ nN/m² for both $\tau = \tau_{\text{AC}}$ and 1000 s, respectively.

Appendix A.4.3. Constant Errors

Resonance frequency error, $\sigma\omega_0 = 5.53 \times 10^{-7}$ s⁻¹⁰. Mean offset from MC simulations, see Appendix A.3.

Mass calibration error, $\sigma m = 1.28 \times 10^{-11}$ kg. Mean offset from MC simulations, see Appendix A.3.

Wavelength offset error, $\sigma \lambda$. Absolute error of the Thorlabs LLD1530 reference laser from manufacturer data, adjusted for better thermal stability at COBS, as described in Section 3.2. During the experiment, this may turn out to be a systematic error. Conservatively, we consider it to be constant here. $\sigma \lambda = 3.4$ fm.

Signal error, σV_{sig} . Propagated constant error of the DC signal V_{sig} . $\sigma V_{\text{sig}} = 0.19 \mu\text{V}$.

Reference signal error, σV_0 . Constant error of the zero-force reference signal. $\sigma V_0 = 0.19 \mu\text{V}$.

Force gradient error, $\sigma \partial_a F$. Constant part as described in Appendix A.3, amounting to $\sigma \partial_a F = 1.16$ nN/m.

Appendix A.5. Other Errors

The radius of the plates is specified with uncertainty 5 μm . It can be measured with slightly better accuracy. To convert the errors on the force and its gradient to a pressure and pressure gradient, we consider a constant error $A \rightarrow A(1 + \sigma A)$ with $\sigma A = 2.5 \times 10^{-3}$, considering the maximal deviation on both plates and alignment errors.

Appendix B. Evaluation of the Out of Thermal Equilibrium Casimir Pressure

In the expression for the non-equilibrium Casimir pressure given in Equation (14), the pure non-equilibrium term, ΔP_{neq} , can be written as the sum of a contribution arising from the evanescent waves ($\Delta P_{\text{neq}}^{\text{EW}}$) and a contribution due to the propagating waves ($\Delta P_{\text{neq}}^{\text{PW}}$) [66,228,233]. Considering local and isotropic materials, the two contributions can be conveniently written as

$$\begin{aligned} \Delta P_{\text{neq}}^{\text{EW}}(a, T_1, T_2) &= -\hbar \int_0^\infty \frac{d\omega}{\pi} \Delta n(\omega, T_1, T_2) \int_{\frac{\omega}{c}}^\infty \frac{dk}{2\pi} k \sum_\sigma \kappa \frac{\text{Im}[r_1^\sigma] \text{Re}[r_2^\sigma] - \text{Re}[r_1^\sigma] \text{Im}[r_2^\sigma]}{|1 - r_1^\sigma r_2^\sigma e^{-2\kappa a}|^2} e^{-2\kappa a} \\ &= -\frac{\hbar}{2} \int_0^\infty \frac{d\omega}{\pi} \Delta n(\omega, T_1, T_2) \int_0^\infty \frac{d\kappa}{2\pi} \sum_\sigma \kappa^2 \frac{2 \text{Im}[r_1^\sigma (r_2^\sigma)^*] e^{-2\kappa a}}{|1 - r_1^\sigma r_2^\sigma e^{-2\kappa a}|^2}, \end{aligned} \quad (\text{A3})$$

$$\begin{aligned} \Delta P_{\text{neq}}^{\text{PW}}(a, T_1, T_2) &= -\frac{\hbar}{2} \int_0^\infty \frac{d\omega}{\pi} \Delta n(\omega, T_1, T_2) \int_0^{\frac{\omega}{c}} \frac{dk}{2\pi} k \sum_\sigma k_z \frac{|r_1^\sigma|^2 - |r_2^\sigma|^2}{|1 - r_1^\sigma r_2^\sigma e^{2ik_z a}|^2} \\ &= -\frac{\hbar}{2} \int_0^\infty \frac{d\omega}{\pi} \Delta n(\omega, T_1, T_2) \int_0^{\frac{\omega}{c}} \frac{dk_z}{2\pi} \sum_\sigma k_z^2 \frac{|r_1^\sigma|^2 - |r_2^\sigma|^2}{|1 - r_1^\sigma r_2^\sigma e^{2ik_z a}|^2}, \end{aligned} \quad (\text{A4})$$

where it is also assumed that each of the plates is locally in thermal equilibrium at the corresponding temperature. In expressions (A3) and (A4), the same conventions and definitions as described after Equation (11) are used, while ** indicates the complex conjugate of the corresponding quantity. In the second line of Equation (A3), given that κ is non-negative over the whole integration range, we changed the variable from k to κ . Similarly, in the second line of Equation (A4), we performed the variable change $k \rightarrow k_z = \sqrt{\omega^2/c^2 - k^2} = i\kappa$ ($\text{Im}[k_z] \geq 0; \text{Re}[k_z] \geq 0$). We have also defined

$$\begin{aligned} \Delta n(\omega, T_1, T_2) &= n(\omega, T_1) - n(\omega, T_2) = \frac{1}{2} \left(\coth \left[\frac{\hbar\omega}{2k_B T_1} \right] - \coth \left[\frac{\hbar\omega}{2k_B T_2} \right] \right) \\ &= \frac{1}{2} \tanh \left[\frac{\hbar\omega}{2k_B} \left(\frac{1}{T_1} - \frac{1}{T_2} \right) \right] \left(1 - \coth \left[\frac{\hbar\omega}{2k_B T_1} \right] \coth \left[\frac{\hbar\omega}{2k_B T_2} \right] \right), \end{aligned} \quad (\text{A5})$$

where $n(\omega, T) = 1/[e^{\frac{\hbar\omega}{k_B T}} - 1]$ is the Bose–Einstein occupation number.

As pointed out in Section 4.1.3, the result (11) allows for the consideration of multilayered structures. In this case, numbering the layers in the stack from the top ($n = 1$

corresponds to the medium above the first interface) to the bottom, the reflection coefficients, as seen from an electromagnetic wave impinging from the top of the layer onto the topmost interface can be obtained using the following recurrence formula [234,235]:

$$r_n^\sigma = \frac{\tilde{r}_n^\sigma + r_{n+1}^\sigma e^{-2t_{n+1}\kappa_{n+1}}}{1 + \tilde{r}_n^\sigma r_{n+1}^\sigma e^{-2t_{n+1}\kappa_{n+1}}}, \tag{A6}$$

where \tilde{r}_n^σ is the interface reflection coefficient between the layer n and $n + 1$, t_n is the thickness of the n th-layer and $\kappa_n = \sqrt{k^2 - \epsilon_n(\omega)\omega^2/c^2}$, with $\epsilon_n(\omega)$ the corresponding permittivity. In the case of a finite multilayer structure having N layers, we set $r_N^\sigma = \tilde{r}_N^\sigma$. For local and isotropic materials, the expression for \tilde{r}_n^σ can be given in terms of Fresnel coefficients [66,233]

$$\begin{aligned} \tilde{r}_n^{TE} &= \frac{\sqrt{k^2 - \epsilon_n(\omega)\frac{\omega^2}{c^2}} - \sqrt{k^2 - \epsilon_{n+1}(\omega)\frac{\omega^2}{c^2}}}{\sqrt{k^2 - \epsilon_n(\omega)\frac{\omega^2}{c^2}} + \sqrt{k^2 - \epsilon_{n+1}(\omega)\frac{\omega^2}{c^2}}}, \\ \tilde{r}_n^{TM} &= \frac{\epsilon_{n+1}(\omega)\sqrt{k^2 - \epsilon_n(\omega)\frac{\omega^2}{c^2}} - \epsilon_n(\omega)\sqrt{k^2 - \epsilon_{n+1}(\omega)\frac{\omega^2}{c^2}}}{\epsilon_{n+1}(\omega)\sqrt{k^2 - \epsilon_n(\omega)\frac{\omega^2}{c^2}} + \epsilon_n(\omega)\sqrt{k^2 - \epsilon_{n+1}(\omega)\frac{\omega^2}{c^2}}}. \end{aligned} \tag{A7}$$

Commonly, multilayer structures are made out of metallic and insulating layers. One of the simplest mathematical expressions for the dielectric function of metals is given by the Drude model (12). For semiconductors or insulators, a relatively simple description is given by the Lorentz model,

$$\epsilon(\omega) = \epsilon_\infty + \frac{(\epsilon_0 - \epsilon_\infty)\Omega_0^2}{\Omega_0^2 - \omega^2 - i\Gamma\omega}. \tag{A8}$$

For example, this expression is used in Figure 12 to describe the optical properties for both silicon and silica. For simplicity, both materials were described using the parameters as given in Ref. [238], to which we add a small dissipation rate to account for the material dissipation near resonance (see Figure 12).

Figure 12 also presents a calculation involving the pressure gradient $P'(a, T_1, T_2)$. Although the expression for $P'(a, T_1, T_2)$ can be obtained analytically from the expression for $P(a, T_1, T_2)$, the numerical evaluation of the corresponding result can be quite unstable. For this reason, the pressure gradient was obtained by applying a symmetric eighth-order numerical differentiation algorithm, which gives an estimate of the derivative of the function $f(x)$ at the point x_0 as

$$\begin{aligned} f'(x_0) \approx \frac{1}{\delta} &\left[\frac{1}{280}f(x_0 - 4\delta) - \frac{4}{105}f(x_0 - 3\delta) + \frac{1}{5}f(x_0 - 2\delta) - \frac{4}{5}f(x_0 - \delta) \right. \\ &\left. + \frac{4}{5}f(x_0 + \delta) - \frac{1}{5}f(x_0 + 2\delta) + \frac{4}{105}f(x_0 + 3\delta) - \frac{1}{280}f(x_0 + 4\delta) \right]. \end{aligned} \tag{A9}$$

for sufficiently small δ . We checked the result (A9) against the corresponding expression for the derivative with respect to the distance of the Lifshitz Formula (11), which can be obtained by using the identity

$$\partial_a \frac{e^{-2\kappa a}}{1 - r_1^\sigma r_2^\sigma e^{-2\kappa a}} = - \frac{2\kappa e^{-2\kappa a}}{(1 - r_1^\sigma r_2^\sigma e^{-2\kappa a})^2}. \tag{A10}$$

The comparison successfully validated the numerical differentiation scheme with $\delta = 1/8 \mu\text{m}$ to the level of one part in a million.

References

1. Keshavarzi, A.; Khaw, K.S.; Yoshioka, T. Muon $g - 2$: A Review. *Nucl. Phys. B* **2022**, *975*, 115675. [CrossRef]
2. Gao, H.; Vanderhaeghen, M. The Proton Charge Radius. *Rev. Mod. Phys.* **2022**, *94*, 015002. [CrossRef]
3. Tiesinga, E.; Mohr, P.J.; Newell, D.B.; Taylor, B.N. CODATA Recommended Values of the Fundamental Physical Constants: 2018. *Rev. Mod. Phys.* **2021**, *93*, 025010. [CrossRef]
4. Burger, F.A.; Corkery, R.W.; Buhmann, S.Y.; Fiedler, J. Comparison of Theory and Experiments on van der Waals Forces in Media—A Survey. *J. Phys. Chem. C* **2020**, *124*, 24179–24186. [CrossRef]
5. Workman, R.L. et al. [Particle Data Group] Review of Particle Physics. *Prog. Theor. Exp. Phys.* **2022**, *2022*, 083C01. [CrossRef]
6. Hardy, J.C.; Towner, I.S. Superallowed $0^+ \rightarrow 0^+$ nuclear β decays: 2020 critical survey, with implications for V_{ud} and CKM unitarity *Phys. Rev. C* **2020**, *102*, 045501. [CrossRef]
7. Peccei, R.D.; Quinn, H.R. CP Conservation in the Presence of Pseudoparticles. *Phys. Rev. Lett.* **1977**, *38*, 1440–1443. [CrossRef]
8. Peccei, R.D.; Quinn, H.R. Constraints Imposed by CP Conservation in the Presence of Pseudoparticles. *Phys. Rev. D* **1977**, *16*, 1791–1797. [CrossRef]
9. Weinberg, S. A New Light Boson? *Phys. Rev. Lett.* **1978**, *40*, 223–226. [CrossRef]
10. Wilczek, F. Problem of Strong P and T Invariance in the Presence of Instantons. *Phys. Rev. Lett.* **1978**, *40*, 279–282. [CrossRef]
11. Zwicky, F. Die Rotverschiebung von extragalaktischen Nebeln. *Helv. Phys. Acta* **1933**, *6*, 110–127. Available online: <https://www.e-periodica.ch/digbib/view?pid=hpa-001:1933:6#112> (accessed on 7 February 2024).
12. Aghanim, N. et al. [Planck Collaboration] Planck 2018 Results. VI. Cosmological Parameters. *Astron. Astrophys.* **2020**, *641*, A6. [CrossRef]
13. Angulo, R.E.; Hahn, O. Large-Scale Dark Matter Simulations. *Liv. Rev. Comput. Astrophys.* **2022**, *8*, 1. [CrossRef]
14. Perlmutter, S.; Aldering, G.; della Valle, M.; Deustua, S.; Ellis, R.S.; Fabbro, S.; Fruchter, A.; Goldhaber, G.; Groom, D.E.; Hook, I.M.; et al. Discovery of a Supernova Explosion at Half the Age of the Universe. *Nature* **1998**, *391*, 51–54. [CrossRef]
15. Riess, A.G.; Filippenko, A.V.; Challis, P.; Clocchiatti, A.; Diercks, A.; Garnavich, P.M.; Gilliland, R.L.; Hogan, C.J.; Jha, S.; Kirshner, R.P.; et al. Observational Evidence from Supernovae for an Accelerating Universe and a Cosmological Constant. *Astrophys. J.* **1998**, *116*, 1009–1038. [CrossRef]
16. Schmidt, B.P.; Suntzeff, N.B.; Phillips, M.M.; Schommer, R.A.; Clocchiatti, A.; Kirshner, R.P.; Garnavich, P.; Challis, P.; Leibundgut, B.; Spyromilio, J.; et al. The High-Z Supernova Search: Measuring Cosmic Deceleration and Global Curvature of the Universe Using Type Ia Supernovae. *Astrophys. J.* **1998**, *507*, 46–63. [CrossRef]
17. Hu, J.P.; Wang, F.Y. Hubble Tension: The Evidence of New Physics. *Universe* **2023**, *9*, 94. [CrossRef]
18. Koch, B.; Käding, C.; Pitschmann, M.; Sedmik, R.I.P. Vacuum Energy, the Casimir Effect, and Newton's Non-Constant. *Universe* **2023**, *9*, 476. [CrossRef]
19. Perivolaropoulos, L.; Skara, F. Challenges for Λ CDM: An Update. *New Astron. Rev.* **2022**, *95*, 101659. [CrossRef]
20. Solà, J. Cosmological Constant and Vacuum Energy: Old and New Ideas. *J. Phys. Conf. Ser.* **2013**, *453*, 012015. [CrossRef]
21. Martin, J. Everything You Always Wanted to Know about the Cosmological Constant Problem (but Were Afraid to Ask). *Comptes Rendus Phys.* **2012**, *13*, 566–665. [CrossRef]
22. Padmanabhan, T. Why Does Gravity Ignore the Vacuum Energy? *Int. J. Mod. Phys. D* **2006**, *15*, 2029–2058. [CrossRef]
23. Weinberg, S. Theories of the Cosmological Constant. *arXiv* **1996**, arXiv:astro-ph/9610044. [CrossRef]
24. Weinberg, S. The Cosmological Constant Problem. *Rev. Mod. Phys.* **1989**, *61*, 1. [CrossRef]
25. Cree, S.S.; Davis, T.M.; Ralph, T.C.; Wang, Q.; Zhu, Z.; Unruh, W.G. Can the Fluctuations of the Quantum Vacuum Solve the Cosmological Constant Problem? *Phys. Rev. D* **2018**, *98*, 063506. [CrossRef]
26. Adler, R.J.; Casey, B.; Jacob, O.C. Vacuum Catastrophe: An Elementary Exposition of the Cosmological Constant Problem. *Am. J. Phys.* **1995**, *63*, 620–626. [CrossRef]
27. Nobbenhuis, S. The Cosmological Constant Problem, an Inspiration for New Physics. Ph.D. Thesis, Utrecht University, Utrecht, The Netherlands, 2006. [CrossRef]
28. Bernabei, R.; Belli, P.; Bussolotti, A.; Cappella, F.; Caracciolo, V.; Cerulli, R.; Dai, C.-J.; D'Angelo, A.; Di Marco, A.; He, H.-L.; et al. First Model Independent Results from DAMA/LIBRA-Phase2. *Universe* **2018**, *4*, 116. [CrossRef]
29. Bulbul, E.; Markevitch, M.; Foster, A.; Smith, R.K.; Loewenstein, M.; Randall, S.W. Detection of an Unidentified Emission Line in the Stacked X-ray Spectrum of Galaxy Clusters. *Astrophys. J.* **2014**, *789*, 13. [CrossRef]
30. Hofmann, F.; Wegg, C. 7.1 keV Sterile Neutrino Dark Matter Constraints from a Deep Chandra X-ray Observation of the Galactic Bulge Limiting Window. *Astron. Astrophys.* **2019**, *625*, L7. [CrossRef]
31. Barkana, R. Possible Interaction between Baryons and Dark-Matter Particles Revealed by the First Stars. *Nature* **2018**, *555*, 71–74. [CrossRef]
32. Colladay, D.; Kostelecký, V.A. Lorentz-Violating Extension of the Standard Model. *Phys. Rev. D* **1998**, *58*, 116002. [CrossRef]
33. Moody, J.E.; Wilczek, F. New Macroscopic Forces? *Phys. Rev. D* **1984**, *30*, 130–138. [CrossRef]
34. Fadeev, P.; Stadnik, Y.V.; Ficek, F.; Kozlov, M.G.; Flambaum, V.V.; Budker, D. Revisiting Spin-Dependent Forces Mediated by New Bosons: Potentials in the Coordinate-Space Representation for Macroscopic- and Atomic-Scale Experiments. *Phys. Rev. A* **2019**, *99*, 022113. [CrossRef]
35. Sponar, S.; Sedmik, R.I.P.; Pitschmann, M.; Abele, H.; Hasegawa, Y. Tests of Fundamental Quantum Mechanics and Dark Interactions with Low-Energy Neutrons. *Nat. Rev. Phys.* **2021**, *3*, 309–327. [CrossRef]

36. Casimir, H.B.G. On the Attraction between Two Perfectly Conducting Plates. *Proc. Kon. Ned. Akad. Wet. B* **1948**, *51*, 793–795. Available online: <https://dwc.knaw.nl/DL/publications/PU00018547.pdf> (accessed on 7 February 2024).
37. Lamoreaux, S. Demonstration of the Casimir Force in the 0.6 to 6 μm Range. *Phys. Rev. Lett.* **1997**, *78*, 5. [CrossRef]
38. Mohideen, U.; Roy, A. Precision Measurement of the Casimir Force from 0.1 to 0.9 μm . *Phys. Rev. Lett.* **1998**, *81*, 4549–4552. [CrossRef]
39. Roy, A.; Mohideen, U. Demonstration of the Nontrivial Boundary Dependence of the Casimir Force. *Phys. Rev. Lett.* **1999**, *82*, 4380–4383. [CrossRef]
40. Tang, L.; Wang, M.; Ng, C.Y.; Nikolic, M.; Chan, C.T.; Rodriguez, A.W.; Chan, H.B. Measurement of Non-Monotonic Casimir Forces between Silicon Nanostructures. *Nat. Photon.* **2017**, *11*, 97. [CrossRef]
41. Garrett, J.L.; Somers, D.A.T.; Munday, J.N. Measurement of the Casimir Force between Two Spheres. *Phys. Rev. Lett.* **2018**, *120*, 040401. [CrossRef]
42. Chen, F.; Mohideen, U.; Klimchitskaya, G.L.; Mostepanenko, V.M. Demonstration of the Lateral Casimir Force. *Phys. Rev. Lett.* **2002**, *88*, 101801. [CrossRef]
43. Chiu, H.C.; Klimchitskaya, G.L.; Marachevsky, V.N.; Mostepanenko, V.M.; Mohideen, U. Demonstration of the Asymmetric Lateral Casimir Force between Corrugated Surfaces in the Nonadditive Regime. *Phys. Rev. B* **2009**, *80*, 121402. [CrossRef]
44. Lisanti, M.; Iannuzzi, D.; Capasso, F. Observation of the Skin-Depth Effect on the Casimir Force between Metallic Surfaces. *Proc. Natl. Acad. Sci. USA* **2005**, *102*, 11989. [CrossRef]
45. Chen, F.; Klimchitskaya, G.L.; Mostepanenko, V.M.; Mohideen, U. Demonstration of the Difference in the Casimir Force for Samples with Different Charge-Carrier Densities. *Phys. Rev. Lett.* **2006**, *97*, 170402. [CrossRef]
46. de Man, S.; Heeck, K.; Wijngaarden, R.J.; Iannuzzi, D. Halving the Casimir Force with Conductive Oxides. *Phys. Rev. Lett.* **2009**, *103*, 040402. [CrossRef]
47. Torricelli, G.; van Zwol, P.J.; Shpak, O.; Binns, C.; Palasantzas, G.; Kooi, B.J.; Svetovoy, V.B.; Wuttig, M. Switching Casimir Forces with Phase-Change Materials. *Phys. Rev. A* **2010**, *82*, 010101. [CrossRef]
48. Torricelli, G.; Pirozhenko, I.; Thornton, S.; Lambrecht, A.; Binns, C. Casimir Force between a Metal and a Semimetal. *Europhys. Lett.* **2011**, *93*, 51001. [CrossRef]
49. Banishev, A.A.; Klimchitskaya, G.L.; Mostepanenko, V.M.; Mohideen, U. Demonstration of the Casimir Force between Ferromagnetic Surfaces of a Ni-Coated Sphere and a Ni-Coated Plate. *Phys. Rev. Lett.* **2013**, *110*, 137401. [CrossRef]
50. Banishev, A.A.; Wen, H.; Xu, J.; Kawakami, R.K.; Klimchitskaya, G.L.; Mostepanenko, V.M.; Mohideen, U. Measuring the Casimir Force Gradient from Graphene on a SiO_2 Substrate. *Phys. Rev. B* **2013**, *87*, 205433. [CrossRef]
51. Liu, M.; Zhang, Y.; Klimchitskaya, G.L.; Mostepanenko, V.M.; Mohideen, U. Demonstration of an Unusual Thermal Effect in the Casimir Force from Graphene. *Phys. Rev. Lett.* **2021**, *126*, 206802. [CrossRef]
52. Ardito, R.; Frangi, A.; Corigliano, A.; Masi, B.D.; Cazzaniga, G. The Effect of Nano-Scale Interaction Forces on the Premature Pull-in of Real-Life Micro-Electro-Mechanical Systems. *Microel. Reliab.* **2012**, *52*, 271. [CrossRef]
53. Broer, W.; Palasantzas, G.; Knoester, J.; Svetovoy, V.B. Significance of the Casimir Force and Surface Roughness for Actuation Dynamics of MEMS. *Phys. Rev. B* **2013**, *87*, 125413. [CrossRef]
54. Somers, D.A.T.; Garrett, J.L.; Palm, K.J.; Munday, J.N. Measurement of the Casimir Torque. *Nature* **2018**, *564*, 386–389. [CrossRef]
55. Lee, S.w.; Sigmund, W.M. Repulsive van der Waals Forces for Silica and Alumina. *J. Colloid Interf. Sci.* **2001**, *243*, 365–369. [CrossRef]
56. Feiler, A.A.; Bergström, L.; Rutland, M.W. Superlubricity Using Repulsive van der Waals Forces. *Langmuir* **2008**, *24*, 2274–2276. [CrossRef]
57. Munday, J.N.; Capasso, F.; Parsegian, V.A. Measured Long-Range Repulsive Casimir–Lifshitz Forces. *Nature* **2009**, *457*, 170–173. [CrossRef]
58. Mostepanenko, V.M. Casimir Puzzle and Casimir Conundrum: Discovery and Search for Resolution. *Universe* **2021**, *7*, 84. [CrossRef]
59. Bimonte, G.; López, D.; Decca, R.S. Isoelectronic Determination of the Thermal Casimir Force. *Phys. Rev. B* **2016**, *93*, 184434. [CrossRef]
60. Chen, F.; Klimchitskaya, G.L.; Mostepanenko, V.M.; Mohideen, U. Control of the Casimir force by the modification of dielectric properties with light. *Phys. Rev. B* **2007**, *76*, 035338. [CrossRef]
61. van Zwol, P.; Svetovoy, V.; Palasantzas, G. Characterization of Optical Properties and Surface Roughness Profiles: The Casimir Force Between Real Materials. In *Casimir Physics*; Dalvit, D., Milonni, P., Roberts, D., da Rosa, F., Eds.; Springer: Berlin/Heidelberg, Germany, 2011; pp. 311–343. [CrossRef]
62. Behunin, R.O.; Intravaia, F.; Dalvit, D.A.R.; Neto, P.A.M.; Reynaud, S. Modeling Electrostatic Patch Effects in Casimir Force Measurements. *Phys. Rev. A* **2012**, *85*, 012504. [CrossRef]
63. Sushkov, A.O.; Kim, W.J.; Dalvit, D.A.R.; Lamoreaux, S.K. Observation of the Thermal Casimir Force. *Nat. Phys.* **2011**, *7*, 230–233. [CrossRef]
64. Klimchitskaya, G.L.; Mostepanenko, V.M. An Alternative Response to the Off-Shell Quantum Fluctuations: A Step Forward in Resolution of the Casimir Puzzle. *Eur. Phys. J. C* **2020**, *80*, 900. [CrossRef]
65. Bezerra, V.B.; Klimchitskaya, G.L.; Mostepanenko, V.M.; Romero, C. Violation of the Nernst Heat Theorem in the Theory of the Thermal Casimir Force between Drude Metals. *Phys. Rev. A* **2004**, *69*, 022119. [CrossRef]

66. Klimchitskaya, G.L.; Mostepanenko, V.M.; Sedmik, R.I.P. Casimir Pressure between Metallic Plates out of Thermal Equilibrium: Proposed Test for the Relaxation Properties of Free Electrons. *Phys. Rev. A* **2019**, *100*, 022511. [CrossRef]
67. Bordag, M.; Geyer, B.; Klimchitskaya, G.L.; Mostepanenko, V.M. Stronger Constraints for Nanometer Scale Yukawa-type Hypothetical Interactions from the New Measurement of the Casimir Force. *Phys. Rev. D* **1999**, *60*, 055004. [CrossRef]
68. Mostepanenko, V.M.; Novello, M. Constraints on Non-Newtonian Gravity from the Casimir Force Measurements between Two Crossed Cylinders. *Phys. Rev. D* **2001**, *63*, 115003. [CrossRef]
69. Decca, R.S.; Fischbach, E.; Klimchitskaya, G.L.; Krause, D.E.; López, D.; Mostepanenko, V.M. Improved Tests of Extra-Dimensional Physics and Thermal Quantum Field Theory from New Casimir Force Measurements. *Phys. Rev. D* **2003**, *68*, 116003. [CrossRef]
70. Decca, R.S.; López, D.; Chan, H.B.; Fischbach, E.; Krause, D.E.; Jamell, C.R. Constraining New Forces in the Casimir Regime Using the Isoelectronic Technique. *Phys. Rev. Lett.* **2005**, *94*, 240401. [CrossRef]
71. Decca, R.; López, D.; Fischbach, E.; Klimchitskaya, G.; Krause, D.; Mostepanenko, V. Novel Constraints on Light Elementary Particles and Extra-Dimensional Physics from the Casimir Effect. *Eur. Phys. J. C* **2007**, *51*, 963–975. [CrossRef]
72. Mostepanenko, V.M.; Decca, R.S.; Fischbach, E.; Klimchitskaya, G.L.; Krause, D.E.; López, D. Stronger Constraints on Non-Newtonian Gravity from the Casimir Effect. *J. Phys. A* **2008**, *41*, 164054. [CrossRef]
73. Masuda, M.; Sasaki, M. Limits on Nonstandard Forces in the Submicrometer Range. *Phys. Rev. Lett.* **2009**, *102*, 171101. [CrossRef]
74. Bezerra, V.B.; Klimchitskaya, G.L.; Mostepanenko, V.M.; Romero, C. Advance and Prospects in Constraining the Yukawa-type Corrections to Newtonian Gravity from the Casimir Effect. *Phys. Rev. D* **2010**, *81*, 055003. [CrossRef]
75. Sushkov, A.O.; Kim, W.J.; Dalvit, D.A.R.; Lamoreaux, S.K. New Experimental Limits on Non-Newtonian Forces in the Micrometer Range. *Phys. Rev. Lett.* **2011**, *107*, 171101. [CrossRef]
76. Klimchitskaya, G.L.; Mohideen, U.; Mostepanenko, V.M. Constraints on Corrections to Newtonian Gravity from Two Recent Measurements of the Casimir Interaction between Metallic Surfaces. *Phys. Rev. D* **2013**, *87*, 125031. [CrossRef]
77. Bezerra, V.B.; Klimchitskaya, G.L.; Mostepanenko, V.M.; Romero, C. Constraints on axion-nucleon coupling constants from measuring the Casimir force between corrugated surfaces. *Phys. Rev. D* **2014**, *90*, 055013. [CrossRef]
78. Chen, Y.J.; Tham, W.K.; Krause, D.E.; López, D.; Fischbach, E.; Decca, R.S. Stronger Limits on Hypothetical Yukawa Interactions in the 30–8000 Nm Range. *Phys. Rev. Lett.* **2016**, *116*, 221102. [CrossRef]
79. Klimchitskaya, G.L.; Mostepanenko, V.M. Constraints on Axionlike Particles and Non-Newtonian Gravity from Measuring the Difference of Casimir Forces. *Phys. Rev. D* **2017**, *95*, 123013. [CrossRef]
80. Kuz'min, V.A.; Tkachev, I.I.; Shaposhnikov, M.E. Restrictions Imposed on Light Scalar Particles by Measurements of van der Waals Forces. *JETP Lett.* **1982**, *36*, 59–62. Available online: http://jetpletters.ru/ps/1330/article_20101.shtml (accessed on 7 February 2024).
81. Behunin, R.O.; Dalvit, D.A.R.; Decca, R.S.; Speake, C.C. Limits on the Accuracy of Force Sensing at Short Separations Due to Patch Potentials. *Phys. Rev. D* **2014**, *89*, 051301. [CrossRef]
82. Wang, J.; Guan, S.; Chen, K.; Wu, W.; Tian, Z.; Luo, P.; Jin, A.; Yang, S.; Shao, C.; Luo, J. Test of Non-Newtonian Gravitational Forces at Micrometer Range with Two-Dimensional Force Mapping. *Phys. Rev. D* **2016**, *94*, 122005. [CrossRef]
83. Adelberger, E.G.; Stubbs, C.W.; Heckel, B.R.; Su, Y.; Swanson, H.E.; Smith, G.; Gundlach, J.H.; Rogers, W.F. Testing the Equivalence Principle in the Field of the Earth: Particle Physics at Masses below 1 μeV ? *Phys. Rev. D* **1990**, *42*, 3267–3292. [CrossRef] [PubMed]
84. Hoyle, C.D.; Kapner, D.J.; Heckel, B.R.; Adelberger, E.G.; Gundlach, J.H.; Schmidt, U.; Swanson, H.E. Submillimeter Tests of the Gravitational Inverse-Square Law. *Phys. Rev. D* **2004**, *70*, 042004. [CrossRef]
85. Adelberger, E.G.; Heckel, B.R.; Hoedl, S.; Hoyle, C.D.; Kapner, D.J.; Upadhye, A. Particle-Physics Implications of a Recent Test of the Gravitational Inverse-Square Law. *Phys. Rev. Lett.* **2007**, *98*, 131104. [CrossRef]
86. Hammond, G.D.; Speake, C.C.; Trenkel, C.; Patón, A.P. New Constraints on Short-Range Forces Coupling Mass to Intrinsic Spin. *Phys. Rev. Lett.* **2007**, *98*, 081101. [CrossRef]
87. Schlamminger, S.; Choi, K.Y.; Wagner, T.A.; Gundlach, J.H.; Adelberger, E.G. Test of the Equivalence Principle Using a Rotating Torsion Balance. *Phys. Rev. Lett.* **2008**, *100*, 041101. [CrossRef]
88. Heckel, B.R.; Adelberger, E.G.; Cramer, C.E.; Cook, T.S.; Schlamminger, S.; Schmidt, U. Preferred-Frame and CP-Violation Tests with Polarized Electrons. *Phys. Rev. D* **2008**, *78*, 092006. [CrossRef]
89. Geraci, A.A.; Smullin, S.J.; Weld, D.M.; Chiaverini, J.; Kapitulnik, A. Improved Constraints on Non-Newtonian Forces at 10 Microns. *Phys. Rev. D* **2008**, *78*, 022002. [CrossRef]
90. Hoedl, S.A.; Fleischer, F.; Adelberger, E.G.; Heckel, B.R. Improved Constraints on an Axion-Mediated Force. *Phys. Rev. Lett.* **2011**, *106*, 041801. [CrossRef]
91. Heckel, B.R.; Terrano, W.A.; Adelberger, E.G. Limits on Exotic Long-Range Spin-Spin Interactions of Electrons. *Phys. Rev. Lett.* **2013**, *111*, 151802. [CrossRef]
92. Terrano, W.A.; Adelberger, E.G.; Lee, J.G.; Heckel, B.R. Short-Range, Spin-Dependent Interactions of Electrons: A Probe for Exotic Pseudo-Goldstone Bosons. *Phys. Rev. Lett.* **2015**, *115*, 201801. [CrossRef]
93. Tan, W.-H.; Yang, S.-Q.; Shao, C.-G.; Li, J.; Du, A.-B.; Zhan, B.-F.; Wang, Q.-L.; Luo, P.-S.; Tu, L.-C.; Luo, J. New Test of the Gravitational Inverse-Square Law at the Submillimeter Range with Dual Modulation and Compensation. *Phys. Rev. Lett.* **2016**, *116*, 131101. [CrossRef] [PubMed]

94. Tan, W.-H.; Du, A.-B.; Dong, W.-C.; Yang, S.-Q.; Shao, C.-G.; Guan, S.-G.; Wang, Q.-L.; Zhan, B.-F.; Luo, P.-S.; Tu, L.-C.; et al. Improvement for Testing the Gravitational Inverse-Square Law at the Submillimeter Range. *Phys. Rev. Lett.* **2020**, *124*, 051301. [CrossRef] [PubMed]
95. Lee, J.G.; Adelberger, E.G.; Cook, T.S.; Fleischer, S.M.; Heckel, B.R. New Test of the Gravitational $1/r^2$ Law at Separations down to 52 μm . *Phys. Rev. Lett.* **2020**, *124*, 101101. [CrossRef] [PubMed]
96. Zhao, Y.-L.; Tan, Y.-J.; Wu, W.-H.; Luo, J.; Shao, C.-G. Constraining the Chameleon Model with the HUST-2020 Torsion Pendulum Experiment. *Phys. Rev. D* **2021**, *103*, 104005. [CrossRef]
97. Sedmik, R.I.P.; Almasi, A.; Iannuzzi, D. Locality of Surface Interactions on Colloidal Probes. *Phys. Rev. B* **2013**, *88*, 165429. [CrossRef]
98. van Zwol, P.J.; Svetovoy, V.B.; Palasantzas, G. Distance upon Contact: Determination from Roughness Profile. *Phys. Rev. B* **2009**, *80*, 235401. [CrossRef]
99. Sedmik, R.I.P.; Pitschmann, M. Next Generation Design and Prospects for CANNEX. *Universe* **2021**, *7*, 234. [CrossRef]
100. Bressi, G.; Carugno, G.; Onofrio, R.; Ruoso, G. Measurement of the Casimir Force between Parallel Metallic Surfaces. *Phys. Rev. Lett.* **2002**, *88*, 041804. [CrossRef] [PubMed]
101. Antonini, P.; Bimonte, G.; Bressi, G.; Carugno, G.; Galeazzi, G.; Messineo, G.; Ruoso, G. An Experimental Apparatus for Measuring the Casimir Effect at Large Distances. *J. Phys. Conf. Ser.* **2009**, *161*, 012006. [CrossRef]
102. Almasi, A.; Brax, P.; Iannuzzi, D.; Sedmik, R.I.P. Force Sensor for Chameleon and Casimir Force Experiments with Parallel-Plate Configuration. *Phys. Rev. D* **2015**, *91*, 102002. [CrossRef]
103. Sedmik, R.; Brax, P. Status Report and First Light from Cannex: Casimir Force Measurements between Flat Parallel Plates. *J. Phys. Conf. Ser.* **2018**, *1138*, 012014. [CrossRef]
104. Sedmik, R.I.P. Casimir and Non-Newtonian Force Experiment (CANNEX): Review, Status, and Outlook. *Int. J. Mod. Phys. A* **2020**, *35*, 2040008. [CrossRef]
105. Fischer, H.; Käding, C.; Sedmik, R.I.P.; Abele, H.; Brax, P.; Pitschmann, M. Search for Environment-Dependent Dilatons. *Phys. Dark Univ.* **2024**, *43*, 101419. [CrossRef]
106. Brax, P.; van de Bruck, C.; Davis, A.C.; Shaw, D.J.; Iannuzzi, D. Tuning the Mass of Chameleon Fields in Casimir Force Experiments. *Phys. Rev. Lett.* **2010**, *104*, 241101. [CrossRef]
107. Stochino, A.; DeSalvo, R.; Huang, Y.; Sannibale, V. Improvement of the Seismic Noise Attenuation Performance of the Monolithic Geometric Anti-Spring Filters for Gravitational Wave Interferometric Detectors. *Nucl. Instrum. Meth. A* **2007**, *580*, 1559–1564. [CrossRef]
108. Stochino, A.; Abbot, B.; Aso, Y.; Barton, M.; Bertolini, A.; Boschi, V.; Coyne, D.; DeSalvo, R.; Galli, C.; Huang, Y.; et al. The Seismic Attenuation System (SAS) for the Advanced LIGO Gravitational Wave Interferometric Detectors. *Nucl. Instr. Methods A* **2009**, *598*, 737. [CrossRef]
109. Blom, M.R.; Beker, M.G.; Bertolini, A.; van den Brand, J.F.J.; Bulten, H.J.; Doets, M.; Hennes, E.; Mul, F.A.; Rabeling, D.S.; Schimmel, A. Vertical and Horizontal Seismic Isolation Performance of the Advanced Virgo External Injection Bench Seismic Attenuation System. *Phys. Procedia* **2015**, *61*, 641–647. [CrossRef]
110. van Heijningen, J.V.; Bertolini, A.; Hennes, E.; Beker, M.G.; Doets, M.; Bulten, H.J.; Agatsuma, K.; Sekiguchi, T.; van den Brand, J.F.J. A Multistage Vibration Isolation System for Advanced Virgo Suspended Optical Benches. *Class. Quant. Grav.* **2019**, *36*, 075007. [CrossRef]
111. Cella, G.; Sannibale, V.; DeSalvo, R.; Márka, S.; Takamori, A. Monolithic Geometric Anti-Spring Blades. *Nucl. Instr. Meth. A* **2005**, *540*, 502–519. [CrossRef]
112. Takamori, A.; Raffai, P.; Márka, S.; DeSalvo, R.; Sannibale, V.; Tariq, H.; Bertolini, A.; Cella, G.; Viboud, N.; Numata, K.; et al. Inverted Pendulum as Low-Frequency Pre-Isolation for Advanced Gravitational Wave Detectors. *Nucl. Instrum. Meth. A* **2007**, *582*, 683–692. [CrossRef]
113. Peterson, J.R. *Observations and Modeling of Seismic Background Noise*; USGS Numbered Series 93-322; U.S. Geological Survey: Reston, VA, USA, 1993. [CrossRef]
114. Beker, M.G.; Bertolini, A.; van den Brand, J.F.J.; Bulten, H.J.; Hennes, E.; Rabeling, D.S. State Observers and Kalman Filtering for High Performance Vibration Isolation Systems. *Rev. Sci. Instrum.* **2014**, *85*, 034501. [CrossRef]
115. Rossi, F.; Opat, G.I. Observations of the Effects of Adsorbates on Patch Potentials. *J. Phys. D Appl. Phys.* **1992**, *25*, 1349–1353. [CrossRef]
116. Garrett, J.L.; Kim, J.; Munday, J.N. Measuring the Effect of Electrostatic Patch Potentials in Casimir Force Experiments. *Phys. Rev. Res.* **2020**, *2*, 023355. [CrossRef]
117. Robertson, N.A.; Blackwood, J.R.; Buchman, S.; Byer, R.L.; Camp, J.; Gill, D.; Hanson, J.; Williams, S.; Zhou, P. Kelvin Probe Measurements: Investigations of the Patch Effect with Applications to ST-7 and LISA. *Class. Quant. Grav.* **2006**, *23*, 2665. [CrossRef]
118. Speake, C.C.; Trenkel, C. Forces between Conducting Surfaces due to Spatial Variations of Surface Potential. *Phys. Rev. Lett.* **2003**, *90*, 160403. [CrossRef]
119. Kim, W.J.; Sushkov, A.O.; Dalvit, D.A.R.; Lamoreaux, S.K. Surface Contact Potential Patches and Casimir Force Measurements. *Phys. Rev. A* **2010**, *81*, 022505. [CrossRef]

120. Fosco, C.D.; Lombardo, F.C.; Mazzitelli, F.D. Electrostatic Interaction due to Patch Potentials on Smooth Conducting Surfaces. *Phys. Rev. A* **2013**, *88*, 062501. [CrossRef]
121. Liu, M.; Schafer, R.; Xu, J.; Mohideen, U. Elimination of Electrostatic Forces in Precision Casimir Force Measurements Using UV and Argon Ion Radiation. *Mod. Phys. Lett. A* **2020**, *35*, 2040001. [CrossRef]
122. de Man, S.; Heeck, K.; Iannuzzi, D. No Anomalous Scaling in Electrostatic Calibrations for Casimir Force Measurements. *Phys. Rev. A* **2009**, *79*, 024102. [CrossRef]
123. Sedmik, R.I.P.; Borghesani, A.F.; Heeck, K.; Iannuzzi, D. Hydrodynamic Force Measurements under Precisely Controlled Conditions: Correlation of Slip Parameters with the Mean Free Path. *Phys. Fluids* **2013**, *25*, 042103. [CrossRef]
124. Sedmik, R.I.P.; Urech, A.; Zalevsky, Z.; Carmeli, I. Efficient Reduction of Casimir Forces by Self-assembled Bio-molecular Thin Films. *arXiv* **2023**, arXiv:2306.16209. [CrossRef]
125. Turetta, N.; Sedona, F.; Liscio, A.; Sambì, M.; Samori, P. Au(111) Surface Contamination in Ambient Conditions: Unravelling the Dynamics of the Work Function in Air. *Adv. Mater. Interf.* **2021**, *8*, 2100068. [CrossRef]
126. Chavan, D.; Gruca, G.; de Man, S.; Slaman, M.; Rector, J.H.; Heeck, K.; Iannuzzi, D. Ferrule-Top Atomic Force Microscope. *Rev. Sci. Instrum.* **2010**, *81*, 123702. [CrossRef]
127. Behunin, R.O.; Dalvit, D.A.R.; Decca, R.S.; Genet, C.; Jung, I.W.; Lambrecht, A.; Liscio, A.; López, D.; Reynaud, S.; Schnoering, G.; et al. Kelvin Probe Force Microscopy of Metallic Surfaces Used in Casimir Force Measurements. *Phys. Rev. A* **2014**, *90*, 062115. [CrossRef]
128. Zerweck, U.; Loppacher, C.; Otto, T.; Grafström, S.; Eng, L.M. Accuracy and Resolution Limits of Kelvin Probe Force Microscopy. *Phys. Rev. B* **2005**, *71*, 125424. [CrossRef]
129. Axt, A.; Hermes, I.M.; Bergmann, V.W.; Tausendpfund, N.; Weber, S.A.L. Know Your Full Potential: Quantitative Kelvin Probe Force Microscopy on Nanoscale Electrical Devices. *Beilstein J. Nanotechnol.* **2018**, *9*, 1809–1819. [CrossRef]
130. Ma, Z.M.; Mu, J.L.; Tang, J.; Xue, H.; Zhang, H.; Xue, C.Y.; Liu, J.; Li, Y.J. Artifacts in KPFM in FM, AM and Heterodyne AM Modes. *Key Engin. Mater.* **2014**, *609–610*, 1362–1368. [CrossRef]
131. Burke, S.A.; LeDue, J.M.; Miyahara, Y.; Topple, J.M.; Fostner, S.; Grütter, P. Determination of the Local Contact Potential Difference of PTCDA on NaCl: A Comparison of Techniques. *Nanotechnol.* **2009**, *20*, 264012. [CrossRef]
132. Garrett, J.L.; Munday, J.N. Fast, High-Resolution Surface Potential Measurements in Air with Heterodyne Kelvin Probe Force Microscopy. *Nanotechnology* **2016**, *27*, 245705. [CrossRef]
133. Sugawara, Y.; Kou, L.; Ma, Z.; Kamijo, T.; Naitoh, Y.; Jun Li, Y. High Potential Sensitivity in Heterodyne Amplitude-Modulation Kelvin Probe Force Microscopy. *Appl. Phys. Lett.* **2012**, *100*, 223104. [CrossRef]
134. Sugawara, Y.; Miyazaki, M.; Li, Y.J. Surface Potential Measurement by Heterodyne Frequency Modulation Kelvin Probe Force Microscopy in MHz Range. *J. Phys. Commun.* **2020**, *4*, 075015. [CrossRef]
135. Ma, Z.M.; Kou, L.; Naitoh, Y.; Li, Y.J.; Sugawara, Y. The Stray Capacitance Effect in Kelvin Probe Force Microscopy Using FM, AM and Heterodyne AM Modes. *Nanotechnology* **2013**, *24*, 225701. [CrossRef]
136. Miyazaki, M.; Sugawara, Y.; Li, Y.J. Dual-Bias Modulation Heterodyne Kelvin Probe Force Microscopy in FM Mode. *Appl. Phys. Lett.* **2022**, *121*, 241602. [CrossRef]
137. Nonnenmacher, M.; O’Boyle, M.P.; Wickramasinghe, H.K. Kelvin Probe Force Microscopy. *Appl. Phys. Lett.* **1991**, *58*, 2921–2923. [CrossRef]
138. Dobosz, M.; Kożuchowski, M. Overview of the Laser-Wavelength Measurement Methods. *Opt. Lasers Engin.* **2017**, *98*, 107–117. [CrossRef]
139. Thorlabs GmbH (Newton, NJ, USA). Private communication, 2023.
140. Rabinovich, S.G. *Measurement Errors and Uncertainties: Theory and Practice*; AIP Press/Springer Science & Business Media: New York, NY, USA, 2005. [CrossRef]
141. Bordag, M.; Klimchitskaya, G.L.; Mohideen, U.; Mostepanenko, V.M. *Advances in the Casimir Effect*; Oxford University Press: New York, NY, 2014. [CrossRef]
142. Lifshitz, E.M. The Theory of Molecular Attractive Force between Solids. *Sov. Phys. JETP* **1956**, *2*, 73–83. Available online: <http://jetp.ras.ru/cgi-bin/e/index/e/2/1/p73?a=list> (accessed on 7 February 2024).
143. Iannuzzi, D.; Lisanti, M.; Capasso, F. Effect of Hydrogen-Switchable Mirrors on the Casimir force. *Proc. Natl. Acad. Sci. USA* **2004**, *101*, 4019–4023. [CrossRef]
144. Lamoreaux, S.K. Reanalysis of Casimir Force Measurements in the 0.6-to-6- μm Range. *Phys. Rev. A* **2010**, *82*, 024102. [CrossRef]
145. Banishev, A.A.; Chang, C.C.; Klimchitskaya, G.L.; Mostepanenko, V.M.; Mohideen, U. Measurement of the Gradient of the Casimir Force between a Nonmagnetic Gold Sphere and a Magnetic Nickel Plate. *Phys. Rev. B* **2012**, *85*, 195422. [CrossRef]
146. Zhao, R.; Li, L.; Yang, S.; Bao, W.; Xia, Y.; Ashby, P.; Wang, Y.; Zhang, X. Stable Casimir Equilibria and Quantum Trapping. *Science* **2019**, *364*, 984–987. [CrossRef]
147. Dzyaloshinskii, I.E.; Lifshitz, E.M.; Pitaevskii, L.P. General Theory of the van der Waals’ Forces. *Sov. Phys. Usp.* **1961**, *4*, 153–176. [CrossRef]
148. Rodriguez, A.W.; Reid, M.T.H.; Intravaia, F.; Woolf, A.; Dalvit, D.A.R.; Capasso, F.; Johnson, S.G. Geometry-Induced Casimir Suspension of Oblate Bodies in Fluids. *Phys. Rev. Lett.* **2013**, *111*, 180402. [CrossRef]
149. Estes, V.; Carretero-Palacios, S.; Míguez, H. Nanolevitation Phenomena in Real Plane-Parallel Systems Due to the Balance between Casimir and Gravity Forces. *J. Phys. Chem. C* **2015**, *119*, 5663–5670. [CrossRef]

150. Estes, V.; Frustaglia, D.; Carretero-Palacios, S.; Míguez, H. Casimir-Lifshitz Optical Resonators: A New Platform for Exploring Physics at the Nanoscale. *Adv. Phys. Res.* **2023**, *3*, 2300065. [CrossRef]
151. Bostrom, M.; Sernelius, B.E. Thermal Effects on the Casimir Force in the 0.1-5 μm Range. *Phys. Rev. Lett.* **2000**, *84*, 4757. [CrossRef]
152. Brevik, I.; Shapiro, B.; Silveirinha, M.G. Fluctuational electrodynamics in and out of equilibrium. *Int. J. Mod. Phys. A* **2022**, *37*, 2241012. [CrossRef]
153. Klimchitskaya, G.L.; Mostepanenko, V.M. Current status of the problem of thermal Casimir force. *Int. J. Mod. Phys. A* **2022**, *37*, 2241002. [CrossRef]
154. Decca, R.S.; López, D.; Fischbach, E.; Klimchitskaya, G.L.; Krause, D.E.; Mostepanenko, V.M. Tests of new physics from precise measurements of the Casimir pressure between two gold-coated plates. *Phys. Rev. D* **2007**, *75*, 077101. [CrossRef]
155. Liu, M.; Xu, J.; Klimchitskaya, G.L.; Mostepanenko, V.M.; Mohideen, U. Precision measurements of the gradient of the Casimir force between ultraclean metallic surfaces at larger separations. *Phys. Rev. A* **2019**, *100*, 052511. [CrossRef]
156. Bimonte, G.; Spreng, B.; Maia Neto, P.A.; Ingold, G.L.; Klimchitskaya, G.L.; Mostepanenko, V.M.; Decca, R.S. Measurement of the Casimir Force between 0.2 and 8 μm : Experimental Procedures and Comparison with Theory. *Universe* **2021**, *7*, 93. [CrossRef]
157. Garcia-Sanchez, D.; Fong, K.Y.; Bhaskaran, H.; Lamoreaux, S.; Tang, H.X. Casimir Force and 'In Situ' Surface Potential Measurements on Nanomembranes. *Phys. Rev. Lett.* **2012**, *109*, 027202. [CrossRef]
158. Behunin, R.O.; Zeng, Y.; Dalvit, D.A.R.; Reynaud, S. Electrostatic Patch Effects in Casimir-force Experiments Performed in the Sphere-Plane Geometry. *Phys. Rev. A* **2012**, *86*, 052509. [CrossRef]
159. Garrett, J.L.; Somers, D.; Munday, J.N. The Effect of Patch Potentials in Casimir Force Measurements Determined by Heterodyne Kelvin Probe Force Microscopy. *J. Phys. Cond. Matter* **2015**, *27*, 214012. [CrossRef]
160. Torgerson, J.R.; Lamoreaux, S.K. Low-frequency Character of the Casimir Force between Metallic Films. *Phys. Rev. E* **2004**, *70*, 047102. [CrossRef]
161. Bimonte, G. Johnson Noise and the Thermal Casimir Effect. *New J. Phys.* **2007**, *9*, 281. [CrossRef]
162. Intravaia, F.; Henkel, C. Casimir Interaction from Magnetically Coupled Eddy Currents. *Phys. Rev. Lett.* **2009**, *103*, 130405. [CrossRef]
163. Klimchitskaya, G.L.; Mostepanenko, V.M. Casimir Effect Invalidates the Drude Model for Transverse Electric Evanescent Waves. *Physics* **2023**, *5*, 952–967. [CrossRef]
164. van Leeuwen, H.J. Problèmes de la théorie électronique du magnétisme. *J. Phys. Radium* **1921**, *2*, 361–377. [CrossRef]
165. Bimonte, G. Bohr–van Leeuwen theorem and the thermal Casimir effect for conductors. *Phys. Rev. A* **2009**, *79*, 042107. [CrossRef]
166. London, F.; London, H. The Electromagnetic Equations of the Supraconductor. *Proc. R. Soc. A Math. Phys. Engin. Sci.* **1935**, *149*, 71–88. [CrossRef]
167. Intravaia, F. How Modes Shape Casimir Physics. *Int. J. Mod. Phys. A* **2022**, *37*, 2241014. [CrossRef]
168. Intravaia, F.; Ellingsen, S.; Henkel, C. Casimir–Foucault Interaction: Free Energy and Entropy at Low Temperature. *Phys. Rev. A* **2010**, *82*, 032504. [CrossRef]
169. Henkel, C.; Intravaia, F. On the Casimir Entropy between 'Perfect Crystals'. *Int. J. Mod. Phys. A* **2010**, *25*, 2328–2336. [CrossRef]
170. Reiche, D.; Busch, K.; Intravaia, F. Quantum Thermodynamics of Overdamped Modes in Local and Spatially Dispersive Materials. *Phys. Rev. A* **2020**, *101*, 012506. [CrossRef]
171. Bimonte, G.; Santamato, E. General Theory of Electromagnetic Fluctuations near a Homogeneous Surface in Terms of Its Reflection Amplitudes. *Phys. Rev. A* **2007**, *76*, 013810. [CrossRef]
172. Guérout, R.; Lambrecht, A.; Milton, K.A.; Reynaud, S. Derivation of the Lifshitz–Matsubara Sum Formula for the Casimir Pressure between Metallic Plane Mirrors. *Phys. Rev. E* **2014**, *90*, 042125. [CrossRef]
173. Svetovoy, V.B.; Esquivel, R. Nonlocal Impedances and the Casimir Entropy at Low Temperatures. *Phys. Rev. E* **2005**, *72*, 036113. [CrossRef]
174. Intravaia, F.; Henkel, C. Casimir Energy and Entropy between Dissipative Mirrors. *J. Phys. A Math. Gen.* **2008**, *41*, 164018. [CrossRef]
175. Klimchitskaya, G.L.; Blagov, E.V.; Mostepanenko, V.M. Problems in the Lifshitz Theory of Atom–Wall Interaction. *Int. J. Mod. Phys. A* **2009**, *24*, 1777–1788. [CrossRef]
176. Klimchitskaya, G.L.; Mohideen, U.; Mostepanenko, V.M. The Casimir Force between real Materials: Experiment and Theory. *Rev. Mod. Phys.* **2009**, *81*, 1827–1885. [CrossRef]
177. Milton, K. The Casimir Force: Feeling the Heat. *Nat. Phys.* **2011**, *7*, 190–191. [CrossRef]
178. Shelden, C.; Spreng, B.; Munday, J.N. Enhanced Repulsive Casimir Forces between Gold and Thin Magnetodielectric Plates. *Phys. Rev. A* **2023**, *108*, 032817. [CrossRef]
179. Banishev, A.A.; Klimchitskaya, G.L.; Mostepanenko, V.M.; Mohideen, U. Casimir Interaction between Two Magnetic Metals in Comparison with Nonmagnetic Test Bodies. *Phys. Rev. B* **2013**, *88*, 155410. [CrossRef]
180. Bordag, M.; Fialkovsky, I.V.; Gitman, D.M.; Vassilevich, D.V. Casimir Interaction between a Perfect Conductor and Graphene Described by the Dirac Model. *Phys. Rev. B* **2009**, *80*, 245406. [CrossRef]
181. Fialkovsky, I.V.; Marachevsky, V.N.; Vassilevich, D.V. Finite-Temperature Casimir Effect for Graphene. *Phys. Rev. B* **2011**, *84*, 035446. [CrossRef]
182. Egerland, C.H.; Busch, K.; Intravaia, F. Polaritonic Contribution to the Casimir Energy between Two Graphene Layers. *Phys. Rev. B* **2019**, *100*, 235418. [CrossRef]

183. Woods, L.M.; Dalvit, D.A.R.; Tkatchenko, A.; Rodriguez-Lopez, P.; Rodriguez, A.W.; Podgornik, R. Materials Perspective on Casimir and van der Waals Interactions. *Rev. Mod. Phys.* **2016**, *88*, 045003. [CrossRef]
184. Fialkovsky, I.; Khusnutdinov, N.; Vassilevich, D. Quest for Casimir Repulsion between Chern-Simons Surfaces. *Phys. Rev. B* **2018**, *97*, 165432. [CrossRef]
185. Chen, L.; Chang, K. Chiral-Anomaly-Driven Casimir-Lifshitz Torque between Weyl Semimetals. *Phys. Rev. Lett.* **2020**, *125*, 047402. [CrossRef]
186. Farias, M.B.; Zyuzin, A.A.; Schmidt, T.L. Casimir Force between Weyl Semimetals in a Chiral Medium. *Phys. Rev. B* **2020**, *101*, 235446. [CrossRef]
187. Intravaia, F.; Lambrecht, A. Surface Plasmon Modes and the Casimir Energy. *Phys. Rev. Lett.* **2005**, *94*, 110404. [CrossRef]
188. Intravaia, F.; Henkel, C.; Lambrecht, A. Role of Surface Plasmons in the Casimir Effect. *Phys. Rev. A* **2007**, *76*, 033820. [CrossRef]
189. Boyer, T.H. Quantum Electromagnetic Zero-Point Energy of a Conducting Spherical Shell and the Casimir Model for a Charged Particle. *Phys. Rev.* **1968**, *174*, 1764–1766. [CrossRef]
190. Graham, N.; Quandt, M.; Weigel, H. Attractive Electromagnetic Casimir Stress on a Spherical Dielectric Shell. *Phys. Lett. B* **2013**, *4–5*, 846–849. [CrossRef]
191. Büscher, R.; Emig, T. Nonperturbative Approach to Casimir Interactions in Periodic Geometries. *Phys. Rev. A* **2004**, *69*, 062101. [CrossRef]
192. Davids, P.S.; Intravaia, F.; Rosa, F.S.S.; Dalvit, D.A.R. Modal Approach to Casimir Forces in Periodic Structures. *Phys. Rev. A* **2010**, *82*, 062111. [CrossRef]
193. Lambrecht, A.; Marachevsky, V.N. Casimir Interaction of Dielectric Gratings. *Phys. Rev. Lett.* **2008**, *101*, 160403. [CrossRef]
194. Intravaia, F.; Davids, P.S.; Decca, R.S.; Aksyuk, V.A.; López, D.; Dalvit, D.A.R. Quasianalytical Modal Approach for Computing Casimir Interactions in Periodic Nanostructures. *Phys. Rev. A* **2012**, *86*, 042101. [CrossRef]
195. Messina, R.; Maia Neto, P.A.; Guizal, B.; Antezza, M. Casimir Interaction between a Sphere and a Grating. *Phys. Rev. A* **2015**, *92*, 062504. [CrossRef]
196. Hartmann, M.; Ingold, G.L.; Neto, P.A.M. Plasma versus Drude Modeling of the Casimir Force: Beyond the Proximity Force Approximation. *Phys. Rev. Lett.* **2017**, *119*, 043901. [CrossRef]
197. Antezza, M.; Chan, H.B.; Guizal, B.; Marachevsky, V.N.; Messina, R.; Wang, M. Giant Casimir Torque between Rotated Gratings and the $\theta = 0$ Anomaly. *Phys. Rev. Lett.* **2020**, *124*, 013903. [CrossRef]
198. Schoger, T.; Spreng, B.; Ingold, G.L.; Lambrecht, A.; Maia Neto, P.A.; Reynaud, S. Universal Casimir Interactions in the Sphere–Sphere Geometry. *Int. J. Mod. Phys. A* **2022**, *37*, 2241005. [CrossRef]
199. Emig, T.; Bimonte, G. Multiple Scattering Expansion for Dielectric Media: Casimir Effect. *Phys. Rev. Lett.* **2023**, *130*, 200401. [CrossRef]
200. Reid, M.T.H.; White, J.; Johnson, S.G. Computation of Casimir Interactions between Arbitrary three-dimensional objects with arbitrary material properties. *Phys. Rev. A* **2011**, *84*, 010503. [CrossRef]
201. Johnson, S. Numerical Methods for Computing Casimir Interactions. In *Casimir Physics*; Dalvit, D., Milonni, P., Roberts, D., da Rosa, F., Eds.; Springer: Berlin/Heidelberg, Germany, 2011; pp. 175–218. [CrossRef]
202. Rodriguez, A.W.; Capasso, F.; Johnson, S.G. The Casimir Effect in Microstructured Geometries. *Nat. Photon.* **2011**, *5*, 211–221. [CrossRef]
203. Reid, M.T.H.; White, J.; Johnson, S.G. Fluctuating Surface Currents: An Algorithm for Efficient Prediction of Casimir Interactions among Arbitrary Materials in Arbitrary Geometries. *Phys. Rev. A* **2013**, *88*, 022514. [CrossRef]
204. Kristensen, P.T.; Beverungen, B.; Intravaia, F.; Busch, K. High-Accuracy Casimir–Polder Force Calculations using the Discontinuous Galerkin Time-Domain method. *Phys. Rev. B* **2023**, *108*, 205424. [CrossRef]
205. Chan, H.B.; Aksyuk, V.A.; Kleiman, R.N.; Bishop, D.J.; Capasso, F. Quantum Mechanical Actuation of Microelectromechanical Systems by the Casimir Force. *Science* **2001**, *291*, 1941–1944. [CrossRef]
206. Chan, H.B.; Aksyuk, V.A.; Kleiman, R.N.; Bishop, D.J.; Capasso, F. Nonlinear Micromechanical Casimir Oscillator. *Phys. Rev. Lett.* **2001**, *87*, 211801. [CrossRef]
207. Derjaguin, B.V.; Abrikosova, I.I.; Lifshitz, E.M. Direct Measurement of Molecular Attraction between Solids Separated by a Narrow Gap. *Quart. Rev. Chem. Soc.* **1956**, *10*, 295–329. [CrossRef]
208. Decca, R.S.; López, D.; Fischbach, E.; Klimchitskaya, G.L.; Krause, D.E.; Mostepanenko, V.M. Precise Comparison of Theory and New Experiment for the Casimir Force Leads to Stronger Constraints on Thermal Quantum Effects and Long-Range Interactions. *Ann. Phys.* **2005**, *318*, 37–80. [CrossRef]
209. Sparnaay, M.J. Attractive Forces between Flat Plates. *Nature* **1957**, *180*, 334–335. [CrossRef]
210. Chan, H.B.; Bao, Y.; Zou, J.; Cirelli, R.A.; Klemens, F.; Mansfield, W.M.; Pai, C.S. Measurement of the Casimir Force between a Gold Sphere and a Silicon Surface with Nanoscale Trench Arrays. *Phys. Rev. Lett.* **2008**, *101*, 030401. [CrossRef]
211. Bao, Y.; Guèrout, R.; Lussange, J.; Lambrecht, A.; Cirelli, R.A.; Klemens, F.; Mansfield, W.M.; Pai, C.S.; Chan, H.B. Casimir Force on a Surface with Shallow Nanoscale Corrugations: Geometry and Finite Conductivity Effects. *Phys. Rev. Lett.* **2010**, *105*, 250402. [CrossRef]
212. Lussange, J.; Guèrout, R.; Lambrecht, A. Casimir Energy between Nanostructured Gratings of Arbitrary Periodic Profile. *Phys. Rev. A* **2012**, *86*, 062502. [CrossRef]

213. Intravaia, F.; Koev, S.; Jung, I.W.; Talin, A.A.; Davids, P.S.; Decca, R.S.; Aksyuk, V.A.; Dalvit, D.A.R.; López, D. Strong Casimir Force Reduction through Metallic Surface Nanostructuring. *Nat. Commun.* **2013**, *4*, 2515. [CrossRef] [PubMed]
214. Wang, M.; Tang, L.; Ng, C.Y.; Messina, R.; Guizal, B.; Crosse, J.A.; Antezza, M.; Chan, C.T.; Chan, H.B. Strong Geometry Dependence of the Casimir Force between Interpenetrated Rectangular Gratings. *Nat. Commun.* **2021**, *12*, 600. [CrossRef] [PubMed]
215. Chen, H.T.; Taylor, A.J.; Yu, N. A Review of Metasurfaces: Physics and Applications. *Rep. Prog. Phys.* **2016**, *79*, 076401. [CrossRef] [PubMed]
216. Kort-Kamp, W.J.M.; Azad, A.K.; Dalvit, D.A.R. Space-Time Quantum Metasurfaces. *Phys. Rev. Lett.* **2021**, *127*, 043603. [CrossRef]
217. Qiu, C.W.; Zhang, T.; Hu, G.; Kivshar, Y. Quo Vadis, Metasurfaces? *Nano Lett.* **2021**, *21*, 5461–5474. [CrossRef]
218. Rahi, S.J.; Emig, T.; Graham, N.; Jaffe, R.L.; Kardar, M. Scattering Theory Approach to Electrodynamic Casimir Forces. *Phys. Rev. D* **2009**, *80*, 085021. [CrossRef]
219. Rahi, S.J.; Emig, T.; Jaffe, R.L. Geometry and Material Effects in Casimir Physics-Scattering Theory. In *Casimir Physics*; Dalvit, D., Milonni, P., Roberts, D., da Rosa, F., Eds.; Springer: Berlin/Heidelberg, Germany, 2011; pp. 129–174. [CrossRef]
220. Lambrecht, A.; Canaguier-Durand, A.; Guérout, R.; Reynaud, S. Casimir Effect in the Scattering Approach: Correlations between Material Properties, Temperature and Geometry. In *Casimir Physics*; Dalvit, D., Milonni, P., Roberts, D., da Rosa, F., Eds.; Springer: Berlin/Heidelberg, Germany, 2011; pp. 97–127. [CrossRef]
221. Ingold, G.L.; Lambrecht, A. Casimir Effect from a Scattering Approach. *Am. J. Phys.* **2015**, *83*, 156–162. [CrossRef]
222. Busch, K.; von Freymann, G.; Linden, S.; Mingaleev, S.; Tkeshelashvili, L.; Wegener, M. Periodic Nanostructures for Photonics. *Phys. Rep.* **2007**, *444*, 101–202. [CrossRef]
223. Matsubara, T. A New Approach to Quantum Statistical Mechanics. *Prog. Theor. Phys.* **1955**, *14*, 351–378. [CrossRef]
224. Chiu, H.C.; Klimchitskaya, G.L.; Marachevsky, V.N.; Mostepanenko, V.M.; Mohideen, U. Lateral Casimir Force between Sinusoidally Corrugated Surfaces: Asymmetric Profiles, Deviations from the Proximity Force Approximation, and Comparison with Exact Theory. *Phys. Rev. B* **2010**, *81*, 115417. [CrossRef]
225. Antezza, M.; Pitaevskii, L.P.; Stringari, S.; Svetovoy, V.B. Casimir-Lifshitz Force Out of Thermal Equilibrium and Asymptotic Nonadditivity. *Phys. Rev. Lett.* **2006**, *97*, 223203. [CrossRef]
226. Volokitin, A.I.; Persson, B.N.J. Near-Field Radiative Heat Transfer and Noncontact Friction. *Rev. Mod. Phys.* **2007**, *79*, 1291–1329. [CrossRef]
227. Reiche, D.; Intravaia, F.; Busch, K. Wading through the Void: Exploring Quantum Friction and Nonequilibrium fluctuations. *APL Photon.* **2022**, *7*, 030902. [CrossRef]
228. Antezza, M.; Pitaevskii, L.P.; Stringari, S.; Svetovoy, V.B. Casimir–Lifshitz Force out of Thermal Equilibrium. *Phys. Rev. A* **2008**, *77*, 022901. [CrossRef]
229. Obrecht, J.M.; Wild, R.J.; Antezza, M.; Pitaevskii, L.P.; Stringari, S.; Cornell, E.A. Measurement of the Temperature Dependence of the Casimir-Polder Force. *Phys. Rev. Lett.* **2007**, *98*, 063201. [CrossRef]
230. Messina, R.; Antezza, M. Scattering-Matrix Approach to Casimir–Lifshitz Force and Heat Transfer out of Thermal Equilibrium between Arbitrary Bodies. *Phys. Rev. A* **2011**, *84*, 042102. [CrossRef]
231. Bartolo, N.; Messina, R.; Dalvit, D.A.R.; Intravaia, F. Nonequilibrium Casimir–Polder Plasmonic Interactions. *Phys. Rev. A* **2016**, *93*, 042111. [CrossRef]
232. Fuchs, S.; Bennett, R.; Krems, R.V.; Buhmann, S.Y. Nonadditivity of Optical and Casimir-Polder Potentials. *Phys. Rev. Lett.* **2018**, *121*, 083603. [CrossRef] [PubMed]
233. Bimonte, G.; Emig, T.; Krüger, M.; Kardar, M. Dilution and Resonance-enhanced Repulsion in Nonequilibrium Fluctuation Forces. *Phys. Rev. A* **2011**, *84*, 042503. [CrossRef]
234. Zhang, B.; Henkel, C.; Haller, E.; Wildermuth, S.; Hofferberth, S.; Krüger, P.; Schmiedmayer, J. Relevance of Sub-Surface Chip Layers for the Lifetime of Magnetically Trapped Atoms. *Eur. Phys. J. D* **2005**, *35*, 97–104. [CrossRef]
235. Yariv, A.; Yeh, P. *Optical Waves in Crystals. Propagation and Control of Laser Radiation*; John Wiley & Sons: New York, NY, USA, 1983.
236. Mendoza Herrera, L.J.; Arboleda, D.M.; Santillán, J.M.J.; Fernández van Raap, M.B.; Scaffardi, L.B.; Schinca, D.C. Nanoscale Dielectric Function of Fe, Pt, Ti, Ta, Al, and V: Application to Characterization of Al Nanoparticles Synthesized by Fs Laser Ablation. *Plasmonics* **2017**, *12*, 1813–1824. [CrossRef]
237. Ordal, M.A.; Bell, R.J.; Alexander, R.W.; Long, L.L.; Querry, M.R. Optical Properties of Fourteen Metals in the Infrared and Far Infrared: Al, Co, Cu, Au, Fe, Pb, Mo, Ni, Pd, Pt, Ag, Ti, V, and W. *Appl. Opt.* **1985**, *24*, 4493–4499. [CrossRef] [PubMed]
238. Pirozhenko, I.; Lambrecht, A. Influence of Slab Thickness on the Casimir Force. *Phys. Rev. A* **2008**, *77*, 013811. [CrossRef]
239. Khoury, J.; Weltman, A. Chameleon Cosmology. *Phys. Rev. D* **2004**, *69*, 044026. [CrossRef]
240. Khoury, J. Les Houches Lectures on Physics beyond the Standard Model of Cosmology. *arXiv* **2013**, arXiv:1312.2006. [CrossRef]
241. Brax, P.; Burrage, C.; Davis, A.C. Screening Fifth Forces in K-Essence and DBI Models. *J. Cosmol. Astropart. Phys.* **2013**, *1*, 020. [CrossRef]
242. Brax, P.; Valageas, P. K-Mouflage Cosmology: The Background Evolution. *Phys. Rev. D* **2014**, *90*, 023507. [CrossRef]
243. Vainshtein, A.I. To the Problem of Nonvanishing Gravitation Mass. *Phys. Lett. B* **1972**, *39*, 393–394. [CrossRef]
244. Damour, T.; Polyakov, A.M. The String Dilaton and a Least Coupling Principle. *Nucl. Phys.* **1994**, *B423*, 532–558. [CrossRef]
245. Brax, P.; van de Bruck, C.; Davis, A.C.; Shaw, D. Dilaton and Modified Gravity. *Phys. Rev. D* **2010**, *82*, 063519. [CrossRef]

246. Sakstein, J.A. Astrophysical Tests of Modified Gravity. Ph.D. Thesis, Downing College, University of Cambridge, Cambridge, UK, 2014. [CrossRef]
247. Cronenberg, G.; Brax, P.; Filter, H.; Geltenbort, P.; Jenke, T.; Pignol, G.; Pitschmann, M.; Thalhammer, M.; Abele, H. Acoustic Rabi Oscillations between Gravitational Quantum States and Impact on Symmetron Dark Energy. *Nat. Phys.* **2018**, *14*, 1022–1026. [CrossRef]
248. Brax, P.; Pitschmann, M. Exact Solutions to Nonlinear Symmetron Theory: One- and Two-Mirror Systems. *Phys. Rev. D* **2018**, *97*, 064015. [CrossRef]
249. Pitschmann, M. Exact Solutions to Nonlinear Symmetron Theory: One- and Two-Mirror Systems. II. *Phys. Rev. D* **2021**, *103*, 084013. [CrossRef]
250. Burrage, C.; Sakstein, J. Tests of Chameleon Gravity. *Living Rev. Relativ.* **2018**, *21*, 1. [CrossRef]
251. Gasperini, M.; Piazza, F.; Veneziano, G. Quintessence as a Runaway Dilaton. *Phys. Rev. D* **2001**, *65*, 023508. [CrossRef]
252. Damour, T.; Piazza, F.; Veneziano, G. Violations of the Equivalence Principle in a Dilaton Runaway Scenario. *Phys. Rev. D* **2002**, *66*, 046007. [CrossRef]
253. Damour, T.; Piazza, F.; Veneziano, G. Runaway Dilaton and Equivalence Principle Violations. *Phys. Rev. Lett.* **2002**, *89*, 081601. [CrossRef] [PubMed]
254. Brax, P.; Burrage, C.; Davis, A.C. Laboratory Constraints. *Int. J. Mod. Phys. D* **2018**, *27*, 1848009. [CrossRef]
255. Burrage, C.; Copeland, E.J.; Hinds, E.A. Probing Dark Energy with Atom Interferometry. *J. Cosmol. Astropart. Phys.* **2015**, *2015*, 042. [CrossRef]
256. Burrage, C.; Copeland, E.J. Using Atom Interferometry to Detect Dark Energy. *Contemp. Phys.* **2016**, *57*, 164–176. [CrossRef]
257. Upadhye, A. Symmetron Dark Energy in Laboratory Experiments. *Phys. Rev. Lett.* **2013**, *110*, 031301. [CrossRef] [PubMed]
258. Jenke, T.; Bosina, J.; Micko, J.; Pitschmann, M.; Sedmik, R.; Abele, H. Gravity Resonance Spectroscopy and Dark Energy Symmetron Fields. *Eur. Phys. J. Spec. Top.* **2021**, *230*, 1131–1136. [CrossRef]
259. Brax, P.; Davis, A.C.; Elder, B. Screened Scalar Fields in Hydrogen and Muonium. *Phys. Rev. D* **2023**, *107*, 044008. [CrossRef]
260. Fischer, H.; Käding, C.; Lemmel, H.; Sponar, S.; Pitschmann, M. Search for Dark Energy with Neutron Interferometry. *Prog. Theor. Exp. Phys.* **2024**, *2*, 023E02. [CrossRef]
261. Brax, P.; Fischer, H.; Käding, C.; Pitschmann, M. The Environment Dependent Dilaton in the Laboratory and the Solar System. *Eur. Phys. J. C* **2022**, *82*, 934. [CrossRef]
262. Ivanov, A.N.; Cronenberg, G.; Höllwieser, R.; Jenke, T.; Pitschmann, M.; Wellenzohn, M.; Abele, H. Exact Solution for Chameleon Field, Self-Coupled through the Ratra–Peebles Potential with $n = 1$ and Confined between Two Parallel Plates. *Phys. Rev. D* **2016**, *94*, 085005. [CrossRef]
263. Keysight Technologies (Santa Rosa, CA, USA). Private communication, 2023.

Disclaimer/Publisher’s Note: The statements, opinions and data contained in all publications are solely those of the individual author(s) and contributor(s) and not of MDPI and/or the editor(s). MDPI and/or the editor(s) disclaim responsibility for any injury to people or property resulting from any ideas, methods, instructions or products referred to in the content.

Casimir Forces between a Dielectric and Metal: Compensation of the Electrostatic Interaction

Vitaly B. Svetovoy

Frumkin Institute of Physical Chemistry and Electrochemistry, Russian Academy of Sciences,
Leninsky Prospect 31 bld. 4, 119071 Moscow, Russia; v.svetovoy@phyche.ac.ru

Abstract: The Casimir forces between metals or good conductors have been checked experimentally. Semiconductors and especially dielectrics have not been investigated because of the surface charges, which generate strong electrostatic forces. Here, it is proposed to study the Casimir interaction of a dielectric and metal using a thin dielectric layer deposited on an optically thick metallic substrate. If the thickness of the layer is a few tens of nanometers, the electrostatic force due to charging can be compensated for by applying an extra voltage between the metallic plates. On the other hand, the contribution of the dielectric layer to the Casimir force is sufficiently large to extract information about the interaction between the bulk dielectric and metal.

Keywords: Casimir force; electrostatic force; charging effect; dielectric layer; compensation potential

1. Introduction

The Casimir forces [1] between bulk bodies have been intensely investigated during the last 20 years (see reviews [2–5]). Critical experiments have been performed in vacuum with a high precision at distances of the order of 100 nm [6–9]. A theoretical description of these forces generated by thermal and quantum fluctuations of the electromagnetic field has been proposed by Evgeniy Lifshitz and later developed along with his colleagues, Igor Dzyaloshinskii and Lev Pitaevskii [10,11]. Predictions of the Lifshitz theory have been checked in special experiments. The dependence of the Casimir forces on the dielectric functions of interacting materials has been verified [12–17], including magnetic materials [18,19]. Shorter distances up to 10 nm have been explored [20,21] and the importance of the effects of surface roughness has been stressed [22,23]. Larger distances in the range of micrometers have been carefully investigated experimentally [24–27] and it was found that there are some systematic deviations in the thermal contribution to the force.

The total force that is directly measured in the experiments includes the Casimir and electrostatic forces. The latter to be considered a background effect and has to be excluded. To minimize the electrostatic force, nearly all experiments have been performed with well-conducted materials but, even for good conductors, the electrostatic contribution to the total force is still important. The electrostatic force originates from the contact potential difference between different materials. However, even for similar interacting materials, the contact potential is nonzero because of the potential difference in the external circuit.

Dielectrics have never been used for force measurements because they contain trapped charges resulting in a strong electrostatic contribution. Even for semiconductors, only a few special cases have been tackled: silicon passivated with hydrogen (H-terminated) [13,28] that prevents oxidation and silicon carbide heavily doped with nitrogen [21], which behaves similar to metals. In general, the effect of charging significantly restricts the choice of materials that can be used for measurements of the Casimir forces.

Investigation of the insulating materials has been concentrated on the space charge in materials [29,30], where the trapped charges in localized states are produced by irradiation, ionization or injection. For thick dielectrics, the charging can be non-homogeneous in depth

Citation: Svetovoy, V.B. Casimir Forces between a Dielectric and Metal: Compensation of the Electrostatic Interaction. *Physics* **2023**, *5*, 814–822. <https://doi.org/10.3390/physics5030051>

Received: 15 June 2023

Accepted: 11 July 2023

Published: 25 July 2023



Copyright: © 2023 by the authors. Licensee MDPI, Basel, Switzerland. This article is an open access article distributed under the terms and conditions of the Creative Commons Attribution (CC BY) license (<https://creativecommons.org/licenses/by/4.0/>).

but, here, one considered homogeneously charged thin dielectric layers on metallic surfaces. The charging mechanisms in general are rather complicated but the total concentration of the surface charges can vary in the range of 10^{10} – 10^{13} cm^{-2} depending on the technological processing, with typical values in the range of 10^{11} – 10^{12} cm^{-2} .

The purpose of this paper is to demonstrate that the electrostatic force between two metals, one of which is covered by a thin dielectric layer, can be compensated for by applying an external potential between the bodies. Only for thick dielectrics is it not possible to compensate for the electrostatic force. It is also demonstrated that a layer with a thickness of a few tens of nanometers is sufficient to extract information about the Casimir interaction of the dielectric and metal. Only metallic substrates are considered here to concentrate on the main idea but not on the technical details. The application of the same idea applied to semiconductor substrates will be considered elsewhere. The problem solved in this paper is rather simple but, to the best of our knowledge, it has not been discussed in relation to the Casimir force measurements.

2. Electrostatic Interaction of Metals Covered by the Dielectric

Let us consider the electrostatic force between two metal plates, one of which is covered by a thin dielectric layer (see Figure 1). The dielectric can be deposited on the metal surface in a controlled way, for example, by magnetron sputtering. The dielectric layer with the thickness d can be made of any chemical compound and is charged with the bulk density ρ_0 . The Casimir force will be larger if only one metal is covered by the dielectric, so let us consider this configuration. In the experiments measuring the Casimir forces, researchers always try to avoid surface charges. When the force is measured between metals, the residual potential difference can be compensated for by applying an external voltage between the metals, as has been carried out in all the experiments [6–9]. If one metal has a dielectric covering, one has to take into account a finite concentration of charges in the dielectric. Here, we are going to answer the question: is it possible to compensate for the electrostatic force in this case?

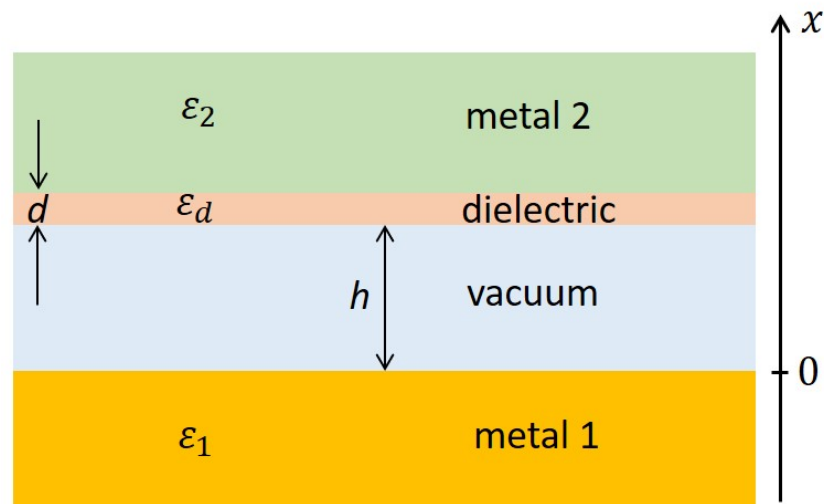


Figure 1. The structure under investigation. The plates are separated by a vacuum gap, h , and the thickness of the dielectric layer on one of the metals is d . The relative dielectric functions ($\epsilon_{1,2}$) of the materials are indicated; they are needed to calculate the Casimir attraction in this structure.

2.1. Solution of the Electrostatic Problem

The structure under investigation is shown in Figure 1. The relative dielectric functions $\epsilon_{1,2}$ and ϵ_d are, in general, functions of frequency, ω , but, for the electrostatic interaction ($\omega \rightarrow 0$), ϵ_d is a constant and $\epsilon_{1,2} \rightarrow \infty$. Let the potential the metal 1 be Ψ_1 ; however, the

potential of metal 2 can be chosen to be zero: $\Psi_2 = 0$. In between the metals, the potential is described by the Poisson equation

$$\frac{d^2\Psi}{dx^2} = \begin{cases} 0, & 0 < x < h, \\ -\rho_0/\epsilon_0\epsilon_{dm}, & h < x < h + d, \end{cases} \quad (1)$$

where ϵ_0 is the permittivity of the vacuum.

The external boundary conditions are chosen as $\Psi(0) = \Psi_1$ and $\Psi(h + d) = 0$. The solution that obeys the external boundary conditions is

$$\Psi(x) = \begin{cases} \Psi_0 + Ax, & 0 < x < h, \\ -\frac{\rho_0(x-h-d)^2}{2\epsilon_0\epsilon_d} + B(x-h-d), & h < x < h + d, \end{cases} \quad (2)$$

where A and B are unknown constants which are defined by the internal boundary conditions. At the vacuum–dielectric interface $x = h$, these are the continuity of the potential and electric displacement. Some surface charges can exist in the dielectric at the interface with the metal. However, in contrast with semiconductors, those charges do not contribute because the static dielectric constant of metals is going to infinity. Thus, the internal boundary conditions are

$$\begin{aligned} \Psi(h - \delta) &= \Psi(h + \delta), \\ \frac{d\Psi}{dx}\Big|_{h-\delta} &= \epsilon_d \frac{d\Psi}{dx}\Big|_{h+\delta}, \quad \delta \rightarrow 0. \end{aligned} \quad (3)$$

The electric field, E , in the vacuum gap is $E = A$ and the electrostatic pressure between the plates is defined by the normal component of the Maxwell stress tensor, $P_e = -\epsilon_0 E^2/2$, (minus sign because the force is attractive). Determining the constant A from the internal boundary conditions, one finds, for the pressure:

$$P_e = -\frac{\epsilon_0}{2} \left[\frac{(\rho_0 d/\epsilon_0)(d/2\epsilon_d) - \Psi_1}{h + d/\epsilon_d} \right]^2. \quad (4)$$

If there are no trapped charges in the dielectric ($\rho_0 = 0$), the only difference in the electrostatic pressure between metals is the effective increase in the distance between the plates, which is $h_{\text{eff}} = h + d/\epsilon_d$. At a finite density of charges, the metal potential, Ψ_1 , is shifted to the value,

$$\Delta U = \left(\frac{\rho_0 d}{\epsilon_0} \right) \left(\frac{d}{2\epsilon_d} \right), \quad (5)$$

where one can interpret $\rho_0 d$ as the projection of the charge density on the surface.

In most of the Casimir force experiments, a sphere–plate configuration is used for measurements and the electrostatic force has to be defined for this configuration. The electrostatic force acting between the sphere and the plate can be immediately found from Equation (4) by applying the proximity force approximation (Derjaguin’s approximation [31,32]), which is true for $h \ll R$, where R is the radius of the sphere. Then, one finds the electrostatic force between the sphere and the plate:

$$F_e \approx -\left(\frac{\pi R \epsilon_0}{2} \right) \frac{[(\rho_0 d/\epsilon_0)(d/2\epsilon_d) - \Psi_1]^2}{h + d/\epsilon_d}. \quad (6)$$

This result also depends on the shifted potential and effective distance. The exact expression for the force can be found analytically, but one can expect that this expression can also depend on the shifted potential and effective distance. It is worth noting that, at

short distances, the roughness of the interacting surfaces starts to contribute. One can deal with the electrostatic forces on the same basis as was proposed for the Casimir forces [23].

2.2. Compensation of the Surface Charges

In all the experiments, both plates (more often it is a sphere and plate) are grounded. Nevertheless, Ψ_1 is nonzero and can be as large as 100 mV or so. This value is due to the contact potential difference, V_c : $\Psi_1 = V_c$. In the case of two metals, this potential can be compensated for by applying the external voltage between the bodies as equal to $-V_c$. Equation (4) shows that one can also compensate for the electrostatic force between two metals, one of which is covered by the dielectric. If the external voltage is U , then $\Psi_1 = V_c + U$ and one finds the compensating potential,

$$U = -V_c + \Delta U. \tag{7}$$

Thus, in the case of the charged dielectric, one has to apply, in addition to $-V_c$, an extra voltage, ΔU , which is proportional to the density of charges in the dielectric. Similarly to the two metals case, the compensating potential does not depend on the distance, h , between the plates.

Consider an example where metal 2 is covered by silicon dioxide with the dielectric constant, $\epsilon_d = 3.9$. It is convenient to consider as a parameter the surface charge density

$$\sigma_s = \rho_0 d_0, \quad d_0 = 10 \text{ nm}. \tag{8}$$

The expected value for this parameter [30] is in the range of $|\sigma_s| = 10^{-8} - 10^{-7} \text{ C/cm}^2$ (concentration of the surface charges $N_s \sim 10^{11} - 10^{12} \text{ cm}^{-2}$). The extra voltage needed to compensate for the electrostatic force is estimated to be in the range of

$$|\Delta U| = (14.5 - 145)(d/d_0)^2 \text{ mV}. \tag{9}$$

If one considers $|\Delta U| < 1 \text{ V}$ as a realistic compensating potential, then Equation (9) restricts the thickness of the dielectric layer. From this restriction, one can conclude that, for the largest charge density, the dielectric film thickness has to be smaller than 26 nm and, for the smallest $|\sigma_s| = 10^{-8} \text{ C/cm}^2$, it has to be smaller than 83 nm. Now, the question is: can one obtain information about the Casimir interaction between the metal and dielectric measuring the force between two metals, one of which is covered by the dielectric with a thickness of approximately 40 nm?

3. Casimir Interaction of Metal Covered by the Dielectric

Let us consider the Casimir force in the configuration shown in Figure 1. The force can be calculated using the Lifshitz formula, where, as the reflection coefficient for plate 2 (the one covered with the dielectric), one has to use the following reflection coefficients [33]:

$$R_2^\nu = \frac{r_{vd}^\nu - r_{md}^\nu \exp(-2k_d d)}{1 - r_{vd}^\nu r_{md}^\nu \exp(-2k_d d)}. \tag{10}$$

This is the same for each polarization state $\nu = s$ or p . The reflection coefficients for vacuum–dielectric (r_{vd}) and for metal–dielectric (r_{md}) interfaces are defined as

$$r_{ab}^s = \frac{k_a - k_b}{k_a + k_b}, \quad r_{ab}^p = \frac{\epsilon_b k_a - \epsilon_a k_b}{\epsilon_b k_a + \epsilon_a k_b}, \tag{11}$$

where $k_{a,b}$ is the normal component of the wave vector in the medium a or b ($a, b = v, d$, or m) that is defined at the imaginary frequency, $\omega = i\zeta$, as

$$k_a = \sqrt{\epsilon_a (i\zeta)^2 / c^2 + q^2}. \tag{12}$$

In Equation (12), q is the absolute value of the wave vector in the plane of the plates, c denotes the speed of light, and the dielectric function of metal 2 is $\epsilon_m = \epsilon_2$. For the reflection coefficient of plate 1, one can use $R_1^v = r_{vm}^v$ where $\epsilon_m = \epsilon_1$ has to be taken.

The Casimir force between the plates is calculated according to the Lifshitz formula [11], which can be presented in the form,

$$P_C(h) = -\frac{k_B T}{\pi} \sum_{n=0}^{\infty} \int_0^{\infty} dq q k_v \sum_{v=s,p} \frac{R_1^v R_2^v e^{-2k_v h}}{1 - R_1^v R_2^v e^{-2k_v h}}, \quad (13)$$

where the sum is running on the Matsubara frequencies, $\zeta_n = 2\pi n k_B T / \hbar$ with k_B the Boltzmann constant, T the temperature, and \hbar the Planck constant, the prime denotes that the term at $n = 0$ has to be taken with the coefficient $1/2$, and $k_B T$ is the thermal energy.

The Casimir pressure is calculated as a function of distance h between two Au plates, one of which is covered by a layer of SiO₂ with the thickness d . The optical data for Au are taken from [34] (sample 3) and the data for SiO₂ are taken from the handbook [35]. Figure 2a shows the results in the zero temperature limit for the dielectric thickness $d = 0, 20$, and 40 nm. Figure 2b shows the relative difference, Δ_R , between the pressures with and without the dielectric layer with respect to the pressure between the metallic plates:

$$\Delta_R(h) = \frac{P_C^{m/d} - P_C^m}{P_C^m}, \quad (14)$$

where the superscripts, 'm' and 'm/d', refer to metal and metal covered by a dielectric, respectively.

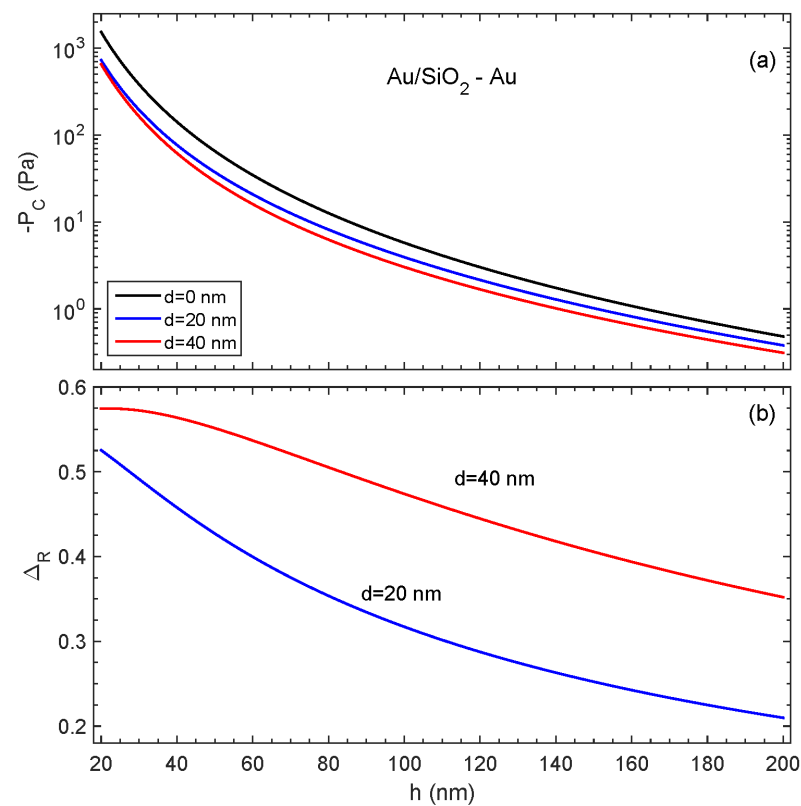


Figure 2. (a) Casimir pressure between two Au plates, one of which is covered by the SiO₂ layer with the thickness d . (b) Difference between the pressures with the dielectric layer and without it related to the pressure between bare metallic plates.

Figure 2a demonstrates that, at small distances, the underlying Au has a weak effect on the pressure since the pressures for $d = 20$ and 40 nm approach each other. At $h = 20$ nm, the pressure for bare Au is 2.35 times larger than that for $d = 40$ nm. At $h = 200$ nm, this ratio is 1.54 and still significant. The situation does not change essentially if one considers the sphere–plate interaction. In this case, the ratio of the forces without and with the dielectric layer is 2.30 and 1.40 at $h = 20$ nm and $h = 200$ nm, respectively. This example shows that the presence of a thin dielectric layer on the metallic plate significantly changes the force. This means that one can investigate the dielectric materials by sputtering thin films on good conductors and comparing the pressures with and without the dielectric layer. The unwanted electrostatic force due to the charging of the dielectric can be compensated for if the layer is sufficiently thin.

The difference between the pressures with and without the dielectric layer can be presented via only two elementary reflection coefficients, r_{vd} and r_{vm} . The coefficient r_{md} is expressed via r_{vd} and r_{vm} by the relation (10) at $d = 0$:

$$r_{md} = \frac{r_{vm} - r_{vd}}{1 - r_{vd}r_{vm}}. \tag{15}$$

Equation (15) is true for both polarizations. The difference, $\Delta = P_C^{m/d} - P_C^m$, between the pressures can be presented using the Lifshitz formula (13) as

$$\Delta = -\frac{k_B T}{\pi} \sum_{n=0}^{\infty} \int_0^{\infty} dq q k_v \sum_{\nu=s,p} \frac{1 - e^{-2k_d d}}{r_{vm}} \times \left[\frac{1 - R_1 r_{vd} e^{-2k_v h}}{r_{vd} - r_{vm}} - \frac{(r_{vd} - R_1 e^{-2k_v h}) e^{-2k_d d}}{1 - r_{vd} r_{vm}} \right]^{-1} \frac{R_1 R_2 e^{-2k_v h}}{1 - R_1 R_2 e^{-2k_v h}}, \tag{16}$$

where the reflection coefficients, $R_{1,2}$, refer to bare metals and coincide with r_{vm} for metal 1 and 2, respectively. If metal 1 and metal 2 are similar, then $R_1 = r_{vm}$.

The pressure difference can be compared with the pressure between the metal and bulk dielectric as shown in Figure 3. Naively, one could expect that the difference, $\Delta = P_C^{m/d} - P_C^m$, is the pressure between the dielectric membrane with the thickness d and the metal. Figure 3a shows that this is not the case since the pressure, P_C^d , between the metal and bulk dielectric is even smaller than Δ . One can also see from Equation (16) that Δ does not coincide with the pressure between the dielectric membrane and metal. The difference, Δ , still keeps information about the underlying metal. Nevertheless, the contribution of the dielectric layer to Δ is significant, as one can see in Figure 3b, which shows the ratio, Δ/P_C^d , as a function of the distance, h .

The effect of the dielectric layer is reduced with its thickness and, for successful experiments, one has to keep the balance between the increasing compensating voltage and the increasing influence of the dielectric layer on the increase in its thickness. To some degree, one can influence the charge in the dielectric by plasma treatment or UV (ultra-violet) irradiation. The less the charge, the thicker the layer of the dielectric that can be used. Note that the thickness of the layer can be well characterized ellipsometrically. It is worth mentioning that the dielectric layer contributes significantly even at rather large distances. For example, at $h = 200$ nm, the relative contribution of the layer (see Equation (14)) is $\Delta_R = 0.352$ and, at $h = 2000$ nm, it is 0.054.

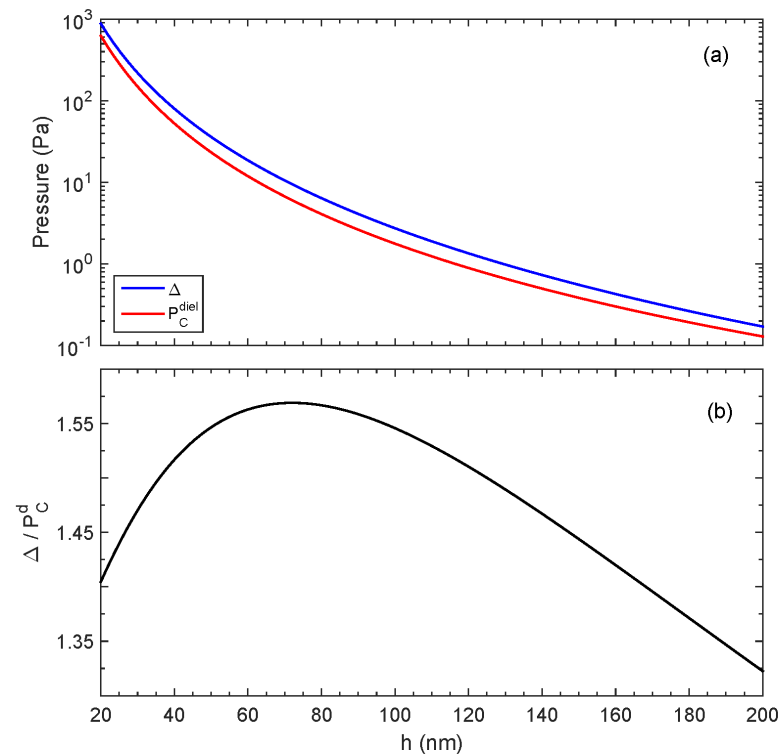


Figure 3. (a) Difference between pressures, $\Delta = P_C^{m/d} - P_C^m$ (blue curve), and the pressure, P_C^d , between Au and bulk SiO₂ (red curve). In $P_C^{m/d}$, the thickness of the dielectric is $d = 40$ nm. (b) Ratio of the pressures presented in (a). The ratio shows that Δ carries significant information about the metal–dielectric interaction.

4. Conclusions

The total force measured experimentally includes a significant contribution from the electrostatic force that has to be separated from the Casimir force. When the force is measured between metals, the problem is solved by applying the compensating potential. The same method cannot be applied to dielectrics, for which the electrostatic force is strong due to the charging effect. The main idea of this paper was to use, instead of a bulk dielectric, a thin layer deposited on a metallic (or metallized) substrate. If the dielectric layer is sufficiently thin, the electrostatic force can be compensated for by applying an extra voltage to the metallic substrates. For a layer thickness above 100 nm, the compensating voltage becomes above 1 V, which is too large for practical use.

At the same time, at separations smaller than or of the order of 100 nm, a dielectric layer thicker than 10 nm contributes significantly to the Casimir force between a metal and the other metal covered with the dielectric. There is an optimal thickness of the layer such that the electrostatic force can be compensated for, but the contribution of the layer to the Casimir force is sufficient to extract information about the Casimir interaction of the metal with the bulk dielectric.

The main idea proposed in this paper can be generalized to the interaction of two dielectrics but, physically, an even more interesting case is the interaction of a semiconductor with metal.

Funding: This research was funded by the Ministry of Education and Science of the Russian Federation.

Data Availability Statement: Not applicable.

Conflicts of Interest: The author declares no conflict of interest.

References

1. Casimir, H.B.G. On the attraction between two perfectly conducting plates. *Proc. Kon. Ned. Akad. Wetensch.* **1948**, *51*, 793–795. Available online: <https://dwc.knaw.nl/DL/publications/PU00018547.pdf> (accessed on 9 July 2023).
2. Klimchitskaya, G.L.; Mohideen, U.; Mostepanenko, V.M. The Casimir force between real materials: Experiment and theory. *Rev. Mod. Phys.* **2009**, *81*, 1827–1885. [CrossRef]
3. Rodriguez, A.W.; Capasso, F.; Johnson, S.G. The Casimir effect in microstructured geometries. *Nat. Photon.* **2011**, *3*, 211–221. [CrossRef]
4. Mostepanenko, V.M. Casimir puzzle and Casimir conundrum: Discovery and search for resolution. *Universe* **2021**, *7*, 84. [CrossRef]
5. Lu, B.S. The Casimir effect in topological matter. *Universe* **2021**, *7*, 237. [CrossRef]
6. Harris, B.W.; Chen, F.; Mohideen, U. Precision measurement of the Casimir force using gold surfaces. *Phys. Rev. A* **2000**, *62*, 052109. [CrossRef]
7. Chan, H.B.; Aksyuk, V.A.; Kleiman, R.N.; Bishop, D.J.; Capasso, F. Quantum mechanical actuation of microelectromechanical systems by the Casimir force. *Science* **2001**, *291*, 1941–1944. [CrossRef]
8. Decca, R.S.; López, D.; Fischbach, E.; Krause, D.E. Measurement of the Casimir force between dissimilar metals. *Phys. Rev. Lett.* **2003**, *91*, 050402. [CrossRef]
9. Decca, R.; López, D.; Fischbach, E.; Klimchitskaya, G.; Krause, D.; Mostepanenko, V. Precise comparison of theory and new experiment for the Casimir force leads to stronger constraints on thermal quantum effects and long-range interactions. *Ann. Phys.* **2005**, *318*, 37–80. [CrossRef]
10. Lifshitz, E.M. The theory of molecular attractive forces between solids. *Sov. Phys. JETP* **1956**, *2*, 73–83. Available online: <http://jetp.ras.ru/cgi-bin/e/index/e/2/1/p73?a=list> (accessed on 9 July 2023).
11. Dzyaloshinskii, I.E.; Lifshitz, E.M.; Pitaevskii, L.P. General theory of van der Waals' forces. *Sov. Phys. Uspekhi* **1961**, *4*, 153–176. [CrossRef]
12. Iannuzzi, D.; Lisanti, M.; Capasso, F. Effect of hydrogen-switchable mirrors on the Casimir force. *Proc. Natl. Acad. Sci. USA* **2004**, *101*, 4019–4023. [CrossRef]
13. Chen, F.; Klimchitskaya, G.L.; Mostepanenko, V.M.; Mohideen, U. Demonstration of optically modulated dispersion forces. *Opt. Express* **2007**, *15*, 4823–4829. [CrossRef] [PubMed]
14. de Man, S.; Heeck, K.; Wijngaarden, R.J.; Iannuzzi, D. Halving the Casimir force with conductive oxides. *Phys. Rev. Lett.* **2009**, *103*, 040402. [CrossRef] [PubMed]
15. Torricelli, G.; van Zwol, P.J.; Shpak, O.; Binns, C.; Palasantzas, G.; Kooi, B.J.; Svetovoy, V.B.; Wuttig, M. Switching Casimir forces with phase-change materials. *Phys. Rev. A* **2010**, *82*, 010101. [CrossRef]
16. Chang, C.C.; Banishev, A.A.; Klimchitskaya, G.L.; Mostepanenko, V.M.; Mohideen, U. Reduction of the Casimir force from Indium tin oxide film by UV treatment. *Phys. Rev. Lett.* **2011**, *107*, 090403. [CrossRef]
17. Banishev, A.A.; Chang, C.C.; Castillo-Garza, R.; Klimchitskaya, G.L.; Mostepanenko, V.M.; Mohideen, U. Modifying the Casimir force between indium tin oxide film and Au sphere. *Phys. Rev. B* **2012**, *85*, 045436. [CrossRef]
18. Banishev, A.A.; Klimchitskaya, G.L.; Mostepanenko, V.M.; Mohideen, U. Demonstration of the Casimir force between ferromagnetic surfaces of a Ni-coated sphere and a Ni-coated plate. *Phys. Rev. Lett.* **2013**, *110*, 137401. [CrossRef]
19. Banishev, A.A.; Klimchitskaya, G.L.; Mostepanenko, V.M.; Mohideen, U. Casimir interaction between two magnetic metals in comparison with nonmagnetic test bodies. *Phys. Rev. B* **2013**, *88*, 155410. [CrossRef]
20. van Zwol, P.J.; Palasantzas, G.; van de Schootbrugge, M.; De Hosson, J.T.M. Measurement of dispersive forces between evaporated metal surfaces in the range below 100 nm. *Appl. Phys. Lett.* **2008**, *92*, 054101. [CrossRef]
21. Sedighi, M.; Svetovoy, V.B.; Palasantzas, G. Casimir force measurements from silicon carbide surfaces. *Phys. Rev. B* **2016**, *93*, 085434. [CrossRef]
22. van Zwol, P.J.; Palasantzas, G.; De Hosson, J.T.M. Influence of random roughness on the Casimir force at small separations. *Phys. Rev. B* **2008**, *77*, 075412. [CrossRef]
23. Broer, W.; Palasantzas, G.; Knoester, J.; Svetovoy, V.B. Roughness correction to the Casimir force at short separations: Contact distance and extreme value statistics. *Phys. Rev. B* **2012**, *85*, 155410. [CrossRef]
24. Sushkov, A.O.; Kim, W.J.; Dalvit, D.A.R.; Lamoreaux, S.K. Observation of the thermal Casimir force. *Nat. Phys.* **2011**, *7*, 230–233. [CrossRef]
25. Liu, M.; Xu, J.; Klimchitskaya, G.L.; Mostepanenko, V.M.; Mohideen, U. Precision measurements of the gradient of the Casimir force between ultraclean metallic surfaces at larger separations. *Phys. Rev. A* **2019**, *100*, 052511. [CrossRef]
26. Bimonte, G.; López, D.; Decca, R.S. Isoelectronic determination of the thermal Casimir force. *Phys. Rev. B* **2016**, *93*, 184434. [CrossRef]
27. Bimonte, G.; Spreng, B.; Maia Neto, P.A.; Ingold, G.L.; Klimchitskaya, G.L.; Mostepanenko, V.M.; Decca, R.S. Measurement of the Casimir force between 0.2 and 8 μm : Experimental procedures and comparison with theory. *Universe* **2021**, *7*, 93. [CrossRef]
28. Chen, F.; Klimchitskaya, G.L.; Mostepanenko, V.M.; Mohideen, U. Control of the Casimir force by the modification of dielectric properties with light. *Phys. Rev. B* **2007**, *76*, 035338. [CrossRef]
29. Wu, Y.H.; Zha, J.W.; Li, W.K.; Wang, S.J.; Dang, Z.M. A remarkable suppression on space charge in isotactic polypropylene by inducing the beta-crystal formation. *Appl. Phys. Lett.* **2015**, *107*, 112901. [CrossRef]

30. Xing, Z.; Zhang, C.; Cui, H.; Hai, Y.; Wu, Q.; Min, D. Space charge accumulation and decay in dielectric materials with dual discrete traps. *Appl. Sci.* **2019**, *9*, 4253. [CrossRef]
31. Derjaguin, B. Untersuchungen über die Reibung und Adhäsion, IV. *Kolloid-Zeitschrift* **1934**, *69*, 155–164. [CrossRef]
32. Derjaguin, B.V.; Abrikosova, I.I.; Lifshitz, E.M. Direct measurement of molecular attraction between solids separated by a narrow gap. *Quart. Rev.* **1968**, *10*, 295–329. [CrossRef]
33. Zhou, F.; Spruch, L. Van der Waals and retardation (Casimir) interactions of an electron or an atom with multilayered walls. *Phys. Rev. A* **1995**, *52*, 297–310. [CrossRef]
34. Svetovoy, V.B.; van Zwol, P.J.; Palasantzas, G.; De Hosson, J.T.M. Optical properties of gold films and the Casimir force. *Phys. Rev. B* **2008**, *77*, 035439. [CrossRef]
35. Palik, E.D. (Ed.) *Handbook of Optical Constants of Solids*; Academic Press, Inc.: San Diego, CA, USA, 1985. [CrossRef]

Disclaimer/Publisher’s Note: The statements, opinions and data contained in all publications are solely those of the individual author(s) and contributor(s) and not of MDPI and/or the editor(s). MDPI and/or the editor(s) disclaim responsibility for any injury to people or property resulting from any ideas, methods, instructions or products referred to in the content.

Article

Casimir Effect Invalidates the Drude Model for Transverse Electric Evanescent Waves

Galina L. Klimchitskaya^{1,2*} and Vladimir M. Mostepanenko^{1,2,3}

¹ Central Astronomical Observatory at Pulkovo of the Russian Academy of Sciences, 196140 Saint Petersburg, Russia; vmostepa@gmail.com

² Peter the Great Saint Petersburg Polytechnic University, 195251 Saint Petersburg, Russia

³ Kazan Federal University, 420008 Kazan, Russia

* Correspondence: g.klimchitskaya@gmail.com

Abstract: We consider the Casimir pressure between two metallic plates and calculate the four contributions to it determined by the propagating and evanescent waves and by the transverse magnetic and transverse electric polarizations of the electromagnetic field. The range of interplate separations is considered where nearly the whole pressure has its origin in the electromagnetic response of conduction electrons. In the Casimir physics, this response is described either by the dissipative Drude model resulting in contradictions with the measurement data or by the experimentally consistent but dissipationless plasma model. It is shown that the total transverse magnetic contribution to the Casimir pressure due to both the propagating and evanescent waves and the transverse electric contribution due to only the propagating waves, computed by means of the Drude model, correlate well with the corresponding results obtained using the plasma model. We conclude that the disagreement between the theoretical predictions obtained using the Drude model and precision measurements of the Casimir force is not caused by the account of dissipation in itself, but arises from an incorrect description of the response of metals to the low-frequency transverse electric evanescent waves by this model. It is demonstrated that the Drude model has no supporting experimental evidence in the range of transverse electric evanescent waves, so that the above conclusion is consistent with all available information. The alternative test of the Drude model for the transverse electric evanescent waves suggested in the framework of classical electrodynamics is discussed.

Keywords: Casimir force; Lifshitz theory; Drude model; plasma mode; propagating waves; evanescent waves; transverse electric and transverse magnetic polarizations; dissipation of conduction electrons

Citation: Klimchitskaya, G.L.; Mostepanenko, V.M. Casimir Effect Invalidates the Drude Model for Transverse Electric Evanescent Waves. *Physics* **2023**, *5*, 952–967. <https://doi.org/10.3390/physics5040062>

Received: 24 July 2023

Revised: 24 August 2023

Accepted: 31 August 2023

Published: 27 September 2023



Copyright: © 2023 by the authors. Licensee MDPI, Basel, Switzerland. This article is an open access article distributed under the terms and conditions of the Creative Commons Attribution (CC BY) license (<https://creativecommons.org/licenses/by/4.0/>).

1. Introduction

The Casimir effect is a relativistic and quantum phenomenon which has attracted widespread attention in the 75 years since its prediction in 1948 [1]. This effect is very popular owing to its unusual character. Casimir predicted that two parallel uncharged ideal metal planes at zero temperature attract each other with the force which depends only on the interplate separation and the fundamental constants \hbar and c . In 1955, Lifshitz demonstrated [2] that the Casimir force falls into the general theory of dispersion forces, which act between any material bodies. From the point of view of the Lifshitz theory, both the van der Waals and Casimir forces are the manifestations of a single dispersion force, but in different regions of separations and temperatures. The Lifshitz theory makes it possible to calculate the Casimir force between two thick material plates by using the response functions of plate materials to the electromagnetic field in the form of frequency-dependent dielectric permittivities.

The Casimir force is unique in being important for such diverse fields of physics as the theory of elementary particles, gravitation and cosmology, quantum electrodynamics, condensed matter physics, atomic physics, and also for nanotechnology. As a result,

a great number of papers was devoted to this subject during recent decades (see the lists of references in the monographs [3–13]). In doing so, much attention has been paid to precision measurements of the Casimir force.

The present stage in measuring the Casimir force started with an experiment [14], which used the configuration of an Au-coated spherical lens of a centimeter-size radius above an Au-coated plate. As was understood later, the presence of the so-called patch potentials [15] and surface imperfections [16] on the centimeter-size surfaces prevents from reaching the highly precise results in measuring the Casimir force. The highly accurate measurements were performed between a microscopic sphere and a plate by means of an atomic force microscope and a micromechanical torsional oscillator pioneered in Refs. [17] and [18], respectively.

The many measurements of the Casimir force performed by means of a micromechanical torsional oscillator [19–24] and an atomic force microscope [25–31] led to unexpected results. It was found that the measurement data are in a very good agreement with theoretical predictions of the Lifshitz theory if the low-frequency response of metals to the electromagnetic field is described by the dissipationless plasma model. If the dissipative Drude model is used, which should describe the conduction electrons correctly, the theoretical predictions are excluded by the data with certainty [19–31]. The force values computed by means of the Drude model were only confirmed in a single experiment [32], but the measurements were performed by means of a centimeter-size spherical lens. As a result, the theoretical uncertainty due to patch potentials removed by means of the fitting procedure exceeded the Casimir force value by an order of magnitude. Moreover, the surface imperfections, which are always present on lens surfaces, were not taken into account in this experiment [16,33].

The contradiction between theoretical predictions of the Lifshitz theory obtained using the apparently well-tested Drude model and measurements of the Casimir force is often named the Casimir puzzle [34–36]. A rich variety of approaches has been suggested in the literature in an effort to resolve it. One could mention an employment of the alternative sets of the optical data [37,38], modeling the patch effect [15,32,39], a more accurate account of the surface roughness [40–42], refined theory for the sphere-plate geometry [43–48], etc. (see [12,49–51] for a review).

Particular emphasis has been placed on the frequency region of the anomalous skin effect where the Drude dielectric function becomes inapplicable due to the spatial nonlocality [52–54]. It was found, however, that the corresponding correction to the Casimir force is too small and cannot explain the discrepancy between the measurement data and theory which uses the Drude model [52].

An important step was made in Refs. [55,56] where it was shown that large thermal correction to the Casimir force predicted by the Drude model arises from the transverse electric (s-polarized) evanescent waves with low frequencies. This result was obtained by analyzing the frequency spectrum of the thermal correction along the real frequency axis. The predicted large thermal correction to the Casimir force, which distinguishes the Drude model from the plasma model and the model of an ideal metal, was also interpreted as arising from the contribution of eddy (Foucault) current modes [57,58].

Furthermore, it was shown that at separations exceeding the thermal length (i.e., above approximately $6 \mu\text{m}$ at $T = 300 \text{ K}$) the contributions of the transverse electric propagating and evanescent waves to the total Casimir force calculated using the Drude model are equal in magnitude and cancel each other [59]. According to Ref. [60], at large separations the contributions of the transverse magnetic (p-polarized) and transverse electric propagating waves are equal regardless of which dielectric model (Drude or plasma) is used in computations. As to the contribution of transverse magnetic evanescent waves, it is equal to zero for both the Drude and plasma models. Thus, at large separations, the difference in Casimir forces computed using the Drude and plasma models originates solely from the contribution of transverse electric evanescent waves.

In this paper, we investigate the contributions of both the transverse magnetic and transverse electric propagating and evanescent waves into the Casimir force per unit area (i.e., the Casimir pressure) for two parallel Au-coated plates in the experimentally relevant separation region from 0.5 to 4 μm where the total force value, in the limits of measurement errors, is determined by the dielectric response of conduction electrons. The contributions of the transverse magnetic and transverse electric propagating and evanescent waves are calculated in the framework of the Lifshitz theory employing either the Drude or the plasma model. For this purpose, we combine the computational results obtained using the formalisms represented in terms of the pure imaginary and real frequencies.

It is shown that the contributions of the transverse magnetic waves to the total Casimir force computed using the Drude and plasma models nearly coincide. The contributions of the transverse electric propagating waves to the Casimir force computed using the Drude and plasma models also turned out to be rather close. As a result, the relatively large difference between the theoretical predictions for the total Casimir force made by means of the Drude and plasma models over the experimentally relevant range of separations comes from different contributions of the transverse electric evanescent waves. Taking into account that this large difference is experimentally excluded by the measurement data of numerous experiments mentioned above, the conclusion is made that the Drude model breaks down in the region of transverse electric evanescent waves. We demonstrate that this conclusion is not in conflict with numerous experimental tests of the Drude model. The obtained results are discussed in connection with the role of dissipation of conduction electrons in the Lifshitz theory.

The paper is organized as follows. In Section 2, we briefly present the formalisms of the Lifshitz theory in terms of either pure imaginary or real frequencies separating the contributions of the transverse magnetic and transverse electric polarizations and the propagating and evanescent waves. Section 3 is devoted to computations of the Casimir pressure between metallic plates using the Drude and the plasma models and the optical data for the complex index of refraction. In Section 4, the contributions of the propagating and evanescent waves are studied for the transverse magnetic and transverse electric polarizations using the Drude and plasma models. Section 5 discusses the failure of the Drude model for the transverse electric evanescent waves, the role of dissipation of conduction electrons, and the possibilities of alternative tests disconnected with the Casimir effect. Section 6 contains our conclusions.

2. Formalisms of the Lifshitz Theory in Terms of Real or Pure Imaginary Frequencies

We consider the Casimir force per unit area of two similar metallic plates described by the dielectric permittivity, $\epsilon(\omega)$, i.e., the Casimir pressure with ω the wave frequency. The plates are at temperature T in thermal equilibrium with the environment and are separated by a distance a . Then, the Casimir pressure can be expressed by the Lifshitz formula [2]. This formula can be presented in terms of real frequencies or pure imaginary (Matsubara) frequencies.

In terms of real frequencies, the Casimir pressure is given by the sum of contributions from the propagating and evanescent waves, each of which, in its turn, consists of two components determined by the transverse magnetic (TM) and transverse electric (TE) polarizations:

$$P(a, T) = P_{\text{TM}}^{\text{prop}}(a, T) + P_{\text{TE}}^{\text{prop}}(a, T) + P_{\text{TM}}^{\text{evan}}(a, T) + P_{\text{TE}}^{\text{evan}}(a, T). \quad (1)$$

Here [12],

$$P_{\text{TM,TE}}^{\text{prop}}(a, T) = -\frac{\hbar}{2\pi^2} \int_0^\infty d\omega \coth \frac{\hbar\omega}{2k_B T} \int_0^{\omega/c} dk_\perp k_\perp \text{Im} \left[q \frac{r_{\text{TM,TE}}^2(\omega, k_\perp) e^{-2aq}}{1 - r_{\text{TM,TE}}^2(\omega, k_\perp) e^{-2aq}} \right] \quad (2)$$

and

$$P_{\text{TM,TE}}^{\text{evan}}(a, T) = -\frac{\hbar}{2\pi^2} \int_0^\infty d\omega \coth \frac{\hbar\omega}{2k_B T} \int_{\omega/c}^\infty dk_\perp k_\perp q \operatorname{Im} \frac{r_{\text{TM,TE}}^2(\omega, k_\perp) e^{-2aq}}{1 - r_{\text{TM,TE}}^2(\omega, k_\perp) e^{-2aq}}. \quad (3)$$

In Equations (1)–(3), the following notations are introduced. T denotes the temperature, \hbar is the reduced Planck’s constant, the Boltzmann constant is k_B , the magnitude of the wave vector projection on the plane of plates is k_\perp , the reflection coefficients for the TM and TE polarizations are

$$r_{\text{TM}}(\omega, k_\perp) = \frac{\varepsilon(\omega)q - p}{\varepsilon(\omega)q + p}, \quad r_{\text{TE}}(\omega, k_\perp) = \frac{q - p}{q + p}, \quad (4)$$

and

$$q \equiv q(\omega, k_\perp) = \left(k_\perp^2 - \frac{\omega^2}{c^2}\right)^{1/2}, \quad p \equiv p(\omega, k_\perp) = \left[k_\perp^2 - \varepsilon(\omega) \frac{\omega^2}{c^2}\right]^{1/2}, \quad (5)$$

where c denotes the speed of light.

Note that by solving the Maxwell equations with the continuity boundary conditions on the surfaces of metallic plates, one determines the Casimir energy via the sum of discrete photon eigenfrequencies (or the cavity modes or the wave guide modes, as they are often referred to Ref. [61]). The continuous frequencies in Equation (3) appear after performing a summation over the discrete frequencies by means of the argument principle.

As is seen from Equation (2), for the propagating waves $k_\perp \leq \omega/c$ in accordance to the mass-shell equation in free space. The quantity q in this case is pure imaginary and the integrand in Equation (2) contains the rapidly oscillating function, $\exp(-2aq)$, that plagues numerical computations. For the evanescent waves in Equation (3), the mass-shell equation is violated because $k_\perp > \omega/c$, but the quantity q takes real values making accessible computations of $P_{\text{TM,TE}}^{\text{evan}}$ by means of Equation (3).

One can conclude that Equations (1)–(3) are not convenient for computations of the total Casimir pressure (1), but the contributions $P_{\text{TM,TE}}^{\text{evan}}$ from the evanescent waves can be computed by (3).

In terms of the pure imaginary Matsubara frequencies, $\omega = i\zeta_l = 2\pi i k_B T l / \hbar$ with $l = 0, 1, 2, \dots$, the Casimir pressure is expressed by the most commonly used Lifshitz formula,

$$P(a, T) = P_{\text{TM}}(a, T) + P_{\text{TE}}(a, T), \quad (6)$$

where [12]

$$P_{\text{TM,TE}}(a, T) = -\frac{k_B T}{\pi} \sum_{l=0}^\infty \int_0^\infty k_\perp dk_\perp q_l \frac{r_{\text{TM,TE}}^2(i\zeta_l, k_\perp) e^{-2aq_l}}{1 - r_{\text{TM,TE}}^2(i\zeta_l, k_\perp) e^{-2aq_l}}. \quad (7)$$

The prime on the summation sign in Equation (7) divides the terms with $l = 0$ by 2, and the reflection coefficients are again defined by Equation (4) with $\omega = i\zeta_l$, so that in line with Equation (5)

$$q = q_l \equiv q(i\zeta_l, k_\perp) = \left(k_\perp^2 + \frac{\zeta_l^2}{c^2}\right)^{1/2}, \quad p = p_l \equiv p(i\zeta_l, k_\perp) = \left(k_\perp^2 + \varepsilon_l \frac{\zeta_l^2}{c^2}\right)^{1/2}, \quad (8)$$

where $\varepsilon = \varepsilon_l \equiv \varepsilon(i\zeta_l)$.

Equation (7) is convenient for numerical computations of $P_{\text{TM,TE}}$, but it alone does not allow computation of the contributions from the propagating and evanescent waves. Actually, all the four components of the Casimir pressure on the right-hand side of Equation (1) can be found by the combined application of the Lifshitz formula (3) in terms of real

frequencies and Equation (7) in terms of the Matsubara frequencies. For this purpose, it is necessary to compute the contributions $P_{TM,TE}^{evan}$ by Equation (3) and the total Casimir pressures $P_{TM,TE}$ by Equation (7). Then, the remaining contributions $P_{TM,TE}^{prop}$ are found from

$$P_{TM,TE}^{prop}(a, T) = P_{TM,TE}(a, T) - P_{TM,TE}^{evan}(a, T). \tag{9}$$

The numerical computations of all four components of the total Casimir pressure between metallic plates using different dielectric functions of a metal are presented in the next sections.

3. Calculation of the Casimir Pressure between Metallic Plates Using the Drude and Plasma Models

It has been known that the dielectric response of metals to the electromagnetic field is determined by the combined action of conduction and bound (core) electrons. In doing so, the corresponding contributions to the dielectric permittivity make a substantially different impact on the Casimir pressure [12]. At short separations between the plates (up to tens of nanometers), the major contribution to the Casimir pressure is given by the region of very high frequencies, where ϵ is fully determined by the core electrons. In the transition region (from tens to hundreds of nanometers), both the conduction and core electrons determine the value of ϵ at the frequencies contributing to the Casimir pressure. Finally, at separations exceeding several hundreds of nanometers, only the conduction electrons determine the dielectric response of metals at the characteristic (low) frequencies.

Taking into account that the problem of disagreement between experiment and theory discussed in Section 1 arises exclusively due to the role of conduction electrons, it is appropriate to consider the separation region where the role of core electrons in computations of the Casimir pressure is negligibly small. In this section, the sought for region is found for two Au plates at room temperature $T = 300$ K (the same results are valid for the plates made of any material coated with an Au layer of thickness exceeding several tens of nanometers [12]).

As discussed in Section 1, the conduction electrons are commonly described by the dielectric permittivity of the dissipative Drude model:

$$\epsilon_D(\omega) = 1 - \frac{\omega_p^2}{\omega(\omega + i\gamma)}, \quad \epsilon_{D,l} = 1 + \frac{\omega_p^2}{\xi_l(\xi_l + \gamma)}, \tag{10}$$

where, for Au, the plasma frequency $\omega_p \approx 1.37 \times 10^{16}$ rad/s and the relaxation parameter, γ , at $T = 300$ K takes the value $\gamma \approx 0.53 \times 10^{14}$ rad/s [62].

The dielectric permittivity of the plasma model, which disregards the dissipation properties of conduction electrons, is obtained from Equation (10) by putting $\gamma = 0$

$$\epsilon_P(\omega) = 1 - \frac{\omega_p^2}{\omega^2}, \quad \epsilon_{P,l} = 1 + \frac{\omega_p^2}{\xi_l^2}. \tag{11}$$

This model is physically applicable only at high frequencies in the region of infrared optics. However, as mentioned in Section 1, the theoretical results obtained using the plasma model at low frequencies, including the zero frequency, agree with measurements of the Casimir force. As to the Drude model, which is physically applicable at low frequencies, it leads to contradictions between theoretical predictions of the Lifshitz theory and the measurement data.

As it was widely discussed in the literature starting from Refs. [63,64], the important formal difference between the dielectric permittivities (10) and (11) is that they lead to

radically different values of the TE reflection coefficient defined in Equation (4) at zero frequency:

$$r_{\text{TE,D}}(0, k_{\perp}) = 0, \quad r_{\text{TE,p}}(0, k_{\perp}) = \frac{ck_{\perp} - \sqrt{c^2k_{\perp}^2 + \omega_p^2}}{ck_{\perp} + \sqrt{c^2k_{\perp}^2 + \omega_p^2}}. \quad (12)$$

It immediately follows that at large separations, where the Casimir pressure is determined by the terms of Equation (7) with $l = 0$,

$$P_{\text{TE,D}}^0(a, T) = 0, \quad P_{\text{TM,D}}^0(a, T) = P_{\text{D}}^0(a, T) = -\frac{k_B T}{8\pi a^3} \zeta(3), \quad (13)$$

where $\zeta(z)$ is the Riemann zeta function. This is one half of the result obtained at large separations for the ideal metal planes.

For the plasma model, the case of ideal metal planes is obtained in the limit $\omega_p \rightarrow \infty$ where

$$\lim_{\omega_p \rightarrow \infty} r_{\text{TE,p}}(0, k_{\perp}) = -1 \quad (14)$$

and the terms of Equation (7) with $l = 0$ are

$$P_{\text{TM,p}}^0(a, T) = P_{\text{TE,p}}^0(a, T) = -\frac{k_B T}{8\pi a^3} \zeta(3), \quad P_{\text{p}}^0(a, T) = -\frac{k_B T}{4\pi a^3} \zeta(3). \quad (15)$$

These are the same results as are obtained for the ideal metal planes. The quantities (13) and (15) do not depend on \hbar . They represent the classical limit of the Casimir pressure at large separations found using the Drude and plasma models, respectively.

To determine the region of separations, where the dielectric permittivities of the Drude and plasma models (10) and (11) determine nearly the total Casimir pressure, we first compute the values of P_{D} and P_{p} and then compare the obtained results with the Casimir pressures computed using the available optical data of Au extrapolated down to zero frequency by means of the Drude or plasma models.

Numerical computations of the Casimir pressure at $T = 300$ K were performed by Equations (6) and (7) with the reflection coefficients (4) and the dielectric permittivities (10) and (11). The computational results for the ratios of obtained pressures to P_{D}^0 defined in Equation (13) are presented in Figure 1 as a function of separation by the top and bottom solid lines computed using the plasma and Drude models, respectively. The two dashed lines indicate the corresponding limiting values of the pressure ratios at large separations.

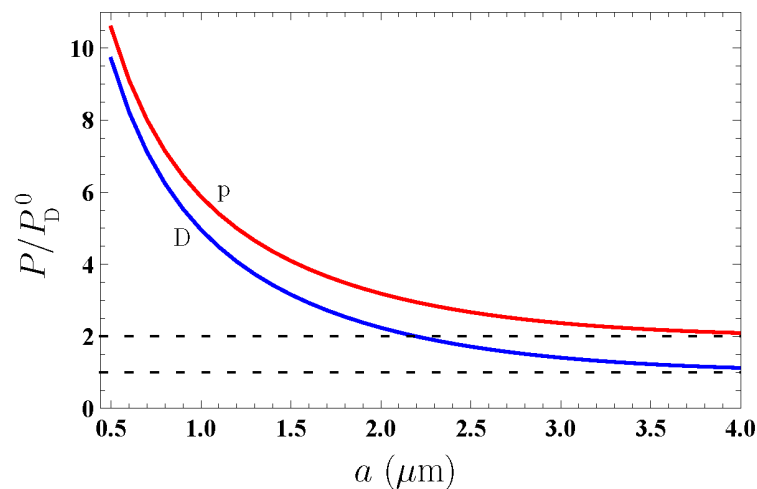


Figure 1. The ratio of the Casimir pressures for Au plates computed at $T = 300$ K using the Drude (D) or the plasma (p) model to the classical limit of the Casimir pressure P_{D}^0 (13) found using the Drude model, is shown as a function of separation.

As is seen in Figure 1, the theoretical predictions obtained using the plasma and Drude models differ by the factors of 1.09 at $a = 0.5 \mu\text{m}$, 1.2 at $a = 1.1 \mu\text{m}$, and 1.86 at $a = 4 \mu\text{m}$. In the limit of large separations (classical limit) the difference is by the factor of 2.

Now we determine the error in Casimir pressures made by omitting the contribution of core electrons in the dielectric permittivity. For this purpose, we find the dielectric permittivity of Au along the imaginary frequency axis by means of the Kramers-Kronig relation where the imaginary part of this permittivity is given by the tabulated optical data of Au [62] extrapolated down to zero frequency by means of the plasma or the Drude model (see, e.g., [12,49] for details). Then the Casimir pressure, $P_{D,p}^{\text{core}}$, is again computed by Equations (4), (6) and (7).

The relative deviation between the Casimir pressures obtained using the simple Drude and plasma models and using the optical data taking into account the core electrons can be characterized by the quantity

$$\delta P_{D,p}(a, T) = \frac{P_{D,p}(a, T) - P_{D,p}^{\text{core}}(a, T)}{P_{D,p}^{\text{core}}(a, T)}. \quad (16)$$

In Figure 2, the computational results for $\delta P_{D,p}$ are shown as a function of separation by the top and bottom lines computed using the Drude and plasma models and corresponding extrapolations of the optical data, respectively. In the inset, the region of separations from 2 to 4 μm , where the two lines are partially overlapping, is shown on an enlarged scale for better visualization.

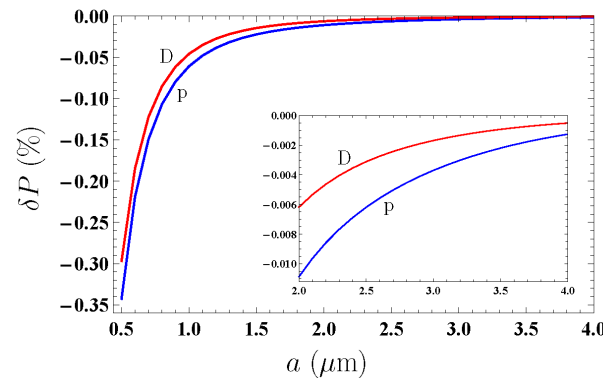


Figure 2. The relative deviation between the Casimir pressures for Au plates computed at $T = 300 \text{ K}$ using the simple Drude (D) or plasma (p) model and the optical data for Au extrapolated to zero frequency by the same models is shown as a function of separation. The inset: the region of large separations is shown on an enlarged scale.

As is seen from Figure 2, at $a = 0.5 \mu\text{m}$ the simple Drude and plasma models reproduce the Casimir pressure computed with due regard for core electrons with the relative errors less than 0.3% and 0.35%, respectively. These errors quickly decrease with increasing separation. Thus, at $a = 1 \mu\text{m}$ they are below 0.05% and 0.052%, respectively.

Note that in the separation region above $0.5 \mu\text{m}$ the already performed precision determinations of the effective Casimir pressure between two parallel plates by measuring the force gradient in the sphere-plate geometry [19–23,25–31] reliably distinguish between the top and bottom lines in Figure 1 in favor of the former at $a < 1.1 \mu\text{m}$. However, at $a > 0.5 \mu\text{m}$ the same experiments cannot discriminate between the theoretical predictions made by means of only the simple Drude or plasma model and taking into account the core electrons. As an example, the total experimental error in measuring the Casimir pressure determined at the 67% confidence level is $\delta P^{\text{expt}} = 1.5\%$ at $a = 0.5 \mu\text{m}$ [21,22] and $\delta P^{\text{expt}} = 27.5\%$ at $a = 1.1 \mu\text{m}$ [30,31] (by measuring the Casimir force in the sphere-plate geometry, the theoretical description using the Drude model was excluded at all separations $a \leq 4.8 \mu\text{m}$ [24]).

4. Comparison Studies of Contributions from the Propagating and Evanescent Waves

Now we are in a position to find all four contributions to the Casimir pressure (1) when using the simple Drude and plasma models and determine which of them is responsible for a disagreement between experiment and theory. In accordance with the results of Section 3, this should be performed at separations between the plates exceeding $0.5 \mu\text{m}$ where the dielectric permittivities of the simple Drude and plasma models contribute nearly the total value of the pressure. There is no point in considering separations which are too large because the experimental situation there is uncertain. We begin with the contribution of the TM polarized waves to the Casimir pressure.

4.1. Transverse Magnetic Polarization

The contribution of the TM polarized waves, P_{TM} , is calculated by Equation (7) where the reflection coefficient r_{TM} is given by the first equality in Equation (4) taken at $\omega = i\zeta_l$. Depending on whether one uses the Drude (10) or the plasma (11) model of the dielectric permittivity, we obtain either $P_{\text{TM,D}}$ or $P_{\text{TM,p}}$.

The computational results for P_{TM} normalized to P_{D}^0 at $T = 300 \text{ K}$ are shown in Figure 3a as a function of separation by the solid and dashed lines computed using the Drude and plasma models, respectively. As can be seen in Figure 3a, the solid and dashed lines almost coincide.

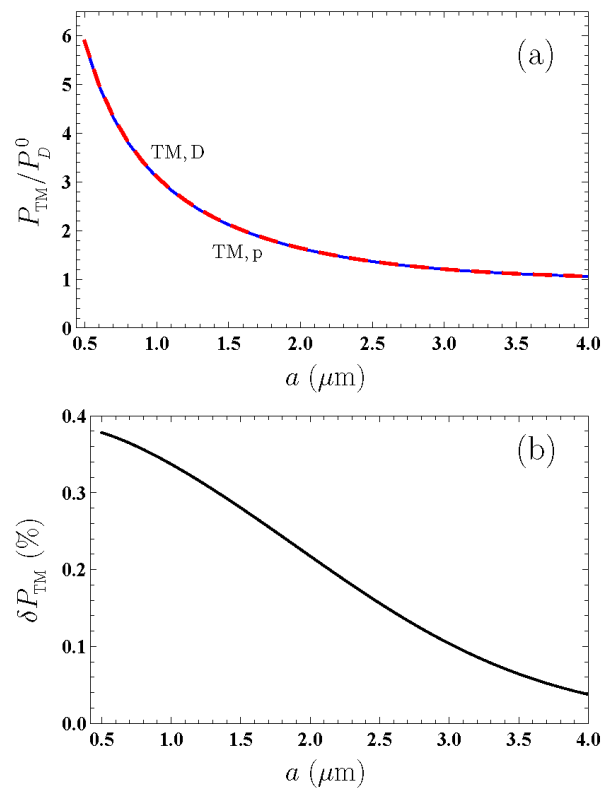


Figure 3. (a) The transverse magnetic contributions to the Casimir pressure for Au plates normalized to P_{D}^0 computed at $T = 300 \text{ K}$ using the simple Drude or plasma model are shown as a function of separation by the solid and dashed lines, respectively. (b) The relative deviation between these contributions is shown by the solid line.

In order to understand the measure of agreement between the theoretical predictions of the Lifshitz theory using the Drude and plasma models, we consider the relative deviation

$$\delta P_{\text{TM}}(a, T) = \frac{P_{\text{TM,D}}(a, T) - P_{\text{TM,p}}(a, T)}{P_{\text{TM,p}}(a, T)}. \quad (17)$$

In Figure 3b, the computational results for δP_{TM} at $T = 300$ K are shown by the solid line as a function of separation. As is seen in Figure 3b, the relative deviation between the predictions obtained using these models decreases from approximately 0.38% at $a = 0.5 \mu\text{m}$ to 0.04% at $a = 4 \mu\text{m}$. Remembering that the Drude model takes into account the dissipation processes, which are fully disregarded by the plasma model, one can conclude that the transverse magnetic contribution to the Casimir pressure between metallic plates is scarcely affected by the dissipation of conduction electrons. It also becomes clear that the impact of dissipation in different contributions to $P_{\text{TM,D}}$ has to be somehow compensated (see below in this section).

Let us now determine the contributions of propagating and evanescent waves to P_{TM} when using the Drude and plasma models in computations. The contribution of evanescent waves is found by Equation (3) with the reflection coefficient r_{TM} defined in Equation (4), whereas the contribution of propagating waves can be obtained by Equation (9), where the total TM contribution to the Casimir pressure is already computed (see Figure 3a).

First of all, it is evident from Equation (3) that

$$P_{\text{TM,p}}^{\text{evan}}(a, T) = 0. \tag{18}$$

This is because the dielectric permittivity of the plasma model (11) and, thus, the reflection coefficient $r_{\text{TM,p}}$ in Equation (4) are the real functions for evanescent waves.

Then, from Equation (9) one concludes that

$$P_{\text{TM,p}}^{\text{prop}}(a, T) = P_{\text{TM,p}}(a, T), \tag{19}$$

where $P_{\text{TM,p}}$ is already shown by the red dashed line in Figure 3a.

For the Drude model, the computations of $P_{\text{TM,D}}^{\text{evan}}$ are again performed by Equation (3) with the reflection coefficient $r_{\text{TM,D}}$ defined in Equation (4) and the dielectric permittivity (10). The quantity $P_{\text{TM,D}}^{\text{prop}}$ is obtained from Equation (9), where the already computed $P_{\text{TM,D}}$ is shown by the solid line in Figure 3a.

Figure 4 shows the computational results for $P_{\text{TM,D}}^{\text{prop}}$ and $P_{\text{TM,D}}^{\text{evan}}$ at $T = 300$ K by the top short-dashed and bottom long-dashed lines as a function of separation. Both these lines are blue. For comparison purposes, in Figure 4 we also reproduce from Figure 3a the blue solid line and the overlapping it red dashed line demonstrating the separation dependence of $P_{\text{TM,D}}$ and $P_{\text{TM,p}}$, respectively (the latter also depicts the behavior of $P_{\text{TM,p}}^{\text{prop}}$).

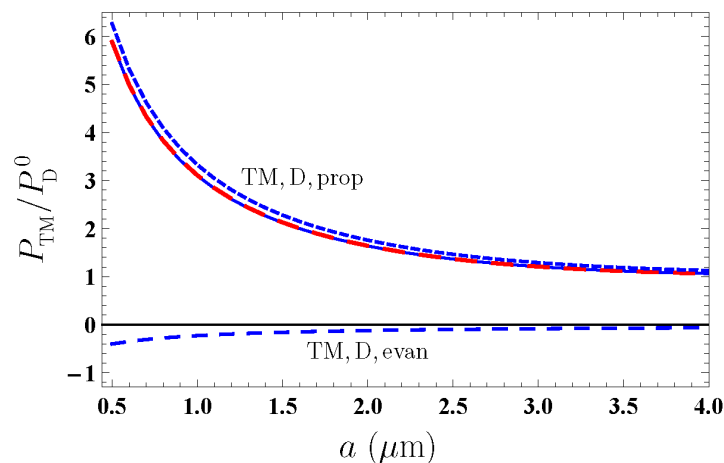


Figure 4. The transverse magnetic contributions to the Casimir pressure for Au plates due to propagating and evanescent waves normalized to P_D^0 computed at $T = 300$ K using the simple Drude model are shown as a function of separation by the top short-dashed and bottom long-dashed blue lines, respectively. The solid blue and long-dashed red lines for the normalized total transverse magnetic contributions to the Casimir pressure computed using the Drude and plasma models are reproduced from Figure 3a.

From Figure 4 it is seen that, although the quantities $P_{TM,D}$ and $P_{TM,p}$ are almost equal, their constituent parts due to the propagating and evanescent waves are different. For the plasma model, $P_{TM,p}$ is determined entirely by the propagating waves, whereas for the Drude model the contribution of $P_{TM,D}^{prop}$ to $P_{TM,D}$ is partially compensated by $P_{TM,D}^{evan}$ which is of the opposite sign, i.e., corresponds to the Casimir repulsion. This explains why there is no eventual impact of dissipation on $P_{TM,D}$, even though the Drude model is dissipative.

4.2. Transverse Electric Polarization

We calculate the contribution of the transverse electric polarization, P_{TE} , to the Casimir pressure by Equation (7) with the reflection coefficient r_{TE} from Equation (4) using the dielectric permittivities of the Drude model (10) and the plasma model (11). In Figure 5, the computational results for $P_{TE,D}$ and $P_{TE,p}$ normalized to P_D^0 at $T = 300$ K are shown as a function of separation by the lower (blue) and upper (red) solid lines for the Drude and plasma models, respectively.

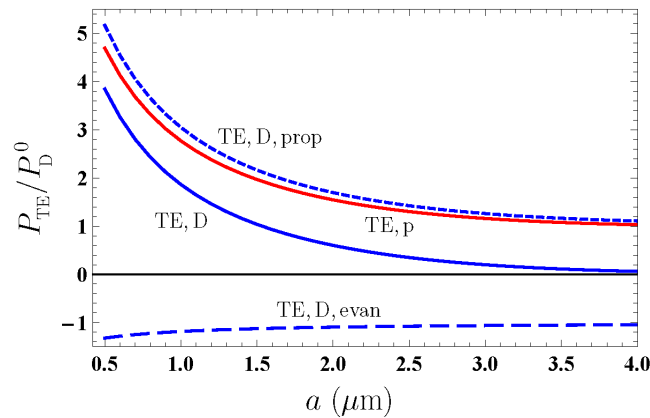


Figure 5. The transverse electric contributions to the Casimir pressure for Au plates due to propagating and evanescent waves normalized to P_D^0 computed at $T = 300$ K using the simple Drude model and the total transverse electric contribution are shown as a function of separation by the top and bottom short-dashed, long-dashed lines, and the lower solid line, respectively. The upper solid line shows similar results for the transverse electric contribution computed using the simple plasma model.

From Figure 5 it is seen that the lower and upper solid lines differ considerably. Keeping in mind that, according to the results of Section 4.1, $P_{TM,D}$ and $P_{TM,p}$ are equal with a high degree of accuracy, it becomes clear that this difference completely determines the discrepancy between the total Casimir pressures computed using the Drude and plasma models, P_D and P_p . The question arises what is the physical origin of this discrepancy.

To answer this question, we compute the quantities $P_{TE,D}^{evan}$ and $P_{TE,p}^{evan}$ by Equation (3). As to the latter, it is evident that

$$P_{TE,p}^{evan}(a, T) = 0, \tag{20}$$

because the dielectric permittivity of the plasma model (11) and the reflection coefficient $r_{TE,p}$ from Equation (4) are the real functions in the region of evanescent waves.

Taking into account Equation (9), one also finds that

$$P_{TE,p}^{prop}(a, T) = P_{TE,p}(a, T), \tag{21}$$

i.e., that for the plasma model the total Casimir pressure determined by the transverse electric polarization is equal to the contribution of TE-polarized propagating waves. This is the same as was proven in Section 4.1 above for the TM polarization. Thus, $P_{TE,p}^{prop}$ is given by the upper solid line in Figure 5a already drawn for $P_{TE,p}$.

The computational results for $P_{TE,D}^{evan}$ obtained by Equations (3), (4) and (10) at $T = 300$ K are shown as a function of separation in Figure 5 by the bottom long-dashed line. As to the computational results for $P_{TE,D}^{prop}$, they are found from Equation (9) and shown by the top short-dashed line in Figure 5 as a function of separation.

All contributions to P_{TE} are now computed using both models of the dielectric response of Au and it is possible to analyze the role of each of them. First of all, from Figure 5 it is seen that the deviation between $P_{TE,D}^{prop}$ and $P_{TE,p}^{prop}$ shown by the top short-dashed line and the upper solid line, respectively (we recall that the latter line also shows $P_{TE,p}$), is reasonably small and cannot be responsible for a much larger discrepancy between P_D and P_p . The latter is equal to the discrepancy between $P_{TE,D}$ and $P_{TE,p}$ shown by the two solid lines. In fact, the deviation between $P_{TE,D}^{prop}$ and $P_{TE,p}^{prop}$ demonstrates the impact of dissipation of conduction electrons on the TE contribution to the Casimir pressure, which is taken into account by the Drude model and disregarded by the plasma one. It is significant that this impact carried out through the TE propagating waves is not in contradiction with the experimental data on measuring the Casimir force.

A completely different type of situation occurs for $P_{TE,D}^{evan}$ shown by the bottom long-dashed line in Figure 5. The magnitude of $P_{TE,D}^{evan}$ is much larger than $P_{TM,D}^{evan}$, and this leads to a significant deviation between $P_{TE,D}$ and $P_{TE,p}$ resulting ultimately in a contradiction between the measurement data and theoretical predictions of the Lifshitz theory obtained using the Drude model.

For better understanding of the situation, one has to take into account that the Drude model has a wealth of alternative experimental confirmations in the area of propagating waves with any polarization, as well as for the transverse magnetic evanescent waves, but lacks confirmation for the transverse electric evanescent waves (see a discussion of experimental situation in Section 5 below). On this basis, one can conclude that experiments on measuring the Casimir force between metallic test bodies invalidate the dielectric permittivity of the Drude model in the area of transverse electric evanescent waves. It is apparent that the alternative experimental confirmations of such a conclusion are highly desirable (see Section 5 below).

5. Discussion: Failure of the Drude Model for Transverse Electric Evanescent Waves, the Role of Dissipation, and Possibilities of Alternative Tests

As discussed in Section 1, the theoretical predictions of the fundamental Lifshitz theory are in conflict with the measurement data of many precision experiments of Casimir physics if the dielectric response of conduction electrons is described by the dissipative Drude model. However, by disregarding the dissipation properties of conduction electrons, i.e., by using the plasma model, one can bring the measurement data in agreement with the theoretical predictions. Such a situation is unacceptable because the dissipation of conduction electrons at low frequencies is the much studied physical effect which is confirmed by many experiments.

According to the results presented above, an account of dissipation by means of the Drude model in the transverse magnetic contribution to the Casimir pressure leads to the same results as are obtained using the dissipationless plasma model. This is because the dissipation-induced terms in the Casimir pressure arising from the evanescent and propagating waves cancel each other. The dissipation-induced term in the contribution to the Casimir pressure from the transverse electric propagating waves is found to be reasonably small and does not bring the theoretical predictions found using the Drude model in contradiction with the measurement data.

The performed computations show that the roots of contradiction are not in the account of dissipation in itself, but in how the Drude model describes the response of metals to the low-frequency transverse electric evanescent waves. These computations compared with the measurement data lead us to conclude that the theoretical description of the electromagnetic response of metals to the transverse electric evanescent waves given by the Drude

model is in error. In this context, it is necessary to discuss the alternative experimental evidence regarding the validity of the Drude model other than the Casimir effect.

In the area of both the transverse magnetic and transverse electric propagating waves, there is an abundance of experimental confirmations of the Drude model in physics, electrotechnics, and even in day-to-day life, so it makes no sense to discuss them. However, direct measurement of the reflection coefficients of a metal in the case of evanescent waves presents complications as soon as all commonly used methods (ellipsometry, for instance) are adapted for the propagating waves.

The great interest paid to the evanescent waves during the last decades is connected with the fact that the evanescent waves made it possible to surmount the optical diffraction limit [65]. Thus, the physics of plasmons polaritons provides the possibility to obtain a great deal of evidence about the reflection of evanescent waves on metallic surfaces, but only for the transverse magnetic polarization [66]. The reflectivity properties of weakly evanescent waves (for which k_{\perp} is only just above ω/c) can be examined by means of the total internal reflection and frustrated total internal reflection [67–69]. Near-field optical microscopy, which is often used in various technological applications, is reasonably sensitive to only the transverse magnetic evanescent waves [70,71] (see also the discussion in Ref. [60] for more details).

The information provided above allows to conclude that the failure of the Drude model demonstrated by experiments on measuring the Casimir force does not contradict to all the available experimental evidences in favor of this model, which are irrelevant to the area of transverse electric evanescent waves.

Despite the fact that there are many experiments mentioned above, which demonstrate the failure of the Drude model resulting from the region of transverse electric evanescent waves, it would be highly desirable to perform one more independent test disconnected from the Casimir effect. Recently, such an alternative test in the field of classical electrodynamics was proposed in Refs. [60,72]. It was shown that the lateral components of the magnetic field of an oscillating magnetic dipole spaced in the proximity of a metallic plate are determined by solely the transverse electric evanescent waves. According to the results of Refs. [60,72], by choosing the suitable dipole frequency and using either the Drude or the plasma model for the dielectric permittivity of the metallic plate, the lateral components of the dipole field are varied by up to several orders of magnitude depending on the model used. Thus, by measuring these components for some fixed dipole parameters, it is possible to reliably conclude whether the Drude model correctly describes the response of plate metal to the transverse electric evanescent waves.

As an example, in Refs. [60,72], a magnetic dipole of 1 mm size with the dipole moment of $3.14 \times 10^{-5} \text{ Am}^2$ oscillating with the frequency of 100 rad/s at 1 cm height above the Cu plate was considered. Small dipoles of such kind are manufactured in the form of coils containing about ten turns [73–75]. In this case, the lateral component of the dipole magnetic field at the same height of 1 cm above the plate computed using the Drude model was found to be $0.027 \text{ A/m} = 3.37 \times 10^{-8} \text{ T}$ [60,72]. If the plasma model is used in computations, a magnetic field larger by a factor of 10 is obtained [60,72]. Keeping in mind that the current resolution limit in measurements of weak magnetic fields is of about 10^{-13} T [76–78], the proposed alternative test of the Drude model in the region of transverse electric evanescent waves seems quite feasible.

Finally, if it is confirmed that the Drude model is really invalid in the region of low-frequency transverse electric evanescent waves, the question arises as to how it could be corrected. Recently, the modifications of the Drude model at low frequencies caused by the spatial dispersion were again considered [79,80] in connection with the problems of Casimir physics. The suggested modifications, however, are incapable to bring the theoretical predictions in agreement with the measurement data for the Casimir force. The phenomenological spatially nonlocal alterations in the Drude model, which bring the theoretical predictions in agreement with all performed experiments on measuring the Casimir force, were suggested in Refs. [81–83], but they are still lacking fundamental

theoretical justification. Thus, the proper form of the response function of metals to the transverse electric evanescent waves remains to be found.

6. Conclusions

To conclude, in this paper we have performed the comparison studies of four contributions to the Casimir pressure between metallic plates caused by the transverse magnetic and transverse electric polarizations of the electromagnetic field and by the propagating and evanescent waves. The region of separations was determined where the major contribution to the pressure is given by the electromagnetic response of free electrons described by the dissipative Drude model or the experimentally consistent but dissipationless plasma model used in comparisons between experiment and theory.

According to our results, the transverse magnetic contributions to the Casimir pressure computed by using the Drude or plasma models are equal to a high degree of accuracy. In so doing, if the Drude model is used, the relatively small contribution from the evanescent waves (which is equal to zero when using the plasma model) is cancelled by an excessive contribution from the propagating waves. Thus, the use of the Drude model for computation of the Casimir pressure determined by the transverse electric polarization does not lead to contradictions between experiment and theory.

It was also shown that the transverse electric contribution to the Casimir pressure caused by the propagating waves, which is computed using the Drude model, deviates slightly from the transverse electric contribution computed using the plasma model (the latter is again determined by the propagating waves alone). This deviation is due to the dissipation processes of propagating waves taken into account by the Drude model. It cannot explain a discrepancy between the theoretical predictions obtained using the Drude model and the measurement data because of its small size.

Next, it was found that the experimental inconsistency of the Drude model is determined by the relatively large contribution of the transverse electric evanescent waves. This leads to a conclusion that the response of metals to the transverse electric evanescent waves is described by the Drude model incorrectly. In such a manner, the reason why the Lifshitz theory using the Drude model is experimentally inconsistent is not that it takes into account dissipation of free electrons, as opposed to the plasma model, but that it takes it into account incorrectly in the region of the transverse electric evanescent waves.

The presented analysis of experimental tests of the Drude model demonstrates that it is lacking experimental confirmation in this important region of the wave vectors and frequencies. Therefore, the recently proposed alternative test of the Drude model as a response function to the transverse electric evanescent waves should shed new light on the problem of disagreement between theoretical predictions of the Lifshitz theory and the measurement data.

Author Contributions: Conceptualization, G.L.K. and V.M.M.; investigation, G.L.K. and V.M.M.; writing—original draft, V.M.M.; writing—review and editing, G.L.K. All authors have read and agreed to the published version of the manuscript.

Funding: G.L.K. was partially funded by the Ministry of Science and Higher Education of Russian Federation (“The World-Class Research Center: Advanced Digital Technologies”, contract No. 075-15-2022-311 dated 20 April 2022). The research of V.M.M. was partially carried out in accordance with the Strategic Academic Leadership Program “Priority 2030” of the Kazan Federal University.

Data Availability Statement: Not applicable.

Conflicts of Interest: The authors declare no conflict of interest.

References

1. Casimir, H.B.G. On the attraction between two perfectly conducting plates. *Proc. Kon. Ned. Akad. Wetensch. B* **1948**, *51*, 793–795. Available online: <https://dwc.knaw.nl/DL/publications/PU00018547.pdf> (accessed on 26 August 2023).
2. Lifshitz, E.M. The theory of molecular attractive forces between solids. *Zh. Eksp. Teor. Fiz.* **1955**, *29*, 94–110 (in Russian); English translation: *Sov. Phys. JETP* **1956**, *2*, 73–83. Available online: <http://jetp.ras.ru/cgi-bin/e/index/e/2/1/p73?a=list> (accessed on 26 August 2023).
3. Mahanty, J.; Ninham, B.W. *Dispersion Forces*; Academic Press: London, UK, 1976.
4. Israelachvili, J.N. *Intermolecular and Surface Forces*; Academic Press: San Diego, CA, USA; Elsevier: San Diego, CA, USA, 2011. [CrossRef]
5. Milonni, P.W. *The Quantum Vacuum. An Introduction to Quantum Electrodynamics*; Academic Press, Inc.: San Diego, CA, USA, 1994. [CrossRef]
6. Mostepanenko, V.M.; Trunov, N.N. *The Casimir Effect and Its Applications*; Clarendon Press/Oxford University Press, Inc.: Oxford, UK; New York, NY, USA, 1997.
7. Milton, K.A. *The Casimir Effect: Physical Manifestations of Zero-Point Energy*; World Scientific: Singapore, 2001. [CrossRef]
8. Parsegian, V.A. *Van der Waals Forces: A Handbook for Biologists, Chemists, Engineers, and Physicists*; Cambridge University Press: Cambridge, UK; New York, NY, USA, 2005. [CrossRef]
9. Buhmann, S.Y. *Dispersion Forces I: Macroscopic Quantum Electrodynamics and Ground-State Casimir, Casimir–Polder and van der Waals Forces*; Springer: Berlin/Heidelberg, Germany, 2012. [CrossRef]
10. Buhmann, S.Y. *Dispersion Forces II: Many-Body Effects, Excited Atoms, Finite Temperature and Quantum Friction*; Springer: Berlin/Heidelberg, Germany, 2012. [CrossRef]
11. Langbein, D. *Theory of Van der Waals Attraction*; Springer: Berlin/Heidelberg, Germany, 2013. [CrossRef]
12. Bordag, M.; Klimchitskaya, G.L.; Mohideen, U.; Mostepanenko, V.M. *Advances in the Casimir Effect*; Oxford University Press Inc.: New York, NY, USA; Oxford, UK, 2015. [CrossRef]
13. Sernelius, B.E. *Fundamentals of van der Waals and Casimir Interactions*; Springer Nature, Switzerland AG: Cham, Switzerland, 2018. [CrossRef]
14. Lamoreaux, S.K. Demonstration of the Casimir Force in the 0.6 to 6 μm Range. *Phys. Rev. Lett.* **1997**, *78*, 5–8. [CrossRef]
15. Speake, C.C.; Trenkel, C. Forces between conducting surfaces due to spatial variations of surface potential. *Phys. Rev. Lett.* **2003**, *90*, 160403. [CrossRef] [PubMed]
16. Bezerra, V.B.; Klimchitskaya, G.L.; Mohideen, U.; Mostepanenko, V.M.; Romero, C. Impact of surface imperfections on the Casimir force for lenses of centimeter-size curvature radii. *Phys. Rev. B* **2011**, *83*, 075417. [CrossRef]
17. Mohideen, U.; Roy, A. Precision measurement of the Casimir force from 0.1 to 0.9 μm . *Phys. Rev. Lett.* **1998**, *81*, 4549–4552. [CrossRef]
18. Decca, R.S.; López, D.; Fischbach, E.; Krause, D.E. Measurement of the Casimir force between dissimilar metals. *Phys. Rev. Lett.* **2003**, *91*, 050402. [CrossRef]
19. Decca, R.S.; Fischbach, E.; Klimchitskaya, G.L.; Krause, D.E.; López, D.; Mostepanenko, V.M. Improved tests of extra-dimensional physics and thermal quantum field theory from new Casimir force measurements. *Phys. Rev. D* **2003**, *68*, 116003. [CrossRef]
20. Decca, R.S.; López, D.; Fischbach, E.; Klimchitskaya, G.L.; Krause, D.E.; Mostepanenko, V.M. Precise comparison of theory and new experiment for the Casimir force leads to stronger constraints on thermal quantum effects and long-range interactions. *Ann. Phys.* **2005**, *318*, 37–80. [CrossRef]
21. Decca, R.S.; López, D.; Fischbach, E.; Klimchitskaya, G.L.; Krause, D.E.; Mostepanenko, V.M. Tests of new physics from precise measurements of the Casimir pressure between two gold-coated plates. *Phys. Rev. D* **2007**, *75*, 077101. [CrossRef]
22. Decca, R.S.; López, D.; Fischbach, E.; Klimchitskaya, G.L.; Krause, D.E.; Mostepanenko, V.M. Novel constraints on light elementary particles and extra-dimensional physics from the Casimir effect. *Eur. Phys. J. C* **2007**, *51*, 963–975. [CrossRef]
23. Bimonte, G.; López, D.; Decca, R.S. Isoelectronic determination of the thermal Casimir force. *Phys. Rev. B* **2016**, *93*, 184434. [CrossRef]
24. Bimonte, G.; Spreng, B.; Maia Neto, P.A.; Ingold, G.-L.; Klimchitskaya, G.L.; Mostepanenko, V.M.; Decca, R.S. Measurement of the Casimir Force between 0.2 and 8 μm : Experimental Procedures and Comparison with Theory. *Universe* **2021**, *7*, 93. [CrossRef]
25. Chang, C.-C.; Banishev, A.A.; Castillo-Garza, R.; Klimchitskaya, G.L.; Mostepanenko, V.M.; Mohideen, U. Gradient of the Casimir force between Au surfaces of a sphere and a plate measured using an atomic force microscope in a frequency-shift technique. *Phys. Rev. B* **2012**, *85*, 165443. [CrossRef]
26. Banishev, A.A.; Chang, C.-C.; Klimchitskaya, G.L.; Mostepanenko, V.M.; Mohideen, U. Measurement of the gradient of the Casimir force between a nonmagnetic gold sphere and a magnetic nickel plate. *Phys. Rev. B* **2012**, *85*, 195422. [CrossRef]
27. Banishev, A.A.; Klimchitskaya, G.L.; Mostepanenko, V.M.; Mohideen, U. Demonstration of the Casimir force between ferromagnetic surfaces of a Ni-coated sphere and a Ni-coated plate. *Phys. Rev. Lett.* **2013**, *110*, 137401. [CrossRef]
28. Banishev, A.A.; Klimchitskaya, G.L.; Mostepanenko, V.M.; Mohideen, U. Casimir interaction between two magnetic metals in comparison with nonmagnetic test bodies. *Phys. Rev. B* **2013**, *88*, 155410. [CrossRef]
29. Xu, J.; Klimchitskaya, G.L.; Mostepanenko, V.M.; Mohideen, U. Reducing detrimental electrostatic effects in Casimir-force measurements and Casimir-force-based microdevices. *Phys. Rev. A* **2018**, *97*, 032501. [CrossRef]

30. Liu, M.; Xu, J.; Klimchitskaya, G.L.; Mostepanenko, V.M.; Mohideen, U. Examining the Casimir puzzle with an upgraded AFM-based technique and advanced surface cleaning. *Phys. Rev. B* **2019**, *100*, 081406. [CrossRef]
31. Liu, M.; Xu, J.; Klimchitskaya, G.L.; Mostepanenko, V.M.; Mohideen, U. Precision measurements of the gradient of the Casimir force between ultraclean metallic surfaces at larger separations. *Phys. Rev. A* **2019**, *100*, 052511. [CrossRef]
32. Sushkov, A.O.; Kim, W.J.; Dalvit, D.A.R.; Lamoreaux, S.K. Observation of the thermal Casimir force. *Nat. Phys.* **2011**, *7*, 230–233. [CrossRef]
33. Klimchitskaya, G.L.; Bordag, M.; Mostepanenko, V.M. Comparison between experiment and theory for the thermal Casimir force. *Int. J. Mod. Phys. A* **2012**, *27*, 1260012. [CrossRef]
34. Klimchitskaya, G.L.; Mostepanenko, V.M. Experiment and theory in the Casimir effect. *Contemp. Phys.* **2006**, *47*, 131–144. [CrossRef]
35. Bimonte, G.; Emig, T.; Kardar, M.; Krüger, M. Nonequilibrium fluctuational quantum electrodynamics: Heat radiation, heat transfer, and force. *Ann. Rev. Condens. Matter Phys.* **2017**, *8*, 119–143. [CrossRef]
36. Milton, K.A.; Li, Y.; Kalauni, P.; Parashar, P.; Guérout, P.; Ingold, G.-L.; Lambrecht, A.; Reynaud, S. Negative entropies in Casimir and Casimir-Polder interactions. *Fortschr. Phys.* **2017**, *65*, 1600047. [CrossRef]
37. Svetovoy, V.B.; van Zwol, P.J.; Palasantzas, G.; De Hosson, J.Th.M. Optical properties of gold films and the Casimir force. *Phys. Rev. B* **2008**, *77*, 035439. [CrossRef]
38. Bimonte, G. Making precise predictions of the Casimir force between metallic plates via a weighted Kramers-Kronig transform. *Phys. Rev. A* **2011**, *83*, 042109. [CrossRef]
39. Behunin, R.O.; Intravaia, F.; Dalvit, D.A.R.; Maia Neto, P.A.; Reynaud, S. Modeling electrostatic patch effects in Casimir force measurements. *Phys. Rev. A* **2012**, *85*, 012504. [CrossRef]
40. van Zwol, P.J.; Palasantzas, G.; De Hosson, J.T.M. Influence of random roughness on the Casimir force at small separations. *Phys. Rev. B* **2008**, *77*, 075412. [CrossRef]
41. Broer, W.; Palasantzas, G.; Knoester, J.; Svetovoy, V.B. Roughness correction to the Casimir force at short separations: Contact distance and extreme value statistics. *Phys. Rev. B* **2012**, *85*, 155410. [CrossRef]
42. Maia Neto, P.A.; Lambrecht, A.; Reynaud, S. Casimir effect with rough metallic mirrors. *Phys. Rev. A* **2005**, *72*, 012115. [CrossRef]
43. Canaguier-Durand, A.; Maia Neto, P.A.; Cervero-Pelaez, I.; Lambrecht, A.; Reynaud, S. Casimir interaction between plane and spherical metallic surfaces. *Phys. Rev. Lett.* **2009**, *102*, 230404. [CrossRef] [PubMed]
44. Fosco, C.D.; Lombardo, F.C.; Mazzitelli, F.D. Proximity force approximation for the Casimir energy as a derivative expansion. *Phys. Rev. D* **2011**, *84*, 105031. [CrossRef]
45. Bimonte, G.; Emig, T.; Jaffe, R.L.; Kardar, M. Casimir forces beyond the proximity force approximation. *Europhys. Lett. (EPL)* **2012**, *97*, 50001. [CrossRef]
46. Teo, L.P. Material dependence of Casimir interaction between a sphere and a plate: First analytic correction beyond proximity force approximation. *Phys. Rev. D* **2013**, *88*, 045019. [CrossRef]
47. Bimonte, G. Going beyond PFA: A precise formula for the sphere-plate Casimir force. *Europhys. Lett.* **2017**, *118*, 20002. [CrossRef]
48. Hartmann, M.; Ingold, G.-L.; Maia Neto, P.A. Plasma versus Drude modeling of the Casimir force: Beyond the proximity force approximation. *Phys. Rev. Lett.* **2017**, *119*, 043901. [CrossRef]
49. Klimchitskaya, G.L.; Mohideen, U.; Mostepanenko, V.M. The Casimir force between real materials: Experiment and theory. *Rev. Mod. Phys.* **2009**, *81*, 1827–1885. [CrossRef]
50. Mostepanenko, V.M. Casimir puzzle and conundrum: Discovery and search for resolution. *Universe* **2021**, *7*, 84. [CrossRef]
51. Klimchitskaya, G.L.; Mostepanenko, V.M. Current status of the problem of thermal Casimir force. *Int. J. Mod. Phys. A* **2022**, *37*, 2241002. [CrossRef]
52. Esquivel, R.; Svetovoy, V.B. Correction to the Casimir force due to the anomalous skin effect. *Phys. Rev. A* **2004**, *69*, 062102. [CrossRef]
53. Svetovoy, V.B.; Esquivel, R. Nonlocal impedances and the Casimir entropy at low temperatures. *Phys. Rev. E* **2005**, *72*, 036113. [CrossRef] [PubMed]
54. Sernelius, B.E. Effects of spatial dispersion on electromagnetic surface modes and on modes associated with a gap between two half spaces. *Phys. Rev. B* **2005**, *71*, 235114. [CrossRef]
55. Torgerson, J.R.; Lamoreaux, S.K. Low-frequency character of the Casimir force between metallic films. *Phys. Rev. E* **2004**, *70*, 047102. [CrossRef]
56. Bimonte, G. Comment on “Low-frequency character of the Casimir force between metallic films”. *Phys. Rev. E* **2006**, *73*, 048101. [CrossRef] [PubMed]
57. Intravaia, F.; Henkel, C. Casimir interaction from magnetically coupled eddy currents. *Phys. Rev. Lett.* **2009**, *103*, 130405. [CrossRef] [PubMed]
58. Intravaia, F.; Ellingsen, S.A.; Henkel, C. Casimir-Foucault interaction: Free energy and entropy at low temperature. *Phys. Rev. A* **2010**, *82*, 032504. [CrossRef]
59. Svetovoy, V.B.; Esquivel, R. The Casimir free energy in high- and low-temperature limits. *J. Phys. A Math. Gen.* **2006**, *39*, 6777–6784. [CrossRef]
60. Klimchitskaya, G.L.; Mostepanenko, V.M.; Svetovoy, V.B. *Experimentum crucis* for electromagnetic response of metals to evanescent waves and the Casimir puzzle. *Universe* **2022**, *8*, 574. [CrossRef]

61. Bordag, M. The Casimir effect for thin plasma sheets and the role of the surface plasmons. *J. Phys. A Math. Gen.* **2006**, *39*, 6173–6185. [CrossRef]
62. Palik, E.D. (Ed.) *Handbook of Optical Constants of Solids. Volume 1*; Academic Press, Inc.: San Diego, CA, USA, 1985. [CrossRef]
63. Boström, M.; Sernelius, B.E. Thermal effects on the Casimir force in the 0.1–5 μm range. *Phys. Rev. Lett.* **2000**, *84*, 4757–4760. [CrossRef] [PubMed]
64. Bordag, M.; Geyer, B.; Klimchitskaya, G.L.; Mostepanenko, V.M. Casimir force at both nonzero temperature and finite conductivity. *Phys. Rev. Lett.* **2000**, *85*, 503–506. [CrossRef] [PubMed]
65. Greffet, J.-J.; Carminati, R. Image formation in near-field optics. *Prog. Surf. Sci.* **1997**, *56*, 133–237. [CrossRef]
66. Törmä, P.; Barnes, W.L. Strong coupling between surface plasmon polaritons and emitters: A review. *Rep. Progr. Phys.* **2015**, *78*, 013901. [CrossRef]
67. Culshaw, W.; Jones, D.S. Effect of a metal plate on total reflection. *Proc. Phys. Soc. B* **1953**, *66*, 859–864. [CrossRef]
68. Brady, J.J.; Brick, R.O.; Pearson, V.D. Penetration of microwaves into the rarer medium in total reflection. *J. Opt. Soc. Am.* **1960**, *50*, 1080–1084. [CrossRef]
69. Zhu, S.; Yu, A.W.; Hawley, D.; Roy, R. Frustrated total internal reflection: A demonstration and review. *Am. J. Phys.* **1986**, *54*, 601–606. [CrossRef]
70. Hsu, J.W.P. Near-field scanning optical microscopy studies of electronic and photonic materials and devices. *Mater. Sci. Engin R Rep.* **2001**, *33*, 1–50. [CrossRef]
71. Aigouy, L.; Lahrech, A.; Grésillon, S.; Cory, H.; Boccarda, A.C.; Rivoal, J.C. Polarization effects in apertureless scanning near-field optical microscopy: An experimental study. *Opt. Lett.* **1999**, *24*, 187–189. [CrossRef]
72. Klimchitskaya, G.L.; Mostepanenko, V.M.; Svetovoy, V.B. Probing the response of metals to low-frequency s-polarized evanescent waves. *Europhys. Lett. (EPL)* **2022**, *139*, 66001. [CrossRef]
73. Ulvr, M. Design of PCB search coils for AC magnetic flux density measurement. *AIP Adv.* **2018**, *8*, 047505. [CrossRef]
74. Ramadan, Q.; Samper, V.; Poenar, D.; Yu, C. On-chip micro-electromagnets for magnetic-based bio-molecules separation. *J. Magn. Magnet. Mater.* **2004**, *281*, 150–172. [CrossRef]
75. Wensink, H.; Benito-Lopez, F.; Hermes, D.C.; Verboom, W.; Gardeniers, H.J.G.E.; Reinhoudt, D.N.; van den Berg, A. Measuring reaction kinetics in a lab-on-a-chip by microcoil NMR. *Lab Chip* **2005**, *5*, 280–284. [CrossRef] [PubMed]
76. Liu, Z.-X.; Wang, B.; Kong, C.; Si, L.-G.; Xiong, H.; Wu, Y. A proposed method to measure weak magnetic field based on a hybrid optomechanical system. *Sci. Rep.* **2017**, *7*, 12521. [CrossRef]
77. Murzin, D.; Mapps, D.J.; Levada, K.; Belyaev, V.; Omelyanchik, A.; Panina, L.; Rodionova, V. Ultrasensitive magnetic field Sensors for biomedical applications. *Sensors* **2020**, *20*, 1569. [CrossRef]
78. Huang, J.-H.; Duan, X.-Y.; Wang, G.-J.; Hu, X.-Y. Enhancing the precision of detecting weak magnetic fields based on weak-value amplification. *J. Opt. Soc. Amer. B* **2022**, *39*, 1289. [CrossRef]
79. Hannemann, M.; Wegner, G.; Henkel, C. No-slip boundary conditions for electron hydrodynamics and the thermal Casimir pressure. *Universe* **2021**, *7*, 108. [CrossRef]
80. Brevik, I.; Shapiro, B. A critical discussion of different methods and models in Casimir effect. *J. Phys. Commun.* **2022**, *6*, 015005. [CrossRef]
81. Klimchitskaya, G.L.; Mostepanenko, V.M. An alternative response to the off-shell quantum fluctuations: A step forward in resolution of the Casimir puzzle. *Eur. Phys. J. C* **2020**, *80*, 900. [CrossRef]
82. Klimchitskaya, G.L.; Mostepanenko, V.M. Casimir effect for magnetic media: Spatially non-local response to the off-shell quantum fluctuations. *Phys. Rev. D* **2021**, *104*, 085001. [CrossRef]
83. Klimchitskaya, G.L.; Mostepanenko, V.M. Theory-experiment comparison for the Casimir force between metallic test bodies: A spatially non-local dielectric response. *Phys. Rev. A* **2022**, *105*, 012805. [CrossRef]

Disclaimer/Publisher’s Note: The statements, opinions and data contained in all publications are solely those of the individual author(s) and contributor(s) and not of MDPI and/or the editor(s). MDPI and/or the editor(s) disclaim responsibility for any injury to people or property resulting from any ideas, methods, instructions or products referred to in the content.

Rectified Lorentz Force from Thermal Current Fluctuations

Carsten Henkel

University of Potsdam, Institute of Physics and Astronomy, Karl-Liebknecht-Str. 24/25, 14476 Potsdam, Germany; henkel@uni-potsdam.de

Abstract: In a conducting medium held at finite temperature, free carriers perform Brownian motion and generate fluctuating electromagnetic fields. In this paper, an averaged Lorentz force density is computed that turns out to be nonzero in a thin subsurface layer, pointing towards the surface, while it vanishes in the bulk. This is an elementary example of rectified fluctuations, similar to the Casimir force or radiative heat transport. The results obtained also provide an experimental way to distinguish between the Drude and so-called plasma models.

Keywords: Lorentz force; Drude model; metal optics

1. Introduction

The Hall effect is a known phenomenon in conducting media where a current in a magnetic field generates a transverse voltage due to the Lorentz force. Due to the large density of free carriers in conductors, significant magnetic fields are also internally generated. The corresponding eddy currents have applications at low frequencies for non-invasive material testing (e.g., reduced conductivity at cracks). Alongside currents induced by oscillating magnetic fields, the Lorentz force also plays a role in this context [1–3]. At frequencies from the infrared through the near-ultraviolet (UV), the Lorentz force is responsible for frequency mixing because it is a product of current and field. This occurs at metal surfaces that provide the necessary broken symmetry and leads to, for example, second-harmonic radiation [4–8]. A similar phenomenon is optical rectification where typically a short and intense laser pulse generates a surge of an electronic current, providing a source of THz radiation [9,10]. In samples with inversion symmetry, the electric and magnetic fields of optical pulses may rectify to a quasi-DC (direct-current) electric field that is assisting second-harmonic generation via the third-order Kerr nonlinearity [11]. Also in these applications, a relatively strong external field provides the force driving the conduction electrons.

In this paper is being discussed the Lorentz (or thermal Hall) force that arises from the Brownian motion of conduction electrons alone, without any external perturbation. A surface is again needed and defines, with its normal, the distinguished direction of the fluctuation-averaged (and hence DC) force. This can be understood as an electromagnetic contribution to the surface or cleavage energy [12–14]. The thermal Hall force will generate some space charge (depletion zone) below the surface and be balanced by the corresponding electric field. Experimental indications would therefore be the temperature dependence of the work function or a transient change in the surface charge density when the temperature of conduction electrons is pushed up, for example, after absorption of an ultrashort laser pulse [15–17].

The problem is addressed within the relatively simple setting of fluctuation electro-dynamics [18] and focussing on the local Drude approximation for the material conductivity. The calculations provide an alternative viewpoint on the challenge of defining fluctuation-induced forces inside a macroscopic medium [19]. The expression for the fluctuation-averaged Lorentz force contains two terms, one of which would be absent if the so-called plasma model were used for the metal permittivity. In line with previous suggestions

Citation: Henkel, C. Rectified Lorentz Force from Thermal Current Fluctuations. *Physics* **2024**, *6*, 568–578. <https://doi.org/10.3390/physics6020037>

Received: 1 December 2023
Revised: 5 February 2024
Accepted: 12 February 2024
Published: 9 April 2024



Copyright: © 2024 by the author. Licensee MDPI, Basel, Switzerland. This article is an open access article distributed under the terms and conditions of the Creative Commons Attribution (CC BY) license (<https://creativecommons.org/licenses/by/4.0/>).

related to low-frequency magnetic dipole radiation [20,21], the proposed thermal Hall force therefore provides another experimental clue to understand the anomalous temperature dependence of the Casimir force and the unusually large radiative heat transfer on the few nm scale [22,23].

2. Model

The electromagnetic force density is given by the familiar expression

$$\mathbf{f} = \rho\mathbf{E} + \mathbf{j} \times \mathbf{B} \tag{1}$$

with charge and current densities ρ and \mathbf{j} , and electric and magnetic fields \mathbf{E} and \mathbf{B} , respectively. For simplicity, pressure terms proportional to the gradient of the carrier density [5] and viscous shear forces [24,25] are neglected here, that lead to spatial dispersion (equivalently, a nonlocal conductivity). If an equilibrium state (with charge density ρ_0 and zero current) is perturbed, the two terms in Equation (1) are of first and second order, respectively, in small deviations from equilibrium. The Coulomb force leads to the resonance frequency Ω_p with $\Omega_p^2 = e\rho_0/\varepsilon_0m_e$ for electronic plasma oscillations (e and m_e are the electron charge and (effective) mass and ε_0 is the vacuum permittivity), while the Lorentz force is responsible for second-harmonic generation [5].

This paper considers the average of the Lorentz force with respect to thermal fluctuations of charges and fields and derives an integral formula for its temperature-dependent DC profile below the surface of a Drude conductor. The starting point is Rytov's fluctuation electrodynamics [18], where the electric current density, $\mathbf{j}(x) = \mathbf{j}(\mathbf{r}, t)$, is a random variable representing both quantum and thermal fluctuations at the position \mathbf{r} and time t . Its symmetrized correlation function is given by the (local) temperature T (fluctuation-dissipation theorem):

$$\begin{aligned} \langle j_i(x), j_k(x') \rangle &= \frac{1}{2} \langle j_i(x)j_k(x') + j_k(x')j_i(x) \rangle - \langle j_i(x) \rangle \langle j_k(x') \rangle \\ &= \delta_{ik} \delta(\mathbf{r} - \mathbf{r}') \int_0^\infty \frac{d\omega}{2\pi} \cos \omega(t - t') S_j(\mathbf{r}, \omega), \end{aligned} \tag{2}$$

$$\text{with } S_j(\mathbf{r}, \omega) = 2\hbar\omega \operatorname{Re} \sigma(\mathbf{r}, \omega) \coth \frac{\hbar\omega}{2k_B T}, \tag{3}$$

Here the indices take values $i, k = x, y, z$, and the brackets $\langle \dots \rangle$ denote the fluctuation average. The conductivity $\sigma(\mathbf{r}, \omega)$ is assumed to be local and isotropic, ω denotes the angular frequency, δ_{ik} the Kronecker delta, $\delta(\cdot)$ the Dirac delta function, and k_B and \hbar are the Boltzmann and the reduced Planck constants.

The Rytov currents generate a magnetic field whose vector potential, \mathbf{A} , solves in the transverse gauge the Ampère–Maxwell equation,

$$-\nabla^2 \mathbf{A} - \mu_0 \omega^2 \varepsilon(\mathbf{r}, \omega) \mathbf{A} = \mu_0 \mathbf{j}_\perp, \tag{4}$$

with the permittivity $\varepsilon(\mathbf{r}, \omega) = \varepsilon_0 + i\sigma(\mathbf{r}, \omega)/\omega$, the vacuum permeability μ_0 and the transverse current \mathbf{j}_\perp . In a homogeneous and isotropic system, one expects $\langle \mathbf{j} \times \mathbf{B} \rangle = \mathbf{0}$, since there is no preferred direction (see also Ref. [19]). The focus in the following is on the simple enough half-space geometry, with the metal filling $z \geq 0$. Parallel to the surface, a Fourier expansion with wave vector $\mathbf{Q} = (q_x, q_y)$ is applied where rotational invariance around the surface normal may be assumed. At fixed \mathbf{Q} , the vector potential is given by a Green tensor

$$\mathbf{A}(\mathbf{Q}, z) = \int_0^\infty dz' \mathbf{G}(\mathbf{Q}, z, z') \cdot \mathbf{j}(\mathbf{Q}, z') \tag{5}$$

$$\text{with } \mathbf{G}(\mathbf{Q}, z, z') = \frac{i\mu_0}{2q} (\bar{\mathbf{T}} e^{-iqz} + \mathbf{R}\bar{\mathbf{T}} e^{+iqz}) e^{iqz'} \quad \text{for } z < z'$$

$$\text{and } \mathbf{G}(\mathbf{Q}, z, z') = \frac{i\mu_0}{2q} (\mathbf{T} e^{-iqz'} + \mathbf{R}\bar{\mathbf{T}} e^{+iqz'}) e^{iqz} \quad \text{for } z' < z, \tag{6}$$

where $q^2 = \mu_0\omega^2\varepsilon(\omega) - Q^2$. This q with $\text{Re } q, \text{Im } q \geq 0$ provides the normal component of the wave vectors $\mathbf{q} = \mathbf{Q} + q\mathbf{e}_z$, $\bar{\mathbf{q}} = \mathbf{Q} - q\mathbf{e}_z$ for reflected and incident waves, respectively. The tensors \mathbf{T} and $\bar{\mathbf{T}}$ are projectors transverse to \mathbf{q} and $\bar{\mathbf{q}}$, respectively. The tensor \mathbf{R} describes the fields reflected from the inner surface. It is diagonal when expanded into principal transverse polarisations— p for the transverse magnetic and s for the transverse electric modes—and contains the reflection amplitudes r_p and r_s , respectively. The average of the vector product $\mathbf{j} \times \mathbf{B}$ with respect to the Rytov currents gives with the local and isotropic correlation (2), a vector structure proportional to

$$\langle \mathbf{j}^* \times [\mathbf{q} \times (\bar{\mathbf{T}} \cdot \mathbf{j})] \rangle \propto \text{tr}(\bar{\mathbf{T}}) \mathbf{q} - \bar{\mathbf{T}} \cdot \mathbf{q} \tag{7}$$

with similar expressions involving $\bar{\mathbf{q}}$, $\mathbf{R}\bar{\mathbf{T}}$, etc. If the tensor \mathbf{T} corresponds to \mathbf{q} , the last term vanishes by transversality. After the integral over the in-plane angle of \mathbf{Q} , only components normal to the surface remain.

Working through the polarisation vectors (see Appendix A.1 for details), it is indeed found that the fluctuation-averaged Lorentz force density $\langle \mathbf{j} \times \mathbf{B} \rangle = f \mathbf{e}_z$ is orthogonal to the surface and is given by

$$f = -\frac{\mu_0}{4\pi} \int_0^\infty d\omega S_j(\omega) \text{Re} \int_0^\infty Q dQ e^{2iqz} (r_p + r_s). \tag{8}$$

Here, the current spectrum S_j is given in Equation (3). The following calculations use the Drude model for the conductivity

$$\sigma(\omega) = \frac{\sigma_0}{1 - i\omega\tau} \tag{9}$$

with the DC conductivity σ_0 and the scattering (collision) rate $1/\tau$. This model describes quite well any conducting material between DC and below additional resonance frequencies. The latter may correspond to optically active phonons (typically in the infrared) or interband transitions (in the visible and above) and depend on the material [26]. The so-called plasma model corresponds to the limit $\sigma_0, \tau \rightarrow \infty$ at a fixed plasma frequency of $\Omega_p^2 = \sigma_0/(\varepsilon_0\tau)$. Physical realisations of this model are superconducting materials below their gap frequency and at temperatures much below critical. Its characteristic feature is a entirely imaginary conductivity, except at zero frequency. The weight of the corresponding δ -function,

$$\text{Re } \sigma(\omega) = \frac{\sigma_0/\tau^2}{1/\tau^2 + \omega^2} \rightarrow \pi \varepsilon_0 \Omega_p^2 \delta(\omega), \tag{10}$$

has been attributed to the density of superconducting carriers (Cooper pairs) [27] and is generally temperature-dependent.

The reflection coefficients from the “inner” side of a metal–vacuum interface are in the Fresnel approximation:

$$r_p = \frac{\varepsilon v - \varepsilon_0 q}{\varepsilon v + \varepsilon_0 q}, \quad r_s = \frac{q - v}{q + v}, \quad v = \sqrt{(\omega/c)^2 - Q^2}, \tag{11}$$

where c denotes the speed of light.

The calculation above focussed on the contribution from fluctuating currents. Within fluctuation electrodynamics, another contribution arises from fluctuating fields [18]. To provide a straightforward motivation for this additional term, consider a toy model with just two normal mode amplitudes a and b . By construction, these amplitudes are uncorrelated. Two generic fields A and B can be written as a linear combination of the normal modes: $A = c_1 a + c_2 b$ and $B = d_1 a + d_2 b$. Their correlation function is

$$\langle A^* B \rangle = c_1^* d_1 \langle a^* a \rangle + c_2^* d_2 \langle b^* b \rangle. \tag{12}$$

To relate the coefficients in this expression with measurable quantities, the term $c_1 a = A_{\text{fl}}$ is attributed to “fluctuations” and $c_2 b = A_{\text{ind}}$ to an “induced” field; and similarly, $d_1 a = B_{\text{ind}}$

and $d_2b = B_{fl}$. Such an identification appears naturally when equations of motion are linearised around an equilibrium, in particular, in the context of Langevin equations. With these notations, the correlation reads

$$\langle A^*B \rangle = \frac{d_1}{c_1} \langle A_{fl}^*A_{fl} \rangle + \frac{c_2^*}{d_2^*} \langle B_{fl}^*B_{fl} \rangle = \frac{\partial B_{ind}}{\partial A_{fl}} \langle A_{fl}^*A_{fl} \rangle + \frac{\partial A_{ind}^*}{\partial B_{fl}^*} \langle B_{fl}^*B_{fl} \rangle. \quad (13)$$

In the last step, the ratio d_1/c_1 is expressed by the linear response of variable B to A and vice versa. With respect to the calculation performed so far, the term $\langle A_{fl}^*A_{fl} \rangle$ in Equation (13) corresponds to current fluctuations, and $\partial B_{ind}/\partial A_{fl}$ describes the magnetic field generated by them. The second term, $\langle B_{fl}^*B_{fl} \rangle$, corresponds to magnetic field fluctuations that are now addressed.

The current responds to \mathbf{B}_{fl} via the associated electric field and Ohm’s law $\mathbf{j}_{ind} = \sigma \mathbf{E}_{fl}$. The thermal Lorentz force is thus determined by the average Poynting vector $\langle \mathbf{E}_{fl} \times \mathbf{B}_{fl} \rangle$. The spectrum of field fluctuations is provided by the fluctuation–dissipation theorem, assuming thermal equilibrium at temperature T . For the purposes of the calculations here, T coincides with the electron temperature because the field responds quite quickly to its sources, in virtue of its wide continuous mode spectrum. Working through the corresponding calculations (Appendix A.2), one finds that an expression similar to Equation (8) has to be added to the Lorentz force. The full result has the explicit form

$$(total) \quad f(z, T) = -\frac{\hbar\mu_0}{2\pi} \operatorname{Re} \int_0^\infty d\omega \omega \sigma(\omega) \coth \frac{\hbar\omega}{2k_B T} \int_0^\infty Q dQ e^{2iqz} (r_p + r_s). \quad (14)$$

Equation (14) is the main result of the present paper. Let us discuss its properties in Section 3 just below.

3. Discussion

3.1. General Features

A net force appears only due to the reflection from the surface at $z = 0$, as expected from broken rotational symmetry. Similar to the Casimir effect, the Lorentz force contains a specific quantum contribution that is UV-dominated, since $\coth \frac{1}{2}\beta\omega \rightarrow 1$ at high frequencies. In practice, the UV transparency of the material makes this contribution finite. Indeed, from the sum of the two Fresnel amplitudes,

$$r_s + r_p = \frac{2vq(\varepsilon - \varepsilon_0)}{(\varepsilon v + \varepsilon_0 q)(q + v)}, \quad (15)$$

it appears explicitly that the integrand decays sufficiently fast at high frequencies. This is illustrated in Figures 1 and 2 where the integrand of Equation (14) is plotted.

In the zero-temperature limit, it is expedient to shift the frequency integration to the imaginary axis, $\omega = i\zeta$. In this representation, relatively large frequencies and wave vectors are exponentially damped by the factor $e^{2iqz} \approx \exp[-2(z/c)\sqrt{\Omega_p^2 + \zeta^2 + c^2Q^2}]$ (this approximation assumes $\zeta \gg 1/\tau$). An approximate estimate of the double integral yields a scaling of the average Lorentz force density according to

$$T = 0 : \quad f(z, 0) \sim \frac{\hbar\Omega_p}{\lambda_p z^3}, \quad (16)$$

where $\lambda_p = c/\Omega_p$ represents the plasma wavelength.

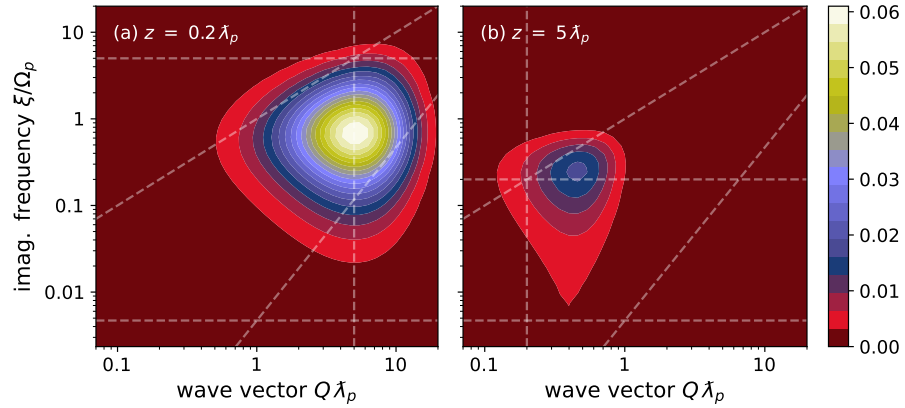


Figure 1. Integrand of the average Lorentz force due to quantum fluctuations ($T = 0$, arbitrary units) for (a) short and (b) large distances, as indicated. A Wick rotation to imaginary frequencies ξ has been applied. Parameters: plasma frequency $\Omega_p \approx 210/\tau$ (typical for Au). The dashed lines in (a,b) mark the values $\xi = c/z$, $\xi = cQ$ (light cone), $\xi = Q^2/(\mu_0\sigma_0)$ (magnetic diffusion), $\xi = 1/\tau$, and $Q = 1/z$. To reduce the dynamics of the data points, the integrand has been multiplied by z^3 . See text for more details.

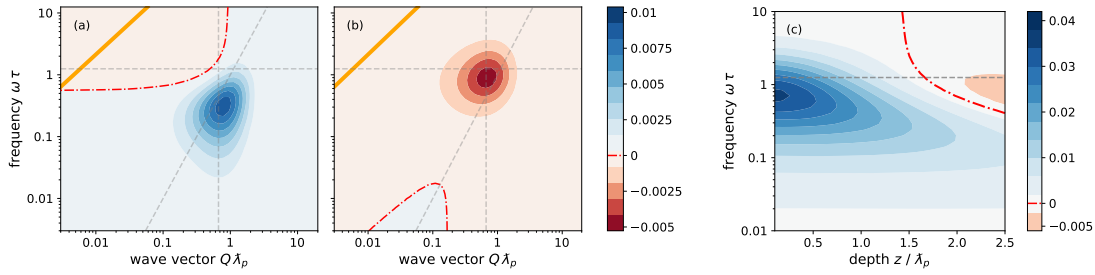


Figure 2. Spectrum of the thermal Lorentz force density (arbitrary units, real frequencies): (a,b) integrand of Equation (14), with the $T = 0$ contribution subtracted and (b) with only the imaginary part of the conductivity kept (similar to the plasma model); (c) the spectrum $f(z, \omega)$ before evaluating the ω -integral. Sign changes occur at the red dashed-dotted lines. Parameters: temperature $k_B T = 1.25 \hbar/\tau$, plasma frequency $\Omega_p \approx 210/\tau$ (as in Figure 1), distance $z = 1.5 \lambda_p$ in (a,b). The dashed lines in (a,b) mark the values $Q = 1/z$, $\hbar\omega = k_B T$, and in solid orange the light cone $\omega = cQ$. The dashed line in (c) indicates $\hbar\omega = k_B T$. To reduce the dynamics of the data points in (c), the force has been multiplied by z^2 .

We expect both the plasma and the Drude model to give comparable contributions, unless distances larger than $c\tau \gg \lambda_p$ are considered. In addition, for frequencies in the visible range and above, it is mandatory to take into account deviations from the Drude (or plasma) models, using, e.g., tabulated optical data [28]. A more detailed discussion is left for future studies.

Deep in the bulk, $z \rightarrow +\infty$, the exponential e^{2iqz} makes the force vanish. Since the medium wave vector q in Equation (14) is complex, one may expect an oscillatory behavior. The exponential e^{2iqz} becomes approximately real deeply below the light cone ($Q \gg \omega/c$). The typical long-range behaviour in the infrared is $q \approx (1+i)/\delta$ with the skin depth $\delta^2 = 2/(\mu_0\sigma_0\omega)$. This corresponds to the diffusive propagation of magnetic fields in a conducting medium.

The limit $z \rightarrow 0$ is beyond the local (Drude or plasma) model because r_p tends towards a constant at large Q , destroying convergence. This is eliminated when using a nonlocal (\mathbf{q} -dependent) conductivity whose magnitude drops for short-wavelength fields. The leading-order behaviour in the local approximation is discussed in Section 3.2 just below.

3.2. Thermal Hall Force

In what follows, the quantum contribution is subtracted, $\coth(\hbar\omega/2k_B T) - 1 = 2\bar{n}(\omega/T)$, so that the thermal component of the Lorentz force is proportional to the Bose–Einstein distribution $\bar{n}(\omega/T)$. The latter is dominated by frequencies with $\hbar\omega \lesssim k_B T$ (mid infrared and below, see Figure 2c). The plots in Figure 2a,b illustrate that the integrand of Equation (14) in the (Q, ω) -plane (Figure 2a) would change sign if only the term due to field fluctuations were kept (Figure 2b).

Note that in the plasma model, where the conductivity is entirely imaginary, the integrand is nonzero only above the light cone ($\omega > cQ$) and approximately above the plasma frequency Ω_p . Otherwise, the medium wave vector q is entirely imaginary, and the reflection coefficients r_s and r_p turn out to be real. This highly suppresses the thermal contribution to the average Lorentz force, since for typical temperatures, one has $\hbar\Omega_p \gg k_B T$. It is therefore instructive to evaluate the contribution from the singular DC conductivity of Equation (10). In calculations along imaginary frequencies, using a generalised plasma model, this term generates a permittivity $\epsilon(i\zeta) \sim \Omega_p^2/\zeta^2$, either by inserting Equation (10) into Kramers–Kronig relations or, more cautiously, by first isolating the zero-frequency pole [29,30]. However, a physical interpretation in terms of current fluctuations for superconductors is not clear enough. Fields penetrate into a superconducting medium down to approximately the same depth (the plasma wavelength λ_p) as the layer where the thermal Lorentz force is nonzero, see Figure 3. However, one would expect from the Meißner effect that in the bulk of a sample, there are neither static currents nor magnetic fields. In Ref. [31], Francesco Intravaia and the present author suggested to interpret the fluctuation electrodynamics of a medium with Equation (10) in terms of an “ideal conductor” model. Its bulk is filled with “frozen currents” and concomitant magnetic field loops. Inserting the conductivity (10) into Equation (14), one obtains for the thermal Lorentz force the expression

$$\text{(ideal conductor)} \quad \Delta f(z, T) = -\frac{k_B T}{\lambda_p^2} \int_0^\infty dQ e^{-2Qz} \frac{Q\kappa}{\kappa + Q} + \text{exp. small terms} \quad (17)$$

with $\kappa^2 = (\Omega_p/c)^2 + Q^2$. The integral here has the asymptotic form $1/(8z^2)$ (or $1/(4z^2)$) for $z \ll \lambda_p$ (for $z \gg \lambda_p$), the same scaling as the Coulomb force due to image charges. The exponentially small terms arise from frequencies $\hbar\omega \gtrsim \hbar\Omega_p \gg k_B T$. The resulting force is shown as dashed-dotted lines in Figure 3.

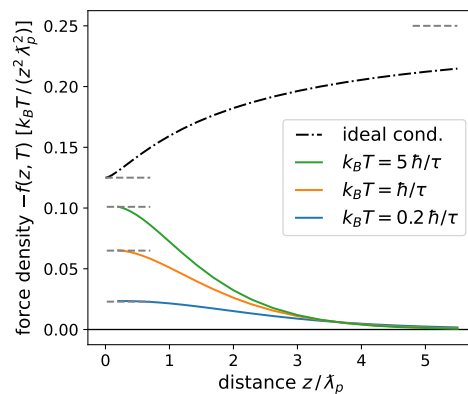


Figure 3. Distance dependence of the DC force density, normalised to T/z^2 and with flipped sign, for different temperatures, calculated for an ideal conductor (17) (black dashed-dotted curve) and a Drude conductor with finite damping time τ (colour curves). The straight dashed gray lines show the short-distance and large-distance limits of Equation (17) and the short-distance limit of Equation (18). The parameters are as in Figure 2: for typical conductors such as Au, the parameters correspond to $\hbar/\tau \approx 400$ K and $\lambda_p = c/\Omega_p \approx 20$ nm.

In good metallic conductors, the reflection coefficients are dominated by $|r_p| \approx 1$, while $r_s \approx -\frac{1}{4}(\epsilon - 1)(\omega/cQ)^2 \rightarrow 0$ for $Q \gg |\epsilon|\omega/c, \omega/c$ (evanescent waves). This allows for an approximate evaluation of the Q -integral in Equation (14). In the leading order, r_s is dropped, and one obtains again the scaling law $f \sim -1/z^2$. It has been checked that this captures well the short-distance behaviour of the force density, $f(z, T) \approx -c_2(T)/z^2$ with a prefactor given by

$$\begin{aligned} c_2(T) &\approx \frac{\hbar\mu_0\sigma_0}{4\pi} \int_0^\infty d\omega \frac{\omega \bar{n}(\omega/T)}{1 + \omega^2\tau^2} \\ &= \frac{k_B T}{8\pi\lambda_p^2} \left(\beta \log \frac{\beta}{2\pi} - \pi - \beta \psi(\beta/2\pi) \right). \end{aligned} \quad (18)$$

Here, $\beta = \hbar/(k_B T \tau)$ and $\psi(\cdot)$ is the digamma function. Recall that τ is the scattering time in the Drude conductivity, and $\bar{n}(\omega/T)$ the Bose–Einstein distribution. This expression is shown in Figure 4 after dividing out the scale factor $k_B T/\lambda_p^2$: one observes only quite minor dynamics, even though the product $k_B T \tau/\hbar$ varies over three orders of magnitude. The agreement with the full numerical integration is particularly good at the short distance $z = 0.2 \lambda_p$.

The distance dependence at a fixed temperature can be found from Figure 3 where the combination $-f(z, T) z^2/(k_B T)$ is shown. The force decays into the bulk with strongly damped oscillations, of which there remains only a crossing of the curves for different temperatures at a depth $z \approx 3.5 \lambda_p$. Beyond this depth, the linear scaling with temperature becomes exact. The rectified Lorentz force is thus restricted to a few plasma penetration depths, typically about 100 nm. The ideal conductor also gives a scaling linear in T , but the weak modifications relative to the $1/z^2$ power law display the opposite trend.

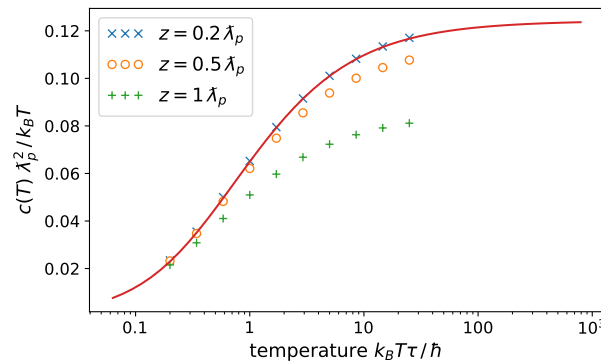


Figure 4. Temperature dependence of the amplitude $c_2(T)$ of the rectified Lorentz force density $f \approx -c_2(T)/z^2$ at short distances, normalised to $k_B T/\lambda_p^2$, calculated using Equation (18) (solid line) and with the numerical integration of Equation (14) with the $T = 0$ contribution subtracted (symbols). Material parameters as in Figure 2. Here, τ is not temperature-dependent.

3.3. Physical Consequences

Among the physical consequences suggested by these calculations, Section 1 mentioned a temperature-dependent shift $\Delta\phi(T)$ in the work function of a metal. Indeed, the Lorentz force is pulling charges towards the surface. To calculate the corresponding energy gain, one needs to regularise the $1/z^2$ divergence as $z \rightarrow 0$. This is physically achieved by adopting a non-local dielectric function (spatial dispersion), as discussed in Refs. [26,32,33]. A characteristic length scale related to the compressibility of the electron gas is the Debye screening length, $\ell_D = v_F/\Omega_p$, where v_F is typically of the order of the Fermi velocity.

If one integrates the Lorentz force density from $z = \infty$ down to a cutoff at $z = \ell_D$ and divides by the equilibrium carrier density n_0 , the following estimate is obtained

$$\Delta\phi(T) \approx -\frac{c_2(T)}{n_0\ell_D} \approx -0.06 k_B T \frac{e^2}{\epsilon_0 \hbar c} \frac{\hbar/\lambda_p}{mv_F}. \tag{19}$$

Both ratios on the right-hand side of Equation (19) are less than unity: the first ratio is $4\pi/137 \approx 0.0917$, and for gold, the second ratio results to ≈ 0.00380 . However, a Kelvin probe locked to a periodic temperature modulation may prove to be sufficiently sensitive.

A complementary phenomenon is the induced subsurface space charge that screens the thermal Lorentz force, restoring electro-chemical equilibrium. From the Coulomb law, its cumulative density $\Delta Q/A$ per unit area is of the order of

$$\frac{\Delta Q}{A} \approx \frac{\epsilon_0}{en_0} \lim_{z \rightarrow \ell_D} f(z) \approx -0.06 \frac{e}{\lambda_p^2} \frac{k_B T}{mv_F^2}. \tag{20}$$

This is again, as just above, a quite small charge, barely an elementary charge per square micron for gold. If this charge shows fluctuations in the MHz frequency band, however, these may be detectable with miniaturised ion traps because the corresponding fluctuations in the Coulomb force work against the laser cooling of the ion to its motional ground state [34].

4. Conclusions

In this paper, a thermal Hall effect has been explored that arises from the correlation between current density and magnetic field in a conducting medium at finite temperature. It turns out that in a thin layer below the material surface (its thickness being comparable to the Meißner penetration depth, λ_p), the Lorentz force density, averaged over thermal fluctuations, is nonzero and points towards the surface, similar to the interaction with image charges. It has been found that a Drude model gives a distinct prediction compared to the so-called plasma model because the corresponding force spectra have opposite signs (see Figure 2a,b). The thermal Hall voltage is relatively small, however.

The next step could be the regularisation on short-length scales, using a spatially dispersive permittivity and suitable boundary conditions. Another interesting perspective is the fluctuation spectrum of the Lorentz force around its thermal average that arises from fourth-order correlations of Rytov currents. This may provide an alternative, physical picture for the unusual electric field fluctuations observed in ion traps (anomalous heating) that are often attributed to surface contaminations [34].

Funding: This research was supported in part by the National Science Foundation (Grant PHY-1748958) and by the Deutsche Forschungsgemeinschaft (Grant 510943930 within CRC 1636, Project No. A01).

Data Availability Statement: No new data were created or analyzed in this study. Data sharing is not applicable to this article.

Acknowledgments: I thank the KITP (University of California at Santa Barbara) for its hospitality while attending the 2022 summer program “Quantum and Thermal Electrodynamic Fluctuations in the Presence of Matter: Progress and Challenges”.

Conflicts of Interest: The author declares no conflicts of interest.

Appendix A. Details of the Calculation

Appendix A.1. Polarisation Vectors

The following transverse polarisation vectors are used to expand the transverse projection tensor $\mathbf{T} = \mathbf{e}_s \otimes \mathbf{e}_s + \mathbf{e}_p \otimes \mathbf{e}_p$:

$$\mathbf{e}_s = \hat{\mathbf{Q}} \times \mathbf{e}_z, \quad \mathbf{e}_p = (q\hat{\mathbf{Q}} - Q\mathbf{e}_z)/k, \tag{A1}$$

where $\hat{\mathbf{Q}}$ is the unit vector parallel to \mathbf{Q} , and $k = \omega[\mu_0\epsilon(\omega)]^{1/2}$. For the wave vector \mathbf{q} of the incident wave (orthogonal projector $\bar{\mathbf{T}}$), the mirror images are used

$$\bar{\mathbf{e}}_s = \mathbf{e}_s, \quad \bar{\mathbf{e}}_p = (q\hat{\mathbf{Q}} + Q\mathbf{e}_z)/k. \tag{A2}$$

This leads to the following compact form of the transverse reflection tensor [35]

$$\mathbf{R}\bar{\mathbf{T}} = r_s \mathbf{e}_s \otimes \bar{\mathbf{e}}_s + r_p \mathbf{e}_p \otimes \bar{\mathbf{e}}_p. \quad (\text{A3})$$

As a consistency check, consider the limit of normal incidence where both polarisations behave in the same way. According to Equation (7), one needs the trace of this tensor:

$$\text{tr } \mathbf{R}\bar{\mathbf{T}} = r_s + r_p (q^2 - Q^2)/k^2 \quad (\text{A4})$$

and the image of the reflected wave vector:

$$\mathbf{R}\bar{\mathbf{T}} \cdot \mathbf{q} = 2r_p \mathbf{e}_p qQ/k. \quad (\text{A5})$$

This expression is nonzero because $\bar{\mathbf{q}}$ and \mathbf{q} differ by one mirror reflection from the surface.

Let us perform the angular integration over the in-plane angle φ of \mathbf{Q} . The reflection coefficients only depend on its magnitude Q . One has

$$\int \frac{d\varphi}{2\pi} \mathbf{q} = q \mathbf{e}_z, \quad \int \frac{d\varphi}{2\pi} \mathbf{e}_p = -(Q/k) \mathbf{e}_z, \quad (\text{A6})$$

so that after integrating over φ , Equation (7) becomes

$$\begin{aligned} & \int \frac{d\varphi}{2\pi} [\text{tr}(\mathbf{R}\bar{\mathbf{T}}) \mathbf{q} - \mathbf{R}\bar{\mathbf{T}} \cdot \mathbf{q}] \\ &= q [r_s + r_p (q^2 - Q^2)/k^2] \mathbf{e}_z + 2q r_p (Q^2/k^2) \mathbf{e}_z = q(r_s + r_p) \mathbf{e}_z. \end{aligned} \quad (\text{A7})$$

One still has to multiply Equation (A7) with the phase factor $e^{iq(z+z')}$ from the Green function (6). The terms without the reflection coefficients (homogeneous medium) cancel thanks to the first integral in Equation (A6): the limits $z' \searrow z$ and $z' \nearrow z$ are combined and the local current correlation function (2) exploited to evaluate the z' -integral. Taking into account the symmetrised correlation function, eventually introduces a real part [36], and one obtains Equation (8).

Appendix A.2. Average Poynting Vector

As outlined after Equation (11), the contribution of field rather than current fluctuations involves the calculation of the correlation function $\langle \mathbf{E}^*(\mathbf{r}, \omega) \times \mathbf{B}(\mathbf{r}, \omega') \rangle$. Using the Faraday equation to express the magnetic field, one has to evaluate

$$\langle \mathbf{E}^*(\mathbf{r}, \omega) \times [\nabla' \times \mathbf{E}(\mathbf{r}', \omega')] \rangle = \nabla' \langle \mathbf{E}^*(\mathbf{r}, \omega) \cdot \mathbf{E}(\mathbf{r}', \omega') \rangle - \langle [\mathbf{E}^*(\mathbf{r}, \omega) \cdot \nabla'] \mathbf{E}(\mathbf{r}', \omega') \rangle, \quad (\text{A8})$$

eventually taking the limit $\mathbf{r}' \rightarrow \mathbf{r}$. The electric field autocorrelation is given by the fluctuation–dissipation theorem [18,37,38]:

$$\langle E_i^*(\mathbf{r}, \omega) E_j(\mathbf{r}', \omega') \rangle = \frac{4\pi\hbar \delta(\omega - \omega')}{e^{\hbar\omega/k_B T} - 1} \text{Im } \mathcal{G}_{ij}(\mathbf{r}, \mathbf{r}', \omega). \quad (\text{A9})$$

Let us assume here for simplicity the medium to be reciprocal so that $\mathcal{G}_{ij}(\mathbf{r}, \mathbf{r}', \omega) = \mathcal{G}_{ji}(\mathbf{r}', \mathbf{r}, \omega)$. Recall that this Green tensor determines the electric field $\mathbf{E}(\mathbf{r}, \omega)$ radiated by a monochromatic point dipole of amplitude \mathbf{d} located at position \mathbf{r}' in the medium, $\mathbf{E} = \mathcal{G} \cdot \mathbf{d}$.

The Green tensor splits into a part relevant for a homogeneous bulk medium that only depends on the difference $\mathbf{r} - \mathbf{r}'$. Its derivative vanishes for $\mathbf{r}' \rightarrow \mathbf{r}$. The remaining part near a planar surface can be written with reflection coefficients (Weyl expansion, $z, z' \geq 0$) [35]:

$$\mathcal{G}^{\text{refl}}(\mathbf{r}, \mathbf{r}', \omega) = i\mu_0\omega^2 \int \frac{d^2Q}{(2\pi)^2} \frac{e^{i(\mathbf{q}\cdot\mathbf{r} - \bar{\mathbf{q}}\cdot\mathbf{r}')} }{2q} \mathbf{R}\bar{\mathbf{T}}. \quad (\text{A10})$$

Performing the derivatives of Equation (A8) under the imaginary part of this expression, leads to a quite similar calculation as in Appendix A.1 and results in

$$\begin{aligned} & \nabla' \operatorname{Im} \operatorname{tr} \mathcal{G}^{\text{refl}}(\mathbf{r}, \mathbf{r}', \omega) - \sum_{i,j} \frac{\partial}{\partial x'_i} \operatorname{Im} \mathcal{G}_{ij}^{\text{refl}}(\mathbf{r}, \mathbf{r}', \omega) \mathbf{e}_j \\ & = -\mathbf{e}_z \frac{\mu_0}{4\pi} \omega^2 \operatorname{Im} \int_0^\infty dQ Q e^{2iqz} (r_s + r_p). \end{aligned} \quad (\text{A11})$$

The final steps are to multiply Equation (A11) by $-i\sigma^*/\omega$ to convert \mathbf{E}^* into \mathbf{j}^* and $\nabla \times \mathbf{E}$ into \mathbf{B} (see Equation (A8)) and to take the real part to obtain the symmetrised correlation. This makes the imaginary part of the conductivity appear. Writing the frequency integral over positive frequencies only, leads in conjunction with Equation (8) to the final result (14).

References

- Uhlig, R.P.; Zec, M.; Brauer, H.; Thess, A. Lorentz force eddy current testing: A prototype model. *J. Nondestruct. Eval.* **2012**, *31*, 357–372. [CrossRef]
- Li, C.; Liu, R.; Dai, S.; Zhang, N.; Wang, X. Vector-based eddy-current testing method. *Appl. Sci.* **2018**, *8*, 2289. [CrossRef]
- Alkhalil, S.; Kolesnikov, Y.; Thess, A. Lorentz force sigmometry: A novel technique for measuring the electrical conductivity of solid and liquid metals. *Meas. Sci. Technol.* **2015**, *26*, 115605. [CrossRef]
- Bloembergen, N.; Chang, R.K.; Jha, S.S.; Lee, C.H. Optical second-harmonic generation in reflection from media with inversion symmetry. *Phys. Rev.* **1969**, *178*, 1528. [CrossRef]
- Sipe, J.E.; So, V.C.Y.; Fukui, M.; Stegeman, G.I. Analysis of second-harmonic generation at metal surfaces. *Phys. Rev. B* **1980**, *21*, 4389–4402. [CrossRef]
- Renger, J.; Quidant, R.; van Hulst, N.; Palomba, S.; Novotny, L. Free-space excitation of propagating surface plasmon polaritons by nonlinear four-wave mixing. *Phys. Rev. Lett.* **2009**, *103*, 266802. [CrossRef] [PubMed]
- Renger, J.; Quidant, R.; van Hulst, N.; Novotny, L. Surface-enhanced nonlinear four-wave mixing. *Phys. Rev. Lett.* **2010**, *104*, 046803. [CrossRef]
- Hille, A.; Moeferd, M.; Wolff, C.; Matyssek, C.; Rodríguez-Oliveros, R.; Prohm, C.; Niegemann, J.; Grafström, S.; Eng, L.M.; Busch, K. Second harmonic generation from metal nano-particle resonators: Numerical analysis on the basis of the hydrodynamic Drude model. *J. Phys. Chem. C* **2016**, *120*, 1163–1169. [CrossRef]
- Kadlec, F.; Kužel, P.; Coutaz, J.-L. Optical rectification at metal surfaces. *Opt. Lett.* **2004**, *29*, 2674–2676. [CrossRef]
- Hoffmann, M.C.; Fülöp, J.A. Intense ultrashort terahertz pulses: Generation and applications. *J. Phys. D Appl. Phys.* **2011**, *44*, 083001. [CrossRef]
- Trinh, M.T.; Smail, G.; Makhali, K.; Yang, D.S.; Kim, J.; Rand, S.C. Observation of magneto-electric rectification at non-relativistic intensities. *Nat. Commun.* **2020**, *11*, 5296. [CrossRef] [PubMed]
- Craig, R.A. Dynamic contributions to the surface energy of simple metals. *Phys. Rev. B* **1972**, *6*, 1134–1142. [CrossRef]
- Morgenstern Horing, N.J.; Kamen, E.; Gumbs, G. Surface correlation energy and the hydrodynamic model of dynamic, nonlocal bounded plasma response. *Phys. Rev. B* **1985**, *31*, 8269–8272. [CrossRef] [PubMed]
- Barton, G. On the surface energy of metals according to the hydrodynamic model with spatial dispersion. *J. Phys. C Sol. State Phys.* **1986**, *19*, 975–980. [CrossRef]
- Prange, R.E.; Kadanoff, L.P. Transport theory for electron–phonon interactions in metals. *Phys. Rev.* **1964**, *134*, A566–A580. [CrossRef]
- Pudell, J.; Maznev, A.; Herzog, M.; Kronseder, M.; Back, C.; Malinowski, G.; von Reppert, A.; Bargheer, M. Layer specific observation of slow thermal equilibration in ultrathin metallic nanostructures by femtosecond X-ray diffraction. *Nat. Commun.* **2018**, *9*, 3335. [CrossRef]
- Bresson, P.; Bryche, J.F.; Besbes, M.; Moreau, J.; Karsenti, P.L.; Charette, P.G.; Morris, D.; Canva, M. Improved two-temperature modeling of ultrafast thermal and optical phenomena in continuous and nanostructured metal films. *Phys. Rev. B* **2020**, *102*, 155127. [CrossRef]
- Rytov, S.M.; Kravtsov, Y.A.; Tatarskii, V.I. *Principles of Statistical Radiophysics. Volume 3: Elements of Random Fields*; Springer: Berlin/Heidelberg, Germany, 1989.
- Griniasty, I.; Leonhardt, U. Casimir stress inside planar materials. *Phys. Rev. A* **2017**, *96*, 032123. [CrossRef]
- Klimchitskaya, G.L.; Mostepanenko, V.M.; Svetovoy, V.B. Experimentum crucis for electromagnetic response of metals to evanescent waves and the Casimir puzzle. *Universe* **2022**, *8*, 574. [CrossRef]
- Klimchitskaya, G.L.; Mostepanenko, V.M.; Svetovoy, V.B. Probing the response of metals to low-frequency s-polarized evanescent fields. *Europhys. Lett.* **2022**, *139*, 66001. [CrossRef]
- Henkel, C. Nano-scale thermal transfer—An invitation to fluctuation electrodynamics. *Z. Naturforsch. A* **2017**, *72*, 99–108. [CrossRef]
- Klimchitskaya, G.L.; Mostepanenko, V.M. Recent measurements of the Casimir force: Comparison between experiment and theory. *Mod. Phys. Lett. A* **2020**, *35*, 2040007. [CrossRef]
- Conti, S.; Vignale, G. Elasticity of an electron liquid. *Phys. Rev. B* **1999**, *60*, 7966–7980. [CrossRef]

25. Hannemann, M.; Wegner, G.; Henkel, C. No-slip boundary conditions for electron hydrodynamics and the thermal Casimir pressure. *Universe* **2021**, *7*, 108. [CrossRef]
26. Dressel, M.; Grüner, G. *Electrodynamics of Solids—Optical Properties of Electrons in Matter*; Cambridge University Press: Cambridge, UK, 2002. [CrossRef]
27. Berlinsky, A.J.; Kallin, C.; Rose, G.; Shi, A.C. Two-fluid interpretation of the conductivity of clean BCS superconductors. *Phys. Rev. B* **1993**, *48*, 4074–4079. [CrossRef] [PubMed]
28. Klimchitskaya, G.L.; Mohideen, U.; Mostepanenko, V.M. The Casimir force between real materials: Experiment and theory. *Rev. Mod. Phys.* **2009**, *81*, 1827–1885. [CrossRef]
29. Klimchitskaya, G.L.; Mohideen, U.; Mostepanenko, V.M. Kramers-Kronig relations for plasma-like permittivities and the Casimir force. *J. Phys. A* **2007**, *40*, F339–F346. [CrossRef]
30. Levine, Z.H.; Cockayne, E. The pole term in linear response theory: An example from the transverse response of the electron gas. *J. Res. Natl. Inst. Stand. Technol.* **2008**, *113*, 299–304. [CrossRef] [PubMed]
31. Henkel, C.; Intravaia, F. On the Casimir entropy between ‘perfect crystals’. *Int. J. Mod. Phys. A* **2010**, *25*, 2328–2336. [CrossRef]
32. Sernelius, B.E. Effects of spatial dispersion on electromagnetic surface modes and on modes associated with a gap between two half spaces. *Phys. Rev. B* **2005**, *71*, 235114. [CrossRef]
33. Svetovoy, V.B.; Esquivel, R. The Casimir free energy in high- and low-temperature limits. *J. Phys. A* **2006**, *39*, 6777–6784. [CrossRef]
34. Brownnutt, M.; Kumph, M.; Rabl, P.; Blatt, R. Ion-trap measurements of electric-field noise near surfaces. *Rev. Mod. Phys.* **2015**, *87*, 1419–1482. [CrossRef]
35. Sipe, J.E. New Green-function formalism for surface optics. *J. Opt. Soc. Am. B* **1987**, *4*, 481–489. [CrossRef]
36. Agarwal, G.S. Quantum electrodynamics in the presence of dielectrics and conductors. I. Electromagnetic-field response functions and black-body fluctuations in finite geometries. *Phys. Rev. A* **1975**, *11*, 230–242. [CrossRef]
37. Lifshitz, E.M.; Pitaevskii, L.P. *Statistical Physics. Part 2: Theory of the Condensed State*; Butterworth–Heinemann Ltd./Elsevier Ltd.: Oxford, UK, 1980. [CrossRef]
38. Buhmann, S.Y. *Dispersion Forces II. Many-Body Effects, Excited Atoms, Finite Temperature and Quantum Friction*; Springer: Berlin/Heidelberg, Germany, 2012. [CrossRef]

Disclaimer/Publisher’s Note: The statements, opinions and data contained in all publications are solely those of the individual author(s) and contributor(s) and not of MDPI and/or the editor(s). MDPI and/or the editor(s) disclaim responsibility for any injury to people or property resulting from any ideas, methods, instructions or products referred to in the content.

Article

The Casimir Force between Two Graphene Sheets: 2D Fresnel Reflection Coefficients, Contributions of Different Polarizations, and the Role of Evanescent Waves

Galina L. Klimchitskaya^{1,2} and Vladimir M. Mostepanenko^{1,2,3,*}

¹ Central Astronomical Observatory at Pulkovo of the Russian Academy of Sciences, 196140 Saint Petersburg, Russia; g.klimchitskaya@gmail.com

² Peter the Great Saint Petersburg Polytechnic University, 195251 Saint Petersburg, Russia

³ Kazan Federal University, 420008 Kazan, Russia

* Correspondence: vmostepa@gmail.com

Abstract: We consider the Casimir pressure between two graphene sheets and contributions to it determined by evanescent and propagating waves with different polarizations. For this purpose, the derivation of the 2-dimensional (2D) Fresnel reflection coefficients on a graphene sheet is presented in terms of the transverse and longitudinal dielectric permittivities of graphene with due account of the spatial dispersion. The explicit expressions for both dielectric permittivities as the functions of the 2D wave vector, frequency, and temperature are written along the real frequency axis in the regions of propagating and evanescent waves and at the pure imaginary Matsubara frequencies using the polarization tensor of graphene. It is shown that in the application region of the Dirac model nearly the total value of the Casimir pressure between two graphene sheets is determined by the electromagnetic field with transverse magnetic (TM) polarization. By using the Lifshitz formula written along the real frequency axis, the contributions of the TM-polarized propagating and evanescent waves into the total pressure are determined. By confronting these results with the analogous results found for plates made of real metals, the way for bringing the Lifshitz theory using the realistic response functions in agreement with measurements of the Casimir force between metallic test bodies is pointed out.

Keywords: graphene; Casimir pressure; Dirac model; spatial dispersion; polarization tensor; propagating waves; evanescent waves

Citation: Klimchitskaya, G.L.; Mostepanenko, V.M. The Casimir Force between Two Graphene Sheets: 2D Fresnel Reflection Coefficients, Contributions of Different Polarizations, and the Role of Evanescent Waves. *Physics* **2023**, *5*, 1013–1030. <https://doi.org/10.3390/physics5040066>

Received: 1 September 2023

Revised: 11 October 2023

Accepted: 19 October 2023

Published: 25 October 2023



Copyright: © 2023 by the authors. Licensee MDPI, Basel, Switzerland. This article is an open access article distributed under the terms and conditions of the Creative Commons Attribution (CC BY) license (<https://creativecommons.org/licenses/by/4.0/>).

1. Introduction

By now, graphene has assumed great importance in the field of fundamental physics and its numerous applications, where it plays a broad spectrum of roles [1,2]. The distinctive characteristic features of graphene, as opposed to ordinary bodies, are the 2-dimensional (2D) crystal structure of carbon atoms and massless quasiparticles described not by the Schrödinger equation, but by the Dirac equation, where the speed of light is replaced with the much smaller Fermi velocity. As a result, at energies below a few eV, the electrical and optical properties of graphene are well described by the relatively simple Dirac model [1–6]. This enables one to investigate the main features of graphene not by using some phenomenological approach, which is the usual practice in condensed matter physics, but on the solid basis of thermal quantum field theory and, more specifically, quantum electrodynamics at nonzero temperature.

The subject of this paper is the Casimir force [7], which acts between any two uncharged closely spaced material bodies owing to the zero-point and thermal fluctuations of the electromagnetic field. In his original publication [7], Casimir calculated the force acting between two ideal metal planes kept at zero temperature. At a later time, E. M. Lifshitz [8–10] developed the general theory expressing the Casimir force between two

plates at any temperature via the reflection coefficients written in terms of the frequency-dependent dielectric permittivities of plate materials. In recent years, the Casimir force continues to grow in popularity due to the role it plays in quantum field theory, elementary particle physics, condensed matter, atomic physics, and even cosmology (see the monographs [11–13]).

Experiments measuring the Casimir force between metallic test bodies faced problems when comparing the measurement data with theoretical predictions of the Lifshitz theory. It turned out that if the low-frequency response of metals is described by the universally used dissipative Drude model, the obtained theoretical predictions are excluded by the measurement data. If, however, the low-frequency response is described by the dissipationless plasma model, which should not be applicable at low frequencies, the theory gives results in agreement with the experiment (see [12,14–17] for a review). Quite recently, it was shown [18] that the roots of the problem are not in the Drude model as a whole, but only in its possible incorrectness in the restricted area of transverse electric evanescent waves where it has no sufficient experimental confirmation.

The response functions of metals, including the Drude model, are of more or less phenomenological character. In this regard, of special interest is the Casimir effect in graphene systems, which has drawn the attention of many authors. At the early stages of investigation, the response of graphene to the electromagnetic field was also described by means of phenomenological methods based on the 2D Drude model, density functional theory, Boltzmann transport equation, random phase approximation, Kubo theory, hydrodynamic model, etc., and the obtained results were used to calculate the Casimir force in graphene systems [19–39]. In doing so, it was found that in the framework of the Dirac model the spatially nonlocal response of graphene at the pure imaginary Matsubara frequencies can be described by the polarization tensor in (2+1)-dimensional space-time and calculated precisely from the first principles of thermal quantum field theory [40,41]. These results were generalized to the entire plane of complex frequencies including the real frequency axis [42,43]. In such a manner, the reflection coefficients of electromagnetic fluctuations on a graphene sheet were expressed directly via the components of the polarization tensor.

The results of first-principles calculations of the Casimir force between two graphene sheets using the polarization tensor were compared [44] with those obtained using various phenomenological methods, and serious limitations of the latter were demonstrated. What is more, the measurement data of two experiments measuring the Casimir force in graphene systems were compared with the predictions of the Lifshitz theory using the reflection coefficients on graphene expressed via the polarization tensor and found to be in excellent agreement [45–48]. Specifically, the most precise measurements [47,48] confirmed the theoretical prediction of [24] that for graphene systems a big thermal effect in the Casimir force arises at much shorter separations than for metallic or dielectric bodies.

Thus, in the case of graphene, the Lifshitz theory does not suffer from a problem arising for metallic plates whose electromagnetic response was determined on partially phenomenological grounds (we recall that the experimental data for the complex index of refraction of metals are available only in the frequency region above some minimum frequency and are usually extrapolated by the Drude model to below this frequency [49]). One can conclude that graphene supplies us with some kind of road map on how to correctly describe the Casimir force between metallic plates. Because of this, it is important to compare both theoretical descriptions in parallel, including the form of reflection coefficients, the contributions of different polarizations of the electromagnetic field, and the propagating and evanescent waves.

In the current study, we underline that the reflection coefficients on a graphene sheet expressed via the polarization tensor are nothing more than the 2D Fresnel reflection coefficients expressed via the spatially nonlocal longitudinal and transverse dielectric permittivities. It is stressed that for a 2D graphene sheet, as opposed to the 3D Casimir configurations, the spatial dispersion can be taken into account exactly on a rigorous theoretical basis. Then, it is shown that in the application region of the Dirac model

the Casimir force between two pristine graphene sheets is completely determined by the transverse magnetic polarization of the electromagnetic field. In doing so, at short separations up to hundreds of nanometers, both the propagating and evanescent waves make essential contributions to the Casimir force, whereas at larger separations the total force value is mostly determined by the contribution of evanescent waves. This is compared with the case of metallic plates where the evanescent waves play an important role in the problem of disagreement between the predictions of the Lifshitz theory using the Drude model and the measurement data.

The paper is organized as follows. In Section 2, we present the detailed derivation of the 2D Fresnel reflection coefficients on a graphene sheet in terms of the dielectric permittivities of graphene with an accurate account of the spatial dispersion. In Section 3, the explicit expressions for the transverse and longitudinal dielectric permittivities of graphene at any temperature are presented. Section 4 contains the results of the numerical computations of contributions to the Casimir pressure between two graphene sheets due to different polarizations of the propagating and evanescent waves. Section 5 provides a discussion of both similarities and distinctions in the Casimir pressures between metallic plates and graphene sheets. Finally, Section 6 contains our conclusions.

2. Fresnel Reflection Coefficients on a Two-Dimensional Sheet

It is known that the Casimir force between two parallel plates is expressed by the Lifshitz formula through the amplitude reflection coefficients of the electromagnetic waves. For the ordinary three-dimensional plates, these are the familiar Fresnel reflection coefficients written in terms of the frequency-dependent dielectric permittivity of the voluminous plate material. Graphene is a two-dimensional sheet of carbon atoms. Its dielectric permittivity is spatially nonlocal and essentially depends not only on the frequency, but on the wave vector and also on temperature. The expressions for the two-dimensional analogues of the Fresnel coefficients presented in terms of the dielectric permittivity of a 2D material are not quite known (see, e.g., [50–52], where the transverse magnetic coefficient [50,51] and both reflection coefficients [52] were expressed in terms of the 2D conductivity with no account of spatial dispersion, or [13,31] where they are presented with no detailed derivation).

Below, we demonstrate in detail that the reflection coefficients on a 2D sheet are obtainable in close analogy to the standard 3D Fresnel reflection coefficients, but with due account of the spatial dispersion.

Let the graphene sheet be in the plane $z = 0$, where the z -axis is directed downward in the plane of Figure 1 and the y -axis is directed upward perpendicular to it.

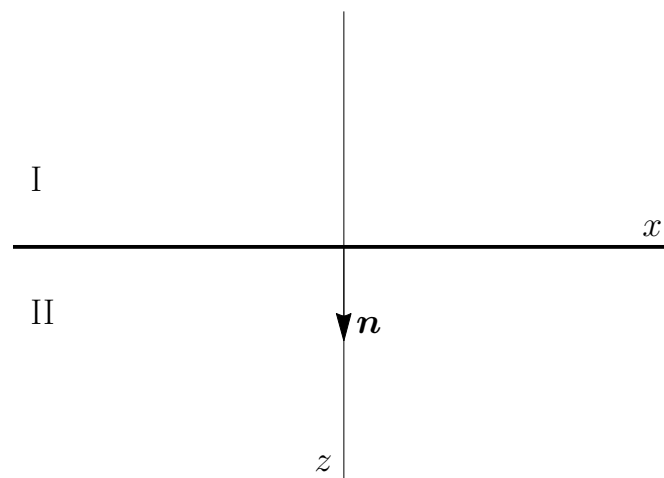


Figure 1. The configuration of a graphene sheet located at the plane (x, y) perpendicular to the plane of the figure. The y -axis is directed upward. The unit normal vector n is directed from the region I to II along the positive direction of the z -axis.

There are empty half spaces I and II on both sides of the graphene sheet. The fluctuating electromagnetic field induces some surface charge density, $q^{2D}(\rho, t)$, and current density, $j^{2D}(\rho, t)$, on the sheet where $\rho = (x, y)$ and t denotes the time. Then, the Maxwell equations in the 3D space take the form

$$\begin{aligned} \nabla D(\mathbf{r}, t) &= 4\pi q^{3D}(\mathbf{r}, t), \\ \nabla B(\mathbf{r}, t) &= 0, \\ \nabla \times E(\mathbf{r}, t) + \frac{1}{c} \frac{\partial B(\mathbf{r}, t)}{\partial t} &= 0, \\ \nabla \times H(\mathbf{r}, t) - \frac{1}{c} \frac{\partial D(\mathbf{r}, t)}{\partial t} &= \frac{4\pi}{c} j^{3D}(\mathbf{r}, t), \end{aligned} \tag{1}$$

where $\mathbf{r} = (x, y, z) = (\rho, z)$, c denotes the speed of light, D is the electric displacement, B is the magnetic induction, and E and H are the electric and magnetic fields, respectively. The 3D charge and current densities in Equation (1) are given by [13,50]

$$q^{3D}(\mathbf{r}, t) = q^{2D}(\rho, t)\delta(z), \quad j^{3D}(\mathbf{r}, t) = j^{2D}(\rho, t)\delta(z). \tag{2}$$

Note that we use the Gaussian units in Equation (1) and below. In these units, j^{3D} has the dimension of $\text{g}^{1/2}\text{cm}^{-1/2}\text{s}^{-2}$, whereas the dimension of j^{2D} is $\text{g}^{1/2}\text{cm}^{1/2}\text{s}^{-2}$.

The standard electrodynamic boundary conditions on the plane $z = 0$ are given by

$$\begin{aligned} [D_{II}(\rho, 0, t) - D_I(\rho, 0, t)] \cdot \mathbf{n} &= 4\pi \rho^{2D}(\rho, t), \\ [B_{II}(\rho, 0, t) - B_I(\rho, 0, t)] \cdot \mathbf{n} &= 0, \\ [E_{II}(\rho, 0, t) - E_I(\rho, 0, t)] \times \mathbf{n} &= 0, \\ [H_{II}(\rho, 0, t) - H_I(\rho, 0, t)] \times \mathbf{n} &= -\frac{4\pi}{c} j^{2D}(\rho, t), \end{aligned} \tag{3}$$

where $\mathbf{n} = (0, 0, 1)$ is the unit vector directed along the z -axis (see Figure 1).

Below we assume that all fields have the form of monochromatic plane waves, e.g.,

$$E(\mathbf{r}, t) = E^0 e^{i(\mathbf{k}\mathbf{r} - \omega t)}, \quad H(\mathbf{r}, t) = H^0 e^{i(\mathbf{k}\mathbf{r} - \omega t)}, \quad B(\mathbf{r}, t) = B^0 e^{i(\mathbf{k}\mathbf{r} - \omega t)}. \tag{4}$$

Here, E^0 , H^0 , and B^0 are the amplitudes; $\mathbf{k} = (k_x, k_y, k_z) \equiv (\mathbf{q}, k_z)$ is the 3D wave vector, and ω is the wave frequency.

For a derivation of the Fresnel reflection coefficients on a 2D sheet, it is suffice to restrict our consideration to the third line of the Maxwell equations (1) and the third and fourth lines in the boundary conditions (3).

Substituting Equation (4) into the third line of Equations (1) and (3), it is readily seen that in both regions I and II

$$\mathbf{k} \times E^0 - \frac{\omega}{c} B^0 = 0 \tag{5}$$

and

$$(E_{II}^0 - E_I^0) \times \mathbf{n} = 0, \tag{6}$$

where E_I^0 and E_{II}^0 are the field amplitudes in the regions I and II, respectively.

Now we look at the fourth line in the boundary conditions (3). Taking into account that the graphene sheet is a spatially nonlocal material, the 2D current density in the fourth line of Equation (3) takes the form

$$j^{2D}(\rho, t) = \int_{-\infty}^t dt' \int d^2\rho' \sigma^{2D}(\rho - \rho', t - t') E_{\text{lat}}(\rho', t'). \tag{7}$$

Here, $\sigma^{2D}(\rho, t)$ is the 2D conductivity of a graphene sheet (it has the dimension cm/s) and E_{lat} is the projection of the electric field on the plane of graphene calculated at $z = 0$:

$$E_{\text{lat}}(\rho, t) = E(\rho, 0, t) - \mathbf{n}(E(\rho, 0, t) \cdot \mathbf{n}) = \mathbf{n} \times [E(\rho, 0, t) \times \mathbf{n}]. \tag{8}$$

Substituting Equations (4) and (7) into the fourth line of Equation (3), one obtains

$$(\mathbf{H}_{\text{II}}^0 - \mathbf{H}_{\text{I}}^0) \times \mathbf{n} = -\frac{4\pi}{c} \sigma^{2D}(\mathbf{q}, \omega) E_{\text{lat}}^0 \tag{9}$$

where $\sigma^{2D}(\mathbf{q}, \omega)$ is the Fourier image of $\sigma^{2D}(\rho, t)$ in the 2D space and time, \mathbf{q} is the 2D wave vector, and E_{lat}^0 is the amplitude of the quantity (8):

$$\begin{aligned} E_{\text{lat}}(\rho, t) &= E_{\text{lat}}^0 e^{i(\mathbf{q}\rho - \omega t)}, \\ E_{\text{lat}}^0 &= \mathbf{n} \times [E^0 \times \mathbf{n}]. \end{aligned} \tag{10}$$

Note that by introducing $\sigma^{2D}(\mathbf{q}, \omega)$ we have used the translational invariance in the plane of a graphene sheet. In the standard Casimir problems, where the plates are made of 3D materials separated by a gap, there is no translational invariance in the 3D space and it is impossible to rigorously introduce the conductivity $\sigma^{3D}(\mathbf{k}, \omega)$ (and the dielectric permittivity) depending on the 3D vector \mathbf{k} . Because of this, for taking into account the effects of spatial dispersion, it is necessary to use some approximations, such as the suggestion of specular reflection [53,54].

We recall also that the spatially dispersive materials are characterized by the two independent conductivities, in our case, $\sigma^{2D,L}(\mathbf{q}, \omega)$ and $\sigma^{2D,Tr}(\mathbf{q}, \omega)$, depending on whether E_{lat}^0 in Equation (9) is parallel or perpendicular to the wave vector \mathbf{q} , respectively [55,56]. These conductivities are called the longitudinal and transverse ones.

We are coming now to the derivation of the amplitude reflection coefficients on a graphene sheet for two independent polarizations of the electromagnetic field using Equations (5), (6) and (9).

Let us start with the case of transverse electric polarization when the amplitudes of the electric field of the incident, E_0^0 , transmitted, E_2^0 , and reflected, E_1^0 , waves are perpendicular to the plane of incidence (x, z) and directed along the positive direction of the y -axis (see Figure 2). The corresponding wave vectors are \mathbf{k}_0 , \mathbf{k}_2 , and \mathbf{k}_1 , and the amplitudes of the magnetic field, which lie in the plane of incidence, are H_0^0 , H_2^0 , and H_1^0 .

Taking into account that the 2D sheet is in the plane (x, y) or, equivalently, $z = 0$ is spatially homogeneous, one finds $k_{0x} = k_{1x} = k_{2x}$. Considering also that $k_0^2 = k_1^2 = k_2^2 = \omega^2/c^2$ because the space outside of a graphene sheet is empty, one obtains

$$\sin \theta_0 = \frac{k_{0x}}{k_0} = \sin \theta_1 = \frac{k_{1x}}{k_1} = \sin \theta_2 = \frac{k_{2x}}{k_2}, \tag{11}$$

i.e., in our case, all the three angles are equal.

According to Figure 2,

$$E_1^0 = E_0^0 + E_2^0, \quad E_{\text{II}}^0 = E_2^0, \tag{12}$$

where $E_0^0 = (0, E_{0y}^0, 0)$, $E_1^0 = (0, E_{1y}^0, 0)$, and $E_2^0 = (0, E_{2y}^0, 0)$.

Taking this into account, the boundary condition (6) reduces to

$$E_{0y}^0 + E_{1y}^0 = E_{2y}^0. \tag{13}$$

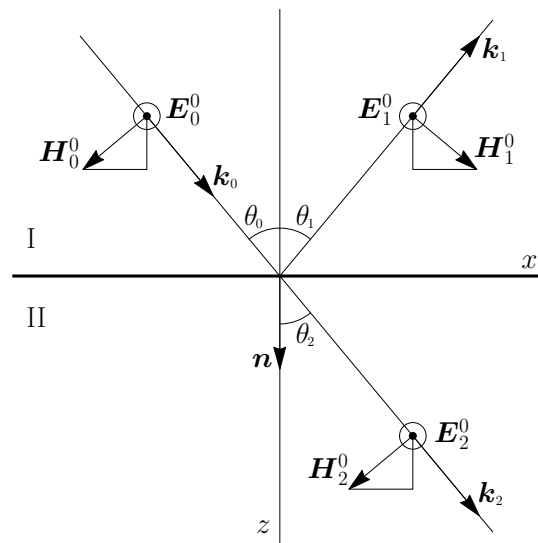


Figure 2. The electromagnetic wave with the transverse electric polarization is incident on a graphene sheet. The amplitudes of the incident, E_0^0 , reflected, E_1^0 , and transmitted, E_2^0 , electric field are perpendicular to the plane of incidence and directed in the positive direction of the y -axis perpendicular to the plane of the figure. The corresponding amplitudes of the magnetic field, H_0^0 , H_1^0 , and H_2^0 , lie in the plane of incidence, whereas k_0 , k_1 , and k_2 are the corresponding wave vectors.

The boundary condition (9), where E_{lat}^0 is defined in Equation (10), is more complicated. In view of Equation (6), both E_I^0 and E_{II}^0 can be substituted into Equation (10) in place of E^0 . We choose E_{II}^0 for the sake of brevity. Then the condition (9) takes the form

$$(H_{II}^0 - H_I^0) \times n = -\frac{4\pi}{c} \sigma^{2D, \text{Tr}}(\mathbf{q}, \omega) [n \times [E_{II}^0 \times n]]. \tag{14}$$

Here, we took into account that the electric field is perpendicular to \mathbf{q} . From Figure 2, it follows that

$$H_I^0 = H_0^0 + H_1^0, \quad H_{II}^0 = H_2^0, \tag{15}$$

where $H_0^0 = (H_{0x}^0, 0, H_{0z}^0)$, $H_1^0 = (H_{1x}^0, 0, H_{1z}^0)$, and $H_2^0 = (H_{2x}^0, 0, H_{2z}^0)$.

Substituting Equations (12) and (15) into the boundary condition (14), one obtains after the elementary algebra:

$$H_{2x}^0 - H_{0x}^0 - H_{1x}^0 = \frac{4\pi}{c} \sigma^{2D, \text{Tr}}(\mathbf{q}, \omega) E_{2y}^0. \tag{16}$$

From the Maxwell equation (5), written for the incident wave in free space where $\mathbf{B}^0 = \mathbf{H}^0$, one obtains

$$H_0^0 = \frac{c}{\omega} [k_0 \times E_0^0]. \tag{17}$$

With account of $k_0 = (k_{0x}, 0, k_{0z})$ and $E_0^0 = (0, E_{0y}^0, 0)$, this reduces to

$$H_{0x}^0 = -\frac{c}{\omega} k_{0z} E_{0y}^0, \tag{18}$$

where, considering Equation (11) and using that in this case k_{0x} plays the role of q ,

$$k_{0z} = \frac{\omega}{c} \cos \theta_0 = \sqrt{\frac{\omega^2}{c^2} - q^2}. \tag{19}$$

In a similar way, from Equation (5) written for the reflected and transmitted waves, one finds

$$H_{1x}^0 = -\frac{c}{\omega}k_{0z}E_{1y}^0, \quad H_{2x}^0 = -\frac{c}{\omega}k_{0z}E_{2y}^0. \quad (20)$$

Substituting Equations (18) and (20) into Equation (16), we finally obtain

$$E_{0y}^0 - E_{1y}^0 - E_{2y}^0 = \frac{4\pi\omega}{c^2k_{0z}}\sigma^{2D,Tr}(\mathbf{q}, \omega)E_{2y}^0. \quad (21)$$

By solving this equation together with Equation (13), the transverse electric (TE) reflection coefficient is found in the form

$$r_{TE}(\mathbf{q}, \omega) = \frac{E_{1y}^0}{E_{0y}^0} = -\frac{2\pi\omega\sigma^{2D,Tr}(\mathbf{q}, \omega)}{c^2k_{0z} + 2\pi\omega\sigma^{2D,Tr}(\mathbf{q}, \omega)}. \quad (22)$$

Note that in Ref. [52] this reflection coefficient was obtained in the special case of normal incidence with ignored spatial dispersion.

By taking into account that for a 2D sheet, the spatially nonlocal dielectric permittivity is expressed via the conductivity as [13,31]

$$\varepsilon^{2D,Tr}(\mathbf{q}, \omega) = 1 + \frac{2\pi i\sigma^{2D,Tr}(\mathbf{q}, \omega)q}{\omega}, \quad (23)$$

and using Equation (19), we rewrite the reflection coefficient (22) in the final form

$$r_{TE}(\mathbf{q}, \omega) = -\frac{\omega^2[\varepsilon^{2D,Tr}(\mathbf{q}, \omega) - 1]}{ic^2q\sqrt{\frac{\omega^2}{c^2} - q^2} + \omega^2[\varepsilon^{2D,Tr}(\mathbf{q}, \omega) - 1]}. \quad (24)$$

This is the transverse electric Fresnel reflection coefficient on a 2D graphene sheet expressed via the spatially nonlocal transverse dielectric permittivity of graphene.

We now proceed to a derivation of the transverse magnetic reflection coefficient on a graphene sheet. In this case, the amplitudes of the magnetic field of the incident, H_0^0 , transmitted, H_2^0 , and reflected, H_1^0 , waves are perpendicular to the plane of incidence and directed along the positive direction of the y -axis (see Figure 3). The amplitudes of the electric field, E_0^0 , E_2^0 , and E_1^0 , lie in the plane of incidence,

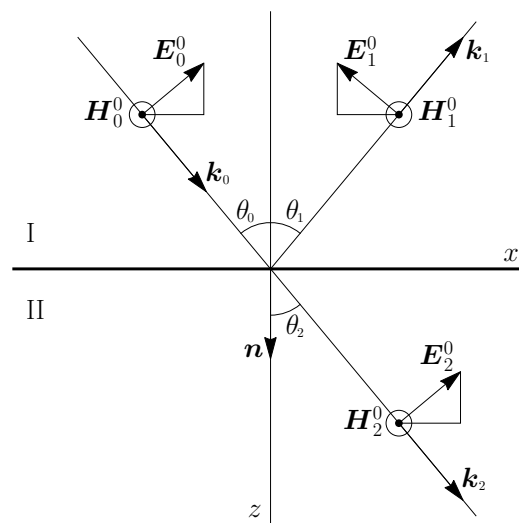


Figure 3. The electromagnetic wave with the transverse magnetic polarization is incident on a graphene sheet. The amplitudes of the incident, H_0^0 , reflected, H_1^0 , and transmitted, H_2^0 , magnetic field are perpendicular to the plane of incidence and directed in the positive direction of the y -axis perpendicular to the plane of the figure. The corresponding amplitudes of the electric field, E_0^0 , E_1^0 , and E_2^0 , lie in the plane of incidence, whereas k_0 , k_1 , and k_2 are the corresponding wave vectors.

According to Figure 3,

$$\mathbf{H}_1^0 = \mathbf{H}_0^0 + \mathbf{H}_1^0, \quad \mathbf{H}_{\text{II}}^0 = \mathbf{H}_2^0, \quad (25)$$

where $\mathbf{H}_0^0 = (0, H_{0y}^0, 0)$, $\mathbf{H}_1^0 = (0, H_{1y}^0, 0)$, and $\mathbf{H}_2^0 = (0, H_{2y}^0, 0)$.

Taking into account that, in this case,

$$\mathbf{E}_{\text{II}}^0 = \mathbf{E}_2^0 = (E_{2x}^0, 0, E_{2z}^0), \quad (26)$$

one obtains

$$\begin{aligned} [\mathbf{E}_2^0 \times \mathbf{n}] &= (0, -E_{2x}^0, 0), \\ \mathbf{n} \times [\mathbf{E}_2^0 \times \mathbf{n}] &= (E_{2x}^0, 0, 0) = (E_2^0 \cos \theta_0, 0, 0), \end{aligned} \quad (27)$$

where $\cos \theta_0$ is defined in Equation (19).

The boundary condition (9), (10) takes the form

$$(\mathbf{H}_{\text{II}}^0 - \mathbf{H}_1^0) \times \mathbf{n} = -\frac{4\pi}{c} \sigma^{2\text{D,L}}(\mathbf{q}, \omega) [\mathbf{n} \times [\mathbf{E}_{\text{II}}^0 \times \mathbf{n}]] \quad (28)$$

The longitudinal conductivity $\sigma^{2\text{D,L}}$ appears in this equation because the 2D wave vector \mathbf{q} is now parallel to $\mathbf{E}_{\text{lat}}^0$.

Substituting Equations (25) and (27) into the boundary condition (28), one finds

$$H_{2y}^0 - H_{0y}^0 - H_{1y}^0 = -\frac{4\pi\sigma^{2\text{D,L}}(\mathbf{q}, \omega)}{c} E_2^0 \cos \theta_0. \quad (29)$$

For the transverse magnetic polarization, the boundary condition (6) reduces to

$$E_{0x}^0 + E_{1x}^0 - E_{2x}^0 = 0. \quad (30)$$

With account of Equation (11), which is valid for both polarizations of the electromagnetic field, Equation (30) is equivalent to

$$E_0^0 \cos \theta_0 - E_1^0 \cos \theta_0 - E_2^0 \cos \theta_0 = 0 \quad (31)$$

and finally to

$$E_0^0 - E_1^0 - E_2^0 = 0. \quad (32)$$

Let us now use the Maxwell equation (5) for the incident wave $\mathbf{H}_0^0 = \mathbf{B}_0^0 = (0, H_{0y}^0, 0)$. Then it takes the form of Equation (17). By using $\mathbf{E}_0^0 = (E_{0x}^0, 0, E_{0z}^0)$, one obtains from Equation (17) with the help of Equations (11) and (19)

$$H_{0y}^0 = \frac{c}{\omega} (k_{0z} E_{0x}^0 - k_{0x} E_{0z}^0) = \frac{c}{\omega} (k_{0z} \cos \theta_0 + k_{0x} \sin \theta_0) E_0^0 = E_0^0. \quad (33)$$

In a similar way, from the Maxwell Equation (17) applied to the reflected and transmitted waves, one obtains

$$H_{1y}^0 = E_1^0, \quad H_{2y}^0 = E_2^0. \quad (34)$$

Substituting Equations (33) and (34) into Equations (29) and (32), one finds

$$\begin{aligned} H_{2y}^0 - H_{0y}^0 - H_{1y}^0 &= -\frac{4\pi\sigma^{2\text{D,L}}(\mathbf{q}, \omega)}{c} H_{2y}^0 \cos \theta_0, \\ H_{0y}^0 - H_{1y}^0 - H_{2y}^0 &= 0. \end{aligned} \quad (35)$$

By solving these equations together, we derive the transverse magnetic (TM) reflection coefficient on a 2D graphene sheet:

$$r_{\text{TM}}(\mathbf{q}, \omega) = \frac{H_{1y}^0}{H_{0y}^0} = \frac{2\pi\sigma^{2\text{D,L}}(\mathbf{q}, \omega) \cos \theta_0}{c + 2\pi\sigma^{2\text{D,L}}(\mathbf{q}, \omega) \cos \theta_0}. \quad (36)$$

The result (36) was obtained in Refs. [50–52] in the spatially local case. In the presence of spatial dispersion, both the results (22) and (36) are presented in Refs. [13,31] with no detailed derivation.

By using an expression for the longitudinal dielectric permittivity of a 2D sheet through its conductivity [13,31]

$$\varepsilon^{2\text{D,L}}(\mathbf{q}, \omega) = 1 + \frac{2\pi i\sigma^{2\text{D,L}}(\mathbf{q}, \omega)q}{\omega}, \quad (37)$$

and Equation (19), one obtains

$$r_{\text{TM}}(\mathbf{q}, \omega) = \frac{[\varepsilon^{2\text{D,L}}(\mathbf{q}, \omega) - 1] \sqrt{\frac{\omega^2}{c^2} - q^2}}{iq + [\varepsilon^{2\text{D,L}}(\mathbf{q}, \omega) - 1] \sqrt{\frac{\omega^2}{c^2} - q^2}}. \quad (38)$$

This is the transverse magnetic Fresnel reflection coefficient on a 2D graphene sheet expressed via the longitudinal dielectric permittivity of graphene.

3. Spatially Nonlocal Dielectric Permittivities of Graphene and the Polarization Tensor

It is common knowledge that at low energies (smaller than approximately 3 eV [57]) graphene is well described by the Dirac model as a set of massless quasiparticles satisfying the Dirac equation, where the speed of light c is replaced with the Fermi velocity $v_F \approx c/300$ [1–3]. In the framework of the Dirac model, it is possible to derive explicit expressions for the polarization tensor of graphene, which describes the response of a graphene sheet to the electromagnetic field [40–43], and thus find both the transverse and longitudinal permittivities of graphene starting from the first principles of quantum electrodynamics. The dielectric permittivities obtained in this way depend on the wave vector, on the frequency, and also on temperature.

The polarization tensor of graphene in (2+1)-dimensional space-time is notated as $\Pi_{\mu\nu}(\mathbf{q}, \omega)$, where $\mu, \nu = 0, 1, 2$ and the dependence on temperature is implied (here, we consider the pristine graphene sheet with no energy gap in the spectrum of quasiparticles and perfect hexagonal crystal lattice). The transverse dielectric permittivity of graphene is expressed as [58]

$$\varepsilon^{2\text{D,Tr}}(\mathbf{q}, \omega) - 1 = -\frac{c^2}{2\hbar q\omega^2} \Pi(\mathbf{q}, \omega), \quad (39)$$

where the quantity Π is the following combination of the components of the polarization tensor:

$$\Pi(\mathbf{q}, \omega) \equiv q^2 \Pi_{\mu}^{\mu}(\mathbf{q}, \omega) + \left(\frac{\omega^2}{c^2} - q^2 \right) \Pi_{00}(\mathbf{q}, \omega), \quad (40)$$

\hbar is the reduced Planck's constant and the summation is made over the repeated indices.

The longitudinal dielectric permittivity of graphene is immediately expressed via the 00 component of the polarization tensor [58]

$$\varepsilon^{2\text{D,L}}(\mathbf{q}, \omega) - 1 = \frac{c^2}{2\hbar q} \Pi_{00}(\mathbf{q}, \omega), \quad (41)$$

The polarization tensor of graphene along the real frequency axis was obtained in Ref. [42]. It was considered for the propagating waves, which satisfy the condition

$$q \leq \frac{\omega}{c}, \quad (42)$$

and for the evanescent waves, which satisfy either the condition

$$\frac{\omega}{c} < q \leq \frac{\omega}{v_F} \approx 300 \frac{\omega}{c} \tag{43}$$

(the so-called plasmonic region [59]) or the condition

$$q > \frac{\omega}{v_F} \approx 300 \frac{\omega}{c}. \tag{44}$$

Using the expression from Ref. [42] for Π in the region of propagating waves (42) and in the plasmonic region (43), the transverse dielectric permittivity of graphene (39) in these regions can be written in the same form:

$$\begin{aligned} \epsilon^{2D,Tr}(q, \omega) - 1 &= i\pi\alpha q \frac{c}{2\omega^2} \sqrt{\omega^2 - v_F^2 q^2} \\ &- \frac{8\alpha c^2}{v_F^2 q} \left\{ \int_0^{u^{(-)}} \frac{du}{e^{\beta u} + 1} \left[1 - \frac{1}{2\omega^2} \sqrt{\omega^2 - v_F^2 q^2} \sum_{\lambda=\pm 1} B(2cu + \lambda\omega) \right] \right. \\ &\left. + \int_{u^{(-)}}^{\infty} \frac{du}{e^{\beta u} + 1} \left[1 - \frac{1}{2\omega^2} \sqrt{\omega^2 - v_F^2 q^2} \sum_{\lambda=\pm 1} \lambda B(2cu + \lambda\omega) \right] \right\}. \tag{45} \end{aligned}$$

Here and below, it is assumed that $\omega > 0$ and the following notations are introduced:

$$u^{(-)} = \frac{1}{2c}(\omega - v_F q), \quad \beta = \frac{\hbar c}{k_B T}, \quad B(x) = \frac{x^2}{\sqrt{x^2 - v_F^2 q^2}}, \tag{46}$$

α denotes the fine structure constant, k_B is the Boltzmann constant and T is the temperature of a graphene sheet.

In the region (44), using the corresponding expression for Π [42], one obtains another expression for the transverse dielectric permittivity of graphene

$$\begin{aligned} \epsilon^{2D,Tr}(q, \omega) - 1 &= -\pi\alpha q \frac{c}{2\omega^2} \sqrt{v_F^2 q^2 - \omega^2} \\ &- \frac{4\alpha c}{v_F^2 q} \sqrt{v_F^2 q^2 - \omega^2} \int_0^{\infty} \frac{dw}{e^{Dw} + 1} \left[1 - \frac{1}{2} \sum_{\lambda=\pm 1} \frac{(\sqrt{v_F^2 q^2 - \omega^2} w + \lambda\omega)^2}{\omega^2 \sqrt{1 - w^2 - \frac{2\lambda\omega w}{\sqrt{v_F^2 q^2 - \omega^2}}}} \right], \tag{47} \end{aligned}$$

where $D = \hbar \sqrt{v_F^2 q^2 - \omega^2} / (2k_B T)$.

In a similar way, using the expression from Ref. [42] for Π_{00} in the region of propagating (42) and plasmonic (43) wave vectors and frequencies, one finds the explicit form of the longitudinal dielectric permittivity of graphene (41) in these regions:

$$\begin{aligned} \epsilon^{2D,L}(q, \omega) - 1 &= i\pi\alpha c q \frac{1}{2\sqrt{\omega^2 - v_F^2 q^2}} \\ &+ \frac{8\alpha c^2}{v_F^2 q} \left\{ \int_0^{u^{(-)}} \frac{du}{e^{\beta u} + 1} \left[1 - \frac{1}{2\sqrt{\omega^2 - v_F^2 q^2}} \sum_{\lambda=\pm 1} F(2cu + \lambda\omega) \right] \right. \\ &\left. + \int_{u^{(-)}}^{\infty} \frac{du}{e^{\beta u} + 1} \left[1 - \frac{1}{2\sqrt{\omega^2 - v_F^2 q^2}} \sum_{\lambda=\pm 1} \lambda F(2cu + \lambda\omega) \right] \right\}, \tag{48} \end{aligned}$$

where

$$F(x) = \sqrt{x^2 - v_F^2 q^2}. \tag{49}$$

Using the expression of Π_{00} [42] in the region (44), for the longitudinal permittivity of graphene (41) in this region, one obtains

$$\begin{aligned} \epsilon^{2D,L}(\mathbf{q}, \omega) - 1 = & \frac{\pi\alpha c q}{2\sqrt{v_F^2 q^2 - \omega^2}} \\ & + \frac{4\alpha c}{v_F^2 q} \sqrt{v_F^2 q^2 - \omega^2} \int_0^\infty \frac{dw}{e^{Dw} + 1} \left[1 - \frac{1}{2} \sum_{\lambda=\pm 1} \sqrt{1 - w^2 - \frac{2\lambda\omega w}{\sqrt{v_F^2 q^2 - \omega^2}}} \right]. \end{aligned} \tag{50}$$

Thus, both the transverse and longitudinal dielectric permittivities of graphene are obtained in all ranges of the wave vectors and frequencies (42)–(44). We emphasize that the first lines of Equations (45), (47), (48) and (50) represent the corresponding dielectric permittivity at zero temperature. The terms in the next lines of these equations define the thermal correction to it found in the framework of the Dirac model. These terms make a profound effect on the reflectivity [42] and conductivity [60] properties of graphene, and also on the Casimir interaction between graphene sheets [44,46–48]. By construction from the polarization tensor, the obtained permittivities satisfy the Kramers–Kronig relations. The specific form of these relations was investigated in the spatially local limit $q \rightarrow 0$ [61] and at zero temperature [62].

For the calculation of the Casimir force in graphene systems, it is helpful to use the reflection coefficients (24) and (38), as well as the dielectric permittivities of graphene, written at the pure imaginary Matsubara frequencies $\omega = i\zeta_l = 2\pi i k_B T l / \hbar$, where $l = 0, 1, 2, \dots$

Substituting $\omega = i\zeta_l$ into Equations (24) and (38), one obtains, respectively,

$$\begin{aligned} r_{TE}(\mathbf{q}, i\zeta_l) = & - \frac{\zeta_l^2 [\epsilon^{2D,Tr}(\mathbf{q}, i\zeta_l) - 1]}{c^2 q \sqrt{q^2 + \frac{\zeta_l^2}{c^2}} + \zeta_l^2 [\epsilon^{2D,Tr}(\mathbf{q}, i\zeta_l) - 1]}, \\ r_{TM}(\mathbf{q}, i\zeta_l) = & \frac{[\epsilon^{2D,Tr}(\mathbf{q}, i\zeta_l) - 1] \sqrt{q^2 + \frac{\zeta_l^2}{c^2}}}{q + [\epsilon^{2D,Tr}(\mathbf{q}, i\zeta_l) - 1] \sqrt{q^2 + \frac{\zeta_l^2}{c^2}}}. \end{aligned} \tag{51}$$

These are the Fresnel reflection coefficients in two dimensions calculated at the pure imaginary Matsubara frequencies. The same expressions are obtained if one substitutes Equations (39) and (41) into the reflection coefficients derived in Refs. [40,41] directly in terms of the polarization tensor.

The spatially nonlocal dielectric permittivities of graphene along the imaginary frequency axis are immediately obtainable from Equations (47) and (50) valid in the interval (44) by putting $\omega = i\zeta_l$. The results are

$$\begin{aligned}
 \varepsilon^{2D,Tr}(\mathbf{q}, i\zeta_l) - 1 &= \pi\alpha q \frac{c}{2\zeta_l^2} \sqrt{v_F^2 q^2 + \zeta_l^2} \\
 &- \frac{4\alpha c}{v_F^2 q} \sqrt{v_F^2 q^2 + \zeta_l^2} \int_0^\infty \frac{dw}{e^{D_l w} + 1} \left[1 + \frac{1}{2} \sum_{\lambda=\pm 1} \frac{(\sqrt{v_F^2 q^2 + \zeta_l^2} w + i\lambda\zeta_l)^2}{\zeta_l^2 \sqrt{1 - w^2 - \frac{2i\lambda\zeta_l w}{\sqrt{v_F^2 q^2 + \zeta_l^2}}}} \right], \\
 \varepsilon^{2D,L}(\mathbf{q}, i\zeta_l) - 1 &= \pi\alpha c q \frac{1}{2\sqrt{v_F^2 q^2 + \zeta_l^2}} \\
 &+ \frac{4\alpha c}{v_F^2 q} \sqrt{v_F^2 q^2 + \zeta_l^2} \int_0^\infty \frac{dw}{e^{D_l w} + 1} \left[1 - \frac{1}{2} \sum_{\lambda=\pm 1} \sqrt{1 - w^2 - \frac{2i\lambda\zeta_l w}{\sqrt{v_F^2 q^2 + \zeta_l^2}}} \right], \quad (52)
 \end{aligned}$$

where now $D_l = \hbar\sqrt{v_F^2 q^2 + \zeta_l^2} / (2k_B T)$.

These expressions are indeed real as it should be. The same dielectric permittivities are obtained at once from Equations (39) and (41) written at $\omega = i\zeta_l$ when substituting expressions for $\Pi(\mathbf{q}, i\zeta_l)$ and $\Pi_{00}(\mathbf{q}, i\zeta_l)$ derived directly along the imaginary frequency axis [63] rather than analytically continued from the real frequency axis as it was made above.

4. Contribution of Different Polarizations and the Role of Evanescent Waves in the Casimir Pressure between Two Graphene Sheets

The Casimir pressure between two parallel graphene sheets at temperature T separated by distance a is given by the Lifshitz formula, which can be presented in terms of either pure imaginary Matsubara or real frequencies [8,12]. In both cases, the total pressure is the sum of contributions from the electromagnetic waves of TM and TE polarizations.

We begin from the representation in terms of the Matsubara frequencies

$$P(a, T) = P_{TM}(a, T) + P_{TE}(a, T), \quad (53)$$

where

$$P_{TM,TE}(a, T) = -\frac{k_B T}{\pi} \sum_{l=0}^{\infty} \int_0^\infty dq q \sqrt{q^2 + \frac{\zeta_l^2}{c^2}} \left[r_{TM,TE}^{-2}(\mathbf{q}, i\zeta_l) e^{2a\sqrt{q^2 + \frac{\zeta_l^2}{c^2}}} - 1 \right]^{-1}. \quad (54)$$

Here, the prime on the summation sign adds the factor 1/2 to the term with $l = 0$, and the reflection coefficients on a graphene sheet for both polarizations are defined in Equation (51) with the dielectric permittivities of graphene presented in Equation (52).

We performed computations of both P_{TM} and P_{TE} in the application region of the Dirac model, i.e., under a condition that the characteristic energy of the Casimir force $\hbar\omega_c = \hbar c / (2a)$ should be less than 3 eV [57]. This condition is well satisfied at $a \geq 200$ nm, where $\hbar\omega_c \leq 0.5$ eV.

The computational results for the magnitudes of P_{TM} and P_{TE} at $T = 300$ K are presented in Figure 4 in the logarithmic scale by the upper and lower lines, respectively, as the function of separation between the graphene sheets. Both P_{TM} and P_{TE} are negative, i.e., they contribute to the Casimir attraction.

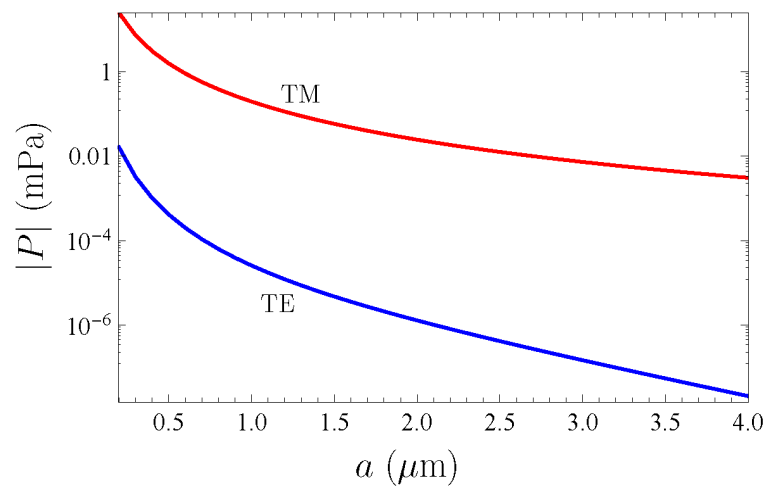


Figure 4. The magnitudes of contributions of the transverse magnetic (TM) and transverse electric (TE) polarizations to the Casimir pressure between two graphene sheets at $T = 300$ K are shown in the logarithmic scale as the function of separation by the upper and lower lines, respectively.

As seen in Figure 4, the major contribution to the Casimir pressure at $a \geq 200$ nm is given by the transverse magnetic polarization, whereas the transverse electric one makes only a negligible small contribution. Thus, at $a = 200$ nm, we have $P_{TM}/P_{TE} = 1530$, i.e., $P_{TM}/P = 0.99935$. The role of the TM polarization only increases with increasing separation. As two more examples, at $a = 2$ and $4 \mu\text{m}$ one finds that $P_{TM}/P_{TE} = 1.92 \times 10^4$ and 1.49×10^5 , respectively. This results in the following respective fractions of P_{TM} in the total Casimir pressure: $P_{TM}/P = 0.99995$ and 0.999993 .

In Section 3, devoted to the nonlocal dielectric permittivities of graphene, they were considered in the region of propagating (42) and evanescent (43) and (44) waves. In so doing, within the region of propagating (42) and in the plasmonic subregion (43) of evanescent waves, these permittivities have a common analytic form. Nevertheless, keeping in mind an especially important role of the propagating waves (42), which are on the mass shell in free space, it is appropriate to consider their contribution to the Casimir pressure separately. Then, the contribution of the evanescent waves is computed as a sum of two terms using two different forms of the dielectric functions depending on whether the condition (43) or (44) is satisfied. Such a separation into the propagating and evanescent waves is also dictated by the form of the Lifshitz formula written in terms of real frequencies (see below).

The representation mathematically equivalent to Equations (53) and (54) of the Lifshitz formula in terms of real frequencies can be written in the form

$$P(a, T) = P_{TM}^{\text{prop}}(a, T) + P_{TE}^{\text{prop}}(a, T) + P_{TM}^{\text{evan}}(a, T) + P_{TE}^{\text{evan}}(a, T). \quad (55)$$

Here, the contributions of the propagating waves with different polarizations are given by [8,12]

$$P_{TM,TE}^{\text{prop}}(a, T) = -\frac{\hbar}{2\pi^2} \int_0^\infty d\omega \coth \frac{\hbar\omega}{2k_B T} \int_0^{\omega/c} q dq \times \text{Im} \left\{ \sqrt{q^2 - \frac{\omega^2}{c^2}} \left[r_{TM,TE}^{-2}(q, \omega) e^{2a\sqrt{q^2 - \frac{\omega^2}{c^2}}} - 1 \right]^{-1} \right\}, \quad (56)$$

where the reflection coefficients are defined in Equations (24) and (38) and the dielectric permittivities in the region (42) are given by Equations (45) and (48).

The contributions of evanescent waves to Equation (55) with different polarizations take the form [8,12]

$$P_{\text{TM,TE}}^{\text{evan}}(a, T) = -\frac{\hbar}{2\pi^2} \int_0^\infty d\omega \coth \frac{\hbar\omega}{2k_B T} \int_{\omega/c}^\infty q dq \sqrt{q^2 - \frac{\omega^2}{c^2}} \times \text{Im} \left[r_{\text{TM,TE}}^{-2}(\mathbf{q}, \omega) e^{2a\sqrt{q^2 - \frac{\omega^2}{c^2}}} - 1 \right]^{-1}, \tag{57}$$

where the reflection coefficients are again defined in Equations (24) and (38). As to the dielectric permittivities entering these reflection coefficients, in the region (43), they are given by Equations (45) and (48), but in the region (44), by Equations (47) and (50).

Equations (56) and (57) are not as convenient for computations as Equation (54). This is most pronounced in $P_{\text{TM,TE}}^{\text{prop}}$ defined in Equation (56), which contains the quickly oscillating functions due to the pure imaginary power in the exponential factor. As to Equation (57), the power of the exponent remains real.

Taking into account that in the application region of the Dirac model nearly the total Casimir pressure is determined by the TM polarized waves, we compute the quantity $P_{\text{TM}}^{\text{evan}}$ by Equations (57) and (38) using the dielectric permittivities defined in Equations (48) and (50). As to the quantity $P_{\text{TM}}^{\text{prop}}$, it is more convenient to not compute it directly by Equation (56), but determine it as a difference

$$P_{\text{TM}}^{\text{prop}}(a, T) = P_{\text{TM}}(a, T) - P_{\text{TM}}^{\text{evan}}(a, T), \tag{58}$$

where P_{TM} is already computed by the Lifshitz formula (54) written in terms of the Matsubara frequencies.

The computational results for P_{TM} , $P_{\text{TM}}^{\text{evan}}$, and $P_{\text{TM}}^{\text{prop}}$ at $T = 300$ K normalized to the Casimir pressure between two ideal metal plates in the classical limit [12]

$$P_{\text{TM}}(a, T) = -\frac{k_B T}{4\pi a^3} \zeta(3), \tag{59}$$

where $\zeta(z)$ is the Riemann zeta function, are presented in Figure 5 as the function of separation by the solid, long-dashed, and short-dashed lines, respectively.

According to Figure 5, at separations of 200–400 nm both the evanescent and propagating transverse magnetic waves contribute significantly to the Casimir pressure. At larger separations, the dominant contribution is given by the evanescent waves. In doing so, the contribution of evanescent waves is attractive at all separation distances. Calculations show, however, that this attraction is combined from the attractive part caused by the plasmonic region (43) and the repulsive part caused by the region (44). The contribution of the TM propagating waves to the Casimir pressure between two graphene sheets changes its character from attraction to repulsion and vice versa with increasing separation.

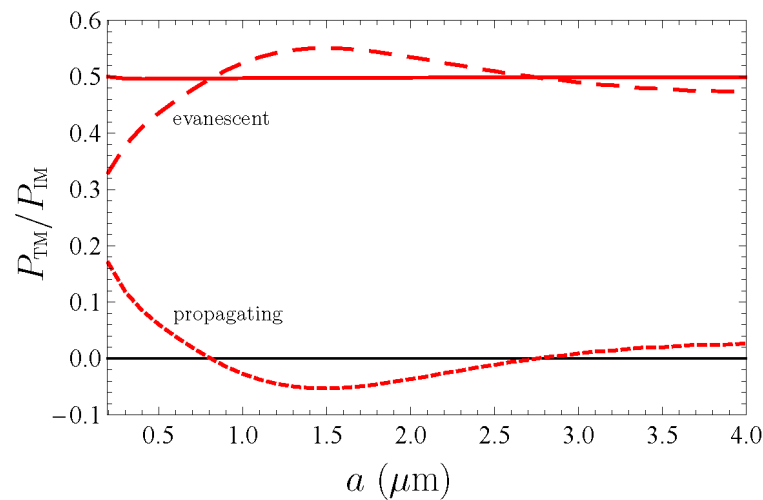


Figure 5. The contributions of the transverse magnetic polarizations to the Casimir pressure between two graphene sheets at $T = 300$ K and to its parts determined by the evanescent and propagating waves normalized to the Casimir pressure between two ideal metal plates in the classical limit are shown as the function of separation by the solid, long-dashed, and short-dashed lines, respectively.

5. Discussion: Whether Graphene Helps to Solve the Problem Arising for Real Metals

The main distinctive feature of the Casimir pressure in the configuration of two graphene sheets considered above is that in the framework of the Dirac model, the spatially nonlocal dielectric permittivities of graphene are found precisely starting from the first principles of thermal quantum field theory. As to the dielectric permittivities of metals used in computations by means of the Lifshitz formula, they contain phenomenological parameters, such as the relaxation parameter of the Drude model, and have not been tested experimentally within all frequency regions essential for the Casimir effect (i.e., in the region of transverse electric evanescent waves).

The formalism of the Lifshitz theory for two graphene sheets presented in Sections 2 and 3 is in perfect analogy with that commonly used for two metallic plates. The Lifshitz formula for the Casimir pressure remains unchanged, and only the 3D Fresnel reflection coefficients are replaced with their 2D analogues as it should be done when considering the Casimir interaction of plane structures. Taking into account the fundamental character of the Lifshitz theory, we obtain the conclusion that only some drawback in the used response functions of metals to the electromagnetic field could cause a disagreement of the theoretical predictions with measurements of the Casimir interaction between Au surfaces.

As shown in Section 4, for two graphene sheets, the total Casimir pressure is determined by the contribution of only the transverse magnetic waves. This is because in the application region of the Dirac model at $a \geq 200$ nm the Casimir force between graphene sheets is already in the classical limit where the contributions of the TE polarized propagating and evanescent waves cancel each other. The same occurs for the Casimir force between metallic plates described by the Drude model at separations exceeding the thermal length [64], i.e., larger than $7.6 \mu\text{m}$ at room temperature. At so large separations, however, there are no reliable measurement data available. As to the experimental separations between metallic plates, both the TM and TE polarizations contribute to the Casimir pressure irrespective of whether the experimentally consistent plasma model or the Drude model excluded by the measurement data is used [18].

By and large, the case of graphene suggests to us that when calculating the Casimir force using the Lifshitz theory, it is important to adequately describe the response of boundary materials to both the propagating and evanescent waves with the transverse magnetic and transverse electric polarizations and take proper account of the effects of spatial dispersion.

6. Conclusions

In the foregoing, we considered the Casimir pressure between two graphene sheets using the Lifshitz theory in the form that is most frequently used for a description of the Casimir effect between conventional 3D materials. For this purpose, we presented the detailed derivation of the 2D Fresnel reflection coefficients on a graphene sheet with due account of the spatial dispersion. As a result, the reflection coefficients for two independent polarizations of the electromagnetic field were expressed via the transverse and longitudinal dielectric permittivities of graphene, which depend on the 2D wave vector, frequency, and temperature. These reflection coefficients are equivalent to those expressed directly via the polarization tensor of graphene.

Next, we presented the explicit expressions for the transverse and longitudinal dielectric permittivities of graphene along the real frequency axis in the regions of both the propagating and evanescent waves and also at the pure imaginary Matsubara frequencies. This was made using the polarization tensor of graphene, which was found earlier in the framework of the Dirac model.

Using the Lifshitz formula written in terms of the Matsubara frequencies, we demonstrated that the total Casimir pressure between two graphene sheets at separations exceeding 200 nm is fully determined by the TM polarized electromagnetic field. By applying the Lifshitz formula along the real frequency axis, the contributions of the TM polarized propagating and evanescent waves to the total pressure were found.

Finally, the above results obtained for graphene sheets were confronted with the corresponding results valid for two metallic plates. This confrontation points the way for bringing the Lifshitz theory in agreement with the measurement data by using the more accurate dielectric functions of metallic test bodies. In the future, it is planned to consider different contributions to the Casimir force between two real graphene sheets possessing the nonzero chemical potential, which prevents from reaching the classical limit at the experimental separations.

Author Contributions: Conceptualization, G.L.K. and V.M.M.; investigation, G.L.K. and V.M.M.; writing—original draft, V.M.M.; writing—review and editing, G.L.K. All authors have read and agreed to the published version of the manuscript.

Funding: G.L.K. was partially funded by the Ministry of Science and Higher Education of the Russian Federation (“The World-Class Research Center: Advanced Digital Technologies”, Contract No. 075-15-2022-311, dated 20 April 2022). The research of V.M.M. was partially carried out in accordance with the Strategic Academic Leadership Program “Priority 2030” of Kazan Federal University.

Data Availability Statement: Not applicable.

Conflicts of Interest: The authors declare no conflict of interest.

References

1. Aoki, H.; Dresselhaus, M.S. (Eds.) *Physics of Graphene*; Springer International Publishing: Cham, Switzerland, 2014. [CrossRef]
2. Katsnelson, M.I. *The Physics of Graphene*; Cambridge University Press: Cambridge, UK, 2020. [CrossRef]
3. Castro Neto, A.H.; Guinea, F.; Peres, N.M.R.; Novoselov, K.S.; Geim, A.K. The electronic properties of graphene. *Rev. Mod. Phys.* **2009**, *81*, 109–162. [CrossRef]
4. Peres, N.M.R. The transport properties of graphene: An introduction. *Rev. Mod. Phys.* **2010**, *82*, 2673–2700. [CrossRef]
5. Goerbig, M.O. Electronic properties of graphene in a strong magnetic field. *Rev. Mod. Phys.* **2011**, *83*, 1193–1244. [CrossRef]
6. Das Sarma, S.; Adam, S.; Hwang, E.H.; Rossi, E. Electronic transport in two-dimensional graphene. *Rev. Mod. Phys.* **2011**, *83*, 407–470. [CrossRef]
7. Casimir, H.B.G. On the attraction between two perfectly conducting plates. *Proc. Kon. Ned. Akad. Wetensch. B* **1948**, *51*, 793–795. Available online: <https://dwc.knaw.nl/DL/publications/PU00018547.pdf> (accessed on 14 October 2023).
8. Lifshitz, E.M. The theory of molecular attractive forces between solids. *Zh. Eksp. Teor. Fiz.* **1955**, *29*, 94–110; English translation: *Sov. Phys. JETP* **1956**, *2*, 73–83. Available online: <http://jetp.ras.ru/cgi-bin/e/index/e/2/1/p73?a=list> (accessed on 14 October 2023).
9. Dzyaloshinskii, I.E.; Lifshitz, E.M.; Pitaevskii, L.P. General theory of van der Waals forces. *Usp. Fiz. Nauk* **1961**, *73*, 381–422; English translation: *Sov. Phys. Uspekhi* **1961**, *4*, 153–176. [CrossRef]

10. Lifshitz, E.M.; Pitaevskii, L.P. *Statistical Physics, Part 2*; Pergamon Press Ltd.: Oxford, UK, 1980. Available online: <https://haidinh89.files.wordpress.com/2015/08/landau-l-d-lifshitz-e-m-course-of-theoretical-physics-vol-09-statistical-physics-part-2-3455.pdf> (accessed on 14 October 2023).
11. Milton, K.A. *The Casimir Effect: Physical Manifestations of Zero-Point Energy*; World Scientific: Singapore, 2001. [CrossRef]
12. Bordag, M.; Klimchitskaya, G.L.; Mohideen, U.; Mostepanenko, V.M. *Advances in the Casimir Effect*; Oxford University Press: Oxford, UK, 2015. [CrossRef]
13. Sernelius, B.E. *Fundamentals of van der Waals and Casimir Interactions*; Springer: Cham, Switzerland, 2018. [CrossRef]
14. Klimchitskaya, G.L.; Mohideen, U.; Mostepanenko, V.M. The Casimir force between real materials: Experiment and theory. *Rev. Mod. Phys.* **2009**, *81*, 1827–1885. [CrossRef]
15. Woods, L.M.; Dalvit, D.A.R.; Tkatchenko, A.; Rodriguez-Lopez, P.; Rodriguez, A.W.; Podgornik, R. Materials perspective on Casimir and van der Waals interactions. *Rev. Mod. Phys.* **2016**, *88*, 045003. [CrossRef]
16. Mostepanenko, V.M. Casimir Puzzle and Conundrum: Discovery and Search for Resolution. *Universe* **2021**, *7*, 84. [CrossRef]
17. Klimchitskaya, G.L.; Mostepanenko, V.M. Current status of the problem of thermal Casimir force. *Int. J. Mod. Phys. A* **2022**, *37*, 2241002. [CrossRef]
18. Klimchitskaya, G.L.; Mostepanenko, V.M. Casimir effect invalidates the Drude model for transverse electric evanescent waves. *Physics* **2023**, *5*, 952–967. [CrossRef]
19. Hult, E.; Hyldgaard, P.; Rossmeisl, J.; Lundqvist, B.I. Density-functional calculation of van der Waals forces for free-electron-like surfaces. *Phys. Rev. B* **2001**, *64*, 195414. [CrossRef]
20. Barton, G. Casimir effect for a flat plasma sheet. I. Energies. *J. Phys. A Math. Gen.* **2005**, *38*, 2997–3020. [CrossRef]
21. Dobson, J.F.; White, A.; Rubio, A. Asymptotics of the dispersion interaction: Analytic benchmarks for van der Waals energy functionals. *Phys. Rev. Lett.* **2006**, *96*, 073201. [CrossRef] [PubMed]
22. Bordag, M. The Casimir effect for thin plasma sheets and the role of the surface plasmons. *J. Phys. A Math. Gen.* **2006**, *39*, 6173–6186. [CrossRef]
23. Bordag, M.; Geyer, B.; Klimchitskaya, G.L.; Mostepanenko, V.M. Lifshitz-type formulas for graphene and single-wall carbon nanotubes: Van der Waals and Casimir interactions. *Phys. Rev. B* **2006**, *74*, 205431. [CrossRef]
24. Gómez-Santos, G. Thermal van der Waals interaction between graphene layers. *Phys. Rev. B* **2009**, *80*, 245424. [CrossRef]
25. Drosdoff, D.; Woods, L.M. Casimir forces and graphene sheets. *Phys. Rev. B* **2010**, *82*, 155459. [CrossRef]
26. Drosdoff, D.; Woods, L.M. Casimir interaction between graphene sheets and metamaterials. *Phys. Rev. A* **2011**, *84*, 062501. [CrossRef]
27. Judd, T.E.; Scott, R.G.; Martin, A.M.; Kaczmarek, B.; Fromhold, T.M. Quantum reflection of ultracold atoms from thin films, graphene and semiconductor heterostructures. *New J. Phys.* **2011**, *13*, 083020. [CrossRef]
28. Sernelius, B.E. Casimir interactions in graphene systems. *Europhys. Lett. (EPL)* **2011**, *95*, 57003. [CrossRef]
29. Sarabadani, J.; Naji, A.; Asgari, R.; Podgornik, R. Many-body effects in the van der Waals–Casimir interaction between graphene layers. *Phys. Rev. B* **2011**, *84*, 155407; Erratum: *Phys. Rev. B* **2013**, *87*, 239905. [CrossRef]
30. Drosdoff, D.; Phan, A.D.; Woods, L.M.; Bondarev, I.V.; Dobson, J.F. Effects of spatial dispersion on the Casimir force between graphene sheets. *Eur. Phys. J. B* **2012**, *85*, 365. [CrossRef]
31. Sernelius, B.E. Retarded interactions in graphene systems. *Phys. Rev. B* **2012**, *85*, 195427. [CrossRef]
32. Phan, A.D.; Woods, L.M.; Drosdoff, D.; Bondarev, I.V.; Viet, N.A. Temperature dependent graphene suspension due to thermal Casimir interaction. *Appl. Phys. Lett.* **2012**, *101*, 113118. [CrossRef]
33. Phan, A.D.; Viet, N.A.; Poklonski, N.A.; Woods, L.M.; Le, C.H. Interaction of a graphene sheet with a ferromagnetic metal plate. *Phys. Rev. B* **2012**, *86*, 155419. [CrossRef]
34. Ribeiro, S.; Scheel, S. Shielding vacuum fluctuations with graphene. *Phys. Rev. A* **2013**, *88*, 042519. [CrossRef]
35. Cysne, T.; Kort-Kamp, W.J.M.; Oliver, D.; Pinheiro, F.A.; Rosa, F.S.S.; Farina, C. Tuning the Casimir-Polder interaction via magneto-optical effects in graphene. *Phys. Rev. A* **2014**, *90*, 052511. [CrossRef]
36. Khusnutdinov, N.; Kashapov, R.; Woods, L.M. Casimir-Polder effect for a stack of conductive planes. *Phys. Rev. A* **2016**, *94*, 012513. [CrossRef]
37. Inui, N. Casimir effect on graphene resonator. *J. Appl. Phys.* **2016**, *119*, 104502. [CrossRef]
38. Knusnutdinov, N.; Kashapov, R.; Woods, L.M. Thermal Casimir and Casimir-Polder interactions in N parallel 2D Dirac materials. *2D Mater.* **2018**, *5*, 035032. [CrossRef]
39. Derras-Chouk, A.; Chudnovsky, E.M.; Garanin, D.A.; Jaafar, R. Graphene cantilever under Casimir force. *J. Phys. D Appl. Phys.* **2018**, *51*, 195301. [CrossRef]
40. Bordag, M.; Fialkovsky, I.V.; Gitman, D.M.; Vassilevich, D.V. Casimir interaction between a perfect conductor and graphene described by the Dirac model. *Phys. Rev. B* **2009**, *80*, 245406. [CrossRef]
41. Fialkovsky, I.V.; Marachevsky, V.N.; Vassilevich, D.V. Finite-temperature Casimir effect for graphene. *Phys. Rev. B* **2011**, *84*, 035446. [CrossRef]
42. Bordag, M.; Klimchitskaya, G.L.; Mostepanenko, V.M.; Petrov, V.M. Quantum field theoretical description for the reflectivity of graphene. *Phys. Rev. D* **2015**, *91*, 045037; Erratum: *Phys. Rev. D* **2016**, *93*, 089907. [CrossRef]
43. Bordag, M.; Fialkovskiy, I.; Vassilevich, D. Enhanced Casimir effect for doped graphene. *Phys. Rev. B* **2016**, *93*, 075414; Erratum: *Phys. Rev. B* **2017**, *95*, 119905. [CrossRef]

44. Klimchitskaya, G.L.; Mostepanenko, V.M. Van der Waals and Casimir interactions between two graphene sheets. *Phys. Rev. B* **2013**, *87*, 075439. [CrossRef]
45. Banishev, A.A.; Wen, H.; Xu, J.; Kawakami, R.K.; Klimchitskaya, G.L.; Mostepanenko, V.M.; Mohideen, U. Measuring the Casimir force gradient from graphene on a SiO₂ substrate. *Phys. Rev. B* **2013**, *87*, 205433. [CrossRef]
46. Klimchitskaya, G.L.; Mohideen, U.; Mostepanenko, V.M. Theory of the Casimir interaction for graphene-coated substrates using the polarization tensor and comparison with experiment. *Phys. Rev. B* **2014**, *89*, 115419. [CrossRef]
47. Liu, M.; Zhang, Y.; Klimchitskaya, G.L.; Mostepanenko, V.M.; Mohideen, U. Demonstration of unusual thermal effect in the Casimir force from graphene. *Phys. Rev. Lett.* **2021**, *126*, 206802. [CrossRef]
48. Liu, M.; Zhang, Y.; Klimchitskaya, G.L.; Mostepanenko, V.M.; Mohideen, U. Experimental and theoretical investigation of the thermal effect in the Casimir interaction from graphene. *Phys. Rev. B* **2021**, *104*, 085436. [CrossRef]
49. Palik, E.D. (Ed.) *Handbook of Optical Constants of Solids*; Academic Press, Inc.: San Diego, CA, USA, 1985; Volume 1. [CrossRef]
50. Falkovsky, L.A.; Pershoguba, S.S. Optical far-infrared properties of a graphene monolayer and multilayer. *Phys. Rev. B* **2007**, *76*, 153410. [CrossRef]
51. Falkovsky, L.A. Optical properties of graphene. *J. Phys. Conf. Ser.* **2008**, *129*, 012004. [CrossRef]
52. Stauber, T.; Peres, N.M.R.; Geim, A.K. Optical conductivity of graphene in the visible region of the spectrum. *Phys. Rev. B* **2008**, *78*, 085432. [CrossRef]
53. Kliewer, K.L.; Fuchs, R. Anomalous skin effect for specular electron scattering and optical experiments at non-normal angles of incidence. *Phys. Rev.* **1968**, *172*, 607–625. [CrossRef]
54. Klimchitskaya, G.L.; Mostepanenko, V.M. Casimir effect for magnetic media: Spatially non-local response to the off-shell quantum fluctuations. *Phys. Rev. D* **2021**, *104*, 085001. [CrossRef]
55. Landau, L.D.; Lifshitz, E.M.; Pitaevskii, L.P. *Electrodynamics of Continuous Media*; Pergamon Press Ltd.: Oxford, UK, 1984. Available online: https://www.aldebaran.cz/studium/books/1984_Landau-Electrodynamics.pdf (accessed on 14 October 2023).
56. Dressel, M.; Grüner, G. *Electrodynamics of Solids: Optical Properties of Electrons in Metals*; Cambridge University Press: Cambridge, UK, 2002. [CrossRef]
57. Zhu, T.; Antezza, M.; Wang, J.-S. Dynamical polarizability of graphene with spatial dispersion. *Phys. Rev. B* **2021**, *103*, 125421. [CrossRef]
58. Klimchitskaya, G.L.; Mostepanenko, V.M.; Sernelius, B.E. Two approaches for describing the Casimir interaction with graphene: Density-density correlation function versus polarization tensor. *Phys. Rev. B* **2014**, *89*, 125407. [CrossRef]
59. Bordag, M.; Pirozhenko, I.G. Surface plasmon on graphene at finite T . *Int. J. Mod. Phys. B* **2016**, *30*, 1650120. [CrossRef]
60. Klimchitskaya, G.L.; Mostepanenko, V.M. Conductivity of pure graphene: Theoretical approach using the polarization tensor. *Phys. Rev. B* **2016**, *93*, 245419. [CrossRef]
61. Klimchitskaya, G.L.; Mostepanenko, V.M. Kramers-Kronig relations and causality conditions for graphene in the framework of Dirac model. *Phys. Rev. D* **2018**, *97*, 085001. [CrossRef]
62. Klimchitskaya, G.L.; Mostepanenko, V.M. Quantum field theoretical framework for the electromagnetic response of graphene and dispersion relations with implications to the Casimir effect. *Phys. Rev. D* **2023**, *107*, 105007. [CrossRef]
63. Bimonte, G.; Klimchitskaya, G.L.; Mostepanenko, V.M. Thermal effect in the Casimir force for graphene and graphene-coated substrates: Impact of nonzero mass gap and chemical potential. *Phys. Rev. B* **2017**, *96*, 115430. [CrossRef]
64. Svetovoy, V.B.; Esquivel, R. The Casimir free energy in high- and low-temperature limits. *J. Phys. A Math. Gen.* **2006**, *39*, 6777–6784. [CrossRef]

Disclaimer/Publisher’s Note: The statements, opinions and data contained in all publications are solely those of the individual author(s) and contributor(s) and not of MDPI and/or the editor(s). MDPI and/or the editor(s) disclaim responsibility for any injury to people or property resulting from any ideas, methods, instructions or products referred to in the content.

Article

Casimir Energy in (2 + 1)-Dimensional Field Theories

Manuel Asorey ^{1,*}, Claudio Iuliano ² and Fernando Ezquerro ¹

¹ Departamento de Física Teórica, Centro de Astropartículas and Física de Altas Energías, Universidad de Zaragoza, 50009 Zaragoza, Spain; fezquerro@unizar.es

² Max Planck Institute for Mathematics in Sciences (MiS), Inselstraße 22, 04103 Leipzig, Germany; iuliano@mis.mpg.de

* Correspondence: asorey@unizar.es

Abstract: We explore the dependence of vacuum energy on the boundary conditions for massive scalar fields in (2 + 1)-dimensional spacetimes. We consider the simplest geometrical setup given by a two-dimensional space bounded by two homogeneous parallel wires in order to compare it with the non-perturbative behaviour of the Casimir energy for non-Abelian gauge theories in (2 + 1) dimensions. Our results show the existence of two types of boundary conditions which give rise to two different asymptotic exponential decay regimes of the Casimir energy at large distances. The two families are distinguished by the feature that the boundary conditions involve or not interrelations between the behaviour of the fields at the two boundaries. Non-perturbative numerical simulations and analytical arguments show such an exponential decay for Dirichlet boundary conditions of SU(2) gauge theories. The verification that this behaviour is modified for other types of boundary conditions requires further numerical work. Subdominant corrections in the low-temperature regime are very relevant for numerical simulations, and they are also analysed in this paper.

Keywords: vacuum energy; (2 + 1)-dimensional field theories; boundary conditions

1. Introduction

The role of boundary effects in quantum field theory is fundamental for many quantum phenomena. One of the earliest applications was the Casimir effect [1]. A quantum field, when confined between two solid bodies, generates a dependence of the renormalized vacuum energy on the boundary conditions at the interfaces of the bodies. This dependence of the vacuum energy generates a force between them which depends on the nature of the boundary conditions of the quantum fields. Although this effect is very tiny, it has been experimentally measured in various setups [2–7].

A remarkable effort has been made in understanding and computing the Casimir effect for different models and setups. Some relevant results were obtained in Ref. [8], where the Casimir vacuum energy at zero temperature was computed for general boundary conditions and arbitrary dimensions for massless scalar fields using heat kernel methods. These results were later extended to finite temperatures in (3 + 1) dimensions [9].

Less known are the characteristics of the effect for interacting theories [10]. Quite recently, the behaviour of the Casimir energy has been investigated in (2 + 1)-dimensional Yang–Mills theories, where some reparametrization of gauge fields in terms of scalar fields allows for an analytic approach to the problem [11–13]. Numerical simulations with Dirichlet boundary conditions on gauge fields confirm the results of this analytic approach [14].

For SU(2) gauge theories, the analytic approach is based on the description of gauge fields in terms of a massive scalar field, whose mass depends on the gauge coupling that in (2 + 1) dimensions is not dimensionless as in (3 + 1) dimensions. In that case, the Casimir energy of the strongly interacting gauge theories with Dirichlet boundary conditions

Citation: Asorey, M.; Iuliano, C.; Ezquerro, F. Casimir Energy in (2 + 1)-Dimensional Field Theories. *Physics* **2024**, *6*, 613–628.

<https://doi.org/10.3390/physics6020040>

Received: 31 December 2023

Revised: 21 February 2024

Accepted: 23 February 2024

Published: 17 April 2024



Copyright: © 2024 by the authors. Licensee MDPI, Basel, Switzerland. This article is an open access article distributed under the terms and conditions of the Creative Commons Attribution (CC BY) license (<https://creativecommons.org/licenses/by/4.0/>).

coincides with the Casimir energy of a scalar field with a magnetic mass $m = g^2/\pi$, where g is the gauge coupling constant.

Some numerical simulations are in progress with different boundary conditions on gauge fields [15] to test if the relation between Casimir energy of massive fields and Yang–Mills theory is robust under the change in boundary conditions. Making comparisons with what happens for scalar fields requires knowing the behaviour of the Casimir energy of the massive scalars for different families of boundary conditions.

In this paper, we study the vacuum energy for massive scalar fields with general boundary conditions in a two-dimensional setup bounded by two homogeneous parallel wires by using a regularization scheme similar to the one used in Refs. [16,17] for massless theories. To compare our results with the lattice gauge theories' results, it is necessary to work at a finite temperature; thus, it is important to understand how the thermal fluctuations affect the Casimir energy at low temperatures in both $(2 + 1)$ -dimensional $SU(2)$ gauge theories and massive scalar field theories in order to have some analytical background reference to compare results to.

Independent of these motivations, some interest has been raised recently on the applications of the thermal Casimir effect in nano-electronic devices [18,19] or the appearance of negative self-entropy related to this effect [20–22], which has boosted interest in new aspects of these thermal effects.

2. Effective Action of a Massive Scalar Field in $(2 + 1)$ Dimensions

We consider a free scalar massive field in $(2 + 1)$ dimensions confined between two homogeneous infinite wires separated by a distance L . Depending on the structure of the wires, the quantum fields have to satisfy some conditions on the boundary wires. Moreover, finite temperature $T \neq 0$ effects can be described in the Euclidean formalism by compactification of the Euclidean time direction into a circle of radius $\beta/(2\pi) = 1/(2\pi T)$. In this case, the partition function can be written as the following determinant:

$$Z(\beta) = \det\left(-\partial_0^2 - \nabla^2 + m^2\right)^{-1/2}, \tag{1}$$

where m is the mass of the fields, ∇^2 is the spatial Laplacian and ∂_0 is the Euclidean time derivative. As already mentioned, the boundary conditions are periodic in time $\psi(t + \beta, \mathbf{x}) = \psi(t, \mathbf{x})$, and because of the homogeneity of the boundary wires, the spatial boundary conditions can be given in terms of 2×2 unitary matrices $U \in U(2)$ [23]

$$\varphi - i\delta\dot{\varphi} = U(\varphi + i\delta\dot{\varphi}), \tag{2}$$

where δ is an arbitrary scale parameter and

$$\varphi = \begin{pmatrix} \varphi(L/2) \\ \varphi(-L/2) \end{pmatrix}, \quad \dot{\varphi} = \begin{pmatrix} \dot{\varphi}(L/2) \\ \dot{\varphi}(-L/2) \end{pmatrix}, \tag{3}$$

are the boundary values $\varphi(\pm L/2) = \psi(t, x_1, \pm L/2)$ of the fields ψ and their outward normal derivatives $\dot{\varphi}(\pm L/2) = \pm\partial_2\psi(t, x_1, \pm L/2)$ on the wires. From now on, we will assume that $\delta = 1$ for simplicity.

In the standard parametrization of $U(2)$ matrices

$$U(\alpha, \gamma, \mathbf{n}) = e^{i\alpha}(\mathbb{I} \cos \gamma + i\mathbf{n} \cdot \boldsymbol{\sigma} \sin \gamma); \quad \alpha \in [0, 2\pi], \quad \gamma \in [-\pi/2, \pi/2], \tag{4}$$

in terms of a unit vector $\mathbf{n} \in S^2$ and Pauli matrices $\boldsymbol{\sigma} = (\sigma_1, \sigma_2, \sigma_3)$, the space of boundary conditions that preserve the non-negativity of the spectrum of the operator $-\nabla^2$ is restricted by the inequalities $0 \leq \alpha \pm \gamma \leq \pi$ [8]. Moreover, since the scalar field is real, the second component of the unit vector n has to vanish, i.e., $n_2 = 0$.

The determinant of the second-order differential operator $-\partial_0^2 - \nabla^2 + m^2$ in Equation (1) is ultraviolet (UV) divergent but can be regularized by means of the zeta

regularization method [24,25]. The effective action is defined by the logarithm of the partition function, which can be expressed as

$$S_{\text{eff}} = -\log Z = -\frac{1}{2} \frac{d}{ds} \zeta(s)|_{s=0}, \tag{5}$$

and in terms of the zeta function as

$$\zeta(L, m, \beta; s) = \mu^{2s} \left(-\partial_0^2 - \nabla^2 + m^2 \right)^{-s} \tag{6}$$

where we have introduced the scale parameter μ , which encodes the standard ambiguity of zeta function renormalization techniques (see, e.g., [26,27] for a detailed discussion and comparison with other renormalization methods), to make the zeta function dimensionless. This ambiguity will be fixed by the renormalization scheme prescription. Actually, the scale parameter μ can be seen as an explicit implementation of the renormalization group.

In our case of a massive scalar field confined between two infinite wires, the eigenvalues of operator $-\partial_0^2 - \nabla^2$ are given by the sum of the square of the temporal modes $2\pi l/\beta$ associated with the Matsubara frequencies, the continuous spatial modes k , and the discrete spatial modes k_i that depend on the boundary conditions imposed by the boundary wires

$$\lambda = \left(\frac{2\pi l}{\beta} \right)^2 + k^2 + k_i^2 + m^2 \quad l \in \mathbb{Z}, i \in \mathbb{N}. \tag{7}$$

Thus, the zeta function in this case reads as follows:

$$\zeta(L, m, \beta; s) = \mu^{2s} \frac{A}{2\pi} \sum_{l,i} \int_{-\infty}^{\infty} dk \left(\left(\frac{2\pi l}{\beta} \right)^2 + k^2 + k_i^2 + m^2 \right)^{-s}, \tag{8}$$

where A is the length of the wires. Now, we can integrate the continuous spatial modes using the analytic extension of the zeta function

$$\zeta(L, m, \beta; s) = \mu^{2s} \frac{A\Gamma(s-1/2)}{2\sqrt{\pi}\Gamma(s)} \sum_{l,i} \left(\left(\frac{2\pi l}{\beta} \right)^2 + k_i^2 + m^2 \right)^{-s+1/2}. \tag{9}$$

It was shown in Ref. [8] that for homogeneous boundary conditions along the wires, the discrete spatial modes are given by the zeros of the spectral function

$$h_U^L(k) = \sin(kL) \left((k^2 - 1) \cos \gamma + (k^2 + 1) \cos \alpha \right) - 2k \sin \alpha \cos(kL) - 2kn_1 \sin \gamma, \tag{10}$$

in the following way

$$\zeta(L, m, \beta; s) = \mu^{2s} \frac{A\Gamma(s-1/2)}{4\pi^{3/2}i\Gamma(s)} \sum_{l=-\infty}^{\infty} \oint dk \left(\left(\frac{2\pi l}{\beta} \right)^2 + k^2 + m^2 \right)^{-s+1/2} \frac{d}{dk} \log h_U^L(k), \tag{11}$$

where the integral is defined along the contour of a thin strip enclosing the positive real axis, where all the zeros of the spectral function $h_U(k)$ are located.

All ultraviolet divergences arise in the zero temperature limit of the vacuum energy and the removal of such divergences requires a consistent prescription method (*renormalization scheme*) with a clear physical meaning. They appear in the leading terms of the zero-temperature expansion that has the following asymptotic behaviour in the large L limit [8,16]:

$$S_{\text{eff}}^{l=0} = \beta E_0 = C_0(m) A \beta L + C_1(m) A \beta + \frac{A\beta}{L} C_c(m, L) + \dots \tag{12}$$

where E_0 is the vacuum energy, $C_0(m)$ the divergent bulk vacuum energy density, $C_1(m)$ the divergent energy density of the boundary wires, and $C_c(m, L)$ is the finite coefficient of the Casimir energy.

One renormalization prescription which allows us to eliminate all these divergences consists of the redefinition of the renormalized effective action as follows [16,17]:

$$S_{\text{eff}}^{\text{ren}} = -\frac{1}{2} \frac{d}{ds} \zeta_{\text{ren}}(L, m, \beta; s) \Big|_{s=0}, \tag{13}$$

where

$$\zeta_{\text{ren}}(L, m, \beta; s) = \lim_{L_0 \rightarrow \infty} (\zeta(L, m, \beta; s) + \zeta(2L_0 + L, m, \beta; s) - 2\zeta(L_0 + L, m, \beta; s)), \tag{14}$$

in terms of an auxiliary length L_0 . Notice that the physical condition which fixes this renormalization scheme is the complete removal of the spurious contributions to the bulk and the boundary vacuum energies, leaving only Casimir energy terms and nonlinear β -temperature-dependent contributions to the effective action. These are precisely the physical requirements that fix the renormalization scheme's prescription.

The sum over Matsubara modes can be explicitly computed in the low-temperature regime.

3. Low-Temperature Regime

In the low-temperature limit $\beta m \gg 1$, we cannot express the result as an infinite series of $1/\beta$. This means that we have to first deal with the Matsubara modes and later with the boundary modes. We start by rewriting (9) as follows:

$$\zeta(L, m, \beta; s) = \left(\frac{\mu\beta}{2\pi}\right)^{2s} \frac{A\sqrt{\pi}\Gamma(s-1/2)}{\beta\Gamma(s)} \sum_i \sum_{l=-\infty}^{\infty} \left(l^2 + \left(\frac{k_i\beta}{2\pi}\right)^2 + \left(\frac{m\beta}{2\pi}\right)^2 \right)^{-s+1/2}. \tag{15}$$

Now, we use the Mellin transform

$$\zeta(L, m, \beta; s) = \left(\frac{\mu\beta}{2\pi}\right)^{2s} \frac{A\sqrt{\pi}}{\beta\Gamma(s)} \sum_i \sum_{l=-\infty}^{\infty} \int_0^{\infty} dt t^{s-3/2} e^{-\left(l^2 + \left(\frac{k_i\beta}{2\pi}\right)^2 + \left(\frac{m\beta}{2\pi}\right)^2\right)t} \tag{16}$$

and apply the Poisson formula for the sum over l modes

$$\zeta(L, m, \beta; s) = \left(\frac{\mu\beta}{2\pi}\right)^{2s} \frac{A\pi}{\beta\Gamma(s)} \sum_i \sum_{l=-\infty}^{\infty} \int_0^{\infty} dt t^{s-2} e^{-\left(\left(\frac{k_i\beta}{2\pi}\right)^2 + \left(\frac{m\beta}{2\pi}\right)^2\right)t - \frac{(\pi l)^2}{t}}. \tag{17}$$

We can compute the integral

$$\begin{aligned} \zeta(L, m, \beta; s) = & \left(\frac{\mu\beta}{2\pi}\right)^{2s} \frac{A\pi}{\beta\Gamma(s)} \left(\Gamma(s-1) \sum_i \left(\left(\frac{k_i\beta}{2\pi}\right)^2 + \left(\frac{m\beta}{2\pi}\right)^2 \right)^{1-s} \right. \\ & \left. + 4 \sum_i \sum_{l=1}^{\infty} (\pi l)^{-1+s} \left(\left(\frac{k_i\beta}{2\pi}\right)^2 + \left(\frac{m\beta}{2\pi}\right)^2 \right)^{1/2-s/2} K_{1-s} \left(\beta l \sqrt{k_i^2 + m^2} \right) \right), \tag{18} \end{aligned}$$

where we have obtained a term ($l = 0$) that has a linear dependence on β , and the rest of the terms can be expressed in terms of the modified Bessel function of the second type K_ν . Let us focus on the first term, which is the zero-temperature one, by replacing the sum of boundary modes with an integral modulated by the spectral function (10). We have

$$\zeta^{l=0}(L, m, \beta; s) = \mu^{2s} \frac{A\beta\Gamma(s-1)}{8\pi^2 i \Gamma(s)} \oint dk \left(k^2 + m^2 \right)^{1-s} \frac{d}{dk} \log h_U^L(k). \tag{19}$$

Thus, the zero-temperature term of the renormalized zeta (14) is

$$\zeta_{\text{ren}}^{l=0}(L, m, \beta; s) = \mu^{2s} \frac{A\beta\Gamma(s-1)}{8\pi^2 i \Gamma(s)} \lim_{L_0 \rightarrow \infty} \oint dk (k^2 + m^2)^{1-s} \frac{d}{dk} \log \frac{h_U^L(k) h_U^{2L_0+L}(k)}{(h_U^{L_0+L}(k))^2}. \quad (20)$$

As it was explained previously, this combination cancels the UV divergences on the integral; thus, the only divergent terms left are the ratio of two Gamma functions whose asymptotic behaviour in the small s expansion is

$$\frac{\Gamma(s-1)}{\Gamma(s)} = -1 - s + \mathcal{O}(s^2) \quad (21)$$

which allows us to calculate the derivative

$$\left. \frac{d}{ds} \left(-(1+s) (k^2 + m^2)^{1-s} \mu^{2s} \right) \right|_{s=0} = (k^2 + m^2) (\log(k^2 + m^2) - 2 \log \mu - 1). \quad (22)$$

Thus, we have

$$\begin{aligned} (\zeta_{\text{ren}}^{l=0})'(L, m, \beta; 0) &= \frac{A\beta}{8\pi^2 i} \lim_{L_0 \rightarrow \infty} \oint dk (k^2 + m^2) (\log(k^2 + m^2) - 2 \log \mu - 1) \\ &\quad \times \left(\frac{d}{dk} \log \frac{h_U^L(k) h_U^{2L_0+L}(k)}{(h_U^{L_0+L}(k))^2} \right). \end{aligned} \quad (23)$$

Since the integrand is holomorphic, we can extend the integration contour to an infinite semicircle limited by the imaginary axis on its left. Also, because the integration over the semicircle is zero, we can reduce the integral to the imaginary axis

$$\begin{aligned} (\zeta_{\text{ren}}^{l=0})'(L, m, \beta; 0) &= \frac{A\beta}{8\pi^2 i} \lim_{L_0 \rightarrow \infty} \int_{-\infty}^{\infty} dk (k^2 - m^2) (\log(m^2 - k^2) - 2 \log \mu - 1) \\ &\quad \times \left(\frac{d}{dk} \log \frac{h_U^L(ik) h_U^{2L_0+L}(ik)}{(h_U^{L_0+L}(ik))^2} \right). \end{aligned} \quad (24)$$

Taking into account that the integrand is parity odd, the integral would vanish if it were not for the contribution of the branching point $k = m$ of the logarithm $\log(m^2 - k^2)$, which gives a factor $2\pi i$ for the interval (m, ∞) , which is absent in the interval $(-\infty, -m)$. Thus, the expression reduces to

$$(\zeta_{\text{ren}}^{l=0})'(L, m, \beta; 0) = \frac{A\beta}{4\pi} \lim_{L_0 \rightarrow \infty} \int_m^{\infty} dk (k^2 - m^2) \frac{d}{dk} \log \frac{h_U^L(ik) h_U^{2L_0+L}(ik)}{(h_U^{L_0+L}(ik))^2}. \quad (25)$$

Since the integral domain begins at m , we can take the limit $L_0 \rightarrow \infty$ on the spectral functions by noticing that

$$\lim_{L_* \rightarrow \infty} h_U^{L_*}(ik) = \lim_{L_* \rightarrow \infty} e^{k(L_*)} \left((k^2 + 1) \cos \gamma + (k^2 - 1) \cos \alpha + 2k \sin \alpha \right). \quad (26)$$

If we define the result in terms of the limit for the spectral function

$$h_U^{\infty}(ik) \equiv \left((k^2 + 1) \cos \gamma + (k^2 - 1) \cos \alpha + 2k \sin \alpha \right), \quad (27)$$

we obtain a simplified formula:

$$\left(\zeta_{\text{ren}}^{l=0}\right)'(L, m, \beta; 0) = -\frac{A\beta}{4\pi} \int_m^\infty dk (k^2 - m^2) \left(L - \frac{d}{dk} \log \frac{h_U^L(ik)}{h_U^\infty(ik)} \right). \tag{28}$$

Temperature-Dependent Terms

Let us now compute the terms with $l \neq 0$ of the zeta function

$$\zeta^{l \neq 0}(L, m, \beta; s) = \left(\frac{\mu\beta}{2\pi}\right)^{2s} \frac{4A\pi}{\beta\Gamma(s)} \sum_{i,l=1}^\infty (\pi l)^{-1+s} \left(\left(\frac{k_i\beta}{2\pi}\right)^2 + \left(\frac{m\beta}{2\pi}\right)^2 \right)^{1/2-s/2} \times \left(K_{1-s} \left(\beta l \sqrt{k_i^2 + m^2} \right) \right). \tag{29}$$

Since the Bessel special function K_1 decreases exponentially as the argument grows, both sums are finite; thus, the only divergent contribution is the Gamma function, which after derivation gives

$$\left(\zeta^{l \neq 0}\right)'(L, m, \beta; 0) = \frac{2A}{\pi} \sum_i \sum_{l=1}^\infty \frac{\sqrt{k_i^2 + m^2}}{l} K_1 \left(\beta l \sqrt{k_i^2 + m^2} \right) \tag{30}$$

and we can we rewrite the sum of the discrete eigenvalues by means of the spectral formula (10)

$$\left(\zeta^{l \neq 0}\right)'(L, m, \beta; 0) = \frac{A}{\pi^2 i} \sum_{l=1}^\infty \oint dk \frac{\sqrt{k^2 + m^2}}{l} K_1 \left(\beta l \sqrt{k^2 + m^2} \right) \frac{d}{dk} \log \left(h_U^L(k) \right). \tag{31}$$

Thus, the temperature-dependent terms of the renormalized zeta function (14) have the following form:

$$\left(\zeta_{\text{ren}}^{l \neq 0}\right)'(L, m, \beta; 0) = \frac{A}{\pi^2 i} \lim_{L_0 \rightarrow \infty} \sum_{l=1}^\infty \oint dk \frac{\sqrt{k^2 + m^2}}{l} K_1 \left(\beta l \sqrt{k^2 + m^2} \right) \frac{d}{dk} \log \frac{h_U^L(k) h_U^{2L_0+L}(k)}{\left(h_U^{L_0+L}(k) \right)^2}.$$

In a similar manner as was carried out for the $l = 0$ term, since the integrand is also holomorphic we can extend the contour to an infinite semi-circle limited by the imaginary axis. Because the integral is zero on the semi-circle, we can reduce the integral to just the imaginary axis

$$\left(\zeta_{\text{ren}}^{l \neq 0}\right)'(L, m, \beta; 0) = -\frac{A}{\pi^2 i} \lim_{L_0 \rightarrow \infty} \sum_{l=1}^\infty \int_{-\infty}^\infty dk \frac{\sqrt{-k^2 + m^2}}{l} K_1 \left(\beta l \sqrt{-k^2 + m^2} \right) \times \left(\frac{d}{dk} \log \frac{h_U^L(ik) h_U^{2L_0+L}(ik)}{\left(h_U^{L_0+L}(ik) \right)^2} \right). \tag{32}$$

Because the integrand is odd, the contribution of $(-m, m)$ is zero, whereas the branching point of $\sqrt{m^2 - k^2}$ introduces a change of sign on the integrand on $(-\infty, -m)$ and also in the argument of the Bessel function. Given that $K_1(\bar{z}) = \overline{K_1(z)}$, the real part of

the integrals between $(-\infty, -m)$ and (m, ∞) is twice one of the integrals, whereas the imaginary part cancels out. In summary, the integral can be reduced to

$$\begin{aligned} (\zeta_{\text{ren}}^{l \neq 0})'(L, m, \beta; 0) = & -\frac{2A}{\pi^2} \lim_{L_0 \rightarrow \infty} \sum_{l=1}^{\infty} \int_m^{\infty} dk \frac{\sqrt{k^2 - m^2}}{l} \Re \left(K_1 \left(i\beta l \sqrt{k^2 - m^2} \right) \right) \\ & \times \left(\frac{d}{dk} \log \frac{h_U^L(ik) h_U^{2L_0+L}(ik)}{\left(h_U^{L_0+L}(ik) \right)^2} \right). \end{aligned} \tag{33}$$

We can take the limit $L_0 \rightarrow \infty$ using Equation (26) as we did for the $l = 0$ term, and the integral is simplified to

$$(\zeta_{\text{ren}}^{l \neq 0})'(L, m, \beta; 0) = \frac{2A}{\pi^2} \sum_{l=1}^{\infty} \int_m^{\infty} dk \frac{\sqrt{k^2 - m^2}}{l} \Re \left(K_1 \left(i\beta l \sqrt{k^2 - m^2} \right) \right) \left(L - \frac{d}{dk} \log \frac{h_U^L(ik)}{h_U^{\infty}(ik)} \right).$$

4. Casimir Energy

The Casimir energy can be derived from the terms we have just computed in the previous sections. We can easily compute the free energy with the effective action simply using the expression $F = S_{\text{eff}}/\beta$. This free energy has two different contributions [22], the non-temperature-dependent part ($l = 0$) which corresponds to the Casimir energy of the system

$$F_U^{l=0}(L, m, \beta) = E_U^c(L, m) = \frac{A}{8\pi} \int_m^{\infty} dk (k^2 - m^2) \left(L - \frac{d}{dk} \log \frac{h_U^L(ik)}{h_U^{\infty}(ik)} \right), \tag{34}$$

and the temperature-dependent part

$$F_U^{l \neq 0}(L, m, \beta) = -\frac{A}{\beta\pi^2} \sum_{l=1}^{\infty} \int_m^{\infty} dk \frac{\sqrt{k^2 - m^2}}{l} \Re \left(K_1 \left(i\beta l \sqrt{k^2 - m^2} \right) \right) \left(L - \frac{d}{dk} \log \frac{h_U^L(ik)}{h_U^{\infty}(ik)} \right).$$

Both terms of the free energy decrease to zero as the distance between the wires L grows to infinite, which is the expected behaviour. The temperature-dependent term also vanishes $F_U^{l \neq 0} \rightarrow 0$ when the temperature does ($\beta \rightarrow \infty$).

Asymptotic Behaviour

Let us now analyse the behaviour of the Casimir energy when $mL \rightarrow \infty$. First, we rewrite the hyperbolic functions of the spectral function as

$$h_U^L(ik) = e^{kL} \left((k^2 + 1) \cos \gamma + (k^2 - 1) \sin \alpha + 2k \sin \alpha \right) \left(1 + n_1 \sin(\gamma) \mathcal{A} e^{-kL} + \mathcal{B} e^{-2kL} \right),$$

where \mathcal{A} and \mathcal{B} are

$$\mathcal{A}(k, \alpha, \gamma) = \frac{4k}{(k^2 + 1) \cos \gamma + (k^2 - 1) \sin \alpha + 2k \sin \alpha}, \tag{35}$$

$$\mathcal{B}(k, \alpha, \gamma) = \frac{-(k^2 + 1) \cos \gamma - (k^2 - 1) \sin \alpha + 2k \sin \alpha}{(k^2 + 1) \cos \gamma + (k^2 - 1) \sin \alpha + 2k \sin \alpha}. \tag{36}$$

We can use this expression to approximate the logarithm of the quotient of spectral functions as

$$\log \frac{h_U^L(ik)}{h_U^{\infty}(ik)} = kL + n_1 \sin \gamma \mathcal{A} e^{-kL} + \left(\mathcal{B} - \frac{\mathcal{A}'}{2} \right) e^{-2kL} + O(e^{-3kL}), \tag{37}$$

where $\mathcal{A}' = (n_1 \sin(\gamma)\mathcal{A})^2$, and we expand the logarithm in powers of e^{-kL} . Now, we introduce this expression on the integral of the Casimir energy formula

$$E_U^c = -\frac{A}{8\pi} \int_m^\infty dk(k^2 - m^2) \frac{d}{dk} \left(n_1 \sin \gamma \mathcal{A} e^{-kL} + \left(\mathcal{B} - \frac{\mathcal{A}'}{2} \right) e^{-2kL} + O(e^{-3kL}) \right) \\ = \frac{A}{4\pi} \int_m^\infty dk k \left(n_1 \sin \gamma \mathcal{A} e^{-kL} + \left(\mathcal{B} - \frac{\mathcal{A}'}{2} \right) e^{-2kL} + O(e^{-3kL}) \right). \tag{38}$$

We can expand this integral as a power series of $1/L$ for each exponential order by integrating by parts as follows:

$$\int_m^\infty dk g(\alpha, \gamma, n_1, k) e^{-jkL} = -\frac{g(\alpha, \gamma, n_1, k)}{jL} e^{-jkL} \Big|_m^\infty + \int_m^\infty dk \frac{g(\alpha, \gamma, n_1, k)'}{jL} e^{-jkL}, \tag{39}$$

and iterate this process since all derivatives of $g(\alpha, \gamma, n_1, k)$ are regular in $[m, \infty]$. Thus, the Casimir energy is given by

$$E_U^c = \sum_{j=1}^\infty \sum_{v=1}^\infty \frac{c_{j,v}(\alpha, \gamma, n_1, m)}{(jL)^v} e^{-jmL}, \tag{40}$$

where the coefficients corresponding to the leading order in the exponential expansion are of the form

$$c_{1,v} = -\frac{n_1 \sin \gamma}{4\pi} \frac{d^v(k\mathcal{A}(\alpha, \gamma, k))}{dk^v} \Big|_m^\infty. \tag{41}$$

This means that when $n_1 \sin \gamma = 0$, all the terms that behave as e^{-mL} vanish and the leading contribution will be of the order of e^{-2mL} . Thus, we have two different families of boundary conditions with different asymptotic behaviours

$$LE_U^c \sim \begin{cases} e^{-mL} & \text{if } \text{tr}(U\sigma_1) \neq 0, \\ e^{-2mL} & \text{if } \text{tr}(U\sigma_1) = 0, \end{cases} \tag{42}$$

depending on whether the matrix U that defines the boundary conditions depends or not on σ_1 .

This is the most important result of this paper because it classifies the boundary conditions into two families. The difference between the two families is the rate of the exponential decay of the Casimir energy (42).

The physical characterization of the two families of boundary conditions with different exponential decays is the vanishing or not of $\text{tr}(U\sigma_1)$. The non-vanishing case corresponds to boundary conditions which connect the values of the fields or its normal derivatives at the two boundary wires, whereas the vanishing case corresponds to families of boundary conditions which only constrains the values of the fields or its normal derivatives at each boundary separately.

The result is obtained for a massive free-field bosonic theory. If the observed rate of decay in gauge theories has the same behaviour, it will provide strong evidence of the scenario that describes the dynamics of gauge theories in $(2 + 1)$ dimensions in terms of a bosonic massive scalar field.

5. Special Cases of Boundary Conditions

Let us analyse some particular cases where the integral of the Casimir energy can be analytically computed and which are of special interest for their potential implementation for gauge fields. An alternative derivation based on the explicit calculation of the spectrum of spatial Laplacian for these cases is postponed to Appendix A.

5.1. Dirichlet and Neumann Boundary Conditions

Dirichlet boundary conditions correspond to the physical case of fields vanishing at both boundary wires $\varphi(L/2) = \varphi(-L/2) = 0$; in our parametrization (4), they are given by $U_D = -\mathbb{I}$. Notice that these boundary conditions do not relate the boundary values of the fields of one boundary with the boundary values at the other one.

The derivative of the logarithm of the quotient of spectral functions is

$$\frac{d}{dk} \log\left(h_{U_D}^L(ik)/h_{U_D}^\infty(ik)\right) = L \coth(kL). \tag{43}$$

We can integrate the Casimir energy formula (34)

$$E_D^c(L, m) = -\frac{A}{16\pi L^2} \left(2mL \operatorname{Li}_2\left(e^{-2mL}\right) + \operatorname{Li}_3\left(e^{-2mL}\right)\right), \tag{44}$$

which, in the massless limit, gives

$$E_D^c(L, 0) = -\frac{A\zeta(3)}{16\pi L^2}. \tag{45}$$

But in the very large $mL \gg 1$ asymptotic limit, the Casimir energy has a fast exponential decay e^{-2mL} , as predicted by the feature that $-\operatorname{Tr} \mathbb{I} \sigma_1 = 0$.

The temperature-dependent terms of the free energy

$$F_D^{l \neq 0}(L, m, \beta) = -\frac{AL}{\beta\pi^2} \sum_{l=1}^{\infty} \int_m^{\infty} dk \frac{\sqrt{k^2 - m^2}}{l} \Re\left(K_1\left(i\beta l \sqrt{k^2 - m^2}\right)\right) (1 - \coth(kL)) \tag{46}$$

cannot be analytically computed, but from the asymptotic expansion of the term

$$1 - \coth(kL) \approx -e^{-2kL}$$

of the integrand, it can be shown that they have the same exponential decay, with mL as the Casimir energy (44).

Neumann boundary conditions correspond to the case where the normal derivative of the fields vanish at the boundary wires $\dot{\varphi}(L/2) = \dot{\varphi}(-L/2) = 0$. They are parameterized by the unitary matrix $U_N = \mathbb{I}$. The derivative of the logarithm of the quotient of spectral functions is the same as for Dirichlet boundary conditions (43), which tell us that the free energy has the same value, $E_N^c = E_D^c$ and $F_{U_D}^{l \neq 0} = F_{U_D}^{l \neq 0}$.

5.2. Periodic Boundary Conditions

The periodicity of the fields and the anti-periodicity of their normal derivatives at the boundaries $\varphi(L/2) = \varphi(-L/2), \dot{\varphi}(L/2) = -\dot{\varphi}(-L/2)$ correspond to periodic boundary conditions associated with the unitary matrix $U_P = \sigma_1$. Notice that, by definition, periodic boundary conditions relate the boundary values of the fields at one boundary to the values of the fields at the other one.

In this case, the derivative of the logarithm of the quotient of spectral functions is

$$\frac{d}{dk} \log\left(h_{U_P}^L(ik)/h_{U_P}^\infty(ik)\right) = L \coth(kL/2). \tag{47}$$

Thus, the Casimir energy is

$$E_P^c(L, m) = -\frac{A}{2\pi L^2} \left(mL \operatorname{Li}_2\left(e^{-mL}\right) + \operatorname{Li}_3\left(e^{-mL}\right)\right) \tag{48}$$

and the massless limit becomes

$$E_P^c(L, 0) = -\frac{A\zeta(3)}{2\pi L^2}. \tag{49}$$

Notice that, in this case, the exponential decay of the Casimir energy e^{-mL} in the asymptotic limit $mL \rightarrow \infty$ is slower than that observed in Dirichlet or Neumann boundary conditions, which corresponds to the feature that $\text{Tr} \sigma_1 \sigma_1 = 2 \neq 0$. The rest of terms of the free energy

$$F_P^{l \neq 0}(L, m, \beta) = -\frac{AL}{\beta\pi^2} \sum_{l=1}^{\infty} \int_m^{\infty} dk \frac{\sqrt{k^2 - m^2}}{l} \Re\left(K_1\left(i\beta l \sqrt{k^2 - m^2}\right)\right) (1 - \coth(kL/2)). \tag{50}$$

share the same behaviour.

5.3. Anti-Periodic Boundary Conditions

Anti-periodic boundary conditions correspond to the values and normal derivatives of the field at the boundary wires satisfying $\varphi(L/2) = -\varphi(-L/2)$, $\dot{\varphi}(L/2) = \dot{\varphi}(-L/2)$, and the associated unitary matrix is $U_A = -\sigma_1$. Again in this case, the boundary conditions relate the boundary values of the fields at one boundary with the boundary values at the other one. In this case, the derivative of the logarithm of the quotient of spectral functions is

$$\frac{d}{dk} \log\left(h_{U_A}^L(ik)/h_{U_A}^{\infty}(ik)\right) = L \tanh(kL/2). \tag{51}$$

Thus, the Casimir energy is

$$E_{U_A}^c(L, m) = -\frac{A}{2\pi L^2} \left(mL \text{Li}_2\left(-e^{-mL}\right) + \text{Li}_3\left(-e^{-mL}\right)\right) \tag{52}$$

which, in the massless limit, agrees with the well-known results

$$E_A^c(L, 0) = \frac{3A\zeta(3)}{8\pi L^2}. \tag{53}$$

Notice that in this case the exponential decay of the Casimir energy e^{-mL} is similar to the case of periodic boundary conditions, corresponding to the feature that $-\text{Tr} \sigma_1 \sigma_1 = -2 \neq 0$. The rest of the terms of the free energy

$$F_{U_A}^{l \neq 0}(L, m, \beta) = -\frac{AL}{\beta\pi^2} \sum_{l=1}^{\infty} \int_m^{\infty} dk \frac{\sqrt{k^2 - m^2}}{l} \Re\left(K_1\left(i\beta l \sqrt{k^2 - m^2}\right)\right) (1 - \tanh(kL/2)) \tag{54}$$

have the same exponential decay because $1 - \tanh(kL/2) \approx e^{-kL}$.

5.4. Zaremba Boundary Conditions

Zaremba boundary conditions correspond to the case where one wire has Dirichlet boundary conditions whereas the other has Neumann boundary conditions. In our parametrization, $U_Z = \pm\sigma_3$, and the derivative of the spectral function is

$$\frac{d}{dk} \log\left(h_{U_Z}^L(ik)/h_{U_Z}^{\infty}(ik)\right) = L \tanh(kL). \tag{55}$$

The Casimir energy is

$$E_{U_Z}^c(L, m) = -\frac{A}{16\pi L^2} \left(2mL \text{Li}_2\left(-e^{-2mL}\right) + \text{Li}_3\left(-e^{-2mL}\right)\right), \tag{56}$$

which, in the massless limit, reduces to

$$E_Z^c(L, 0) = \frac{3A\zeta(3)}{64\pi L^2}. \tag{57}$$

The temperature-dependent part of the free energy is

$$F_Z^{l \neq 0}(L, m, \beta) = -\frac{AL}{\beta\pi^2} \sum_{l=1}^{\infty} \int_m^{\infty} dk \frac{\sqrt{k^2 - m^2}}{l} \Re\left(K_1\left(i\beta l \sqrt{k^2 - m^2}\right)\right) (1 - \tanh(kL)). \tag{58}$$

In both cases, the exponential suppression e^{-2mL} coincides with that of Dirichlet or Neumann boundary conditions, and again in this case, the boundary conditions do not relate the boundary values of the fields at one boundary with the values at the other one.

5.5. Asymptotic Behaviour

The asymptotic behaviour of the Casimir energy for these boundary conditions follow the rule (42) in which Dirichlet, Neumann (44), and Zaremba (56) conditions decay as follows:

$$LE_U^c \sim e^{-2mL} \tag{59}$$

since for these cases $\text{tr}(U\sigma_1) = 0$, whereas the periodic (48) and anti-periodic (52) behave as follows:

$$LE_U^c \sim e^{-mL} \tag{60}$$

because these boundary conditions satisfy the inequality $\text{tr}(U\sigma_1) \neq 0$. We can also appreciate the difference in the factor of the exponential decaying behaviour plotting the Casimir energy for these boundary conditions (Figure 1).

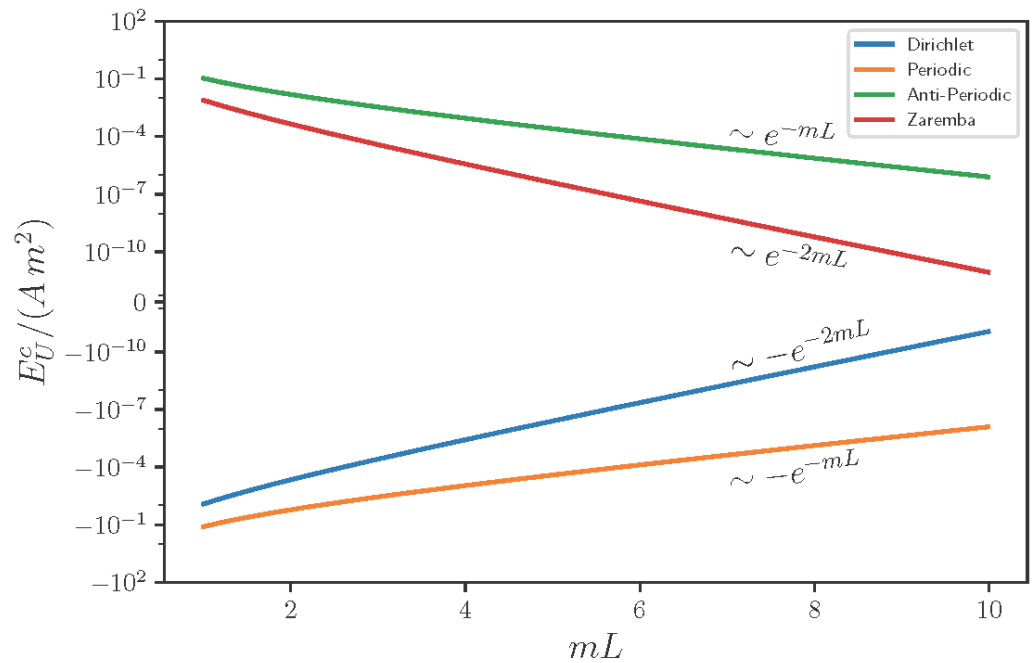


Figure 1. Dependence of the Casimir energy in logarithmic scale as a function of the effective distance mL between the two boundary wires for different boundary conditions.

By plotting the temperature-dependent part of the free energy $F_U^{l \neq 0}$ (see Figure 2), it can also be seen how these terms exponentially decay to zero as mL grows.

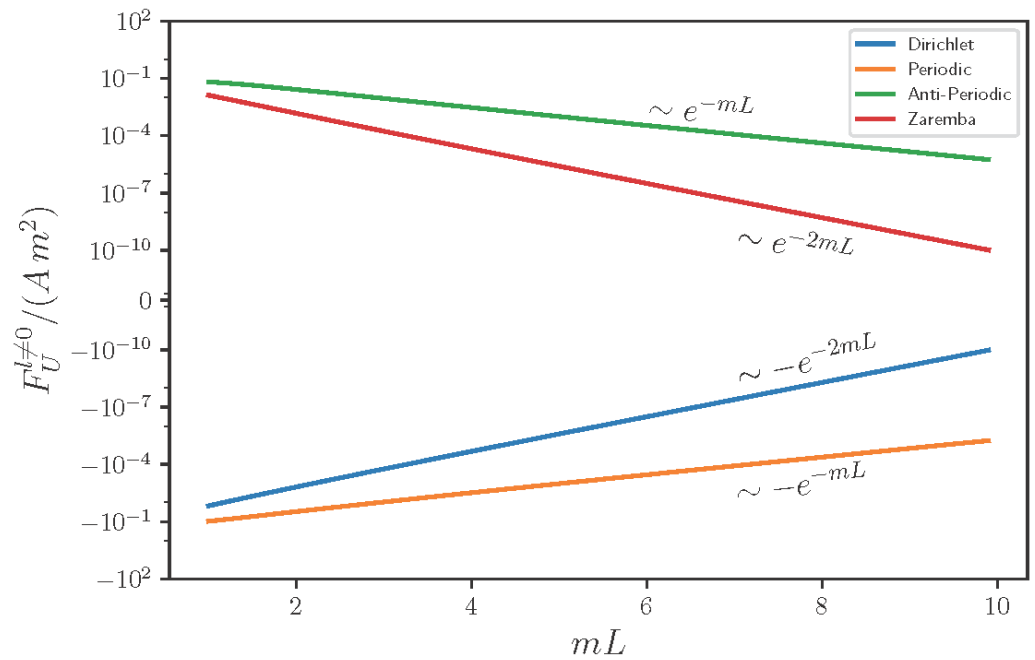


Figure 2. Free energy behaviour of the temperature-dependent part in logarithmic scale as a function of the effective distance mL between the two boundary wires for different boundary conditions, with $m\beta = 1$.

The physical difference between the two families gives rise to different asymptotic behaviours: the families with faster decays (Dirichlet, Neumann, Zaremba) are conditions imposed on each boundary wire separately, whereas in the second family (periodic, anti-periodic, pseudo-periodic) with slower decay rates, the boundary conditions involve a relationship between the values of the fields in both wires, establishing an interconnection between them.

6. Conclusions

We have shown the existence of two types of boundary conditions which give rise to different regimes of exponential decay of the Casimir energy at large distances for scalar field theories. The two types are distinguished by the feature that the boundary conditions involve or not interconnections between the behaviour of the fields at the two boundaries.

The fast exponential decays of the Casimir energy associated with all massive fields make Casimir energy negligible when compared with the contribution of massless fields coming from electrodynamics. This means that there is no hope of measuring its effects experimentally. However, from a conceptual point of view, it can become of crucial importance to understand the confining infrared behaviour of non-Abelian gauge theories if this regime can be effectively driven by a massive scalar field.

Indeed, analytic arguments [11,12] and non-perturbative numerical simulations [14] show that there is a similar exponential decay in gauge theories with Dirichlet boundary conditions. The verification that such a behaviour is modified for other types of boundary conditions would provide further evidence to the claim that the low-energy behaviours of non-Abelian SU(2) gauge theories are governed by an effective scalar field with a fixed non-vanishing mass. A remarkable feature is that the mass of this scalar field is considerably smaller than the lowest mass of the glueball spectrum [11,12].

In particular, the confirmation of the existence of the two regimes for different boundary conditions will be crucial for the verification of this conjecture. Numerical simulations are in progress to clarify this issue.

Author Contributions: All authors contributed equally to this work. All authors have read and agreed to the published version of the manuscript.

Funding: This research is partially supported by Spanish Grants No. PGC2022-126078NB-C21 funded by MCIN/AEI/10.13039/501100011033, Erasmus+ Programme, ERDF A way of making Europe Grant; the Quantum Spain project of the QUANTUM ENIA of the Ministry of Economic Affairs and Digital Transformation, the Diputación General de Aragón-Fondo Social Europeo (DGA-FSE) Grant No. 2020-E21-17R of the Aragon Government; and the European Union, NextGenerationEU Recovery and Resilience Program on ‘Astrofísica y Física de Altas Energías’, CEFCA-CAPA-ITAINNOVA.

Data Availability Statement: No external data used.

Acknowledgments: We thank José M. Muñoz-Castañeda and V. Parameswaran Nair for their discussions. C.I. is grateful to the University of Zaragoza for the hospitality.

Conflicts of Interest: The authors declare no conflicts of interest.

Appendix A. Alternative Calculation of the Free Energy

As an additional check of previous calculations derived by using the spectral function of the spatial Laplacian, let us calculate the free energy directly in some cases where the spectrum of the spatial Laplacian is explicitly known.

Appendix A.1. Dirichlet Boundary Conditions

In this case, the discrete eigenvalues of the spatial Laplacian are given by $k_j = \pi j/L$ with $j = 1, \dots, \infty$.

Let us consider the low-temperature limit of the effective action. The corresponding zeta function (9) is

$$\zeta(L, m, \beta; s) = \left(\frac{\mu\beta}{2\pi}\right)^{2s} \frac{A\sqrt{\pi}\Gamma(s-1/2)}{\beta\Gamma(s)} \sum_{j=1}^{\infty} \sum_{l=-\infty}^{\infty} \left(l^2 + \left(\frac{j\beta}{2L}\right)^2 + \left(\frac{m\beta}{2\pi}\right)^2\right)^{-s+1/2}, \quad (A1)$$

with which, using the Mellin transform (16) and the Poisson formula (17) on the Matsubara modes, we arrive at

$$\zeta(L, m, \beta; s) = \left(\frac{\mu\beta}{2\pi}\right)^{2s} \frac{A\pi}{\beta\Gamma(s)} \sum_{j=1}^{\infty} \sum_{l=-\infty}^{\infty} \int_0^{\infty} dt t^{s-2} e^{-\left(\left(\frac{j\beta}{2L}\right)^2 + \left(\frac{m\beta}{2\pi}\right)^2\right)t - \frac{(\pi l)^2}{t}}. \quad (A2)$$

After integration, the expression (A2) reduces to

$$\begin{aligned} \zeta(L, m, \beta; s) = & \left(\frac{\mu\beta}{2\pi}\right)^{2s} \frac{A\pi}{\beta\Gamma(s)} \left(\Gamma(s-1) \sum_{j=1}^{\infty} \left(\left(\frac{j\beta}{2L}\right)^2 + \left(\frac{m\beta}{2\pi}\right)^2 \right)^{1-s} \right. \\ & \left. + 4 \sum_{j,l=1}^{\infty} (\pi l)^{s-1} \left(\left(\frac{j\beta}{2L}\right)^2 + \left(\frac{m\beta}{2\pi}\right)^2 \right)^{1/2-s/2} K_{1-s} \left(\beta l \sqrt{\left(\frac{\pi j}{L}\right)^2 + m^2} \right) \right). \end{aligned} \quad (A3)$$

To obtain the contribution of the second term to the effective action, we just have to derive the gamma function $\Gamma(s)$ on the denominator. We obtain

$$\left(\zeta^{l \neq 0}\right)'(L, m, \beta; 0) = \frac{2A}{L} \sum_{j,l=1}^{\infty} \frac{1}{l} \sqrt{j^2 + \left(\frac{mL}{\pi}\right)^2} K_1 \left(\frac{\pi\beta l}{L} \sqrt{j^2 + \left(\frac{mL}{\pi}\right)^2} \right) \quad (A4)$$

Now, we rewrite the first term of (A3) as

$$\zeta^{l=0}(L, m, \beta; s) = \left(\frac{\mu L}{\pi}\right)^{2s} \frac{A\pi\beta\Gamma(s-1)}{4L^2\Gamma(s)} \sum_{j=1}^{\infty} \left(j^2 + \left(\frac{mL}{\pi}\right)^2\right)^{1-s}, \quad (A5)$$

and by applying the Mellin transform (16) and the Poisson formula (17), which in this case reads

$$\sum_{n=1}^{\infty} e^{-2\pi\alpha n^2} = \frac{1}{\sqrt{2\alpha}} \sum_{n=1}^{\infty} e^{-\frac{\pi n^2}{2\alpha}} + \frac{1}{2} \left(\frac{1}{\sqrt{2\alpha}} - 1 \right), \quad (\text{A6})$$

for the sum in the modes j , we have

$$\begin{aligned} \zeta^{l=0}(L, m, \beta; s) &= \left(\frac{\mu L}{\pi} \right)^{2s} \frac{A\pi\sqrt{\pi}\beta}{4L^2\Gamma(s)} \left(\sum_{j=1}^{\infty} \int_0^{\infty} dt t^{s-\frac{5}{2}} e^{-\left(\frac{mL}{\pi}\right)^2 t - \frac{(\pi j)^2}{t}} \right. \\ &\quad \left. + \frac{1}{2} \int_0^{\infty} dt t^{s-\frac{5}{2}} e^{-\left(\frac{mL}{\pi}\right)^2 t} \left(1 - \frac{\sqrt{t}}{\sqrt{\pi}} \right) \right). \end{aligned} \quad (\text{A7})$$

After integrating out the t variable, we obtain

$$\begin{aligned} \zeta^{l=0}(L, m, \beta; s) &= \left(\frac{\mu L}{\pi} \right)^{2s} \frac{A\pi\sqrt{\pi}\beta}{8L^2\Gamma(s)} \left(\Gamma\left(s - \frac{3}{2}\right) \left(\frac{mL}{\pi} \right)^{3-2s} - \frac{\Gamma(s-1)}{\sqrt{\pi}} \left(\frac{mL}{\pi} \right)^{2-2s} \right. \\ &\quad \left. + 4 \sum_{j=1}^{\infty} (\pi j)^{s-3/2} \left(\frac{mL}{\pi} \right)^{3/2-s} K_{3/2-s}(2jmL) \right). \end{aligned} \quad (\text{A8})$$

Upon derivation, the only non-vanishing contribution of this term comes from the derivative of $\Gamma(s)$ in the first and third terms, whereas we have to use the asymptotic expansion (21) for the second. The result is

$$\begin{aligned} (\zeta^{l=0})'(L, m, \beta; 0) &= \frac{AL\beta m^3}{6\pi} + \frac{Am^2\beta}{4\pi} \left(\log(\mu/m) + \frac{1}{2} \right) \\ &\quad + \frac{A\beta}{8L^2\pi} \left(2mL \text{Li}_2(e^{-2mL}) + \text{Li}_3(e^{-2mL}) \right). \end{aligned} \quad (\text{A9})$$

From the renormalized effective action (13), we can compute the Casimir energy

$$E_D^c(L, m) = -\frac{A}{16L^2\pi} \left(2mL \text{Li}_2(e^{-2mL}) + \text{Li}_3(e^{-2mL}) \right) \quad (\text{A10})$$

which is the same as what we obtained in Equation (44) with the spectral function. The temperature-dependent component of the free energy

$$F_D^{l \neq 0}(L, m, \beta) = -\frac{A}{\beta L} \sum_{j,l=1}^{\infty} \frac{1}{l} \sqrt{j^2 + \left(\frac{mL}{\pi}\right)^2} K_1 \left(\frac{\pi\beta l}{L} \sqrt{j^2 + \left(\frac{mL}{\pi}\right)^2} \right) \quad (\text{A11})$$

$$- \frac{1}{2\beta} \lim_{L_0 \rightarrow \infty} \left((\zeta^{l \neq 0})'(2L_0 + L, m, \beta; 0) - 2(\zeta^{l \neq 0})'(L_0 + L, m, \beta; 0) \right). \quad (\text{A12})$$

can be shown to be equivalent to Equation (46).

Appendix A.2. Periodic Boundary Conditions

The discrete eigenvalues of the spatial Laplacian in this case are $k_j = 2\pi j/L$ with $j \in \mathbb{Z}$. We can derive the effective action directly from the spectrum by rewriting (8)

$$\zeta(L, m, \beta; s) = \left(\frac{\mu\beta}{2\pi} \right)^{2s} \frac{A\sqrt{\pi}\Gamma(s-1/2)}{\Gamma(s)} \sum_{l,j=-\infty}^{\infty} \left(l^2 + \left(\frac{j\beta}{L}\right)^2 + \left(\frac{m\beta}{2\pi}\right)^2 \right)^{-s+1/2}, \quad (\text{A13})$$

and by using the Mellin transform and the Poisson formula on the Matsubara modes, we have

$$\zeta(L, m, \beta; s) = \left(\frac{\mu\beta}{2\pi}\right)^{2s} \frac{A\pi}{\Gamma(s)} \sum_{l, j=-\infty}^{\infty} \int_0^{\infty} dt t^{s-2} e^{-\left(\left(\frac{j\beta}{L}\right)^2 + \left(\frac{m\beta}{2\pi}\right)\right)t - \frac{(\pi l)^2}{t}}, \tag{A14}$$

which, after integration, becomes

$$\begin{aligned} \zeta(L, m, \beta; s) = & \left(\frac{\mu\beta}{2\pi}\right)^{2s} \frac{A\pi}{\beta\Gamma(s)} \sum_{j=-\infty}^{\infty} \left(\Gamma(s-1) \left(\left(\frac{j\beta}{L}\right)^2 + \left(\frac{m\beta}{2\pi}\right)^2\right)^{1-s}\right. \\ & \left.+ 4 \sum_{l=-\infty}^{\infty} (\pi l)^{s-1} \left(\left(\frac{j\beta}{L}\right)^2 + \left(\frac{m\beta}{2\pi}\right)^2\right)^{1/2-s/2} K_{1-s} \left(\beta l \sqrt{\left(\frac{2\pi j}{L}\right)^2 + m^2}\right)\right). \end{aligned} \tag{A15}$$

The derivative of the second term gives

$$\left(\zeta^{l \neq 0}\right)'(L, m, \beta; 0) = \frac{4A}{L} \sum_{j=-\infty}^{\infty} \sum_{l=1}^{\infty} \frac{1}{l} \sqrt{j^2 + \left(\frac{mL}{2\pi}\right)^2} K_1 \left(\frac{2\pi\beta l}{L} \sqrt{j^2 + \left(\frac{mL}{2\pi}\right)^2}\right). \tag{A16}$$

We rewrite Equation (A15) as

$$\zeta^{l=0}(L, m, \beta; s) = \left(\frac{\mu L}{2\pi}\right)^{2s} \frac{A\beta\Gamma(s-1)\pi}{L^2\Gamma(s)} \sum_{j=-\infty}^{\infty} \left(j + \left(\frac{mL}{2\pi}\right)^2\right)^{1-s} \tag{A17}$$

and follow the same strategy as for Dirichlet boundary conditions from Equation (A5) to Equation (A9) with these particular spatial modes. We thus arrive at

$$\left(\zeta^{l=0}\right)'(L, m, \beta; 0) = \frac{AL\beta m^3}{6\pi} + \frac{A\beta}{L^2\pi} \left(mL \operatorname{Li}_2(e^{-mL}) + \operatorname{Li}_3(e^{-mL})\right) \tag{A18}$$

and the Casimir energy is

$$E_P^c(L, m) = -\frac{A}{2\pi L^2} \left(mL \operatorname{Li}_2(e^{-mL}) + \operatorname{Li}_3(e^{-mL})\right) \tag{A19}$$

which coincides with result obtained by the general spectral function method (48). Meanwhile, the temperature-dependent component of the free energy is

$$\begin{aligned} F_P^{l \neq 0}(L, m, \beta) = & -\frac{2A}{\beta L} \sum_{j=-\infty}^{\infty} \sum_{l=1}^{\infty} \frac{1}{l} \sqrt{j^2 + \left(\frac{mL}{2\pi}\right)^2} K_1 \left(\frac{2\pi\beta l}{L} \sqrt{j^2 + \left(\frac{mL}{2\pi}\right)^2}\right) \\ & - \frac{1}{2\beta} \lim_{L_0 \rightarrow \infty} \left(\left(\zeta^{l \neq 0}\right)'(2L_0 + L, m, \beta; 0) - 2\left(\zeta^{l \neq 0}\right)'(L_0 + L, m, \beta; 0)\right) \end{aligned} \tag{A20}$$

which also agrees with Equation (50).

References

1. Casimir, H.B.G. On the attraction between two perfectly conducting plates. *Proc. Kon. Ned. Akad. Wetensch. B* **1948**, *51*, 793–795. Available online: <https://dwc.knaw.nl/DL/publications/PU00018547.pdf> (accessed on 22 February 2024).
2. Sparnaay, M.J. Attractive forces between flat plates. *Nature* **1957**, *180*, 334–335. [CrossRef]
3. Sparnaay, M.J. Measurements of attractive forces between flat plates. *Physica* **1958**, *24*, 751–764. [CrossRef]
4. Lamoreaux, S.K. Demonstration of the Casimir force in the 0.6 to 6 μm range. *Phys. Rev. Lett.* **1997**, *78*, 5–8. [CrossRef]
5. Mohideen, U.; Roy, A. Precision measurement of the Casimir force from 0.1 to 0.9 μm. *Phys. Rev. Lett.* **1998**, *81*, 4549–4552. [CrossRef]

6. Chan, H.B.; Aksyuk, V.A.; Kleiman, R.N.; Bishop, D.J.; Capasso, F. Nonlinear micromechanical Casimir oscillator. *Phys. Rev. Lett.* **2001**, *87*, 211801. [CrossRef]
7. Dalvit, D.; Milonni, P.; Roberts, D.; da Rosa, F. *Casimir Physics*; Springer: Berlin/Heidelberg, Germany, 2011. . [CrossRef]
8. Asorey, M.; Muñoz-Castañeda, J. Attractive and repulsive Casimir vacuum energy with general boundary conditions. *Nucl. Phys. B* **2013**, *874*, 852–876. [CrossRef]
9. Muñoz-Castañeda, J.; Santamaría-Sanz, L.; Donaire, M.; Tello-Fraile, M. Thermal Casimir effect with general boundary conditions. *Eur. Phys. J. C* **2020**, *80*, 793. [CrossRef]
10. Symanzik, K. Schrödinger representation and Casimir effect in renormalizable quantum field theory. *Nucl. Phys. B* **1981**, *190*, 1–44. [CrossRef]
11. Karabali, D.; Nair, V.P. Casimir effect in $(2 + 1)$ -dimensional Yang-Mills theory as a probe of the magnetic mass. *Phys. Rev. D* **2018**, *98*, 105009. [CrossRef]
12. Karabali, D.; Kim, C.; Nair, V. Planar Yang-Mills theory: Hamiltonian, regulators and mass gap. *Nucl. Phys. B* **1998**, *524*, 661–694. [CrossRef]
13. Karabali, D.; Nair, V. On the origin of the mass gap for non-Abelian gauge theories in $(2 + 1)$ dimensions. *Phys. Lett. B* **1996**, *1*, 141–147. [CrossRef]
14. Chernodub, M.N.; Goy, V.A.; Molochkov, A.V.; Nguyen, H.H. Casimir Effect in Yang-Mills Theory in $D = 2 + 1$. *Phys. Rev. Lett.* **2018**, *121*, 191601. [CrossRef]
15. Asorey, M.; Ezquerro, F. Energy preserving boundary conditions in field theory. *Phys. Rev. D* **2023**, *4*, 045008. [CrossRef]
16. Asorey, M.; Beneventano, C.; D’Ascanio, D.; Santangelo, E. Thermodynamics of conformal fields in topologically non-trivial space-time backgrounds. *J. High Energy Phys.* **2012**, *2013*, 68. [CrossRef]
17. Asorey, M.; Beneventano, C.G.; Cervero-Peláez, I.; D’Ascanio, D.; Santangelo, E.M. Topological entropy and renormalization group flow in 3-dimensional spherical spaces. *J. High Energy Phys.* **2015**, *2015*, 78. [CrossRef]
18. Zou, J.; Marcet, Z.; Rodriguez, A.W.; Reid, M.T.H.; McCauley, A.P.; Kravchenko, I.I.; Lu, T.; Bao, Y.; Johnson, S.G.; Chan, H.B. Casimir forces on a silicon micromechanical chip. *Nat. Commun.* **2013**, *4*, 1845. [CrossRef]
19. Terças, H.; Ribeiro, S.; Pezzutto, M.; Omar, Y. Quantum thermal machines driven by vacuum forces. *Phys. Rev. E* **2017**, *95*, 022135. [CrossRef]
20. Geyer, B.; Klimchitskaya, G.; Mostepanenko, V. Thermal corrections in the Casimir interaction between a metal and dielectric. *Phys. Rev. A* **2005**, *72*, 022111. [CrossRef]
21. Milton, K.; Kalauni, P.A.; Parashar, P.; Li, Y. Casimir self-entropy of a spherical electromagnetic δ -function shell. *Phys. Rev. D* **2017**, *96*, 085007. [CrossRef]
22. Bordag, M. Free energy and entropy for thin sheets. *Phys. Rev. D* **2018**, *98*, 085010. [CrossRef]
23. Asorey, M.; Ibort, A.; Marmo, G. Global theory of quantum boundary conditions and topology change. *Int. J. Mod. Phys. A* **2005**, *20*, 1001–1025. [CrossRef]
24. Dowker, J.S.; Critchley, R. Effective Lagrangian and energy-momentum tensor in de Sitter space. *Phys. Rev. D* **1976**, *13*, 3224–3232. [CrossRef]
25. Blau, S.; Visser, M.; Wipf, A. Zeta functions and the Casimir energy. *Nucl. Phys. B* **1988**, *310*, 163–180. [CrossRef]
26. Moretti, V. Direct ζ -function approach and renormalization of one-loop stress tensors in curved spacetimes. *Phys. Rev. D* **1997**, *56*, 7797–7819. [CrossRef]
27. Moretti, V. One-loop stress-tensor renormalization in curved background: The relation between ζ -function and point-splitting approaches, and an improved point-splitting procedure. *J. Math. Phys.* **1999**, *40*, 3843–3875. [CrossRef]

Disclaimer/Publisher’s Note: The statements, opinions and data contained in all publications are solely those of the individual author(s) and contributor(s) and not of MDPI and/or the editor(s). MDPI and/or the editor(s) disclaim responsibility for any injury to people or property resulting from any ideas, methods, instructions or products referred to in the content.

Article

Casimir Forces in CFT with Defects and Boundaries

Philippe Brax ^{1,*} and Sylvain Fichet ²¹ Institut de Physique Théorique, Université Paris-Saclay, CEA, CNRS, F-91191 Gif-sur-Yvette Cedex, France² Centro de Ciências Naturais e Humanas, Universidade Federal do ABC, Santo André 09210-580, SP, Brazil; sylvain.fichet@gmail.com

* Correspondence: philippe.brax@ipht.fr

Abstract: We investigate the quantum forces occurring between the defects and/or boundaries of a conformal field theory (CFT). We propose to model imperfect defects and boundaries as localized relevant double-trace operators that deform the CFT. Our focus is on pointlike and codimension-one planar defects. In the case of two parallel membranes, we point out that the CFT 2-point function tends to get confined and develops a tower of resonances with a constant decay rate when the operator dimension approaches the free field dimension. Using a functional formalism, we compute the quantum forces induced by the CFT between a variety of configurations of pointlike defects, infinite plates and membranes. Consistency arguments imply that these quantum forces are attractive at any distance. Forces of the Casimir–Polder type appear in the UV (ultraviolet), while forces of the Casimir type appear in the IR (infrared), in which case the CFT gets repelled from the defects. Most of the forces behave as a non-integer power of the separation, controlled by the dimension of the double-trace deformation. In the Casimir regime of the membrane–membrane configuration, the quantum pressure behaves universally as $1/\ell^d$; however, information about the double-trace nature of the defects still remains encoded in the strength of the pressure.

Keywords: Casimir force; Casimir–Polder forces; conformal field theory

1. Introduction

Quantum field theory (QFT) predicts that macroscopic bodies can experience forces of a purely quantum nature [1,2]. Such quantum forces are usually computed within the framework of weakly coupled QFT; see, e.g., Refs. [3–8] for modern reviews. In this paper, we propose to explore the quantum forces that arise in a particular class of QFTs for which calculations are possible, even with strong coupling: conformal field theories (CFTs).

Conformal field theories are ubiquitous in the real world. Many thermodynamic and quantum critical points exhibit conformal invariance. For example, the liquid–vapor critical points, the superfluid transition in liquid helium, and Heisenberg magnets are all described by the same family of scalar 3D (3-dimensional) CFTs; see, e.g., Refs. [9,10]. CFTs are also ubiquitous in the space of quantum field theories: most renormalisation group (RG) flows end on a CFT, either in the infrared (IR) or the ultraviolet (UV). Reversing the logic, one can also think of generic weakly coupled QFTs as CFTs deformed by operators that are either relevant or irrelevant.

The CFTs that appear in the real world are not ideal. Critical systems obtained in the laboratory certainly have boundaries. Moreover, real-world CFTs can contain impurities of various codimensions. A subfield of CFT studies focuses on extracting data from CFTs with boundaries and defects using inputs from symmetry, unitarity and causality; see, e.g., Refs. [11–15] for some seminal papers, Refs. [16–27] for recent progresses, and Refs. [28,29] for recent reviews. The present study does not pursue this approach. Our focus is rather a set of observable phenomena that we compute via QFT methods adapted to the CFT context.

Citation: Brax, P.; Fichet, S. Casimir Forces in CFT with Defects and Boundaries. *Physics* **2024**, *6*, 544–567. <https://doi.org/10.3390/physics6020036>

Received: 29 November 2023

Revised: 31 January 2024

Accepted: 7 February 2024

Published: 9 April 2024



Copyright: © 2024 by the authors. Licensee MDPI, Basel, Switzerland. This article is an open access article distributed under the terms and conditions of the Creative Commons Attribution (CC BY) license (<https://creativecommons.org/licenses/by/4.0/>).

Boundaries and defects in the real world are not ideal either. Physical defects cannot, in general, be thought as ideal truncations of the spatial support of a field theory with fluctuations of any wavelength. A more realistic description of defects should feature some notion of smoothness. The modeling of such imperfect defects and boundaries is somewhat familiar from weakly coupled QFT. There, a defect is sometimes modeled by a bilinear operator, whose spatial support represents the defect [30–32]. Within such a model, the defect ideally repels the field only asymptotically in the IR. More generally, for arbitrary wavelengths, the quantum field propagates to some extent inside the defect [33,34]. One of the points of this paper is to model imperfect defects in CFTs in an analogous manner. This is performed in Section 3.

The second aim of this paper is the computation of observable quantities: the quantum forces induced by the CFT between pairs of defects and/or boundaries. We assume that spacetime dimension is equal to or larger than three; see, e.g., Refs. [35–39] for Casimir-type computations in 2d CFT. We mainly focus on quantum fluctuations in spacetime; however, our approach can analogously apply to thermal fluctuations in Euclidean space since quantum and statistical field theories are related via Wick rotation. In the thermodynamic context, the fluctuating field describes an order parameter of a continuous phase transition. One commonly uses the term critical Casimir forces [10] to refer to forces appearing near criticality, where the system becomes a CFT. The quantities computed in the thermal case are, however, slightly different from the ones in QFT. In QFT, one computes a force or potential between non-relativistic bodies, while in the thermal case, one typically computes the free energy at criticality.

Our results on quantum forces are presented in Section 5, where we also discuss monotonicity and the connection to critical Casimir forces. In the process, we analyze the properties of 2-point correlators confined between membranes in Section 4. Section 2 contains the necessary introductory material, and Section 6 contains a summary of our results.

2. Basics

2.1. CFT Rudiments

A conformal field theory is a field theory that is invariant under the conformal group $SO(d, 2)$ —or $SO(d + 1, 1)$ in Euclidean space. The symmetries of the conformal group are so strong that they fully constrain both the 2-point and 3-point correlation functions of any operator. Still due to symmetries, operators and states are in one-to-one correspondence, and the operator product expansion (OPE) has a finite radius of convergence. The OPE, combined with crossing symmetry, provides nontrivial constraints on 4-point correlators, which is the theme of the “Conformal Bootstrap” program; see [40–45] for modern reviews on CFTs. In this paper, we only need the most basic features of CFTs, and no prior CFT knowledge is needed.

The symmetries of the conformal group impose that so-called primary operators \mathcal{O}_i have 2-point position correlators of the form

$$\langle \mathcal{O}_i(x_1) \mathcal{O}_j(x_2) \rangle = \frac{a_i \delta_{ij}}{x_{12}^{2\Delta_i}}, \tag{1}$$

with $x_{12}^2 = (x_1 - x_2)^\mu (x_1 - x_2)_\mu$. Δ_i is the scaling dimension of \mathcal{O}_i under the dilation operator, δ_{ij} is the Kronecker delta, the brackets $\langle \dots \rangle$ denote the quantum averaging, the Latin letter indexes labelling the primary operators, and the Greek letter indexes taking 0 (temporal), $1, \dots, d - 1$ (space) values.

The overall constant a_i is not fixed by symmetries. In this paper, we adopt the normalization $a_i \equiv 1$. CFT unitarity implies that an operator is a free field if and only if $\Delta = (d - 2)/2$, where d denotes the dimension of space-time. For a canonically normalized 4D free field, we have $a_i \rightarrow 1/(4\pi^2)$. We convert to this normalization when comparing with the 4D free field results throughout this paper.

The formal CFT operators O_i can be understood as traces of combinations of matrices, such as the irreducible representations of an internal $SU(N)$ group. This is why operators of the form $[\mathcal{O}(x)]^n$ are commonly called n -uple trace operators. In this paper, a central role is played by the double-trace operators $[\mathcal{O}(x)]^2$. An operator is said to be relevant, marginal and irrelevant if $\Delta < d$, $\Delta = d$, and $\Delta > d$, respectively.

We further assume that the CFT has a large enough number of degrees of freedom, i.e., large N such that 't Hooft's large- N expansion applies. This assumption renders many calculations possible; here, we only need to work at the leading order of the large N expansion. (Moreover, we only focus on 2-point correlators. At large enough N , the 2-point correlators that we compute amount to those of a scalar generalized free field (GFF), i.e., a free scalar with dimension $\Delta > (d - 2)/2$ [46]. An actual GFF would appear by taking $N \rightarrow \infty$, in which case all the higher-point correlators of a GFF are trivially expressed as a function of the 2-point GFF correlator via Wick's theorem; see, e.g., Ref. [47]. In this paper, we do not need to take infinite N , which is known to be an ill-defined limit in CFT and beyond; see, e.g., Refs. [48,49]. We assume large enough but finite N , and all our results are given up to $O(1/N^2)$ corrections.) In this regime, the scaling dimension of the double-trace operator is only $\Delta_{\mathcal{O}^2} = 2\Delta + O(1/N^2)$.

CFTs in the real world live in finite volumes with boundaries. Furthermore, they may contain impurities. This has triggered a formal program of studies constraining CFTs with boundaries and defects—the boundary conformal bootstrap; see [46–49] for general references. In this paper, we do not use bootstrap techniques. It might be fruitful to apply bootstrap techniques to the class of defects and boundaries that we introduce further below; this is left for future work.

2.1.1. Momentum Space

We compute the CFT 2-point function of a scalar primary \mathcal{O} in momentum space (p^M). The Fourier transform convention is $\mathcal{O}(x) = \int \frac{d^d p}{(2\pi)^d} \mathcal{O}(p) e^{-ip \cdot x}$. We introduce the reduced correlator

$$\langle \mathcal{O}(p_1) \mathcal{O}(p_2) \rangle = (2\pi)^d \delta^{(d)}(p_1 + p_2) \langle\langle \mathcal{O}(p_1) \mathcal{O}(p_2) \rangle\rangle, \tag{2}$$

where $\delta^{(d)}(\cdot)$ is the d -dimensional Dirac delta function and the brackets $\langle\langle \cdot \cdot \rangle\rangle$ denotes the reduced correlator where the momentum conservation has been used.

One has $\langle \mathcal{O}(x_1) \mathcal{O}(x_2) \rangle = \int \frac{d^d p}{(2\pi)^d} e^{-ip \cdot x_{12}} \langle\langle \mathcal{O}(p) \mathcal{O}(-p) \rangle\rangle$ and obtain

$$\langle\langle \mathcal{O}(p) \mathcal{O}(-p) \rangle\rangle = -i \frac{\pi^{d/2} \Gamma(d/2 - \Delta)}{\Gamma(\Delta)} \left(\frac{4}{-p^2} \right)^{d/2 - \Delta}, \tag{3}$$

where Γ represents the gamma function.

A convenient way to compute the Fourier transform is via the Schwinger parametrization; see Appendix A.

2.1.2. Momentum–Position Space

Since we are interested in codimension-one defects, it is also useful to single out one of the spatial dimensions corresponding to the orthogonal direction to the defects, $x^M = (y^\mu, z)$. We compute the CFT correlator in mixed position–momentum space (p^μ, z) . For this, we introduce the reduced mixed-space correlator

$$\langle \mathcal{O}(p_1, z_1) \mathcal{O}(p_2, z_2) \rangle = (2\pi)^{d-1} \delta^{(d-1)}(p_1 + p_2) \langle\langle \mathcal{O}(p_1, z_1) \mathcal{O}(p_2, z_2) \rangle\rangle. \tag{4}$$

We have $\langle \mathcal{O}(x_1) \mathcal{O}(x_2) \rangle = \int \frac{d^{d-1}p}{(2\pi)^d} \langle\langle \mathcal{O}(p, z_1) \mathcal{O}(-p, z_2) \rangle\rangle e^{-ip \cdot y_{12}}$ and obtain

$$\langle\langle \mathcal{O}(p, z_1) \mathcal{O}(-p, z_2) \rangle\rangle = -i \frac{2\pi^{\frac{d-1}{2}}}{\Gamma(\Delta)} \left(\frac{4z_{12}^2}{-p^2} \right)^{\frac{d-1-2\Delta}{4}} K_{\frac{d-1}{2}-\Delta} \left(\sqrt{-p^2 z_{12}^2} \right), \tag{5}$$

that, again, as in Section 2.1.2, can be obtained using the Schwinger parametrization; see Appendix A. K_α is the modified Bessel function of the second kind of order α . A useful integral representation is

$$K_\alpha(z) = \frac{1}{2} \left(\frac{2}{z} \right)^\alpha \int_0^\infty \frac{dt}{t} t^\alpha e^{-t - \frac{z^2}{4t}}. \tag{6}$$

We further introduce

$$\langle\langle \mathcal{O}(p, z_1) \mathcal{O}(-p, z_2) \rangle\rangle \equiv iG(p; z_1, z_2). \tag{7}$$

With this definition, $G(p; z_1, z_2)$ is real for spacelike momenta ($p^2 < 0$) or if one Wick-rotates p to Euclidean space.

2.2. Casimir Forces in the Functional Formalism

In this paper, our interest lies in computing Casimir and Casimir-type forces between the defects and/or boundaries of a CFT. To this end, we use a variational approach introduced long ago in, for example, Ref. [50], and recently exploited/developed in Ref. [34]. In Ref. [51] a similar approach was used; see also [52] for related developments.

In this formalism, one considers the generating functional of the correlators of the system (i.e., the free energy in Euclidean space) in the presence of a static source $J(x)$,

$$E[J] = iT \log Z[J], \quad Z[J] = \int \mathcal{D}\Phi e^{iS[\Phi, J]}, \tag{8}$$

where Φ refers collectively to the set of quantum fields.

The quantity $E[J]$ can be referred to as the vacuum energy evaluated in the presence of the source J . In the present study, the source is ultimately identified with the defects and/or boundaries of the system.

A variation of the source produces a variation in the vacuum energy. This variation in energy is identified as a quantum version of the notion of the work. We write this quantum work as

$$W_\lambda = -\partial_\lambda E[J_\lambda], \tag{9}$$

where λ is a deformation parameter, and $\partial_\lambda \equiv \partial/\partial\lambda$. In cases where the deformation of the source is simple enough, the quantum work can be factored out as displacement times force. The force that emerges from W_λ encodes all the effects of the quantum fluctuations. This is how we compute quantum forces in this note.

The functional formalism sketched above applies, by definition, to any field theory (either weakly or strongly coupled), and admits any kind of deformation. While the principle of the approach is conceptually straightforward, the precise formulation is slightly technical due to the finding that one needs to parametrize a generic deformation of the source. Assuming for simplicity that the density is constant in λ and x , i.e., that the source is incompressible and homogeneous, the source is written as $J_\lambda(x) \equiv n\mathbf{1}_J(x) \equiv n\Theta[l_\lambda(x)]$ with the support function $l_\lambda(x) > 0$ on the support of J , $l_\lambda(x) = 0$ at its boundary and is negative otherwise. (The general case including compressible, heterogenous sources is presented in Ref. [34].) The deformation of J_λ is described by a vector field \mathbf{L} referred to as the deformation flow such that

$$l_{\lambda+d\lambda}(x) = l_\lambda(x - \mathbf{L}(x)d\lambda). \tag{10}$$

Introducing ∂_λ , one obtains the definition of the quantum work as a variation in λ , written in Equation (9).

If the fields couple bilinearly to the source,

$$S[\Phi, J] = \int dx^d \left(\mathcal{L}[\Phi(x)] - \frac{\xi}{2} \Phi^2(x) J(x) \right), \tag{11}$$

then the quantum work is found to be [34]

$$W_\lambda = -\frac{\xi}{2} \int d^{d-1} \mathbf{x} \langle \Phi(x) \Phi(x) \rangle_J \partial_\lambda J_\lambda(x). \tag{12}$$

Here, $\langle \Phi(x) \Phi(x) \rangle_J$ is the 2-point correlator of Φ evaluated in the presence of the J source and taken at the coincident point. Equation (12) is the general formula we use in this paper. When the deformation is simple enough, the quantum work can be written as $W_\lambda = \mathbf{L} \cdot \mathbf{F}$, where \mathbf{F} is identified as the quantum force.

A crucial feature highlighted by the quantum work formalism is that the matter in the source must be conserved [34]. Otherwise, nonphysical divergences would appear in the quantum work, while it must be finite by definition. At constant density, i.e., for an incompressible homogeneous source, the statement of matter conservation becomes that the deformation flow must be divergence-less, $\partial \cdot L(x) = 0$, where ∂ denote the This is a firm condition that constrains the admissible deformations of J . An example of the arbitrary deformation of an arbitrary source is shown in Figure 1.

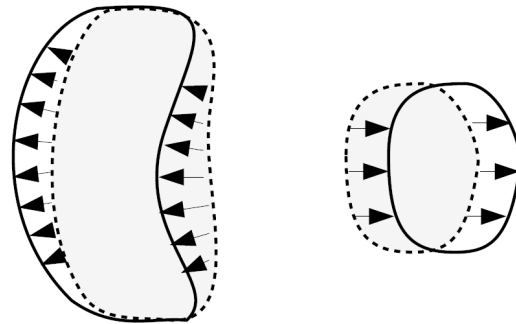


Figure 1. Deformation of a source. The arrows represent the divergence-less deformation flow.

3. Double-Trace Deformations as Defects and Boundaries

3.1. Modeling Imperfect Defects and Boundaries

In weakly coupled QFTs, it is common to model an imperfect boundary using a mass term localized in space, $J(x) = m^2 \mathbf{1}_J(x)$ where $\mathbf{1}_J$ is the function whose value is unity on the support of J . This mass term dresses the ϕ propagator, forming a Born series $G_\phi(x_1, x_2) - i \int d^d x G_\phi(x_1, x) J(x) G_\phi(x, x_2) + \dots$ (the Born series can be derived by integrating out the ϕ field in the partition function of the theory). In the $m^2 \rightarrow \infty$ limit, the ϕ field is repelled from the support of J , and thus acquires a Dirichlet boundary condition on ∂J . This can be shown at the level of the equation of motion [34], or by inspecting the dressing of the propagator as shown further below.

The mass term is, in any d , a relevant operator. Accordingly, the $m^2 \rightarrow \infty$ limit can be understood as the limit of low momentum, i.e., the infrared regime of the RG flow. With this viewpoint, one deduces that the field is repelled from J at a long distance while it propagates to some extent inside J at a short distance. This provides a straightforward picture of an imperfect defect/boundary in weakly coupled QFT. We now define a model that reproduces such a behavior in CFT.

The natural CFT analogue of a mass term is the CFT double-trace deformation. A double-trace deformation can be just thought as a term added to the CFT action,

$$S_{\text{deformed}}^{\text{CFT}} = S^{\text{CFT}} - \frac{\xi}{2} \int dx^d \mathcal{O}^2(x) J(x), \tag{13}$$

where ξ is coupling constant.

The deformation breaks the conformal symmetry unless $\Delta_{\mathcal{O}^2} = d$ exactly. Still, in the large- N limit, we can compute the correlator of the deformed 2-point CFT by dressing the correlator in the absence of defect.

Following the features of weakly coupled QFT, we require that the \mathcal{O}^2 be relevant. At the leading order in the large- N limit, this implies that the dimension of \mathcal{O} must satisfy

$$\frac{d-2}{2} \leq \Delta < \frac{d}{2}. \tag{14}$$

In this Section, we further motivate this bound.

Let us first review the effect of a double-trace operator occupying the whole space. In that case, $J = 1$. The CFT 2-point correlator is straightforwardly expressed in momentum space (at the leading order in the large- N limit, the leading effect in the dressing comes from insertions of the $-i\xi$ vertex; the contributions built from higher-point correlators are automatically N -suppressed and thus negligible):

$$\langle \mathcal{O}\mathcal{O} \rangle_J = \frac{1}{\langle \mathcal{O}\mathcal{O} \rangle^{-1} + i\xi}. \tag{15}$$

Like in the weakly coupled case, this can be derived from the partition function, which produces a Born series representing the 2-point CFT correlator dressed by insertions of $-iJ$. If the \mathcal{O} operator satisfies Equation (14), the dressed correlator takes the form

$$\langle \mathcal{O}\mathcal{O} \rangle_J = -\frac{i}{\xi} + \frac{1}{\xi^2} \langle \mathcal{O}\mathcal{O} \rangle^{-1} + O(\xi^{-3}), \tag{16}$$

in the IR. The first term is a mere contact term. The second term features the inverse 2-point correlator, that turns out to be proportional to the 2-point correlator of an operator $\tilde{\mathcal{O}}$ with dimension $\tilde{\Delta} = d - \Delta$ with $d/2 < \tilde{\Delta} < d/2 + 1$. One says that the deformations induce a RG flow from a UV CFT with an operator of dimension Δ to an IR CFT with an operator of dimension $d - \Delta$. See [53] and the references therein, and the seminal papers [54,55].

Let us now model imperfect defects and boundaries in CFT via a localized relevant double-trace deformation. Like in the weakly coupled case, the 2-point correlator can be expressed as a Born series. To express it rigorously in position space, we introduce the convolution product \star as $f \star g(x_1, x_2) = \int d^d x f(x_1, x) g(x, x_2)$ and introduce the inverse

$$A \star A^{-1}(x) = \delta^d(x). \tag{17}$$

We also introduce $\Sigma(x, x') = -iJ(x)\delta^d(x - x')$. Using this notation, we can write the propagator entirely using convolutions. The exact resummed Born series is expressed as

$$\langle \mathcal{O}(x_1)\mathcal{O}(x_2) \rangle_J = \sum_{r=0}^{\infty} \langle \mathcal{O}\mathcal{O} \rangle [\star \xi \Sigma \star \langle \mathcal{O}\mathcal{O} \rangle]^r(x_{12}) \tag{18}$$

$$= [\langle \mathcal{O}\mathcal{O} \rangle^{-1} - \xi \Sigma]^{-1}(x_{12}). \tag{19}$$

If \mathcal{O}^2 is relevant, then in the infrared, the ξ term must dominate at any point of the J support. We thus obtain that, for any x_1 or x_2 in J ,

$$\langle \mathcal{O}(x_1)\mathcal{O}(x_2) \rangle_J = \frac{1}{\xi} \delta^d(x_{12}) + \frac{1}{\xi^2} \langle \mathcal{O}(x_1)\mathcal{O}(x_2) \rangle^{-1} + O(\xi^{-3}). \tag{20}$$

One can see that the deformed CFT 2-point correlator tends not to propagate inside J in the infrared regime. Asymptotically in the IR, when $\xi \rightarrow \infty$, we obtain that $\langle \mathcal{O}(x_1)\mathcal{O}(x_2) \rangle_J \rightarrow 0$ anywhere on J and its boundary. Therefore, the 2-point correlator

satisfies a Dirichlet condition on the boundary of J in the IR. Such a behavior appropriately models an imperfect defect/boundary for a CFT.

3.2. The Double-Trace Membrane

A simple extended double-trace defect is the one whose support is a codimension-one plane. We refer to it as a membrane. The support of the membrane is defined (from now on, we include the coupling constants ξ in J) as follows:

$$J(\mathbf{x}) = \xi \delta(z - z_0). \tag{21}$$

To compute the dressed propagator, one uses the position–momentum space 2-point correlator Equation (5). Dressing the propagator with a membrane necessarily involves evaluating $\langle\langle \mathcal{O}(p, z_1) \mathcal{O}(-p, z_2) \rangle\rangle$ at $z_{12} = 0$. Let us investigate its behavior for relatively small z_{12} at fixed p . In this limit, the Bessel function has quite a small argument expansion. We find

$$\langle\langle \mathcal{O}(p, z_1) \mathcal{O}(-p, z_2) \rangle\rangle_d = \left(\langle\langle \mathcal{O}(p) \mathcal{O}(-p) \rangle\rangle_{d-1} + \frac{c}{z_{12}^{2\Delta-d+1}} \right) \left[1 + \mathcal{O}\left((pz_{12})^2\right) \right], \tag{22}$$

with

$$c = -i \frac{\Gamma(\Delta + \frac{1-d}{2})}{\Gamma(\Delta)}. \tag{23}$$

The two terms shown in Equation (22) are the leading non-analytical and analytical ones. These two terms correspond respectively to the regions of relatively small and large p_z momenta covered by the corresponding Fourier integral. The $\langle\langle \mathcal{O}(p) \mathcal{O}(-p) \rangle\rangle_{d-1}$ correlator, which is independent of z_{12} , corresponds exactly to the 2-point correlator of an operator of dimension Δ in $d - 1$ dimensions. One could equivalently obtain it by averaging over z_{12} in the original position space correlator.

The $c/z_{12}^{2\Delta-d+1}$ term corresponds to a relatively large p_z momentum. One could equivalently obtain it by averaging the transverse coordinates in the original position space correlator. One can see that this term diverges when $z_{12} \rightarrow 0$ if $\Delta > (d - 1)/2$. This divergence might need to be treated via renormalization of the defect. This would deserve a separate treatment that is beyond the scope of this note. Therefore, in the presence of a membrane, we restrict Δ as

$$\frac{d-2}{2} \leq \Delta < \frac{d-1}{2}. \tag{24}$$

We denote the 2-point function in the presence of the defect J as

$$\langle\langle \mathcal{O}(p, z_1) \mathcal{O}(-p, z_2) \rangle\rangle_J \equiv iG_J(p; z_1, z_2). \tag{25}$$

In the case of the membrane (21), we obtain

$$G_J(p; z_1, z_2) = G(p; z_1, z_2) + G(p; z_1, z_0) \frac{\xi}{1 - \xi G_0(p)} G(p; z_0, z_2). \tag{26}$$

where $G_0(p) = G(p; z_0, z_0) = \langle\langle \mathcal{O}(p) \mathcal{O}(-p) \rangle\rangle_{d-1}$ corresponds to the 2-point function in $(d - 1)$ space defined in Equation (22). Explicitly,

$$G_0(p) = -\frac{\pi^{\frac{d-1}{2}} \Gamma(\frac{d-1}{2} - \Delta)}{\Gamma(\Delta)} \left(\frac{4}{-p^2} \right)^{\frac{d-1}{2} - \Delta}. \tag{27}$$

If the double-trace operator is relevant, $G_0(p)$ grows when p decreases. In the limit for which $\xi G_0(p) \gg 1$, we have, therefore,

$$G_J(p; z_1, z_2) \xrightarrow{\text{small } p} G(p; z_1, z_2) - G(p; z_1, z_0) G_0^{-1}(p) G(p; z_0, z_2), \tag{28}$$

which satisfies the Dirichlet boundary condition on the membrane.

The membrane defect can serve as an approximation for a plate-shaped defect of finite width. The approximation appears in the IR regime when the plate width is smaller than all other distance scales of the problem such that, by dimensional analysis, the correlator must see the plate approximately as a membrane.

3.3. AdS/CFT Motivation

Another motivation for implementing relevant double-trace deformations as defects and boundaries comes from the AdS/CFT correspondence; see [47,56–58] for some anti-de Sitter AdS/CFT reviews.

Let us consider the $(d + 1)$ -dimensional Poincaré patch with a boundary at $y = y_0$, $ds^2 = L^2(dx^\mu dx_\mu + dy^2)/y^2$, $y \geq y_0$. Consider a scalar field in the bulk of AdS with mass $m_\Phi^2 = \Delta(\Delta - d)L^2$. For any $\Delta > (d - 2)/2$, the brane-to-brane propagator of Φ behaves as the one of a d -dimensional free field ϕ mixing with the 2-point function of a CFT operator of dimension Δ via an operator $\phi\mathcal{O}$. The same is true for higher-point correlators. This is sometimes referred to as the Δ_+ branch of the correspondence.

When $\Delta < d/2$, a second possibility appears: the brane-to-brane correlators can be directly identified as the CFT correlators of an operator with dimension $d - \Delta$; see [59,60] and, for example, Refs. [53,61,62] for more recent studies. We refer to this identification as the Δ_- branch of the correspondence. Here, we write the general statement of the Δ_- branch as

$$\int \mathcal{D}\phi_{\text{CFT}} e^{iS_{\text{CFT}} + iS_0[\mathcal{O}, J]} \equiv \int \mathcal{D}\Phi_0 e^{iS_0[\Phi_0, J]} \int_{\Phi_0} \mathcal{D}\Phi e^{iS_{\text{AdS}}[\Phi]}, \tag{29}$$

where Φ_0 denotes the value of the fields on the boundary, here $\Phi_0 = \Phi|_{z=z_0}$. (The S_0 action can contain a linear source term $S_0[X, J] = \int d^d x X J$, that can be used to define the correlators on both sides upon functional derivative in J .)

In our model of defect CFT, the general double-trace deformation (13) corresponds to setting the S_0 action to

$$S_0[X, J] \equiv -\frac{\xi}{2} \int d^d x X^2 J. \tag{30}$$

Using Equation (29), one sees that this corresponds to a boundary-localized mass term for Φ on the AdS side. Therefore, the double-trace deformation on the CFT side is encoded as a deformation of the boundary condition of Φ on the AdS side. The double-trace defect of the CFT is realized as a boundary mass term with a support that is localized along the boundary volume. In brief, the defect is on the boundary (Figure 2).

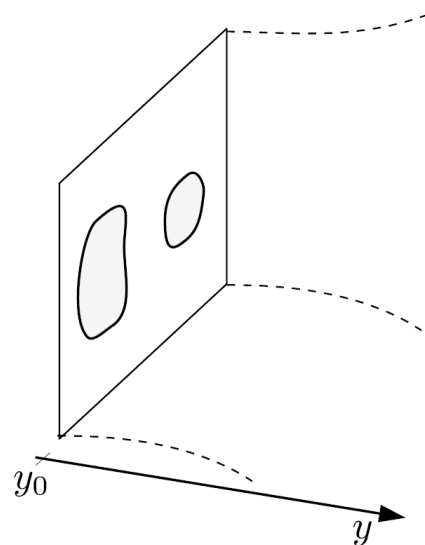


Figure 2. The double-trace defect of the CFT. See text for details.

The domain for which the Δ_- correspondence applies is precisely the range given in Equation (14). Thus, our model of defect CFT can always be realized holographically from the AdS viewpoint: the double-trace deformation defined via AdS is automatically relevant.

At the level of the vacuum energies, we have the identification

$$E_{\text{CFT}}[J] = E_{\text{AdS}}[J] \tag{31}$$

with

$$E_{\text{AdS}}[J] = iT \log Z_{\text{AdS}}[J], \quad Z_{\text{AdS}}[J] = \int \mathcal{D}\Phi_0 e^{i \int_{\partial} d^d x \frac{\xi}{2} J(x) \Phi_0^2} \int_{\Phi_0} \mathcal{D}\Phi e^{i S_{\text{AdS}}[\Phi]}. \tag{32}$$

When the correspondence (31) holds, applying the functional formalism of Section 2.2 to E_{CFT} means on the AdS side that we deform the support of the boundary-localized mass term. In other words, the boundary condition for the bulk fields gets deformed. The phenomenon of the 2-point correlator being repelled from the defect in the IR is understood on the AdS side as the bulk field being repelled from the boundary due to the mass term. For $\xi \rightarrow \infty$, the AdS propagator vanishes on the boundary of the defect localized on the AdS boundary.

We do not use further the AdS picture in the following.

4. A CFT between Two Membranes

We explore further the properties of the 2-point CFT correlators in the presence of two double-trace membranes. The full defect is given by

$$J(x) = J_a(x) + J_b(x) = \frac{\xi_a}{2} \delta(z - z_a) + \frac{\xi_b}{2} \delta(z - z_b). \tag{33}$$

We define $|z_b - z_a| = L$. A convenient way to obtain the 2-point function is by dressing it successively with the two membranes J_a and J_b . We obtain

$$G_a(p; z_1, z_2) = G(p; z_1, z_2) + G(p; z_1, z_a) \frac{\xi_a}{1 - \xi_a G(p; z_a, z_a)} G_0(p; z_a, z_2), \tag{34}$$

$$\begin{aligned} G_{a,b}(p; z_1, z_2) &= G_a(p; z_1, z_2) + G_a(p; z_1, z_b) \frac{\xi_b}{1 - \xi_b G_a(p; z_b, z_b)} G_a(p; z_b, z_2) \\ &= G_{12} + \frac{\xi_b G_{1b} (\xi_a G_{ab} G_{a2} + (1 - \xi_a G_0) G_{b2}) + \xi_a G_{1a} (\xi_b G_{ab} G_{b2} + (1 - \xi_b G_0) G_{a2})}{(\xi_a G_0 - 1)(\xi_b G_0 - 1) - \xi_a \xi_b G_{ab}^2}. \end{aligned} \tag{35}$$

In the second line of Equation (35), we introduce the notation $G(p; z_i, z_j) \equiv G_{ij}$.

4.1. Dirichlet Limit

To understand the behavior of this 2-point function, we take the $\xi_{a,b} \rightarrow \infty$. At finite $\xi_{a,b}$, this corresponds to the asymptotic limit associated to the infrared regime. In this limit, the CFT gets literally confined inside the $[0, L]$ interval. The 2-point correlator becomes

$$G_D(p; z_1, z_2) = G_{12} + \frac{G_{1b} G_{ab} G_{a2} - G_{1b} G_0 G_{b2} + G_{1a} G_{ab} G_{b2} - G_{1a} G_0 G_{a2}}{G_0^2 - G_{ab}^2}. \tag{36}$$

4.2. Poles

We stay in the Dirichlet limit for simplicity. Due to the denominator in Equation (36), it turns out that G_D features a series of poles in the complex plane of p determined by the condition

$$G(p; z_a, z_b) = \pm G_0(p). \tag{37}$$

Explicitly, the poles in p are determined by solving

$$\frac{1}{\Gamma(\alpha)} \left(\sqrt{-p^2} L \right)^\alpha K_\alpha(\sqrt{-p^2} L) = \pm 1, \quad \alpha = \frac{d-1}{2} - \Delta, \tag{38}$$

with $-\frac{1}{2} < \alpha < \frac{1}{2}$. We denote the complex values of p solving Equation (38) by m_n^\pm . There is no massless pole ($p = 0$) nor light pole ($p \ll 1/L$) thanks to the asymptotic behavior at relatively small p is $G_{ab} \rightarrow G_0$ (see Equation (22)), in which case Equation (37) is either trivial or impossible to satisfy.

4.3. Residues

The residues associated to the $p = m_n^\pm$ poles take quite a simple factorized form, $(G_{a1} \mp G_{b1})(G_{a2} \mp G_{b2})$,

$$G(p; z_1, z_2) \stackrel{p \sim m_n^\pm}{\approx} -\frac{1}{2} \frac{f_n^\pm(z_1) f_n^\pm(z_2)}{G_{ab} \mp G_0}, \quad f_n(z) \equiv G(m_n^\pm, z, z_a) \mp G(m_n^\pm, z, z_b). \tag{39}$$

This factorized form is reminiscent of weakly coupled QFT on an interval, which develops a sequence of discrete modes. In the weakly coupled case, the poles lie on the real line up to the corrections due to the interactions. Equation (39) then corresponds to the Källén–Lehmann representation of the propagator confined in the $[0, L]$ interval. Here, we see that the factorized structure remains true even if the poles lie anywhere in the complex plane.

4.4. Free Limit

In the case of the free field in $d = 4$, we have $\Delta = 1$. The 2-point correlator becomes

$$iG^{\text{free}}(p; z_1, z_2) = -i4\pi^2 a \frac{e^{-\sqrt{-p^2}|z_1-z_2|}}{2\sqrt{-p^2}}, \tag{40}$$

where, for a canonically normalized field, $a = 1/(4\pi^2)$. In this case, the poles determined by Equation (38) are real, with $m_n^{\text{free}} = n\pi/L$, $n \in \mathbb{N}^*$. The propagator dressed by the two membranes takes the form

$$iG^{\text{free}}(p; z_1, z_2) = i \frac{\sinh\left(\sqrt{-p^2}(z_a - z_<)\right) \sinh\left(\sqrt{-p^2}(z_> - z_b)\right)}{\sqrt{-p^2} \sinh\left(\sqrt{-p^2}(z_b - z_a)\right)}, \tag{41}$$

where we assume $z_a < z_b$ and define $z_{<(>)} = \min(\max)(z, z')$. This matches the result obtained by solving the free field equation of motion on the interval with Dirichlet boundary conditions on the membranes (see, for example, the Appendix of Ref. [63]).

4.5. Resonances

Slightly away from the free field case, for $\Delta - (d-2)/2 \ll 1$, it turns out that the set of poles of the CFT behaves as a tower of narrow resonances at values $p = m_n \equiv m_n^{\text{free}} - i\Gamma_n/2$ with $\Gamma_n \ll m_n^{\text{free}}$. Expanding the relation (38), we find that the resonances feature a common decay rate Γ_n :

$$\Gamma_n \approx \left(\Delta - \frac{d-2}{2} \right) \pi/L. \tag{42}$$

Details of the computation are given in Appendix B.

One obtains, thus, a notion of unstable particle states directly from a CFT. Since the CFT has internal degrees of freedom, one may think of these resonances as collective excitations. The fact that the resonances decay reflects the fact that, for $\Delta > (d-2)/2$, the theory is interacting. However, the decay width is independent of the underlying physics

of the CFT; it is controlled by the dimension of the double-trace operator that causes the CFT confinement on the interval.

5. CFT Casimir Forces between Defects and Boundaries

We compute the quantum forces induced by the CFT between localized double-trace operators with pointlike and planar supports. The planar geometry includes the case of a flat boundary (for example, $z > 0$) of a membrane and also the case of a plate of any width. We consider two disjoint defects, described by

$$S = S_{\text{CFT}} - \frac{1}{2} \int d^d x \mathcal{O}^2(x) J(x), \quad J(x) = \xi_a J_a(x) + \xi_b J_b(x). \quad (43)$$

The $\xi_{a,b}$ parameters have mass dimension: $[\xi_{a,b}] = d - [J_{a,b}] - 2\Delta$.

We consider a rigid deformation of J such that J_b gets shifted along a constant \mathbf{L} while J_a remains identical,

$$J_{a,\lambda+d\lambda}(x) = J_{a,\lambda}(x), \quad J_{b,\lambda+d\lambda}(x) = J_{b,\lambda}(x - \mathbf{L}d\lambda), \quad (44)$$

exemplified as shown in Figure 3.

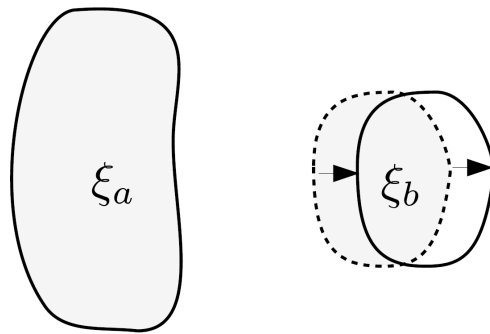


Figure 3. Rigid deformation. See text for details.

The quantum work is then expressed as

$$W = -\frac{\xi_b}{2} \int d^{d-1} x \langle \mathcal{O}(x) \mathcal{O}(x) \rangle_J \partial_\lambda J_{b,\lambda}(x). \quad (45)$$

Equation (45) is the formula we apply throughout this Section.

The CFT propagator in the presence of J can always be written in the form of a Born series as described in Equation (19). Evaluating the expression in a closed form for, for example, a plate is more challenging. Here, we limit ourselves to computing analytical results for the force between J_a and J_b in two limiting cases: the asymptotic Casimir–Polder and Casimir regimes.

5.1. CFT Casimir–Polder Forces

In the UV regime, i.e., in the limit of short separation, the effect of the J insertion in the Born series tends to be quite small. In this limit, the first terms of the series dominate. It turns out that the leading contribution to the quantum work is [34]

$$W = -i \frac{\xi_a \xi_b}{2} \int d^{d-1} x d^{d-1} x' \langle \mathcal{O}(x') \mathcal{O}(x) \rangle J_a(x) \langle \mathcal{O}(x) \mathcal{O}(x') \rangle \mathbf{L} \cdot \partial J_b(x') + O(\xi^3). \quad (46)$$

Upon integration by part, we recognize the structure of a potential $W = -\mathbf{L} \cdot \partial V_{ab}$ with

$$V_{ab} = -i \frac{\xi_a \xi_b}{2} \int d^{d-1} x d^{d-1} x' J_a(x) J_b(x') \int dt \langle \mathcal{O}(0, x) \mathcal{O}(t, x') \rangle^2. \quad (47)$$

The V_{ab} potential has a Casimir–Polder-like structure; it is a loop made of two CFT correlators that connects the two defects. Hence, we refer to this limit as the Casimir–Polder limit.

5.1.1. Point–Point Geometry

We first consider two defects that are pointlike,

$$J_a(\mathbf{x}) = \delta^{d-1}(\mathbf{x}), \quad J_b(\mathbf{x}) = \delta^{d-1}(\mathbf{x} - \mathbf{r}). \tag{48}$$

The potential becomes

$$V(r) = -i \frac{\tilde{\xi}_a \tilde{\xi}_b}{2} \int dt \langle \mathcal{O}(0) \mathcal{O}(t, r) \rangle^2, \tag{49}$$

with $r = |\mathbf{r}|$.

We compute Equation (49) by going to the full momentum space. The momentum space correlator is Equation (3). In momentum space, the potential is given by

$$V(p) = i \frac{\tilde{\xi}_a \tilde{\xi}_b}{2} \frac{\pi^d \Gamma^2(d/2 - \Delta)}{\Gamma^2(\Delta)} \int \frac{d^d k}{(2\pi)^d} \left(\frac{4}{-k^2} \right)^{d/2-\Delta} \left(\frac{4}{-(k+p)^2} \right)^{d/2-\Delta}, \tag{50}$$

where $p_0 = 0$. We rotate the integral to Euclidean space with Euclidean momentum q^M satisfying $q^2 = -k^2$, and go to spherical coordinates,

$$V(p) = -\frac{\tilde{\xi}_a \tilde{\xi}_b}{2} \frac{\pi^d \Gamma^2(d/2 - \Delta)}{\Gamma^2(\Delta)} \int \frac{d^d q}{(2\pi)^d} \left(\frac{4}{q^2} \right)^{d/2-\Delta} \left(\frac{4}{(q+p)^2} \right)^{d/2-\Delta}. \tag{51}$$

We need to evaluate

$$\int \frac{d^d q}{(2\pi)^d} \left((p+q)^2 \right)^a \left(q^2 \right)^b, \tag{52}$$

for some a, b . We apply the identity

$$\left((p+q)^2 \right)^a \left(q^2 \right)^b = \int_0^1 dx \frac{(x(p+q)^2 + (1-x)q^2)^{a+b}}{x^{a+1}(1-x)^{b+1}} \frac{\Gamma(-a-b)}{\Gamma(-a)\Gamma(-b)}. \tag{53}$$

The integral on the right-hand side converges for $\text{Re}(a), \text{Re}(b) < 0$. However, provided the final result of the calculation is analytic in a, b , the result can be extended by analytical continuation such that restrictions on a, b are ultimately lifted. Shifting the loop momentum $l \equiv q + px$, one obtains for Equation (52):

$$\int_0^1 dx \int \frac{d^d l}{(2\pi)^d} \frac{(l^2 + x(1-x)p^2)^{a+b}}{x^{a+1}(1-x)^{b+1}} \frac{\Gamma(-a-b)}{\Gamma(-a)\Gamma(-b)}. \tag{54}$$

We evaluate the loop integral with

$$\int \frac{d^d l}{(2\pi)^d} (l^2 + \Delta)^c = \frac{\Gamma\left(-c - \frac{d}{2}\right)}{\Gamma(-c)} \frac{\Delta^{c+d/2}}{(4\pi)^{d/2}}. \tag{55}$$

Again, the loop integrals are performed in the domain of (c, d) , where the integral on the left-hand side converges. The functions on the right-hand side are analytic in c anywhere away from the integral values of c ; hence, the final result will be ultimately analytically continued in c . For certain values of Δ at even d , a physical divergence appears, which requires renormalization. However, such divergences are irrelevant for our study as soon as it is ultimately only the branch cut of $V(p)$ that contributes to the spatial potential;

see [64]. Hence, no divergence appears in the position space propagators when Δ is set to integer values.

Putting Equations (53) and (55) together yields for Equation (52):

$$\frac{1}{(4\pi)^{\frac{d}{2}}} (p^2)^{a+b+\frac{d}{2}} \frac{\Gamma(-a-b-\frac{d}{2})}{\Gamma(-a)\Gamma(-b)} \int_0^1 dx x^{b+\frac{d}{2}-1} (1-x)^{a+\frac{d}{2}-1}. \tag{56}$$

We identify the remaining integral as being the integral representation of the Beta function. Evaluating the integral, one obtains for Equation (52):

$$\frac{1}{(4\pi)^{d/2}} (p^2)^{a+b+d/2} \frac{\Gamma(-a-b-d/2)}{\Gamma(-a)\Gamma(-b)} \frac{\Gamma(a+d/2)\Gamma(b+d/2)}{\Gamma(a+b+d)}. \tag{57}$$

The potential in momentum space is thus

$$V(p) = -\frac{\xi_a \xi_b}{2} \frac{\pi^d \Gamma^2(d/2 - \Delta)}{\Gamma^2(\Delta)} 4^{d-2\Delta} \frac{1}{(4\pi)^{d/2}} (p^2)^{2\Delta-d/2} \frac{\Gamma(-2\Delta+d/2)}{\Gamma(\frac{d}{2}-\Delta)\Gamma(\frac{d}{2}-\Delta)} \frac{\Gamma^2(\Delta)}{\Gamma(2\Delta)}. \tag{58}$$

Simplifying,

$$V(p) = -\frac{\xi_a \xi_b}{2} \left(\frac{p^2}{4}\right)^{2\Delta-d/2} \frac{\pi^{d/2} \Gamma(-2\Delta+d/2)}{\Gamma(2\Delta)}. \tag{59}$$

We can recognize that Equation (59) is proportional to the momentum space 2-point correlator of the double-trace operator \mathcal{O}^2 with $p_0 = 0$. That is, due to the properties of the CFT, the loop of \mathcal{O} can be understood as a tree exchange of \mathcal{O}^2 . (Particle physics models involving such processes have been considered in Refs. [65–67].) The overall coefficient is nontrivial; however, our loop calculation is required to determine it. This phenomenon occurs only in the Casimir–Polder regime.

One may notice that the numerator diverges if $\Delta \rightarrow d/4$, which is allowed when $d \leq 4$ since $\Delta \geq (d-2)/2$. However, the expression for the potential in position space computed below is automatically finite even in the case $\Delta \rightarrow d/4$. This is because this is a quantity computed at separated points. Keeping a general, non-integer, dimension Δ throughout the calculation plays the same role as dimensional regularization weakly coupled QFT. Finally, we can go back to position space with a $(d-1)$ Fourier transform, $V(r) = \int \frac{d^{d-1}p}{(2\pi)^{d-1}} e^{ipr} V(p)$. We obtain the final result for the CFT Casimir–Polder potential between two pointlike double-trace deformations,

$$V(r) = -\sqrt{\pi} \frac{\xi_a \xi_b}{2} \frac{\Gamma(2\Delta - \frac{1}{2})}{\Gamma(2\Delta)} \frac{1}{r^{4\Delta-1}}. \tag{60}$$

As a cross check, taking $\Delta = 1$ and using the $a = \frac{1}{4\pi}$ normalization for each correlator, we recover exactly the Casimir–Polder potential from the exchange of 4D free massless scalars, $V(r) = -\zeta^2 / (64\pi^3 r^3)$. Notice that $[\xi_{a,b}] = 1 - 2\Delta$; thus, $[V] = 1$.

5.1.2. Point-Plate

We calculate the Casimir–Polder potential between a point particle and an infinite plate located at $z < 0$. In terms of the support functions, this is described by

$$J_a(\mathbf{x}) = \Theta(-z), \quad J_b(\mathbf{x}) = \delta^{d-2}(\mathbf{x}_{\parallel}) \delta(z - \ell), \tag{61}$$

where $\Theta(\cdot)$ is the Heaviside function.

We assume that the deformation moves J_b along the z direction, i.e., $\mathbf{L} = (\mathbf{0}, 1)$. The x_{\parallel} are the coordinates parallel to the plate.

The CFT force between the point and the membrane can be straightforwardly obtained by integrating the point–point Casimir–Polder potential over J_a . This simplified approach is valid only in the Casimir–Polder limit. The $\tilde{\zeta}_{a,b}$ are defined such that the parametrization (43) holds, now with the defect (61). $\tilde{\zeta}_a$ is related to the pointlike source coupling by $\tilde{\zeta}_a = n\tilde{\zeta}_a^{\text{point}}$, where n is the number density of J_a .

The Casimir–Polder force is given by the potential

$$V(\ell) = n \int_{-\infty}^0 dz \int d^2x_{\parallel} \int \frac{d^3p}{(2\pi)^3} e^{ip_z(\ell-z)} e^{ip_{\parallel}x_{\parallel}} V(p). \tag{62}$$

The p_{\parallel} is the momentum component along the plate. The integral reduces to

$$V(\ell) = -\frac{\pi^{d/2} \tilde{\zeta}_a \tilde{\zeta}_b}{2} \frac{\Gamma(-2\Delta + d/2)}{\Gamma(2\Delta)} \int_{-\infty}^0 dz \int \frac{dp_z}{2\pi} e^{ip_z(\ell-z)} \left(\frac{p^2}{4}\right)^{2\Delta-d/2}. \tag{63}$$

The momentum integral can be performed and gives

$$\int \frac{dp_z}{2\pi} e^{ip_z(\ell-z)} \left(\frac{p^2}{4}\right)^{2\Delta-d/2} = \frac{\Gamma(2\Delta + \frac{1-d}{2})}{\sqrt{\pi}\Gamma(\frac{d}{2} - 2\Delta)} \frac{1}{(\ell-z)^{4\Delta+1-d}}. \tag{64}$$

The integral over z converges, provided $\Delta > d/4$. When computing the force further below, the divergence matters only when for a free field in $d = 3$. In the convergent case, we have

$$V(\ell) = -\frac{\pi^{(d-1)/2}}{2(4\Delta-d)} \frac{\Gamma(2\Delta + \frac{1-d}{2})}{\Gamma(2\Delta)} \frac{\tilde{\zeta}_a \tilde{\zeta}_b}{\ell^{4\Delta-d}}, \tag{65}$$

where $d > 4$. The force is then given by $F = -\partial V/\partial \ell$, which gives

$$F(\ell) = -\frac{\pi^{(d-1)/2} \Gamma(2\Delta + \frac{1-d}{2})}{2\Gamma(2\Delta)} \frac{\tilde{\zeta}_a \tilde{\zeta}_b}{\ell^{4\Delta-d+1}}. \tag{66}$$

For a free field in $d = 4$, one obtains

$$F(\ell) = -\frac{\pi^2 \tilde{\zeta}_a \tilde{\zeta}_b}{2 \ell}. \tag{67}$$

This correctly reproduces the $\propto \frac{1}{\ell}$ scalar Casimir–Polder force derived in Ref. [34], $-\frac{\tilde{\zeta}_a \tilde{\zeta}_b}{32\pi^2 \ell}$, once one takes into account the canonical normalization of the free fields, which introduces the factor $a^2 = (\frac{1}{4\pi^2})^2$. (A factor of $\frac{1}{2}$ is missing in Equation (6.29) of Ref. [34]).

The case of the free field in $d = 3$ necessitates the assumption that the plane has finite width L . We obtain

$$F(\ell) = -\frac{\pi \Gamma(2\Delta - 1)}{2\Gamma(2\Delta)} \tilde{\zeta}_a \tilde{\zeta}_b \log\left(1 + \frac{L}{\ell}\right). \tag{68}$$

5.1.3. Plate–Plate CFT Casimir–Polder

We similarly compute the Casimir–Polder pressure between two infinite plates. This is described by

$$J_a(\mathbf{x}) = \Theta(-z), \quad J_b(\mathbf{x}) = \Theta(z - \ell). \tag{69}$$

We assume that the deformation moves J_b along the z direction, i.e., $\mathbf{L} = (0, 1)$. (In general, one should require that the plates end far away, i.e., are not formally infinite, in order for the deformation flow to be divergence-free [34]; while this is necessary in general, this detail does not affect the present Casimir–Polder calculation.)

The $\tilde{\zeta}_{a,b}$ are defined such that the parametrization Equation (43) holds, now in the presence of the defect (61). $\tilde{\zeta}_{a,b}$ is related to the pointlike source coupling by $\tilde{\zeta}_{a,b} = n_{a,b} \tilde{\zeta}_{a,b}^{\text{point}}$

with $n_{a,b}$, the number density of $J_{a,b}$. Similarly to the point–plate case, we integrate the point–point potential over the two defects, with, for example,

$$F_{\text{plate–plate}}(\ell) = -n_b S_{d-2} \int_{\ell}^{\infty} dz F_{\text{point–plate}}(z), \tag{70}$$

where $S_{d-2} = \int d^{d-2} \mathbf{x}_{\parallel}$ is the volume integral in Equation (70) in the directions parallel to the plate. As long as $\Delta > d/4$, the integral is IR convergent and gives

$$\frac{F(\ell)}{S_{d-2}} = -\frac{\pi^{(d-1)/2}}{2(4\Delta - d)} \frac{\Gamma(2\Delta + \frac{1-d}{2})}{\Gamma(2\Delta)} \frac{\zeta_a \zeta_b}{\ell^{4\Delta-d}}. \tag{71}$$

The case of a free field in $d = 4$ is logarithmically divergent. This is a physical divergence that signals that we should consider finite plates instead of approximating them as infinite. It is sufficient to assume that one of the plates, here, the second plate integrated in Equation (70), has finite width L . We find

$$\frac{F(\ell)}{S_1} = -\frac{\pi^2}{2} \zeta_a \zeta_b \ln\left(1 + \frac{L}{\ell}\right). \tag{72}$$

The IR divergent behavior also appears in the result of Ref. [34], in the case where the free field is massless. There is no IR divergence if the free field is massive.

5.2. CFT Casimir Forces

We compute forces beyond the Casimir–Polder approximation. Our focus is on membranes. Computing analytical results for plates of finite widths is more challenging. However, in the IR regime for which the plate width is smaller than other distance scales of the problem, we expect the results to reproduce the one obtained with membranes.

Since the chosen defects feature membranes, we restrict Δ to the interval (24). The case $\Delta \geq (d - 1)2$ deserves a separate analysis.

5.2.1. Point–Membrane CFT Casimir

We first compute the force between a membrane at $z = 0$ and a point at distance $z = \ell$. The two defects are parametrized as

$$J_a(\mathbf{x}) = \delta(z), \quad J_b(\mathbf{x}) = \delta^{d-2}(\mathbf{x}_{\parallel}) \delta(z - \ell). \tag{73}$$

The membrane is infinitely thin in contrast with the point–plate case of the previous section, where the plate had a large width. We choose that the deformation moves the pointlike defect along z , while the membrane stays in place, i.e., it is given by Equation (44), where \mathbf{L} is oriented along z . The deformation of the defect is then given by

$$\partial_{\lambda} J = -\zeta_b L \delta^{d-2}(\mathbf{x}_{\parallel}) \partial_z \delta(z - \ell). \tag{74}$$

The quantum force is given by

$$F(\ell) = -\frac{1}{2} \int d^{d-1} \mathbf{x} \langle \mathcal{O}(x) \mathcal{O}(x) \rangle_J \partial_{\lambda} J_{b,\lambda}(x) \tag{75}$$

$$= -\frac{\zeta_b}{2} \partial_z \langle \mathcal{O}(x^{\alpha}, z) \mathcal{O}(x^{\alpha}, z) \rangle_J \Big|_{z \rightarrow \ell}. \tag{76}$$

Here, $\langle \mathcal{O}(x^{\alpha}, z) \mathcal{O}(x^{\alpha}, z) \rangle_J$ is the CFT 2-point function dressed by the membrane at $z = 0$. This correlator is computed in Equation (26). Going to the position–momentum space, one has

$$G_J(p; z, z) = G_0(p) + G^2(p; 0, z) \frac{\zeta_a}{1 - \zeta_a G_0(p)}, \tag{77}$$

where $G_0(p)$ is defined in Equation (27).

The quantum force is then expressed as

$$F(\ell) = -\frac{i\tilde{\zeta}_b}{2} \int \frac{d^{d-1}p}{(2\pi)^{d-1}} \partial_z G_J(p; z, z)|_{z \rightarrow \ell} \tag{78}$$

$$= -\frac{i}{2} \int \frac{d^{d-1}p}{(2\pi)^{d-1}} \frac{\tilde{\zeta}_a \tilde{\zeta}_b}{1 - \tilde{\zeta}_a G_0(p)} \partial_z \left(G^2(p; 0, z) \right)_{z \rightarrow \ell'} \tag{79}$$

where $G_0(p)$ does not contribute since it is constant in z .

The derivative piece takes a straightforward form:

$$\partial_z \left(G^2(p; 0, z) \right)_{z \rightarrow \ell} = -\frac{16\pi^{d-1}\ell}{\Gamma^2(\Delta)} \left(\frac{4\ell^2}{-p^2} \right)^{\frac{d-2-2\Delta}{2}} K_{\frac{1-d}{2}+\Delta} \left(\sqrt{-p^2\ell} \right) K_{\frac{3-d}{2}+\Delta} \left(\sqrt{-p^2\ell} \right). \tag{80}$$

One may notice it is proportional to the product of two correlators with dimension Δ and $\Delta + 1$.

We can identify the potential directly from the line (79), where the ∂_z derivative is equivalent to ∂_ℓ . We rotate to Euclidean momentum q^M and use spherical coordinates. We find the general result:

$$V(\ell) = -\frac{\pi^{\frac{d-1}{2}}}{2^{d-3}\Gamma(\frac{d-1}{2})\Gamma^2(\Delta)} \int dq q^{d-2} \frac{\tilde{\zeta}_a \tilde{\zeta}_b}{1 - \tilde{\zeta}_b G_0(q)} \left(\frac{2\ell}{q} \right)^{d-1-2\Delta} K_{\frac{1-d}{2}+\Delta}^2(q\ell), \tag{81}$$

$$F(\ell) = -\frac{\pi^{\frac{d-1}{2}}\ell}{2^{d-5}\Gamma(\frac{d-1}{2})\Gamma^2(\Delta)} \int dq q^{d-2} \frac{\tilde{\zeta}_a \tilde{\zeta}_b}{1 - \tilde{\zeta}_b G_0(q)} \left(\frac{2\ell}{q} \right)^{d-2-2\Delta} K_{\frac{1-d}{2}+\Delta}(q\ell) K_{\frac{3-d}{2}+\Delta}(q\ell). \tag{82}$$

One can evaluate the loop integral in both the Casimir–Polder regime $\tilde{\zeta}_a G_0(p) \ll 1$ and the Casimir regime $\tilde{\zeta}_a G_0(p) \gg 1$. We write the two Bessel functions using the representation (6), and perform the loop momentum integral and then the t and t' integrals. The intermediate steps involve hypergeometric functions, but the final results are remarkably simple.

In the Casimir–Polder regime, we obtain the potential

$$V(\ell) = -\frac{\pi^{(d-1)/2} \Gamma(2\Delta + \frac{1-d}{2})}{2 \Gamma(2\Delta)} \frac{\tilde{\zeta}_a \tilde{\zeta}_b}{\ell^{4\Delta-d+1}}. \tag{83}$$

It is attractive for any Δ satisfying the unitarity bound. For $d = 3$ and 4 the Casimir–Polder force is

$$F_{d=3}(\ell) = -\frac{\pi \tilde{\zeta}_a \tilde{\zeta}_b}{\ell^{4\Delta-1}} \text{ and} \tag{84}$$

$$F_{d=4}(\ell) = \frac{\pi^{3/2} \Gamma(2\Delta - \frac{1}{2})}{\Gamma(2\Delta)} \frac{\tilde{\zeta}_a \tilde{\zeta}_b}{\ell^{4\Delta-2}}, \tag{85}$$

respectively.

For the free field in $d = 4$, including two factors of $a = \frac{1}{4\pi^2}$ to recover canonical normalization, we find $F(\ell) = -\frac{\tilde{\zeta}_a \tilde{\zeta}_b}{32\pi^2 \ell^2}$. Notice that this Casimir–Polder limit corresponds to a loop between a point and an infinitely thin membrane; it differs from the point–plate geometry of Section 5.1.2, where the width of the plate is quite large.

In the Casimir regime, one obtains

$$V(\ell) = -\frac{\sqrt{\pi d} \Gamma(d-1-\Delta)}{2^d \Gamma(1 + \frac{d}{2}) \Gamma(\frac{d-1-2\Delta}{2})} \frac{\tilde{\zeta}_b}{\ell^{2\Delta}}. \tag{86}$$

The potential depends only on ξ_b and is attractive for Δ in the interval of interest, $\frac{d-2}{2} \leq \Delta < \frac{d-1}{2}$. For $d = 3$ and 4 , one obtains the forces

$$F_{d=3}(\ell) = \Delta(\Delta - 1) \frac{\xi_b}{\ell^{2\Delta+1}} \quad \text{and} \quad (87)$$

$$F_{d=4}(\ell) = -\frac{\sqrt{\pi}\Delta\Gamma(3-\Delta)}{4\Gamma(\frac{3}{2}-\Delta)} \frac{\xi_b}{\ell^{2\Delta+1}}, \quad (88)$$

respectively.

For the free field in $d = 4$, including one factor of $a = \frac{1}{4\pi^2}$ to recover canonical normalization, one finds $F(\ell) = -\xi_b/(16\pi^2\ell^3)$. This reproduces exactly the Casimir force obtained from the plate–point configuration taken in the Dirichlet limit computed in Ref. [34]. This illustrates that, in the Casimir regime, only the boundary of the defect matters. The $V(\ell) \propto \ell^{-2\Delta}$ dependence in the Casimir regime is reminiscent of the feature that the \mathcal{O}^2 operator in a boundary CFT admits a vev with profile $\langle \mathcal{O}^2 \rangle \propto z^{-2\Delta}$.

5.2.2. Membrane–Membrane CFT Casimir

We turn to the force between two membranes at $z = 0$ and $z = \ell$. The two defects are parametrized as

$$J_a(\mathbf{x}) = \delta(z), \quad J_b(\mathbf{x}) = \delta(z - \ell). \quad (89)$$

The deformation of the defect is given by

$$\partial_\lambda J = -\xi_b L \partial_z \delta(z - \ell). \quad (90)$$

Following the same steps as in Section 5.1.1, we arrive at the quantum pressure

$$\frac{F(\ell)}{S_{d-2}} = -\frac{i\xi_b}{2} \int \frac{d^{d-1}p}{(2\pi)^{d-1}} \partial_z G_J(p; z, z)|_{z \rightarrow \ell}, \quad (91)$$

with $S_{d-2} = \int d^{d-2}x_\parallel$. The 2-point correlator in the presence of two membranes is computed in Equation (35).

Unlike in the other cases previously treated (see Equation (81)), it is not possible to identify a potential directly from Equation (91). This is due to the feature that the ∂_z derivative cannot be traded for a derivative in ℓ as soon as the dressed 2-point correlator depends nontrivially on ℓ ; see Equation (35). Rather, we first compute the force, which is the fundamental quantity, then one may optionally infer a potential from it.

Our focus is on the Casimir limit, which amounts to taking quite large $\xi_{a,b}$. Notice that one cannot use in Equation (91) the Dirichlet limit (36), for which $\xi_{a,b} = \infty$. This would lead to an indefinite $0 \times \infty$ form in Equation (91). Instead, one should compute the expansion of G_J for relatively large but finite $\xi_{a,b}$. The self-consistency of the quantum work formalism ensures that this expansion and the ξ_b factor in Equation (91) will conspire to give a finite result for the pressure.

One finds

$$\partial_z G_J(p; z, z)|_{z \rightarrow \ell} = \frac{1}{\xi_b} \frac{\partial_z(G^2(0, z))_{z \rightarrow \ell}}{G_0^2(p) - G^2(p; 0, \ell)} + O\left(\frac{1}{\xi_a}, \frac{1}{\xi_b}\right). \quad (92)$$

To obtain this result, we use that $\partial_z G(p; z, z')|_{z' \rightarrow z} = 0$ by symmetry. This sets to zero the would-be leading term $\xi_{a,b}^0$. As a result, the $1/\xi_b$ term is the leading one.

The quantum pressure between the membranes is then

$$\frac{F(\ell)}{S_{d-2}} = \frac{\pi^{\frac{d-1}{2}}}{2^{d-1}\Gamma(\frac{d-1}{2})} \int dq q^{d-2} \frac{\partial_z(G^2(q; 0, z))_{z \rightarrow \ell}}{G_0^2(q) - G^2(q; 0, \ell)}. \quad (93)$$

Using the identity

$$\partial_z \log(G(q; 0, z))|_{z \rightarrow \ell} = -\frac{qK_{\Delta-\frac{d}{2}+\frac{3}{2}}(q\ell)}{K_{\Delta-\frac{d}{2}+\frac{1}{2}}(q\ell)}, \tag{94}$$

one finds the final form

$$\frac{F(\ell)}{S_{d-2}} = \frac{\pi^{\frac{d-1}{2}}}{2^{d-5-2\Delta}\Gamma(\frac{d-1}{2})} \int dq q^{d-1} \frac{(q\ell)^{2d} K_{\Delta-\frac{d}{2}+\frac{3}{2}}(q\ell) K_{\Delta-\frac{d}{2}+\frac{1}{2}}(q\ell)}{2^{3+2\Delta}(q\ell)^{2d} K_{\Delta-\frac{d}{2}+\frac{1}{2}}^2(q\ell) - 2^d (q\ell)^{2\Delta+2d+1} \Gamma^2(\frac{d-1-2\Delta}{2})}. \tag{95}$$

As a sanity check, for a free field ($\Delta = (d - 2)/2$), one recovers exactly the known Casimir pressure between two membranes in any dimension [68]. The quantum pressure between the membranes is negative on the $\frac{d-2}{2} < \Delta < \frac{d-1}{2}$ interval. It is independent on $\xi_{a,b}$ and scales as $F(\ell)/S_{d-2} \propto 1/\ell^d$ as can be seen from Equation (95).

One can see that the Casimir regime displays a sense of universality. In the Casimir regime, the pressure does not depend on the strength of the double-trace couplings $\xi_{a,b}$. The pressure scales as ℓ^{-d} just like for a weakly coupled CFT; this scaling is dictated by the geometry of the problem. The sign of the force is also fixed; see Section 5.3 just below. The only non-trivial data are the strength of the force. One can check via numerical integration that the strength of the force does depend on Δ . Hence, in spite of the screening, information about the double-trace nature of the boundary still remains encoded in the overall coefficient of the pressure.

5.3. Monotonicity from Consistency

In all the previous results, it may seem that the $\xi_{a,b}$ coefficients can be arbitrary real numbers such that the $\xi_a \xi_b$ product can get both signs and thus that some of the forces may be either attractive or repulsive. Let us show that this is not the case.

From Section 5.1, it is clear that the quantum force between any two bodies in the Casimir–Polder (i.e., UV) regime has the sign of $-\xi_a \xi_b$, i.e., it is attractive (repulsive) if $\xi_a \xi_b > 0$ ($\xi_a \xi_b < 0$). On the other hand, we have found in Section 5.2 that the force between two membranes in the Casimir (i.e., IR) regime is negative independently of $\xi_{a,b}$. None of these observations in themselves constrain $\xi_{a,b}$, but one may note that if $\xi_a \xi_b < 0$, then the force would have to flip sign in the transition from Casimir–Polder to Casimir. To understand whether such a behavior is allowed, we need to consider the exact formulas that interpolate between the UV and IR regimes.

First, consider the point–membrane configuration given in Equation (79). We focus on the dressed 2-point correlator shown Equation (77). For $\frac{d-2}{2} \leq \Delta < \frac{d-1}{2}$, one has $G_0(p) \in \mathbb{R}_-$ for the spacelike or Euclidean momentum. This implies that if $\xi_a < 0$, then the dressed correlator features a pole at real negative p^2 . This is a tachyon, whose mass is

$$m_{\text{tachyon}}^2 = -4 \left(-\frac{\Gamma(\Delta)}{\pi^{\frac{d-1}{2}} \Gamma(\frac{d-1-2\Delta}{2}) \xi_a} \right)^{\frac{2}{2\Delta-d+1}}. \tag{96}$$

The presence of the tachyon pole has a firm consequence: having $\xi_a < 0$ would make the loop integral in Equation (79) divergent. Since the force must be finite, this possibility is ruled out. Therefore, ξ_a must be positive.

Similar analysis can be performed in the membrane–membrane configuration. For example, the same tachyon mass Equation (96) shows up if one lets one of the ξ_i be quite small. The tachyon pole also exists if, for example, $\xi_a = \xi_b$, in which case the tachyon mass receives a ℓ -dependent correction from the $G^2(p; 0, \ell)$ term. One concludes that again ξ_a and ξ_b must be positive.

Having $\xi_{a,b} > 0$ implies that the force does not change sign for any value of the separation ℓ . In other words, the absence of the tachyon is tied to the potential being monotonic.

A similar reasoning involving a tachyon has been applied for a double-trace deformation occupying all spacetime in Ref. [53]. In this study, the existence of the tachyon for $\zeta < 0$ is understood as an obstruction to the RG flow—while for $\zeta > 0$, there is no obstruction. Our argument here can be seen as an analogous version of this obstruction statement for a case where the double-trace deformation is localized on a membrane. The said obstruction appears particularly when computing the quantum force.

Let us briefly mention that in the $\frac{d-1}{2} < \Delta < \frac{d}{2}$ case, the sign of the $\Gamma(\frac{d-1-2\Delta}{2})$ factor that appears in Equation (96) becomes positive. Applying the above chain of arguments would then imply that ζ should be negative in this range of Δ . However, as pointed out in Section 3.2, the computations likely cannot be trusted in this domain—extra effort would be needed to appropriately treat the divergent piece in G_0 (see Equation (22)).

Finally, let the support of the defect, $J(x)$, be interpreted not just as an abstract distribution but as a physical density of matter. At the level of the Lagrangian, this is straightforwardly written covariantly by coupling \mathcal{O}^2 to the trace of the stress–energy tensor T_μ^μ , with

$$\mathcal{L} = -\frac{\zeta}{2m} \mathcal{O}^2 T_\mu^\mu(x), \tag{97}$$

with m as the mass of the matter particle. In the presence of non-relativistic static matter, we simply have $T_\mu^\mu(x) = \rho(x) = mn(x)$ with $n(x)$, the number density. Then, the generic $\zeta_{a,b}$ parameters that we have been using for each defect are related to a single fundamental coupling $\zeta_i = n_i \zeta$. In that view, any of the above arguments that constrain some of the ζ_a to be positive implies that $\zeta > 0$. It then follows that the ζ_i of any defects are positive; therefore, the potential between any two defects is monotonic. In other words, under the condition that J is interpretable as a physical density, the quantum force between any two defects is attractive at any value of their separation. (The notion of J being interpretable as a physical density is also needed to ensure the finiteness of the quantum work [34].)

5.4. Critical Casimir Forces

Here, we briefly connect our results to critical Casimir forces. We just present the scalings predicted from our double trace model in the geometries considered in Sections 5.1 and 5. For thermal fluctuations at criticality, the relevant quantity is $\beta_c \delta F$ with $\beta_c = 1/T_c$, where T_c is the critical temperature and δF is the geometry-dependent term of the free energy. $\beta_c \delta F$ has a vanishing mass dimension.

In the Euclidean field theory, the coupling of the double trace operator to the source is $\frac{1}{2} \int d^d x_E \zeta \mathcal{O}^2(x_E) J(x_E)$. The ζ coupling has a scaling dimension $[\zeta] = d - [J] - 2\Delta$. The behavior of the forces follows by dimensional analysis.

The free energy in the short distance limit gives non-retarded van der Waals forces. In the point–point, plate–point and plate–plate geometries, one obtains

$$\beta_c \delta F|_{\text{pt-pt}} \propto \frac{\zeta_a \zeta_b}{\ell^{4\Delta}}, \quad \beta_c \delta F|_{\text{plate-pt}} \propto \frac{\zeta_a \zeta_b}{\ell^{4\Delta-d}}, \quad \beta_c \delta F|_{\text{plate-plate}} \propto \frac{\zeta_a \zeta_b}{\ell^{4\Delta-2d}}. \tag{98}$$

In the long distance limit, this gives Casimir-type forces. The membrane–point and membrane–membrane results are:

$$\beta_c \delta F|_{\text{memb-pt}} \propto \frac{\zeta}{\ell^{2\Delta}}, \quad S_{d-1}^{-1} \beta_c \delta F|_{\text{memb-memb}} \propto \frac{1}{\ell^{d-1}}. \tag{99}$$

ζ is the coupling to the pointlike defect. The couplings to the membranes do not appear in the Casimir limit. In the membrane–membrane case, we give the free energy per units of area of the membrane, S_{d-1} . The point–point and membrane–point results match the predictions made from limits of the sphere–sphere geometry in the critical Ising model [69–71].

6. Summary

We explore the quantum forces occurring between the defects and/or boundaries of conformal field theories. While defect CFTs are often investigated formally, our approach here is much firmer. Since such CFTs do exist in the laboratory, our focus is to predict phenomena that may, at least in principle, be experimentally observed. Our computations only require basic notions of CFT and a solid formalism to derive quantum forces in arbitrary situations.

Defects and boundaries in the real world are not ideal, in the sense that no real-world material can truncate the spatial support of a field theory fluctuating at all wavelengths. Inspired by models used in weakly coupled QFT, we propose to model the imperfect defects of CFTs as localized relevant double-trace operators. This idea is nicely supported by the Δ_- branch of the AdS/CFT correspondence, in which case the defects are identified as mass terms localized on the (regularized) boundary of the Poincaré patch.

In order to compute quantum forces, one needs to know the 2-point CFT correlators in the presence of such “double-trace” defects. Assuming relatively large N , this is described by a Born series that dresses the CFT correlator with insertions of the defect.

We first clarify that the CFT correlators get repelled from the defects in the infrared regime. Asymptotically in the IR, the CFT satisfies a Dirichlet condition on the boundary of the defect. In this limit, the interior of the defect becomes irrelevant.

The archetype of an extended defect is the codimension-one hyperplane, i.e., the membrane. In the presence of a membrane, we restrict the conformal dimension to $\frac{d-2}{2} \leq \Delta < \frac{d-1}{2}$ to avoid dealing with a divergence in the membrane-to-membrane correlator. A careful analysis of the $\Delta > \frac{d-1}{2}$ case remains to be performed.

We compute the 2-point correlator in the presence of two parallel membranes and investigate some of its features. We find that the CFT between the membranes develops a sequence of poles away from the real axis, which should be understood as a set of resonances, or collective excitations, of the CFT constituents. In the near-free limit, these resonances are narrow with the decay rate depending only on the separation between the two membranes and on the dimension of the double-trace operator. It would be interesting to study further the properties of these resonances, including their interactions.

We then explore the quantum forces between pointlike and/or planar double-trace defects in the asymptotic Casimir–Polder and Casimir regimes. The Casimir–Polder regime typically appears at a short separation, i.e., in the UV, when the first term of the Born series is leading. The CFT Casimir–Polder force between a pointlike defect and another pointlike defect, a membrane, or an infinite plate, is respectively proportional to $1/\ell^{4\Delta-2}$, $1/\ell^{4\Delta-d+2}$, $1/\ell^{4\Delta-d+1}$. The force between two infinite plates is in $1/\ell^{4\Delta-d}$.

The Casimir regime appears at large enough separation, i.e., in the IR, when the Born series must be resummed. The Casimir force between a point and a membrane is $1/\ell^{2\Delta+1}$, while the pressure between two membranes is $1/\ell^d$. The membrane–membrane quantum pressure has, in a sense, a universal behavior analogous to the one induced from free fields. However, information about the double-trace nature of the boundary still remains in the overall coefficient of the force, which is Δ -dependent.

In membrane configurations, we show that the sign of the double-trace operator is constrained in order for the potential to be well defined at any distance. This is tied to requiring the absence of a tachyon in the spectrum of the 2-point correlator. In turn, this constraint guarantees that the potential is monotonic. Assuming that the support of the defects can be interpreted as a physical matter distribution—an assumption that is also needed to ensure the finiteness of the quantum work—one concludes that the potential between any two defects is monotonic. Hence, the quantum forces between any two double-trace defects are attractive at any distance.

It would be interesting to determine real-world systems—either quantum or critical—for which the defects and boundaries may, at least approximately, be described by double-trace deformations. It would also be interesting to devise laboratory experiments that can test

some of the phenomena predicted in this paper. The exploration of these possibilities is left for future work.

Author Contributions: Conceptualization, P.B. and S.F.; writing—original draft preparation, P.B. and S.F.; writing—review and editing, P.B. and S.F. All authors have read and agreed to the published version of the manuscript.

Funding: This research received no external funding.

Data Availability Statement: No data used in this work.

Conflicts of Interest: The authors declare no conflict of interest.

Appendix A. 2-Point Correlator in Mixed Space

The Schwinger parametrization is

$$\frac{1}{x_{12}^{2\Delta}} = \frac{1}{\Gamma(\Delta)} \int_0^\infty \frac{dt}{t} t^\Delta e^{-tx_{12}^2}. \tag{A1}$$

We use parametrization (A1) to compute the Fourier transform

$$\begin{aligned} \langle\langle \mathcal{O}(p, z_1) \mathcal{O}(-p, z_2) \rangle\rangle &= \int d^{d-1} y_{12} e^{iy_{12} \cdot p} \frac{1}{x_{12}^{2\Delta}} \\ &= \frac{1}{\Gamma(\Delta)} \int_0^\infty \frac{dt}{t} t^\Delta e^{-tz_{12}^2} \int d^{d-1} y_{12} e^{iy_{12} \cdot p} e^{-ty_{12}^2} \\ &= -i \frac{\pi^{\frac{d-1}{2}}}{\Gamma(\Delta)} \int_0^\infty \frac{dt}{t} t^{\Delta - \frac{d-1}{2}} e^{-tz_{12}^2 + \frac{p^2}{4t}}. \end{aligned} \tag{A2}$$

In Equation (A2), the time integral is evaluated upon Wick rotation to the Euclidean space, $y_{12}^0 = -iy_{12}^{0,E}$, which makes the overall $-i$ factor appear. In Equation (A2), one recognizes the integral representation of the Bessel K (6), which one can put in the form

$$\int_0^\infty \frac{dt}{t} t^{\Delta - \frac{d-1}{2}} e^{-tz^2 - \frac{q^2}{4t}} = 2 \left(\frac{q}{2z}\right)^{\Delta - \frac{d-1}{2}} K_{\Delta - \frac{d-1}{2}}(qz). \tag{A3}$$

We remind that $K_\alpha(z) = K_{-\alpha}(z)$. Identifying Equation (A3) in Equation (A2), one obtains the momentum–position representation of the 2-point correlator (5).

Appendix B. Computation of the Decay Widths

Consider the denominator of Equation (36),

$$D(p) = G_0^2(p) - G^2(p; 0, L). \tag{A4}$$

For $\Delta = d - 2/2$, one has

$$D(p) = \frac{4\pi^d}{\Gamma^2\left(\frac{d-2}{2}\right)} \frac{1 - e^{-2L\sqrt{-p^2}}}{p^2}. \tag{A5}$$

In that case, $D(p)$ has a set of zeros on the real line $D(m_n^{\text{free}}) = 0$ at the values $p = m_n^{\text{free}} \equiv n\pi/L$, $n \in \mathbb{N}_{/0}$. These are the familiar modes of the free field confined in a $[0, L]$ Dirichlet interval.

For Δ close to the free field dimension, one can expand the denominator in $\epsilon = \Delta - \frac{d-2}{2}$. This produces a relatively small correction to Equation (A5). One obtains

$$D(p) \approx \frac{4\pi^d}{\Gamma^2\left(\frac{d-2}{2}\right)} \left(\frac{\sqrt{-p^2}}{L}\right)^\epsilon \frac{\left(L\sqrt{-p^2}\right)^{2\epsilon} - e^{-2L\sqrt{-p^2}}}{p^2}. \tag{A6}$$

By continuity, the poles are given by $m_n = m_n^{\text{free}} + \epsilon\delta_{n,r} + i\epsilon\delta_{n,i} + O(\epsilon^2)$.

We assume that the imaginary part of the δ -correction is negative, $\delta_{n,i} < 0$. Plugging this form into Equation (A6) and expanding in ϵ determines the δ corrections. One finds

$$\delta_{n,r} = -\epsilon \log\left(\frac{n\pi}{L}\right), \quad (\text{A7})$$

$$\delta_{n,i} = -\epsilon \frac{\pi}{2L}. \quad (\text{A8})$$

One has, thus, $\delta_{n,i} < 0$, consistent with our hypothesis. These poles describe narrow resonances. In particle physics, the imaginary part is commonly written as

$$\delta_{n,i} \equiv -\frac{\Gamma_n}{2}, \quad (\text{A9})$$

where $\Gamma_n \ll m_n$ is the decay rate, i.e., the width of the resonance. This leads to the formula (42).

References

1. Casimir, H.B.G.; Polder, D. The influence of retardation on the London–van der Waals forces. *Phys. Rev.* **1948**, *73*, 360–372. [CrossRef]
2. Casimir, H.B.G. On the attraction between two perfectly conducting plates. *Proc. Kon. Ned. Akad. Wetensch. B* **1948**, *51*, 793–795. Available online: <https://dwc.knaw.nl/DL/publications/PU00018547.pdf> (accessed on 2 February 2024).
3. Milton, K.A. The Casimir effect: Recent controversies and progress. *J. Phys. A Math. Gen.* **2004**, *37*, R209–R277. [CrossRef]
4. Klimchitskaya, G.L.; Mohideen, U.; Mostepanenko, V.M. The Casimir force between real materials: Experiment and theory. *Rev. Mod. Phys.* **2009**, *81*, 1827–1885. [CrossRef]
5. Woods, L.M.; Dalvit, D.A.R.; Tkatchenko, A.; Rodriguez-Lopez, P.; Rodriguez, A.W.; Podgornik, R. Materials perspective on Casimir and van der Waals interactions. *Rev. Mod. Phys.* **2016**, *88*, 045003. [CrossRef]
6. Bimonte, G.; Emig, T.; Kardar, M.; Krüger, M. Nonequilibrium fluctuational quantum electrodynamics: Heat radiation, heat transfer, and force. *Ann. Rev. Condens. Matter Phys.* **2017**, *8*, 119–143. [CrossRef]
7. Bimonte, G.; Emig, T.; Graham, N.; Kardar, M. Something can come of nothing: Quantum fluctuations and the Casimir force. *Annu. Rev. Nucl. Part. Sci.* **2022**, *72*, 93–118. [CrossRef]
8. Bordag, M.; Klimchitskaya, G.L.; Mohideen, U.; Mostepanenko, V.M. *Advances in the Casimir Effect*; Oxford University Press: New York, NY, USA, 2009. [CrossRef]
9. Poland, D.; Simmons-Duffin, D. Snowmass white paper: The numerical conformal bootstrap. *arXiv* **2022**, arXiv:2203.08117. [CrossRef]
10. Dantchev, D.M.; Dietrich, S. Critical Casimir effect: Exact results. *Phys. Rep.* **2023**, *1005*, 1–130. [CrossRef]
11. McAvity, D.M.; Osborn, H. Conformal field theories near a boundary in general dimensions. *Nucl. Phys. B* **1995**, *455*, 522–576. [CrossRef]
12. Liendo, P.; Rastelli, L.; van Rees, B.C. The bootstrap program for boundary CFT_d. *J. High Energy Phys.* **2013**, *2013*, 113. [CrossRef]
13. Gaiotto, D.; Mazac, D.; Paulos, M.F. Bootstrapping the 3d Ising twist defect. *J. High Energy Phys.* **2014**, *2014*, 100. [CrossRef]
14. Gliozzi, F.; Liendo, P.; Meineri, M.; Rago, A. Boundary and interface CFTs from the conformal bootstrap. *J. High Energy Phys.* **2015**, *2015*, 36. [CrossRef]
15. Billò, M.; Gonçalves, V.; Lauria, E.; Meineri, M. Defects in conformal field theory. *J. High Energy Phys.* **2016**, *2016*, 91. [CrossRef]
16. Behan, C.; Di Pietro, L.; Lauria, E.; Van Rees, B.C. Bootstrapping boundary-localized interactions. *J. High Energy Phys.* **2020**, *2020*, 182. [CrossRef]
17. Behan, C.; Di Pietro, L.; Lauria, E.; van Rees, B.C. Bootstrapping boundary-localized interactions II. Minimal models at the boundary. *J. High Energy Phys.* **2022**, *2022*, 146. [CrossRef]
18. Barrat, J.; Gimenez-Grau, A.; Liendo, P. A dispersion relation for defect CFT. *J. High Energy Phys.* **2023**, *2023*, 255. [CrossRef]
19. Bianchi, L.; Bonomi, D. Conformal dispersion relations for defects and boundaries. *SciPost Phys.* **2023**, *2023*, 55. [CrossRef]
20. Gimenez-Grau, A.; Lauria, E.; Liendo, P.; van Vliet, P. Bootstrapping line defects with O₂ global symmetry. *J. High Energy Phys.* **2022**, *2022*, 18. [CrossRef]
21. Antunes, A.; Behan, C. Coupled minimal conformal field theory models revisited. *Phys. Rev. Lett.* **2023**, *130*, 071602. [CrossRef]
22. Bianchi, L.; Bonomi, D.; de Sabbata, E. Analytic bootstrap for the localized magnetic field. *J. High Energy Phys.* **2023**, *2023*, 69. [CrossRef]
23. Gimenez-Grau, A. Probing magnetic line defects with two-point functions. *arXiv* **2022**, arXiv:2212.02520. [CrossRef]
24. Söderberg Rousu, A. The discontinuity method in a BCFT. *arXiv* **2023**, arXiv:2304.02271. [CrossRef]
25. Barrat, J.; Liendo, P.; van Vliet, P. Line defect correlators in fermionic CFTs. *arXiv* **2023**, arXiv:2304.13588. [CrossRef]
26. Cuomo, G.; Zhang, S. Spontaneous symmetry breaking on surface defects. *J. High Energ. Phys.* **2024**, *2024*, 22. [CrossRef]

27. Behan, C.; Lauria, E.; Nocchi, M.; van Vliet, P. Analytic and numerical bootstrap for the long-range Ising model. *J. High Energy Phys.* **2024**, *2024*, 136. [CrossRef]
28. Andrei, N.; Bissi, A.; Buican, M.; Cardy, J.; Dorey, P.; Drukker, N.; Erdmenger, J.; Friedan, D.; Fursaev, D.; Konechny, A.; et al. Boundary and defect CFT: Open problems and applications. *J. Phys. A Math. Gen.* **2020**, *53*, 453002. [CrossRef]
29. Herzog, C.P. Conformal Field Theory with Boundaries and Defects. Lectures at the Lezioni Avanzate di Campi E Stringhe (LACES), Arcetri, Italy, 29 November–17 December 2021. Available online: <https://www.ggi.infn.it/laces/LACES21/CFTdefects21.html> (accessed on 2 February 2024).
30. Graham, N.; Jaffe, R.L.; Khemani, V.; Quandt, M.; Scandurra, M.; Weigel, H. Casimir energies in light of quantum field theory. *Phys. Lett. B* **2003**, *572*, 196–201. [CrossRef]
31. Graham, N.; Jaffe, R.L.; Khemani, V.; Quandt, M.; Scandurra, M.; Weigel, H. Calculating vacuum energies in renormalizable quantum field theories: A New approach to the Casimir problem. *Nucl. Phys. B* **2002**, *645*, 49–84. [CrossRef]
32. Graham, N.; Jaffe, R.L.; Khemani, V.; Quandt, M.; Schroeder, O.; Weigel, H. The Dirichlet Casimir problem. *Nucl. Phys. B* **2004**, *677*, 379–404. [CrossRef]
33. Brax, P.; Fichet, S. Quantum chameleons. *Phys. Rev. D* **2019**, *99*, 104049. [CrossRef]
34. Brax, P.; Fichet, S. Scalar-mediated quantum forces between macroscopic Bodies and interferometry. *Phys. Dark Univ.* **2023**, *42*, 101294. [CrossRef]
35. Cardy, J.L. Effect of boundary conditions on the operator content of two-dimensional conformally invariant theories. *Nucl. Phys. B* **1986**, *275*, 200–218. [CrossRef]
36. Kleban, P.; Vassileva, I. Free energy of rectangular domains at criticality. *J. Phys. A Math. Gen.* **1991**, *24*, 3407–3412. [CrossRef]
37. Eisenriegler, E. Anisotropic colloidal particles in critical fluids. *J. Chem. Phys.* **2004**, *121*, 3299–3322. [CrossRef] [PubMed]
38. Bimonte, G.; Emig, T.; Kardar, M. Conformal Field theory of critical Casimir interactions in 2D. *EPL (Europhys. Lett.)* **2013**, *104*, 21001. [CrossRef]
39. Geng, H.; Lüst, S.; Mishra, R.K.; Wakeham, D. Holographic BCFTs and communicating black holes. *J. High Energy Phys.* **2021**, *2021*, 3. [CrossRef]
40. Rychkov, S. *EPFL Lectures on Conformal Field Theory in $D \geq 3$ Dimensions*; Springer: Cham, Switzerland, 2017. [CrossRef]
41. Simmons-Duffin, D. The conformal bootstrap. In *TASI 2015: New Frontiers in Fields and Strings*; Polchinski, J., De Wolfe, O., Eds.; World Scientific Co., Ltd.: Singapore, 2017; pp. 1–74. [CrossRef]
42. Poland, D.; Rychkov, S.; Vichi, A. The conformal bootstrap: Theory, numerical techniques, and applications. *Rev. Mod. Phys.* **2019**, *91*, 015002. [CrossRef]
43. Chester, S.M. Weizmann lectures on the numerical conformal bootstrap. *Phys. Rep.* **2023**, *1045*, 1–44. [CrossRef]
44. Qualls, J.D. Lectures on conformal field theory. *arXiv* **2015**, arXiv:1511.04074. [CrossRef]
45. Gillioz, M. *Conformal Field Theory for Particle Physicists: From QFT Axioms to the Modern Conformal Bootstrap*; Springer: Berlin/Heidelberg, Germany, 2023. [CrossRef]
46. Greenberg, O.W. Generalized free fields and models of local field theory. *Ann. Phys.* **1961**, *16*, 158–176. [CrossRef]
47. Kaplan, J. Lectures on AdS/CFT from the Bottom Up. Available online: <https://sites.krieger.jhu.edu/jared-kaplan/writing/> (accessed on 2 February 2024).
48. Dymarsky, A.; Farnsworth, K.; Komargodski, Z.; Luty, M.A.; Prilepina, V. Scale invariance, conformality, and generalized free fields. *J. High Energy Phys.* **2016**, *2016*, 99. [CrossRef]
49. Fichet, S.; Megias, E.; Quiros, M. Continuum effective field theories, gravity, and holography. *Phys. Rev. D* **2023**, *107*, 096016. [CrossRef]
50. Schwinger, J.S.; DeRaad, L.L., Jr.; Milton, K.A. Casimir effect in dielectrics. *Ann. Phys.* **1979**, *115*, 1–23. [CrossRef]
51. Franchino-Viñas, S.A.; Mantiñan, M.N.; Mazzitelli, F.D. Quantum vacuum fluctuations and the principle of virtual work in inhomogeneous backgrounds. *Phys. Rev. D* **2022**, *105*, 085023. [CrossRef]
52. Bimonte, G.; Emig, T. Unifying theory for Casimir forces: Bulk and surface formulations. *Universe* **2021**, *7*, 225. [CrossRef]
53. Porrati, M.; Yu, C.C.Y. Notes on relevant, irrelevant, marginal and extremal double trace perturbations. *J. High Energy Phys.* **2016**, *2016*, 40. [CrossRef]
54. Brézin, E.; Wallace, D.J. Critical behavior of a classical Heisenberg ferromagnet with many degrees of freedom. *Phys. Rev. B* **1973**, *7*, 1967–1974. [CrossRef]
55. Wilson, K.G.; Kogut, J.B. The Renormalization group and the epsilon expansion. *Phys. Rep.* **1974**, *12*, 75–199. [CrossRef]
56. Aharony, O.; Gubser, S.S.; Maldacena, J.M.; Ooguri, H.; Oz, Y. Large N field theories, string theory and gravity. *Phys. Rep.* **2000**, *323*, 183–386. [CrossRef]
57. Zaffaroni, A. Introduction to the AdS–CFT correspondence. *Class. Quant. Grav.* **2000**, *17*, 3571–3597. [CrossRef]
58. Nastase, H. Introduction to AdS–CFT. *arXiv* **2007**, arXiv:0712.0689. [CrossRef]
59. Klebanov, I.R.; Witten, E. AdS/CFT correspondence and symmetry breaking. *Nucl. Phys. B* **1999**, *556*, 89–114. [CrossRef]
60. Mueck, W. An Improved correspondence formula for AdS/CFT with multitrace operators. *Phys. Lett. B* **2002**, *531*, 301–304. [CrossRef]
61. Giombi, S.; Kirilin, V.; Perlmutter, E. Double-trace deformations of conformal correlations. *J. High Energy Phys.* **2018**, *2018*, 175. [CrossRef]
62. Geng, H. Open AdS/CFT via a double trace deformation. *arXiv* **2023**, arXiv:2311.13633. [CrossRef]

63. Fichtel, S. Braneworld effective field theories—Holography, consistency and conformal effects. *J. High Energy Phys.* **2020**, 2020, 16. [CrossRef]
64. Brax, P.; Fichtel, S.; Pignol, G. Bounding quantum dark forces. *Phys. Rev. D* **2018**, *97*, 115034. [CrossRef]
65. Brax, P.; Fichtel, S.; Tanedo, P. The warped dark sector. *Phys. Lett. B* **2019**, *798*, 135012. [CrossRef]
66. Costantino, A.; Fichtel, S.; Tanedo, P. Exotic spin-dependent forces from a hidden sector. *J. High Energy Phys.* **2020**, 2020, 148. [CrossRef]
67. Chaffey, I.; Fichtel, S.; Tanedo, P. Continuum-mediated self-interacting dark matter. *J. High Energy Phys.* **2021**, 2021, 8. [CrossRef]
68. Ambjorn, J.; Wolfram, S. Properties of the vacuum. 1. Mechanical and thermodynamic. *Ann. Phys.* **1983**, *147*, 1–32. [CrossRef]
69. Burkhardt, T.W.; Eisenriegler, E. Casimir interaction of spheres in a fluid at the critical point. *Phys. Rev. Lett.* **1995**, *74*, 3189–3192. [CrossRef] [PubMed]
70. Eisenriegler, E.; Ritschel, U. Casimir forces between spherical particles in a critical fluid and conformal invariance. *Phys. Rev. B* **1995**, *51*, 13717–13734. [CrossRef]
71. Hanke, A.; Schlesener, F.; Eisenriegler, E.; Dietrich, S. Critical Casimir forces between spherical particles in fluids. *Phys. Rev. Lett.* **1998**, *81*, 1885–1888. [CrossRef]

Disclaimer/Publisher’s Note: The statements, opinions and data contained in all publications are solely those of the individual author(s) and contributor(s) and not of MDPI and/or the editor(s). MDPI and/or the editor(s) disclaim responsibility for any injury to people or property resulting from any ideas, methods, instructions or products referred to in the content.

Article

The Normal Casimir Force for Lateral Moving Planes with Isotropic Conductivities

Nail Khusnutdinov * and Natalia Emelianova

Centro de Matemática, Computação e Cognição, Universidade Federal do ABC, Santo André 09210-170, SP, Brazil; natalia7emelianova@gmail.com

* Correspondence: nail.khusnutdinov@gmail.com

Abstract: We consider the two planes at zero temperature with isotropic conductivity that are in relative lateral motion with velocity v and interplane distance a . Two models of conductivity are taken into account—the constant and frequency-dependent Drude models. The normal (perpendicular to planes) Casimir force is analyzed in detail for two systems—(i) two planes with identical conductivity and (ii) one plane that is a perfect metal. The velocity correction to the Casimir energy, $\Delta_v \mathcal{E} \propto v^2$, for small enough velocities is used for all considered cases. In the case of constant conductivity, η , the energy correction is $\Delta_v \mathcal{E} \propto \eta/a^3 (v/\eta)^2$ for $v \ll \eta \ll 1$.

Keywords: dynamic Casimir effect; lateral motion; constant conductivity

1. Introduction

The Casimir effect was initially considered for perfect conductive plates, and has now been extended to many non-ideal and new materials [1,2]. Hendrik Casimir noted in Ref. [3] that Niels Bohr suggested considering the zero-point energy as an origin of this effect and simplifying the derivation of the force. In the case of perfect conductive planes, the Casimir effect relies solely on fundamental constants and interplane distance. However, for actual materials, the Casimir effect depends on various factors, such as the shape and structure of the material, conductivity, chemical potential, temperature, and the presence of impurities [1,2].

The Casimir force between bodies is further influenced by their relative motions (see the recent review on the dynamic Casimir effect [4] and Refs. [1,5,6]). The relative motions are lateral (parallel to the planes), perpendicular to planes, or, in general, a combination of these. The Casimir effect for perpendicularly and uniformly moving slabs was first considered in Refs. [7,8] for electromagnetic and massless scalar fields. It is a direct consequence of the quantum field theory with moving boundaries [9]. In the non-relativistic scenario, the velocity correction to the Casimir pressure is quadratic, $\propto v^2$ ($\propto v^2/c^2$ in dimensional units, where c denotes the speed of light) for both fields, but with opposite signs. For the scalar field, the relative velocity correction for Casimir pressure is $\delta \mathcal{P} = (\mathcal{P} - \mathcal{P}_{v=0})/\mathcal{P} = \frac{8}{3}v^2$, while for the electromagnetic field is $\delta \mathcal{P} = -(10/\pi^2 - 2/3)v^2$.

For the massless scalar field, $\delta \mathcal{P}$, while is negative for the electromagnetic case.

The lateral relative motion of different planes gives rise to two distinct Casimir pressures in perpendicular directions. One of these pressures acts normally to planes, similar to perpendicular motion, while the other acts along planes, known as quantum, non-contact, or Casimir friction. The study of normal force has been carried out in earlier studies [10,11] for layers in stratified dielectric media with magneto-electric and non-reciprocal constant coupling, and for plates with general electric permittivity and magnetic permeability, respectively. For a three-layer system [10], the force can be either attractive or repulsive depending on the velocity directions of the extreme layers. In the non-relativistic case, the velocity correction to the force becomes repulsive when the extreme

Citation: Khusnutdinov, N.; Emelianova, N. The Normal Casimir Force for Lateral Moving Planes with Isotropic Conductivities. *Physics* **2024**, *6*, 148–163. <https://doi.org/10.3390/physics6010011>

Received: 13 November 2023

Revised: 16 December 2023

Accepted: 2 January 2024

Published: 26 January 2024



Copyright: © 2024 by the authors. Licensee MDPI, Basel, Switzerland. This article is an open access article distributed under the terms and conditions of the Creative Commons Attribution (CC BY) license (<https://creativecommons.org/licenses/by/4.0/>).

layers have the same velocity directions with respect to the middle layer, and becomes attractive for opposite velocity directions. The velocity correction to the Casimir energy follows a similar order of magnitude, approximately proportional to v^2 . For relativistic velocities, both attractive and repulsive effects can occur. A general expression for the normal force between two plates was obtained in Ref. [11] using the Fresnel reflection coefficients. It was shown that the same quadratic correction $\propto v^2$, applies to the ordinary Casimir force.

Quantum friction is a more challenging topic for analysis and is currently a subject of debate [11–24], with some even negating its existence [11]. Two dielectric planes at different temperatures with lateral relative motion have been considered in Refs. [12,13]. The quantum friction force was calculated within the framework of Rytov fluctuation theory [25]. It was demonstrated that the force is proportional to the first power of the velocity v , but can have different signs, resulting in either the deceleration or acceleration of the planes. Mkrtchian investigated two conductive planes with relative lateral motion and calculated the force and viscosity of vacuum for different plane impedance models [14]. The dependence of the force on the interplane distance heavily relies on the chosen model, but in any case, the velocity correction to the typical Casimir force proportional v emerges as the typical dependence for Casimir friction. The quantum friction for planes with temporally dispersive conductivity was analyzed in Ref. [15], revealing a cubic, v^3 , dependence at relatively small velocities and a $v^{-1} \ln v$ -dependence at quite high velocities. In Ref. [16] a general theory for quantum friction within the framework of fluctuation electrodynamics was developed. Though Ref. [11] claims the absence of quantum friction as a whole, the existence of a normal force remains without doubt (see Ref. [17]).

The study of quantum friction using scattering theory was carried out in Refs. [18,19], demonstrating the existence of a quantum friction threshold: the friction force is zero when the relative velocity is smaller than the speed of light within the slabs' materials. The origin of quantum friction was connected to quantum Cherenkov radiation: the super-luminally moving object spontaneously emits photons. This concept is closely related to super-radiance, where a rotating body amplifies incident waves [26]. In Refs. [20,21], quantum friction was calculated for two graphene sheets using the effective action approach, revealing a velocity threshold: the friction is zero when the relative velocity is smaller than the Fermi velocity. The correlation of threshold with the findings of Refs. [18,19] arises from the feature that the Dirac electron in graphene is described by the Dirac equation with the Fermi velocity instead of the speed of light. The threshold was confirmed through different calculations in Ref. [24]. The nonperturbative approach was employed to study quantum friction in Ref. [22], where the friction force was associated with electromagnetic instability: the kinetic energy of the relative motion transforms into exponentially growing coherent radiation.

In this study, we investigate the normal force between two laterally moving planes with isotropic conductivities. Previously [24], a general approach was developed for two conductive planes with relative lateral motion, which allowed for the calculation of both normal and tangential forces. The normal force was found to reduce to the typical Casimir force for planes with tensorial conductivities [27], with a specific form for the tensor of the moving plane being used. Quantum friction was also found to arise as an imaginary part of the energy calculated for complex frequencies, as discussed in the earlier papers [28–30].

In the current paper, we focus specifically on the normal force for laterally moving planes with isotropic conductivities. As noted in the earlier studies [31,32], Ohm's law for the moving plane needs to be considered carefully. The Lorentz transformation for a moving plane with scalar constant conductivity is not straightforward, as it involves a coefficient between three vectors of the electric current and an electric field. The transformation law of the conductivity tensor was discussed previously in Ref. [32] utilizing a linear response tensor [33]. In the case of graphene, the linear response tensor plays the role of polarization tensor [24,34]. To obtain the isotropic conductivity of a moving plane, we adopt the approach suggested in Ref. [24] for graphene and consider the formal limit

where the Fermi velocity and mass gap tend to zero. In this limit, the conductivity tensor becomes isotropic in the co-moving frame of the plane. However, in the laboratory frame, the conductivity is not diagonal and depends on the velocity. It is worth noting that here we employ the graphene approach as a computational tool only. The results obtained are applicable to various compositions with isotropic conductivity, including those with temporal dispersion (not considered in Ref. [10]).

In previous studies [6,35–37], the Casimir and Casimir–Polder effects for planes with isotropic conductivity were explored. Two models of conductivity were employed: (i) the constant conductivity, $\sigma = \sigma_0 \mathbf{I}$, where σ_0 denotes the scalar constant conductivity, and \mathbf{I} is the 2×2 unit matrix, and (ii) the Drude–Lorentz model with seven oscillators $\sigma = \sigma_{\text{DL}}(\omega) \mathbf{I}$,

$$\sigma_{\text{DL}}(\omega) = \frac{f_0 \omega_p^2}{\gamma_0 - i\omega} + \sum_{j=1}^7 \frac{i\omega f_j \omega_p^2}{\omega^2 - \omega_j^2 + i\omega \gamma_j},$$

with the parameters of this model obtained from experimental data for graphite from Ref. [38]. Here, f_j, ω_j and γ_j denote parameters of the model, ω is the frequency and 0 subscript notifies the Drude contribution. The first term in the model represents a Drude-like contribution, while the other terms have a Lorentz-like form. Since graphene is a single layer of graphite, the conductivity of graphene is obtained by multiplying the above expression by the interplane distance in graphite. The estimation of the binding energy per single sheet of graphene in graphite (a stack of graphenes) made in Ref. [36] revealed that the constant conductivity model underestimates the binding energy, whereas the Drude–Lorentz seven-oscillator model aligns well with the experimental data.

Both models were employed to describe the Casimir effect in a stack of graphene layers and the Casimir–Polder effect for a micro-particle near the stack. The general case of a layered system consisting of conductive planes with tensorial conductivities was analyzed in Ref. [39]. This study demonstrated that the expressions for force and energy have the same form as those obtained for the case of scalar constant conductivity, but with corresponding reflection coefficients for transverse electric (TE) and transverse magnetic (TM) modes.

In the case of constant conductivity, the Casimir energy exhibits a $1/a^3$ -dependence for all interplane distances. However, this relationship only holds for large interplane distances in the case of graphene, where the parameter ma is much greater than one (m is mass gap). This can be straightforwardly explained by noting that in the constant conductivity model, there are no dimensional parameters other than the interplane distance. For the case of small conductivity ($\eta_{\text{gr}} = 2\pi\sigma_{\text{gr}} = 0.0114$ for graphene), the TM mode contributes linearly in η , while the TE mode contributes as η^2 . However, this is not the case for two graphenes, where both modes contribute quadratically. As previously mentioned in Ref. [24], the spatial dispersion of conductivity plays an important role in the Casimir effect, causing the contribution to change from linear to quadratic.

The paper is organized as follows. In Section 2, we re-derive the conductivity of a moving graphene sheet by applying boundary conditions and obtain the main formula for normal Casimir energy. We discuss the problem of determining the eigenvalues of the product of reflection matrices. The Fresnel matrices do not commute, and their eigenvalues are not simply the product of the eigenvalues of the individual reflection matrices. Additionally, we briefly discuss the general property of lateral force along the planes and demonstrate that the necessary condition for this force is that the modulus of the Fresnel matrices is greater than one, indicating the production of photons. In Section 3, we obtain the expressions for the normal Casimir force for isotropic conductivity in two scenarios: (i) two identical planes and (ii) an isotropic plane and a perfect metal. We perform numerical calculations of the Casimir energy and analytically derive the v^2 -dependence for the velocity correction to the energy and pressure. We also evaluate the Drude-like model of isotropic conductivity numerically and demonstrate that, for large distances, the Drude-like model yields quite similar results to the constant conductivity model. Finally, in the conclusion in Section 4, we discuss the results obtained in this study.

Throughout this paper, the natural units with $\hbar = c = 1$ are used; here, \hbar represents the reduced Planck's constant.

2. The Casimir Energy of Moving Planes

We use the approach for the Casimir effect of lateral moving graphene developed in Ref. [24] as a computational trick. In order to provide a comprehensive understanding of this approach, let us review the key steps of derivations of the normal force outlined in Ref. [24] with some expanded explanations.

The system under consideration involves two parallel conductive planes with isotropic conductivities and an interplane distance, a . The first plane remains stationary in the laboratory frame, while the second plane undergoes lateral motion with a velocity v . The fluctuating electric field induces a current in the second plane following Ohm's law. This current affects the boundary condition and ultimately alters the energy spectrum. The current induced in the second conductive plane, which is in motion, is described by Ohm's law in its co-moving frame. To solve the scattering problem in the laboratory frame, it is necessary to determine the conductivity of the second plane in laboratory frame. The Lorentz transformation of Ohm's law was discussed in Ref. [31,32]. Given that Ohm's law has no covariant form, as it represents a linear relationship between the three-vector of the electric field and current density, the method of linear response tensor, $\Pi^{\mu\nu}$ [33], is preferred in this particular case. Within the framework of this approach, the four-vector, J^μ , of the current density and the four-potential, A^ν , are linearly connected through a tensor of linear response: $J^\mu = \Pi^\mu_\nu A^\nu$. Here, the Greek letter indices denote the time (0) and space (1, 2, 3) coordinates, x^μ , under the space-time metric (+, −, −, −). The latter represents a covariant relation that can be Lorentz-transformed into another inertial frame. This approach was successfully implemented in Refs. [31,32], where it was demonstrated that the transformation of the conductivity tensor assumes a complex and non-standard form.

A similar methodology was applied in Ref. [24] for a graphene sheet, where the polarization tensor serves as the linear response tensor. The complete action, which includes the Dirac electron, the classical electromagnetic field, and the effective action due to fermion loop correction [34], yields the following set of Maxwell equations:

$$\partial_\mu F^{\mu\nu} = -\delta(z - a)\Pi^{\nu\alpha} A_\alpha = -4\pi J^\nu, \tag{1}$$

where $z = a$ represents the position of the graphene plane and $\Pi^{\nu\alpha}$ denotes the polarization tensor resulting from the Dirac electron fermion loop. The current density assumes the form of a boundary condition. Here, $\partial_\mu \equiv \partial/\partial x_\mu$, $F_{\mu\nu}$ represents the electromagnetic tensor, and $\delta(z - a)$ is the Dirac delta function. By integrating the relationship (1) over an infinitesimally small interval ($a - \varepsilon, a + \varepsilon$) with ε approaching zero, Equation (1) can be transformed into Ohm's law with the conductivity tensor,

$$\sigma^{ab} = \frac{\Pi^{ab}}{i\omega},$$

where the lower-case Latin letter indices take the values 1, 2.

The invariance of the boundary conditions with respect to 3-boosts,

$$\Lambda = \begin{pmatrix} u^0 & -\mathbf{u} \\ -\mathbf{u} & \mathbf{I} + \frac{\mathbf{u} \otimes \mathbf{u}}{u^0 + 1} \end{pmatrix}, \quad \mathbf{u} = (u^1, u^2), \tag{2}$$

along the graphene plane was utilized in Ref. [24] to determine the transformation of the conductivity tensor of graphene to the laboratory frame, with u denoting the spacial velocity and \otimes representing the tensor product. In the current study, we employ this approach to calculate the boost transformation of the isotropic conductivity tensor. The conductivity tensor in the laboratory frame is represented by

$$\sigma = \frac{\omega'}{\omega} \mathbf{G} \sigma' \mathbf{G}^T, \tag{3}$$

where

$$\mathbf{G} = \mathbf{I} - \frac{\omega}{(ku)} \frac{\mathbf{u} \otimes \mathbf{u}}{u_0 + 1} + \frac{\mathbf{u} \otimes \mathbf{k}}{(ku)},$$

k represents the wave vector and the prime denotes the quantities defined in the co-moving frame.

In the framework of the scattering matrix approach [27], the Casimir energy density, \mathcal{E} , per unit area can be expressed in terms of the scattering matrix, \mathcal{S} :

$$\mathcal{E} = \frac{i}{4\pi} \iint \frac{d^2k}{(2\pi)^2} \int_0^\infty \ln \det \mathcal{S} \frac{k_3 dk_3}{\sqrt{k^2 + k_3^2}}, \tag{4}$$

where the \mathcal{S} -matrix of the total system consists of the reflection, \mathbf{R} , and transmission, \mathbf{T} , matrices:

$$\mathcal{S} = \begin{pmatrix} \mathbf{R} & \mathbf{T}' \\ \mathbf{T} & \mathbf{R}' \end{pmatrix}.$$

The matrix (2) describes the scattering of the electromagnetic field:

$$\begin{pmatrix} \overleftarrow{\mathbf{E}}_l \\ \overrightarrow{\mathbf{E}}_r \end{pmatrix} = \mathcal{S} \begin{pmatrix} \overrightarrow{\mathbf{E}}_l \\ \overleftarrow{\mathbf{E}}_r \end{pmatrix},$$

where the direction of the vector indicates the direction of the wave, $\overrightarrow{\mathbf{E}} \propto e^{+ik_3z}$, $\overleftarrow{\mathbf{E}} \propto e^{-ik_3z}$ and indexes "l" and "r" stand for electromagnetic field on the left and right sides of the total system, correspondingly. The system, in general, can consist of a set of planes. The vectors over the fields denote the wave direction. The scattering matrix \mathcal{S} cannot be reduced to a product of matrices for each plane [39].

The general relation can be transformed [27] into the following expressions for the energy density, \mathcal{E} , and the pressure, \mathcal{P} , for real frequencies:

$$\mathcal{E} = -\frac{1}{2i} \iint \frac{d^2k}{(2\pi)^3} (I_- - I_+) \quad \text{and} \quad \mathcal{P} = \iint \frac{d^2k}{(2\pi)^3} (I_- + I_+), \tag{5}$$

where

$$I_\pm = \int_k^\infty d\omega \ln \det [1 - e^{\pm 2iak_3} \mathcal{R}(\pm k_3)], \tag{6}$$

$$J_\pm = \int_k^\infty d\omega k_3 \frac{e^{\pm 2iak_3} (\text{tr} \mathcal{R}(\pm k_3) - 2e^{\pm 2iak_3} \det \mathcal{R}(\pm k_3))}{\det [1 - e^{\pm 2iak_3} \mathcal{R}(\pm k_3)]}, \tag{7}$$

$\mathcal{R}(\pm k_3) = r'_I(\pm k_3)r_{II}(\pm k_3)$, $k_3 = \sqrt{\omega^2 - k^2}$ and r_A with $A = I, II$ denote the reflection matrices. The integration in Equation (5) is taken over the xy -plane. Formulas (5) only consider the propagating waves, because $\omega \geq k$. The subscript $I(II)$ indicates that all reflection matrices are related to the rest (moving) plane.

The scattering matrix for each part of the system (each plane) has the following form:

$$\mathcal{S}_A = \begin{pmatrix} r_A & t'_A \\ t_A & r'_A \end{pmatrix},$$

with the corresponding index $A = I, II$ and argument. It connects the electromagnetic waves on the left side (l) of the specific plane of the system with that on the right (r) side by relation:

$$\begin{pmatrix} \overleftarrow{\mathbf{E}}_l \\ \overrightarrow{\mathbf{E}}_r \end{pmatrix} = \mathcal{S}_A \begin{pmatrix} \overrightarrow{\mathbf{E}}_l \\ \overleftarrow{\mathbf{E}}_r \end{pmatrix}.$$

The reflection matrices for the conductive plane were derived in Ref. [27] using the boundary condition on the plane:

$$r_A = r'_A = -\frac{\omega^2 \eta_A - \mathbf{k} \otimes (\mathbf{k} \eta_A) + \mathbf{I} \omega k_3 \det \eta_A}{\omega^2 \text{tr} \eta_A - \mathbf{k} \mathbf{k} \eta_A + \omega k_3 (1 + \det \eta_A)}, \tag{8}$$

where $\eta_A = 2\pi\sigma_A$, and σ_i is the conductivity tensor of the plane $A = I, II$. In domain $\omega < k$, there are evanescent and waveguide modes [40], but, as demonstrated in this Section below, through the rotation of the contour of integration to the imaginary axis, the contribution of these modes is cancelled out with the energy of the boundary states of corresponding modes.

Then, a rotation of the integration contour over the real axis, $\Re \omega$, in I_{\pm} (6) and J_{\pm} (7) is applied to the imaginary axis, $\Im \omega$; see Figure 1.

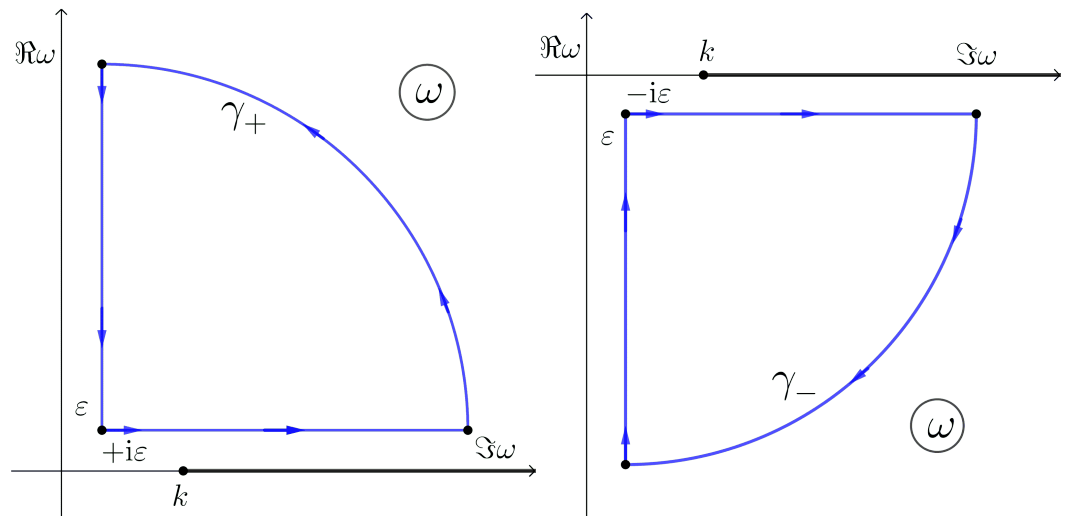


Figure 1. The contours γ_{\pm} of integration for I_{\pm} (6) and J_{\pm} (7) in the ω -plane. The integration over imaginary frequency, $\zeta = -i\omega$, yields the energy, \mathcal{E}^{\perp} . The potential presence of poles within the contours may contribute to a non-zero energy \mathcal{E}^{\parallel} . ϵ denotes an infinitely small distance to the axes and k is the wave vector.

After the rotation of the contour to the imaginary axis, two contributions survive, which we refer to as \mathcal{E}^{\perp} and \mathcal{E}^{\parallel} , corresponding to normal (real) and parallel (imaginary) to the planes, respectively. The first contribution with integration along the imaginary frequency, $\zeta = -i\omega$, is given by

$$\mathcal{E}^{\perp} = \iint \frac{d^2k}{2(2\pi)^3} \int_{-\infty}^{+\infty} d\zeta \ln \det \left[1 - e^{-2ak_E} \mathcal{R}(ik_E) \right], \tag{9}$$

where $k_E = \sqrt{\zeta^2 + k^2}$. The corresponding force is perpendicular to the planes, as is typical for the Casimir force. This expression can be simplified by using the eigenvalues of matrix \mathcal{R} and can be represented as a sum of TE and TM contributions. The matrices r'_I and r_{II} do not commute (see below in this Section), and therefore the eigenvalues of \mathcal{R} are not a product of the eigenvalues of r'_I and r_{II} . The eigenvalues of \mathcal{R} can be found in closed, albeit complicated, forms [24], corresponding to the contributions of the TM and TE modes separately. Instead of applying this approach, we use the expression for energy in the form [27] straightforwardly including the conductivity matrices, η_A :

$$\mathcal{E}^\perp = \int \frac{d^2k}{2(2\pi)^3} \int_{-\infty}^{\infty} d\zeta \ln \left(1 + e^{-4ak_E} \frac{\zeta^2 k_E^2}{b_I b_{II}} \det \boldsymbol{\eta}_I \det \boldsymbol{\eta}_{II} - e^{-2ak_E} \left[\frac{\zeta^2 k_E^2}{b_I b_{II}} [(1 - \det \boldsymbol{\eta}_I)(1 - \det \boldsymbol{\eta}_{II}) + \det(\boldsymbol{\eta}_I - \boldsymbol{\eta}_{II})] - \frac{\zeta k_E}{b_I} - \frac{\zeta k_E}{b_{II}} + 1 \right] \right), \quad (10)$$

where $b_A = \zeta^2 \text{tr } \boldsymbol{\eta}_A + (\mathbf{k} \boldsymbol{\eta}_A) + \zeta k_E (1 + \det \boldsymbol{\eta}_A)$. The \mathcal{E}_\parallel contribution represents the Casimir friction.

If the conductivity tensor is given by

$$\boldsymbol{\eta}_A = \eta_A^{\text{TE}} \mathbf{I} + (\eta_A^{\text{TM}} - \eta_A^{\text{TE}}) \frac{\mathbf{k} \otimes \mathbf{k}}{k^2}, \quad (11)$$

it possesses the eigenvalues η_A^{TM} and η_A^{TE} , corresponding to the TM and TE modes, respectively. In particular, the graphene conductivity tensor has such a structure [34] with corresponding conductivities of modes. The Hall conductivity gives an additional antisymmetric term [41]. In this case, the expression (10) for Casimir energy can be transformed to the known [1] form of sum contributions for the TE and TM modes:

$$\mathcal{E}^\perp = \int \frac{d^2k}{2(2\pi)^3} \int_{-\infty}^{\infty} d\zeta \left[\ln \left(1 - \frac{e^{-2ak_E}}{\left(1 + \frac{k_E}{\zeta \eta_I^{\text{TE}}}\right) \left(1 + \frac{k_E}{\zeta \eta_{II}^{\text{TE}}}\right)} \right) + \ln \left(1 - \frac{e^{-2ak_E}}{\left(1 + \frac{k_E}{\zeta \eta_I^{\text{TM}}}\right) \left(1 + \frac{k_E}{\zeta \eta_{II}^{\text{TM}}}\right)} \right) \right].$$

In the case considered here, the conductivity of the moving plane does not have form (11), and we use the Casimir energy in the form (10).

In Ref. [24], the normal force was considered for moving graphene with the following conductivity in a co-moving frame:

$$\boldsymbol{\eta} = \eta_{\text{gr}} \frac{\tilde{\mathbf{k}}}{\omega} \left(\mathbf{I} + v_F^2 \frac{\mathbf{k} \otimes \mathbf{k}}{\tilde{k}^2} \right) \tilde{\Phi} \left(\frac{\tilde{\mathbf{k}}}{2m} \right), \quad (12)$$

where $\eta_{\text{gr}} = \pi e^2 / 2$ with e the electron charge, v_F is the Fermi velocity,

$$\tilde{\Phi}(y) = \frac{2i}{\pi y} \left(1 - \frac{y^2 + 1}{y} \text{arctanh } y \right) \text{ and } \tilde{k} = \sqrt{\omega^2 - v_F^2 k^2}. \quad (13)$$

In the laboratory frame, the general structure of the moving plane's conductivity tensor (3) takes the form [24]

$$\boldsymbol{\eta}_{II} = i_1 \mathbf{I} + i_2 \mathbf{k} \otimes \mathbf{k} + i_3 (\mathbf{k} \otimes \mathbf{v} + \mathbf{v} \otimes \mathbf{k}), \quad (14)$$

where

$$\begin{aligned} i_1 &= \frac{\eta_{\text{gr}} \tilde{\Phi}'}{\omega k^2 \tilde{k}'} \left(k^2 \tilde{k}'^2 + \frac{1 - v_F^2}{1 - v^2} ((\mathbf{k}\mathbf{v})^2 - k^2 v^2) k_3^2 \right), \\ i_2 &= \frac{\eta_{\text{gr}} \tilde{\Phi}'}{\omega k^2 \tilde{k}'} \left(k^2 v_F^2 + \frac{1 - v_F^2}{1 - v^2} v^2 k_3^2 \right), \\ i_3 &= \frac{\eta_{\text{gr}} \tilde{\Phi}'}{k^2 \tilde{k}'} \frac{1 - v_F^2}{1 - v^2} (k^2 - \omega(\mathbf{k}\mathbf{v})), \end{aligned} \quad (15)$$

and

$$\tilde{k}' = \sqrt{\tilde{k}^2 + \frac{1 - v_F^2}{1 - v^2} [\omega^2 v^2 + (\mathbf{k}\mathbf{v})^2 - 2\omega(\mathbf{k}\mathbf{v})]}, \quad (16)$$

is the Lorentz transformation of \tilde{k} (13).

The reflection matrices r_i (8), on the basis of eigenvectors, are given as

$$\hat{r}_I(k_3) = - \begin{pmatrix} \frac{k_3\eta}{\eta k_3 + \tilde{k}} & 0 \\ 0 & \frac{\eta \tilde{k}}{\eta \tilde{k} + k_3} \end{pmatrix} \text{ and } \hat{r}_{II}(k_3) = - \begin{pmatrix} \frac{k_3\eta'}{\eta' k_3 + \tilde{k}'} & 0 \\ 0 & \frac{\eta' \tilde{k}'}{\eta' \tilde{k}' + k_3} \end{pmatrix}, \quad (17)$$

where the hat denotes the diagonalized reflection matrices, $\eta = \eta_{gr} \tilde{\Phi}(y)$, $\eta' = \eta_{gr} \tilde{\Phi}(y')$, and

$$\mathbf{T}_A^{-1} r_A \mathbf{T}_A = \hat{r}_A \Leftrightarrow r_A = \mathbf{T}_A \hat{r}_A \mathbf{T}_A^{-1}. \quad (18)$$

The matrices \mathbf{T}_i diagonalize the reflection matrices r_i and have the form

$$\mathbf{T}_I = \begin{pmatrix} k_2 & k_1 \\ -k_1 & k_2 \end{pmatrix} \text{ and } \mathbf{T}_{II} = \begin{pmatrix} k_2 - v_2 \frac{k_3^2}{\omega - (kv)} & k_1 - v_1 \omega \\ -k_1 + v_1 \frac{k_3^2}{\omega - (kv)} & k_2 - v_2 \omega \end{pmatrix}.$$

It is worth noting that the eigenvalues of r_{II} can be obtained from the eigenvalues of r_I through a Lorentz transformation. Specifically, $k_3 \rightarrow k_3$, $\tilde{k} \rightarrow \tilde{k}'$, and $\eta \rightarrow \eta'$ under these transformations, resulting in $\hat{r}_I \rightarrow \hat{r}_{II}$. This is expected, as eigenvalues are invariants of a matrix.

The eigenvector basis of r_I ,

$$\mathbf{a}_1 = (k_2, -k_1), \mathbf{a}_2 = (k_1, k_2) = \mathbf{k},$$

is orthogonal with $\mathbf{a}_1 \cdot \mathbf{a}_2 = 0$, and $\mathbf{a}_1^2 = \mathbf{a}_2^2 = k^2$. On the other hand, the eigenvector basis of r_{II} ,

$$\mathbf{c}_1 = \left(k_2 - v_2 \frac{k_3^2}{\omega - (kv)}, -k_1 + v_1 \frac{k_3^2}{\omega - (kv)} \right), \\ \mathbf{c}_2 = (k_1 - v_1 \omega, k_2 - v_2 \omega),$$

is not orthogonal:

$$\mathbf{c}_1 \cdot \mathbf{c}_2 = \frac{k^2 - \omega(kv)}{\omega - (kv)} (kvn) \neq 0, \quad (19)$$

where $n^a = \delta_3^a$ with δ_b^a the Kronecker delta. Through straightforward calculations, the following expression for the commutator is obtained:

$$[r_I, r_{II}] = \eta\eta' \frac{(1 - v_F^2)^2}{1 - v^2} \frac{\omega((kv)\omega - k^2)}{\tilde{k}\tilde{k}' b_I b_{II}} (k_3^2 \mathbf{k} \otimes \mathbf{v} - \omega^2 \mathbf{v} \otimes \mathbf{k}), \quad (20)$$

Therefore, the commutator $[r_I, r_{II}] \neq 0$ and the r_I and r_{II} cannot be diagonalized simultaneously; this means that the eigenvalues of $r_I \cdot r_{II}$ are not a product of the eigenvalues of the matrices r_I and r_{II} .

The straightforward calculations give the following expression for the eigenvalues of matrix \mathcal{R} :

$$r_{TM/TE}(k_3) = \frac{\eta\eta'}{2PQP'Q'} \left\{ \alpha \left(k_3 \left(k^2 Q' + Q \left((ku)^2 - k_3^2 \right) \right) + \alpha \left((ku)\omega - k_3^2 u_0 \right)^2 \right) + 2k_3^2 QQ' \right. \\ \left. \pm \alpha \sqrt{\left(k_3 \left(k^2 Q' + Q \left((ku)^2 - k_3^2 \right) \right) + \alpha \left((ku)\omega - k_3^2 u_0 \right)^2 \right)^2 + 4k_3^4 QQ' \left((ku)^2 - k^2 u^2 \right)} \right\}, \quad (21)$$

where $\alpha = 1 - v_F^2$, \pm defines the TM (plus sign) and TE (minus sign),

$$Q = \tilde{k}\eta + k_3, P = \tilde{k} + \eta k_3, \text{ and } Q' = \tilde{k}'\eta' + k_3, P' = \tilde{k}' + \eta' k_3.$$

In the case of zero velocity, $\mathbf{u} = \mathbf{0}$, $\hat{\mathbf{r}} = \hat{\mathbf{r}}_1^2$, is obtained, as expected. To establish the correct correspondence, the following square root sign convention is employed:

$$\sqrt{(\alpha k^2 + 2k_3 Q)^2} = \alpha k^2 + 2k_3 Q, \tag{22}$$

The eigenvalues (21) have quite a complex form. Hence, expression (10) is used where the Casimir energy is directly expressed in terms of the tensors' conductivities.

Let us briefly discuss the contribution \mathcal{E}_{\parallel} , which can contribute to the force along the planes. The contribution to the Casimir pressure takes the form

$$\begin{aligned} \mathcal{P}^{\parallel} = & \iint \frac{d^2k}{(2\pi)^3} \left\{ \oint_{\gamma_-} d\omega k_3 \frac{e^{-2iak_3} (\text{tr } \mathcal{R}(-k_3) - 2e^{-2iak_3} \det \mathcal{R}(-k_3))}{\det[\mathbf{I} - e^{-2iak_3} \mathcal{R}(-k_3)]} \right. \\ & \left. + \oint_{\gamma_+} d\omega k_3 \frac{e^{2iak_3} (\text{tr } \mathcal{R}(k_3) - 2e^{2iak_3} \det \mathcal{R}(k_3))}{\det[\mathbf{I} - e^{2iak_3} \mathcal{R}(k_3)]} \right\}, \end{aligned} \tag{23}$$

with the contours γ_{\pm} as shown in Figure 1. This expression only has a non-zero value if poles appear inside the contours, satisfying the relations

$$\det[\mathbf{I} - e^{\pm 2iak_3} \mathbf{r}'_1(\pm k_3) \mathbf{r}_2(\pm k_3)] = 0. \tag{24}$$

The relation (24), within various contexts, has been noted in the earlier studies [19,28–30,42]. If the matrix \mathcal{R} has the eigenvalues r_{TM} and r_{TE} , this relation can be separated into the two scalar relations:

$$1 - e^{\pm 2iak_3} r_{\text{TM}}(\pm k_3) = 0 \quad \text{and} \quad 1 - e^{\pm 2iak_3} r_{\text{TE}}(\pm k_3) = 0, \tag{25}$$

respectively.

The solutions of the relations (25) must possess imaginary parts to contribute as residues. It can be demonstrated that solutions to these relations exist if, and only if,

$$|r_{\text{TM}}(\pm k_3)| > 1 \quad \text{and} \quad |r_{\text{TE}}(\pm k_3)| > 1. \tag{26}$$

Since $\text{sign}(\Im k_3) = \text{sign}(\Im \omega)$, then

$$\left| e^{\pm 2iak_3} \right| = \left[e^{\pm 2iak_3} e^{\mp 2iak_3^*} \right]^{1/2} = e^{\mp 2a \Im k_3} = e^{-2a |\Im k_3|} < 1.$$

Given this inequality, one can obtain the inequalities (26) from the relations (25).

Then, it follows that the condition $\mathcal{P}^{\parallel} \neq 0$ is associated with virtual photon production because the modulus of the reflection coefficients is greater than 1. Lifshitz demonstrated [43] that without relative velocity, Equation (24) has no solutions since the inequalities (26) cannot be satisfied. This statement can be proven for graphene with zero mass gap (for simplicity). For velocity $v = 0$ and $m = 0$,

$$\begin{aligned} r_{\text{TM}}^{-1}(\pm k_3) &= \left(1 \pm \frac{\tilde{k}}{\eta k_3} \right)^2 = \left(1 + \frac{\tilde{k}}{\eta_{\text{gr}} k_3} \right)^2, \\ r_{\text{TE}}^{-1}(\pm k_3) &= \left(1 \pm \frac{k_3}{\eta \tilde{k}} \right)^2 = \left(1 + \frac{k_3}{\eta_{\text{gr}} \tilde{k}} \right)^2, \end{aligned} \tag{27}$$

are obtained. Then,

$$\left| r_{\text{TM}}^{-1}(\pm k_3) \right| = \left(1 + \frac{|\tilde{k}|^2}{\eta_{\text{gr}}^2 |k_3|^2} + 2 \frac{\Re \tilde{k} \Re k_3 + \Im \tilde{k} \Im k_3}{\eta_{\text{gr}} |k_3|^2} \right)^2. \tag{28}$$

It can be straightforwardly shown that $\Re k \Re k_3 + \Im k \Im k_3 > 0$, thus, satisfying

$$\left| r_{\text{TM}}^{-1}(\pm k_3) \right| > 1. \tag{29}$$

Hence, one concludes that the inequalities (26) cannot be satisfied in the case considered in this paper, indicating there are no solutions for Equation (24). However, one would expect that solutions may exist due to relative motion of the planes.

3. The Case of Isotropic Conductivity

The case of isotropic conductivity can be obtained by taking the formal limits $v_F \rightarrow 0$ and $\tilde{\Phi} \rightarrow 1$ ($m \rightarrow 0$) in Equation (12) and replacing the graphene conductivity, η_{gr} , with the conductivity, η_i , of the corresponding plane. After taking these limits, the conductivity tensor for the plane at rest becomes diagonal $\eta_I = \eta_I \mathbf{I}$ and $k' = \gamma \omega_v$, where $\omega_v = \omega - \mathbf{k}v$, $\gamma = 1/\sqrt{1 - v^2}$ is the relativistic factor, and

$$\eta_{II} = i'_1 \mathbf{I} + i'_2 \mathbf{k} \otimes \mathbf{k} + i'_3 (\mathbf{k} \otimes \mathbf{v} + \mathbf{v} \otimes \mathbf{k}), \tag{30}$$

where

$$i'_1 = \frac{\eta_{II} \gamma (\mathbf{k}^2 \omega_v^2 + ((\mathbf{k}v)^2 - \mathbf{k}^2 v^2) k_3^2)}{k^2 \omega \omega_v}, \quad i'_2 = \frac{\eta_{II} \gamma v^2 k_3^2}{k^2 \omega \omega_v}, \quad i'_3 = \frac{\eta_{II} \gamma}{k^2 \omega_v} (\mathbf{k}^2 - \omega(\mathbf{k}v)). \tag{31}$$

The quantity $\omega_v \gamma$ represents the frequency of photons in a laboratory that was emitted in a co-moving frame.

By performing straightforward calculations at the imaginary axis $\omega = i\zeta$, one obtains:

$$b_I = (\eta_I \zeta + k_E)(\zeta + \eta_I k_E), \quad b_{II} = \frac{\zeta}{\gamma \zeta_v} (\eta_{II} \gamma \zeta_v + k_E)(\gamma \zeta_v + \eta_{II} k_E),$$

$$\det(\eta_I - \eta_{II}) = (\eta_I - \eta_{II})^2 + \eta_I \eta_{II} \left(\gamma v^2 \frac{k_E^2}{\zeta \zeta_v} + 2(1 - \gamma) \right), \quad \det \eta_A = \eta_A^2, \tag{32}$$

where $\zeta_v = \zeta + i\mathbf{k}v$. Then, we use the polar coordinates for \mathbf{k} in Equation (10), $\mathbf{k}v = kv \cos \varphi$ and transform the coordinates of the plane $k \in [0, \infty)$, $\zeta \in (-\infty, \infty)$ to polar coordinates $\zeta = k_E \cos \theta$, $k = k_E \sin \theta$. After these changes, the dependence of k_E only survives in the exponents. Changing $ak_E = y$, one observes that the energy depends on the interplane distance as $1/a^3$ for constant conductivities, as expected [35]. Thus, the energy and pressure have the following form ($x = \cos \theta$):

$$\mathcal{E}_{1,2}^\perp = \Re \int_0^\infty \frac{y^2 dy}{(2\pi a)^3} \int_0^1 dx \int_0^\pi d\varphi E_{1,2}, \quad \mathcal{P}_{1,2}^\perp = \frac{3}{a} \mathcal{E}_{1,2}^\perp, \tag{33}$$

where

$$E_{1,2} = \ln \left\{ 1 + e^{-4y} \frac{x^2 \eta_I^2 \eta_{II}^2}{\beta_I \beta_{II}} \right. \\ \left. - e^{-2y} \left[\frac{x^2}{\beta_I \beta_{II}} \left((1 - \eta_I \eta_{II})^2 + \eta_I \eta_{II} \left(\frac{\gamma v^2}{xx_v} + 2(1 - \gamma) \right) \right) - \frac{x}{\beta_I} - \frac{x}{\beta_{II}} + 1 \right] \right\}, \tag{34}$$

and

$$\beta_I = (\eta_I x + 1)(x + \eta_I), \quad \beta_{II} = \frac{x}{\gamma x_v} (\eta_{II} \gamma x_v + 1)(\gamma x_v + \eta_{II}), \quad x_v = x + iv\sqrt{1 - x^2} \cos \varphi. \tag{35}$$

If the first plane (at rest) is a perfect (ideal) conductor, one takes the limit $\eta_1 \rightarrow \infty$ and obtains

$$E_{id,2} = \ln \left[1 + e^{-4y} \frac{x\eta_{II}^2}{\beta_{II}} - e^{-2y} \left(\frac{x\eta_{II}^2}{\beta_{II}} - \frac{x}{\beta_{II}} + 1 \right) \right], \tag{36}$$

whereas for two ideal planes,

$$E_{id,id} = 2 \ln(1 + e^{-2y}), \tag{37}$$

the energy does not depend on the velocity.

The expressions (33) and (34) coincide with those obtained in Ref. [11], where two planes of finite thickness with relative lateral motion were considered. As noted in Ref. [44], the typical reflection coefficients cannot be used for 2D (two-dimensional) materials due to the impossibility of taking the limit of zero thickness. The reflection coefficients in this case have to be calculated using scattering theory [45] or 2D quantum electrodynamics[34]. In the case under consideration here, one needs to use the reflection coefficients (27) for the plane at rest and the same expressions, but with a boosted wave vector (16), for the moving plane. Then, one takes limit $v_F \rightarrow 0$ to obtain the isotropic conductivity. Finally, one arrives at Equations (33) and (34). For example, the coefficient at e^{-4y} in Equation (34) reads

$$\frac{x^2 \eta_I^2 \eta_{II}^2}{\beta_I \beta_{II}} = r_{E1} r_{E2} r_{B1} r_{B2}$$

in the notations of Ref. [11].

Without a relative movement, $v = 0$, the results obtained in Ref. [35] are reproduced:

$$E = \ln \left(1 - e^{-2y} \frac{\eta_I \eta_{II}}{(\eta_I + x)(\eta_{II} + x)} \right) + \ln \left(1 - e^{-2y} \frac{\eta_I \eta_{II} x^2}{(x\eta_I + 1)(x\eta_{II} + 1)} \right) = E_{TM} + E_{TE}, \tag{38}$$

the sum of TM and TE contributions.

Let us consider the constant conductivities case with equal conductivities: $\eta_I = \eta_{II} = \eta = \text{const}$. For $v = 0$, one obtains from Equation (33) the sum of the TM and TE mode contributions,

$$\begin{aligned} E_{1,2}^0 &= \ln \left(1 - e^{-2y} \frac{\eta^2}{(x + \eta)^2} \right) + \ln \left(1 - e^{-2y} \frac{x^2 \eta^2}{(1 + x\eta)^2} \right), \\ E_{id,2}^0 &= \ln \left(1 - e^{-2y} \frac{\eta}{x + \eta} \right) + \ln \left(1 - e^{-2y} \frac{x\eta}{1 + x\eta} \right), \end{aligned} \tag{39}$$

respectively.

In the case with $\eta \ll 1$, the Casimir energies read for $v = 0$:

$$\begin{aligned} \mathcal{E}_{1,2}^0 &= \frac{\eta}{a^3} \frac{180\zeta_R(3) + \pi^4 + 60\pi^2 - 1440 \ln 2}{2880\pi^2} = -3.2 \times 10^{-3} \frac{\eta}{a^3}, \\ \mathcal{E}_{id,2}^0 &= \frac{\eta}{a^3} \left[\frac{\ln \eta}{32\pi^2} + \frac{90\zeta_R(3) + \pi^4 + 15\pi^2 - 405}{2880\pi^2} \right] = - \left[3.1 \ln \eta^{-1} + 1.8 \right] \times 10^{-3} \frac{\eta}{a^3}. \end{aligned} \tag{40}$$

To move to the dimensional SI (International System) units, one has to multiply the relations (39) and (40) by $\hbar c = 3.16 \times 10^{-26} \text{ J} \cdot \text{m}$.

For small velocity and conductivity, specifically if $v \ll \eta \ll 1$, one obtains Equation (33):

$$\frac{\Delta_v \mathcal{E}_{1,2}^\perp}{\mathcal{E}_{1,2}^0} = \frac{\Delta_v \mathcal{P}_{1,2}^\perp}{\mathcal{P}_{1,2}^0} \approx -0.19 \left(\frac{v}{\eta} \right)^2, \quad \frac{\Delta_v \mathcal{E}_{id,2}^\perp}{\mathcal{E}_{id,2}^0} = \frac{\Delta_v \mathcal{P}_{id,2}^\perp}{\mathcal{P}_{id,2}^0} \approx - \frac{0.3}{\ln \eta^{-1} + 0.57} \left(\frac{v}{\eta} \right)^2, \tag{41}$$

where $\Delta_v \mathcal{E}_{i,k}^\perp = \mathcal{E}_{i,k}^\perp - \mathcal{E}_{i,k}^0$. The relative velocity correction is quadratic in the velocity and is negative, meaning the force is decreased due to the motion of the planes.

Numerical evaluations of Equation (33) are shown in Figure 2 for two systems: (1,2)—two conductive planes with constant conductivity η (solid lines) and (id,2)—the first plane at rest, which is a perfect metal (dashed lines). We calculated the velocity correction to the energy: $\Delta_v \mathcal{E}_\perp / \mathcal{E}_0 = (\mathcal{E}_\perp - \mathcal{E}_0) / \mathcal{E}_0$, where \mathcal{E}_0 is the energy without relative movement. The velocity correction is negative for both systems and exhibits quadratic behavior, proportional to v^2 , for small velocities, $v \ll \eta \ll 1$. The absolute value of the correction is larger for the first system.

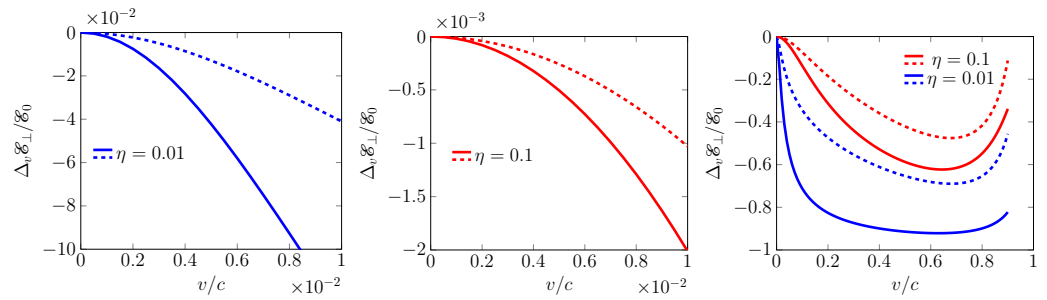


Figure 2. The velocity correction $\Delta_v \mathcal{E}_\perp / \mathcal{E}_0 = (\mathcal{E}_\perp - \mathcal{E}_0) / \mathcal{E}_0$ for $\eta = 0.01, 0.1$. In the case of small velocity and conductivity, $v \ll \eta \ll 1$ (**left** and **middle**), a quadratic correction is observed in accordance with Equation (41). The **right** plot shows the correction for all possible velocities. The solid lines represent two planes with equal conductivity, as given by Equation (34), while the dashed lines represent systems where one plane is stationary with perfect conductivity (described by Equation (36)), and the second plane possesses isotropic conductivity (described by Equation (34)). Here, c denotes the speed of light.

The above derivation is applicable for isotropic, but frequency-dependent (temporal dispersion), conductivity, $\eta = \eta(\omega)$. Let us consider the simple enough case of Drude-like conductivity with

$$\eta_1 = \frac{\eta \Gamma}{\Gamma + \xi}, \quad \eta_2 = \frac{\eta \Gamma}{\Gamma + \gamma \xi v}, \tag{42}$$

where parameters are considered for graphene: $\Gamma = 6.365$ eV and $\eta = \eta_{gr} = e^2/4$, where Γ denotes a scattering parameter [36]. After changing the integrand variables as in Equation (33) the Casimir energy acquires an additional dependence on the interplane distance through conductivity:

$$\eta_I = \frac{\eta_{gr}(a\Gamma)}{(a\Gamma) + yx}, \quad \eta_{II} = \frac{\eta_{gr}(a\Gamma)}{(a\Gamma) + \gamma yxv}. \tag{43}$$

For $a = 100$ nm and $\Gamma = 6.365$ eV, one has $a\Gamma = 3.225$. For large values of $a\Gamma \gg 1$, the conductivities $\eta_I = \eta_{II} = \eta_{gr}$, consistent with the constant conductivity model, are valid for large interplane distances.

The Casimir energy is numerically evaluated and presented in Figure 3. It can be observed that as the interplane distance increases, the energy approaches that of the constant conductivity case (blue lines), as expected.

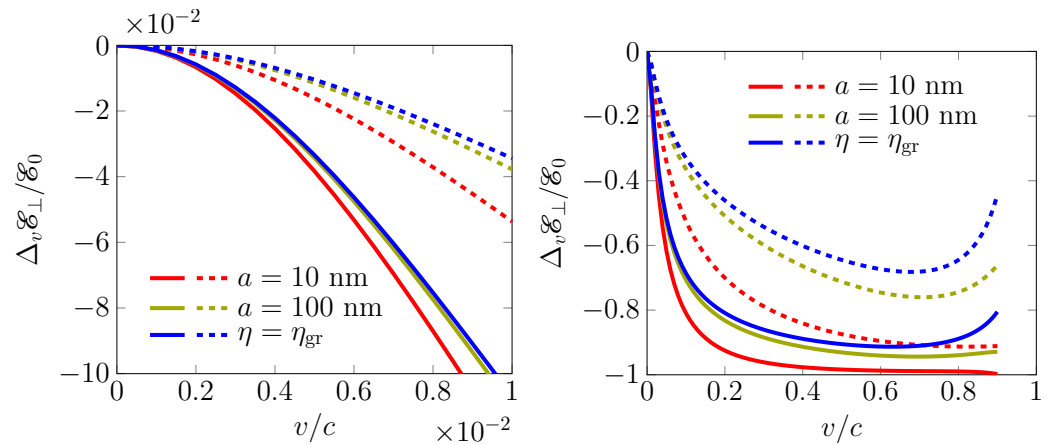


Figure 3. The velocity correction $\Delta_v \epsilon_{\perp} / \epsilon_0 = (\epsilon_{\perp} - \epsilon_0) / \epsilon_0$ for the Drude model with the parameters of the interplane distance, $a = 10$ nm and 100 nm, and constant conductivity, $\eta = \eta_{gr}$, the graphene conductivity, for small velocities, $v \ll 1$ (left), and the entire range of v (right). The solid lines correspond to two planes with equal conductivity, and the dashed lines represent a scenario where one plane is stationary with perfect conductivity. It is worth noting that as the interplane distance increases, the curves approach the scenario of constant conductivity.

To compare the results obtained here with the analysis of graphene in Ref. [24], let us consider the case of two graphene sheets. The energy initially increases with velocity and then becomes negative, reaching a maximum at $v_c = v_F + (ma)/2$. When $m = v_F = 0$, the region with positive energy disappears. Conversely, for two planes with constant conductivity, the energy is always negative for all values of velocity. Both cases exhibit a velocity correction of v^2 order. Regarding the interplane distance, different behaviors are observed. For two planes with constant conductivity, the energy has the $1/a^3$ -dependence for any a distance, while for graphene, this dependence is only evident for large distances. This is expected, as the constant conductivity model for graphene is valid for large interplane distances. In the case of a system consisting of a perfect conductor and graphene, the energy is zero up to a specific velocity, while in the aforementioned scenario, a quadratic behavior is observed at the beginning. The same conclusion holds for the Drude model of conductivity (42). For large interplane distances, both models closely align, while for small distances, a weak dependence on distance is observed.

4. Conclusions

In this paper, we investigated the normal (perpendicular to the planes) Casimir force between two conductive planes with an isotropic conductivity that moves laterally with a relative velocity v . Within the framework of scattering theory, the main challenge lies in determining the conductivity of a moving plane in a laboratory frame. In a co-moving frame, the isotropic conductivity is represented by a coefficient in Ohm’s law, $J' = \sigma' E'$, where E' and J' denote fluctuations in the electric field and corresponding current density. Transforming this relation to the laboratory frame, where the first plane is at rest, is not a trivial task. A simplified approach [31,32] to address this issue is to start from the linear relation between current density and electromagnetic vector potential, $J^\mu = \Pi_v^\mu A^\nu$, which is commonly used in plasma physics [33]. A similar approach was employed in Ref. [34], where the polarization tensor served as the linear response tensor Π_v^μ .

Even in the case of constant conductivity, the transformation of conductivity does not have quite a simple form [32]. A similar methodology was applied in Ref. [24], where the linear relations for current and electromagnetic potential, as well as the conservation of boundary conditions, were utilized. To obtain isotropic conductivity, we adapted the expressions derived for graphene, taking the limits $v_F \rightarrow 0$ for Fermi velocity and $m \rightarrow 0$ for mass gap. With these limits, the conductivity tensor in the co-moving frame becomes

diagonal. In the laboratory frame, it has the form (30). Using these tensors, the Casimir energy can be calculated using expression (10), originally derived in Ref. [27].

The expressions (34) obtained for two conductive planes and for the system (perfect conductivity)/(constant conductivity) involve two small dimensionless parameters: the velocity v of the plane and the conductivity $\eta = 2\pi\sigma$ (dimensionless for 2D systems). In the case where $v \ll \eta \ll 1$, the relative energy correction due to velocity is approximately given by the $(v/\eta)^2$ behaviour (41). This quadratic v -dependence is typical for normal force and different directions of motion [7,8,10,24]. The energy dependence on the interplane distance is $1/a^3$ for any distance, which is typical for the constant conductivity case [35], as the constant conductivity model is valid for large distances where the Casimir regime is satisfied. The Drude model of conductivity shows similar behavior of the system with a weak dependence on the interplane distances (see Figure 3).

The constant conductivity model, discussed in Refs. [6,35–37], quite well describes the Casimir effect for graphenes. However, in the case of the normal force considered in this paper, there is a significant qualitative difference. When the mass gap $m \neq 0$, the velocity correction is positive up to its maximum value of $v = v_F + am/2$, whereas the constant conductivity model gives a negative correction. As stated in Ref. [24], spatial dispersion plays a crucial role in the Casimir effect. For low conductivity values, the Casimir effect exhibits a linear dependence on conductivity in the constant conductivity case, whereas it becomes quadratic when the spatial dispersion of conductivity is taken into account.

Our future investigation concerns the quantum friction in the case of constant and isotropic conductivity. It is anticipated that the magnitude of the friction force is smaller by orders of magnitude [16] compared to the normal force. Nevertheless, the study is of importance due to quite a wide range of the different results obtained for quantum friction.

Author Contributions: Investigation: N.K. and N.E.; Writing—original draft: N.K. and N.E.; Writing—review & editing: N.K. and N.E. All authors have read and agreed to the published version of the manuscript.

Funding: N.K. was supported in part by the grants 2022/08771-5 and 2021/10128-0 from the São Paulo Research Foundation (FAPESP).

Data Availability Statement: The data are available upon reasonable request.

Conflicts of Interest: The authors declare no conflicts of interest.

References

- Bordag, M.; Klimchitskaya, G.L.; Mohideen, U.; Mostepanenko, V.M. *Advances in the Casimir Effect*; Oxford University Press: Oxford, UK, 2009; p. 768. [CrossRef]
- Woods, L.M.; Dalvit, D.A.R.; Tkatchenko, A.; Rodriguez-Lopez, P.; Rodriguez, A.W.; Podgornik, R. Materials Perspective on Casimir and van der Waals Interactions. *Rev. Mod. Phys.* **2016**, *88*, 045003. [CrossRef]
- Casimir, H.B.G. Some Remarks on the History of the so called Casimir Effect. In *Casimir Effect 50 Years Later*; Bordag, M., Ed.; World Scientific Publishing Co.: Singapore, 1998; pp. 3–9. [CrossRef]
- Dodonov, V. Fifty Years of the Dynamical Casimir Effect. *Physics* **2020**, *2*, 67–104. [CrossRef]
- Bordag, M.; Mohideen, U.; Mostepanenko, V.M. New Developments in the Casimir Effect. *Phys. Rep.* **2001**, *353*, 1–205. [CrossRef]
- Khusnutdinov, N.; Woods, L.M. Casimir Effects in 2D Dirac Materials (Scientific Summary). *JETP Lett.* **2019**, *110*, 183–192. [CrossRef]
- Bordag, M.; Petrov, G.; Robaschik, D. Calculation of the Casimir Effect for Scalar Fields with the Simplest Nonstationary Boundary Conditions. *Sov. J. Nucl. Phys.* **1984**, *39*, 828–831. Available online: <https://lib-extopc.kek.jp/preprints/PDF/1983/8308/8308199.pdf> (accessed on 30 December 2023). (In Russian)
- Bordag, M.; Dittes, F.-M.; Robaschik, D. Casimir Effect With Uniformly Moving Mirrors. *Sov. J. Nucl. Phys.* **1986**, *43*, 1034–1038. Available online: <https://lib-extopc.kek.jp/preprints/PDF/1985/8508/8508324.pdf> (accessed on 30 December 2023).
- Fulling, S.A.; Davies, P.C.W. Radiation from a Moving Mirror in Two Dimensional Space-Time: Conformal Anomaly. *Proc. R. Soc. Lond. A* **1976**, *348*, 393–414. [CrossRef]
- Maslovski, S.I. Casimir Repulsion in Moving Media. *Phys. Rev. A* **2011**, *84*, 22506. [CrossRef]
- Philbin, T.G.; Leonhardt, U. No Quantum Friction between Uniformly Moving Plates. *New J. Phys.* **2009**, *11*, 33035. [CrossRef]
- Polevoi, V.G. Tangential Molecular Forces Caused between Moving Bodies by a Fluctuating Electromagnetic Field. *Sov. Phys. JETP* **1990**, *71*, 1119–1124. Available online: <http://jetp.ras.ru/cgi-bin/e/index/e/71/6/p1119?a=list> (accessed on 30 December 2023).

13. Dedkov, G.V.; Kyasov, A.A. Friction and Radiative Heat Exchange in a System of Two Parallel Plates Moving Sideways: Levin–Polevoi–Rytov Theory Revisited. *Chin. J. Phys.* **2018**, *56*, 3002–3011. [CrossRef]
14. Mkrtchian, V.E. Interaction between Moving Macroscopic Bodies: Viscosity of the Electromagnetic Vacuum. *Phys. Lett. A* **1995**, *207*, 299–302. [CrossRef]
15. Pendry, J.B. Shearing the Vacuum - Quantum Friction. *J. Phys. Condens. Matter* **1997**, *9*, 10301–10320. [CrossRef]
16. Volokitin, A.I.; Persson, B.N.J. Near-Field Radiative Heat Transfer and Noncontact Friction. *Rev. Mod. Phys.* **2007**, *79*, 1291–1329. [CrossRef]
17. Pendry, J.B. Quantum Friction—Fact or Fiction? *New J. Phys.* **2010**, *12*, 33028. [CrossRef]
18. Maghrebi, M.F.; Golestanian, R.; Kardar, M. Scattering Approach to the Dynamical Casimir Effect. *Phys. Rev. D* **2013**, *87*, 25016. [CrossRef]
19. Maghrebi, M.F.; Golestanian, R.; Kardar, M. Quantum Cherenkov Radiation and Noncontact Friction. *Phys. Rev. A* **2013**, *88*, 42509. [CrossRef]
20. Belén Farias, M.; Fosco, C.D.; Lombardo, F.C.; Mazzitelli, F.D. Quantum Friction between Graphene Sheets. *Phys. Rev. D* **2017**, *95*, 65012. [CrossRef]
21. Belén Farias, M.; Kort-Kamp, W.J.M.; Dalvit, D.A.R. Quantum Friction in Two-Dimensional Topological Materials. *Phys. Rev. B* **2018**, *97*, 161407. [CrossRef]
22. Brevik, I.; Shapiro, B.; Silveirinha, M.G. Fluctuational Electrodynamics in and out of Equilibrium. *Int. J. Mod. Phys. A* **2022**, *37*, 22410123. [CrossRef]
23. Guo, X.; Milton, K.A.; Kennedy, G.; Pourtolami, N. Quantum Friction in the Presence of a Perfectly Conducting Plate. *Phys. Rev. A* **2023**, *107*, 62812. [CrossRef]
24. Antezza, M.; Emelianova, N.; Khusnutdinov, N. Casimir-Lifshitz Force for Moving Graphene. *arXiv* **2023**, arXiv:2303.03115. <https://doi.org/10.48550/arXiv.2303.03115>.
25. Levin, M.L.; Rytov, S.M. *Theory of Equilibrium Thermal Fluctuations in Electrodynamics*; Nauka: Moscow, Russia, 1967. (In Russian)
26. Zel'dovich, Y.B. Generation of Waves by a Rotating Body. *JETP Lett.* **1971**, *14*, 270–272. Available online: http://jetpletters.ru/ps/1604/article_24607.shtml (accessed on 30 December 2023).
27. Fialkovsky, I.; Khusnutdinov, N.; Vassilevich, D. Quest for Casimir Repulsion between Chern-Simons Surfaces. *Phys. Rev. B* **2018**, *97*, 165432. [CrossRef]
28. Van Kampen, N.G.; Nijboer, B.N.A.; Schram, K. On the Macroscopic Theory of van der Waals Forces. *Phys. Lett. A* **1968**, *26*, 307–308. [CrossRef]
29. Gerlach, E. Equivalence of van der Waals Forces between Solids and the Surface–Plasmon Interaction. *Phys. Rev. B* **1971**, *4*, 393–396. [CrossRef]
30. Silveirinha, M.G. Optical Instabilities and Spontaneous Light Emission by Polarizable Moving Matter. *Phys. Rev. X* **2014**, *4*, 31013. [CrossRef]
31. Starke, R.; Schober, G.A.H. Functional Approach to Electrodynamics of Media. *Photonics Nanostruct. Fundam. Appl.* **2015**, *14*, 1–34. [CrossRef]
32. Starke, R.; Schober, G.A.H. Relativistic Covariance of Ohm’s Law. *Int. J. Mod. Phys. D* **2016**, *25*, 1640010. [CrossRef]
33. Melrose, D.B. *Quantum Plasmadynamics: Unmagnetized Plasmas*; Springer: New York, NY, USA, 2008. [CrossRef]
34. Bordag, M.; Fialkovsky, I.V.; Gitman, D.M.; Vassilevich, D.V. Casimir Interaction between a Perfect Conductor and Graphene Described by the Dirac Model. *Phys. Rev. B* **2009**, *80*, 245406. [CrossRef]
35. Khusnutdinov, N.; Drosdoff, D.; Woods, L.M. Casimir Energy for Surfaces with Constant Conductivity. *Phys. Rev. D* **2014**, *89*, 85033. [CrossRef]
36. Khusnutdinov, N.; Kashapov, R.; Woods, L.M. Casimir Effect for a Stack of Conductive Planes. *Phys. Rev. D* **2015**, *92*, 45002. [CrossRef]
37. Khusnutdinov, N.; Kashapov, R.; Woods, L.M. Casimir-Polder Effect for a Stack of Conductive Planes. *Phys. Rev. A* **2016**, *94*, 12513. [CrossRef]
38. Djurišić, A.B.; Li, E.H. Optical Properties of Graphite. *J. Appl. Phys.* **1999**, *85*, 7404–7410. [CrossRef]
39. Emelianova, N.; Khusnutdinov, N.; Kashapov, R. Casimir Effect for a Stack of Graphene Sheets. *Phys. Rev. B* **2023**, *107*, 235405. [CrossRef]
40. Bordag, M. Electromagnetic Vacuum Energy for Two Parallel Slabs in Terms of Surface, Waveguide, and Photonic Modes. *Phys. Rev. D* **2012**, *85*, 25005. [CrossRef]
41. Antezza, M.; Fialkovsky, I.; Khusnutdinov, N. Casimir-Polder Force and Torque for Anisotropic Molecules Close to Conducting Planes and Their Effect on CO₂. *Phys. Rev. B* **2020**, *102*, 195422. [CrossRef]
42. Henkel, C.; Joulain, K.; Mulet, J.P.; Greffet, J.J. Coupled Surface Polaritons and the Casimir Force. *Phys. Rev. A* **2004**, *69*, 23808. [CrossRef]
43. Lifshitz, E.M. The Theory of Molecular Attractive Forces between Solids. *Sov. Phys. JETP* **1956**, *2*, 73–83. Available online: <http://jetp.ras.ru/cgi-bin/e/index/e/2/1/p73?a=list> (accessed on 30 December 2023).

44. Bordag, M.; Geyer, B.; Klimchitskaya, G.L.; Mostepanenko, V.M. Lifshitz-Type Formulas for Graphene and Single-Wall Carbon Nanotubes: van der Waals and Casimir Interactions. *Phys. Rev. B* **2006**, *74*, 205431. [CrossRef]
45. Jaekel, M.T.; Reynaud, S. Casimir Force between Partially Transmitting Mirrors. *J. Phys. Fr.* **1991**, *1*, 1395–1409. [CrossRef]

Disclaimer/Publisher's Note: The statements, opinions and data contained in all publications are solely those of the individual author(s) and contributor(s) and not of MDPI and/or the editor(s). MDPI and/or the editor(s) disclaim responsibility for any injury to people or property resulting from any ideas, methods, instructions or products referred to in the content.

Article

Casimir–Lifshitz Frictional Heating in a System of Parallel Metallic Plates

George V. Dedkov

Institute of Informatics, Electronics and Robotics, Kabardino-Balkarian State University, Chernysheskogo 174, Nalchik 360004, Russia; gv_dedkov@mail.ru

Abstract: The Casimir–Lifshitz force of friction between neutral bodies in relative motion, along with the drag effect, causes their heating. This paper considers this frictional heating in a system of two metal plates within the framework of fluctuation electromagnetic theory. Analytical expressions for the friction force in the limiting cases of low (zero) temperature and low and high speeds, as well as general expressions describing the kinetics of heating, have been obtained. It is shown that the combination of low temperatures ($T < 10$ K) and velocities of $10\text{--}10^3$ m/s provides the most favorable conditions when measuring the Casimir–Lifshitz friction force from heat measurements. In particular, the friction force of two coaxial disks of gold 10 cm in diameter and 500 nm in thickness, one of which rotates at a frequency of $10\text{--}10^3$ rps (revolutions per second), can be measured using the heating effect of 1–2 K in less than 1 min. A possible experimental layout is discussed.

Keywords: Casimir–Lifshitz friction force; quantum friction; radiative heating

1. Introduction

Over the past two decades, much effort has been spent investigating the static [1,2] and dynamic [3,4] Casimir effect in various geometric configurations, including a system of two parallel metal (dielectric) plates separated by a narrow vacuum gap. The main objectives of these studies are the properties of a fluctuating electromagnetic field and its interaction with matter on the nanoscale. Measurement of these effects paves the way to the core of nonequilibrium quantum field theory [5–8].

In addition to the attractive (in most cases) Casimir forces between electrically neutral bodies at rest, a dissipative tangential force arises when one or both bodies move relative to each other. The sources of these forces are dissipative effects within the plates (Joule losses). In this case, the corresponding fluctuation electromagnetic forces are called “van der Waals” [9], “Casimir” [10], or “quantum” [11] forces of friction. As it looks, it is convenient to use the general name “Casimir–Lifshitz” (CL) friction force, which incorporates all the features of these dissipative forces regarding their distance, temperature, and material properties.

It is worth noting that, despite of many intense efforts, no convincing experimental measurements of CL friction forces have been carried out to date. This is due not only to the small magnitude of these forces relative to the “ordinary” Casimir forces (forces of attraction) but also to the imperfections of the measurement layout. In particular, the effective interaction area and relative velocity are significantly limited in the “pendulum” measurement scheme used in Ref. [12]. Other experimental scenarios [9,13–17] seem to be more exotic. Recently, in Refs. [15–17], to measure traces of quantum friction, the authors suggested a scenario in which the nitrogen vacancy center in diamond acquires the geometric phase during rotation at a frequency of $10^3\text{--}10^4$ rps (revolutions per second) near the Si- or Au-coated surface. Nitrogen vacancy centers have been proposed for use as the main components of quantum computer processors [18].

Nearly all experiments to measure Casimir–Lifshitz forces (both conservative and dissipative) have been performed with well-conducting materials (metals like gold) under

Citation: Dedkov, G.V.

Casimir–Lifshitz Frictional Heating in a System of Parallel Metallic Plates. *Physics* **2024**, *6*, 13–30. <https://doi.org/10.3390/physics6010002>

Received: 2 September 2023

Revised: 21 November 2023

Accepted: 28 November 2023

Published: 27 December 2023



Copyright: © 2023 by the author. Licensee MDPI, Basel, Switzerland. This article is an open access article distributed under the terms and conditions of the Creative Commons Attribution (CC BY) license (<https://creativecommons.org/licenses/by/4.0/>).

near-normal temperature conditions. Regarding Casimir–Lifshitz friction forces, it has usually been assumed that they decrease with decreasing temperature as the resistivity of metals and ohmic losses decrease. Therefore, at first glance, the friction force also does. The conclusion that for metals, the temperature behavior of CL friction is not that simple was first made in Ref. [19] and later discussed in [20,21]. It has been shown that at temperatures $T \ll \theta_D$ (θ_D is the Debye temperature), the force of friction can increase by several orders of magnitude compared with normal conditions. However, several issues have not been elucidated, in particular, the relation between friction and heating effects at thermal nonequilibrium, the relation between quantum friction and friction at close to zero temperature, and the kinetics of radiation heating, etc. In particular, the interplay between nonequilibrium dynamics, the quantum and thermal properties of the radiation, and the confinement of light at the vacuum-surface interface may lead to several intriguing features caused by nonequilibrium thermodynamics of quantum friction [22–25]. Some other effects were considered in Refs. [26–30].

The main objective of this paper, in addition to studying CL friction and heating in a system of parallel metallic plates of nonmagnetic metals like gold, is to substantiate the possibility of determining the friction force from thermal measurements. In the calculations, the general results of fluctuation electrodynamics [31,32] are used, without a linear expansion in velocity in the basic expressions. It is shown that identical metal plates with different initial temperatures, moving with a constant nonrelativistic velocity, V , relative to each other, rapidly reach a state of quasithermal equilibrium and continue to heat up further. The heating rate is then determined by the power of the friction force.

The outline of this paper is as follows. In Section 2, the general relations between radiative heating and friction force for parallel plates in relative nonrelativistic motion are given. In Sections 2.2, 2.3, 2.4, and 2.5 I consider the simplest case of identical plates of Drude metals having the same material parameters and temperature, T . Analytical expressions are obtained for the friction force of metal plates in the limiting cases of low (zero) temperature and low and high speeds, as well as general expressions describing the kinetics of heating. In Section 3, the results of the numerical calculations (heating rates of plate 1 and friction parameter, $\eta = F_x/V$, with F_x the x -component of the friction force) are given for different thermal configurations and velocities. The analytical results of Section 2 are compared with the results of numerical integration according to the general formulas. Section 4 is devoted to a brief discussion of a possible layout of an experiment for determining the CL friction force by measuring the heating rates of gold plates. Concluding remarks are given in Section 5. Appendixes A–C contain the details of the analytical calculations. All formulas are written in the Gaussian units, \hbar and c are the reduced Planck constant and the speed of light in vacuum, respectively, T denotes the absolute temperature and is given in units of energy.

2. General Results

2.1. Radiative Heating and Friction Force for Parallel Plates in Relative Motion

Here, we use the standard formulation of the problem, in which the plates are assumed to be made of homogeneous and isotropic materials with permittivities, ϵ_1 , ϵ_2 , and permeabilities, μ_1 , μ_2 , depending on the frequency, ω , and local temperatures, T_1 and T_2 (Figure 1).

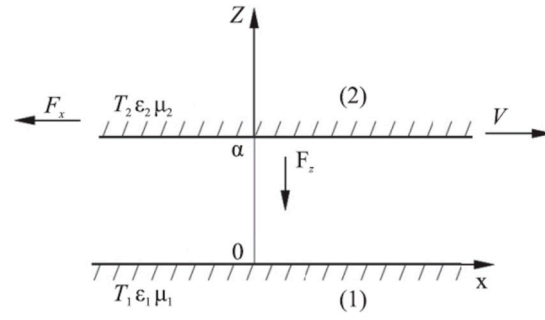


Figure 1. Configuration of parallel plates in relative motion. See text for details.

In line with Refs. [31,32], the power, $F_x V$, of the friction force x -component, F_x , per unit surface area applied to plate 2 in the laboratory coordinate system associated with plate 1 is calculated using

$$F_x V = P_1 + P_2 / \gamma. \quad (1)$$

Here, P_1 and P_2 are the heat fluxes of the plates from a unit surface area per unit time, and $\gamma = (1 - V^2/c^2)^{-1/2}$. For all quantities, indices 1 and 2 here and in what follows correspond to the numbering in Figure 1. Moreover, P_1 and P_2 are calculated in the rest frames of the plates. General relativistic expressions for P_1 and P_2 were obtained in Ref. [31]. In the nonrelativistic case, $V/c \ll 1$, but taking retardation into account, a more compact form of P_1 and P_2 reads [32]:

$$P_1 = \frac{\hbar}{4\pi^3} \int_0^\infty d\omega \omega \int d^2k \frac{|q|^2}{|Q_\mu|^2} \text{Im} \left(\frac{q_1}{\mu_1} \right) \text{Im} \left(\frac{\tilde{q}_2}{\mu_2} \right) \left[\coth \left(\frac{\hbar\omega}{2T_1} \right) - \coth \left(\frac{\hbar\omega^-}{2T_2} \right) \right] + (\mu_{1,2} \leftrightarrow \varepsilon_{1,2}), \quad (2)$$

$$P_2 = -\frac{\hbar}{4\pi^3} \int_0^\infty d\omega \omega \int d^2k \omega^- \frac{|q|^2}{|Q_\mu|^2} \text{Im} \left(\frac{q_1}{\mu_1} \right) \text{Im} \left(\frac{\tilde{q}_2}{\mu_2} \right) \left[\coth \left(\frac{\hbar\omega}{2T_1} \right) - \coth \left(\frac{\hbar\omega^-}{2T_2} \right) \right] + (\mu_{1,2} \leftrightarrow \varepsilon_{1,2}), \quad (3)$$

$$Q_\mu = \left(q + q_1 / \mu_1 \right) \left(q + \tilde{q}_2 / \tilde{\mu}_2 \right) \exp(qa) - \left(q - q_1 / \mu_1 \right) \left(q - \tilde{q}_2 / \tilde{\mu}_2 \right) (-qa), \quad Q_\mu \leftrightarrow Q_\varepsilon. \quad (4)$$

Here, $\omega^- = \omega - k_x V$, $q = \sqrt{k^2 - \omega^2/c^2}$, $q_{1,2} = \sqrt{k^2 - \varepsilon_{1,2}\mu_{1,2}\omega^2/c^2}$, and a is the gap width in Figure 1. Variables with a tilde, such as \tilde{q}_2 , should be used replacing $\omega \rightarrow \omega^-$. The terms $(\mu_{1,2} \leftrightarrow \varepsilon_{1,2})$ are defined by the same expressions with appropriate replacements. In the general case, the expressions depending on $\varepsilon_{1,2}$ and $\mu_{1,2}$ correspond to the contributions of electromagnetic modes with P (transverse magnetic, TM) and S (transverse electric, TE) polarizations. The quantities P_1 and P_2 are directly related to the heating (cooling) rates of the plates: $dQ_1/dt = -P_1$ and $dQ_2/dt = -P_2$, where t denotes the time.

Using Equations (1)–(4), the power of the friction force $F_x V = P_1 + P_2$ takes the form:

$$F_x V = \frac{\hbar}{4\pi^3} \int_0^\infty d\omega \int d^2k (k_x V) \frac{|q|^2}{|Q_\mu|^2} \text{Im} \left(\frac{q_1}{\mu_1} \right) \text{Im} \left(\frac{\tilde{q}_2}{\mu_2} \right) \left[\coth \left(\frac{\hbar\omega}{2T_1} \right) - \coth \left(\frac{\hbar\omega^-}{2T_2} \right) \right] + (\mu_{1,2} \leftrightarrow \varepsilon_{1,2}). \quad (5)$$

Formula (5) can be also recast into a more familiar form in terms of the Fresnel reflection coefficients [9,32].

At $T_1 = T_2 = T$, due to the symmetry of the system, the heating rates of identical plates are equal. One then has $F_x V = 2P_{1,2}$, and the friction force can be determined using the heating rate of any plate. For $T_1 \neq T_2$, it follows that $P_1 \neq P_2$, but $P_1(T_1, T_2) = P_2(T_2, T_1)$ and, correspondingly, $P_1(T_1, T_2) + P_2(T_1, T_2) = P_1(T_1, T_2) + P_1(T_2, T_1) = P_2(T_1, T_2) + P_2(T_2, T_1)$. This means that when measuring the CL friction force, it is sufficient to control the temperature of only one plate.

2.2. Metal Plates in the Drude Model

In order to treat the problem of temperature-dependent CL friction force between ordinary metals, they are described using the Drude model in terms of plasma frequency, ω_p , and damping parameter, $\nu(T) = \omega_p^2 \rho(T) / 4\pi$, with $\rho(T)$ being the resistivity:

$$\epsilon(\omega) = 1 - \frac{\omega_p^2}{\omega(\omega + i\nu(T))}. \tag{6}$$

Figure 2 plots the dependences $\rho(T)$ corresponding to the Bloch–Grüneisen (BG) model [33] and the modified Bloch–Grüneisen (MBG) model (BG scaled in Figure 2 to the data from Ref. [34]). In the former case, the residual resistance is zero or can be specified by indicating the effective temperature, below which it is constant. In the MBG model, the residual resistivity is $\rho_0 = 2.3 \times 10^{-10} \Omega \cdot m$ (see Figure 2).

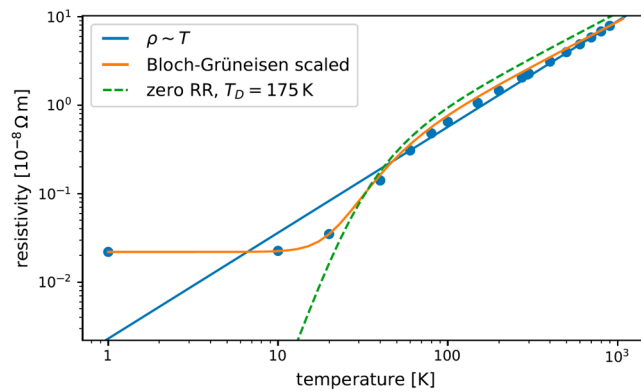


Figure 2. Resistivity of gold [34]. To obtain resistivity in the Gaussian units, one should use the relation $\Omega \cdot m = (1/9)10^{-9}s$. The ‘zero RR’ stands for zero residual resistance, T_D is the Debye temperature, and $\rho \sim T$ denotes a linear fit. See text for more details.

Hereinafter, for simplicity, the plates are assumed been made of similar nonmagnetic metal ($\mu_1 = \mu_2 = 1$) with the same plasma frequency ω_p , but different $\nu(T)$ dependence.

Since $\epsilon(\omega) \gg 1$ for good conductors and the inequality becomes stronger as $T \rightarrow 0$, the terms with $\epsilon_{1,2}$ in Equations (2), (3) and (5), corresponding to modes with P-polarization, are negligible compared to the terms with $\mu_{1,2}$, corresponding to modes with S-polarization. Therefore, in what follows, the contributions of P modes are omitted.

When calculating the integrals in (2), (3), and (5), it is convenient to introduce a new frequency variable $\omega = \nu_m(T_1, T_2)t$, with $\nu_m(T_1, T_2) = \max(\nu_1(T_1), \nu_2(T_2))$ and $\nu_i(T_i)$, $i = 1, 2$, being the damping parameters of plates 1 and 2 depending on their temperatures T_1 and T_2 , respectively. The absolute value k of the two-dimensional wave vector (using the polar coordinates k, ϕ in the plane (k_x, k_y)) is expressed as $k = (\omega_p/c) \sqrt{y^2 + \beta_m^2 t^2}$ in the evanescent sector $k > \omega/c$ ($0 \leq y < \infty$) and $k = (\omega_p/c) \sqrt{\beta_m^2 t^2 - y^2}$ in the radiation sector $k < \omega/c$ ($0 \leq y \leq \beta_m t$). Here, the parameters $\beta_m = \nu_m/\omega_p$, $\alpha_i = \hbar\nu_i/T_i$, $\gamma_i = \nu_i/\nu_m$, $\lambda = \omega_p a/c$, $\zeta = (V/c)\beta_m^{-1}$, and $K = \frac{\hbar\nu_m^2(\omega_p/c)^2}{2\pi^3}$ are introduced. With these definitions, for $k > \omega/c$, Equations (2), (3) and (5) take the form:

$$P_1 = K \int_0^\infty dt \int_0^\infty dy y^3 f_1(t, y), \tag{7}$$

$$P_2 = -K \int_0^\infty dt \int_0^\infty dy y^3 f_2(t, y), \tag{8}$$

$$F_x V = K \int_0^\infty dt \int_0^\infty dy y^3 \sqrt{y^2 + \beta_m^2 t^2} f_3(t, y), \tag{9}$$

$$f_1(t, y) = t \int_0^\pi d\phi \frac{\text{Im}w_1 \text{Im}w_2}{|D|^2} Z(t, y, \phi), \tag{10}$$

$$f_2(t, y) = \int_0^\pi d\phi t^- \frac{\text{Im}w_1 \text{Im}w_2}{|D|^2} Z(t, y, \phi), \tag{11}$$

$$f_3(t, y) = \zeta \int_0^\pi d\phi \cos\phi \frac{\text{Im}w_1 \text{Im}w_2}{|D|^2} Z(t, y, \phi), \tag{12}$$

$$Z(t, y, \phi) = \coth\left(\frac{\alpha_1 t}{2}\right) - \coth\left(\frac{\alpha_2 t^-}{2}\right), \tag{13}$$

$$w_1 = \sqrt{y^2 + \frac{t}{t + i\gamma_1}}, \quad w_2 = \sqrt{y^2 + \frac{t^-}{t^- + i\gamma_2}}, \quad t^- = t - \zeta \cos\phi \sqrt{y^2 + \beta_m^2 t^2}, \tag{14}$$

$$D = (y + w_1)(y + w_2)\exp(\lambda y) - (y - w_1)(y - w_2)\exp(-\lambda y). \tag{15}$$

In the sector $k < \omega/c$, Formulas (14) and (15) should be modified by replacing $y \rightarrow iy$ and substituting $\beta_m t$ for ∞ in Equations (7)–(9) in the integrals over y . The expressions for $\text{Im}w_{1,2}$ can be additionally simplified. For example, it follows that

$$\text{Im}w_1 = \frac{\left(\sqrt{\{\gamma_1^2 y^2 + (1 + y^2)t^2\}^2 + \gamma_1^2 t^2 - \gamma_1^2 y^2 - (1 + y^2)t^2}\right)^{1/2} \text{sgn}(-t)}{\sqrt{2(\gamma_1^2 + t^2)}}. \tag{16}$$

The $\text{Im}w_2$ is defined by the same expression (16), substituting γ_2 for γ_1 and t^- for t . For two identical plates at quasithermal equilibrium, it follows that $\gamma_1 = \gamma_2 = 1$, and a simpler useful expression is obtained by expanding the square root in Equation (16) and leaving the expansion terms up to the second order:

$$\text{Im}w_1 \approx \frac{|t| \cdot \text{sgn}(-t)}{2\sqrt{(1 + t^2)(y^2 + (1 + y^2)t^2)}}. \tag{17}$$

In this case, an approximate analytical calculations can be done.

2.3. Quantum Friction

In the case $T_1 = T_2 = 0$, corresponding to the conditions of quantum friction, the main role is played by the evanescent modes $k > \omega/c$. At finite temperatures, the evanescent modes make the dominant contribution at $a < 1 \mu\text{m}$. This range of distances is highly promising experimentally. For this reason, hereinafter, let us consider only evanescent modes, omitting the small term $\beta_m^2 t^2$ in Equations (9), (14) and other formulas. Therefore, at zero temperature, substituting the identity $Z(t, y, \phi) = \text{sgn}(t) - \text{sgn}(t - \zeta y \cos(\phi))$ into Equation (9) yields:

$$F_x V = 2K\zeta \int_0^\infty dy y^4 \int_0^{\frac{\pi}{2}} d\phi \cos\phi \int_0^{\zeta y \cos\phi} dt \frac{\text{Im}w_1 \text{Im}w_2}{|D|^2}. \tag{18}$$

The most straightforward asymptotics of Equation (18) can be worked out for two identical plates in the limit of low velocities, $\zeta \ll 1$. Using Equations (15) and (17), one obtains:

$$\text{Im}w_1\text{Im}w_2 \rightarrow -\frac{t(\zeta y \cos\phi - t)}{4y^2}, |D|^2 \rightarrow \frac{1}{16}y^{-4}\exp(-2\lambda y). \quad (19)$$

Inserting Equation (19) into Equation (18) yields:

$$F_x V = -\frac{\pi K \zeta^4}{2^{12} \lambda^2} = -\frac{\hbar \omega_p^2}{2^{13} \pi^2} \left(\frac{\omega_p}{c}\right)^2 \left(\frac{V}{c}\right)^2 \left(\frac{V}{av_0}\right)^2 = -\frac{1}{2^9} \frac{\hbar}{\rho_0^2 a^2} \left(\frac{V}{c}\right)^4, \quad (20)$$

where ρ_0 is the residual resistivity corresponding to the zero-temperature damping factor $\nu_0 = \nu(0)$. The limit of high velocities, $\zeta \gg 1$ is more laborious. A reasonable representation of the double integral in Equation (9) can be worked out using an approximate expression for $\text{Im}w_1\text{Im}w_2$, based on Equation (17):

$$\text{Im}w_1\text{Im}w_2 = \frac{|t(b-t)|\text{sgn}(t)\text{sgn}(b-t)}{4 \left[(1+t^2)(1+(t-b)^2)(y^2+t^2(1+y^2))(y^2+(t-b)^2(1+y^2)) \right]^{1/2}}. \quad (21)$$

where $b = \zeta y \cos\phi$. The product $\text{Im}w_1\text{Im}w_2$, as a function of t in the range $0 \leq t \leq b$, reaches its maximum close to the point $t = b/2$, with zeroing at the end points $t = 0, t = b$ of the integration domain of the inner integral in Equation (9). At the same time, the dependence on t in $|D|^2$ is much weaker. By virtue of this, $t = b/2$ was inserted into the denominator of Equation (21) and into $|D|^2$ (in the latter case, $\cos\phi \approx 1$ is also used). Expression (21) then takes the form

$$\text{Im}w_1\text{Im}w_2 \approx -\frac{t(b-t)}{4[(1+b^2/4)(y^2+b^2(1+y^2)/4)]}. \quad (22)$$

With these transformations, it follows that (see Appendix A):

$$F_x V = -\frac{K\zeta}{2} \int_0^\infty dy \frac{y^4}{|D|^2} \int_0^{\pi/2} d\phi \frac{\cos\phi}{\psi(y,\phi)} \int_0^{\zeta y \cos\phi} dt t(\zeta y \cos\phi - t), \quad (23)$$

where $|D|^2$ and $\psi(y,\phi)$ are calculated using Equations (A2) and (A3). The integrals over t and ϕ are calculated explicitly, and finally, we obtain (see Equations (A4) and (A6)):

$$F_x V = -\frac{\hbar v_0^2}{3\pi^2} \left(\frac{\omega_p}{c}\right)^2 \int_0^\infty dy \frac{y^5 \exp(-2\lambda y)}{(y + \sqrt{1+y^2})^4} \left(\frac{1}{y^2(1+y^2)} - \frac{2}{y^2 \sqrt{y^2 \zeta^2 + 4}} + \frac{2}{(1+y^2) \sqrt{(1+y^2)\zeta^2 + 4}} \right). \quad (24)$$

As follows from Equation (24), in this approximation, the power of the quantum friction force does not depend on the velocity. However, it is worth noting that the condition $\zeta \gg 1$ implies $\rho_0 \omega_p \ll 4\pi V/c$, and along with $V/c \ll 1$, it can only be satisfied if ρ_0 is more than three orders of magnitude smaller than the MBG value shown in Figure 2. Interestingly, for $\zeta \ll 1$, Equation (24) also agrees quite well with the numerical calculations and approximation (20) (see Section 3.2 below).

2.4. Low Temperatures, Linear in Velocity Approximation

In the quasiequilibrium thermal regime, $T_1 = T_2 = T$, for two identical metal plates in the linear in velocity approximation, Equations (5) and (9) can be recast into the form of [19,20]:

$$F_x V = -\frac{\hbar V^2}{8\pi^2} \left(\frac{\omega_p}{c}\right)^4 \alpha^{-1} Y_1(\lambda, \alpha), \quad (25)$$

$$Y_1(\lambda, \alpha) = \alpha^2 \int_0^\infty \frac{dt}{\sinh^2(\alpha t/2)} \int_0^\infty dy y^5 \frac{(\text{Im}w_1)^2}{|D|^2}. \tag{26}$$

In this limit, the friction parameter, $\eta = F_x/V$, does not depend on V . It is the dependence $F_x \propto \alpha^{-1}$ in Equation (25) that leads to a large enhancement of friction at low temperatures, when $\alpha = \hbar\nu(T)/T \rightarrow 0$, because the function $Y_1(\lambda, \alpha)$ weakly depends on α . The main contribution to $Y_1(\lambda, \alpha)$ in this case makes the values $t < 1$, $y \sim 1/2\lambda \sim 1$, and one can again use Equation (17) for $\text{Im}w_1$. Meantime, $\alpha^2 \sinh^{-2}(\alpha t/2) \approx 4/t^2$ (this is a suitable approximation at $\alpha < 0.3$) and $|D|^2 \approx 16y^4 \exp(2\lambda y)$. Making use of these simplifications in Equation (26), one arrives at (see Appendix B)

$$Y_1(\lambda, \alpha) \approx \chi(\lambda) = \frac{\pi}{32} \left\{ \frac{\pi}{4\lambda} [\text{H}_1(2\lambda) - N_1(2\lambda)] - \frac{1}{4\lambda^2} \right\}, \tag{27}$$

where $\text{H}_1(x)$ and $N_1(x)$ are the Struve and Neumann functions [35], respectively. Using the series representations of these functions yields:

$$\chi(\lambda) = \begin{cases} \frac{\pi}{64} \left(\frac{1}{\lambda} - \frac{1}{2\lambda^2} + \frac{1}{4\lambda^3} + \dots \right), & \lambda \gg 1, \\ \frac{\pi}{32} \left(\frac{1}{4} + \frac{2\lambda}{3} - 2\lambda(\ln\lambda + 0.577) \right), & \lambda \ll 1. \end{cases} \tag{28}$$

A more straightforward and physically transparent low-temperature representation of Equation (25) is obtained by using the relation $\nu(T) = \omega_p^2 \rho(T)/4\pi$ between the damping factor and resistivity, yielding

$$F_x V = -\frac{1}{2\pi} \left(\frac{V}{c} \right)^2 \left(\frac{\omega_p}{c} \right)^2 \frac{T}{\rho(T)} \chi(\lambda). \tag{29}$$

Combining the relation $\alpha \ll 1$, which implies $\hbar\nu(T) \ll T$, and $\zeta \ll 1$, which implies the limit of low velocities $V/c \ll \nu(T)/\omega_p$, one concludes that the Formula (29) holds at

$$\hbar\omega_p V/c \ll \hbar\nu(T) \ll T. \tag{30}$$

As a result, the conditions of a low-temperature increase in friction and the applicability of the low-speed approximation are met at $V/c \ll T/\omega_p \hbar$. For gold, at $T = 1$ K, this implies $V/c \ll 1.5 \times 10^{-5}$.

According to Refs. [19,20], the dependence (29) is associated with a growing penetration depth of S-polarized electromagnetic modes and an increase in their density at low temperatures. A significant low-temperature increase in the friction parameter was also noted in the case of the movement of a metal particle above the metal surface [21].

2.5. Low Temperatures, High-Velocity Limit

The limit $\zeta \gg 1$ at finite but low temperatures ($\alpha \ll 1$) can be analyzed similarly to the case of zero temperatures using the properties of the function (21). When substituting Equation (21) into Equation (9) with allowance for Equation (13), the first exponential term in Equation (13) makes the dominant contribution at $t \sim 1 \ll b = \zeta y \cos\phi$. Due to this, let us take an advantage of the substitution $|t - b| \rightarrow b$ in the denominator of Equation (21). For the second term in Equation (13), a new variable $t' = t - b$ is introduced and the substitution $|t' + b| \rightarrow b$ is made in the denominator of Equation (21), while the integral (9) is then determined using the large exponential factor $(\exp(\alpha t') - 1)^{-1}$ at $t' \sim 1 \ll b$. Then,

taking into account these transformations in Equation (9), and summing both contributions, the double integral in Equation (9) finally takes the form (see Appendix C)

$$I \approx \frac{\zeta^2}{2} \int_0^\infty dy y^4 |D|^{-2} \int_0^{\frac{\pi}{2}} d\phi \psi_1(y, \phi) \int_0^\infty dt \frac{t}{(e^{\alpha t} - 1)} \psi_2(y, \phi), \quad (31)$$

where

$$|D|^{-2} \approx \left(y + \sqrt{1 + y^2} \right)^{-4} \exp(-2\lambda y), \quad (32)$$

$$\psi_1(y, \phi) = \cos^2 \phi \left(1 + \zeta^2 y^2 \cos^2 \phi \right)^{-1/2} \left(1 + \zeta^2 \left(1 + y^2 \right) \cos^2 \phi \right)^{-1/2}, \quad (33)$$

and

$$\psi_2(y, t) = \frac{1}{[(1 + t^2)(y^2 + t^2(1 + y^2))]^{1/2}}. \quad (34)$$

To proceed further, we replace the function $t/(e^{\alpha t} - 1)$ with $1/\alpha$ in the inner integral (31), which is again a good approximation for $\alpha < 0.3$. The remaining integral yields:

$$\int_0^\infty dt \frac{t}{(e^{\alpha t} - 1)} \psi_2(y, t) \approx \frac{1}{\alpha} \frac{K(q)}{\sqrt{1 + y^2}}, \quad q = \left(1 + y^2 \right)^{-1/2}, \quad (35)$$

where $K(q)$ is a complete elliptic integral [35]. Taking this into account, the ϕ -integral in Equation (31) can be evaluated as the arithmetic mean between the integrals calculated with the limit functions on the left and right sides of the inequality (see Appendix C):

$$\cos^2 \phi \left(1 + \zeta^2 \left(1 + y^2 \right) \cos^2 \phi \right)^{-1} < \psi_1(y, \phi) < \cos^2 \phi \left(1 + \zeta^2 y^2 \cos^2 \phi \right)^{-1}. \quad (36)$$

Substituting Equation (A20) into Equations (31) and (9) finally yields:

$$F_x V = -\frac{T}{8\pi^2} V \left(\frac{\omega_p}{c} \right)^3 Y_2(\lambda, \zeta), \quad (37)$$

where $Y_2(\lambda, \zeta)$ is calculated using:

$$Y_2(\lambda, \zeta) = \int_0^\infty dy \frac{y^4 e^{-2\lambda y}}{\left(y + \sqrt{y^2 + 1} \right)^4 (1 + y^2)^{\frac{1}{2}}} K \left(\frac{1}{\sqrt{1 + y^2}} \right) \left[\frac{\sqrt{1 + \zeta^2 y^2} - 1}{y^2 \sqrt{1 + \zeta^2 y^2}} + \frac{\sqrt{1 + \zeta^2 (1 + y^2)} - 1}{(1 + y^2) \sqrt{1 + \zeta^2 (1 + y^2)}} \right]. \quad (38)$$

Similar to the case of quantum friction (24), the power of the friction force (37) does not depend on velocity.

To date, there are no other relevant calculations for the friction forces between metal plates, corresponding to low-temperature conditions. However, it is interesting to compare the results obtained here with those in the case of an atom moving above the metal surface [22,23]. Let us compare the dependences on the velocity and resistivity of metal for quantum friction ($T = 0$). Equation (20) has the same low-speed dependence, $F_x \sim V^3$, but the opposite dependence on resistivity (Equation (16) in Ref. [22]): $F_x \sim \rho_0^{-2}$ (yet the additional condition $\rho_0 \omega_p \gg 4\pi V/c$ should be met). At high but nonrelativistic velocities ($\rho_0 \omega_p \ll 4\pi V/c$), Equation (24) yields $F_x \sim \rho_0^2$ in contrast to $F_x \sim \rho_0$ (Equation (19) in Ref. [22]). The dependence on velocity in Equation (24) is more moderate, $F_x \sim V^{-1}$, which qualitatively agrees with that in Ref. [22]. The case $T > 0$, when the friction force is linear in velocity, is less informative, because the results of Refs. [22,23] correspond to room conditions. Yet, Formula (29) yields $F_x \sim 1/\rho_0$ (assuming the condition (30)), which is different from that in Ref. [23]: $F_x \sim \rho(T)^2$.

In general, one should not expect close qualitative similarity between the plate–plate and atom–plate configurations because in the latter case, the radiative energy exchange processes, according to Refs. [22,23], are determined by the specific thermal nonequilibrium in the system. In the case of macroscopic bodies, such as two plates, the system must reach a state of thermal quasiequilibrium; see Section 2.6 just below.

2.6. Kinetics of Heating of Plates

The heat transfer of plates is described using the equations

$$P_1(T_1, T_2)\Delta t = -h_1\rho_1c_1(T_1)\Delta T_1 \text{ and } P_2(T_1, T_2)\Delta t = -h_2\rho_2c_2(T_2)\Delta T_2. \quad (39)$$

With $c_i(T_i)$ being the specific heat capacities, h_i and ρ_i are the thicknesses and densities of materials, $P_1(T_1, T_2)$ and $P_2(T_1, T_2)$ are defined using Equations (2) and (3), and the temperature gains ΔT_i correspond to the interval of time Δt . The dependences $T_2(T_1)$ and $T_1(T_2)$ can be determined using the equation

$$\frac{dT_2}{dT_1} = \frac{P_1(T_1, T_2)c_1(T_1)h_1\rho_1}{P_2(T_1, T_2)c_2(T_2)h_2\rho_2}. \quad (40)$$

For identical plates, in Equation (40), one can use the replacements $P_2(T_1, T_2) \rightarrow P_1(T_2, T_1)$, $P_1(T_1, T_2) \rightarrow P_2(T_2, T_1)$. In what follows, only this case is considered.

When writing Equations (39) and (40), it is also assumed that the heat exchange due to radiative heat transfer occurs much slower than under thermal diffusion, and the plates acquire equal temperature at all points because of high thermal conductivity. Using the thermal diffusion equation along the normal to the plates, $\partial T/\partial t = a^2\partial^2 T/\partial z^2$, the characteristic time of the heat diffusion necessary to reach thermal quasiequilibrium, is $\tau = h^2/a^2$ (where $a^2 = \kappa/c\rho$, and κ is the thermal conductivity). Then it follows that $\tau = h^2c\rho/\kappa$ and in the case of gold at $T = 10$ K and $h_{1,2} = h = 500$ μm $c = 2.2$ J/(kg·K), $\kappa = 3200$ W/(m·K), $\rho = 19.8 \cdot 10^3$ kg/m³ [36]) one obtains $\tau \simeq 3$ μs . In turn, the kinetics of heating induced by friction takes dozens of seconds or minutes (see Section 3.3 below), depending on the velocity and other parameters. Assuming that $P_i(T, T) = -0.5\eta(T, V)V^2$, from Equation (39) one obtains:

$$t = \frac{2h\rho}{V^2} \int_{T_0}^T \frac{c(T)}{\eta(T, V)} dT, \quad (41)$$

the heating time from the initial temperature T_0 to the final temperature T . In the simplest case of $\eta = \text{const}$ and $c(T) = a_1T + a_2T^3$ (this is a typical low-temperature dependence for metals), it follows from Equation (41) that

$$T(t) = \left(-\beta + \sqrt{\beta^2 + T_0^4 + 2\beta T_0^2 + 2\eta V^2 t/h\rho a_2} \right)^{1/2}, \quad (42)$$

where $\beta = a_1/a_2$. At $T_1 \neq T_2$ and relatively low velocities of plate 2, as follows from numerical calculations (see Section 3.1 below), the heating/cooling rates of metal plates differ only in sign, i.e., $P_1(T_1, T_2) = -P_2(T_1, T_2)$. This is the normal mode of heat transfer, when a hotter body cools down, and a colder one heats up. Then the left sides of Equation (39) can be equated, and the corresponding quasistationary temperature of the plates is calculated using:

$$T = \left(-\beta + \sqrt{\beta^2 + \beta(T_1^2 + T_2^2) + T_1^4 + T_2^4} \right)^{1/2}, \quad (43)$$

where T_1 and T_2 are their initial temperatures. After establishing quasithermal equilibrium, the temperature of the plates will increase according to Equations (41) and (42).

3. Numerical Results

For an ideal metal without impurities and defects, within the BG model, the damping frequency $\nu(T)$ in Equation (6) is defined using the formula [33]:

$$\nu(T) = 0.0212(\Theta/T)^5 \int_0^{\Theta/T} dx x^5 \sinh^{-2}(x/2) \text{ (eV)}. \quad (44)$$

Numerical calculations were performed using Equation (44) and the MBG approximation shown in Figure 2 (BG scaled). The used plasma frequency of gold is $\omega_p = 9.03$ eV. All calculations were performed with a gap width of $a = 10$ nm (Figure 1) unless another value is indicated. It should be noted that at distances of $a > 10$ nm, the processes of radiative heat transfer and friction due to tunneling of electrons and phonons [37,38] seem do not occur or become insignificant [39–41].

3.1. Quantum Friction

Figure 3 shows the velocity-dependent quantum friction force between the plates of gold, calculated using Formulas (20) (green line), (9) (red line) and (24) (blue line).

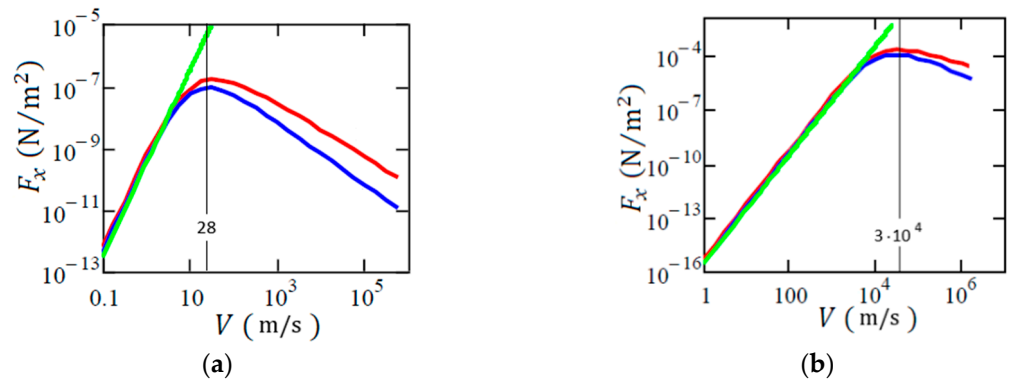


Figure 3. Quantum friction force of the plates of gold as a function of the velocity of a moving plate 2: (a) residual resistance of gold corresponds to Bloch–Grüneisen (BG) model at $T = 5$ K; (b) residual resistance corresponds to modified BG (MBG) model at $T = 0$ (see Figure 2). The red lines represent complete numerical integration in Equation (9), the green and blue lines are calculations using Formulas (20) and (24). The positions of the maxima and the corresponding velocities are shown, respectively, by vertical lines and the numbers indicated.

The curves in Figure 3a,b were calculated at residual resistances of $2.13 \times 10^{-13} \Omega \cdot \text{m}$ and $2.3 \times 10^{-10} \Omega \cdot \text{m}$, which correspond to the BG model (44) at $T = 5$ K and the MBG model at $T = 0$ K. Note that in the latter case, the residual resistance coincides with that defined using Formula (44) at $T = 20.9$ K.

3.2. Temperature-Dependent Friction at Thermal Quasiequilibrium

Figure 4 shows the plots of the friction parameter, $\eta = F_x/V$, depending on the temperature T of the gold plates, corresponding to the BG and MBG models. The curves with symbols were calculated using Equation (9) for $V = 1$ m/s. Solid curves were plotted using approximation (25) along with Equation (26) (green lines) or Equation (28) at $\lambda \gg 1$ (blue lines). In Figure 4a, both solid lines merge. The presence of maxima and their positions on the curves agree with Equations (29) and (30), respectively. These results show that the linear-in-velocity approximation is valid only to the right of the maxima of the $\eta(T)$ dependences.

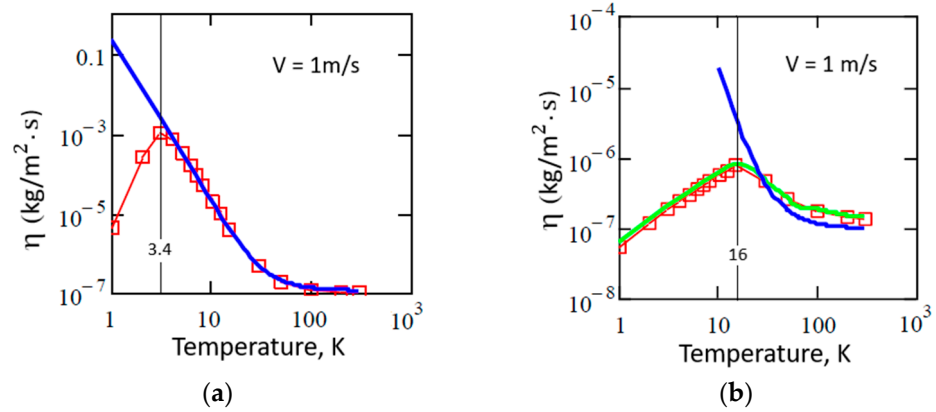


Figure 4. Friction parameter of gold plates as a function of their quasiequilibrium temperature for (a) BG and (b) MBG models. The curves with symbols were calculated using complete numerical integration in Equation (9). Solid lines correspond to the calculations using Equation (25) with Equation (26) (green lines) and (28) (blue lines); in (a), the blue and green lines merge. The vertical numbered lines show the temperatures corresponding to the maxima of the curves.

Figure 5a,b demonstrates the velocity dependences of η in the BG and MBG models. The red, blue, and green lines correspond to quasiequilibrium temperatures of 5 K, 10 K, and 77 K, respectively. The different (temperature) order of lines in Figure 5a compared to Figure 5b is explained by the high residual resistance of gold in the MBG model: the condition $\hbar v(T) < T$, which is necessary for the low-temperature increase in friction, is violated at $T = 5$ and 10 K.

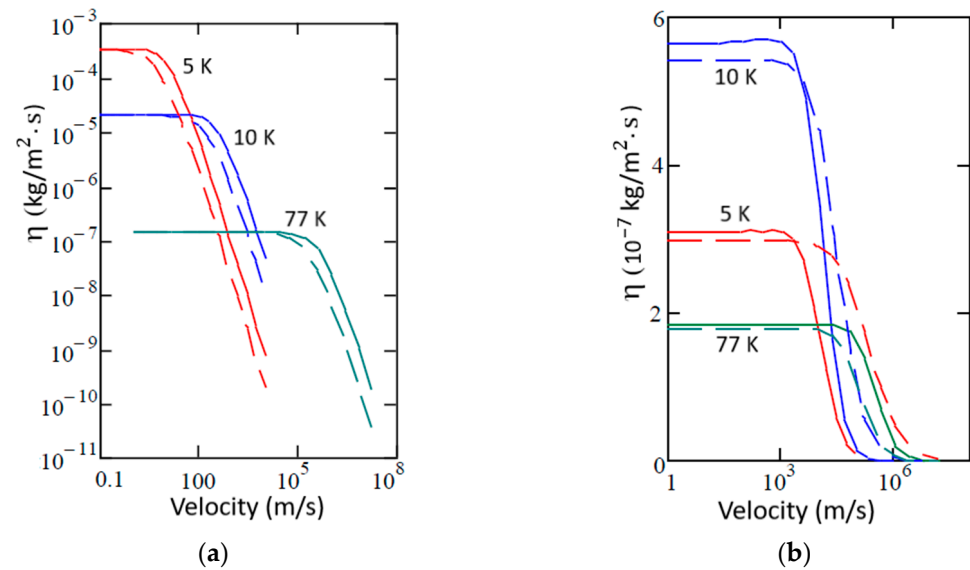


Figure 5. Friction parameter of gold plates as a function of the velocity of plate 2 for the (a) BG and (b) MBG models. The solid lines represent the calculations using Equation (9), dashed lines—Equations (37) and (38). The red, blue, and green lines correspond to quasistationary temperatures of 5 K, 10 K, and 77 K, respectively, for both plates. The different temperature order of the curves in (b) is explained by a different sequence of parameters $\alpha = \hbar v/T$: $\alpha(10) < \alpha(5) < \alpha(77)$. The plateau in the curves corresponds to the linear velocity dependence of the friction force.

Table 1 shows the calculated values of the friction parameter η of the gold plates at $V = 1$ m/s, depending on the temperature, T , and separation distance, a . Similar to that in Figure 4, one can note the effect of increasing friction (up to a maximum) with decreasing temperature at $T < \theta_D$, which is more better expressed in the BG model. The height of

this maximum depends on the velocity-to-resistivity ratio. When the temperature becomes sufficiently low, condition (30) is violated, and the coefficient of friction decreases.

Table 1. Friction parameter η (in $\text{kg}/(\text{m}^2 \cdot \text{s})$) of gold plates for velocity $V = 1 \text{ m/s}$ at thermal quasiequilibrium, Equation (9).

Temperature of Plates, K	$a = 10 \text{ nm}$	$a = 20 \text{ nm}$	$a = 10 \text{ nm}$	$a = 20 \text{ nm}$
	Model BG		Model MBG	
1	4.81×10^{-6}	2.77×10^{-6}	5.60×10^{-8}	2.80×10^{-8}
2	2.63×10^{-4}	1.47×10^{-4}	1.22×10^{-7}	5.98×10^{-8}
3	1.10×10^{-3}	5.73×10^{-4}	1.87×10^{-7}	9.13×10^{-8}
5	3.44×10^{-4}	1.67×10^{-4}	3.08×10^{-7}	1.50×10^{-7}
10	2.15×10^{-5}	1.04×10^{-5}	5.63×10^{-7}	2.73×10^{-7}
15	4.30×10^{-5}	2.09×10^{-6}	7.77×10^{-7}	3.76×10^{-7}
20	1.52×10^{-6}	7.35×10^{-7}	7.19×10^{-7}	3.33×10^{-7}
50	2.04×10^{-7}	9.90×10^{-8}	2.56×10^{-7}	1.25×10^{-7}
100	1.30×10^{-7}	6.30×10^{-8}	1.77×10^{-7}	8.63×10^{-8}
200	1.14×10^{-7}	5.54×10^{-8}	1.42×10^{-7}	6.81×10^{-8}
300	1.11×10^{-7}	5.41×10^{-8}	1.39×10^{-7}	6.81×10^{-8}

The dependence of η on the separation distance a in all the cases is close to inverse proportionality ($\eta \propto a^{-1}$). This is clearly seen from the data in Table 1 and agrees with our previous results [19,20,32].

3.3. Friction and Heating under Different Conditions

Figures 6 and 7 show the calculated heating rates of plate 1 (Figures 6a and 7a) and friction parameters (Figures 6b and 7b), depending on the velocity V of plate 2 for various thermal configurations.

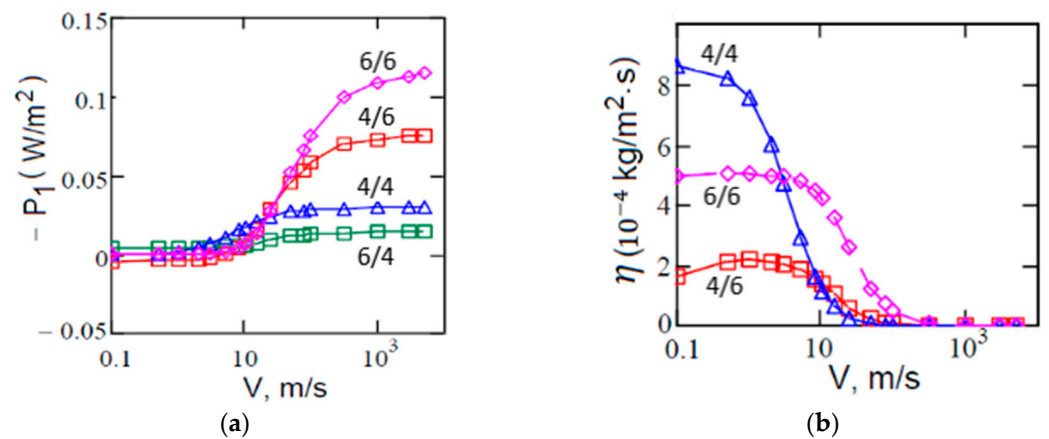


Figure 6. Heating rate of plate 1 (a) and friction parameter $\eta = F_x/V$ (b) as a function of velocity V of plate 2 in the BG model. The temperature configuration for the plates are indicated on the curves as follows: e.g., 6/4 denotes $T_1 = 6 \text{ K}$, $T_2 = 4 \text{ K}$. Thermal configurations $T_1 = 6 \text{ K}$, $T_2 = 4 \text{ K}$ and $T_1 = 4 \text{ K}$, $T_2 = 6 \text{ K}$ have the same friction parameters, configurations $T = 4$ and 6 K correspond to a quasiequilibrium thermal mode. The data shown by open triangles (Δ) (a) and by open diamonds (\diamond) (b) are multiplied by 3 (cf. [42], where all numerical data to be reduced by π times).

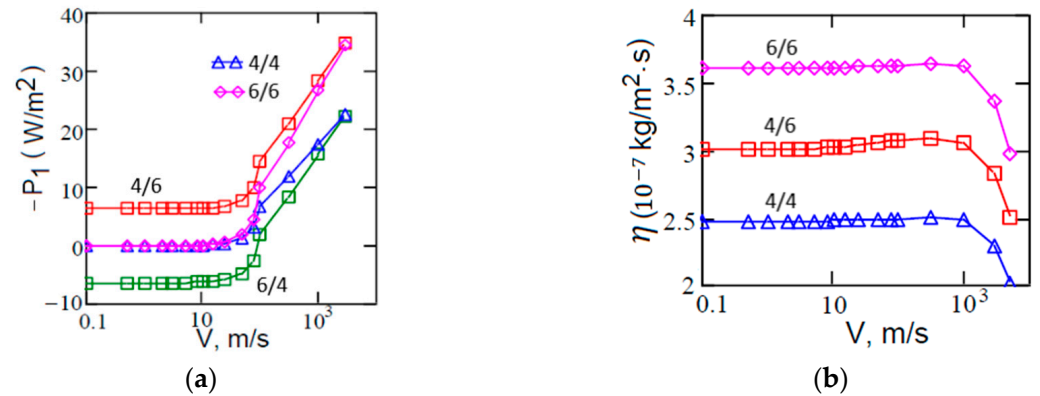


Figure 7. Same as in Figure 6 but in the MBG model. No additional numerical factors for the data are used.

One can see that at $V < 10$ m/s (Figure 6a) and $V < 10^2$ m/s (Figure 7a), the heating rates of plates 1 and 2 are equal in absolute value, differing in sign. According to their temperatures, $T_1 = 4$ K and $T_2 = 6$ K, plate 1 heats up and plate 2 cools down, realizing the “normal” heat exchange regime. At the same time, the friction parameters weakly depend on the temperature (Figures 6b and 7b). When the speed of plate 2 increases, both plates heat up faster. Then, one can see the effect of the “anomalous” heating of plate 2 for some time, when it continues to heat up despite the higher temperature. This is similar to the case of heating a hotter metal particle moving above a cold surface [21]. However, due to different absolute values of the heating rates (cf. the upper and lower lines shown with open squares (□) in Figures 6a and 7a), the temperature of plate 1 “catches up” with the temperature of plate 2, and further on, both plates heat up at the same rate.

The drop in friction parameters for high velocities of plate 2 (Figures 6b and 7b) is explained by the change in sign of the Doppler-shifted frequency $\omega^- = \omega - k_x V = \omega - kV \cos \phi$ in Equation (5). This occurs at $V > v(T)a$ because the characteristic absorption frequency is $\omega \sim v(T)$ and the characteristic wave vector is $k \sim 1/a$. The positions of the “kinks” on the curves $\eta(V)$ in Figures 6 and 7 correlate with resistivity because $v(T) \sim \rho(T)$. Indeed, it follows from Figure 2 that $\rho_{\text{MBG}}/\rho_{\text{BG}} = 10^2\text{--}10^3$ at $T = 4\text{--}6$ K. At the same time, the ratio $\eta_{\text{MBG}}/\eta_{\text{BG}}$ in this case is inversely proportional to resistivities (see Equation (29) and Table 1).

In general, as follows from the calculations for all considered temperatures and velocities (Figures 5–7, Table 1), the maximum friction parameter in the BG and MBG models (at $a = 10$ nm) is $10^{-6} - 10^{-3}$ kg/(m²·s).

Figure 8 shows the heating time of the plates versus the velocity of plate 2, calculated using numerical integration of Equation (40) from 4 K to 5 K and from 4 K to 8 K. In these calculations, the fitting parameters $a_1 = 0.0035$ J/(kg·K²) and $a_2 = 0.0023$ J/(kg·K⁴) of the dependence $c(T) = a_1 T + a_2 T^3$ were determined using the data [36] for gold at $T < 20$ K.

As follows from Figure 8, quite comfortable (from the experimental point of view) values of the plate heating times (1–100 s) can be obtained in the velocity range 1–10³ m/s. On the contrary, heating by 1 K at $T_0 = 300$ K, $a = 10$ nm, and $V = 10^3$ m/s will take about 2 h. Thus, low-temperature thermal measurements have exceptional advantages over measurements under normal conditions due to a significant reduction in measurement time and the elimination of noise and other undesirable effects.

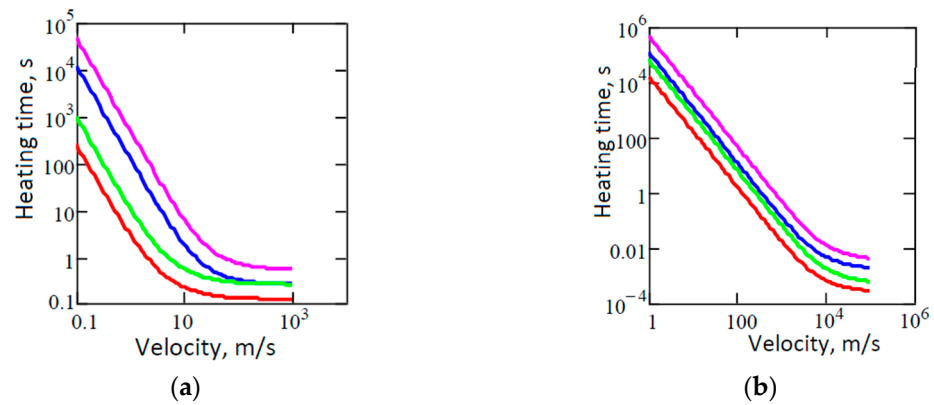


Figure 8. Heating time of gold plates as a function of the velocity of plate 2 at $h = 500 \mu\text{m}$ according to BG (a) and MBG (b) models. Two upper lines correspond to heating from 4 K to 8 K at $a = 20 \text{ nm}$ (crimson) and $a = 10 \text{ nm}$ (blue), and two lower lines correspond to heating from 4 K to 5 K at $a = 20 \text{ nm}$ (green) and $a = 10 \text{ nm}$ (red).

4. Experimental Proposal

Initiated by the advantage of the experimental design [15–17] to measure the quantum friction force, I suggested [42] using another experimental layout, as shown schematically in Figure 9. Unlike in Ref. [17], where the setup includes a disk 10 cm in diameter rotating with an angular frequency of up to $7 \times 10^3 \text{ rps}$, it is proposed to use two identical disks placed in one thermostat, one of which rotates at a controlled speed. In the peripheral region, the disks have an annular metal coating with an effective area πDw . The non-inertiality of the reference system of disk 2 does not appear in this case because the rotation frequency is small compared to the characteristic frequencies of the fluctuation electromagnetic field. Accordingly, the original expressions (2) and (3), for heating rates remain valid.

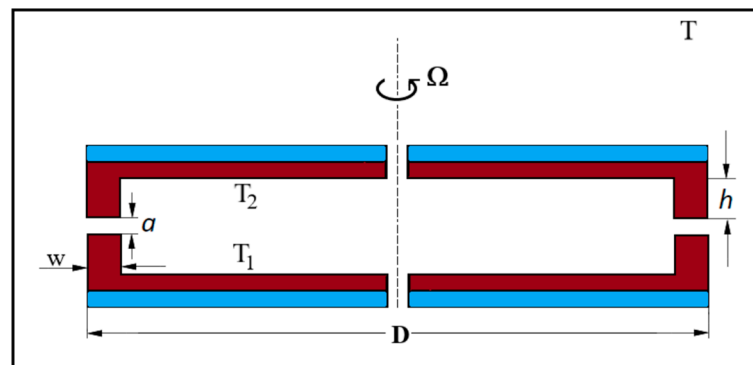


Figure 9. A possible setup for measuring Casimir–Lifshitz friction force (side view). The thermal protection layer is shown in blue, the metal coating is shown in brown. When the upper disk rotates, the circular sections of disks locating at a distance a move at a linear velocity of $0.5 \Omega D$ relative to each other. At rotation frequencies $n = 1\text{--}10^4 \text{ rps}$ (revolutions per second) and disk diameter $D = 0.1 \text{ m}$, the velocity range to be $0.3\text{--}3000 \text{ m/s}$.

A possible measurement scenario in this case is the quasiequilibrium thermal mode, in which the temperatures of plates increase from the initial temperature T_0 at the same rate. It should be noted that the experimental design must take into account possible limitations on angular velocity imposed by the tensile strength of the material used. Assuming that the main body of the plate is made of gold, a quite moderate assessment of the linear velocity of the far-distant annular parts of the plate yields $V < (\sigma_0/\rho)^{0.5}$, with $\sigma_0 = 1.5 \times 10^8 \text{ N/m}^2$ and $\rho = 1.93 \times 10^4 \text{ kg/m}^3$ being the tensile strength and density of gold [35]. By plugging the numerical numbers into the above condition, one obtains $V \sim 10^2 \text{ m/s}$, or $n \sim 300 \text{ rps}$, which seems to be a well acceptable value.

5. Concluding Remarks

The Casimir–Lifshitz friction force mediated by the fluctuating electromagnetic field between metal plates moving with constant velocity relative to each other causes their heating. In a state out of thermal equilibrium, “anomalous” heating of the moving plate can be observed when it is heated for some time despite the higher temperature. However, the system rapidly reaches a state of thermal quasiequilibrium. At low temperatures $T \ll \theta_D$, the Casimir–Lifshitz friction and heating of metal plates increase significantly (see Equations (29) and (30)) while the heat capacity decreases. In combination with a fairly high speed of movement, this provides a fairly short heating time, which is convenient for experiments (see Equation (41)).

Funding: This research received no external funding.

Data Availability Statement: Data can be obtained upon reasonable request.

Acknowledgments: I am grateful to Carsten Henkel for fruitful remarks at the preliminary stage of the work and for providing data on the low-temperature resistivity of gold.

Conflicts of Interest: The author declares no conflicts of interest.

Appendix A. Evaluation of the Integral (24)

Substituting $t = b/2 = \zeta y \cos\phi/2$ into Equation (22) takes into account that typically, $\zeta y \cos\phi/2 \gg 1$ (since $\zeta \gg 1$, $y \sim 1/2\lambda \sim 1$) and $|w_{1,2}| \approx \sqrt{y^2 + 1}$. Then $|D|^2$ takes the form

$$|D|^2 \approx \left(y + \sqrt{y^2 + 1}\right)^4 \exp(-2\lambda y). \tag{A1}$$

With these simplifications, Formula (18) reads:

$$F_x V = -\frac{K\zeta}{2} \int_0^\infty dy \frac{y^2}{\left(y + \sqrt{y^2 + 1}\right)^4} e^{-2\lambda y} \int_0^{\pi/2} d\phi \frac{\cos\phi}{\psi(y, \phi)} \int_0^{\zeta y \cos\phi} dt t (\zeta y \cos\phi - t), \tag{A2}$$

$$\psi(y, \phi) = \left(1 + \zeta^2 y^2 \cos^2\phi/4\right) \left(1 + \zeta^2 (1 + y^2) \cos^2\phi/4\right). \tag{A3}$$

The t -integral in Equation (A2) is just $\zeta^3 y^3 \cos^3\phi/6$, while the integral over ϕ is

$$I_\phi = \frac{\zeta^3 y^3}{6} \int_0^{\pi/2} d\phi \frac{\cos^4\phi}{\psi(y, \phi)} = \frac{8y^3}{3\zeta} \int_0^{\pi/2} d\phi \frac{\cos^4\phi}{(u^2 + y^2 \cos^2\phi) \left(u^2 + (1 + y^2) \cos^2\phi\right)}, \tag{A4}$$

where $u = 2/\zeta$. The integral in Equation (A4) is calculated explicitly using the table integral [35]

$$\int_0^{\pi/2} \frac{d\phi}{a^2 + b^2 \cos^2\phi} = \frac{\pi}{2} \frac{1}{a\sqrt{a^2 + b^2}}. \tag{A5}$$

Using Equation (A5) yields:

$$I_\phi = \frac{4\pi y^3}{3\zeta} \left(\frac{1}{y^2(1 + y^2)} - \frac{2}{y^2 \sqrt{y^2 \zeta^2 + 4}} + \frac{2}{(1 + y^2) \sqrt{(1 + y^2) \zeta^2 + 4}} \right). \tag{A6}$$

Substituting Equation (A6) into Equation (A2) yields Equation (24).

Appendix B. Evaluation of the Integral (26)

In the case $\alpha \ll 1$, the main contribution to Equation (26) makes the values $t < 1$, $y \sim 1/2\lambda \sim 1$. Then, from Equation (14), it follows that $|w_{1,2}| = |(y^2 + t/(t+i))^{1/2}| \approx y$. Using this, one finds:

$$|D|^{-2} \approx 16y^4 \exp(-2\lambda y). \tag{A7}$$

Meantime, from Equation (21) it follows that

$$(\text{Im}w_{1,2})^2 = \frac{t^2}{4(1+t^2)(y^2+t^2(1+y^2))}. \tag{A8}$$

Substituting Equations (A7) and (A8) into Equation (26) yields:

$$Y(\lambda, \alpha) = \frac{\alpha^2}{64} \int_0^\infty dy y e^{-2\lambda y} \int_0^\infty dt \frac{t^2}{\sinh(\alpha t/2)^2} \frac{1}{(1+t^2)(y^2+t^2(1+y^2))}. \tag{A9}$$

Using the approximation $\frac{t^2}{\sinh(\alpha t/2)^2} \rightarrow 4/\alpha^2$ and the table integral [35]

$$\int_0^\infty dx \frac{1}{(a^2+x^2)} \frac{1}{(b^2+x^2)} = \frac{\pi}{2ab(a+b)}, \tag{A10}$$

one obtains:

$$Y_1(\lambda, \alpha) \approx \chi(\lambda) = \frac{\pi}{32} \int_0^\infty dy \frac{e^{-2\lambda y}}{(y + \sqrt{1+y^2})} = \frac{\pi}{32} \left\{ \frac{\pi}{4\lambda} [H_1(2\lambda) - N_1(2\lambda)] - \frac{1}{4\lambda^2} \right\}, \tag{A11}$$

where $H_1(x)$ and $N_1(x)$ are the Struve and Neumann functions [35].

Appendix C. Evaluation of the Integral (31)

Let us rewrite Equation (13) in the form

$$Z(t, y, \phi) = \frac{2}{\exp(\alpha t) - 1} - \frac{2}{\exp(\alpha|t^-|) - 1}, \quad t^- = t - \zeta y \cos\phi. \tag{A12}$$

The integral in Equation (9) includes two exponential factors, defined by Equation (A12). By changing the order of integration in the first term, one obtains:

$$I = 2\zeta \int_0^\infty dy y^4 \int_0^\pi d\phi \cos\phi \int_0^\infty dt \frac{\text{Im}w_1 \text{Im}w_2}{|D|^2} \frac{1}{\exp(\alpha t) - 1}. \tag{A13}$$

Similar to Appendix B, one can again take advantage of the behavior of the t -integral in Equation (A13) for $\alpha \ll 1$, and $\zeta \gg 1$, substituting $\frac{1}{\exp(\alpha t) - 1} \approx 1/\alpha t$ and using Equation (A1) for $|D|^2$. For $\text{Im}w_1 \text{Im}w_2$, let us use Equation (21) with the replacement $|t-b| \rightarrow \zeta y |\cos\phi|$. Then Equation (21) takes the form

$$\text{Im}w_1 \text{Im}w_2 = - \frac{t \cdot \zeta |\cos\phi| \cdot \text{sign}(t - \zeta y \cos\phi)}{4[(1 + \zeta^2 y^2 \cos^2\phi)(1 + \zeta^2(1+y^2)\cos^2\phi)(1+t^2)(y^2+t^2(1+y^2))]^{1/2}}. \tag{A14}$$

Inserting Equation (A14) into Equation (A13) yields:

$$I = \frac{\zeta^2}{\alpha} \int_0^\infty dy \frac{y^4 e^{-2\lambda y}}{(y + \sqrt{y^2 + 1})^4 (1+y^2)^{1/2}} \int_0^{\pi/2} d\phi \psi_1(y, \phi) \int_0^\infty dt \psi_2(t, y), \tag{A15}$$

where

$$\psi_1(\phi, y) = \cos^2\phi \left[\left(1 + \zeta^2 y^2 \cos^2\phi \right) \left(1 + \zeta^2 \left(1 + y^2 \right) \cos^2\phi \right) \right]^{-1/2}, \quad (\text{A16})$$

$$\psi_2(t, y) = \frac{1}{\left[(1+t^2) \left(\frac{y^2}{(1+y^2)} + t^2 \right) \right]^{1/2}}. \quad (\text{A17})$$

Substituting Equations (A16) and (A17) into Equation (A15) and taking into account Equations (A10) and (35), the inner integrals are calculated yielding

$$I_\phi(y) = \int_0^\infty d\phi \frac{\cos^2\phi}{\psi_1(\phi, y)} \approx \frac{\pi}{2\zeta^2} \left[\frac{\sqrt{1+\zeta^2 y^2}-1}{y^2 \sqrt{1+\zeta^2 y^2}} + \frac{\sqrt{1+\zeta^2(1+y^2)}-1}{(1+y^2) \sqrt{1+\zeta^2(1+y^2)}} \right], \quad (\text{A18})$$

$$I_t(y) = \int_0^\infty dt \psi_2(t, y) = \frac{1}{\sqrt{1+y^2}} K\left(\frac{1}{\sqrt{1+y^2}}\right), \quad (\text{A19})$$

where $K(x)$ is the elliptic integral. Finally, substituting Equations (A18) and (A19) into Equation (A15) yields:

$$I = \frac{\pi}{4\alpha} \int_0^\infty dy \frac{y^4 e^{-2\lambda y}}{\left(y + \sqrt{y^2 + 1} \right)^4 (1+y^2)^{1/2}} K\left(\frac{1}{\sqrt{1+y^2}}\right) \left[\frac{\sqrt{1+\zeta^2 y^2}-1}{y^2 \sqrt{1+\zeta^2 y^2}} + \frac{\sqrt{1+\zeta^2(1+y^2)}-1}{(1+y^2) \sqrt{1+\zeta^2(1+y^2)}} \right]. \quad (\text{A20})$$

The second integral in Equation (9) by including t^- in Equation (A12) gets to the same result (but ultimately having the opposite sign) by introducing a new variable $t' = t - b$, and using the substitution $|t' + b| \rightarrow \zeta y |\cos\phi|$ in Equation (21).

References

1. Casimir, H.B.G. On the attraction between two perfectly conducting plates. *Proc. Kon. Ned. Akad. Wetensch. B* **1948**, *51*, 793–795. Available online: <https://dwc.knaw.nl/DL/publications/PU00018547.pdf> (accessed on 25 November 2023).
2. Lifshitz, E.M. The theory of molecular attractive forces between solids. *Sov. Phys. JETP* **1956**, *2*, 73–83. Available online: <http://jetp.ras.ru/cgi-bin/e/index/e/2/1/p73?a=list> (accessed on 25 November 2023).
3. Yablonovitch, E. Accelerating reference frame for electromagnetic waves in a rapidly growing plasma: Unruh-Davies-Fulling-DeWitt radiation and the nonadiabatic Casimir effect. *Phys. Rev. Lett.* **1956**, *62*, 1742–1746. [CrossRef] [PubMed]
4. Dodonov, V.V.; Klimov, A.B.; Man'ko, V.I. Nonstationary Casimir effect and oscillator energy level shift. *Phys. Rev. Lett. A* **1989**, *142*, 511–513. [CrossRef]
5. Schwinger, J. Casimir energy for dielectrics. *Proc. Nat. Acad. Sci. USA* **1989**, *89*, 4091–4093. [CrossRef] [PubMed]
6. Dodonov, V. Fifty years of the dynamic Casimir effect. *Physics* **2020**, *2*, 67–104. [CrossRef]
7. Mostepanenko, V.M. Casimir puzzle and Casimir conundrum: Discovery and search for resolution. *Universe* **2021**, *7*, 84. [CrossRef]
8. Reiche, D.; Intravaia, F.; Busch, K. Wading through the void: Exploring quantum friction and vacuum fluctuations. *APL Photonics* **2022**, *7*, 030902. [CrossRef]
9. Volokitin, A.I.; Persson, B.N.J. Near-field radiation heat transfer and noncontact friction. *Rev. Mod. Phys.* **2007**, *79*, 1291–1329. [CrossRef]
10. Milton, K.A.; Høye, J.S.; Brevik, I. The reality of Casimir friction. *Symmetry* **2016**, *8*, 29–83. [CrossRef]
11. Pendry, J.B. Shearing the vacuum—quantum friction. *J. Phys. C Condens. Matter* **1997**, *9*, 10301–10320. [CrossRef]
12. Stipe, B.C.; Stowe, T.D.; Kenny, T.W.; Rugar, D. Noncontact friction and force fluctuations between closely spaced bodies. *Phys. Rev. Lett.* **2001**, *87*, 096801. [CrossRef] [PubMed]
13. Volokitin, A.I. Casimir friction force between a SiO₂ probe and a graphene-coated SiO₂ substrate. *JETP Lett.* **2016**, *104*, 534–539. [CrossRef]
14. Volokitin, A.I. Effect of an electric field in the heat transfer between metals in the extreme near field. *JETP Lett.* **2019**, *110*, 749–754. [CrossRef]
15. Viotti, L.; Farias, M.B.; Villar, P.I.; Lombardo, F.C. Thermal corrections to quantum friction and decoherence: A closed time-path approach to atom-surface interaction. *Phys. Rev. D* **2019**, *99*, 105005. [CrossRef]
16. Farias, M.B.; Lombardo, F.C.; Soba, A.A.; Villar, P.I.; Decca, R.S. Towards detecting traces of non-contact quantum friction in the corrections of the accumulated geometric phase. *npj Quantum Inf.* **2020**, *6*, 25. [CrossRef]
17. Lombardo, F.C.; Decca, R.S.; Viotti, L.; Villar, P.I. Detectable signature of quantum friction on a sliding particle in vacuum. *Adv. Quant. Technol.* **2021**, *4*, 2000155. [CrossRef]

18. Gurudev Dutt, M.V.; Childress, L.; Jiang, L.; Togan, E.; Maze, J.; Jelezko, F.; Zibrov, A.S.; Hemmer, P.R.; Lukin, D. Quantum register based on individual electronic and nuclear spin qubits in diamond. *Science* **2007**, *316*, 1312. [CrossRef]
19. Dedkov, G.V. Low-temperature increase in the van der Waals friction force with the relative motion of metal plates. *JETP Lett.* **2021**, *114*, 779–784. [CrossRef]
20. Dedkov, G.V. Puzzling low-temperature behavior of the van der Waals friction force between metallic plates in relative motion. *Universe* **2021**, *7*, 427. [CrossRef]
21. Dedkov, G.V. Nonequilibrium Casimir-Lifshitz friction force and anomalous radiation heating of a small particle. *Appl. Phys. Lett.* **2022**, *121*, 231603. [CrossRef]
22. Reiche, D.; Intravaia, F.; Hsiang, J.-T.; Busch, K.; Hu, B.-L. Nonequilibrium thermodynamics of quantum friction. *Phys. Rev.* **2020**, *102*, 050203. [CrossRef]
23. Oelschläger, M.; Reiche, D.; Egerland, C.H.; Busch, K.; Intravaia, F. Electromagnetic viscosity in complex structured environments: From black-body to quantum friction. *Phys. Rev. A* **2022**, *106*, 052205. [CrossRef]
24. Brevik, I.; Shapiro, B.; Silveirinha, M. Fluctuational electrodynamics in and out of equilibrium. *Int. J. Mod. Phys. A* **2022**, *37*, 2241012. [CrossRef]
25. Intravaia, F. How modes shape Casimir physics. *Int. J. Mod. Phys. A* **2022**, *37*, 2241014. [CrossRef]
26. Jentschura, U.D.; Lach, G.; De Kiviet, M.; Pachucki, K. One-loop dominance in the imaginary part of the polarizability: Application to blackbody and noncontact van der Waals friction. *Phys. Rev. Lett.* **2015**, *114*, 043001. [CrossRef]
27. Klatt, J.; Bennett, R.; Buhmann, S.Y. Spectroscopic signatures of quantum friction. *Phys. Rev. A* **2016**, *94*, 063803. [CrossRef]
28. Guo, X.; Milton, K.A.; Kennedy, G.; McNulty, W.P.; Pourtolami, N.; Li, Y. Energetics of quantum friction: Field fluctuations. *Phys. Rev. D* **2021**, *104*, 116006. [CrossRef]
29. Guo, X.; Milton, K.A.; Kennedy, G.; McNulty, W.P.; Pourtolami, N.; Li, Y. Energetics of quantum friction. II: Dipole fluctuations and field fluctuations. *Phys. Rev. D* **2022**, *106*, 016008. [CrossRef]
30. Milton, K.A.; Guo, X.; Kennedy, G.; Pourtolami, N.; DelCol, D.M. Vacuum torque, propulsive forces, and anomalous tangential forces: Effects of nonreciprocal media out of thermal equilibrium. *arXiv* **2023**, arXiv:2306.02197. [CrossRef]
31. Polevoi, V.G. Tangential molecular forces caused between moving bodies by a fluctuating electromagnetic field. *Sov. Phys. JETP* **1990**, *71*, 1119–1124. Available online: <http://jetp.ras.ru/cgi-bin/e/index/e/71/6/p1119?a=list> (accessed on 25 November 2023).
32. Dedkov, G.V.; Kyasov, A.A. Friction and radiative heat exchange in a system of two parallel plate moving sideways: Levin-Polevoi-Rytov theory revisited. *Chin. Phys.* **2018**, *56*, 3002. [CrossRef]
33. Condon, E.U.; Odishaw, H. (Eds.) *Handbook of Physics*; McGraw-Hill Book Company, Inc.: New York, NY, USA, 1967.
34. Baptiste, J. Resistivity of gold. In *The Physics Factbook*; Elert, G., Ed.; 2004. Available online: <https://hypertextbook.com/facts/2004/JennelleBaptiste.shtml> (accessed on 25 November 2023).
35. Gradshteyn, I.S.; Ryzhik, I.M. *Table of Integrals, Series and Products*; Academic Press/Elsevier Inc.: Waltham, MA, USA, 2014. [CrossRef]
36. Grigoriev, I.S.; Meilikhov, E.Z. (Eds.) *Handbook of Physical Quantities*; CRC Press/Taylor & Francis Group: Boca Raton, FL, USA, 1996. Available online: https://archive.org/details/handbookofphysic0000unse_b1e4 (accessed on 25 November 2023).
37. Biehs, S.-A.; Kittel, A.; Ben-Abdallah, P. Fundamental limitations of the mode temperature concept in strongly coupled system. *Z. Naturforsch. A* **2020**, *75*, 803–807. [CrossRef]
38. Vioria, M.G.; Guo, Y.; Merabia, S.; Ben-Abdallah, P.; Messina, R. Role of Nottingham effect in the heat transfer in extreme near field regime. *Phys. Rev.* **2023**, *107*, 125414. [CrossRef]
39. Pendry, J.B.; Sasiithlu, K.; Kraster, R.V. Phonon-assisted heat transfer between vacuum-separated surfaces. *Phys. Rev. B* **2016**, *94*, 075414. [CrossRef]
40. Sasiithlu, K.; Pendry, J.B. Van der Waals force assisted heat transfer. *Z. Naturforsch. A* **2017**, *72*, 181–188. [CrossRef]
41. Kuehn, S.; Loring, R.F.; Marohn, J.A. Dielectric fluctuations and the origins of noncontact friction. *Phys. Rev.* **2006**, *96*, 156103. [CrossRef]
42. Dedkov, G.V. Casimir-Lifshitz friction force and kinetics of radiative heat transfer between metal plates in relative motion. *JETP Lett.* **2023**, *117*, 952–957. [CrossRef]

Disclaimer/Publisher’s Note: The statements, opinions and data contained in all publications are solely those of the individual author(s) and contributor(s) and not of MDPI and/or the editor(s). MDPI and/or the editor(s) disclaim responsibility for any injury to people or property resulting from any ideas, methods, instructions or products referred to in the content.

Article

Stabilizing Diamagnetic Levitation of a Graphene Flake through the Casimir Effect

Norio Inui

Graduate School of Engineering, University of Hyogo, Shosha 2167, Himeji 671-2201, Japan; inui@eng.u-hyogo.ac.jp

Abstract: Graphene exhibits diamagnetism, enabling it to be lifted by the repulsive force produced in an inhomogeneous magnetic field. However, the stable levitation of a graphene flake perpendicular to the magnetic field is impeded by its strong anisotropic of magnetic susceptibility that induces rotation. A method to suppress this rotation by applying the Casimir force to the graphene flake is presented in this paper. As a result, the graphene flake can archive stable levitation on a silicon plate when the gravitational force is small.

Keywords: Casimir effect; Casimir force; Casimir torque; diamagnetic levitation

1. Introduction

One of the promising applications of the Casimir effect [1,2] is the actuation of microelectromechanical systems (MEMS) [3–6]. Unlike conventional actuation methods that rely on electric power sources, the Casimir force, which arises from vacuum fluctuations, does not require an external energy source such as a battery. This advantage makes it a desirable option for MEMS actuation. However, the Casimir force can also lead to unexpected adhesion [7] between different parts of MEMS, causing their function to cease due to the omnipresence of vacuum fluctuations. To prevent this adhesion, a straightforward approach is to generate a repulsive force that levitates the MEMS parts. While the repulsive Casimir force [8] has been studied and observed in liquid environments [9], its utilization in atmospheric conditions has not been explored [10].

Levitating MEMS parts without them adhering to substrates can reduce friction and enhance the sensitivity sensors. Numerous methods for levitating objects in the atmosphere have been proposed, with magnetic levitation being a well-known technique. According to Earnshaw's theorem, the stable levitation of magnets cannot be achieved through a combination of static magnetic or gravitational force alone; additional control is required. However, the unique property of diamagnetism enables levitation in the atmosphere without the need for control [11,12].

Graphite, a highly diamagnetic material [13], can be stably levitated above neodymium magnets, and more recently, multi-layer graphene flakes have also been successfully levitated [14,15]. However, achieving stable levitation of a single-layer graphene flake above a magnet in an atmosphere setting remains an unmet challenge. When a magnetic field is applied perpendicularly to the surface of graphene, a strong magnetic moment is induced. In contrast, applying a magnetic field parallel to the surface results in minimal magnet moment induction. Consequently, the graphene rotates to align itself parallel to the magnetic field, leading to a loss of the levitation force.

This study investigates the levitation of a single graphene flake above a substrate, considering the interplay between the diamagnetic force and the Casimir force within the framework of the proximity force approximation (PFA) [16]. Normally, the Casimir force between a graphene sheet and a substrate is attractive, thereby reducing the levitation force. However, it is demonstrated that the Casimir effect can counteract rotation and enable the stable levitation of graphene.

Citation: Inui, N. Stabilizing Diamagnetic Levitation of a Graphene Flake through the Casimir Effect. *Physics* **2023**, *5*, 923–935. <https://doi.org/10.3390/physics5030060>

Received: 20 June 2023

Revised: 28 July 2023

Accepted: 7 August 2023

Published: 1 September 2023



Copyright: © 2023 by the authors. Licensee MDPI, Basel, Switzerland. This article is an open access article distributed under the terms and conditions of the Creative Commons Attribution (CC BY) license (<https://creativecommons.org/licenses/by/4.0/>).

For a configuration involving a small square plate and an infinitely large substrate arranged in parallel, the Casimir energy between them is negative and proportional to the area of the small plate. When the small plate tilts around an axis passing through its center and parallel to its sides, the projection area onto the substrate decreases due to the inclination. This decrease in the projection area contributes to an increase in the Casimir energy. Additionally, the distance between one side of the small plate and the substrate increases, further increasing the Casimir energy. However, the distance between the other side of the small plate and the substrate decreases, leading to a decrease in the Casimir energy. The stability of the parallel state relative to the substrate is determined by the summation of these contributions. For large separations, the last contribution is smaller than the others, resulting in a stable parallel state. If the torque induced by magnetic interaction can be canceled out by the Casimir effect, a graphene flake can be levitated stably in a vacuum.

The remainder of this paper is organized as follows: In Section 2, the magnetic properties of a graphene flake based on the tight-binding model is explained. Section 3 focuses on the levitation of a graphene flake, considering the balance between the force induced by a magnetic field and gravity. In Section 4, the approximation of the Casimir energy between a single-layer graphene and a silicon substrate as a summation of power functions is given. In Section 5, the change in the Casimir energy which is expressed as a power function, due to the rotation being is calculated. This also explores the relationship between the stability of the parallel state and the separation distance. In Section 6, the stability of a levitated graphene flake above a silicon substrate through the application of diamagnetic force is examined. In Section 7, the optimizing the applied magnetic field can lead to stabilization through the Casimir effect on Earth is demonstrated. Additionally, the calculation method beyond PFA is discussed. Finally, in the conclusion, the essential conditions required to achieve stable levitation are summarized.

2. Magnetic Properties of Graphene

The potential energy of a graphene flake in the presence of an external magnetic field is examined. In this study, the magnetic field is generated by passing an electric current through a coil. When the electric current is sufficiently large, the graphene flake can be levitated above the coil, as depicted in Figure 1a. The coil, with a radius R , is positioned above a silicon substrate at a separation distance d as illustrated in Figure 1b. It is important to note that the discussion focuses solely on the levitation achieved through the magnetic force, while the influence of the Casimir effect on the levitation is explored in subsequent Sections.

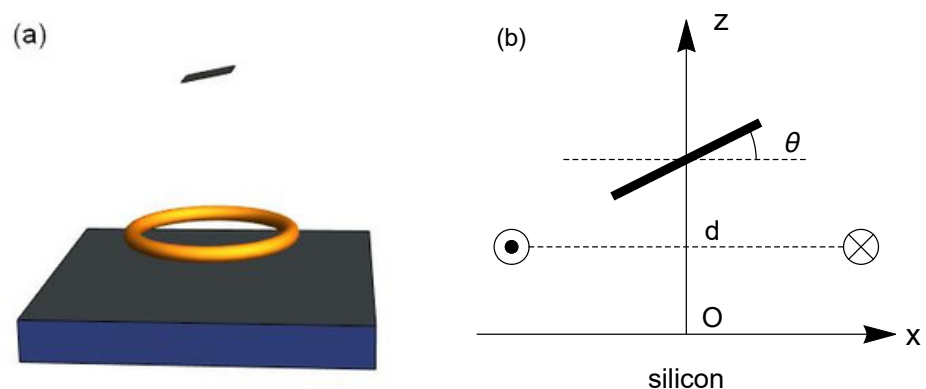


Figure 1. (a) Illustration of the levitation of a graphene flake in a magnetic field generated by an electric current flowing through a coil positioned above a silicon plate. (b) Positional relationship between the inclined graphene, coil, and silicon plate.

The magnetic flux density along the z -axis is expressed as follows:

$$B_z(z) = \frac{\mu_0 I R^2}{2[(z-d)^2 + R^2]^{3/2}}, \tag{1}$$

where I is the electric current through the coil, and $\mu_0 = 1.257 \times 10^{-6} \text{ NA}^{-2}$ is the permeability in the vacuum. The direction of the electric current is counterclockwise when observed from above the ring. On the z -axis, the component of the magnetic flux density parallel to the substrate is zero.

The diamagnetic characteristics of graphene stem from the interaction between the induced electric current and the magnetic field. This study neglects the spin interactions and focus on the calculation of the energy eigenvalues of graphene, denoted as $\epsilon_i(B)$, which depend on the magnetic field. These eigenvalues are typically determined using the tight-binding model and the Peierls substitution method [17–19]. The Hamiltonian can be expressed as follows:

$$H = -\gamma_0 \sum_{\langle n,m \rangle} e^{i\phi_{nm}} \hat{c}_n^\dagger \hat{c}_m, \tag{2}$$

where γ_0 ($=3 \text{ eV}$) is the transfer energy; \hat{c}_n^\dagger and \hat{c}_n are the annihilation and creation operators of an electron at site n , respectively. The magnetic dependence of the Hamiltonian is represented by Peierls phase, ϕ_{nm} , defined by

$$\phi_{nm} = \frac{e}{\hbar} \int_{\vec{r}_n}^{\vec{r}_m} d\vec{r} \cdot \vec{A}, \tag{3}$$

where $\vec{A}(r)$ is the vector potential, and \vec{r}_s is the position of site s . The symbols e and \hbar denote the elementary charge and the reduced Planck constant, respectively. If the applied uniform magnetic field, B , is perpendicular to the graphene surface, the vector potential can be expressed by $(0, Bx, 0)$ in the Landau gauge.

By calculating eigenvalues $\epsilon_i(B)$ of the Hamiltonian, the free energy of graphene including the contribution from the orbital current induced by applying the magnetic field at temperature T is expressed as

$$\mathcal{F}_m(B) = -2k_b T \sum_i \ln \left[1 + \exp \left(\frac{\mu - \epsilon_i(B)}{k_b T} \right) \right], \tag{4}$$

where k_b and μ denote the Boltzmann constant and the chemical potential, respectively. In Equation (4), the factor of 2 is the spin degeneracy of the levels. The present study considers only the case of $\mu = 0$. When considering small magnetic fields, the induced magnetic moment of the graphene flake is directly proportional to the applied magnetic field. Consequently, the magnetic potential can be described as proportional to the inner product of the magnetic moment and the magnetic field. Thus, the magnetic potential for the small magnetic field is expressed as $c_m B^2$. The coefficient c_m depends on the size and edge type of graphene and is expressed as follows:

$$c_m = \left. \frac{1}{2} \frac{\partial^2 \mathcal{F}_m(B)}{\partial B^2} \right|_{B=0}. \tag{5}$$

3. Levitation by Diamagnetic Force

In the case when the angle of inclination is zero and the change in the magnetic field within the graphene flake is disregarded, the total energy of the graphene system can be expressed as the sum of the magnetic energy and the gravitational energy:

$$U_{mg}(z, d) = c_m \frac{\mu_0^2 I^2 R^4}{4[(z-d)^2 + R^2]^3} + mgz, \tag{6}$$

where m is the mass of graphene and g is gravitational acceleration. If $d = 0$ and the normalized position, $\zeta \equiv z/R$, is introduced, the total energy is expressed as

$$U_{mg}(\zeta) = c_0 \left[\frac{1}{(\zeta^2 + 1)^3} + \gamma \zeta \right], \tag{7}$$

where

$$c_0 = \frac{c_m \mu_0^2 I^2}{4R^2}, \tag{8}$$

$$\gamma = \frac{mgR}{c_0}. \tag{9}$$

Figure 2a shows the dependence of U_{mg} on ζ for a different γ . For a small γ , there is a local minimum of U_{mg} , at which the magnetic force balances. Furthermore, this equilibrium point is stable. Thus, the graphene can be levitated stably along the z -axis. If $\gamma > \gamma_c \equiv 1.329$, no local minimum exists and the graphene falls to the substrate. Figure 2b shows the dimensionless levitation height, ζ_m , where U_{mg} takes a minimum values a function of γ . The dimensionless levitation height approaches 0.378 in the limit of $\gamma \rightarrow \gamma_c$.

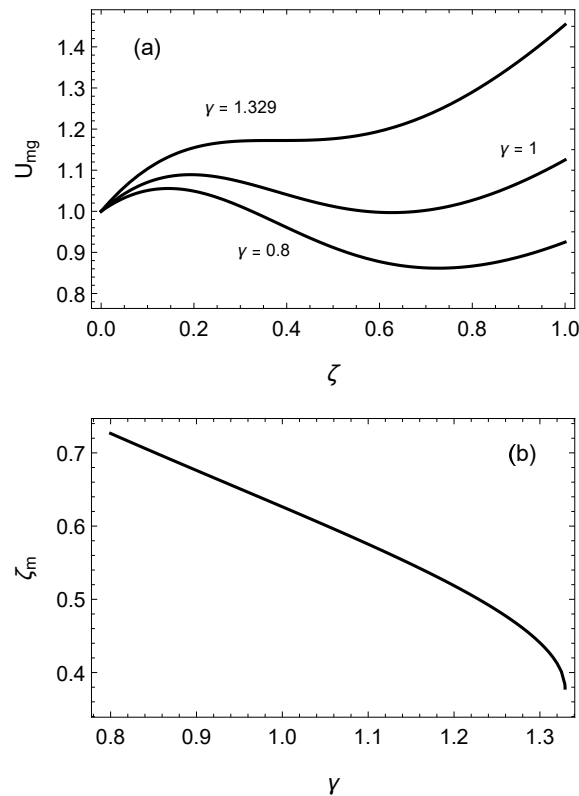


Figure 2. (a) The sum, U_{mg} (7), of magnetic and gravitational potential energies as a function of the nondimensional height, ζ , for different ratios, γ (9). (b) Relationship between the nondimensional levitation height, ζ_m , and γ .

The magnetic susceptibility of graphite vertical to the surface per mass, χ_{\perp} , is $-2.7 \times 10^{-7} \text{ m}^3/\text{kg}$ and one parallel to the surface per mass, χ_{\parallel} , is $-6.3 \times 10^{-9} \text{ m}^3/\text{kg}$. Similarly, the orbital magnetic susceptibility of graphene when aligned parallel to the surface is expected to be significantly smaller than that when aligned perpendicularly to

the surface. Thus, it is assumed that χ_{\parallel} is zero in the following calculations. Accordingly, the magnetic energy of the inclined graphene with the angle θ of inclination is given by

$$U_m(\zeta, \theta) = \frac{c_0 \cos^2 \theta}{(\zeta^2 + 1)^3}. \tag{10}$$

The gravitational energy of a graphene flake remains unaffected by its rotation. Consequently, the flake will rotate until it aligns as parallel to the magnetic field, causing the levitation force to diminish. As a result, the graphene flake descends and eventually comes in contact with the substrate.

4. Casimir Force between a Graphene Flake and a Silicon Plate

To address the issue of rotation, the utilization of the Casimir effect becomes crucial. According to the Lifshitz theory, the Casimir free energy per unit area between a single-layer graphene sheet and a dielectric plate, separated by a separation a and at a temperature T , can be expressed as the sum of contributions for different polarizations η of the electromagnetic field, namely transverse magnetic (TM) and transverse electric (TE):

$$\mathcal{F}_C(a) = \mathcal{F}_{TM}(a) + \mathcal{F}_{TE}(a), \tag{11}$$

where

$$\mathcal{F}_\eta(a) = \frac{k_B T}{8\pi a^2} \sum_{l=0}^{\infty} \int_{\zeta_l}^{\infty} y dy \ln[1 - r_\eta^{(g)}(i\zeta_l, y)r_\eta^{(p)}(i\zeta_l, y)e^{-y}]. \tag{12}$$

Here, ζ_l with nonnegative integer variable l is the dimensionless Matsubara frequencies defined by $4\pi a k_B T l / \hbar c$, with c denoting the speed of light, and $r_\eta^{(g)}$ and $r_\eta^{(p)}$ are the reflection coefficients on graphene and on a plate for the polarization η , respectively [20–25].

The reflection coefficients on a silicon plate are expressed as

$$r_{TM}^{(p)}(i\zeta_l, y) = \frac{\epsilon_l y - \sqrt{y^2 + \zeta_l^2(\epsilon_l - 1)}}{\epsilon_l y + \sqrt{y^2 + \zeta_l^2(\epsilon_l - 1)}}, \tag{13}$$

$$r_{TE}^{(p)}(i\zeta_l, y) = \frac{y - \sqrt{y^2 + \zeta_l^2(\epsilon_l - 1)}}{y + \sqrt{y^2 + \zeta_l^2(\epsilon_l - 1)}}, \tag{14}$$

where ϵ_l is the dielectric permittivity of silicon at the imaginary frequency, $2\pi i k_B T l / \hbar$, and calculated from the optical data [26] based on the Kramers–Kronig relation,

$$\epsilon(i\zeta) = 1 + \frac{2}{\pi} \int_0^{\infty} \frac{\omega \text{Im}\epsilon(\omega)}{\omega^2 + \zeta^2} d\omega. \tag{15}$$

The reflection coefficients on graphene using the Dirac model are expressed as follows:

$$r_{TM}^{(g)}(i\zeta_l, y) = \frac{y\Pi_{00}}{y\Pi_{00} + \frac{\hbar}{a}(y^2 - \zeta_l^2)}, \tag{16}$$

$$r_{TE}^{(g)}(i\zeta_l, y) = -\frac{(y^2 - \zeta_l^2)\Pi_{tr} - y^2\Pi_{00}}{(y^2 - \zeta_l^2)(\Pi_{tr} + \frac{\hbar}{a}y) - y^2\Pi_{00}}, \tag{17}$$

where Π_{00} is the 00-component of the polarization tensor, Π , and $\Pi_{tr} = \Pi_1^1 + \Pi_2^2$. The polarization tensor is determined by the temperature [27], mass gap parameter, δ_g , chemical potential, μ , and the Fermi velocity, $v_F = c/300$. The polarization tensor is described in detail in Ref. [21].

The circles in Figure 3 show the dependence of the Casimir energy per area between graphene with $\delta_g = \mu = 0$ and a silicon plate on the separation distance at temperature 300 K. The line represents a fitting function,

$$u_C(z) = -\frac{c_3}{z^3} - \frac{c_2}{z^2}, \tag{18}$$

where $c_3 = 1.11 \times 10^{-12}$ Jm and $c_2 = 7.96 \times 10^{-11}$ J.

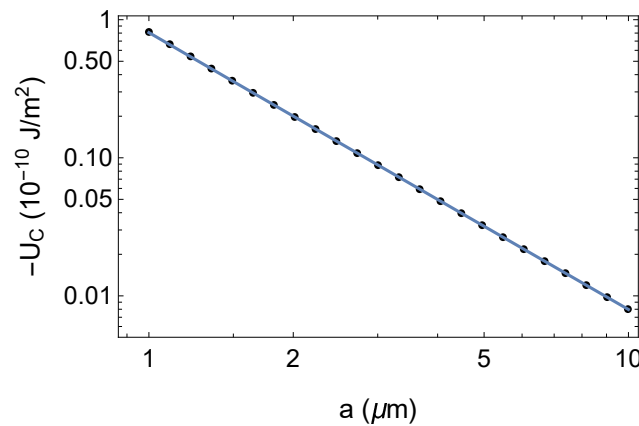


Figure 3. Casimir energy per area between a graphene sheet and a silicon plate calculated using the Lifshitz formula (circles) and the fitting function (line).

5. Change in the Casimir Energy by Inclining

The calculation of the Casimir energy between an inclined plate and a flat plate can be a computationally intensive task [28–30]. As an alternative approach, the PFA is employed. Within the PFA framework, the Casimir energy between an inclined square plate, with one side measuring $2L$, and an infinite substrate can be approximated by the following expression:

$$U_C(a, \theta) = 2L \int_{-L \cos \theta}^{L \cos \theta} u[a - (\tan \theta)x] dx, \tag{19}$$

where $u(z)$ is the Casimir energy per area. If the Casimir energy per area obeys the power function, $u(z) = -c_\beta z^{-\beta}$, where c_β is a constant and $\beta > 1$, its dependence on θ is expressed as

$$U_C(a, \theta, \beta) = -\frac{2c_\beta L}{(1 - \beta) \tan \theta} \left[(a + L \sin \theta)^{1-\beta} - (a - L \sin \theta)^{1-\beta} \right]. \tag{20}$$

By introducing a dimensionless coordinate $\alpha \equiv a/L$, the normalized energy, \tilde{U} , with the absolute value at $\theta = 0$ is expressed as

$$\tilde{U}(\alpha, \theta, \beta) \equiv \frac{U(a, \theta, \beta)}{|U(a, 0, \beta)|}, \tag{21}$$

$$= -\frac{\alpha^\beta}{2(1 - \beta)} \frac{(\alpha + \sin \theta)^{1-\beta} - (\alpha - \sin \theta)^{1-\beta}}{\tan \theta}. \tag{22}$$

Figure 4a shows $\tilde{U}(\alpha, \theta, 2)$ for $\alpha = 1.2, \sqrt{2}$, and 3. For the small values of α , representing small separation distances, a local minimum is present at the nonzero inclination angle and the flat state ($\theta = 0$) becomes unstable. As the separation increases above a threshold, $\alpha_c = \sqrt{2}$, the Casimir energy takes the minimum value at $\theta = 0$, and the flat state becomes stable. Figure 4b shows the relationship between the threshold α_c and exponent β . The thresholds α_c are 2 and $2\sqrt{5/3}$ for $\beta = 3$ and 4, respectively. A smaller exponent in the

Casimir energy equation enables the suppression of plate rotation to suppress from a smaller separation distance.

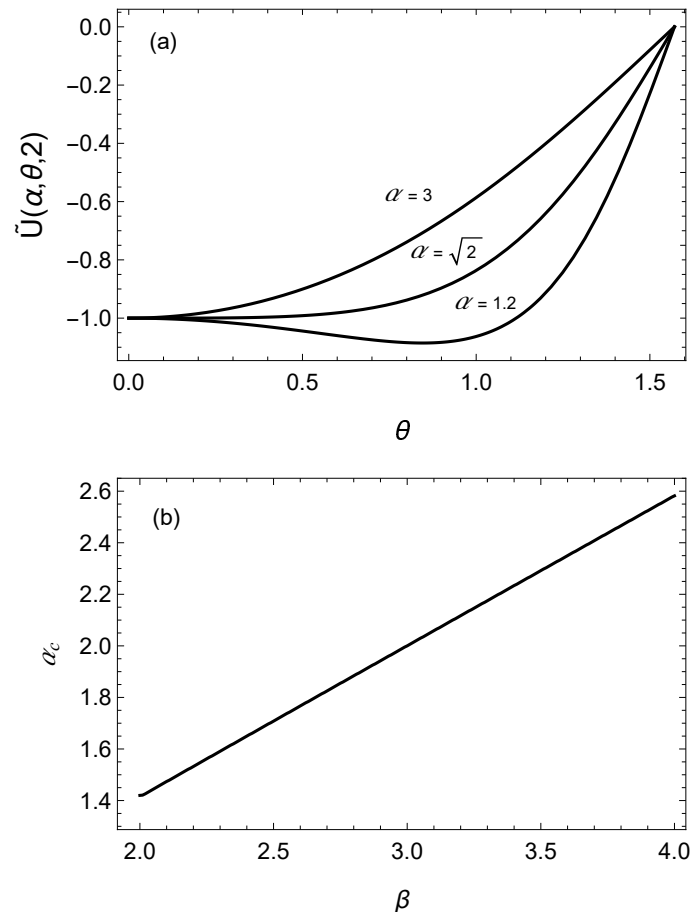


Figure 4. (a) Dependence of the potential energy, $U(\alpha, \theta, \beta = 2)$ (21), of an inclined plate on the angle, θ , of inclination for different dimensional heights, α . (b) Relationship between the threshold, α_c , above which the flat state is stable and the exponent, β , of the potential energy.

6. Levitation of a Graphene Flake above a Silicon Plate in a Magnetic Field

Let us proceed to investigate whether the suppression of rotation, discussed in Section 5, can contribute to stabilizing the levitation of a graphene flake in the presence of a magnetic field. If the graphene flake is levitated on a silicon plate, as depicted in Figure 1b, the total potential energy can be approximated given the following expression:

$$\begin{aligned}
 U(z, \theta) &= U_C(z, \theta, 2) + U_C(z, \theta, 3) + U_{mg}(z), \\
 &= -\frac{2c_2 L \cos \theta}{L^2 \sin^2 \theta - z^2} - \frac{2c_3 L z \cos \theta}{(L^2 \sin^2 \theta - z^2)^2}
 \end{aligned}
 \tag{23}$$

$$+ \frac{c_m \mu_0^2 I^2 R^4}{4[(z-d)^2 + R^2]^3} + mgz,
 \tag{24}$$

where the Casimir energy between a graphene flake and a coil is neglected. Figure 5a shows the relationship between the total energy of a flat graphene flake and a silicon plate, and the separation distance, considering the gravitational acceleration $g = 0$ and 0.1 m/s^2 . The parameters employed in the calculation are summarized in Table 1. Notably, one of the parameters, c_m , plays an important role in determining the magnetic force. Its value is specific to a graphene flake with hexagonal armchair edges at a temperature of 300 K (see Ref. [17] for details).

Table 1. Parameters used in the calculations. See text for details.

Parameters	Values
L	11.58 nm
R	4 μm
d	2.5 μm
I	0.3 A
c_m	1.24×10^{-5} eV/T ²
c_2	7.96×10^{-11} J
c_3	1.11×10^{-12} J m

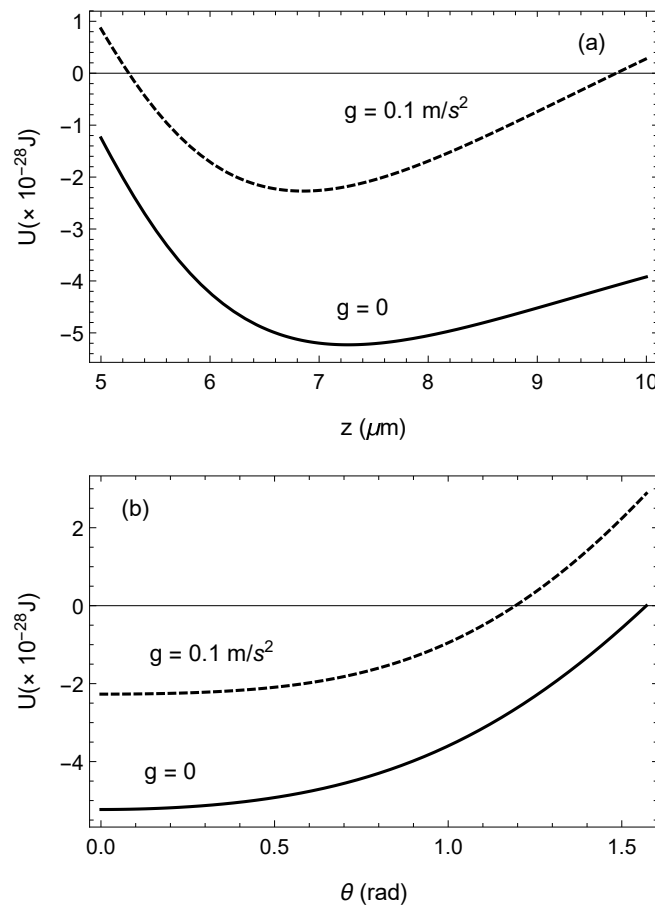


Figure 5. (a) Dependence of the total Casimir energy, magnetic energy, and gravitational energy on the separation distance for gravitational acceleration $g = 0$ and 0.1 m/s^2 . (b) Dependence of the total energy at equilibrium heights on the inclined angle.

The levitation heights are measured to be 7.3 and 6.9 μm for the gravitational acceleration of 0 and 0.1 m/s^2 , respectively. Figure 5b displays the change in the total energy due to inclination, with the minimum value of ΔU set to zero. The total energy monotonously increases as the graphene flake tilts away from $\theta = 0$, indicating stable levitation when the gravitational acceleration is small. As the gravitational acceleration increases, the levitation height decreases. The results for $g = 0.3 \text{ m/s}^2$ and 0.4 m/s^2 are presented in Figure 6a,b and illustrate the dependence of total energy on the position and inclination angle, respectively. When the graphene flake deviates from $\theta = 0$, the total energy decreases, reaching its minimum at $\theta = 0.52$ rad for $g = 0.3 \text{ m/s}^2$. The inclined angle increases with an increase in gravitational acceleration. For $g = 0.4 \text{ m/s}^2$, the angle of inclination, at which the total energy is minimized, is 0.67 rad. Figure 6c shows the total energy of inclined graphene flakes at $\theta = 0.52$ rad for $g = 0.3$ and $\theta = 0.67$ rad for $g = 0.4 \text{ m/s}^2$. In the case of $g = 0.3 \text{ m/s}^2$,

a local minimum exists in the total energy, enabling the levitation of the graphene flake in the inclined state. However, for $g = 0.4 \text{ m/s}^2$, no local minimum exists, causing the graphene flake to fall onto the substrate after tilting.

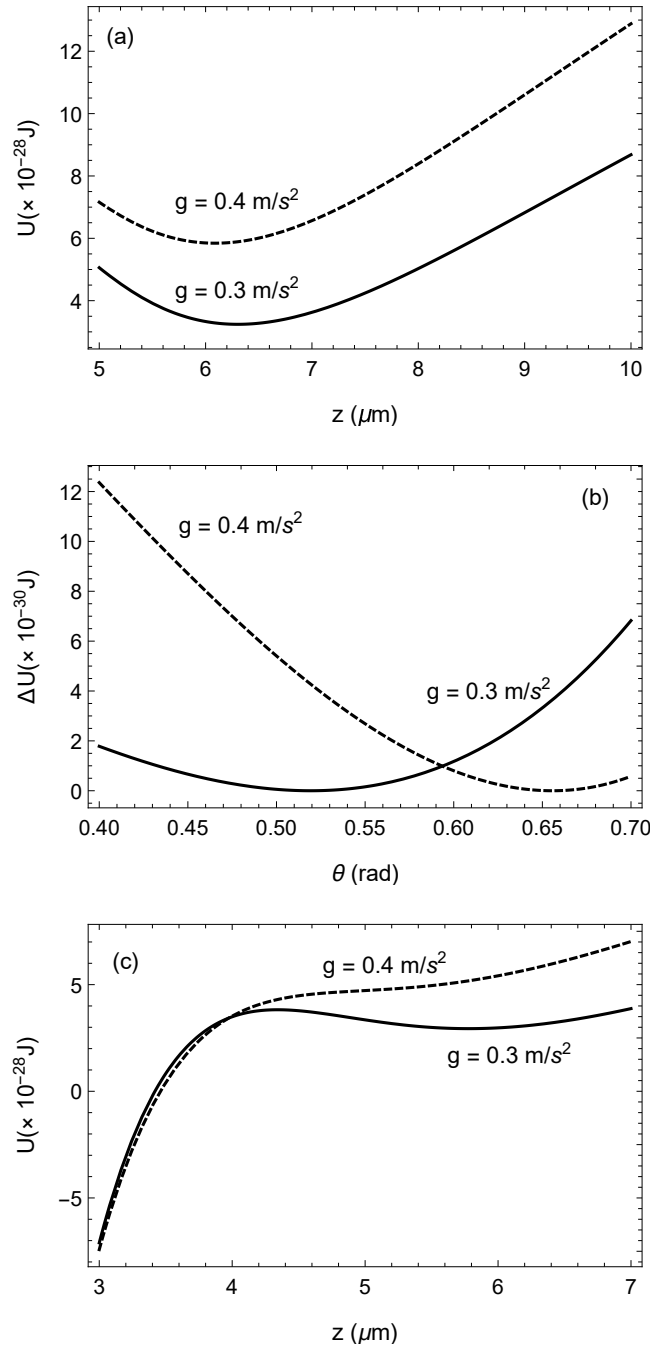


Figure 6. (a) Dependence of the total energy of the flat graphene flake for $g = 0.4$ and 0.3 m/s^2 on the vertical position. (b) Dependence of the total energy at equilibrium heights on the inclined angle for $g = 0.4$ and 0.3 m/s^2 . The angle at which takes the minimum potential energy exists at non-zero inclined angle. (c) Dependence of the total energy of the graphene flakes that incline with the equilibrium angle on the separation distance.

7. Role of a Diamagnetic Force and the Casimir Torque

A diamagnetic force and the Casimir torque must be effectively combined to achieve stable levitation. In previous calculations, the magnetic field is generated by a circular current and the levitation was unsuccessful for large gravitational accelerations. However,

if an appropriate magnetic field is generated, then stable levitation can be realized. For example, when the magnetic flux density, which is expressed by $0.5 - 0.35z + 0.08z^2$ T, (where z is in μm) near $z = 2 \mu\text{m}$ is generated, the total energy of the flat graphene flake for $g = 9.8 \text{ m/s}^2$ takes a minimum at $2 \mu\text{m}$ as shown in Figure 7a. Furthermore, Figure 7b shows the total energy at the levitation height and takes the minimum in the flat state ($\theta = 0$), and indicates that stable levitation can be achieved on Earth if the appropriate magnetic field is generated.

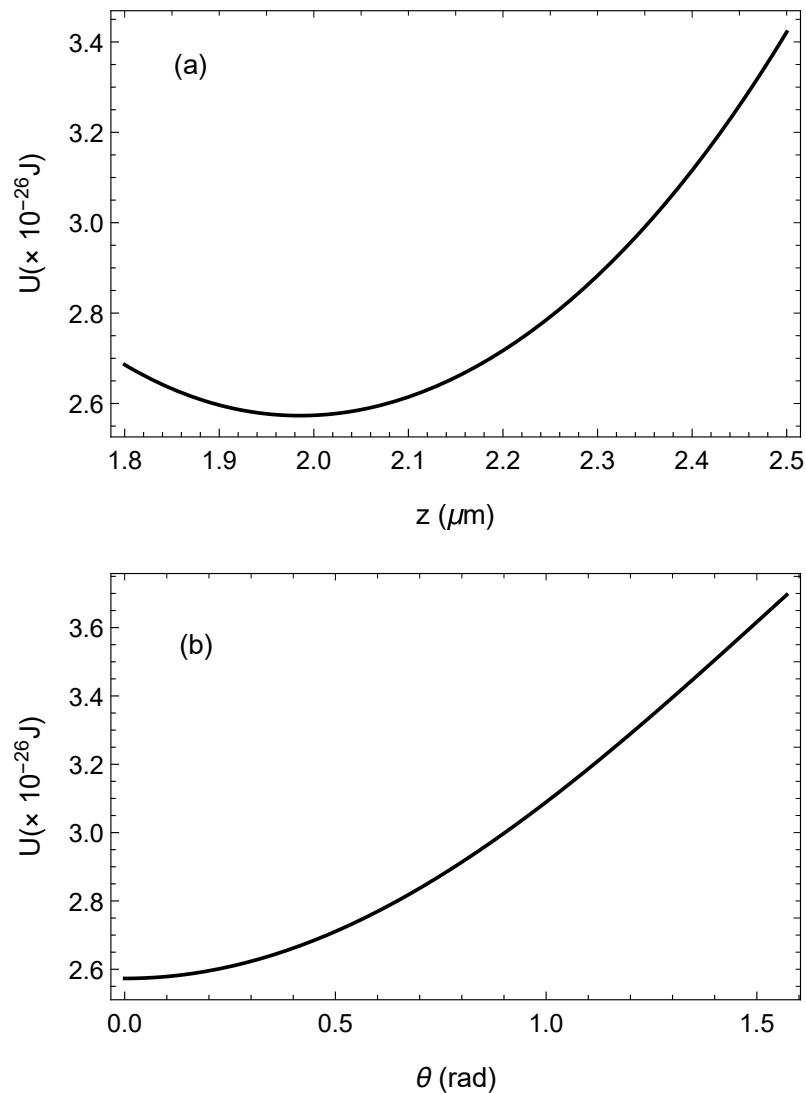


Figure 7. (a) Dependence of the total energy of the flat graphene flake for $g = 9.8 \text{ m/s}^2$ on the vertical position. (b) Dependence of the total energy at equilibrium heights of $2 \mu\text{m}$ on the inclined angle for $g = 9.8 \text{ m/s}^2$.

The stabilization of levitation results from the feature that the Casimir energy takes a minimum value when the plates are parallel for large separations. PFA worsens as the separation distance increases. However, the predicted stability of parallel configurations may be correct. For perfectly conductive plates, an analytical formula of the Casimir energy between non-parallel plates was presented in Ref. [30] using the optical approximation, which is one of the calculation methods beyond PFA [31–33]. Figure 8 shows the inclination angle of a square plate with side of size L above an infinite plate in a stable configuration, calculated using the optics approximation; θ^* is a function of the ratio of the separation distance between the square center and the infinite plate (δ). The parallel configuration with a zero inclination angle stabilizes when $\delta > 0.81$. Although sophisticated calculation

methods are necessary to determine the magnetic field accurately to realize levitation, the guideline indicating that stabilization through the Casimir effect is highly effective for large separations can be useful.

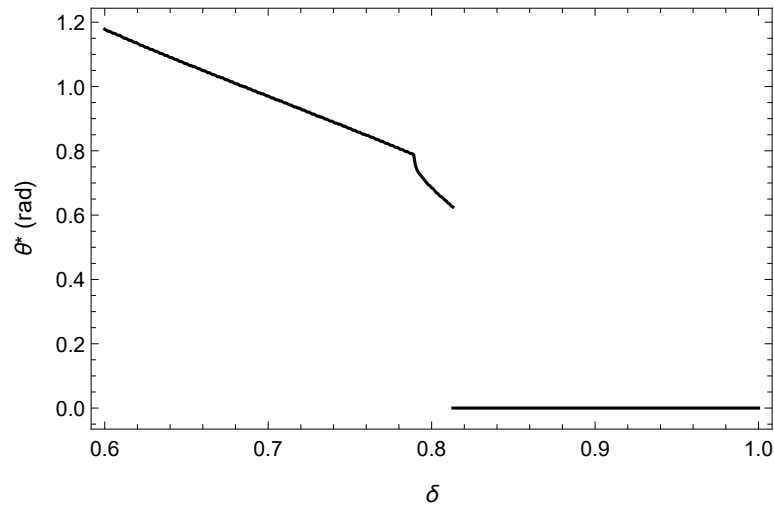


Figure 8. Dependence of the equilibrium of inclination angle, θ^* , obtained by the optical approximation on normalized separation distance with the size of a plate, δ . The parallel configuration is stable for $\delta > 0.81$.

8. Conclusions

The coexistence of attractive and repulsive forces is crucial for achieving the levitation of objects. Furthermore, the behavior of these forces near the equilibrium point is of great importance. If they follow the power functions with the same exponent, the resulting function becomes monotonic, rendering stable levitation impossible.

The Casimir energy between objects is influenced by various physical parameters, such as the objects' shapes, distance between objects, permittivity, and temperature [27,34]. It is often represented by a power function. In the case of perfectly conductive plates, Casimir energy is inversely proportional to the cube of the separation distance, i.e., a^{-3} , regardless of the distance. However, if the permittivity is finite, Casimir energy varies as a^{-2} for small separations. This implies that the force between objects and its derivative can be manipulated by selecting appropriate materials and separation distances from an engineering perspective.

To counteract the rotation of the graphene flake and achieve stable levitation, a diamagnetic force was employed as a repulsive force. In order for the flake's surface to remain perpendicular to the magnetic field, it is necessary to fixate the surface and ensure that the product of the applied magnetic field and its derivative is sufficiently large. However, in a vacuum environment, the graphene flake tends to rotate, causing its surface to become parallel to the magnetic field. To address this issue, the Casimir torque was utilized as one of the methods for stabilization.

The numerical analysis revealed that the Casimir effect can provide some degree of stabilization for the diamagnetic levitation of a graphene flake. However, its effectiveness is limited, and it is insufficient to fully suppress the rotation in Earth's gravity by the magnetic field generated through the circular electric current. This limitation arises from the feature that the suppression of the rotation by the Casimir effect is most effective at larger separation distances. As the separation distance increases, the Casimir energy rapidly diminishes, resulting in a weaker restoring torque. Therefore, in order to achieve magnetic levitation in a strong gravitational field, furthering the optimization of the magnetic field is necessary as shown in Section 7.

As the separation distance approaches zero, the magnetic energy remains finite. However, the Casimir energy diverges to negative infinity. This implies that the levitation state

is metastable [35–37], and a potential barrier is present near the surface. The height of this potential barrier is not significant. Therefore, to maintain the levitation state, it is necessary to maintain a high vacuum and low temperature. These conditions help to stabilize the system and prevent the graphene flake from falling onto the substrate.

Funding: This research was funded by the Ministry of Education, Culture, Sports, Science and Technology, Grant-in-Aid for Scientific Research(C), MEXT KAKENHI, Japan, Grant Number 21K04895.

Data Availability Statement: Not applicable.

Conflicts of Interest: The author declares no conflicts of interest.

References

1. Milonni, P.W. *The Quantum Vacuum*; Academic Press, Inc.: San Diego, CA, USA, 1994. [CrossRef]
2. Bordag, M.; Klimchitskaya, G.L.; Mohideen, U.; Mostepanenko, V.M. *Advances in the Casimir Effect*; Oxford University Press: Oxford, UK, 2009. [CrossRef]
3. Chan, H.B.; Aksyuk, V.A.; Kleiman, R.N.; Bishop, D.J.; Capasso, F. Quantum mechanical actuation of microelectromechanical systems by the Casimir force. *Science* **2001**, *291*, 1941–1944. [CrossRef]
4. Capasso, F.; Munday, J.N.; Iannuzzi, D.; Chan, H.B. Casimir forces and quantum electrodynamic torques: Physics and nanomechanics. *IEEE J. Sel. Top. Quantum Electron.* **2007**, *13*, 400–414. [CrossRef]
5. Decca, R.; Aksyuk, V.; López, D. Casimir force in micro and nano electro mechanical systems. In *Casimir Physics*; Dalvit, D., Milonni, P., Roberts, D., da Rosa, F., Eds.; Springer: Berlin/Heidelberg, Germany, 2011; pp. 287–309. [CrossRef]
6. Zou, J.; Marcet, Z.; Rodriguez, A.W.; Reid, M.T.H.; McCauley, A.P.; Kravchenko, I.I.; Lu, T.; Bao, Y.; Johnson, S.G.; Chan, H.B. Casimir forces on a silicon micromechanical chip. *Nat. Commun.* **2013**, *4*, 1845. [CrossRef] [PubMed]
7. Palasantzas, G.; Sedighi, M.; Svetovoy, V.B. Applications of Casimir forces: Nanoscale actuation and adhesion. *Appl. Phys. Lett.* **2020**, *117*, 120501. [CrossRef]
8. Kenneth, O.; Klich, I.; Mann, A.; Revzen, M. Repulsive Casimir forces. *Phys. Rev. Lett.* **2002**, *89*, 033001. [CrossRef] [PubMed]
9. Munday, J.N.; Capasso, F.; Parsegian, V.A. Measured long-range repulsive Casimir–Lifshitz forces. *Nature* **2009**, *457*, 170–173. [CrossRef]
10. Kenneth, O.; Klich, I. Opposites attract: A theorem about the Casimir force. *Phys. Rev. Lett.* **2006**, *97*, 160401. [CrossRef]
11. Geim, A.K.; Simon, M.D.; Boamfa, M.I.; Heflinger, L.O. Magnet levitation at your fingertips. *Nature* **1999**, *400*, 323–324. [CrossRef]
12. Simon, M.D.; Geim, A.K. Diamagnetic levitation: Flying frogs and floating magnets (invited). *J. Appl. Phys.* **2000**, *87*, 6200–6204. [CrossRef]
13. McClure, J.W. Diamagnetism of graphite. *Phys. Rev.* **1956**, *104*, 666–671. [CrossRef]
14. Niu, C.; Lin, F.; Wang, Z.M.; Bao, J.; Hu, J. Graphene levitation and orientation control using a magnetic field. *J. Appl. Phys.* **2018**, *123*, 044302. [CrossRef]
15. Lin, F.; Niu, C.; Hu, J.; Wang, Z.; Bao, J. Graphene diamagnetism: Levitation, transport, rotation, and orientation alignment of graphene flakes in a magnetic field. *IEEE Nanotechnol. Mag.* **2020**, *14*, 14–22. [CrossRef]
16. Błocki, J.; Randrup, J.; Świątecki, W.J.; Tsang, C.F. Proximity forces. *Ann. Phys.* **1977**, *105*, 427–462. [CrossRef]
17. Ominato, Y.; Koshino, M. Orbital magnetism of graphene flakes. *Phys. Rev. B* **2013**, *87*, 115433. [CrossRef]
18. Espinosa-Ortega, T.; Luk'yanchuk, I.A.; Rubo, Y.G. Magnetic properties of graphene quantum dots. *Phys. Rev. B* **2013**, *87*, 205434. [CrossRef]
19. Deyo, S.; Hershfield, S. Magnetism in graphene flakes with edge disorder. *Phys. Rev. B* **2021**, *104*, 014404. [CrossRef]
20. Fialkovsky, I.V.; Marachevsky, V.M.; Vassilevich, D.M. Finite-temperature Casimir effect for graphene. *Phys. Rev. B* **2011**, *84*, 35446. [CrossRef]
21. Bordag, M.; Klimchitskaya, G.L.; Mostepanenko, V.M. Thermal Casimir effect in the interaction of graphene with dielectrics and metals. *Phys. Rev. B* **2012**, *86*, 165429. [CrossRef]
22. Klimchitskaya, G.L.; Mostepanenko, V.M. van der Waals and Casimir interactions between two graphene sheets. *Phys. Rev. B* **2013**, *87*, 75439. [CrossRef]
23. Banishev, A.A.; Wen, H.; Xu, J.; Kawakami, R.K.; Klimchitskaya, G.L.; Mostepanenko, V.M.; Mohideen, U. Measuring the Casimir force gradient from graphene on a SiO₂ substrate. *Phys. Rev. B* **2013**, *87*, 205433. [CrossRef]
24. Henkel, C.; Klimchitskaya, G.L.; Mostepanenko, V.M. Influence of the chemical potential on the Casimir-Polder interaction between an atom and gapped graphene or a graphene-coated substrate. *Phys. Rev. A* **2018**, *97*, 32504. [CrossRef]
25. Klimchitskaya, G.L.; Mostepanenko, V.M. Casimir and Casimir-Polder forces in graphene systems: Quantum field theoretical description and thermodynamics. *Universe* **2020**, *6*, 150. [CrossRef]
26. Palik, E.D. (Ed.) *Handbook of Optical Constants of Solids*; Academic Press, Inc.: San Diego, CA, USA, 1985; Volume 1. [CrossRef]
27. Liu, M.; Zhang, Y.; Klimchitskaya, G.L.; Mostepanenko, V.M.; Mohideen, U. Experimental and theoretical investigation of the thermal effect in the Casimir interaction from graphene. *Phys. Rev. B* **2021**, *104*, 085436. [CrossRef]
28. Mostepanenko, V.M.; Trunov, N.N. *The Casimir Effect and Its Applications*; Clarendon Press/Oxford University Press, Inc.: New York, NY, USA, 1997.

29. Scardicchio, A.; Jaffe, R.L. Casimir effects: An optical approach I. Foundations and examples. *Nucl. Phys. B* **2005**, *704*, 552–582. [CrossRef]
30. Guifoyle, B.; Klingenberg, W.; Sen, S. The Casimir effect between non-parallel plates by geometric optics. *Rev. Math. Phys.* **2005**, *17*, 859–880. [CrossRef]
31. Bordag, M.; Nikolaev, V. Casimir force for a sphere in front of a plane beyond proximity force approximation. *J. Phys. A* **2008**, *41*, 164002. [CrossRef]
32. Reynaud, S.; Maia Neto, P. A.; Lambrecht, A. Casimir energy and geometry: Beyond the proximity force approximation. *J. Phys. A* **2008**, *41*, 164004. [CrossRef]
33. Inui, N.; Kushiro, T.; Mochiji, K.; Moritani, M. Stable position of a micro torsion balance under the Casimir force. *e-J. Surf. Sci. Nanotech.* **2013**, *11*, 60–64. [CrossRef]
34. Sushkov, A.O.; Kim, W.J.; Dalvit, D.A.R.; Lamoreaux, S.K. Observation of the thermal Casimir force. *Nat. Phys.* **2011**, *7*, 230–233. [CrossRef]
35. Kramers, H.A. Brownian motion in a field of force and the diffusion model of chemical reactions. *Physica* **1940**, *7*, 284–304. [CrossRef]
36. Hanggi, P. Escape from a metastable state. *J. Stat. Phys.* **1986**, *42*, 105–148. [CrossRef]
37. Inui, N.; Maebuchi, K. Dynamic and fluctuation properties of a graphene disk levitated by a diamagnetic force in air. *J. Phys. D* **2022**, *55*, 285002. [CrossRef]

Disclaimer/Publisher’s Note: The statements, opinions and data contained in all publications are solely those of the individual author(s) and contributor(s) and not of MDPI and/or the editor(s). MDPI and/or the editor(s) disclaim responsibility for any injury to people or property resulting from any ideas, methods, instructions or products referred to in the content.

Review

Axion Electrodynamics and the Casimir Effect

Iver Brevik ^{1,*}, Subhojit Pal ², Yang Li ^{3,4}, Ayda Gholamhosseinian ⁵ and Mathias Boström ^{2,6}

¹ Department of Energy and Process Engineering, Norwegian University of Science and Technology, NO-7491 Trondheim, Norway

² Centre of Excellence ENSEMBLE3 Sp. z o. o., Wolczynska Str. 133, 01-919 Warsaw, Poland; subhojit.pal@ensemble3.edu (S.P.); mathias.bostrom@ensemble3.eu (M.B.)

³ Department of Physics, Nanchang University, Nanchang 330031, China; leon@ncu.edu.cn

⁴ School of Physics and Materials Science, Nanchang University, Nanchang 330031, China

⁵ Department of Physics, Ferdowsi University of Mashhad, Mashhad 9177948974, Iran; ayda.gholamhosseinian@mail.um.ac.ir

⁶ Chemical and Biological Systems Simulation Laboratory, Centre of New Technologies, University of Warsaw, Banacha 2C, 02-097 Warsaw, Poland

* Correspondence: iver.h.brevik@ntnu.no

Abstract: We present a concise review of selected parts of axion electrodynamics and their application to Casimir physics. We present the general formalism including the boundary conditions at a dielectric surface, derive the dispersion relation in the case where the axion parameter has a constant spatial derivative in the direction normal to the conducting plates, and calculate the Casimir energy for the simple case of scalar electrodynamics using dimensional regularization.

Keywords: axion electrodynamics; Casimir effect; topological insulators

1. Introduction

The axion concept has actually a long history. It was introduced by Roberto Peccei and Helen Quinn back in 1977 [1,2] in connection with the CP (charge conjugation and parity symmetry) problem in high-energy physics. However, later it was understood as related to a natural extra term in the electromagnetic Lagrangian with a direct formal connection to materials like topological insulators and thus of obvious practical interest. So, we first describe the basic properties of topological materials. Topological insulators (TIs) are the new phases of matter, which exhibit unique electronic properties due to their nontrivial topological characteristics, and were discovered in 2005 [3,4]. These materials have insulating states inside the bulk with a bulk energy gap separating the highest occupied electronic band from the lowest empty band, like an ordinary insulator, while conducting states exist on their surfaces in the case of three-dimensional TIs or on their edges in the case of two-dimensional (2D) TIs, which are topologically protected (robust to local defects, imperfections, and disorders) by time-reversal symmetry [5]. In 2006, the TI phase was theoretically predicted [6] and experimentally realized in a CdTe-HgTe-CdTe quantum well; this quantum well behaves in bulk as an insulator. However, the electric current was observed across the interface, i.e., it behaves like a conductor in the surface region [7]. Additionally, one knows from band theory that conductors do not have a gap between their valence and conduction bands. In contrast, insulators are defined as materials with a gap between them. The most notable aspect is that Maxwell's equations are unable to explain the experimental behaviors of topological insulators. Notably, this kind of behavior was previously suggested by Frank Wilczek [8] in 1987, along with the possibility that it could be described by the axion electrodynamics he [9] and Steven Weinberg [10] developed. Their initial aim was to explain the breaking of combined symmetries of charge conjugation and parity in strong interactions.

With a topological invariant called the \mathbb{Z}_2 invariant, one can distinguish trivial insulators from topological insulators. Topological materials have interesting features, and one

Citation: Brevik, I.; Pal, S.; Li, Y.; Gholamhosseinian, A.; Boström, M. Axion Electrodynamics and the Casimir Effect. *Physics* **2024**, *6*, 407–421. <https://doi.org/10.3390/physics6010027>

Received: 24 November 2023

Revised: 13 January 2024

Accepted: 5 February 2024

Published: 14 March 2024



Copyright: © 2024 by the authors. Licensee MDPI, Basel, Switzerland. This article is an open access article distributed under the terms and conditions of the Creative Commons Attribution (CC BY) license (<https://creativecommons.org/licenses/by/4.0/>).

of them is the magnetoelectric effect caused by a term called the θ term. Since this term, referred to as the magnetoelectric polarizability, has exactly the same form as the action describing the coupling between a photon and an axion, these magnetoelectric phenomena are often depicted with axion electrodynamics. In the presence of time-reversal symmetry, θ takes on a quantized value $\theta = \pi(\text{mod } 2\pi)$ for topological insulators and $\theta = 0$ for ordinary insulators [11–14]. The value of θ , nevertheless, can be arbitrary in systems with broken time-reversal symmetry, even depending on space and time as $\theta(r, t)$, like in various semimetallic phases. Moreover, when the dynamics of the axion field is included, the existence of new quasiparticles, such as the axion polariton [15], is also proposed. For more details, see [14] and the references therein.

In a separate paper [16] we reviewed the semiclassical electrodynamics and its link to Casimir physics. Notably, the history of this remarkable effect dates back to 1948 when it was predicted by Hendrik Casimir [17,18]. A formidable, and highly effective, theory for the retarded dispersion force between a pair of planar surfaces interacting across an intervening medium was developed in the 1950s by Evgeny Lifshitz and collaborators [19,20]. From the late 1960s, groups from around the world explored if a theory based upon the classical Maxwell's equations combined with the Planck quantization of light could by itself lead to a simple and useful semiclassical theory for van der Waals, Lifshitz, and Casimir interactions [21,22]. As one important example, a semiclassical derivation of Casimir effects in magnetic media was presented by Peter Richmond and Barry Ninham [23] already in 1971. Many theoretical [24–36] and experimental studies [37–44] have followed in the last 50 years. More information related to Casimir effects in traditional systems can be found in the extensive literature [45–51]. A number of studies have been carried out with a focus on predictive theories, nanobiotechnological applications, and novel materials' growth and characterization. Notably, going beyond the standard applications, specific ion effects in both biological systems and colloid chemistry have been proposed to occur partly due to ionic dispersion potentials [52] acting on ions in salt solutions [53–59]. This leads to a nonlinear coupling of electrodynamical and electrostatic interactions with a proposed role behind the so-called (ion-specific) Hofmeister effect [60]. Most interestingly, Casimir and van der Waals interactions may also have an impact on the growth of ice clusters within mist [61] and clouds [62,63]. It has been, and still is, relevant to explore the limits of validity of the different theories for dispersion forces (e.g., between two layered surfaces). A most natural extension of this conventional semiclassical electrodynamics, as well as quantum electrodynamics, in media is to allow for an extra pseudoscalar field, called conventionally the axion field $a(x)$ (x means here spacetime), pervading in the whole volume. Some of the pioneering papers on axion electrodynamics are listed in Refs. [1,2,10,64–69]. More recent investigations can be found in Refs. [70–94]. Here, we present an easy-to-follow and concise review of the current understanding of axion electrodynamics from our point of view.

2. Axion Electrodynamics

Different methods have been suggested to investigate the electromagnetic characteristics of 3D magnetic topological insulators (see, for example, Refs. [10,64]), which are based on axion field theory [95,96]. This approach introduces an additional term to the conventional Maxwell electromagnetic action, expressed as follows:

$$S_A = \frac{e^2}{32\pi^2\hbar c} \int d^3\vec{r} dt \theta \varepsilon^{\mu\nu\alpha\beta} F_{\mu\nu} F_{\alpha\beta}, \quad (1)$$

where e denotes the elementary charge, \hbar is the reduced Planck constant, c denotes the speed of light. Here and elsewhere below, $\varepsilon^{\mu\nu\alpha\beta}$ represents the completely antisymmetric tensor, $F_{\mu\nu}$ is the Maxwell field strength tensor, the Greek letter indices take the 0 (time, t), 1, 2, and 3 (space) values, \vec{r} is the space vector, and θ denotes the axion coupling strength. Originally proposed in the context of quantum chromodynamics (QCD) to address the strong CP problem [1,97], the axion is a hypothetical pseudoscalar particle and has also been considered a potential candidate for cosmological dark matter. Since Equation (1)

bears mathematical similarities to the description of cosmological/QCD axions, the term “axion” is used in the context of topological insulators. However, the axial coupling in topological insulators is related to the presence of a surface quantum Hall effect [98].

The reason why $a(x)$ is a pseudoscalar quantity is that the mentioned extra term in the Lagrangian implies a two-photon interaction with the electromagnetic field, and the pseudoscalar property of $a(x)$ ensures that its product with the polar vector \mathbf{E} together with the axial vector \mathbf{B} becomes a scalar in the Lagrangian. We shall in the following highlight some essential properties of the axion formalism, assuming a dielectric environment with the permittivity ϵ and the permeability μ being constants. It means that the constitutive relations are simply $\mathbf{D} = \epsilon\mathbf{E}$, $\mathbf{B} = \mu\mathbf{H}$. The presentation in the following is largely based upon our earlier papers [91–94]. When magnetoelectric effects occur in topological material, the magnetic induction \mathbf{B} changes the electric displacement vector \mathbf{D} , and the magnetic field intensity \mathbf{H} is in turn influenced by the electric field. Then, the relations for \mathbf{D} and \mathbf{B} should be changed, $\mathbf{D} = \epsilon\mathbf{E} - \theta\alpha\mathbf{B}/\pi$, $\mathbf{H} = \mathbf{B}/\mu + \theta\alpha\mathbf{E}/\pi$, where α is the fine-structure constant. These constitutive relations were given in [99] and in references therein; see also the later Ref. [100]. As a result, these two polarizations are coupled, meaning that the electromagnetic boundary conditions are off-diagonal components of the Fresnel coefficients [101].

In relation to our previous comments in Section 1, it is quite important to note parallelism between two analogous yet distinct phenomena. In the following discussion, our focus will be on the axion approach rooted in the Peccei–Quinn formalism, while a formal analogy arises with polariton excitations in condensed media. Our coupling constant $g_{a\gamma\gamma}$, below, will thus refer to the axion case. One might be interested in the corresponding coupling constant in the polarization case also, but this is a complicated subject into which we will not enter here. Interested readers may consult, for instance, the paper [102], to obtain detailed information about a strong coupling between a topological insulator and a III-V heterostructure.

2.1. Basic Equations

We choose the metric convention with signature $g_{00} = -1$ and introduce two field tensors, $F_{\alpha\beta}$ and $H^{\alpha\beta}$. The components of the original field tensor $F_{\alpha\beta}$ are as in vacuum, $F_{0i} = -E_i$, $F_{jk} = \epsilon_{ijk}B_i$ (where the indices in Latin letters denote the space coordinates), while the components of the contravariant response tensor $H^{\alpha\beta}$ are $H^{0i} = D_i$, $H_{jk} = \epsilon_{ijk}H_i$.

Including the pseudoscalar axion field $a = a(x)$, we obtain for the Lagrangian

$$\mathcal{L} = -\frac{1}{4}F_{\alpha\beta}H^{\alpha\beta} + \mathbf{A} \cdot \mathbf{J} - \rho\Phi - \frac{1}{2}\partial_\mu a\partial^\mu a - \frac{1}{2}m_a^2 a^2 - \frac{1}{4}\theta(x)F_{\alpha\beta}\tilde{F}^{\alpha\beta}, \tag{2}$$

in which \mathbf{A} denotes the magnetic potential, \mathbf{J} denotes the current, ρ denotes the energy density, Φ denotes the scalar potential, m_a is the axion mass, $\tilde{F}^{\alpha\beta} = \epsilon^{\alpha\beta\gamma\delta}F_{\gamma\delta}/2$, and we have defined the nondimensional field amplitude as

$$\theta(x) = g_{a\gamma\gamma}a(x). \tag{3}$$

The constant for the coupling of the axion with two photons can be defined as follows,

$$g_{a\gamma\gamma} = g_\gamma \frac{\alpha}{\pi} \frac{1}{f_a}, \tag{4}$$

where g_γ is a constant depending on the specific model used and is usually taken to be 0.36 [75]. The f_a represents the axion decay constant and for f_a , it is commonly assumed that its value is on the order of 10^{12} GeV. The Lagrangian’s last term (2), $\mathcal{L}_{a\gamma\gamma}$, can be written as $\mathcal{L}_{a\gamma\gamma} = \theta(x)\mathbf{E} \cdot \mathbf{B}$, explicitly showing the pseudoscalar property of $\theta(x)$.

The expression (2) can be used to obtain the generalized Maxwell equations

$$\nabla \cdot \mathbf{D} = \rho - \mathbf{B} \cdot \nabla\theta, \tag{5}$$

$$\nabla \times \mathbf{H} = \mathbf{J} + \frac{\partial}{\partial t} \mathbf{D} + \frac{\partial \theta}{\partial t} \mathbf{B} + \nabla \theta \times \mathbf{E}, \quad (6)$$

$$\nabla \cdot \mathbf{B} = 0, \quad (7)$$

$$\nabla \times \mathbf{E} = -\frac{\partial}{\partial t} \mathbf{B}. \quad (8)$$

These equations are general, and there are no restrictions on the spacetime variation of $a(x)$. The equations are relativistically covariant. It is crucial that the constitutive relations stated previously maintain their quite simple form $\mathbf{D} = \epsilon \mathbf{E}$, $\mathbf{B} = \mu \mathbf{H}$ only in the rest system, and the electromagnetic formalism's covariance is achieved by introducing *two* distinct field tensors, $F_{\mu\nu}$ and $H^{\mu\nu}$. The field equations describing the system are

$$\nabla^2 \mathbf{E} - \epsilon \mu \frac{\partial^2}{\partial t^2} \mathbf{E} = \nabla(\nabla \cdot \mathbf{E}) + \mu \frac{\partial}{\partial t} \mathbf{J} + \mu \frac{\partial}{\partial t} \left[\frac{\partial \theta}{\partial t} \mathbf{B} + \nabla \theta \times \mathbf{E} \right], \quad (9)$$

$$\nabla^2 \mathbf{H} - \epsilon \mu \frac{\partial^2}{\partial t^2} \mathbf{H} = -\nabla \times \mathbf{J} - \nabla \times \left[\frac{\partial \theta}{\partial t} \mathbf{B} + \nabla \theta \times \mathbf{E} \right]. \quad (10)$$

In practice, the influence from axions is typically small in our case here. We do not consider the field equations for the axions explicitly for simplicity and clarity.

The field equations above contain the second-order derivatives of θ . These may conveniently be removed if we assume there is a strong external magnetic field $\mathbf{B}_e = B_e \hat{\mathbf{z}}$ present, where $\hat{\mathbf{z}}$ is the normal vector. Then, assuming the axion field

$$a(t) = a_0 \cos \omega_a t, \quad (11)$$

one can separate out the part $\mathbf{E}_a(t)$ related to the $\ddot{\theta}$ term, where the dot on the top denotes the time derivative. From the governing equation for $\mathbf{E}_a(t)$, ignoring the current \mathbf{J} as the axion-related field,

$$\nabla^2 \mathbf{E}_a - \epsilon \mu \frac{\partial^2}{\partial t^2} \mathbf{E}_a = \mu \ddot{\theta} \mathbf{B}_e. \quad (12)$$

Then,

$$\mathbf{E}_a(t) = -\frac{1}{\epsilon} E_0 \cos \omega_a t \hat{\mathbf{z}}, \quad (13)$$

where

$$E_0 = \theta_0 B_e. \quad (14)$$

After this separation, the field equations (9) and (10) take the reduced forms

$$\nabla^2 \mathbf{E} - \epsilon \mu \frac{\partial^2}{\partial t^2} \mathbf{E} = \nabla(\nabla \cdot \mathbf{E}) + \mu \frac{\partial}{\partial t} \mathbf{J} + \mu \left[\dot{\theta} \frac{\partial}{\partial t} \mathbf{B} + \nabla \theta \times \frac{\partial}{\partial t} \mathbf{E} \right], \quad (15)$$

$$\nabla^2 \mathbf{H} - \epsilon \mu \frac{\partial^2}{\partial t^2} \mathbf{H} = -\nabla \times \mathbf{J} - \left[\dot{\theta} \nabla \times \mathbf{B} + (\nabla \theta) \nabla \cdot \mathbf{E} - (\nabla \theta \cdot \nabla) \mathbf{E} \right]. \quad (16)$$

In the following, we allow θ to be spatially varying but neglect the second-order derivatives, i.e., $\partial_i \partial_j \theta \approx 0$. This means that the model excludes situations where spatial boundaries lead to δ - and δ' -type terms. Actually, as shown in Equation (25) below, we in the mathematical analysis take θ to vary linearly in space over the field region of interest. There will accordingly be no second-order terms in the field region, while the electromagnetic boundary conditions must be imposed at the boundaries.

It is to be noted that the equations contain the dynamical fields \mathbf{E} and \mathbf{B} only.

2.2. Hybrid Form of Maxwell's Equations. Boundary Conditions

It turns out that one can construct a hybrid form of Maxwell's equations from which the generalized boundary conditions at a dielectric surface follow in a very transparent way. We introduce new fields \mathbf{D}_γ and \mathbf{H}_γ via

$$\begin{pmatrix} \mathbf{D}_\gamma \\ \mathbf{H}_\gamma \end{pmatrix} = \begin{pmatrix} \varepsilon & \theta \\ -\theta & 1/\mu \end{pmatrix} \begin{pmatrix} \mathbf{E} \\ \mathbf{B} \end{pmatrix}, \quad (17)$$

which shows how $\mathbf{D}_\gamma, \mathbf{H}_\gamma$ relate to the response tensor $H^{\mu\nu}$. The hybrid Maxwell equations thus become similar to those in the usual electrodynamics,

$$\nabla \times \mathbf{H}_\gamma = \mathbf{J} + \frac{\partial}{\partial t} \mathbf{D}_\gamma, \quad \nabla \cdot \mathbf{D}_\gamma = \rho, \quad (18)$$

$$\nabla \times \mathbf{E} = -\frac{\partial}{\partial t} \mathbf{B}, \quad \nabla \cdot \mathbf{B} = 0. \quad (19)$$

The boundary conditions at a dielectric boundary are then immediate:

$$E_\perp = E_{\gamma,\perp} + E_{a,\perp} \quad \text{is continuous}, \quad (20)$$

$$E_\perp, H_{\gamma,\perp} \quad \text{are continuous}, \quad (21)$$

$$D_{\gamma,\parallel}, B_\parallel \quad \text{are continuous}, \quad (22)$$

(the symbols \perp and \parallel mean perpendicular and parallel to the normal, thus parallel and perpendicular to the surface). A key quantity is the property of Poynting's vector, $\mathbf{S} = \mathbf{E} \times \mathbf{H}$. Taking the z component S_z orthogonal to a dielectric surface, one sees that

$$S_{1z} = S_{2z}, \quad (23)$$

showing that the energy flux density is continuous across the surface, dividing media 1 and 2. This is as one would expect as the surface is *at rest*; the force acting on it is not able to perform any mechanical work.

2.3. Dispersion Relations

We use now the standard plane wave expansion

$$\mathbf{E} \propto e^{i(\mathbf{k}\cdot\mathbf{x}-\omega t)}, \quad \mathbf{k} = (k_x, k_y, k_z) \quad (24)$$

with \mathbf{k} the wave number and the frequency ω .

We start from the reduced Maxwell Equations (15) and (16) and restrict ourselves to the case where $a(x)$ will vary with space only,

$$\boldsymbol{\beta} = \nabla\theta, \quad (25)$$

with $\boldsymbol{\beta}$ assumed constant. This form is mathematically convenient and often used in the literature. The form is of the same kind as assumed for Weyl semimetals [103,104], where the gradient of the axion is related to the separation of Weyl nodes in the Brillouin zone. One may here note that the case of topological insulators is different, as in such a case the gradient of the axion is taken to be zero except at the interfaces between trivial and nontrivial phases. The situation is, however, complex, and it should be mentioned that the configuration given here is very close to the one reported in Ref. [105], where a topological insulator slab is placed between two perfect conducting plates. We also point out that instructive papers on the new material, for example, those showing exotic Hall

effects, those on TRS-broken semimetals, those on Chern insulators, etc., can be found in the Refs. [101,106,107].

Starting from Equations (15) and (16), assuming $\rho = \mathbf{J} = 0$, we find the determinant equation determining the dispersion relations. There are two dispersive branches. The first is a “normal” one, satisfying

$$\epsilon\mu\omega^2 = \mathbf{k}^2, \tag{26}$$

corresponding to waves independent of the axions and polarizing parallel to β . The second branch, polarizing perpendicular to β , should have

$$\epsilon\mu\omega^2 = \mathbf{k}^2 \pm \mu\beta\omega. \tag{27}$$

showing the splitting of this branch into two modes, equally separated from the normal mode on both sides. This sort of splitting has been encountered before under various circumstances; see, for instance, Refs. [75,76,108].

The following property of this kind of material should be noticed: the dispersive property does not influence the electromagnetic energy density. In a complex representation, the energy density can be written as

$$W_{\text{disp}} = \frac{1}{4} \left[\frac{d(\epsilon_{\text{eff}}\omega)}{d\omega} |\mathbf{E}|^2 + |\mathbf{H}|^2 \right], \tag{28}$$

where we have assumed for a moment that the medium is nonmagnetic, and we have introduced an effective permittivity ϵ_{eff} such that

$$\mathbf{k}^2 = \epsilon_{\text{eff}}(\omega)\omega^2. \tag{29}$$

It then follows that

$$\frac{d(\epsilon_{\text{eff}}\omega)}{d\omega} = \epsilon, \tag{30}$$

which shows that the dispersive correction disappears. The energy density is the same as if dispersion were absent. This property is not quite trivial.

2.4. Dispersion Relations, When θ Is Time-Dependent

We introduce the variable α as

$$\alpha = \dot{\theta} \tag{31}$$

and assume α constant. The dispersion takes the form

$$\epsilon\mu\omega^2 = \mathbf{k}^2 \pm \mu\alpha|\mathbf{k}|. \tag{32}$$

We may here for a nonmagnetic medium introduce the refractive index, $n_{\text{eff}} = \sqrt{\epsilon_{\text{eff}}}$, and so obtain

$$n_{\text{eff}}(\omega) = \sqrt{\epsilon + \frac{\alpha^2}{4\omega^2}} \pm \frac{\alpha}{2\omega}. \tag{33}$$

Given the assumed smallness of the axion contributions, we restrict the parameter values to the region $(\beta + \alpha)/k_z \ll 1$.

If k_z is the wave number for photons in the z direction, corresponding to axions with mass $m_a \sim \omega = 10^{-5}$ eV, we have $k_z = 10^{-5}$ eV, so that the condition above can be rewritten as

$$\beta + \alpha \ll 10^{-5} \text{ eV} \left(\frac{m_a}{10^{-5} \text{ eV}} \right). \tag{34}$$

3. Energy–Momentum Considerations

It is interesting to consider the electromagnetic energy–momentum tensor in interaction with the axion field. As this is a nonclosed physical system, the four-force density will in general be different from zero. The system is in this way analogous to the electromag-

netic field in a medium in ordinary electrodynamics, since also, in that case, the system is nonclosed because the influence from the mechanical system itself is not accounted for (this is the point giving rise to the classic Abraham–Minkowski problem). We assume in this section that ϵ and μ can vary in space and time but do not restrict the derivatives with respect to space or time to be constants.

We may start with the electromagnetic energy density,

$$W = \frac{1}{2}(\mathbf{E} \cdot \mathbf{D} + \mathbf{H} \cdot \mathbf{B}). \quad (35)$$

Together with the Poynting vector,

$$\mathbf{S} = \mathbf{E} \times \mathbf{H}, \quad (36)$$

this leads to the energy conservation equation

$$\nabla \cdot \mathbf{S} + \dot{W} = -\mathbf{E} \cdot \mathbf{J} - \dot{\theta}(\mathbf{E} \cdot \mathbf{B}). \quad (37)$$

There is thus an exchange of electromagnetic energy with the axion “medium” if \mathbf{E} and \mathbf{B} are different from zero and $\theta(t)$ is time-varying, even if $\mathbf{J} = 0$.

A more delicate question is the expression for the momentum density \mathbf{g} . In accordance with Planck’s principle of inertia of energy, $\mathbf{g} = \mathbf{S}/c^2$, one would expect the Abraham momentum density \mathbf{g}^A to be right,

$$\mathbf{g}^A = \mathbf{E} \times \mathbf{H}. \quad (38)$$

We notice that the Maxwell stress tensor,

$$T_{ik} = E_i D_k + H_i B_k - \frac{1}{2} \delta_{ik} (\mathbf{E} \cdot \mathbf{D} + \mathbf{H} \cdot \mathbf{B}), \quad (39)$$

is common for the Abraham and Minkowski alternatives, $T_{ik}^A = T_{ik}^M \equiv T_{ik}$. Here δ_{ik} is the Kronecker delta. The momentum conservation equation can thus be expressed in the form

$$\partial_k T_{ik} - \dot{g}_i^A = f_i^A, \quad (40)$$

where f_i^A are the components of Abraham’s force density

$$\mathbf{f}^A = \rho \mathbf{E} + (\mathbf{J} \times \mathbf{B}) + (\epsilon\mu - 1) \frac{\partial}{\partial t} (\mathbf{E} \times \mathbf{H}) - g_{a\gamma\gamma} (\mathbf{E} \cdot \mathbf{B}) \nabla a. \quad (41)$$

The third term on the right-hand side of Equation (41), the Abraham term, has experimentally turned up only in a few experiments, mainly at low frequencies where the mechanical oscillations of a test body are directly detectable.

In optics, the Abraham force will fluctuate out. It is therefore mathematically simpler, and in accordance with all observational experience in optics, to include the Abraham momentum (physically, a mechanical accompanying momentum) in the effective field momentum. Therewith, the momentum density becomes just the Minkowski momentum \mathbf{g}^M , given by

$$\mathbf{g}^M = \mathbf{D} \times \mathbf{B}. \quad (42)$$

The momentum conservation equation in the Minkowski case yields

$$\partial_k T_{ik} - \frac{\partial}{\partial t} g_i^M = f_i^M, \quad (43)$$

where

$$\mathbf{f}^M = \rho \mathbf{E} + (\mathbf{J} \times \mathbf{B}) - (\mathbf{E} \cdot \mathbf{B}) \nabla \theta. \quad (44)$$

Consider the relativistically covariant form for the energy–momentum balance: Minkowski’s energy–momentum tensor,

$$S_{\mu}^{M\nu} = F_{\mu\alpha}H^{\nu\alpha} - \frac{1}{4}g_{\mu}^{\nu}F_{\alpha\beta}H^{\alpha\beta}, \tag{45}$$

has the same form in all inertial frames. The conservation equations for electromagnetic energy and momentum can be written as

$$-\partial_{\nu}S_{\mu}^{M\nu} = f_{\mu}^M, \tag{46}$$

where $f_{\mu}^M = (f_0, \mathbf{f}^M)$ is the four-force density. In the rest system,

$$f_0 = \mathbf{E} \cdot \mathbf{J} + (\mathbf{E} \cdot \mathbf{B})\dot{\theta}, \tag{47}$$

where $f_0^M = f_0^A \equiv f_0$.

4. Casimir Effect between Two Plates

We here restrict ourselves to the simplest case, namely, scalar electrodynamics, meaning that the photons’ vector property is included but not their spin. We assume $\alpha = 0$ and also zero temperature. Assume the usual setup where there are two large metallic plates, with a gap L , orthogonal to the z direction. In the intervening region, there is an axion field $a(z)$ whose amplitude increases linearly with z ,

$$a(z) = \frac{a_0z}{L} = \beta z, \quad 0 < z < L, \tag{48}$$

where a_0 , the amplitude at $z = L$, is fixed. There is no external magnetic field. The magnitude of β is not restricted to be small. The smallness expansion in the present theory applies rather to the spatial variation of the axion field, as embodied in the restriction $\partial_i\partial_j\theta \approx 0$, as also mentioned above.

We mention that the reduced Maxwell equations in this case can be written as

$$\nabla^2\mathbf{E} - \epsilon\mu\ddot{\mathbf{E}} = g_{a\gamma\gamma}\mu\beta\hat{\mathbf{z}} \times \dot{\mathbf{E}}, \tag{49}$$

$$\nabla^2\mathbf{H} - \epsilon\mu\ddot{\mathbf{H}} = g_{a\gamma\gamma}\beta\partial_z\mathbf{E}. \tag{50}$$

We obtain two dispersive branches, as before. The first, corresponding to Equation (26), can now be written

$$|\mathbf{k}| = \sqrt{\epsilon\mu}\omega, \quad k_z = \frac{\pi n}{L}, \quad n = 1, 2, 3, \dots, \tag{51}$$

showing no dependence on the axions. The second branch can be written as

$$\epsilon\mu\omega^2 = \mathbf{k}^2 \pm g_{a\gamma\gamma}\beta\omega, \tag{52}$$

which can be recast in the form

$$\omega = \frac{1}{\sqrt{\epsilon\mu}} \left(|\mathbf{k}| \pm \frac{1}{2}g_{a\gamma\gamma}\beta\sqrt{\frac{\mu}{\epsilon}} \right), \tag{53}$$

in view of the smallness of $g_{a\gamma\gamma}^2$. This branch, composed of two modes, lies very close to the first mode above. For a given ω , there are in all three different values of $|\mathbf{k}|$.

Consider now the zero-temperature zero-point energy \mathcal{E} of the field, defined by

$$\mathcal{E} = \frac{1}{2} \sum \omega. \tag{54}$$

From the second branch (53) only, one obtains, per unit plate area,

$$\mathcal{E} = \frac{1}{2\sqrt{\varepsilon\mu}} \sum_{n=1}^{\infty} \left[\int \frac{d^2k_{\perp}}{(2\pi)^2} \sqrt{k_{\perp}^2 + \frac{\pi^2 n^2}{L^2}} \pm \frac{g_{a\gamma\gamma}}{2L^2} \sqrt{\frac{\mu}{\varepsilon}} \right], \tag{55}$$

where \mathbf{k}_{\perp} is the component of \mathbf{k} orthogonal to the surface normal (note that the present definition of β differs from that in Ref. [108]). This expression can be further treated using dimensional regularization (see, for instance, Ref. [46]), with the result [108]

$$\mathcal{E} = \frac{1}{\sqrt{\varepsilon\mu}} \left(-\frac{\pi^2}{1440} \frac{1}{L^3} \mp \frac{g_{a\gamma\gamma}\beta}{4L^2} \sqrt{\frac{\mu}{\varepsilon}} \right). \tag{56}$$

Of main interest is the contribution from the photons and axions moving in the z direction. We associate this with the Casimir energy \mathcal{E}_C . Mathematically, the derivation involves the Hurwitz zeta function. One obtains

$$\mathcal{E}_C = \frac{1}{4\sqrt{\varepsilon\mu}} \left(-\frac{\pi}{6L} \pm \frac{1}{2} g_{a\gamma\gamma}\beta \sqrt{\frac{\mu}{\varepsilon}} \right) \frac{1}{L^2}. \tag{57}$$

Here, the first term comes from scalar photons propagating in the z direction, while the second term is the axionic contribution. With respect to the inverse L dependence, the Casimir energies for the electrodynamic and the axion parts behave similarly, as one would expect. In the above, the upper and lower signs match. In Equation (57), the small axion-induced increase in the Casimir energy arises from the superluminal mode in the dispersion relation (53) (meaning that the group velocity is larger than $1/\sqrt{\varepsilon\mu}$). This mode corresponds to a weak repulsive Casimir force. The other mode corresponds to a weak attractive force.

5. An Axion Echo from Reflection in Outer Space

Assume that the axion field is of the form $a = a(t) = a_0 \sin \omega_a t$, as is often chosen for outer space, and assume $\varepsilon = \mu = 1$. In view of the smallness of the axion velocity, $v \sim 10^{-3}c$, one has approximately $\omega_a = m_a$. An estimated value of $m_a = 10 \mu\text{eV}$ is common. If the axions are associated with dark matter, we have to make do with a very low energy density, $\rho_{\text{DM}} = 0.45 \text{ GeV}/\text{cm}^3$ [71]. We will adopt the simple form

$$\rho_a = \frac{1}{2} m_a^2 a_0^2. \tag{58}$$

Assume now that an electromagnetic beam is sent from the Earth to an axion cloud. We take the initial form of the beam to be Gaussian,

$$\mathbf{A}_0(x, t) = c e^{-x^2/2D^2} \cos k_0 x \hat{\mathbf{y}}, \tag{59}$$

with \mathbf{A}_0 as the vector potential and the constant D as the Gaussian width. Making a Fourier decomposition,

$$\mathbf{A}_0(x, t) = \frac{1}{2} \int_{-\infty}^{\infty} \left[\mathbf{A}_0(k) e^{i(kx - \omega t)} + \mathbf{A}_0^*(k) e^{-i(kx - \omega t)} \right] dk, \tag{60}$$

one has as inversion

$$\mathbf{A}_0(k) = \frac{1}{2\pi} \int_{-\infty}^{\infty} e^{-ikx} \left[\mathbf{A}_0(x, 0) + \frac{i}{\omega} \frac{\partial \mathbf{A}_0}{\partial t}(x, 0) \right] dx. \tag{61}$$

Then, imposing the condition $\partial \mathbf{A}_0 / \partial t(x, 0) = 0$, we obtain

$$\mathbf{A}_0(k) = \mathbf{A}_0^+(k) + \mathbf{A}_0^-(k), \tag{62}$$

where

$$\mathbf{A}_0^+(k) = \frac{cD}{2\sqrt{2\pi}} \exp\left[-\frac{1}{2}D^2(k - k_0)^2\right] \hat{\mathbf{y}}. \quad (63)$$

The expression for $\mathbf{A}_0^-(k)$ implies that $k - k_0 \rightarrow k + k_0$. The right-moving wave, to be considered henceforth, is

$$\mathbf{A}_0^+(x, t) = \int_0^\infty \mathbf{A}_0^+(k) \cos(kx - \omega t) dk, \quad \omega = k > 0. \quad (64)$$

In what follows, we omit the superscript. The incident wave fields are $\mathbf{E}_0(x, t) = -\dot{\mathbf{A}}_0(x, t)$, $\mathbf{H}_0(x, t) = \nabla \times \mathbf{A}_0(x, t)$.

The incident wave will interact with the axion cloud. As $\rho = \mathbf{J} = 0$, we see from Equations (41) or (44) that $\mathbf{f} = 0$, in accordance with the assumed homogeneity of the cloud. Furthermore, the component f_0 in (47) is zero, because \mathbf{E}_0 and \mathbf{H}_0 are orthogonal. We therefore go back to the field equations, from which we obtain

$$\nabla^2 \mathbf{A} - \ddot{\mathbf{A}} = -g_{a\gamma\gamma} \dot{a} \nabla \times \mathbf{A}. \quad (65)$$

We here let $\mathbf{A} \rightarrow \mathbf{A}_0$ on the right-hand side of Equation (65). Neglecting $\nabla^2 \mathbf{A}$ on the left-hand side, and using Equation (64), we obtain

$$\ddot{\mathbf{A}}(x, t) = -g_{a\gamma\gamma} a_0 \omega_a \int_0^\infty A_0(k) k \sin(kx - \omega t) \cos \omega_a t \, dk \hat{\mathbf{z}}, \quad (66)$$

still with $\omega = k$.

In complex notation, extracting the resonance term,

$$\ddot{\mathbf{A}}(x, t) = \frac{1}{2} g_{a\gamma\gamma} a_0 \omega_a \text{Im} \int_0^\infty A_0(k) k e^{i(kx - \omega t + \omega_a t)} \hat{\mathbf{z}}. \quad (67)$$

We construct a new quantity $\mathbf{A}(k, t)$ as

$$\mathbf{A}(x, t) = \text{Im} \int_0^\infty e^{ikx} \mathbf{A}(k, t) dk, \quad (68)$$

and can thus write

$$\ddot{\mathbf{A}}(k, t) = -\frac{1}{2} g_{a\gamma\gamma} a_0 \omega_a A_0(k) k e^{-i(\omega - \omega_a)t} \hat{\mathbf{z}}. \quad (69)$$

With yet another quantity

$$\mathcal{A}(k, t) = \mathbf{A}(k, t) e^{-i\omega t}, \quad (70)$$

we have

$$\ddot{\mathbf{A}}(k, t) = \ddot{\mathcal{A}}(k, t) e^{i\omega t} + 2i\omega \dot{\mathcal{A}}(k, t) e^{i\omega t} - \omega^2 \mathcal{A}(k, t) e^{i\omega t}, \quad (71)$$

Now, keeping the resonance term only, we obtain

$$\dot{\mathcal{A}}(k, t) = \frac{i}{4} g_{a\gamma\gamma} a_0 \omega_a A_0(k) e^{-i(2\omega - \omega_a)t} \hat{\mathbf{z}}. \quad (72)$$

Integrating over t ,

$$\mathcal{A}(k, t) = -g_{a\gamma\gamma} a_0 \omega_a \frac{cD}{8\sqrt{2\pi}} \exp\left[-\frac{1}{2}D^2(k - k_0)^2\right] \frac{e^{-i(2\omega - \omega_a)t}}{2\omega - \omega_a} \hat{\mathbf{z}}. \quad (73)$$

The resonance at $\omega = \omega/2$ is as expected: an incoming photon 2ω can split an axion into two components with the same mass, $m_a = \omega_a$. We focus on the imaginary part of the above expression and use the relation

$$\lim_{\alpha \rightarrow \infty} \frac{\sin \alpha x}{\pi x} = \delta(x), \quad (74)$$

(with $\delta(x)$ the Dirac delta function) to obtain

$$\text{Im} \mathcal{A}(k, t) = g_{a\gamma\gamma} a_0 \omega_a \frac{cD}{16} \sqrt{\frac{\pi}{2}} \exp\left[-\frac{1}{2} D^2 (k - k_0)^2\right] \delta\left(\omega - \frac{1}{2} \omega_a\right) \hat{\mathbf{z}}. \quad (75)$$

From this, the axion echo can be found. This sort of calculation was pioneered by Pierre Sikivie and collaborators [75,82]. The present generalized form, containing the Gaussian width D , was given by one of the authors of this paper and Masud Chaichian [91].

6. Discussions and Future Outlooks

We would like to conclude with the following brief points.

1. As already mentioned, the influence of axions, at least in cosmology, is expected to be very weak. The cosmological axion energy density is often expected to be about 0.40 GeV/cm^3 , corresponding to an axion mass of about 10^{-5} eV and a relative velocity of about 10^{-3} . Various experiments and proposals of experiments have been launched:
 - (a) The haloscope experiment, proposed by Sikivie [75], in which the aim is to detect resonances between the electromagnetic eigenfrequencies of a dielectric cylinder and the axions (see also Refs. [70,91]). To date, no such resonance has been detected.
 - (b) The idea, also due to Sikivie [75], to observe the axions via their electromagnetic “echo” returned back to the Earth from an outer cloud (see also Ref. [91]).
 - (c) The broadband solenoidal haloscope proposed in Ref. [71], which proposes to make use of the axion “antenna” effect to focus the electromagnetic radiation emitted from dielectric boundaries towards a detector.
2. The above treatment provides a general review of axion electrodynamics and is, in principle, not limited to the semiclassical case. This constraint applies similarly to ordinary electrodynamics, usually when distances are small or temperatures are high.
3. The axion formalism is useful as regards application to topological insulators. Thus, the constitutive relations (17) can formally be taken over to this kind of modern material science as they stand. The case of chiral materials, for instance, a Faraday material, is more complicated since the coupling parameter θ becomes imaginary; see, for instance, Ref. [74].
4. To conclude, we have presented a concise summary of the basics of axion electrodynamics, linking it to the general field of Casimir physics. Notably, additional contributions to the Casimir interaction are observed that occur as direct consequences of the extra pseudoscalar axion field. Novel physics, based on improved materials characterization requiring new and improved physical models, is likely to be discovered in the years to come.

Author Contributions: Initialization, conceptualization, supervision, project administration, funding acquisition, I.B. Writing—original draft preparation, writing—review and editing, I.B., M.B., A.G., Y.L., and S.P. All authors have read and agreed to the published version of the manuscript.

Funding: This research is part of the project No. 2022/47/P/ST3/01236 cofunded by the National Science Centre and the European Union’s Horizon 2020 research and innovation programme under the Marie Skłodowska-Curie grant agreement No. 945339. We also thank the “ENSEMBLE3—Centre of Excellence for nanophotonics, advanced materials and novel crystal growth-based technologies”

project (GA No. MAB/2020/14) carried out within the International Research Agendas programme of the Foundation for Polish Science cofinanced by the European Union under the European Regional Development Fund, the European Union's Horizon 2020 research and innovation programme Teaming for Excellence (GA. No. 857543) for support of this work.

Conflicts of Interest: The authors declare no conflicts of interest.

References

1. Peccei, R.D.; Quinn, H.R. CP Conservation in the presence of pseudoparticles. *Phys. Rev. Lett.* **1977**, *38*, 1440–1443. [CrossRef]
2. Peccei, R.D. The strong CP problem and axions. In *Axions: Theory, Cosmology, and Experimental Searches*; Kuster, M., Raffelt, G., Beltrán, B., Eds.; Springer: Berlin/Heidelberg, Germany, 2008. pp. 3–17. [CrossRef]
3. Kane, C.L.; Mele, E.J. Z_2 topological order and the quantum spin Hall effect. *Phys. Rev. Lett.* **2005**, *95*, 146802. [CrossRef]
4. Kane, C.L.; Mele, E.J. Quantum spin Hall effect in graphene. *Phys. Rev. Lett.* **2005**, *95*, 226801. [CrossRef]
5. Hasan, M.Z.; Kane, C.L. Colloquium: Topological insulators. *Rev. Mod. Phys.* **2010**, *82*, 3045–3067. [CrossRef]
6. Bernevig, B.A.; Hughes, T.L.; Zhang, S.C. Quantum spin Hall effect and topological phase transition in HgTe quantum wells. *Science* **2006**, *314*, 1757–1761. [CrossRef]
7. Qi, X.L.; Zhang, S.C. The quantum spin Hall effect and topological insulators. *Phys. Today* **2010**, *63*, 33–38. [CrossRef]
8. Wilczek, F. Two applications of axion electrodynamics. *Phys. Rev. Lett.* **1987**, *58*, 1799–1802. [CrossRef]
9. Wilczek, F. Problem of strong P and T invariance in the presence of instantons. *Phys. Rev. Lett.* **1978**, *40*, 279–282. [CrossRef]
10. Weinberg, S. A new light boson? *Phys. Rev. Lett.* **1978**, *40*, 223–226. [CrossRef]
11. Fu, L.; Kane, C.L. Topological insulators with inversion symmetry. *Phys. Rev. B* **2007**, *76*, 045302. [CrossRef]
12. Liu, C.C.; Feng, W.; Yao, Y. Quantum spin Hall effect in silicene and two-dimensional germanium. *Phys. Rev. Lett.* **2011**, *107*, 076802. [CrossRef]
13. Fukui, T.; Hatsugai, Y.; Suzuki, H. Chern numbers in discretized Brillouin zone: Efficient method of computing (spin) Hall conductances. *J. Phys. Soc. Jpn.* **2005**, *74*, 1674–1677. [CrossRef]
14. Sekine, A.; Nomura, K. Axion electrodynamics in topological materials. *J. Appl. Phys.* **2021**, *129*, 141101. [CrossRef]
15. Li, R.D.; Wang, J.; Qi, X.L.; Zhang, S.C. Dynamical axion field in topological magnetic insulators. *Nat. Phys.* **2010**, *6*, 284–288. [CrossRef]
16. Boström, M.; Gholamhosseini, A.; Pal, S.; Li, Y.; Brevik, I. Semi-classical electrodynamics and the Casimir effect. *Physics* **2024**, *6*, 456–467. [CrossRef]
17. Casimir, H.B.G. On the attraction between two perfectly conducting plates. *Proc. Kon. Ned. Akad. Wetensch. B* **1948**, *51*, 793–795. Available online: <https://dwc.knaw.nl/DL/publications/PU00018547.pdf> (accessed on 1 February 2024).
18. Casimir, H.B.G.; Polder, D. The influence of retardation on the London–van der Waals forces. *Phys. Rev.* **1948**, *73*, 360–372. [CrossRef]
19. Lifshitz, E.M. The theory of molecular attractive forces between solids. *Sov. Phys. JETP* **1956**, *2*, 73–83. Available online: <http://jetp.ras.ru/cgi-bin/e/index/e/2/1/p73?a=list> (accessed on 1 February 2024).
20. Dzyaloshinskii, I.E.; Lifshitz, E.M.; Pitaevskii, L.P. The general theory of van der Waals forces. *Adv. Phys.* **1961**, *10*, 165–209. [CrossRef]
21. Parsegian, V.A.; Ninham, B.W. Application of the Lifshitz theory to the calculation of van der Waals forces across thin lipid films. *Nature* **1969**, *224*, 1197–1198. [CrossRef]
22. Ninham, B.W.; Parsegian, V.A.; Weiss, G.H. On the macroscopic theory of temperature-dependent van der Waals forces. *J. Stat. Phys.* **1970**, *2*, 323–328. [CrossRef]
23. Richmond, P.; Ninham, B.W. A note on the extension of the Lifshitz theory of van der Waals forces to magnetic media. *J. Phys. C Solid State Phys.* **1971**, *4*, 1988–1993. [CrossRef]
24. Richmond, P.; Ninham, B.W. Calculations, using Lifshitz theory, of the height vs. thickness for vertical liquid helium films. *Solid State Commun.* **1971**, *9*, 1045–1047. [CrossRef]
25. Richmond, P.; Ninham, B.W.; Ottewill, R.H. A theoretical study of hydrocarbon adsorption on water surfaces using Lifshitz theory. *J. Coll. Interf. Sci.* **1973**, *45*, 69–80. [CrossRef]
26. Boström, M.; Sernelius, B.E. Thermal effects on the Casimir force in the 0.1–5 μm range. *Phys. Rev. Lett.* **2000**, *84*, 4757–4760. [CrossRef]
27. Bordag, M.; Geyer, B.; Klimchitskaya, G.L.; Mostepanenko, V.M. Casimir force at both nonzero temperature and finite conductivity. *Phys. Rev. Lett.* **2000**, *85*, 503–506. [CrossRef]
28. Ninham, B.W.; Boström, M.; Persson, C.; Brevik, I.; Buhmann, S.Y.; Sernelius, B.E. Casimir forces in a plasma: Possible connections to Yukawa Potentials. *Eur. Phys. J. D* **2014**, *68*, 328. [CrossRef]
29. Dou, M.; Lou, F.; Boström, M.; Brevik, I.; Persson, C. Casimir quantum levitation tuned by means of material properties and geometries. *Phys. Rev. B* **2014**, *89*, 201407. [CrossRef]
30. Esteso, V.; Carretero-Palacios, S.; Miguez, H. Nanolevitation phenomena in real plane-parallel systems due to the balance between Casimir and gravity forces. *J. Phys. Chem. C* **2015**, *119*, 5663–5670. [CrossRef] [PubMed]

31. Boström, M.; Dou, M.; Malyi, O.I.; Parashar, P.; Parsons, D.F.; Brevik, I.; Persson, C. Fluid-sensitive nanoscale switching with quantum levitation controlled by α -Sn/ β -Sn phase transition. *Phys. Rev. B* **2018**, *97*, 125421. [CrossRef]
32. Estes, V.; Carretero-Palacios, S.; Míguez, H. Casimir–Lifshitz force based optical resonators. *J. Phys. Chem. Lett.* **2019**, *10*, 5856–5860. [CrossRef] [PubMed]
33. Estes, V.; Carretero-Palacios, S.; MacDowell, L.G.; Fiedler, J.; Parsons, D.F.; Spallek, F.; Míguez, H.; Persson, C.; Buhmann, S.Y.; Brevik, I.; et al. Premelting of ice adsorbed on a rock surface. *Phys. Chem. Chem. Phys.* **2020**, *22*, 11362–11373. [CrossRef] [PubMed]
34. Li, Y.; Brevik, I.; Malyi, O.I.; Boström, M. Different pathways to anomalous stabilization of ice layers on methane hydrates. *Phys. Rev. E* **2023**, *108*, 034801. [CrossRef] [PubMed]
35. Boström, M.; Khan, M.R.; Gopidi, H.R.; Brevik, I.; Li, Y.; Persson, C.; Malyi, O.I. Tuning the Casimir–Lifshitz force with gapped metals. *Phys. Rev. B* **2023**, *108*, 165306. [CrossRef]
36. Klimchitskaya, G.L.; Mostepanenko, V.M. Casimir effect invalidates the Drude model for transverse electric evanescent waves. *Physics* **2023**, *5*, 952–967. [CrossRef]
37. Hauxwell, F.; Ottewill, R. A study of the surface of water by hydrocarbon adsorption. *J. Coll. Interf. Sci.* **1970**, *34*, 473–479. [CrossRef]
38. Anderson, C.H.; Sabisky, E.S. Phonon interference in thin films of liquid helium. *Phys. Rev. Lett.* **1970**, *24*, 1049–1052. [CrossRef]
39. Lamoreaux, S.K. Demonstration of the Casimir force in the 0.6 to 6 μ m range. *Phys. Rev. Lett.* **1997**, *78*, 5–8. [CrossRef]
40. Harris, B.W.; Chen, F.; Mohideen, U. Precision measurement of the Casimir force using gold surfaces. *Phys. Rev. A* **2000**, *62*, 052109. [CrossRef]
41. Decca, R.S.; López, D.; Fischbach, E.; Krause, D.E. Measurement of the Casimir force between dissimilar metals. *Phys. Rev. Lett.* **2003**, *91*, 050402. [CrossRef]
42. Feiler, A.A.; Bergström, L.; Rutland, M.W. Superlubricity using repulsive van der Waals forces. *Langmuir* **2008**, *24*, 2274–2276. [CrossRef]
43. Munday, J.N.; Capasso, F.; Parsegian, V.A. Measured long-range repulsive Casimir–Lifshitz forces. *Nature* **2009**, *457*, 170–173. : [CrossRef] [PubMed]
44. Somers, D.; Garrett, J.; Palm, K.; Munday, J.N. Measurement of the Casimir torque. *Nature* **2018**, *564*, 386–389. [CrossRef]
45. Mahanty, J.; Ninham, B.W. *Dispersion Forces*; Academic Press Inc. Ltd.: London, UK, 1976.
46. Milton, K.A. *The Casimir Effect: Physical Manifestations of Zero-Point Energy*; World Scientific Co. Ltd.: Singapore, 2001. [CrossRef]
47. Parsegian, V.A. *Van der Waals Forces: A Handbook for Biologists, Chemists, Engineers, and Physicists*; Cambridge University Press: New York, NY, USA, 2006. [CrossRef]
48. Bordag, M.; Klimchitskaya, G.L.; Mohideen, U.; Mostepanenko, V.M. *Advances in the Casimir Effect*; Oxford Science Publications: New York, NY, USA, 2009. [CrossRef]
49. Sernelius, B.E. *Surface Modes in Physics*; Wiley-VCH Verlag Berlin GmbH: Berlin, Germany, 2005. [CrossRef]
50. Buhmann, S.Y. *Dispersion Forces I: Macroscopic Quantum Electrodynamics and Ground-State Casimir, Casimir–Polder and Van der Waals Forces*; Springer: Berlin/Heidelberg, Germany, 2012. [CrossRef]
51. Sernelius, B.E. *Fundamentals of van der Waals and Casimir Interactions*; Springer Nature Switzerland AG: Cham, Switzerland, 2018. [CrossRef]
52. Boström, M.; Williams, D.R.M.; Ninham, B.W. Specific ion effects: Why DLVO theory fails for biology and colloid systems. *Phys. Rev. Lett.* **2001**, *87*, 168103. [CrossRef]
53. Parsons, D.F.; Ninham, B.W. Ab initio molar volumes and Gaussian radii. *J. Phys. Chem. A* **2009**, *113*, 1141–1150. [CrossRef]
54. Parsons, D.F.; Ninham, B.W. Nonelectrostatic ionic forces between dissimilar surfaces: A mechanism for colloid separation. *J. Phys. Chem. C* **2012**, *116*, 7782–7792. [CrossRef]
55. Medda, L.; Barse, B.; Cugia, F.; Boström, M.; Parsons, D.F.; Ninham, B.W.; Monduzzi, M.; Salis, A. Hofmeister challenges: Ion binding and charge of the BSA protein as explicit examples. *Langmuir* **2012**, *28*, 16355–16363. [CrossRef] [PubMed]
56. Duignan, T.T.; Parsons, D.F.; Ninham, B.W. A continuum model of solvation energies including electrostatic, dispersion, and cavity contributions. *J. Phys. Chem. B* **2013**, *117*, 9421–9429. [CrossRef]
57. Parsons, D.F.; Salis, A. The impact of the competitive adsorption of ions at surface sites on surface free energies and surface forces. *J. Chem. Phys.* **2015**, *142*, 134707. [CrossRef]
58. Boström, M.; Malyi, O.I.; Thiyam, P.; Berland, K.; Brevik, I.; Persson, C.; Parsons, D.F. The influence of Lifshitz forces and gas on premelting of ice within porous materials. *EPL (Europhys. Lett.)* **2016**, *115*, 13001. [CrossRef]
59. Thiyam, P.; Fiedler, J.; Buhmann, S.Y.; Persson, C.; Brevik, I.; Boström, M.; Parsons, D.F. Ice particles sink below the water surface due to a balance of salt, van der Waals, and buoyancy forces. *J. Phys. Chem. C* **2018**, *122*, 15311–15317. [CrossRef]
60. Ninham, B.W.; Yaminsky, V. Ion binding and ion specificity: The Hofmeister effect and Onsager and Lifshitz theories. *Langmuir* **1997**, *13*, 2097–2108. [CrossRef]
61. Boström, M.; Li, Y.; Brevik, I.; Persson, C.; Carretero-Palacios, S.; Malyi, O.I. van der Waals induced ice growth on partially melted ice nuclei in mist and fog. *Phys. Chem. Chem. Phys.* **2023**, *25*, 32709–32714. [CrossRef]
62. Luengo-Márquez, J.; MacDowell, L.G. Lifshitz theory of wetting films at three phase coexistence: The case of ice nucleation on Silver Iodide (AgI). *J. Coll. Interf. Sci.* **2021**, *590*, 527–538. [CrossRef]

63. Luengo-Marquez, J.; Izquierdo-Ruiz, F.; MacDowell, L.G. Intermolecular forces at ice and water interfaces: Premelting, surface freezing, and regelation. *J. Chem. Phys.* **2022**, *157*, 044704. [CrossRef] [PubMed]
64. Sikivie, P. Experimental tests of the “invisible” axion. *Phys. Rev. Lett.* **1983**, *51*, 1415–1417. [CrossRef]
65. Preskill, J.; Wise, M.B.; Wilczek, F. Cosmology of the invisible axion. *Phys. Lett. B* **1983**, *120*, 127–132. [CrossRef]
66. Abbott, L.F.; Sikivie, P. A cosmological bound on the invisible axion. *Phys. Lett. B* **1983**, *120*, 133–136. [CrossRef]
67. Dine, M.; Fischler, W. The not-so-harmless axion. *Phys. Lett. B* **1983**, *120*, 137–141. [CrossRef]
68. Sikivie, P. Axion cosmology. In *Axions: Theory, Cosmology, and Experimental Searches*; Kuster, M., Raffelt, G., Beltrán, B., Eds.; Springer: Berlin/Heidelberg, Germany, 2008; pp. 19–50. [CrossRef]
69. Sikivie, P.; Sullivan, N.; Tanner, D.B. Proposal for axion dark matter detection using an LC circuit. *Phys. Rev. Lett.* **2014**, *112*, 131301. [CrossRef] [PubMed]
70. Millar, A.J.; Redondo, J.; Steffen, F.D. Dielectric haloscopes: Sensitivity to the axion dark matter velocity. *J. Cosmol. Astropart. Phys.* **2017**, *2017*, 006. [CrossRef]
71. Liu, J.; et al. [BREAD Collaboration]. Broadband solenoidal haloscope for terahertz axion detection. *Phys. Rev. Lett.* **2022**, *128*, 131801. [CrossRef] [PubMed]
72. Li, X.; Shi, X.; Zhang, J. Generalized Riemann ζ -function regularization and Casimir energy for a piecewise uniform string. *Phys. Rev. D* **1991**, *44*, 560–562. [CrossRef] [PubMed]
73. Lawson, M.; Millar, A.J.; Pancaldi, M.; Vitagliano, E.; Wilczek, F. Tunable axion plasma haloscopes. *Phys. Rev. Lett.* **2019**, *123*, 141802. [CrossRef] [PubMed]
74. Jiang, Q.D.; Wilczek, F. Chiral Casimir forces: Repulsive, enhanced, tunable. *Phys. Rev. B* **2019**, *99*, 125403. [CrossRef]
75. Sikivie, P. Invisible axion search methods. *Rev. Mod. Phys.* **2021**, *93*, 015004. [CrossRef]
76. McDonald, J.I.; Ventura, L.B. Optical properties of dynamical axion backgrounds. *Phys. Rev. D* **2020**, *101*, 123503. [CrossRef]
77. Zyla, P.A.; et al. [Particle Data Group]. Review of Particle Physics. *Prog. Theor. Exp. Phys* **2020**, *2020*, 083C01. Ch. 79. [CrossRef]
78. Arza, A.; Schwetz, T.; Todarello, E. How to suppress exponential growth—On the parametric resonance of photons in an axion background. *J. Cosmol. Astropart. Phys.* **2020**, *2020*, 013. [CrossRef]
79. Carenza, P.; Mirizzi, A.; Sigl, G. Dynamical evolution of axion condensates under stimulated decays into photons. *Phys. Rev. D* **2020**, *101*, 103016. [CrossRef]
80. Leroy, M.; Chianese, M.; Edwards, T.D.; Weniger, C. Radio signal of axion-photon conversion in neutron stars: A ray tracing analysis. *Phys. Rev. D* **2020**, *101*, 123003. [CrossRef]
81. Ouellet, J.; Bogorad, Z. Solutions to axion electrodynamics in various geometries. *Phys. Rev. D* **2019**, *99*, 055010. [CrossRef]
82. Arza, A.; Sikivie, P. Production and detection of an axion dark matter echo. *Phys. Rev. Lett.* **2019**, *123*, 131804. [CrossRef]
83. Qiu, Z.; Cao, G.; Huang, X.G. Electrodynamics of chiral matter. *Phys. Rev. D* **2017**, *95*, 036002. [CrossRef]
84. Dror, J.A.; Murayama, H.; Rodd, N.L. Cosmic axion background. *Phys. Rev. D* **2021**, *103*, 115004. [CrossRef]
85. Fukushima, K.; Imaki, S.; Qiu, Z. Anomalous Casimir effect in axion electrodynamics. *Phys. Rev. D* **2019**, *100*, 045013. [CrossRef]
86. Tobar, M.E.; McAllister, B.T.; Goryachev, M. Modified axion electrodynamics as impressed electromagnetic sources through oscillating background polarization and magnetization. *Phys. Dark Univ.* **2019**, *26*, 100339. [CrossRef]
87. Bae, S.; Youn, S.; Jeong, J. Tunable photonic crystal haloscope for high-mass axion searches. *Phys. Rev. D* **2023**, *107*, 015012. [CrossRef]
88. Adshead, P.; Draper, P.; Lillard, B. Time-domain properties of electromagnetic signals in a dynamical axion background. *Phys. Rev. D* **2020**, *102*, 123011. [CrossRef]
89. Tobar, M.E.; McAllister, B.T.; Goryachev, M. Poynting vector controversy in axion modified electrodynamics. *Phys. Rev. D* **2022**, *105*, 045009. [CrossRef]
90. DeRocco, W.; Hook, A. Axion interferometry. *Phys. Rev. D* **2018**, *98*, 035021. [CrossRef]
91. Brevik, I.H.; Chaichian, M.M. Axion electrodynamics: Energy–momentum tensor and possibilities for experimental tests. *Int. J. Mod. Phys. A* **2022**, *37*, 2250151. [CrossRef]
92. Brevik, I.H.; Chaichian, M.M. Electric current and heat production by a neutral carrier: An effect of the axion. *Eur. Phys. J. C* **2022**, *82*, 202. [CrossRef]
93. Brevik, I.; Favitta, A.M.; Chaichian, M. Axionic and nonaxionic electrodynamics in plane and circular geometry. *Phys. Rev. D* **2023**, *107*, 043522. [CrossRef]
94. Brevik, I.; Chaichian, M.; Favitta, A.M. On the Axion Electrodynamics in a two-dimensional slab and the Casimir effect. *arXiv* **2023**, arXiv:2310.05575. [CrossRef]
95. Qi, X.L.; Zhang, S.C. Topological insulators and superconductors. *Rev. Mod. Phys.* **2011**, *83*, 1057–1110. [CrossRef]
96. Qi, X.L.; Hughes, T.L.; Zhang, S.C. Topological field theory of time-reversal invariant insulators. *Phys. Rev. B* **2008**, *78*, 195424. [CrossRef]
97. Peccei, R.D.; Quinn, H.R. Constraints imposed by CP conservation in the presence of pseudoparticles. *Phys. Rev. D* **1977**, *16*, 1791–1797. [CrossRef]
98. Lu, B.S. The Casimir effect in topological matter. *Universe* **2021**, *7*, 237. [CrossRef]
99. Martín-Ruiz, A.; Cambiaso, M.; Urrutia, L. The magnetoelectric coupling in electrodynamics. *Int. J. Mod. Phys. A* **2019**, *34*, 1941002. [CrossRef]

100. Nogueira, F.S.; van den Brink, J. Absence of induced magnetic monopoles in Maxwellian magnetoelectrics. *Phys. Rev. Res.* **2022**, *4*, 013074. [CrossRef]
101. Woods, L.M.; Krüger, M.; Dodonov, V.V. Perspective on some recent and future developments in Casimir interactions. *Appl. Sci.* **2020**, *11*, 293. [CrossRef]
102. To, D.Q.; Wang, Z.; Ho, D.Q.; Hu, R.; Acuna, W.; Liu, Y.; Bryant, G.W.; Janotti, A.; Zide, J.M.; Law, S.; et al. Strong coupling between a topological insulator and a III-V heterostructure at terahertz frequency. *Phys. Rev. Mater.* **2022**, *6*, 035201. [CrossRef]
103. Kargarian, M.; Randeria, M.; Trivedi, N. Theory of Kerr and Faraday rotations and linear dichroism in topological Weyl semimetals. *Sci. Rep.* **2015**, *5*, 12683. [CrossRef]
104. Wilson, J.H.; Allocca, A.A.; Galitski, V. Repulsive Casimir force between Weyl semimetals. *Phys. Rev. B* **2015**, *91*, 235115. [CrossRef]
105. Martín-Ruiz, A.; Cambiaso, M.; Urrutia, L. A Green's function approach to the Casimir effect on topological insulators with planar symmetry. *Europhys. Lett.* **2016**, *113*, 60005. [CrossRef]
106. Woods, L.; Dalvit, D.A.R.; Tkatchenko, A.; Rodriguez-Lopez, P.; Rodriguez, A.W.; Podgornik, R. Materials perspective on Casimir and van der Waals interactions. *Rev. Mod. Phys.* **2016**, *88*, 045003. [CrossRef]
107. Khusnutdinov, N.; Woods, L.M. Casimir effects in 2D Dirac materials (Scientific Summary). *JETP Lett.* **2019**, *110*, 183–192. [CrossRef]
108. Brevik, I. Axion electrodynamics and the axionic Casimir effect. *Universe* **2021**, *7*, 133. [CrossRef]

Disclaimer/Publisher's Note: The statements, opinions and data contained in all publications are solely those of the individual author(s) and contributor(s) and not of MDPI and/or the editor(s). MDPI and/or the editor(s) disclaim responsibility for any injury to people or property resulting from any ideas, methods, instructions or products referred to in the content.

Article

Semi-Classical Electrodynamics and the Casimir Effect

Mathias Boström ^{1,2,*}, Ayda Gholamhosseinian ³, Subhojit Pal ¹, Yang Li ^{4,5} and Iver Brevik ^{6,*}

¹ Centre of Excellence ENSEMBLE3 Sp. z o. o., Wolczynska Str. 133, 01-919 Warsaw, Poland; subhojit18@iiserb.ac.in

² Chemical and Biological Systems Simulation Lab, Centre of New Technologies, University of Warsaw, Banacha 2C, 02-097 Warsaw, Poland

³ School of Physics and Materials Science, Ferdowsi University of Mashhad, Mashhad 9177948974, Iran; ayda.gholamhosseinian@mail.um.ac.ir

⁴ School of Physics and Materials Science, Nanchang University, Nanchang 330031, China; leon@ncu.edu.cn

⁵ Institute of Space Science and Technology, Nanchang University, Nanchang 330031, China

⁶ Department of Energy and Process Engineering, Norwegian University of Science and Technology, NO-7491 Trondheim, Norway

* Correspondence: mathias.bostrom@ensemble3.eu (M.B.); iver.h.brevik@ntnu.no (I.B.)

Abstract: From the late 1960s onwards, the groups of Barry Ninham and Adrian Parsegian, and their many collaborators, made a number of essential contributions to theory and experiment of intermolecular forces. In particular, they explored the semi-classical theory: Maxwell's equations and Planck quantization of light leads to Lifshitz and Casimir interactions. We discuss some selected thought-provoking results from Ninham and his group. Some of the results have been conceived as controversial but, we would say, never uninteresting.

Keywords: Lifshitz forces; Casimir effect; semi-classical electrodynamics

1. Introduction

Since the prediction of the Casimir effect in 1948, and its experimental confirmation in the period after that, there has been a significant interest in studying the forces caused by fluctuations both theoretically and experimentally [1,2]. Before reviewing some contributions to Casimir physics from semi-classical electrodynamics theory, that is Maxwell's equations and Planck quantization of light leading to Lifshitz and Casimir interactions, with particular emphasis on the paper by Barry Ninham and collaborators, we first present some historical reflections. The history of intermolecular forces actually goes back to the early history of science. Thomas Young notably wrote a paper on molecular forces in 1805 [3,4]. Young deduced that they had to obey $1/r^6$ -power-law, where r is the average distance between molecules. Reverend Pam Challis of Trinity College, in a major address to the British Association 1836 [5], reviewed the state of molecular forces between colloidal particles, suggested interferometry for direct measurements, quoting Augustin-Jean Fresnel, and referred to the subject as "this the highest Department of Science" for which he coined the term Mathematical Physics. The renowned article by James Clerk Maxwell in the ninth edition of Encyclopaedia Britannica [6] discussed capillary action and molecular forces, updated by Lord Rayleigh in the 11th edition [7]. Roger Boscovich (Ruđer Bošković), a Croatian Jesuit Priest based in Rome after whom the Ruđer Bošković Institute in Zagreb is named, developed a system of the world essentially inventing statistical mechanics (his book [8] appeared around 1600). To do so, Boscovich needed a molecular potential. His effective potential oscillated with the period a molecular diameter tailing off into a gravitational $1/r^2$. The basis of the study of intermolecular forces was laid by Johannes Diderik van der Waals in 1873 [9] (see English translation in Ref. [10]). He clarified the concept of interparticle forces and how molecules interact. Quantum fluctuations create intermolecular forces that exist throughout macroscopic bodies. At the molecular separations

Citation: Boström, M.; Gholamhosseinian, A.; Pal, S.; Li, Y.; Brevik, I. Semi-Classical Electrodynamics and the Casimir Effect. *Physics* **2024**, *6*, 456–467. <https://doi.org/10.3390/physics6010030>

Received: 24 November 2023

Revised: 10 January 2024

Accepted: 18 January 2024

Published: 19 March 2024



Copyright: © 2024 by the authors. Licensee MDPI, Basel, Switzerland. This article is an open access article distributed under the terms and conditions of the Creative Commons Attribution (CC BY) license (<https://creativecommons.org/licenses/by/4.0/>).

of about a few nanometres or less, these interactions causing the attraction and repulsion between molecules, are the familiar van der Waals forces.

As discussed by Boris Derjaguin, Irina Abrikosova, and Evgeny Lifshitz in their 1956 review paper [11], the correct understanding of the nature of molecular forces was initially proposed by Peter (Pyotr) N. Lebedev, back in 1894 [11,12]: “There exist intermolecular forces whose origin is closely connected with radiation processes.” In general, it is necessary to understand van der Waals forces and understand their importance compared to other molecular forces.

Fundamental and applied research on molecular forces continued until Fritz London proposed the general theory of molecular forces in 1930 [13]. This theoretically improved the understanding of molecular dispersion forces, and contributed to the interpretation of van der Waals forces and other molecular forces. Also, the significant contributions of Lifshitz should be addressed. In 1955, Lifshitz explained how the oscillating charge distribution in molecules leads to the creation of attractive forces [14]. These explanations contribute to a deeper understanding of molecular forces and their role in various phenomena.

Ever since Derjaguin and Abrikosova [11] performed their force measurements, there has been a strong focus on the phenomena. The first set of experiments, notably measuring interactions between quartz and metal plates, studied only the so-called retarded region. Experiments of David Tabor and Ralph Winterton [15] and subsequently of Jacob Israelachvili and Tabor [16,17] fitted the measured force to a power law function of $1/L^p$ (where L is the distance), where p varied from non-retarded ($p = 3$) to fully retarded ($p = 4$) value. In these early experiments, a gradual transition was observed from non-retarded to retarded interaction, as the distance between the surfaces increased from around 12 nm upto 130 nm [16]. Surface force measurements [11,15–18] and theoretical clarifications and extensions of the Lifshitz formula [19–23] to include, for example, magnetic [24] and conducting particles [25,26], and liquids between unequal surfaces, were pioneered in the 1970s by the group of Ninham, Israelachvili, and their collaborators at the Department of Applied Mathematics in the Australian National University.

According to the fundamental theory, the Lifshitz force can also be repulsive, which is an interesting feature that has attracted quite some of attention [19,27,28]. Charles Anderson and Edward Sabiski demonstrated this phenomenon in their research on liquid helium films on smooth surfaces of calcium fluorite (CaF_2), among other similar molecularly smooth surfaces [29]. The thickness of the films in the experiment ranged from 10 Å to 200 Å, and could be measured with an accuracy of a few percent in most cases. Several past publications by Ninham have explored the history of intermolecular forces in more detail. The book by Ninham and Pierandrea Lo Nostro [30] is of a particular interest.

We focus first on reviewing a study that our close and distinguished collaborator Barry Ninham wrote in 1970 together with Adrian V. Parsegian and George H. Weiss [21]. The reason to highlight this paper is that it seems to us it is not recognized well enough in the field. The theories of intermolecular dispersion forces have occupied such a vast literature that one would suspect quite little should remain to be said. However, even lately, new applications of the fundamental theory have arisen. We firstly address the semi-classical theory itself, and then briefly discuss our contribution to the theory of Casimir interaction between real metal plates at high temperatures/large separations. A controversial, as well as especially intriguing, idea is briefly explored in the current paper, highlighting that the high-temperature Casimir effect might have a role even in nuclear physics [31]. To be more specific: it was shown in an unpublished note by Ninham and Colin Pask [32] more than 50 years ago how Maxwell’s equations for the electromagnetic field with Planck quantization of allowed modes appear to provide a semiclassical account of nuclear interactions. The direct consequence if this idea has any relevance is that mesons would emerge as plasmons, collective excitations in an electron–positron pair-sea [31]. We then proceed to present a study that was initiated by Ninham around 1970 on excited state interaction between atoms [33]. Related self-energies and excited state interactions

are, for example, essential in photobiochemistry. We finally wrap up our study with a few concluding words.

2. The Ninham, Parsegian and Weiss Semi-Classical Derivation of Lifshitz Theory

The theory due to Lifshitz was readdressed by Lifshitz, Igor Dzyaloshinskii and Lev Pitaevski [19] via some lengthy arguments that exploited Green’s function techniques in quantum field theory. We outline the general ideas behind the considerably simpler semi-classical theory of dispersion interactions. The paper [21], which we follow in this Section with some changes in notation, expanded on general ideas presented by Nicolaas van Kampen and collaborators [34]. Here, we point out that Ref. [34] only considered the zero-temperature and non-retarded limit. We use the electrodynamics boundary conditions given in the book [35] that the components of $(\mathbf{E}_\omega, \mathbf{H}_\omega)$, E_x , E_y , ϵE_z , H_x , H_y , and μH_z (with μ the permeability) are continuous at interfaces between the media, parallel to the xy -plane at $z = 0$ and $z = d$. We are thus considering the simple enough case of two half-spaces interacting across a media. We assume that the dielectric permittivities are different, $\epsilon_1(\omega) \neq \epsilon_2(\omega)$ where ω denoteds the frequency, and the magnetic permeabilities equal to one. The solutions $(\mathbf{Y} = \sum_\omega \mathbf{Y}_\omega e^{-i\omega t}$ where $\mathbf{Y}_\omega \in \{ \mathbf{H}_\omega, \mathbf{E}_\omega \}$) has normal mode frequencies from the wave equation [21],

$$\nabla^2 \mathbf{Y}_\omega + (\epsilon\omega^2/c^2)\mathbf{Y}_\omega = 0, \tag{1}$$

together with $\nabla \cdot \mathbf{Y}_\omega = 0$. Here, c denotes the speed of light in the vacuum. For the separate components of \mathbf{E}_ω and \mathbf{H}_ω , one assumes the form [21] $\Theta(z)e^{i(ux+vy)}$, where u and v are the wave vector components parallel to the surface, and $\Theta''(z) = \gamma^2\Theta(z)$, where the prime denotes the z -derivative. Here, $\gamma^2 = \kappa^2 - [\omega^2\epsilon(\omega)/c^2]$ and $\kappa = \sqrt{u^2 + v^2}$ is the real component of the wave vector parallel to the slab of the intermediate film. Ninham, Parsegian and Weiss showed [21] that normal modes (ω_i) are solutions of transverse magnetic (TM) and transverse electric (TE) dispersion relations,

$$D_1(\omega; d) = 1 - \Delta_{\text{TM}}^2 e^{-2\gamma_2 d} = 0 = D_2(\omega; d) = 1 - \Delta_{\text{TE}}^2 e^{-2\gamma_2 d}, \tag{2}$$

where

$$\Delta_{\text{TE}} = \frac{\gamma_2 - \gamma_1}{\gamma_2 + \gamma_1}; \quad \Delta_{\text{TM}} = \frac{\epsilon_1\gamma_2 - \epsilon_2\gamma_1}{\epsilon_1\gamma_2 + \epsilon_2\gamma_1}. \tag{3}$$

The two types of electromagnetic modes are TE and TM, and there are no TE evanescent modes. This is put into question for the Drude-plasma model for real metal surfaces, as discussed briefly in Section 3 below. The requirement of the surface-type solutions (those that are well-behaved and vanish at infinity), $\text{Re}(\gamma_2) > 0$ implies that $\kappa \geq (\omega/c)\text{Re}(\epsilon_2^{1/2})$ in what follows. Ultimately, the fundamental dispersion relations in Equation (2) combine into a simple enough relation: $D = D_1 D_2 = 0$. The Gibbs interaction free energy is given by

$$F(d, T) = \frac{1}{2\pi} \int_0^\infty [F_d(r) - F_\infty(r)] r dr, \tag{4}$$

where T denotes the temperature; the next step is to integrate over wave vector \mathbf{r} ,

$$F_d(r) = kT \sum_j \ln[2 \sinh(\beta \hbar \omega_j(r)/2)] \tag{5}$$

(with k and \hbar are the Boltzmann and the reduced Planck constants, respectively, and $\beta = 1/(kT)$) in the subsequent steps, the sum must be taken over all the available real roots of Equation (2). From this it follows that

$$\sum_j g(\omega_j) = \frac{1}{2\pi i} \oint_C g(\omega) [1/D(\omega)] [dD(\omega)/d\omega] d\omega. \tag{6}$$

In the Formula (6), the path C includes the important points where D has zeros, but does not include the poles of this function (for details, see [21]). To ensure the validity of Equation (6), the functions $g(z)$ and $D(z)$ must exhibit analyticity or smoothness, where the contour C includes the relevant zeros of D , and excludes poles of $g(\omega)$. Note that $g(z)$ and $D(z)$ are assumed analytic for Equation (6) to hold. Since $g(\omega) = \ln[2 \sinh(\beta\hbar\omega/2)]$ has branch cuts, it is convenient to expand it as

$$\begin{aligned} g(\omega) &= \ln[2 \sinh(\beta\hbar\omega/2)] \\ &= \ln \left[e^{\frac{\beta\hbar\omega}{2}} - e^{-\frac{\beta\hbar\omega}{2}} \right] \\ &= \frac{\beta\hbar\omega}{2} + \ln \left[1 - e^{-\beta\hbar\omega} \right] \\ &= \frac{\beta\hbar\omega}{2} - \sum_{n=1}^{\infty} \frac{1}{n} e^{-n\beta\hbar\omega} \end{aligned} \tag{7}$$

and consider each term separately. To proceed formally, we choose the path in Equation (6) starting from $-\infty$ to $i\infty$ along the imaginary axis, then move around the right half-plane along a semicircular path with an infinity radius. Since $\varepsilon(|\omega|) \rightarrow 1$ as $|\omega| \rightarrow \infty$, $D(|\omega|) = 1$ on the semicircle and one can write

$$\begin{aligned} F_d(r) &= \frac{1}{2\pi i} \int_{\infty}^{-\infty} g(i\zeta) \frac{d \ln D(i\zeta; d)}{d\zeta} d\zeta \\ &= \frac{\hbar}{2} \sum_j \omega_j + \frac{\hbar}{2\pi} \sum_{n=1}^{\infty} \int_{-\infty}^{\infty} \cos(n\beta\hbar\zeta) \ln D_r(i\zeta; d) d\zeta \\ &\quad - \frac{i\hbar}{2\pi} \sum_{n=1}^{\infty} \int_0^{\infty} \sin(n\beta\hbar\zeta) \ln \left[\frac{D_r(i\zeta; d)}{D_r(-i\zeta; d)} \right] d\zeta, \end{aligned} \tag{8}$$

where D_r refers to the real roots. Using standard mathematics we exploit the identity

$$\sum_{n=1}^{\infty} \cos(nx) = \pi \sum_{n=-\infty}^{\infty} \delta(x - 2\pi n) - \frac{1}{2}, \tag{10}$$

where $\delta(\cdot)$ is the Dirac delta function. When the delta functions are substituted into the integrals, the integrations can be carried out:

$$\frac{\hbar}{2} \sum_j \omega_j + \frac{\hbar}{2\pi} \sum_{n=1}^{\infty} \int_{-\infty}^{\infty} \cos(n\beta\hbar\zeta) \ln D_r(i\zeta; d) d\zeta = \frac{kT}{2} \sum_{n=-\infty}^{\infty} \ln D_r(i\zeta_n; d), \tag{11}$$

where the Matsubara frequency $\zeta_n = 2\pi kTn/\hbar$ so that

$$F_d(r) = \frac{kT}{2} \sum_{n=-\infty}^{\infty} \ln D_r(i\zeta_n; d) - \frac{i\hbar}{2\pi} \sum_{n=1}^{\infty} \int_0^{\infty} \sin(n\beta\hbar\zeta) \ln \left[\frac{D_r(i\zeta; d)}{D_r(-i\zeta; d)} \right] d\zeta. \tag{12}$$

Noteworthy for dielectric functions depending on ω^2 only, one term in Equation (12) turns out to be zero by symmetry and Equation (12) reduces to

$$F_d(r) = kT \sum_{n=0}^{\infty} ' \ln D_r(i\zeta_n; d) \tag{13}$$

The prime notation here represents that the term corresponding to $n = 0$ is multiplied by $1/2$. This equation is, for instance, valid for the so-called plasma model discussed in Section 3 just below.

3. A High-Temperature Semi-Classical Application: The Drude-Plasma Controversy

The Casimir interaction between real metal surfaces has caused controversy in the field of Casimir physics. The paper [21] discussed above could be relevant to this problem. As is known [36,37], a real metal has a finite static conductivity. The so-called Drude model is a suitable model for the optical and dielectric properties of a real metal for small frequencies. The dielectric function can be described within the Drude model as

$$\varepsilon(\omega) = 1 + \frac{4\pi i\sigma(\omega)}{\omega} = 1 - \frac{\omega_{pl}^2}{\omega(\omega + i\gamma)}. \quad (14)$$

Setting the dissipation parameter γ equal to zero is commonly called using the plasma model,

$$\varepsilon(\omega) = 1 - \frac{\omega_{pl}^2}{\omega^2}. \quad (15)$$

Notably, for metal surfaces using the Drude dielectric function, the condition used to pass from Equation (12) to Equation (13) is not fulfilled. However, the dissipation parameter has an actual physical basis. It is not zero for any real metal. Its origin is via scattering of carriers against impurities within the lattice. Importantly, when using the plasma model, one by quite a simple ad hoc decision neglects these effects and, as a result, the static conductivity becomes infinite. In Ref. [36] it is demonstrated how including the dissipation parameter has a critical effect on the predicted interaction at large surface separations, where temperature effects impact the results strongly. The plasma model predicts a result coinciding with that of the classical Gedanken experiment by Casimir between two perfectly reflecting half-spaces, while the Drude model predicts that this result is reduced by a factor of two. To understand how these drastic effects occur, one needs to look at the TM and TE normal modes involved in the problem. When dissipation is included, there are also TE evanescent modes. At separations where the temperature is essential, the contribution to the interaction from these TE evanescent modes completely cancels those from the TE propagating modes. It is known that experimental results in general agree better with the zero-temperature results between real metal surfaces and well enough with the zero-temperature result for the Casimir Gedanken experiment. The agreement is better still with the theoretical room-temperature result obtained when using the so-called plasma model. This was the seed of the long-standing controversy in the field. The finite temperature Casimir effect between metallic surfaces is a complex phenomenon, and care has to be taken about the electrostatic patch potentials, which have caused uncertainties in the actual interpretation of the data in experiments. Different theoretical groups have found fundamentally different results [36,38]. A particularly useful aspect of the original Lamoreaux experiment [39] was that it was carried out at large enough separations where finite temperature corrections can be expected. Steve Lamoreaux with collaborators later presented results using a similar experimental setup where separations were varied from 0.7 to 7 μm [40]. The theoretical predictions based upon the Drude model were found to agree with the observed results to acceptable accuracy. Let us stress, however, that other experiments [41–45] (more references can be found in the recent review by Vladimir Mostepanenko and Galina Klimchitskaya [46]), yielded results in quite good accordance with the plasma model rather than the Drude model. The reason for contradictory results (both theoretical and experimental) is not known to the authors of the present paper. There is still a need for more experiments and theoretical analysis focusing on Casimir–Lifshitz forces in different systems that include interacting conducting (metallic) objects. However, it is not the purpose of the current study to explore this problem. For one side of this long story (and relevant references), we refer to a very recent paper by Mostepanenko and Klimchitskaya [46]; see also [47]. For another side of the story, one could, for example, consult the well-explaining paper by Sernelius [37]. More information can be found in elsewhere [48–51]. But, perhaps, a correct calculation for high-temperature/large-separation Casimir force between real metal surfaces has still

not been carried out. The solution might from a fundamental point of view, if perhaps not necessary from a practical point of view, involve both the use of our Equation (12) and the inclusion in the theory of any intervening plasma as in the following Section 4.

4. Another Intriguing Semi-Classical Story: Casimir Interaction Energy across a Plasma

Researchers have been looking into Casimir forces over time because of a fundamental role of those forces in electron stability, particle physics, and nuclear interactions [52–54]. We recently looked at a Casimir–Yukawa problem that is similar to the classic story of electron stability, often known as “the Casimir mousetrap” [54]. This problem explores how negative charges on an electron surface create a repulsive force between surface parts, which has to be counteracted by an attractive force to retain a finite electron radius. Casimir proposed that the attractive Poincaré stresses could be caused by the zero-point energy present in electromagnetic vacuum fluctuations [54]. Nevertheless, the study of Timothy Boyer and others showed that although the interaction’s magnitude was correct, it had the wrong sign and resulted in a repulsive force [54]. Other relevant models, such as the dielectric ball, also exhibit their respective problems, some of which are still triggering discussions recently. Around 50 years ago, Ninham and Pask [32] found that the zero-temperature Casimir vacuum fluctuation energy was enough to provide the binding energy of nucleons in a nucleus. At finite temperatures, the expression (4) discussed in Section 2 reads [19]

$$F(d, T) = \frac{kT}{\pi} \sum_{n=0}^{\infty} ' \int_0^{\infty} dq q \ln[1 - e^{-2d\sqrt{q^2 + \xi_n^2/c^2}}]. \tag{16}$$

Explicitly, in vacuum (i.e., in the complete absence of an intervening electron–positron plasma), the following useful expansion [31,52,55,56] were derived,

$$F(d, T) \approx \frac{-\pi^2 \hbar c}{720d^3} - \frac{\zeta(3)k^3T^3}{2\pi\hbar^2c^2} + \frac{\pi^2 dk^4T^4}{45\hbar^3c^3} + \dots, \tag{17}$$

where zeta function $\zeta(3) \approx 1.202$. One observes that the initial term corresponds to the attractive zero temperature Casimir result. The third term in this expression corresponds to a black body radiation energy (in vacuum and at equilibrium). More than twenty years ago, Ninham and one of the authors of this paper discussed how this term opposes the attractive Casimir term [52]. The remaining term is a chemical potential term that in the Gibbs free energy is well recognized as being due to an electron–positron plasma formed from the photons inside the nuclear gap ($e^- + e^+ \leftrightarrow \gamma$) [57]. The second term can be analysed using the known density of an electron–positron plasma [57],

$$\rho_- + \rho_+ = \frac{3\zeta(3)k^3T^3}{\pi^2\hbar^3c^3}. \tag{18}$$

For a pair of perfectly conducting plates, the Casimir interaction energy across an electron–positron plasma is

$$F(d, T) = \frac{kT}{\pi} \sum_{n=0}^{\infty} ' \int_0^{\infty} dq q \ln \left[1 - e^{-2d\sqrt{q^2 + (\xi_n/c)^2 + \kappa^2}} \right], \tag{19}$$

Recall that $\kappa = \omega_p/c$, where ω_p denotes the plasma frequency. For any separation at high enough temperatures, or for any finite temperature at large enough separations, it follows [52,55,56] an expansion of the form,

$$F(d, T) = -\frac{kT\kappa}{4\pi} \frac{e^{-2\kappa d}}{d} \left[1 + \frac{1}{2d\kappa} \right] - \frac{(kT)^2 e^{-2\eta d}}{\hbar c} \frac{e^{-\rho^* \eta d}}{d} + \mathcal{O}(e^{-4\eta d}), \tag{20}$$

where $\rho^* = \rho e^2 \hbar^2 / (\pi m_e k^2 T^2)$, $\eta = 2kT / (\hbar c)$ and κ is defined above. Both the $n = 0$ and $n > 0$ terms behave similarly to the Yukawa potential [31,56]. Both provide contributions to the Casimir–Yukawa binding energy, depending on the separation (about 0.9 MeV from the $n = 0$ term and about 3.6 MeV from the $n > 0$ term), and surprisingly close to the experimentally observed binding energy per nucleon (1.1 MeV to about 8.8 MeV) [31]. The idea that there ought to be some kind of link between electromagnetic and nuclear forces goes back to Richard Feynman (via private communication in the late 1960s between Ninham and Freeman Dyson, who told Ninham that Richard Feynman had believed there ought to be a connection between electromagnetic theory and nuclear interactions). This idea was first explored by Ninham and Pask in early 1970s [32]. We have revived and expanded on this idea in a series of publications [52,55,56]. The explicit derivation of meson mass, nuclear binding energy and lifetimes [58] were recently discussed at length in Ref. [31].

5. Semi-Classical Derivation of Resonance Interaction between Excited State Atom Pair

The semi-classical formalism was also able to describe in detail the ground state van der Waals potentials between a pair of molecules, or between a molecule and a surfaces [23]. Here, as one in some sense more controversial example [33,59–62], we explore what predictions come out from semi-classical theory for the resonance interaction energy between two identical atoms in an excited configuration. The results in this Section were, in the zero-temperature limit, derived about 50 years ago by Ninham, John Mitchell, and others, and finally, after deep contemplation and a final extension to finite temperatures [33], published 20 years ago. Notably, the results are, in the non-retarded limit, identical to the perturbation theory results [60–63], but in the retarded and finite-temperature limits, non-oscillatory results are found. This contrast against the oscillatory long-range retarded resonance interaction obtained from perturbation theory [60,61].

The normal mode expression used to calculate ground state van der Waals interactions in the case of two identical atoms in air,

$$1 - \alpha(1|\omega)\alpha(2|\omega)T(d|\omega)^2 = 0, \tag{21}$$

can be separated into one anti-symmetric and one symmetric part. Here, $T(d|\omega)$ is the field susceptibility [59] in a material with dielectric function $\epsilon(\omega)$, and $\alpha(j|\omega)$ represent the polarizability of atom j . The excited symmetric state has a substantially shorter lifetime than the excited anti-symmetric state, which can cause the system to end up in an excited anti-symmetric state [33]. The first-order dispersion energy of such an anti-symmetric state comes from

$$U(d) = \hbar[\omega_r(d) - \omega_r(\infty)], \tag{22}$$

where ω_r denotes resonance frequency. The solution of Equation (21) is the pole of the anti-symmetric part (of the underlying Green’s function). We change the integration path around this pole to obtain an expression for the first order excited state resonance interaction energy,

$$U(d) = (\hbar/\pi) \int_0^\infty d\zeta \ln[1 + \alpha(1|i\zeta)T(d|i\zeta)]. \tag{23}$$

As pointed out in the past, any finite temperature systems can approximately be dealt with in the same way as for the corresponding ground state problem [55,64]. The temperature (T) dependence follows when replacing the integration over imaginary frequencies by a summation over discrete frequencies [14]. The leading term, at large separation when the modes in the $(\pm;x)$ branch are excited, is

$$U(d, T) \simeq \pm \frac{2kT}{d^3} \sum_{n=0}^\infty \alpha(i\zeta_n) e^{-xn} [1 + xn + x^2n^2], \tag{24}$$

where $x = 2\pi kTd/(\hbar c)$. In a standard way we approximate the polarizability with $\alpha(0)$ at large enough separations. Within this approximation, the resonance free-energy is [33],

$$U(d, T) \simeq \pm \frac{2kT\alpha(0)}{2d^3(e^x - 1)^3} [1 + e^{3x} - e^x(1 + 2x - 2x^2) + e^{2x}(-1 + 2x + 2x^2)]. \quad (25)$$

For small values of x , this free energy of resonance interaction goes as $1/d^4$. However, for any finite temperature, the long-range interaction within the Ninham model is dominated by the $n = 0$ term. This term is here

$$U(d, T)_{n=0} = \pm kT\alpha(0)/d^3. \quad (26)$$

This manifestation of the correspondence principle is identical in nature to the result obtained for the retarded van der Waals interaction between two ground-state atoms [55,64]. This highlights that the quantum nature of light has an essential role behind the softening of intermolecular interactions between ground state or excited state atoms (and indeed in the same way for Lifshitz interactions between macroscopic surfaces).

6. Discussions and Future Outlooks

This concise review primarily aims to engage an insightful discussion concerning the semi-classical theory of interactions with ground and excited state van der Waals, Lifshitz, and Casimir forces. This paper also aims to shed new light on a small, but missing, element of information that might provide some understanding to settle the Drude-plasma controversy. To be more precise, as we have already discussed in the study by Ninham, Parsegian, and Weiss [21], the conventional Lifshitz theory left out one extra term. Further investigations of the Casimir effect at high-temperatures/short-range regimes may offer more evidence for its potential influence in both meson and atom-atom physics. The modern research on van der Waals, Lifshitz, and Casimir interactions was pioneered by Ninham and Parsegian more than 50 years ago. Their respective groups demonstrated how to use the complicated Lifshitz theory and how to derive it in a much-simplified way. Researchers from around the world have developed the field for the last 50–60 years (notably, Russian researchers, including Yuri Barash and Vitaly Ginzburg [65], presented some classic works that are similar to those that came from Ninham's group in Australia). However, it is still an intensive active research field [36,46]. The field was, for instance, energized by Michael Elbaum and Michael Schick, who predicted that ice can have a nanometer sized premelted water layer on an ice surface caused by van der Waals, Lifshitz, intermolecular forces [66]. In general surface charges, ions, and impurities can induce water films many orders of magnitude thicker [67–69]. The effects caused by ionic interactions are in general complicated enough, due partly to the fact that the polarizability of ions leads to a non-linear coupling of van der Waals and ionic forces leading to the macroscopic double-layer and Lifshitz forces acting across salt solutions [70–75]. An impact from such intermolecular forces has also been proposed for frost heaving [76] and thunder cloud charging [77–79]. Ice melting at surfaces and interfaces could be relevant as habitats for life on planets and moons in permafrost regions, but also on other planets and moons in the solar system and beyond [80] (for more discussions on planetary science, see [81–83]). The reverse reaction with ice forming on a water surface via Lifshitz interactions was ruled out by the study of Elbaum and Schick [84]. However, in contrast, recent re-investigations of the optical properties of water and ice suggest such a role [85,86]. Following along these lines, we investigated how the Lifshitz interaction can contribute to some geophysical effects, including ice layer formation on gas hydrate surfaces [87]. We have recently proposed such dispersion interactions as potential energy sources behind a secondary ice growth mechanism on partially melted ice clusters within mist, fog, and potentially also in clouds [88]. The contributions from intermolecular forces to geophysics is an evolving research field with essential contributions from Luis McDowell and collaborators [86,89].

Dispersion interactions between particles and surfaces occur at finite temperatures and in the presence of a background plasma. This is not only of vital importance for various biological applications and catalysis, but it may also surprisingly enough be of interest for hidden aspects in fundamental quantum electrodynamics. All interactions between particles take place in the presence of the plasma of the fluctuating electron–positron pairs; constantly created and annihilated. This is particularly true for the interaction between nuclear particles. Strong similarities were found, suggesting a potential role for screened Casimir forces as one major contribution to the nuclear interaction. When non-relativistic plasma [56] is used, the relativistic energy, mc^2 , enters the interaction energy in a quite an intriguing way: it replaces the temperature. This indicates that there could be some interesting physics hidden in this problem, and we may need to use the relativistic mass from the beginning. To make further progress, one seems may need to extend these quite simple consideration to include a relativistic plasma response function and to include magnetic (spin) susceptibilities. These are problems of the same importance as occurring in physical chemistry [90]. A fundamental ansatz commonly used, assumes that all electrostatic interactions (generally analysed in a nonlinear theory) and electrodynamic interactions (often treated within a linear approximation) can be treated separately. This, in general, is in violation of the fundamental physical laws [90]. For further progress, one needs to carefully ponder the foundations of the theory of these attractive and repulsive intermolecular interactions [91].

Author Contributions: Initialization, conceptualization, supervision, project administration, funding acquisition, M.B. Writing—original draft preparation, writing—review and editing, M.B., A.G., S.P., Y.L. and I.B. All authors have read and agreed to the published version of the manuscript.

Funding: This research is part of the project No. 2022/47/P/ST3/01236 co-funded by the National Science Centre and the European Union’s Horizon 2020 research and innovation programme under the Marie Skłodowska-Curie grant agreement No. 945339. We also thank the “ENSEMBLE3—Centre of Excellence for nanophotonics, advanced materials and novel crystal growth-based technologies” project (GA No. MAB/2020/14) carried out within the International Research Agendas programme of the Foundation for Polish Science co-financed by the European Union under the European Regional Development Fund, the European Union’s Horizon 2020 research and innovation programme Teaming for Excellence (GA. No. 857543) for support of this work.

Data Availability Statement: The data is contained within the article.

Conflicts of Interest: The authors declare no conflicts of interest.

References

1. Casimir, H.B.G. On the attraction between two perfectly conducting plates. *Proc. Kon. Ned. Akad. Wetensch. B* **1948**, *51*, 793–795. Available online: <https://dwc.knaw.nl/DL/publications/PU00018547.pdf> (accessed on 15 January 2024).
2. Casimir, H.B.G.; Polder, D. The influence of retardation on the London–van der Waals forces. *Phys. Rev.* **1948**, *73*, 360–372. [CrossRef]
3. Young, T. An essay on the cohesion of fluids. *Phil. Trans. R. Soc. Lond.* **1805**, *95*, 65–87. [CrossRef]
4. Craik, A.D.D. Thomas Young on fluid mechanics. *J. Eng. Math.* **2010**, *67*, 95–113. [CrossRef]
5. Challis, J. On capillary attraction and the molecular forces of fluids. *Lond. Edinb. Dublin Philos. Mag. J. Sci.* **1836**, *8*, 89–96. [CrossRef]
6. Capillary Action. In *Encyclopedia Britannica: Dictionary of Arts, Sciences, and General Literature. Volume V*; Adam and Charles Black: Edinburgh, UK, 1876; pp. 56–71. Available online: <https://digital.nls.uk/encyclopaedia-britannica/archive/193322694> (accessed on 15 January 2023).
7. Capillary Action. In *Encyclopedia Britannica: Dictionary of Arts, Sciences, and General Literature. Volume XI*; University Press: Cambridge, UK, 1910; pp. 256–275. Available online: <https://archive.org/details/encyclopaediabrit05chisrich/page/256/> (accessed on 15 January 2023).
8. Boscovich, P.R.J.; Societatis Jesu. *Theoria Philosophiæ Naturalis*. Venetiis: Vienna, Austria, 1563. English translation: Boscovich, R.J.; Societatis Jesu. *A Theory of Natural Philosophy*; The M.I.T. Press: Cambridge, MA, USA, 1966. Available online: <https://archive.org/details/theoryofnaturalp0000rugg> (accessed on 15 January 2024).
9. van der Waals, J.D. *Over de Continuïteit van den Gas- en Vloeistofoestand*; Boekdrukkerij van A.W. Sijthoff: Leiden, The Netherlands, 1873. [CrossRef]

10. van der Waals, J.D. *On the Continuity of the Gaseous and Liquid States*; Elsevier Science Publishers B.V.: Amsterdam, The Netherlands, 1988.
11. Derjaguin, B.V.; Abrikosova, I.I.; Lifshitz, E.M. Direct measurement of molecular attraction between solids separated by a narrow gap. *Quart. Rev. Chem. Soc.* **1956**, *10*, 295–329. [CrossRef]
12. Lebedew, P. Ueber die mechanische Wirkung der Wellen auf ruhende Resonatoren. I. Electromagnetische Wellen. *Ann. Phys.* **1894**, *288*, 621–640. [CrossRef]
13. London, F. Zur Theorie und Systematik der Molekularkräfte. *Z. Phys.* **1930**, *63*, 245–279. [CrossRef]
14. Lifshitz, E.M. The theory of molecular attractive forces between solids. *Sov. Phys. JETP* **1956**, *2*, 73–83. Available online: <http://jetp.ras.ru/cgi-bin/e/index/e/2/1/p73?a=list> (accessed on 15 January 2024).
15. Tabor, D.; Winterton, W.H.S. The direct measurement of normal and retarded van der Waals forces. *Proc. Roy. Soc. Lond. A Math. Phys. Sci.* **1969**, *312*, 435. [CrossRef]
16. Israelachvili, J.N.; Tabor, D. The measurement of van der Waals dispersion forces in the range 1.5 to 130 nm. *Proc. R. Soc. Lond. A Math. Phys. Sci.* **1972**, *331*, 19–38. [CrossRef]
17. White, L.R.; Israelachvili, J.N.; Ninham, B.W. Dispersion interaction of crossed mica cylinders: A reanalysis of the Israelachvili–Tabor experiments. *J. Chem. Soc. Faraday Trans. 1 Phys. Chem. Cond. Phases* **1976**, *72*, 2526–2536. [CrossRef]
18. Tabor, D.; Winterton, R. Surface forces: Direct measurement of normal and retarded van der Waals forces. *Nature* **1968**, *219*, 1120–1121. [CrossRef]
19. Dzyaloshinskii, I.E.; Lifshitz, E.M.; Pitaevskii, L.P. The general theory of van der Waals forces. *Adv. Phys.* **1961**, *10*, 165–209. [CrossRef]
20. Parsegian, V.A.; Ninham, B.W. Application of the Lifshitz theory to the calculation of van der Waals forces across thin lipid films. *Nature* **1969**, *224*, 1197–1198. [CrossRef]
21. Ninham, B.W.; Parsegian, V.A.; Weiss, G.H. On the macroscopic theory of temperature-dependent van der Waals forces. *J. Stat. Phys.* **1970**, *2*, 323–328. [CrossRef]
22. Ninham, B.W.; Parsegian, V.A. van der Waals forces: Special characteristics in lipid-water systems and a general method of calculation based on the Lifshitz theory. *Biophys. J.* **1970**, *10*, 646–663. [CrossRef] [PubMed]
23. Mahanty, J.; Ninham, B.W. *Dispersion Forces*; Academic Press Inc. Ltd.: London, UK, 1976.
24. Richmond, P.; Ninham, B.W. A note on the extension of the Lifshitz theory of van der Waals forces to magnetic media. *J. Phys. C Solid State Phys.* **1971**, *4*, 1988–1993. [CrossRef]
25. Richmond, P.; Davies, B.; Ninham, B.W. van der Waals attraction between conducting molecules. *Phys. Lett. A* **1972**, *39*, 301–302. [CrossRef]
26. Davies, B.; Ninham, B.W.; Richmond, P. van der Waals forces between thin cylinders: New features due to conduction processes. *J. Chem. Phys.* **2003**, *58*, 744–750. [CrossRef]
27. Richmond, P.; Ninham, B.W. Calculations, using Lifshitz theory, of the height vs. thickness for vertical liquid helium films. *Solid State Commun.* **1971**, *9*, 1045–1047. [CrossRef]
28. Richmond, P.; Ninham, B.W.; Ottewill, R.H. A theoretical study of hydrocarbon adsorption on water surfaces using Lifshitz theory. *J. Coll. Interf. Sci.* **1973**, *45*, 69–80. [CrossRef]
29. Anderson, C.H.; Sabisky, E.S. Phonon interference in thin films of liquid helium. *Phys. Rev. Lett.* **1970**, *24*, 1049–1052. [CrossRef]
30. Ninham, B.W.; Lo Nostro, P. *Molecular Forces and Self Assembly in Colloid, Nano Sciences and Biology*; Cambridge University Press: Cambridge, UK, 2010. [CrossRef]
31. Ninham, B.W.; Brevik, I.; Boström, M. Equivalence of electromagnetic fluctuation and nuclear (Yukawa) forces: The π_0 meson, its mass and lifetime. *Substantia* **2022**, *7*, 7–14. [CrossRef]
32. Ninham, B.W.; Pask, C. Observations on the the possible electromagnetic nature of nucleon interactions and pions. Australian National University, Canberra, Australia, 1969. Unpublished.
33. Boström, M.; Longdell, J.J.; Mitchell, D.J.; Ninham, B.W. Resonance interaction between one excited and one ground state atom. *Eur. Phys. J. D At. Mol. Opt. Plasma Phys.* **2003**, *22*, 47–52. [CrossRef]
34. Van Kampen, N.G.; Nijboer, B.R.A.; Schram, K. On the macroscopic theory of Van der Waals forces. *Phys. Lett. A* **1968**, *26*, 307–308. [CrossRef]
35. Jackson, J.D. *Classical Electrodynamics*; John Wiley & Sons, Inc.: New York, NY, USA, 1975. Available online: <https://archive.org/details/ClassicalElectrodynamics2nd> (accessed on 15 January 2024).
36. Boström, M.; Sernelius, B.E. Thermal effects on the Casimir force in the 0.1–5 μm range. *Phys. Rev. Lett.* **2000**, *84*, 4757. [CrossRef]
37. Sernelius, B.E. *Fundamentals of van der Waals and Casimir Interactions*; Springer Nature Switzerland AG: Cham, Switzerland, 2018. [CrossRef]
38. Bordag, M.; Geyer, B.; Klimchitskaya, G.L.; Mostepanenko, V.M. Casimir force at both nonzero temperature and finite conductivity. *Phys. Rev. Lett.* **2000**, *85*, 503–506. [CrossRef]
39. Lamoreaux, S.K. Demonstration of the Casimir force in the 0.6 to 6 μm range. *Phys. Rev. Lett.* **1997**, *78*, 5–8. [CrossRef]
40. Sushkov, A.O.; Kim, W.J.; Dalvit, D.A.R.; Lamoreaux, S.K. Observation of the thermal Casimir force. *Nat. Phys.* **2011**, *7*, 230–233. [CrossRef]
41. Harris, B.W.; Chen, F.; Mohideen, U. Precision measurement of the Casimir force using gold surfaces. *Phys. Rev. A* **2000**, *62*, 052109. [CrossRef]

42. Decca, R.S.; López, D.; Fischbach, E.; Krause, D.E. Measurement of the Casimir force between dissimilar metals. *Phys. Rev. Lett.* **2003**, *91*, 050402. [CrossRef] [PubMed]
43. Klimchitskaya, G.L.; Mohideen, U.; Mostepanenko, V.M. The Casimir force between real materials: Experiment and theory. *Rev. Mod. Phys.* **2009**, *81*, 1827–1885. [CrossRef]
44. Chang, C.-C.; Banishev, A.A.; Castillo-Garza, R.; Klimchitskaya, G.L.; Mostepanenko, V.M.; Mohideen, U. Gradient of the Casimir force between Au surfaces of a sphere and a plate measured using an atomic force microscope in a frequency-shift technique. *Phys. Rev. B* **2012**, *85*, 165443. [CrossRef]
45. Klimchitskaya, G.L.; Mohideen, U.; Mostepanenko, V.M. The Casimir effect in graphene systems: Experiment and theory. *Int. J. Mod. Phys. A* **2022**, *37*, 2241003. [CrossRef]
46. Klimchitskaya, G.L.; Mostepanenko, V.M. Casimir effect invalidates the Drude model for transverse electric evanescent waves. *Physics* **2023**, *5*, 952–967. [CrossRef]
47. Bordag, M.; Klimchitskaya, G.L.; Mohideen, U.; Mostepanenko, V.M. *Advances in the Casimir Effect*; Oxford Science Publications: New York, NY, USA, 2009. [CrossRef]
48. Milton, K.A. *The Casimir Effect: Physical Manifestations of Zero-Point Energy*; World Scientific Co. Ltd.: Singapore, 2001. [CrossRef]
49. Sernelius, B.E. *Surface Modes in Physics*; John Wiley-VCH Verlag Berlin GmbH: Berlin, Germany, 2005. [CrossRef]
50. Buhmann, S.Y. *Dispersion Forces I: Macroscopic Quantum Electrodynamics and Ground-State Casimir, Casimir–Polder and Van Der Waals Forces*; Springer: Berlin/Heidelberg, Germany, 2012. [CrossRef]
51. Buhmann, S.Y. *Dispersion Forces II: Many-Body Effects, Excited Atoms, Finite Temperature and Quantum Friction*; Springer: Berlin/Heidelberg, Germany, 2012. [CrossRef]
52. Ninham, B.W.; Boström, M. Screened Casimir force at finite temperatures: A possible role in nuclear interactions. *Phys. Rev. A* **2003**, *67*, 030701. [CrossRef]
53. Casimir, H.B.G. Introductory remarks on quantum electrodynamics. *Physica* **1953**, *19*, 846–849. [CrossRef]
54. Boyer, T.H. Quantum electromagnetic zero-Point energy of a conducting spherical shell and the Casimir model for a charged particle. *Phys. Rev.* **1968**, *174*, 1764–1776. [CrossRef]
55. Ninham, B.W.; Daicic, J. Lifshitz theory of Casimir forces at finite temperature. *Phys. Rev. A* **1998**, *57*, 1870–1880. [CrossRef]
56. Ninham, B.W.; Boström, M.; Persson, C.; Brevik, I.; Buhmann, S.Y.; Sernelius, B.E. Casimir forces in a plasma: Possible connections to Yukawa potentials. *Eur. Phys. J. D* **2014**, *68*, 328. [CrossRef]
57. Landau, L.D.; Lifshitz, E.M. *Statistical Physics*; Elsevier Ltd./Butterworth–Heinemann: Oxford, UK, 1999. [CrossRef]
58. Ninham, B.W.; Powell, C.J.; Swanson, N. Plasmon Damping in Metals. *Phys. Rev.* **1966**, *145*, 209–217. [CrossRef]
59. McLachlan, A.D. Resonance transfer of molecular excitation energy. *Molec. Phys.* **1964**, *8*, 409–423. [CrossRef]
60. Avery, J.S. Resonance energy transfer and spontaneous photon emission. *Proc. Phys. Soc.* **1966**, *88*, 1–8. [CrossRef]
61. Power, E.A.; Thirunamachandran, T. Dispersion forces between molecules with one or both molecules excited. *Phys. Rev. A* **1995**, *51*, 3660–3666. [CrossRef] [PubMed]
62. Andrews, D.L.; Sherborne, B.S. Resonant excitation transfer: A quantum electrodynamic study. *J. Chem. Phys.* **1987**, *86*, 4011–4017. [CrossRef]
63. Andrews, D.; Curutchet, C.; Scholes, G. Resonance energy transfer: Beyond the limits. *Laser Photon. Rev.* **2011**, *5*, 114–123. [CrossRef]
64. Wennerström, H.; Daicic, J.; Ninham, B.W. Temperature dependence of atom-atom interactions. *Phys. Rev. A* **1999**, *60*, 2581–2584. [CrossRef]
65. Barash, Y.S.; Ginzburg, V.L. Electromagnetic fluctuations and molecular forces in condensed matter. In *The Dielectric Function of Condensed Systems*; Keldysh, L.V., Kirzhnits, D.A., Maradudin, A.A., Eds.; Elsevier: Amsterdam, The Netherlands, 1989; pp. 389–457. [CrossRef]
66. Elbaum, M.; Schick, M. Application of the theory of dispersion forces to the surface melting of ice. *Phys. Rev. Lett.* **1991**, *66*, 1713–1716. [CrossRef] [PubMed]
67. Elbaum, M.; Lipson, S.; Dash, J. Optical study of surface melting on ice. *J. Cryst. Growth* **1993**, *129*, 491–505. [CrossRef]
68. Wilen, L.A.; Wettlaufer, J.S.; Elbaum, M.; Schick, M. Dispersion-force effects in interfacial premelting of ice. *Phys. Rev. B* **1995**, *52*, 12426–12433. [CrossRef] [PubMed]
69. Wettlaufer, J.S. Impurity effects in the premelting of ice. *Phys. Rev. Lett.* **1999**, *82*, 2516–2519. [CrossRef]
70. Parsons, D.F.; Ninham, B.W. Ab initio molar volumes and Gaussian radii. *J. Phys. Chem. A* **2009**, *113*, 1141–1150. [CrossRef]
71. Parsegian, V.A. *Van der Waals Forces: A Handbook for Biologists, Chemists, Engineers, and Physicists*; Cambridge University Press: New York, NY, USA, 2006. [CrossRef]
72. Parsons, D.F.; Ninham, B.W. Nonelectrostatic ionic forces between dissimilar surfaces: A mechanism for colloid separation. *J. Phys. Chem. C* **2012**, *116*, 7782–7792. [CrossRef]
73. Duignan, T.T.; Parsons, D.F.; Ninham, B.W. A continuum model of solvation energies including electrostatic, dispersion, and cavity contributions. *J. Phys. Chem. B* **2013**, *117*, 9421–9429. [CrossRef] [PubMed]
74. Parsons, D.F.; Salis, A. The impact of the competitive adsorption of ions at surface sites on surface free energies and surface forces. *J. Chem. Phys.* **2015**, *142*, 134707. [CrossRef] [PubMed]
75. Thiyam, P.; Fiedler, J.; Buhmann, S.Y.; Persson, C.; Brevik, I.; Boström, M.; Parsons, D.F. Ice Particles sink below the water surface due to a balance of salt, van der Waals, and buoyancy forces. *J. Phys. Chem. C* **2018**, *122*, 15311–15317. [CrossRef]

76. Wilen, L.A.; Dash, J.G. Frost heave dynamics at a single crystal interface. *Phys. Rev. Lett.* **1995**, *74*, 5076–5079. [CrossRef]
77. Dash, J.G.; Fu, H.; Wettlaufer, J.S. The premelting of ice and its environmental consequences. *Rep. Prog. Phys.* **1995**, *58*, 115–167. [CrossRef]
78. Dash, J.G.; Wettlaufer, J.S. The surface physics of ice in thunderstorms. *Can. J. Phys.* **2003**, *81*, 201–207. [CrossRef]
79. Wettlaufer, J.S. Surface phase transitions in ice: From fundamental interactions to applications. *Phil. Trans. R. Soc. A Math. Phys. Eng. Sci.* **2019**, *377*, 20180261. [CrossRef]
80. Boxe, C.S.; Hand, K.P.; Neelson, K.H.; Yung, Y.L.; Yen, A.S.; Saiz-Lopez, A. Adsorbed water and thin liquid films on Mars. *Int. J. Astrobiol.* **2012**, *11*, 169–175. [CrossRef]
81. de Pater, I.; Lissauer, J.J. *Planetary Sciences*; Cambridge University Press: Cambridge, UK, 2015. [CrossRef]
82. Catling, D.C.; Kasting, J.F. *Atmospheric Evolution on Inhabited and Lifeless Worlds*; Cambridge University Press: Cambridge, UK, 2017. [CrossRef]
83. Schenk, P.M.; Clark, R.N.; Howett, C.J.A.; Verbiscer, A.J.; Waite, J.H., Eds. *Enceladus and the Icy Moons of Saturn*; The University of Arizona Press: Tucson, AZ, USA, 2018. Available online: <https://www.jstor.org/stable/j.ctv65sw2b> (accessed on 15 January 2024).
84. Elbaum, M.; Schick, M. On the failure of water to freeze from its surface. *J. Phys. France* **1991**, *1*, 1665–1668. [CrossRef]
85. Fiedler, J.; Boström, M.; Persson, C.; Brevik, I.H.; Corkery, R.W.; Buhmann, S.Y.; Parsons, D.F. Full-spectrum high resolution modeling of the dielectric function of water. *J. Phys. Chem. B* **2020**, *124*, 3103–3113. [CrossRef]
86. Luengo-Marquez, J.; Izquierdo-Ruiz, F.; MacDowell, L.G. Intermolecular forces at ice and water interfaces: Premelting, surface freezing, and regelation. *J. Chem. Phys.* **2022**, *157*, 044704. [CrossRef]
87. Boström, M.; Estes, V.; Fiedler, J.; Brevik, I.; Buhmann, S.Y.; Persson, C.; Carretero-Palacios, S.; Parsons, D.F.; Corkery, R.W. Self-preserving ice layers on CO₂ clathrate particles: Implications for Enceladus, Pluto and similar ocean worlds. *Astron. Astrophys.* **2021**, *650*, A54. [CrossRef]
88. Boström, M.; Li, Y.; Brevik, I.; Persson, C.; Carretero-Palacios, S.; Malyi, O.I. van der Waals induced ice growth on partially melted ice nuclei in mist and fog. *Phys. Chem. Chem. Phys.* **2023**, *25*, 32709–32714. [CrossRef] [PubMed]
89. Luengo-Márquez, J.; MacDowell, L.G. Lifshitz theory of wetting films at three phase coexistence: The case of ice nucleation on Silver Iodide (AgI). *J. Coll. Interf. Sci.* **2021**, *590*, 527–538. [CrossRef] [PubMed]
90. Ninham, B.W.; Yaminsky, V. Ion binding and ion specificity: The Hofmeister effect and Onsager and Lifshitz theories. *Langmuir* **1997**, *13*, 2097–2108. [CrossRef]
91. Dou, M.; Lou, F.; Boström, M.; Brevik, I.; Persson, C. Casimir quantum levitation tuned by means of material properties and geometries. *Phys. Rev. B* **2014**, *89*, 201407. [CrossRef]

Disclaimer/Publisher's Note: The statements, opinions and data contained in all publications are solely those of the individual author(s) and contributor(s) and not of MDPI and/or the editor(s). MDPI and/or the editor(s) disclaim responsibility for any injury to people or property resulting from any ideas, methods, instructions or products referred to in the content.

Article

Casimir Interaction of Chern–Simons Layers on Substrates via Vacuum Stress Tensor

Valery N. Marachevsky * and Arseny A. Sidelnikov

Saint-Petersburg State University, 7/9 Universitetskaya nab., 199034 St. Petersburg, Russia;
st074065@student.spbu.ru

* Correspondence: maraval@mail.ru or v.marachevsky@spbu.ru

Abstract: We develop a Green’s functions scattering method for systems with Chern–Simons plane boundary layers on dielectric half-spaces. The Casimir pressure is derived by evaluation of the stress tensor in a vacuum slit between two half-spaces. The sign of the Casimir pressure on a Chern–Simons plane layer separated by a vacuum slit from the Chern–Simons layer at the boundary of a dielectric half-space is analyzed for intrinsic Si and SiO₂ glass substrates.

Keywords: Casimir pressure; stress tensor; Chern–Simons layer

1. Introduction

Quantum interaction between macroscopic bodies in the ground state is studied via the Casimir effect [1,2]—various reviews and books are dedicated to the subject [3–24]. The Lifshitz formula [25] determines the interaction between two dielectric half-spaces separated by a vacuum slit; it determines interaction due to fluctuations in the relevant case when transverse electric (TE) and transverse magnetic (TM) polarizations of the electromagnetic field do not mix after reflection from flat boundaries of dielectrics. In this case, the Casimir pressure is attractive for dielectric half-spaces separated by a vacuum slit [26].

Nevertheless, there exist systems with plane boundaries and Casimir repulsive pressure. The Casimir pressure is repulsive for three dielectric media with plane-parallel boundaries when the inequality for dielectric permittivities $\epsilon_1(i\omega) < \epsilon_2(i\omega) < \epsilon_3(i\omega)$ holds [27] with ω the frequency; here, the medium with a dielectric permittivity $\epsilon_2(\omega)$ fills the space between dielectrics with permittivities $\epsilon_1(\omega)$ and $\epsilon_3(\omega)$. The experiment [28] has demonstrated that the sign of the Casimir–Lifshitz force can indeed be changed from attractive to repulsive by a suitable selection of interacting materials immersed in a fluid. The contribution of surface modes in three-layered systems guaranteeing repulsion has been investigated in Ref. [29], where it was demonstrated that at short separations, surface modes play a decisive role in the Casimir repulsion. The repulsive critical Casimir forces emerging in a critical binary liquid mixture near the critical temperature can be used to counteract attraction due to fluctuating Casimir–Lifshitz forces [30].

Another possibility to obtain the Casimir repulsion is to study the interaction between plates with dielectric, diamagnetic and magnetodielectric properties [31–35]. The pressure between a perfectly conducting plate and an infinitely permeable plate is derived by Timothy Boyer [36]; the pressure is purely repulsive in this case: its magnitude is 7/8 that of the Casimir pressure between two perfectly conducting plates [2]. Casimir pressure and repulsion between metamaterials were investigated in Refs. [37–40].

One can also obtain Casimir repulsion in systems with plane-parallel Chern–Simons layers [41,42]. There is a mixing of TE and TM polarizations of the electromagnetic field after reflection from the Chern–Simons layer [42]. The general result for the Casimir energy of two arbitrary Chern–Simons layers in vacuum is expressed through nondiagonal reflection matrices on the basis of TE and TM polarizations [42]. This structure of reflection

Citation: Marachevsky, V.N.; Sidelnikov, A.A. Casimir Interaction of Chern–Simons Layers on Substrates via Vacuum Stress Tensor. *Physics* **2024**, *6*, 496–515.
<https://doi.org/10.3390/physics6020033>

Received: 30 December 2023

Revised: 21 January 2024

Accepted: 4 February 2024

Published: 2 April 2024



Copyright: © 2024 by the authors. Licensee MDPI, Basel, Switzerland. This article is an open access article distributed under the terms and conditions of the Creative Commons Attribution (CC BY) license (<https://creativecommons.org/licenses/by/4.0/>).

matrices leads to the Casimir attraction or the Casimir repulsion in systems with plane-parallel Chern–Simons layers in vacuum and at the boundaries of dielectrics, depending on the parameters of the layers [41–44]. The Monte Carlo method was used to calculate the Casimir energy of interacting Chern–Simons layers in vacuum in Refs. [45,46].

Maxwell–Chern–Simons (2 + 1) space-time dimensional Abelian electrodynamics with the Chern–Simons term was considered in Ref. [47]; there is a massive spin-1 excitation in this case. The constant of the Chern–Simons action is dimensionless in the (3 + 1) case. The study of the Casimir energy in systems with Chern–Simons terms in (3 + 1) dimensions was started in Refs. [48,49] in the framework of rigid, nonpenetrable boundary conditions.

Physical systems are known to be described by the Chern–Simons action with a quantized constant of the action. In the low-energy effective theory of topological insulators, the term proportional to $\theta \mathbf{E} \mathbf{H}$, with \mathbf{E} and \mathbf{H} the electric and magnetic fields, respectively, is added to the standard electromagnetic energy density; integration of this term over the volume of the topological insulator yields boundary Chern–Simons action. Chern–Simons boundary action is defined in this case by a dimensionless quantized parameter $a: a = \alpha\theta/(2\pi)$, $\theta = (2n + 1)\pi$, where α is a fine structure constant of quantum electrodynamics and n is an integer number [50]. The Casimir effect for topological insulators was studied in Refs. [51–56].

In the non-dispersive case, Chern insulators [57–59] are described by the Chern–Simons action with a quantized parameter $a = C\alpha$, where C is a Chern number equal to the winding number of a map from a two-dimensional torus to a two-dimensional unit sphere. The Casimir effect for Chern insulators was investigated in Refs. [42,60,61].

For quantum Hall layers in an external magnetic field, the quantized parameter of the Chern–Simons action characterizing Hall plateaus takes the values $a = \nu\alpha$, where ν is an integer or a fractional number [43,62,63].

Recently, the formalism based on Green’s functions scattering has been worked out [3,64]; in this approach, one evaluates the Casimir pressure in an explicit gauge-invariant derivation. The formalism yields gauge-invariant results for electric and magnetic Green’s functions by construction. Note that due to disregard of gauge invariance, the electric and the magnetic Green’s functions for the Lifshitz problem (two dielectric half-spaces separated by a vacuum slit) obtained in the book [4] contradict the result for the Casimir–Polder potential of a polarizable neutral atom located between two dielectric half-spaces [3,64].

The Casimir–Polder potential of a neutral anisotropic atom added to a multi-body system is expressed in the second-order perturbation theory in terms of electric Green’s functions for this system [3,65–68]. The Casimir–Polder potential of an anisotropic atom is repulsive at distances close to the hole in a plane conductor or grooves of a diffraction grating when the atomic polarizability is aligned in a direction perpendicular to the conductor [69,70] or a diffraction grating [71], in cylindrical and other geometries [72–76]. Note that the repulsion of the point charge from the axisymmetric conductor with an opening is present in electrostatics [77]. The curvature-induced repulsive effect on the lateral Casimir–Polder force is studied in Refs. [78–80]. The fundamental limits on the Casimir–Polder repulsive and attractive forces have been determined in Ref. [81].

The Casimir–Polder potential of a neutral anisotropic atom in the presence of a single Chern–Simons plane layer has been derived in Ref. [82]. The symmetric part of the polarizability for a nonmagnetic ground-state molecule yields potential proportional to the Casimir–Polder potential in front of a perfectly conducting plane; the asymmetric part of the polarizability also contributes to the Casimir–Polder potential [82]. Chiral media are actively studied in the Casimir effect [83,84]; the Casimir–Polder potential of a molecule with an isotropic chiral polarizability interacting with a chiral medium has been studied in Ref. [85]. Charge–parity violating effects [86] for the Casimir–Polder potential in the presence of a Chern–Simons layer have been studied in Ref. [87]: the Chern–Simons layer induces Casimir–Polder interaction both with a molecule that is not chiral but has an electric–magnetic cross polarizability and with a molecule having an anisotropic, asymmetric chiral polarizability. Recently, the formalism of Green’s functions scattering has been

applied to derive analytic results for the Casimir–Polder potentials of an anisotropic neutral atom in the presence of Chern–Simons plane boundary layers on dielectric half-spaces and in vacuum [88]. A novel three-body vacuum parity effect has been discovered in the system Chern–Simons layer–atom–Chern–Simons layer, which manifests as different values of the Casimir–Polder potential after a 180 degree rotation of one of the layers [88].

In this paper, we develop a Green’s functions scattering method and derive the Casimir pressure in geometries with Chern–Simons plane boundary layers on dielectric substrates by evaluation of the Casimir fluctuation pressure via vacuum stress tensor [3,4,25,64,89]. We proceed as follows. In Section 2, we derive expressions for the field of a point dipole in vacuum in terms of electric and magnetic fields. Then, we derive electric and magnetic Green’s functions in a slit between two dielectric substrate half-spaces covered by Chern–Simons layers. The Casimir pressure is expressed in terms of electric and magnetic Green’s functions through evaluation of the vacuum stress tensor in the slit. In Section 3, we study the sign of the Casimir pressure on a Chern–Simons plane layer separated by a vacuum slit from the Chern–Simons layer at the boundary of a dielectric half-space for intrinsic Si and SiO₂ glass substrates. Connection between representations of the Casimir energy in the local polar basis and the local basis of TE and TM polarizations in momentum space is established in Appendix A.

The magnetic permeability of materials $\mu = 1$ throughout the text. We use $\hbar = c = 1$ for the reduced Planck constant, \hbar , and the speed of light, c , and Heaviside–Lorentz units.

2. Casimir Pressure in the System of Two Dielectric Half-Spaces with Chern–Simons Boundary Layers

Consider the volume charge density (ρ) and the current density (\mathbf{j}) of a dipole source at the point $\mathbf{r}' = (0, 0, z')$ [82]:

$$\rho(t, \mathbf{r}) = -p^l(t) \frac{\partial \delta^3(\mathbf{r} - \mathbf{r}')}{\partial x^l}, \tag{1}$$

$$j^l(t, \mathbf{r}) = \frac{\partial p^l(t)}{\partial t} \delta^3(\mathbf{r} - \mathbf{r}'), \tag{2}$$

where \mathbf{p} is an electric dipole moment vector, $\mathbf{r} = (x, y, z)$, t denotes time, the Latin letter indices denote the space components and $\delta^3(\cdot)$ is the three-dimensional Dirac delta function. The four-current density (1)–(2) satisfies the continuity equation $\partial\rho/\partial t + \text{div}\mathbf{j} = 0$.

The Weyl formula, [90]

$$\frac{e^{i\omega|\mathbf{r}' - \mathbf{r}|}}{4\pi|\mathbf{r}' - \mathbf{r}|} = i \iint \frac{e^{i(k_x(x' - x) + k_y(y' - y) + \sqrt{\omega^2 - k_x^2 - k_y^2}(z' - z))}}{2\sqrt{\omega^2 - k_x^2 - k_y^2}} \frac{dk_x dk_y}{(2\pi)^2}, \tag{3}$$

valid for $z' - z > 0$, can be substituted into the solution of equations for scalar (ϕ) and vector (\mathbf{A}) potentials:

$$(\Delta + \omega^2)\phi(\omega, \mathbf{r}) = -\rho(\omega, \mathbf{r}), \tag{4}$$

$$(\Delta + \omega^2)\mathbf{A}(\omega, \mathbf{r}) = -\mathbf{j}(\omega, \mathbf{r}) \tag{5}$$

to find electric and magnetic fields from a dipole source (1)–(2) in free space. As a result, electric and magnetic fields propagating upwards from the dipole source (1)–(2) in free space have the form [3]

$$\mathbf{E}_{\text{up}}^{(0)}(\omega, \mathbf{r}) = \int \mathbf{N}(\omega, \mathbf{k}_{\parallel}) e^{i\mathbf{k}_{\parallel} \cdot \mathbf{r}_{\parallel}} e^{ik_z(z-z')} d^2\mathbf{k}_{\parallel}, \quad (6)$$

$$\mathbf{H}_{\text{up}}^{(0)}(\omega, \mathbf{r}) = \frac{1}{\omega} \int [\mathbf{k} \times \mathbf{N}(\omega, \mathbf{k}_{\parallel})] e^{i\mathbf{k}_{\parallel} \cdot \mathbf{r}_{\parallel}} e^{ik_z(z-z')} d^2\mathbf{k}_{\parallel}, \quad (7)$$

$$\mathbf{N}(\omega, \mathbf{k}_{\parallel}) = \frac{i}{8\pi^2 k_z} \left(-(\mathbf{p} \cdot \mathbf{k})\mathbf{k} + \omega^2 \mathbf{p} \right), \quad (8)$$

where $\mathbf{k}_{\parallel} = (k_x, k_y, 0)$, $k_z = \sqrt{\omega^2 - k_{\parallel}^2}$, $\mathbf{k} = (\mathbf{k}_{\parallel}, k_z)$ and $\mathbf{r}_{\parallel} = (x, y, 0)$.

We start from a solution of the diffraction problem of a dipole field when the dielectric medium is filling the half-space $z > d$. Scalar and vector functions defining the half-space $z \geq d$ or diffraction from it are denoted by index 1. A homogeneous dielectric half-space $z > d$ is characterized by a frequency dispersion of a dielectric permittivity $\epsilon_1(\omega)$ at every point. In addition, there is a Chern–Simons plane layer at the boundary $z = d$. The Chern–Simons layer at $z = d$ is described by the action

$$S_{\text{CS}} = \frac{a_1}{2} \int \epsilon^{z\nu\rho\sigma} A_{\nu} F_{\rho\sigma} dt dx dy \quad (9)$$

with a dimensionless parameter a_1 , ϵ the Levi-Civita symbol, A_{ν} the electromagnetic four-potential, $F_{\rho\sigma} \equiv \partial_{\rho} A_{\sigma} - \partial_{\sigma} A_{\rho}$, the Greek letter indices take Minkowski space-time values, and $\partial_{\rho} \equiv \partial/\partial x^{\rho}$ over space-time coordinates.

Consider an upward propagation of the electromagnetic field from a point dipole (1)–(2). In the presence of a dielectric medium for $z > d$, one writes the solution of the Maxwell equations for $z < d$ in the form

$$\mathbf{E}^{(V_1)}(\omega, \mathbf{r}) = \int \mathbf{N} e^{i\mathbf{k}_{\parallel} \cdot \mathbf{r}_{\parallel}} e^{ik_z(z-z')} d^2\mathbf{k}_{\parallel} + \int \mathbf{v}_1 e^{i\mathbf{k}_{\parallel} \cdot \mathbf{r}_{\parallel}} e^{-ik_z z} d^2\mathbf{k}_{\parallel}, \quad (10)$$

$$\begin{aligned} \mathbf{H}^{(V_1)}(\omega, \mathbf{r}) &= \frac{1}{\omega} \int [\mathbf{k} \times \mathbf{N}] e^{i\mathbf{k}_{\parallel} \cdot \mathbf{r}_{\parallel}} e^{ik_z(z-z')} d^2\mathbf{k}_{\parallel} \\ &+ \frac{1}{\omega} \int \left([\mathbf{k}_{\parallel} \times \mathbf{v}_1] - k_z [\mathbf{n} \times \mathbf{v}_1] \right) e^{i\mathbf{k}_{\parallel} \cdot \mathbf{r}_{\parallel}} e^{-ik_z z} d^2\mathbf{k}_{\parallel}. \end{aligned} \quad (11)$$

The transmitted fields for $z > d$ are written in the form

$$\mathbf{E}^{(D_1)}(\omega, \mathbf{r}) = \int \mathbf{u}_1 e^{i\mathbf{k}_{\parallel} \cdot \mathbf{r}_{\parallel}} e^{iK_{z1}z} d^2\mathbf{k}_{\parallel}, \quad (12)$$

$$\mathbf{H}^{(D_1)}(\omega, \mathbf{r}) = \frac{1}{\omega} \int \left([\mathbf{k}_{\parallel} \times \mathbf{u}_1] + K_{z1} [\mathbf{n} \times \mathbf{u}_1] \right) e^{i\mathbf{k}_{\parallel} \cdot \mathbf{r}_{\parallel}} e^{iK_{z1}z} d^2\mathbf{k}_{\parallel}, \quad (13)$$

where $K_{z1} = \sqrt{\epsilon_1(\omega)\omega^2 - k_x^2 - k_y^2}$ and $\mathbf{n} = (0, 0, 1)$. Vector functions $\mathbf{v}_1(\omega, \mathbf{k}_{\parallel})$ and $\mathbf{u}_1(\omega, \mathbf{k}_{\parallel})$ are found from the transversality of the reflected and transmitted fields and the boundary conditions imposed on the fields:

$$\text{div}(\mathbf{E}^{(V_1)} - \mathbf{E}_{\text{up}}^{(0)}) = 0, \quad (14)$$

$$\text{div} \mathbf{E}^{(D_1)} = 0, \quad (15)$$

$$E_x^{(V_1)}|_{z=d} = E_x^{(D_1)}|_{z=d}, \quad (16)$$

$$E_y^{(V_1)}|_{z=d} = E_y^{(D_1)}|_{z=d}, \quad (17)$$

$$H_x^{(D_1)}|_{z=d+} - H_x^{(V_1)}|_{z=d-} = 2a_1 E_x^{(V_1)}|_{z=d}, \quad (18)$$

$$H_y^{(D_1)}|_{z=d+} - H_y^{(V_1)}|_{z=d-} = 2a_1 E_y^{(V_1)}|_{z=d}. \tag{19}$$

Boundary conditions (18)–(19) have been used to describe the diffraction of a plane electromagnetic wave in a medium with a piecewise constant axion field [91] and in a medium with Chern–Simons layers [92].

Boundary conditions (14)–(19) can be imposed in cylindrical coordinates in a local orthogonal basis $\mathbf{e}_r, \mathbf{e}_\varphi, \mathbf{e}_z$ in momentum space so that $\mathbf{k}_\parallel = k_r \mathbf{e}_r, k_r = |\mathbf{k}_\parallel|$:

$$u_{1r}k_r + K_{z1}u_{1z} = 0, \tag{20}$$

$$v_{1r}k_r - k_z v_{1z} = 0, \tag{21}$$

$$u_{1r}e^{iK_{z1}d} = v_{1r}e^{-ik_z d} + N_r e^{ik_z(d-z')}, \tag{22}$$

$$u_{1\varphi}e^{iK_{z1}d} = v_{1\varphi}e^{-ik_z d} + N_\varphi e^{ik_z(d-z')}, \tag{23}$$

$$k_z v_{1\varphi}e^{-ik_z d} - k_z N_\varphi e^{ik_z(d-z')} + K_{z1}u_{1\varphi}e^{iK_{z1}d} = -2a_1 u_{1r}e^{iK_{z1}d}, \tag{24}$$

$$-k_z v_{1r}e^{-ik_z d} - k_r v_{1z}e^{-ik_z d} + k_z N_r e^{ik_z(d-z')} - k_r N_z e^{ik_z(d-z')} - (K_{z1}u_{1r}e^{iK_{z1}d} - k_r u_{1z}e^{iK_{z1}d}) = -2a_1 u_{1\varphi}e^{iK_{z1}d}. \tag{25}$$

The solution of the transversality conditions (20)–(21) and boundary conditions (22)–(25) imposed at $z = d$ yields

$$v_{1r} = \left[-\frac{r_{TM_1} + a_1^2 T_1}{1 + a_1^2 T_1} N_r + \frac{k_z}{\omega} \frac{a_1 T_1}{1 + a_1^2 T_1} N_\varphi \right] e^{ik_z(2d-z')}, \tag{26}$$

$$v_{1\varphi} = \left[-\frac{\omega}{k_z} \frac{a_1 T_1}{1 + a_1^2 T_1} N_r + \frac{r_{TE_1} - a_1^2 T_1}{1 + a_1^2 T_1} N_\varphi \right] e^{ik_z(2d-z')}, \tag{27}$$

$$v_{1z} = -\frac{k_r}{k_z} \left[\frac{r_{TM_1} + a_1^2 T_1}{1 + a_1^2 T_1} N_r - \frac{k_z}{\omega} \frac{a_1 T_1}{1 + a_1^2 T_1} N_\varphi \right] e^{ik_z(2d-z')}, \tag{28}$$

where the Fresnel reflection coefficients

$$r_{TM_1} = \frac{\varepsilon_1(\omega)k_z - K_{z1}}{\varepsilon_1(\omega)k_z + K_{z1}}, \quad r_{TE_1} = \frac{k_z - K_{z1}}{k_z + K_{z1}} \tag{29}$$

and

$$T_1 = \frac{4k_z K_{z1}}{(k_z + K_{z1})(\varepsilon_1(\omega)k_z + K_{z1})}. \tag{30}$$

depend on the dielectric permittivity $\varepsilon_1(\omega)$ of the half-space $z > d$.

Electric and magnetic fields propagating downwards from the dipole source (1)–(2) in free space have the form [3]

$$\mathbf{E}_{\text{down}}^{(0)}(\omega, \mathbf{r}) = \int \tilde{\mathbf{N}}(\omega, \mathbf{k}_\parallel) e^{i\mathbf{k}_\parallel \cdot \mathbf{r}_\parallel} e^{-ik_z(z-z')} d^2 \mathbf{k}_\parallel, \tag{31}$$

$$\mathbf{H}_{\text{down}}^{(0)}(\omega, \mathbf{r}) = \frac{1}{\omega} \int [\tilde{\mathbf{k}} \times \tilde{\mathbf{N}}(\omega, \mathbf{k}_\parallel)] e^{i\mathbf{k}_\parallel \cdot \mathbf{r}_\parallel} e^{-ik_z(z-z')} d^2 \mathbf{k}_\parallel, \tag{32}$$

$$\tilde{\mathbf{N}}(\omega, \mathbf{k}_\parallel) = \frac{i}{8\pi^2 k_z} \left(-(\mathbf{p} \cdot \tilde{\mathbf{k}}) \tilde{\mathbf{k}} + \omega^2 \mathbf{p} \right), \tag{33}$$

where $\tilde{\mathbf{k}} = (\mathbf{k}_\parallel, -k_z)$.

The next step is to find a solution of the diffraction problem of a dipole field when the medium is filling half-space $z < 0$. Scalar and vector functions defining the half-space $z \leq 0$ or diffraction from it are denoted by index 2. A homogeneous dielectric half-space $z < 0$ is characterized by a frequency dispersion of a dielectric permittivity $\varepsilon_2(\omega)$ at every point. There is a Chern–Simons plane layer characterized by a dimensionless parameter a_2 at the boundary $z = 0$.

In the presence of a dielectric medium for $z < 0$, one adds the reflected parts of fields to a solution (31)–(32) and writes the solution of the Maxwell equations for $z > 0$ in the form

$$\mathbf{E}^{(V_2)}(\omega, \mathbf{r}) = \int \tilde{\mathbf{N}}(\omega, \mathbf{k}_{\parallel}) e^{i\mathbf{k}_{\parallel} \cdot \mathbf{r}_{\parallel}} e^{-ik_z(z-z')} d^2\mathbf{k}_{\parallel} + \int \mathbf{v}_2(\omega, \mathbf{k}_{\parallel}) e^{i\mathbf{k}_{\parallel} \cdot \mathbf{r}_{\parallel}} e^{ik_z z} d^2\mathbf{k}_{\parallel}, \quad (34)$$

$$\begin{aligned} \mathbf{H}^{(V_2)}(\omega, \mathbf{r}) &= \frac{1}{\omega} \int [\tilde{\mathbf{k}} \times \tilde{\mathbf{N}}(\omega, \mathbf{k}_{\parallel})] e^{i\mathbf{k}_{\parallel} \cdot \mathbf{r}_{\parallel}} e^{-ik_z(z-z')} d^2\mathbf{k}_{\parallel} \\ &+ \frac{1}{\omega} \int [\mathbf{k}_{\parallel} \times \mathbf{v}_2(\omega, \mathbf{k}_{\parallel})] e^{i\mathbf{k}_{\parallel} \cdot \mathbf{r}_{\parallel}} e^{ik_z z} d^2\mathbf{k}_{\parallel}. \end{aligned} \quad (35)$$

For $z < 0$, one writes the transmitted fields in the form

$$\mathbf{E}^{(D_2)}(\omega, \mathbf{r}) = \int \mathbf{u}_2(\omega, \mathbf{k}_{\parallel}) e^{i\mathbf{k}_{\parallel} \cdot \mathbf{r}_{\parallel}} e^{-iK_{z2}z} d^2\mathbf{k}_{\parallel}, \quad (36)$$

$$\mathbf{H}^{(D_2)}(\omega, \mathbf{r}) = \frac{1}{\omega} \int \left([\mathbf{k}_{\parallel} \times \mathbf{u}_2(\omega, \mathbf{k}_{\parallel})] - K_{z2}[\mathbf{n} \times \mathbf{u}_2(\omega, \mathbf{k}_{\parallel})] \right) e^{i\mathbf{k}_{\parallel} \cdot \mathbf{r}_{\parallel}} e^{-iK_{z2}z} d^2\mathbf{k}_{\parallel}, \quad (37)$$

where $K_{z2} = \sqrt{\varepsilon_2(\omega)\omega^2 - k_x^2 - k_y^2}$ and $\mathbf{n} = (0, 0, 1)$. Vector functions $\mathbf{v}_2(\omega, \mathbf{k}_{\parallel})$ and $\mathbf{u}_2(\omega, \mathbf{k}_{\parallel})$ are found from the transversality of the reflected and transmitted fields and the boundary conditions imposed on the fields:

$$\text{div}(\mathbf{E}^{(V_2)} - \mathbf{E}_{\text{down}}^{(0)}) = 0, \quad (38)$$

$$\text{div} \mathbf{E}^{(D_2)} = 0, \quad (39)$$

$$E_x^{(V_2)}|_{z=0} = E_x^{(D_2)}|_{z=0}, \quad (40)$$

$$E_y^{(V_2)}|_{z=0} = E_y^{(D_2)}|_{z=0}, \quad (41)$$

$$H_x^{(V_2)}|_{z=0+} - H_x^{(D_2)}|_{z=0-} = 2a_2 E_x^{(V_2)}|_{z=0}, \quad (42)$$

$$H_y^{(V_2)}|_{z=0+} - H_y^{(D_2)}|_{z=0-} = 2a_2 E_y^{(V_2)}|_{z=0}. \quad (43)$$

It is convenient to write boundary conditions (38)–(43) in cylindrical coordinates in a local orthogonal basis $\mathbf{e}_r, \mathbf{e}_\varphi, \mathbf{e}_z$ in momentum space so that $\mathbf{k}_{\parallel} = k_r \mathbf{e}_r, k_r = |\mathbf{k}_{\parallel}|$:

$$v_{2r}k_r + k_z v_{2z} = 0, \quad (44)$$

$$u_{2r}k_r - K_{z2}u_{2z} = 0, \quad (45)$$

$$u_{2r} = v_{2r} + \tilde{N}_r e^{ik_z z'}, \quad (46)$$

$$u_{2\varphi} = v_{2\varphi} + \tilde{N}_\varphi e^{ik_z z'}, \quad (47)$$

$$-k_z v_{2\varphi} + k_z \tilde{N}_\varphi e^{ik_z z'} - K_{z2} u_{2\varphi} = 2\omega a_2 u_{2r}, \tag{48}$$

$$k_z v_{2r} - k_r v_{2z} - k_z \tilde{N}_r e^{ik_z z'} - k_r \tilde{N}_z e^{ik_z z'} + K_{z2} u_{2r} + k_r u_{2z} = 2\omega a_2 u_\varphi \tag{49}$$

and get

$$v_{2r} = \left[-\frac{r_{TM_2} + a_2^2 T_2}{1 + a_2^2 T_2} \tilde{N}_r + \frac{k_z}{\omega} \frac{a_2 T_2}{1 + a_2^2 T_2} \tilde{N}_\varphi \right] e^{ik_z z'}, \tag{50}$$

$$v_{2\varphi} = \left[-\frac{\omega}{k_z} \frac{a_2 T_2}{1 + a_2^2 T_2} \tilde{N}_r + \frac{r_{TE_2} - a_2^2 T_2}{1 + a_2^2 T_2} \tilde{N}_\varphi \right] e^{ik_z z'}, \tag{51}$$

$$v_{2z} = \frac{k_r}{k_z} \left[\frac{r_{TM_2} + a_2^2 T_2}{1 + a_2^2 T_2} \tilde{N}_r - \frac{k_z}{\omega} \frac{a_2 T_2}{1 + a_2^2 T_2} \tilde{N}_\varphi \right] e^{ik_z z'}, \tag{52}$$

where Fresnel reflection coefficients r_{TM_2} , r_{TE_2} and T_2 depend on the dielectric permittivity $\epsilon_2(\omega)$ of the half-space $z < 0$. The local matrix R resulting from Equations (26), (27), (50) and (51) is defined as follows:

$$R(a, \epsilon(\omega), \omega, k_r) \equiv \frac{1}{1 + a^2 T} \begin{pmatrix} -r_{TM} - a^2 T & \frac{k_z}{\omega} a T \\ -\frac{\omega}{k_z} a T & r_{TE} - a^2 T \end{pmatrix}. \tag{53}$$

The solution of a diffraction problem when both half-spaces are present simultaneously and the point dipole is located at $\mathbf{r}' = (0, 0, z')$, $0 < z' < d$ can be derived as follows. Denote the upper dielectric half-space ($z > d$) by index 1 and the lower dielectric half-space ($z < 0$) by index 2. The Chern–Simons boundary layers at $z = d$ and $z = 0$ are defined by the parameters a_1 and a_2 as before (Figure 1). From (53) and the solutions for the diffraction cases considered above, we define local matrices R_1 and R_2 for reflection of the tangential components of the electric field from media above and below the point dipole, respectively:

$$R_1(\omega) \equiv R(a_1, \epsilon_1(\omega), \omega, k_r), \quad R_2(\omega) \equiv R(a_2, \epsilon_2(\omega), \omega, k_r). \tag{54}$$

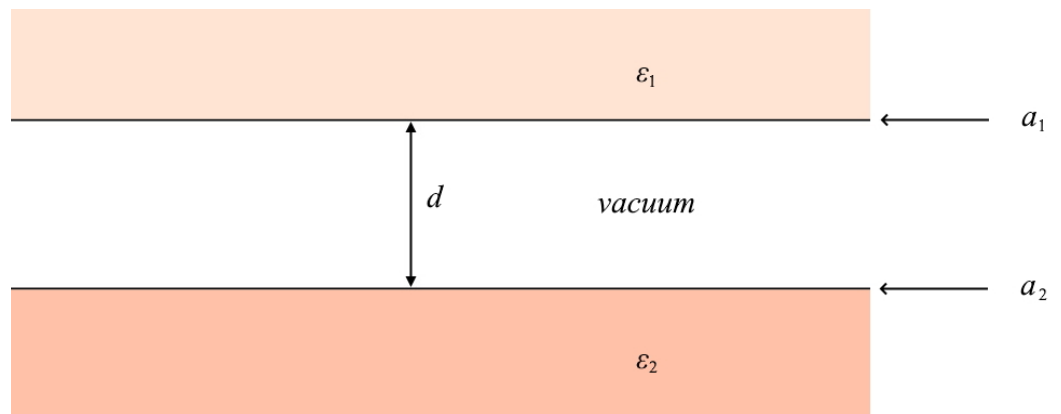


Figure 1. Two dielectric half-spaces with Chern–Simons boundary layers are separated by a distance d . The permittivity of the upper dielectric half-space is ϵ_1 ; the permittivity of the lower dielectric half-space is ϵ_2 . The upper Chern–Simons boundary layer is defined by a_1 ; the lower Chern–Simons boundary layer is defined by a_2 .

Tangential local components of the electric field in the interval $0 < z < d$ from the point dipole (1)–(2) are expressed in terms of R_1, R_2 after the summation of multiple reflections from media with indices 1 and 2:

$$\begin{pmatrix} E_r \\ E_\varphi \end{pmatrix} = \frac{I}{I - R_2 R_1 e^{2ik_z d}} e^{ik_z z} \left[R_2 R_1 \begin{pmatrix} N_r \\ N_\varphi \end{pmatrix} e^{ik_z (2d - z')} + R_2 \begin{pmatrix} \widetilde{N}_r \\ \widetilde{N}_\varphi \end{pmatrix} e^{ik_z z'} \right] \\ + \frac{I}{I - R_1 R_2 e^{2ik_z d}} e^{2ik_z d} e^{-ik_z z} \left[R_1 R_2 \begin{pmatrix} \widetilde{N}_r \\ \widetilde{N}_\varphi \end{pmatrix} e^{ik_z z'} + R_1 \begin{pmatrix} N_r \\ N_\varphi \end{pmatrix} e^{-ik_z z'} \right], \quad (55)$$

where I is the identity matrix. From Equation (55), we define four matrices:

$$M^{(1)} \equiv (I - R_2(\omega)R_1(\omega)e^{i2k_z d})^{-1}R_2(\omega)R_1(\omega), \quad (56)$$

$$M^{(2)} \equiv (I - R_2(\omega)R_1(\omega)e^{i2k_z d})^{-1}R_2(\omega), \quad (57)$$

$$M^{(3)} \equiv (I - R_1(\omega)R_2(\omega)e^{i2k_z d})^{-1}R_1(\omega)R_2(\omega), \quad (58)$$

$$M^{(4)} \equiv (I - R_1(\omega)R_2(\omega)e^{i2k_z d})^{-1}R_1(\omega) \quad (59)$$

and write components of the electric field in a cylindrical local system of coordinates explicitly from Formulas (21), (44), (55) and (56)–(59):

$$E_r = e^{ik_z z} \left[e^{-ik_z z'} e^{2ik_z d} (M_{11}^{(1)} N_r + M_{12}^{(1)} N_\varphi) + e^{ik_z z'} (M_{11}^{(2)} \widetilde{N}_r + M_{12}^{(2)} \widetilde{N}_\varphi) \right] \\ + e^{-ik_z z} e^{2ik_z d} \left[e^{ik_z z'} (M_{11}^{(3)} \widetilde{N}_r + M_{12}^{(3)} \widetilde{N}_\varphi) + e^{-ik_z z'} (M_{11}^{(4)} N_r + M_{12}^{(4)} N_\varphi) \right], \quad (60)$$

$$E_\varphi = e^{ik_z z} \left[e^{-ik_z z'} e^{2ik_z d} (M_{21}^{(1)} N_r + M_{22}^{(1)} N_\varphi) + e^{ik_z z'} (M_{21}^{(2)} \widetilde{N}_r + M_{22}^{(2)} \widetilde{N}_\varphi) \right] \\ + e^{-ik_z z} e^{2ik_z d} \left[e^{ik_z z'} (M_{21}^{(3)} \widetilde{N}_r + M_{22}^{(3)} \widetilde{N}_\varphi) + e^{-ik_z z'} (M_{21}^{(4)} N_r + M_{22}^{(4)} N_\varphi) \right], \quad (61)$$

$$E_z = -\frac{k_r}{k_z} e^{ik_z z} \left[e^{-ik_z z'} e^{2ik_z d} (M_{11}^{(1)} N_r + M_{12}^{(1)} N_\varphi) + e^{ik_z z'} (M_{11}^{(2)} \widetilde{N}_r + M_{12}^{(2)} \widetilde{N}_\varphi) \right] \\ - e^{-ik_z z} e^{2ik_z d} \left[e^{ik_z z'} (M_{11}^{(3)} \widetilde{N}_r + M_{12}^{(3)} \widetilde{N}_\varphi) + e^{-ik_z z'} (M_{11}^{(4)} N_r + M_{12}^{(4)} N_\varphi) \right], \quad (62)$$

where $M_{11}^{(s)}, M_{12}^{(s)}, M_{21}^{(s)}, M_{22}^{(s)}$ ($s = 1, \dots, 4$) are components of the four matrices (56)–(59).

For convenience, we rewrite \mathbf{N} and $\widetilde{\mathbf{N}}$ in a cylindrical system of coordinates:

$$\mathbf{N} = \frac{i}{8\pi^2 k_z} \left(-(p_r k_r + k_z p_z)(\mathbf{e}_r k_r + \mathbf{e}_z k_z) + \omega^2 \mathbf{p} \right), \quad (63)$$

$$\widetilde{\mathbf{N}} = \frac{i}{8\pi^2 k_z} \left(-(p_r k_r - k_z p_z)(\mathbf{e}_r k_r - \mathbf{e}_z k_z) + \omega^2 \mathbf{p} \right). \quad (64)$$

The scattered part of the electric field at the point \mathbf{r} from the source (1)–(2) at the point \mathbf{r}' for $0 < z, z' < d$ is given by

$$\mathbf{E}(\mathbf{r}, \mathbf{r}') = \int d^2 \mathbf{k}_\parallel e^{i\mathbf{k}_\parallel \cdot (\mathbf{r}_\parallel - \mathbf{r}'_\parallel)} (E_r \mathbf{e}_r + E_\varphi \mathbf{e}_\varphi + E_z \mathbf{e}_z). \quad (65)$$

The rotation formulas between a cylindrical local basis and a Cartesian basis for every given \mathbf{k}_{\parallel} are standard:

$$E_x = E_r \cos \varphi + E_{\varphi} \sin \varphi, \quad (66)$$

$$E_y = E_r \sin \varphi - E_{\varphi} \cos \varphi, \quad (67)$$

$$p_r = p_x \cos \varphi + p_y \sin \varphi, \quad (68)$$

$$p_{\varphi} = p_x \sin \varphi - p_y \cos \varphi, \quad (69)$$

where p_x and p_y denote the Cartesian components of an electric dipole moment vector.

The Cartesian components of the scattered electric Green's functions are expressed in terms of components of the reflected electric Green's functions in a cylindrical local basis from (66)–(69) for $\mathbf{r}_{\parallel} = \mathbf{r}'_{\parallel}$:

$$D_{xx}^E(\omega, z, z') = \int (D_{rr}^E(\omega, k_r, z, z') \cos^2 \varphi + D_{\varphi\varphi}^E(\omega, k_r, z, z') \sin^2 \varphi) \frac{d^2 \mathbf{k}_{\parallel}}{(2\pi)^2}, \quad (70)$$

$$D_{yy}^E(\omega, z, z') = \int (D_{rr}^E(\omega, k_r, z, z') \sin^2 \varphi + D_{\varphi\varphi}^E(\omega, k_r, z, z') \cos^2 \varphi) \frac{d^2 \mathbf{k}_{\parallel}}{(2\pi)^2}, \quad (71)$$

$$D_{zz}^E(\omega, z, z') = \int D_{zz}^E(\omega, k_r, z, z') \frac{d^2 \mathbf{k}_{\parallel}}{(2\pi)^2}, \quad (72)$$

In Equations (70)–(72), we omit nondiagonal contributions to scattered Green’s functions in a cylindrical local basis proportional to either $\cos \varphi \sin \varphi$, $\cos \varphi$ or $\sin \varphi$ since integrals over angle φ equal zero for these terms for coinciding arguments $\mathbf{r}_{\parallel} = \mathbf{r}'_{\parallel}$.

The components of the scattered electric Green’s functions in a cylindrical local basis entering (70)–(72) are found from (60)–(64):

$$D_{rr}^E(\omega, k_r, z, z') = \frac{ik_z}{2} \times \left[e^{ik_z(z-z')} e^{2ik_z d} M_{11}^{(1)} + e^{ik_z(z+z')} M_{11}^{(2)} + e^{ik_z(z'-z)} e^{2ik_z d} M_{11}^{(3)} + e^{-ik_z(z+z')} e^{2ik_z d} M_{11}^{(4)} \right], \quad (73)$$

$$D_{\varphi\varphi}^E(\omega, k_r, z, z') = \frac{i\omega^2}{2k_z} \times \left[e^{ik_z(z-z')} e^{2ik_z d} M_{22}^{(1)} + e^{ik_z(z+z')} M_{22}^{(2)} + e^{ik_z(z'-z)} e^{2ik_z d} M_{22}^{(3)} + e^{-ik_z(z+z')} e^{2ik_z d} M_{22}^{(4)} \right], \quad (74)$$

$$D_{zz}^E(\omega, k_r, z, z') = \frac{ik_r^2}{2k_z} \times \left[e^{ik_z(z-z')} e^{2ik_z d} M_{11}^{(1)} - e^{ik_z(z+z')} M_{11}^{(2)} + e^{ik_z(z'-z)} e^{2ik_z d} M_{11}^{(3)} - e^{-ik_z(z+z')} e^{2ik_z d} M_{11}^{(4)} \right]. \quad (75)$$

After integration over the polar coordinates, we express scattered electric Green’s functions for coinciding arguments $\mathbf{r} = \mathbf{r}'$ in terms of matrix elements of matrices (56)–(59) [88]:

$$D_{xx}^E(\omega, \mathbf{r} = \mathbf{r}') = D_{yy}^E(\omega, \mathbf{r} = \mathbf{r}') = \frac{i}{8\pi} \int_0^{\infty} dk_r k_r \times \left[k_z (e^{2ik_z d} M_{11}^{(1)} + e^{2ik_z z'} M_{11}^{(2)} + e^{2ik_z d} M_{11}^{(3)} + e^{2ik_z(d-z')} M_{11}^{(4)}) + \frac{\omega^2}{k_z} (e^{2ik_z d} M_{22}^{(1)} + e^{2ik_z z'} M_{22}^{(2)} + e^{2ik_z d} M_{22}^{(3)} + e^{2ik_z(d-z')} M_{22}^{(4)}) \right], \quad (76)$$

$$D_{zz}^E(\omega, \mathbf{r} = \mathbf{r}') = -\frac{i}{4\pi} \int_0^{\infty} dk_r \frac{k_r^3}{k_z} \times \left[-e^{2ik_z d} M_{11}^{(1)} + e^{2ik_z z'} M_{11}^{(2)} - e^{2ik_z d} M_{11}^{(3)} + e^{2ik_z(d-z')} M_{11}^{(4)} \right]. \quad (77)$$

Scattered magnetic Green’s functions can be evaluated from reflected electric Green’s functions:

$$D_{il}^H(\omega, \mathbf{r}, \mathbf{r}') = \frac{1}{\omega^2} \epsilon_{ijk} \epsilon_{lmn} \frac{\partial}{\partial x^j} \frac{\partial}{\partial x'^m} D_{kn}^E(\omega, \mathbf{r}, \mathbf{r}'). \quad (78)$$

The components of the scattered magnetic Green's functions in a cylindrical local basis are found from (78) and (73)–(75):

$$D_{rr}^H(\omega, k_r, z, z') = \frac{ik_z}{2} \times \left[e^{ik_z(z-z')} e^{2ik_z d} M_{22}^{(1)} + e^{ik_z(z+z')} M_{22}^{(2)} + e^{ik_z(z'-z)} e^{2ik_z d} M_{22}^{(3)} + e^{-ik_z(z+z')} e^{2ik_z d} M_{22}^{(4)} \right], \quad (79)$$

$$D_{\varphi\varphi}^H(\omega, k_r, z, z') = \frac{i\omega^2}{2k_z} \times \left[e^{ik_z(z-z')} e^{2ik_z d} M_{11}^{(1)} - e^{ik_z(z+z')} M_{11}^{(2)} + e^{ik_z(z'-z)} e^{2ik_z d} M_{11}^{(3)} - e^{-ik_z(z+z')} e^{2ik_z d} M_{11}^{(4)} \right], \quad (80)$$

$$D_{zz}^H(\omega, k_r, z, z') = \frac{ik_r^2}{2k_z} \times \left[e^{ik_z(z-z')} e^{2ik_z d} M_{22}^{(1)} + e^{ik_z(z+z')} M_{22}^{(2)} + e^{ik_z(z'-z)} e^{2ik_z d} M_{22}^{(3)} + e^{-ik_z(z+z')} e^{2ik_z d} M_{22}^{(4)} \right]. \quad (81)$$

The Cartesian components of the scattered magnetic Green's functions are evaluated in complete analogy to the evaluation of the Cartesian components of the scattered electric Green's functions.

For every $0 < z' < d$ and the coinciding arguments of the reflected local Green's functions $z' = z$, these identities hold:

$$D_{rr}^E(\omega, k_r, z', z') + D_{\varphi\varphi}^H(\omega, k_r, z', z') - D_{zz}^E(\omega, k_r, z', z') = ik_z e^{i2k_z d} \left(M_{11}^{(1)} + M_{11}^{(3)} \right), \quad (82)$$

$$D_{zz}^H(\omega, k_r, z', z') + D_{\varphi\varphi}^E(\omega, k_r, z', z') - D_{rr}^H(\omega, k_r, z', z') = ik_z e^{i2k_z d} \left(M_{22}^{(1)} + M_{22}^{(3)} \right). \quad (83)$$

The Casimir pressure P equals the T_{zz} component of the fluctuation stress tensor in a slit between half-spaces; it is expressed in terms of the scattered electric and magnetic Green's functions:

$$P = -\frac{i}{2} \int_{-\infty}^{+\infty} \frac{d\omega}{2\pi} \left[D_{xx}^E(\omega, \mathbf{r}, \mathbf{r}) + D_{yy}^E(\omega, \mathbf{r}, \mathbf{r}) - D_{zz}^E(\omega, \mathbf{r}, \mathbf{r}) + D_{xx}^H(\omega, \mathbf{r}, \mathbf{r}) + D_{yy}^H(\omega, \mathbf{r}, \mathbf{r}) - D_{zz}^H(\omega, \mathbf{r}, \mathbf{r}) \right]. \quad (84)$$

We use Formulas (70)–(72), identities (82)–(83) and the Wick rotation to express the Casimir pressure in terms of the reflection matrices $R_1(i\omega)$ and $R_2(i\omega)$:

$$P = \frac{1}{(2\pi)^2} \int_0^\infty d\omega \int_0^\infty dk_r k_r \times \left[D_{rr}^E(i\omega, k_r, z', z') + D_{\varphi\varphi}^E(i\omega, k_r, z', z') - D_{zz}^E(i\omega, k_r, z', z') + D_{rr}^H(i\omega, k_r, z', z') + D_{\varphi\varphi}^H(i\omega, k_r, z', z') - D_{zz}^H(i\omega, k_r, z', z') \right] = -\frac{1}{(2\pi)^2} \int_0^\infty d\omega \int_0^\infty dk_r k_r \tilde{k}_z \text{Tr} \left[\left(I - R_2(i\omega) R_1(i\omega) e^{-2\tilde{k}_z d} \right)^{-1} R_2(i\omega) R_1(i\omega) e^{-2\tilde{k}_z d} + \left(I - R_1(i\omega) R_2(i\omega) e^{-2\tilde{k}_z d} \right)^{-1} R_1(i\omega) R_2(i\omega) e^{-2\tilde{k}_z d} \right], \quad (85)$$

where “Tr” defines the trace operation and $\tilde{k}_z \equiv \sqrt{\omega^2 + k_r^2}$.

The corresponding Casimir energy on a unit surface has the form

$$\frac{E}{S} = \frac{1}{(2\pi)^2} \int_0^\infty d\omega \int_0^\infty dk_r k_r \text{Tr} \ln \left(I - R_1(i\omega) R_2(i\omega) e^{-2\tilde{k}_z d} \right). \quad (86)$$

The equivalence of the Casimir energy (86) to the result for the Casimir energy obtained within the scattering approach [43] is proved in Appendix A.

3. Casimir Interaction in Systems with Chern–Simons Layers on Realistic Substrates

The scattering approach yields finite expressions for the Casimir energy of several interacting objects; it has been applied to diffraction gratings [93–96], spheres, cylinders and other geometries [97–107]. Planes with conductivity have also been studied in the framework of the scattering approach in Refs. [3,108–112]. The experiment [113] has confirmed the (2 + 1) finite temperature polarization operator approach in the description of graphene layers and the strong temperature dependence of the Casimir pressure for interacting layers of graphene [108].

The Casimir energy of two Chern–Simons layers in vacuum for arbitrary Chern–Simons constants a_1 and a_2 was derived in Ref. [42] in the framework of the scattering approach. For $a_1 = a_2$, the Casimir force is repulsive over an interval $a_1 \in [0, a_{\max}]$, where $a_{\max} \approx 1.032502$ [41,43]. For $a_1 = -a_2$, the Casimir force is always attractive for two Chern–Simons layers in vacuum [42].

Suppose there is a quantization of Chern–Simons parameters a_1 and a_2 as in quantum Hall systems: $a_1 = \alpha m, a_2 = \alpha n$, where m and n are integer numbers and α is a fine structure constant. The Casimir repulsion for two half-spaces covered by Chern–Simons layers was studied for Au, intrinsic Si and SiO₂ glass substrate materials in Refs. [43,44]. In Ref. [43], it was shown that for two Au substrate half-spaces separated by a vacuum slit, the Casimir repulsion can be achieved at the maximum distance $d = 3.65$ nm for $a_1 = a_2 = 0.565$, and for two Si substrate half-spaces, the Casimir repulsion can be achieved at the maximum distance $d = 6.39$ nm for $a_1 = a_2 = 0.567$. It was demonstrated in Ref. [44] that for two SiO₂ substrate half-spaces separated by a vacuum slit, the Casimir repulsion can be realized at the maximum distance $d = 26.52$ nm between half-spaces; the maximum distance at which the Casimir repulsion occurs in this system corresponds to Chern–Simons constants $a_1 = a_2 = 0.542$ or $m = n = 74$. In Ref. [44], it was shown that the minimum of the Casimir energy with $d > 10$ nm is achieved for integer $m = n \in [34, 115]$. The Casimir interaction of Chern–Simons layers in the presence of realistic substrate materials was not studied for small enough and different values of a_1 and a_2 or for geometries different from two half-space substrates with boundary Chern–Simons layers.

In this Section, we study the Casimir interaction of Chern–Simons layers for small enough values of a_1 and a_2 and explore the transition between the regimes of Casimir attraction and repulsion in the presence of a realistic dielectric substrate. Consider the Chern–Simons plane layer defined by the constant a_1 separated by a vacuum slit of width d from a dielectric half-space characterized by a dielectric permittivity $\epsilon_2(\omega)$ and the boundary Chern–Simons layer defined by the constant a_2 (Figure 2). We emphasize that $\epsilon_1(\omega) = 1$ in this case. We evaluate the Casimir energy in this system for two dielectric substrate materials: intrinsic Si and SiO₂ glass. For the dielectric permittivity of intrinsic Si, the model from Ref. [114] is used. For SiO₂ glass, we use data from [115] to evaluate dielectric permittivity at imaginary frequencies. We apply Equation (86) to evaluate the Casimir energy.

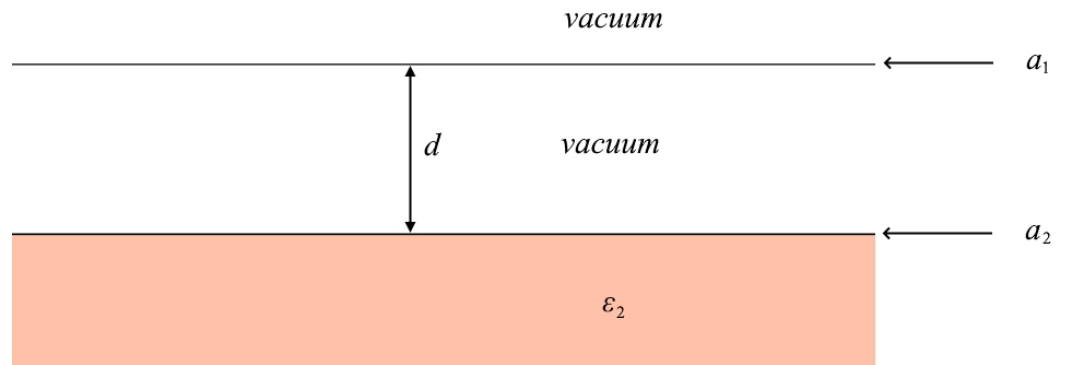


Figure 2. The Chern–Simons layer defined by a_1 is separated by a distance d from a dielectric half-space, with the boundary Chern–Simons layer defined by a_2 . The permittivity of a dielectric half-space is ϵ_2 .

The Casimir energy for the Si substrate and Chern–Simons layers with $m = n = 1$ is presented in Figure 3; the minimum of the energy is at the distance $d = 35.5$ nm. For $n = 1, m = 2$, the minimum is at the distance $d = 17.6$ nm; for $n = 1, m = 3$, the minimum is at the distance $d = 11.9$ nm.

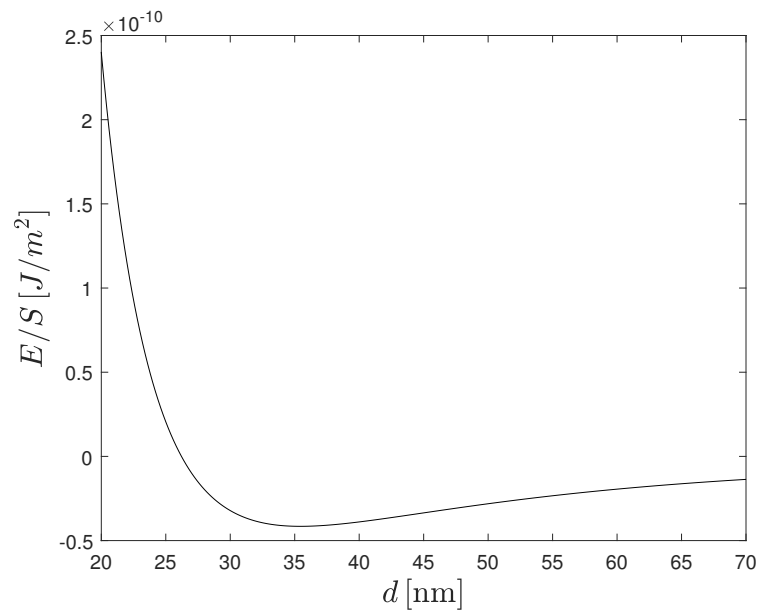


Figure 3. The Casimir energy (86) as a function of a distance d between the Chern–Simons layer defined by $a_1 = \alpha$ and the Chern–Simons layer defined by $a_2 = \alpha$ at the boundary of intrinsic Si half-space substrate.

The Casimir energy for the SiO₂ glass substrate and Chern–Simons plane layers with $n = 1, m = 6$ is shown in Figure 4; the minimum of the energy is at the distance $d = 13.7$ nm. For $n = 1, m = 5$, the minimum is at the distance $d = 20$ nm; for $n = 1, m = 4$, the minimum is at the distance $d = 38.2$ nm; for $n = 1, m = 3$, the minimum is at the distance $d = 276$ nm; for $n = 1, m = 2$, the minimum is at the distance $d = 1547$ nm. For $n = 1, m = 1$, there is no minimum of the Casimir energy: the Casimir repulsion occurs at all distances between the Chern–Simons layers.

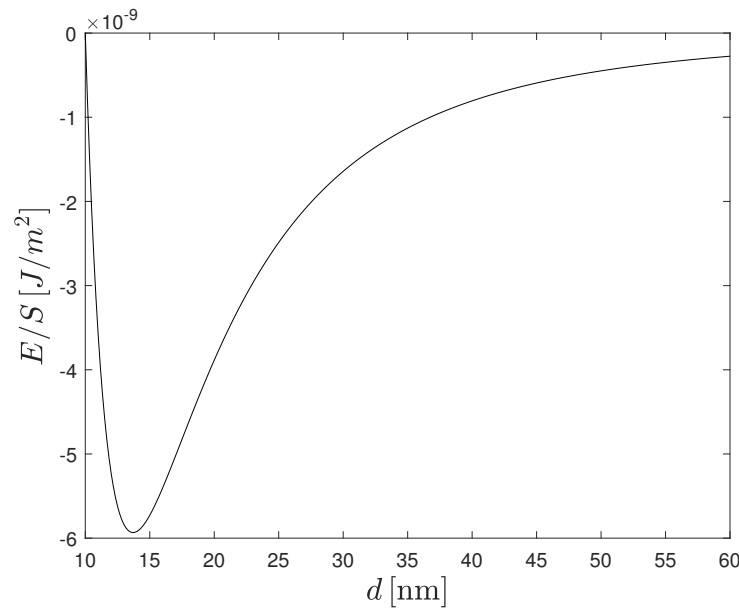


Figure 4. The Casimir energy (86) as a function of a distance d between the Chern–Simons layer defined by $a_1 = 6\alpha$ and the Chern–Simons layer defined by $a_2 = \alpha$ at the boundary of SiO₂ glass half-space substrate.

4. Discussion and Summary

The Green’s functions scattering method [3,64] is explicitly gauge-invariant by construction; it is based on a direct evaluation of electric and magnetic Green’s functions and the fluctuation stress tensor in a vacuum slit between objects. In Refs. [3,64], the Casimir pressure is derived for flat geometries and boundary conditions when there is no mixing between transverse electric and transverse magnetic polarizations after reflection from flat boundaries. In Ref. [88] and in this paper, the method is generalized to systems with Chern–Simons plane layers; in this case, there is mixing between the transverse electric and transverse magnetic polarizations after reflection from the Chern–Simons layers.

In the present paper, the Casimir pressure is derived for dielectric half-spaces with Chern–Simons plane-parallel boundary layers via evaluation of the fluctuation stress tensor in a vacuum slit. Section 2, presents derivation of the Casimir pressure (85) expressed in terms of reflection matrices through evaluation of the fluctuation stress tensor in a vacuum slit. The fluctuation stress tensor is expressed through electric and magnetic Green’s functions in a vacuum slit. We start from evaluation of the electric Green’s functions in a vacuum slit [88]. The derivation of the magnetic Green’s functions and the stress tensor in a vacuum slit is new. To our knowledge, the Casimir pressure expressed in terms of nondiagonal reflection matrices has not been previously derived through evaluation of the vacuum stress tensor. In Appendix A, we prove the equivalence of the Casimir energy (86) to the result for the Casimir energy obtained with the scattering approach [43].

The Casimir pressure on a Chern–Simons plane layer separated by a vacuum slit from the boundary Chern–Simons layer on intrinsic Si or SiO₂ glass half-spaces has remarkable properties for experimental study. In Section 3, we concentrate on the case of quite small parameters a_1, a_2 for the boundary Chern–Simons layers: the case that is easier to implement experimentally. The case of relatively small and different values of a_1, a_2 was not investigated before. The geometry of the Chern–Simons plane layer separated by a vacuum slit from a dielectric half-space with the boundary Chern–Simons layer was not studied before. It is convenient to consider quantum Hall quantization of the parameters $a_1 = m\alpha, a_2 = n\alpha$, where m and n are integer numbers. For $m = n = 1$, the Casimir pressure is repulsive at all separations for the SiO₂ substrate; however, there exists a minimum of the Casimir energy in this case for the Si substrate. For $n = 1$ and integers $m > 1$, there is a

minimum of the Casimir energy both for the Si and SiO₂ substrates; the Casimir pressure is attractive when the separation between the layers is greater than the separation at the position of the minimum of the energy, and it is repulsive at shorter separations. We find the positions of the minimum of the Casimir energy for $n = 1$ and $m = 1, 2, 3$ for the intrinsic Si substrate and for $n = 1$ and integers $m \in [2, 6]$ for the SiO₂ glass substrate.

The results obtained in this paper demonstrate that intrinsic Si and SiO₂ glass are natural substrate materials for the study of transitions from an attractive regime of the Casimir pressure to a repulsive one. The positions of the minimum of the Casimir energy are found at experimentally realizable distances between the layers for quite small integer numbers of quantization parameters for both Chern–Simons layers, which is important for experimental realization of the repulsive Casimir force.

Author Contributions: Both authors contributed equally to this work. All authors have read and agreed to the published version of the manuscript.

Funding: This research has received financial support from a grant from the Russian Science Foundation (RSF project N^o 22-13-00151).

Data Availability Statement: Data are contained within the article.

Acknowledgments: Research was performed at the Research park of the St. Petersburg State University Computing Center, Russia.

Conflicts of Interest: The authors declare no conflicts of interest.

Appendix A. Representations of the Casimir Energy in Two Bases

Here, we prove the equivalence of the Casimir energy (86) to the result for the Casimir energy obtained with the scattering approach [43,44]. In the present paper, we use the local polar basis vectors \mathbf{e}_r and \mathbf{e}_φ in momentum space; in Ref. [43], the local basis vectors \mathbf{e}_s and \mathbf{e}_p of the TE and TM polarizations in momentum space have been used. The amplitudes of the incident electric fields in the two bases are related by the matrix A^f :

$$\begin{pmatrix} N_r \\ N_\varphi \end{pmatrix} = A^f \begin{pmatrix} N_s \\ N_p \end{pmatrix}. \tag{A1}$$

The amplitudes of the reflected electric field v_i are expressed through the amplitudes of the incident field N_i by the matrix R defined in Equation (53):

$$\begin{pmatrix} v_r \\ v_\varphi \end{pmatrix} = R \begin{pmatrix} N_r \\ N_\varphi \end{pmatrix}. \tag{A2}$$

The amplitudes of the reflected electric field in the two bases are related by the transition matrix A^g :

$$\begin{pmatrix} v_s \\ v_p \end{pmatrix} = A^g \begin{pmatrix} v_r \\ v_\varphi \end{pmatrix} = A^g R A^f \begin{pmatrix} N_s \\ N_p \end{pmatrix} = R' \begin{pmatrix} N_s \\ N_p \end{pmatrix}. \tag{A3}$$

One immediately finds the relation between the reflection matrices in the two bases:

$$R' = A^g R A^f. \tag{A4}$$

The transformation matrices for a reflection from the upper half-space have the form

$$A^{g1} = \begin{pmatrix} 0 & -1 \\ \omega/k_z & 0 \end{pmatrix}, \tag{A5}$$

$$A^{f1} = \begin{pmatrix} 0 & -k_z/\omega \\ -1 & 0 \end{pmatrix}. \tag{A6}$$

For a reflection from the lower half-space, the transformation matrices have the form

$$A^{s_2} = \begin{pmatrix} 0 & -1 \\ -\omega/k_z & 0 \end{pmatrix}, \quad (\text{A7})$$

$$A^{f_2} = \begin{pmatrix} 0 & k_z/\omega \\ -1 & 0 \end{pmatrix}. \quad (\text{A8})$$

From (53), (54), (A4) and (A5)–(A8), we obtain reflection matrices in agreement with the scattering approach [43]:

$$R'_1 = \frac{1}{1 + a_1^2 T_1} \begin{pmatrix} r_{\text{TE}_1} - a_1^2 T_1 & -a_1 T_1 \\ -a_1 T_1 & r_{\text{TM}_1} + a_1^2 T_1 \end{pmatrix}, \quad (\text{A9})$$

$$R'_2 = \frac{1}{1 + a_2^2 T_2} \begin{pmatrix} r_{\text{TE}_2} - a_2^2 T_2 & a_2 T_2 \\ a_2 T_2 & r_{\text{TM}_2} + a_2^2 T_2 \end{pmatrix}. \quad (\text{A10})$$

One can write the product of the reflection matrices from the upper and the lower half-spaces:

$$\begin{aligned} R'_1 R'_2 &= \begin{pmatrix} 0 & -1 \\ \omega/k_z & 0 \end{pmatrix} R_1 \begin{pmatrix} 0 & -k_z/\omega \\ -1 & 0 \end{pmatrix} \begin{pmatrix} 0 & -1 \\ -\omega/k_z & 0 \end{pmatrix} R_2 \begin{pmatrix} 0 & k_z/\omega \\ -1 & 0 \end{pmatrix} \\ &= \begin{pmatrix} 0 & -1 \\ \omega/k_z & 0 \end{pmatrix} R_1 R_2 \begin{pmatrix} 0 & k_z/\omega \\ -1 & 0 \end{pmatrix}. \end{aligned} \quad (\text{A11})$$

The equality of the trace operations in two different bases follows:

$$\text{Tr}(R'_1 R'_2)^L = \text{Tr}(R_1 R_2)^L, \quad (\text{A12})$$

where L is a positive integer number. The equivalence of the Casimir energy (86) to the result for the Casimir energy obtained with the scattering approach [43] follows from the equality (A12).

References

1. Casimir, H.B.G.; Polder, D. The influence of retardation on the London–van der Waals forces. *Phys. Rev.* **1948**, *73*, 360–372. [CrossRef]
2. Casimir, H.B.G. On the attraction between two perfectly conducting plates. *Proc. Kon. Ned. Akad. Wetensch. B* **1948**, *51*, 793–795. Available online: <https://dwc.knaw.nl/DL/publications/PU00018547.pdf> (accessed on 1 February 2024).
3. Marachevsky, V.N.; Sidelnikov, A.A. Green functions scattering in the Casimir effect. *Universe* **2021**, *7*, 195. [CrossRef]
4. Lifshitz, E.M.; Pitaevskii, L.P. *Statistical Physics. Part 2: Theory of Condensed States*; Butterworth–Heinemann Ltd/Elsevier Ltd.: Oxford, UK, 1980. [CrossRef]
5. Barash, Y.S.; Ginzburg, V.L. Electromagnetic fluctuations in matter and molecular (Van-der-Waals) forces between them. *Sov. Phys. Usp.* **1975**, *18*, 305–322. [CrossRef]
6. Barash, Y.S.; Ginzburg, V.L. Some problems in the theory of van der Waals forces. *Sov. Phys. Usp.* **1984**, *27*, 467–491. [CrossRef]
7. Plunien, G.; Müller, B.; Greiner, W. The Casimir effect. *Phys. Rep.* **1986**, *134*, 87–193. [CrossRef]
8. Bordag, M.; Mohideen, U.; Mostepanenko, V.M. New developments in the Casimir effect. *Phys. Rep.* **2001**, *353*, 1–205. [CrossRef]
9. Santangelo, E.M. Evaluation of Casimir energies through spectral functions. *Theor. Math. Phys.* **2002**, *131*, 527–542. [CrossRef]
10. Milton, K.A. The Casimir effect: Recent controversies and progress. *J. Phys. A Math. Gen.* **2004**, *37*, R209–R277. [CrossRef]
11. Jaffe, R.L. Casimir effect and the quantum vacuum. *Phys. Rev. D* **2005**, *72*, 021301(R). [CrossRef]
12. Scheel, S.; Buhmann, S.Y. Macroscopic quantum electrodynamics—Concepts and applications. *Acta Phys. Slovaca* **2008**, *58*, 675–809. Available online: <http://www.physics.sk/aps/pub.php?y=2008&pub=aps-08-05> (accessed on 1 February 2024). [CrossRef]
13. Klimchitskaya, G.L.; Mohideen, U.; Mostepanenko, V.M. The Casimir force between real materials: Experiment and theory. *Rev. Mod. Phys.* **2009**, *81*, 1827–1885. [CrossRef]
14. Rodriguez, A.; Capasso, F.; Johnson, S. The Casimir effect in microstructured geometries. *Nat. Photon.* **2011**, *5*, 211–221. [CrossRef]
15. Marachevsky, V.N. The Casimir effect: Medium and geometry. *J. Phys. A Math. Theor.* **2012**, *45*, 374021. [CrossRef]
16. Woods, L.M.; Dalvit, D.A.R.; Tkatchenko, A.; Rodriguez-Lopez, P.; Rodriguez, A.W.; Podgornik, R. Materials perspective on Casimir and van der Waals interactions. *Rev. Mod. Phys.* **2016**, *88*, 045003. [CrossRef]

17. Woods, L.M.; Krüger, M.; Dodonov, V.V. Perspective on some recent and future developments in Casimir interactions. *Appl. Sci.* **2021**, *11*, 293. [CrossRef]
18. Lu, B.-S. The Casimir effect in topological matter. *Universe* **2021**, *7*, 237. [CrossRef]
19. Elizalde, E. *Ten Physical Applications of Spectral Zeta Functions*; Springer: Berlin/Heidelberg, Germany, 2012. . [CrossRef]
20. Kirsten, K. *Spectral Functions in Mathematics and Physics*; Chapman & Hall/CRC Press/Taylor & Francis Group: Boca Raton, FL, USA, 2002. . [CrossRef]
21. Fursaev, D.; Vassilevich, D. *Operators, Geometry and Quanta: Methods of Spectral Geometry in Quantum Field Theory*; Springer Science+Business Media B.V.: Dordrecht, The Netherlands, 2011.
22. Buhmann, S.Y. *Dispersion Forces I. Macroscopic Quantum Electrodynamics and Ground-State Casimir, Casimir–Polder and van der Waals Forces*; Springer: Berlin/Heidelberg, Germany, 2012. . [CrossRef]
23. Buhmann, S.Y. *Dispersion Forces II. Many-Body Effects, Excited Atoms, Finite Temperature and Quantum Friction*; Springer: Berlin/Heidelberg, Germany, 2012. . [CrossRef]
24. Bordag, M.; Klimchitskaya, G.L.; Mohideen, U.; Mostepanenko, V.M. *Advances in the Casimir Effect*; Oxford University Press: Oxford, UK, 2015. [CrossRef]
25. Lifshitz, E.M. The theory of molecular attractive forces between solids. *Zh. Eksp. Teor. Fiz.* **1955**, *29*, 94–110. (In Russian) English translation: *Sov. Phys. JETP* **1956**, *2*, 73–83. Available online: <http://jetp.ras.ru/cgi-bin/e/index/e/2/1/p73?a=list> (accessed on 1 February 2024).
26. Renne, M.J. Microscopic theory of retarded van der Waals forces between macroscopic dielectric bodies. *Physica* **1971**, *56*, 125–137. [CrossRef]
27. Dzyaloshinskii, I.E.; Lifshitz, E.M.; Pitaevskii, L.P. General theory of van der Waals' forces. *Sov. Phys. Usp.* **1961**, *4*, 153–176. . [CrossRef]
28. Munday, J.N.; Capasso, F.; Parsegian, V.A. Measured long-range repulsive Casimir–Lifshitz forces. *Nature* **2009**, *457*, 170–173. [CrossRef] [PubMed]
29. Pirozhenko, I.; Lambrecht, A. Repulsive Casimir forces and the role of surface modes. *Phys. Rev. A* **2009**, *80*, 042510. [CrossRef]
30. Schmidt, F.; Callegari, A.; Daddi-Moussa-Ider, A.; Munkhbat, B.; Verre, R.; Shegai, T.; Käll, M.; Löwen, H.; Gambassi, A.; Volpe, G. Tunable critical Casimir forces counteract Casimir–Lifshitz attraction. *Nat. Phys.* **2023**, *19*, 271–278. [CrossRef]
31. Tomaš, M.S. Casimir force between dispersive magnetodielectrics. *Phys. Lett. A* **2005**, *342*, 381–388. [CrossRef]
32. Geyer, B.; Klimchitskaya, G.L.; Mostepanenko, V.M. Thermal Casimir interaction between two magnetodielectric plates. *Phys. Rev. B* **2010**, *81*, 104101. [CrossRef]
33. Inui, N. Thickness dependence of the Casimir force between a magnetodielectric plate and a diamagnetic plate. *Phys. Rev. A* **2011**, *84*, 052505. [CrossRef]
34. Brevik, I.; Parashar, P.; Shajesh, K.V. Casimir force for magnetodielectric media. *Phys. Rev. A* **2018**, *98*, 032509. [CrossRef]
35. Shelden, C.; Spreng, B.; Munday, J.N. Enhanced repulsive Casimir forces between gold and thin magnetodielectric plates. *Phys. Rev. A* **2023**, *108*, 032817. [CrossRef]
36. Boyer, T.H. Van der Waals forces and zero-point energy for dielectric and permeable materials. *Phys. Rev. A* **1974**, *9*, 2078–2084. [CrossRef]
37. Rosa, F.S.S.; Dalvit, D.A.R.; Milonni, P.W. Casimir–Lifshitz theory and metamaterials. *Phys. Rev. Lett.* **2008**, *100*, 183602. [CrossRef]
38. Rosa, F.S.S.; Dalvit, D.A.R.; Milonni, P.W. Casimir interactions for anisotropic magnetodielectric metamaterials. *Phys. Rev. A* **2008**, *78*, 032117. [CrossRef]
39. Yannopoulos, V.; Vitanov, N.V. First-principles study of Casimir repulsion in metamaterials. *Phys. Rev. Lett.* **2009**, *103*, 120401. [CrossRef] [PubMed]
40. Zhao, R.; Zhou, J.; Koschny, T.; Economou, E.N.; Soukoulis, C.M. Repulsive Casimir force in chiral metamaterials. *Phys. Rev. Lett.* **2009**, *103*, 103602. [CrossRef] [PubMed]
41. Markov, V.N.; Pis'mak, Y.M. Casimir effect for thin films in QED. *J. Phys. A Math. Gen.* **2006**, *39*, 6525–6532. [CrossRef]
42. Marachevsky, V.N. Casimir effect for Chern–Simons layers in the vacuum. *Theor. Math. Phys.* **2017**, *190*, 315–320. [CrossRef]
43. Marachevsky, V.N. Casimir interaction of two dielectric half spaces with Chern–Simons boundary layers. *Phys. Rev. B* **2019**, *99*, 075420. [CrossRef]
44. Marachevsky, V.N. Chern–Simons boundary layers in the Casimir effect. *Mod. Phys. Lett. A* **2020**, *35*, 2040015. [CrossRef]
45. Pavlovsky, O.; Ulybyshev, M. Casimir energy calculations within the formalism of noncompact lattice QED. *Int. J. Mod. Phys. A* **2010**, *25*, 2457–2473. [CrossRef]
46. Pavlovsky, O.V.; Ulybyshev, M.V. Casimir energy in noncompact lattice electrodynamics. *Theor. Math. Phys.* **2010**, *164*, 1051–1063. [CrossRef]
47. Milton, K.A.; Ng, Y.J. Maxwell–Chern–Simons Casimir effect. *Phys. Rev. D* **1990**, *42*, 2875–2880. [CrossRef]
48. Elizalde, E.; Vassilevich, D.V. Heat kernel coefficients for Chern–Simons boundary conditions in QED. *Class. Quantum Gravity* **1999**, *16*, 813–822. [CrossRef]
49. Bordag, M.; Vassilevich, D.V. Casimir force between Chern–Simons surfaces. *Phys. Lett. A* **2000**, *268*, 75–80. [CrossRef]
50. Qi, X.-L.; Li, R.; Zang, J.; Zhang, S.-C. Inducing a magnetic monopole with topological surface states. *Science* **2009**, *323*, 1184–1187. [CrossRef] [PubMed]

51. Grushin, A.G.; Cortijo, A. Tunable Casimir repulsion with three-dimensional topological insulators. *Phys. Rev. Lett.* **2011**, *106*, 020403. [CrossRef] [PubMed]
52. Grushin, A.G.; Rodriguez-Lopez, P.; Cortijo, A. Effect of finite temperature and uniaxial anisotropy on the Casimir effect with three-dimensional topological insulators. *Phys. Rev. B* **2011**, *84*, 045119. [CrossRef]
53. Chen, L.; Wan, S. Casimir interaction between topological insulators with finite surface band gap. *Phys. Rev. B* **2011**, *84*, 075149. [CrossRef]
54. Chen, L.; Wan, S. Critical surface band gap of repulsive Casimir interaction between three-dimensional topological insulators at finite temperature. *Phys. Rev. B* **2012**, *85*, 115102. [CrossRef]
55. Martín-Ruiz, A.; Cambiaso, M.; Urrutia, L.F. A Green's function approach to the Casimir effect on topological insulators with planar symmetry. *Europhys. Lett.* **2016**, *113*, 60005. [CrossRef]
56. Fialkovsky, I.; Khusnutdinov, N.; Vassilevich, D. Quest for Casimir repulsion between Chern–Simons surfaces. *Phys. Rev. B* **2018**, *97*, 165432. [CrossRef]
57. Weng, H.; Yu, R.; Hu, X.; Dai, X.; Fang, Z. Quantum anomalous Hall effect and related topological electronic states. *Adv. Phys.* **2015**, *64*, 227–282. [CrossRef]
58. Liu, C.-X.; Zhang, S.-C.; Qi, X.-L. The quantum anomalous Hall effect: Theory and experiment. *Annu. Rev. Cond. Matter. Phys.* **2016**, *7*, 301–321. [CrossRef]
59. Ren, Y.; Qiao, Z.; Niu, Q. Topological phases in two-dimensional materials: A review. *Rep. Prog. Phys.* **2016**, *79*, 066501. [CrossRef] [PubMed]
60. Rodriguez-Lopez, P.; Grushin, A.G. Repulsive Casimir effect with Chern insulators. *Phys. Rev. Lett.* **2014**, *112*, 056804. [CrossRef] [PubMed]
61. Muniz, Y.; Farina, C.; Kort-Kamp, W.J.M. Casimir forces in the flatland: Interplay between photoinduced phase transitions and quantum Hall physics. *Phys. Rev. Res.* **2021**, *3*, 023061. [CrossRef]
62. Tse, W.-K.; MacDonald, A.H. Quantized Casimir force. *Phys. Rev. Lett.* **2012**, *109*, 236806. [CrossRef] [PubMed]
63. Ezawa, Z.F. *Quantum Hall Effects: Field Theoretical Approach and Related Topics*; World Scientific: Singapore, 2008. . [CrossRef]
64. Marachevsky, V.N.; Sidelnikov, A.A. Gauge-invariant derivation of the Casimir–Lifshitz pressure. *Phys. Part. Nucl. Lett.* **2023**, *20*, 1114–1116. . [CrossRef]
65. Barton, G. Quantum-electrodynamic level shifts between parallel mirrors: Analysis. *Proc. R. Soc. Lond. A* **1987**, *410*, 141–174.
66. Brevik, I.; Lygren, M.; Marachevsky, V.N. Casimir–Polder effect for a perfectly conducting wedge. *Ann. Phys.* **1998**, *267*, 134–142. [CrossRef]
67. Messina, R.; Dalvit, D.A.R.; Maia Neto, P.A.; Lambrecht, A.; Reynaud, S. Dispersive interactions between atoms and nonplanar surfaces. *Phys. Rev. A* **2009**, *80*, 022119. [CrossRef]
68. Bender, H.; Stehle, C.; Zimmermann, C.; Slama, S.; Fiedler, J.; Scheel, S.; Buhmann, S.Y.; Marachevsky, V.N. Probing atom-surface interactions by diffraction of Bose–Einstein condensates. *Phys. Rev. X* **2014**, *4*, 011029. [CrossRef]
69. Levin, M.; McCauley, A.P.; Rodriguez, A.W.; Homer Reid, M.T.; Johnson, S.G. Casimir repulsion between metallic objects in vacuum. *Phys. Rev. Lett.* **2010**, *105*, 090403. [CrossRef] [PubMed]
70. Eberlein, C.; Zietal, R. Casimir–Polder interaction between a polarizable particle and a plate with a hole. *Phys. Rev. A* **2011**, *83*, 052514. [CrossRef]
71. Buhmann, S.Y.; Marachevsky, V.N.; Scheel, S. Impact of anisotropy on the interaction of an atom with a one-dimensional nano-grating. *Int. J. Mod. Phys. A* **2016**, *31*, 1641029. [CrossRef]
72. Milton, K.A.; Abalo, E.K.; Parashar, P.; Pourtolami, N.; Brevik, I.; Ellingsen, S.A. Casimir–Polder repulsion near edges: Wedge apex and a screen with an aperture. *Phys. Rev. A* **2011**, *83*, 062507. [CrossRef]
73. Milton, K.A.; Parashar, P.; Pourtolami, N.; Brevik, I. Casimir–Polder repulsion: Polarizable atoms, cylinders, spheres, and ellipsoids. *Phys. Rev. D* **2012**, *85*, 025008. [CrossRef]
74. Milton, K.A.; Abalo, E.K.; Parashar, P.; Pourtolami, N.; Brevik, I.; Ellingsen, S.A. Repulsive Casimir and Casimir–Polder forces. *J. Phys. A Math. Theor.* **2012**, *45*, 374006. [CrossRef]
75. Shajesh, K.V.; Schaden, M. Repulsive long-range forces between anisotropic atoms and dielectrics. *Phys. Rev. A* **2012**, *85*, 012523. [CrossRef]
76. Marchetta, J.J.; Parashar, P.; Shajesh, K.V. Geometrical dependence in Casimir–Polder repulsion. *Phys. Rev. A* **2021**, *104*, 032209. [CrossRef]
77. Savin, V.P.; Koksharov, Y.A. Electrostatic repulsion between an uncharged or slightly charged conductor and a point charge. *J. Electrostat.* **2022**, *120*, 103769. [CrossRef]
78. Nogueira, E.C.M.; Queiroz, L.; Alves, D.T. Sign inversion in the lateral van der Waals force. *Phys. Rev. A* **2022**, *105*, 062816. [CrossRef]
79. Queiroz, L.; Nogueira, E.C.M.; Alves, D.T. Sign inversion in the lateral van der Waals force between an anisotropic particle and a plane with a hemispherical protuberance: An exact calculation. *J. Phys. A Math. Theor.* **2023**, *56*, 115301. [CrossRef]
80. Alves, D.T.; Queiroz, L.; Nogueira, E.C.M.; Peres, N.M.R. Curvature-induced repulsive effect on the lateral Casimir–Polder–van der Waals force. *Phys. Rev. A* **2023**, *107*, 062821. [CrossRef]
81. Venkataram, P.S.; Molesky, S.; Chao, P.; Rodriguez, A.W. Fundamental limits to attractive and repulsive Casimir–Polder forces. *Phys. Rev. A* **2020**, *101*, 052115. [CrossRef]

82. Marachevsky, V.N.; Pis'mak, Y.M. Casimir–Polder effect for a plane with Chern–Simons interaction. *Phys. Rev. D* **2010**, *81*, 065005. [CrossRef]
83. Jiang, Q.-D.; Wilczek, F. Chiral Casimir forces: Repulsive, enhanced, tunable. *Phys. Rev. B* **2019**, *99*, 125403. [CrossRef]
84. Høye, J.S.; Brevik, I. Casimir force between ideal metal plates in a chiral vacuum. *Eur. Phys. J. Plus* **2020**, *135*, 271. [CrossRef]
85. Butcher, D.T.; Buhmann, S.Y.; Scheel, S. Casimir–Polder forces between chiral objects. *New J. Phys.* **2012**, *14*, 113013. [CrossRef]
86. Khriplovich, I.B. *Parity Nonconservation in Atomic Phenomena*; Gordon and Breach Science Publishers S.A.: Philadelphia, PA, USA, 1991.
87. Buhmann, S.Y.; Marachevsky, V.N.; Scheel, S. Charge-parity-violating effects in Casimir–Polder potentials. *Phys. Rev. A* **2018**, *98*, 022510. [CrossRef]
88. Marachevsky, V.N.; Sidelnikov, A.A. Casimir–Polder interaction with Chern–Simons boundary layers. *Phys. Rev. D* **2023**, *107*, 105019. [CrossRef]
89. Brown, L.S.; Maclay, G.J. Vacuum stress between conducting plates: An image solution. *Phys. Rev.* **1969**, *184*, 1272–1279. [CrossRef]
90. Weyl, H. Ausbreitung elektromagnetischer Wellen über einen Leiter. *Ann. Der Phys.* **1919**, *365*, 481–500. [CrossRef]
91. Obukhov, Y.N.; Hehl, F.W. Measuring a piecewise constant axion field in classical electrodynamics. *Phys. Lett. A* **2005**, *341*, 357–365. [CrossRef]
92. Pis'mak, D.Y.; Pis'mak, Y.M.; Wegner, F.J. Electromagnetic waves in a model with Chern–Simons potential. *Phys. Rev. E* **2015**, *92*, 013204. [CrossRef] [PubMed]
93. Lambrecht, A.; Marachevsky, V.N. Casimir interaction of dielectric gratings. *Phys. Rev. Lett.* **2008**, *101*, 160403. [CrossRef] [PubMed]
94. Lambrecht, A.; Marachevsky, V.N. Theory of the Casimir effect in one-dimensional periodic dielectric systems. *Int. J. Mod. Phys. A* **2009**, *24*, 1789–1795. [CrossRef]
95. Antezza, M.; Chan, H.B.; Guizal, B.; Marachevsky, V.N.; Messina, R.; Wang, M. Giant Casimir torque between rotated gratings and the $\theta = 0$ anomaly. *Phys. Rev. Lett.* **2020**, *124*, 013903. [CrossRef]
96. Marachevsky, V.N. The Casimir effect for diffraction gratings, symmetry breaking and geometric transitions. *Phys. Part. Nucl. Lett.* **2023**, *20*, 255–258. [CrossRef]
97. Emig, T.; Graham, N.; Jaffe, R.L.; Kardar, M. Casimir forces between arbitrary compact objects. *Phys. Rev. Lett.* **2007**, *99*, 170403. [CrossRef]
98. Rahi, S.J.; Emig, T.; Graham, N.; Jaffe, R.L.; Kardar, M. Scattering theory approach to electromagnetic Casimir forces. *Phys. Rev. D* **2009**, *80*, 085021. [CrossRef]
99. Emig, T.; Jaffe, R.L.; Kardar, M.; Scardicchio, A. Casimir interaction between a plate and a cylinder. *Phys. Rev. Lett.* **2006**, *96*, 080403. [CrossRef]
100. Canaguier-Durand, A.; Maia Neto, P.A.; Cavero-Pelaez, I.; Lambrecht, A.; Reynaud, S. Casimir interaction between plane and spherical metallic surfaces. *Phys. Rev. Lett.* **2009**, *102*, 230404. [CrossRef] [PubMed]
101. Canaguier-Durand, A.; Gérardin, A.; Guérout, R.; Maia Neto, P.A.; Nesvizhevsky, V.V.; Voronin, A.Y.; Lambrecht, A.; Reynaud, S. Casimir interaction between a dielectric nanosphere and a metallic plane. *Phys. Rev. A* **2011**, *83*, 032508. [CrossRef]
102. Bordag, M.; Nikolaev, V. Casimir force for a sphere in front of a plane beyond proximity force approximation. *J. Phys. A Math. Theor.* **2008**, *41*, 164002. [CrossRef]
103. Bordag, M.; Pirozhenko, I. Vacuum energy between a sphere and a plane at finite temperature. *Phys. Rev. D* **2010**, *81*, 085023. [CrossRef]
104. Bordag, M.; Pirozhenko, I.G. On the Casimir entropy for a ball in front of a plane. *Phys. Rev. D* **2010**, *82*, 125016. [CrossRef]
105. Rodriguez-Lopez, P.; Rahi, S.J.; Emig, T. Three-body Casimir effects and nonmonotonic forces. *Phys. Rev. A* **2009**, *80*, 022519. [CrossRef]
106. Graham, N.; Shpunt, A.; Emig, T.; Rahi, S.J.; Jaffe, R.L.; Kardar, M. Electromagnetic Casimir forces of parabolic cylinder and knife-edge geometries. *Phys. Rev. D* **2011**, *83*, 125007. [CrossRef]
107. Rodriguez-Lopez, P.; Emig, T.; Noruzifar, E.; Zandi, R. Effect of curvature and confinement on the Casimir–Polder interaction. *Phys. Rev. A* **2015**, *91*, 012516. [CrossRef]
108. Fialkovsky, I.V.; Marachevsky, V.N.; Vassilevich, D.V. Finite-temperature Casimir effect for graphene. *Phys. Rev. B* **2011**, *84*, 035446. [CrossRef]
109. Klimchitskaya, G.L.; Mostepanenko, V.M. Casimir and Casimir–Polder forces in graphene systems: Quantum field theoretical description and thermodynamics. *Universe* **2020**, *6*, 150. [CrossRef]
110. Khusnutdinov, N.; Kashapov, R.; Woods, L.M. Casimir–Polder effect for a stack of conductive planes. *Phys. Rev. A* **2016**, *94*, 012513. [CrossRef]
111. Khusnutdinov, N.; Kashapov, R.; Woods, L.M. Thermal Casimir and Casimir–Polder interactions in N parallel 2D Dirac materials. *2D Mater.* **2018**, *5*, 035032. [CrossRef]
112. Antezza, M.; Fialkovsky, I.; Khusnutdinov, N. Casimir–Polder force and torque for anisotropic molecules close to conducting planes and their effect on CO₂. *Phys. Rev. B* **2020**, *102*, 195422. [CrossRef]
113. Liu, M.; Zhang, Y.; Klimchitskaya, G.L.; Mostepanenko, V.M.; Mohideen, U. Demonstration of an unusual thermal effect in the Casimir force from graphene. *Phys. Rev. Lett.* **2021**, *126*, 206802. [CrossRef]

114. Lambrecht, A.; Pirozhenko, I.; Duraffourg, L.; Andreucci, P. The Casimir effect for silicon and gold slabs. *Europhys. Lett.* **2007**, *77*, 44006. [CrossRef]
115. Palik, E.D. (Ed.) *Handbook of Optical Constants of Solids*; Academic Press/Elsevier Inc.: Cambridge, MA, USA, 1997. Available online: <https://www.sciencedirect.com/book/9780125444156/handbook-of-optical-constants-of-solids> (accessed on 1 February 2024).

Disclaimer/Publisher's Note: The statements, opinions and data contained in all publications are solely those of the individual author(s) and contributor(s) and not of MDPI and/or the editor(s). MDPI and/or the editor(s) disclaim responsibility for any injury to people or property resulting from any ideas, methods, instructions or products referred to in the content.

Larmor Temperature, Casimir Dynamics, and Planck's Law

Evgenii Ievlev^{1,2,3} and Michael R. R. Good^{1,4,*}

- ¹ Physics Department & Energetic Cosmos Laboratory, Nazarbayev University, Astana 010000, Kazakhstan; evgenii.ievlev@nu.edu.kz
² Theoretical & Nuclear Physics Department, al-Farabi Qazaq National University, Almaty 050040, Kazakhstan
³ National Research Center "Kurchatov Institute", Petersburg Nuclear Physics Institute, St. Petersburg 188300, Russia
⁴ Leung Center for Cosmology and Particle Astrophysics, National Taiwan University, Taipei 10617, Taiwan
* Correspondence: michael.good@nu.edu.kz

Abstract: Classical radiation from a single relativistically accelerating electron is investigated where the temperature characterizing the system highlights the dependence on acceleration. In the context of the dynamic Casimir effect with Planck-distributed photons and thermal black hole evaporation, we demonstrate analytic consistency between the ideas of constant acceleration and equilibrium thermal radiation. For ultra-relativistic speeds, we demonstrate a long-lasting constant peel acceleration and constant power emission, which is consistent with the idea of balanced equilibrium of Planck-distributed particle radiation.

Keywords: moving mirrors; beta decay; black hole evaporation; acceleration radiation

1. Introduction

It is fascinating that black holes (BH), with surface gravity, $\kappa_{\text{BH}} = c^4/4GM$, have 'quantum' (with the reduced Planck constant, \hbar) temperature [1],

$$T_{\text{BH}} = \frac{\hbar\kappa_{\text{BH}}}{2\pi ck_B}, \quad (1)$$

because, in part, the radiated particles in equilibrium are frequency-distributed with a Planck factor, and the power emitted scales according to $P \sim T^2$, substantiating black holes as one-dimensional information channels [2]. Here, G is the Newtonian constant of gravitation, M is the BH mass, c is the speed of light, and k_B is the Boltzmann constant.

In this paper, we help to make the case for a classical analog to Equation (1). We present new details supporting the idea of a moving point charge radiation effect, quite similar in form to Equation (1) yet fully classical in origin. The thermal radiation originates from a single accelerating electron. For clarity, we provide overlap with [3], but the novel results here focus on temperature and the analytic expressions of time dependence. Our results are concerned with the equilibrium period of an electron's radiation: when the power emitted is uniform and classical thermodynamics applies, the emission has a temperature proportional to the peel acceleration, κ , of the electron; the latter term is defined and explained in Section 3.3. One finds the 'classical' (no \hbar) temperature [4],

$$T_{\text{electron}} = \frac{\mu_0 e^2 \kappa}{2\pi k_B}, \quad (2)$$

which is commensurate with constant power emission [3]. This temperature is in the Stoney scale [5]; see [6]. Here, e denotes the electron's charge and μ_0 is the vacuum magnetic permeability. Interestingly, this occurs during Planck-distributed radiation from an analog moving mirror (dynamical Casimir effect [7–9]) accelerated along the same specific trajectory (provided in Ref. [3]). A horizontal leveling of the power is visually

Citation: Ievlev, E.; Good, M.R.R. Larmor Temperature, Casimir Dynamics, and Planck's Law. *Physics* **2023**, *5*, 797–813. <https://doi.org/10.3390/physics5030050>

Received: 18 May 2023
Accepted: 25 June 2023
Published: 18 July 2023



Copyright: © 2023 by the authors. Licensee MDPI, Basel, Switzerland. This article is an open access article distributed under the terms and conditions of the Creative Commons Attribution (CC BY) license (<https://creativecommons.org/licenses/by/4.0/>).

observed at extremely ultra-relativistic final speeds of the electron. A notion of temperature is congruent with the power P , emitted by the electron scaling according to $P \sim T^2$ (this quantity is the \bar{P}_c defined in Equation (18)), revealing similar Bekenstein one-dimensional behavior and power–temperature scaling [2]. In this paper, we investigate the arguments supporting this conjecture and the classical temperature (2), as well as the analogy to the quantum temperature (1).

1.1. Analog Bridge

First, let us consider the straightforward action correspondence between Equations (1) and (2),

$$\hbar \rightarrow \frac{e^2}{\epsilon_0 c} = \mu_0 c e^2, \tag{3}$$

where the \hbar value is,

$$\hbar = 1.054 \times 10^{-34} \text{ J s}, \tag{4}$$

and the smaller action (or angular momentum) classical quantity is

$$\mu_0 c e^2 = 9.671 \times 10^{-36} \text{ J s}. \tag{5}$$

Notice that

$$\frac{\hbar}{\mu_0 c e^2} \approx 10.91. \tag{6}$$

For a given acceleration scale, κ , the classical temperature (2) is nominally about a magnitude order smaller than the quantum temperature (1). The analog ‘substitution’ (3) can help one bridge the analog connection between the elementary particle and black hole via a substitution $\hbar \rightarrow \mu_0 c e^2$ in Equation (1) gives Equation (2). We justify and generalize this in what follows.

1.2. Temperature Definition

Temperature is a collective property and is almost always defined with an assemblage of particles. The helpfulness of thermodynamics is particularly salient in a regime with a large number of particles (in this case, the large amount of radiated particles are infinite soft thermal photons).

We emphasize that what is meant by ‘the temperature of electron radiation’ in Equation (2) is a temperature extracted by averaging the photon energy radiated over many realizations of the same decay experiment with a single asymptotically ultra-relativistic electron. Only in this context does it make sense to consider a single electron radiating photons with a defined temperature.

Here, the frequency distribution is also analogous to the moving mirror particle production, which is Planck-distributed; see Section 4 below. The connection to black hole temperature is limited in the sense that an explicit Planck distribution has not been derived for classical electron radiation, unlike the moving mirror Planck distribution, which is a result of the Bogolubov beta coefficients originating from the quantum fields in a curved space approach, see e.g., [8–11]. However, the connection is explicitly tethered by the power–temperature scaling of the (1+1)-dimensional Stefan–Boltzmann law; see Section 5 below. Importantly, this notion of electron radiation temperature is dynamically convenient because it signals a corresponding period of uniform peel acceleration (which is defined in Section 3.3).

1.3. Extension Bridge

The bridge (3) is not limited to Equations (1) and (2). It proves helpful as an action correspondence in general (see Refs. [12–15]) between the quantum moving mirror model

(denoted below by the q subscript) and the classical moving point charge model (denoted by the c subscript). This is observed, respectively, in the power (see, e.g., [16,17]),

$$P_q = \frac{\hbar\alpha^2}{6\pi c^2}, \quad P_c = \frac{\mu_0 e^2 \alpha^2}{6\pi c}, \tag{7}$$

where α is the proper acceleration of the mirror or electron, and self-force [18,19],

$$F_q = \frac{\hbar\alpha'(\tau)}{6\pi c^2}, \quad F_c = \frac{\mu_0 e^2 \alpha'(\tau)}{6\pi c}, \tag{8}$$

with the prime indicating the derivative with respect to proper time, τ , (not coordinate time, t) (see, e.g., [18,20]), for any limited horizonless trajectory whose acceleration is asymptotically zero (asymptotic inertia).

Moreover, the bridge also occurs specifically between the spectral radiance of a particular moving mirror model and lowest-order inner bremsstrahlung (IB) during beta decay [3], contained therein. More generally, if one examines the infrared limit, this is observed in the frequency independence of the spectral energy per unit bandwidth (see, e.g., [16,21]),

$$I_q = \frac{\hbar}{2\pi^2} \left(\frac{\eta}{s} - 1\right), \quad I_c = \frac{\mu_0 c e^2}{2\pi^2} \left(\frac{\eta}{s} - 1\right), \tag{9}$$

where $s = \tanh \eta$ is the final speed of the mirror or electron as a fraction of c , and η is the final rapidity.

In what follows, we check the consistency of our claims by analyzing the correspondence from different sides. In Section 2, we consider the radiation from an accelerated electron more closely, discussing the relevant scales of the problem. In Section 3, we show that such an electron is characterized by constant-in-time characteristic quantities, thus supporting the thermal regime. Section 4 presents the Planck spectrum for a moving mirror model and its connection to the moving point charge and black holes, also supporting thermality and the analog bridge of Equations (1) and (2). In Section 5, we provide several derivations of the Stefan–Boltzmann law in the relevant contexts; the results serve as an independent confirmation of the quadratic dependence in temperature. Section 6 gives the conclusions.

2. Energy Radiated by an Electron

2.1. Total Energy Emitted

To obtain the energy per unit bandwidth from Equation (9), one associates the ultraviolet (UV) scale, ω_{\max} , of the system with the acceleration scale, κ :

$$\omega_{\max} = \frac{\pi\kappa}{12c}, \tag{10}$$

such that, using the first equation of Equation (9), the quantum spectral energy per unit bandwidth,

$$I_q = \frac{dE_q}{d\omega} \quad \rightarrow \quad E_q = \frac{\hbar\kappa}{24\pi c} \left(\frac{\eta}{s} - 1\right), \tag{11}$$

or with the second equation of Equation (9), the classical spectral energy per bandwidth,

$$I_c = \frac{dE_c}{d\omega} \quad \rightarrow \quad E_c = \frac{\mu_0 e^2 \kappa}{24\pi} \left(\frac{\eta}{s} - 1\right). \tag{12}$$

With the clarity of the International System of Units (SI), this demonstrates that the two different models have analogous energy emission scaling. Notice that energy (12) can be expressed as

$$E_c = \frac{\mu_0 e^2 \kappa}{48\pi} \left[\frac{1}{s} \ln \left(\frac{1+s}{1-s} \right) - 2 \right], \tag{13}$$

where, again, as in Equation (9), s is the final constant speed of the electron as a fraction of the speed of light. As shown in Section 3 below, for a thermal plateau, ultra-relativistic speeds are required, $s \sim 1$ (although this is not required in order to obtain the Planck-distributed photon thermal spectrum). Only the classical version Equation (12) [22] or lowest-order IB energy [23] have been directly observed in experiments; see, e.g., [24].

2.2. UV Cutoff and Temperature

For some orientations, consider now re-expressing the temperature (2) of the electron radiation in terms of the maximum appreciable energy emitted, $\hbar\omega_{\max} = \hbar\pi\kappa/12c$ (see Equation (10)),

$$T = \frac{6}{\pi^2} \frac{\mu_0 c e^2}{\hbar} \frac{E_\gamma}{k_B}, \tag{14}$$

where energy range of the detected photons is UV-limited by $E_\gamma = \hbar\omega_{\max}$ and can be expressed from Equation (14) as

$$E_\gamma = \frac{\pi^2}{6} \frac{\hbar}{\mu_0 c e^2} k_B T \approx 18 k_B T. \tag{15}$$

This provides some perspective on the dependence of the system on the cutoff when in thermal equilibrium. Consistency of the temperature Formulas (2) and (14) is confirmed below; see Sections 2.3, 3, 4, and 5 below.

Including these UV limits, experimental evidence of lowest-order IB energy emitted during beta decay confirms the consistency of the theoretically derived frequency independence of the spectral energy per unit bandwidth (9); see, e.g., [24]. In what follows, we support the physical notion of temperature in this context by providing corroborative analytic results confirming the mathematical validity of Equation (2).

2.3. Scale Dependence

The analog between black hole temperature and electron radiation temperature, introduced in Section 1, has limitations. Black hole temperature, $T = \hbar\kappa/2\pi c k_B$, varies dependent on the surface gravity, $\kappa_{\text{BH}} = c^4/4GM$, of the black hole, while electron radiation temperature, $T = \mu_0 e^2 \kappa / 2\pi k_B$, varies on the acceleration scale, $\kappa = 12c\omega_{\max}/\pi$, inherently a function of the UV scale of the system, ω_{\max} . Hence, because the charge of every electron is the same, the fine structure does not change in this context, and the temperature of the electron's acceleration radiation is UV-dependent, so the two expressions differ with respect to both intuition and scale. In this context, it is convenient to consider the universality of the soft factor [25] and the thermal character of the infinite zero-energy photons emitted in this regime. Indeed, the thermality here is connected to every scattering process in the deep infrared, at least in the instantaneous collision reference frame [26]. Thus, there is an argument for the relevance of Equation (2) beyond the bremsstrahlung context.

To this end, we point out that Equation (2) is relevant for Feddeev–Kulish dressed states, where equivalent particle count and energy results [27] suggest one can derive a ‘cloud temperature’. Analog systems with corresponding results are also subject to thermal character. For instance, ‘mirror temperature’ is an appropriate assignment in the context of the dynamical Casimir effect [28], as we demonstrate straightforwardly with the spectral computation (see Equation (26) below). Moreover, since the internal structure of the source cannot be discerned by long wavelengths, these results can necessarily be extended in analog to curved spacetime final states [29], where ‘black hole temperature’ leading to a leftover remnant becomes a helpful characterization of the system. We leave these extensions for future investigations.

3. Thermal Plateaus

In a system with well-defined thermality, one naturally expects to observe an equilibrium, which implies that characteristic quantities describing this system remain constant in

time (up to small fluctuations). For example, a black body immersed in a heat bath radiates the same amount of energy each second, i.e., the radiation power remains constant.

Since we talk about temperature and thermality for the electron/mirror setup, it is desirable to see that this system is indeed in a regime where its characteristic quantities remain constant; in this Section, we explore this in detail. We find that indeed there is a time window where the characteristic quantities remain constant and exhibit plateaus. In the ultrarelativistic limit, $s \rightarrow 1$, of high final speeds, these plateaus become wide, thus validating the regime of thermality.

3.1. Constant Power Emission

As expected for thermal equilibrium, a stable emission period of constant power is measured by a far-away observer. This is best represented as the change in energy with respect to retarded time, $u = t - r/c$ (r is the distance to the origin), and written as Larmor power, $\bar{P} = dE/du$, such that $\bar{P} = P dt/du = P/(1 - \beta)$, where $P = \mu_0 e^2 \alpha^2 / 6\pi c$, see Equation (7). Here, β is the velocity normalized by c .

The main example here is the trajectory directly related to the lowest-order inner bremsstrahlung in the radiative beta decay [3],

$$\mathbf{r}(t) = \frac{sc}{\kappa} W(e^{\kappa t/c}) \hat{\mathbf{r}}, \tag{16}$$

Here, $\hat{\mathbf{r}}$ is the unit vector in the \mathbf{r} direction, while W is the Lambert product logarithm defined as a solution to equation, $w e^w = x$, such that $w = W(x)$ and $W(0) = 0$. The Larmor power can be computed analytically. Its expression, formulated in terms of u , reads:

$$\bar{P}(u) = \frac{\mu_0 e^2 \kappa^2 s^2 W^2(W + 1 - s)}{6\pi c (W + 1)^4 ((1 + s)W + 1 - s)^3}, \text{ where } W \equiv W[e^{\kappa u/c} (1 - s)]. \tag{17}$$

Equation (17) has a plateau when the final speed of the electron is near the causal limit, $s \rightarrow 1$. Consider analytically two separate limits of high speeds and late times, which reveal, using Equation (2),

$$\bar{P}_c \equiv \lim_{u \rightarrow \infty} \lim_{s \rightarrow 1} \bar{P}(u) = \frac{\mu_0 e^2 \kappa^2}{48\pi c} = \frac{\pi}{12} \frac{k_B^2}{\mu_0 c e^2} T^2. \tag{18}$$

Figure 1 shows $\bar{P}(u)$ at high final asymptotic speeds, $s \sim 1$, and illustrates the constant power plateau indicative of thermal emission.

Keep in mind that we are working with classical (3+1)-dimensional radiation of an electron. Therefore, we notice that Equation (18) is a (1+1)-dimensional classical power-temperature relation, with scaling identical to the standard quantum (1+1)-dimensional Stefan-Boltzmann law [30], which describes (3+1)-dimensional black hole power radiance (see, e.g., [2]),

$$P_q = \frac{\pi k_B^2}{12 \hbar} T^2. \tag{19}$$

In the same way that a single-spatial-dimensional Planck distribution yields Equation (19), an analog Planck distribution, J (without \hbar), or spectral energy density in angular frequency space,

$$J(\omega) = \frac{1}{2\pi} \frac{\mu_0 c e^2 \omega}{e^{\mu_0 c e^2 \omega / k_B T} - 1}, \tag{20}$$

where Equation (3), $\hbar \rightarrow \mu_0 c e^2$, can be applied (as an example), integrated over angular frequency,

$$\int_0^\infty J(\omega) d\omega = \frac{\pi}{12} \frac{k_B^2}{\mu_0 c e^2} T^2, \tag{21}$$

which results in Equation (18). It is natural to suppose a distribution similar to $J(\omega)$ (20) might be responsible for Equation (18); see, e.g., [4]. Such a distribution could lend support for the action correspondence (3), but also corroborate the temperature (2)). It appears that such a distribution would only characterize the radiation during a long-lived constant power emission phase at sufficiently high speeds, $s \sim 1$. Nevertheless, independent of any $J(\omega)$ supposition and the difficulties commensurate with such speculation, the power emission (17) possesses a plateau consistent with Equation (18).

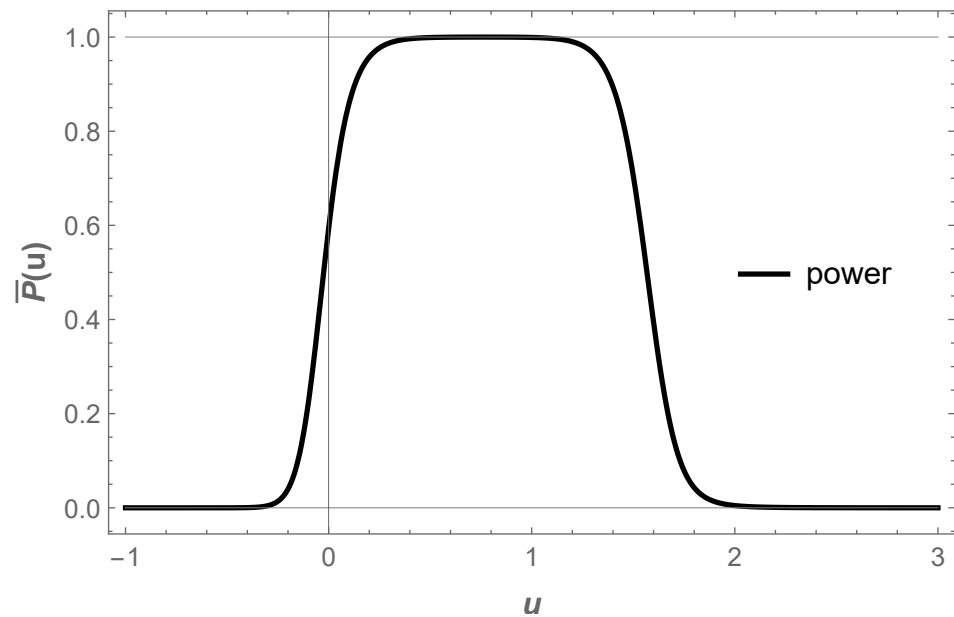


Figure 1. The power, $\bar{P}(u)$ (17), with a plateau demonstrating constant emission when the final speed, s , of the electron is extremely ultra-relativistic, $s = 1 - 10^{-9}$ (or rapidity, $\eta = 10.7$, $s = \tanh \eta$). Here, $\kappa = \sqrt{48\pi}$ and $\mu_0 = c = 1$ and unit charge so that the plateau is at height $\bar{P}(u) = 1$. The Larmor power plateau corroborates the conclusion that, at high electron speeds, the photons, as with the Planck-distributed particles, produced by the mirror (see Equation (26)), find themselves with the temperature, $T = \kappa/2\pi$ (2). The integral of (17) under the curve, is the experimentally observed soft inner bremsstrahlung (IB) energy, E_c (12) or (13).

3.2. Constant Radiation Reaction

Having seen the power plateau in $\bar{P}(u)$ originating from $P = \mu_0 e^2 \alpha^2 / 6\pi c$, let us now turn to the self-force, $F = \mu_0 e^2 \alpha'(\tau) / 6\pi c$, and the associated power, which we call ‘Feynman power’ [31], $\bar{F}(u) = F dr/du = F\beta/(1 - \beta)$, as a function of u ,

$$\bar{F}(u) = \frac{\mu_0 e^2 \kappa^2 s W (s - W - 1) (2(s + 1)W^2 + s + W - 1)}{6\pi c (W + 1)^4 ((s + 1)W - s + 1)^3}, \quad W \equiv W[e^{\kappa u/c} (1 - s)]. \quad (22)$$

Taking the same two separate consecutive limits of high speeds and late times, as in Equation (18), reveals

$$\lim_{u \rightarrow \infty} \lim_{s \rightarrow 1} \bar{F}(u) = -\frac{\mu_0 e^2 \kappa^2}{48\pi c} = -\frac{\pi}{12} \frac{k_B^2}{\mu_0 c e^2} T^2. \quad (23)$$

Figure 2 shows the period of constant Feynman power. This plot, similar to Figure 1 of the Larmor power, \bar{P} , also exhibits a constant period during which the electron emits particles in thermal equilibrium. Equation (23) substantiates Equation (2).

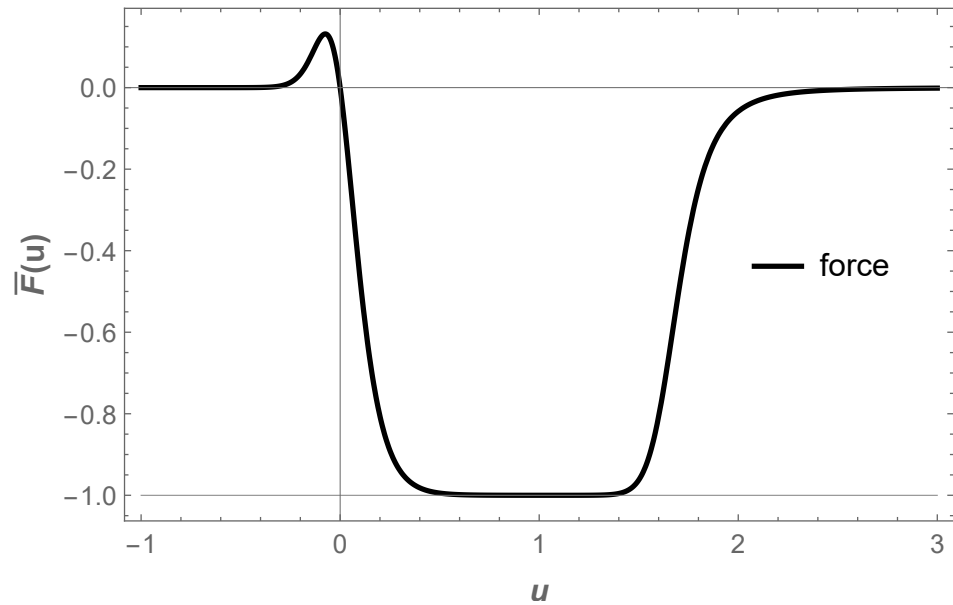


Figure 2. The Feynman power or ‘self-force measure’, $\bar{F}(u)$ (22), with a plateau demonstrating constant self-force when the final speed of the electron is extremely ultra-relativistic, $s = 1 - 10^{-9}$ (or rapidity, $\eta = 10.7$). Here, $\kappa = \sqrt{48\pi}$ and $\mu_0 = c = 1$ and unit charge so that the plateau is at height $\bar{F}(u) = -1$. The Feynman power plateau corroborates the temperature, $T = \kappa/2\pi$ (14). The integral of (22) under the curve is sign-flipped experimentally observed soft IB energy, E_c (13).

3.3. Constant Peel Acceleration

Direct corroboration of an extended period of thermal equilibrium is given by the object $\bar{\kappa}(u) = v''(u)/v'(u)$, where $v = t + r/c$ is the advanced coordinate and the prime denotes a partial derivative with respect to the independent variable, the retarded time, u , in this case. This quantity is called the ‘peeling function’ and has been used in the relativity literature; see, e.g., [32,33]. Following precedent, we call it the ‘peel acceleration’ or ‘peel’ for short.

The peel acceleration typically accompanies thermal particle radiation. For instance, it has been used as a measure of what Carlitz–Willey [34] called ‘local acceleration’. The result for IB is [3]

$$\bar{\kappa}(u) = \frac{2\kappa s W}{(W + 1)^2(1 + (s + 1)W - s)}, \quad W \equiv W[e^{\kappa u/c}(1 - s)]. \tag{24}$$

In the limit of high speeds and late times, one finds:

$$\lim_{u \rightarrow \infty} \lim_{s \rightarrow 1} \bar{\kappa}(u) = \kappa. \tag{25}$$

The peel acceleration, $\bar{\kappa}(u)$, is related to the Lorentz-invariant proper acceleration, α , via the relation, $\bar{\kappa} = 2\alpha e^\eta$, or via the first derivative of the rapidity with respect to retarded time, $\bar{\kappa}(u) = 2\eta'(u)$.

Figure 3 shows the peel acceleration. A quasi-constant peel acceleration is in agreement with the equilibrium of a thermal distribution and constant power emission; however, it is important to underscore the fact that a constant peel acceleration does not describe uniform proper acceleration of the electron.

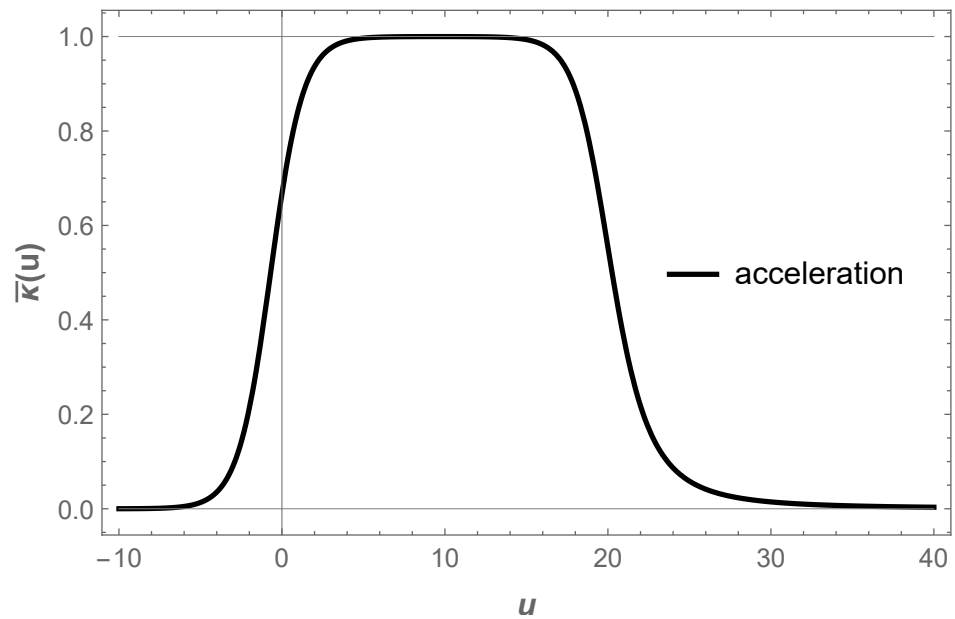


Figure 3. The peel acceleration, $\bar{\kappa}(u)$ (24), with a plateau demonstrating constant local acceleration when the final speed of the electron is extremely ultra-relativistic, $s = 1 - 10^{-9}$ (or rapidity $\eta = 10.7$). Here, $\kappa = c = 1$ so that the plateau is at height $\bar{\kappa}(u) = 1$. The peel acceleration plateau directly substantiates the temperature, $T = \kappa/2\pi$ (2).

4. Planck Spectrum

4.1. Moving Mirror Model

In the moving mirror model (see, e.g., [9,10]), the Bogolubov beta coefficients corroborate radiative equilibrium via an explicit Planck distribution. For IB during beta decay, the Planck distribution is explicitly manifest in Equation (26). Accelerating boundaries radiate soft particles whose long wavelengths lack the capability to probe the internal structure of the source [25]. In the spirit of the analogy, the moving mirror spectrum, with the peel acceleration, κ , supports the appropriate notion of temperature for the soft spectrum of the electron’s IB. Combining the results for each side of the mirror [28] by adding the squares of the Bogolubov beta coefficients, the overall spectrum reads [3]:

$$|\beta_{\omega\omega'}|^2 = \frac{2cs^2\omega\omega'}{\pi\kappa(\omega + \omega')} \frac{a^{-2} + b^{-2}}{e^{2\pi c(\omega+\omega')/\kappa} - 1}. \tag{26}$$

Here, $a = \omega(1 + s) + \omega'(1 - s)$, and $b = \omega(1 - s) + \omega'(1 + s)$, where ω is the out-frequency mode and ω' is the in-frequency mode of the massless scalar field [10]; Davies-Fulling notation [9] is used here. See Figure 4 for an illustration of the symmetry between the frequency modes of the beta modulus (26).

For a consistency check, using the retarded time clock of the observer, the following integrations hold:

$$E_c = - \int_{-\infty}^{\infty} \bar{F}(u) du = \int_{-\infty}^{\infty} \bar{P}(u) du, \tag{27}$$

along with

$$E_q = \int_0^{\infty} \int_0^{\infty} \hbar\omega |\beta_{\omega\omega'}|^2 d\omega d\omega', \tag{28}$$

or

$$E_q = \int_0^{\infty} \int_0^{\infty} \hbar\omega' |\beta_{\omega\omega'}|^2 d\omega d\omega', \tag{29}$$

demonstrating consistency with the conservation of energy. Importantly, this also demonstrates the consistency of the analogy between quantum mirrors and classical electrons.

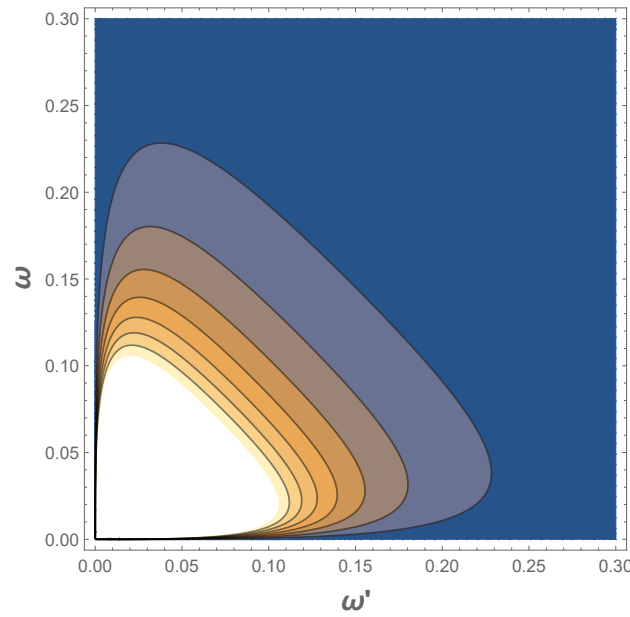


Figure 4. The $|\beta_{\omega\omega'}|^2$ spectrum of Equation (26) in a contour plot. Here, $\kappa = 1$ and $s = 1/2$. Notice the symmetry between the frequency modes ω and ω' . The qualitative shape is indicative of the Bose–Einstein statistics explicit in the Planck factor of Equation (26).

The Planck spectrum of Equation (26) is robust to both high-frequency approximations and low-frequency approximations. This is made particularly explicit by considering high final speeds, $s \approx 1$, then using either frequency approximation. Consider the high frequency, $\omega' \gg \omega$ approximation [1]. To leading order, one retrieves

$$|\beta_{\omega\omega'}|^2 = \frac{c}{2\pi\kappa\omega} \frac{1}{e^{2\pi c\omega'/\kappa} - 1}. \tag{30}$$

Likewise, considering high final speeds and the low-frequency, $\omega' \ll \omega$, approximation switches the prime on the ω' s, leading to (see, e.g., [35])

$$|\beta_{\omega\omega'}|^2 = \frac{c}{2\pi\kappa\omega'} \frac{1}{e^{2\pi c\omega/\kappa} - 1}, \tag{31}$$

demonstrating Planck factor validity to either frequency approximation. The spectrum plot of the moving mirror radiation (Figure 4) illustrates the explicit Planck factor, which demonstrates the particles are distributed with a temperature given in Equation (2): $N(\omega) = \int d\omega' |\beta_{\omega\omega'}|^2$.

4.2. Relation to Electrons and Black Holes

The moving mirror model, or dynamical Casimir effect (DCE), is closely related to electron radiation and black holes. Having the radiation spectrum of the mirror, it is possible to obtain the radiation spectra for these related systems. Let us explain the details.

The connection between DCE and point charge radiation has been suggested long ago (by Unruh and Wald [19] and by Ford and Vilenkin [18]), and has been developing since; see [12–16,36]. Eventually, this led to the realization that there is an exact functional identity between the radiation spectra in these models [4,37]. In papers [4,37], the corresponding transformation recipe was derived and checked; it was established that an electron corresponding to the mirror equation (26) radiates with the spectrum,

$$I(\omega) = \frac{\mu_0 c e^2}{2\pi^2} \left(\frac{\tanh^{-1} s/c}{s/c} - 1 \right) \frac{2\pi c\omega/\kappa}{e^{2\pi c\omega/\kappa} - 1}. \tag{32}$$

One can immediately see the aforementioned Planck form of the spectrum with the same temperature as the mirror.

Thermal emission is not so surprising considering the Larmor power plateau (Figure 1), Feynman power plateau (Figure 2), and acceleration plateau (Figure 3). It is also in agreement with the close analogy for quantum and classical quantities of powers [16,17] and self-forces [18,20] between mirrors and electrons.

Black hole evaporation [1], and, in particular, the collapse of a null shell in the s -wave approximation, can also be described as a DCE [29,38]. This black hole–moving mirror correspondence has been successfully applied, for example, to such important spacetimes as Schwarzschild [39,40], Reissner–Nordström [41], and Kerr [42] metrics. In the triarchy ‘moving mirrors–electrons–black holes’, the quantum-classical temperature relation between Equation (1) and Equation (2) has been found, supporting the analog bridge of Section 1.1. It is an interesting question about which geometry corresponds to mirror Equation (26); we leave this for a future investigation.

5. Stefan–Boltzmann Law

It is natural to consider how the classical power scales according to the (1+1)-dimensional Stefan–Boltzmann law [30],

$$P \sim T^2, \tag{33}$$

rather than the (3+1)-dimensional Stefan–Boltzmann law,

$$P \sim AT^4, \tag{34}$$

which governs the power radiated from a black body in terms of its temperature. A first heuristic answer is the classical electron is a point particle with no area. We note that in flat spacetime, Equation (34) is the relevant contrasting expression for the energy transmission of a single photon polarization out of a closed hot black body surface with temperature T and area A into 3-dimensional space.

Ultimately, a better understanding may be related to black hole radiance. The scaling could occur for the same reason that black holes are one-dimensional information channels [2], whose power also scales according to $P \sim T^2$. In the context of Equation (2), the electron’s constant power peaks at exactly Equation (18), which is the analog of the known all-time constant equilibrium emission of the quantum stress tensor for the eternal thermal Carlitz–Willey moving mirror [11] and the late-time Schwarzschild mirror [39]. The 1+1 spacetimes corresponding to these mirrors exhibit horizons and have been considered as analogous to black holes; see, e.g., [29].

A complete investigation concerning the entropy and information flow related to the quadratic temperature dependence of the electron’s power emission is a worthwhile study but is outside the scope of this study. Nevertheless, in Sections 5.1–5.4, we make some necessary preliminary progress regarding exploring this Stefan–Boltzmann law in the context of its origin from electromagnetic spectral analysis, statistically maximized entropy, and classical thermodynamics.

5.1. Classical Stefan–Boltzmann

Using the aforementioned Stoney scale [5], the classical temperature of radiation from an electron is, regarding Equation (2),

$$T = \frac{\mu_0 e^2 \kappa}{2\pi k_B}. \tag{35}$$

Contrast this with the Kelvin scale and the temperature resembles the quantum Davies–Fulling–Unruh effect,

$$T = \frac{\hbar \kappa}{2\pi c k_B}, \tag{36}$$

except, here, κ is the peel (not uniform proper acceleration). The Davies–Fulling–Unruh expression is well-understood as a quantum effect and the proposed temperature of radiation emitted by an electron in the literature, e.g., [43–46].

However, the classical reasoning for Equation (35) is two-fold: dynamics and spectral analysis. Dynamically, one can compute the power [3] and find it agrees with the Stefan–Boltzmann law, $P \sim T^2$, at the plateau for high speeds, $s \approx 1$. The spectral analysis done in Ref. [3] confirms the Planck distribution, using the spectral distribution, $dI(\omega)/d\Omega = dE/d\omega d\Omega$ [4],

$$I(\omega) = \frac{\mu_0 c e^2}{2\pi^2} \left(\frac{\eta}{s} - 1\right) \frac{M}{e^M - 1}, \tag{37}$$

where the dimensionless M is an analog to $\hbar\omega/(k_B T)$:

$$M \equiv \frac{\mu_0 c e^2}{k_B T} \omega, \tag{38}$$

with temperature (35). Moreover, as we see in the next sub-section; the characteristic frequency of the photons confirms the Stefan–Boltzmann law using basic classical electromagnetic spectral analysis.

5.2. Stefan–Boltzmann from Spectra

Let us assume thermal emission is described by a heuristic and characteristic frequency of the radiation when the electron is ultra-relativistic. Then, this frequency is

$$\frac{P}{k_B T} = \int_0^\infty \mathcal{I}(f) df, \tag{39}$$

where the left-hand side is the ratio of the thermal power divided by the average energy in equilibrium, $k_B T$, as given by the equipartition theorem for the canonical ensemble. Here,

$$\mathcal{I}(f) = \frac{I(f)}{I_{\text{infra}}} = \frac{M}{e^M - 1} \tag{40}$$

is the dimensionless spectrum, as a function of frequency, $f = \omega/(2\pi)$, so that $M = \frac{\mu_0 c e^2}{k_B T} 2\pi f$. Here, I_{infra} is the infrared limit of the spectrum; see Equation (58) in Ref. [4] and Equation (9) above. Integrating Equation (39) over f provides the required result for the power,

$$P = \frac{\pi}{12} \frac{k_B^2}{\mu_0 c e^2} T^2, \tag{41}$$

which is same T^2 temperature scaling as the (1+1)-dimensional Stefan–Boltzmann law [30] describing black hole radiance [47] and electron radiance [3], as derived straight from the dynamics of the trajectory using the proper acceleration via the Larmor power.

While the quadratic scaling of temperature in Equation (41) describes thermal noise power transfer in one-dimensional optical systems [30],

$$P = \frac{\pi}{6} \frac{k_B^2}{\hbar} T^2, \tag{42}$$

the most known case of one-dimensional thermal radiation is Johnson noise or Nyquist noise of electrical circuits [48],

$$P = \frac{\pi}{12} \frac{k_B^2}{\hbar} T^2, \tag{43}$$

which is also proportional to temperature squared, yet with an emissivity of $\epsilon = 1/2$. This lower emissivity arises from the fact that photons in electrical networks are polarised, and thus the resistors act as gray bodies rather than black bodies.

5.3. Stefan–Boltzmann from Entropy

Consider the classical accelerating electron in thermal equilibrium with its environment. By the second law of thermodynamics, the probability distribution, $p(n)$, must be such as to maximize the system entropy. Following Oliver [48], we determine $p(n)$, where n is an integer. Here, n is the number of photons emitted by the ensemble system. We start with the definition of Gibbs entropy for the electron,

$$S_e = -k_B \sum_{n=0}^{\infty} p(n) \ln p(n), \tag{44}$$

with constraints of unitarity and averaging

$$\sum_{n=0}^{\infty} p(n) = 1, \quad \sum_{n=0}^{\infty} n p(n) = \bar{n}. \tag{45}$$

The first constraint demands n must be some integer. The second constraint provides the average number of photons present where \bar{n} need not be an integer.

The above summations will not vary as the distribution is varied as long as the entropy is maximized. A linear sum of all three,

$$\sum p(n) \ln p(n) + \mathcal{A} \sum n p(n) + \mathcal{B} \sum p(n), \tag{46}$$

where \mathcal{A} and \mathcal{B} are constants, have then zero variation,

$$\sum [\ln p(n) + 1 + \mathcal{A}n + \mathcal{B}] \delta p(n) = 0, \tag{47}$$

for small perturbations, $\delta p(n)$, of $p(n)$. This is satisfied if

$$\ln p(n) + 1 + \mathcal{A}n + \mathcal{B} = 0, \tag{48}$$

which provides a probability distribution,

$$p(n) = e^{-1-\mathcal{B}} e^{-\mathcal{A}n}. \tag{49}$$

Using the averaging and unitarity constrain, one obtains:

$$p(n) = (1 - e^{-\mathcal{A}}) e^{-n\mathcal{A}}, \quad \bar{n} = \frac{1}{e^{\mathcal{A}} - 1}. \tag{50}$$

Using the distribution $p(n)$ in the entropy, one then finds:

$$\frac{S_e}{k_B} = \frac{\ln(e^{\mathcal{A}} - 1)}{e^{\mathcal{A}} - 1} - \frac{\ln(-e^{-\mathcal{A}} + 1)}{-e^{-\mathcal{A}} + 1}. \tag{51}$$

The electron can be imagined to absorb an average non-integer classical energy (no \hbar),

$$\bar{W}(\omega) = \bar{n} \mu_0 c e^2 \omega, \tag{52}$$

in analog to $\bar{n} \hbar \omega$, suitable for the Stoney scale (nominally, $\mu_0 c e^2$ is, as we have seen, more than ten times smaller than \hbar). For a gray body with absorptivity a , average absorbed radiation is $\bar{n} \hbar \omega \cdot a$. In our setup, $a \sim \mu_0 c e^2 / \hbar$; see Section 5.5.

The average energy (52) comes from the surrounding outside thermal environment, producing an entropy change,

$$S_o = -\frac{\bar{n} \mu_0 c e^2 \omega}{T} = k_B \frac{1}{e^{\mathcal{A}} - 1} M, \tag{53}$$

in the rest of the system ‘outside’ the electron. The dimensionless M is the Stoney temperature scale version of $\hbar\omega/(k_B T)$:

$$M \equiv \frac{\mu_0 c e^2}{k_B T} \omega. \tag{54}$$

The total change, $\Delta S = S_e + S_o$, in entropy will progress until, in equilibrium, ΔS is maximized. Taking a derivative of ΔS with respect to \mathcal{A} provides

$$\frac{1}{4} \operatorname{csch}^2\left(\frac{\mathcal{A}}{2}\right) (M - \mathcal{A}) = 0. \tag{55}$$

This is true if $\mathcal{A} = M$. The probability distribution and \bar{n} is then written as

$$p(n) = (1 - e^{-M}) e^{-nM}, \quad \bar{n} = \frac{1}{e^M - 1}. \tag{56}$$

The average classical energy absorbed by the electron is, therefore

$$\bar{W}(\omega) = \bar{n} \mu_0 c e^2 \omega = \frac{1}{e^M - 1} M k_B T. \tag{57}$$

The total thermal power is found by

$$P = \int_0^\infty \bar{W}(\omega) \frac{d\omega}{2\pi} = \frac{(k_B T)^2}{\mu_0 c e^2} \frac{1}{2\pi} \int_0^\infty \frac{M}{e^M - 1} dM, \tag{58}$$

whose integral is $\pi^2/6$, so that

$$P = \frac{\pi}{12} \frac{k_B^2}{\mu_0 c e^2} T^2, \tag{59}$$

which scales as the (1+1)-dimensional Stefan–Boltzmann law. This is classical thermal noise from a single accelerating electron [4].

5.4. Stefan–Boltzmann from Thermodynamics

The Stefan–Boltzmann law can be derived from thermodynamics alone in two steps (see the original paper [49]). In this derivation, we do not assume any particular form of the spectral frequency distribution.

5.4.1. Maxwell Relations

First, consider the Maxwell relations for the entropy. Let U be the radiation energy, and then $U = \rho(T) V$, where $\rho(T)$ is the energy density (we suppose that it depends only on the temperature T). Then, one has:

$$dU = T dS - p dV, \tag{60}$$

from which it follows that

$$dS = \frac{1}{T} (dU + p dV) = \frac{1}{T} \left(V \frac{d\rho}{dT} dT + (\rho + p) dV \right). \tag{61}$$

From this, one can read off the first derivatives:

$$\begin{aligned} \left(\frac{\partial S}{\partial T}\right)_V &= \frac{V}{T} \frac{d\rho}{dT}, \\ \left(\frac{\partial S}{\partial V}\right)_T &= \frac{\rho + p}{T}. \end{aligned} \tag{62}$$

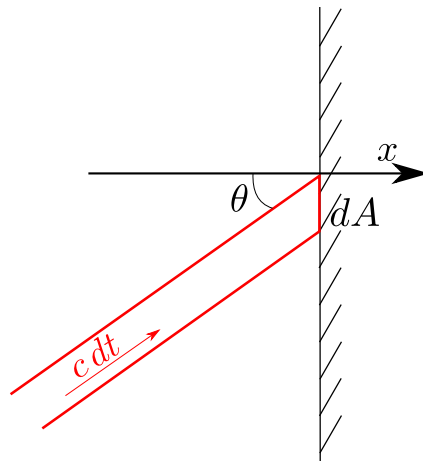


Figure 5. Radiation in a box. See text for details.

Computing the second derivative, $\partial^2 S / \partial T \partial V$, in two different ways, one obtains:

$$\left(\frac{\partial p}{\partial T}\right)_V = \frac{\rho + p}{T}. \tag{63}$$

To finish the derivation, one needs an equation of state. Let us derive it.

5.4.2. Equation of State in 3+1 Dimensions

We start with the (3+1)-dimensional case. Consider the radiation inside a perfectly reflecting box (the perfect reflectivity assumption is actually not mandatory, but it simplifies the derivations.); see Figure 5. When radiation waves hit the box wall, the waves are reflected and therefore transfer some of the momentum to the wall. Take some area element, dA , of the wall, and let the x axis be perpendicular to the wall in this vicinity. Let θ be the angle between the x axis and the wavevector of an incoming electromagnetic wave. Total momentum of the radiation coming from the solid angle, $d\Omega$, is given by the energy divided by c :

$$|\vec{P}| = \frac{1}{c} \cdot \rho \cdot c \, dt \cos \theta \cdot dA \cdot \frac{d\Omega}{4\pi} = \rho \cos \theta \frac{d\Omega}{4\pi} dA \, dt. \tag{64}$$

The momentum transfer is twice the x -projection:

$$\Delta P_x = 2|\vec{P}| \cos \theta = 2\rho \cos^2 \theta \frac{d\Omega}{4\pi} dA \, dt. \tag{65}$$

Dividing the momentum Equation (65) by dt , one obtains the force, and then, dividing by dA , the pressure. Integration over the solid angle, $d\Omega$, one side of the wall finally provides

$$p = \frac{2\rho}{4\pi} \int_0^{2\pi} d\phi \int_0^1 \cos^2 \theta \, d \cos \theta = \frac{1}{3} \rho. \tag{66}$$

Plugging Equation (66) into Equation (63) yields an ordinary differential equation, whose solution,

$$\rho = C \cdot T^4, \tag{67}$$

is determined only up to an arbitrary constant, C . Note that, in general, this constant must be positive, but, otherwise, it is not restricted by the above derivation.

5.4.3. Other Dimensions

What happens in lower dimensions?

Consider a lower dimensional system embedded in 3-dimensional space. This means that one can still consider electromagnetic waves even for a one-dimensional system. Then, the only point to modify in the derivation in Section 5.4.2 is the solid angle part.

When the space is two-dimensional, there is no solid angle, and θ represents the polar angle. The integration in this case provides the result $p = \rho/2$. In a one-dimensional system, there are no angles at all, and one obtains: $p = \rho$.

From this, one can derive the corresponding Stefan–Boltzmann laws. We summarize the results in Table 1. For a body immersed in an equilibrium radiation heat bath, the radiated energy per second is proportional to the energy density of the ambient radiation (the proportionality coefficient depends on the surface area and absorptivity).

Table 1. Stefan–Boltzmann law in various dimensions. See text for details.

Dimension	Equation of State	Stefan–Boltzmann Law
1	$p = \rho$	$P \sim T^2$
2	$p = \rho/2$	$P \sim T^3$
3	$p = \rho/3$	$P \sim T^4$

5.4.4. Lessons

Using only thermodynamics, the Stefan–Boltzmann law is determined by the dimensionality of the space, up to a coefficient. The coefficient is undetermined in this derivation: it depends on the physical system under consideration and is not fixed. In particular, Equation (41) is acceptable because of the scaling.

It is quite instructive to find that Equation (41) represents the Stefan–Boltzmann law in one-dimensional space; indeed what one would expect from a moving mirror in one spatial and one temporal dimension.

5.5. Electron as a Gray Body

In general, the Stefan–Boltzmann law relates the total power to the temperature. In 1+1 dimensions [30],

$$P_{\text{black body}} = \frac{\pi k_B^2}{6\hbar} AT^2 ; \tag{68}$$

see, e.g., the discussion below Equation (10) in Ref. [30]. Here, A is the body’s “surface area”: in 1+1 dimensions, $A = 1$ (one side) or $A = 2$ (two sides). In the moving mirror setup, it is natural to take $A = 1$ as the observer is most often on one (the right) side of the mirror.

We can compare Equation (68) to the power in our setup. Regarding the quantum radiation power in Equation (19),

$$P_q = \frac{\pi k_B^2}{12\hbar} T^2 , \tag{69}$$

one can see that Equation (69) corresponds to a gray body with absorptivity, $a = 1/2$ (see, e.g., Section 3 in Ref. [30]).

The classical radiation power in Equation (18), when re-expressed in terms of the quantum temperature scale (see Equation (3)), becomes

$$\bar{P}_e = \frac{\mu_0 e^2 \kappa^2}{48\pi c} = \frac{\mu_0 c e^2}{\hbar} \frac{\pi}{12} \frac{k_B^2}{\hbar} T^2 , \tag{70}$$

which is also proportional to the square of the temperature, T^2 . One can see that Equations (68) and (70) are not quite the same; they are off by a factor (we take $A = 1$, which is natural from the mirror’s perspective):

$$\bar{P}_e = \frac{\mu_0 c e^2}{2\hbar} P_{\text{black body}}, \quad \frac{\mu_0 c e^2}{2\hbar} \approx 0.0458. \quad (71)$$

The existence of a coefficient tells us that the electron may be considered a (1+1)-dimensional quantum-radiating gray body that absorbs only about 4.58% of the incoming radiation.

The physical meaning of this absorptivity is intriguing and deserves further investigation, which we leave for future studies.

6. Conclusions

In this paper, we have helped to develop the analogy between the dynamical Casimir, black hole, and electron radiation temperature. We have found periods of constant power and radiation reaction, indicative of thermal equilibrium. Indeed, by analogy with the dynamical Casimir effect, we have demonstrated thermality, in part, by the symmetry between frequency modes in the analog spectrum for the radiation of an accelerated electron, which, at ultra-relativistic speeds, manifests explicit uniform plateau radiation emission commensurate with the spectral Planck distribution. The constant temperature is consistent with the constant periods of power, self-force, and peel acceleration.

Author Contributions: Conceptualization, methodology, validation, formal analysis, investigation, M.R.R.G. and E.I.; writing—original draft preparation, M.R.R.G.; writing—review and editing, M.R.R.G. and E.I.; visualization, M.R.R.G. and E.I.; funding acquisition, M.R.R.G. All authors have read and agreed to the published version of the manuscript.

Funding: Funding comes in part from the FY2021-SGP-1-STMM Faculty Development Competitive Research Grant No. 021220FD3951 at Nazarbayev University, Kazakhstan.

Data Availability Statement: Not applicable.

Acknowledgments: We extend thanks to Paul Davies, Eric Linder, and Morgan Lynch for insightful discussion.

Conflicts of Interest: The authors declare no conflict of interest.

References

- Hawking, S. Particle creation by black holes. *Commun. Math. Phys.* **1975**, *43*, 199–220. [CrossRef]
- Bekenstein, J.D.; Mayo, A.E. Black holes are one-dimensional. *Gen. Rel. Grav.* **2001**, *33*, 2095–2099. [CrossRef]
- Good, M.R.R.; Davies, P.C.W. Infrared acceleration radiation. *Found. Phys.* **2023**, *53*, 53. [CrossRef]
- Ievlev, E.; Good, M.R.R. Thermal Larmor radiation. *arXiv* **2023**. <https://doi.org/10.48550/arXiv.2303.03676>.
- Johnstone Stoney, G. VIII. On the physical units of nature. *Sci. Proc. R. Dublin Soc.* **1883**, *3*, 51–60. Available online: <https://books.google.ch/books?id=R79WAAAIAAJ&pg=PA51> (accessed on 21 June 2023).
- Barrow, J.D. Natural Units Before Planck. *Q. J. R. Astron. Soc.* **1983**, *24*, 24–26. Available online: <https://ui.adsabs.harvard.edu/abs/1983QJRAS...24...24B/abstract> (accessed on 21 June 2023).
- Moore, G.T. Quantum theory of the electromagnetic field in a variable-length one-dimensional cavity. *J. Math. Phys.* **1970**, *11*, 2679–2691. [CrossRef]
- DeWitt, B.S. Quantum field theory in curved space-time. *Phys. Rep.* **1975**, *19*, 295–357. [CrossRef]
- Davies, P.; Fulling, S. Radiation from moving mirrors and from black holes. *Proc. R. Soc. Lond. A* **1977**, *A356*, 237–257. [CrossRef]
- Fulling, S.A.; Davies, P.C.W. Radiation from a moving mirror in two dimensional space-time: Conformal anomaly. *Proc. R. Soc. Lond. A* **1976**, *348*, 393–414. [CrossRef]
- Carlitz, R.D.; Willey, R.S. Reflections on moving mirrors. *Phys. Rev. D* **1987**, *36*, 2327–2335. [CrossRef]
- Ritus, V. The Symmetry, inferable from Bogoliubov transformation, between the processes induced by the mirror in two-dimensional and the charge in four-dimensional space-time. *J. Exp. Theor. Phys.* **2003**, *97*, 10–23.
- Ritus, V. Vacuum-vacuum amplitudes in the theory of quantum radiation by mirrors in 1+1-space and charges in 3+1-space. *Int. J. Mod. Phys. A* **2002**, *17*, 1033–1040. [CrossRef]
- Ritus, V. Symmetries and causes of the coincidence of the radiation spectra of mirrors and charges in (1+1) and (3+1) spaces. *J. Exp. Theor. Phys.* **1998**, *87*, 25–34. [CrossRef]
- Nikishov, A.; Ritus, V. Emission of scalar photons by an accelerated mirror in 1+1 space and its relation to the radiation from an electrical charge in classical electrodynamics. *J. Exp. Theor. Phys.* **1995**, *81*, 615–624. Available online: <http://jetp.ras.ru/cgi-bin/e/index/e/81/4/p615?a=list> (accessed on 21 June 2023).

16. Zhakenuly, A.; Temirkhan, M.; Good, M.R.R.; Chen, P. Quantum power distribution of relativistic acceleration radiation: Classical electrodynamic analogies with perfectly reflecting moving mirrors. *Symmetry* **2021**, *13*, 653. [CrossRef]
17. Good, M.R.R.; Linder, E.V. Quantum power: A Lorentz invariant approach to Hawking radiation. *Eur. Phys. J. C* **2022**, *82*, 204. [CrossRef]
18. Ford, L.; Vilenkin, A. Quantum radiation by moving mirrors. *Phys. Rev. D* **1982**, *25*, 2569–2575. [CrossRef]
19. Unruh, W.G.; Wald, R.M. Acceleration radiation and generalized second law of thermodynamics. *Phys. Rev. D* **1982**, *25*, 942–958. [CrossRef]
20. Myrzakul, A.; Xiong, C.; Good, M.R.R. CGHS black hole analog moving mirror and its relativistic quantum information as radiation reaction. *Entropy* **2021**, *23*, 1664. [CrossRef]
21. Zangwill, A. *Modern Electrodynamics*; Cambridge University Press: Cambridge, UK, 2013. [CrossRef]
22. Jackson, J.D. *Classical Electrodynamics*; John Wiley & Sons, Inc.: Hoboken, NJ, USA, 1999. Available online: <https://www.scribd.com/doc/200995304/Classical-Electrodynamics-3rd-Ed-1999-John-David-Jackson> (accessed on 21 June 2023).
23. Chang, C.S.W.; Falkoff, D.L. On the continuous gamma-radiation accompanying the beta-decay of nuclei. *Phys. Rev.* **1949**, *76*, 365–371. [CrossRef]
24. Ballagh, H.C. Observation of muon inner bremsstrahlung in deep inelastic neutrino scattering. *Phys. Rev. Lett.* **1983**, *50*, 1963–1966. [CrossRef]
25. Strominger, A. Lectures on the infrared structure of gravity and gauge theory. *arXiv* **2017**. [CrossRef]
26. Cardoso, V.; Lemos, J.P.S.; Yoshida, S. Electromagnetic radiation from collisions at almost the speed of light: An Extremely relativistic charged particle falling into a Schwarzschild black hole. *Phys. Rev. D* **2003**, *68*, 084011. [CrossRef]
27. Tomaras, T.N.; Toumbas, N. IR dynamics and entanglement entropy. *Phys. Rev. D* **2020**, *101*, 065006. [CrossRef]
28. Good, M.R.R. Reflecting at the speed of light. In *Memorial Volume for Kerson Huang*; Phua, K.K., Low, H.B., Xiong, C., Eds.; World Scientific: Singapore, 2017; pp. 113–116. [CrossRef]
29. Wilczek, F. Quantum purity at a small price: Easing a black hole paradox. In *Proceedings of the International Symposium on Black holes, Membranes, Wormholes and Superstrings*, Huston, TX, USA, 16–18 January 1992; Kalara, S., Nanopoulos, D.V., Eds.; World Scientific: Singapore, 1993; pp. 1–21. [CrossRef]
30. Landsberg, P.T.; De Vos, A. The Stefan-Boltzmann constant in n -dimensional space. *J. Phys. A Math. Gen.* **1989**, *22*, 1073. [CrossRef]
31. Feynman, R.P. *Feynman Lectures on Gravitation*; CRC Press/Taylor & Francis Group: Boca Raton, FL, USA, 2003. [CrossRef]
32. Bianchi, E.; Smerlak, M. Entanglement entropy and negative energy in two dimensions. *Phys. Rev. D* **2014**, *90*, 041904. [CrossRef]
33. Barcelo, C.; Liberati, S.; Sonego, S.; Visser, M. Minimal conditions for the existence of a Hawking-like flux. *Phys. Rev. D* **2011**, *83*, 041501. [CrossRef]
34. Carlitz, R.D.; Willey, R.S. Lifetime of a black hole. *Phys. Rev. D* **1987**, *36*, 2336–2341. [CrossRef]
35. Fulling, S.A. Review of some recent work on acceleration radiation. *J. Mod. Opt.* **2005**, *52*, 2207–2213. [CrossRef]
36. Ritus, V.I. Finite value of the bare charge and the relation of the fine structure constant ratio for physical and bare charges to zero-point oscillations of the electromagnetic field in the vacuum. *Phys. Usp.* **2022**, *65*, 468–486. [CrossRef]
37. Ievlev, E.; Good, M.R.R.; Linder, E.V. Thermal radiation from an electron with Schwarzschild-Planck acceleration. *arXiv* **2023**. [CrossRef]
38. Cong, W.; Tjoa, E.; Mann, R.B. Entanglement harvesting with moving mirrors. *J. High Energy Phys.* **2019**, *6*, 21. [CrossRef]
39. Good, M.R.R.; Anderson, P.R.; Evans, C.R. Mirror reflections of a black hole. *Phys. Rev. D* **2016**, *94*, 065010. [CrossRef]
40. Good, M.R.R. Spacetime continuity and quantum information loss. *Universe* **2018**, *4*, 122. [CrossRef]
41. Good, M.R.R.; Ong, Y.C. Particle spectrum of the Reissner–Nordström black hole. *Eur. Phys. J. C* **2020**, *80*, 1169. [CrossRef]
42. Good, M.R.R.; Foo, J.; Linder, E.V. Accelerating boundary analog of a Kerr black hole. *Class. Quant. Grav.* **2021**, *38*, 085011. [CrossRef]
43. Bell, J.S.; Leinaas, J.M. Electrons as accelerated thermometers. *Nucl. Phys. B* **1983**, *212*, 131–150. [CrossRef]
44. Myhrvold, N.P. Thermal Radiation from accelerated electrons. *Ann. Phys.* **1985**, *160*, 102–113. [CrossRef]
45. Kolbenstvedt, H. Unruh-Davies effect and the Larmor radiation formula in hyperbolic motion. *Phys. Scr.* **2001**, *63*, 313–315. [CrossRef]
46. Landulfo, A.G.; Fulling, S.A.; Matsas, G.E. Classical and quantum aspects of the radiation emitted by a uniformly accelerated charge: Larmor-Unruh reconciliation and zero-frequency Rindler modes. *Phys. Rev. D* **2019**, *100*, 045020. [CrossRef]
47. Bekenstein, J.D. Black holes and information theory. *Contemp. Phys.* **2003**, *45*, 31–43. [CrossRef]
48. Nyquist, H. Thermal agitation of electric charge in conductors. *Phys. Rev.* **1928**, *32*, 110–113. [CrossRef]
49. Stefan, J. Über die Beziehung zwischen der Wärmestrahlung und der Temperatur. *Sitzungsber. Kaiserl. Akad. Wiss. Math.-Naturwiss. Cl.* **1879**, *LXXIX*, 391–428. Available online: <http://www.ing-buero-ebel.de/strahlung/Original/Stefan1879.pdf> (accessed on 21 June 2023).

Disclaimer/Publisher’s Note: The statements, opinions and data contained in all publications are solely those of the individual author(s) and contributor(s) and not of MDPI and/or the editor(s). MDPI and/or the editor(s) disclaim responsibility for any injury to people or property resulting from any ideas, methods, instructions or products referred to in the content.

Article

First- and Second-Order Forces in the Asymmetric Dynamical Casimir Effect for a Single $\delta - \delta'$ Mirror

Matthew J. Gorban ^{1,2,*}, William D. Julius ^{1,2}, Patrick M. Brown ^{1,2}, Jacob A. Matulevich ^{1,2},
Ramesh Radhakrishnan ^{1,2} and Gerald B. Cleaver ^{1,2}

¹ Early Universe, Cosmology and Strings (EUCOS) Group, Center for Astrophysics, Space Physics and Engineering Research (CASPER), Baylor University, Waco, TX 76798, USA; william_julius1@baylor.edu (W.D.J.); patrick_brown2@baylor.edu (P.M.B.); jacob_matulevich1@baylor.edu (J.A.M.); ramesh_radhakrishna1@baylor.edu (R.R.); gerald_cleaver@baylor.edu (G.B.C.)

² Department of Physics, Baylor University, Waco, TX 76798, USA

* Correspondence: matthew_gorban1@baylor.edu

Abstract: Here, we consider an asymmetric $\delta - \delta'$ mirror undergoing time-dependent interactions with a massless scalar field in $1 + 1$ dimensions. Using fluctuation-dissipation theory for a mirror in vacuum, we compute the force on a moving $\delta - \delta'$ mirror with time-dependent material properties. We investigate the first-order forces arising from the two distinct fluctuation sources and calculate the linear susceptibility in each case. We then plot the resulting forces. At the second order, we also find the independent contributions to the total force as well as the force that arises from the interference phenomena between the two fluctuation sources.

Keywords: quantum vacuum; vacuum fluctuation; dynamical Casimir effect; Casimir forces; asymmetry; asymmetric excitations; asymmetric dynamical Casimir effect

1. Introduction

A mirror subject to time-dependent interactions with the quantum vacuum, in which its position or boundary (material) properties may fluctuate, will experience the dynamical Casimir effect (DCE) and produce real particles. This phenomenon has been thoroughly investigated for numerous theoretical configurations (see [1–3] for several detailed reviews of this topic) and has also been experimentally verified [4]. There has been recent interest in understanding the consequences of modifying DCE systems by introducing asymmetric boundary conditions to a mirror undergoing time-dependent interactions with the quantum vacuum [5–9]. This asymmetry leads to an asymmetric spectrum of produced particles in what is now known as the asymmetric dynamical Casimir effect (ADCE). To better understand the ADCE, it is convenient to investigate the interaction between the quantum vacuum and a partially transparent mirror in a $(1 + 1)D$ (dimensional) spacetime. This is achieved by modeling the mirror as $\delta - \delta'$ potential [5,6,10–16] (δ' being the spatial derivative of the Dirac δ function). Previous literature has explored the ADCE spectrum of a moving $\delta - \delta'$ mirror [5] and a $\delta - \delta'$ mirror with time-dependent material properties [6] as well as when the mirror possesses both of these independent fluctuation sources. In this latter case, there is an interference effect between the two sources that modifies the total asymmetric spectrum of produced particles [9].

An asymmetric production of photons on either side of the mirror leads to an unbalanced force on the mirror due to the imbalance in the number of particles produced by the two sides of the mirror [6–8,17]. Specifically, in the case of a $\delta - \delta'$ mirror with time-dependent properties, the initially stationary mirror will be perturbed in such a way that the imbalance in particle production will induce motion upon the mirror [6]. The quantum vacuum will, in turn, act as a dissipative medium and react to the motion of

Citation: Gorban, M.J.; Julius, W.D.; Brown, P.M.; Matulevich, J.A.; Radhakrishnan, R.; Cleaver, G.B. First- and Second-Order Forces in the Asymmetric Dynamical Casimir Effect for a Single $\delta - \delta'$ Mirror. *Physics* **2024**, *6*, 760–779. <https://doi.org/10.3390/physics6020047>

Received: 31 December 2023

Revised: 16 February 2024

Accepted: 1 March 2024

Published: 14 May 2024



Copyright: © 2024 by the authors. Licensee MDPI, Basel, Switzerland. This article is an open access article distributed under the terms and conditions of the Creative Commons Attribution (CC BY) license (<https://creativecommons.org/licenses/by/4.0/>).

objects moving through it. For a perfectly reflective mirror moving in (1 + 1)D spacetime, a dissipative reaction force acts on the mirror:

$$F(t) = \frac{\hbar}{6\pi c^2} \frac{d^3}{dt^3} q(t), \tag{1}$$

which is proportional to the third time derivative of the mirror’s position, $q(t)$. Here, \hbar is the reduced Planck constant and c is the speed of light. Thus, to fully understand the forces present in the $\delta - \delta'$ system, one must account for both the force from the radiation pressure generated by the asymmetry in particles and the dissipative effects of the object moving through the quantum vacuum.

In this paper, we compute the full spectrum of forces for a moving $\delta - \delta'$ mirror with time-dependent boundary conditions using fluctuation–dissipation theory [18–20]. At first-order, we calculate the independent force contributions from both the motion of the mirror and from its time-dependent material properties by first calculating the linear susceptibility. By prescribing a specific form to the fluctuation sources, we are able to plot the mean force on the mirror for different magnitudes of λ_0 , which controls the degree of asymmetry in the $\delta - \delta'$ mirror. In addition to explicit first-order forces, the second-order forces are presented after first deriving the second-order correction to the output field. At second-order, the forces resulting from the two independent fluctuation sources are again found along with the addition of a third force that results from the interference between the motion of the mirror and its changing properties.

The remainder of this paper is organized as follows. In Section 2, we review fluctuation–dissipation theory [18], which is used to calculate the susceptibility and force. Section 3 goes over the scattering formalism, which describes the interaction between the quantum vacuum and the $\delta - \delta'$ mirror. Here, we also derive the necessary second-order corrections to the output field. The first-order forces are then calculated in Section 4, which also includes numerically integrated plots of the resulting forces. Section 5 contains the calculations of the second-order forces, including the additional term arising from the interference of the two fluctuation sources. We conclude with ending remarks in Section 6.

Unless otherwise stated, it is assumed throughout this paper that $\hbar = c = 1$. We also use square brackets on a function $f[\omega]$ to denote that this frequency domain function is the Fourier transform of some function $f(t)$ in the time domain. Additionally, we take $\eta = \text{diag}(1, -1)$. Throughout the paper we will use primes in two distinct ways. A prime on a function is understood to mean the spatial derivative of that function, where as primes on variables are understood to simply index distinct variables.

2. Quantum Fluctuation–Dissipation Theorem

This Section reviews the notation and terminology necessary to understand the fluctuation–dissipation theorem applied to quantum interactions with the vacuum. Following the conventions in Ref. [18], we decompose a (1 + 1)D scalar field into the sum of two counter-propagating fields, which are denoted as $\varphi(t - x)$ and $\psi(t + x)$. We denote the incoming fields with an “in” subscript and the outgoing fields with an “out” subscript. In what follows, we adopt a scattering framework, taking our ingoing field as the initial field which scatters by some interaction and is perturbatively modified into an outgoing field. We then specialize this to the case of the background quantum vacuum scattering off partially reflecting mirrors. We make use of the following column matrix notation to write the field as

$$\Phi(t, x) = \begin{pmatrix} \varphi(t - x) \\ \psi(t + x) \end{pmatrix}. \tag{2}$$

In the frequency domain, the field $\Phi[\omega, x]$ can be expressed in terms of the stationary field $\Phi[\omega, 0]$ at $x = 0$,

$$\Phi[\omega, x] = \begin{pmatrix} \varphi[\omega]e^{i\omega x} \\ \psi[\omega]e^{-i\omega x} \end{pmatrix} = e^{i\eta\omega x}\Phi[\omega, 0], \tag{3}$$

with the frequency ω .

Going forward, we employ a shorthand for this stationary field by taking $\Phi(t, 0) = \Phi(t)$ and $\Phi[\omega, 0] = \Phi[\omega]$. The two stationary incoming counter-propagating fields can be related to the standard creation and annihilation operators. Explicitly, these are

$$\varphi_{\text{in}}[\omega] = (2|\omega|)^{-1/2} [\Theta(\omega)a_L[\omega] + \Theta(-\omega)a_L^\dagger[-\omega]] \quad (4)$$

and

$$\psi_{\text{in}}[\omega] = (2|\omega|)^{-1/2} [\Theta(\omega)a_R[\omega] + \Theta(-\omega)a_R^\dagger[-\omega]]. \quad (5)$$

Here, $a_j[\omega]$ and $a_j^\dagger[\omega]$ ($j = L, R$) are the annihilation and creation operators for the left (L) and right (R) sides of the mirror, and $\Theta(\omega)$ is the Heaviside function.

Two important quantities we use below are the energy density, $e(t, x)$, and impulsion density, $p(t, x)$. One may write these quantities in terms of the counter-propagating fields:

$$e(t, x) = \varphi'(t - x)^2 + \psi'(t + x)^2, \quad p(t, x) = \varphi'(t - x)^2 - \psi'(t + x)^2. \quad (6)$$

We show below that the mean (expectation) value of these terms can be used to directly calculate the force on the mirror. In order to calculate these quantities, will use two-point correlation functions, written in terms of the covariance, which are defined as

$$\text{cov}(\Phi(t, x), \Phi(t', x')) \equiv C_{x,x'}(t, t') = \langle \Phi(t, x)\Phi(t', x')^T \rangle. \quad (7)$$

The flux densities are then

$$\langle e(t, x) \rangle = \{ \text{Tr} [\partial_t \partial_{t'} C_{x,x'}(t, t')] \}_{t=t'}, \quad \langle p(t, x) \rangle = \{ \text{Tr} [\eta \partial_t \partial_{t'} C_{x,x'}(t, t')] \}_{t=t'}, \quad (8)$$

where “Tr” denotes the trace operation.

Using the following expression for the correlator in the frequency domain,

$$C_{x,x'}[\omega, \omega'] = \langle \Phi_x[\omega]\Phi_{x'}[\omega']^T \rangle = e^{i\eta\omega x} C[\omega, \omega'] e^{i\eta\omega' x'}, \quad (9)$$

we implicitly define the Fourier transforms of the energy and impulsion densities as, respectively,

$$\langle e(t, x) \rangle = \int \frac{d\omega}{2\pi} \int \frac{d\omega'}{2\pi} e^{i\omega t - i\omega' t} i\omega i\omega' \text{Tr} [C_{x,x}[\omega, \omega']] \quad (10)$$

and

$$\langle p(t, x) \rangle = \int \frac{d\omega}{2\pi} \int \frac{d\omega'}{2\pi} e^{i\omega t - i\omega' t} i\omega i\omega' \text{Tr} [\eta C_{x,x}[\omega, \omega']]. \quad (11)$$

One can now compute the outgoing field (Φ_{out}), and the resulting forces, by expressing the outgoing field in terms of the ingoing field (Φ_{in}). The ingoing state corresponds to a stationary state, whose covariance matrices depend only upon one parameter, and whose correlator now becomes

$$C(t, t') = c(t - t'), \quad C[\omega, \omega'] = 2\pi\delta(\omega + \omega')c[\omega]. \quad (12)$$

For a vacuum ingoing state, we have

$$c_{\text{vac}}[\omega] = \frac{\Theta(\omega)}{2\omega} I_2, \quad (13)$$

where I_2 is the identity matrix.

We now use this framework to analyze an asymmetric $\delta - \delta'$ mirror. This is a partially transparent mirror whose interaction with the ingoing vacuum state can be linearly related to its modified outgoing field via

$$\Phi_{\text{out}}[\omega] = S[\omega]\Phi_{\text{in}}[\omega], \quad (14)$$

where $S[\omega]$ is the scattering matrix. We see that for partially transparent mirrors, the outgoing correlator can be related to the ingoing correlator as

$$C_{\text{out}}[\omega, \omega'] = S_0[\omega]C_{\text{in}}[\omega, \omega']S_0[\omega']^T, \tag{15}$$

where S_0 is the zeroth-order scattering matrix (see Equation (49)).

Some authors make use of an overbar to denote quantities taken to be comoving with the mirror [18]. We do not make use of this notation, except when introducing the moving mirror in Sections 3.1 and 3.2, as in all other instances we will be able to explicitly work in the laboratory frame.

The perturbed, outgoing fields is eventually expressed as the zeroth, first, and second-order corrections from the scattering matrix for both moving mirrors and stationary mirrors with time-dependent boundary conditions:

$$\Phi_{\text{out}}[\omega] = S_0[\omega]\Phi_{\text{in}}[\omega] + \int \frac{d\omega'}{2\pi} \delta S[\omega, \omega']\Phi_{\text{in}}[\omega'] + \int \frac{d\omega'}{2\pi} \int \frac{d\omega''}{2\pi} \delta S[\omega, \omega', \omega'']\Phi_{\text{in}}[\omega'']. \tag{16}$$

Force on a Mirror

In the (1 + 1)D spacetime considered here, the force on a single, stationary mirror is given by

$$F(t) = \phi'_{\text{in}}(t)^2 + \psi'_{\text{out}}(t)^2 - \phi'_{\text{out}}(t)^2 - \psi'_{\text{in}}(t)^2. \tag{17}$$

The resulting force can be interpreted as the difference between the impulsion densities of the ingoing and outgoing fields evaluated at the mirror’s position. The force takes the form

$$F(t) = p_{\text{in}} - p_{\text{out}}. \tag{18}$$

This is also related to the T_{xx} component of the stress-energy tensor (radiation pressure) obtained by taking the difference between the energy densities of the left and right half of the mirror

$$F(t) = e_L - e_R. \tag{19}$$

One can freely pull through the time averaging to obtain the mean force relation

$$\langle F(t) \rangle = \langle p_{\text{in}} \rangle - \langle p_{\text{out}} \rangle = \langle e_L \rangle - \langle e_R \rangle. \tag{20}$$

Using Equations (11) and (15) in Equation (20), one can now express the mean force as

$$\langle F(t) \rangle = \int \frac{d\omega}{2\pi} \int \frac{d\omega'}{2\pi} e^{i\omega t - i\omega' t} i\omega i\omega' \text{Tr}[\mathbb{F}[\omega, \omega']C_{\text{in}}[\omega, \omega']], \tag{21}$$

where $\mathbb{F}[\omega, \omega']$ is the matrix

$$\mathbb{F}[\omega, \omega'] = \eta - S_0[\omega']^T \eta S_0[\omega], \tag{22}$$

which possesses the symmetry $\mathbb{F}[\omega, \omega']^T = \mathbb{F}[\omega', \omega]$. Equation (21) allows us to calculate the mean force for any ingoing state. For any stationary ingoing state, whose correlators take the form in Equation (12), the mean force becomes

$$\langle F \rangle = \int \frac{d\omega}{2\pi} \omega^2 \text{Tr}[\mathbb{F}[\omega, -\omega]c_{\text{in}}[\omega]], \tag{23}$$

which vanishes in the case of stationary ingoing states [18]. The energy exchange between the field and the mirror is

$$\langle G \rangle = \int \frac{d\omega}{2\pi} \omega^2 \text{Tr}[\mathbb{G}[\omega, -\omega]c_{\text{in}}[\omega]], \tag{24}$$

where

$$\mathbb{G}[\omega, \omega'] = I_2 - S[\omega']^T S[\omega]. \tag{25}$$

The energy exchange for any stationary state is zero due to the unitarity of the scattering matrix S .

In general, the perturbed field Φ_{out} takes the form in Equation (16). Using this, one can compute the mean force due to the perturbation δS in the laboratory frame:

$$\langle \delta F(t) \rangle = -\langle \delta p_{\text{out}}(t) \rangle = -\left\{ \partial_t \partial_{t'} \text{Tr} [\eta \delta C_{\text{out}}(t, t')] \right\}_{t=t'}, \tag{26}$$

which becomes, to first-order,

$$\langle \delta F(t) \rangle = \int \frac{d\omega}{2\pi} \int \frac{d\omega'}{2\pi} e^{-i\omega t - i\omega' t} \omega \omega' \text{Tr} [\eta \delta C_{\text{out}}[\omega, \omega']], \tag{27}$$

$$\delta C_{\text{out}}[\omega, \omega'] = \int \frac{d\omega''}{2\pi} \left(\delta S[\omega, \omega''] C_{\text{in}}[\omega'', \omega'] S_0[\omega']^T + S_0[\omega] C_{\text{in}}[\omega, \omega''] \delta S[\omega', \omega'']^T \right). \tag{28}$$

The force in Equation (27) can be further expressed as

$$\langle \delta F(t) \rangle = \int \frac{d\omega}{2\pi} \int \frac{d\omega'}{2\pi} e^{-i\omega t - i\omega' t} \chi[\omega, \omega'] f[\omega + \omega'], \tag{29}$$

where $f[\omega]$ is the equation that governs the form of time-dependent fluctuations. We eventually use this form to write the force as a linear response to the mirror’s perturbation,

$$\langle \delta F[\omega] \rangle = \chi[\omega] \delta f[\omega], \tag{30}$$

expressed in terms of the susceptibility, given by

$$\chi[\omega] = \int \frac{d\omega'}{2\pi} \chi[\omega', \omega - \omega']. \tag{31}$$

3. The Scattering Matrix

The mirror is initially located at $x = 0$, which allows us to decompose our field as

$$\phi(t, x) = \Theta(x) \phi_+(t, x) + \Theta(-x) \phi_-(t, x), \tag{32}$$

where ϕ_+ (ϕ_-) is the field on the right (left) side of the mirror. In general, we will use “+” (“−”) subscripts to refer to any quantities that pertain to only the right (left) side of the mirror. Using the fact that both ϕ_{\pm} obey the Klein–Gordon equation, One may represent each as the sum of two freely counterpropagating fields. Explicitly, these are

$$\phi_+(t, x) = \int \frac{d\omega}{\sqrt{2\pi}} \left[\phi_{\text{out}}[\omega] e^{i\omega x} + \psi_{\text{in}}[\omega] e^{-i\omega x} \right] e^{-i\omega t} \tag{33}$$

and

$$\phi_-(t, x) = \int \frac{d\omega}{\sqrt{2\pi}} \left[\phi_{\text{in}}[\omega] e^{i\omega x} + \psi_{\text{out}}[\omega] e^{-i\omega x} \right] e^{-i\omega t}, \tag{34}$$

which depend on the incoming and outgoing fields introduced in Section 2. We assume here that the ingoing and outgoing fields are linearly related as

$$\Phi_{\text{out}}[\omega] = S[\omega] \Phi_{\text{in}}.$$

Thus far, we have not specified any properties of our mirror except that it is partially reflecting. In this case, $S[\omega]$ can be taken to be the most general partially reflecting scattering matrix, which is written explicitly as

$$S[\omega] = \begin{pmatrix} s_+[\omega] & r_+[\omega] \\ r_-[\omega] & s_-[\omega] \end{pmatrix}. \tag{35}$$

Here, $r_{\pm}[\omega]$ and $s_{\pm}[\omega]$ are the reflection and transmission coefficients, respectively. Going forward, we consider the mirror interaction to be described by the asymmetric, partially reflected $\delta - \delta'$ mirror, whose potential is given as

$$U(x) = \mu\delta(x) + \lambda\delta'(x). \tag{36}$$

Here, μ is related to the plasma frequency of the mirror and λ is a dimensionless factor. With this, it is now possible to derive explicit forms of the transmission and reflection components [5]:

$$r_{\pm}[\omega] = \frac{-i\mu_0 \pm 2\omega\lambda_0}{i\mu_0 + \omega(1 + \lambda_0^2)} \tag{37}$$

and

$$s_{\pm}[\omega] = \frac{\omega(1 - \lambda_0^2)}{i\mu_0 + \omega(1 + \lambda_0^2)}. \tag{38}$$

Here, we introduce the notation μ_0 and λ_0 to denote the zeroth-order terms. This distinction is important when considering perturbative effects due to field interactions with the mirror.

3.1. First-Order Corrections

We start by solving for the ADCE corrections for the $\delta - \delta'$ mirror with time-dependent $\mu(t)$. For this analysis, we assume that the mirror is held at rest. Here, we require that the fluctuations in $\mu(t)$ take the form of small oscillations about a fixed value μ_0 . Specifically,

$$\mu(t) = \mu_0[1 + \epsilon f(t)], \tag{39}$$

where $\mu_0 \geq 1$ is a constant and $f(t)$ is an arbitrary function such that $|f(t)| \leq 1$, with $\epsilon \ll 1$.

To find the modified outgoing field, we apply the field equation of the system, determined by the potential in Equation (36), to Equations (33) and (34). From here, the matching conditions can be solved to the first order by following Ref. [5], where the final form becomes

$$\Phi_{\text{out}}[\omega] = S_0[\omega]\Phi_{\text{in}}[\omega] + \epsilon \int \frac{d\omega'}{2\pi} \delta S_{\mu}^{(1)}[\omega, \omega']\Phi_{\text{in}}[\omega']. \tag{40}$$

The first-order correction to the scattering matrix due to the introduction of $f(t)$ takes the form

$$\delta S_{\mu}^{(1)}[\omega, \omega'] = -i\mu_0 h(\omega) f[\omega - \omega'] \mathbb{S}_{\mu}[\omega'], \tag{41}$$

where $h(\omega) = [i\mu_0 + \omega(1 + \lambda_0^2)]^{-1}$ and

$$\mathbb{S}_{\mu}[\omega'] = J_2 + S_0[\omega'] = \begin{pmatrix} s_+[\omega'] & 1 + r_+[\omega'] \\ 1 + r_-[\omega'] & s_-[\omega'] \end{pmatrix}. \tag{42}$$

Here, J_2 is the column-reversed identity matrix. This is in agreement with Ref. [6]. Throughout this paper, we use the superscripts “(1)” and “(2)” to denote the first- and second-order contributions, respectively. Additionally, the subscript μ represents the contribution from the time-varying material properties.

Let us now calculate the first-order corrections due to the $\delta - \delta'$ mirror undergoing mechanical oscillations about $x = 0$. Scattering is still linear with

$$\bar{\Phi}_{\text{out}}[\omega] = S[\omega]\bar{\Phi}_{\text{in}}, \tag{43}$$

in the co-moving frame (denoted by the overbar in this Section only). In this frame, the mirror is instantaneously at rest. The movement is assumed to be nonrelativistic ($|\dot{q}(t)| \ll 1$, where the dot denotes the time-derivative) and limited by a small amplitude, such that

$$q(t) = \epsilon g(t), \tag{44}$$

with $|g(t)| \leq 1$ and $\epsilon \ll 1$. To solve this in the laboratory frame, we use the relation

$$\bar{\Phi}(t', 0) = \Phi(t, \epsilon g(t)) = [1 - \epsilon g(t)\eta\partial_t]\Phi(t, 0) + \mathcal{O}(\epsilon^2). \tag{45}$$

Taking advantage of the fact that $d\bar{t} = dt$ at the first order, Equation (45) can be rewritten as

$$\bar{\Phi}(t, 0) = [1 - \epsilon g(t)\eta\partial_t]\Phi(t, 0). \tag{46}$$

One finds that applying this transform to Equation (43) in the frequency domain yields

$$\Phi_{\text{out}}[\omega] = S_0[\omega]\Phi_{\text{in}}[\omega] + \epsilon \int \frac{d\omega'}{2\pi} \delta S_q^{(1)}[\omega, \omega']\Phi_{\text{in}}[\omega'], \tag{47}$$

where the subscript q denotes the motion of the mirror. The first-order S -matrix perturbation, $\delta S_q^{(1)}[\omega, \omega']$, takes the form

$$\delta S_q^{(1)}[\omega, \omega'] = i\omega'g[\omega - \omega']\mathbb{S}_q^{(1)}[\omega, \omega'], \tag{48}$$

where

$$\mathbb{S}_q^{(1)}[\omega, \omega'] = S_0[\omega]\eta - \eta S_0[\omega'] \tag{49}$$

and S_0 is the zeroth-order scattering matrix found from Equations (37) and (38). This is in agreement with Ref. [5].

3.2. Second-Order Corrections

The second-order perturbation due to the time dependence of $\mu(t)$ can be found by carrying through the derivation of the first-order term to second-order in the matching conditions. With this in mind, one finds that the expression for Φ_{out} in Equation (40) to the second-order term is now

$$\Phi_{\text{out}}[\omega] = S_0[\omega]\Phi_{\text{in}}[\omega] + \epsilon \int \frac{d\omega'}{2\pi} \delta S_\mu^{(1)}[\omega, \omega']\Phi_{\text{in}}[\omega'] + \epsilon^2 \int \frac{d\omega'}{2\pi} \int \frac{d\omega''}{2\pi} \delta S_\mu^{(2)}[\omega, \omega', \omega'']\Phi_{\text{in}}[\omega''], \tag{50}$$

with the first-order perturbation term, $\delta S_\mu^{(1)}[\omega, \omega']$, given in Equation (41), and the second-order term,

$$\delta S_\mu^{(2)}[\omega, \omega', \omega''] = -\mu_0^2 h(\omega)h(\omega')f[\omega - \omega']f[\omega' - \omega'']\mathbb{S}_\mu[\omega''], \tag{51}$$

which agrees with Ref. [6].

The second-order correction due to the motion of the mirror is more complicated. Let us start by evaluating the fields at the time-dependent position of the mirror. This is the frame in which the mirror is instantaneously at rest whereby the field and its Fourier transform can be written as, respectively

$$\bar{\Phi}(\tau) = \Phi_{q_i}(t) = \left\{ e^{-x\eta\partial_t}\Phi(t) \right\}_{x=q_i}, \quad \bar{\Phi}(\tau) = \int \frac{d\omega}{2\pi} \Phi'[\omega]e^{-i\omega\tau}, \tag{52}$$

where τ is the mirror's proper time and $q_t \equiv q(t)$. The proper time and laboratory time are related by

$$d\tau = \sqrt{1 - \dot{q}_t^2} dt. \tag{53}$$

The first- and second-order expansions in q_t of the mirror's trajectory around $q = 0$, or $\bar{\Phi}(\tau, 0) = \Phi(\tau, \epsilon q(t))$, lead to

$$\bar{\Phi}(\tau) = \Phi(t) - q_t \eta \partial_t \Phi(t) + \frac{1}{2} q_t^2 \partial_t^2 \Phi(t). \tag{54}$$

Now, unlike in the first-order expansion when the mirror's proper time and laboratory time coincide, $d\tau$ is no longer equal to dt . One can see for the second-order time correction, in the nonrelativistic limit ($|\dot{q}(t)| \ll 1$):

$$d\tau \approx \left(1 - \frac{1}{2} \delta q_t^2\right) dt. \tag{55}$$

Therefore,

$$\tau = t - \frac{1}{2} \int dt \delta q_t^2. \tag{56}$$

Using Equation (44), we obtain the explicit result:

$$\bar{\Phi}(\tau, 0) = \left[1 - \epsilon g(t) \eta \partial_t + \frac{1}{2} \epsilon^2 g(t)^2 \partial_t^2\right] \Phi(t, 0) + \mathcal{O}(\epsilon^3) \tag{57}$$

and

$$\tau = t - \frac{1}{2} \epsilon^2 \int dt \dot{g}(t)^2 + \mathcal{O}(\epsilon^3). \tag{58}$$

To find the field in the frequency domain, we substitute the new form of τ in Equation (58) into the field's Fourier transform from Equation (52). We find its second-order approximation to be

$$\bar{\Phi}(\tau) = \int \frac{d\omega}{2\pi} \Phi'[\omega] e^{-i\omega\tau} \approx \int \frac{d\omega}{2\pi} \left[1 + \frac{i\omega\epsilon^2}{2} \int dt \dot{g}(t)^2\right] \Phi'[\omega] e^{-i\omega t}. \tag{59}$$

We can equate this quantity to the Fourier transform of the right-hand side of Equation (54), where we now arrive at the following relationship

$$\left[1 + \frac{i\omega\epsilon^2}{2} \int dt \dot{g}(t)^2\right] \Phi'[\omega] = \Phi[\omega] + i\epsilon\eta \int \frac{d\omega'}{2\pi} \omega' g[\omega - \omega'] \Phi[\omega'] - \frac{\epsilon^2}{2} \int \frac{d\omega'}{2\pi} \int \frac{d\omega''}{2\pi} \omega''^2 g[\omega - \omega'] g[\omega' - \omega''] \Phi[\omega'']. \tag{60}$$

Solving for $\bar{\Phi}[\omega]$ in Equation (60), and using $(1 + x)^{-1} \approx 1 - x$, leads to the second-order correction to the field in the laboratory frame,

$$\bar{\Phi}^{(2)}[\omega] = -\frac{i\omega\epsilon^2}{2} \int dt \dot{g}(t)^2 \Phi[\omega] - \frac{\epsilon^2}{2} \int \frac{d\omega'}{2\pi} \int \frac{d\omega''}{2\pi} \omega''^2 g[\omega - \omega'] g[\omega' - \omega''] \Phi[\omega'']. \tag{61}$$

With Equation (61), which describes the relationship between the field in the instantaneous frame of mirror with the field in the laboratory frame for the second order, one can now calculate the output field as a function of the input field using Equation (43). The full first- and second-order corrections to the outgoing field due to the motion of the mirror are

$$\Phi_{\text{out}}[\omega] = S_0[\omega] \Phi_{\text{in}}[\omega] + \epsilon \int \frac{d\omega'}{2\pi} \delta S_q^{(1)}[\omega, \omega'] \Phi_{\text{in}}[\omega'] + \epsilon^2 \int \frac{d\omega'}{2\pi} \int \frac{d\omega''}{2\pi} \delta S_q^{(2)}[\omega, \omega', \omega''] \Phi_{\text{in}}[\omega''], \tag{62}$$

with the definition of $\delta S_q^{(1)}$ from Equation (48) and

$$\delta S_q^{(2)}[\omega, \omega', \omega''] = \frac{1}{2} \omega''^2 g[\omega - \omega'] g[\omega' - \omega''] \mathbb{S}_q^{(2)}[\omega, \omega''], \tag{63}$$

where

$$\mathbb{S}_q^{(2)}[\omega, \omega''] = S_0[\omega''] - S_0[\omega]. \tag{64}$$

4. First-Order Forces

The first-order (in ϵ) contribution to the mean force due to the modification of $\delta S^{(1)}$ is (see Equations (27) and (28))

$$\begin{aligned} \langle \delta F^{(1)}(t) \rangle &= \int \frac{d\omega}{2\pi} \int \frac{d\omega'}{2\pi} e^{-i\omega t - i\omega' t} \omega \omega' \text{Tr} \left[\eta \delta C_{\text{out}}^{(1)}[\omega, \omega'] \right], \\ \delta C_{\text{out}}^{(1)}[\omega, \omega'] &= \int \frac{d\omega''}{2\pi} \left(\delta S^{(1)}[\omega, \omega''] c_{\text{in}}[\omega'', \omega'] S_0[\omega']^T + S_0[\omega] c_{\text{in}}[\omega, \omega''] \delta S^{(1)}[\omega', \omega'']^T \right). \end{aligned}$$

With a stationary ingoing state (see Equations (12) and (13)), $\delta C_{\text{out}}^{(1)}$ reads

$$\delta C_{\text{out}}^{(1)}[\omega, \omega'] = \delta S^{(1)}[\omega, -\omega'] c_{\text{in}}[-\omega'] S_0[\omega']^T + S_0[\omega] c_{\text{in}}[\omega] \delta S^{(1)}[\omega', -\omega]^T. \tag{65}$$

Recall that the force appears as a linear response to the mirror's perturbation,

$$\langle \delta F[\omega] \rangle = \chi[\omega] \delta f[\omega],$$

which is expressed in terms of the susceptibility,

$$\chi[\omega] = \int \frac{d\omega'}{2\pi} \chi[\omega', \omega - \omega'].$$

4.1. Moving Mirror

Here, we calculate the force on a moving $\delta - \delta'$ mirror whose position $q(t)$ fluctuates about $x = 0$ with a small amplitude $\epsilon g(t)$. Using the first-order correction to the scattering matrix $\delta S_q^{(1)}$ from Equation (48) into Equation (65), $\delta C_q^{(1)}$ becomes

$$\begin{aligned} \delta C_q^{(1)}[\omega, \omega'] &= -i\omega' g[\omega + \omega'] (S_0[\omega] \eta - \eta S_0[-\omega']) c_{\text{in}}[-\omega'] S_0[\omega']^T \\ &\quad - i\omega g[\omega + \omega'] S_0[\omega] c_{\text{in}}[\omega] (\eta S_0[\omega']^T - S_0[-\omega]^T \eta). \end{aligned} \tag{66}$$

Applying the properties of the trace, Equation (66) can be used to find

$$\text{Tr} \left[\eta \delta C_q^{(1)}[\omega, \omega'] \right] = g[\omega + \omega'] \text{Tr} \left[\mathbb{F}[\omega, \omega'] (i\omega c_{\text{in}}[\omega] \eta + i\omega' \eta c_{\text{in}}[-\omega']) \right], \tag{67}$$

with the matrix $\mathbb{F}[\omega, \omega']$ from Equation (22). Under a double integral over the full domain of ω and ω' , one may freely swap these variables. This allows us to modify certain quantities in a way that enables simplification of the integrand without changing the result of the integral. Explicitly, we perform the following swap:

$$g[\omega + \omega'] \text{Tr} \left[\mathbb{F}[\omega, \omega'] i\omega c_{\text{in}}[\omega] \eta \right] \implies g[\omega' + \omega] \text{Tr} \left[\mathbb{F}[\omega', \omega] i\omega' c_{\text{in}}[\omega'] \eta \right], \tag{68}$$

Then, one may use the argument swapping symmetry on \mathbb{F} and the definition of c_{in} (where $c_{\text{in}} = c_{\text{vac}}$ from Equation (13)) to re-express Equation (67) as

$$\text{Tr} \left[\eta \delta C_q^{(1)}[\omega, \omega'] \right] \implies \frac{i}{2} \text{sgn}(\omega') g[\omega + \omega'] \text{Tr} \left[\mathbb{F}[\omega, \omega'] \eta \right]. \tag{69}$$

In Equations (68) and (69), we use the arrow instead of the equation sign to indicate that, while these expressions are not equivalent, they lead to the same final result when integrating. Additionally, when simplifying Equation (69), we used the following definition for the sign function:

$$\text{sgn}(\omega) = \Theta(\omega) - \Theta(-\omega). \tag{70}$$

With Equation (69), we write the first-order motional force in terms of $\chi[\omega, \omega']$ in the following manner:

$$\langle \delta F_q^{(1)}(t) \rangle = \int \frac{d\omega}{2\pi} \int \frac{d\omega'}{2\pi} e^{-i\omega t - i\omega' t} \chi_q^{(1)}[\omega, \omega'] g[\omega + \omega'], \tag{71}$$

$$\chi_q^{(1)}[\omega, \omega'] = \frac{i\omega\omega'}{2} \text{sgn}(\omega') \text{Tr}[\mathbb{F}[\omega, \omega']\eta], \tag{72}$$

where Equation (72) can be rewritten as

$$\chi_q^{(1)}[\omega, \omega'] = \text{sgn}(\omega') \omega \omega' h(\omega) h(\omega') \left[-2i\mu_0^2 + 8i\lambda_0^2 \omega \omega' - \mu_0(1 + \lambda_0^2)(\omega + \omega') \right]. \tag{73}$$

The susceptibility is then

$$\begin{aligned} \chi_q^{(1)}[\omega] &= \int \frac{d\omega'}{2\pi} \chi[\omega', \omega - \omega'] \\ &= \frac{i}{2} \int \frac{d\omega'}{2\pi} \text{sgn}(\omega - \omega') \omega' (\omega - \omega') \text{Tr}[\mathbb{F}[\omega', \omega - \omega']\eta]. \end{aligned} \tag{74}$$

Taking $\beta = (1 + \lambda_0^2)/\mu_0$, we can determine various expansions when the term $\beta\omega$ is assumed to be large or small. The real and imaginary parts of the susceptibility in Equation (74) are,

$$\text{Re} \chi_q^{(1)}[\omega] = \frac{1}{2\pi\beta^3(1 + \lambda_0^2)^2} \frac{2\mathcal{A}(\omega) \arctan(\beta\omega) - \mathcal{C}_R(\omega) - \mathcal{B}(\omega) \log(1 + (\beta\omega)^2)}{(4 + (\beta\omega)^2)}, \tag{75}$$

$$\text{Im} \chi_q^{(1)}[\omega] = \frac{1}{2\pi\beta^3(1 + \lambda_0^2)^2} \frac{2\mathcal{B}(\omega) \arctan(\beta\omega) + \mathcal{C}_I(\omega) + \mathcal{A}(\omega) \log(1 + (\beta\omega)^2)}{(4 + (\beta\omega)^2)}, \tag{76}$$

where

$$\begin{aligned} \mathcal{A}(\omega) &= \beta\omega \left[4(1 - 4\lambda_0^2 + \lambda_0^4) + (\beta\omega)^2(1 - 6\lambda_0^2 + \lambda_0^4) \right], \\ \mathcal{B}(\omega) &= 4(\lambda_0^2 - 1)^2 + (\beta\omega)^2(1 + \lambda_0^2)^2, \\ \mathcal{C}_R(\omega) &= (\beta\omega)^2(4 + (\beta\omega)^2) \left[1 - 6\lambda_0^2 + \lambda_0^4 \right], \\ \mathcal{C}_I(\omega) &= \frac{2}{3}\beta\omega(4 + (\beta\omega)^2) \left[2(\beta\omega)^2\lambda_0^2 - 3(\lambda_0^2 - 1)^2 \right]. \end{aligned} \tag{77}$$

For $\beta\omega \ll 1$:

$$\begin{aligned} \text{Re} \chi_q^{(1)}[\omega] &= -\frac{1}{2\pi\beta^3(1 + \lambda_0^2)^2} \left[\frac{(\beta\omega)^4(1 + \lambda_0^2)^2}{6} - \frac{(\beta\omega)^6(1 + 6\lambda_0^2 + \lambda_0^4)}{15} + \mathcal{O}[(\beta\omega)^8] \right], \\ \text{Im} \chi_q^{(1)}[\omega] &= \frac{1}{6\pi\beta^3(1 + \lambda_0^2)^2} \left[(\beta\omega)^3(1 + \lambda_0^2)^2 - \frac{(\beta\omega)^5(3 + 14\lambda_0^2 + 3\lambda_0^5)}{10} + \mathcal{O}[(\beta\omega)^7] \right], \end{aligned} \tag{78}$$

and for $\beta\omega \gg 1$:

$$\begin{aligned}
 \operatorname{Re} \chi_q^{(1)}[\omega] &= -\frac{1}{2\pi\beta^3(1+\lambda_0^2)^2} \left[(\beta\omega)^2(1-6\lambda_0^2+\lambda_0^4) + \beta\omega\pi(-1+6\lambda_0^2-\lambda_0^4) + 2(1-6\lambda_0^2+\lambda_0^4) \right. \\
 &\quad \left. + 2\log(\beta\omega)(1+\lambda_0^2)^2 - \frac{8\pi\lambda_0^2}{\beta\omega} + \frac{1+66\lambda_0^2+\lambda_0^4-96\lambda_0^2\log(\beta\omega)}{3(\beta\omega)^2} + \mathcal{O}[(\beta\omega)^{-3}] \right], \\
 \operatorname{Im} \chi_q^{(1)}[\omega] &= \frac{1}{6\pi\beta^3(1+\lambda_0^2)^2} \left[4(\beta\omega)^3\lambda_0^3 - 6\beta\omega(1-2\lambda_0^2+\lambda_0^4 - \log(\beta\omega)(-1+6\lambda_0^2+\lambda_0^4)) \right. \\
 &\quad \left. + 3\pi(1+\lambda_0^2)^2 - \frac{3(1+10\lambda_0^2-\lambda_0^4+16\lambda_0^2\log(\beta\omega))}{\beta\omega} - \frac{48\pi\lambda_0^2}{(\beta\omega)^2} + \mathcal{O}[(\beta\omega)^{-3}] \right].
 \end{aligned} \tag{79}$$

The limits in Equations (78) and (79) correspond to the low- and high-frequency limits of the susceptibility, respectively. One should exercise caution though, as using these to produce time-domain quantities can lead to misleading results as the inverse Fourier transform requires an integral over the entire frequency domain.

When $\lambda_0 = 1$, which corresponds to the spectrum of a perfectly reflective $\delta - \delta'$ mirror, the relationship $\beta = 2/\mu_0$ holds, where β is now the Robin parameter. In the limits from Equations (78) and (79), which contain the corrections to the Dirichlet ($\beta \rightarrow 0$) and Neumann ($\beta \rightarrow \infty$) limits of a moving Robin mirror, respectively, we find that the correct leading order linear susceptibility,

$$\chi[\omega] = i\frac{\omega^3}{6\pi}, \tag{80}$$

is recovered, which leads to the dissipative force in Equation (1).

Notice that when $\lambda_0 = 0$, which corresponds to a perfectly reflective δ mirror with no asymmetry in particle production (the spectrum is identical for both sides of the mirror), the susceptibility does not completely vanish. This is due to the fact that there is still a reaction force from the vacuum onto the mirror originating from the motion of the mirror itself. This is not the case, as one sees in Section 4.2 below, for the stationary mirror with time-dependent $\mu(t)$.

The expression in Equation (71) can be directly computed when an appropriate form of the motion, $g(t)$, is introduced. Here, we use

$$g(t) = \cos(\omega_0 t) \exp(-|t|/\mathcal{T}), \tag{81}$$

where ω_0 is the characteristic frequency of the oscillation and \mathcal{T} is the effective time of the oscillation. Integrals of the type present in Equation (71) do not have analytic solutions to the best of our knowledge. Thus, we numerically integrate this expression; see Figure 1, where we plot with different values of λ_0 and compare these results to the force on a moving Dirichlet mirror using Equation (80). One sees that as the asymmetry between the two sides of the $\delta - \delta'$ mirror grows larger ($\lambda_0 \rightarrow \infty$), the magnitude of the force on the mirror grows along with it. Along with this increase in magnitude, the force becomes more sharply peaked. The increase in force arises from the increase in the magnitude of the asymmetric dynamical Casimir effect; the larger imbalance of generated particles leads to an increase in the force on the mirror due to increasingly asymmetric radiation reaction forces.

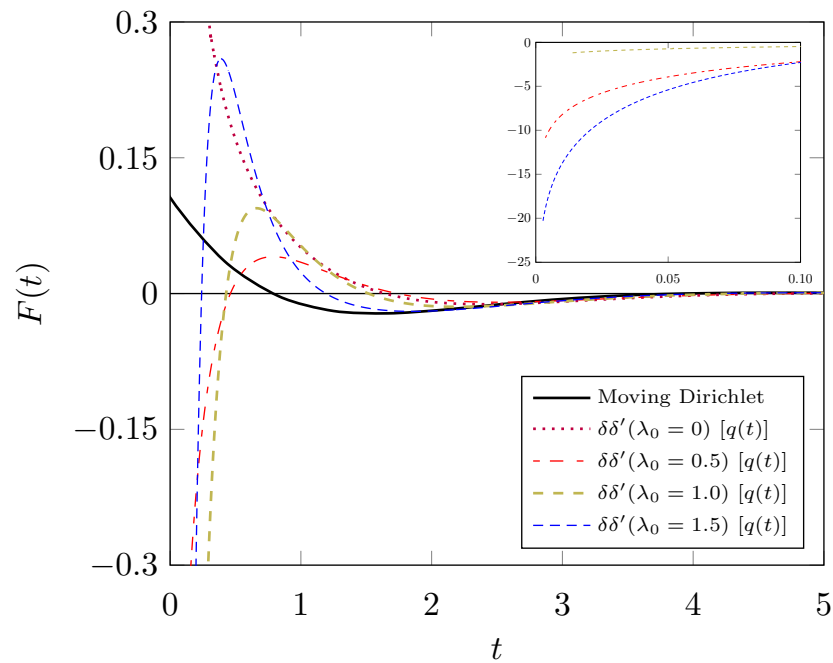


Figure 1. The force (see Equation (71)) on a moving $\delta - \delta'$ mirror (indicated as $\delta\delta'$) as a function of time, presented in natural units, for some values of λ_0 , where $\mu_0 = \omega_0 = \mathcal{T} = 1$. The force on a moving Dirichlet mirror is presented for comparison. Inset: the behavior of the moving $\delta - \delta'$ mirror's forces near zero. See text for details.

Compared to the dissipative Dirichlet mirror, the signature of the asymmetry present in the force is apparent. Instead of a positive dissipative force acting on the mirror as it begins to move, there is an initially negative force that corresponds to non-zero dynamical Casimir effect forces that arise due to the asymmetry in particle production. This behavior becomes more obvious when we consider the force on the moving $\delta - \delta'$ mirror for $\lambda_0 = 0$. The force plot now resembles that of the Dirichlet mirror, where the force is once again positive near zero, albeit greater.

Presented in Figure 2, the force as a function of time is plotted for two different values of ω_0 . As the frequency of oscillation increases, the number of peaks increases along with it. Compared to the analogous plot for the $\delta - \delta'$ mirror with time-dependent properties, there is a larger increase in the magnitude of the force for the moving mirror. This is expected, as the asymmetry in particle production for the moving $\delta - \delta'$ mirror scales as ω_0^2 when compared to that of the $\delta - \delta'$ mirror with time-dependent material properties [7,8]. Thus, there is an accompanying increase in net force on the moving mirror as the frequency of oscillation increases.

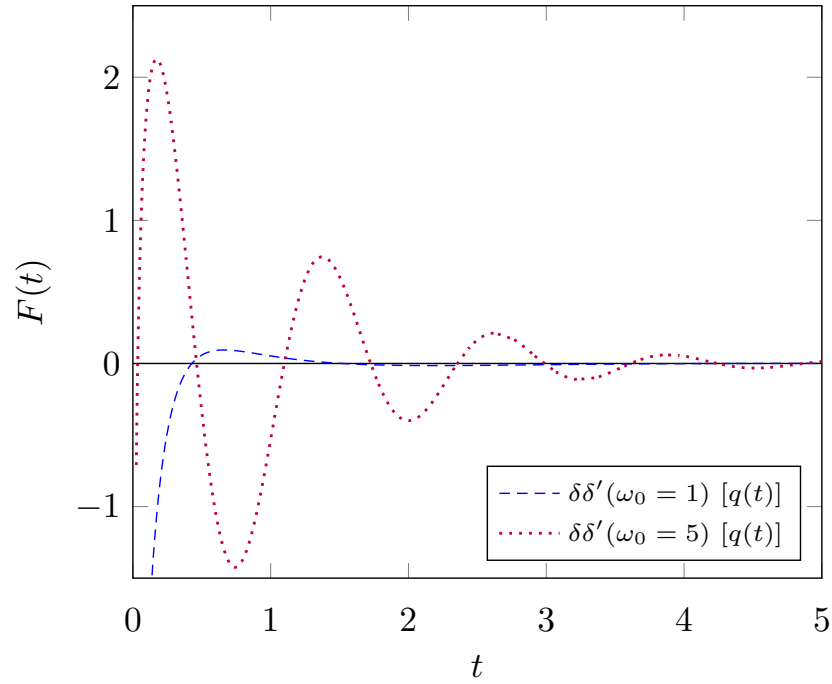


Figure 2. The force (see Equation (71)) on a moving $\delta - \delta'$ mirror as a function of time, presented in natural units, for two values of ω_0 , where $\mu_0 = \lambda_0 = \mathcal{T} = 1$. See text for details.

4.2. Mirror with Time-Dependent Properties

To find the first-order force on a stationary $\delta - \delta'$ mirror with time-dependent $\mu(t)$ (see Equation (39)), let us start by using $\delta S_\mu^{(1)}[\omega, \omega']$ from Equation (41) in Equation (65) to find

$$\delta C_\mu^{(1)}[\omega, \omega'] = -i\mu_0 f[\omega + \omega'] \left(h(\omega) \mathbb{S}_\mu[-\omega'] c_{in}[-\omega'] S_0[\omega']^T + h(\omega') S_0[\omega] c_{in}[\omega] \mathbb{S}_\mu[-\omega]^T \right). \tag{82}$$

Again using the definition of $c_{in}[\omega]$ from Equation (13), and implementing a change of variables in the second term as done in Equation (68), $\delta C_\mu^{(1)}$ becomes

$$\delta C_\mu^{(1)}[\omega, \omega'] = -\frac{i\mu_0}{2\omega'} h(\omega) f[\omega + \omega'] \left(\Theta(\omega') S_0[\omega'] \mathbb{S}_\mu[-\omega']^T - \Theta(-\omega') \mathbb{S}_\mu[-\omega'] S_0[\omega']^T \right), \tag{83}$$

which yields

$$\text{Tr} \left[\eta \delta C_\mu^{(1)}[\omega, \omega'] \right] = -\frac{i\mu_0}{2\omega'} \text{sgn}(\omega') h(\omega) f[\omega + \omega'] \text{Tr} \left[\eta S_0[\omega'] \mathbb{S}_\mu[-\omega']^T \right]. \tag{84}$$

Performing the direct calculation

$$\text{Tr} \left[\eta S_0[\omega'] \mathbb{S}_\mu[-\omega']^T \right] = 4\lambda_0 \omega' h(\omega'), \tag{85}$$

one sees that

$$\text{Tr} \left[\eta \delta C_\mu^{(1)}[\omega, \omega'] \right] = -2i\lambda_0 \mu_0 \text{sgn}(\omega') h(\omega) h(\omega') f[\omega + \omega']. \tag{86}$$

From Equation (86), we write the motional force in terms of $\chi[\omega, \omega']$ in the following manner

$$\langle \delta F_\mu^{(1)}(t) \rangle = \int \frac{d\omega}{2\pi} \int \frac{d\omega'}{2\pi} e^{-i\omega t - i\omega' t} \chi_\mu^{(1)}[\omega, \omega'] f[\omega + \omega'], \tag{87}$$

$$\chi_\mu^{(1)}[\omega, \omega'] = -2i\lambda_0 \mu_0 \text{sgn}(\omega') \omega \omega' h(\omega) h(\omega'). \tag{88}$$

Plugging in Equation (88) into Equation (31) gives the explicit first-order susceptibility for the time-dependent $\delta - \delta'$ mirror,

$$\chi_{\mu}^{(1)}[\omega] = \frac{\lambda_0}{\pi\beta^2(1 + \lambda_0^2)} \left[\frac{2 + (\beta\omega)^2 - 2i\beta\omega}{4 + (\beta\omega)^2} \left[2i \arctan(\beta\omega) - \log(1 + \beta^2\omega^2) \right] - i\beta\omega \right], \tag{89}$$

which is in agreement with Ref. [6], up to discrepancy of a factor of 2 on the entire term. Unlike in the motional case presented in Equation (74), when the asymmetry is no longer present ($\lambda_0 = 0$), the susceptibility in Equation (89) completely vanishes. This is expected, as there are no longer any time-dependent interactions occurring between the mirror and the vacuum, and thus there is no force present.

The susceptibility's real and imaginary components are

$$\text{Re } \chi_{\mu}^{(1)}[\omega] = \frac{\lambda_0}{\pi\beta^2(1 + \lambda_0^2)} \left[\frac{2\beta\omega \arctan(\beta\omega) - (2 + \beta^2\omega^2) \log(1 + \beta^2\omega^2)}{4 + \beta^2\omega^2} \right], \tag{90}$$

$$\text{Im } \chi_{\mu}^{(1)}[\omega] = \frac{\lambda_0}{\pi\beta^2(1 + \lambda_0^2)} \left[\frac{-4\beta\omega - \beta^3\omega^3 + (2 + \beta^2\omega^2) 2 \arctan(\beta\omega) + \beta\omega \log(1 + \beta^2\omega^2)}{4 + \beta^2\omega^2} \right]. \tag{91}$$

For $\beta\omega \ll 1$:

$$\begin{aligned} \text{Re } \chi_{\mu}^{(1)}[\omega] &= \frac{\lambda_0}{\pi\beta^2(1 + \lambda_0^2)} \left[-\frac{(\beta\omega)^4}{6} + \frac{(\beta\omega)^6}{10} + \mathcal{O}[(\beta\omega)^8] \right], \\ \text{Im } \chi_{\mu}^{(1)}[\omega] &= \frac{\lambda_0}{\pi\beta^2(1 + \lambda_0^2)} \left[\frac{(\beta\omega)^3}{6} - \frac{2(\beta\omega)^5}{15} + \mathcal{O}[(\beta\omega)^7] \right]. \end{aligned} \tag{92}$$

For $\beta\omega \gg 1$:

$$\begin{aligned} \text{Re } \chi_{\mu}^{(1)}[\omega] &= \frac{\lambda_0}{\pi\beta^2(1 + \lambda_0^2)} \left[-2 \log(\beta\omega) + \frac{\pi}{\beta\omega} + \frac{-3 + 4 \log(\beta\omega)}{(\beta\omega)^2} - \frac{4\pi}{(\beta\omega)^3} + \mathcal{O}[(\beta\omega)^{-4}] \right], \\ \text{Im } \chi_{\mu}^{(1)}[\omega] &= \frac{\lambda_0}{\pi\beta^2(1 + \lambda_0^2)} \left[-\beta\omega + \pi - \frac{2(1 - \log(\beta\omega))}{\beta\omega} - \frac{2\pi}{(\beta\omega)^2} + \frac{17 - 24 \log(\beta\omega)}{3(\beta\omega)^3} + \mathcal{O}[(\beta\omega)^{-4}] \right]. \end{aligned} \tag{93}$$

Similar to the moving mirror case of Section 4.1, the limits in Equations (92) and (93) correspond to the low- and high-frequency limits of the susceptibility, respectively. One should still exercise caution, as again, using these to produce time-domain quantities can lead to misleading results as the inverse Fourier transform requires an integral over the entire frequency domain.

As in the first-order motional case, we again plot the force that arises from the time-dependent perturbation, now due to $\mu(t)$, in Figure 3. The behavior is similar to that of the moving mirror; the magnitude of the force increases as the asymmetry grows. Compared to the moving mirror, the positive force peaks have been shifted toward zero slightly but still dies off just as quickly. While the positive force peaks due to the time-dependent material properties are of the same order as the force from the motion of the mirror, the initial negative force is approximately an order of magnitude lower. In Figure 4, the behavior of the $\delta - \delta'$ mirror with time-dependent material properties is plotted. As in the moving mirror case there is an increase in the number of peaks and the magnitude of the peaks, although the increase is not as dramatic as the moving case.

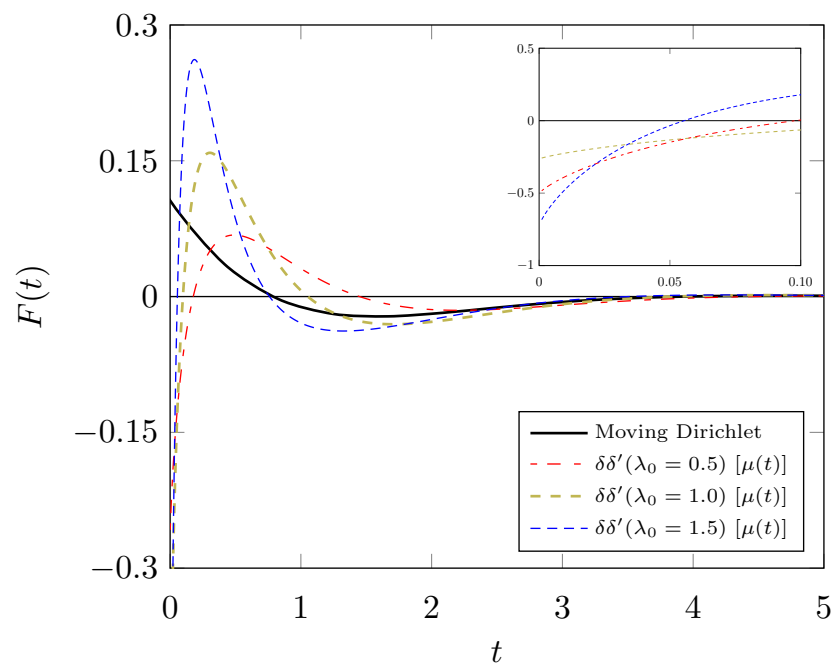


Figure 3. The force (see Equation (87)) on a $\delta - \delta'$ mirror with time-dependent $\mu(t)$ as function of time, presented in natural units, for some values of λ_0 , where $\mu_0 = \omega_0 = \mathcal{T} = 1$. The force on a moving Dirichlet mirror is presented for comparison. Inset: the behavior of the time-dependent $\delta - \delta'$ mirror's forces near zero. See text for details.

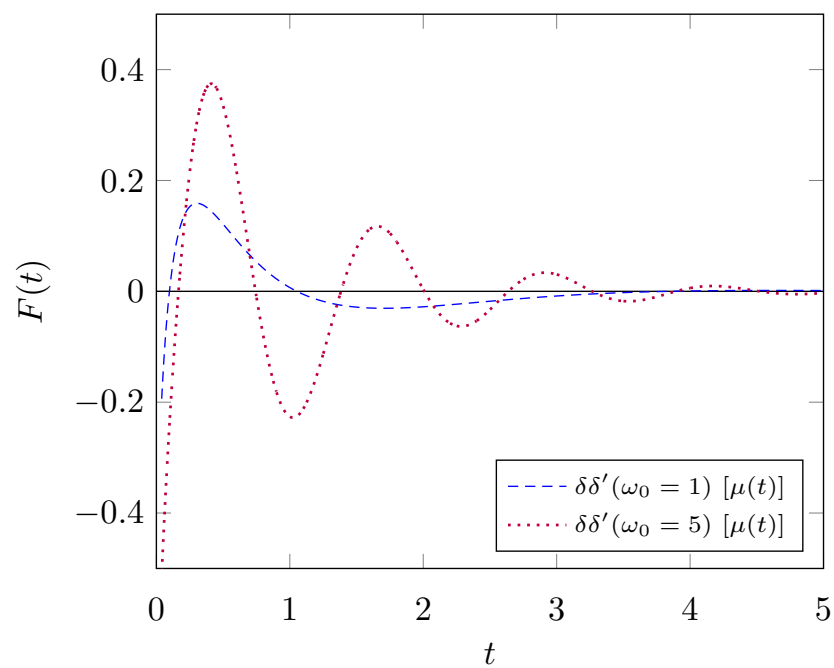


Figure 4. The force (see Equation (87)) on a $\delta - \delta'$ mirror with time-dependent $\mu(t)$ (see Equation (39)) as a function of time, presented in natural units, for two values of ω_0 , where $\mu_0 = \lambda_0 = \mathcal{T} = 1$. See text for details.

5. Second-Order Forces

The second-order contribution (of order ϵ^2) to the non-vanishing mean force that arises due to the terms $\delta S^{(1)}$ and $\delta S^{(2)}$ (see Equations (41) and (51), respectively) is

$$\langle \delta F^{(2)}(t) \rangle = \int \frac{d\omega}{2\pi} \int \frac{d\omega'}{2\pi} e^{-i\omega t - i\omega' t} \omega \omega' \text{Tr} \left[\eta \delta C_{\text{out}}^{(2)}[\omega, \omega'] \right], \quad (94)$$

where

$$\begin{aligned} \delta C_{\text{out}}^{(2)}[\omega, \omega'] &= \int \frac{d\omega''}{2\pi} \int \frac{d\omega'''}{2\pi} \left(\delta S^{(1)}[\omega, \omega''] C_{\text{in}}[\omega'', \omega'''] \delta S^{(1)}[\omega', \omega''']^T \right. \\ &\quad \left. + S_0[\omega] C_{\text{in}}[\omega, \omega'''] \delta S^{(2)}[\omega', \omega'', \omega''']^T + \delta S^{(2)}[\omega, \omega'', \omega'''] C_{\text{in}}[\omega''', \omega'] S_0[\omega']^T \right). \end{aligned} \quad (95)$$

With a stationary ingoing state (see Equations (12) and (13)), this becomes

$$\begin{aligned} \delta C_{\text{out}}^{(2)}[\omega, \omega'] &= \int \frac{d\omega''}{2\pi} \left(\delta S^{(1)}[\omega, \omega''] c_{\text{in}}[\omega''] \delta S^{(1)}[\omega', -\omega'']^T \right. \\ &\quad \left. + S_0[\omega] c_{\text{in}}[\omega] \delta S^{(2)}[\omega', \omega'', -\omega]^T + \delta S^{(2)}[\omega, \omega'', -\omega'] c_{\text{in}}[-\omega'] S_0[\omega']^T \right). \end{aligned} \quad (96)$$

It is helpful to simplify $\delta C_{\text{out}}^{(2)}$ here using the definition $c_{\text{in}}[\omega]$ from Equation (13). This becomes

$$\begin{aligned} \delta C_{\text{out}}^{(2)}[\omega, \omega'] &= \int \frac{d\omega''}{2\pi} \left(\frac{\Theta(\omega'')}{2\omega''} \delta S^{(1)}[\omega, \omega''] \delta S^{(1)}[\omega', -\omega'']^T \right. \\ &\quad \left. + \frac{\Theta(\omega)}{2\omega} S_0[\omega] \delta S^{(2)}[\omega', \omega'', -\omega]^T - \frac{\Theta(-\omega')}{2\omega'} \delta S^{(2)}[\omega, \omega'', -\omega'] S_0[\omega']^T \right). \end{aligned} \quad (97)$$

Again, as in Section 4.2, using the fact that exchanging ω and ω' under the double integral does not change the result of the integral, we may modify the expression (97) to

$$\begin{aligned} \text{Tr} \left[\eta \delta C_{\text{out}}^{(2)}[\omega, \omega'] \right] &\implies \int \frac{d\omega''}{2\pi} \left(\frac{\Theta(\omega'')}{2\omega''} \text{Tr} \left[\eta \delta S^{(1)}[\omega, \omega''] \delta S^{(1)}[\omega', -\omega'']^T \right] \right. \\ &\quad \left. + \frac{\text{sgn}(\omega')}{2\omega'} \text{Tr} \left[\eta S_0[\omega'] \delta S^{(2)}[\omega, \omega'', -\omega']^T \right] \right). \end{aligned} \quad (98)$$

5.1. Moving Mirror

Now, using the definition of the first-order perturbation from Equation (48) and the second-order perturbation from Equation (63) for a moving $\delta - \delta'$ mirror one sees that Equation (98) becomes

$$\begin{aligned} \text{Tr} \left[\eta \delta C_q^{(2)}[\omega, \omega'] \right] &= \int \frac{d\omega''}{2\pi} \left(\frac{\Theta(\omega'')}{2} \omega'' g[\omega - \omega''] g[\omega' + \omega''] \text{Tr} \left[\eta \mathbb{S}_q^{(1)}[\omega, \omega''] \mathbb{S}_q^{(1)}[\omega', -\omega'']^T \right] \right. \\ &\quad \left. + \frac{\text{sgn}(\omega')}{4} \omega' g[\omega - \omega''] g[\omega' + \omega''] \text{Tr} \left[\eta S_0[\omega'] \mathbb{S}_q^{(2)}[\omega, \omega'', -\omega']^T \right] \right). \end{aligned} \quad (99)$$

We find

$$\text{Tr} \left[\eta \mathbb{S}_q^{(1)}[\omega, \omega''] \mathbb{S}_q^{(1)}[\omega', -\omega'']^T \right] = 8i\lambda_0 \mu_0^3 \mathcal{Q}[\omega, \omega', \omega''] h(\omega) h(\omega') h(\omega'') h(-\omega''), \quad (100)$$

$$\text{Tr} \left[\eta S_0[\omega'] \mathbb{S}_q^{(2)}[\omega, \omega'', -\omega']^T \right] = 4i\lambda_0 \mu_0 (\omega + \omega') h(\omega) h(\omega'), \quad (101)$$

where

$$\mathcal{Q}[\omega, \omega', \omega''] = \left[1 + (\beta\omega'')^2 \right] (\omega + \omega') - i\beta(\omega - \omega'')(\omega' + \omega''). \quad (102)$$

Let us now express the second-order force from Equation (94) in terms of $\chi_q^{(2)}$:

$$\langle \delta F_q^{(2)}(t) \rangle = \int \frac{d\omega}{2\pi} \int \frac{d\omega'}{2\pi} \int \frac{d\omega''}{2\pi} e^{-i\omega t - i\omega' t} \chi_q^{(2)}[\omega, \omega', \omega''] g[\omega - \omega''] g[\omega' + \omega''], \quad (103)$$

where

$$\begin{aligned} \chi_q^{(2)}[\omega, \omega', \omega''] &= i\omega\omega' \lambda_0 \mu_0 h(\omega) h(\omega') \\ &\times \left[4\mu_0^2 \Theta(\omega'') \omega'' \mathcal{Q}[\omega, \omega', \omega''] h(\omega'') h(-\omega'') + \text{sgn}(\omega') \omega' (\omega + \omega') \right], \end{aligned} \quad (104)$$

and thus

$$\langle \delta F_q^{(2)}[\omega] \rangle = \int \frac{d\omega'}{2\pi} \int \frac{d\omega''}{2\pi} \chi_q^{(2)}[\omega', \omega - \omega', \omega''] g[\omega' - \omega''] g[\omega - \omega' + \omega'']. \quad (105)$$

5.2. Mirror with Time-Dependent Properties

Now, using the definition of the first-order perturbation from Equation (41) and the second-order perturbation from Equation (51) for a $\delta - \delta'$ mirror with time dependent material properties Equation (98) becomes

$$\begin{aligned} \text{Tr} \left[\eta \delta C_\mu^{(2)}[\omega, \omega'] \right] &= - \int \frac{d\omega''}{2\pi} \frac{\Theta(\omega'')}{2\omega''} \mu_0^2 h(\omega) h(\omega') f[\omega - \omega''] f[\omega' + \omega''] \text{Tr} \left[\eta \mathbb{S}_\mu[\omega''] \mathbb{S}_\mu[-\omega'']^T \right] \\ &- \int \frac{d\omega''}{2\pi} \frac{\text{sgn}(\omega')}{2\omega'} \mu_0^2 h(\omega) h(\omega'') f[\omega - \omega''] f[\omega' + \omega''] \text{Tr} \left[\eta S_0[\omega'] \mathbb{S}_\mu[-\omega']^T \right] \end{aligned} \quad (106)$$

We find:

$$\text{Tr} \left[\eta \mathbb{S}_\mu[\omega''] \mathbb{S}_\mu[-\omega'']^T \right] = \frac{8\lambda_0(1 + \lambda_0^2)\omega''^2}{\mu_0^2 + \omega''^2(1 + \lambda_0^2)} = -8\lambda_0(1 + \lambda_0^2)\omega''^2 h(\omega'') h(-\omega''), \quad (107)$$

$$\text{Tr} \left[\eta S_0[\omega'] \mathbb{S}_\mu[-\omega']^T \right] = \frac{4\lambda_0\omega'}{i\mu_0 + \omega'(1 + \lambda_0^2)^2} = 4\omega' \lambda_0 h(\omega'), \quad (108)$$

Expressing the second-order force in terms of $\chi_\mu^{(2)}$:

$$\langle \delta F_\mu^{(2)}(t) \rangle = \int \frac{d\omega}{2\pi} \int \frac{d\omega'}{2\pi} \int \frac{d\omega''}{2\pi} e^{-i\omega t - i\omega' t} \chi_\mu^{(2)}[\omega, \omega', \omega''] f[\omega - \omega''] f[\omega' + \omega''], \quad (109)$$

where

$$\chi_\mu^{(2)}[\omega, \omega', \omega''] = 2\omega\omega' \lambda_0 \mu_0^2 h(\omega) h(\omega') h(\omega'') \left[2(1 + \lambda_0^2) \Theta(\omega'') \omega'' h(-\omega'') - \text{sgn}(\omega') \right], \quad (110)$$

leads to

$$\langle \delta F_\mu^{(2)}[\omega] \rangle = \int \frac{d\omega'}{2\pi} \int \frac{d\omega''}{2\pi} \chi_\mu^{(2)}[\omega', \omega - \omega', \omega''] f[\omega' - \omega''] f[\omega - \omega' + \omega'']. \quad (111)$$

While the first-order force calculation (see Equation (71)) agrees with that from Ref. [6], the corresponding second-order force calculation (see Equation (111)) does not. The susceptibility in Equation (110) differs substantially and includes an additional term dependant on $(1 + \lambda_0^2)$. We believe our derivation of the second-order force term is correct and indicates an issue in the corresponding calculation in Ref. [6].

5.3. Force from the Interference Effect

A system that possesses two distinct sources of time-dependent fluctuations experiences an interference effect due to the interaction between these two sources [9,21]. This interaction occurs as a second-order effect, as there is no first-order mixing term present. Thus, in addition to the independent force terms that are present at the second order,

there is a mixing of the first-order perturbation terms, $\delta S_\mu^{(1)}[\omega, \omega']$ (see Equation (41)) and $\delta S_q^{(1)}[\omega, \omega']$ (see Equation (48)):

$$\langle \delta F_{\text{int}}^{(2)}(t) \rangle = \int \frac{d\omega}{2\pi} \int \frac{d\omega'}{2\pi} e^{-i\omega t - i\omega' t} \omega \omega' \text{Tr} \left[\eta \delta C_{\text{int}}^{(2)}[\omega, \omega'] \right], \quad (112)$$

where

$$\delta C_{\text{int}}^{(2)}[\omega, \omega'] = \int \frac{d\omega''}{2\pi} \int \frac{d\omega'''}{2\pi} \left(\delta S_\mu^{(1)}[\omega, \omega''] C_{\text{in}}[\omega'', \omega'''] \delta S_q^{(1)}[\omega', \omega''']^T + \delta S_q^{(1)}[\omega, \omega''] C_{\text{in}}[\omega'', \omega'''] \delta S_\mu^{(1)}[\omega', \omega''']^T \right). \quad (113)$$

With $C_{\text{in}}[\omega, \omega'] = 2\pi \delta(\omega + \omega') c_{\text{in}}[\omega]$, as in Equation (12), this becomes

$$\delta C_{\text{int}}^{(2)}[\omega, \omega'] = \int \frac{d\omega''}{2\pi} \left(\delta S_\mu^{(1)}[\omega, \omega''] c_{\text{in}}[\omega''] \delta S_q^{(1)}[\omega', -\omega'']^T + \delta S_q^{(1)}[\omega, \omega''] c_{\text{in}}[\omega''] \delta S_\mu^{(1)}[\omega', -\omega'']^T \right), \quad (114)$$

which can be further simplified with the definition of $c_{\text{in}}[\omega]$ as in Equation (13) to obtain

$$\delta C_{\text{int}}^{(2)}[\omega, \omega'] = \int \frac{d\omega''}{2\pi} \frac{\Theta(\omega'')}{2\omega''} \left(\delta S_\mu^{(1)}[\omega, \omega''] \delta S_q^{(1)}[\omega', -\omega'']^T + \delta S_q^{(1)}[\omega, \omega''] \delta S_\mu^{(1)}[\omega', -\omega'']^T \right). \quad (115)$$

Now, to simplify this expression, we make a change of variables in the second term of Equation (115). We take $\omega'' \rightarrow -\omega''$ and swap $\omega \leftrightarrow \omega'$ to arrive at

$$\delta C_{\text{int}}^{(2)}[\omega, \omega'] = \int \frac{d\omega''}{2\pi} \left(\frac{\Theta(\omega'')}{2\omega''} \delta S_\mu^{(1)}[\omega, \omega''] \delta S_q^{(1)}[\omega', -\omega'']^T + \frac{\Theta(-\omega'')}{2\omega''} \delta S_q^{(1)}[\omega, \omega''] \delta S_\mu^{(1)}[\omega', \omega'']^T \right) \quad (116)$$

Using the properties of the trace, we find:

$$\text{Tr} \left[\eta \delta C_{\text{int}}^{(2)}[\omega, \omega'] \right] = \int \frac{d\omega''}{2\pi} \frac{1}{2\omega''} \text{Tr} \left[\eta \delta S_\mu^{(1)}[\omega, \omega''] \delta S_q^{(1)}[\omega', -\omega'']^T \right], \quad (117)$$

where the identity $\Theta(\omega) + \Theta(-\omega) = 1$ is used. Now, using the definition of the two first-order perturbation terms $\delta S_\mu^{(1)}[\omega, \omega']$ (see Equation (41)) and $\delta S_q^{(1)}[\omega, \omega']$ (see Equation (48)) we find:

$$\text{Tr} \left[\eta \delta C_{\text{int}}^{(2)}[\omega, \omega'] \right] = - \int \frac{d\omega''}{2\pi} \frac{\mu_0}{2} h(\omega) f[\omega - \omega''] g[\omega' + \omega''] \text{Tr} \left[\eta \mathbb{S}_\mu[\omega''] \mathbb{S}_q^{(1)}[\omega', -\omega'']^T \right]. \quad (118)$$

The trace term becomes

$$\text{Tr} \left[\eta \mathbb{S}_\mu[\omega''] \mathbb{S}_q^{(1)}[\omega', -\omega'']^T \right] = 4i\omega'' h(\omega') h(\omega'') h(-\omega'') \mathcal{I}[\omega, \omega', \omega''], \quad (119)$$

where

$$\mathcal{I}[\omega, \omega', \omega''] = i\mu_0^2(1 + \lambda_0^2) + \mu_0(1 - \lambda_0^2)^2 \omega' - 4i\lambda_0^2(1 + \lambda_0^2) \omega' \omega'' \quad (120)$$

We can now express the second-order force due to the interference of the two sources (see Equation (112)) in terms of $\chi_{\text{int}}^{(2)}$:

$$\langle \delta F_{\text{int}}^{(2)}(t) \rangle = \int \frac{d\omega}{2\pi} \int \frac{d\omega'}{2\pi} \int \frac{d\omega''}{2\pi} e^{-i\omega t - i\omega' t} \chi_{\text{int}}^{(2)}[\omega, \omega', \omega''] f[\omega - \omega''] g[\omega' + \omega''], \quad (121)$$

where

$$\chi_{\text{int}}^{(2)}[\omega, \omega', \omega''] = 2i\mu_0 \omega \omega' \omega'' h(\omega) h(\omega') h(\omega'') h(-\omega'') \mathcal{I}[\omega, \omega', \omega'']. \quad (122)$$

The force for the interference term now reads

$$\langle \delta F_{\text{int}}^{(2)}[\omega] \rangle = \int \frac{d\omega'}{2\pi} \int \frac{d\omega''}{2\pi} \chi_{\text{int}}^{(2)}[\omega', \omega - \omega', \omega''] f[\omega' - \omega''] g[\omega - \omega' + \omega'']. \quad (123)$$

6. Conclusions

When a mirror in a vacuum undergoes time-dependent fluctuations, it produces real particles via the dynamical Casimir effect. In the case when such a mirror possesses asymmetric boundary properties, its spectrum of particles is also be asymmetric. This asymmetry in particle production results in a perturbation in the position of the mirror; that is, the imbalance in radiation reaction forces results in induced motion of the mirror [6–8]. The vacuum, in turn, acts as a dissipative medium and resists the motion of the mirror, which is described in part by fluctuation–dissipation theory [18]. Here, we have used fluctuation–dissipation theory to calculate the vacuum-induced response to the time-dependent fluctuations of an asymmetric $\delta - \delta'$ mirror which is both moving and possesses time-dependent material properties. We find that the resulting forces are both dissipative and motion inducing, since the asymmetry in particle production generates a secondary force in addition to the dissipative force of the vacuum, which seeks to suppress the motion of the mirror.

The linear susceptibility, used to calculate the mean force, is calculated to the first- and second-order for both the contribution from the motion of the moving mirror and from the time-dependent boundary conditions. For the first-order, we are able to provide exact results for the susceptibility as well as expansions in the limits $\beta\omega \gg 1$ and $\beta\omega \ll 1$. We plot the resulting force numerically for different values of λ_0 and compare them to the purely dissipative force of a moving Dirichlet mirror. Additionally, we have also looked at the resulting changes to the force when the fluctuation oscillation frequency is increased. The resulting second-order forces are calculated, which also include a mixed interference term in addition to the second-order contributions from the two separate fluctuation sources.

Thus far, our numerical analysis has been restricted to first-order forces with only a single type of oscillation. In the future, we wish to extend these numerical methods to a higher order in force and study other physically interesting types of fluctuations, which would cause novel interactions with the vacuum. Additionally, these methods could be used to analyze work and impulse delivered to the Casimir system, allowing us to determine optimal system configurations along with parameters for generating motion.

Author Contributions: Conceptualization, M.J.G.; data curation, W.D.J.; formal analysis, M.J.G. and W.D.J.; investigation, M.J.G., W.D.J., P.M.B., J.A.M., R.R. and G.B.C.; methodology, M.J.G. and W.D.J.; project administration, G.B.C.; resources, G.B.C.; software, M.J.G., W.D.J. and P.M.B.; supervision, G.B.C.; validation, M.J.G., W.D.J., P.M.B. and J.A.M.; visualization, M.J.G. and W.D.J.; writing—original draft, M.J.G. and W.D.J.; writing—review and editing, M.J.G., W.D.J., P.M.B., J.A.M., R.R. and G.B.C. All authors have read and agreed to the published version of the manuscript.

Funding: This research received no external funding.

Data Availability Statement: The data presented in this study are available on request from the corresponding author.

Acknowledgments: The authors would like to thank Eric Davis for beneficial discussion and review.

Conflicts of Interest: The authors declare no conflicts of interest.

References

1. Dodonov, V.V. Dynamical Casimir effect: Some theoretical aspects. *J. Phys. Conf. Ser.* **2009**, *161*, 012027. [CrossRef]
2. Dodonov, V.V. Current status of the dynamical Casimir effect. *Phys. Scr.* **2010**, *82*, 038105. [CrossRef]
3. Dodonov, V. Fifty years of the dynamical Casimir effect. *Physics* **2020**, *2*, 67–104. [CrossRef]
4. Wilson, C.M.; Johansson, G.; Pourkabirian, A.; Simoen, M.; Johansson, J.R.; Duty, T.; Nori, F.; Delsing, P. Observation of the dynamical Casimir effect in a superconducting circuit. *Nature* **2011**, *479*, 376–379. [CrossRef]
5. Silva, J.D.L.; Braga, A.N.; Alves, D.T. Dynamical Casimir effect with $\delta - \delta'$ mirrors. *Phys. Rev. D* **2016**, *94*, 105009. [CrossRef]
6. Silva, J.D.L.; Braga, A.N.; Rego, A.L.C.; Alves, D.T. Motion induced by asymmetric excitation of the quantum vacuum. *Phys. Rev. D* **2020**, *102*, 125019. [CrossRef]
7. Gorban, M.J.; Julius, W.D.; Brown, P.M.; Matulevich, J.A.; Cleaver, G.B. The asymmetric dynamical Casimir effect. *Physics* **2023**, *5*, 398–422. [CrossRef]

8. Gorban, M.J.; Julius, W.D.; Brown, P.M.; Matulevich, J.A.; Cleaver, G.B. Correction: Gorban et al. The asymmetric dynamical Casimir effect. *Physics* 2023, 5, 398–422. *Physics* 2024, 6, 422–425. [CrossRef]
9. Gorban, M.J.; Julius, W.D.; Radhakrishnan, R.; Cleaver, G.B. Interference phenomena in the asymmetric dynamical Casimir effect for a single $\delta - \delta'$ mirror. *Phys. Rev. D* 2023, 108, 096037. [CrossRef]
10. Barton, G.; Calogeracos, A. On the quantum electrodynamics of a dispersive mirror: I. Mass shifts, radiation, and radiative reaction. *Ann. Phys.* 1995, 238, 227–267. [CrossRef]
11. Nicolaevici, N. Quantum radiation from a partially reflecting moving mirror. *Class. Quant. Grav.* 2001, 18, 619–628. [CrossRef]
12. Nicolaevici, N. Semitransparency effects in the moving mirror model for Hawking radiation. *Phys. Rev. D* 2009, 80, 125003. [CrossRef]
13. Dalvit, D.A.R.; Maia Neto, P.A. Decoherence via the dynamical Casimir effect. *Phys. Rev. Lett.* 2000, 84, 798–801. [CrossRef]
14. Muñoz-Castañeda, J.M.; Mateos Guilarte, J. $\delta - \delta'$ generalized Robin boundary conditions and quantum vacuum fluctuations. *Phys. Rev. D* 2015, 91, 025028. [CrossRef]
15. Braga, A.N.; Silva, J.D.L.; Alves, D.T. Casimir force between $\delta - \delta'$ mirrors transparent at high frequencies. *Phys. Rev. D* 2016, 94, 125007. [CrossRef]
16. Rego, A.L.C.; Braga, A.N.; Silva, J.D.L.; Alves, D.T. Dynamical Casimir effect enhanced by decreasing the mirror reflectivity. *Phys. Rev. D* 2022, 105, 025013. [CrossRef]
17. Silva, H.O.; Farina, C. Simple model for the dynamical Casimir effect for a static mirror with time-dependent properties. *Phys. Rev. D* 2011, 84, 045003. [CrossRef]
18. Jackel, M.-T.; Reynaud, S. Fluctuations and dissipation for a mirror in vacuum. *Quant. Opt.* 1992, 4, 39–53. [CrossRef]
19. Jaekel, M.-T.; Reynaud, S. Quantum fluctuations of position of a mirror in vacuum. *J. Phys.* 1993, 3, 1–20. [CrossRef]
20. Jaekel, M.-T.; Reynaud, S. Movement and fluctuations of the vacuum. *Rep. Prog. Phys.* 1997, 60, 863–887. [CrossRef]
21. Silva, J.D.L.; Braga, A.N.; Rego, A.L.C.; Alves, D.T. Interference phenomena in the dynamical Casimir effect for a single mirror with Robin conditions. *Phys. Rev. D* 2015, 92, 025040. [CrossRef]

Disclaimer/Publisher’s Note: The statements, opinions and data contained in all publications are solely those of the individual author(s) and contributor(s) and not of MDPI and/or the editor(s). MDPI and/or the editor(s) disclaim responsibility for any injury to people or property resulting from any ideas, methods, instructions or products referred to in the content.

Article

Mass and Magnetic Moment of the Electron and the Stability of QED—A Critical Review

Michael Bordag* and Irina G. Pirozhenko

Bogoljubov Laboratory of Theoretical Physics, Joint Institute for Nuclear Research, 141980 Dubna, Russia; pirozhen@theor.jinr.ru

* Correspondence: bordag@mail.ru

Abstract: The anomalous magnetic moment of the electron, first calculated by Schwinger, lowers the ground state energy of the electron in a weak magnetic field. It is a function of the field and changes signs for large fields, ensuring the stability of the ground state. This has been shown in the past 50 years in numerous papers. The corresponding corrections to the mass of the electron have also been investigated in strong fields using semiclassical methods. We critically review these developments and point out that the calculation for low-lying excited states raises questions. Also, we calculate the contribution from the tadpole diagram, the relevance of which was observed only quite recently.

Keywords: QED; electron mass; magnetic moment

1. Introduction

Quantum electrodynamics (QED) is the fundamental theory for describing the interaction of matter and light. On the classical level, these are the Maxwell theory and the relativistic mechanics, joined by a covariant coupling. QED is the quantum version of these. It was formulated quite early in the history of quantum mechanics, beginning with the paper of Paul Dirac. One of the first calculations of QED effects was the effective Lagrangian of Werner Heisenberg and Hans Euler [1], and the first new effect predicted using QED was the scattering of light on light. About ten years later, in 1948, Hendrick Casimir found [2] a vacuum interaction between neutral conducting plates caused by the quantized electromagnetic field confined between the plates. These two effects can be interpreted as loop correction, or radiative correction, to external influences. In the first case, such influence is provided by a classical electromagnetic field, and in the second case, it is provided by a conductor boundary condition on the plates (or by the freely movable charges within the plates), which also constitute a classical object.

It must be mentioned that there is a different interpretation for these effects saying that the vacuum of QED is filled with a fluctuating electromagnetic field, the interaction of which with the mentioned influences causes the effects. However, in a more formal approach, there is no need to speak about fluctuating fields. Namely, the mentioned effects can be equivalently described as vacuum-to-vacuum transition amplitude in an external field or as the vacuum expectation value of the energy–momentum tensor in the presence of external influences. For details, we refer to one of many books on this topic [3].

Beyond the two mentioned effects go the radiative, or loop, corrections like the anomalous magnetic moment of the electron and the Lamb shift. The former one can be viewed as a correction to the mass of the electron and to its magnetic moment, μ . The magnetic moment can be expressed as $\mu = g\mu_B$ in terms of the Bohr magneton, μ_B , and the gyromagnetic ratio, g . From the Dirac equation, $g = 2$ follows, whereas the radiative corrections cause a deviation, $a_e = (g - 2)/2$, called the anomaly of the magnetic moment. In 1948, Julian Schwinger found [4] $a_e = \alpha/(2\pi)$ in the lowest order in the fine structure constant, α . This anomaly lowers the energy of the ground state of an electron in a magnetic

Citation: Bordag, M.; Pirozhenko, I.G. Mass and Magnetic Moment of the Electron and the Stability of QED—A Critical Review. *Physics* **2024**, *6*, 237–250. <https://doi.org/10.3390/physics6010017>

Received: 22 November 2023

Revised: 22 January 2024

Accepted: 26 January 2024

Published: 18 February 2024



Copyright: © 2024 by the authors. Licensee MDPI, Basel, Switzerland. This article is an open access article distributed under the terms and conditions of the Creative Commons Attribution (CC BY) license (<https://creativecommons.org/licenses/by/4.0/>).

field. Also, it results in a split of the excited energy levels. This split was measured in the so-called $g - 2$ experiments with high precision and showed an excellent agreement with the theory (including higher powers of α).

In a weak magnetic field, the lowering of the ground state energy is proportional to the magnetic field. However, for an increasing field (as well as for higher excited states), it becomes a function of the field and it changes sign before the total energy can reach zero, ensuring the stability of the ground state. It must be mentioned that in theories with higher spin ($s > 1/2$), there is no stability. An example is quantum chromodynamics (QCD), where the so-called Savvidy vacuum is unstable, as shown in Ref. [5]; for a recent review, see [6].

In line with these examples, the Casimir effect is not only a phenomenon arising from vacuum fluctuations, but it may also bear instabilities under certain boundary conditions. In Appendix A, we refer to the Robin boundary conditions as an example. Like in a strong magnetic field, for certain values of the parameters, the energy of the lowest state may be below zero and constitute the instability of the system. It must be mentioned that in the literature on the Casimir effect, a situation with instabilities is rarely considered, although it well deserves more attention.

The present paper is a critical review on the question of the stability of QED in a magnetic field. The point is the following. While for the ground state the stability can be shown using a quite simple calculation and for high excited states and/or strong magnetic field using asymptotic methods, for lower excited states and medium fields, one is left with numerical investigation. Such analysis was performed in Ref. [7].

However, as we point out here, there are questions about the methods used in Ref. [7]. In addition, recently, in Ref. [8], it was observed that a class of diagrams (one-particle irreducible ones) do not vanish in distinction from earlier belief and may give an additional contribution.

For this reason, in what follows, we are interested only in the one-loop correction to the mass of the electron in a homogeneous magnetic field. Therefore, we do not consider the motion of the electron in the direction of the field and use the simplified notation.

It worth noting that the motion of an electron in a magnetic field is a field of vital interest, not so much in connection with the stability of QED as in connection with the synchrotron radiation which appears on the tree level as well as from the imaginary part of the radiative correction to the electron mass, see [9] and the book [10], for example. An essential tool is the semiclassical approximation, i.e., mass correction for high excited levels, see [11–13].

The paper is organized as follows. In Section 2, we reproduce and discuss the formulas known in the literature with a focus on the proper time representation. In Sections 2.1 and 2.2, we discuss the problems which appear. In Section 3, we consider the one-particle irreducible (1PI) contribution. Section 4 gives conclusions of the study.

Throughout the paper, we use notations with $\hbar = c = 1$ for the reduced Planck's constant, \hbar , and the speed of light, c .

2. The Mass and the Magnetic Moment of the Electron in a Magnetic Field

We consider the effective Dirac equation, i.e., the Dirac equation with loop corrections,

$$(i\mathcal{D} - m)\psi(x) + \int dx' \Sigma(x, x')\psi(x') = 0, \tag{1}$$

in one loop approximation. Here, x represents a four-dimensional coordinate, ψ is the wave function, m denotes the mass of a particle. The covariant derivative is $\mathcal{D} = \gamma^\mu D_\mu$, with γ_μ the Dirac matrices, $D_\mu = \partial_\mu - ieA_\mu$, where e is the elementary charge, A_μ denotes the electromagnetic potential, the Greek indices take the values 0 (for the time coordinate), 1, 2, and 3 (space), and the self-energy operator, $\Sigma(x, x')$, reads

$$\Sigma(x, x') = \begin{array}{c} \text{wavy line} \\ \text{---} \\ \text{doubled line} \end{array} = -ie^2 D_{\mu\nu}(x, x') \gamma^\mu S(x, x') \gamma^\nu, \quad (2)$$

where the wavy line represents the photon propagator, $D_{\mu\nu}(x, x')$, the doubled line represents dressed electron propagator and the dots represent interaction vertices. The spinor propagator $S(x, x')$, which is 'exact' in the field A_μ , obeys

$$(i\mathcal{D} - m)S(x, x') = \delta(x - x'), \quad (3)$$

where $\delta(x - a)$ is the Dirac delta function.

From Equation (1), for the electron, a mass,

$$M = m + \Delta M, \quad (4)$$

follows with a mass correction ΔM . In the given order of approximation, ΔM is the expectation value of the self-energy operator in the unperturbed states.

From here on, we consider a homogeneous magnetic field, H . Then, the mass correction is the average

$$\begin{aligned} \Delta M(N, \zeta) &= \langle N, \zeta | \Sigma(x, x') | N, \zeta \rangle, \\ &= \int d^3x \int d^3x' \bar{\psi}_{M, \zeta}(\vec{x}) \Sigma(x, x') \psi_{M, \zeta}(\vec{x}) \end{aligned} \quad (5)$$

and it depends on the state of the electron. The eigenfunctions, taken in coordinate representation, read $\langle x | N, \sigma \rangle = e^{-iE_N t} \psi_{N, \zeta}(\vec{x})$, and they obey the Dirac equation

$$(i\mathcal{D} - m) | N, \zeta \rangle = 0. \quad (6)$$

The $\psi_{N, \zeta}(\vec{x})$ are the known eigenspinors, and the one-particle energy is

$$E_N = \sqrt{m^2 + p_3^2 + 2eHN}, \quad N = 0, 1, \dots, \quad (7)$$

where p_3 is the momentum third space-component.

The states are numbered by N , and the spin projection is $\zeta = \pm 1$. The number N consists of two parts,

$$N = n + \frac{1}{2}(1 - \zeta) \quad (8)$$

where $n = 0, 1, \dots$ numbers the Landau levels in the magnetic field. The ground state has $n = 0$ and $\zeta = 1$ (spin projection parallel to the field). The excited states are doublets, which are degenerated on the tree level and split by the radiative correction.

As soon as $\zeta^2 = 1$, the mass correction (5) can be written in the form

$$\Delta M(N, \zeta) = \Delta M_0(N) + \zeta \Delta M_\zeta(N), \quad N = 1, 2, \dots, \quad (9)$$

for the excited states. For the ground state, one has only

$$\Delta M(N, \zeta) = \Delta M_0(0). \quad (10)$$

A split like in the excited states is formally possible, but physically meaningless. Making a non-relativistic approximation in (7), one comes to

$$E_N = m + \frac{p_3^2}{2m} + \mu_B H \left(2n + 1 - g \frac{\zeta}{2} \right) + \dots \quad (11)$$

For the free Dirac equation, $g = 2$ follows, and from the loop correction, one has

$$g = 2(1 + a_e), \tag{12}$$

where a_e is the anomaly factor and $\mu_B a_e$ is the so-called anomalous magnetic moment. Comparing Equation (11) with Equation (7), one identifies

$$\Delta M(N, \zeta) = \mu_B H a_e. \tag{13}$$

This way, the anomaly factor becomes a function of both the field and the state.

For the calculation of the mass correction, there are two known methods. The first starts from the representation of the electron propagator in terms of the eigenspinors $\psi_{N,\zeta}(x)$ and the one-particle energies E_N , which is an eigenfunction representation. This way was used in Refs. [14,15]. The representation of the mass correction is in terms of an integral over the photon loop momentum (in polar coordinates $|k|$ and $\cos \theta$) and a sum over the intermediate states of the electron. It is convenient for strong fields since in that case only the lowest intermediate state contributes.

The second method uses the proper time representation of the propagators. In Ref. [16], the spinor propagator in the magnetic field was represented this way by performing the sum over the intermediate states. In Ref. [17], this representation was used to obtain an integral representation of the self-energy operator, $\Sigma(x, x')$.

In Ref. [18], a similar result was obtained using the algebraic procedure of Schwinger [19]. This method allows us to obtain the result through bypassing the summation of the eigenfunctions. The method was refined in a subsequent paper [20], and we follow the representation given there.

We use the following notations instead of the ones used in Ref. [20]. We change the integration variable $y \rightarrow x$. For the energy E , we insert E_N (7), and set $p_3 = 0$. In addition, we set $m = 1$ (except in the factor in front) and also $e = 1$ so that one has: $E/m \rightarrow E_N$, $(E^2 - m^2)/m^2 \rightarrow 2NH$ and $(E^2 - m^2)/(eH) \rightarrow 2N$. Finally, the prime is dropped: $\zeta' \rightarrow \zeta$. With this notation, Equation (32) from Ref. [20] reads

$$\Delta M(N, \zeta) = \frac{\alpha m}{2\pi} \int_0^\infty \frac{dx}{x} \int_0^1 du e^{-iux/H} (F - F_{\text{sub}}), \tag{14}$$

where

$$F_{\text{sub}} = 1 + u \tag{15}$$

is the ultraviolet subtraction and

$$\begin{aligned} F &= e^{-i(\beta-(1-u)x)2N} W, \tag{16} \\ W &= \frac{1}{\sqrt{\Delta}} \{ \cos(\beta - x) - i\zeta E_N \sin(\beta - x) + u[\cos(\beta + x) - i\zeta E_N \sin(\beta + x)] \\ &\quad + (1 - u)2NH W_0 \}, \\ W_0 &= \frac{1 - u}{\Delta} \cos(\beta - x) + \frac{u \sin(x)}{\Delta x} \cos(\beta) - \cos(\beta + x). \end{aligned}$$

Equation (25) from Ref. [20] defines β as

$$\tan(\beta) = \frac{(1 - u) \sin(x)}{(1 - u) \cos(x) + u \sin(x)/x} \tag{17}$$

and Equation (29) of Ref. [20] defines

$$\Delta = (1 - u)^2 + 2u(1 - u) \frac{\sin(x) \cos(x)}{x} + u^2 \left(\frac{\sin(x)}{x} \right)^2, \tag{18}$$

which appears in the denominator.

Actually, these notations are not convenient enough. For that reason, we rewrite the notations. We start with the definition

$$h = 1 - u + u \frac{\sin(x)}{x} e^{-ix}. \tag{19}$$

Multiplying h by its complex conjugate, one can see that Δ factorizes,

$$\Delta = h h^*. \tag{20}$$

Further, let us consider

$$1 + i \tan(\beta) = \frac{h e^{ix}}{(1 - u) \cos(x) + u \sin(x)/x}, \tag{21}$$

which allows one to write

$$e^{2i(\beta-x)} = \frac{h}{h^*}. \tag{22}$$

Next, let us consider W_0 in Equation (16). We write the trigonometric functions as sum/difference of the corresponding exponentials, and with Equation (22) one arrives at

$$W_0 = \frac{1 - h e^{2ix}}{2\sqrt{h h^*}} + \text{c.c.}, \tag{23}$$

where ‘c.c.’ denotes the complex conjugate. Using these formulas, we rewrite F in Equation (16) in the form

$$F = \left(\frac{h^*}{h}\right)^N e^{-2iuxN} W, \tag{24}$$

$$W = \frac{1}{2h} (1 + \zeta E_N) (1 + u e^{-2ix}) + \frac{1}{2h^*} (1 - \zeta E_N) (1 + u e^{2ix})$$

$$+ (1 - u) \left[\frac{1 - h e^{2ix}}{2h h^*} + \text{c.c.} \right] 2NH.$$

In this representation, the first two terms are interrelated by the complex conjugation and spin reversal: $\zeta \rightarrow -\zeta$. The third term is of a real value.

The expression (24) can be simplified by keeping in the third term only the contributions from the ‘1’ in the numerator,

$$W = \frac{1}{2h} \left[(1 + u e^{-2ix}) (1 + \zeta E_N) - (1 - u) e^{-2ix} 2NH \right] \tag{25}$$

$$+ \frac{1}{2h^*} \left[(1 + u e^{2ix}) (1 - \zeta E_N) - (1 - u) e^{2ix} 2NH \right]$$

$$+ \frac{1 - u}{h h^*} 2NH.$$

Finally, one arrives at

$$W = \frac{e^{-ix}}{h} \left[\cos(x) (1 + \zeta E_N) - \frac{1 - u}{2} e^{-ix} E_N (E_N + \zeta) \right] \tag{26}$$

$$+ \frac{e^{ix}}{h^*} \left[\cos(x) (1 - \zeta E_N) - \frac{1 - u}{2} e^{ix} E_N (E_N - \zeta) \right]$$

$$+ \frac{1 - u}{h h^*} 2NH.$$

The expression (26) coincides with that in Refs. [17] with $\sigma = -\zeta$, up to an overall factor E_N , of which Ref. [17] has more in the denominator (probably a typo).

In Ref. [7], the expression for ΔM was taken over from Ref. [17] (using different notations). Also using the operator method, in Ref. [21], a representation—Equation (3.18) in Ref. [21]—was derived which coincides with the above one. This representation was also taken over in Ref. [22], Equation (1), where, however, new notations were introduced, $s(x) = 1 - \sin(x)/x$, for instance. Regrettably, the last term in the second line in Equation (1) [22] has a misprint and coincides with Equation (1) if one substitutes $-us(x) \rightarrow 1 + usin(x)/x$.

In Ref. [7], a further set of notations was introduced. In Equation (8), the energy correction is split into real and imaginary parts. This is the expression which in Ref. [7] was used for the numerical evaluation. It can be obtained from Equation (26) with the application of Equation (7), which here takes the form $E_N^2 = 1 + 2NH$. Equation (26) then reads:

$$W = \frac{1}{h h^*} (A + 2NH B + i\zeta E_N C) \tag{27}$$

with

$$\begin{aligned} A &= (1 - u)(1 + u \cos(2x)) + u(1 + u) \frac{\sin(2x)}{2x}, \\ B &= (1 - u) \left(1 - (1 - u) \cos(2x) - u \frac{\sin(2x)}{2x} \right), \\ C &= 2u(1 - u) \sin(x) \left(-\cos(x) + \frac{\sin(x)}{2x} \right). \end{aligned} \tag{28}$$

Actually, Equation (28) is Equations (25) or (26), taken on a common denominator.

In order to investigate the structure of the expression F in Equation (14), it is necessary to look for the singularities in the complex plane. Denoting $x = \zeta + i\eta$, let us first look for the zeros of the expression h (19),

$$h = \frac{1}{2ix} \left(2i(\zeta + i\eta)(1 - u) + u - ue^{2\eta}(\cos(2\zeta) - i \sin(2\zeta)) \right). \tag{29}$$

For $h = 0$, one obtains two equations:

$$e^{2\eta} \cos(2\zeta) = 1 - 2 \frac{1 - u}{u} \eta, \tag{30}$$

$$e^{2\eta} \sin(2\zeta) = -2 \frac{1 - u}{u} \zeta. \tag{31}$$

Equation (31) can be resolved for η , and from the quotient of Equations (30) and (31), one obtains:

$$\eta = \frac{1}{2} \ln \left(\frac{1 - u}{u} \frac{-2\zeta}{\sin(2\zeta)} \right), \tag{32}$$

$$\tan(2\zeta) = \frac{-2(1 - u)\zeta}{u - 2(1 - u)\eta}. \tag{33}$$

Inserting η (32) into Equation (33), it can be seen that there are solutions for

$$\pi(k + 1/2) < \zeta < \pi(k + 1), \quad k = 0, 1, \dots \tag{34}$$

For solutions (34), from Equation (32), follows that $\eta > 0$.

This way, the zeros of h are in the upper half-plane. Straightforwardly, h^* has its zeros in the lower half-plane. For $u = 1$, these zeros reach the real axis in $\zeta = \pi k$. For $u \rightarrow 0$, the zeros go to infinity, $x = \pi\left(k - \frac{1}{2}\right)\left(1 + \frac{1}{\ln(1/u)}\right)$, $\eta \sim \frac{1}{2} \ln \frac{1}{u}$. The zeros are shown in Figure 1.

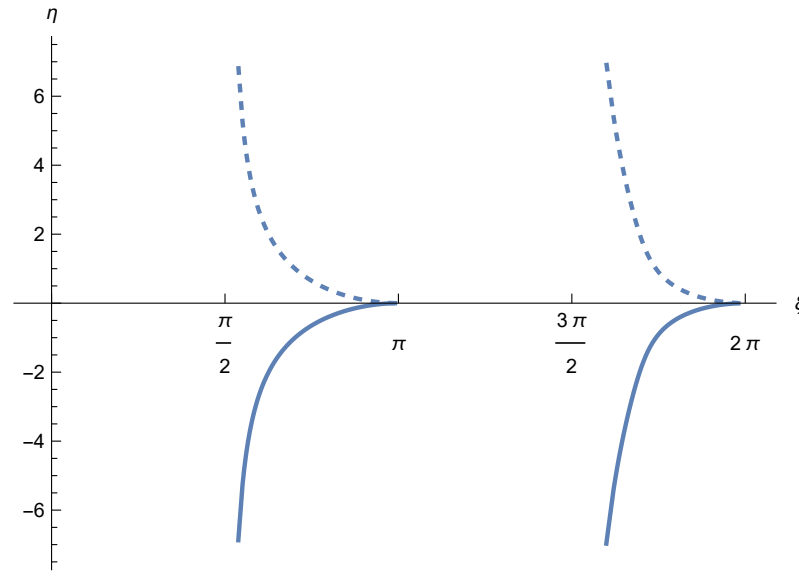


Figure 1. In the complex plane, $x = \zeta + i\eta$, the locations of the zeros of h (19) (upper half-plane, dashed) and of h^* (lower half-plane). In these curves, the parameter u takes values from $u = 1$ at $\eta = 0$ to $u \rightarrow 0$ at $\eta \rightarrow \pm\infty$.

For the ground state, $N = 0$, $\zeta = 1$, the expressions simplify, and using Equations (24) and (25), one comes to

$$F_{\text{ground state}} = \frac{1}{h} \left(1 + ue^{-2ix}\right). \tag{35}$$

Since h has zeros only in the upper half-plane, according to the exponential factor in Equation (14), one may rotate the integration path towards the negative imaginary axis, $x \rightarrow -iy$. The result is a well-converging expression which allows for an immediate numerical evaluation. We repeat here in Figure 2 the representation given in Ref. [23].

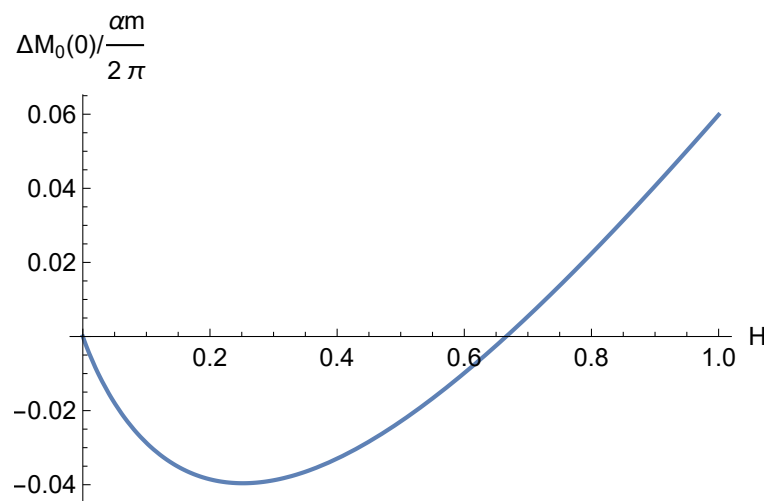


Figure 2. The mass correction $\Delta M_0(0)$, see Equation (10), for the ground state, divided by $\alpha m / (2\pi)$, as a function of the magnetic field. In the minimum, this function takes small values and must be additionally multiplied by α to compare with the rest mass.

For the excited states, the numerical evaluation is considerably more complicated. So far, only one attempt has been undertaken [7], which we consider in Section 2.1 just below.

2.1. On the Numerical Evaluation in Ref. [7] for the Excited States

In Section III of Ref. [7], it is mentioned that a numerical integration over the real x -axis is complicated because of the singularities in $x = \pi n$. A rotation of the integration path downwards in the complex plane, $x \rightarrow -iy$, would cross the singularities (see Figure 1). In Ref. [7], the authors use the following method. The u -integration is divided into two parts at some u_0 . For $0 \leq u \leq u_0$, there are no problems on the real axis and a numerical integration is possible. For $u_0 \leq u \leq 1$, they turn the integration path towards the imaginary axis, see Equation (11) in Ref. [7]. However, this is not possible. As one can see in Figure 1, there are zeros in the denominator for all values of u . From this, we conclude that the numerical results in Ref. [7] are questionable.

2.2. On the Strong Field Limit

The limit of the strong magnetic field, $H \rightarrow \infty$, was calculated for the ground state in Refs. [18,24]. Recently, using an expression similar to Equation (35) from Ref. [23], the limit was recalculated, including the constant term,

$$\Delta M_0(0) = \frac{\alpha m}{2\pi} \frac{5}{2} \left(\ln(2H) - \gamma_E - \frac{3}{2} \right)^2 + a + \mathcal{O}\left(\frac{1}{H}\right), \tag{36}$$

$$a \simeq 4.028717,$$

where γ_E is the Euler’s constant.

For the low excited states ($N = 1, 2, \dots$), there is only one calculation of the strong field limit [24]. It is in terms of the eigenfunction method and it is only for the spin-dependent part. It delivered

$$\Delta M_\zeta(N) \simeq \frac{\alpha m \ln(2H)}{2\pi N}. \tag{37}$$

This way, for a strong field, the mass correction is also positive.

2.3. The Mass Correction for Low-Lying Excited States

An attempt to calculate this mass correction from the formulas which were reproduced in Section 2.2 above hits the following problem. When turning the integration path in (14) into the complex plane, $x \rightarrow -iy$, besides the contributions from the poles which one crosses, the following integral shows up:

$$\Delta M(N, \zeta) = \frac{\alpha m}{2\pi} \int_0^\infty \frac{dy}{y} \int_0^1 du e^{-uy/H} (F - F_{\text{sub}}) + \text{pole terms}. \tag{38}$$

However, for $y \rightarrow \infty$, one observes an asymptotic behavior, using Equations (19) and (30) with $x \rightarrow -iy$,

$$F = \left(\frac{u e^{2(1-u)y}}{u + 2(1-u)y} + \mathcal{O}(1) \right)^N \left[\frac{y}{u} (1 - E_N \zeta) + \frac{y}{u + 2(1-u)y} (1 + E_N \zeta) + \mathcal{O}(e^{-2y}) \right], \tag{39}$$

where

$$h = 1 - u + \frac{u}{2y} + \mathcal{O}(e^{-2y}), \quad h^* = \frac{u}{2y} e^{2y} + \mathcal{O}(1) \tag{40}$$

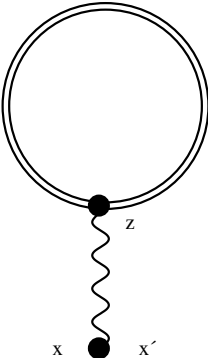
was used. In addition, there is the factor $e^{-uy/H}$ in the integrand. This way, one observes an exponential growth in the integrand for $y \rightarrow \infty$ for $H < \frac{uy}{2(1-u)N}$, i.e., for all finite H . Let us mention that this divergence is absent in the ground state, i.e., for $N = 0$. Also, this

divergence cannot be related to the infrared divergence of the mass operator $\Sigma(x, x')$ in Equation (2), since ΔM in Equation (5) is taken in states. Now, one could speculate on a cancellation from the pole contributions. But this is quite unlikely.

One may wonder how under such circumstances the weak-field expansion derived in Refs. [18,25,26] may be possible. The point is that for real x an expansion in the powers of u and x brings the power N down to factors N , and the resulting, oscillating integrals well may give finite answers. And they do, as follows from the mentioned papers. However, it is clear that the low-field expansion must be an asymptotic one.

3. The Contribution from the Tadpole Diagram

As observed quite recently in Ref. [8], 1PI diagrams can contribute to the effective Lagrangian in a homogeneous background field. The feature is that a tadpole diagram does not vanish. It contributes to the electron self-energy,



$$\Sigma^{1PI}(x, x) = \text{diagram} = ie\gamma_\nu D^{\mu\nu}(x, z) j_\mu(z) \delta(x - x'). \quad (41)$$

The tadpole diagram can be derived from the one-loop Heisenberg–Euler (HE) Lagrangian (see, e.g., [27]) that

$$L_{HE}^{1\text{-loop}} = \frac{1}{8\pi^2} \int \frac{dT}{T^3} e^{-mT^2} \left[\frac{\sqrt{2\mathcal{F}} T}{\tanh(\sqrt{2\mathcal{F}} T)} - \frac{2}{3} T^2 \mathcal{F} - 1 \right], \quad (42)$$

with $\mathcal{F} = \frac{1}{4}(F_{\mu\nu}F^{\mu\nu})$. To mention is the possibility of deriving it from the worldline methods as performed, for example, in Ref. [28] for the spinor propagator. Such a diagram contributes a current (in Ref. [8] called a *photon current*),

$$j_\nu(k) = ieB\varepsilon_{\mu\nu 3} k^\mu \delta^{(4)}(k) \frac{\partial L_{HE}^{1\text{-loop}}}{\partial \mathcal{F}}, \quad (43)$$

where, for a constant purely magnetic field, B , directed along the z -axis, $F_{\mu\nu} = -\varepsilon_{\mu\nu 3} B$, $\mathcal{F} = B^2/2$, k^μ is the 4-momentum, $\varepsilon_{\mu\nu 3}$ is the antisymmetric Levi-Civita symbol, $\delta^{(4)}(k)$ is the four-dimensional Dirac delta, with [8]

$$\frac{\partial L_{HE}^{1\text{-loop}}}{\partial \mathcal{F}} = \frac{e^2}{8\pi} \left[4\zeta'(-1, \chi) - \chi (\zeta'(0, \chi) - \ln \chi + \chi) - \frac{1}{3} \ln \chi - \frac{1}{2} \right], \quad \chi = \frac{m^2}{2eB}, \quad (44)$$

following. In Equation (43), the indices μ and ν take only values 1 and 2. In Equation (44), $\zeta(s, \chi)$ stands for the Hurwitz zeta function.

As it stands, the expression (44) is zero due to the factor k in front of the delta function and the general theory of distributions, and from symmetry reasons as well. However, a more detailed investigation [8] made a regularization of the delta function by considering a non-constant background field. The reason for the vanishing of Equation (43) is that a constant background field cannot support momentum transfer and therefore the momentum k must be zero. However, in a non-constant field, this argument cannot be applied and, in the limit of removing the regularization, one comes to an undefined expression of the

type zero times infinity, to be considered in more details. The calculation realization rests on the ‘local constant field approximation’ [29], which allows us to use the expression of the one-loop effective Lagrangian for constant fields. This way, Ref. [8] calculated the 1PI contribution to the two-loop HE Lagrangian.

A similar effect appears also for the mass correction of the electron. From the Feynman rules and from Equation (41), a mass correction,

$$\Delta M^{1PI}(N, \zeta) = \langle N, \zeta | \Sigma^{1PI}(x, x') | N, \zeta \rangle, \tag{45}$$

follows, which adds to $\Delta M(N, \zeta)$ in Equation (5).

In the sense of some regularization, we take for the delta function in Equation (43) the expression

$$\delta_\epsilon^{(4)}(k) = \frac{e^{-k^2/4\epsilon}}{(4\pi\epsilon)^2}, \tag{46}$$

which is most convenient in the given case. Then, the mass correction $\Delta M^{1PI}(n, \zeta)$ in Equation (45) can be calculated using the states $|n, \zeta\rangle$; these states are known, see, e.g., [30]. In order to be close to the notations of Ref. [30], we change the notation from N from Section 2 to n , and note

$$|n, s, \zeta\rangle = \frac{e^{ip_3z}}{\sqrt{L}} \frac{e^{i\ell\varphi}}{\sqrt{2\pi}} \frac{\sqrt{\gamma}}{\sqrt{K_n(K_n + m)}} (\zeta_+ \delta_{\zeta,1} + \zeta_- \delta_{\zeta,-1}). \tag{47}$$

where the following notations, also close to those in Ref. [30], are used: $\gamma = B/2$, $K_n = \sqrt{m^2 + p_3^2 + 4\gamma n}$ and

$$\zeta_+ = \begin{pmatrix} (K_n + m) I_{n-1,s}(\rho) e^{-i\varphi/2} \\ 0 \\ p_3 I_{n-1,s}(\rho) e^{-i\varphi/2} \\ i\sqrt{4\gamma n} I_{n,s}(\rho) e^{i\varphi/2} \end{pmatrix}, \quad \zeta_- = \begin{pmatrix} 0 \\ i(K_n + m) I_{n,s}(\rho) e^{i\varphi/2} \\ \sqrt{4\gamma n} I_{n-1,s}(\rho) e^{-i\varphi/2} \\ -p_3 I_{n,s}(\rho) e^{i\varphi/2} \end{pmatrix}, \tag{48}$$

where $\rho = Br^2/2$ is the radial variable, ζ_\pm are the spinor factors for spin projection $\zeta = \pm 1$ and $n = 0, 1, \dots$ enumerates the energy levels (7). These levels are degenerated with respect to the orbital quantum number l , which is related by

$$l = n + s \tag{49}$$

to the principal quantum number $s = 0, 1, \dots$ and takes values $-\infty < l < n$. The radial wave functions $I_{n,s}(\rho)$ are given by

$$I_{n,s}(\rho) = (-1)^l \sqrt{\frac{n!}{s!}} \rho^{-1/2} e^{-\rho/2} L_n^{-1}(\rho) \tag{50}$$

in terms of Laguerre polynomials. Below, we set the electron mass $m = 1$.

Using Equations (47)–(50), the calculation of the matrix elements becomes just a computing task. Since the dependence on the momentum p_3 in the direction of the magnetic field can be restored by a Lorentz transform, we restrict ourselves to $p_3 = 0$. The mass correction reads

$$\langle n, s, \zeta | \Sigma^{1PI}(x, x') | n', s', \zeta' \rangle = \int d^4x \bar{\psi}_\zeta^{n,s}(x) i e \gamma_\nu \psi_{\zeta'}^{n',s'}(x) \int d^4z j_\mu(z) D^{\mu\nu}(z, x). \tag{51}$$

Using momentum representation for the current j_μ and the Euclidean propagator, one obtains:

$$\int d^4z j_\mu(z) D_{\mu\nu}(z, x) = \frac{1}{(2\pi)^4} \int d^4k \frac{e^{-ikx}}{k^2} j_\nu(k) \tag{52}$$

$$= \frac{2eB\varepsilon_{\nu\mu 3}}{(4\pi\varepsilon)^2} \int_0^\infty dt \frac{\partial}{\partial x_\mu} \int d^4k e^{-\frac{k^2}{4\varepsilon} - ikx - tk^2} = \frac{ieB}{32} \frac{\partial L_{HE}^{1-loop}}{\partial \mathcal{F}} \varepsilon_{\nu\mu 3} x_\mu. \tag{53}$$

We represent the vector x in Equation (53) as $x = r \begin{pmatrix} \cos \varphi \\ \sin \varphi \end{pmatrix}$. It is to be multiplied by the gamma matrices. Then,

$$x_2 \gamma_1 - x_1 \gamma_2 = \frac{r}{2i} \left((\gamma_1 - i\gamma_2) e^{i\varphi} - (\gamma_1 + i\gamma_2) e^{-i\varphi} \right). \tag{54}$$

With Equation (48), the spinor diagonal matrix elements turn into

$$\zeta_\pm^\dagger (x_2 \gamma_1 - x_1 \gamma_2) \zeta_\pm = -2i\sqrt{n}(K_n + m) I_{n,s}(\rho) I_{n-1,s}(\rho). \tag{55}$$

These matrix elements (55) are independent of the spin projection and, thanks to this, cannot contribute to the anomalous magnetic moment. Further, there is no contribution to the ground state ($n = 0$) and no contribution to a spin flip. As well, one can observe that the dependence on the azimuthal angle, φ , dropped out so that, from Equation (47), the conservation of angular momentum for non-diagonal matrix elements follows. Finally, one has to insert Equations (47) and Equation (55) into Equation (45) and are left with a radial integration,

$$\int_0^\infty d\rho \sqrt{\rho} I_{n,n-l}(\rho) I_{n-1,n-l}(\rho) = \sqrt{n}. \tag{56}$$

so that one arrives at

$$\begin{aligned} \Delta M^{1PI}(n, s) &= \frac{eB}{16} \frac{\partial L_{HE}^{1-loop}}{\partial \mathcal{F}} \frac{\sqrt{n}}{K_n} \int_0^\infty d\rho \sqrt{\rho} I_{n,n-l}(\rho) I_{n-1,n-l}(\rho). \\ &= \frac{eB}{16} \frac{\partial L_{HE}^{1-loop}}{\partial \mathcal{F}} \frac{n}{\sqrt{1 + 2eB n}}. \end{aligned} \tag{57}$$

Here, $\partial L_{HE}^{1-loop} / \partial \mathcal{F}$ is defined in Equation (44). As it turns out, this contribution to the mass corrections does not depend on the orbital momentum, l , similar to Equation (5). Examples for the dependence on the magnetic field are shown in Figure 3.

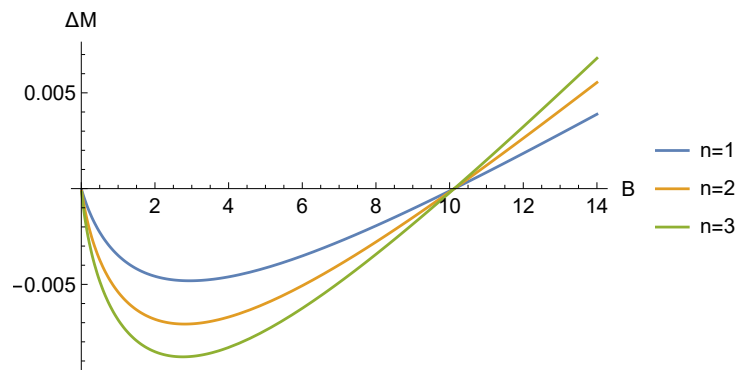


Figure 3. The mass correction ΔM^{1PI} in Equation (57), as a function of the magnetic field, B , for a few n values as indicated.

For the mass correction in a strong field, using the asymptotics of $\partial L_{\text{HE}}^{1\text{-loop}}/\partial\mathcal{F}$ derived in Equation B.6 of Ref. [8] one obtains

$$\Delta M^{1\text{PI}}(n,s) = \frac{\alpha e}{48\sqrt{2}\pi} \sqrt{eBn} \ln\left(\frac{eB}{\sqrt{2}}\right) + \mathcal{O}(\sqrt{B}). \tag{58}$$

This way, the contribution from the tadpole graph follows the general expectation, a negative contribution for small fields and a positive contribution for strong fields.

4. Conclusions

We reconsidered the calculation of the one-loop mass correction of the electron in a homogeneous magnetic field. There are two kind of representations known in the literature. One is in terms of eigenfunctions, and the other one uses the proper time representation and the operator method. We focused on the second case and compared the corresponding results obtained by different authors. In convenient notations, the result can be best written in the form $\Delta M(N, \zeta)$ in Equation (14), with W (26) (or (27)). Quite obvious misprints in the various papers are identified.

For studying the structure of the integrand F , Equation (26) is the most convenient since it has the simplest form of the denominators. On the real x -axis, one observes for $u = 1$, simple poles in $x = \pi\left(n + \frac{1}{2}\right)$, $n = 0, 1, \dots$. The ratio h/h^* in front is regular, and the last term in Equation (26) also has a simple pole if accounting for the integration over u and the factor $(1 - u)$ in the nominator. In the complex plane, one observes simple poles, the locations of which are shown in Figure 1.

As for the ground state, there are coinciding results from all the studies referred to here. The mass correction is shown in Figure 2 and its asymptotics for $H \rightarrow \infty$ are given in Equation (36). The finding demonstrates the stability of the ground state for arbitrary strength of the magnetic field.

For the low excited states, a similar result was obtained numerically in Ref. [7]. However, the method used for the calculation, as laid out in Section III in Ref. [7], raises questions as discussed in Section 2.1 here. More questions arise from the attempt to use the formulas shown in Section 2 for $N > 0$. As shown in Section 2.3, the rotation into the complex plane, $x \rightarrow -iy$, results in an exponential growth for $y \rightarrow \infty$, which should not have been there.

In addition, we calculated the so-far-overlooked contribution to the mass correction from the tadpole. The findings show no addition to the anomalous magnetic moment as well as no addition to the ground state energy. The tadpole contribution to the low excited states is shown in Figure 3. However, in order to compare this contribution with the contribution from Equation (2), more studies are necessary.

It worth mentioning that for high excited states, $N \gg 1$, which is of interest primarily for synchrotron radiation, a semiclassical approach delivers quite simple formulas which all demonstrate a growth in the mass correction in a magnetic field. We did not consider those calculations in the present paper.

In summary, the existing calculation for the mass correction of the electron in a magnetic field suggests no instability in QED. However, there are doubts in the correctness of the mentioned calculations, and a recalculation is advised.

Author Contributions: All authors contributed equally to this work. All authors have read and agreed to the published version of the manuscript.

Funding: This research received no external funding.

Data Availability Statement: Data is contained within the article.

Acknowledgments: The authors thank Sergey L. Lebedev for interesting discussions. The authors also thank the editors for English corrections.

Conflicts of Interest: The authors declare no conflicts of interest.

Appendix A. Robin Boundary Condition

In this Appendix, we refer to the basic formulas with the Robin boundary conditions, which are of interest in context with the Casimir effect and instabilities. The simplest case is a scalar field in four dimensions, obeying the wave equation and the boundary condition

$$(\partial_t^2 - \partial_{\parallel}^2 - \partial_z^2)\phi(\underline{x}) = 0, \quad (1 + \beta\partial_z)\phi(\underline{x})|_{z=0} = 0, \quad (\text{A1})$$

where $\partial_t = \partial/\partial t$, $\partial_{\parallel} = (\partial/\partial x, \partial/\partial y)$ the underlining in \underline{x} denotes a four-vector, β is some parameter and we consider $z \geq 0$. After a Fourier transform in time and with the directions parallel to the plate,

$$\phi(\underline{x}) = e^{-i\omega t + ik_{\parallel} x_{\parallel}} \varphi(z), \quad (\text{A2})$$

the equation $(-\omega^2 + k_{\parallel}^2 - \partial_z^2)\varphi(z) = 0$ follows. With the ansatz $\varphi(z) = e^{-\kappa z}$, from the boundary condition (A1), $\kappa = 1/\beta$ follows. One must assume $\beta > 0$ to obtain a normalizable solution and to arrive at

$$\omega^2 = k_{\parallel}^2 - \kappa^2 \quad (\text{A3})$$

for the frequency. For $k_{\parallel}^2 > \kappa^2$, the frequency is real. This solution describes a surface mode (known, for example, on the surface of metals). However, for $k_{\parallel}^2 < \kappa^2$, the frequency becomes imaginary and there will be a solution exponentially increasing in time. This is the mentioned instability, which is typically excluded from investigating the Casimir effect. It is interesting to note the similarities between Equations (A3) and (11).

References

1. Heisenberg, W.; Euler, H. Folgerungen aus der Diracschen Theorie des Positrons. *Z. Phys.* **1936**, *98*, 714–732. English translation: Consequences of Dirac's theory of positrons. Available online: <http://neo-classical-physics.info/electromagnetism.html> (accessed on 24 January 2024). [CrossRef]
2. Casimir, H.B.G. On the attraction between two perfectly conducting plates. *Proc. Kon. Ned. Akad. Wetensch.* **1948**, *51*, 793–795. Available online: <https://dwc.knaw.nl/DL/publications/PU00018547.pdf> (accessed on 24 January 2024).
3. Bordag, M.; Klimchitskaya, G.L.; Mohideen, U.; Mostepanenko, V.M. *Advances in the Casimir Effect*; Oxford University Press: Oxford, UK, 2009. [CrossRef]
4. Schwinger, J. On quantum-electrodynamics and the magnetic moment of the electron. *Phys. Rev.* **1948**, *73*, 416–417. [CrossRef]
5. Nielsen, N.K.; Olesen, P. Unstable Yang-Mills field mode. *Nucl. Phys. B* **1978**, *144*, 376–396. [CrossRef]
6. Savvidy, G. From Heisenberg-Euler Lagrangian to the discovery of chromomagnetic gluon condensation. *Eur. Phys. J. C* **2020**, *80*, 165. [CrossRef]
7. Geprägs, R.; Riffert, H.; Herold, H.; Ruder, H.; Wunner, G. Electron self-energy in a homogeneous magnetic field. *Phys. Rev. D* **1994**, *49*, 5582–5589. [CrossRef]
8. Gies, H.; Karbstein, F. An addendum to the Heisenberg-Euler effective action beyond one loop. *J. High Energy Phys.* **2017**, *2017*, 108. [CrossRef]
9. Erber, T. High-energy electromagnetic conversion processes in intense magnetic fields. *Rev. Mod. Phys.* **1966**, *38*, 626–659. [CrossRef]
10. Sokolov, A.A.; Ternov, I.M. *Synchrotron Radiation*; Akademie-Verlag GmbH/Pergamon Press Ltd.: Berlin/Braunschweig, Germany, 1968. Available online: https://archive.org/details/isbn_080129455 (accessed on 24 January 2024).
11. Ternov, I.; Tumanov, W. On question of the movement of polarized electrons in magnetic field. *Izv. VUZov SSSR Ser. Fiz. [Bull. High Educ. Establ. USSR Ser. Phys.]* **1960**, *1*, 155. (In Russian)
12. Nikishov, A.I.; Ritus, V.I. Interaction of electrons and photons with a very strong electromagnetic field. *Sov. Phys. Uspekhi* **1970**, *13*, 303–305. [CrossRef]
13. Baier, V.N.; Katkov, V.M.; Fadin, V.S. *Radiation from Relativistic Electrons*; Atomizdat: Moscow, Russia, 1973. (In Russian)
14. Ternov, I.M.; Bagrov, V.G.; Bordovitsyn, V.A.; Dorofeev, O.F. Vacuum magnetic moment of an electron moving in a uniform magnetic field. *Sov. Phys. J.* **1968**, *11*, 11–16. [CrossRef]
15. Kobayashi, M.; Sakamoto, M. Radiative-corrections in a strong magnetic-field. *Prog. Theor. Phys.* **1983**, *70*, 1375–1384. [CrossRef]
16. Géhéniau, J.; Demeur, M. Solutions singulières des équations de Dirac, tenant compte d'un champ magnétique extérieur. *Physica* **1951**, *17*, 71–75. [CrossRef]
17. Constantinescu, D.H. Electron self-energy in a magnetic field. *Nucl. Phys. B* **1972**, *44*, 288–300. [CrossRef]

18. Tsai, W.-Y.; Yildiz, A. Motion of an electron in a homogeneous magnetic-field—Modified propagation function and synchrotron radiation. *Phys. Rev. D* **1973**, *8*, 3446–3460. [CrossRef]
19. Schwinger, J. Classical radiation of accelerated electrons. II. A quantum viewpoint. *Phys. Rev. D* **1973**, *7*, 1696–1701. [CrossRef]
20. Tsai, W.-Y. Modified electron propagation function in strong magnetic fields. *Phys. Rev. D* **1974**, *10*, 1342–1345. [CrossRef]
21. Baĭer, V.N.; Katkov, V.M.; Strakhovenko, V.M. Operator approach to quantum electrodynamics in an external field: The mass operator. *Sov. Phys. JETP* **1975**, *40*, 225–232. Available online: <http://jetp.ras.ru/cgi-bin/e/index/e/40/2/p225?a=list> (accessed on 24 January 2024).
22. Baĭer, V.N.; Katkov, V.M.; Strakhovenko, V.M. Structure of the electron mass operator in a homogeneous magnetic field close to the critical strength. *Sov. Phys. JETP* **1990**, *71*, 657–666. Available online: <http://jetp.ras.ru/cgi-bin/e/index/e/71/4/p657?a=list> (accessed on 24 January 2024).
23. Bordag, M. On instabilities caused by magnetic background fields. *Symmetry* **2023**, *15*, 1137. [CrossRef]
24. Ternov, I.M.; Bagrov, V.G.; Bordovitsyn, V.A.; Dorofeev, O.F. Concerning the anomalous magnetic moment of the electron. *Sov. Phys. JETP* **1969**, *28*, 1206–1209. Available online: <http://jetp.ras.ru/cgi-bin/e/index/e/28/6/p1206?a=list> (accessed on 24 January 2024).
25. Newton, R.G. Radiative effects in a constant field. *Phys. Rev.* **1954**, *96*, 523–528. [CrossRef]
26. Consoli, M.; Preparata, G. On the stability of the perturbative ground state in non-abelian Yang-Mills theories. *Phys. Lett. B* **1985**, *154*, 411–417. [CrossRef]
27. Dunne, G.V. Heisenberg-Euler effective lagrangians: Basics and extensions. In *From Fields to Strings: Circumnavigating Theoretical Physics*; Shifman, M., Vainstein, A., Wheeler, J., Eds.; World Scientific: Singapore, 2005; pp. 445–522. [CrossRef]
28. Ahmadianiaz, N.; Bastianelli, F.; Corradini, O.; Edwards, J.P.; Schubert, C. One-particle reducible contribution to the one-loop spinor propagator in a constant field. *Nucl. Phys. B* **2017**, *924*, 377–386. [CrossRef]
29. Karbstein, F.; Shaisultanov, R. Stimulated photon emission from the vacuum. *Phys. Rev. D* **2015**, *91*, 113002. [CrossRef]
30. Sokolov, A.A.; Ternov, I.M. *Radiation from Relativistic Electrons*; American Institute of Physics Translation Series; American Institute of Physics: New York, NY, USA, 1986. Available online: <https://archive.org/details/radiationfromrel0000soko/> (accessed on 24 January 2024).

Disclaimer/Publisher’s Note: The statements, opinions and data contained in all publications are solely those of the individual author(s) and contributor(s) and not of MDPI and/or the editor(s). MDPI and/or the editor(s) disclaim responsibility for any injury to people or property resulting from any ideas, methods, instructions or products referred to in the content.

Article

Surface Casimir Densities on Branes Orthogonal to the Boundary of Anti-De Sitter Spacetime

Aram Saharian

Institute of Physics, Yerevan State University, 1 Alex Manogian Street, Yerevan 0025, Armenia; saharian@ysu.am

Abstract: The paper investigates the vacuum expectation value of the surface energy–momentum tensor (SEMT) for a scalar field with general curvature coupling in the geometry of two branes orthogonal to the boundary of anti-de Sitter (AdS) spacetime. For Robin boundary conditions on the branes, the SEMT is decomposed into the contributions corresponding to the self-energies of the branes and the parts induced by the presence of the second brane. The renormalization is required for the first parts only, and for the corresponding regularization the generalized zeta function method is employed. The induced SEMT is finite and is free from renormalization ambiguities. For an observer living on the brane, the corresponding equation of state is of the cosmological constant type. Depending on the boundary conditions and on the separation between the branes, the surface energy densities can be either positive or negative. The energy density induced on the brane vanishes in special cases of Dirichlet and Neumann boundary conditions on that brane. The effect of gravity on the induced SEMT is essential at separations between the branes of the order or larger than the curvature radius for AdS spacetime. In the considerably large separation limit, the decay of the SEMT, as a function of the proper separation, follows a power law for both massless and massive fields. For parallel plates in Minkowski bulk and for massive fields the fall-off of the corresponding expectation value is exponential.

Keywords: Casimir effect; anti-de Sitter space; surface energy; Robin boundary conditions

Citation: Saharian, A. Surface Casimir Densities on Branes Orthogonal to the Boundary of Anti-De Sitter Spacetime. *Physics* **2023**, *5*, 1145–1162. <https://doi.org/10.3390/physics5040074>

Received: 11 October 2023
Revised: 18 November 2023
Accepted: 22 November 2023
Published: 14 December 2023



Copyright: © 2023 by the author. Licensee MDPI, Basel, Switzerland. This article is an open access article distributed under the terms and conditions of the Creative Commons Attribution (CC BY) license (<https://creativecommons.org/licenses/by/4.0/>).

1. Introduction

Among the interesting directions in the development of the Casimir effect theory (for a general introduction and applications, see, e.g., [1–6]) is the study of the dependence of expectation values of physical characteristics for quantum fields on the bulk and boundary geometries, as well as on the spatial topology. The interest is motivated by applications in gravitational physics, in cosmology, and in condensed matter physics. Exact analytic expressions for physical characteristics are obtained in geometries with a sufficient degree of symmetry. In particular, the corresponding background geometries include maximally symmetric spacetimes sourced by positive and negative cosmological constants. These geometries, referred as de Sitter (dS) and anti-de Sitter (AdS) spacetimes, respectively, are among the most popular bulks in quantum field theory on curved backgrounds.

The goal of this paper is to investigate the surface Casimir densities on two parallel branes for a scalar field in AdS spacetime. Quantum field theoretical effects on a fixed AdS background have been extensively studied in the literature. These investigations are important for several reasons. The AdS spacetime is a non-globally hyperbolic manifold with a timelike boundary at spatial infinity and the early interest in the formulation of quantum field theory in that geometry was related to principal questions of quantization [7–9] (see also the references in Ref. [10]). The necessity to control the information through the spatial infinity requires the imposition of boundary conditions on quantum fields (for a discussion of possible boundary conditions on the AdS boundary, see, e.g., [11,12]). The different boundary conditions correspond to physically different field theories. The AdS boundary at spatial infinity plays a central role in models of AdS/conformal field

theory (AdS/CFT) correspondence [13–16]. The latter establishes duality between conformal field theory living on the boundary of AdS spacetime and supergravity or string theory on AdS bulk. This holographic correspondence between two different theories provides an efficient computational framework for non-perturbative effects, mapping them to the perturbative region of the dual theory. Within this approach interesting results have been obtained in high energy physics, in quantum chromodynamics, and in condensed matter physics [14,17,18]. The braneworld models [19] with large extra dimensions, both phenomenological- and string-theory-motivated, present another interesting setup where the properties of AdS spacetime play a crucial role. They provide a geometrical solution to the hierarchy problem between the electroweak and gravitational energy scales and serve as an interesting framework to discuss the problems in high energy physics, gravitation, and cosmology.

The braneworld models contain two types of field: fields propagating in the bulk and fields localized on the branes. In simplified models, the interaction between branes and bulk fields is reduced to boundary conditions on the branes. Those conditions modify the spectrum of vacuum fluctuations of bulk quantum fields and give rise to the Casimir-type contributions in the expectation values of physical observables, such as the ground state energy and the vacuum forces acting on the branes. The Casimir energy and forces in the geometry of branes parallel to the AdS boundary have been widely studied in the literature (see [20–35] for early investigations and [36] for a more complete list of references). The Casimir forces can be used as a possible mechanism for stabilization of the interbrane distance that is required to escape the variations in physical constants in the effective theory on the branes. The vacuum fluctuations of the bulk field may also provide a mechanism for the generation of the cosmological constant on branes. More detailed information on the properties of the vacuum state is contained in the expectation values of bilinear combinations of fields, such as the field squared and the energy–momentum tensor. In braneworld models on AdS bulk, those expectation values are considered in Refs. [32,37–45] for scalar, fermionic, and electromagnetic fields.

In the references cited above, the branes are parallel to the AdS boundary (Randall–Sundrum-type models [46,47]). In a number of recent developments in conformal field theories, additional boundaries are present (see, e.g., [48] and references therein). In the context of AdS/CFT correspondence, the corresponding dual theory on the AdS bulk contains boundaries intersecting the AdS boundary (AdS/BCFT correspondence) [49,50]. Another interesting problem on AdS bulk with surfaces crossing its boundary is related to the evaluation of the entanglement entropy of a quantum system in conformal field theory with a boundary. In accordance with the procedure suggested in Refs. [51,52], the entanglement entropy in a bounded region from the CFT side on the AdS boundary is expressed in terms of the area of the minimal surface in the AdS bulk that asymptotes the boundary of CFT (see also [53,54] for reviews). Motivated by those developments, the influence of branes orthogonally intersecting the AdS boundary on the local properties of the scalar vacuum in a general number of spatial dimensions was studied in Refs. [55,56]. As local characteristics of the vacuum state, the expectation values of the field squared and of the energy–momentum tensor were considered. By using the corresponding vacuum stresses, the Casimir forces acting on the branes were investigated as well. It was shown that, in addition to the component perpendicular to the brane, those forces have a nonzero parallel component (shear force). In quantum field theory with boundaries, the expectation values of physical quantities may contain contributions localized on the boundary. The expression for the surface energy–momentum tensor of a scalar field with a general curvature coupling parameter, and for general bulk and boundary geometries, was derived in Ref. [57] by using the standard variational procedure. The corresponding vacuum expectation value in the problem with branes parallel to the AdS boundary was investigated in Refs. [58,59]. The present paper considers the vacuum expectation value of the surface energy–momentum tensor (SEMT) for a scalar field in the problem with two parallel branes orthogonal to the AdS boundary.

The organization of the paper is as follows. Section 2 describes the geometry of the problem and present the expression for the surface energy–momentum tensor. The corresponding vacuum expectation value (VEV) is investigated in Section 3 by using the two-point function from [56]. The surface energy density is decomposed into contributions corresponding to the self-energy of the brane when the second brane is absent and the part induced by the second brane. The renormalization is required only for the first contribution. In the limit of infinite curvature radius, the result for parallel plates in the Minkowski bulk is recovered. Another special case with conformal relation to the Casimir problem in Minkowski spacetime corresponds to a conformally coupled massless field. The behavior of the SEMT in asymptotic regions of the parameters is discussed in Section 4. A numerical analysis for the induced surface energy density is presented as well. The main results of the paper are summarized in Section 5. The regularization of the self-energy contribution, by using the generalized zeta function approach, is considered in Appendix A. The finite part is separated on the basis of principal part prescription.

2. Geometry of the Problem

AdS spacetime is the maximally symmetric solution of the Einstein equations with a negative cosmological constant Λ as the only source of the gravitational field. In Poincaré coordinates (t, x^1, \mathbf{x}, z) , with t denoting the time, $\mathbf{x} = (x^2, \dots, x^{D-1})$ the space coordinates with the spatial dimension $D > 1$, the corresponding metric tensor, g_{ik} , is given by

$$ds^2 = g_{ik}dx^i dx^k = \left(\frac{\alpha}{z}\right)^2 \left[dt^2 - (dx^1)^2 - d\mathbf{x}^2 - dz^2 \right]. \tag{1}$$

Here, the parameter $\alpha = \sqrt{D(1 - D)/(2\Lambda)}$ determines the curvature radius of the background spacetime, $-\infty < x^i < +\infty$ for $i, k = 0, 1, 2, \dots, D - 1$, and $0 \leq z < \infty$. The D -dimensional hypersurfaces $z = 0$ and $z = \infty$ present the AdS boundary and horizon, respectively. The proper distance along the z -direction is measured by the coordinate $y = \alpha \ln(z/\alpha)$, $-\infty < y < +\infty$. In the coordinate system (t, x^1, \mathbf{x}, y) one has $g'_{DD} = 1$ and $g'_{ik} = g_{ik} = e^{-2y/\alpha} \eta_{ik}$, with η_{ik} being the metric tensor for Minkowski spacetime.

The aim is to investigate the surface Casimir densities induced by quantum fluctuations of a scalar field $\varphi(x)$ on codimension one parallel branes located at $x^1 = a_1$ and $x^1 = a_2$, $a_1 < a_2$ (see Figure 1 for the geometry of the problem). Throughout the paper, it is assumed that the field is prepared in the Poincaré vacuum state. For a scalar field with curvature coupling parameter ζ , the corresponding field equation reads

$$\left(\square + \zeta R + m^2 \right) \varphi(x) = 0, \tag{2}$$

where $\square = g^{ik} \nabla_i \nabla_k$ is the covariant d'Alembertian, m is the mass, and $R = 2\Lambda(D + 1)/(D - 1)$ is the Ricci scalar for AdS spacetime. On the branes, the field operator is constrained by Robin boundary conditions,

$$(A_j + B_j n^i_{(j)} \nabla_i) \varphi(x) = 0, \quad x^1 = a_j, \tag{3}$$

where $n^i_{(j)}$ is the normal to the brane at $x^1 = a_j$ pointing into the region under consideration. The branes divide the background space into three regions: $x^1 \leq a_1$, $a_1 \leq x^1 \leq a_2$, and $x^1 \geq a_2$. In the first and third regions, one has $n^i_{(1)} = -\delta^i_1 z/\alpha$ and $n^i_{(2)} = \delta^i_1 z/\alpha$, respectively, where δ^i_k is the Kronecker symbol. For the region $a_1 \leq x^1 \leq a_2$, the normal in Equation (3) is expressed as $n^i_{(j)} = (-1)^{j-1} \delta^i_1 z/\alpha$. In the discussion below, the region between the branes is considered. The VEVs for the regions $x^1 \leq a_1$ and $x^1 \geq a_2$ are obtained in the limits $a_2 \rightarrow \infty$ and $a_1 \rightarrow -\infty$. For the sets of the coefficients $(A_j, B_j) = (A_j, 0)$ and $(A_j, B_j) = (0, B_j)$ the constraints (3) are reduced to Dirichlet and Neumann boundary conditions, respectively. For Robin boundary conditions, here the special case $B_j/A_j = \alpha\beta_j/z$ is assumed, with β_j ,

$j = 1, 2$, being constants. For this choice, the boundary conditions (3), written in terms of the coordinate $x_{(p)}^1 = \alpha x^1/z$, take the form

$$(1 + \beta_j n_{(j)}^1 \partial_{x_{(p)}^1}) \varphi(x) = 0, \quad x^1 = a_j, \tag{4}$$

where $\partial_a \equiv \partial/\partial a$.

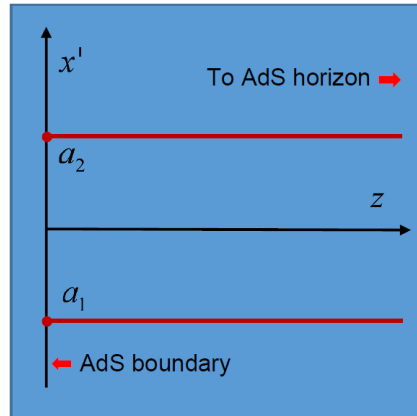


Figure 1. The geometry of two branes orthogonal to the AdS boundary. See text for details.

The latter is the Robin boundary condition with constant coefficient β_j . This coefficient characterizes the properties of the brane and can be used to model the finite penetration length of quantum fluctuations. Note that the coordinate $x_{(p)}^1$ in Equation (4) measures the proper distance from the brane for a fixed z .

For the scalar field modes in the region between the branes, the eigenvalues of the quantum number k^1 , corresponding to the momentum along the direction x^1 , are quantized by the boundary conditions (4). Those eigenvalues are roots of the transcendental equation (see [56])

$$(\beta_1 + \beta_2)k^1 a \cos(k^1 a) + [\beta_1 \beta_2 (k^1)^2 - 1] \sin(k^1 a) = 0, \tag{5}$$

where $a = a_2 - a_1$. Depending on the values of the Robin coefficients, this equation, in addition to an infinite set of roots with real k^1 , may have purely imaginary roots $k^1 = i\chi$ (for the corresponding conditions, see [60]). The energy of the scalar modes, with the momentum $\mathbf{k} = (k^2, \dots, k^{D-1})$, $-\infty < k^i < +\infty$, $i = 2, \dots, D - 1$, in the subspace with coordinates \mathbf{x} , is expressed as $E = \sqrt{(k^1)^2 + \mathbf{k}^2 + \gamma^2}$, where $0 \leq \gamma < \infty$ is the quantum number corresponding to the z -direction. The dependence of the mode functions on the coordinate z is expressed in terms of the function $z^{D/2} J_\nu(\gamma z)$, with $J_\nu(u)$ being the Bessel function and

$$\nu = \sqrt{\frac{D^2}{4} - D(D+1)\xi + m^2 a^2}. \tag{6}$$

Note that, in contrast to the Minkowski bulk, the energy of the scalar modes with given momentum does not depend on the mass of the field quanta. The mass enters in the problem through the parameter $\nu \geq 0$. Now, one can see that in the presence of imaginary roots $k^1 = i\chi$, for the scalar field modes with $\mathbf{k}^2 + \gamma^2 < \chi^2$, the energy becomes imaginary. This signals the instability of the vacuum state under consideration. In the discussion below, the values of the coefficients β_1 and β_2 , for which there are no imaginary roots of the eigenvalue Equation (5), are assumed. The corresponding conditions read [60]

$$\beta_{1,2} \leq 0 \cup \{\beta_1 \beta_2 \leq 0, \beta_1 + \beta_2 > 1/a\}. \tag{7}$$

For a general $(D + 1)$ -dimensional spacetime with a smooth boundary ∂M_s , the SEMT $T_{ik}^{(s)}(x) = \tau_{ik}\delta(x; M_s)$, localized on the boundary by the one-sided Dirac delta function $\delta(x; M_s)$, is given by [57]

$$\tau_{ik} = (1/2 - 2\zeta)h_{ik}\varphi n^l \nabla_l \varphi + \zeta K_{ik}\varphi^2. \tag{8}$$

Here, $h_{ik} = g_{ik} + n_i n_k$ is the induced metric on the boundary, with n_i being the inward-pointing unit normal vector for M_s , and $K_{ik} = h_i^l h_k^m \nabla_l n_m$ is the corresponding extrinsic curvature tensor. The expression (8) was obtained in Ref. [57] by using the standard variational procedure for the action of a scalar field with general curvature coupling parameter and with an appropriate boundary term localized on M_s . Denoting the vacuum state by $|0\rangle$, the VEV of the SEMT is presented as

$$\langle 0|T_{ik}^{(s)}(x)|0\rangle = \delta(x; M_s)\langle 0|\tau_{ik}(x)|0\rangle, \tag{9}$$

where the VEV $\langle \tau_{ik}(x) \rangle \equiv \langle 0|\tau_{ik}(x)|0\rangle$ is written in terms of the Hadamard function $G^{(1)}(x, x') = \langle 0|\varphi(x)\varphi(x') + \varphi(x')\varphi(x)|0\rangle$ by the formula

$$\langle \tau_{ik}(x) \rangle = \frac{1}{2} \lim_{x' \rightarrow x} \left[(1/2 - 2\zeta)h_{ik}n^l \nabla_l + \zeta K_{ik} \right] G^{(1)}(x, x'). \tag{10}$$

The limit contains two types of divergences. The first type of the divergences is present already in the case when the point x does not belong to the boundary. The corresponding divergent part is the same as that in the problem where the branes are absent and is removed by the subtraction from the Hadamard function in Equation (10), the corresponding function in the brane-free geometry. The SEMT is absent in the latter geometry and the brane-free Hadamard function does not contribute to the VEV of the SEMT. The second type of divergences originates from the surface divergences in quantum field theory with boundaries and arises when the point x belongs to the boundary.

3. VEV of the SEMT

3.1. General Expression

In the problem under consideration, and for the region $a_1 \leq x^1 \leq a_2$, the inward-pointing normal is given by $n_i = n_{(j)i} = (-1)^j \delta_i^1 \alpha / z$ for the brane at $x^1 = a_j$. The corresponding induced metric reads $h_{ik} = g_{ik}$, $i, k \neq 1$, and $h_{11} = 0$. Now, it can be immediately checked that the extrinsic curvature tensor for the branes vanishes, $K_{ik} = 0$. Hence, the VEV of the SEMT is expressed as

$$\langle \tau_{ik}(x) \rangle = \left(\frac{1}{4} - \zeta \right) h_{ik} n^l \lim_{x' \rightarrow x} \nabla_l G^{(1)}(x, x'). \tag{11}$$

The expression for the Hadamard function in the region between the branes is obtained from the corresponding expression for the Wightman function derived in Ref. [56]. The Wightman function is presented in the decomposed form

$$\begin{aligned} G^{(1)}(x, x') &= G_j^{(1)}(x, x') + \frac{2(zz')^{D/2}}{(2\pi\alpha)^{D-1}} \int d\mathbf{k} e^{i\mathbf{k}\Delta\mathbf{x}} \int_0^\infty d\gamma \gamma J_\nu(\gamma z) J_\nu(\gamma z') \\ &\times \int_w^\infty d\lambda \frac{\cosh(\sqrt{\lambda^2 - w^2}\Delta t)}{\sqrt{\lambda^2 - w^2}} \frac{2 \cosh[\lambda(x^1 - x'^1)] + \sum_{l=\pm 1} \left[e^{|\lambda x^1 + x'^1 - 2a_j|\lambda} c_j(\lambda) \right]^l}{c_1(\lambda)c_2(\lambda)e^{2a\lambda} - 1}, \end{aligned} \tag{12}$$

where $\Delta\mathbf{x} = \mathbf{x} - \mathbf{x}'$, $w = \sqrt{\gamma^2 + k^2}$, $k = |\mathbf{k}|$, J_ν is the Bessel function, and

$$c_j(\lambda) = \frac{\beta_j \lambda - 1}{\beta_j \lambda + 1}. \tag{13}$$

In Equation (12),

$$G_j^{(1)}(x, x') = G_0^{(1)}(x, x') + \frac{(zz')^{D/2}}{(2\pi\alpha)^{D-1}} \int d\mathbf{k} e^{i\mathbf{k}\Delta\mathbf{x}} \int_0^\infty d\gamma \gamma J_\nu(\gamma z) J_\nu(\gamma z') \times \int_0^\infty d\lambda \frac{e^{-i\sqrt{\lambda^2+w^2}\Delta t}}{\sqrt{\lambda^2+w^2}} \sum_{l=\pm 1} \left[e^{i|x^1+x'^1-2a_j|\lambda} c_j(i\lambda) \right]^l, \tag{14}$$

is the Hadamard function in the problem with a brane at $x^1 = a_j$ when the second brane is absent. Again, it is obtained from the corresponding Wightman function given in Refs. [55,56]. The first term in the right-hand side, $G_0^{(1)}(x, x')$, is the Hadamard function in AdS spacetime without branes. The last term in Equation (12) is interpreted as the contribution to the Hadamard function in the region $a_1 \leq x^1 \leq a_2$, induced by the brane at $x^1 = a_j$ when this term is added to the problem with a single brane at $x^1 = a_j$. Here, and below, $j' = 1$ for $j = 2$ and $j' = 2$ for $j = 1$.

Combining (11) and (12), the SEMT on the brane at $x^1 = a_j$ is decomposed as

$$\langle \tau_{ik} \rangle_j = \langle \tau_{ik} \rangle_j^{(0)} + \langle \tau_{ik} \rangle_j^{\text{ind}}. \tag{15}$$

Here, $\langle \tau_{ik} \rangle_j^{(0)}$ is the VEV of the SEMT when the second brane is absent and $\langle \tau_{ik} \rangle_j^{\text{ind}}$ is induced by the second brane at $x^1 = a_{j'}$. The VEV $\langle \tau_{ik} \rangle_j^{(0)}$ is obtained from Equation (11) with the Hadamard function (14). By taking into account that in the AdS spacetime without branes the SEMT is absent, one obtains:

$$\langle \tau_i^k \rangle_j^{(0)} = (4\xi - 1) \frac{\delta_i^k \beta_j z^{D+1}}{(2\pi)^{D-1} \alpha^D} \int d\mathbf{k} \int_0^\infty d\gamma \gamma J_\nu^2(\gamma z) \int_0^\infty d\lambda \frac{1}{\sqrt{\lambda^2 + b^2}} \frac{\lambda^2}{1 + \lambda^2 \beta_j^2}. \tag{16}$$

The vacuum SEMT induced by the second brane comes from the last term in Equation (12). It is presented in the form

$$\langle \tau_i^k \rangle_j^{\text{ind}} = (4\xi - 1) \frac{2\delta_i^k \beta_j z^{D+1}}{(2\pi)^{D-1} \alpha^D} \int d\mathbf{k} \int_0^\infty d\gamma \gamma J_\nu^2(\gamma z) \int_b^\infty d\lambda \frac{\lambda^2}{\sqrt{\lambda^2 - b^2}} \times \frac{\beta_{j'} \lambda + 1}{\beta_{j'} \lambda - 1} \frac{1}{(\beta_1 \lambda - 1)(\beta_2 \lambda - 1)e^{2a\lambda} - (\beta_1 \lambda + 1)(\beta_2 \lambda + 1)}. \tag{17}$$

The expression (16) for the self-SEMT is divergent and needs a regularization with a subsequent renormalization removing the divergences. This type of surface divergence is well known in quantum field theory with boundaries.

Note that for an observer living on the brane $x^1 = a_j$, the D -dimensional line element is obtained from Equation(1), taking $dx^1 = 0$. It describes D -dimensional AdS spacetime generated by a cosmological constant $\Lambda' = (1 - 2/D)\Lambda$. From the point of view of an observer on the brane, the energy–momentum tensor $\langle \tau_i^k \rangle_j$ is a source of gravitation, with the energy density $\varepsilon_j = \langle \tau_0^0 \rangle_j$ and isotropic effective pressure $p_j = -\langle \tau_2^2 \rangle_j = \dots = -\langle \tau_D^D \rangle_j$. The corresponding equation of state reads $p_j = -\varepsilon_j$, hence $\langle \tau_i^k \rangle_j$ is a source of the cosmological constant type. Certainly, the latter property is a consequence of the symmetry in the problem under consideration. In accordance with Equation (15), the surface energy density is decomposed into the self-energy and the contribution induced by the second brane:

$$\varepsilon_j = \varepsilon_j^{(0)} + \varepsilon_j^{\text{ind}}, \tag{18}$$

where $\varepsilon_j^{\text{ind}} = \langle \tau_0^0 \rangle_j^{\text{ind}}$.

The regularization of the divergent expression on the right-hand side of Equation (16), based on the generalized zeta function approach, is discussed in Appendix A. The expres-

sion is decomposed into pole and finite contributions obtained from Equation (A15) in combination with Equation (A2). In the principal part prescription the finite self-energy, $\epsilon_j^{(0)}$ is identified with the finite part of the corresponding Laurent expansion near the physical point $s = 1$. In order to remove the divergent part, to note is that the VEV $\langle \tau_{ik} \rangle_j$ is a part of a theory which contains other contributions localized on the brane and the divergences in $\langle \tau_{ik} \rangle_j$ are absorbed by renormalizing the parameters in those contributions. The finite part of the SEMT $\langle \tau_{ik} \rangle_j^{(0)}$ is given by Equation (A19). This part contains renormalization ambiguities, which can be fixed by imposing additional renormalization conditions. Here, the situation is completely parallel to that for the case of the total Casimir energy discussed, for example, in Ref. [4]. Similar to Equation (15), the Casimir energy for a system composed of separate bodies is decomposed into the self-energies and the interaction energy. The renormalization is required only for the self-energies.

Unlike the self-energy part, $\epsilon_j^{(0)}$, the surface energy density, ϵ_j^{ind} , and the related SEMT, $\langle \tau_i^k \rangle_j^{\text{ind}}$, are finite and uniquely defined. The main concern in the discussion below is that part of the energy–momentum tensor. Integrating over the angular coordinates of \mathbf{k} and introducing the polar coordinates in the plane (k, u) , one integrates over the related polar angle:

$$\begin{aligned} \langle \tau_i^k \rangle_j^{\text{ind}} &= \frac{(4\xi - 1)\delta_i^k \beta_j z^{D+1}}{2^{D-2} \pi^{\frac{D-1}{2}} \Gamma(\frac{D-1}{2}) \alpha^D} \int_0^\infty d\gamma \gamma J_\nu^2(\gamma z) \int_0^\infty dr r^{D-2} \frac{\beta_j \lambda + 1}{\beta_j \lambda - 1} \\ &\times \frac{\lambda}{(\beta_1 \lambda - 1)(\beta_2 \lambda - 1)e^{2a\lambda} - (\beta_1 \lambda + 1)(\beta_2 \lambda + 1)} \Big|_{\lambda = \sqrt{\gamma^2 + r^2}}. \end{aligned} \tag{19}$$

Next, let us introduce polar coordinates in the plane (γ, r) . The angular integral is evaluated by using the result [61]

$$\int_0^1 dx x(1 - x^2)^{\frac{D-3}{2}} J_\nu^2(ux) = \frac{\Gamma(\frac{D-1}{2})}{2^{2\nu+1}} u^{2\nu} F_\nu(u), \tag{20}$$

with the function

$$F_\nu(u) = \frac{{}_1F_2(\nu + \frac{1}{2}; \frac{D+1}{2} + \nu, 1 + 2\nu; -u^2)}{\Gamma(\frac{D+1}{2} + \nu)\Gamma(1 + \nu)}. \tag{21}$$

Here, Γ is the gamma function and ${}_1F_2(a; b, c; x)$ is the hypergeometric function. This gives:

$$\langle \tau_i^k \rangle_j^{\text{ind}} = \frac{(4\xi - 1)\delta_i^k \beta_j z^{D+2\nu+1}}{2^{D+2\nu-1} \pi^{\frac{D-1}{2}} \alpha^D} \int_0^\infty d\lambda \frac{\beta_j \lambda + 1}{\beta_j \lambda - 1} \frac{\lambda^{D+2\nu+1} F_\nu(\lambda z)}{(\beta_1 \lambda - 1)(\beta_2 \lambda - 1)e^{2a\lambda} - (\beta_1 \lambda + 1)(\beta_2 \lambda + 1)}. \tag{22}$$

From this it follows that the induced SEMT on the brane $x^1 = a_j$ vanishes for special cases of Dirichlet and Neumann boundary conditions on that brane. Depending on the coefficients β_j and on the separation between the branes, the induced energy density ϵ_j^{ind} can be either positive or negative (see numerical examples below). Introducing a new integration variable $u = \lambda z$, one can see that the product $\alpha^D \langle \tau_i^k \rangle_j^{\text{ind}}$ depends on the quantities z, a_j, β_j , having dimension of length, in the form of two dimensionless ratios $a/z, \beta_j/z$. Those ratios are the proper values of the quantities, measured by an observer with fixed z , in units of the curvature radius α . This feature is a consequence of the AdS maximal symmetry.

3.2. Minkowskian Limit and a Conformally Coupled Massless Field

To clarify the features of the SEMT on the branes, let us consider special cases and asymptotic regions of the parameters. First, let us discuss the Minkowskian limit corresponding to $\alpha \rightarrow \infty$ for fixed coordinate y . For the coordinate z , in the leading or-

der, one has $z \approx \alpha$ and the line element (1) tends to the Minkowskian interval $ds_M^2 = dt^2 - (dx^1)^2 - dx^2 - dy^2$. The geometry of the corresponding problem consists of two parallel plates at $x^1 = a_1$ and $x^1 = a_2$ with the boundary condition $(1 - (-1)^j \beta_j \partial_1) \varphi(x) = 0$ at $x^1 = a_j$ in the region $a_1 \leq x^1 \leq a_2$; here, $\partial_1 \equiv \partial/\partial_{x^1}$. For relatively large values of α and for a massive field, the parameter ν is large, $\nu \approx m\alpha$, and one needs the asymptotic of the function $F_\nu(\lambda z)$ when both the argument and the order are considerably large. The corresponding analysis in Ref. [55] shows that the function $F_\nu(\nu\lambda/m)$ is exponentially suppressed for $\nu \gg 1$ and $\lambda < m$. For $\lambda > m$, the leading behavior is approximated by [55]

$$F_\nu\left(\frac{\nu}{m}\lambda\right) \approx \frac{(\lambda^2 - m^2)^{D/2-1} (2m/\nu)^{2\nu+1}}{2\sqrt{\pi}\Gamma(\frac{D}{2})\lambda^{D+2\nu-1}}. \tag{23}$$

By using this asymptotic for the part of the integral in Equation (22) over the region $m \leq \lambda < \infty$, one obtains the SEMT on the plate $x^1 = a_j$ in Minkowski spacetime, $\langle \tau_i^k \rangle_{(M)j}^{\text{ind}} = \lim_{\alpha \rightarrow \infty} \langle \tau_i^k \rangle_j^{\text{ind}}$, given by

$$\langle \tau_i^k \rangle_{(M)j}^{\text{ind}} = \frac{(4\zeta - 1)\delta_i^k \beta_j}{2^{D-1}\pi^{D/2}\Gamma(\frac{D}{2})} \int_m^\infty d\lambda \frac{\beta_j \lambda + 1}{\beta_j \lambda - 1} \frac{\lambda^2 (\lambda^2 - m^2)^{D/2-1}}{(\beta_1 \lambda - 1)(\beta_2 \lambda - 1)e^{2a\lambda} - (\beta_1 \lambda + 1)(\beta_2 \lambda + 1)}. \tag{24}$$

This result for a massive field was obtained in Ref. [58] as a limiting case of the problem with two branes in AdS spacetime parallel to the AdS boundary. In the case of a massless field, the expression for $\langle \tau_i^k \rangle_{(M)1}^{\text{ind}} + \langle \tau_i^k \rangle_{(M)2}^{\text{ind}}$, obtained from Equation (24), coincides with the result derived in Ref. [60]. The VEV of the SEMT for a single Robin boundary in background of $(3 + 1)$ -dimensional Minkowski spacetime has also been considered in Refs. [62,63].

In the case of a massless field with conformal coupling, one has $\zeta = \zeta_D = \frac{D-1}{4D}$ and $\nu = 1/2$. By taking into account that $J_{1/2}(x) = \sqrt{\frac{\pi}{2x}} \sin x$, from Equation (20) one obtains [55]:

$$F_{1/2}(u) = \frac{2}{\sqrt{\pi}u^2} \left[\frac{1}{\Gamma(\frac{D}{2})} - \frac{J_{\frac{D}{2}-1}(2u)}{u^{\frac{D}{2}-1}} \right]. \tag{25}$$

Substituting this expression into Equation (22) one obtains

$$\varepsilon_j^{\text{ind}} = (z/\alpha)^D \varepsilon_{(M)j}^{\text{ind}}, \tag{26}$$

with

$$\begin{aligned} \varepsilon_{(M)j}^{\text{ind}} &= -\frac{2^{1-D}\beta_j}{D\pi^{\frac{D}{2}}} \int_0^\infty d\lambda \frac{\beta_j \lambda + 1}{\beta_j \lambda - 1} \left[\frac{1}{\Gamma(\frac{D}{2})} - \frac{J_{\frac{D}{2}-1}(2\lambda z)}{(\lambda z)^{D/2-1}} \right] \\ &\times \frac{\lambda^D}{(\beta_1 \lambda - 1)(\beta_2 \lambda - 1)e^{2a\lambda} - (\beta_1 \lambda + 1)(\beta_2 \lambda + 1)}. \end{aligned} \tag{27}$$

For a conformally coupled massless scalar field, the problem considered here is conformally related to the problem of two Robin plates at $x^1 = a_j, j = 1, 2$, in Minkowski spacetime, described by the interval $ds_M^2 = dt^2 - (dx^1)^2 - dx^2 - dz^2$, intersected by a Dirichlet plate located at $z = 0$. The presence of the latter is related to the boundary condition for scalar field modes imposed on the AdS boundary $z = 0$. The surface energy density (27) is induced on the plate $x^1 = a_j$ by the presence of the second plate $x^1 = a_j$. The part of $\varepsilon_{(M)j}^{\text{ind}}$ coming from the first term in the square brackets is the corresponding quantity in the geometry where the plate $z = 0$ is absent (see Equation (24) for $m = 0$). The part with the second term is a consequence of the presence of the plate $z = 0$. Note that

$\varepsilon_{(M)j}^{\text{ind}}$ vanishes on that plate: $\varepsilon_{(M)j}^{\text{ind}}|_{z=0} = 0$. This is a consequence of Dirichlet boundary conditions at $z = 0$.

4. Asymptotics and Numerical Analysis

In this Section, the behavior of the VEV for SEMT in asymptotic regions of the parameters is studied. Let us start with the asymptotics at relatively small and large separations between the branes. For a given z , the proper separation between the branes is given by $a_{(p)} = \alpha a/z$. For quite small proper separations compared to the curvature radius, one has $a/z \ll 1$ and the integral in Equation (22) is dominated by the contribution of the region with large enough values of the argument of the function $F_\nu(\lambda z)$. By using the corresponding asymptotic [55],

$$F_\nu(u) \approx \frac{2^{2\nu}}{\sqrt{\pi}\Gamma\left(\frac{D}{2}\right)u^{2\nu+1}}, \quad u \gg 1, \tag{28}$$

one can see that the relation

$$\langle \tau_i^k \rangle_j^{\text{ind}} \approx (z/\alpha)^D \langle \tau_i^k \rangle_{(M)j}^{\text{ind}}|_{m=0}, \tag{29}$$

takes place, where $\langle \tau_i^k \rangle_{(M)j}^{\text{ind}}|_{m=0}$ is given by Equation (24) with $m = 0$. In the limit under consideration, the main contribution to the SEMT comes from the zero-point fluctuations with wavelengths smaller than the curvature radius and the effect of the gravitational field is weak. The asymptotic (29) is further simplified if the separation a is smaller than the length scales determined by the boundary conditions, $a/|\beta_l| \ll 1, l = 1, 2$. For Dirichlet boundary conditions on the brane $x^1 = a_j, \beta_j = 0$, the condition $a/|\beta_j| \ll 1$ is assumed. Under those conditions, $\lambda|\beta_l| \gg 1$ ($\lambda|\beta_j| \gg 1$ in the case $\beta_j = 0$) for the region of λ that dominates in the integral on the right-hand side of Equation (24) (with $m = 0$). In the leading order one obtains:

$$\langle \tau_i^k \rangle_j^{\text{ind}} \approx \delta_i^k \frac{(z/\alpha)^D (4\zeta - 1)}{2^D \pi^{\frac{D+1}{2}} a^{D-1}} \zeta(D-1) \Gamma\left(\frac{D-1}{2}\right) \begin{cases} 1/\beta_j, & \beta_j \neq 0 \\ (2^{2-D} - 1)/\beta_j, & \beta_j = 0 \end{cases}, \tag{30}$$

with $\zeta(u)$ being the Riemann zeta function. Note that the asymptotic (29) also describes the behavior of the SEMT near the AdS horizon. As is seen from Equation (30), in the special cases of minimally ($\zeta = 0$) and conformally ($\zeta = \zeta_D$) coupled fields and for quite small separations between the branes, the energy density induced on the brane $x^1 = a_j$ by the second brane is positive for $\beta_j < 0$ and negative for $\beta_j > 0$. For the Dirichlet boundary condition on the second brane ($\beta_j = 0$), the sign of the induced energy density coincides with the sign of the product $(1 - 4\zeta)\beta_j$.

In the opposite limit of considerably large proper separations compared with the curvature radius, one has $a/z \gg 1$ and the main contribution to the integral in Equation (22) gives the region near the lower limit, corresponding to $\lambda z \ll 1$. In the leading order, replacing the function $F_\nu(\lambda z)$ by

$$F_\nu(0) = \frac{1}{\Gamma(\nu+1)\Gamma\left(\frac{D+1}{2} + \nu\right)}, \tag{31}$$

one obtains

$$\langle \tau_i^k \rangle_j^{\text{ind}} \approx \frac{8(4\zeta - 1)\delta_i^k (z/2)^{D+2\nu+2} \beta_j/z}{\pi^{\frac{D-1}{2}} \Gamma(\nu+1)\Gamma\left(\frac{D+1}{2} + \nu\right) \alpha^D} \int_0^\infty d\lambda \frac{\lambda \beta_j + 1}{\lambda \beta_j - 1} \frac{\lambda^{D+2\nu+1}}{(\lambda \beta_1 - 1)(\lambda \beta_2 - 1)e^{2\lambda a} - (\lambda \beta_1 + 1)(\lambda \beta_2 + 1)}. \tag{32}$$

This expression is further simplified for separations larger than the length scales in Robin boundary conditions. Assuming $a \gg |\beta_l|, l = 1, 2$, one can see that $\lambda|\beta_l| \ll 1$ for the

region, giving the dominant contribution to the integral in Equation (32). For the case of Neumann boundary conditions on the brane $x^1 = a_j$, corresponding to the limit $|\beta_j| \rightarrow \infty$, for separations $a \gg |\beta_j|$, one has $\lambda|\beta_j| \ll 1$ in the region with the dominant contribution to the integral. For the leading order term in the VEV of the SEMT and for non-Neumann ($A_j \neq 0$) boundary conditions on the second brane, one finds:

$$\langle \tau_i^k \rangle_j^{\text{ind}} \approx \delta_i^k \frac{(1 - 4\tilde{\xi})\zeta(D + 2\nu + 2)\beta_j/a}{\pi^{\frac{D}{2}} \Gamma(\nu + 1)\alpha^D (2a/z)^{D+2\nu+1}} (D + 2\nu + 1)\Gamma\left(\frac{D}{2} + \nu + 1\right). \quad (33)$$

For Neumann boundary conditions on the second brane, an additional factor $(2^{-D-2\nu-1} - 1)$ should be added to the right-hand side of Equation (33). One can see that at considerably large distances between the branes the decay of the SEMT, as a function of the proper separation, is a power law for both massive and massless fields. This feature for massive fields is in contrast with the corresponding behavior for parallel plates in the Minkowski bulk, where the suppression is exponential, by the factor e^{-2ma} . Let us note that the Formula (32) also gives the asymptotic of the SEMT near the AdS boundary. As seen, for fixed β_j , the SEMT tends to zero on the AdS boundary, like $z^{D+2\nu+1}$. The asymptotic estimate (33) shows that for $\beta_j < 0$, and for non-Neumann boundary conditions on the second brane ($1/\beta_j \neq 0$), at quite large separations between the branes the induced energy density ϵ_j^{ind} is negative for minimally and conformally coupled fields.

Figure 2 presents the VEV of the energy density, induced on the brane at $x^1 = a_1$ by the brane at $x^1 = a_2$ as a function of the proper separation between the branes a/z . The graphs are plotted for a scalar field in $(4 + 1)$ -dimensional AdS spacetime ($D = 4$), for the Robin boundary condition with $\beta_1/z = -0.5$ and with the mass corresponding to $m\alpha = 0.5$. The dependence on the proper separation is displayed for different values of the ratio β_2/z (the numbers near the curves) and for Dirichlet and Neumann boundary conditions on the second brane. Figure 2, left, and Figure 2, right, correspond to conformally and minimally coupled fields, respectively. In accordance with the asymptotic analysis given above, for minimally and conformally coupled fields and at relatively small separations between the branes, the energy density, induced by the second brane, is positive (negative) for non-Dirichlet (Dirichlet) boundary conditions on the second brane. At considerably large separations, the energy density is negative for non-Neumann boundary conditions on the second brane and is positive for Neumann boundary conditions. The inset in Figure 2, right, is given to emphasize the change in the sign of the surface energy density as a function of the separation between the branes.

In Figure 3, for conformally (Figure 3, left) and minimally (Figure 3, right) coupled scalar fields in $D = 4$ spatial dimensions, the dependence of the energy density ϵ_1^{ind} on the Robin coefficient β_1/z is plotted for different values of the Robin coefficient β_2/z (the numbers marking the curves) on the second brane and for Dirichlet and Neumann boundary conditions. The graphs are plotted for $m\alpha = 0.5$ and $a/z = 1$.

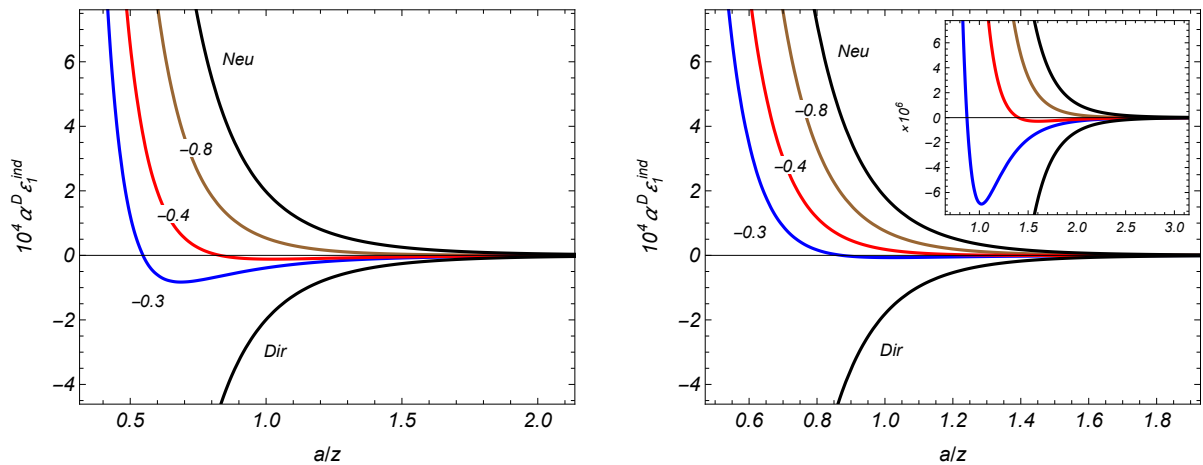


Figure 2. The induced surface energy density on the brane for conformally (left) and minimally (right) coupled fields at $x^1 = a_1$, in units of α^{-D} , versus the proper separation between the branes for $D = 4$, $m\alpha = 0.5$, and $\beta_1/z = 0.5$. The graphs are presented for different values of the ratio β_2/z (the numbers marking the curves) and for Dirichlet (marked "Dir") and Neumann ("Neu") boundary conditions on the second brane ($\beta_2/z = 0$ and $\beta_2/z = \infty$, respectively). See text for details.

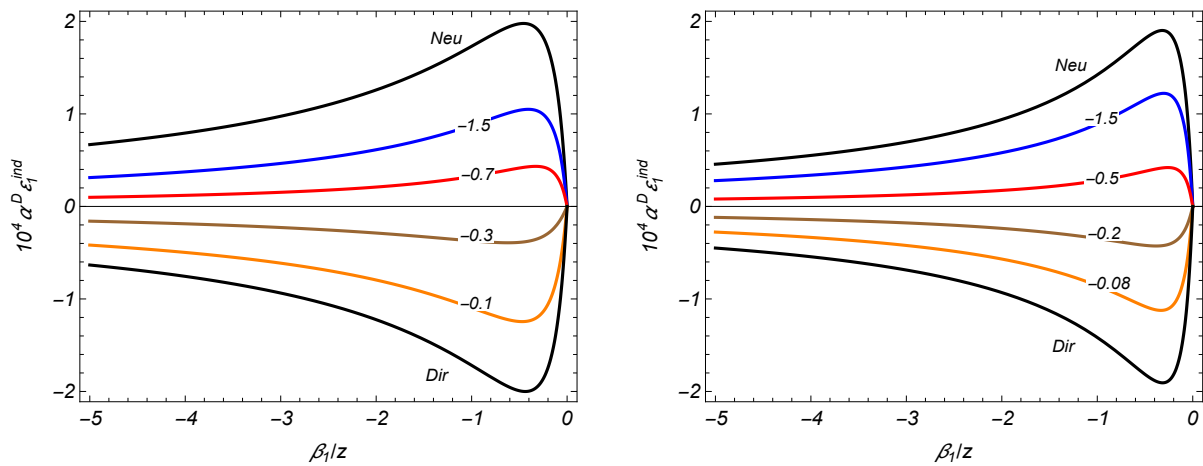


Figure 3. The induced surface energy density on the brane for conformally (left) and minimally (right) coupled fields at $x^1 = a_1$ for $D = 4$, $m\alpha = 0.5$, and $a/z = 1$ versus the Robin coefficient β_1/z for different values of β_2/z (the numbers marking the curves), $\beta_2/z = 0$ and $\beta_2/z = -\infty$ for Dirichlet (marked "Dir") and Neumann ("Neu") boundary conditions). See text for details.

The dependence of the surface energy density on the mass of the field (in units of $1/\alpha$) is displayed in Figure 4 for conformally (Figure 4, left) and minimally (Figure 4, right) coupled scalar fields in spatial dimensions $D = 4$. The graphs are plotted for $a/z = 1$, $\beta_1/z = -0.5$, and for different values of the ratio β_2/z (the numbers marking the curves). The graphs corresponding to Robin boundary conditions, $-\infty < \beta_2/z < 0$, are located between the graphs corresponding to Neumann and Dirichlet boundary conditions on the second brane ($\beta_2/z = -\infty$ and $\beta_2/z = 0$, respectively). As seen, the induced energy density, in general, is not a monotonic function of the field mass. In addition, for fixed values of the other parameters it may change the sign as a function of the mass. In particular, that is the case for a minimally coupled field with the boundary conditions corresponding to $\beta_1/z = -0.5$ and $\beta_2/z = -0.25$ (see Figure 4, right).

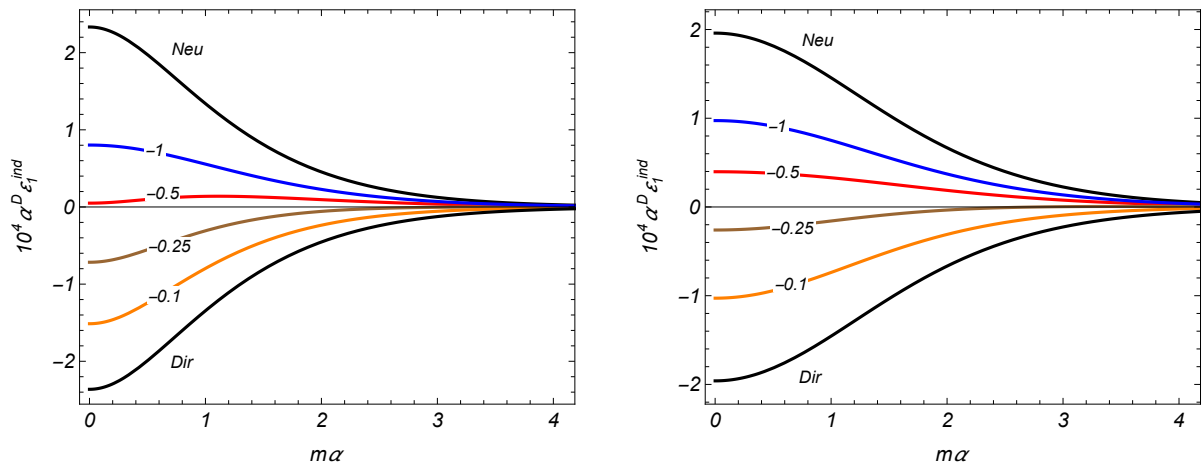


Figure 4. The dependence of the surface energy density on the first brane, induced by the second brane for conformally (left) and minimally (right) coupled fields versus the field mass for $D = 4$, $a/z = 1$, $\beta_1/z = -0.5$ and for separate values of β_2/z (the numbers marking the curves). The graphs for Dirichlet (marked “Dir”) and Neumann (“Neu”) boundary conditions on the second brane are presented as well. See text for details.

5. Conclusions

For a scalar field with general curvature coupling, the VEV of the SEMT induced on branes in AdS spacetime orthogonal to its boundary has been studied. On the branes, the field operator is constrained by the boundary conditions (3) or, equivalently, by the conditions (4). To ensure the stability of the vacuum state, the values of the parameters in Robin boundary conditions are restricted by (7). For the geometry of the branes under consideration, the extrinsic curvature tensor is zero and the general formula for the SEMT is simplified to Equation (11). From the viewpoint of observers living on the branes this SEMT presents a gravitational source with the equation of state for a cosmological constant. In order to evaluate the corresponding VEV, the Hadamard function is used, obtained from the positive frequency Wightman function from Ref. [56]. In the region between the branes, the Hadamard function is decomposed into single-brane and the second-brane-induced contributions. This allows the separation of the part generated by the second brane from the total VEV of the SEMT. The surface divergences are contained in the self-energy contributions on the branes and the renormalization is required for those parts only. In order to extract the finite parts in the corresponding VEVs, in Appendix A, the regularization procedure based on the generalized zeta function approach is employed. The divergences, appearing in the form of simple poles, are absorbed by the renormalization of the corresponding parameters in the “classical” action localized on the branes. The finite part of the SEMT separated in this way contains renormalization ambiguities and additional conditions are required to obtain a unique result. This is fully similar to the case of the self-energy in the Casimir effect in the geometry of a single boundary (see, for example, the corresponding discussion in Ref. [4]).

The part of the SEMT induced on the brane by the presence of the second brane is finite and uniquely defined. The induced SEMT on the brane $x^1 = a_j$ is given by the expression (22). It vanishes for special cases of Dirichlet and Neumann boundary conditions on that brane. As a consequence of the maximal symmetry of AdS spacetime, for the general case of Robin boundary conditions, the dimensionless quantity $\alpha^D \langle \tau_i^k \rangle_j^{ind}$ is completely determined by the dimensionless ratios a/z and β_j/z , $j = 1, 2$. The first one is the proper separation between the branes, measured by an observer with fixed z in units of the curvature radius α . The VEV of the SEMT for Robin parallel plates in the Minkowski bulk is obtained from Equation (22) in the limit $\alpha \rightarrow \infty$ and is expressed as Equation (24). The latter includes special cases previously discussed in the literature and coincides with the result obtained in Ref. [58] as a limit $\alpha \rightarrow \infty$ of the SEMT in the geometry of branes

parallel to the AdS boundary. For a conformally coupled massless field, the problem in the AdS bulk is conformally related to the problem in Minkowski spacetime consisting of two parallel Robin plates perpendicularly intersected by a Dirichlet plate, the latter being the image of the AdS boundary. The VEV in the Minkowski counterpart is given by the Formula (27), where the contribution of the Dirichlet plate comes from the term in the square brackets with the Bessel function.

At quite small separations between the branes, compared to the curvature radius and length scales determined by the Robin coefficients, the influence of the gravitational field on the SEMT is small enough and the leading term in the corresponding expansion is expressed by Equation (30). In this limit, and for non-Dirichlet (Dirichlet) boundary conditions on the brane $x^1 = a_j$, the sign of the surface energy density induced on the brane $x^1 = a_j$ coincides with the sign of the product $(4\tilde{\xi} - 1)\beta_j$, $((1 - 4\tilde{\xi})\beta_j)$. The effects of the gravitational field are essential at proper separations between the branes of the order or larger than the curvature scale of the background geometry. Additionally, assuming that the separation is larger than the length scales fixed by the boundary conditions, the leading behavior of the induced SEMT is described by Equation (33) for non-Neumann boundary conditions on the second brane. The sign of the energy density coincides with the sign of $(1 - 4\tilde{\xi})\beta_j$. For Neumann conditions on the second brane, an additional factor $(2^{-D-2\nu-1} - 1)$ needs to be added on the right-hand side of Equation (33) and the energy density at quite large distances has an opposite sign. An important feature of the large-distance behavior of the SEMT is the power law decay as a function of the proper separation. For parallel plates in Minkowski spacetime, the corresponding decay for massive fields is exponential. The induced surface energy density vanishes on the AdS boundary like $z^{D+2\nu+1}$ and behaves as $(z/\alpha)^D$ near the AdS horizon.

The investigations of the brane-induced effects on the properties of the scalar vacuum in AdS spacetime have discussed the branes parallel or perpendicular to the AdS boundary. An interesting generalization, that includes these special cases, would be the geometry of branes crossing the AdS boundary at an arbitrary angle. In this case, the dependence of the scalar mode functions on the coordinates parallel and perpendicular to the AdS boundary are not separable and the problem is more complicated. It is expected that for a general crossing angle, in addition the normal and shear Casimir forces, a rotational momentum to appear generated by the vacuum fluctuations.

The study of the boundary-induced effects on the fermionic and electromagnetic vacua for branes perpendicular to the AdS boundary is another direction for further research. The dependence of the mode functions on the coordinate z is expressed in terms of the functions $J_{m\alpha\pm 1/2}(\gamma z)$ for the fermionic field (with m being the mass of the field) and in terms of the function $J_{D/2-1}(\gamma z)$ for the vector potential of the electromagnetic field. Similar to the case of a scalar field, it is expected that the equation determining the eigenvalues of the quantum number corresponding to the direction normal to the branes to be the same as that in the Minkowski bulk, with the same boundary conditions on planar boundaries. The summation over those eigenvalues in the corresponding mode sum for the VEV of the energy-momentum tensor can be achieved using the generalized Abel-Plana formula. This allows the explicit extraction of the brane-induced contribution. Note that previous investigations of the vacuum energy-momentum tensor for fermionic and electromagnetic fields have considered branes parallel to the AdS boundary (see [41–45]). The bag boundary condition has been imposed for the fermionic field, and for the electromagnetic field, the perfect conductor and confining boundary conditions have been discussed.

Funding: This research was funded by the grant no. 21AG-1C047 of the Higher Education and Science Committee of the Ministry of Education, Science, Culture and Sport (Republic of Armenia).

Data Availability Statement: Data are contained within the article.

Conflicts of Interest: The author declares no conflict of interest.

Appendix A. Surface Densities for a Single Brane

It was shown above that the VEV of the SEMT for a single brane at $x^1 = a_j$ is presented in the form (16). The corresponding expression is divergent and can be regularized by using the generalized zeta function approach (for a general introduction and applications in the theory of the Casimir effect, see, e.g., [64–66]). Let us consider the function

$$F(s, z) = \frac{\mu^{s-1} \beta_j z^{D+1}}{(2\pi)^{D-1}} \int_0^\infty d\gamma \gamma J_\nu^2(\gamma z) \int_0^\infty d\lambda \lambda^2 \int d\mathbf{k} \frac{(\lambda^2 + \gamma^2 + k^2)^{-\frac{s}{2}}}{1 + \lambda^2 \beta_j^2}, \quad (A1)$$

with, in general, complex argument s . As seen below, the expression on the right-hand side is finite for $\text{Re } s > D$. The scale parameter μ , having dimension of inverse length, is introduced to keep the function $F(s, z)$ dimensionless. Following the principal part prescription, considered previously in the literature for the total Casimir energy in ultrastatic manifolds with boundaries (see [64,65,67]), the SEMT in the geometry of a single brane is obtained as

$$\langle \tau_i^k \rangle_j^{(0)} = \delta_i^k \frac{4\zeta - 1}{\alpha^D} \text{PP}[F(s, z)]_{s=1}, \quad (A2)$$

where $\text{PP}[F(s, z)]_{s=1}$ corresponds to the finite part of the Laurent expansion of the function $F(s, z)$ near $s = 1$. The evaluation of that part is reduced to the extraction of the pole term.

The integral over \mathbf{k} in Equation (A1) is expressed in terms of the gamma function and one obtains

$$F(s, z) = \frac{\mu^{s-1} \beta_j z^{D+1}}{2^{D-1} \pi^{D/2}} \frac{\Gamma(1 - \frac{D-s}{2})}{\Gamma(\frac{s}{2})} \int_0^\infty d\gamma \gamma J_\nu^2(\gamma z) \int_0^\infty d\lambda \lambda^2 \frac{(\lambda^2 + \gamma^2)^{\frac{D-s}{2}-1}}{1 + \lambda^2 \beta_j^2}. \quad (A3)$$

For the further transformation of the expression on the right-hand side of Equation (A3) the integral representation

$$(\lambda^2 + \gamma^2)^{\frac{D-s}{2}-1} = \frac{1}{\Gamma(1 - \frac{D-s}{2})} \int_0^\infty dx x^{\frac{s-D}{2}} e^{-(\lambda^2 + \gamma^2)x} \quad (A4)$$

is used.

With this representation, the integral over γ is evaluated by the formula [61]

$$\int_0^\infty d\gamma \gamma J_\nu^2(\gamma z) e^{-\gamma^2 x} = \frac{1}{2x} \exp\left(-\frac{z^2}{2x}\right) I_\nu\left(\frac{z^2}{2x}\right), \quad (A5)$$

with $I_\nu(u)$ being the modified Bessel function. Passing to a new integration variable $u = z^2/(2x)$, one finds

$$F(s, z) = \frac{\mu^{s-1} \beta_j z^{s+1}}{2^{\frac{D+s}{2}} \pi^{D/2} \Gamma(\frac{s}{2})} \int_0^\infty du u^{\frac{D-s}{2}-1} e^{-u} I_\nu(u) \int_0^\infty d\lambda \frac{\lambda^2 e^{-\lambda^2 \frac{z^2}{2u}}}{1 + \lambda^2 \beta_j^2}. \quad (A6)$$

The λ -integral is evaluated in terms of the complementary incomplete gamma function $\Gamma(-1/2, x)$. As a result, the function $F(s, z)$ is presented as

$$F(s, z) = \frac{(\mu z)^{s-1} \beta_j z^2}{2^{\frac{D+s}{2}+2} \pi^{\frac{D-1}{2}} \Gamma(\frac{s}{2}) |\beta_j|^3} \int_0^\infty du u^{\frac{D-s}{2}-1} S(2\beta_j^2/z^2, u), \quad (A7)$$

where the function

$$S(b, u) = e^{-u} I_\nu(u) e^{\frac{1}{bu}} \Gamma\left(-\frac{1}{2}, \frac{1}{bu}\right) \quad (A8)$$

is used.

In the limit $u \rightarrow \infty$, the function (A8) tends to the limiting value $\sqrt{2b/\pi}$ and $\lim_{u \rightarrow 0} S(b, u) = 0$. This shows that the representation (A7) is valid in the region $\text{Re } s > D$ of the complex plane s .

The divergence of the integral in Equation (A8) at $s = 1$ comes from the divergence in the upper limit of the integral. By using the expansions of the functions $e^{-u} I_\nu(u)$ and $e^{\frac{1}{bu}} \Gamma\left(-\frac{1}{2}, \frac{1}{bu}\right)$ (see, e.g., [68]) for quite large values of u , the following expansion is obtained:

$$S(b, u) = \sqrt{\frac{2b}{\pi}} \sum_{n=0}^{\infty} \left[\frac{A_n(b)}{u^n} - \sqrt{\pi} \frac{B_n(b)}{u^{n+\frac{1}{2}}} \right]. \tag{A9}$$

For the coefficients, one has:

$$\begin{aligned} A_0 &= 1, \quad A_1 = \frac{2}{b} - \frac{1}{2} \left(v^2 - \frac{1}{4} \right), \\ A_2 &= \frac{4}{3b^2} + \left(v^2 - \frac{1}{4} \right) \left[\frac{1}{8} \left(v^2 - \frac{9}{4} \right) - \frac{1}{b} \right], \end{aligned} \tag{A10}$$

and

$$\begin{aligned} B_0 &= \frac{1}{\sqrt{b}}, \quad B_1 = \frac{1}{b^{\frac{3}{2}}} - \frac{1}{2\sqrt{b}} \left(v^2 - \frac{1}{4} \right), \\ B_2 &= \frac{1}{2\sqrt{b}} \left[\frac{1}{b^2} + \left(v^2 - \frac{1}{4} \right) \left(\frac{1}{4} \left(v^2 - \frac{9}{4} \right) - \frac{1}{b} \right) \right]. \end{aligned} \tag{A11}$$

In order to separate the pole term in Equation (A7), let us rewrite the function $F(s, z)$ in the form

$$\begin{aligned} F(s, z) &= \frac{(\mu z)^{s-1} \beta_j z^2}{2^{\frac{D+s}{2}+2} \pi^{\frac{D-1}{2}} \Gamma\left(\frac{s}{2}\right) |\beta_j|^3} \left\{ \int_0^1 du u^{\frac{D-s}{2}-1} S(b_j, u) \right. \\ &\quad \left. + \int_1^{\infty} du u^{\frac{D-s}{2}-1} [S(b_j, u) - S_N(b_j, u)] + \int_1^{\infty} du u^{\frac{D-s}{2}-1} S_N(b_j, u) \right\}, \end{aligned} \tag{A12}$$

where $b_j = 2\beta_j^2/z^2$ and

$$S_N(b, u) = \sqrt{\frac{2b}{\pi}} \sum_{n=0}^N \left[\frac{A_n(b)}{u^n} - \sqrt{\pi} \frac{B_n(b)}{u^{n+\frac{1}{2}}} \right]. \tag{A13}$$

For $N > (D - 3)/2$, the first two integrals in the curly brackets in Equation (A12) are convergent for $s = 1$. By using Equation (A13) in the last integral in Equation (A12), the corresponding contribution to the function $F(s, z)$ is presented as

$$\bar{F}(s, z) = -\frac{(\mu z/\sqrt{2})^{s-1} z}{2^{\frac{D+1}{2}} \pi^{\frac{D}{2}} \Gamma\left(\frac{s}{2}\right) \beta_j} \sum_{n=0}^N \left[\frac{A_n(b_j)}{s + 2n - D} - \frac{\sqrt{\pi} B_n(b_j)}{s + 1 + 2n - D} \right]. \tag{A14}$$

The function $\bar{F}(s, z)$ has a simple pole at $s = 1$. The pole comes from the term with $n = (D - 1)/2$ for odd D and from the term with $n = D - 1$ for even D .

Expanding the function (A14) near the physical point $s = 1$, the function $F(s, z)$ is decomposed as

$$F(s, z) = \frac{F_{(p)}(s, z)}{s - 1} + F_{(f)}(z) + \dots, \tag{A15}$$

where the unshown terms represent the part vanishing in the limit $s \rightarrow 1$. Here, the coefficient in the pole term reads

$$F_{(p)}(s, z) = -\frac{zC_D(b_j)}{(2\pi)^{\frac{D+1}{2}}\beta_j}, \tag{A16}$$

and the finite term reads

$$F_{(f)}(z) = \frac{\beta_j z^2}{2^{\frac{D+1}{2}+2}\pi^{\frac{D}{2}}|\beta_j|^3} \left\{ \int_0^1 du u^{\frac{D-3}{2}} S(b_j, u) + \int_1^\infty du u^{\frac{D-3}{2}} [S(b_j, u) - S_N(b_j, u)] \right\} + \frac{z}{(2\pi)^{\frac{D+1}{2}}\beta_j} \left\{ C_D(b_j) \left[\ln\left(\frac{\mu z}{\sqrt{2}}\right) + \frac{1}{2}\psi(1/2) \right] - \sum_{n=0}^{N'} \left[\frac{A_n(b_j)}{1+2n-D} - \frac{\sqrt{\pi}B_n(b_j)}{2+2n-D} \right] \right\}, \tag{A17}$$

where the prime in the sum indicates that the term $n = (D - 1)/2$ for odd D and the term $n = D/2 - 1$ for even D to be omitted. In Equation (A17), $\psi(x)$ is the digamma function with $\psi(1/2) \approx -1.964$ and

$$C_D(b) = \begin{cases} A_{\frac{D-1}{2}}(b) & \text{for odd } D, \\ -\sqrt{\pi}B_{\frac{D}{2}-1}(b) & \text{for even } D. \end{cases} \tag{A18}$$

In the principal part prescription, the physical value extracted from the divergent expectation value of the SEMT $\langle \tau_i^k \rangle_j^{(0)}$ is identified with

$$\langle \tau_i^k \rangle_j^{(0)} = \delta_i^k \frac{4\zeta - 1}{\alpha^D} F_{(f)}(z). \tag{A19}$$

Note that this result contains a scale ambiguity. Under scale change it transforms to

$$\langle \tau_i^k \rangle_j^{(0)}(\mu') = \langle \tau_i^k \rangle_j^{(0)}(\mu) + \delta_i^k (4\zeta - 1) \frac{\ln(\mu'/\mu)C_D(b_j)z}{(2\pi)^{\frac{D+1}{2}}\alpha^D\beta_j}. \tag{A20}$$

The logarithmic dependence on the scale μ is a distinctive feature of the regularization procedure.

References

1. Mostepanenko, V.M.; Trunov, N.N. *The Casimir Effect and Its Applications*; Clarendon Press/Oxford University Press: Oxford, UK, 1997. [CrossRef]
2. Milton, K.A. *The Casimir Effect: Physical Manifestation of Zero-Point Energy*; World Scientific: Singapore, 2002. [CrossRef]
3. Parsegian, V.A. *Van der Waals Forces: A Handbook for Biologists, Chemists, Engineers, and Physicists*; Cambridge University Press: Cambridge, UK, 2005. [CrossRef]
4. Bordag, M.; Klimchitskaya, G.L.; Mohideen, U.; Mostepanenko, V.M. *Advances in the Casimir Effect*; Oxford University Press: Oxford, UK, 2009. [CrossRef]
5. Klimchitskaya, G.L.; Mohideen, U.; Mostepanenko, V.M. The Casimir force between real materials: Experiment and theory. *Rev. Mod. Phys.* **2009**, *81*, 1827–1885. [CrossRef]
6. Dalvit, D.; Milonni, P.; Roberts, D.; da Rosa, F. (Eds.) *Casimir Physics*; Springer: Berlin/Heidelberg, Germany, 2011. [CrossRef]
7. Avis, S.J.; Isham, C.J.; Storey, D. Quantum field theory in anti-de Sitter space-time. *Phys. Rev. D* **1978**, *18*, 3565–3576. [CrossRef]
8. Breitenlohner, P.; Freedman, D.Z. Stability in gauged extended supergravity. *Ann. Phys.* **1982**, *144*, 249–281. [CrossRef]
9. Mezzinescu, L.; Townsend, P.K. Stability at a local maximum in higher dimensional anti-deSitter space and applications to supergravity. *Ann. Phys.* **1985**, *160*, 406–419. [CrossRef]
10. Saharian, A.A. Wightman function and Casimir densities on AdS bulk with application to the Randall-Sundrum braneworld. *Nucl. Phys. B* **2005**, *712*, 196–228. [CrossRef]
11. Ishibashi, A.; Wald, R.M. Dynamics in non-globally-hyperbolic static spacetimes: III. Anti-de Sitter spacetime. *Class. Quantum Grav.* **2004**, *21*, 2981–3014. [CrossRef]

12. Morley, T.; Taylor, P.; Winstanley, E. Quantum field theory on global anti-de Sitter space-time with Robin boundary conditions. *Class. Quantum Grav.* **2022**, *38*, 035009. [CrossRef]
13. Aharony, O.; Gubser, S.S.; Maldacena, J.; Ooguri, H.; Oz, Y. Large N field theories, string theory and gravity. *Phys. Rep.* **2000**, *323*, 183–386. [CrossRef]
14. Papantonopoulos, E. (Ed.) *From Gravity to Thermal Gauge Theories: The AdS/CFT Correspondence*; Springer: Berlin/Heidelberg, Germany, 2011. [CrossRef]
15. Năstase, H. *Introduction to AdS/CFT Correspondence*; Cambridge University Press: Cambridge, UK, 2015. [CrossRef]
16. Ammon, M.; Erdmenger, J. *Gauge/Gravity Duality: Foundations and Applications*; Cambridge University Press: Cambridge, UK, 2015. [CrossRef]
17. Pires, A.S.T. *AdS/CFT Correspondence in Condensed Matter*; Morgan & Claypool Publishers: San Rafael, CA, USA, 2014. [CrossRef]
18. Zaanen, J.; Sun, Y.-W.; Liu, Y.; Schalm, K. *Holographic Duality in Condensed Matter Physics*; Cambridge University Press: Cambridge, UK, 2015. [CrossRef]
19. Maartens, R.; Koyama, K. Brane-world gravity. *Living Rev. Relativ.* **2010**, *13*, 5. [CrossRef]
20. Fabinger, M.; Horava, P. Casimir effect between world-branes in heterotic M-theory. *Nucl. Phys. B* **2000**, *580*, 243–263. [CrossRef]
21. Nojiri, S.; Odintsov, S. Brane world inflation induced by quantum effects. *Phys. Lett. B* **2000**, *484*, 119–123. [CrossRef]
22. Nojiri, S.; Odintsov, S.; Zerbini, S. Quantum (in)stability of dilatonic AdS backgrounds and the holographic renormalization group with gravity. *Phys. Rev. D* **2000**, *62*, 064006. [CrossRef]
23. Toms, D.J. Quantised bulk fields in the Randall-Sundrum compactification model. *Phys. Lett. B* **2000**, *484*, 149–153. [CrossRef]
24. Nojiri, S.; Obregon, O.; Odintsov, S. (Non)-singular brane-world cosmology induced by quantum effects in five-dimensional dilatonic gravity. *Phys. Rev. D* **2000**, *62*, 104003. [CrossRef]
25. Goldberger, W.D.; Rothstein, I.Z. Quantum stabilization of compactified AdS₅. *Phys. Lett. B* **2000**, *491*, 339–344. [CrossRef]
26. Garriga, J.; Pujolàs, O.; Tanaka, T. Radion effective potential in the brane-world. *Nucl. Phys. B* **2001**, *605*, 192–214. [CrossRef]
27. Flachi, A.; Toms, D.J. Quantized bulk scalar fields in the Randall-Sundrum brane model. *Nucl. Phys. B* **2001**, *610*, 144–168. [CrossRef]
28. Flachi, A.; Moss, I.G.; Toms, D.J. Fermion vacuum energies in brane world models. *Phys. Lett. B* **2001**, *518*, 153–156. [CrossRef]
29. Brevik, I.H.; Milton, K.A.; Nojiri, S.; Odintsov, S.D. Quantum (in)stability of a brane-world AdS₅ universe at nonzero temperature. *Nucl. Phys. B* **2001**, *599*, 305–318. [CrossRef]
30. Flachi, A.; Moss, I.G.; Toms, D.J. Quantized bulk fermions in the Randall-Sundrum brane model. *Phys. Rev. D* **2001**, *64*, 105029. [CrossRef]
31. Naylor, W.; Sasaki, M. Casimir energy for de Sitter branes in bulk AdS₅. *Phys. Lett. B* **2002**, *542*, 289–294. [CrossRef]
32. Saharian, A.A.; Setare, M.R. The Casimir effect on background of conformally flat brane-world geometries. *Phys. Lett. B* **2003**, *552*, 119–126. [CrossRef]
33. Garriga, J.; Pomarol, A. A stable hierarchy from Casimir forces and the holographic interpretation. *Phys. Lett. B* **2003**, *560*, 91–97. [CrossRef]
34. Elizalde, E.; Nojiri, S.; Odintsov, S.D.; Ogushi, S. Casimir effect in de Sitter and anti-de Sitter braneworlds. *Phys. Rev. D* **2003**, *67*, 063515. [CrossRef]
35. Moss, I.G.; Naylor, W.; Santiago-Germán, W.; Sasaki, M. Bulk quantum effects for de Sitter branes in AdS₅. *Phys. Rev. D* **2003**, *67*, 125010. [CrossRef]
36. Saharian, A.A. Quantum vacuum effects in braneworlds on AdS bulk. *Universe* **2020**, *6*, 181. [CrossRef]
37. Knapman, A.; Toms, D.J. Stress-energy tensor for a quantized bulk scalar field in the Randall-Sundrum brane model. *Phys. Rev. D* **2004**, *69*, 044023. [CrossRef]
38. Saharian, A.A.; Mkhitarian, A.L. Wightman function and vacuum densities for a Z₂-symmetric thick brane in AdS spacetime. *J. High Energy Phys.* **2007**, *08*, 063. [CrossRef]
39. Saharian, A.A. Wightman function and vacuum fluctuations in higher dimensional brane models. *Phys. Rev. D* **2006**, *73*, 044012. [CrossRef]
40. Saharian, A.A. Bulk Casimir densities and vacuum interaction forces in higher dimensional brane models. *Phys. Rev. D* **2006**, *73*, 064019. [CrossRef]
41. Shao, S.-H.; Chen, P.; Gu, J.-A. Stress-energy tensor induced by a bulk Dirac spinor in the Randall-Sundrum model. *Phys. Rev. D* **2010**, *81*, 084036. [CrossRef]
42. Elizalde, E.; Odintsov, S.D.; Saharian, A.A. Fermionic Casimir densities in anti-de Sitter spacetime. *Phys. Rev. D* **2013**, *87*, 084003. [CrossRef]
43. Kotanjyan, A.S.; Saharian, A.A. Electromagnetic quantum effects in anti-de Sitter spacetime. *Phys. At. Nucl.* **2017**, *80*, 562–571. [CrossRef]
44. Kotanjyan, A.S.; Saharian, A.A.; Saharyan, A.A. Electromagnetic Casimir Effect in AdS Spacetime. *Galaxies* **2017**, *5*, 102. [CrossRef]
45. Saharian, A.A.; Kotanjyan, A.S.; Sargsyan, H.G. Electromagnetic field correlators and the Casimir effect for planar boundaries in AdS spacetime with application in braneworlds. *Phys. Rev. D* **2020**, *102*, 105014. [CrossRef]
46. Randall, L.; Sundrum, R. Large mass hierarchy from a small extra dimension. *Phys. Rev. Lett.* **1999**, *83*, 3370–3373. [CrossRef]
47. Randall, L.; Sundrum, R. An alternative to compactification. *Phys. Rev. Lett.* **1999**, *83*, 4690–4693. [CrossRef]

48. Cuomo, G.; Mezei, M.; Raviv-Moshe, A. Boundary conformal field theory at large charge. *J. High Energy Phys.* **2021**, *10*, 143. [CrossRef]
49. Takayanagi, T. Holographic dual of a boundary conformal field theory. *Phys. Rev. Lett.* **2011**, *107*, 101602. [CrossRef]
50. Fujita, M.; Takayanagi, T.; Tonni, E. Aspects of AdS/BCFT. *J. High Energy Phys.* **2011**, *11*, 043. [CrossRef]
51. Ryu, S.; Takayanagi, T. Holographic derivation of entanglement entropy from the anti-de Sitter space/conformal field theory correspondence. *Phys. Rev. Lett.* **2006**, *96*, 181602. [CrossRef] [PubMed]
52. Ryu, S.; Takayanagi, T. Aspects of holographic entanglement entropy. *J. High Energy Phys.* **2006**, *08*, 045. [CrossRef]
53. Nishioka, T.; Ryu, S.; Takayanagi, T. Holographic entanglement entropy: An overview. *J. Phys. A Math. Theor.* **2009**, *42*, 504008. [CrossRef]
54. Chen, B.; Czech, B.; Wang, Z.-Z. Quantum information in holographic duality. *Rep. Prog. Phys.* **2022**, *85*, 046001. [CrossRef] [PubMed]
55. Bezerra de Mello, E.R.; Saharian, A.A.; Setare, M.R. Vacuum densities for a brane intersecting the AdS boundary. *Phys. Rev. D* **2015**, *92*, 104005. [CrossRef]
56. Bellucci, S.; Saharian, A.A.; Kotanjyan, V.K. Vacuum densities and the Casimir forces for branes orthogonal to the AdS boundary. *Phys. Rev. D* **2022**, *106*, 065021. [CrossRef]
57. Saharian, A.A. Energy-momentum tensor for a scalar field on manifolds with boundaries. *Phys. Rev. D* **2004**, *69*, 085005. [CrossRef]
58. Saharian, A.A. Surface Casimir densities and induced cosmological constant on parallel branes in AdS spacetime. *Phys. Rev. D* **2004**, *70*, 064026. [CrossRef]
59. Saharian, A.A. Surface Casimir densities and induced cosmological constant in higher dimensional braneworlds. *Phys. Rev. D* **2006**, *74*, 124009. [CrossRef]
60. Romeo, A.; Saharian, A.A. Casimir effect for scalar fields under Robin boundary conditions on plates. *J. Phys A Math. Gen.* **2002**, *35*, 1297–1320. [CrossRef]
61. Prudnikov, A.P.; Brychkov, Y.A.; Marichev, O.I. *Integrals and Series. Volume 2: Special Functions*; Gordon and Breach Science Publishers: Amsterdam, The Netherlands, 1998. Available online: <https://archive.org/details/integralseries0002prud> (accessed on 20 November 2023).
62. Lebedev, S.L. Casimir effect in the presence of an elastic boundary. *J. Exp. Theor. Phys.* **1996**, *83*, 423–434. Available online: <http://jetp.ras.ru/cgi-bin/e/index/e/83/3/p423?a=list> (accessed on 20 November 2023).
63. Lebedev, S.L. Vacuum energy and Casimir force in the presence of a dimensional parameter in the boundary condition. *Phys. At. Nucl.* **2001**, *64*, 1337–1346. [CrossRef]
64. Elizalde, E.; Odintsov, S.D.; Romeo, A.; Bytsenko, A.A.; Zerbini, S. *Zeta Regularization Techniques with Applications*; World Scientific: Singapore, 1994. [CrossRef]
65. Kirsten, K. *Spectral Functions in Mathematics and Physics*; Chapman and Hall/CRC Press: Boca Raton, FL, USA, 2002. Available online: http://lib.yzu.edu.tw/disciplines_bk/70c8c6cffe7f1534b131c208088b6f4.pdf (accessed on 20 November 2023).
66. Elizalde, E. *Ten Physical Applications of Spectral Zeta Functions*; Springer: Heidelberg/Berlin, Germany, 2012. [CrossRef]
67. Blau, S.K.; Visser, M.; Wipf, A. Zeta functions and the Casimir energy. *Nucl. Phys. B* **1988**, *310*, 163–180. [CrossRef]
68. Abramowitz, M.; Stegun, I.A. (Eds.) *Handbook of Mathematical Functions: With Formulas, Graphs, and Mathematical Tables*; US Department of Commerce, National Bureau of Standards: Washington, DC, USA, 1972. Available online: https://personal.math.ubc.ca/~cbm/aands/abramowitz_and_stegun.pdf (accessed on 20 November 2023).

Disclaimer/Publisher’s Note: The statements, opinions and data contained in all publications are solely those of the individual author(s) and contributor(s) and not of MDPI and/or the editor(s). MDPI and/or the editor(s) disclaim responsibility for any injury to people or property resulting from any ideas, methods, instructions or products referred to in the content.

Vacuum Interaction of Topological Strings at Short Distances

Yuri V. Grats and Pavel Spirin *

Theoretical Physics Department, Faculty of Physics, M. V. Lomonosov Moscow State University,
119991 Moscow, Russia; grats@phys.msu.ru

* Correspondence: salotop@list.ru

Abstract: The paper provides an extended overview of recent results obtained by the authors in the process of studying the vacuum interaction of topological cosmic strings at short distances, taking into account their transverse size a and the mass m of the quantized field. We consider the case of a massive real-valued scalar field with minimal coupling. It is shown that at the interstring distances significantly larger than the Compton length, $l_c = 1/m$, the Casimir effect is damped exponentially. On the other hand, at distances smaller than l_c but much larger than the typical string width, the field-mass influence becomes insignificant. In this case, the partial contribution of a massive field to the Casimir energy is of the same order as the contribution of a massless one. At these distances, the string's transverse size is insignificant also. However, at the interstring distances of the same order as a string radius, the energy of the vacuum interaction of thick strings may significantly surpass the one for two infinitely thin strings with the same mass per unit length.

Keywords: Casimir effect; topological strings; effective action; dimensional regularization

1. Introduction

Seventy-five years ago, a phenomenon was predicted [1] and then named the Casimir effect in honor of the author. Being experimentally confirmed, it became direct evidence of the close relationship between the macroscopic external conditions and quantized fields. Since those times, it has shown great development, both in experimental investigations and at the level of theoretical research. Now, it is a subject of study not only by specialists in quantum field theory and physics of condensed matter and nanotechnology but also by scientists working in various fields of gravity and cosmology (see, e.g., [2]).

One of the problems related to modern astrophysics, which was considered in the literature, is the problem of the vacuum interaction of cosmic strings.

Cosmic strings are considered as one-dimensional-extended topological defects (closed or infinite), which might be created under cosmological phase transitions during the Universe evolution [3,4]. In what follows, we use the term “string” for this kind of cosmic string (so-called topological cosmic strings) and do not consider the case of non-topological F-strings and D-strings, which may be formed during the interaction of multidimensional branes.

A special interest in these types of defects arose in connection with the hypothesis that they might represent one of the basic sources of primary fluctuations in the Hot Universe. The hypothesis was not confirmed, but the cosmic strings are still considered to be a possible origin of some observable effects (a review of the possible appearance and indirect effects of cosmic strings is to be found in Ref. [5]). This stimulates the searches for ways to detect cosmic strings and, consequently, the investigation of features concerning how classical (or quantum) matter behaves in the corresponding curved backgrounds.

The study of the evolution of the cosmic-string net during its formation in the Early Universe phase transitions implies that the investigations of processes happened under close contact of strings and collisions [3,4]. In these processes, the account of the vacuum (Casimir) string interaction may turn out to be significant.

Citation: Grats, Y.; Spirin, P. Vacuum Interaction of Topological Strings at Short Distances. *Physics* **2023**, *5*, 1163–1180. <https://doi.org/10.3390/physics5040075>

Received: 7 October 2023

Revised: 6 November 2023

Accepted: 10 November 2023

Published: 14 December 2023



Copyright: © 2023 by the authors. Licensee MDPI, Basel, Switzerland. This article is an open access article distributed under the terms and conditions of the Creative Commons Attribution (CC BY) license (<https://creativecommons.org/licenses/by/4.0/>).

The first estimate of the energy of Casimir of two parallel infinitely thin strings was obtained in Ref. [6]. Subsequently, the result of this study was corrected in Refs. [7–9].

In papers [7,9], the authors proceeded within the framework of a local formalism, where the object of study was the renormalized vacuum average of the energy–momentum tensor (EMT) operator. In paper [8], a global formalism was applied, which allowed us to work directly with the renormalized total vacuum energy. In studies [7–9], the direct product of the two-dimensional Minkowski space and a two-dimensional locally flat surface with two conical singularities was chosen as the spacetime model.

Meanwhile, the creation and evolution of cosmic strings do not imply that they are necessarily parallel. In Ref. [10], the global formalism was extended to the different mutual directions of strings. The Casimir energy due to the massless scalar field and infinitely thin strings was computed for two interacting straight strings.

However, the string’s radius is determined by the energy scale of that phase transition with broken symmetry when the string was created, and for the GUT strings, the radius has an estimate of $a \sim 10^{-28}$ cm. At these scales, the cone vertex represents not just a point-like singularity but also the curvature, distributed over a cylindrical region of radius a , while the metric should smoothly transit to the external conical domain. Therefore, it raises the following question: how does the transverse string size influence the quantum field effects near the strings?

In the meantime, another problem concerns the influence of the quantized field’s mass on the Casimir effect. It is natural to suppose that the characteristic length scale, where the mass is significant, is a Compton length. Quantitatively, the latter is much larger (for all known elementary particles) than the transverse size of Grand Unified Theory (GUT) strings.

The effects of the finite core on the vacuum polarization around a single cosmic string have been investigated earlier, and some nontrivial field-theory effects have been discovered [11–17]. In the present paper, we perform the next step and consider the Casimir effect arising in the net of parallel cosmic strings, taking into account not only the non-zero strings’ widths but also the non-zero field’s mass.

The striking feature of the multi-string background is that, due to translational symmetry along the z -axis, it is enough to analyze the geometry in the two-dimensional plane transverse to the string net. Inside this plane, the scalar curvature does not vanish only on a system of non-overlapping compact domains. As a result, the direct gravitational inter-string interaction is absent. However, the global distinction of the spacetime considered here, from the Minkowski one, leads to a change in the spectrum of vacuum fluctuations and, consequently, to the appearance of the interstring attraction force, the Casimir effect.

Let us start with a qualitative analysis of the problem. First, to notice is that the energy (per unit string’s length) of vacuum interaction has a dimensionality of the inverse length square. Thus, from the dimensional quantities in the problem considered here, it can depend only upon the interstring distance, d , the string radius, a , and the field’s Compton length, $l_c = 1/m$.

Then the relative energy (per unit length) of the interaction of two similar strings, parallel to the z -axis, in the units of $G = \hbar = c = 1$ (where G denotes the Newtonian constant of gravity, \hbar the Planck’s constant, and c the speed of light) can be presented in the form

$$\frac{\mathcal{E}_{\text{Cas}}}{Z} = -\frac{4}{15\pi} \frac{\mu_1\mu_2}{d^2} \mathcal{F}\left(\frac{a}{d}, md\right), \quad Z = \int dz, \tag{1}$$

where $\mu_{1,2}$ is the strings’ masses per unit length, while \mathcal{F} is a real-valued function. The pre-factor just in front of \mathcal{F} is determined using dimensional analysis and is specified to be equal to the Casimir energy of two infinitely thin strings interacting via the massless scalar field with minimal coupling. Let us note that with that choice of the pre-factor, the function \mathcal{F} tends to unit as $a/d \rightarrow 0^+$ or $md \rightarrow 0^+$. Actually, the vanishing of these arguments can be interpreted both as neglect of the strings’ radii and as a transition to the massless field.

Hereafter, we restrict the study to the case of the scalar field with minimal coupling. It is related to the observation that for the case of the infinitely thin string, the non-zero coupling leads to the appearance of a potential with the Aharonov-Bohm δ -like singularities in the field equation. Such an appearance takes special attention, and the computational results may drastically vary, in dependence on how one interprets these singularities [18,19].

However, the Compton length of the most massive currently known particle (the t-quark) is $l_c \sim 10^{-15}$ cm, while the width of GUT strings is estimated as $a \sim 10^{-28}$ cm, what is of many orders less. If one considers the distances $d \gg a$ then strings are to be approximately considered to be infinitely thin, and hence, in Equation (1), one can replace

$$\mathcal{F}\left(\frac{a}{d}, md\right) \rightarrow \mathcal{F}_1(md) = \mathcal{F}(0, md).$$

Now let us estimate the behavior of $\mathcal{F}_1(md)$ as md tends to zero. This limit can be regarded as a transition to the massless field limit with finite values d , and consequently, with the choice of a pre-factor in Equation (1), one has $\mathcal{F}_1 = 1$ in this limit. On the other hand, equally, this limit can be regarded as a transition $d \rightarrow 0^+$ (for infinitely thin strings), keeping the mass fixed. Therefore, the scale where the mass influence is significant is a Compton length. Thus, at interstring distances of the order of l_c or smaller, the influence of mass is significant, and the partial contribution of massive modes into the vacuum energy is comparable with the one of a massless field. But for finite strings' width, if one considers the distances $2a < d \ll l_c$, then the string transverse size cannot be neglected. However, if the above estimates hold, in this regime, one can neglect the field's mass and carry out another substitution in Equation (1):

$$\mathcal{F}\left(\frac{a}{d}, md\right) \rightarrow \mathcal{F}_2\left(\frac{a}{d}\right) = \mathcal{F}\left(\frac{a}{d}, 0\right).$$

In what follows, the length scale, where the transverse strings' size is significant, is the string radius. Thus again, as soon as $\tilde{z} = a/d \rightarrow 0^+$ the function \mathcal{F}_2 tends to unity. Actually, if this limit is to be regarded as limit $d \rightarrow \infty$, then it is quite evident that at these distances, strings interact as infinitely thin ones. Consequently, the result should reproduce the Casimir energy of interaction of two infinitely thin strings, with the coefficient $\mathcal{F}_2 = 1$. The same limit is to be valid if a tends to zero. But for the finite-width (or, equivalently, "thick") strings, one has $d \geq 2a$. Hence, the significant difference \mathcal{F}_2 from unity (and the significant difference of the Casimir energy from the strings' width) should take place if the interstring distance does not significantly exceed $2a$.

Below, it is explicitly shown that these qualitative estimates are fully confirmed.

Actually, there is a variety of string models. Some of them imply that the gravity-induced Casimir force is not the only interaction. We compute a partial contribution to the total interstring interaction within any model, for which the above assumptions on the metric hold.

The computation is carried out within the so-called tr-ln formalism for the effective action, where one starts from the expression for the total vacuum energy, expressed in terms of the effective action.

Throughout the paper, we use the system of units $G = \hbar = c = 1$; the metric signature is $(+, -, -, -)$.

2. Multi-String Spacetime

Consider the following four-dimensional spacetime, which represents the Cartesian product of two-dimensional Minkowski space and two-dimensional Riemannian manifold. The observation that any two-dimensional Riemannian surface is locally conformal to the Euclidean plane allows the reduction, by the appropriate coordinate transformation, of the four-dimensional metric to the form

$$ds^2 = dt^2 - dz^2 - e^{-\sigma(x)}(dx_1^2 + dx_2^2), \tag{2}$$

where x_1 and x_2 are the two-dimensional Riemannian space coordinates and t denotes the time.

Let

$$\sigma(\mathbf{x}) = \sum_{\alpha} \sigma_{\alpha}(|\mathbf{x} - \mathbf{x}_{\alpha}|), \quad |\mathbf{x} - \mathbf{x}_{\alpha}| = \left[(x_1 - x_{\alpha 1})^2 + (x_2 - x_{\alpha 2})^2 \right]^{1/2}. \tag{3}$$

Then the Ricci scalar reads:

$$R = \sum_{\alpha} R_{\alpha} = \sum_{\alpha} e^{\sigma} \Delta \sigma_{\alpha}, \tag{4}$$

where Δ stands for the Laplacian associated with two-dimensional *Euclidean* metric in the transverse subspace. If the supports of partial contributions, $\Delta \sigma_{\alpha}$, are compact and do not intersect each other, one deals with ultra-static spacetime, where the curvature is non-zero in a series of non-overlapping domains.

Choose the functions σ_{α} in the form

$$\sigma_{\alpha}(\mathbf{x}) = 2(1 - \beta_{\alpha}) f_{\alpha}(r_{\alpha}) \theta(a_{\alpha} - r_{\alpha}) + 2(1 - \beta_{\alpha}) \ln \frac{r_{\alpha}}{a_{\alpha}} \theta(r_{\alpha} - a_{\alpha}), \tag{5}$$

where a_{α} is a conformal radius of α th string, all parameters $\beta_{\alpha} \leq 1$, $\theta(\cdot)$ stands for the Heaviside step-function, and f is a twice-differentiable function of an argument $r_{\alpha} = |\mathbf{x} - \mathbf{x}_{\alpha}|$, which satisfies the following boundary conditions:

$$f_{\alpha} \Big|_{r_{\alpha}=a_{\alpha}} = 0, \quad \frac{df_{\alpha}}{dr_{\alpha}} \Big|_{r_{\alpha}=a_{\alpha}} = \frac{1}{a_{\alpha}}. \tag{6}$$

With such a choice of the conformal factor, $e^{-\sigma}$, the scalar curvature vanishes everywhere if $|\mathbf{x} - \mathbf{x}_{\alpha}| > a_{\alpha}$ holds for all α . Moreover, in this domain, the metric coincides with that of a system of parallel infinitely thin cosmic strings [20]. Furthermore, the criterion of the perturbation smallness and thus the validity of calculations within the perturbation theory is a smallness of parameters $(1 - \beta_{\alpha})$. It is assumed that for the GUT strings, the estimate of these parameters is 10^{-6} .

Therefore, the space defined above is to be regarded as a spacetime generated by the net of parallel cosmic strings with non-zero width. The scalar curvature of this spacetime reads:

$$R(\mathbf{x}) = \begin{cases} e^{\sigma} \Delta \sigma_{\alpha}, & \text{if exists } \alpha : |\mathbf{x} - \mathbf{x}_{\alpha}| \leq a_{\alpha}; \\ 0, & \text{if for all } \alpha \quad |\mathbf{x} - \mathbf{x}_{\alpha}| > a_{\alpha}. \end{cases} \tag{7}$$

The metric under consideration satisfies the Einstein equation, where on the right-hand side, the energy-momentum tensor has the following time component:

$$T_{tt} = \frac{R}{16\pi} = \frac{1}{16\pi} e^{\sigma} \sum_{\alpha} \Delta \sigma_{\alpha}.$$

Hence, the energy per unit length of a system of thick strings equals

$$\int T_{tt} \sqrt{-g} d^2x = \frac{1}{16\pi} \sum_{\alpha} \int d^2x \Delta \sigma_{\alpha} = \frac{1 - \beta_{\alpha}}{8\pi} \sum_{\alpha} \int d^2x \Delta f_{\alpha},$$

where g is the determinant of the metric tensor.

In what follows, the quantity

$$\mu_{\alpha} := \frac{1 - \beta_{\alpha}}{8\pi} \int d^2x \Delta f_{\alpha} \tag{8}$$

is to be regarded as the energy per unit length of the α th string.

The transition to the infinitely thin strings implies the limit of any support $\Delta\sigma_\alpha$ to be the single dot $x = x_\alpha$, preserving the value of integrals over d^2x . This limit (as $a_\alpha \rightarrow 0^+$) corresponds to the fixation of the linear energy density of any string. In this limit, the exponential power in Equation (2) goes to

$$\sigma(x) = 2 \sum_\alpha (1 - \beta_\alpha) \ln |x - x_\alpha|. \tag{9}$$

Then, regarding the limit in the distributional sense, one obtains:

$$\lim_{a_\alpha \rightarrow 0^+} \Delta\sigma_\alpha = 4\pi(1 - \beta_\alpha) \delta^2(x - x_\alpha). \tag{10}$$

Therefore, in addition to Equation (6), when specifying the functions f_α , one has to demand

$$\int d^2x \Delta f_\alpha = 2\pi.$$

Then from Equation (8), one obtains

$$\mu_\alpha = \frac{1 - \beta_\alpha}{4},$$

and, in the limit $a_\alpha \rightarrow 0^+$, the heuristic expression,

$$T_{tt}(x) = e^{\sigma(x)} \sum_\alpha \mu_\alpha \delta^2(x - x_\alpha), \tag{11}$$

holds.

As shown in Ref. [20], any two-dimensional x_1x_2 -plane represents the locally flat surface with a series of conical singularities located at the points x_α , while the parameter $(1 - \beta_\alpha)$ represents the angular deficit, related to α th conical vertex

$$\delta\varphi_\alpha = 8\pi \mu_\alpha = 2\pi(1 - \beta_\alpha).$$

Hereafter, we assume that the conformal coordinates cover the x_1x_2 -plane globally. In the case of single singularity, it takes place if $\mu < 1/4$, while in the case of more singularities—if the restriction $\sum \mu_\alpha < 1/2$ holds and thus the conical subspace does not acquire the sphere topology [21–24].

In the case of a single infinitely thin string, the spacetime metric has two striking features: (i) the absence of any length parameters and (ii) higher symmetry. The first allows us to state that for a massless field, the vacuum expectation value of the EMT depends upon the distance, r , from the observation point to the singularity. In four dimensions of a spacetime the EMT scales as

$$\langle T_{\mu\nu} \rangle_{\text{vac}} \sim r^{-4}$$

with μ, ν the four-dimensional indices.

The second feature allows the separation of variables in the field equation to construct Green’s function analytically and to compute the renormalized $\langle T_{\mu\nu} \rangle_{\text{vac}}$. In the case of two strings and more, the problem becomes too complicated, and the perturbation theory techniques become of particular significance [7–9].

The transition to the finite-width strings complicates the problem and demands the concretization of functions σ_α . The smoothing of the cone vertices can be realized with the following choice of the functions f_α [25,26]:

$$f_\alpha(r_\alpha) = -\frac{1}{2} \left(1 - \frac{r_\alpha^2}{a_\alpha^2} \right). \tag{12}$$

Now, the Ricci scalar is given by

$$R(x) = \begin{cases} 4(1 - \beta_\alpha)e^\sigma / a_\alpha^2, & \text{if exists } \alpha : |x - x_\alpha| \leq a_\alpha ; \\ 0, & \text{if for all } \alpha \quad |x - x_\alpha| > a_\alpha . \end{cases}$$

This model is known as the "ballpoint-pen" model, and below, when considering the Casimir effect in a system of thick strings, we restrict ourselves to this particular case.

For a single cosmic string, the schematic illustrations of a two-dimensional section for the infinitely thin string and the "smoothed" one are shown in Figure 1.

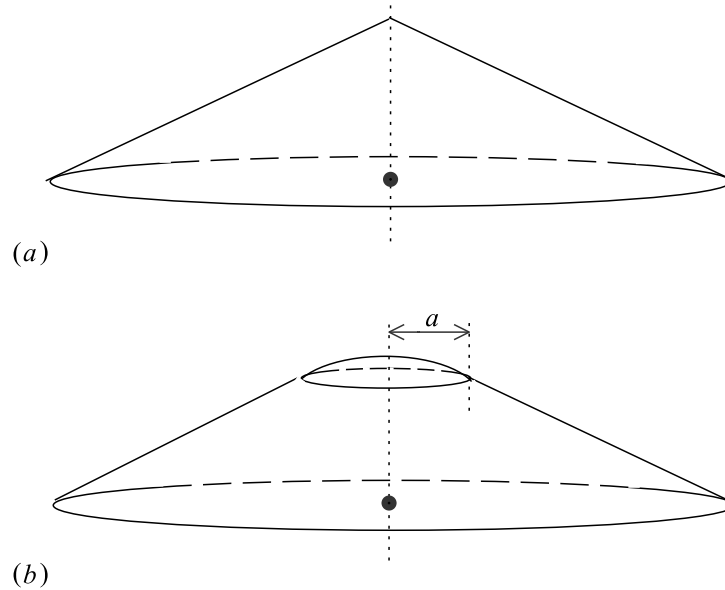


Figure 1. Schematic illustration of two-dimensional sections of two models of cosmic-string space: (a) a cone which corresponds to the infinitely thin cosmic string; (b) the so-called "ballpoint-pen" model, which corresponds to the cosmic string with radius a and is of use in this paper.

3. The Setup

The action of the real-valued scalar field ϕ with mass m can be chosen in the form

$$S_\phi = -\frac{1}{2} \int d^4x \phi(x) L(x, \partial) \phi(x) ,$$

where the field operator $L(x, \partial) = \sqrt{-g} (\square + m^2)$ and $\square = \nabla_\mu \nabla^\mu$ —the curvilinear Laplace–Beltrami operator.

Represent operator $L(x, \partial)$ in the form

$$L(x, \partial) = (\partial^2 + m^2) + \delta L(x, \partial) , \quad \partial^2 = \partial_t^2 - \partial_1^2 - \partial_2^2 - \partial_z^2 , \tag{13}$$

where $\partial_\mu \equiv \partial / \partial x^\mu$.

Hereafter, the scalar products of 4-vectors are regarded in the sense of the Minkowski spacetime metric. The operator $\delta L(x, \partial)$, corresponding to the metric (2), equals

$$\delta L(x, \partial) = \Lambda(x) (\partial_t^2 - \partial_z^2 + m^2) , \quad \Lambda(x) = e^{-\sigma(x)} - 1 . \tag{14}$$

Therefore, $\Lambda(x)$ does not depend on t and z and thus can be equivalently denoted as $\Lambda(x)$.

In the case considered in this paper, all the external factors (the metric, matter, boundaries, external fields, etc.) are static, hence the effective action, W_{eff} , is just proportional to the total vacuum energy, \mathcal{E}_{vac} , namely:

$$W_{\text{eff}} = -T\mathcal{E}_{\text{vac}},$$

where T denotes the total time [27].

On the other hand, the effective action can be reexpressed as [28]

$$W_{\text{eff}} = \frac{i}{2} \text{tr} \ln L = \frac{i}{2} \ln \det L$$

and consequently, within the tr-ln formalism, we infer:

$$\mathcal{E}_{\text{vac}} = -\frac{i}{2T} \ln \det L. \tag{15}$$

If δL can be considered to be a small perturbation, then one has

$$\begin{aligned} \ln \det L &= \ln \det(\partial^2 + m^2 + \delta L) \\ &= \ln \det(\partial^2 + m^2) + \ln \det[1 + (\partial^2 + m^2)^{-1} \delta L] \\ &= \text{tr} \ln(\partial^2 + m^2) + \text{tr} \ln[1 + (\partial^2 + m^2)^{-1} \delta L] \\ &= \text{tr} \ln(\partial^2 + m^2) + \text{tr}[(\partial^2 + m^2)^{-1} \delta L] - \frac{1}{2} \text{tr}[(\partial^2 + m^2)^{-1} \delta L (\partial^2 + m^2)^{-1} \delta L] + \dots \end{aligned} \tag{16}$$

However, the latter formal expansion is well-defined iff all its operator constituents represent the trace-class operators [29]. In the problem considered here, this is not the case. Hence, in the computation of traces, one requires some regularization. Here, we use the dimensional regularization. However, the usage of it can generate another difficulty. As shown by Hawking [30], in the case of curved spacetime, there is no natural recipe for which dimensions should be specified for the dimensional analytical continuation. The final result may depend upon this choice and, moreover, may differ from the results obtained by other regularization schemes. The way, proposed in Ref. [30], consists of the construction of the direct product of the curved four-dimensional spacetime and fictitious $(d - 4)$ -dimensional flat space. Such a continuation leads to the result, which coincides with that obtained with the help of generalized zeta-function. In our case, the spacetime under consideration represents the direct product of a two-dimensional curved Riemann surface times a two-dimensional flat Minkowski. Thus, we make the dimensional continuation of the Minkowski subspace and keep the dimensionality of transverse curved subspace; thus, the prescript, proposed in Ref. [30], works as well.

Within the dimensional regularization technique, the computation of the first two terms in Equation (16) yields:

$$\begin{aligned} \text{tr} \ln(\partial^2 + m^2) + \text{tr}((\partial^2 + m^2)^{-1} \delta L) &= -iTZ m^D \frac{\Gamma[-D/2]}{(4\pi)^{D/2}} \int (\Lambda(x) + 1) d^2x \\ &= -iTZ m^D \frac{\Gamma[-D/2]}{(4\pi)^{D/2}} \int \sqrt{-g(x)} d^2x, \end{aligned} \tag{17}$$

where Γ is the gamma function and $D = 4 - 2\epsilon$. The corresponding contribution to the effective action coincides with the first term of deWitt–Schwinger expansion and should be neglected in the subsequent renormalization procedure [28].

Therefore, for the separation of the Casimir contribution to the total vacuum energy to the first non-zero perturbational order, one must take the third term of the expansion (16):

$$\mathcal{E}_{\text{vac}} = \frac{i}{4T} \text{tr} \left[(\partial^2 + m^2)^{-1} \delta L (\partial^2 + m^2)^{-1} \delta L \right]. \tag{18}$$

In the Fourier basis, the latter expression becomes

$$\mathcal{E}_{\text{vac}} = \frac{i}{4T} \int \frac{d^4k}{(2\pi)^4} \frac{d^4p}{(2\pi)^4} \frac{\delta L(k, i(p+k)) \delta L(-k, ip)}{[p^2 - m^2][(p+k)^2 - m^2]}, \tag{19}$$

where

$$\delta L(k, ip) = \int d^4x e^{ikx} \left[\delta L(x, \partial) \Big|_{\partial \rightarrow -ip} \right]. \tag{20}$$

In our problem, from Equation (14) we infer:

$$\delta L(k, ip) = -\Lambda(k) \left(p_0^2 - p_z^2 - m^2 \right), \tag{21}$$

(where $\Lambda(k)$ denotes the four-dimensional Fourier-transform of $\Lambda(x)$). The direct n -dimensional Fourier-transform (with the indication of dimensionality in text) is defined as

$$f(k) = \int e^{ikx} f(x) d^n x.$$

Thus, the vacuum energy is determined by the following expression:

$$\mathcal{E}_{\text{vac}} = \frac{i}{4T} \int \frac{d^4k}{(2\pi)^4} \frac{d^4p}{(2\pi)^4} \frac{(p_0^2 - p_z^2 - m^2)^2}{[p^2 - m^2][(p+k)^2 - m^2]} \Lambda(k) \Lambda(-k). \tag{22}$$

Under the derivation of Equation (22), it was taken into account that

$$\Lambda(k) = 4\pi^2 \delta(k^0) \delta(k^z) \Lambda(\mathbf{k}), \tag{23}$$

where $\Lambda(\mathbf{k})$ stands for the two-dimensional Fourier-transform of $\Lambda(x)$, $\mathbf{k} = (k^1, k^2)$, and $\delta(\cdot)$ is the Dirac delta function. Consequently, in the expressions below, one has to fix $k^0 = k^z = 0$.

The integral over d^4p in Equation (22) diverges, but it has a standard form appropriate for the usage of the dimensional regularization method.

The Wick rotation,

$$p^0 = i p_E^0, \quad d^4p = i d^4p_E, \quad p^2 = -p_E^2,$$

where the subscript 'E' indicates the Euclidean space, and subsequent substitution of d^4p by $\tilde{\mu}^{4-D} d^D p_E$ reduce the expression (22) to the form

$$\mathcal{E}_{\text{vac}}^{\text{reg}} = -\frac{\tilde{\mu}^{4-D}}{4T} \int \frac{d^4k}{(2\pi)^4} \Lambda(k) \Lambda(-k) \int \frac{d^D p_E}{(2\pi)^D} \frac{(p_0^2 + p_z^2 + m^2)_E^2}{(p^2 + m^2)_E [(p+k)_E^2 + m^2]}, \tag{24}$$

where $\tilde{\mu}$ is an arbitrary mass scale factor introduced to preserve the physical dimension of regularized expression (24).

The internal integral over $d^D p_E$ has a typical quantum field theory (QFT) form. Thus, it can be computed with the help of the Feynman parametrization (see, e.g., [31]). In the subsequent integration over d^4k , we encounter the observation that the integrand contains $\Lambda(k)$ squared (23), i.e., squares $\delta(k^0)$ and $\delta(k^z)$, respectively. We resolve this problem in a standard way:

$$[\delta(k^0)]^2 = \delta(k^0) \delta(0) = \frac{\delta(k^0)}{2\pi} \int e^{ik^0 t} dt \Big|_{k^0=0} = \frac{T}{2\pi} \delta(k^0).$$

The same for the delta-function of k^z yields:

$$[\delta(k^z)]^2 = \frac{Z}{2\pi} \delta(k^z).$$

As a result, for the regularized vacuum energy one has the following expression:

$$\begin{aligned} \mathcal{E}_{\text{vac}}^{\text{reg}} = & -\frac{Z}{4(4\pi)^2} \int \frac{d^2k}{(2\pi)^2} \Lambda(\mathbf{k}) \Lambda(-\mathbf{k}) \times \\ & \times \int_0^1 d\eta \left[2\Gamma(-2 + \varepsilon)\Psi^2 + 2m^2\Gamma(-1 + \varepsilon)\Psi + m^4\Gamma(\varepsilon) \right] \left(\frac{\Psi}{4\pi\tilde{\mu}^2} \right)^{-\varepsilon}, \end{aligned} \quad (25)$$

where

$$\Psi = \eta(1 - \eta)k^2 + m^2.$$

Then one expands $(\Psi/\tilde{\mu}^2)^{-\varepsilon}$ with respect to small ε :

$$\left(\frac{\Psi}{\tilde{\mu}^2} \right)^{-\varepsilon} = 1 - \varepsilon \ln \frac{\Psi}{\tilde{\mu}^2} + \mathcal{O}(\varepsilon^2). \quad (26)$$

The first term in Equation (26) leads to the appearance of terms proportional to the “pole-valued” Γ -functions, in the expression for $\mathcal{E}_{\text{vac}}^{\text{reg}}$ (25). These terms are to be excluded in our renormalization scheme [28].

The procedure of dimensional regularization on curved background in four dimensions reduces to separation and discarding the terms proportional to $\Gamma(\varepsilon)$, $\Gamma(-1 + \varepsilon)$, $\Gamma(-2 + \varepsilon)$. It is shown (see, e.g., [28]) that the renormalized effective action obtained under this prescription coincides with the analogous expressions obtained under other often used regularization techniques.

Thus, one obtains:

$$\begin{aligned} \mathcal{E}_{\text{vac}}^{\text{ren}} = & \frac{Z}{4(4\pi)^2} \int \frac{d^2k}{(2\pi)^2} \Lambda(\mathbf{k}) \Lambda(-\mathbf{k}) \int_0^1 d\eta (\Psi - m^2)^2 \ln \frac{\Psi}{\tilde{\mu}^2} \\ = & \frac{Z}{4(4\pi)^2} \int \frac{d^2k}{(2\pi)^2} \Lambda(\mathbf{k}) \Lambda(-\mathbf{k}) k^4 \int_0^1 d\eta \eta^2 (1 - \eta)^2 \ln \frac{\Psi}{\tilde{\mu}^2}. \end{aligned} \quad (27)$$

This expression is taken as the starting point for further research, which is developed in Sections 4 and 5 below.

4. Vacuum Interaction of Strings: $d \gg 2a$

As mentioned in Section 1, in the regime $d \gg 2a$, the strings can be considered to be infinitely thin. If so, the functions σ_α are to be specified in the form (9), hence their Fourier-transforms equal

$$\sigma_\alpha(\mathbf{k}) = -\frac{16\pi\mu_\alpha}{k^2} e^{ikx_\alpha}. \quad (28)$$

Assuming that the exponential power σ in Equation (14) is small enough and the substitution

$$\Lambda(\mathbf{x}) \longrightarrow -\sum_\alpha \sigma_\alpha(\mathbf{x}),$$

is valid, one arrives at the following expression:

$$\mathcal{E}_{\text{vac}}^{\text{ren}} = \frac{Z}{4(4\pi)^2} \sum_{\alpha, \beta} \int \frac{d^2k}{(2\pi)^2} \sigma_\alpha(\mathbf{k}) \sigma_\beta^*(\mathbf{k}) k^4 \int_0^1 d\eta \eta^2 (1-\eta)^2 \ln \frac{\Psi}{\tilde{\mu}^2}. \quad (29)$$

Within the problem formulation, common for the Casimir effect, the criterion of elicitation of the Casimir contribution from the total vacuum energy is a dependence upon the distance between "walls". It was shown (see, e.g., [2]) that for the finite-sized bodies, separated by the finite distance, the corresponding Casimir contribution into the total (generally, diverging) vacuum energy turns out to be finite. In the problem considered here, this prescript allows the neglect of those terms in the integrand, which contain products $\sigma_\alpha \sigma_\alpha$.

One can see that only the summand terms with $\alpha \neq \beta$ are responsible for the Casimir interaction since the latter depends upon the relative interstring distances. Thus, with the computational perturbation-order accuracy used here, the Casimir interaction is to be regarded as pairwise.

Taking into account Equation (28), the integration with respect to η reduces the Casimir energy expression into

$$\mathcal{E}_{\text{Cas}} = \frac{8Z\mu_1\mu_2}{15} \int \frac{d^2k}{(2\pi)^2} e^{ikd} \left[\ln \frac{m}{\tilde{\mu}} + A(x) \left(1 - \frac{2}{x^2} + \frac{6}{x^4} \right) - \left(\frac{47}{60} - \frac{3}{2x^2} + \frac{6}{x^4} \right) \right], \quad (30)$$

where

$$x = \frac{|k|}{m}, \quad A(x) = \sqrt{1 + (2/x)^2} \operatorname{arcsinh} \frac{x}{2}.$$

Being integrated, the constant terms in the square brackets yield $\delta^2(d)$, and therefore, they do not contribute to \mathcal{E}_{Cas} , by virtue of $d > 0$.

Furthermore, at small values of x the function $A(x)$ behaves like

$$A(x) = 1 + \frac{1}{12} x^2 - \frac{1}{120} x^4 + \frac{1}{840} x^6 + \mathcal{O}(x^8), \quad (31)$$

and, as is straightforward to verify, the integrand has no non-integrable singularity as $|k| \rightarrow 0^+$.

On the other hand, as $(x \gg 1)$ the following expansion holds

$$A(x) = \ln x + \frac{2 \ln x + 1}{x^2} - \frac{2 \ln x - 1/2}{x^4} + \mathcal{O}\left(\frac{\ln x}{x^6}\right), \quad (32)$$

so the integral (regarded in the Riemann sense) diverges at large $|k|$.

This divergence occurs due to the logarithmic behavior of the function $A(x)$ at infinity, so we proceed as follows. Add and subtract $\ln x$ inside the square brackets in Equation (30). The minus-logarithm is to remain inside the integrand, while the Fourier-transform of the plus-logarithm is to be separated as an independent term. Therefore, we represent Equation (30) in the form

$$\mathcal{E}_{\text{Cas}} = \frac{8Z\mu_1\mu_2}{15} \int \frac{d^2k}{(2\pi)^2} e^{ikd} \left[A(x) \left(1 - \frac{2}{x^2} + \frac{6}{x^4} \right) - \ln x + \left(\frac{3}{2x^2} - \frac{6}{x^4} \right) \right] - \frac{4Z\mu_1\mu_2}{15d^2}. \quad (33)$$

We took the help of the point that the Fourier-transform of the logarithm is well-defined in the sense of distributions [32]. The latter yields a non-integral term in Equation (33). Now, the remaining integral in Equation (33) is well-defined as a Riemannian one.

Subsequent integration with respect to the polar angle φ in the (k_1, k_2) -plane with help of the table integral [33]

$$\int_0^{2\pi} d\varphi e^{iqr \cos \varphi} = 2\pi J_0(qr), \tag{34}$$

where J_0 is a zeroth-order Bessel function of the 1st kind, yields

$$\mathcal{E}_{\text{Cas}} = \frac{4Z\mu_1\mu_2}{15\pi} \int_0^\infty dk k J_0(kd) \left[A\left(\frac{k}{m}\right) \left(1 - 2\frac{m^2}{k^2} + 6\frac{m^4}{k^4}\right) - \ln \frac{k}{m} + \frac{3}{2} \frac{m^2}{k^2} - 6\frac{m^4}{k^4} \right] - \frac{4Z\mu_1\mu_2}{15d^2}. \tag{35}$$

Notice that the non-integral term in Equation (35) coincides with the known result for the massless scalar field. Therefore, the dependence of the Casimir effect upon mass, which is of interest here, is completely determined by the integral term in Equation (35). Thus, for the function $\mathcal{F} = \mathcal{E}_{\text{vac}}(m) / \mathcal{E}_{\text{vac}}(0)$, introduced formally in Equation (1), one obtains a definite expression

$$\mathcal{F} = -d^2 \int_0^\infty dk k J_0(kd) \left[A\left(1 - 2\frac{m^2}{k^2} + 6\frac{m^4}{k^4}\right) - \ln \frac{k}{m} + \frac{3}{2} \frac{m^2}{k^2} - 6\frac{m^4}{k^4} \right] + 1. \tag{36}$$

After the variable change $s = k/2m$, the integral splits as follows:

$$\mathcal{F}(z) = 1 - z^2 \left[h_0(z) - \frac{1}{2} h_1(z) + \frac{3}{8} h_2(z) \right], \quad z = 2md,$$

where $h_n(z)$ are defined as

$$\begin{aligned} h_0(z) &= \int_0^\infty ds J_0(sz) \left[\sqrt{1+s^2} \operatorname{arcsinh} s - s \ln 2s \right], \\ h_1(z) &= \int_0^\infty ds \frac{J_0(sz)}{s^2} \left[\sqrt{1+s^2} \operatorname{arcsinh} s - s \right], \\ h_2(z) &= \int_0^\infty ds \frac{J_0(sz)}{s^4} \left[\sqrt{1+s^2} \operatorname{arcsinh} s - s - \frac{s^3}{3} \right]. \end{aligned} \tag{37}$$

These integrals can be computed:

$$\begin{aligned} h_0(z) &= \frac{1}{z^2} + \frac{1}{4} \left[K_0^2\left(\frac{z}{2}\right) - K_1^2\left(\frac{z}{2}\right) \right], \\ h_1(z) &= \frac{z}{2} U(z), \\ h_2(z) &= -\frac{z^2}{9} \left[K_0^2\left(\frac{z}{2}\right) - K_1^2\left(\frac{z}{2}\right) \right] - \frac{z^3}{18} U(z) - \frac{z}{6} K_0\left(\frac{z}{2}\right) K_1\left(\frac{z}{2}\right), \end{aligned} \tag{38}$$

where $K_n(\cdot)$ are Macdonald functions (modified Bessel functions of the 3rd kind), while $U(\cdot)$ stands for the following special integral Macdonald function:

$$U(z) = \int_z^\infty \frac{dx}{x^2} K_0^2\left(\frac{x}{2}\right). \tag{39}$$

As a result, for $\mathcal{F}(z)$ one obtains eventually:

$$\mathcal{F}(z) = \frac{z^2}{4} \left[\left(\frac{z^2}{6} - 1 \right) \left[K_0^2\left(\frac{z}{2}\right) - K_1^2\left(\frac{z}{2}\right) \right] + \left(\frac{z^2}{12} + 1 \right) zU(z) + \frac{z}{4} K_0\left(\frac{z}{2}\right) K_1\left(\frac{z}{2}\right) \right]. \quad (40)$$

The plot of $\mathcal{F}(z)$ is presented in Figure 2.

In what follows, for $z \gg 1$, the asymptotic expansion reads:

$$\mathcal{F}(z) = \frac{\pi}{16} e^{-z} \left(15 - \frac{75}{2z} + \frac{25,031}{128z^2} + \mathcal{O}(z^{-3}) \right).$$

Therefore, at large (with respect to the Compton length) distances, the Casimir effect is damped exponentially.

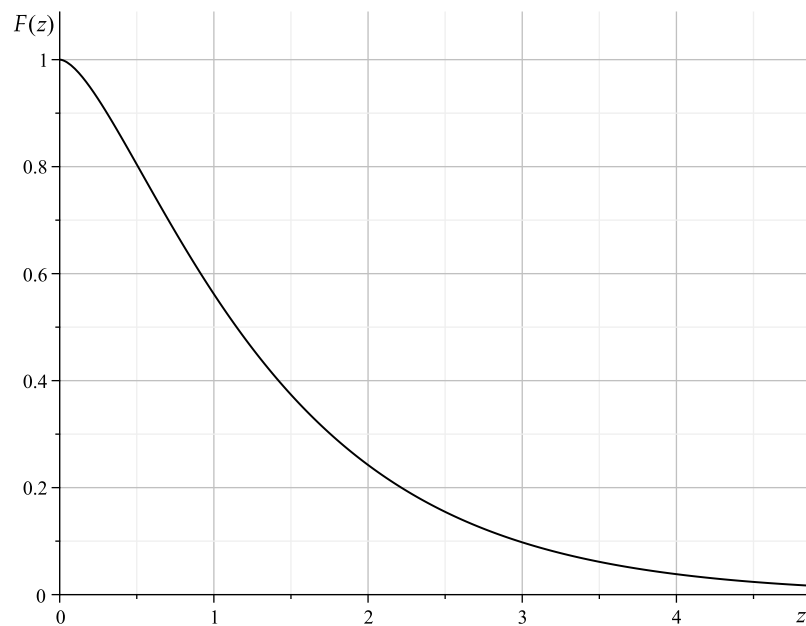


Figure 2. $\mathcal{F}(z)$ function given by Equation (40).

In the opposite case, for $z \ll 1$, the expansion is given by

$$\mathcal{F}(z) = 1 + \frac{5}{8} z^2 \left(\ln \frac{z}{4} + \gamma + \frac{1}{3} \right) + \mathcal{O}(z^4 |\ln z|),$$

and thus, one can see that for $d \ll l_c$, the contribution of massive modes into the Casimir energy turns out to be comparable to the contribution of massless modes, as follows from the qualitative speculations.

The plot of dependence of the Casimir energy,

$$\mathcal{E}_{\text{Cas}} = -\frac{4Z\mu_1\mu_2}{15d^2} \mathcal{F}(2md), \quad (41)$$

as a function of interstring distance in doubly logarithmic scale is presented in Figure 3. The dashed line corresponds to the massless limit.

The corresponding attraction force per unit strings' length is to be found as a derivative of the Casimir energy \mathcal{E}_{Cas} with respect to the strings-separation distance d . Therefore, both the Casimir energy and the Casimir force (both per unit length) are given by finite expressions.

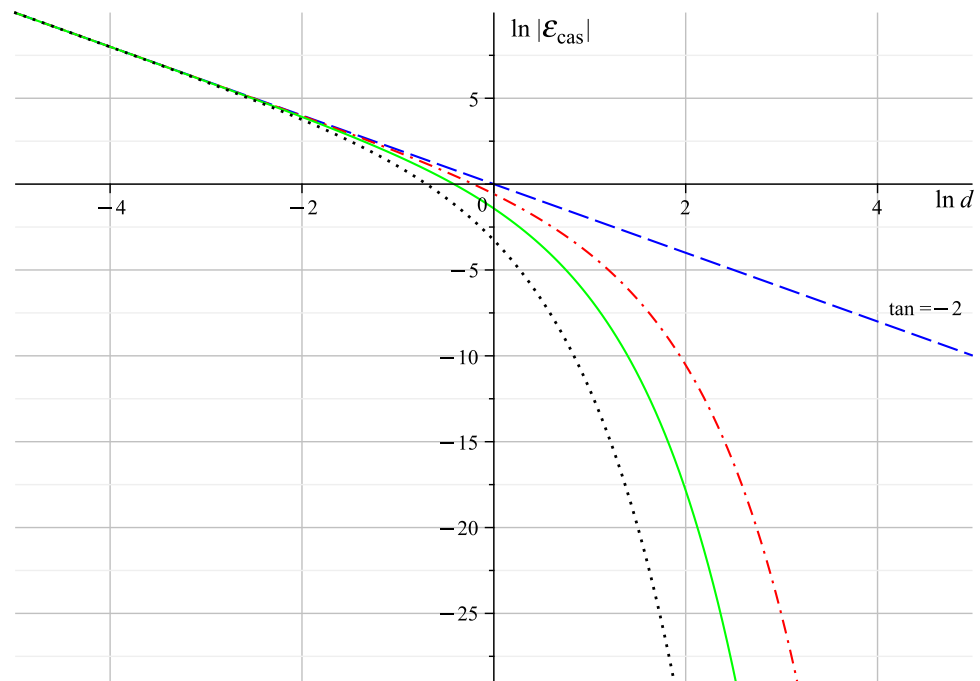


Figure 3. Energy of the Casimir attraction of two strings as a function of interstring distance (in units $l_c^{(m=1)} = 1$) in doubly logarithmic scale: for the massive fields with $m = 0.5$ (red, dashdotted), $m = 1$ (green, solid), $m = 2$ (black, dotted), and for the massless field (blue, dashed). See text for details.

5. Vacuum Interaction of Strings: $2a < d \ll l_c$

As was noted in Section 1, the case $d \ll l_c$ corresponds to the observation that the field can be considered to be massless.

Then, returning to Equation (27) and fixing $m = 0$, one obtains:

$$\mathcal{E}_{\text{vac}}^{\text{ren}} = \frac{Z}{4(4\pi)^2} \int \frac{d^2k}{(2\pi)^2} \Lambda(\mathbf{k}) \Lambda(-\mathbf{k}) k^4 \int_0^1 d\eta \eta^2 (1-\eta)^2 \ln \frac{\eta(1-\eta)k^2}{\tilde{\mu}^2}, \quad (42)$$

and after the η -integration:

$$\mathcal{E}_{\text{vac}}^{\text{ren}} = \frac{Z}{60(4\pi)^2} \int \frac{d^2k}{(2\pi)^2} \Lambda(\mathbf{k}) \Lambda(-\mathbf{k}) k^4 [\ln |k| + \mathcal{O}(1)]. \quad (43)$$

Now after the substitution $\Lambda(\mathbf{k}) \rightarrow -\sigma(\mathbf{k})$ the expression (43) is rewritten as a sum of two integrals. One of them reads:

$$\int \frac{d^2k}{(2\pi)^2} |k|^4 \sigma(\mathbf{k}) \sigma(-\mathbf{k}) = \int d^2x [\Delta\sigma(\mathbf{x})]^2 \simeq \int d^2x R^2(\mathbf{x}). \quad (44)$$

The integral, which contains a logarithm in Equation (43), also can be transformed into the coordinate representation:

$$\begin{aligned} \int \frac{d^2k}{(2\pi)^2} |k|^4 \ln |k| \sigma(\mathbf{k}) \sigma(-\mathbf{k}) &= -\frac{1}{2\pi} \int d^2x d^2x' \frac{\Delta\sigma(\mathbf{x}) \Delta'\sigma(\mathbf{x}')}{|\mathbf{x} - \mathbf{x}'|^2} \\ &\simeq -\frac{1}{2\pi} \int d^2x d^2x' \frac{R(\mathbf{x}) R(\mathbf{x}')}{|\mathbf{x} - \mathbf{x}'|^2}. \end{aligned} \quad (45)$$

In the expressions (44) and (45), it was taken into account that to the lowest order of $(1 - \beta)$, which is of interest here,

$$\Delta\sigma(\mathbf{x}) = \sum_{\alpha} \Delta\sigma_{\alpha}(\mathbf{x}) \simeq R(\mathbf{x}) = \sum_{\alpha} R_{\alpha}(\mathbf{x}). \tag{46}$$

For two strings separated by distance $d > a_1 + a_2$ ($\mathbf{d} = \mathbf{x}_1 - \mathbf{x}_2$), the supports of the partial contributions R_{α} and R_{β} do not overlap. Hence, that contribution to Equation (44), which depends upon the distance d , vanishes, and the Casimir contribution to the total vacuum energy (46) is completely determined by the contribution due to the integral (45). This contribution can be presented in the form

$$\mathcal{E}_{\text{Cas}} = -\frac{Z}{15(4\pi)^3} \int_{\substack{|x| < a_1, \\ |x'| < a_2}} d^2x d^2x' \frac{R_1(\mathbf{x}) R_2(\mathbf{x}')}{|\mathbf{x} - \mathbf{x}' + \mathbf{d}|^2}. \tag{47}$$

Introduce two polar coordinate systems (ϱ, φ) and (ϱ', φ') (with suggestive notations) with origins in the centers of strings. Then, both angular integrations are carried out with the help of the table integral [33]

$$\int_0^{2\pi} \frac{d\varphi}{A + B \cos \varphi} = \frac{2\pi}{\sqrt{A^2 - B^2}}.$$

It results in the following expression for the Casimir energy per unit length:

$$\frac{\mathcal{E}_{\text{Cas}}}{Z} = -\frac{16}{15\pi} \frac{\mu_1 \mu_2}{a_1^2 a_2^2} \int_0^{a_1} \varrho d\varrho \int_0^{a_2} \varrho' d\varrho' \frac{\varrho' d\varrho'}{\sqrt{[(d + \varrho')^2 - \varrho^2][(d - \varrho')^2 - \varrho^2]}}.$$

Integrating with respect to ϱ , one has:

$$\frac{\mathcal{E}_{\text{Cas}}}{Z} = -\frac{8}{15\pi} \frac{\mu_1 \mu_2}{a_1^2 a_2^2} \int_0^{a_2} \varrho' d\varrho' \left(\ln \frac{d}{\varrho'} - \operatorname{arccosh} \frac{d^2 + \varrho'^2 - a_1^2}{2d\varrho'} \right). \tag{48}$$

The final integration yields:

$$\begin{aligned} \frac{\mathcal{E}_{\text{Cas}}}{Z} = \frac{8}{15\pi} \frac{\mu_1 \mu_2}{a_1^2 a_2^2} & \left[\frac{d^2 - 2a_1^2}{8} - \frac{1}{8} \sqrt{(d^2 + a_1^2 - a_2^2)^2 - 4d^2 a_1^2} + \right. \\ & \left. + \frac{a_1^2}{2} \left(\operatorname{arccosh} \frac{d^2 + a_1^2 - a_2^2}{2da_1} - \ln \frac{d}{a_1} \right) + \{a_1 \leftrightarrow a_2\} \right]. \tag{49} \end{aligned}$$

In the case of GUT strings, both the mass per unit length and the string's width are determined by the energy scale of the corresponding phase transition, $\eta_{\text{GUT}} \sim 10^{16}$ GeV. Hence it is reasonable to fix

$$a_1 = a_2 = a = a_{\text{GUT}} \sim \eta_{\text{GUT}}^{-1}, \quad \mu_1 = \mu_2 = \mu = \mu_{\text{GUT}} \sim \eta_{\text{GUT}}^2$$

and consider two similar strings. Then, introducing

$$\xi = \frac{a}{d} < \frac{1}{2},$$

the energy of the Casimir attraction per unit length of two finite-width strings equals [34]

$$\frac{\mathcal{E}_{\text{Cas}}}{Z} = \frac{4}{15\pi} \frac{\mu^2}{d^2} \frac{1}{\zeta^4} \int_0^{\zeta^2} dx \ln \frac{1+x-\zeta^2 + \sqrt{(1+x-\zeta^2)^2 - 4x}}{2}. \tag{50}$$

Finally, integrating with respect to x , the Casimir energy of two equivalent strings is given by

$$\frac{\mathcal{E}_{\text{Cas}}}{Z} = -\frac{4}{15\pi} \frac{\mu^2}{d^2} \frac{1}{\zeta^2} \left[1 - 2 \ln \frac{1 + \sqrt{1 - 4\zeta^2}}{2} - \frac{1 - \sqrt{1 - 4\zeta^2}}{2\zeta^2} \right]. \tag{51}$$

The dependence of the Casimir energy (normalized by $(-4\mu^2/15\pi)$) of attraction of two similar strings upon the interstring distance is plotted in Figure 4.

In the case $d \gg a$, the direct expansion in $\zeta \ll 1$ yields

$$\frac{\mathcal{E}_{\text{Cas}}}{Z} = -\frac{4}{15\pi} \frac{\mu^2}{d^2} \left[1 + \frac{a^2}{d^2} + \frac{5}{3} \frac{a^4}{d^4} + \mathcal{O}(d^{-6}) \right], \tag{52}$$

what to the leading (in a/d) order coincides with the result for infinitely thin strings [7–9].

In Figure 5, we plot the curve of a ratio of the Casimir energy for the ballpoint-pen model with respect to the same quantity for infinitely thin strings.

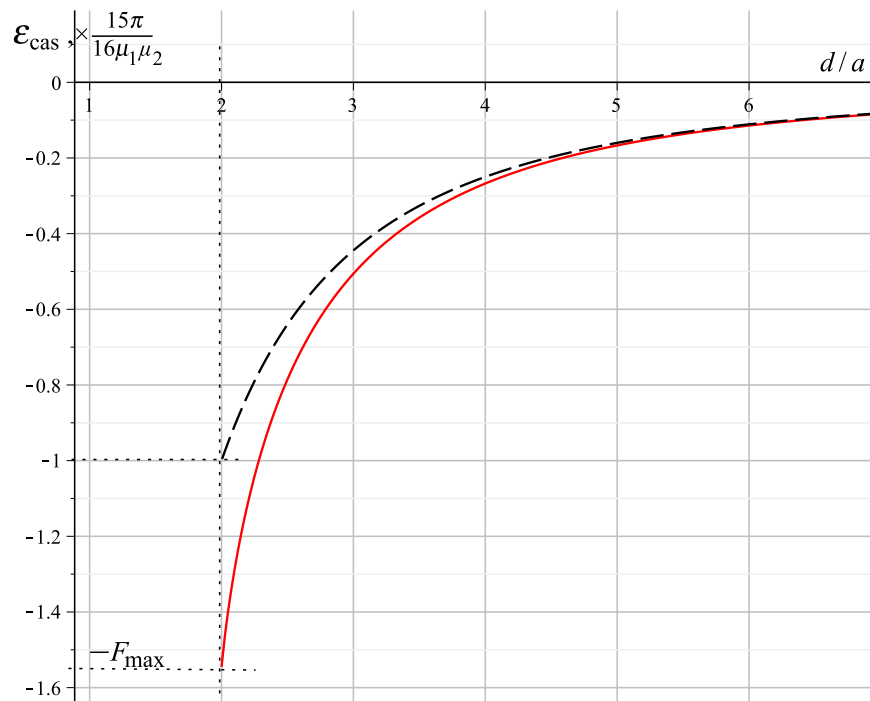


Figure 4. Casimir energy (normalized by the factor $16\mu_1\mu_2/15\pi$) versus the distance between centers for fixed equal string radii (red solid) in $a = 1$ units, compared with the infinitely thin string (black dashed). See text for details.

Let us consider the case $a_1 \ll a_2 < d$ separately. It can be considered to be a case when one of the strings (namely, a_2) was formed under the electroweak (EW) phase transition. It happened with considerably lower energies ($\eta_{\text{EW}} \sim 10^3$ GeV) and corresponds to the transverse size of the created strings of $a_{\text{EW}} \sim 10^{-15}$ cm, what significantly exceeds the corresponding width of a typical GUT-string ($a_{\text{GUT}} \sim 10^{-28}$ cm).

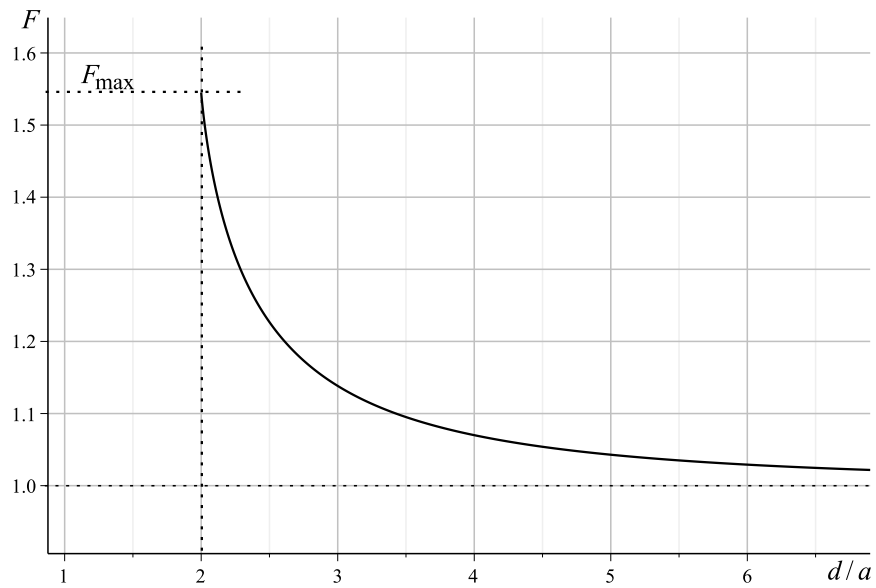


Figure 5. Relative Casimir attraction energy versus the interstring distance, with respect to the attraction of infinitely thin strings.

Then from the expression (48) we infer:

$$\frac{\mathcal{E}_{\text{Cas}}}{Z} = -\frac{8}{15\pi} \frac{\mu_1\mu_2}{a_2^2} \int_0^{a_2} \frac{q'dq'}{d^2 - q'^2} + \mathcal{O}(a_1^2/d^2). \tag{53}$$

In what follows, in the limit $a_1 \rightarrow 0^+$, denoting $a_2 = a$, one obtains

$$\frac{\mathcal{E}_{\text{Cas}}}{Z} = \frac{4}{15\pi} \frac{\mu_1\mu_2}{a^2} \ln\left(1 - \frac{a^2}{d^2}\right), \tag{54}$$

so, for $d \gg a$, we return to the result valid for two infinitely thin strings.

However, in the case of close contact, where the interstring gap, $\delta = d - a$, is considerably smaller than the interstring distance d , Equation (54) gives logarithmic singularity ($\mathcal{E}_{\text{Cas}} \sim \ln(2\delta/d)$) as $(\delta \rightarrow 0^+)$. This implies that if δ becomes of the same order as the width of the thinner string, one cannot neglect string's radius.

Let us demonstrate that under a contact of the strings of any finite width, the Casimir energy per unit length is finite within the model under interest. Then, two radii are related by $a_2 = d - a_1$. Define $a = \min\{a_1, a_2\}$ now and introduce $\bar{\zeta} := a/d$. Then for any $0 < \bar{\zeta} \leq 1/2$,

$$\frac{\mathcal{E}_{\text{Cas}}}{Z} = -\frac{4}{15\pi} \frac{\mu_1\mu_2}{d^2} \frac{1}{\bar{\zeta}^2} \left[\frac{\bar{\zeta}^2(1 - \ln \bar{\zeta}) - \bar{\zeta}}{(1 - \bar{\zeta})^2} - \ln(1 - \bar{\zeta}) \right]. \tag{55}$$

For $\bar{\zeta} = 1/2$ one reproduces the result (51) with $\zeta = 1/2$:

$$\mathcal{F} = 4(2\ln 2 - 1), \tag{56}$$

while, in the opposite limiting case ($\bar{\zeta} \ll 1$), the expansion in relatively small a reads:

$$\frac{\mathcal{E}_{\text{Cas}}}{Z} = -\frac{4}{15\pi} \frac{\mu_1\mu_2}{d^2} \left(\ln \frac{d}{a} - \frac{1}{2} \right) + \mathcal{O}(a|\ln a|). \tag{57}$$

From the quantitative viewpoint, this case (applied to the pair GUT-plus-EW strings) is of a significantly lower interest than the case of two similar GUT strings discussed in this

Section. It happens since the energy per unit length, $\mu_{EW} \sim \eta_{EW}^2$, of the EW string is many orders smaller than the same energy, μ_{GUT} , for the GUT string. But from the qualitative viewpoint, for the EW strings, these effects take place already at the distances of the order of $d \sim 1/\eta_{EW} \sim 10^{-15}$ cm, in contrast to the orders 10^{-28} cm for the Casimir interaction of two GUT strings. Also, the model considered above once again illustrates the nontrivial dependence of this effect on the strings' size.

6. Discussion

We have presented an extended overview of recent results obtained by the authors in the process of studying the vacuum interaction of topological cosmic strings at short distances [34,35]. Within the tr-ln formalism, we have considered the vacuum interaction of finite-width topological cosmic strings, which interact via a massive scalar field with minimal coupling. It is shown that at distances much less than the Compton length but significantly larger than the strings' width, the partial contribution of massive fields to the Casimir energy is comparable with the contribution of massless fields. Therefore, at such small (in the sense mentioned above) distances, one can neglect the mass. Nevertheless, if the interstring distance becomes comparable with the strings' width, one cannot neglect the string radius. Furthermore, if the interstring gap is of the order of the string's width, the energy of the Casimir interaction may significantly surpass the same quantity for the infinitely thin strings with the same mass per unit length.

The results obtained here may be useful in subsequent issues on the interaction of strings at short distances, on their collisions, and on accompanying intertangles and reconnections.

Author Contributions: Conceptualization, Y.V.G.; investigation, Y.V.G. and P.S.; writing—original draft, P.S.; writing—review and editing, Y.V.G. All authors have read and agreed to the published version of the manuscript.

Funding: This research received no external funding.

Data Availability Statement: Data is contained within the article.

Acknowledgments: This study was conducted within the scientific program of the National Center for Physics and Mathematics, section #5 "Particle Physics and Cosmology" (stage 2023–2025), Russia.

Conflicts of Interest: The authors declare no conflict of interest.

Abbreviations

The following abbreviations are used in this manuscript:

EMT	Energy-momentum tensor
GUT	Grand Unified Theory
QFT	Quantum field theory
EW	Electroweak

References

1. Casimir, H.B.G. On the attraction between two perfectly conducting plates. *Proc. Kon. Ned. Akad. Wetensch. B* **1948**, *51*, 793–795. Available online: <https://dwc.knaw.nl/DL/publications/PU00018547.pdf> (accessed on 10 November 2023).
2. Bordag, M.; Klimchitskaya, G.L.; Mohideen, U.; Mostepanenko, V.M. *Advances in the Casimir Effect*; Oxford University Press: Oxford, UK, 2009. [CrossRef]
3. Gibbons, G.W.; Hawking, S.W.; Vachaspati, T. (Eds.) *The Formation and Evolution of Cosmic Strings*; Cambridge University Press: Cambridge, UK, 1990.
4. Vilenkin, A.; Shellard, E.P.S. *Cosmic Strings and Other Topological Defects*; Cambridge University Press: Cambridge, UK, 1994.
5. Copeland, E.J.; Pogasian, L.; Vachaspati, T. Seeking string theory in the cosmos. *Class. Quant. Grav.* **2011**, *28*, 204009. [CrossRef]
6. Bordag, M. On the vacuum interaction of two parallel cosmic strings. *Ann. Phys.* **1990**, *502*, 93–100. [CrossRef]
7. Muñoz-Castañeda, J.M.; Bordag, M. Quantum vacuum interaction between two cosmic strings revisited. *Phys. Rev. D* **2014**, *89*, 065034. [CrossRef]
8. Grats, Y.V. Vacuum interaction of conic singularities. *Theor. Math. Phys.* **2016**, *186*, 205–212. [CrossRef]

9. Gal'tsov, D.V.; Grats, Y.V.; Lavrent'ev, A.B. Vacuum polarization and topological selfinteraction of a charge in multiconic space. *Phys. Atom. Nucl.* **1995**, *58*, 516–521.
10. Pirozhenko, I. Vacuum interaction of crossed cosmic strings. *Universe* **2021**, *7*, 217. [CrossRef]
11. Allen, B.; Ottewill, A.C. Effects of curvature couplings for quantum fields on cosmic-string space-times. *Phys. Rev. D* **1990**, *42*, 2669–2677. [CrossRef]
12. Allen, B.; McLaughlin, J.G.; Ottewill, A.C. Photon and graviton Green's functions on cosmic string space-times. *Phys. Rev. D* **1992**, *45*, 4486–4503. [CrossRef]
13. Allen, B.; Kay, B.S.; Ottewill, A.C. Long range effects of cosmic string structure. *Phys. Rev. D* **1996**, *53*, 6829–6841. [CrossRef]
14. Khusnutdinov, N.R.; Bordag, M. Ground state energy of massive scalar field in the background of finite thickness cosmic string. *Phys. Rev. D* **1999**, *59*, 064017. [CrossRef]
15. Bezerra de Mello, E.R.; Bezerra, V.B.; Saharian, A.A.; Tarloyan, A.S. Vacuum polarization induced by a cylindrical boundary in the cosmic string spacetime. *Phys. Rev. D* **2006**, *74*, 025017. [CrossRef]
16. Bezerra de Mello, E.R.; Bezerra, V.B.; Saharian, A.A.; Harutyunyan, H.H. Vacuum currents induced by a magnetic flux around a cosmic string with finite core. *Phys. Rev. D* **2015**, *91*, 064034. [CrossRef]
17. Bezerra de Mello, E.R.; Saharian, A.A. Vacuum polarization by a global monopole with finite core. *J. High Energy Phys.* **2006**, *10*, 049. [CrossRef]
18. Grats, Y.V.; Spirin, P. Vacuum polarization and classical self-action near higher-dimensional defects. *Eur. Phys. J. C* **2017**, *77*, 101. [CrossRef]
19. Grats, Y.V.; Spirin, P. Vacuum polarization in the background of conical singularity. *Int. J. Mod. Phys. A* **2020**, *35*, 2040030. [CrossRef]
20. Letelier, P.C. Multiple cosmic strings. *Class. Quant. Grav.* **1987**, *4*, L75. [CrossRef]
21. Deser, S.; Jackiw, R.; 't Hooft, G. Three-dimensional Einstein gravity: Dynamics of flat space. *Ann. Phys.* **1984**, *152*, 220–235. [CrossRef]
22. Gott, J.R.; Alpert, M. General relativity in a (2+1)-dimensional space-time. *Gen. Relat. Gravit.* **1984**, *16*, 243–247. [CrossRef]
23. Giddings, S.; Abbott, J.; Kuchar, K. Einstein's theory in a three-dimensional space-time. *Gen. Relat. Gravit.* **1984**, *16*, 751–775. [CrossRef]
24. Jackiw, R. Lower dimensional gravity. *Nucl. Phys. B* **1985**, *252*, 343–356. [CrossRef]
25. Gott, J.R., III. Gravitational lensing effects of vacuum strings: Exact solutions. *Astrophys. J.* **1985**, *288*, 422–427. [CrossRef]
26. Hiscock, W.A. Exact gravitational field of a string. *Phys. Rev. D* **1985**, *31*, 3288–3290. [CrossRef]
27. Peskin, M.E.; Schroeder, D.V. *An Introduction to Quantum Field Theory*; CRC Press/Taylor & Francis Group LLC: Boca Raton, FL, USA, 1995. [CrossRef]
28. Birrell, N.D.; Davies, P.C.W. *Quantum Fields in Curved Space*; Cambridge University Press: Cambridge, UK, 1982. [CrossRef]
29. Reed, M.; Simon, B. *Methods of Modern Mathematical Physics. Volume 3: Scattering Theory*; Academic Press, Inc.: New York, NY, USA, 1979.
30. Hawking, S.W. Zeta function regularization of path integrals in curved spacetime. *Commun. Math. Phys.* **1977**, *55*, 133–138. [CrossRef]
31. Itzykson, C.; Zuber, J.B. *Quantum Field Theory*; McGraw-Hill Inc.: New-York, NY, USA, 1980. Available online: <https://archive.org/details/quantumfieldtheo0000itzy> (accessed on 10 November 2023).
32. Gel'fand, I.M.; Shilov, G.E. *Generalized Functions. Volume 1: Properties and Operations*; Academic Press Inc.: New York, NY, USA, 1964. Available online: <https://archive.org/details/gelfand-shilov-generalized-functions-vol-1-properties-and-operations> (accessed on 10 November 2023).
33. Prudnikov, A.P.; Brychkov, Y.A.; Marichev, O.I. *Integrals and Series. Volume 2: Special Functions*; Gordon and Breach Science Publishers: Amsterdam, The Netherlands, 1998. Available online: <https://archive.org/details/integralseries0002prud> (accessed on 10 November 2023).
34. Grats, Y.V.; Spirin, P. Casimir interaction of finite-width strings. *Phys. Rev. D* **2023**, *108*, 045001. [CrossRef]
35. Grats, Y.V.; Spirin, P. Casimir interaction of cosmic strings: massive field. *J. Exp. Theor. Phys.* **2024**, *138*, in press.

Disclaimer/Publisher's Note: The statements, opinions and data contained in all publications are solely those of the individual author(s) and contributor(s) and not of MDPI and/or the editor(s). MDPI and/or the editor(s) disclaim responsibility for any injury to people or property resulting from any ideas, methods, instructions or products referred to in the content.

Review

The Casimir Effect in Finite-Temperature and Gravitational Scenarios

Valdir Barbosa Bezerra ^{1,*}, Herondy Francisco Santana Mota ¹, Augusto P. C. M. Lima ², Geová Alencar ³ and Celio Rodrigues Muniz ⁴

¹ Departamento de Física, Universidade Federal da Paraíba, Caixa Postal 5008, João Pessoa 58051-900, Paraíba, Brazil; hmota@fisica.ufpb.br

² Instituto Federal de Educação, Ciência e Tecnologia do Piauí, Campus Corrente, Rua Projetada 06, S/n, Corrente 64980-000, Piauí, Brazil; augusto.placido@ifpi.edu.br

³ Departamento de Física, Universidade Federal do Ceará, Caixa Postal 6030, Campus do Pici, Fortaleza 60455-760, Ceará, Brazil; geova@fisica.ufc.br

⁴ Faculdade de Educação, Ciências e Letras de Iguatu, Universidade Estadual do Ceará, Iguatu 63500-000, Ceará, Brazil; celio.muniz@uece.br

* Correspondence: valdir@fisica.ufpb.br

Abstract: In this paper, we review some recent findings related to the Casimir effect. Initially, the thermal corrections to the vacuum Casimir energy density are calculated, for a quantum scalar field, whose modes propagate in the (3+1)-dimensional Euclidean spacetime, subject to a nontrivial compact boundary condition. Next, we analyze the Casimir effect induced by two parallel plates placed in a weak gravitational field background. Finally, we review the three-dimensional wormhole solutions sourced by the Casimir density and pressures associated with the quantum vacuum fluctuations of the Yang-Mills field.

Keywords: Casimir effect; finite-temperature effect; nontrivial compact boundary condition; weak gravitational field; wormhole; Yang–Mills field

1. Introduction

From the classical physics point of view, the phenomenon called the Casimir effect [1] cannot find its explanation. The effect manifests itself as an attractive force between the two parallel electrically neutral ideal metallic plates at zero temperature placed at a certain distance in a vacuum, according to the original configuration. According to classical electrodynamics, there is no force in such a scenario. Thus, this phenomenon can only be understood in the context of quantum physics, and its origin is related to the oscillations of the zero-point (vacuum) energy or, equivalently, to the fluctuations of the quantum electromagnetic field as a consequence of boundary conditions imposed to the field due to the presence of the plates. This is the most basic configuration that leads to the Casimir effect. This phenomenon associated with the vacuum fluctuations of the quantum electromagnetic field was predicted by Hendrik Casimir [1] in 1948, who obtained an intriguing and remarkably simple formula for this force per unit area of the plates:

$$F = -\frac{\pi^2 \hbar c}{240 L^4}, \quad (1)$$

where L denotes the distance between the two plates and \hbar and c are the reduced Planck constant and the speed of light in vacuum, respectively. That is, the force depends on a geometrical factor, the distance between the plates, and the two fundamental constants, the former related to the quantum physics and the latter one to the relativistic consideration.

Originally, the Casimir effect was associated with the electromagnetic field and material boundaries made of a perfect conductor. Thus, taking into account that the Casimir

Citation: Bezerra, V.B.; Mota, H.F.S.; Lima, A.P.C.M.; Alencar, G.; Muniz, C.R. The Casimir Effect in Finite-Temperature and Gravitational Scenarios. *Physics* **2024**, *6*, 1046–1071. <https://doi.org/10.3390/physics6030065>

Received: 11 January 2024

Revised: 8 June 2024

Accepted: 5 July 2024

Published: 13 August 2024



Copyright: © 2024 by the authors. Licensee MDPI, Basel, Switzerland. This article is an open access article distributed under the terms and conditions of the Creative Commons Attribution (CC BY) license (<https://creativecommons.org/licenses/by/4.0/>).

effect, as originally conceived, is a direct consequence of the vacuum fluctuations of physical photons, whose propagating behavior depends on the presence of boundaries as compared with the free spacetime, and assuming the predictions of the quantum field theory that boundaries, independent of their nature, if material or due to the topology, induce nonzero vacuum expectation values, it is natural to expect that similar phenomena occur for countless configurations of quantum fields with different spins subject, for example, to boundary conditions dictated by the nontrivial topology associated with flat or curved spacetime [2–5].

During seventy-five years, since the discovery of this remarkable pure quantum effect, specifically from the seventies of the twentieth century up to nowadays, the line of research along the generalization described just above, in particular, concerning the role played by the nontrivial topology of spacetime on the quantum vacuum energy in the framework of the general theory of relativity, has been extensively investigated, with the breakthrough findings. As pioneering papers about this topic, we mention firstly the one that investigates the zero-point energy of quantum fields placed in background gravitational fields with a nontrivial topology [6]. As the second point, we call a cosmological model with a nontrivial topology, namely the Einstein universe with a topology $\mathcal{R}^1 \times \mathcal{S}^2$. In this cosmological scenario, considering a conformally coupled massless scalar field, the Casimir energy density and pressure are given by [7]

$$\varepsilon_0 = \frac{\hbar c}{480\pi^2 R^4} \quad \text{and} \quad P_0 = \frac{\varepsilon_0}{3}, \quad (2)$$

respectively, where R denotes the radius of the universe.

These pioneering studies inspired investigations concerning the role of the global structure of spacetime or, in other words, the role of the nontrivial topology, on the zero-point energy of quantum fields, placed in flat or curved backgrounds. Some of these studies related to the role played by boundary conditions imposed by the nontrivial topology in locally or globally flat spacetimes are given in Refs. [5,8–21]. Concerning the presence of gravitational fields, some interesting investigations were performed [4,13,22–51].

Over these seventy-five years, since its discovery [1], the Casimir effect has been actively investigated from theoretical point of view as well as experimentally. Particularly in the last three decades, and more recently, due to the possibility of numerous applications of this physical manifestation of zero-point energy, not only in fundamental sciences but also in applied sciences. It is a multidisciplinary phenomenon that arises when any quantum field is submitted to boundary conditions caused by material bodies or associated with a nontrivial space topology. It arises in different contexts, namely, quantum electrodynamics, condensed matter physics, quantum chromodynamics, gravitation and cosmology, and nanotechnology.

This paper reviews three different scenarios in which this phenomenon manifests, confirming the multifaceted and interdisciplinary features of the Casimir effect and its importance. In order to emphasize this multifaceted character, a revision is made about three different topics. The first one is related to the thermal corrections to the Casimir energy of massive and massless scalar fields, under boundary conditions with a nontrivial topology, in flat spacetime using the zeta function formalism [52]. The second concerns the investigation on how the Casimir effect manifests itself when the plates are embedded in a weak gravitational field sourced by a certain mass [50]. The third topic addressed in this review proposes the generation of wormholes in 2+1 dimensions by the Casimir energy associated to a Yang–Mills field [53]. Therefore, there is a progression in the scenarios discussed with respect to spacetime, ranging from flat one, then a slightly curved and finally a highly curved one.

The different topics considered in this review are believed to give us a better understanding of how the structure of spacetime influences a quantum phenomenon, shedding light on the relation between quantum fields, geometry and topology.

We begin by reviewing the generalized zeta function method, in Section 2. We calculate the Casimir energy for a massless scalar field and its respective thermal correction, taking into account a nontrivial compact boundary condition. In Section 3, we review the formalism to calculate the Casimir energy in a weak static gravitational field and revisit previous results of the literature. In Section 4, we study what is termed Casimir wormholes, and, in Sections 5 and 6, the summary of the results obtained and the conclusions are presented.

2. Thermal Corrections to the Casimir Energy Density: Scalar Field Subject to a Nontrivial Compact Boundary Condition

In what follows, the generalized zeta function method is used to obtain the thermal corrections to the Casimir energy density of a scalar field, initially calculated at zero temperature, by imposing a nontrivial compact boundary condition on the field. This condition was originally called the helix boundary condition in Refs. [18,54].

The expressions for the heat kernel function and free energy density are obtained in exact and analytic forms. In these calculations, quantum scalar fields with mass and those massless are taken into account. In particular, for the massless case, the internal energy density is analyzed concerning the limits corresponding to high and low temperatures. The influence of the boundary condition is the focus of the analysis along with the contribution by the thermal corrections to the Casimir energy density of the quantum scalar fields. It is worth noticing that all calculations are performed in a flat spacetime. Therefore, all modifications to the local features of the zero-point energy are due to the boundary conditions imposed on the fields.

2.1. Generalized Zeta Function Method

Let us review in what follows the vacuum energy and its temperature corrections for a real quantum scalar field with a nontrivial compact boundary condition following studies presented in Refs. [18,54,55] at zero temperature and in Ref. [52], at finite temperature. We adopt the method of the generalized zeta function defined as [56–58]

$$\zeta_4(s) = \sum_j \lambda_j^{-s}, \tag{3}$$

where λ_j represents the eigenvalues of a four-dimensional Laplace–Beltrami operator, \hat{A}_4 , where the subindex refers to the spacetime dimension, and j takes the values $1, 2, \dots, \infty$.

It is worth noticing that $\zeta_4(s)$ (3) converges for $\{\text{Re}(s) > 2$ and it is regular at $s = 0$, in four dimensions. It can be analytically extended to the interval $\text{Re}(s) < 2$, with poles at $s = 2$ and $s = 1$. As concerns its spectrum of eigenvalues denoted by λ_j , it is not necessarily discrete [58]. The path integral formulation of quantum field theory allows us to link the zeta function (3) with the partition function, Z , thus providing a way to study the thermodynamic properties of a quantum system. This connection is made through \hat{A}_4 and is given by [52,56,58]

$$Z = \det\left(\frac{4}{\pi\mu^2} \hat{A}_4\right), \tag{4}$$

where the parameter μ is a constant with a dimension of mass and stands for an integration measure in the functional space, and should be suppressed by the renormalization. Note that, in the case we are considering, the operator \hat{A}_4 is identified as the Laplace–Beltrami operator in the four-dimensional Euclidean space. Hence, in natural units, the operator has a dimension of mass squared, what makes Equation (4) dimensionless.

Upon using the known identity $e^{-\zeta_4'(0)} = \det(\hat{A}_4)$, where the prime denotes the s -derivative, from Equation (4), one finds [52,56,58]:

$$\ln Z = \frac{1}{2}\zeta_4'(0) + \frac{1}{2} \ln\left(\frac{\pi\mu^2}{4}\right)\zeta_4(0). \tag{5}$$

From Equation (5), we conclude that the partition function (4) can be determined if the zeta function (3) and its s -derivative at $s = 0$ are known.

The trace of the operator \hat{A}_4 defines the heat kernel $K(\eta)$:

$$K(\eta) = \text{Tr} \left[e^{-\eta \hat{A}_4} \right] = \sum_j e^{-\Omega_j \eta}, \tag{6}$$

where Ω_j is the set of eigenvalues of \hat{A}_4 . The generalized zeta function (3) can be written in terms of Equation (6) as

$$\zeta(s) = \frac{1}{\Gamma(s)} \int_0^\infty \eta^{s-1} \text{Tr} \left[e^{-\eta \hat{A}_4} \right] d\eta, \tag{7}$$

where $\Gamma(s)$ is the Gamma function.

Equation (7) corresponds to another representation of the generalized zeta function (3). Note that, in representation (7), the generalized zeta function does not depend on the spacetime coordinates. The form (7) is quite helpful to calculate the vacuum free energy when the eigenvalues of the operator \hat{A}_4 are known. With the zeta function in hand, we just use Equation (5) to calculate the partition function and, immediately, the vacuum-free energy.

The temperature corrections enter when a periodic boundary condition is imposed on the imaginary time, τ coordinate, of the scalar field, $\phi_j(x)$, whose solution can be written as

$$\phi_j(x) = e^{-i\omega_n \tau} \varphi_\ell(\mathbf{r}) \quad \text{with} \quad \omega_n^2 = \left(\frac{2\pi n}{\beta} \right)^2, \tag{8}$$

where $n = 0, \pm 1, \pm 2, \dots, j = (n, \ell)$ are the quantum modes and $\beta = 1/k_B T$ is the period, with k_B being the Boltzmann constant and T the temperature.

The eigenvalues are given by $\lambda_n = \omega_n^2 + \mathbf{k}^2 + m^2$, with \mathbf{k} being the three-momentum and m the mass of the field. The factor $\varphi_\ell(\mathbf{r})$ is the part of the solution of the quantum scalar field $\phi_j(x)$, which depends on the spatial coordinates.

It is worth pointing out that the approach we are adopting to calculate the thermal corrections are, in general, applicable, when the spacetime is ultra static [59–62], in which case, the solution can be written according to Equation (8).

Using the solution given by Equation (8), the general expression for the zeta function (7) turns into

$$\zeta_4(s) = \frac{\beta}{\sqrt{4\pi}\Gamma(s)} \left\{ \Gamma(s - 1/2) \zeta_3(s - 1/2) + 2 \sum_{n=1}^\infty \int_0^\infty \eta^{s-\frac{3}{2}} e^{-\frac{(n\beta)^2}{4\eta}} \text{Tr} \left[e^{-\eta \hat{A}_3} \right] d\eta \right\}, \tag{9}$$

where the operator \hat{A}_3 with eigenvalues \mathbf{k} corresponds to the spatial part of the operator \hat{A}_4 and $\zeta_3(s)$ is the zeta function whose general expression is given by Equation (7).

Now, Equations (5) and (9) can be used to calculate the free energy, which is given as follows:

$$\begin{aligned} F &= -\frac{\ln Z}{\beta} \\ &= \frac{1}{2} \zeta_3(-1/2) - \frac{\bar{C}_2}{2(4\pi)^2} \ln(C^2) - \frac{1}{\sqrt{4\pi}} \sum_{n=1}^\infty \int_0^\infty \eta^{-\frac{3}{2}} e^{-\frac{(n\beta)^2}{4\eta}} \text{Tr} \left[e^{-\eta \hat{A}_3} \right] d\eta, \end{aligned} \tag{10}$$

where $\sqrt{\pi}e^2\mu/8$, with e being the elementary charge.

The first two terms correspond to the vacuum energy at zero temperature, and the third one furnishes the thermal corrections. Note that the result given by Equation (10)

presents an ambiguity in the definition of the vacuum energy at zero temperature if the coefficient \bar{C}_2 is different from zero. Let us write \bar{C}_2 as [4]

$$\bar{C}_2 = C_2 - C_1 m^2 + \frac{C_0 m^4}{2}, \tag{11}$$

where C_0 , C_1 , and C_2 are the heat kernel coefficients. It is worth calling attention to the feature that, in the massless case, the ambiguity disappears when C_2 vanishes.

The heat kernel coefficients are introduced using the heat kernel expansion [4]:

$$K(\eta) = \frac{e^{-m^2 \eta}}{(4\pi\eta)^{3/2}} \sum_{p=0}^{\infty} C_{p/2} \eta^{p/2} + \text{ES}, \tag{12}$$

where $C_{p/2}$ are the heat kernel coefficients and "ES" stands for exponentially suppressed terms.

To proceed with the regularization of the vacuum energy, we can write the first two terms of Equation (10) as [4]

$$E_0(s) = \frac{C^{2s}}{2} \zeta_3(s - 1/2). \tag{13}$$

Therefore, the renormalized vacuum energy reads

$$E_0^{\text{ren}} = \lim_{s \rightarrow 0} [E_0(s) - E_0^{\text{div}}(s)], \tag{14}$$

where $E_0^{\text{div}}(s)$ is the divergent contribution of the regularized expression in Equation (13) [4]. This divergent contribution is given in terms of the heat kernel coefficients $C_{p/2}$. As shown in Section 2.2 below, the only divergent contribution is given in terms of C_0 , which is related to the Euclidean heat kernel divergent contribution to the zeta function $\zeta_3(s - 1/2)$. In the massive case, other coefficients appear, and thus, it is necessary to include an additional normalization condition to obtain the renormalized vacuum energy, and thus justifying the subtraction of terms proportional to the positive powers of the mass m [4]. Then, the normalization condition is given by

$$\lim_{m \rightarrow \infty} E_0^{\text{ren}} = 0, \tag{15}$$

which is satisfied in the case under consideration, as expected. The condition (15) has been suggested in Ref. [63] and provides a unique physical meaning for the renormalized vacuum energy, since, in the large (infinite) mass limit, there should be no quantum vacuum fluctuations. The condition (15) implies that it is necessary to implement a renormalization of finite terms proportional to the positive powers of mass, in addition to the renormalization of infinite terms which, in general, takes place in vacuum energy configurations.

2.2. Nontrivial Compact Boundary Condition, Heat Kernel, and Thermal Corrections

In what follows, we assume that the quantum modes of the scalar field propagate in a (3+1)-dimensional Euclidean spacetime and experience a boundary condition given by

$$\varphi(x + a, y, z) = \varphi(x, y + h, z), \tag{16}$$

which is also known as the helix boundary condition in the literature [18,54]. According to Refs. [18,54], the condition (16) is topologically equivalent to a helix and the geometric parameters h and a are the pitch and the helix radius, respectively. The boundary condition expressed by Equation (16) was also considered by investigating the Casimir effect at zero [18,54] and nonzero [52] temperatures. The helix-like topology of the spacetime codified in Equation (16) is constructed using the mathematical notion of the equivalence relation, equivalence classes, and quotient space as discussed in Refs. [18,54]

(see also Ref. [64]). For instance, the points (x, y) and $(x + n_x a, y + n_y a)$ in \mathbb{R}^2 , with $n_x, n_y = 0, \pm 1, \pm 2, \pm 3, \dots$, present an equivalence relation if $x \rightarrow x + n_x a$ and $y \rightarrow y + n_y a$. A quotient space may be obtained by separately identifying the endpoints in each dimension x and y to form a compact space with topology $S^1 \times S^1$. Thus, we end up with two independently compactified dimensions. However, in the present case, a quotient space \mathbb{R}^2 / \sim is obtained by identifying the points $(a, 0)$ and $(0, h)$, for instance, and consequently, making the direction along the green solid line in Figure 1 compact, with length $d = \sqrt{a^2 + h^2}$. Hence, the nontrivial compact condition described in Equation (16) is presented as $\mathbb{R}^2 \times \mathbb{R}^2 / \sim$.

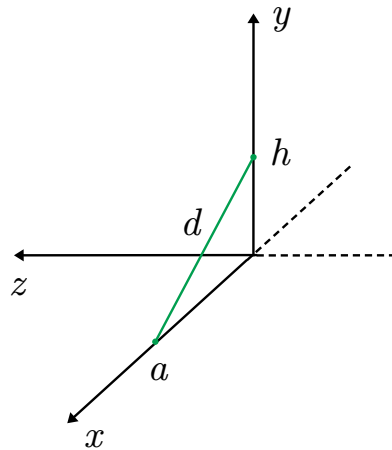


Figure 1. Illustration of the direction of the compactification. According to the condition given by Equation (16), the scalar field has the same value at $(a, 0)$ and $(0, h)$ if one considers $(x, y) = (0, 0)$. The parameters a and h can be topologically associated with a helix [18,54].

In the present study, we are interested in reviewing some important aspects of the problem related to heat kernel coefficient contributions and also to divergences associated with these coefficients.

The corresponding eigenvalues of the problem are written as [52]

$$\begin{aligned} \lambda_\ell &= k_x^2 + \left(\frac{k_x a}{h} - \frac{2\pi n}{h}\right)^2 + k_z^2 + m^2 \\ &= \left(\frac{k_y h}{a} + \frac{2\pi n}{a}\right)^2 + k_y^2 + k_z^2 + m^2. \end{aligned} \tag{17}$$

As the components of the momentum k_x and k_y are related, the spatial quantum modes are indexed by $\ell = (n, k_y, k_z)$ or $\ell = (n, k_x, k_z)$. In the calculation that follows, the latter option is assumed. Taking into account the recently obtained result concerning the heat kernel for the problem under consideration [52]:

$$K(\eta) = V \frac{e^{-m^2 \eta}}{(4\pi\eta)^{3/2}} \sum_{n=-\infty}^{\infty} e^{-\frac{n^2 d^2}{4\eta}}, \tag{18}$$

where the Euclidean contribution to the heat kernel is given by [60–62]

$$K_E(\eta) = V \frac{1}{(4\pi\eta)^{3/2}} e^{-m^2 \eta}, \tag{19}$$

where only the term $n = 0$ was taken into account. Note that the heat kernel (18) can be interpreted as the one obtained from space with topology $\mathbb{R}^2 \times S^1$, with d being the size of

the compact dimension. This becomes clear if, in the first line of Equation (17), we perform the substitution

$$k_x = \frac{h}{d} \left(k_X + \frac{2a\pi n}{hd} \right), \tag{20}$$

where k_X is the momentum in the new direction, X . Hence, Equation (17) can be written as

$$\lambda_\ell = k_X^2 + \frac{4\pi^2 n^2}{d^2} + k_z^2 + m^2. \tag{21}$$

The problem considered here is equivalent to the one in a four-dimensional spacetime with Cartesian coordinates (t, X, Y, z) , with the Y dimension compactified into a circle of length d [65]. In other words, the spacetime topology characterized by the condition (16) is effectively equivalent to a space with topology $\mathbb{R}^2 \times S^1$, as previously noted. That is why we have also called Equation (16) a nontrivial compact boundary condition.

Comparing the heat kernel (18) with the heat kernel expansion (18), we find that the C_0 is only coefficient different from zero and given by $C_0 = V$, where V is the volume of the (3+1)-dimensional Euclidean spacetime. It is worth calling attention to the feature that C_0 is responsible for the divergent contribution to the zeta function (7) and, thus, should be cancelled to obtain a finite result for the Casimir energy density. On the other hand, the contribution of the third term of the free energy (10), which arises from the Euclidean heat kernel (19), corresponds to the scalar thermal (blackbody) radiation contribution [56]. To find a renormalized result for the thermal correction contributions [39,40], the appropriate subtractions have to be performed. As a result, the classical limit for the free energy is recovered for high temperatures, as expected.

Now, subtracting the Euclidean heat kernel contribution equation (19) from the heat kernel (18) and assuming the boundary condition given by Equation (16), the renormalized heat kernel for the field $\varphi_\ell(\mathbf{r})$ reads as :

$$K_{\text{ren}}(\eta) = V \frac{e^{-m^2\eta}}{4(\pi\eta)^{3/2}} \sum_{n=1}^{\infty} e^{-\frac{n^2(a^2+h^2)}{4\eta}}. \tag{22}$$

Let us return to the generalized zeta function (7), which can be written as

$$\zeta_3(s - 1/2) = V \frac{2^{3-s} m^{4-2s}}{(4\pi)^{3/2} \Gamma(s - 1/2)} \sum_{n=1}^{\infty} f_{2-s}(mnd). \tag{23}$$

where

$$f_\mu(x) = \frac{K_\mu(x)}{x^\mu}, \tag{24}$$

with $K_\mu(x)$ being the modified Bessel function of the second kind.

Let us consider the free energy (10), where the first two terms correspond to the Casimir energy at zero temperature. Thus, using Equations (13) and (14), the following expression is obtained:

$$E_0^{\text{ren}} = -V \frac{m^4}{2\pi^2} \sum_{n=1}^{\infty} f_2(mnd). \tag{25}$$

The result given by Equation (25) is the renormalized Casimir energy at zero temperature [18,54,55]. Taking into account the massless field, the renormalized Casimir energy can be obtained from Equation (25) assuming that the arguments of the modified Bessel function are very small, such that $K_\mu(x) \simeq (2/x)^\mu \Gamma(\mu)/2$ [66,67]. Thus, the following result is obtained [18,54,55]:

$$E_0^{\text{ren}} = -V \frac{\pi^2}{90d^4}, \tag{26}$$

where the Riemann zeta function, $\zeta_R(4) = \pi^4/90$, was used [58,66,67].

Notice that the results obtained do not depend on the energy scale, M , and as a consequence, there is no ambiguity. One should remember that the term containing the parameter M in Equation (10), which introduces an ambiguity in the definition of the vacuum energy at zero temperature, is nonzero only when the coefficient \bar{C}_2 in Equation (11) exists. As in the the case considered here, where $\bar{C}_2 = C_0 m^4/2$, with $C_0 = V$, as already stated in this Section. Actually, the second term on the right-hand side of Equation (10) is nonzero. However, as we expect a decreasing in the vacuum energy for large masses, this term should be discarded, since it grows with the mass m and must be subtracted in order to obey the normalization (15). Such a process, in the massive case, leads to the renormalized vacuum energy in Equation (25). On the other hand, the massless vacuum energy case does not carry the term depending on M in Equation (10) since $\bar{C}_2 = 0$. So, naturally, one obtains Equation (26).

As discussed above, the results for the Casimir energies given by Equations (25) and (26) can be obtained, effectively, by considering a space with topology $\mathbb{R}^2 \times S^1$, where one of the dimensions has been compactified into a circle of length d . But, then, what are the new features here? To answer this question, one should remember that the length d is defined in terms of the radius a and pitch h of the helix in Figure 1, i.e., $d = \sqrt{a^2 + h^2}$. This makes it possible to calculate the Casimir force both along h and a , as shown in Ref. [18]. In Ref. [18], it is also shown that the Casimir force in the h direction behaves according to Hooke’s law in the regime when the parameter ratio, $r = h/a$, is exceptionally small, i.e., $r \ll 1$, whereas in the opposite regime, $r \gg 1$, the Casimir force behaves according to an inverse square law. The helix-like topology also allows us to apply the results presented here to investigate the influence of the Casimir energy in an RNA structure of a virus like SARS-CoV-2, as has been performed in a simplified initial study in Ref. [68].

In what follows, the thermal corrections to the renormalized Casimir energy densities given by Equations (25) and (26), for the massive and massless cases, respectively, will be calculated. To do this end, the following results will be considered:

$$F_T^E = -V \frac{m^4}{2\pi^2} \sum_{n=1}^{\infty} f_2(mn\beta), \tag{27}$$

and

$$F_T^E = -V \frac{\pi^2}{90} (k_B T)^4 \tag{28}$$

for the massive and massless cases, respectively. Equations (27) and (28) are obtained using the Euclidean heat kernel (19). Equation (28) corresponds to the massless scalar thermal (blackbody) radiation contribution [56]. It should be subtracted from the temperature correction to obtain the classical limit at high temperatures [39,40].

The normalized temperature correction, F_T^{ren} (25), to the Casimir energy density is obtained with the use of the renormalized heat kernel equation (22).

Then, we arrives at

$$F_T^{\text{ren}} = -V \frac{m^4}{\pi^2} \sum_{j=1}^{\infty} \sum_{n=1}^{\infty} f_2 \left[m\beta(j^2 + n^2\gamma^2)^{1/2} \right], \tag{29}$$

where $\gamma = d/\beta = k_B T d$. It is worth calling attention to the feature that the result (29) is exponentially suppressed at low temperatures, which means that $\beta m \gg 1$, in which case, $K_\mu(x) \simeq \sqrt{\frac{\pi}{2x}} e^{-x}$ [66,67]. Thus, the result expressed by Equation (29) is consistent with the requirement that the temperature corrections must vanish for low temperatures. For high temperatures, which means $\beta m \ll 1$, we obtain:

$$F_T^{\text{ren}} = -V \frac{2}{\pi^2} \sum_{n=1}^{\infty} \sum_{j=1}^{\infty} \frac{1}{(j^2\beta^2 + n^2d^2)^2}. \tag{30}$$

Taking into account the massive case, the renormalized free energy is given by

$$F_T^{\text{ren}} = -V \frac{m^4}{2\pi^2} \sum_{n=1}^{\infty} f_2(mnd) - V \frac{m^4}{\pi^2} \sum_{j=1}^{\infty} \sum_{n=1}^{\infty} f_2 \left[m\beta(j^2 + n^2\gamma^2)^{\frac{1}{2}} \right], \quad (31)$$

where the sum of Equations (25) and (29) was considered. Note that the second term in Equation (31) is exponentially suppressed, and only the first term contributes [18,54,55].

In the massless case, Equations (26) and (30) can be combined and written as

$$F^{\text{ren}} = -V \frac{\pi^2}{90d^4} - V \frac{2}{\pi^2} \sum_{n=1}^{\infty} \sum_{j=1}^{\infty} \frac{1}{(j^2\beta^2 + n^2d^2)^2}. \quad (32)$$

In this case, the low and high temperatures limit can be analyzed and interesting results are obtained. Firstly, let us perform the sum in j in Equation (32), to obtain the high-temperature limit. In what concerns the limit of low temperatures, it is obtained by performing the sum in n , firstly. Taking these procedures into account, the result obtained for the high-temperature limit, $k_B Td \gg 1$, is as follows:

$$F_{\text{ren}} \simeq -\frac{k_B T}{2\pi d^3} \zeta_3 - \frac{2(k_B T)^2}{d^2} e^{-2\pi\gamma}. \quad (33)$$

Note that the second term in Equation (33) is exponentially suppressed, while the first one corresponds to the classical scenario and dominates in this limit.

In the low-temperature limit, Equation (32) turns into

$$F_{\text{ren}} \simeq -\frac{\pi^2}{90d^4} + \frac{\pi^2}{90} (k_B T)^4 - \frac{(k_B T)^3}{2\pi d} \zeta(3) - \frac{2(k_B T)^3}{\pi d} e^{-\frac{2\pi}{k_B Td}}. \quad (34)$$

Note that the first term corresponds to the Casimir energy at zero temperature and is the dominant one. In what concerns to the third term, it is exponentially suppressed.

3. Casimir Energy in Weak Static Gravitational Field

When comprehensively examining the Casimir Effect in curved spacetime, special consideration should be given to scenarios involving weak background gravity. This assertion stems from the anticipation that feasible laboratory conditions for assessing the interaction between vacuum energy and gravity will likely involve relatively small gravitational effects. For instance, the Archimedes experiment [69,70] aims to measure the weight of the vacuum and is expected to occur in such a setting. The initial results of this experiment are eagerly awaited, as they may offer a means to scrutinize the reality of the vacuum fluctuation energy and its gravitational behavior further. From a theoretical standpoint, researchers generally expect the vacuum energy to behave following the principle of equivalence, a fundamental aspect of general relativity. However, experimental confirmation is still pending.

In this Section, we review the fundamentals of the Casimir effect in curved spacetime and revisit several works from the literature that delve into the simplest case of a Casimir apparatus subjected to weak, spherically symmetrical gravity, a suitable approximation for Earth’s gravitational field. We begin with an elegant and explicit calculation introduced by Francesco Sorge in Ref. [44], along with similar findings from other sources. Subsequently, we discuss the corrections proposed by Augusto Lima and colleagues in Ref. [50], leading to a somewhat surprising prediction of null corrections to the measured “vacuum weight” at the first relevant order. This contradicts some earlier works that suggest that the Casimir energy should be affected by gravity like any other form of energy. We then briefly outline how Sorge resolves this issue in Ref. [71].

3.1. General Method

Firstly, let us review the method for computing the Casimir effect in curved spacetime highlighting a simplified approach proposed in Ref. [44]. This involves studying the

Casimir effect in the basic scenario of rectangular parallel plates under Dirichlet boundary conditions, considering a real massless scalar field within a static weak gravitational field. The configuration is shown in Figure 2.

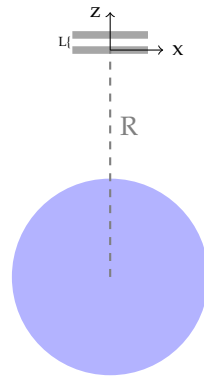


Figure 2. Diagram illustrating the placement of plates and the observer’s coordinate system.

In a curved spacetime, the action of the scalar field, ϕ , can be written as

$$S = \int d^4x \sqrt{g} \left[\frac{1}{2} g^{\mu\nu} \partial_\mu \phi \partial_\nu \phi + \frac{1}{2} \epsilon \mathcal{R} \phi^2 \right], \tag{35}$$

and the field equation as

$$\frac{1}{\sqrt{g}} \partial_\mu [\sqrt{g} g^{\mu\nu} \partial_\nu \phi] + \epsilon \mathcal{R} \phi = 0, \tag{36}$$

where $g^{\mu\nu}$ is the 4-dimensional metric tensor with a signature $(+, -, -, -)$, the Greek indices take the values 0 (temporal component), 1, 2, and 3 (spatial components), g is the determinant of $g^{\mu\nu}$, ϵ denotes the vacuum energy, \mathcal{R} is the Ricci scalar, and $\partial_\mu \equiv \partial/\partial x_\mu$.

In order to get a simple enough expression for the energy density, we consider a static observer who performs measurements with the four-velocity:

$$u^\mu = g_{00}^{-1/2} \delta_0^\mu, \tag{37}$$

where δ_ν^μ is the Kronecker delta.

The orthonormal mode solutions obey the scalar product:

$$\langle \phi_n, \phi_m \rangle = \int_\Sigma \sqrt{g_\Sigma} n^\mu [\phi_n^* \partial_\mu \phi_m - (\partial_\mu \phi_n^*) \phi_m] d\Sigma, \tag{38}$$

where Σ stands for the boundaries, and

$$\langle (\phi_n, \vec{k}_n), (\phi_m, \vec{k}_m) \rangle = \delta(\vec{k}_n - \vec{k}_m) \delta_{nm}, \tag{39}$$

with n and m representing discrete modes, while \vec{k} refers to the transverse wave numbers, and $\delta(\vec{k}_n - \vec{k}_m)$ is the Dirac delta function.

The mean vacuum energy is defined as

$$\bar{\epsilon} = \frac{1}{V_p} \int_\Sigma d^3x \sqrt{g_\Sigma} u^\mu u^\nu \langle 0 | T_{\mu\nu} | 0 \rangle, \tag{40}$$

where V_p is the proper volume of the cavity $V_p = \int_{\Sigma} d^3x \sqrt{g_{\Sigma}}$ and $T_{\mu\nu}$ represents the stress–momentum–energy of the scalar field. In terms of the field modes, Equation (40) can be written in terms of the orthonormal mode solutions as [44]

$$\bar{\epsilon} = \frac{1}{V_p} \sum_n \int d^2k \sqrt{g_{\Sigma}} (g_{00})^{-1} T_{00}[\phi_n^*, \phi_n], \tag{41}$$

where, $T_{00}[\phi_n^*, \phi_n]$ represents a bilinear form analogous to the time–time component of the stress–energy tensor:

$$T_{00}[\phi_n^*, \phi_n] = \partial_0 \phi_n^* \partial_0 \phi_n - g_{00} g^{\mu\nu} \partial_{\mu} \phi_n^* \partial_{\nu} \phi_n. \tag{42}$$

3.2. Sorge’s Result and Generalizations

The field is governed by the ordinary Klein–Gordon equation; the boundaries are planes with coordinate separation, L ; and field obeys the conditions $\phi(z = 0) = \phi(z = L) = 0$. The orthonormal solutions are given by

$$\phi(x) = \frac{1}{2\pi\sqrt{\omega_{nF}L}} \sin\left(\frac{n\pi z}{L}\right) \exp[i(\omega_{nF}t - k_{\perp}x_{\perp})], \tag{43}$$

where $\omega_{nF} = \sqrt{k_{\perp}^2 + (n\pi/L)^2}$ is the mode frequency (with the \perp subscript denoting the transverse component and the “ F ” subscript standing for a flat spacetime). Using these mode solutions in Equations (41) and (42), we obtain:

$$\bar{\epsilon} = \frac{1}{8\pi^2L} \sum_n \int d^2k_{\perp} \omega_{nF}. \tag{44}$$

Employing Schwinger’s proper time representation and zeta function regularization, we arrive at the renormalized value for the Casimir energy in Minkowski spacetime:

$$\bar{\epsilon}_{\text{Cas}} = -\frac{\pi^2}{1440L^4}. \tag{45}$$

To explore the curved case, we commence with the explicit calculation proposed by Sorge [44]. The spacetime metric is defined as

$$ds^2 = -(1 + 2\Phi(r))dt^2 + (1 - 2\Phi(r))(dr^2 + r^2d\Omega^2), \tag{46}$$

where r is the radius-vector, Ω is the space solid angle, $\Phi(r) = -\mathcal{M}/r$ is the Newtonian gravitational potential, with \mathcal{M} being the mass parameter, in the framework of the weak field approximation of the Schwarzschild spacetime. In this background, the Casimir energy is sought in a scenario where two parallel rectangular plates are present. To simplify the calculations, a Cartesian-like coordinate system is employed between the plates, whose origin is located at the center of the lower plate, and the z -axis is aligned parallel with the radial direction (see Figure 2).

Concerning the metric, it is written as

$$ds^2 = -(1 + 2\Phi_0 + 2Yz)dt^2 + (1 - 2\Phi_0 - 2Yz)(dx^2 + dy^2 + dz^2). \tag{47}$$

Applying the following coordinate changes: $dt \rightarrow (1 + 2\Phi_0)^{-1}dt$, $\vec{dx} \rightarrow (1 - 2\Phi_0)^{-1}\vec{dx}$, the metric (47) turns into

$$ds^2 = -(1 + 2Yz)dt^2 + (1 - 2Yz)\vec{dx}^2, \tag{48}$$

which reduces to Equation (47) with $\Phi_0 = 0$. Therefore, up to order $(\mathcal{M}/R)^2$, the relevant parameter is Y . Notice that, in the case where there are no crossing terms in the metric, the

Casimir energy for a general constant perturbation measured by the observer, given by Equation (37), remains unaltered [72]. This is what is expected because this spacetime is equivalent to the Minkowski one.

The vacuum expected value of the energy–momentum tensor can then be determined by the standard manner using orthonormal solutions of the Klein–Gordon Equation (36) and substituting into Equation (41).

The perturbative calculation is performed, order by order [44], starting with the zeroth order (flat spacetime) and, in the sequel, to the first order (up to Φ_0 in Equation (47)). An intriguing observation is that, when calculating to the order of Φ_0 —constant perturbative terms relative to Minkowski spacetime—it is demonstrated that there is no correction to the conventional flat spacetime Casimir energy. This stems from the observation that setting $Y = 0$ in Equation (47) results in a flat spacetime with a gauge transformation [44]. Then, we proceed to the second-order calculation following these steps.

The case $Y = 0$ corresponds to the first-order approximation being calculated explicitly, with a null result [44]. In the sequel, the correction of the second order of the metric (48) is taken into account. In this case, the field equation turns into

$$-(1 - 4Yz)\partial_t^2\phi + \nabla^2\phi = 0, \tag{49}$$

where $\nabla^2 \equiv \delta^{ij}\partial_i\partial_j$. The solutions are, then, given by

$$\phi_{n,k} = \chi_n(z)e^{i\omega_n t - ik_\perp x_\perp}, \tag{50}$$

and asymptotically turn into

$$\chi_n(u) = A_n u^{-1/4} \sin\left(\frac{2}{3}u^{3/2} + \varphi\right), \tag{51}$$

where

$$u(z) = -(z - p/q)q^{1/3}, \quad q = 4Y\omega_n^2, \quad p = \omega_n^2 - k_\perp^2, \tag{52}$$

and $\omega_n = (1 + YL)\omega_{nF}$ are the frequencies. In the results obtained in Ref. [44], the expansion is performed in terms of the solution for the flat case, as follows:

$$\phi_n = \phi_n^{(0)} + \delta\phi_n. \tag{53}$$

Using this approach, the energy–momentum tensor and Casimir energy can be written as

$$T_{00}[\phi_n^*, \phi_n] = T_{00}[\phi_n^{(0)*}, \phi_n^{(0)}] + \{T_{00}[\delta\phi_n^*, \phi_n^{(0)}] + \text{c.c.}\}, \tag{54}$$

and $\bar{\epsilon} = \bar{\epsilon}^{(0)} + \delta\bar{\epsilon}$. Here, “c.c.” stands for complex conjugate.

Substituting the first term on the right-hand side of Equation (54) into Equation (41) and subsequently renormalizing, we obtain:

$$\bar{\epsilon}_{\text{ren}}^{(0)} = -(1 - 2YL_p)\frac{\pi^2}{1440L_p^4}. \tag{55}$$

In the expression (55), $L_p = \int dz \sqrt{|g_{33}|}$ represents the proper separation distance between the plates.

Considering the second term, which is analogous to the flat spacetime expression (44), the calculation is performed by integrating the frequency change of the modes (neglecting other terms since $\delta\phi$ itself is of order Y):

$$\delta\bar{\epsilon} = \frac{1}{8\pi^2 L} \sum_n \int d^2k_\perp \delta\omega_n = YL_p \left(-\frac{\pi^2}{1440L_p^4} \right), \tag{56}$$

with the following result:

$$\bar{\epsilon}_{\text{Cas}} = -(1 - YL_p) \frac{\pi^2}{1440L_p^4} = -(1 - YL)\bar{\epsilon}_0, \tag{57}$$

with $\bar{\epsilon}_0$ being the standard flat spacetime result. Notably, in Ref. [44] it is meticulously ensured that the result is expressed exclusively in terms of proper quantities, not in the coordinate ones. This constitutes the original outcome presented in Ref. [44].

Several generalizations to the result (57) have been proposed, such as one in Ref. [73] where a general weak field metric is suggested by considering distinct Φ and Y parameters as follows:

$$ds^2 = -(1 + 2\Phi_0 + 2Y_0z)dt^2 + (1 - 2\Phi_1 - 2Y_1z)(dx^2 + dy^2 + dz^2). \tag{58}$$

Taking into account the Neumann boundary conditions, a calculation can be carried out for both scalar and vector fields. In particular, for a real scalar massless field, the following result for the proper energy density is obtained:

$$\bar{\epsilon} = -(1 + \Phi_0 + Y_0 \frac{L_p}{2})\bar{\epsilon}_0. \tag{59}$$

This approach can be applied to specific cases, including the far-field limit of Kerr spacetime (also discussed in Ref. [74]), Fermi spacetime, and the scenario of Horava–Lifshitz gravity with a cosmological constant. This can be achieved by adjusting the coefficients Φ and Y . It is important to note however, that Equation (59) does not seem to recover the result obtained in Equation (57). Several additional examples involving spacetimes sharing some similarity with Equation (58) are explored. These include the study of a similar model for extended theories of gravity [75], the Casimir effect in post-Newtonian gravity with Lorentz violation [76], and the Casimir effect in quadratic theories of gravity [77].

3.3. Revisiting

Recently, Lima and colleagues [50] have revisited the the problem we consider here addressed by Sorge in Ref. [44]. Let us first revisit Sorge’s approach [44] to calculate second-order corrections. The same reasoning that leads to the second-order calculations can be applied to compute the first-order correction; let us examine the outcome.

Assuming that $\Phi = \Phi_0$ in Equation (46) and substituting Equation (45) into Equation (42) and integrating, we obtain

$$\bar{\epsilon}^0 = \frac{1}{V_p} \frac{1}{(2\pi)^{22}L} (1 - 3\Phi_0) \sum_n \int d^2k \omega_0. \tag{60}$$

Performing the renormalization and writing the result in terms of L_p , we find

$$\bar{\epsilon}_{\text{ren}}^0 = -(1 - 4\Phi_0) \frac{\pi^2}{1440L_p^4}. \tag{61}$$

The frequencies are $\omega \simeq (1 + 2\Phi_0)\omega_0$, so we should have

$$\delta\bar{\epsilon} = -2\Phi_0 \frac{\pi^2}{1440L_p^4}. \tag{62}$$

Adding the contributions given in Equations (61) and (62), a nonzero energy shift is found. The method falters due to the assumption that $\delta\bar{\epsilon}$ can be computed by substituting ω_0 for $\delta\omega$, as in the flat spacetime case.

Lima and colleagues [50] demonstrated that this is not the case and that the correction factor is linked to a geometrical term reminiscent of the normalization condition (38). In what follows, the details are presented.

Let us begin by writing Equation (51) as a perturbative expansion in terms of Y , as follows

$$\chi(z) = \frac{1}{2\pi\sqrt{\omega_0 L}} \sin\left(\frac{n\pi z}{L}\right) + Y\chi^{(1)}(z) + \mathcal{O}(M/R)^3, \tag{63}$$

where $\chi^{(1)}$ defines the first order correction. To obtain $\chi^{(1)}$, we have to determine A_n , φ and ω_n . The frequencies are obtained by imposing the periodicity of the solution, namely, $\phi(0) = \phi(L) = 0$, which gives us

$$\omega_n \simeq (1 + YL)\omega_0, \text{ where } \omega_0 = [k^2 + (n\pi/L)^2]^{1/2}. \tag{64}$$

Imposing that $\chi(z = 0) = 0$, the following solution is obtained:

$$\phi = -\frac{2}{3}u^{3/2}(0). \tag{65}$$

To obtain the coefficients A_n , let us write Equation (38) by restricting to the hypersurface $t = 0$. Thus, the following normalization condition is obtained:

$$\langle \chi(n, k_1), \chi(n, k_2) \rangle = \delta^2(k_{1\perp} - k_{2\perp})\delta_{nm}, \tag{66}$$

and as a consequence,

$$A_n = \left[(2\pi)^2 2\omega \int_V d^3x (1 - 4Yz) \Theta_n^2 \right]^{-1/2} \text{ with } \Theta_n = u^{-1/4} \sin\left(\frac{2}{3}u^{3/2} + \varphi\right). \tag{67}$$

Now, let us use the results for A_n , φ and ω_n in the expansion of Equation (51) in powers of Y , similarly to Equation (63). As a result, we get

$$\begin{aligned} \chi^{(1)}(z) = & [2n\pi\omega_0^2 L^2 (L - z)z \cos(n\pi z/L) \\ & + L(2n^2\pi^2 z + 2k^2 L^2 z - k^2 L^3) \sin(n\pi z/L)] / 4Ln^2\pi^3 \sqrt{\omega_0 L}. \end{aligned} \tag{68}$$

The solution given by Equation (63), can be used to verify that the Klein–Gordon equation given by Equation (36), along with the boundary condition and normalization relation, is satisfied up to order $(M/R)^2$.

Now, we have all the necessary information to write Equation (41). In order to do this, let us express Equation (42) in terms of $\chi(z)$, as

$$T_{00}[\psi_n^*, \psi_n] = \frac{1}{2}\omega_n^2 \chi_n^2 + \frac{1}{2}(1 + 4Yz)[k_\perp^2 \chi_n^2 + (\partial_z \chi_n)^2]. \tag{69}$$

Thus, the unnormalized vacuum energy density reads

$$\bar{\epsilon} = \frac{1}{V_p} \frac{S}{8\pi^2 L} (1 + YL/2) \sum_n \int d^2 k_\perp \omega_0, \tag{70}$$

while the renormalized Casimir energy density is given by

$$\bar{\epsilon}_{\text{Cas}} = -\frac{\pi^2}{1440L^4} (1 + 2YL) = -\frac{\pi^2}{1440L_p^4} = \bar{\epsilon}_0. \tag{71}$$

Therefore, regarding the proper length of the cavity, measured by a static observer, the mean value of the Casimir energy density is identical to the one obtained in a flat spacetime case, for a rigid cavity.

Verify if the result (71) has important consequences is challenging. As it is written in generalized coordinates, this verification should be not straightforward.

To distinguish between physical effects and those arising due to the choice of coordinates. The Casimir energy density appears to be the same as that obtained in the case of flat spacetime, where there is no imposition of boundary conditions, for instance. Setting aside these considerations from a heuristic perspective, it is intriguing that the shift in the field solution found in this calculation is sufficient to compensate for the geometrical factors.

Furthermore, in Ref. [50], it is demonstrated that the above conclusion also holds for the case of the more general metric (58). According to the this new result (71), there would be no correction to the Casimir energy and, consequently, no correction to the force between the plates, in the presence of weak field gravity. The initial calculation seems to yield a seemingly controversial result, which might not align with the equivalence principle.

The question of whether or not the vacuum should gravitate by the principle of equivalence has been explored in earlier papers [78–81]. These papers are dedicated to the question “How does Casimir energy fall?” and conduct in-depth analyses with a seemingly general agreement that the buoyancy of the vacuum energy should indeed obey the equivalence principle. Following this line of reasoning, we conclude that, although the calculations following from the definition given by Equation (40) have been performed correctly, the obtained result, given by Equation (71), is not consistent with the equivalence principle, since to obey this principle in the order of approximation considered, a term of Newtonian potential energy would be expected, highly suggesting there is a problem with the initial proposition.

Returning to the earlier discussion, presented in Section 3.2, a new calculation for the Casimir energy in the presence of weak gravity was conducted in Ref. [31], this time and using the Schwinger method [82,83], the same result given by Equation (57) was obtained. With respect to the results expressed by Equation (71), it was also obtained in Ref. [84].

Going deeper, in Ref. [71], Sorge proposes another method of obtaining the vacuum energy by calculating the quasi-local Tolman mass of the vacuum between the plates. Additional insight is provided for the meaning (or lack thereof) of expression (41), which represents a summation of the expectation value for the energy–momentum tensor taken in the frame of a series of different observers. Since a single observer cannot simultaneously measure values for the entire region with infinite points, this does not reflect a measurable experimental result.

Through a detailed formal calculation, the Sorge demonstrates that the total measured energy for the system at a specific instant in time should be

$$E_t = \int_{\Sigma} d^3x \sqrt{|g|} \langle T^0_0 \rangle_{\text{vac}}. \tag{72}$$

When compared to the density definition (41), it becomes apparent that the former is missing an extra $\sqrt{|g_{00}|}$ factor, attributed to a redshift factor between the local observer and an ideal one at spatial infinity.

It is then demonstrated through a Lagrangian method that the energy attributed to the Casimir apparatus subjected to a weak gravitational field at a given time t , in the laboratory frame of a Fermi observer, is

$$E = - \left[1 + Y \left(H + \frac{L_p}{2} \right) \right] S_p \frac{\pi^2}{1400 L_p^3} = \left[1 + Y \left(H + \frac{L_p}{2} \right) \right] V_p \bar{\epsilon}_0, \tag{73}$$

where H is the reference height of the lower plate in the laboratory frame. This implies that the correction,

$$\delta E = Y \left(H + \frac{L_p}{2} \right) V_p \bar{\epsilon}_0, \tag{74}$$

acts as a gravitational potential energy, where $z_{\text{cm}} \equiv H + L_p/2$ is the vertical coordinate of the center of mass of the vacuum field, being then in concordance with the principle of equivalence. Notice that this result is in accordance with the one obtained in Ref. [73] if one takes $H \rightarrow R$. Nazari also proposes a quasi-local stress–tensor formalism in Ref. [85], although the results differ from those obtained by Sorge [31].

As it is stressed by Sorge and Nazari, for typical values of the Y factor on Earth's surface, corrections proposed to the Casimir energy due to the planet's gravitational field are quite small (approximately 10^{-22} -times the value of the ordinary Casimir interaction), but the possibilities of measuring these effects have been discussed since Ref. [43]. Those discussions may be of help to fuel the idealization of the Archimedes experiment [69,70].

In Ref. [86], an instructive analysis is carried out for the problem of a rigid Casimir cavity radially falling in geodesic motion towards a Schwarzschild event horizon. In this case, on the comoving observer frame, the horizon gives rise to a non-static background. It is found that, still in a perturbative approach (although it is outlined that the method proposed could be a starting point to a nonperturbative one), through the effective action method, somewhat small corrections to the proper energy density related to vacuum polarization (static Casimir effect) and the creation of quanta inside the cavity. It is shown that the energy variations considering both aspects coincide precisely, suggesting the two contributions might be intrinsically related, although, as already pointed out this is quite complicated to ensure because of the perturbative first-order nature of the calculations carried out.

In Ref. [87], several earlier results are generalized in the analysis of a Casimir apparatus orbiting in a background described by the Kerr spacetime. In paper [87], rather than calculating the effects due to the variation of the geometry inside the cavity, the metric components are taken as approximately constant inside the plates, and instead, lower order (bigger magnitude) corrections due to the nonstatic nature of spacetime are obtained, related to the loss of azimuthal symmetry in this scenario. Some limiting cases are considered such as those when the orbit is close to a null path, and thus, the measured energy approaches zero; this case is also close to the case of the innermost stable circular orbits of extremal Kerr black holes, as pointed out in Ref. [87]. Another noticeable result of Ref. [87] is that observers with zero angular momentum relative to the source will detect no disturbance in the ordinary Casimir interaction.

References [86,87] exemplify even more relevant subjects such as tidal and dynamic effects on the vacuum state, which may be found considering time-dependent backgrounds and stronger gravitational effects. Further details of the Casimir effect in gravitational spacetimes such as Kerr and Schwarzschild ones are foreseeing to be uncovered in the forthcoming years, although more detailed calculations involving variations of the energy-momentum tensor in small Casimir cavities involving factors such as plate finiteness and anisotropies in the field solutions may prove to be cumbersome. Likewise, one may also expect many exciting results to arise from the study of vacuum energy in the context of other feature-rich objects, such as wormholes.

Different extensions of the elementary particles Standard Model predict the existence of light massive and massless elementary particles [88,89], which can be exchanged between atoms of material bodies separated by a given distance implying the appearance of corrections to Newton's gravitational law of the Yukawa-type as well as the power type [90]. The deviation from Newtonian gravity is commonly investigated by fixing the constraints on the parameters of non-Newtonian gravity performed using the experiments of Eötvös and Cavendish types [90]. One limitation of this kind of experiments is that the strength of the obtained constraints quickly decreases when the bodies are separated by distances below a few micrometers. At such distances, the Casimir force [1] becomes dominant as compared to Newton's gravitational force. In this case, the investigations concerning non-Newtonian interactions are of crucial importance as may reveal some insight into how to connect the two apparently incompatible theoretical pillars of modern physics, namely quantum mechanics and general relativity. This makes the search for non-Newtonian gravity at considerably short separations an important scientific problem to be considered, and, in addition, the measurements of the Casimir force appear as important data that can be used to obtain stronger constraints on the parameters that measure the deviations from Newtonian gravity, due to hypothetical interactions predicted in different unification schemes beyond the Standard Model. During the last two decades, measurements of the Casimir interaction

were performed using different configurations [91–99], and, as a consequence, there was a significant improvement concerning the constraints on the Yukawa-type corrections to Newton’s gravitational law. The present generation of experiments to measure the Casimir force permits us to impose strong constraints on chameleon cosmological models [100]. Concerning the symmetrons [101], some results were addressed recently [102], even in a scenario of a hypothetical Casimir experiment. As was shown above, to explain the deviations from Newton’s law of gravitation at sub-millimeter separations between macroscopic bodies, the measure of the Casimir force with high accuracy has a fundamental role, not only concerning the comprehension of this specific point, but also to clarify on the questions related to the dark sector and a new physics phenomenology. To improve the acquisition of data related to this measurements. The Casimir And Non-Newtonian force EXperiment (CANNEX) is a project to allow for the measurements of the force between parallel macroscopic plates separated by distances between 3 and 30 micrometers [103,104]. The improvement of the apparatus sensitivity, with the CANNEX, may potentially open a window to detect several physical phenomena beyond the Standard Model and general relativity based on the quantum phenomenon termed the Casimir effect.

4. Casimir Wormholes

The distinctive feature of the Casimir energy density lies in its ability to violate energy conditions, notably attaining negative values for specific configurations. This unique property turns the Casimir energy density a rare energy source with the potential to facilitate the existence of traversable wormholes, as discussed in Ref. [105]. These objects are solutions to Einstein’s equations, akin to hypothetical spacetime tunnels connecting distant points in the universe. Traversable wormholes typically necessitate the presence of exotic matter, as outlined in Ref. [106]. However, it is worth noting that certain modified theories of gravity, as explored in Ref. [107], have offered alternative perspectives on this requirement, which has proven to be instrumental in the study of such exotic structures [108,109].

The pioneering exploration of the energy–momentum tensor associated with the Casimir effect as a potential contributor to the building of four-dimensional traversable wormholes within the framework of general relativity emerged in 2019 through the research of Remo Garattini [110]. Garattini’s study [110] resulted in the derivation of the following “Casimir” wormhole solution, characterized by a throat radius denoted as r_0 . In the form of a Morris–Thorne solution, one has:

$$ds^2 = -e^{2\Phi(r)} dt^2 + \frac{dr^2}{1 - b(r)/r} + r^2 d\Omega^2, \tag{75}$$

with the shape function $b(r)$ given by

$$b(r) = \frac{2r_0}{3} + \frac{r_0^2}{3r}, \tag{76}$$

and the redshift function $\Phi(r)$ is

$$\Phi(r) = \log \left(\frac{3r}{3r + r_0} \right). \tag{77}$$

It is worth calling attention to the feature that such a solution obeys the traversability conditions that should be satisfied by a wormhole, namely:

- (i) the flaring-out condition, determined by the minimality of the wormhole throat, which imposes that $(b - b')/b^2 > 0$, where the “prime” means derivative with respect to r and at the throat, $b(r_0) = r_0$;
- (ii) the condition to guarantee the existence of wormholes, given by $1 - b/r \geq 0$; and finally,

- (iii) the condition that there are no horizons, which are identified by the existence of surfaces with $e^\Phi \rightarrow 0$, so that $\Phi(r)$ is finite everywhere [106].

It is worth mentioning that the solution given by Equations (75)–(77) adheres to the Casimir equation of state (EoS), $p_r = 3\rho = -3\pi^2/(720r^4)$, where the radial coordinate replaces the customary separation between plates, hence the denomination “Casimir wormholes”. A criticism that can be made to this direct approach is that, to build a complete wormhole solution using quantum fields, one must simultaneously solve the quantum field theory and the gravitational equations, thus accounting for the backreaction of the renormalized stress–energy tensor of the quantum fields beyond the linearized (or perturbative) approximation.

Soon after, the Garattini study [110] was followed by various others in the same line of investigation, including modified theories [111–118], and expanded to encompass d spacetime dimensions, as documented in Ref. [119]. Nonetheless, the research of Geová Alencar, Valdir Bezerra and Celio Muniz [120] has revealed that, within the context of 2+1 dimensions, the Casimir energy density and pressure alone do not have the necessary attributes to support a wormhole structure. Consequently, it is not feasible to create what may be referred to as “pure” Casimir wormholes within this reduced dimension, as elaborated upon in Ref. [120].

Three-Dimensional Casimir–Yang–Mills Wormholes

Motivated by earlier investigations that explored the utilization of quarkonic matter as a catalyst for wormholes, as referenced in Ref. [121], the pursuit of discovering traversable Casimir wormholes confined to 2+1 dimensions has been revisited. This re-evaluation was prompted by adopting a perspective based on the Casimir effect of gluon fields, as expounded upon in Ref. [53]. This new approach involves considering the potentials derived from lattice simulations based on first principles within the Yang–Mills theory, characterizing the interactions between perfect chromoelectric conductors at both short and long distances, as initially presented in Ref. [122]. In Ref. [122], the lattice calculation of the Casimir energy for the $SU(N)$ gauge theory was fitted by the following expression:

$$\frac{\mathcal{E}}{L} = -\text{DimG} \frac{\zeta(3)}{16\pi} \frac{(R\sqrt{\sigma})^{-\nu}}{R^2} e^{-M_{\text{Cas}}R}, \tag{78}$$

where DimG is the dimension of the group ($\text{Dim}(SU(3)) = 3$; for the group $SU(3)$, L is the length of each wire, R is the distance between them, and σ is the tension of the confining (fundamental) Yang–Mills string at zero temperature). The exponent ν represents an anomalous dimension of the Casimir potential at short distances and M_{Cas} represents the effective Casimir mass associated with the nonperturbative mass gap at large distances. The quantities ν and M_{Cas} are free parameters that can be controlled to obtain the best lattice fit. It is worth mentioning that the Casimir energy of the non-interacting case (short distances) is obtained by performing $\nu = M_{\text{Cas}} = 0$ in the expression (78) above.

With this motivation, an innovative approach has been introduced in the quest for a traversable Casimir wormhole solution within lower dimensions in the context of the vacuum fluctuations of Yang–Mills fields. This approach entails introducing a subtle perturbation to the EoS, which relates Casimir energy density to the corresponding pressure, by incorporating a series of functions characterized by inverse power laws relative to the radial coordinate. This perturbation was taken into account in both the short- and long-range interactions of the referenced quantum fields, as comprehensively detailed in Ref. [53], yielding distinct classes of static and circularly symmetric Casimir wormhole solutions. By averaging such deformation in the EoS, the authors identified that the original equation of state is maintained, and therefore, it forms a legitimate Casimir source on average. The energy conditions and stability of these novel solutions were studied in detail.

In this context of three-dimensional Casimir–Yang–Mills wormholes, we focus on the long-range interaction case, where a Casimir mass, denoted as M_{Cas} , is associated with gluons. The simplest wormhole solution within the obtained spectrum of solutions can succinctly be described as follows. In terms of the shape function, we have [53]:

$$b(r) = r_0 + 2\kappa\lambda\sigma^{-\frac{\nu}{2}}M_{\text{Cas}}^{\nu+1}r[\Gamma(-\nu - 1, M_{\text{Cas}}r) - \Gamma(-\nu - 1, M_{\text{Cas}}r_0)], \tag{79}$$

where $\Gamma(a, z)$ is the incomplete gamma function. For the redshift function, we obtain

$$\Phi(r) = \frac{r_0}{2r}(2 + \nu + M_{\text{Cas}}r_0) + \frac{1}{2}M_{\text{Cas}}r_0 \ln\left(\frac{r}{r_0}\right) - \frac{r_0(\nu - M_{\text{Cas}}r_0)}{r - r_0} \ln\left(\frac{r}{r_0}\right). \tag{80}$$

The metric functions (79) and (80) ensure the asymptotic local flatness and flaring-out conditions of the wormhole solution. It is interesting to note the nontrivial topology that emerges from this solution, since asymptotically, it presents a conical singularity behavior, i.e.,

$$\frac{b(r)}{r} \approx -2\kappa\lambda\sigma^{-\frac{\nu}{2}}M_{\text{Cas}}\Gamma(-\nu - 1, M_{\text{Cas}}r_0), \tag{81}$$

which does not happen in the short-distance scenario.

Another interesting aspect of the analysis involves the examination of the solution stability through the adiabatic sound velocity, v_s , within the source, v_s , defined as

$$v_s^2(r) = \frac{1}{2} \left[\frac{d(p_r + p_\theta)}{d\rho} \right] = \frac{1}{2} \left[\frac{p'_r(r) + p'_\theta(r)}{\rho'(r)} \right]. \tag{82}$$

In the expression (82), p_r and p_θ represent the radial and lateral pressures, respectively. It is worth noting that, in contrast to the short-range case, only the long-range interaction case exhibits stability ($v_s \geq 0$), and the sound velocity remains less than 1 nearby and on the wormhole throat, lending physical significance to this solution as can be seen in the parameter space depicted in Figure 3.

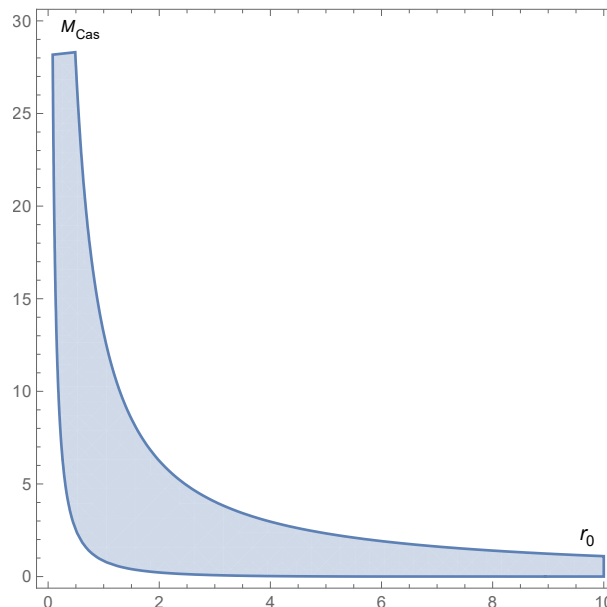


Figure 3. Parameter space (r_0, M_{Cas}) nearby the Casimir–Yang–Mills wormhole throat ($r \approx r_0$) for the simplest solution of the interacting scenario, pointing out the region in which $0 \leq v_s^2 \leq 1$, with $\nu = 0.05$, $\lambda = 3\zeta(3)/(16\pi)$. See text for details.

Energy conditions also were evaluated, and as anticipated, violations were indeed observed. This finding is in line with the expectations, since it is consistent with the negative Casimir energy density serving as the primary source for these wormhole solutions.

5. Summary of Results

The generalized zeta function method and the heat kernel expansion were used to obtain the renormalized free energy for massive and massless scalar fields, at zero temperature, as well as the thermal corrections, in a closed and analytic form. These studies were performed in Minkowski spacetime, by imposing on the fields a nontrivial compact boundary condition. In the massless case, the limits of high and low temperatures were obtained and discussed.

A discussion was presented about the explicit derivation of the Casimir interaction from quantum field orthonormal solutions. It emphasizes the problem related to the energy definition in the equation and its implications, in particular the conclusion of the absence of sensible corrections to the Casimir force due to gravity. This is a reminder that energy, as a non-local quantity, presents difficulty with its definition in curved spacetime. It was shown that this problem is solved with more thorough treatment involving the quasi-local formalism, and the results were reconciled with the principle of equivalence.

Finally, a traversable wormhole solution was obtained by considering the Casimir energy associated with the quantum vacuum fluctuations of the Yang–Mills field in a three-dimensional spacetime, as a source of the gravitating body.

Quantum fields, as exemplified in this study, are confined to a bounded domain with nontrivial compact boundary conditions. These fields experience influences due to the bounded nature of the space and the imposed boundary conditions. Additionally, when a finite temperature is considered, it also impacts the Casimir effect, as expected.

Concerning the Casimir energy of a scalar field placed in a weak gravitational field, between two parallel plates, the obtained result tells us that this energy depends exclusively on the proper values of the quantities involved in the energy expression.

Finally, the wormhole solution sourced by a Casimir energy of Yang–Mills origin was considered. It was shown that the energy conditions are violated, as expected. Another point analyzed concerns the stability of the solution, which is present only in the long-range interaction regime. In this regime, an asymptotic conical singularity also occurs.

6. Conclusions and Discussion

Let us summarize the findings of this study.

First, we have obtained the Casimir energy density with thermal corrections for a quantum scalar field, with and without mass, in a (3+1)-dimensional Euclidean spacetime, under the restriction that the field obeys a nontrivial compact boundary condition. To find this result, we used the generalized zeta function method and the renormalized heat kernel expansion given by Equation (22), which can be written as the sum of the $n = 0$ term, corresponding to the Euclidean contribution, given by Equation (19). When using the Euclidean heat kernel to obtain the free energy at zero temperature, we faced a problem, namely the appearance of a divergence term. This problem is solved by appropriately subtracting this divergence. Concerning the thermal corrections, in the massive case, the Euclidean heat kernel gives a finite contribution, while for the massless case, a blackbody radiation contribution is obtained, as shown in Equation (27)). Even being finite, these contributions should also be subtracted, to obtain the correct classical limit at high temperature, for the massless scalar field. The renormalization approach used to calculate the vacuum energy at zero temperature and nonzero temperatures gives us exact and analytic results for the renormalized free energy (31) and (32) for both cases, namely massive and massless, respectively.

In the particular case of the massless field, it was shown that the free energy density (32) has asymptotic behaviors, concerning the temperature, which permits us to write down the free energy density in a relatively simple and appropriate form to analyze the high-temperature and low-temperature limits. Performing the sum concerning j , the high-temperature limit is obtained as in Equation (33), and the correct classical limit is confirmed, as one would expect. On the other hand, when the sum is firstly performed over n in Equation (32), the low-temperature limit is achieved, as shown in Equation (34).

As a final observation related to this topic on the influence of nontrivial compact boundary conditions, as well as of the finite temperature, the results obtained show explicitly the changes in the physical observables due to the nontrivial condition imposed on the quantum scalar fields, for both cases, massive and massless, as well as the changes due to the finite-temperature effect, expressed by the thermal correction.

In Section 3, in the second part of this paper, we briefly discussed the explicit derivation of the Casimir interaction from quantum field orthonormal solutions in a weak gravitational field. However, as demonstrated, an issue arises due to the energy definition in Equation (41), leading to the conclusion that meaningful corrections to the Casimir force caused by gravity are absent. This highlights the challenge of obtaining total energies, which are non-local quantities in curved spacetime. A more comprehensive treatment involving quasi-local formalism reconciles the results with the equivalence principle. Although it is predicted that vacuum energy should gravitate like any other form of energy, experimental confirmation is still pending. Therefore, the results of the Archimedes experiment are eagerly awaited as they are believed to bring breakthrough measurements.

The Casimir energy's capacity to violate energy conditions has moved researchers to explore its potential in forming traversable wormholes, which connect distant regions or universes. Garattini's paper introduced the concept of Casimir wormholes [110], but integrating quantum field theory and gravity to form complete solutions consistently is still a challenge. Studies exploring modified theories and higher dimensions have demonstrated that Casimir energy does not provide support for wormholes in 2+1 dimensions. However, as we have shown, a recent investigation into the Casimir effects associated with Yang–Mills fields ([53]) uncovered various feasible classes of three-dimensional traversable Casimir wormholes by introducing perturbations to the linear equation of state. While energy condition violations were observed, stable solutions emerged in the long-range interaction scenario hinting at potential physical validity. In addition, an asymptotic conical singularity-like behavior emerged due to the intricate interplay between the strong Yang–Mills field dynamics and the spacetime geometry. The study aimed to enhance the comprehension of the relationship between the Casimir energy and the emergence of spacetime structures including those with nontrivial topologies.

Thus, we reviewed three theoretical scenarios that have been approached in recent years. The one scenario considered was one related to thermal corrections of the Casimir effect considering the influence of helix boundary conditions dictated by the topology. In the other case, the influence of a weak gravitational field on a Casimir apparatus formed by two parallel plates placed in a vacuum with this field was considered. Finally, a three-dimensional configuration corresponding to a non-Abelian field as a source to shape a static and circularly symmetric traversable wormhole was considered where the Casimir effect is present.

There are several directions research connected with the Casimir effect. For example, those concerning the interaction between two mirrors mediated by massive fermion fields, such as quarks or neutrinos, and the effect of the topology, among many others. However, despite the intensive researches in the field over the last seventy-five years, quite a number of problems stay unsolved up to nowadays. Thus, after seventy-five years, scientists will have several mysteries to discover and applications to find, certainly, related to the Casimir effect, a pure quantum manifestation of zero-point energy.

Author Contributions: Conceptualization, H.F.S.M., C.R.M., G.A. and V.B.B.; methodology, H.F.S.M., C.R.M., G.A., A.P.C.M.L. and V.B.B.; software, H.F.S.M., C.R.M., A.P.C.M.L. and G.A.; validation, H.F.S.M., C.R.M., G.A. and V.B.B.; formal analysis, H.F.S.M., C.R.M., G.A., A.P.C.M.L. and V.B.B.; investigation, H.F.S.M., C.R.M., G.A., A.P.C.M.L. and V.B.B.; resources, H.F.S.M., C.R.M., A.P.C.M.L. and G.A.; writing—original draft preparation, H.F.S.M., C.R.M., G.A. and V.B.B.; writing—review and editing, H.F.S.M., C.R.M., G.A., A.P.C.M.L. and V.B.B.; visualization, H.F.S.M., C.R.M., G.A., A.P.C.M.L. and V.B.B.; supervision, V.B.B.; project administration, V.B.B.; funding acquisition, H.F.S.M., C.R.M., G.A. and V.B.B. All authors have read and agreed to the published version of the manuscript.

Funding: This research was funded by Conselho Nacional de Desenvolvimento Científico e Tecnológico (CNPq)-Brazil. V.B.B. is partially supported by the Conselho Nacional de Desenvolvimento Científico e Tecnológico (CNPq)-Brazil, through the Research Project No. 307211/2020-7. H.E.S.M. is partially supported by the Conselho Nacional de Desenvolvimento Científico e Tecnológico (CNPq)-Brazil, through the Research Project No. 308049/2023-3. G.A. is partially supported by the Conselho Nacional de Desenvolvimento Científico e Tecnológico (CNPq)-Brazil, through the Research Project No. 315568/2021-6. C.R.M. is partially supported by the Conselho Nacional de Desenvolvimento Científico e Tecnológico (CNPq)-Brazil, through the Research Project No. 308168/2021-6.

Data Availability Statement: No new data were created or analyzed in this study. Data sharing is not applicable to this article.

Conflicts of Interest: The authors declare no conflicts of interest.

References

1. Casimir, H.B.G. On the attraction between two perfectly conducting plates. *Proc. Kon. Nederland. Akad. Wetensch. B* **1948**, *51*, 793–795. Available online: <https://dwc.knaw.nl/DL/publications/PU00018547.pdf> (accessed on 1 July 2024).
2. Mostepanenko, V.M.; Trunov, N.N. *The Casimir Effect and Its Applications*; Clarendon Press/Oxford University Press Inc.: New York, NY, USA, 1997. [CrossRef]
3. Milton, K.A. *The Casimir Effect: Physical Manifestations of Zero-Point Energy*; World Scientific Ltd.: Singapore, 2001. [CrossRef]
4. Bordag, M.; Klimchitskaya, G.L.; Mohideen, U.; Mostepanenko, V.M. *Advances in the Casimir Effect*; Oxford University Press Inc.: New York, NY, USA, 2009. [CrossRef]
5. Bordag, M.; Mohideen, U.; Mostepanenko, V.M. New developments in the Casimir effect. *Phys. Rep.* **2001**, *353*, 1–205. [CrossRef]
6. DeWitt, B.S. Quantum field theory in curved space–time. *Phys. Rep.* **1975**, *19*, 295–357. [CrossRef]
7. Ford, L.H. Quantum vacuum energy in general relativity. *Phys. Rev. D* **1975**, *11*, 3370–3377. [CrossRef]
8. Müller, D.; Fagundes, H.V.; Opher, R. Casimir energy in multiply connected static hyperbolic universes. *Phys. Rev. D* **2002**, *66*, 083507. [CrossRef]
9. Ferrer, E.J.; de la Incera, V.; Romeo, A. Photon propagation in spacetime with a compactified spatial dimension. *Phys. Lett. B* **2001**, *515*, 341–347. [CrossRef]
10. Lima, M.P.; Müller, D. Casimir effect in E^3 closed spaces. *Class. Quant. Grav.* **2007**, *24*, 897–914. [CrossRef]
11. Cao, C.; van Caspel, M.; Zhitnitsky, A.R. Topological Casimir effect in Maxwell electrodynamics on a compact manifold. *Phys. Rev. D* **2013**, *87*, 105012. [CrossRef]
12. Bessa, C.H.G.; Bezerra, V.B.; Silva, J.C.J. Casimir effect in spacetimes with cosmological constant. *Int. J. Mod. Phys. D* **2016**, *25*, 1641017. [CrossRef]
13. Bezerra de Mello, E.R.; Saharian, A.A. Topological Casimir effect in compactified cosmic string spacetime. *Class. Quant. Grav.* **2012**, *29*, 035006. [CrossRef]
14. Mota, H.F.; Bezerra, V.B. Topological thermal Casimir effect for spinor and electromagnetic fields. *Phys. Rev. D* **2015**, *92*, 124039. [CrossRef]
15. Bellucci, S.; Saharian, A.A.; Saharyan, N.A. Casimir effect for scalar current densities in topologically nontrivial spaces. *Eur. Phys. J. C* **2015**, *75*, 378. [CrossRef]
16. Dowker, J.S. Spherical universe topology and the Casimir effect. *Class. Quant. Grav.* **2004**, *21*, 4247–4272. [CrossRef]
17. Asorey, M.; García-Álvarez, D.; Muñoz-Castañeda, J.M. Casimir effect and global theory of boundary conditions. *J. Phys. A Math. Gen.* **2006**, *39*, 6127–6136. [CrossRef]
18. Feng, C.-J.; Li, X.-Z. Quantum spring from the Casimir effect. *Phys. Lett. B* **2010**, *691*, 167–172. [CrossRef]
19. Bezerra, V.B.; Mota, H.F.; Muniz, C.R. Remarks on a gravitational analogue of the Casimir effect. *Int. J. Mod. Phys. D* **2016**, *25*, 1641018. [CrossRef]
20. Kleinert, H.; Zhuk, A. The Casimir effect at nonzero temperatures in a universe with topology $S^1 \times S^1 \times S^1$. *Theor. Math. Phys.* **1996**, *108*, 1236–1248. [CrossRef]
21. Tanaka, T.; Hiscock, W.A. Massive scalar field in multiply connected flat spacetimes. *Phys. Rev. D* **1995**, *52*, 4503–4511. [CrossRef] [PubMed]
22. Dowker, J.S.; Critchley, R. Covariant Casimir calculations. *J. Phys. A Math. Gen.* **1976**, *9*, 535–540. [CrossRef]

23. Ford, L.H. Quantum vacuum energy in a closed universe. *Phys. Rev. D* **1976**, *14*, 3304–3313. [CrossRef]
24. Dowker, J.S. Thermal properties of Green's functions in Rindler, de Sitter, and Schwarzschild spaces. *Phys. Rev. D* **1978**, *18*, 1856. [CrossRef]
25. Altaie, M.B.; Dowker, J.S. Spinor Fields in an Einstein universe: Finite temperature effects. *Phys. Rev. D* **1978**, *18*, 3557–3564. [CrossRef]
26. Baym, S.S.; Oezcan, M. Casimir energy in a curved background with a spherical boundary: An exactly solvable case. *Phys. Rev. D* **1993**, *48*, 2806–2812. [CrossRef]
27. Karim, M.; Bokhari, A.H.; Ahmedov, B.J. The Casimir force in the Schwarzschild metric. *Class. Quant. Grav.* **2000**, *17*, 2459–2462. [CrossRef]
28. Setare, M.R.; Mansouri, R. Casimir effect for spherical shell in de Sitter space. *Class. Quant. Grav.* **2001**, *18*, 2331–2338. [CrossRef]
29. Elizalde, E.; Nojiri, S.; Odintsov, S.D.; Ogushi, S. Casimir effect in de Sitter and anti-de Sitter brane worlds. *Phys. Rev. D* **2003**, *67*, 063515. [CrossRef]
30. Aliev, A.N. Casimir effect in the spacetime of multiple cosmic strings. *Phys. Rev. D* **1997**, *55*, 3903–3904. [CrossRef]
31. Sorge, F. Casimir effect in a weak gravitational field: Schwinger's approach. *Class. Quant. Grav.* **2019**, *36*, 235006. [CrossRef]
32. Konno, K.; Takahashi, R. Spacetime rotation-induced Landau quantization. *Phys. Rev. D* **2012**, *85*, 061502. [CrossRef]
33. Elizalde, E. Uses of zeta regularization in QFT with boundary conditions: A cosmo-topological Casimir effect. *J. Phys. A Math. Gen.* **2006**, *39*, 6299–6307. [CrossRef]
34. Bezerra de Mello, E.R.; Bezerra, V.B.; Saharian, A.A. Electromagnetic Casimir densities induced by a conducting cylindrical shell in the cosmic string spacetime. *Phys. Lett. B* **2007**, *645*, 245–254. [CrossRef]
35. Elizalde, E.; Odintsov, S.D.; Saharian, A.A. Repulsive Casimir effect from extra dimensions and Robin boundary conditions: From branes to pistons. *Phys. Rev. D* **2009**, *79*, 065023. [CrossRef]
36. Elizalde, E.; Saharian, A.A.; Vardanyan, T.A. Casimir effect for parallel plates in de Sitter spacetime. *Phys. Rev. D* **2010**, *81*, 124003. [CrossRef]
37. Nouri-Zonoz, M.; Nazari, B. Vacuum energy and the spacetime index of refraction: A new synthesis. *Phys. Rev. D* **2010**, *82*, 044047. [CrossRef]
38. Saharian, A.A.; Setare, M.R. Casimir effect for curved boundaries in Robertson–Walker spacetime. *Class. Quant. Grav.* **2010**, *27*, 225009. [CrossRef]
39. Bezerra, V.B.; Klimchitskaya, G.L.; Mostepanenko, V.M.; Romero, C. Thermal Casimir effect in closed Friedmann universe revisited. *Phys. Rev. D* **2011**, *83*, 104042. [CrossRef]
40. Bezerra, V.B.; Mostepanenko, V.M.; Mota, H.F.; Romero, C. Thermal Casimir effect for neutrino and electromagnetic fields in closed Friedmann cosmological model. *Phys. Rev. D* **2011**, *84*, 104025. [CrossRef]
41. Nazari, B.; Nouri-Zonoz, M. Electromagnetic Casimir effect and the spacetime index of refraction. *Phys. Rev. D* **2012**, *85*, 044060. [CrossRef]
42. Milton, K.; Saharian, A.A. Casimir densities for a spherical boundary in de Sitter spacetime. *Phys. Rev. D* **2012**, *85*, 064005. [CrossRef]
43. Calloni, E.; Di Fiore, L.; Esposito, G.; Milano, L.; Rosa, L. Vacuum fluctuation force on a rigid Casimir cavity in a gravitational field. *Phys. Lett. A* **2002**, *297*, 328–333. [CrossRef]
44. Sorge, F. Casimir effect in a weak gravitational field. *Class. Quant. Grav.* **2005**, *22*, 5109–5119. [CrossRef]
45. Bimonte, G.; Esposito, G.; Rosa, L. From Rindler space to the electromagnetic energy–momentum tensor of a Casimir apparatus in a weak gravitational field. *Phys. Rev. D* **2008**, *78*, 024010. [CrossRef]
46. Lin, F.L. Casimir effect of graviton and the entropy bound. *Phys. Rev. D* **2001**, *63*, 064026. [CrossRef]
47. Ruser, M.; Durrer, R. Dynamical Casimir effect for gravitons in bouncing braneworlds. *Phys. Rev. D* **2007**, *76*, 104014. [CrossRef]
48. Drut, J.E.; Porter, W.J. Convexity of the entanglement entropy of $SU(2N)$ -symmetric fermions with attractive interactions. *Phys. Rev. Lett.* **2015**, *114*, 050402. [CrossRef] [PubMed]
49. Sorge, F. Gravitational memory of Casimir effect. *Phys. Rev. D* **2023**, *108*, 104003. [CrossRef]
50. Lima, A.P.C.M.; Alencar, G.; Muniz, C.R.; Landim, R.R. Null second order corrections to Casimir energy in weak gravitational field. *J. Cosmol. Astropart. Phys.* **2019**, *07*, 011. [CrossRef]
51. Muniz, C.R.; Bezerra, V.B.; Cunha, M.S. Casimir effect in the Hořava–Lifshitz gravity with a cosmological constant. *Annals Phys.* **2015**, *359*, 55–63. [CrossRef]
52. Aleixo, G.; Mota, H.F.S. Thermal Casimir effect for the scalar field in flat spacetime under a helix boundary condition. *Phys. Rev. D* **2021**, *104*, 045012. [CrossRef]
53. Santos, A.C.L.; Muniz, C.R.; Maluf, R.V. Yang–Mills Casimir wormholes in $D = 2 + 1$. *J. Cosmol. Astropart. Phys.* **2023**, *09*, 022. [CrossRef]
54. Zhai, X.-H.; Li, X.-Z.; Feng, C.-J. The Casimir force of quantum spring in the $(D + 1)$ -dimensional spacetime. *Mod. Phys. Lett. A* **2011**, *26*, 669–679. [CrossRef]
55. Feng, C.-J.; Li, X.-Z. Quantum spring. *Int. J. Mod. Phys. Conf. Ser.* **2012**, *7*, 165–173. [CrossRef]
56. Hawking, S.W. Zeta function regularization of path integrals in curved spacetime. *Commun. Math. Phys.* **1977**, *55*, 133–148. [CrossRef]

57. Elizalde, E. Zeta function regularization in Casimir effect calculations and J.S. Dowker's contribution. *Int. J. Mod. Phys. Conf. Ser.* **2012**, *14*, 57–72. [CrossRef]
58. Elizalde, E.; Odintsov, S.D.; Romeo, A.; Bytsenko, A.A.; Zerbini, S. *Zeta Regularization Techniques with Applications*; World Scientific Publishing: Singapore, 1994. [CrossRef]
59. Sonego, S. Ultrastatic space-times. *J. Math. Phys.* **2010**, *51*, 092502. [CrossRef]
60. Pontual, I.; Moraes, F. Casimir effect around a screw dislocation. *Philos. Mag. A* **1998**, *78*, 1073–1084. [CrossRef]
61. Cognola, G.; Kirsten, K.; Vanzo, L. Free and selfinteracting scalar fields in the presence of conical singularities. *Phys. Rev. D* **1994**, *49*, 1029–1038. [CrossRef] [PubMed]
62. Bytsenko, A.A.; Cognola, G.; Vanzo, L. Vacuum energy for (3+1)-dimensional spacetime with compact hyperbolic spatial part. *J. Math. Phys.* **1992**, *33*, 3108–3111. [CrossRef]
63. Bordag, M. Ground state energy for massive fields and renormalization. *arXiv* **1998**, arXiv:hep-th/9804103. [CrossRef]
64. Nakahara, M. *Geometry, Topology and Physics*; CRC Press/Taylor & Francis Group: Boca Raton, FL, USA, 2003. [CrossRef]
65. Farias Junior, A.J.D.; Mota Santana, H.F. Loop correction to the scalar Casimir energy density and generation of topological mass due to a helix boundary condition in a scenario with Lorentz violation. *Int. J. Mod. Phys. D* **2022**, *31*, 2250126. [CrossRef]
66. Abramowitz, M.; Stegun, I.A. (Eds.) *Handbook of Mathematical Functions with Formulas, Graphs, and Mathematical Tables*; Dover Publications, Inc.: New York, NY, USA, 1972. Available online: <https://archive.org/details/handbookofmathe000abra/> (accessed on 1 July 2024).
67. Gradshteyn, I.S.; Ryzhik, I.M. *Table of Integrals, Series, and Products*; Academic Press/Elsevier Inc.: San Diego, CA, USA, 2014. [CrossRef]
68. Nogueira, B.; Lavor, I.; Muniz, C. Ribonucleic acid genome mutations induced by the Casimir effect. *Biosystems* **2023**, *226*, 104888. [CrossRef]
69. Calloni, E.; De Laurentis, M.; De Rosa, R.; Garufi, F.; Rosa, L.; Di Fiore, L.; Esposito, G.; Rovelli, C.; Ruggi, P.; Tafuri, F. Towards weighing the condensation energy to ascertain the Archimedes force of vacuum. *Phys. Rev. D* **2014**, *90*, 022002. [CrossRef]
70. Avino, S.; Calloni, E.; Caprara, S.; De Laurentis, M.; De Rosa, R.; Di Girolamo, T.; Errico, L.; Gagliardi, G.; Grilli, M.; Mangano, V.; et al. Progress in a vacuum weight search experiment. *Physics* **2020**, *2*, 1–13. [CrossRef]
71. Sorge, F. Quasi-local Casimir energy and vacuum buoyancy in a weak gravitational field. *Class. Quant. Grav.* **2020**, *38*, 025009. [CrossRef]
72. Zhang, A. Theoretical analysis of Casimir and thermal Casimir effect in stationary space–time. *Phys. Lett. B* **2017**, *773*, 125–128. [CrossRef]
73. Nazari, B. Casimir effect of two conducting parallel plates in a general weak gravitational field. *Eur. Phys. J. C* **2015**, *75*, 501. [CrossRef]
74. Bezerra, V.B.; Mota, H.F.; Muniz, C.R. Casimir effect due to a slowly rotating source in the weak field approximation. *Phys. Rev. D* **2014**, *89*, 044015. [CrossRef]
75. Lambiase, G.; Stabile, A.; Stabile, A. Casimir effect in extended theories of gravity. *Phys. Rev. D* **2017**, *95*, 084019. [CrossRef]
76. Blasone, M.; Lambiase, G.; Petruzzello, L.; Stabile, A. Casimir effect in Post-Newtonian gravity with Lorentz-violation. *Eur. Phys. J. C* **2018**, *78*, 976. [CrossRef]
77. Buoninfante, L.; Lambiase, G.; Petruzzello, L.; Stabile, A. Casimir effect in quadratic theories of gravity. *Eur. Phys. J. C* **2019**, *79*, 41. [CrossRef]
78. Fulling, S.A.; Milton, K.A.; Parashar, P.; Romeo, A.; Shajesh, K.V.; Wagner, J. How does Casimir energy fall? *Phys. Rev. D* **2007**, *76*, 025004. [CrossRef]
79. Milton, K.A.; Parashar, P.; Shajesh, K.V.; Wagner, J. How does Casimir energy fall? II. Gravitational acceleration of quantum vacuum energy. *J. Phys. A Math. Theor.* **2007**, *40*, 10935–10943. [CrossRef]
80. Shajesh, K.V.; Milton, K.A.; Parashar, P.; Wagner, J.A. How does Casimir energy fall? III. Inertial forces on vacuum energy. *J. Phys. A Math. Theor.* **2008**, *41*, 164058. [CrossRef]
81. Milton, K.A.; Shajesh, K.V.; Fulling, S.A.; Parashar, P. How does Casimir energy fall? IV. Gravitational interaction of regularized quantum vacuum energy. *Phys. Rev. D* **2014**, *89*, 064027. [CrossRef]
82. Schwinger, J. Casimir effect in source theory. *Lett. Math. Phys.* **1975**, *1*, 43–47. [CrossRef]
83. Schwinger, J. Casimir effect in source theory II. *Lett. Math. Phys.* **1992**, *24*, 59–61. [CrossRef]
84. Lima, A.P.C.M.; Alencar, G.; Landim, R.R. Null second order corrections to Casimir energy in weak gravitational field: The Schwinger's approach. *J. Cosmol. Astropart. Phys.* **2021**, *01*, 056. [CrossRef]
85. Nazari, B. Quasi-local stress–tensor formalism and the Casimir effect. *Mod. Phys. Lett. A* **2022**, *37*, 2250160. [CrossRef]
86. Sorge, F.; Wilson, J.H. Casimir effect in free fall towards a Schwarzschild black hole. *Phys. Rev. D* **2019**, *100*, 105007. [CrossRef]
87. Sorge, F. Casimir energy in Kerr spacetime. *Phys. Rev. D* **2014**, *90*, 084050. [CrossRef]
88. Ferrara, S.; Scherk, J.; Zumino, B. Algebraic properties of extended supergravity theories. *Nucl. Phys. B* **1977**, *121*, 393–402. [CrossRef]
89. Deser, S.; Zumino, B. Broken Supersymmetry and Supergravity. *Phys. Rev. Lett.* **1977**, *38*, 1433–1436. [CrossRef]
90. Lämmerzahl, C.; Dittus, H. Book Review: The Search for Non-Newtonian Gravity by E. Fischbach und C. L. Talmadge. *Gen. Rel. Grav.* **2000**, *32*, 2105–2107. [CrossRef]

91. Bordag, M.; Geyer, B.; Klimchitskaya, G.L.; Mostepanenko, V.M. New constraints for non-Newtonian gravity in the nanometer range from the improved precision measurement of the Casimir force. *Phys. Rev. D* **2000**, *62*, 011701. [CrossRef]
92. Mostepanenko, V.M.; Decca, R.S.; Fischbach, E.; Klimchitskaya, G.L.; Krause, D.E.; Lopez, D. Stronger constraints on non-Newtonian gravity from the Casimir effect. *J. Phys. A Math. Theor.* **2008**, *41*, 164054. [CrossRef]
93. Bezerra, V.B.; Klimchitskaya, G.L.; Mostepanenko, V.M.; Romero, C. Advance and prospects in constraining the Yukawa-type corrections to Newtonian gravity from the Casimir effect. *Phys. Rev. D* **2010**, *81*, 055003. [CrossRef]
94. Klimchitskaya, G.L.; Romero, C. Strengthening constraints on Yukawa-type corrections to Newtonian gravity from measuring the Casimir force between a cylinder and a plate. *Phys. Rev. D* **2010**, *82*, 115005. [CrossRef]
95. Bezerra, V.B.; Klimchitskaya, G.L.; Mostepanenko, V.M.; Romero, C. Constraints on non-Newtonian gravity from measuring the Casimir force in a configuration with nanoscale rectangular corrugations. *Phys. Rev. D* **2011**, *83*, 075004. [CrossRef]
96. Mostepanenko, V.M.; Bezerra, V.B.; Klimchitskaya, G.L.; Romero, C. New constraints on Yukawa-type interactions from the Casimir effect. *Int. J. Mod. Phys. A* **2012**, *27*, 1260015. [CrossRef]
97. Klimchitskaya, G.L.; Mohideen, U.; Mostepanenko, V.M. Constraints on non-Newtonian gravity and light elementary particles from measurements of the Casimir force by means of a dynamic atomic force microscope. *Phys. Rev. D* **2012**, *86*, 065025. [CrossRef]
98. Klimchitskaya, G.L.; Mohideen, U.; Mostepanenko, V.M. Constraints on corrections to Newtonian gravity from two recent measurements of the Casimir interaction between metallic surfaces. *Phys. Rev. D* **2013**, *87*, 125031. [CrossRef]
99. Klimchitskaya, G.L.; Kuusk, P.; Mostepanenko, V.M. Constraints on non-Newtonian gravity and axionlike particles from measuring the Casimir force in nanometer separation range. *Phys. Rev. D* **2020**, *101*, 056013. [CrossRef]
100. Khoury, J.; Weltman, A. Chameleon cosmology. *Phys. Rev. D* **2004**, *69*, 044026. [CrossRef]
101. Hinterbichler, K.; Khoury, J. Symmetron fields: Screening long-range forces through local symmetry restoration. *Phys. Rev. Lett.* **2010**, *104*, 231301. [CrossRef] [PubMed]
102. Elder, B.; Vardanyan, V.; Akrami, Y.; Brax, P.; Davis, A.C.; Decca, R.S. Classical symmetron force in Casimir experiments. *Phys. Rev. D* **2020**, *101*, 064065. [CrossRef]
103. Sedmik, R.I.P. Casimir and non-Newtonian force experiment (CANNEX): Review, status, and outlook. *Int. J. Mod. Phys. A* **2020**, *35*, 2040008. [CrossRef]
104. Klimchitskaya, G.L.; Mostepanenko, V.M.; Sedmik, R.I.P.; Abele, H. Prospects for searching thermal effects, non-Newtonian gravity and axion-like particles: Cannex test of the quantum vacuum. *Symmetry* **2019**, *11*, 407. [CrossRef]
105. Tripathy, S.K. Modelling Casimir wormholes in extended gravity. *Phys. Dark Univ.* **2021**, *31*, 100757. [CrossRef]
106. Morris, M.S.; Thorne, K.S. Wormholes in spacetime and their use for interstellar travel: A tool for teaching general relativity. *Am. J. Phys.* **1988**, *56*, 395–412. [CrossRef]
107. Pavlovic, P.; Sossich, M. Wormholes in viable $f(R)$ modified theories of gravity and weak energy condition. *Eur. Phys. J. C* **2015**, *75*, 117. [CrossRef]
108. De Falco, V.; Battista, E.; Capozziello, S.; De Laurentis, M. Testing wormhole solutions in extended gravity through the Poynting–Robertson effect. *Phys. Rev. D* **2021**, *103*, 044007. [CrossRef]
109. De Falco, V.; Battista, E.; Capozziello, S.; De Laurentis, M. Reconstructing wormhole solutions in curvature based Extended Theories of Gravity. *Eur. Phys. J. C* **2021**, *81*, 157. [CrossRef]
110. Garattini, R. Casimir wormholes. *Eur. Phys. J. C* **2019**, *79*, 951. [CrossRef]
111. Garattini, R. Yukawa–Casimir wormholes. *Eur. Phys. J. C* **2021**, *81*, 824. [CrossRef]
112. Carvalho, I.D.D.; Alencar, G.; Muniz, C.R. Gravitational bending angle with finite distances by Casimir wormholes. *Int. J. Mod. Phys. D* **2022**, *31*, 2250011. [CrossRef]
113. Samart, D.; Tangphati, T.; Channuie, P. Charged traversable wormholes supported by Casimir energy with and without GUP corrections. *Nucl. Phys. B* **2022**, *980*, 115848. [CrossRef]
114. Avalos, R.; Fuenmayor, E.; Contreras, E. Traversable wormholes with like-Casimir complexity supported with arbitrarily small amount of exotic matter. *Eur. Phys. J. C* **2022**, *82*, 420. [CrossRef]
115. Sokoliuk, O.; Baransky, A.; Sahoo, P.K. Probing the existence of the ZTF Casimir wormholes in the framework of $f(R)$ gravity. *Nucl. Phys. B* **2022**, *980*, 115845. [CrossRef]
116. Hassan, Z.; Ghosh, S.; Sahoo, P.K.; Bamba, K. Casimir wormholes in modified symmetric teleparallel gravity. *Eur. Phys. J. C* **2022**, *82*, 1116. [CrossRef]
117. Hassan, Z.; Ghosh, S.; Sahoo, P.K.; Rao, V.S.H. GUP corrected Casimir wormholes in $f(Q)$ gravity. *Gen. Rel. Grav.* **2023**, *55*, 90. [CrossRef]
118. de Oliveira, P.H.F.; Alencar, G.; Jardim, I.C.; Landim, R.R. On the Traversable Yukawa–Casimir wormholes. *Symmetry* **2023**, *15*, 383. [CrossRef]
119. Oliveira, P.H.F.; Alencar, G.; Jardim, I.C.; Landim, R.R. Traversable Casimir wormholes in D dimensions. *Mod. Phys. Lett. A* **2022**, *37*, 2250090. [CrossRef]
120. Alencar, G.; Bezerra, V.B.; Muniz, C.R. Casimir wormholes in $2 + 1$ dimensions with applications to the graphene. *Eur. Phys. J. C* **2021**, *81*, 924. [CrossRef]

121. Harko, T.; Lobo, F.S.N.; Mak, M.K. Wormhole geometries supported by quark matter at ultra-high densities. *Int. J. Mod. Phys. D* **2014**, *24*, 1550006. [CrossRef]
122. Chernodub, M.N.; Goy, V.A.; Molochkov, A.V.; Nguyen, H.H. Casimir effect in Yang–Mills theory in $D = 2 + 1$. *Phys. Rev. Lett.* **2018**, *121*, 191601. [CrossRef]

Disclaimer/Publisher’s Note: The statements, opinions and data contained in all publications are solely those of the individual author(s) and contributor(s) and not of MDPI and/or the editor(s). MDPI and/or the editor(s) disclaim responsibility for any injury to people or property resulting from any ideas, methods, instructions or products referred to in the content.

MDPI AG
Grosspeteranlage 5
4052 Basel
Switzerland
Tel.: +41 61 683 77 34

Physics Editorial Office
E-mail: physics@mdpi.com
www.mdpi.com/journal/physics



Disclaimer/Publisher's Note: The statements, opinions and data contained in all publications are solely those of the individual author(s) and contributor(s) and not of MDPI and/or the editor(s). MDPI and/or the editor(s) disclaim responsibility for any injury to people or property resulting from any ideas, methods, instructions or products referred to in the content.



Academic Open
Access Publishing

mdpi.com

ISBN 978-3-7258-2143-3